PREPRINTS

# 5TH INTERNATIONAL WORKSHOP ON WAVE HINDCASTING AND FORECASTING

**JANUARY 26-30, 1998** **MELBOURNE, FL**

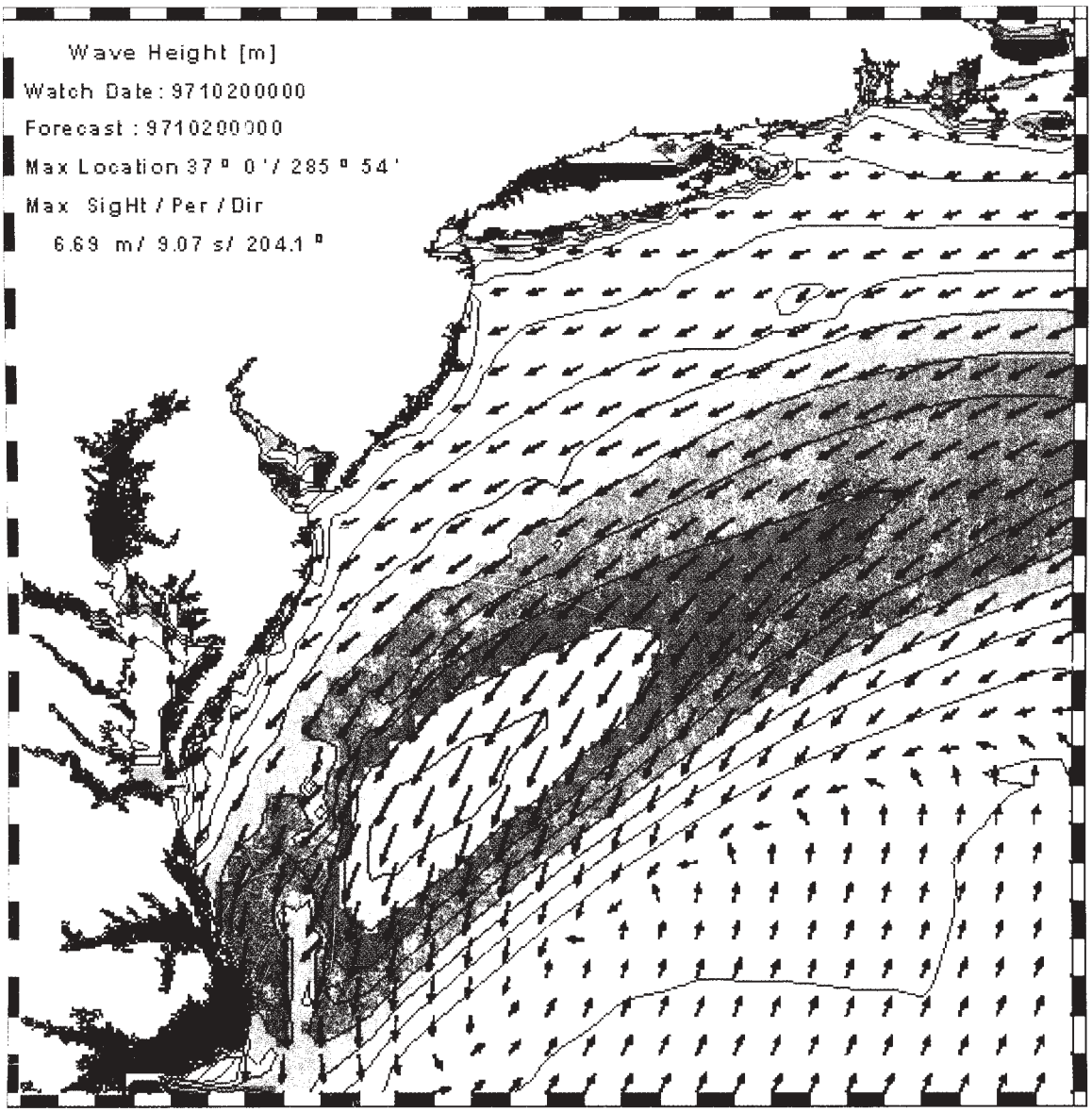


USAE WATERWAYS EXPERIMENT STATION

FLEET NUMERICAL METEOROLOGY AND OCEANOGRAPHY CENTER

FLORIDA INSTITUTE OF TECHNOLOGY

ATOMOPHERIC ENVIRONMENT SERVICE CANADA

# PREPRINTS
# 5TH INTERNATIONAL WORKSHOP ON
# WAVE HINDCASTING AND FORECASTING

## MELBOURNE, FLORIDA
## JANUARY 26-30, 1998

**Published by:**

**Environment Canada**
**Atmospheric Environment Service**
**4905 Dufferin Street**
**Downsview, Ontario**
**M3H 5T4**

AUTHOR INDEX

TABLE OF CONTENTS

## ACKNOWLEDGMENTS

The organizers are indebted to many people who provided valuable assistance in planning of the workshop. We would especially like to thank the sponsors, the U.S. Army Engineer Waterways Experiment Station's Coastal and Hydraulics Laboratory, the Fleet Numerical meteorological Oceanography Center, the Florida Institute of Technology, and the Atmospheric Environment Service. The committee would also like to thank those who submitted papers and posters for the workshop program, and those who served as chairmen for the various sessions. Special thanks are due to Ms. Claudette Doiron and Ms. Patricia Oldham who assisted in the assembly and production of this preprint volume, and to Dr. Robert Jensen who produced the cover photography.

**Cover:** Color contour plot of significant wave height and mean wave direction estimates during the SandyDuck field experiment at the U.S. Army Corps of Engineers Field Research Facility, Duck, NC. Wind fields provided by the Fleet Numerical Meteorology and Oceanography Center (Monterey, CA). 3GWAM (Komen et al. 1994) was used in a multi-level grid nest approach, where the finest resolution grid is displayed.

D. T. Resio, Chairman, Workshop Organizing Committee

TABLE OF CONTENTS



***abstract only - full paper not available**

***abstract only - full paper not available**



AUTHOR INDEX

***abstract only - full paper not available**



AUTHOR INDEX

***abstract only - full paper not available**



AUTHOR INDEX

***abstract only - full paper not available**

***abstract only - full paper not available**

## Author Index



*abstract only - full paper not available

*abstact only - full paper not available

# A LONG TERM NORTH ATLANTIC WAVE HINDCAST

V.R Swail[1], V.J. Cardone[2] and A.T. Cox[2]

[1]Environment Canada
Downsview, Ontario

[2]Oceanweather, Inc.
Cos Cob, CT

## 1. INTRODUCTION

The variability of the ocean wave climate of the North Atlantic (NA) Ocean has been studied in recent years using measured data (Bacon and Carter, 1991), and a long term wave hindcast (WASA Group, 1995). However, the measured data suffer from gaps within the past four decades, are available at only a few locations and in some parts of the data base include visual observations. The wave hindcast was produced using operational wind fields spliced together from various sources and, therefore, does not provide homogeneous forcing for the wave model used, thereby rendering the results of the hindcasts inconclusive. Evidence has also been presented (Kushnir *et al.*, 1997) of a worsening of the wave climate in the eastern NA within the past few decades associated with North Atlantic Oscillation (NAO).

The objective of this study is to utilize the National Centers for Environmental Prediction (NCEP) global reanalysis (NRA) products (Kalnay *et al.*, 1996) to drive a third-generation wave model adapted to the NA on a high-resolution grid to produce a high-quality, homogeneous, long term wind and wave data base for assessment of trend and variability in the wave climate of the NA. To remove potential biases in the historical wind fields, all wind observations from ships and buoys are re-assimilated into the analysis taking account of the method of observation, anemometer height and stability. Wind fields for all significant storms are kinematically reanalyzed with the aid of an interactive Wind Workstation (Cox *et al.*, 1995). Furthermore, high resolution surface wind fields for all tropical cyclones, as specified by a proven tropical cyclone boundary layer model, are assimilated into the wind fields to provide greater skill and resolution in the resulting wave hindcasts.

Sections 2 and 3 of this report describe the wave model used in the hindcast, and the wind fields used to drive the wave model; Section 4 describes how the long-term production hindcast was carried out. Section 5 shows preliminary results from comparative wind and wave climatologies based on the hindcast and selected *in-situ* measurements for both sides of the North Atlantic.

## 2. WAVE MODEL

### 2.1 Physics

The wave model used for this hindcast is a discrete spectral type called OWI 3-G. The spectrum is resolved at each grid point in 24 directional bins and 23 frequency bins. The bin centre frequencies range from 0.039 Hz to 0.32 Hz increasing in geometric progression with a constant ratio 1.10064. Deep water physics is assumed in both the propagation algorithm and the source terms. The propagation scheme (Greenwood *et al.*, 1985) is a downstream interpolatory scheme that is rigorously energy conserving with great circle propagation effects included. The source term formulation and integration is a third-generation type (WAMDI, 1988) but with different numerics and with the following modifications of the source terms in official WAMDI. First, a linear excitation source term is added to the input source term to allow the sea to grow from a flat calm condition without an artificial warm start sea state. The exponential wind input source is taken as the Snyder *et al.* (1981) linear function of friction velocity, as in WAMDI. However, unlike WAM, in which friction velocity is computed from the input 10-m wind speed following the drag law of Wu (1982), a different drag law is used in OWI 3-G. That law follows Wu closely up to wind speed of 20 m/s and then becomes asymptotic to a constant at hurricane wind speeds. The dissipation source term is taken from WAMDI except that the frequency dependence is cubic rather than quadratic. Finally, the

discrete interaction approximation to the non-linear source term is used as in WAMDI except that two modes of interaction are included (in WAMDI the second mode is ignored). Further details on this model and its validation may be found in Khandekar *et al.* (1994) and Cardone *et al.* (1996).

### 2.2 Adaptation to North Atlantic

OWI 3-G is adapted on a latitude-longitude grid consisting of a 122 (in latitude) by 126 (in longitude) array of points. The grid spacing is 0.625° in latitude by 0.833° in longitude, which is within 10% of square (i.e. $\Delta x = \Delta y$) between 38° and 45° N. After deductions for land there are 9023 grid points, as shown in Figure 1. The south edge of the grid is at the equator. This boundary is treated as open. Time histories of two-dimensional spectra are prescribed at all grid points along the equator as interpolated from the output of a lower resolution global first generation model driven by unmodified NCEP reanalysis 10 m wind fields. The eastern boundary is at 20° E longitude and the northern boundary is at 75.625° N latitude. The basic model integration time step is 0.5 hours and consists of one 30 propagation time step and two 15 minute growth cycles.

This wave model has been shown to reproduce observed wave heights very well when driven by accurate wind fields (Cardone *et al.*, 1995, 1996).

## 3. WIND FIELDS

In the production phase of the project, currently underway, the NCEP surface winds are brought into the Wind WorkStation every 6 hours in monthly segments for evaluation by a trained marine-meteorologist. The NCEP surface (10 m) wind fields on the Gaussian grid were identified in the evaluation phase of this project, described elsewhere in this volume by Cox *et al.* (1998), as being the most appropriate to drive the North Atlantic wave hindcast model. The NCEP surface winds are further refined by computing an equivalent neutral wind using the NCEP 2m surface temperature and sea-surface temperature fields and the algorithm described by Cardone *et al.* (1990). All available marine surface data, including buoy observations, ship reports (from COADS), C-MAN stations and ERS 1/2 scatterometer winds are displayed and selectively assimilated (as determined by the analyst) into the final wind field. All wind observations are subjected to a vigorous quality control and are adjusted for height and stability. Altimeter measurements are adjusted as recommended by Cotton and Carter (1994).

Winds for tropical systems are generated using a proven tropical cyclone model as described by Cardone *et al.* (1994) and Thompson and Cardone (1996). Track and initial estimates of intensity are taken, with some modification, from the NOAA Tropical Prediction Center's (TPC) HURDAT database. The radius of maximum wind is determined using a pressure profile fit to available surface observations and aircraft reconnaissance. Reconnaissance data are taken from TPC's Annual Data and Verification Tabulation diskettes from 1989-1996, digitally scanned from manuscript records for the period 1974-1988, and manually scanned from reconnaissance microfilm for periods prior to 1974. Figure 3 shows a pressure model fit to reconnaissance data adjusted to surface via Jordan (1957). Surface winds generated from the model are then evaluated against available surface data and aircraft reconnaissance wind observations adjusted to the surface as described by Powell *et al.* (1989). Model winds within 240 nautical miles from the centre are then exported on a 0.5° latitude/longitude grid for inclusion in the Wind WorkStation.

The interactive hindcast methodology used by the analysts follows similar previous hindcast studies (Cardone *et al.*, 1995, 1996). Particular attention is spent on strong extra-tropical systems, blending tropical model winds into the NCEP surface wind field, and in the quality control of surface data. Kinematically analyzed winds from previous hindcasts of severe extratropical storms in the northwest Atlantic (Swail *et al.*, 1995) are incorporated into the present analysis on the North Atlantic wave model grid.

Altimeter measurements are used in an inverse wave-modelling approach as follows. First, a global coarse wave run is made and hindcast wave heights over the North Atlantic Ocean are compared to altimeter wave measurements. The global wave fields are generated using the Oceanweather wave model adapted to a 1.25° by 2.5° latitude/longitude grid for the entire globe (Figure 4). NCEP surface winds (adjusted to neutral stability) are used to drive the global wave model. Areas where the resulting wave fields are deficient, as indicated by the altimeter, are brought to the analysts' attention and the analyst subjectively rectifies the deficiencies in the backward space-time evolution of the wind field causing the discrepancy.

Final wind fields for each month were interpolated onto the 0.625° by 0.833° latitude-longitude wave model grid using the IOKA (Interactive Objective Kinematic Analysis) algorithm (Cox *et al.*, 1995) and then time interpolated to a one-hour timestep.

## 4. PRODUCTION HINDCAST

The production hindcast was carried out in monthly segments using the OWI 3-G wave model in deep water mode driven by the final kinematically reanalysed wind fields as described above.

Final IOKA winds are run through the North Atlantic wave model as during the evaluation phase with the following modifications: First, a spectral save file is generated at the end of each month of integration and used to initialize the spectrum for the run of the succeeding month. Second, ice-cover is specified for each month from mid-monthly ice tables specified on the wave grid from Walsh & Johnson (1979) (prior to 1972), Arctic and Antarctic Sea Ice Data CD-ROM 1972-1994, and hand-digitized maps produced from the joint Navy/NOAA Ice Center data sets. The 5/10 ice concentration contour was used as the definition of the ice edge - points with ice concentrations greater than 5/10 were considered as land by the model, those with concentrations 5/10 or less were considered as open water. Third, wave spectra from the coarse global wave model noted above are used as boundary conditions along the equator. Wave spectra are saved along the equator every 2.5 degrees at a 3-hour time step and interpolated to the North Atlantic wave grid's time step and spatial resolution.

Quality control of the production hindcast consists mainly of comparisons of the wave hindcast against measurements evaluated against 12 deep-water buoys (Figure 2) and ERS 1/2 altimeter wave measurements.

The output of the model consists of 17 so-called 'fields' quantities (Table 1) at all grid points and the full two-dimensional spectrum at the 233 grid points shown in Figure 1. These points were selected to allow even coverage of the basin, as well as to allow the possibility to drive finer mesh models especially for the US East Coast, the Scotian Shelf and Grand Banks of Newfoundland and the European West Coast. Spectra were also output at the locations of selected moored buoys and offshore platforms.

## 5. PRELIMINARY RESULTS - CLIMATOLOGY

The following paragraphs describe various intercomparisons of the preliminary wind and wave climatology produced from the hindcast and from *in-situ* measurements on both sides of the North Atlantic ocean. The locations where the comparisons were carried out are shown in Figure 2.

At the time of writing hindcasts covering nearly 6 years had been completed (1990-1995). While this time period is not sufficient to accurately describe the real wind and wave climate at the selected locations, it is adequate to undertake some aspects of a comparative climatology of hindcasts versus measurements; however, it is not yet long enough to compare extremal analysis results, or to evaluate possible climate trends and variability. Such analyses will have to wait until the completion of the full hindcast.

The hindcasts produced a continuous smoothly varying time series of winds and waves at each point on the grid; data were archived at 6-hour intervals for the climatology.

The measured data came from a variety of sources. U.S. buoy data came from the NOAA Marine Environmental Buoy Database on CD-ROM; the Canadian buoy data came from the Marine Environmental Data Service marine CD-ROM; the remaining data came from the Comprehensive Ocean Atmosphere Data Set (COADS). The wave measurements are comprised of 20-minute samples (except for Canadian buoys which were 40 minutes) once per hour. The wind measurements were taken as 10 minute samples, scalar averaged, except vector averaged at the Canadian buoys, also once per hour. The wind and wave values selected for comparison with the hindcast were 3-hour mean values centered on each six hour synoptic time with equal (1,1,1) weighting. The wind speeds were adjusted to 10 m neutral winds in both the measured and hindcast data.

The measured data sets contained some gaps and some erroneous data. Where a gap existed in the measured data the corresponding data from the hindcast were ignored. There were many obvious spikes (high and low) in the measured data, particularly from the eastern Atlantic data sets accessed from COADS, or otherwise bad or suspicious data. These data points were removed along with the corresponding hindcast data. There may still remain more subtle errors in some measurements, in spite of our best efforts to identify and remove them. Removal of the hindcast

data corresponding to measurements gaps is necessary to achieve a valid intercomparison between hindcast and measurements; as a result, however, the climatologies may not be an accurate depiction of the "true" climatic conditions of the 6-year period 1990-95.

A series of comparative climate statistics for 8 of the locations shown in Figure 2 is given in Table 2, for significant wave height (HS), wind speed (WS) and spectral peak period (TP). A discussion of the climate comparisons is given in the following sections.

### 5.1 Wave Height Climatology Comparisons

From Table 2 it is clear that the hindcast represents the wave climate very well at the selected locations. The hindcast mean wave heights typically exceed the measurements by a few centimetres. The standard deviations are also very closely approximated, with the buoy measurements being slightly more variable than the hindcasts, and the platforms slightly lower. The higher order moments of the distribution are also remarkably close, except at 44011, where the distribution deviates in both skewness and kurtosis, likely a reflection of the relatively shallow water depths surrounding the buoy. In all cases the skewness and kurtosis of the hindcast waves exceeds that of the measurements. The 90, 95 and 99 percentile wave heights are typically within a few centimetres at the buoys, with the measurements tending usually to be slightly higher than the hindcasts; at the platforms the model is noticeably higher than the measurements. Comparisons of the maximum hindcast and measured waves shows no clear pattern. In some cases the measurements are higher, most notably at 44137 where the 15.8 m maximum came from the Halloween storm documented by Cardone *et al.* (1996), which showed an inability of all the models tested to reproduce the extreme wave heights generated by the storm. Generally, except for 44011 and LF5U, the differences in the wave height maxima were less than 1 m.

Figure 5 shows quantile-quantile plots for model versus measured wave height for each of the 8 selected sites. In quantile scatterplots, the quantiles of one variable are plotted against the quantiles of another variable in order to assess the similarity of the empirical distributions of the two variables. If the data points fall on the regression line, then it can be concluded that the two variables follow the same distribution. Q-Q plots are particularly useful in comparisons of the right-hand (extreme) tails of the distributions. These plots show very good agreement across the entire frequency distribution. There is a slight tendency for the model to overestimate the wave height compared to the measurements for low values of sea state. The model also is consistently higher at the platforms, although the differences are negligible for the few highest observations. The effect of the Halloween storm is clearly seen at 44137 and 44138, where the peak measured waves clearly exceed the hindcast values. At 44011, in relatively shallow water, the 8 points for which the model greatly exceeds the measured wave heights all come from the same 48-hour period during the extreme Halloween storm.

### 5.2 Wind Speed Climatology Comparisons

The hindcast and measured wind speed climatologies are not independent since all of the wind data used contributed heavily to the data assimilation scheme in the NCEP re-analysis, and again in the kinematic re-analysis. Nevertheless, it is useful to compare the two data sets to verify that the various adjustments for elevation and interpolation onto the wave model grid have not compromised the hindcast data set.

Table 2 shows that the mean wind speeds are within a few cm/s, except at the two platforms where the differences are about 0.6-0.7 m/s; the model mean winds were generally equal to or slightly higher at all locations. The wind speed standard deviations were quite similar with the measured winds being slightly more variable. As for waves, the higher order moments were also comparable, with the hindcast having consistently higher values of skewness and also higher kurtosis except at the platforms. The 90, 95 and 99 percentile wind speeds were nearly identical, although the model winds at the platforms were 0.6-0.7 m/s higher than the measurements. There were some differences in the maximum wind speeds, split evenly between the two data sources as to which was higher. Differences were typically on the order of 2-3 m/s.

Figure 6 shows quantile-quantile plots for model versus measured wind speed for each of the 8 selected sites. These plots show very good agreement across the entire frequency distribution. There is a tendency for the model winds to be slightly higher at the Canadian buoys, particularly for the highest wind speeds, possibly related to the vector averaging of the buoy wind samples as opposed to scalar averages elsewhere. There is also a noticeable difference in the highest values at 44011, with the hindcast values exceeding the buoy. However, as for the wave height the top 8 values were all associated with the Halloween storm. At the platforms the model is noticeably higher than the

measurements for the low end of the wind speed distribution.

### 5.3 Wave Period Climate Comparisons

The wave period comparisons were particularly difficult to carry out. The spectral peak wave period is the reciprocal of the peak frequency. For the measurements this is computed from the one frequency band containing the most energy. In bi-modal seas this may fluctuate from one value to another. The hindcast peak frequency is computed by taking the spectral density in each frequency bin, and fitting a parabola to the highest density and one neighbor on each side. If highest density is in the 0.32157 Hz bin, the peak period reported is the peak period of a Pierson-Moskowitz spectrum having the same total variance as the hindcast spectrum. Thus we are not comparing exactly equal quantities. Other problems relate to the measured data in the various archives. For the platforms and the 62108 buoy (the COADS-based observations) the wave period information was discretized into a very few bins (only 4 in one case). This made meaningful analysis very difficult. In the case of 41001 there were some problems with the measured data base which were not fully resolved. Therefore detailed analysis was only carried out at 4 sites (41010, 44011, 44137 and 44138).

Table 2 shows the statistics for all of the buoys. As noted above the information for the other 4 buoys should not be considered reliable. Some clear indications can be seen from the table. The means of the peak wave periods are consistently higher for the measurements than for the hindcast, by 0.5-1.5 seconds. The standard deviations of the measurements were also consistently higher. The skewness and kurtosis were usually higher for the measurements (except at 44011 in both cases). The 90, 95 and 99 percentile wave periods continued the low bias apparent in the hindcast mean period values with differences reaching almost 3 seconds in the 99 percentile value at the two Canadian buoys. Maximum values were similarly biased, although inexplicably the difference in the maxima for all except 41010 was less than the difference in the percentile values.

Figure 7 shows quantile-quantile plots for model versus measured spectral peak wave period for each of the 4 sites considered to be relatively reliable. The shapes of the plots for the Canadian buoys (44137, 44138) show a small but consistent bias even in the lowest periods, growing slowly to periods of about 11s, then growing more quickly. However, for the few highest values of peak period the measurement is only slightly larger than the model values. Buoy 44011 shows a similar tendency, although without the relatively large bias at longer periods demonstrated by the other two. For buoy 41010 the bias grows more quickly from the outset, and continues to grow rapidly; unlike the other 3 buoys the maxima are widely divergent. A more detailed analysis of the reasons for this behaviour is required.

## 6. SUMMARY AND FUTURE WORK

In summary, a comprehensive wind and wave hindcast is presently being produced for the North Atlantic Ocean using a long term, consistent wind field forcing based on the NCEP re-analysis. The NCEP surface wind fields are kinematically re-analysed to reproduce small-scale features such as tropical storms and to reduce the inherent low bias in extreme extratropical storms due to the limited grid resolution in the NCEP wind fields. The wind fields are used to drive a 3$^{rd}$ generation wave model on a fine mesh grid covering the entire North Atlantic Ocean. The output from the wave model, consisting of 17 different fields is archived at 6-hour intervals at each grid location; 2-D wave spectra are archived every 6 hours at 233 grid points covering the entire basin, but particularly along the continental margins.

The wind speed and wave height climatology produced from the hindcast closely resembles that obtained from measured wind and wave data from buoys and offshore platforms on both sides of the Atlantic Ocean, in terms of the various statistical moments and the shape and scale of the frequency distributions. This confirms that the wave hindcast results may be used as a high-quality estimate of the actual wave climate.

The full wave hindcast should be completed in late 1998, thus providing a high-quality, long-term homogeneous data base of winds and waves over the entire North Atlantic Ocean. At that time more extensive climate analysis, including an investigation of the trend and variability of North Atlantic wave heights, and an extremal analysis of waves can be carried out. Investigation of the spatial patterns of wave height variability and relationships to large scale circulation features such as the North Atlantic Oscillation is also planned.

## 7. REFERENCES

Bacon, S., and D.J. Carter, 1991. *Wave climate changes in the North Atlantic and North Sea.* Int. J. Climatology, 11, 545-558.

Cardone, V.J., J.G. Greenwood and M.A. Cane, 1990. *On trends in historical marine wind data*. J. Climate, 3, 113-127.

Cardone, V.J., A.T. Cox, J.A. Greenwood, and E.F. Thompson, 1994. *Upgrade of tropical cyclone Surface wind field model.* U.S. Corps of Engineers Misc. Paper CERC-94-14.

Cardone, V.J., H.C. Graber, R.E. Jensen, S. Hasselmann, and M.J. Caruso, 1995. *In search of the true surface wind field in SWADE IOP-1: ocean wave modelling perspective*. The Global Ocean Atmopshere System, 3, 107-150.

Cardone, V.J., R.E. Jensen, D.T. Resio, V.R. Swail and A.T. Cox, 1996. *Evaluation of contemporary ocean wave models in rare extreme events: "Halloween storm of October, 1991; "storm of the century" of March, 1993".* J. Atmos. and Oceanic Tech., Vol. 13, No. 1, p. 198-230.

Cotton, P.D., and D.J.T. Carter, 1994. *Cross calibration of TOPEX, ERS-1, and Geosat wave heights.* J. of Geophysical Research, Vol 99, No. C12, pp. 25,025-25,033.

Cox, A.T., J.A. Greenwood, V.J. Cardone and V.R. Swail, 1995. *An interactive objective kinematic analysis system.* Proceedings 4th International Workshop on Wave Hindcasting and Forecasting, October 16-20, 1995, Banff, Alberta, p. 109-118.

Cox, A.T., V.J. Cardone and V.R. Swail, 1998. *Evaluation of NCEP/NCAR reanalysis project marine surface wind products for a long term North Atlantic wave hindcast*. Proc. 5th International Workshop on Wave Hindcasting and Forecasting, Melbourne, FL

Greenwood, J.A., V.J. Cardone and L.M. Lawson, 1985. *Intercomparison test version of the SAIL wave model.* Ocean Wave Modelling, the SWAMP Group, Plenum Press, 221-233.

Jordan, C.L. 1957. *Estimation of surface central pressures in tropical cyclones from aircraft observations.* Bull. AMS, Vol. 39, No. 7 pp.345-352.

Kalnay, E., *et al*, 1996. *The NCEP/NCAR 40-Year reanalysis project*. Bull. AMS, 77(3), 437-471.

Khandekar, M.L., R. Lalbeharry and V.J. Cardone, 1994: *The performance of the Canadian spectral ocean wave model (CSOWM) during the Grand Banks ERS-1 SAR wave spectra validation experiment.* Atmosphere-Ocean 32(1), 31-60.

Kushnir, Y. V.J. Cardone, J.G. Greenwood and M.A. Cane, 1997. *On the recent increase in North Atlantic wave heights*. Accepted in J. Climate.

Kushnir, Y., 1994. *Interdecadal variations in North Atlantic sea surface temperature and associated atmospheric conditions*. J. Climate, 7, 141-157.

Powell, M.D., and P.G. Black, 1989. *The relationship of hurricane reconnaissance flight-level wind measured by NOAA's oceanic platforms.* 6th National Conference on Wind Engineering, March 7-10, 1989.

Snyder, R., F.W. Dobson, J.A. Elliott and R.B. Long, 1981. *Array measurements of atmospheric prressure fluctuations above surface gravity waves.* J. Fluid Mech., 102, 1-59.

Swail, V.R., M. Parsons, B.T. Callahan and V.J. Cardone, 1995. *A revised extreme wave climatology for the east coast of Canada*. Proc. 4th International Workshop on Wave Hindcasting and Forecasting, October 16-20, 1995, Banff, Alberta, p. 81-91.

Thompson, E.F., and V.J. Cardone, 1996. *Practical modeling of hurricane surface wind fields.* Journal of Waterway, Port, Coastal, and Ocean Engineering, July/August 1996, pp. 195-205.

Walsh, J.E., and C.M. Johnson, 1979. *An analysis of Arctic sea ice fluctuations, 1953-1977*. J. Phys. Ocean., 9, 580-591.

WAMDI Group, 1988. *The WAM model - a third generation ocean wave prediction model*. J. Phys. Ocean. 18: 1775-1810.

WASA,1995. *The WASA Project: changing storm and wave climate in the Northeast Atlantic and adjacent seas?* Proc. 4th International Workshop on Wave Hindcasting and Forecasting, Banff, Canada, October 16-20, 1995, 31-44; also: GKSS Report 96/E/61

Wu, J., 1982. *Wind-stress coefficients over the sea surface from breeze to hurricane*. J. Geophys. Res., (87), 9704-9706.

| | | |
|---|---|---|
| WS | Wind Speed | 1-hour average of the effective neutral wind at a height of 10 metres, units in metres/second. |
| WD | Wind Direction | From which the wind is blowing, clockwise from true north in degrees (meteorological convention). Winds are 1-hour averages of the effective neutral wind at a height of 10 metres. |
| ETOT | Total Variance of Total Spectrum: | The sum of the variance components of the hindcast spectrum, over the 552 bins of the 3G wave model, in metres squared. |
| TP | Peak Spectral Period of Total Spectrum: | Peak period is the reciprocal of peak frequency, in seconds. Peak frequency is computed by taking the spectral density in each frequency bin, and fitting a parabola to the highest density and one neighbor on each side. If highest density is in the .32157 Hz bin, the peak period reported is the peak period of a Pierson-Moskowitz spectrum having the same total variance as the hindcast spectrum. |
| VMD | Vector Mean Direction of Total Spectrum | To which waves are traveling, clockwise from north in degrees (oceanographic convention). |
| ETOT1 | Total Variance of Primary Partition | The sum of the variance components of the hindcast spectrum, over the 552 bins of the 3G model, in metres squared. To partition sea (primary) and swell (secondary) we compute a P-M (Pierson-Moskowitz) spectrum, with a cos^3 spreading, from the adopted wind speed and direction. For each of the 552 bins, the lesser of the hindcast variance component and P-M variance component is thrown into the sea partition; the excess, if any, of hindcast over P-M is thrown into the swell partition. |
| TP1 | Peak Spectral Period of Primary Partition | |
| VMD1 | Vector Mean Direction of Primary Partition | |
| ETOT2 | Total Variance of Secondary Partition | |
| TP2 | Peak Spectral Period of Secondary Partition | |
| VMD2 | Vector Mean Direction of Secondary Partition | |
| MO1 | First Spectral Moment of Total Spectrum | Following Haring and Heideman (OTC 3280, 1978) the first and second moments contain powers of omega = 2pi f; thus:<br><br>M1 = ΣΣ 2pi f dS<br>M2 = ΣΣ (2pi f)^2 dS<br><br>where dS is a variance component and the double sum extends over 552 bins. |
| MO2 | Second Spectral Moment of Total Spectrum | |
| HS | Significant Wave Height | 4.000 times the square root of the total variance, in metres |

Table 1. List of archived fields and definitions.

| | | |
|---|---|---|
| | | solution of the equations<br><br>Acos 2 psi = ΣΣ cos 2 theta pi dS<br>Asin 2 psi = ΣΣ sin 2 theta pi dS<br><br>The angle psi is determined only to within 180 degrees. Haring and Heideman choose from the pair (psi,psi+180) the value closer to the peak direction. |
| ANGSPR | Angular Spreading Function | The angular spreading function is the mean value, over the 552 bins, of cos(theta-VMD), weighted by the variance component in each bin. If the angular spectrum is uniformly distributed over 360 degrees, this statistic is zero if uniformly distributed over 180 degrees, 2/pi if all variance is concentrated at the VMD, 1. |
| INLINE | In-Line Variance Ratio | Called directional spreading by Haring and Heideman, p 1542. Computed as:<br><br>Rat = [ΣΣcos^2(theta-psi) dS]/[ΣΣ dS]<br><br>If spectral variance is uniformly distributed over the entire compass, or over a semicircle, Rat = 0.5; if variance is confined to one angular band, or to two band 180 degrees apart, Rat = 1.00 . According to Haring and Heideman, cos^2 spreading corresponds to Rat = 0.75 . |

Table 1 (cont.). List of archived fields and definitions.

| | HS-model (m) | HS-meas (m) | WS-model (m/s) | WS-meas (m/s) | TP-model (sec) | TP-meas (sec) |
|---|---|---|---|---|---|---|
| **41001** | | | | | | |
| MEAN | 1.96 | 1.96 | 7.69 | 7.55 | 5.29 | 6.47 |
| STDEV | 1.02 | 1.08 | 3.52 | 3.56 | 0.77 | 1.66 |
| COEF_VAR | 0.52 | 0.55 | 0.46 | 0.47 | 0.15 | 0.26 |
| SKEW | 1.89 | 1.72 | 0.64 | 0.51 | 1.35 | 1.38 |
| KURT | 5.31 | 4.19 | 0.25 | 0.06 | 3.09 | 2.62 |
| MAX | 9.27 | 10.00 | 23.60 | 23.89 | 10.05 | 16.50 |
| 90%ILE | 3.28 | 3.47 | 12.51 | 12.39 | 6.27 | 8.50 |
| 95%ILE | 3.99 | 4.10 | 14.32 | 14.03 | 6.75 | 10.50 |
| 99%ILE | 5.45 | 5.63 | 17.12 | 16.92 | 7.87 | 12.50 |
| | | | | | | |
| **41010** | | | | | | |
| MEAN | 1.66 | 1.56 | 6.48 | 6.51 | 5.24 | 5.83 |
| STDEV | 0.79 | 0.83 | 3.08 | 3.13 | 0.74 | 1.08 |
| COEF_VAR | 0.47 | 0.53 | 0.47 | 0.48 | 0.14 | 0.18 |
| SKEW | 1.72 | 1.64 | 0.64 | 0.59 | 1.41 | 1.46 |
| KURT | 4.25 | 3.76 | 0.39 | 0.27 | 3.87 | 4.70 |
| MAX | 8.36 | 7.53 | 23.10 | 23.03 | 10.74 | 14.60 |
| 90%ILE | 2.72 | 2.67 | 10.66 | 10.75 | 6.19 | 7.17 |
| 95%ILE | 3.21 | 3.23 | 12.16 | 12.26 | 6.58 | 7.77 |
| 99%ILE | 4.36 | 4.43 | 14.80 | 14.84 | 7.67 | 9.28 |
| | | | | | | |
| **44011** | | | | | | |
| MEAN | 1.95 | 1.96 | 6.58 | 6.38 | 5.46 | 5.81 |
| STDEV | 1.14 | 1.16 | 3.79 | 3.71 | 0.88 | 1.03 |
| COEF_VAR | 0.59 | 0.59 | 0.58 | 0.58 | 0.16 | 0.18 |
| SKEW | 2.27 | 1.70 | 0.80 | 0.71 | 1.21 | 0.88 |
| KURT | 10.08 | 4.21 | 0.51 | 0.27 | 2.47 | 1.14 |
| MAX | 13.99 | 11.43 | 27.59 | 25.28 | 10.85 | 10.97 |
| 90%ILE | 3.48 | 3.53 | 11.93 | 11.61 | 6.61 | 7.17 |
| 95%ILE | 4.22 | 4.30 | 13.74 | 13.33 | 7.10 | 7.73 |
| 99%ILE | 5.92 | 5.89 | 16.84 | 16.44 | 8.20 | 8.87 |
| | | | | | | |
| **44137** | | | | | | |
| MEAN | 2.65 | 2.58 | 9.11 | 8.99 | 8.31 | 9.30 |
| STDEV | 1.50 | 1.55 | 4.35 | 4.45 | 1.84 | 2.16 |
| COEF_VAR | 0.57 | 0.60 | 0.48 | 0.50 | 0.22 | 0.23 |
| SKEW | 1.95 | 1.86 | 0.53 | 0.45 | 0.59 | 0.90 |
| KURT | 6.13 | 5.65 | 0.08 | -0.13 | 0.37 | 0.99 |
| MAX | 15.09 | 15.80 | 28.73 | 28.38 | 17.59 | 17.87 |
| 90%ILE | 4.51 | 4.57 | 15.08 | 15.09 | 10.78 | 12.20 |
| 95%ILE | 5.49 | 5.63 | 16.87 | 16.98 | 11.72 | 13.56 |
| 99%ILE | 8.12 | 7.90 | 20.38 | 20.27 | 13.03 | 15.93 |
| | | | | | | |

Table 2. Comparison statistics for hindcast and *in-situ* climatology at selected sites.

| | HS-model (m) | HS-meas (m) | WS-model (m/s) | WS-meas (m/s) | TP-model (sec) | TP-meas (sec) |
|---|---|---|---|---|---|---|
| **44138** | | | | | | |
| MEAN | 2.69 | 2.67 | 8.67 | 8.57 | 8.86 | 10.22 |
| STDEV | 1.47 | 1.54 | 4.18 | 4.18 | 2.03 | 2.38 |
| COEF_VAR | 0.55 | 0.58 | 0.48 | 0.49 | 0.23 | 0.23 |
| SKEW | 2.05 | 1.77 | 0.70 | 0.57 | 0.53 | 0.69 |
| KURT | 6.79 | 5.03 | 0.55 | 0.21 | 0.29 | 0.68 |
| MAX | 13.43 | 13.40 | 29.27 | 26.35 | 17.62 | 21.33 |
| 90%ILE | 4.52 | 4.65 | 14.40 | 14.21 | 11.62 | 13.50 |
| 95%ILE | 5.46 | 5.66 | 16.27 | 16.21 | 12.54 | 14.78 |
| 99%ILE | 8.36 | 8.00 | 20.16 | 19.84 | 14.13 | 17.09 |
| | | | | | | |
| **62108** | | | | | | |
| MEAN | 3.44 | 3.32 | 9.94 | 9.94 | 6.48 | 7.54 |
| STDEV | 1.82 | 1.87 | 4.53 | 4.62 | 1.18 | 1.70 |
| COEF_VAR | 0.53 | 0.56 | 0.46 | 0.46 | 0.18 | 0.23 |
| SKEW | 1.45 | 1.36 | 0.49 | 0.48 | 0.62 | 0.81 |
| KURT | 2.85 | 2.51 | 0.18 | 0.21 | -0.04 | 0.56 |
| MAX | 13.55 | 13.50 | 33.78 | 34.45 | 10.65 | 14.50 |
| 90%ILE | 5.83 | 6.00 | 15.89 | 15.92 | 8.16 | 10.50 |
| 95%ILE | 6.86 | 7.00 | 17.77 | 17.84 | 8.68 | 10.50 |
| 99%ILE | 9.64 | 9.70 | 22.03 | 22.11 | 9.64 | 12.50 |
| | | | | | | |
| **LF3J** | | | | | | |
| MEAN | 3.19 | 2.87 | 9.71 | 8.96 | 6.19 | 7.18 |
| STDEV | 1.84 | 1.70 | 4.67 | 4.77 | 1.14 | 1.28 |
| COEF_VAR | 0.57 | 0.59 | 0.48 | 0.53 | 0.18 | 0.18 |
| SKEW | 1.21 | 1.04 | 0.69 | 0.68 | 0.36 | 0.94 |
| KURT | 1.64 | 1.16 | 0.19 | 0.26 | -0.60 | 3.13 |
| MAX | 11.89 | 12.00 | 32.08 | 30.05 | 10.05 | 18.50 |
| 90%ILE | 5.70 | 5.00 | 16.16 | 15.52 | 7.77 | 8.50 |
| 95%ILE | 6.72 | 6.00 | 18.49 | 17.80 | 8.20 | 8.50 |
| 99%ILE | 9.11 | 8.00 | 22.23 | 21.80 | 8.85 | 10.50 |
| | | | | | | |
| **LF5U** | | | | | | |
| MEAN | 2.47 | 2.19 | 9.34 | 8.58 | 5.42 | 5.77 |
| STDEV | 1.54 | 1.33 | 4.17 | 4.24 | 1.03 | 1.00 |
| COEF_VAR | 0.62 | 0.61 | 0.45 | 0.49 | 0.19 | 0.17 |
| SKEW | 1.55 | 1.33 | 0.65 | 0.65 | 0.68 | 1.29 |
| KURT | 3.34 | 2.67 | 0.13 | 0.30 | 0.11 | 1.80 |
| MAX | 12.42 | 11.00 | 29.68 | 33.44 | 9.91 | 10.50 |
| 90%ILE | 4.48 | 4.00 | 15.27 | 14.53 | 6.84 | 6.50 |
| 95%ILE | 5.43 | 4.50 | 17.13 | 16.37 | 7.36 | 8.50 |
| 99%ILE | 8.03 | 6.50 | 20.48 | 19.78 | 8.26 | 8.50 |

Table 2 (cont.). Comparison statistics for hindcast and *in-situ* climatology at selected sites.

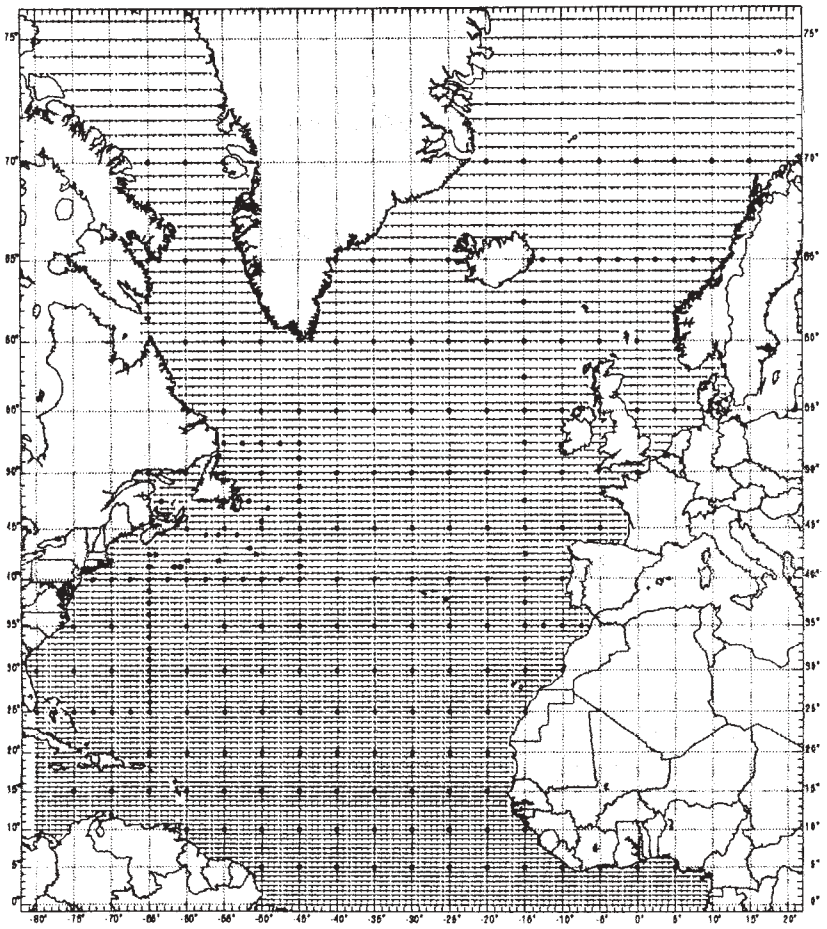

Figure 1. Wave Model Grid and Spectral Save Points

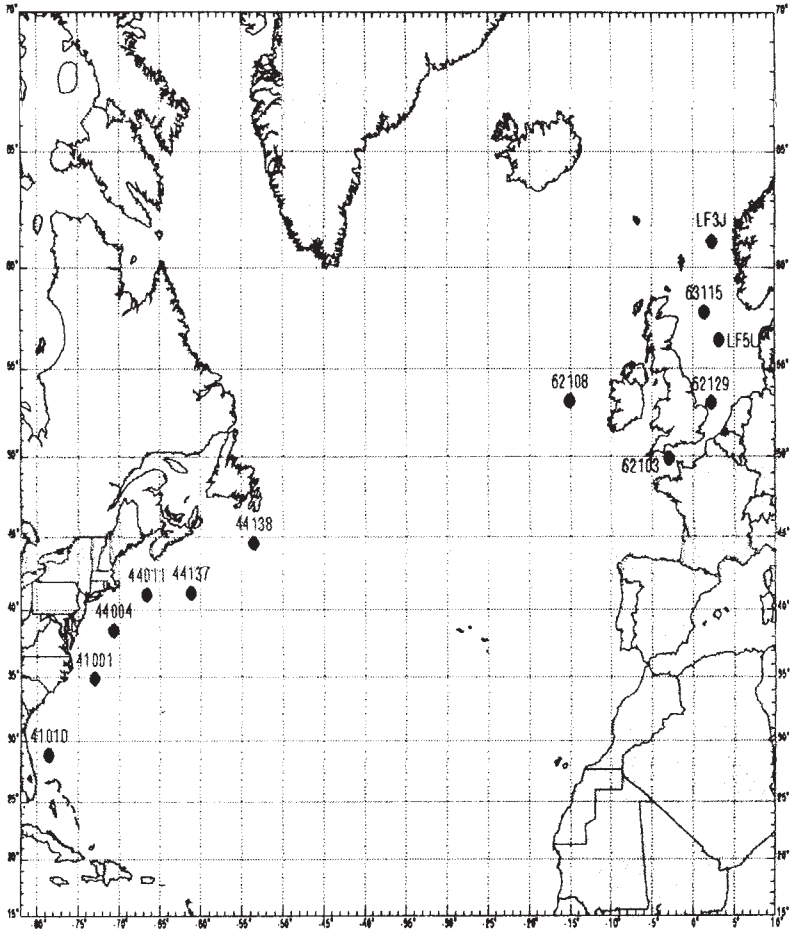


Figure 2. Locations of Wave Climatology Comparison Sites



TABLE OF CONTENTS

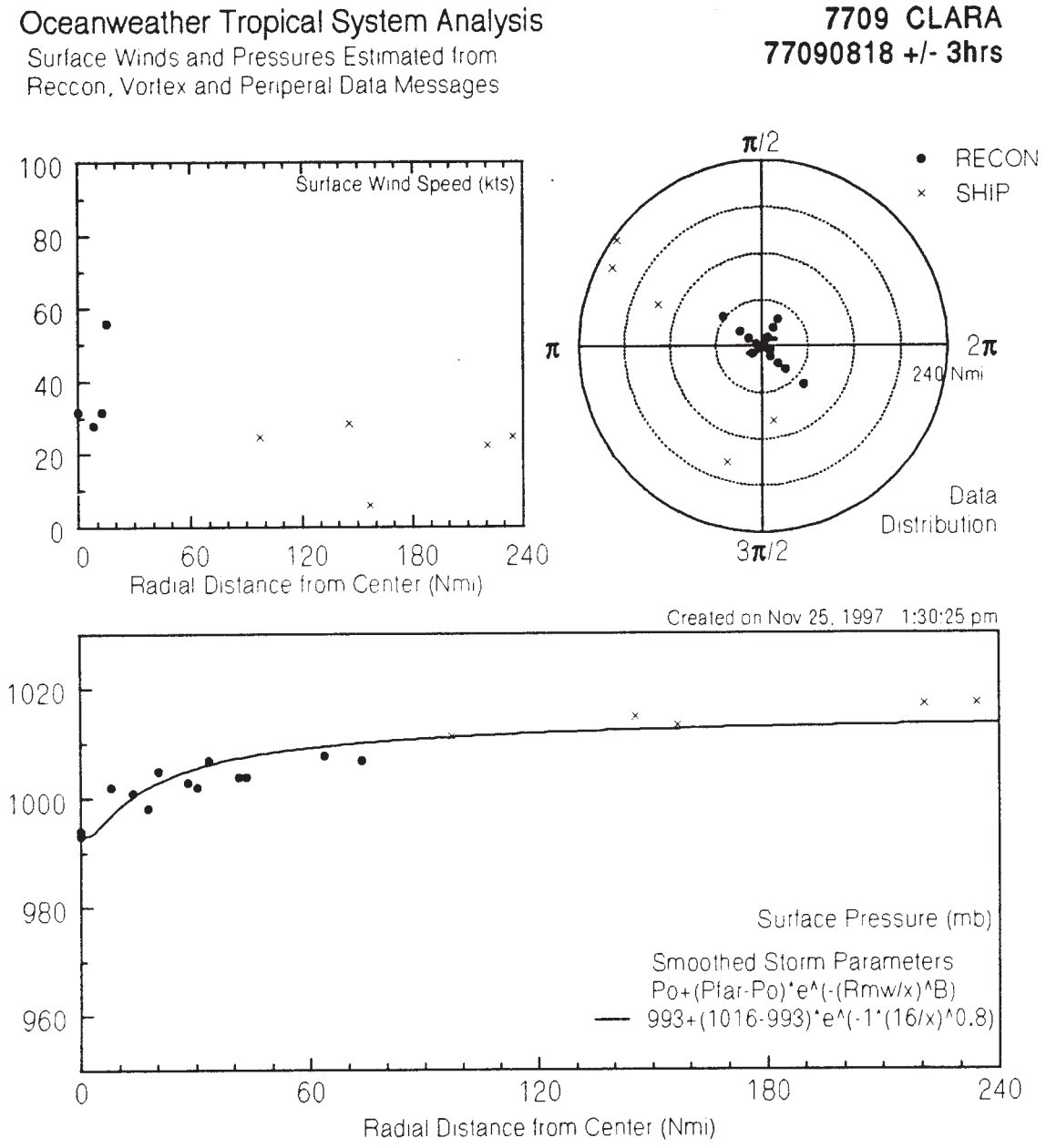


**Figure 3. Sample pressure profile fit to available aircraft reconnaissance and surface data.**

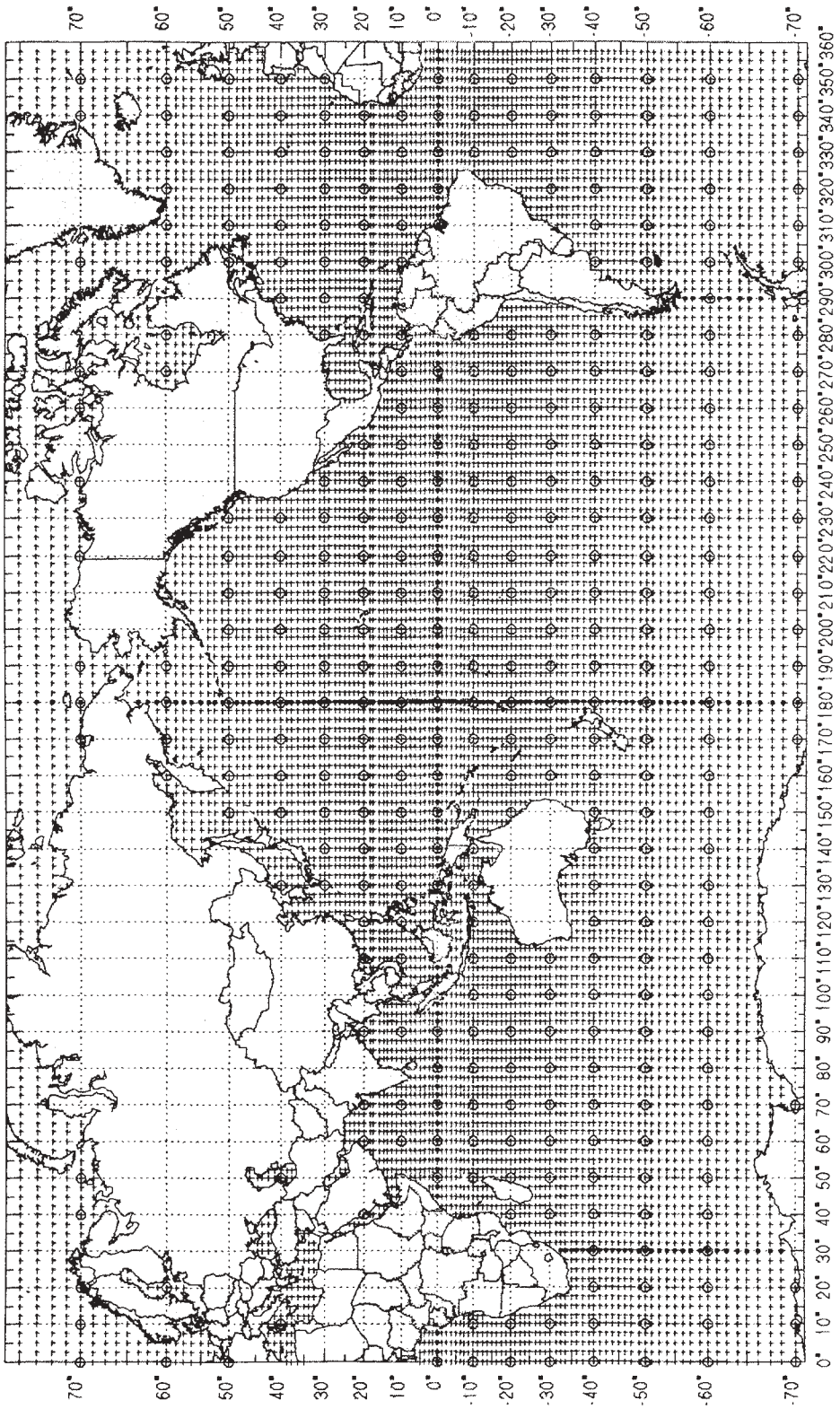


**Figure 4. Global wave grid with spectral save points (circles).**

**Figure 5. Q-Q plots of significant wave height for selected locations.**

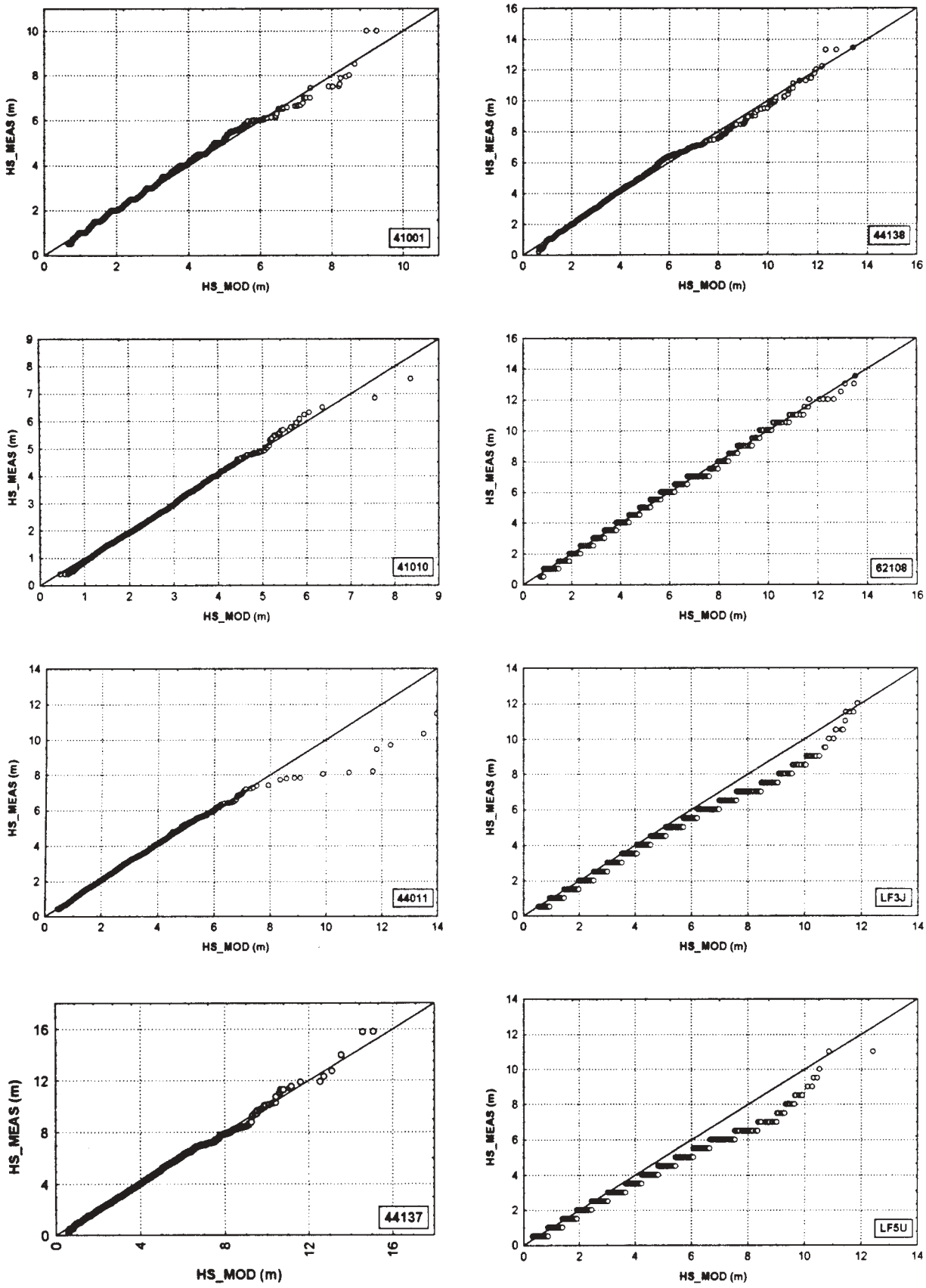


AUTHOR INDEX

TABLE OF CONTENTS

**Figure 6. Q-Q plots of wind speed for selected locations.**

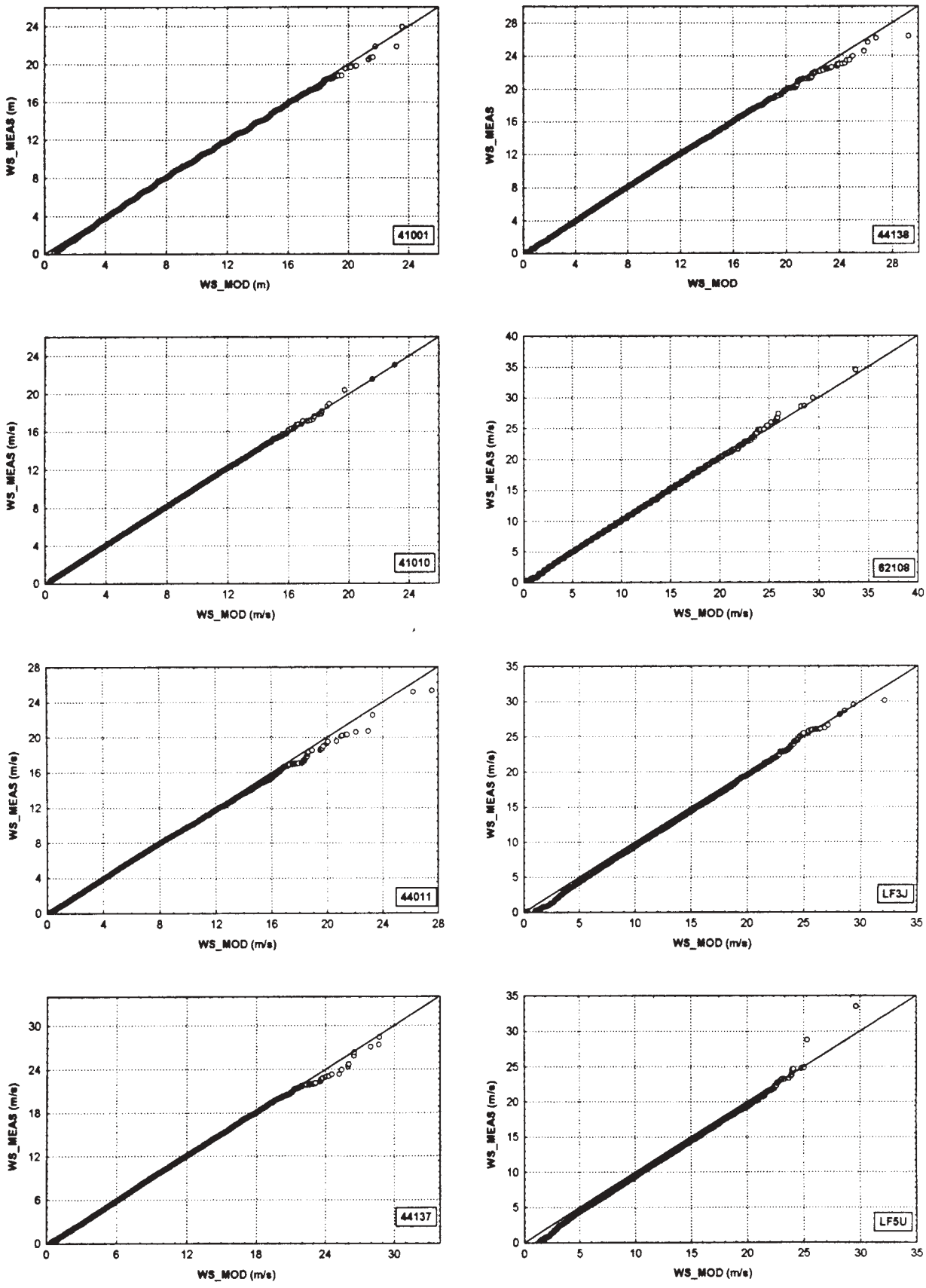


AUTHOR INDEX

TABLE OF CONTENTS

**Figure 7. Q-Q plots of spectral peak wave period for selected locations.**

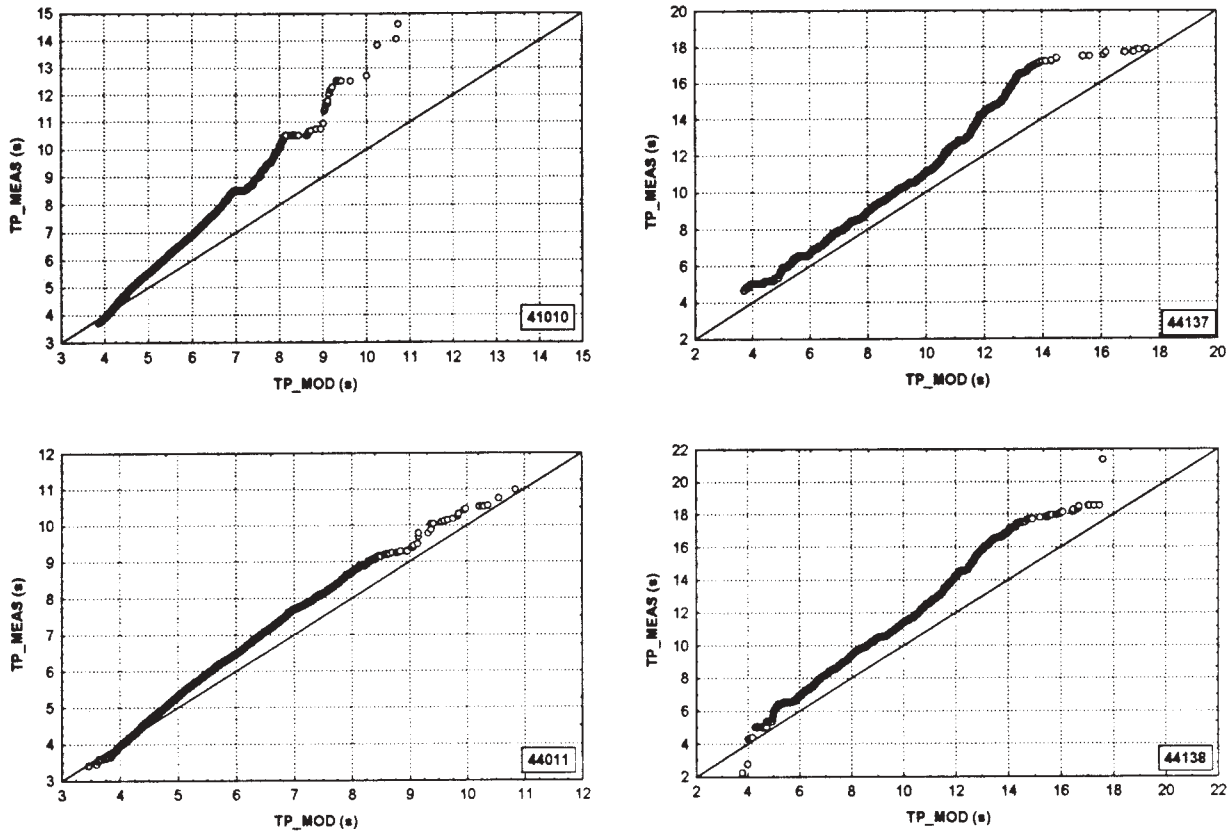


AUTHOR INDEX

TABLE OF CONTENTS

# RESULTS OF THE WASA WAVE HINDCAST

H. Günther[1], W. Rosenthal[1], M. Stawarz[1],
J.C. Carretero[2], M. Gomez[2], I. Lozano[2], O. Serrano[2], M. Reistad[3]

[1] GKSS Forschungszentrum Geesthacht, Geesthacht, Germany
[2] Clima Maritimo, Madrid, Spain
[3] Det Norske Meteorological Institutt, Bergen, Norway

## 1. INTRODUCTION

In recent years there has been a growing concern among many people, especially in coastal areas and in the marine industry, about a climate change over the past several decades. There have been many reports of increased wind speeds, wave heights and storm surges heights, as well as increased storm frequency. The European project "Waves and Storms in the North Atlantic" (WASA), funded by the European Union's Environment Program, has been set up to prove, or to disprove, hypotheses of a worsening storm and wave climate in the Northeast Atlantic and adjacent seas in the present century. A major obstacle for assessing changes in storm and wave conditions are inhomogeneities in the observational records, both in the local observations and in the analysed products, which usually produce an artificial increase of extreme winds and waves. Therefore, changes in the wave climate were assessed with a state-of-the-art wave model using wind analyses.

This article summarises the ocean wave subtask of WASA. A full description of the work is presented in Günther et al. (1997).

The reconstruction of the wave climate in the North Atlantic for last 40 years (1955-1994) was achieved by running the WAM model in two nested grids: a coarse grid covering the whole North Atlantic and a fine grid covering only the North-East Atlantic (cf. section 2).

For running the numerical simulation, two different wind data sets were used (cf. chapter 3): operational analyses of the Fleet Numerical Meteorology and Oceanography Center (FNMOC) for the coarse grid, and wind estimates from the air-pressure analyses prepared routinely by Det Norske Meteorologisk Institutt (DNMI) for the fine grid.

The homogeneity of the input wind fields is an important aspect for the assessment of changes in the wave climate obtained from the hindcast data. With a homogeneous wind data set we may expect, within the limitations of the wave models, to receive a detailed space and time evolution of wave parameters, such as significant wave height (SWH), which may be considered to be a reality "substitute". Even if the hindcasted substitute reality does not capture all details, it is expected that the low-frequency variations of wave statistics, including interdecadal variability and trends, are reliably reproduced.

Inhomogeneities, i.e. changing non physical factors influencing the weather analyses, can be either "creeping" or "sudden" (Karl et al., 1993; Jones, 1995). Creeping inhomogeneities are present in operational analyses, which are prepared with forecast models subjected to ongoing improvements. Another source are ongoing modifications of the observational network (e.g. gradually changing ship routes, increasing ship speeds and instrument heights). The availability of satellite imagery in the 60s may have persuaded human weather forecasters to describe a low pressure system over the Atlantic as more intense than if he had only ship observations as in the 50s.

Sudden inhomogeneities are introduced by abrupt, often documented, changes in the analysis scheme. These may be the change from manual to automatic analysis techniques, the rectification of outright errors in the analysis procedure, the creation or the withdrawal of an observational platform in a data sparse area (such as ocean weather stations). If sudden changes are not already known from the documentation, they may often be identified by screening the time series for jumps in the moments of the time series calculated for moving windows.

In our case, we could not completely assess the degree of homogeneity in the driving wind fields. We objectively identified sudden inhomogeneities, but for creeping inhomogeneities we had to refer to plausibility arguments. The comparison with observed records is in many cases inconclusive as these data have already entered

the analysis, so that they do not offer independent information. Furthermore, local observations, which in many cases are not instrumental observations but are based on subjective assessments (wind force estimated from wave heights), may already suffer from the creeping inhomogeneities, which are then inherited by the 2-d mapped analysis.

We argue in Section 3 that the FNMOC winds are homogeneous enough for producing boundary conditions for our 40 year fine grid hindcast. This view is supported by the relative uniformity of the monthly mean statistics in this data set; while over the whole 40 years of the hindcast the frequency of strong wind events has undergone changes which are not supported by the DNMI analyses and analyses from pressure gradients.

The degree to which the DNMI analyses were contaminated by creeping inhomogeneities was examined with the help of maps of the ratio of storm-related standard deviations of air pressure calculated for consecutive 10 year intervals. It was found that this standard deviation has undergone a steady increase in data from sparse areas far from coasts, while it remained almost constant in an area surrounding the British Isles and covering the North Sea (see Section 3.2). Based on this observation, we concluded that the DNMI analyses suffer from an artificial worsening of the storm climate in data sparse areas, and that we could expect minor inhomogeneities in the area covering the North Sea and the Atlantic adjacent to the British Isles, approximately between 70°N and 40°N and east of 20°W.

In section 4 the model output was compared with weather ship measurements and other observational data sets. Furthermore, the data obtained from the numerical simulation were compared with data retrieved from ship routing charts (Bouws et al., 1996). In general there was a good agreement between model results and observations. As a conclusion from this comparison, we believe that the real trends of wave statistics are reliably reconstructed by the hindcast.

To examine the hypothesis of worsening of the wave climate in the North Atlantic published by many authors in last years (i.e. Carter and Draper, 1988; Bacon and Carter, 1991; Hogben, 1994), model data time series from different locations were analysed. The trends in average wave heights derived from model data were much smaller than those given in recent publications.

Trends of SWH and wind speed were computed for each grid point, and the two-dimensional distribution of changes per year were presented section 5. The maxima, and 99th and 90th percentiles of SWH have steadily increased in the Northeast Atlantic, while in the near-coastal areas of Northwest Europe the storm climate has not systematically worsened. The upper estimates for this increase are 7-10 cm/year for the maxima, 3-4 cm/year for the 99th percentile and 2-3 cm/year for the 90th percentile of annual wave height distribution.

A further objective of the WASA project described in this paper is extreme value analysis (Section 6). The extreme wave analysis was performed in four slices of ten years. The values of SWH with a return period of 100 years obtained in each decade showed a clear spatial pattern. Two distinct regions can be identified: one between Iceland and Scotland with a tendency towards higher extreme waves, and another southwest of Ireland with a slight decrease. These trends took place during the four decades without interruption or large oscillations.

## 2. WAVE MODEL SET-UP

A 40 year reconstruction, 1955 to 1994, of wave conditions was prepared by running the WAM (cycle four) wave model (WAMDI 1988; Günther et al. 1992 and Komen et al. 1994). The wave model was applied to two nested grids:

A coarse grid in the North Atlantic: resolution 1.5° x 1.5° latitude x longitude, covering the whole North Atlantic from 80°N to 9.5°N and from 78°W to 48°E.

A nested fine grid in the Northeast Atlantic: resolution 0.5° x 0.75° latitude x longitude covering the Northeast Atlantic: 77°N to 38°N, 30°W to 45°E .

Bottom effects were neglected in the coarse North Atlantic grid but included in the fine grid model runs of the Northeast Atlantic. In both models an angular resolution of 15° and 25 logarithmically spaced frequencies from 0.042 Hz to 0.411 Hz were used.

The standard WAM model was modified to handle variable sea ice cover updated once per simulation month. The sea ice data were provided by the DNMI. To follow the aims of the WASA project and to facilitate possible future analysis, model data (3 integrated spectral parameters and two-dimensional wave spectra in the full

frequency-angular resolution) were stored for both grids at all sea points every three hours for the entire 40 year hindcast period.

## 3. HINDCAST WIND FIELDS

### 3.1 FNMOC winds

The operational wind analysis done by FNMOC was used to force the coarse grid model. Unfortunately, the FNMOC winds suffer from a few gaps, e.g. all of 1994 is missing. These gaps were filled by temporal interpolation if the gaps were one day or less. The European Centre for Medium-Range Weather Forecasts (ECMWF) analysis was used to fill longer gaps.

The wind fields were interpolated on the WASA coarse grid using a polynomial method. For interpolation in time, a linear method (standard WAM cycle 4) was applied.

Several inconsistencies in the wind data set were found. In some periods the winds were given at 19.5 m, while in other periods they were given at 10 m, the reference level required by the WAM model. This inconsistency was removed by applying a standard logarithmic wind speed profile.

Several changes in the preparation of the analysis have taken place over the past 40 years. For example, until 1971 the pressure maps were prepared by manual analysis, after 1971 numerical analysis models were used. This change was associated with an abrupt change of about 1 m/s in average wind speed. Surface winds for the period 1954 to 1977 were geostrophically derived, while afterwards a Planetary Boundary Layer Model (PBLM) was used. The overlapping period of eight months was used for consistency tests. The distribution of wind direction of both data sets agree quite well. The geostrophic wind speeds were found to be systematically lower than the PBLM wind speeds. Therefore, the geostrophically derived wind speeds were adjusted using the correction derived from the statistical comparison of the overlapping period. Because of the shortness of this period, it is uncertain whether the chosen correction applies for the whole geostrophic period.

Comparisons between PBLM and ECMWF winds showed good agreement in direction and modulus for values of up to around 15 m/s. Higher values were found to be lower in the ECMWF winds. For the comparison between model wind data and observation the Comprehensive Ocean-Atmosphere Data Set (COADS) was used. Time series were compared with mean values of the observations from ships in the area (square box of $1^{o}$ x $1^{o}$). All points were located in areas with high density of observations and in general there was a good agreement between both data sets.

Comparison (Fig. 1) between model coarse grid data and measurements at Ekofisk (position: $56.5^{o}$N, $3.2^{o}$E) from 1980 to 1994 also showed a good agreement in annual mean wind speeds and annual 90th percentiles (up to values of around 15 m/s). The annual 99th percentiles of the model wind were slightly overestimated. Mean errors in wind speed at Ekofisk vary between 1.6 m/s and 2.9 m/s. Comparison with wind observations at Gulfaks ($61.2^{o}$N, $2.3^{o}$E) over the same period gave similar results.

For the comparison between wind input and Ocean Weather Ships (OWS) data a German data

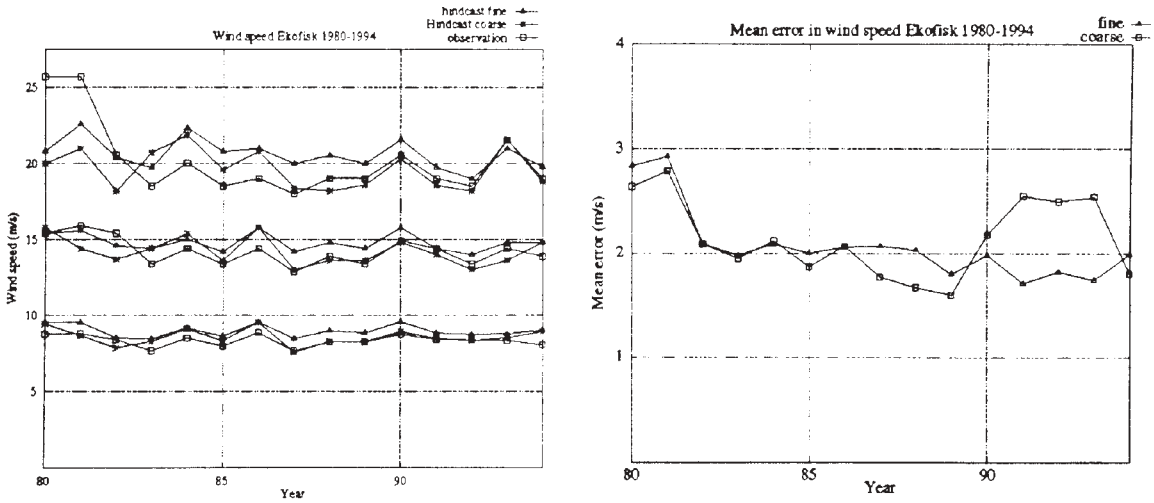


Fig.1: Comparison between model input wind (coarse and fine grid) an measurements at Ekofisk. Left side from top to bottom: 99th, 90th persentiles and mean; right side mean wind speed error.

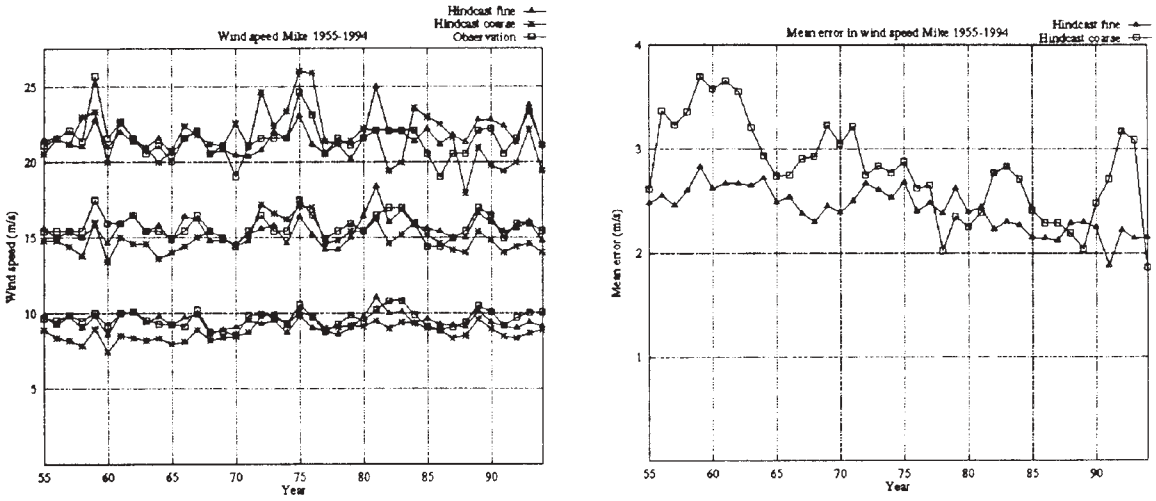


Fig.2: Comparison between model input wind (coarse and fine grid) an measurements at OWS Mike. Left side from top to bottom: 99th, 90th persentiles and mean; right side mean wind speed error.

archive at the German Met. Office and DNMI data were used. A typical result of these comparisons is presented in Fig 2. which shows the comparison at OWS Mike (66°N, 2°E) over the full hindcast period 1955 to 1994.

The comparison between 99th and 90th percentiles of the annual model input wind speeds and observed wind speeds showed mixed results (Fig. 2). In the period 1955 to 1970 input wind speeds are underestimated. In this period the mean wind speed error varies between 2.6 and 3.7 m/s. The agreement is better after 1970, but there are still periods (e.g. 1982-85, 1990-93) with rather poor agreement between model and observations.

## 3.2 DNMI winds

The fine resolution simulation was forced with wind data from DNMI (Reistad and Iden, 1995). These winds were calculated from mean sea level air pressure fields. The data were taken at 6-hour intervals on a rectangular grid with a stereographic map projection with a grid distance of 75km at 60°N. The data were interpolated to the WASA fine grid. The DNMI wind data do not cover the most southern part of the WASA fine grid model area, so the DNMI wind data were supplemented by the wind data from FNMOC.

The DNMI data were considered to be more accurate than the FNMOC wind fields, but the data were not homogeneous for the whole 40 year period. The most severe inhomogeneity was in 1982, coinciding with the first use of pressure fields from numerical weather prediction systems. There were also inhomogeneities in the pressure and wind data due to changing numbers of observations used in the analyses through the years 1955-1981, and after 1982 there were changes and improvements of the numerical weather prediction systems that affect the pressure analyses.

Comparison between fine grid model winds and observations at Ekofisk from 1980 to 1994 (Fig. 1) showed a good agreement in annual mean and 90th percentiles of the wind speed. The agreement between 99th percentiles of model and observations is worse, especially in the period 1980-81. However, observed values show much uncertainty in this time. The mean error in wind speed varied between 1.7 m/s and 2.9 m/s . The analysis of the wind speed at Gulfaks showed similar results but the agreement for the 99th percentiles was better.

Comparisons between wind speed records of different OWS's and DNMI winds also showed that, generally, model and observed winds agreed well. Fig. 2 shows time series of the annual wind speed at OWS Mike as well as the mean error between model and observation.

In general, the model winds and the observations at various sites were in quite good agreement. This holds for coarse (FNMOC) and fine (DNMI) winds and for the comparisons of the mean wind speeds and the checked percentiles. Only the mean errors indicated a small advantage in the quality of DNMI winds over some periods. It has to be taken into account that these observations were used to generate the wind fields with the techniques described above. Therefore, the differences mainly reflect the weight given by the wind and pressure analysis to

the quality of the observations.

The most important aspect of the reliability of computed trends in wave conditions in the North Atlantic is the homogeneity of the wind fields used in the wave hindcast. The analyses of both FNMOC and DNMI wind fields showed that the DNMI winds seemed to be homogeneous in most parts of the fine grid area, approximately between 70°N and 40°N and east of 20°W. The ratio of high-pass filtered standard deviations of air-pressure variations in winter in the decade 1984-93 and in the decade 1964-73 showed small variability in this area. In contrast, the variability increased severely after the 1960's in areas where few or no in-situ observations were available (WASA, 1995).

We concluded that the high quality and homogeneity of the DNMI wind fields in the area mentioned above allowed us to make reliable predictions about the development of wave conditions in this area over the past 40 years. However, the reduced quality of the wind fields in areas near the boundary of the fine grid (west of 20°W, north of 70°N and south of 40°N) indicated that the trends obtained there had to be handled with great care.

## 4. WAVE ANALYSIS AT SELECTED POINTS

The wave parameters obtained from the numerical simulations were compared with the observational data and with the data retrieved from the KNMI ship routing charts. Two-dimensional distributions of the wind and wave parameters were also computed.

A number of storms hindcasted with the fine resolution model were compared with observational records. The agreement between model data and observation was fair. Statistics of year-to-year variation were also computed and compared with those of observations. Some of the statistics for the Northern North Sea and for the Northeast Atlantic show good correlation between model and observation, while others show severe overestimations by the model. This may be partly due to the tuning of the WAM model to the ECMWF-wind fields, which are usually lower than the wind fields used in this study. Other reasons for the overestimation were insufficient resolution of the grid to show sheltering from islands (e.g. the Shetland and Faroe Islands are not resolved) and some model problems with wave dissipation in the shallower southern parts of the North Sea. Fig. 3 shows the comparisons of the monthly maximum SWH, the monthly 90th percentile and the monthly mean SWH at Statfjord (61.2°N, 2.3°E) for two different five year periods.

Also within the framework of WASA, wave heights were retrieved from a set of wave charts produced by KNMI Ship Routing Office during its existence between 1960 and 1988 (Bouws et al., 1996). The results based on maximum SWH for one of the selected areas west of Ireland

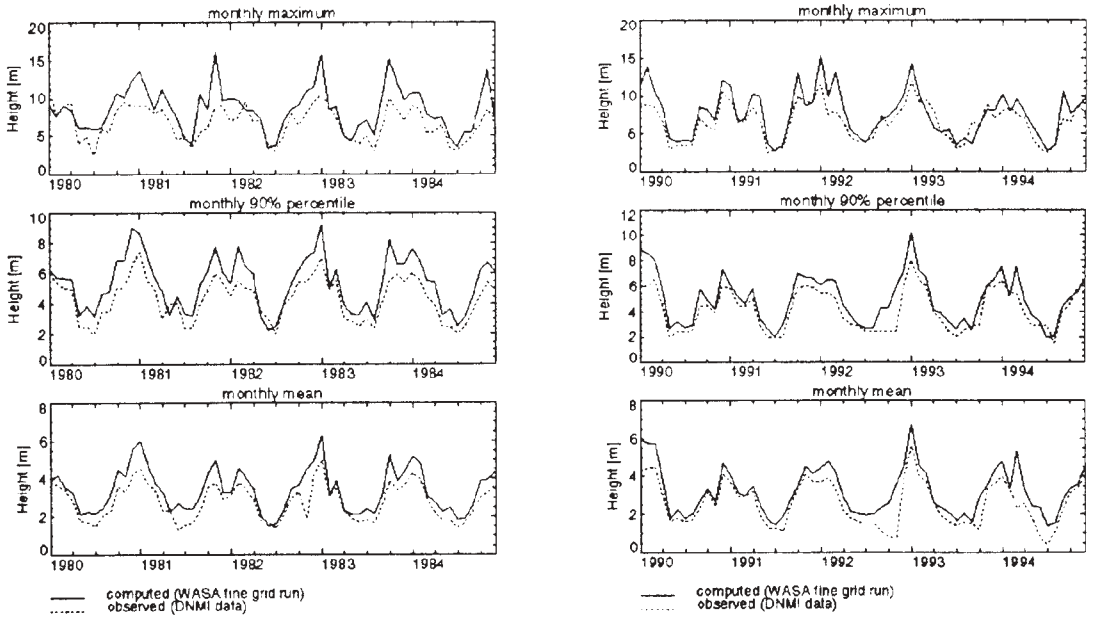


Fig. 3: Comparison between model SWH (fine grid) an measurements at Statfjord. From top to bottom: monthly maximum, 90th persentiles and mean; Left side 1980-84, right side 1990-94

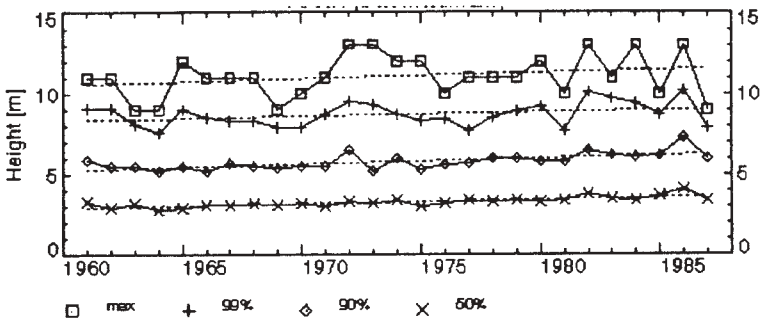


Fig.4: Time series of maximum, 99th, 90th and 50th persentiles (from top to bottom) of the annual SWH retrieved for the area west of Ireland from ship routing maps.

(50°N-55°N, 20°W-10°W) over the period 1961-1987 are presented in Fig. 4. Positive trends in yearly maxima, 99th, 90th and 50th percentiles of significant wave height were found. Yearly averages (not shown in the figure) also increased in this period.

The regression coefficients obtained from a linear regression representing the yearly change of the wave height for the given exceedance levels are listed in Tab. 1. The trends seem to be persistent during the whole period. It should be noted that the procedures for making wave charts at the KNMI Ship Routing Office hardly changed during this whole period. The increase of SWH during the period 1970-1982 was found to be about 15%, compared to 30% found by Neu (1984).

| | max | 99% | 90% | 50% |
|---|---|---|---|---|
| KNMI maps 1961-1987 | 3,80 | 2,70 | 3,80 | 3,80 |
| Hindcast 1961-1987 | 5,48 | 1,01 | 0,54 | 1,01 |
| Hindcast 1955-1994 | 2,18 | -1,51 | -0,38 | 0,05 |

Table 1: Estimated change per year in cm/year of the yearly maxima, 99th, 90th and 50th percentiles of SWH in the area west of Ireland.

Tab. 1 also shows the statistics from the WASA data in the area west of Ireland over the same period, and over the entire simulation period 1955-94 (Fig.5). The trends found for the yearly maxima, 99th, 90th and 50th percentiles of SWH were positive as well. Except for the yearly maxima, where WASA data resulted in the greater trend, the trends computed for 99th, 90th and 50th percentiles of SWH were smaller. But over the last 40 years, only maxima of SWH increased about 2.2 cm/year, while the 99th and 90th percentiles of SWH decreased by about 1.5 and 0.4 cm/year respectively.

The same statistical analysis of the WASA data was made for an area north of Scotland (60°-65°N, 10°-0°W). Tab. 2 shows the results of the wind speed and SWH analysis for both areas. The wave maxima in both areas increased. This increase was more significant north of Scotland (about 8.7 cm/year) than that west of Ireland (about 2.2 cm/year).

Other representatives for the aspect of possible changes in the wave climate are 99th or 90th percentiles of SWH. The regression coefficients obtained for these percentiles were much smaller than those for wave maxima (see Tab. 2). The changes in SWH corresponded very well to changes in wind speed in the chosen areas.

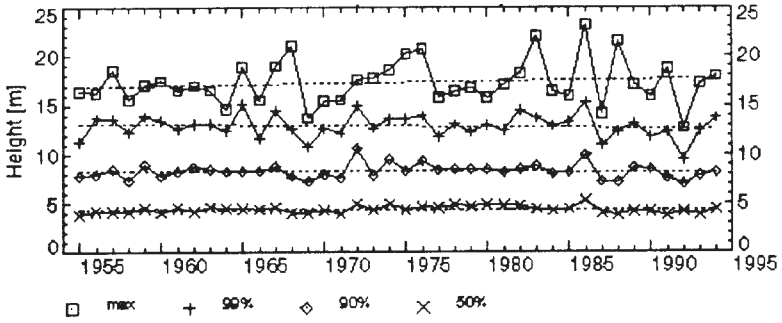


Fig.5: Same as Fig 4 but from the WASA analysis over 40 years.

At selected locations from the 40 years time series of SWH and wind speed the annual maxima, 99th, 90th and 50th percentiles were calculated. The computed trends are presented in Tab. 3. Generally, the variability of the wave climate was large and there were sometimes significant changes in the statistics of wave and wind fields over time scales of decades.

| Percen-tile | SWH | | Wind speed | |
|---|---|---|---|---|
| | West of Ireland | North of Scotland | West of Ireland | North of Scotland |
| max | 2,18 | 8,73 | 2,46 | 7,78 |
| 99 | -1,51 | 4,03 | 0,31 | 5,94 |
| 90 | -0,38 | 1 | -0,1 | 1,34 |
| 50 | 0,05 | 0,04 | -0,1 | -0,31 |

Table 2: Estimated change per year of the yearly maxima, 99th, 90th and 50th percentiles of SWH [cm/year] and wind speed [cm/s/year] in the area west of Ireland and north of Scotland.

The results at the different locations are:

- Southern North Sea - Euro location:
  Trends for maxima and 99th percentiles of the wind speed and total significant wave heights slightly decreased, 90th and 50th percentiles were mostly constant. At this station the maxima are definitely overestimated by the model.
- Central North Sea - Ekofisk location:
  Wind speed maxima and 99th and 90th percentiles increased (4.8, 3.9 and 3.1 cm/s/year). The increase in the wind speed could be determined by the increase of total SWH. The trend for the maxima is 3.5 cm/year, and the 99th and 90th percentiles also increased slightly.
- Northern North Sea - Brent location:
  Wind speed slightly increased: max 4.9 and 99th percentile 3.2 cm/s/year, 90th percentile 2.6 cm/s/year. Total SWH also increased: 3.4, 2.2 and 1.1 cm/year respectively.
- Northeast Atlantic - Mike location:
  Wind max, 99th percentile: 6.3, 2.6 cm/s/year, total SWH: 8.4 and 2.6 cm/year, respectively.
- North Atlantic - Juliett (west of Ireland):
  Relatively strong increase in wind speed. Trend for the maxima is 13.7, for the 99th percentile 6.8 cm/s/year. But the total SWH at this position increase only slightly: max 0.9 cm/year. 99th percentile decreased by 1.9 cm/year.
- North Atlantic- India, Lima (northwest of Ireland):
  At India wind speed and SWH increased significantly. The maxima of the wind speed increased on the order of 17.5 cm/s/year, SWH 9.4 cm/year. However, the statistics of wind speed and SWH at Lima were quite different. There the maxima of wind speed decreased, as well as the maxima of total SWH.

Past analyses of data on wave height, gathered from ships of opportunity or from ocean weather stations, had led to the conclusion of a substantial worsening of the wave climate in the North Atlantic (Carter and Draper 1988, Bacon and Carter 1991, Hogben 1994). Hogben found that mean wave heights have increased at a rate on the order of 1% or 2% per annum since 1950. He supported this with data from a series of locations mainly between 50° and 60°N. However, such local data must be considered with great care. Upward trends could have various non-physical reasons (WASA, 1994). For example, before 1979 wave height data were based on visual assessments, and they seem to be systematically too low, while after 1979 they were based on instrumental data. The poor quality of visual

| Position | SWH [cm/year] | | | | | Wind speed [cm/s/year] | | | | |
|---|---|---|---|---|---|---|---|---|---|---|
| | max | 99% | 90% | 50% | mean | max | 99% | 90% | 50% | mean |
| Euro | -0,89 | -0,96 | 0,12 | 0,00 | 0,00 | -2,97 | -2,70 | -0,02 | -0,07 | -0,12 |
| Ekofisk | 3,47 | 1,73 | 1,04 | 0,28 | 0,41 | 4,81 | 3,86 | 3,08 | 1,61 | 1,65 |
| Brent | 3,38 | 2,18 | 1,10 | 0,41 | 0,57 | 4,92 | 3,17 | 2,62 | 1,61 | 1,54 |
| OWS Mike | 8,39 | 2,62 | 1,01 | 0,22 | 0,38 | 6,30 | 2,56 | 0,89 | -0,57 | -0,25 |
| OWS Juliett | 0,90 | -1,99 | 0,55 | 0,49 | 0,43 | 13,68 | 6,75 | 5,73 | 2,37 | 2,83 |
| OWS India | 9,40 | 0,16 | 0,11 | 0,08 | 0,18 | 17,49 | 6,28 | 2,16 | 0,68 | 1,10 |
| OWS Lima | -3,40 | -3,99 | -0,38 | 0,06 | -0,08 | -3,83 | -2,56 | 0,90 | 0,37 | 0,37 |

Table 3: Estimated change per year in cm/year of the yearly maxima, 99th, 90th, 50th percentiles and mean value of SWH and wind speed at selected positions.

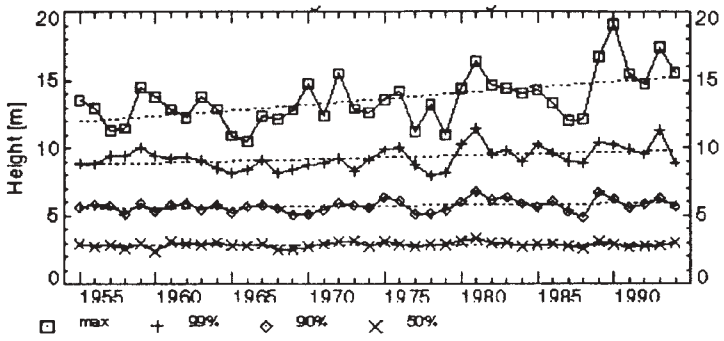


Fig.6: Same as Fig 4 but from the WASA analysis over 40 years at OWS Mike.

wave observations (especially at night) makes any analysis of year-to-year variability unreliable.

In fact, there was an increase in model SWH at OWS Mike (Fig. 6) over the whole simulation period 1955-1994 of the order of 8 cm/year for the annual maxima, or a rate of 0.7% per annum. The regression coefficients obtained for the 99th and 90th percentiles of SWH were much lower, 2.6 cm/year and 1.0 cm/year, respectively (see Tab. 3).

The increase in wave height at OWS Mike was more significant in the second part of the simulation period, 1975-1994. During that time, the maxima of SWH increased by more than 17 cm/year (1.4% per annum) and 99th percentile by about 3.5 cm/year (0.3% per annum). For the mean values, there was no evidence of a significant trend over the last 40 years. The simulated mean SWH at OWS Mike increased by 0.3 cm/year, which corresponds to 0.09% per annum. The median of SWH increased by 0.2 cm/year.

The model data confirmed that swell waves were dominant at low wind speeds. The slight increase in mean SWH at OWS Mike could, in fact, be explained by the increase in the mean swell height, especially since the mean wind speed at this station decreased by an annual rate of 0.25 cm/s. Also mean wind waves decreased slightly (0.026 cm/year) but mean swell height increased by 0.44 cm/year.

There have been many other publications (Barratt, 1991; Bacon and Carter, 1991), based both on measurements and visual observations, with evidence of an increase in average wave heights over the Northeast Atlantic. Generally, an upward trend in the annual mean value of significant wave height between 1% and 2% per annum was found. At OWS India, a rate of 2.5% per annum was reached. The analysis of WASA wave data at the same locations did not confirm such large trends in annual mean wave height. The rate varied between 1% per annum at OWS Juliet (1960-74) and -0.4% per annum at OWS Lima (1978-85).

The trends for average wave heights derived from model data were much smaller than those found in recent publications. Similarly, the annual rates of increase in mean wave heights computed over the whole simulation period 1955-94 were small. The following rates were obtained:

OWS India: 0.1 cm/year
OWS Juliett: 0.04 cm/year
OWS Lima: 0.0 cm/year
Brent and Statfjord: 0.5 cm/year

Evidence of a strong upward trend in the wave heights was also reported by Neu (1984). His analysis based on data derived from synoptic charts for separated $5^{o}$ square areas of the North Atlantic from 1970 to 1982. He found that the annual 50th percentiles of wave heights increased during this period by an average 3.93% per year. For the area west of Ireland (15-$10^{o}$ W, 50-$55^{o}$ N) he found an increase in median wave height from 2.65 m to 3.65 m, which is 8.3 cm/year or 3.14%. The analysis of WASA data for selected areas in the North Atlantic did not verify Neu's rates of increase. The computed rates are about 50% smaller than Neu's rate of increase.

The differences between the WASA hindcast results and earlier estimates of wave height trends described in this section were partly significant. There are several possible explanations for these discrepancies. Two of these are:

The development of the shipborne wave recorder, which took place between 1962 and 1980. This instrument was improved over the years and visual observations of wave heights on weather ships were probably influenced by its objective measurements of wave heights.

The bias of ship observations towards lower waves, since ships tend to avoid storms. However, modern ships have improved sea keeping capability and can now sail more often under heavy storm conditions than previously without risk to ship and cargo.

## 5. TRENDS IN THE FINE GRID AREA

The detection of possible changes in the wave and storm climate in the North Atlantic was focused on regional changes in the trends of SWH and wind speed. The annual maxima, averages and the 50th, 90th and 99th percentiles were computed for each grid point in the 40 year wave hindcast (1955-1994). To study possible trends, a straight line was fitted to the yearly variation. The linear regression coefficients are presented for the homogeneous part of the fine grid area as contour plots in figures 7,and 8. The contour line "Ice" marked the maximum extension of the sea-ice.

### 5.1 Extreme conditions

The significant wave height and wind speed maximum, and the 99th and 90th percentiles have steadily increased in the Northeast Atlantic in the last 40 years, while in the near-coastal areas of the North Sea the storm climate has not systematically worsened. In the southwestern part of the fine grid area the significant wave height and wind speed maximum, 99th and 90th percentiles have decreased.

The most characteristic feature in the trend distribution for annual maxima of SWHs was the area between Iceland and Scotland (Fig. 7) here is quite distinct. The annual rates of increase in maximum SWH lie between 7.5 and 10 cm/year, partly between 10-12 cm/year. Positive trends are also found in the Norwegian Sea, where upper-bound estimates were 7.5-10 cm/year. The maxima of the wind speed also clearly increased in this area. Upper-bound estimates were 10-14 cm/s/year. In contrast, in the area southwest of Ireland wind maxima became lower and wave heights became smaller. The distribution in the North Sea was quite complex. In the central part wind speed showed a tendency towards higher maxima, while in the Southern North Sea they decreased. The trends for the maxima of SWH were similar: increased waves in the central part and decreased waves along the south coast from the Netherlands to Denmark.

### 5.2 Mean conditions

The trends in average SWHs derived from model data were likewise small (Fig. 8). Only in the Northern North Sea, in the Northeast Atlantic (north of the Faroe Islands), and on the northwest coast of Ireland were the trends in average SWH slightly greater, between 0.5 and 0.75 cm/year. In the Central North Atlantic (west of OWS Juliett) the rates were between 0.75 and 1 cm/year. The small changes in average SWH could be seen as a result of small changes in mean wind speeds. The computed trends in the mean wind speed in the Northeast Atlantic were almost negligible (Fig. 9). Only on the northwest coast of Spain and in the central North Atlantic did the mean wind velocity increase significantly and the rate of year-to-year variation exceeds 6 cm/s/year, an increment in the mean wind speed of about 2.5 m/s over the 40 year period. However, the average wave parameters showed comparable variability over time scales of decades as

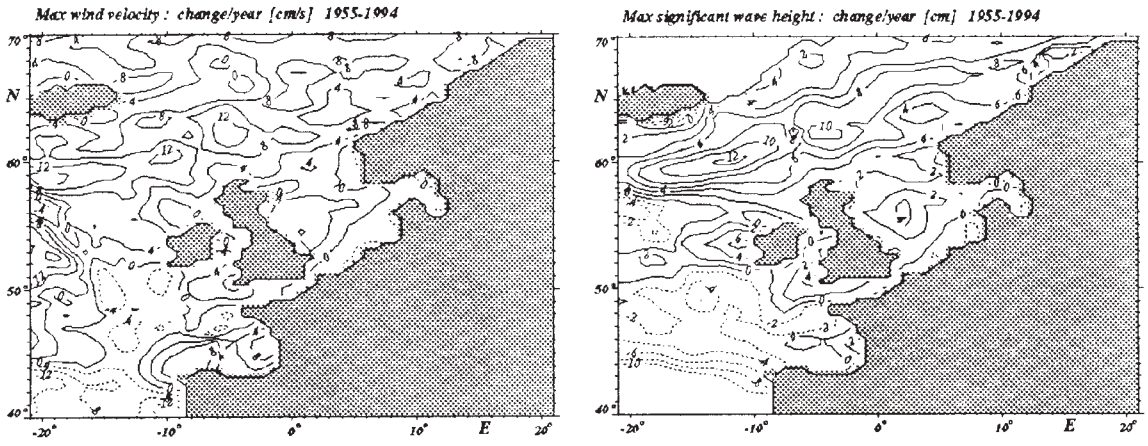


Fig. 7: Spacial distribution of changes per year of the yearly maximum wind speed and maximum SWH over the period 1955-1994.

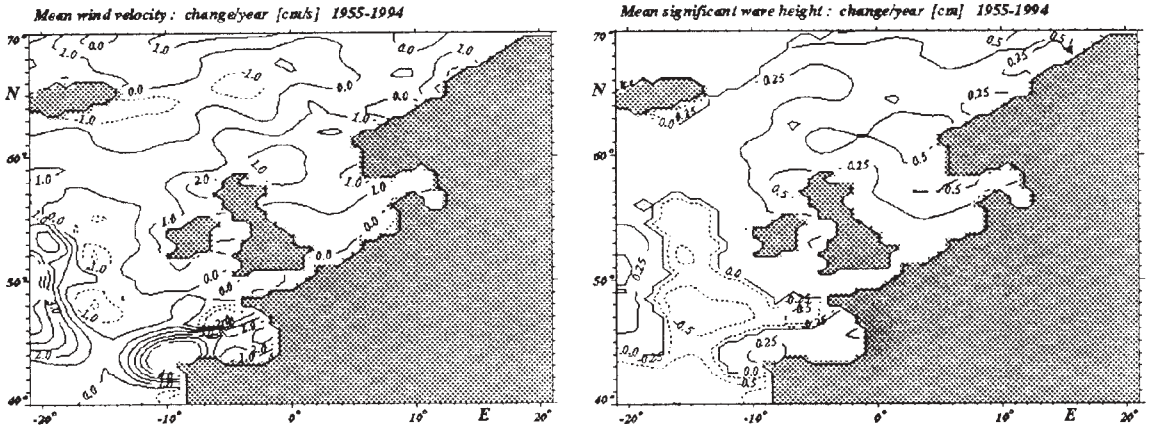


Fig.8: Same as Fig. 7, but changes of annual mean.

discussed for the 90th percentile of wind speed and SWH. In contrast to the whole simulation period, the average annual SWH decreased almost everywhere over the last 20 years. A positive trend in mean SWH over the last two decades was computed in the Irish Sea and on the west coast of Norway. The rate of changes obtained for these areas reached 0.5 cm/year. More significant increases in annual mean SWH took place on the northwest Norwegian coast

## 6 EXTREME VALUE ANALYSIS

The common approach used to calculate the risk of extreme wave conditions is the theory of extreme value statistics. The method is well established and the output has been used as the environmental characteristic for loads on offshore construction, shipbuilding, downtimes of ship operation. The typical parameter in this theory is the average return period of an extreme significant wave height. For finding the distribution function for the high wave tail of the overall distribution of SWH we used the peak over threshold selection of wave height maxima. These extreme peaks are then ordered by height and a suitable parametrized distribution function is fitted.

Details of the calculation method of extreme regimes have been previously described by Muri and El-Shaarawi (1986), Goda (1988), Serrano and Nieto (1992) and Carretero (1994).

In order to determine the size of the sample in the extreme analysis, a sensitivity analysis was carried out. In the final analysis we used 160 peaks, which corresponds to a mean of 4 peaks per year in the hindcast period. This seemed to be a reasonable number of severe storms per year and gave support to this choice of the number of peaks.

The Fisher-Tippett III distribution was selected to calculate the wave heights associated with long return periods (50, 100 and 200 years), since the analysis showed that it was the best distribution for most points. Fig. 9 shows the SWH in the Northeast Atlantic for a return period of 100 years.

Using the 40-year wave hindcast and the statistical techniques described above, the

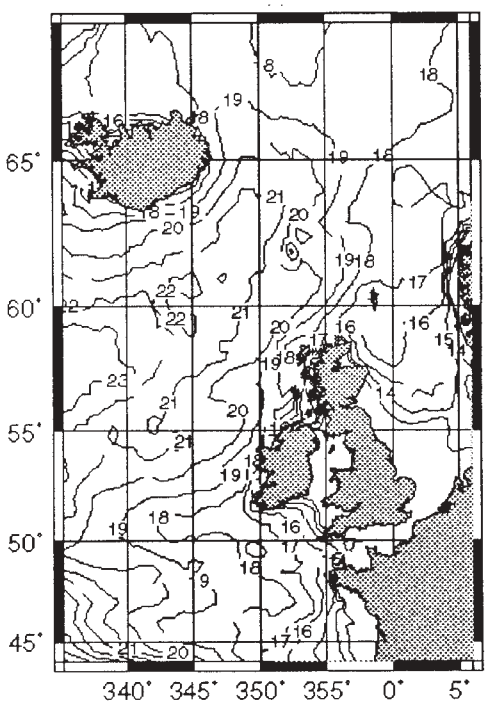


Fig.9: Spacial distribution of 100 years return SWH calculated with Fisher-Tippett distribution fitting 160 peaks over the period 1955-94.

extreme wave analysis was performed in slices of ten years: 1955-64, 1965-74, 1975-84, 1985-94. A comparison of the results for the long return period along the four decades can shed some light on the question of an increase of wave heights in the North Atlantic. As a collateral result of this analysis, it is possible to check the underlying assumption of stationarity of the statistical distribution of the extreme wave heights, which was used to describe the extreme wave occurrence in the future.

For the extreme analysis of the 10-year periods we used 50 peaks per slice (five peaks per year on the average) in order to have a sufficient number of peaks for the analysis.

This study was done in all the reduced area of the fine grid. The 100 year return period waves obtained for each decade showed a clear spatial pattern when fitted to a linear regression model, and the slope was calculated for every point in the grid. Two distinct regions can be identified: one between Iceland and Scotland, where a tendency towards higher extreme waves appeared, and the other southwest of Ireland, with a slight decrease (Fig. 10) in SWH.

Furthermore, the results of the extreme value analysis showed that the assumption of stationarity of the statistical distribution of the extreme wave heights cannot be verified. The method of return period calculation presented here does not take into account long-term changes in the extreme wave statistics. Due to this lack of stationarity and the existence of an upward trend, the return values derived from the 40 year hindcast (Fig 9) underestimate the actual values.

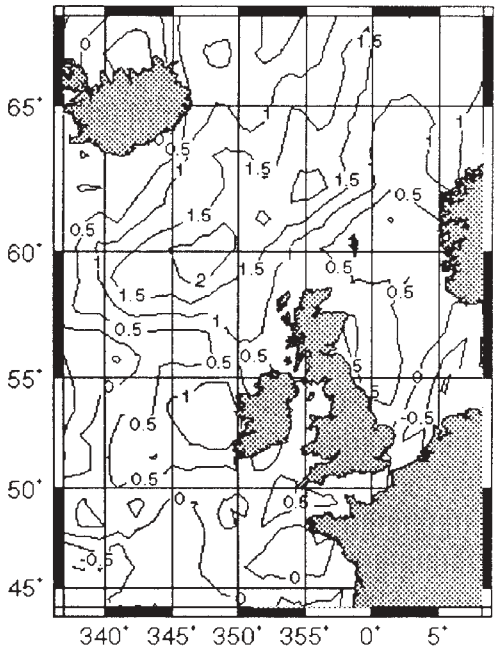


Fig.10: Spacial distribution of the trend of 100 years return SWH.

## 7 CONCLUSIONS

The wave data obtained within the WASA project make it possible to make more reliable predictions of changes in wave conditions in the North Atlantic since 1955 than other wave data sets allow. The analysis of the model output data revealed that statistics of significant wave height in the Northern North Sea and in the Norwegian Sea have undergone a steady increase in the last 40 years. Upper bound estimates were 3-4 cm/year for the 99th and 1-2 cm/year for the 90th annual percentiles. But average SWH increased during this time only at a rate of 0.25-0.75 cm/year, which correspond to about 0.2% per annum. Consequently, a continuous upward trend in average wave heights of the order of 1% or 2% per annum reported in recent years cannot be supported using WASA wave model output.

For the credibility of the trends in SWH and changes in wave climate obtained from the WASA hindcast data, the homogeneity (i.e. absence of non-physical signals) of the input wind fields play a key role. Without uniform quality throughout the entire hindcast period the predicted changes are unreliable. The results of the analysed hindcast data showed that the trends obtained from the WASA data are reliable for most of the fine grid model area, the area approximately between 70°N and 40°N and east of 20°W. The comparison between model data and observations in this area showed good agreement and gradients of the computed trends were smooth. Previous analyses have also shown that the DNMI winds are relatively homogeneous in this area (WASA, 1995).

The regional variability of the trends computed from the WASA data shows that wind speed and wave height tendencies are closely correlated. In areas where SWH increased (i.e. between Scotland and Iceland) wind speed increased as well. Consequently, the upward trend in significant wave height in the WASA hindcast can be explained by the increase in wind speed. However, further analysis of the derived data set is necessary to confirm the one-to-one correspondence between the increases of these two parameters. The increasing wind speed in the region of interest is also shown by the WASA investigations on changes of the geostrophic

wind (Alexandersson et al., 1997). The 90th percentile of the large-scale geostrophic wind has changed in the Torshavn-Aberdeen-Bergen triangle in the period 1960 to 1995 from about 26 m/s to about 30 m/s. The regional variability of our data indicates that a one-parameter description for the change of wind and wave climate is not appropriate. Nevertheless, it is interesting that the North Atlantic Oscillation index (NAO), which is built from the pressure difference between Iceland and Azores and is a major mode of atmospheric variability, has significantly intensified in the past 30 years (Hurrel, 1995). The analysis of wind and wave variability showed that variations in wave climate in the North Atlantic may be related to variations in the NAO (Kushnir et al., 1995). The WASA hindcast results supported the connection between NAO index and wind and wave climate in the North Atlantic over the last four decades. It follows that the wave climate changes in this period are explainable by the large scale feature of the circulation. In contrast to this, the stormy decades around and before 1900 were in general years with low or normal NAO index ( Alexandersson et al., 1997).

Interesting results with regard to the possible changes in the wave climate in the North Atlantic were given by the extreme value analysis. We used the well-established extreme value statistic to construct return periods for extreme waves from the 40 year hindcast. The underlying assumption is the stationarity of the extreme wave statistics over the involved return period. We checked this assumption for the return period calculation a posteriori in four slices of ten years. The results showed that the values of SWH for prescribed return periods have been growing during the last four decades in a distended area southeast of Iceland and in a small area west of Ireland. Southwest of Iceland a slight tendency towards smaller extreme waves appeared. These results fit very well with the analysis of percentiles of SWH performed in the fine grid area for the same period. The results of the extreme value analysis showed also that the presented method of return period calculation does not take into account the long term changes of the extreme wave statistics.

It is also notable that the anomalies found with climate change scenario computations (double concentration of CO2) show the same pattern as the trends of the extreme waves for the 40 year hindcast (Rider et al., 1996). There is an area south of Iceland with positive values for the anomalies (growth) and an area southwest of Ireland with negative values (decrease).

## 8 REFERENCES


Alexandersson, H., T. Schmith, K. Iden and H. Tuomenvirta, 1997: Long-term trend variations of the storm climate over NW Europe, submitted to GAOS.

Bacon, S. and D.J.T. Carter, 1991: Wave climate changes in the North Atlantic and the North Sea, Int. J. Climat. 11, 545-558.

Barratt, M.J., 1991: Waves in the North East Atlantic, Offshore Technology Report OTI 90 545, HMSO.

Bouws, E., D. Jannink and G.J. Komen, 1996: The increasing wave height in the North Atlantic Ocean, BAMS, 77 (10), 2275-2277.

Carretero, Juan C., 1994: An extreme wave analysis for the Atlantic Coast of Spain, Clima Marítimo No. 55.

Carter, D.J.T. and L. Draper, 1988: Has the Northeast Atlantic become rougher?, Nature 332, 494.

Goda, Y., 1988: On the methodology of Selecting Design Wave Height, 21. int. Conf. Coastal Engineering (ICCE).

Günther, H., S. Hasselmann, P.A.E.M. Jansen, 1992: The WAM Model cycle 4, DKRZ Technical Report No. 4.

Günther, H., W. Rosenthal, M. Stawarz, J.C. Carretero, M. Gomez, I. Lozano, O. Serrano, M. Reistad, 1997: The wave climate of the Northeast Atlantic over the period 1955-1994: the WASA wave hindcast. submitted to GAOS.

Hogben, N., 1994: Increase in wave heights over the North Atlantic: A review of the evidence and some implications for the naval architect, Trans Roy. Inst. Naval Arch., 93-101.

Hurrel, J.W., 1995: Decadal trends in the North Atlantic Oscillation: Regional temperature and precipitation, Science 269, p 676-679.

Jones, P.D., 1995: The Instrumental Data Record: Its Accuracy and Use in Attempts to Identify the "CO2 Signal". In: H. von Storch and A. Navarra (eds) "Analysis of Climate Variability: Applications of Statistical Techniques", Springer Verlag, 53-76, (ISBN 3-540-58918-X).

Karl, T.R., R.G. Quayle and P.Y. Groisman, 1993: Detecting climate variations and change: New challenges for observing and data management systems. J. Climate 6, 1481-1494.

Komen, G.J., L. Cavaleri, M. Donelan, K. Hasselmann, S. Hasselmann and P.A.E.M. Jansen, 1994: Dynamics and Modelling of Ocean Waves, Cambridge University Press, 532 pp.

Kushnir, Y., V.J. Cardone, J.G. Greenwood and M.A. Cane, 1995: Link between North Atlantic climate variability of surface wave height and sea level pressure, Proc. Fourth Int. Workshop on Wave Hindcasting and Forecasting, Banff, Alberta, Canada, Enviroment Canada, 59-64.

Neu, H.J.A., 1984: Interannual variations and longer-term changes in the sea state of the North Atlantic from 1970 to 1982, J. Geophys. Res. 89 (C4), 6397-6402.

Reistad, M., K.A. Iden, 1995: Updating, correction and evaluation of a hindcast data base of air pressure, winds and waves for the North Sea, Norwegian Sea and the Barents Sea, Tech. Rep. 9, Det Norske Meteorologiske Institutt.

Rider, K., G.J. Komen, J.J. Beersma, 1996: Simulation of the response of the ocean waves in the North Atlantic and the North Sea to CO2 doubling in the atmosphere. KNMI Scientific Report WR 96-05.

Serrano, O. and J.C. Nieto, 1992: Análisis extremal Técnicas de simulatión estadística, Clima Marítimo No. 53.

WAMDI group, S. Hasselmann, K. Hasselmann, E. Bauer, P.A.E.M. Jansen, G.J. Komen, L. Bertotti, P. Lionello, A. Guillaume, V.C. Cardone, J.A. Greenwood, M. Reistad, L. Zambresky and J.A. Ewing, 1988: The WAM Model - A Third Generation Ocean Wave Prediction Model, J. Phys. Oceanogr., Vol. 18, 1775-1810.

WASA group, K. Iden, H. Reichardt, M. Reistad, W. Rosenthal, A. Ruiz de Elvira and H. von Storch, 1994: Comment on "Increase in Wave Heights over the North Atlantic: A Review of the Evidence and some Implications for the Naval Architect" by N. Hogben, Trans Roy. Inst. Naval Arch., 107-110.

WASA group, 1995: The WASA project: Changing Storm and Wave Climate in the Northeast Atlantic and adjacent seas?, Proc. 4th International Workshop on Wave Hindcasting and Forecasting, Oct 16-20, 1995, Banff, Alberta, Canada, 31-44.

# EVALUATION OF NCEP/NCAR REANALYSIS PROJECT MARINE SURFACE WIND PRODUCTS FOR A LONG TERM NORTH ATLANTIC WAVE HINDCAST

Andrew T. Cox[1], Vincent J. Cardone[1] and Val R. Swail[2]

[1]Oceanweather, Inc.
Cos Cob, CT

[2]Environment Canada
Downsview, Ontario

## 1. INTRODUCTION

This study is a part of a larger research program, described elsewhere in this volume by Swail *et al.* (1998), to utilize the NCEP reanalysis (NRA) products (Kalnay *et al.*, 1996) to produce a high-quality homogeneous long-term wind and wave database for assessment of trend and variability in the wave climate of the North Atlantic (NA). This paper describes the evaluation phase of the program. In the evaluation phase we compared three alternative NCEP sources of marine boundary layer winds: (1) the 1000 mb wind fields on the 2.5° latitude-longitude grid; (2) the lowest sigma level (0.995) wind fields on the 2.5° latitude-longitude grid; (3) the 10 m surface wind fields on the Gaussian grid. Since the reanalysis process itself involved, at least to some extent, the assimilation of measured surface marine data into each of these products, it is not possible to derive an independent assessment of the accuracy of the alternative wind fields only from comparisons with wind measurements.

An alternative evaluation approach is suggested by recent studies with advanced third generation (3-G) ocean wave prediction models (Cardone *et al.*, 1995). Those studies show that, when such models are driven by accurate surface wind fields, nearly perfect simulations of the principal scale and shape (significant wave height and spectral peak period) properties of the surface gravity wave field result. On the other hand, if erroneous winds are used, the ocean response is modelled with obvious bias and/or scatter when compared to wave measurements. Copious high quality wave measurements have been provided within the past two decades from buoys moored near the continental margins and satellite altimeters which provide full-basin coverage. Our approach, therefore, is to hindcast the surface wave field in the North Atlantic Ocean from alternative NRA surface marine wind fields for selected months using a proven 3-G wave model, and then to assess the errors in the wind fields through a comprehensive evaluation of the resulting wave hindcasts against all available wave measurements.

The best of the NRA alternatives identified in this evaluation provides a background wind field for use in the production phase of the hindcast. In the production phase of the long term hindcast, which is also outlined briefly herein, the NRA wind fields are improved by adding details of the evolution of tropical and extratropical cyclone wind field features missed in the NRA objective analyses. The efficacy of this approach is also illustrated briefly in this paper. A preliminary evaluation of the first decade or so of production hindcasts is given at this conference by Swail *et al.* (1998).

## 2. EVALUATION METHODOLOGY

Eight months were chosen from the available period, 1979 through 1995, for the wind field evaluation. Months 8103 and 8301 were chosen for having the highest and lowest values, respectively, of the mean North Atlantic atmospheric zonal circulation index described by Kushnir (1994). The months 9110, 9303 and 9504 each contained extreme western North Atlantic storms hindcast in recent studies (Cardone *et al.*, 1996 and Swail *et al.*, 1995), while 9509 was chosen as a hurricane dominated month. The remaining months (7906, 8808) were added to provide more even representation over time of the part of the NRA available at the time this evaluation was carried out.

Wind fields for each month were interpolated from the NRA source grids onto a 0.625° by 0.833° latitude-longitude wave model grid covering the North Atlantic Ocean (see Swail *et al.*, 1998) using the IOKA (Interactive Objective Kinematic Analysis)

algorithm (Cox *et al.*, 1995), and then time interpolated to a one-hour time step. Oceanweather's third generation (3-G) wave model (Khandekar *et al.*, 1994) was used in deep water mode for all hindcasts. Wave and interpolated wind results were then compared (time series, scatter plots and statistics) to all available deep-water buoys (U.S., Canadian, European), offshore North Sea platforms, U.S. C-MAN (Coastal Marine Automated Network) and ERS-1/2 altimeter and scatterometer measurements. All measured winds were adjusted for height and stratification to 10 meter reference height and neutral stability, while hourly wind and wave measurements were smoothed over ±1 hours using equal weights (1,1,1). ERS-1/2 altimeter and scatterometer measurements were extracted from Ifremer's CD-ROM set using the recommended quality controls, temporally binned within a 6-hour window, and then spatially binned onto the wave model grid every 6 hours.

## 3. EVALUATION RESULTS

The results of the statistical comparisons of the three sets of NCEP winds and the waves they produced with all buoys, platforms and C-MAN stations on the western and eastern Atlantic continental margins, and with ERS-1/2 satellite altimeter winds and waves are summarized in Tables 1 and 2. Table 1 shows statistical comparisons for March 1993 - the other evaluation months showed generally comparable results. While the statistics for correlation coefficient and scatter index for winds were largely similar among all wind fields, there were clear advantages in bias, scatter index, and ratio for the waves produced by the surface wind fields. From these results it was clear that there was no advantage in selecting the 1000 mb winds; therefore the 1000 mb winds were dropped from further consideration. Table 2 shows the bias and scatter index comparisons for all 8 evaluation months versus the *in situ* measurements, and for the 3 months for which ERS-1/2 altimeter data were available. It is clear from Table 2 that the best wind field was the surface wind. The bias for the surface wind field was generally lower for both winds and resulting waves; the scatter indices for winds were similar for both data sets, although the independent satellite comparisons always favored the surface winds. The scatter index for waves hindcast from the surface winds was always superior.

While the NCEP surface wind fields produce the least biased and most skillful wave hindcasts overall, the scatter index values are much higher than found in hindcast studies of continuous periods (Cardone *et al.*, 1995) or storms (Cardone *et al.*, 1996) where kinematically reanalyzed wind fields are used to drive the wave model. The hindcasts were also found to systematically underestimate storm peaks. The overall skill in the hindcasts is improved and the underestimation of storm peaks is greatly reduced when the NCEP surface winds are kinematically reanalyzed with the aid of an interactive Wind Workstation. Figure 1 (left) shows the impact of this kinematic reanalysis at a buoy off the US east coast during SWADE IOP-1 relative to the hindcast made with unmodified NRA surface winds. It was also found that tropical storms are poorly resolved in the NCEP wind fields. Figure 2 compares the NCEP winds and final IOKA winds during Hurricane Emily (September 1993). The improvement is achieved through a combination of interactive kinematic analysis of the wind fields in conjunction with winds generated by a proven tropical cyclone model. The resulting wave comparison at buoy 44014 is shown in Figure 1 (right).

## 4. PRODUCTION PHASE

The production phase, whereby wave hindcasts will be carried out for the entire 40 years of the NCEP reanalysis period, is described in detail by Swail *et al.* (1998); that paper also includes a preliminary evaluation of the climatological aspects of the production wave hindcasts completed to date. Presented here is a description of the quality control products generated by the hindcast which show the impact of the IOKA methodology.

Quality control of the production hindcast consists mainly of comparisons of the wave hindcast against measurements evaluated against 12 deep-water buoys (Figure 3) and ERS 1/2 altimeter wave measurements. Table 3 shows the standard difference statistics computed for a typical month (9211) based on differences between 6-hourly hindcast and measurement time series. Note that the mean difference in wave height over all buoys is only 10 cm and scatter indices are in the range 0.15-0.21 at most buoys, which are comparable to those exhibited for peak-peak comparisons in the very best hindcast studies. The small negative bias in hindcast wave period is due at least in part to the wave model. Several other hindcast studies carried out with 3-G wave models (e.g. Cardone *et al.*, 1996) also show

that most variants of the 3-G wave model tend to underpredict wave period.

Figure 4 shows a typical example of the time series comparison of wind speed, wind direction, wave height, wave period and wave direction for buoy 44137 during December 1992. The excellent agreement in the winds is a consequence of the IOKA, which has naturally assimilated the buoy observation into each 6-hourly analysis. The buoy wave height and period (there is no wave direction measurement at this buoy) time series, however, provides an independent assessment of the wave hindcast. Mean and maximum monthly wind speed and wave height fields are also extracted as part of the quality control process (Figure 5). Finally, the wave model grid-averaged altimeter wave measurements are binned every 0.5 meters and compared with the matching hindcast (within 3-hours) waves as shown in Figure 6, which shows all wave height residuals for bins with greater than 15 comparisons. While the buoy comparisons indicate the skill in the hindcasts near the continental margins, the altimeter samples the entire North Atlantic basin more or less evenly in space and time. It is encouraging, therefore, that wave hindcasts shows very good agreement with the altimeter throughout the range of wave heights. The mean difference in wave height over all 10,910 observations in this month is only -0.04 m and within ± 20 cm in most individual bins. Hindcast wave heights under 1.5 meters show a slight systematic overestimation which may be attributed to a natural tendency for the gridded wind and wave fields to fail to resolve small areas of calm winds and seas.

Given the emphasis in the IOKA on specification of storm wind fields, it is interesting to compare the production wave hindcasts with wave hindcasts made with the unmodified NRA surface winds during storm peaks. Figure 7 shows the comparison of storm peaks greater than 3 meters (as measured by the buoy) at buoy 44138 for the 4 overlapping evaluation and production months.

## 5. CONCLUSIONS

Three alternative NCEP reanalysis marine boundary layer wind fields were evaluated by hindcasting the surface wave field in the North Atlantic from each, and then assessing the errors in the wind fields through evaluation of the resulting wave hindcasts against wave measurements. The NCEP surface 10 m wind fields produced the least biased and most skillful wave hindcasts overall, and also produced the best wind field comparisons when compared to independent wind data from ERS 1/2. However, the skill in the hindcasts is greatly enhanced, particularly in storm peaks, when the NCEP surface winds are kinematically reanalyzed with the aid of interactive techniques in general, and, for tropical storms specifically, of a proven tropical cyclone wind model. In the production phase of this study, currently underway and scheduled for completion in late 1998, all wind fields for the 40 years are kinematically reanalyzed as described above.

## 6. REFERENCES


Cardone, V.J., H.C. Graber, R.E. Jensen, S. Hasselmann, M.J. Caruso, 1995. *In search of the true surface wind field in SWADE IOP-1: ocean wave modelling perspective*. The Global Ocean Atmopshere System, 3, 107-150.

Cardone, V.J., R.E. Jensen, D.T. Resio, V.R. Swail and A.T. Cox, 1996. *Evaluation of contemporary ocean wave models in rare extreme events: "Halloween storm of October, 1991; "storm of the century" of March, 1993"*. J. Atmos. and Oceanic Tech., Vol. 13, No. 1, p. 198-230.

Cox, A.T., J.A. Greenwood, V.J. Cardone and V.R. Swail, 1995. *An interactive objective kinematic analysis system.* Proceedings 4th International Workshop on Wave Hindcasting and Forecasting, October 16-20, 1995, Banff, Alberta, p. 109-118.

Kalnay, E., *et al*, 1996. *The NCEP/NCAR 40-Year reanalysis project*. Bull. AMS, 77(3), 437-471.

Khandekar, M.L., R. Lalbeharry and V.J. Cardone. *The performance of the Canadian Spectral Ocean Wave Model (CSOWM) during the Grand Banks ERS-1 SAR wave spectra validation experiment.* Atmosphere-Ocean 31 (1) 1994, pp. 31-60.

Kushnir, Y., 1994. *Interdecadal variations in North Atlantic sea surface temperature and associated atmospheric conditions*. J. Climate, 7, 141-157.

Swail, V.R., M. Parsons, B.T. Callahan and V.J. Cardone, 1995. *A revised extreme wave climatology for the east coast of Canada*. Proceedings 4th International Workshop on Wave Hindcasting and

Forecasting, October 16-20, 1995, Banff, Alberta, p. 81-91.

Swail, V.R., V.J. Cardone and A.T. Cox, 1998. *A long term North Atlantic wave hindcast.* Proc. 5th International Workshop on Wave Hindcasting and Forecasting, Melbourne, FL, January 26-30, 1998.

| Wind Field | Bias (H-M) m (m/s) | rms error m (m/s) | Scatter Index | Ratio | Corr. Coeff. |
|---|---|---|---|---|---|
| Surface | 0.0 (0.0) | 0.98 (2.74) | 0.44 (0.35) | 0.52 (0.51) | 0.83 (0.82) |
| Sigma | 1.0 (2.0) | 1.65( 3.36) | 0.60 (0.34) | 0.85 (0.79) | 0.81 (0.83) |
| 1000 mb | 0.6 (1.2) | 1.36 (3.13) | 0.54 (0.36) | 0.76 (0.68) | 0.78 (0.80) |

Table 1. Comparison wave summary statistics (wind statistics in brackets) for March 1993 for NCEP surface, sigma and 1000 mb wind fields. (Scatter index is standard deviation/ mean measurement; ratio is percentage of points above/below the 1:1 line)

| | WIND SPEED | | | | SIGNIFICANT WAVE HEIGHT | | | |
|---|---|---|---|---|---|---|---|---|
| | BIAS (H-M) | | SCATTER INDEX | | BIAS (H-M) | | SCATTER INDEX | |
| | Surface | Sigma | Surface | Sigma | Surface | Sigma | Surface | Sigma |
| Vs in-situ | | | | | | | | |
| 7906 | ***-0.4*** | 1.1 | ***0.44*** | 0.45 | ***0.0*** | 0.4 | ***0.56*** | 0.60 |
| 8103 | ***-0.4*** | 1.2 | 0.27 | 0.27 | -0.4 | 0.4 | ***0.27*** | 0.33 |
| 8301 | ***0.1*** | 0.8 | 0.27 | ***0.23*** | -0.3 | ***0.1*** | ***0.27*** | 0.29 |
| 8808 | ***0.2*** | 2.2 | ***0.48*** | 0.50 | ***-0.2*** | 0.4 | ***0.51*** | 0.61 |
| 9110 | ***-0.5*** | 1.4 | 0.39 | ***0.37*** | -0.4 | 0.4 | ***0.61*** | 0.72 |
| 9303 | ***0.0*** | 2.0 | 0.35 | ***0.34*** | ***0.0*** | 1.0 | ***0.44*** | 0.60 |
| 9504 | -1.2 | ***0.3*** | 0.38 | ***0.35*** | ***-0.2*** | 0.4 | ***0.44*** | 0.46 |
| 9509 | -1.2 | ***0.5*** | 0.36 | ***0.32*** | -0.4 | ***0.2*** | ***0.36*** | 0.43 |
| vs altimeter | | | | | | | | |
| 9110 | ***0.1*** | 1.4 | ***0.30*** | 0.34 | ***0.0*** | 0.8 | ***0.34*** | 0.54 |
| 9303 | ***0.6*** | 2.2 | ***0.33*** | 0.37 | ***0.1*** | 1.2 | ***0.45*** | 0.63 |
| 9504 | ***0.2*** | 1.6 | ***0.3*** | 0.33 | ***0.1*** | 0.9 | ***0.41*** | 0.56 |

Table 2. Comparison of wind and wave bias and scatter index values by month for NCEP re-analysis sigma and surface winds (bold italics show closer agreement with measurements)

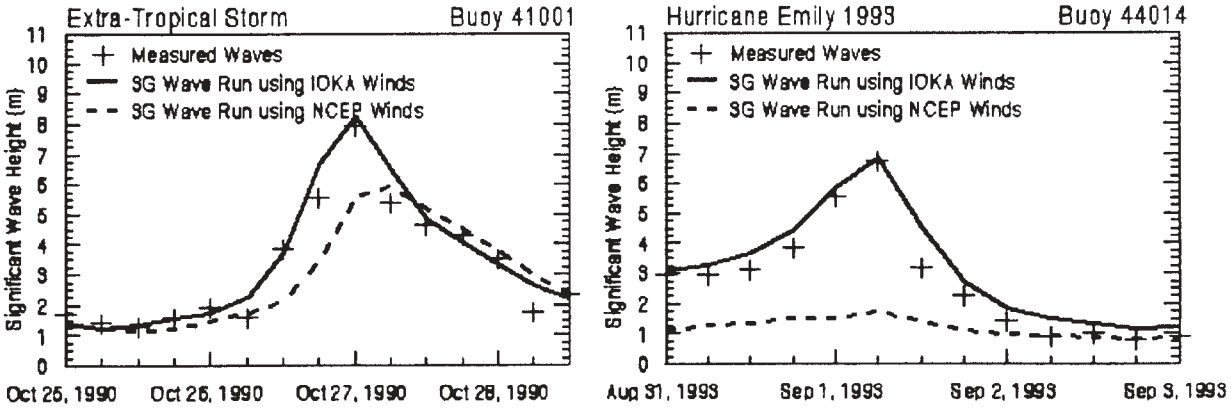


Figure 1. Effect of kinematic analysis on wave hindcast

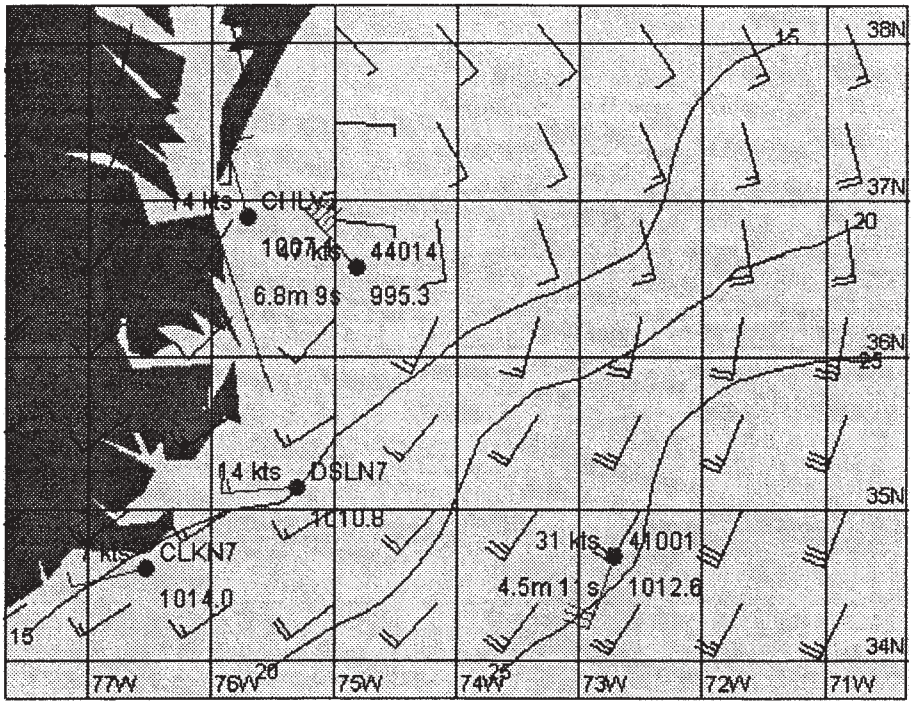


Figure 2a. NCEP surface wind field (unmodified).

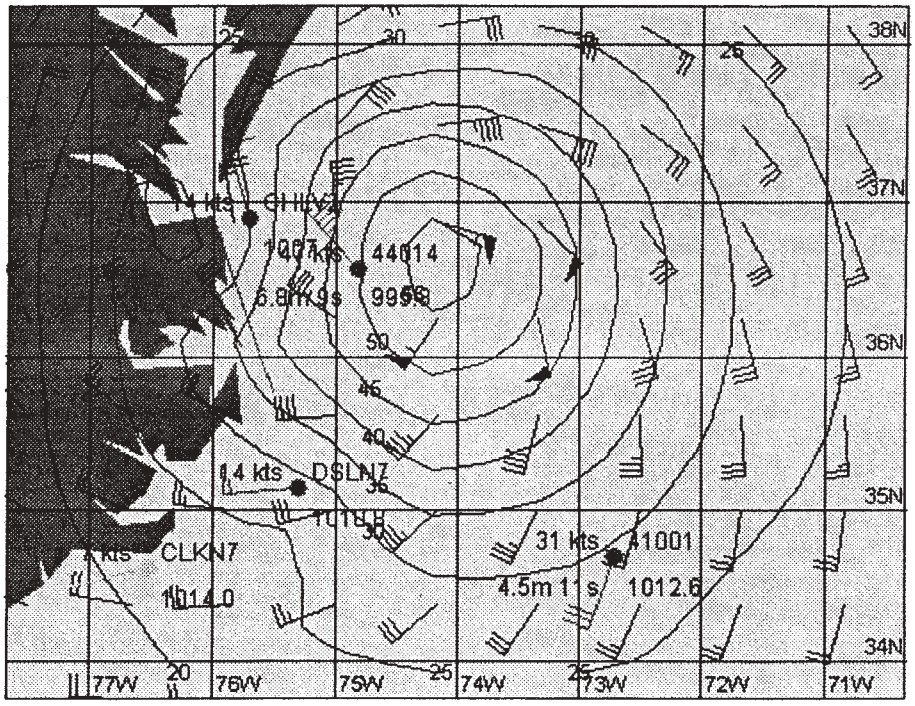


Figure 2b. IOKA final wind field with tropical vortex model winds incorporated.

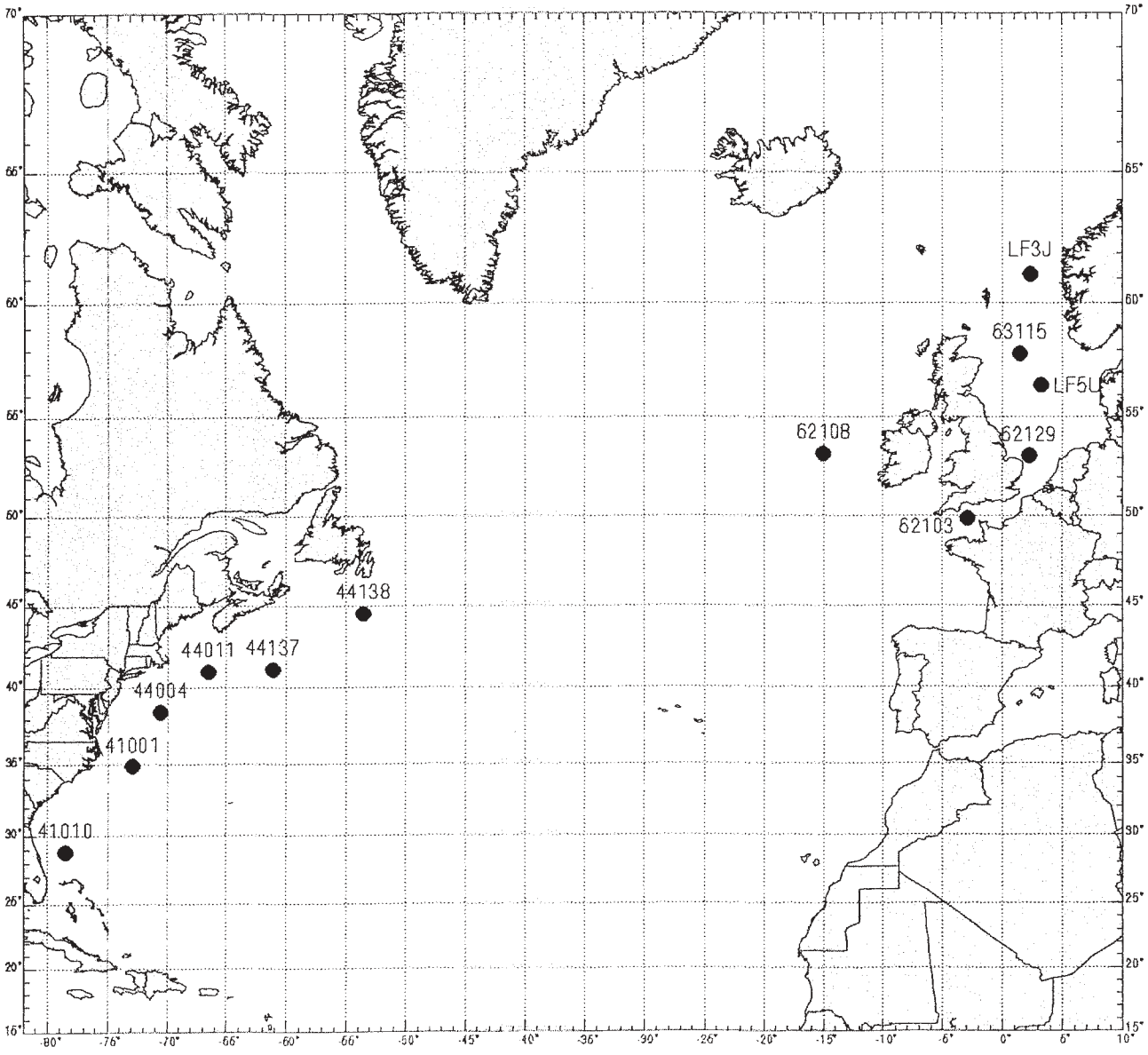


Figure 3. Buoy locations used in production verification.

**AES North Atlantic Reference Wind and Wave Climatology**
**Hindcast Period: 1992100100 through 1992110100**

| | Station | Number of Pts | Mean Meas | Mean Hind | Diff (H-M) | RMS Error | Stnd Dev | Scat Index | Ratio | Corr Coeff |
|---|---|---|---|---|---|---|---|---|---|---|
| Wind Spd. (m/s) | 41001 | 125 | 7.79 | 7.78 | -0.01 | 0.52 | 0.52 | 0.07 | 0.54 | 0.99 |
| Wind Dir. (deg) | 41001 | 125 | 294.08 | 293.67 | 0.35 | N/A | 5.95 | 0.02 | N/A | N/A |
| Sig Wave Ht (m) | 41001 | 125 | 2.00 | 2.07 | 0.07 | 0.33 | 0.32 | 0.16 | 0.66 | 0.95 |
| Ave. Period (s) | 41001 | 125 | 5.81 | 5.39 | -0.41 | 0.65 | 0.51 | 0.09 | 0.20 | 0.83 |
| Wind Spd. (m/s) | 41010 | 125 | 7.08 | 7.01 | -0.07 | 0.24 | 0.23 | 0.03 | 0.33 | 1.00 |
| Wind Dir. (deg) | 41010 | 125 | 40.30 | 47.79 | -0.25 | N/A | 3.99 | 0.01 | N/A | N/A |
| Sig Wave Ht (m) | 41010 | 125 | 1.94 | 1.98 | 0.04 | 0.32 | 0.32 | 0.16 | 0.64 | 0.96 |
| Ave. Period (s) | 41010 | 125 | 6.09 | 5.56 | -0.52 | 0.76 | 0.55 | 0.09 | 0.18 | 0.90 |
| Wind Spd. (m/s) | 44004 | 125 | 7.63 | 7.66 | 0.03 | 0.32 | 0.31 | 0.04 | 0.54 | 1.00 |
| Wind Dir. (deg) | 44004 | 125 | 332.41 | 310.77 | 0.42 | N/A | 4.52 | 0.01 | N/A | N/A |
| Sig Wave Ht (m) | 44004 | 125 | 1.90 | 1.97 | 0.07 | 0.38 | 0.38 | 0.20 | 0.63 | 0.90 |
| Ave. Period (s) | 44004 | 125 | 5.72 | 5.27 | -0.45 | 0.93 | 0.81 | 0.14 | 0.22 | 0.58 |
| Wind Spd. (m/s) | 44011 | 125 | 7.34 | 7.39 | 0.05 | 0.17 | 0.16 | 0.02 | 0.58 | 1.00 |
| Wind Dir. (deg) | 44011 | 125 | 339.35 | 297.73 | 0.78 | N/A | 3.20 | 0.01 | N/A | N/A |
| Sig Wave Ht (m) | 44011 | 125 | 1.87 | 2.01 | 0.15 | 0.32 | 0.29 | 0.15 | 0.68 | 0.93 |
| Ave. Period (s) | 44011 | 125 | 5.77 | 5.41 | -0.36 | 0.69 | 0.59 | 0.10 | 0.25 | 0.65 |
| Wind Spd. (m/s) | 44137 | 125 | 9.79 | 9.74 | -0.05 | 0.32 | 0.32 | 0.03 | 0.34 | 1.00 |
| Wind Dir. (deg) | 44137 | 125 | 340.56 | 299.26 | 0.83 | N/A | 8.22 | 0.02 | N/A | N/A |
| Sig Wave Ht (m) | 44137 | 125 | 2.73 | 2.80 | 0.07 | 0.56 | 0.56 | 0.21 | 0.58 | 0.90 |
| Peak Period (s) | 44137 | 125 | 9.92 | 8.73 | -1.18 | 3.53 | 3.33 | 0.34 | 0.38 | 0.11 |
| Wind Spd. (m/s) | 44138 | 124 | 8.66 | 8.65 | -0.01 | 0.22 | 0.22 | 0.03 | 0.50 | 1.00 |
| Wind Dir. (deg) | 44138 | 124 | 354.68 | 290.63 | -0.52 | N/A | 1.96 | 0.01 | N/A | N/A |
| Sig Wave Ht (m) | 44138 | 118 | 2.64 | 2.87 | 0.23 | 0.79 | 0.75 | 0.29 | 0.64 | 0.86 |
| Peak Period (s) | 44138 | 118 | 10.18 | 9.05 | -1.13 | 3.99 | 3.82 | 0.38 | 0.40 | -0.12 |
| Wind Spd. (m/s) | 62108 | 123 | 9.86 | 9.83 | -0.03 | 0.16 | 0.15 | 0.02 | 0.33 | 1.00 |
| Wind Dir. (deg) | 62108 | 123 | 350.76 | 333.74 | -0.08 | N/A | 1.94 | 0.01 | N/A | N/A |
| Sig Wave Ht (m) | 62108 | 123 | 3.15 | 3.22 | 0.07 | 0.58 | 0.57 | 0.18 | 0.61 | 0.95 |
| Ave. Period (s) | 62108 | 123 | 7.74 | 6.30 | -1.45 | 1.82 | 1.10 | 0.14 | 0.07 | 0.74 |
| Wind Spd. (m/s) | 63115 | 7 | 11.45 | 9.33 | -2.11 | 4.27 | 3.71 | 0.32 | 0.43 | 0.36 |
| Wind Dir. (deg) | 63115 | 7 | 359.07 | 306.43 | -21.42 | N/A | 50.51 | 0.14 | N/A | N/A |
| Sig Wave Ht (m) | 63115 | 7 | 2.29 | 2.25 | -0.03 | 0.86 | 0.86 | 0.38 | 0.71 | 0.66 |
| Ave. Period (s) | 63115 | 7 | 5.86 | 5.28 | -0.58 | 1.21 | 1.06 | 0.18 | 0.43 | 0.12 |
| Wind Spd. (m/s) | LF3J | 104 | 7.35 | 8.06 | 0.71 | 1.03 | 0.75 | 0.10 | 0.81 | 0.99 |
| Wind Dir. (deg) | LF3J | 104 | 2.34 | 36.98 | 3.09 | N/A | 12.44 | 0.03 | N/A | N/A |
| Sig Wave Ht (m) | LF3J | 95 | 2.31 | 2.52 | 0.21 | 0.53 | 0.48 | 0.21 | 0.65 | 0.93 |
| Ave. Period (s) | LF3J | 95 | 6.90 | 5.97 | -0.93 | 1.19 | 0.74 | 0.11 | 0.11 | 0.74 |
| Wind Spd. (m/s) | LF5U | 111 | 7.42 | 8.08 | 0.66 | 1.17 | 0.96 | 0.13 | 0.77 | 0.95 |
| Wind Dir. (deg) | LF5U | 111 | 355.96 | 333.63 | -2.02 | N/A | 12.04 | 0.03 | N/A | N/A |
| Sig Wave Ht (m) | LF5U | 110 | 2.10 | 2.12 | 0.02 | 0.38 | 0.38 | 0.18 | 0.54 | 0.91 |
| Ave. Period (s) | LF5U | 110 | 5.73 | 5.33 | -0.40 | 0.73 | 0.62 | 0.11 | 0.31 | 0.74 |
| Wind Spd. (m/s) | ALL BUOYS | 1094 | 8.14 | 8.25 | 0.11 | 0.65 | 0.65 | 0.08 | 0.52 | 0.99 |
| Wind Dir. (deg) | ALL BUOYS | 1094 | 341.72 | 325.42 | 0.17 | N/A | 8.02 | 0.02 | N/A | N/A |
| Sig Wave Ht (m) | ALL BUOYS | 1078 | 2.29 | 2.39 | 0.10 | 0.49 | 0.48 | 0.21 | 0.63 | 0.93 |
| Period (s) | ALL BUOYS | 1078 | 7.09 | 6.33 | -0.76 | 2.01 | 1.86 | 0.26 | 0.24 | 0.66 |

Table 3. Verification statistics for 12 buoys.

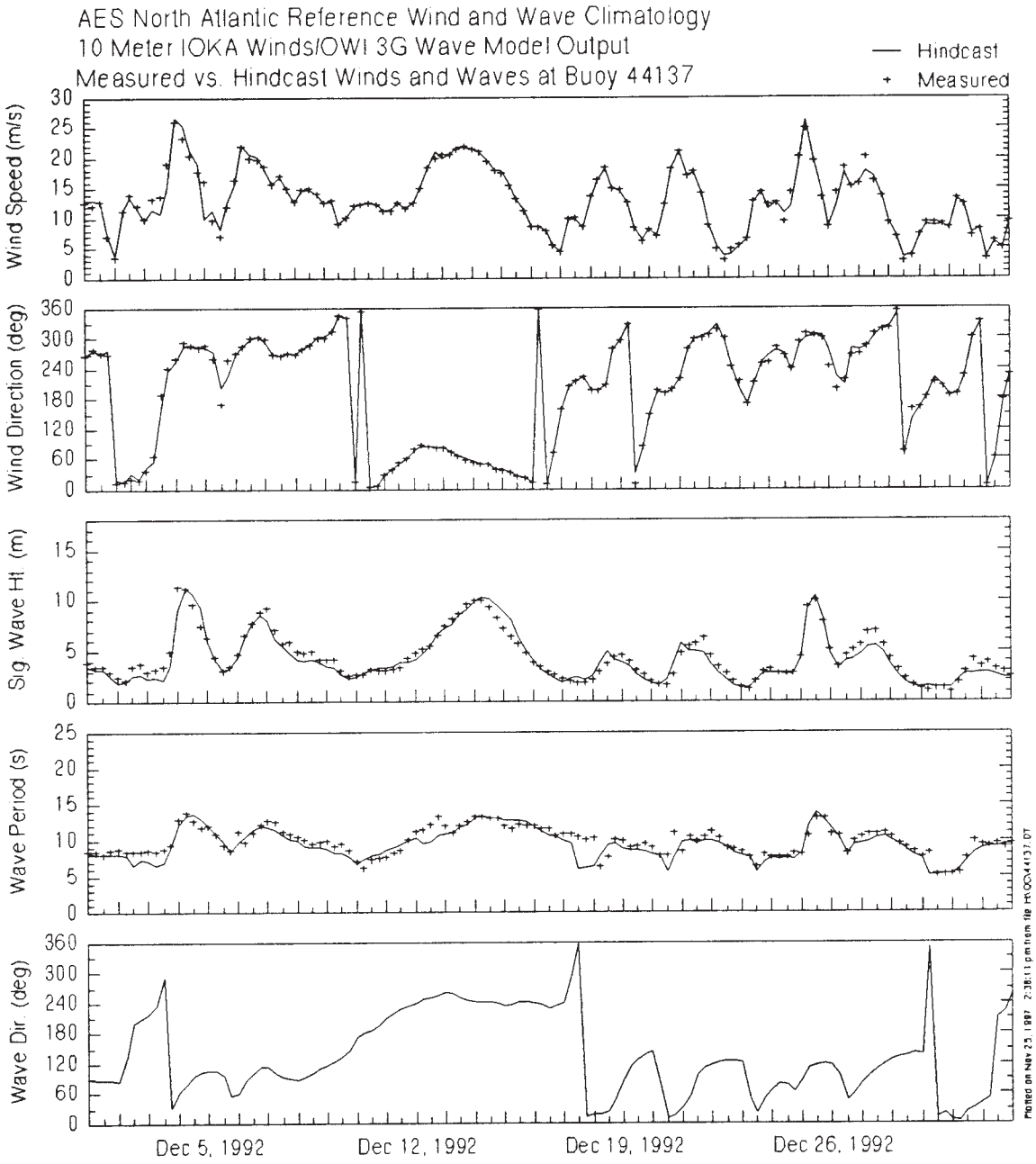


Figure 4. Time series comparison at Buoy 44137 during December 1992.

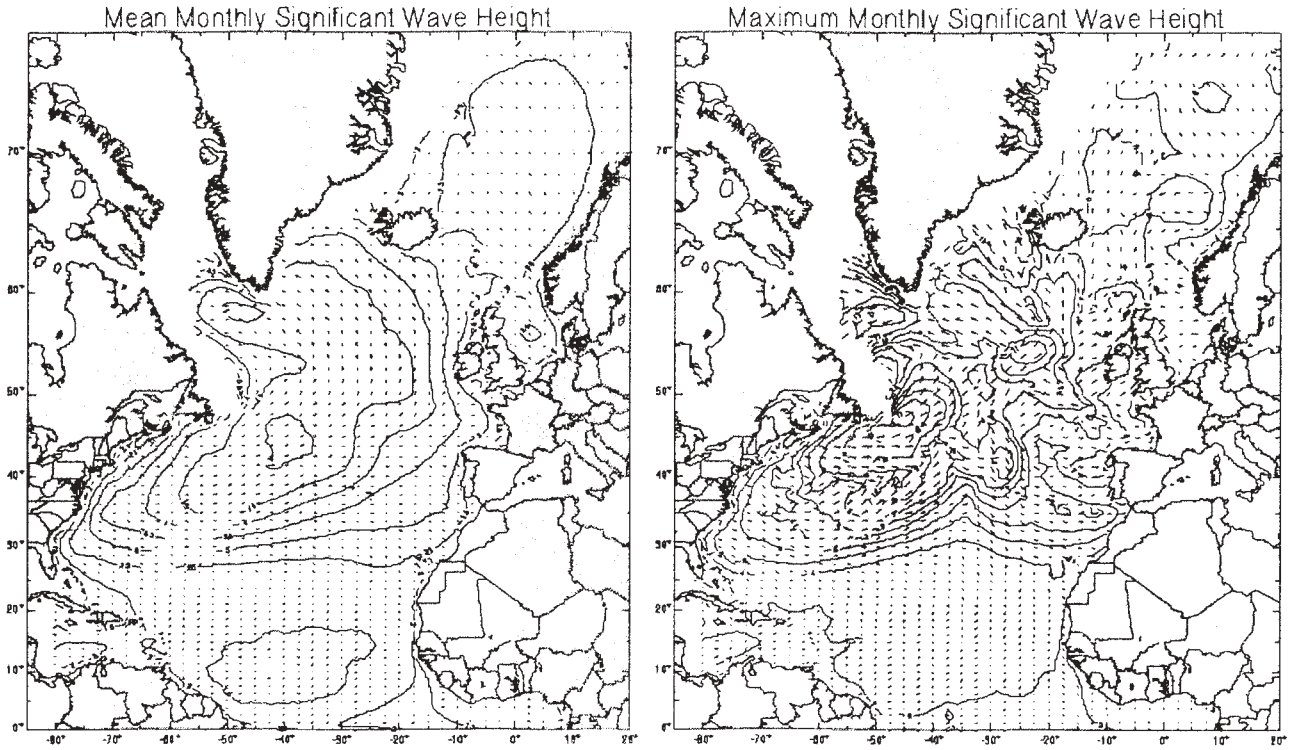


Figure 5. Mean and maximum wave heights for January 1985.

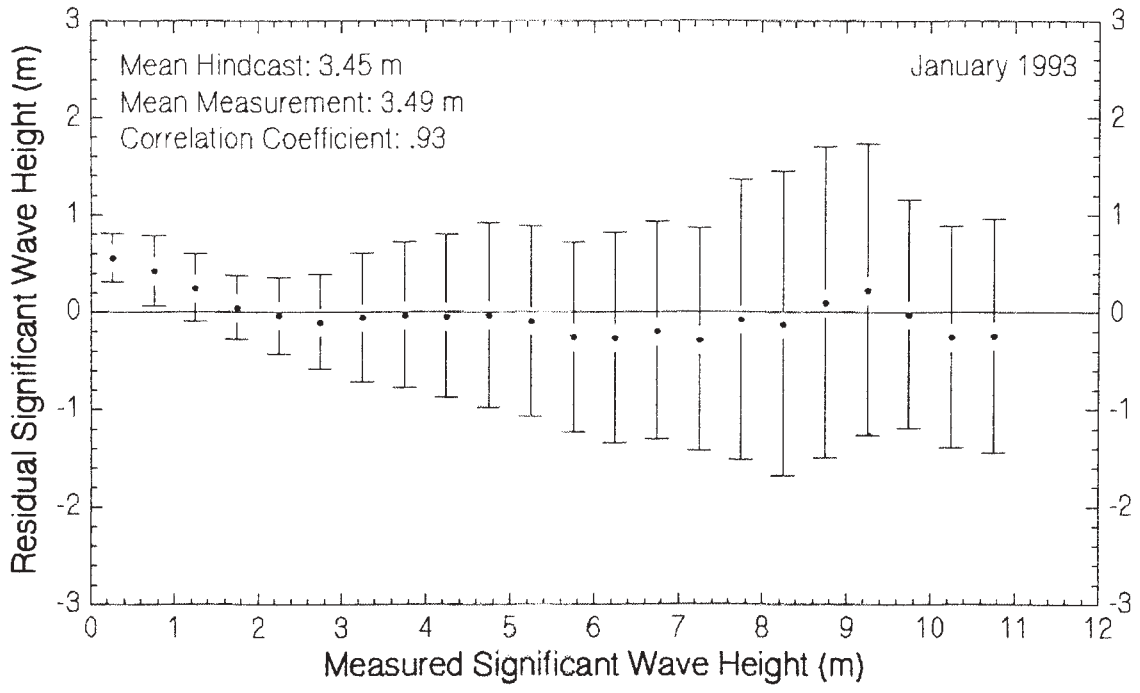


Figure 6. Comparison of hindcast vs. ERS altimeter significant wave height residuals in .5 meter bins.



AUTHOR INDEX
TABLE OF CONTENTS

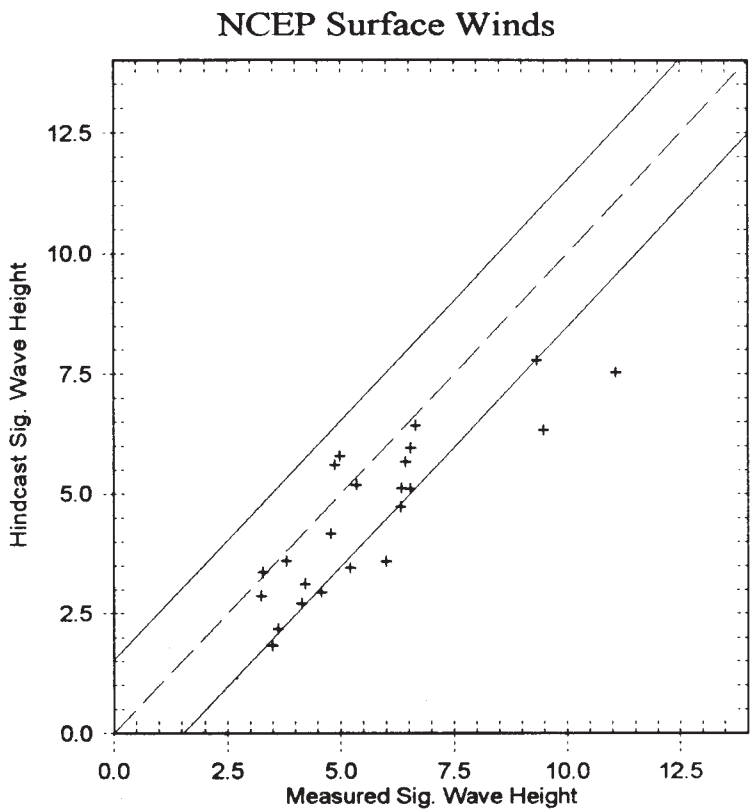


| | |
|---|---|
| Total Points: | 23 |
| Mean X: | 5.666 |
| Mean Y: | 4.569 |
| Mean Diff: | -1.097 |
| Root Mean Square: | 1.524 |
| Standard Dev.: | 1.058 |
| Scatter Index: | 0.187 |
| Ratio: | 0.130 |
| Correlation Coeff: | 0.852 |

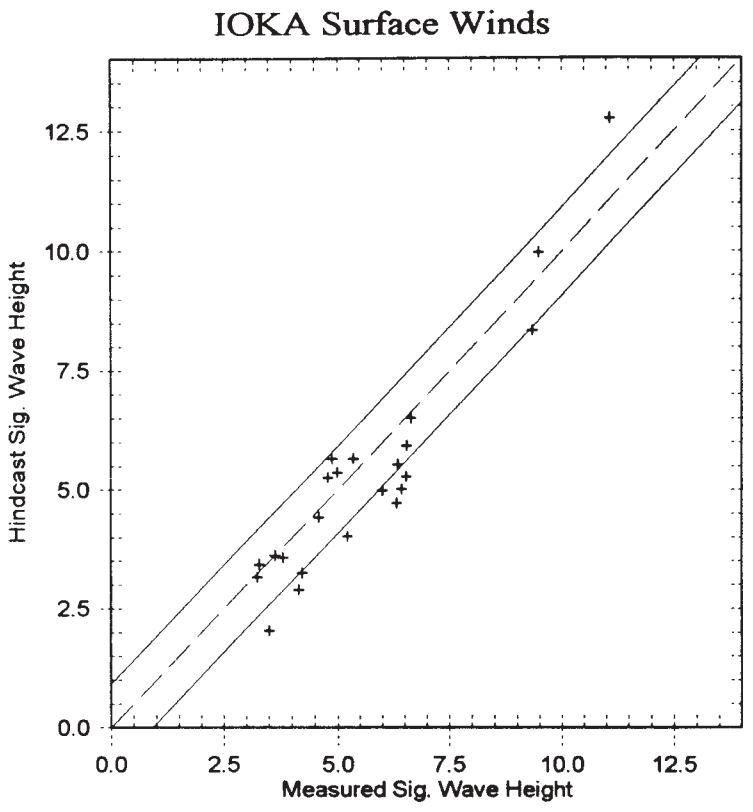


| | |
|---|---|
| Total Points: | 23 |
| Mean X: | 5.666 |
| Mean Y: | 5.280 |
| Mean Diff: | -0.386 |
| Root Mean Square: | 0.919 |
| Standard Dev.: | 0.834 |
| Scatter Index: | 0.147 |
| Ratio: | 0.304 |
| Correlation Coeff: | 0.938 |

Figure 7. Comparison of peak-to-peak wave height using NCEP and IOKA wind fields to drive 3-G wave model for 4 months.

# WAVE CLIMATE ON THE BRITISH COLUMBIA COAST

**Diane Masson**

Institute of Ocean Sciences
P.O. Box 6000
Sidney, B.C.
Canada V8L 4B2

## ABSTRACT

Since 1970, a Waverider buoy located in about 30 m water on the coast of British Columbia has been collecting data almost continuously. This provides us with a valuable homogeneous wave climate data set. The wave spectra have been quality controlled and analyzed to look at possible long term trends in characteristics of the wave field such as significant wave height and peak period. The time series of monthly mean peak periods indicates a significant increase over the 26-year period. However, this trend in the wave period is not associated with a change in the energy content of the wave field. A time series of the joint probability distribution function of the peak period and significant wave height was constructed to better identify the nature of the changes in wave climate, as well as possible links to change in storm characteristics.

# Analysis Of Hurricane Cycles In Florida

Lihwa Lin[1] and Robert G. Dean[2]

## Abstract

Hurricane cycles were studied for the hurricanes affecting Florida, USA, over the 110 years from 1886 to 1995. A total of 111 hurricanes which affected Florida during this period as identified from the North Atlantic Tropical Cyclone Climatology Data complied by the National Hurricane Center were used for the study. The data show that occurrences of Florida hurricanes were less frequent from 1970 to 1995 as compared to that from 1886 to 1970. By using a spectral analysis, the occurrences of Florida hurricanes were found to peak at the intervals of 11, 18, and 55 years. The occurrences of hurricanes were also seen to be more frequent and uniformly distributed from 1886 to 1995 along the west/northwest coast than east coast of Florida. On the average, the return periods of Florida hurricanes were found to be equal to 1.71 years on the west/northwest coast and 4.28 years on the east coast.

## 1. Introduction

It has been a well-observed phenomenon that different intensity hurricanes tend to cluster in certain years and in certain areas (Jordan, 1966; Sheets, 1992; Hebert, *et al.*, 1995). Therefore, it is not surprising to see hurricanes come to the same area at certain time intervals. Then, the question is how often and to what extent that hurricanes may attack the same area. The present study aims at analyzing the frequency of occurrence of historical hurricanes in Florida.

---

[1]Research Hydraulic Engineer. US Army Engineer Waterways Experiment Station, CEWES-CN-C, 3909 Halls Ferry rd., Vicksburg, Mississippi 39180-6199, USA.

[2]Graduate Research Professor. Coastal and Oceanographic Engineering Dept., 336 Weil Hall, University of Florida. Gainesville, Florida 32611, USA.

Table 1: Saffir/Simpson Hurricane Scale Ranges

| Category | Central Pressure (millibar) | Maximum Winds (knots) | Storm Surge (ft) | Damage |
|---|---|---|---|---|
| 1 | >980 | 65--82 | 4--5 | Minimal |
| 2 | 965--979 | 83--95 | 6--8 | Moderate |
| 3 | 945--964 | 96--113 | 9--12 | Extensive |
| 4 | 920--944 | 114--135 | 13--18 | Extreme |
| 5 | <920 | >135 | >18 | Catastrophic |

A total of 111 hurricanes which affected Florida from 1886 to 1995 were analyzed. Among them, 91 hurricanes made landfalls on the Florida Peninsula and 47 hurricanes were classified as Categories 3, 4 and 5 hurricanes with maximum wind exceeding 96 knot (110 mph) according to a Saffir/Simpson Scale as presented in Table 1. On the average, nearly one hurricane per year affected Florida, while about four hurricanes struck Florida every five years. In reality, however, the number of hurricane occurrences in Florida is quite unevenly distributed on the yearly basis. In the present study, the cyclical nature of these hurricanes was investigated by analyzing hurricanes with different type of storm paths in different regions.

## 2. Histograms

Florida hurricanes are defined as those with storm track crossing through a pentagonal area as delineated in Figure 1. A total of 111 historical hurricanes with still hurricane wind strength affecting Florida were selected in the present study. The information of Florida hurricane track were from the North Atlantic Tropical Cyclone Climatology Data compiled at the National Hurricane Center (Jarvinen and Neumann, 1978; Hebert, *et al.*, 1995). Figure 2 shows a histogram of occurrences of all historical Florida hurricanes from 1886 to 1995. Figure 3 shows a histogram of those Florida hurricanes with intensity above Category 3. The width of each cell used in the histogram is 5 year.

It is noticed in Figures 2 and 3 that hurricanes are less frequent from 1970 to 1995 compared to the period from 1886 to 1970. However, some cyclical patterns of hurricane occurrences are clearly noticeable in Figures 2 and 3.

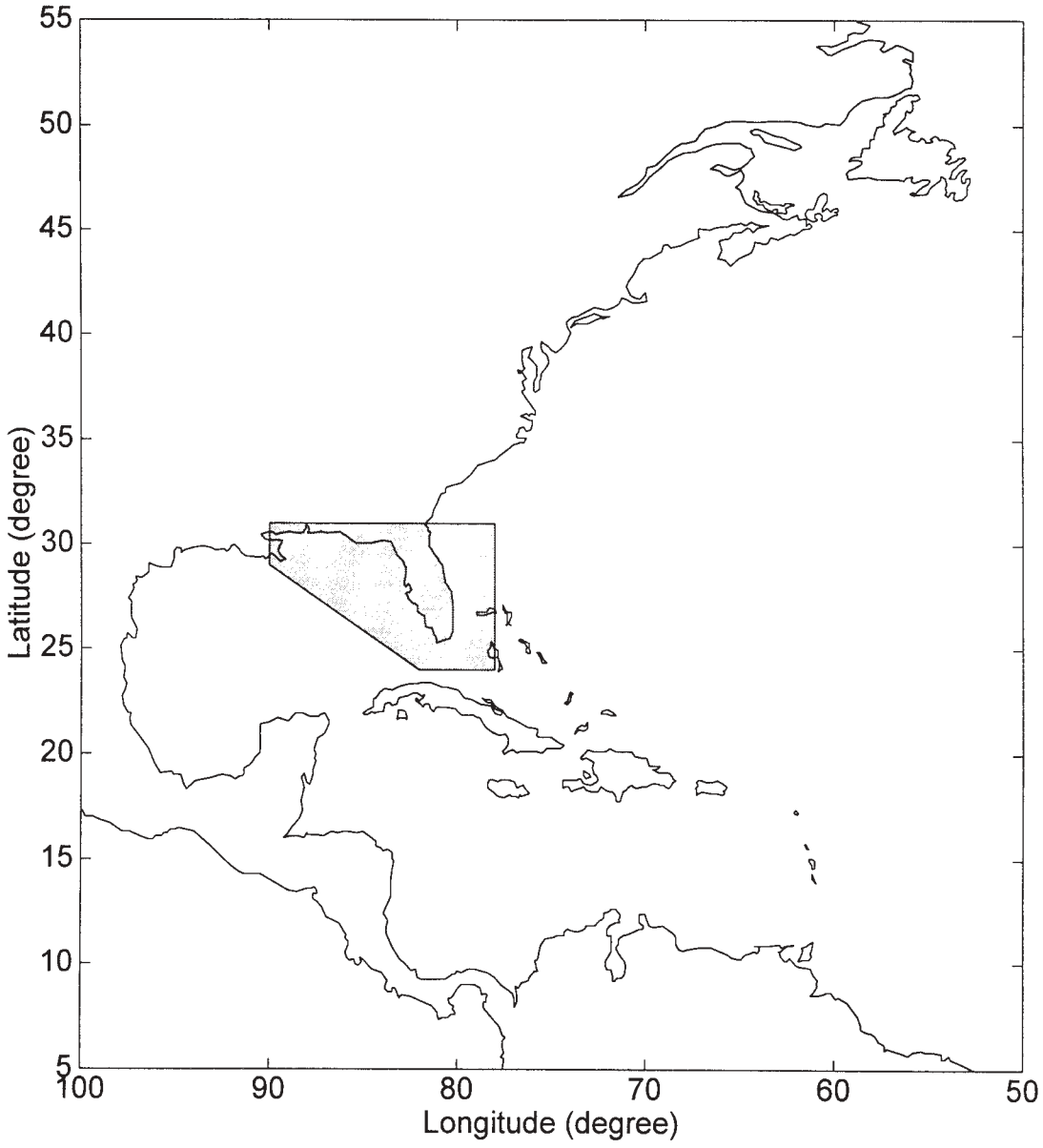


Figure 1: Florida hurricane affecting zone (shading area).

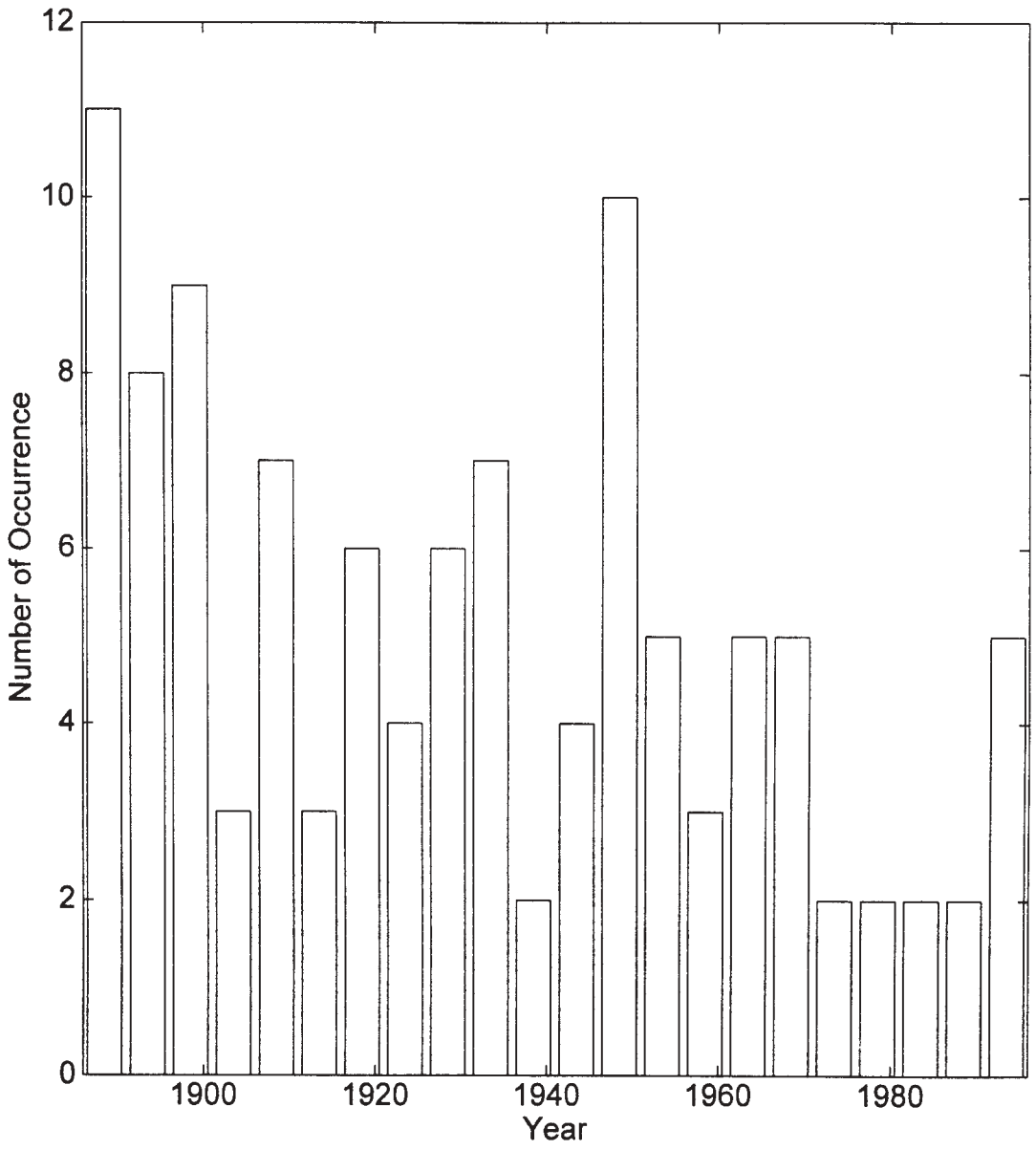


Figure 2: Histogram of all 111 Florida hurricanes (1886-1995).

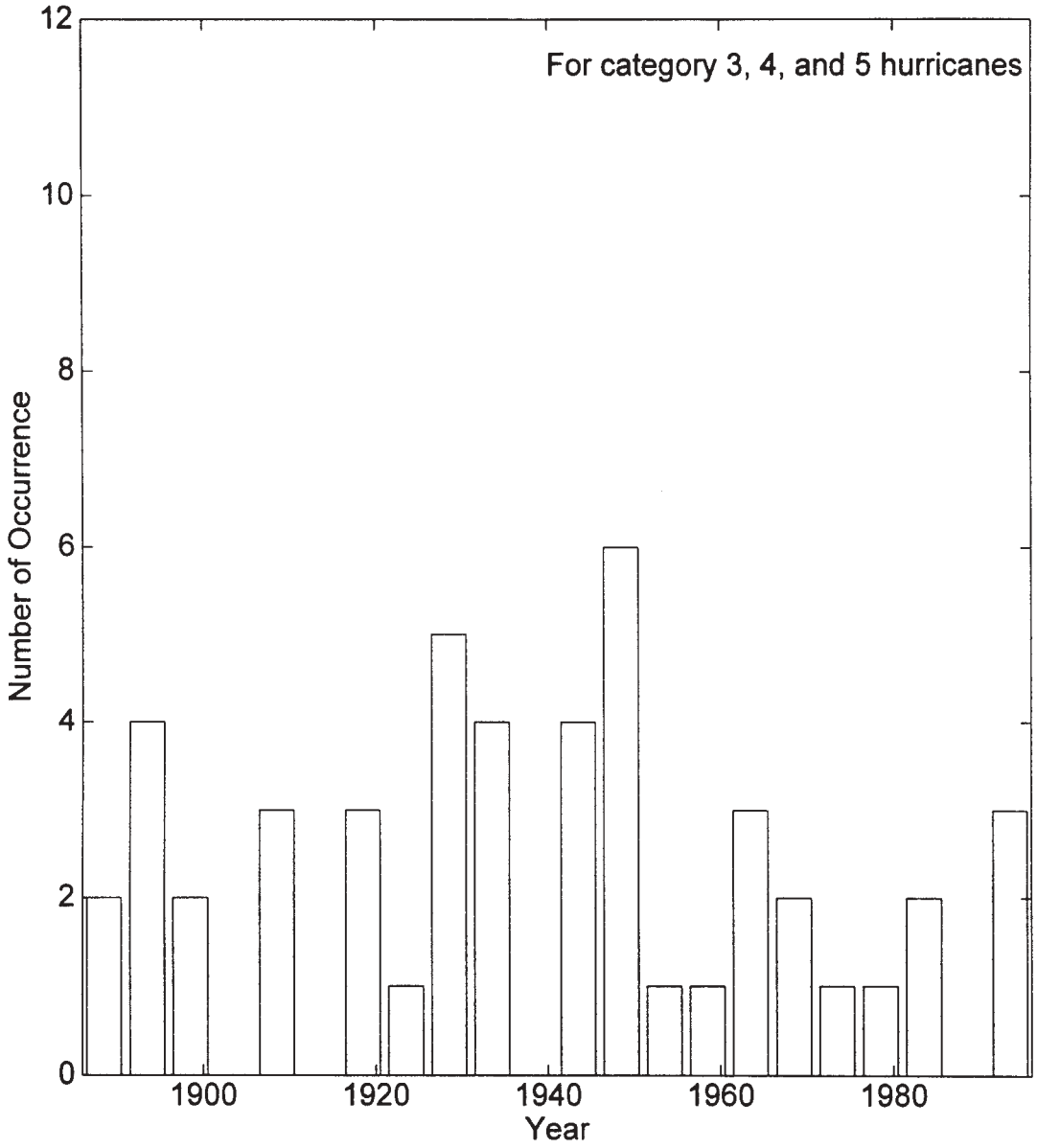


Figure 3: Histogram of Category 3, 4, and 5 hurricanes (1886-1995).

## 3. Spectral Analysis

A standard spectral method which finds the frequency components in a noisy time domain signal through the use of Fourier transforms of the signal is applied to analyze the characteristics of hurricane cycles. The method is used in two cases: (1) annual data of accumulation of hurricane categories in each year, and (2) the numbers of hurricane occurrences in the 5-year basis from 1886 to 1995. The analysis of Case (1) is intended to find the return period of stronger hurricanes while analysis of Case (2) is to find the cyclical peak of hurricane occurrences in the 5-year basis.

Figures 4 and 5 show the results of spectral analyses for Cases (1) and (2). In Figure 4, the spectrum exhibits that major hurricanes can return to Florida in the smallest intervals of 2.07 and 2.44 years, which correspond to frequencies of 0.48 and 0.41 per year, respectively. Figure 5 shows that occurrences of hurricanes in the 5-year basis generally peaked at the intervals of 11,18, and 55 years, which corresponding to frequencies of 0.09, 0.056, and 0.018 per year, respectively. It is especially interesting that the occurrences of major hurricanes, which include all Category 3, 4, and 5 hurricanes, peaked more predominantly about every 18 years.

## 4. Hurricanes of Different Types of Storm Path

A more logical and valid approach to study the cyclical nature is to analyze the hurricanes with different characteristics of storm routes. This approach seems more promising since different Florida hurricanes may have different causes as being formed in the Gulf of Mexico or Caribbean Sea, and in the tropical Atlantic Ocean (Jordan, 1966; Neumann, 1976). By examining all the historical Florida hurricanes from 1886 to 1995, five different types of hurricane path can be distinguished. They are: (A) a storm path of a parabolic type curve originating over the tropical Atlantic or Caribbean Sea, recurving into the North Atlantic off the east Florida coast without landfalling, and continuously moving northwards to the northeast U.S. coast or higher latitude area in the North Atlantic Ocean, (B) a storm path similar to (A) but landfalling on the east coast of Florida, (C) a storm path commencing a northwesterly or westerly track from the tropical Atlantic, crossing the lower or central Florida, and continuing a northwestly course in the Gulf of Mexico before landfalling on the northwest coast of Florida, (D) a storm track starting from either the tropical Atlantic, Gulf of Mexico, or Caribbean Sea, moving generally northwards in the Gulf, and making landfall on the northwest coast of Florida, and (E) a storm path similar to (D) but landfalling on the central or lower west coast of Florida. Of these five different types of hurricane path, Types (B) and (C) can be combined in the case of which hurricanes made landfall on the east coast of Florida, Types (C) and (D) can be combined in the case of which hurricanes made landfall on the northwest coast of Florida, whereas Types (C)+(D)+(E) together can represent hurricanes with landfalling on the west and northwest coast of Florida.

TABLE OF CONTENTS

AUTHOR INDEX

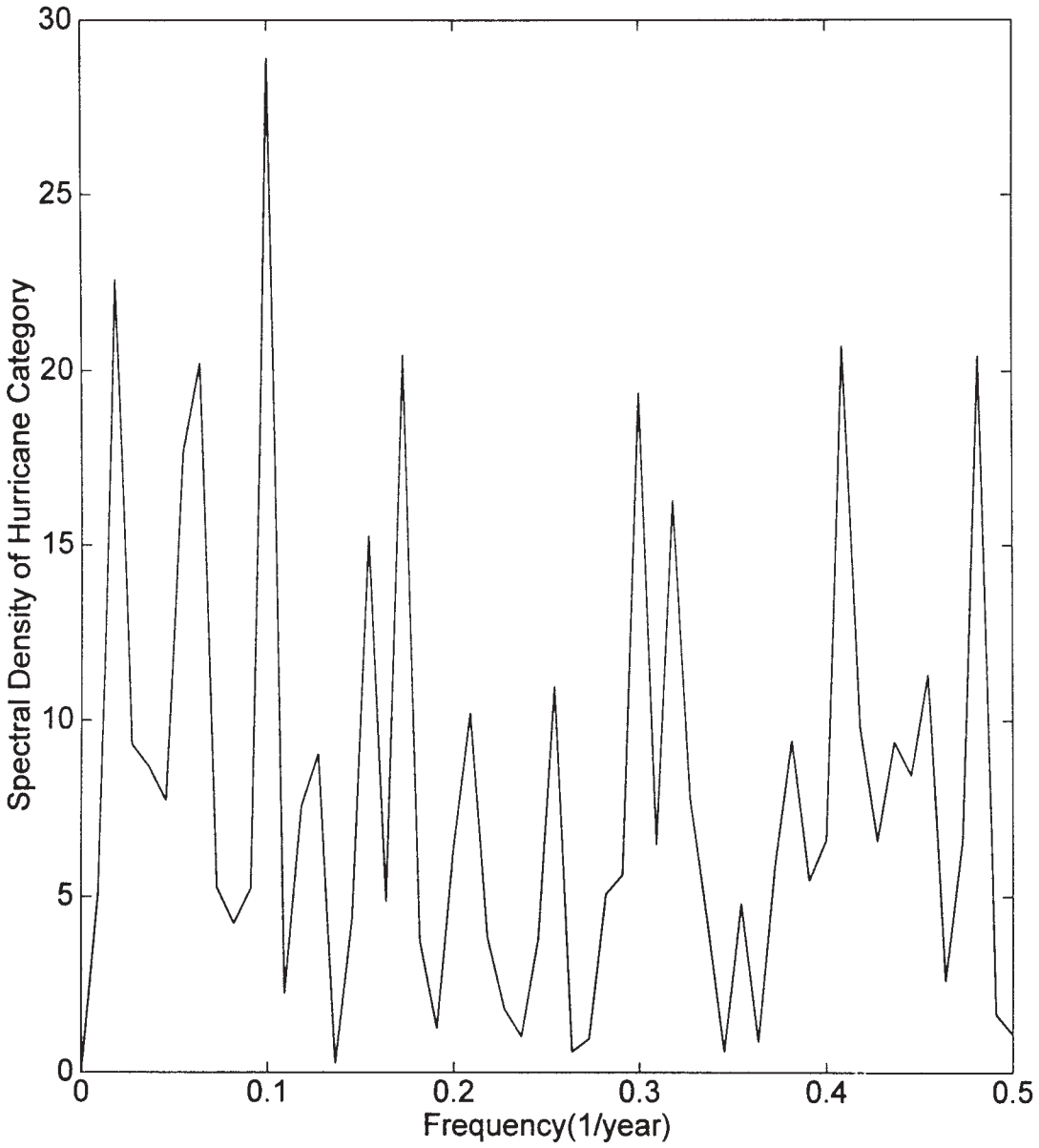


Figure 4: Spectrum of annual data of accumulation of hurricane categories (1886-1995).

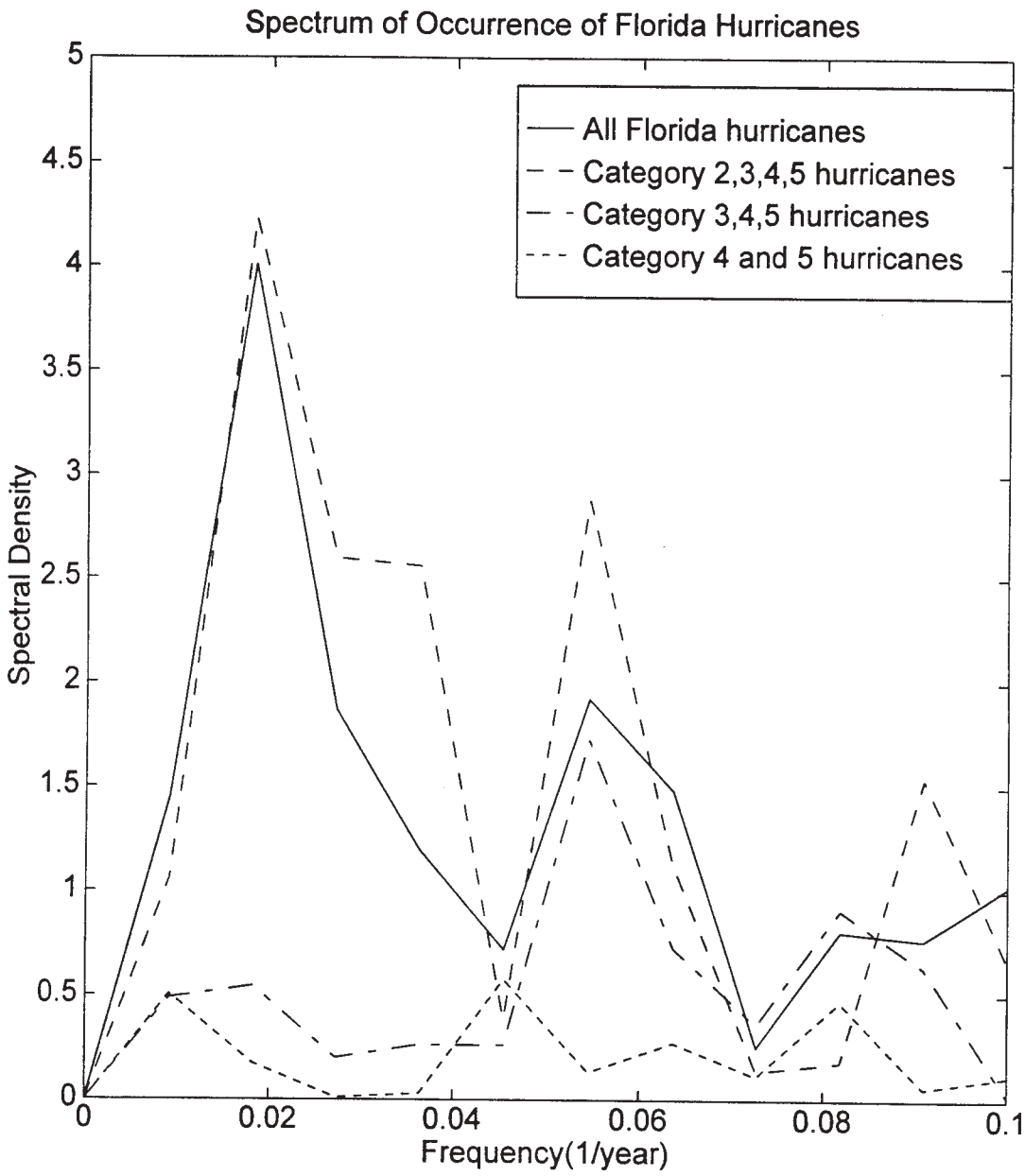


Figure 5: Spectral presentation of occurrences of Florida hurricanes (1886-1995).

Table 2: Average Return Period of Florida Hurricanes from 1886 to 1995

| Type of Path | Number of Occurrence | Average Return Period (year) | Standard Deviation (year) |
|---|---|---|---|
| (A) | 21 | 5.06 | 5.30 |
| (B) | 12 | 8.00 | 10.11 |
| (C) | 14 | 8.23 | 8.93 |
| (D) | 30 | 3.77 | 4.98 |
| (E) | 21 | 5.12 | 5.28 |
| (B)+(C) | 26 | 4.28 | 5.48 |
| (C)+(D) | 44 | 2.54 | 1.95 |
| (C)+(D)+(E) | 65 | 1.71 | 1.54 |

From all historical Florida hurricanes occurred from 1886 to 1995, a total number of 98 hurricanes clearly fell into one of the five type paths aforementioned above with still hurricane wind intensity affecting Florida. Figure 6 displays the hurricane tracks separated into the five type paths. Table 2 presents the average return period of hurricanes and the associated standard deviation for the five different path types and combined Types (B)+(C), (C)+(D), and (C)+(D)+(E). For each of Types (A), (B), (C), (D), (E), there is no indication of a cyclical pattern of hurricane occurrences as evidenced by the corresponding large standard deviations of return period shown in Table 2.

For Type (B)+(C), in which hurricanes made direct hit on the east coast of Florida, a cyclical pattern was also not found. However, for Type (B)+(C), it is interesting to see that hurricanes were most likely to make landfall only in the lower half part of the east coast of Florida. In summary, 25 out of a total of 26 hurricanes of Type (B)+(C) from 1886 to 1995 made landfall from a mid east coast near Cape Canaveral to the lower east coast in the Florida Keys. On the other hand, the cyclical patterns of the hurricanes of Type (C)+(D), and (C)+(D)+(E), which struck the northwest and west/northwest coasts, respectively, were noted from smaller standard deviations of return periods. In fact, the occurrences of hurricanes in the northwest and west/northwest coasts are more uniformly over the 110 years from 1886 to 1995 as shown by the time history plots of corresponding hurricane occurrences in Figures 7 and 8. On the average, the return periods of hurricanes which impacted the east, northwest, and west/northwest coasts are equal to 4.28, 2.54, and 1.71 years, respectively.

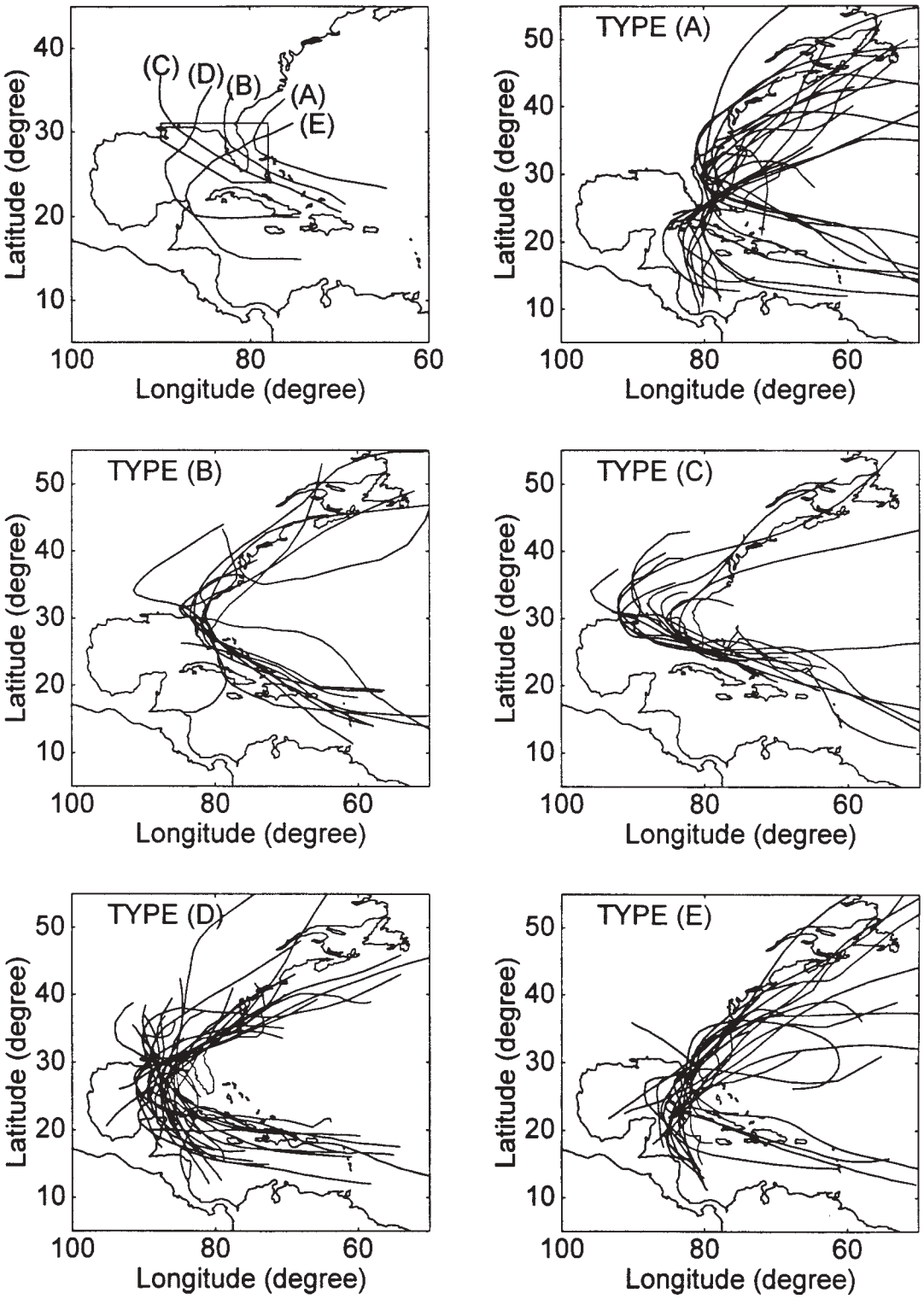


Figure 6: Five different types of hurricane paths (1886-1995).

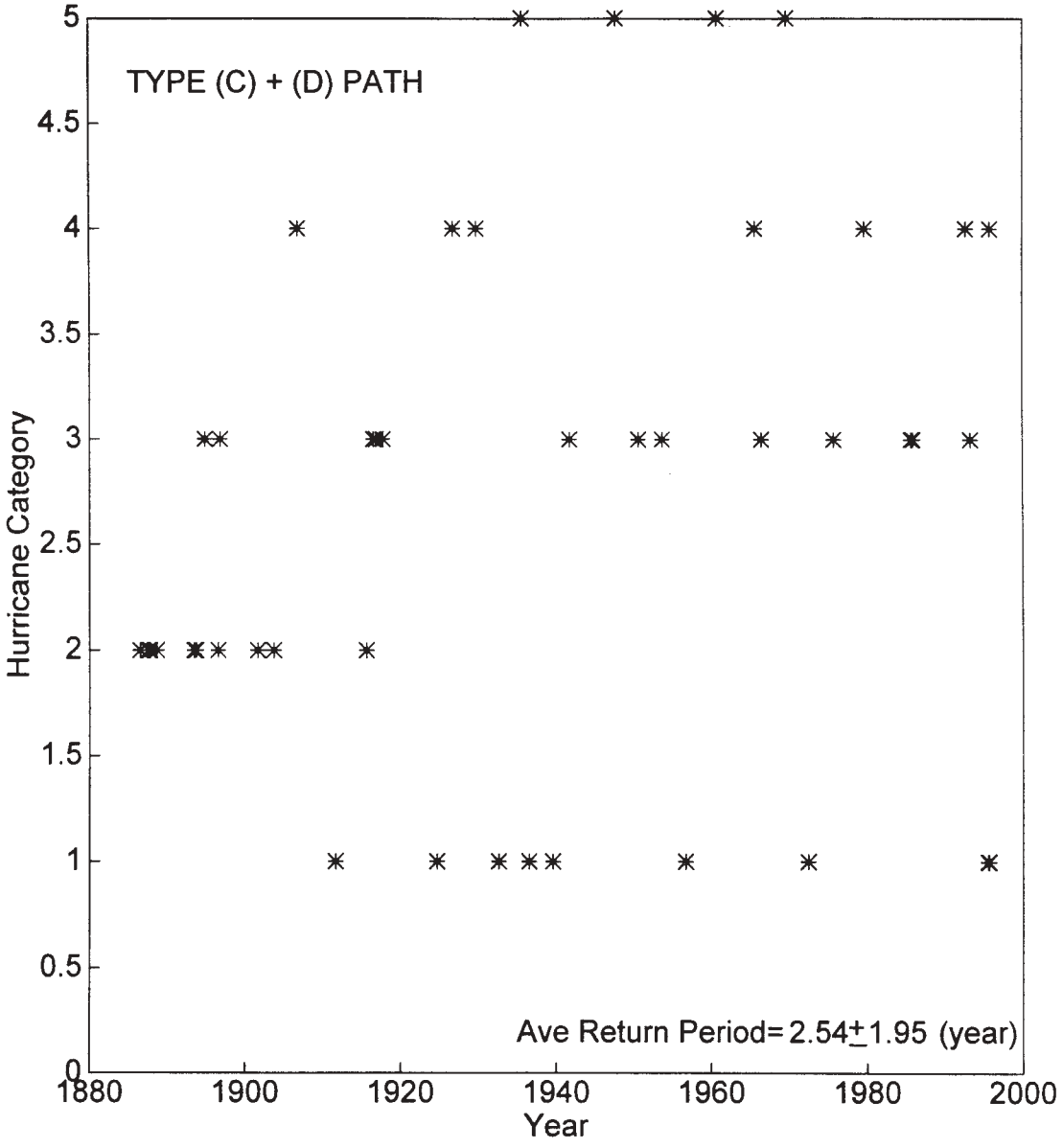


Figure 7: Plot of hurricane category versus time for Type (C)+(D) path hurricanes.

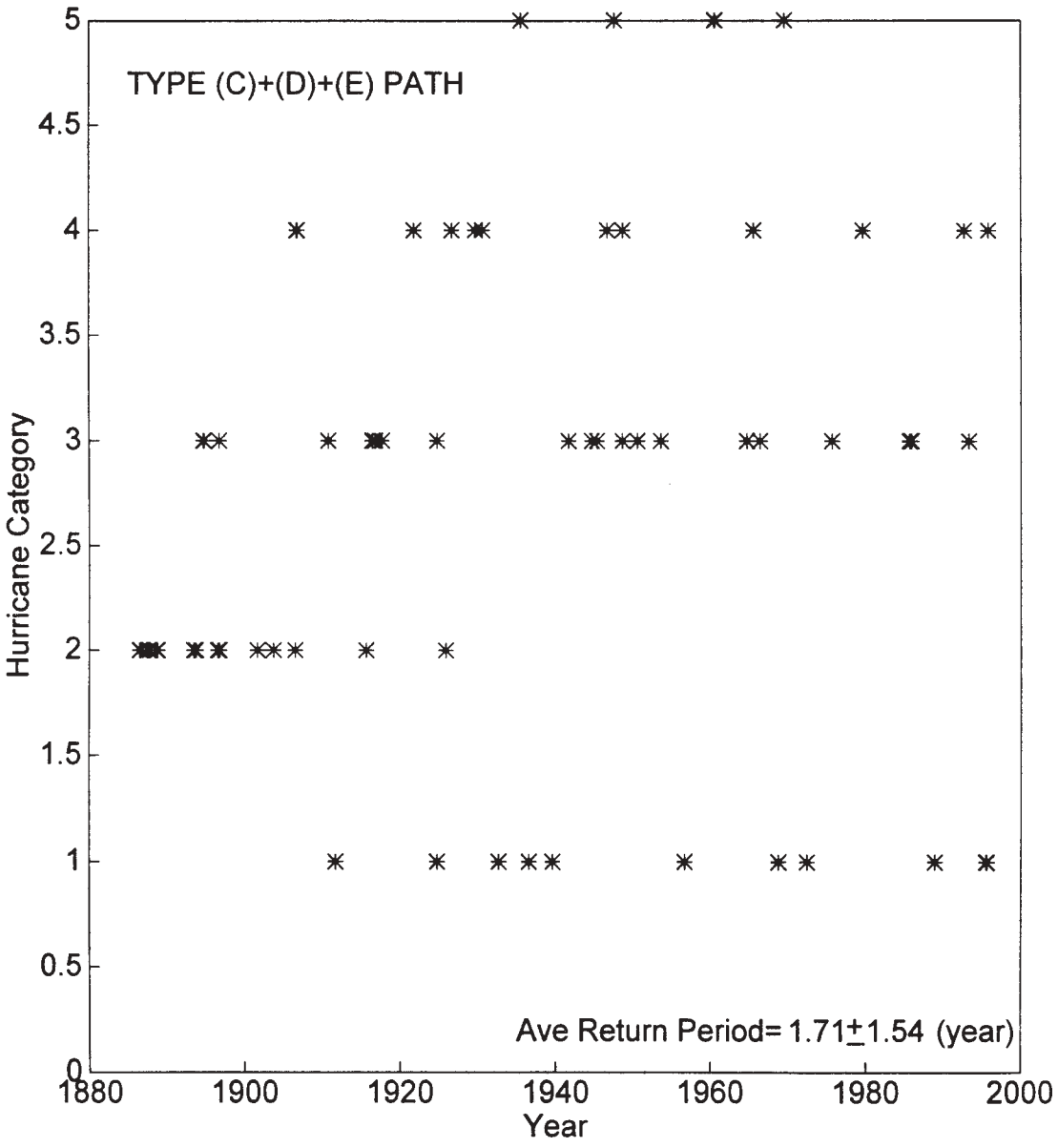


Figure 8: Plot of hurricane category versus time for Type (C)+(D)+(E) hurricanes.

## 5. El Niño Effect

El Niño means sea temperature rise about 1 or 2 degrees centigrade warmer than normal in the tropical Pacific Ocean. When the El Niño is present, the upper-air winds can blow in a westerly direction from the Pacific Ocean across to the Atlantic Ocean and, accordingly, shear off weather systems from developing into hurricanes in the Atlantic Ocean. As a result, the El Niño events can reduce hurricane activity in the Atlantic and they will certainly influence the hurricane cycles in Florida.

Since 1949, there have been 12 El Niño years observed in the Pacific Ocean. The average return period of El Niño events is 4.18 years and the associated standard deviation is 1.72 years. Table 3 presents the list of El Niño years (Gray, 1984). It is interested to see that a pattern of occurrences of El Niño years may exist in about every 18 to 20 years. This seems to agree well with the occurrences of major hurricanes which tend to peak more predominantly about every 18 years.

Table 3: List of El Niño years from 1949 to 1997

| El Niño Year | | | | | | | | | | | |
|---|---|---|---|---|---|---|---|---|---|---|---|
| 1951 | 1957 | 1963 | 1965 | 1969 | 1972 | 1976 | 1982 | 1986 | 1987 | 1991 | 1997 |
| ⟨---- repeated pattern ----⟩ | | | | | | ⟨---- repeated pattern ----⟩ | | | | | |

## 6. Conclusions

Based on the best hurricane track information from the North Atlantic Tropical Cyclone Climatology Data compiled at the National Hurricane Center, a total of 111 hurricanes which affected Florida from 1886 to 1995 were analyzed for frequency of occurrence study. Among them, 91 hurricanes made landfalls on the Florida Peninsula whereas 20 came only closer to the coast without landfalling in Florida. By expressing the number of occurrences of these hurricanes in a histogram, it is seen that the occurrences of Florida hurricanes were less frequent from 1970 to 1995 as compared to that from 1886 to 1970. Patterns of hurricane cycle are, however, observed from the histogram. The occurrences of Florida hurricanes were noticed, according to a spectral analysis, to peak at the intervals of 11, 18, and 55 years. The cyclical pattern is particularly interesting for the occurrences of major hurricanes, which include all Category 3, 4, and 5 hurricanes based on a Saffir/Simpson Scale, that these hurricanes tend to peak more predominantly about every 18 years in the 5-year basis. This cyclical pattern of major hurricanes was also found to agree well with the pattern of occurrences of the El Niño events.

The cyclical characteristics of the historical Florida hurricanes were further investigated for the hurricanes in five different type paths. In the case of that

hurricanes came from the tropical Atlantic and made landfall on the east coast of Florida, no clear cyclical figure of hurricane occurrences was found. In the case of that hurricanes struck the west and northwest coasts, the occurrences of hurricanes were more frequent and uniformly distributed from 1886 to 1995. Over the 110 years from 1886 to 1995, there are 65 hurricanes made landfall on the west/northwest coast and 26 hurricanes on the east coast of Florida. On the average, the return periods of Florida hurricanes are found to be equal to 1.71 years on the west/northwest coast and 4.28 years on the east coast.

## References


1. Gray, W.M., 1984. "Atlantic Seasonal Hurricane Frequency. Part I: El Niño and 30 mb Quasi-Biennial Oscillation Influences. Monthly Weather Review, v.112, 1649-1668.

2. Hebert, P.J., J.D. Jarrell, and M. Mayfield, 1995. "The Deadliest, Costliest, and Most Intense United States Hurricanes of This Century," Proceedings of the 17th Annual National Hurricane Conference. Atlantic City, New Jersey. April 11-14, 1995. pp.12-50.

3. Jarvinen, B.R., and C.J. Neumann, 1978. "Atlantic Tropical Cyclone Tracks by 5, 10, 15, and 30 day periods," NOAA Technical Memorandum, NWS/NHC/5, National Hurricane Center, Miami, Florida.

4. Jordan, C.L., 1966. "Climatological Features of the Formation and Tracks of Hurricanes,"
Proceedings of Hurricane Symposium. Houston, Texas. American Society for Oceanography. October 10-11, 1966. pp.82-101.

5. Neumann, C.J., 1976. "Computerized Tropical Cyclone Climatology," Mariners Weather Log, Vol.20, No.5. National Weather Service, NOAA. Coral Gables, Florida. Sep. 1976.

6. Sheets, R.C., 1992. "The United States Hurricane Problem: An Assessment for the 1990's," Proceedings of the14th Annual National Hurricane Conference. Norfolk, Virginia. April 8-10, 1992. pp. 1-46.

# WAVE CLIMATE STUDIES FOR SEBASTIAN INLET

W.R. Dally[1], W.G. Grosskopf[2], and L.E. Harris[1]

[1]Ocean Engineering Program, Florida Institute of Technology, 150 W. University Blvd., Melbourne, Florida, 32901

[2]Offshore and Coastal Technologies, Inc. - East ; 510 Spencer Road; Avondale, PA, 19311

## 1. INTRODUCTIONI

Reliable wave information, including hindcasts, real-time measurements, and forecasts, is essential to many engineering and coastal management activities being conducted at Sebastian Inlet. This tidal inlet is a small, stabilized navigable entrance located on the east central coast of Florida, approximately 65 km south of Cape Canaveral (see Figure 1). This paper describes 1) use of the archived data base of hindcasted wave climate available from the U.S. Army Corps of Engineers Wave Information Study (WIS), 2) attempts to verify the WIS data for the region by comparison to the NOAA buoy located off Cape Canaveral, and 3) new tests of the WISWAVE model against wave data recently collected at Sebastian Inlet, as well as the Canaveral buoy. The ultimate goal is to develop reliable long-term hindcasts specifically for the Sebastian Inlet site.

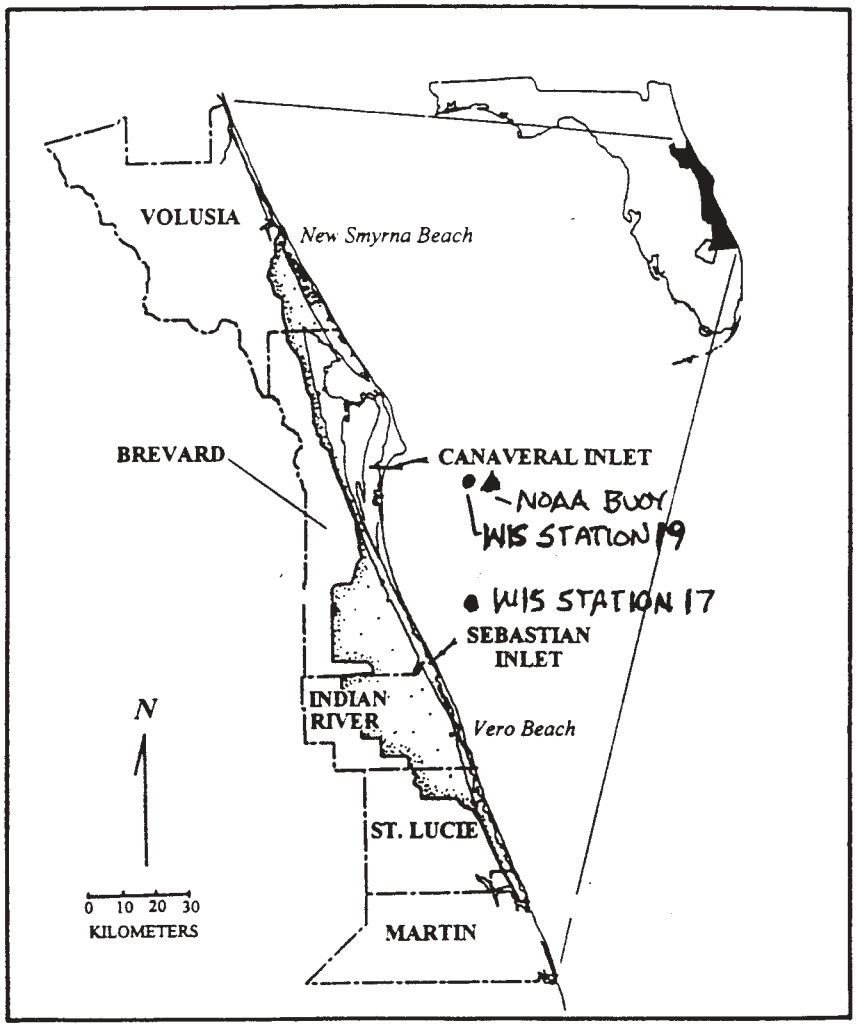


Figure 1 - Location map for Sebastian Inlet, also showing approximate locations of NOAA buoy 41009, WIS Site 19, and WIS Site 17.

## 2. ARCHIVED WIS HINDCASTS

The WIS data used in this study were developed in WIS Report 30 (Hubertz, et al., 1993) and WIS Report 33 (Brooks and Brandon, 1995), and were downloaded from CERC's library archive (ftp bigfoot.cerc.wes.army.mil). The closest station to Sebastian Inlet is WIS Site 17 (28.00°N and 80.25°W), which is 15.6 km north and 25.6 km east of the inlet, in a water depth of 24 m, as shown in Figure 1. Hindcast results for this site are available from 1956 to 1993; however, the period from 1956 to 1975 does not include modeling of tropical storms or hurricanes.

These data, being the only source of long-term wave information available for the region, are being used in performing basic coastal engineering analyses and design for the Sebastian Inlet, including establishing a sediment budget, designing jetties and other structures, and identifying stormy epochs that have affected the neighboring beaches. The hindcast wave parameters utilized thus far include energy-based significant wave height ($H_{mo}$), spectral peak period ($T_p$), and spectral peak direction ($\theta_p$). To make the data more manageable, the record was decimated from the original eight entries per day format to four entries per day, at 0000, 0600, 1200, and 1800 hrs. - nevertheless, over 55,500 entries in all.

Figures 2, 3, and 4 present the histograms of the $H_{mo}$, $T_p$, and $\theta_p$ WIS data, respectively, as well as sample results of probabilistic modeling conducted by Leyden (1997). Using the method of moments to establish model parameters, for $H_{mo}$ it appears from Figure 2 that the shifted-gamma model captures the peak of the WIS histogram to some degree, whereas the shifted-lognormal model better represents the low-energy tail. Both models appear to capture the high-energy tail of the WIS data. For $T_p$, Figure 3 demonstrates that the lognormal and gamma models are almost indistinguishable; however, both miss the peak of the histogram. Finally, in Figure 4 the $\theta_p$ histogram contains two peaks, and so a cosine-power model can represent only its basic shape.

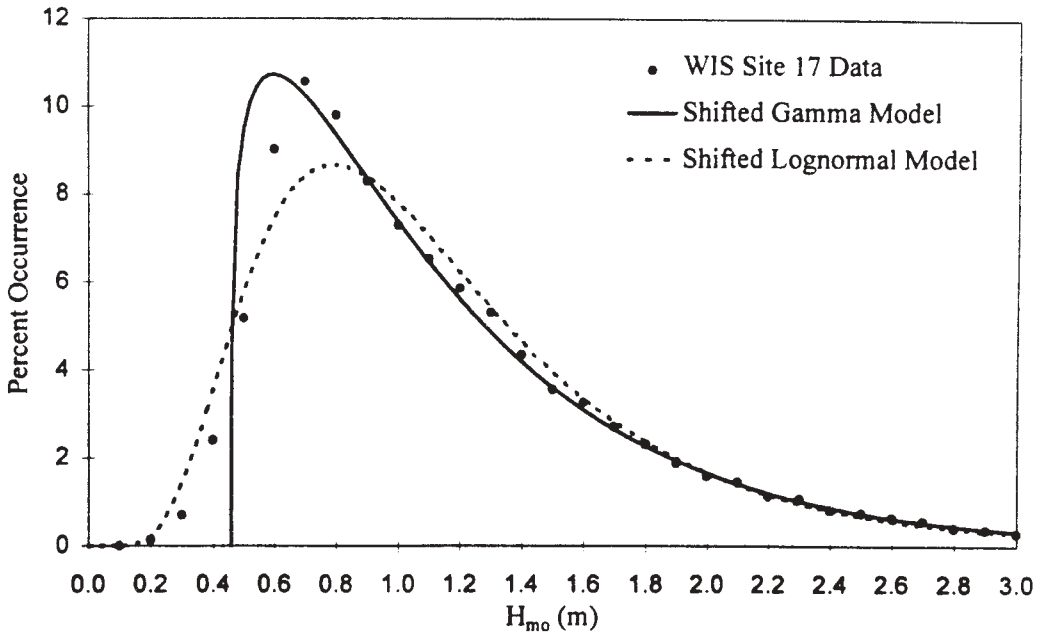


Figure 2 - Histogram of energy-based significant wave height data from WIS Site 17, and comparison of the shifted gamma and shifted lognormal models (from Leyden, 1997).

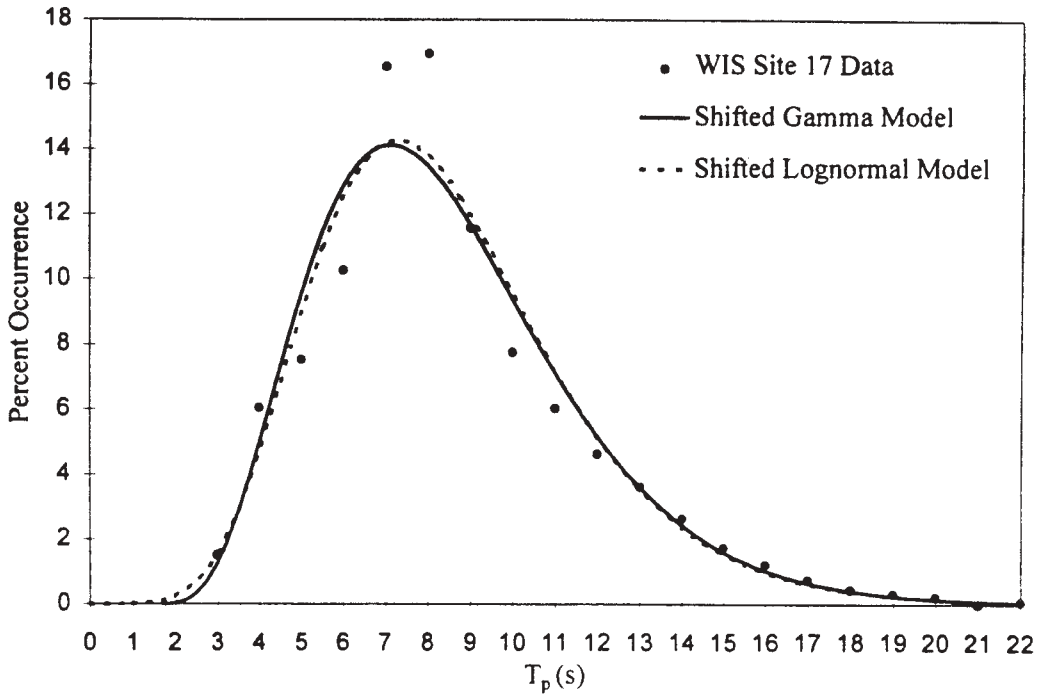


Figure 3 - Histogram of spectral peak period data from WIS Site 17, and comparison of shifted gamma and shifted lognormal models (from Leyden, 1997).

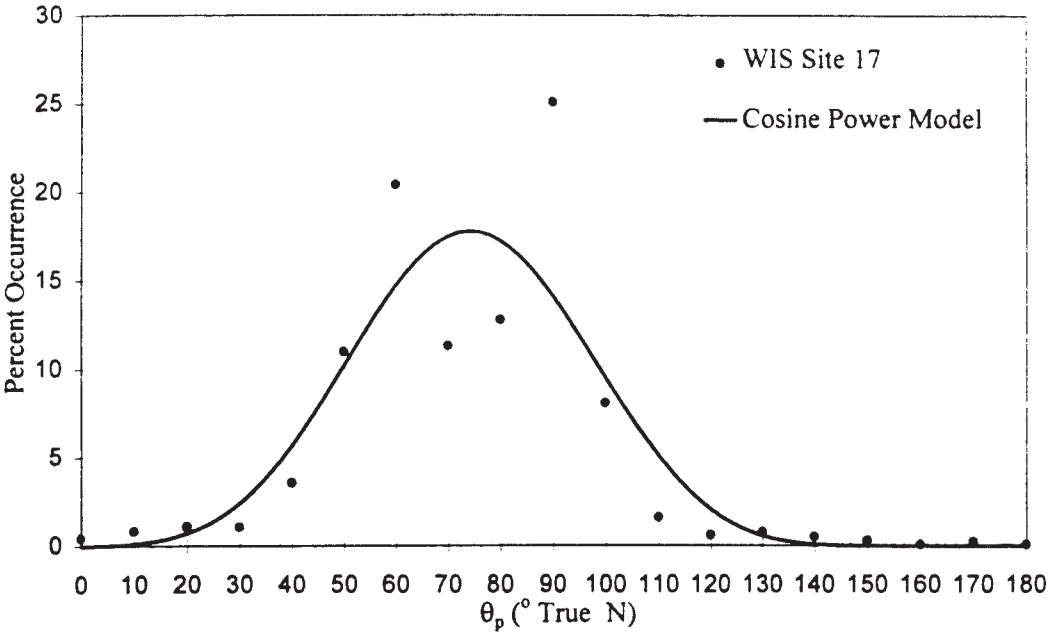


Figure 4 - Histogram of spectral peak direction data from WIS Site 17, and comparison of cosine-power model (from Leyden, 1997)

As an example of one application of hindcasted data for Sebastian Inlet, estimates of the cross-product Radiation Stress, $S_{xy}$, have also been computed by Leyden (1997) in order to study the forcing climate of longshore currents and sand transport in the region. A histogram of $S_{xy}$ is presented in Figure 5. The mean value of +6.61 N/m indicates a small net southerly forcing, as should be expected for the region. However, the gross forcing is approximately 130 N/m, indicating that the mean is a small difference between two large quantities. The standard deviation of $S_{xy}$ is 247 N/m, indicating that wave-forcing of the longshore current in the region is highly variable.

## 3. WIS VALIDATION AT CAPE CANAVERAL

In attempt to validate the Site 17 hindcast results, Leyden (1997) compared WIS data from Site 19 off Cape Canaveral to in situ measurements from NOAA Buoy 41009 (see Figure 1 for locations) for the time period for which buoy and WIS data overlap (1998-1993). Comparative histograms are provided in Figures 6 and 7. Results indicate that the WIS model does a reasonable job at hindcasting $H_{mo}$, with average correlation of 0.785. This confirms the findings of Brooks and Brandon (1995) who performed a similar comparison. However, the ability of the WIS model to hindcast $T_p$ was found to be poor (correlation of 0.27). The ability to model $\theta_p$ in the region remains untested because the NOAA Buoy does not provide wave direction.

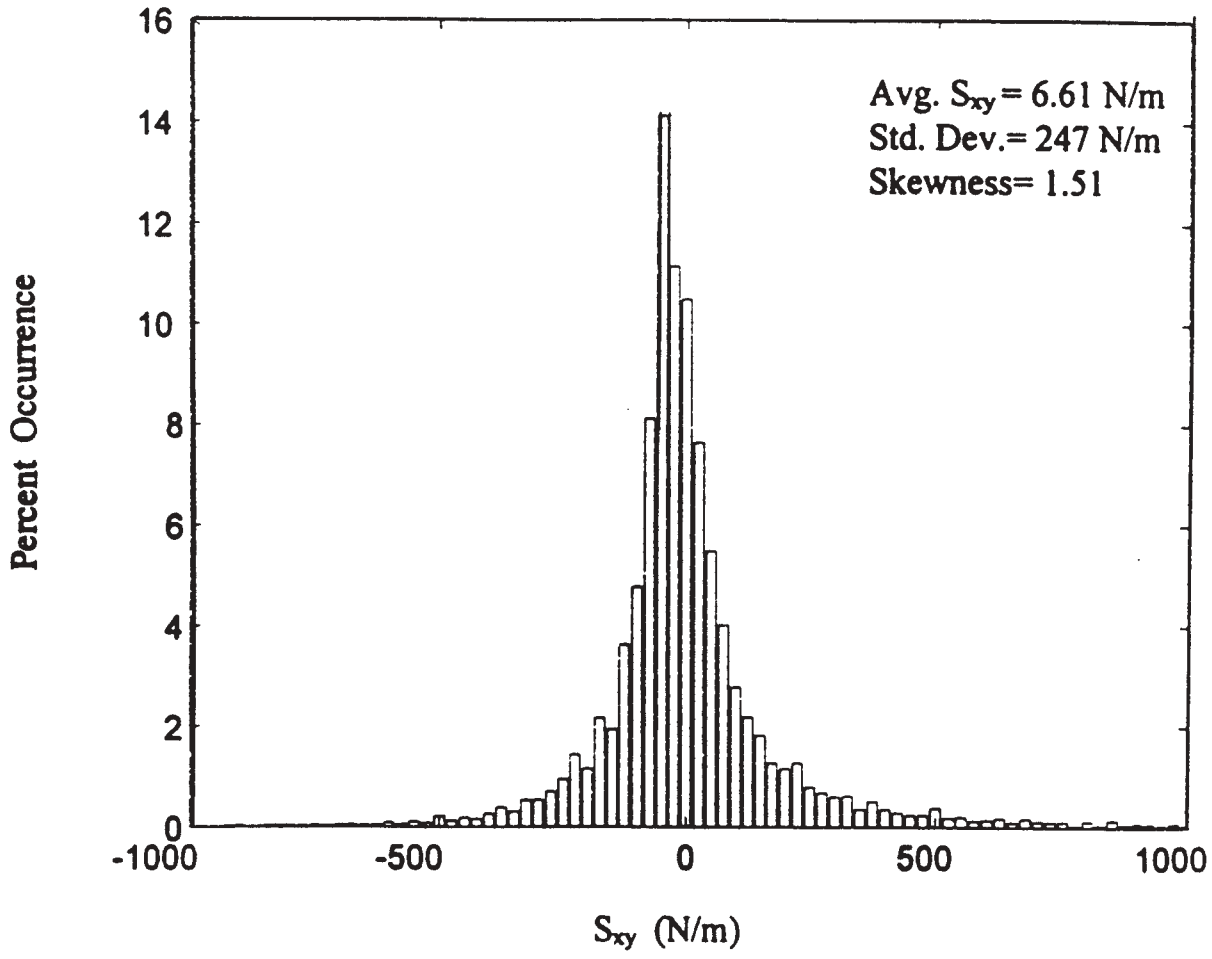


Figure 5 - Histogram of Radiation Stress, $S_{xy}$, calculated from WIS Site 17 data (1956-1993). Small net stress is to the south.

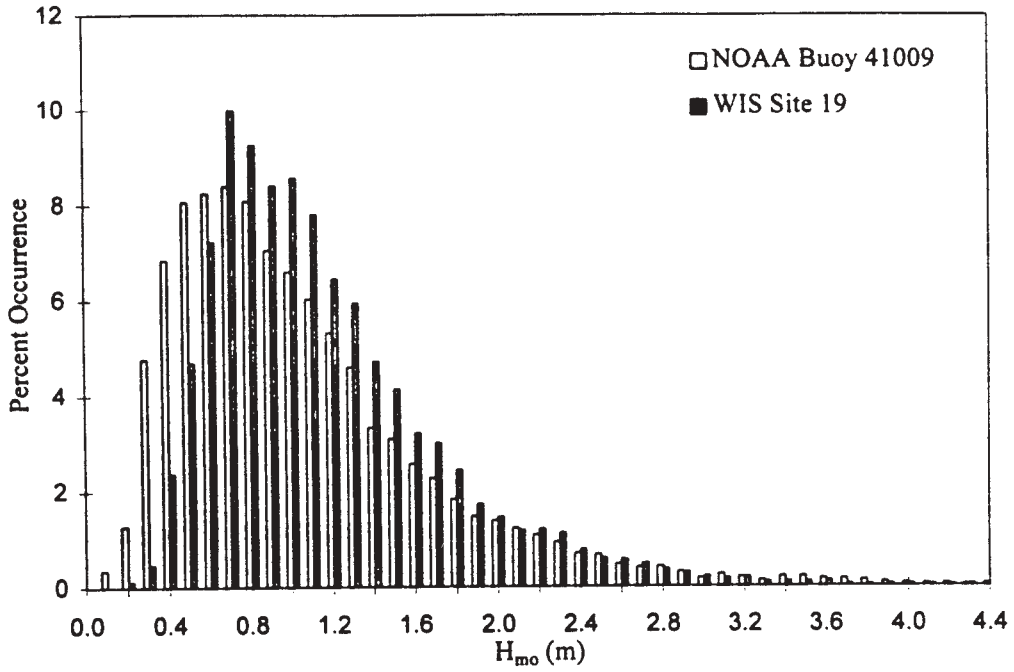


Figure 6 - Histogram comparison of energy-based significant wave height from NOAA Buoy 41009 and WIS Site 19 (1988-1993) (from Leyden, 1997).

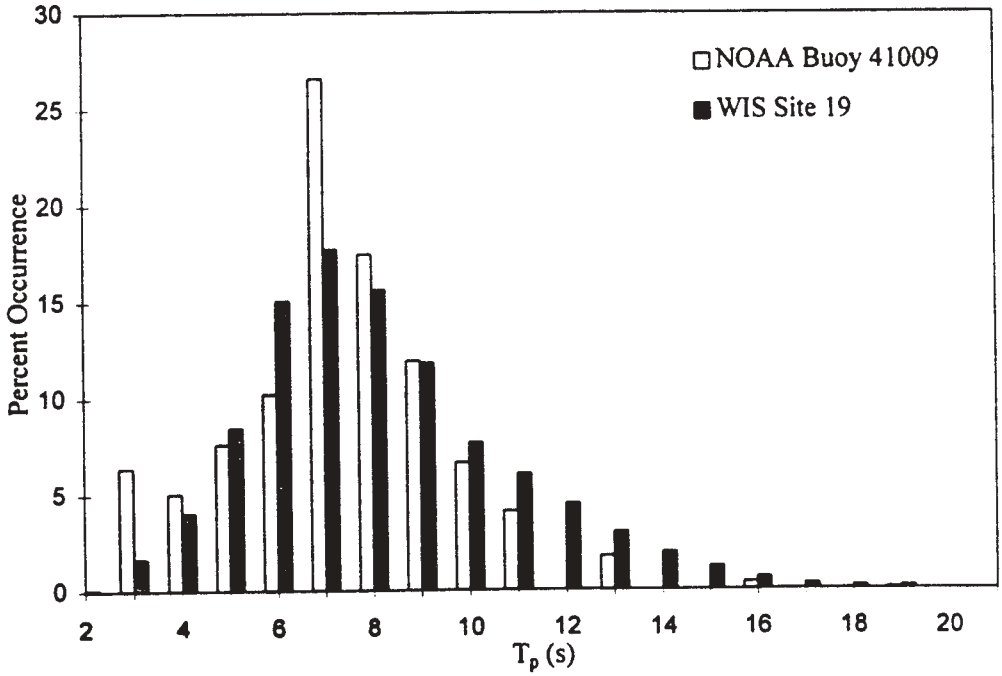


Figure 7 - Histogram comparison of spectral peak period from NOAA Buoy 41009 and WIS Site 19 (1988-1993) (from Leyden, 1997).

4. ONGOING MEASUREMENT PROGRAM

Real-time wave and tide data have been collected by Florida Institute of Technology offshore of Sebastian Inlet since August 1996 (Harris and Childress, 1998). Two directional SeaPac™ 2100 PUV wave gages manufactured by the Woods Hole Group are used for measuring, recording and transmitting the wave data. The second gage provides a backup for quick-swapping of the gages, thereby minimizing data loss during wave gage service and maintenance.

The PUV wave gage consists of four sensors:
(1) Paroscientific pressure transducer to measure pressure variations due to water level changes,
(2) Marsh-McBirney electromagnetic (EM) current sensor to measure the two horizontal velocity components,
(3) Paroscientific temperature sensor to measure seawater temperature (T), and
(4) KVH Industries digital fluxgate compass to determine gage orientation .

The aerial photograph in Figure 8 shows the location of the wave gage, approximately 300 m north of the north jetty, and approximately 300 m offshore in a nominal water depth of 8 m. The pressure sensor is located about 1.2 m above the bottom, with the current sensor 1.2 m above the transducer. A 500-meter long double-armored steel cable buried under the sand runs to the shore and to a small shed. The cable is used to send power to the wave gage, monitor the instrument, and to transmit wave data directly to shore as it is collected, which provides real-time data access. Data are also recorded internally in the instrument. The internal recording of the data provides a backup of the data in the event of data transmission loss due to the loss of electricity or telephone service to the shore-based computer (especially during severe storm events). The wave gage is inspected and cleaned every two to four months, and swapped out every four to six months.

The wave gage sampling scheme is designed to resolve wave energy in the frequency range from 0.01 to 0.3 Hz (100 to 3 s periods). This is done by sampling the pressure at 2 Hz for seventeen minutes. The sample burst interval was set to three hours, i.e. 8 times per day. Processing of the data was done using Wavepro™ software, developed by the Woods Hole Group. This software is run in the MATLAB™ environment.

The high-frequency pressure variations with periods from 3 to 100 seconds are used to determine the wave heights and periods, and the lower frequency water level variations (including the tides) are determined from continuous pressure measurements averaged over 3.5-minute intervals. The wave direction is determined from the high frequency variations of the water particle velocity components (u and v) due to the waves. The lower frequency water current velocity components are measured by averaging the u and v components of the water particle velocities.

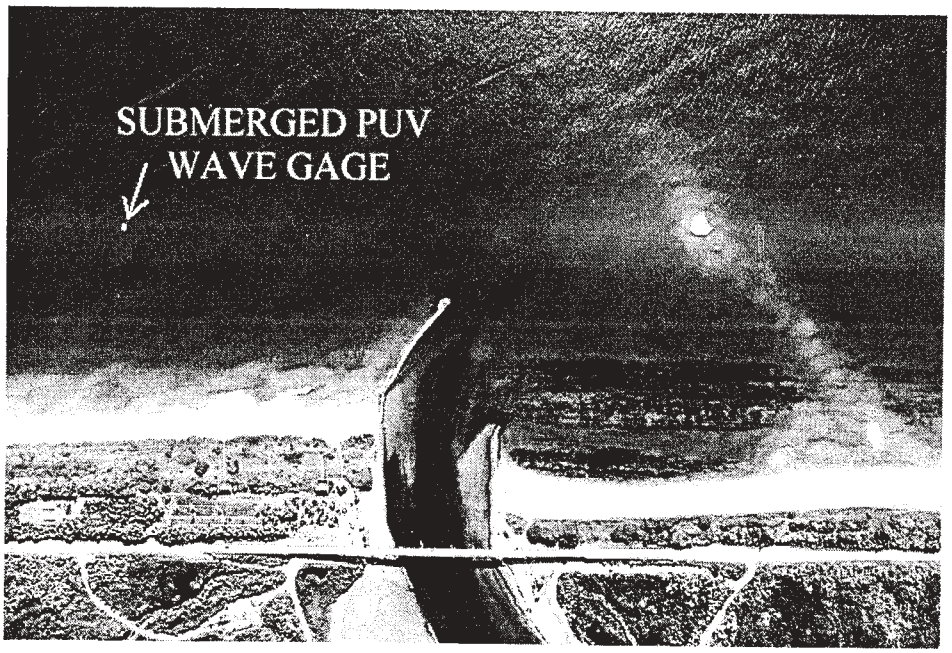


Figure 8 - Aerial photograph of Sebastian Inlet showing location of PUV wave gage.

## 5. NEW HINDCASTING EFFORTS

The in situ data are being used to both verify the WISWAVE hindcasting model specifically for the Sebastian Inlet site, as well as to further investigate its ability to model peak period and direction. A wave hindcast for the region from Cape Canaveral to Sebastian Inlet area was performed for the period August 1996-December 1996. Although in situ data from the Sebastian gage are available through October, 1997, at the time this paper was written, suitable wind field input was not yet available for the 1997 calendar year.

### 5.1 Model Input

Numerical wave hindcasting requires the use of the best possible wind fields and bathymetry as input to the computer model. For the long term simulations, wind fields for this study were developed using atmospheric data developed by the NOAA National Center for Environmental Prediction/National Center for Atmospheric Research (NCEP/NCAR) reanalysis effort. The project reanalyzed historic weather information since 1985 to improve the quality of the archived data set (Kalnay, et al., 1995). The weather products include various gridded historic weather parameters, including the 10-meter wind fields on a gaussian-spaced Latitude grid that has an average spacing of 1.905 degrees. The Longitude grid spacing is constant at 1.875 degrees. That data set was used for this study and obviates the traditional digitization of hard copy pressure charts or the use of lesser quality digital weather information.

The gaussian 10-m wind fields were extracted from the NCEP/NCAR data and interpolated to the regular grids used for wave modeling at a 12-hour increment of time through the period of interest (August-December, 1996). The wind fields were interpolated to three nested grids used for wave modeling:

Grid 1 (Western Atlantic): 1 degree resolution 20.00-45.00 degN 50.00-85.00 degW
Grid 2 (Eastern Florida): 15 min. resolution 78.75-82.25 degN 25.75-30.25 degW
Grid 3 (Local): 2.5 min. resolution 80.21-81.04 degN 27.71-29.04 degW

Grid coverage was specified to include the entire wave generation domain relevant to the eastern Florida region so that both locally-generated seas and swell from distant events would be propagated into the area (Figures 9 and 10). Grid resolutions were selected so as to include the spatial variations in the winds and bathymetry. It should be noted that this approach is generally acceptable for long term hindcasts, but is less appropriate for detailed storm hindcasting where fine scale features of storms must be supplemented from independent data sources.

The model grids are designed in a nested fashion so as to propagate larger-scale wave conditions to the site in addition to locally-generated waves at successively finer resolution. The wind fields are interpolated to each grid and used to generate waves as larger-scale waves are brought in as a boundary condition along the outer edge of the grid. Therefore, the simulation is carried out three times, once for each grid. Bathymetries for each grid were developed from the latest NOAA/NOS navigation charts.

### 5.2 Wave Model

Hindcasted wave conditions for this study were simulated using a discrete directional spectral wave model that is applicable in all water depths. The model includes a nonlinear wave-wave interaction source term and shallow water wave transformations. The model has been applied to many locations around the world by government and commercial entities and is used by the U.S. Army Corps of Engineers Wave Information Study.

The wave model is a FORTRAN code which simulates wave growth, dissipation and propagation in deep or shallow water. Spectra are represented as fully two-dimensional spectra in discretized frequency and direction bands. Propagation effects and source/sink mechanisms are computed in terms of variations of energy levels in each of these frequency-direction elements. All wave parameters such as significant wave height, frequency of the spectral peak, mean wave direction, etc. are computed from these discrete elements. The physics embodied in the model represents a time-tested yet advanced wave generation formulation. It is the first discrete spectral model to be based upon an f-4 equilibrium range formulation. As such, it represents a model that is consistent with energy conservation in the equilibrium range as calculable from the complete or reduced Boltzmann integrals. The fetch-growth characteristics of the model are similar to the JONSWAP relationships, i.e. wave energy increases linearly with fetch; and the duration-growth characteristics are similar to those of Resio (1981) and the Navy's Spectral Ocean Wave Model (SOWM). The model includes energy source and sink terms describing wave shoaling, refraction, wind effects, wave-wave interactions and bottom interaction effects.

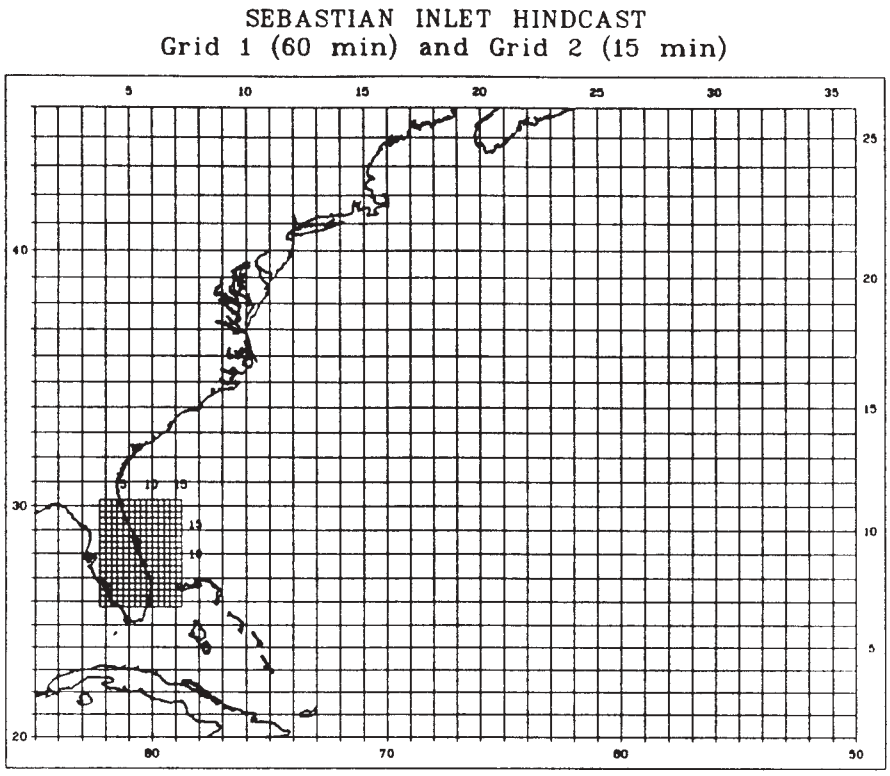


Figure 9 - Wave model grids #1 and #2 used in Canaveral/Sebastian hindcasting validation.

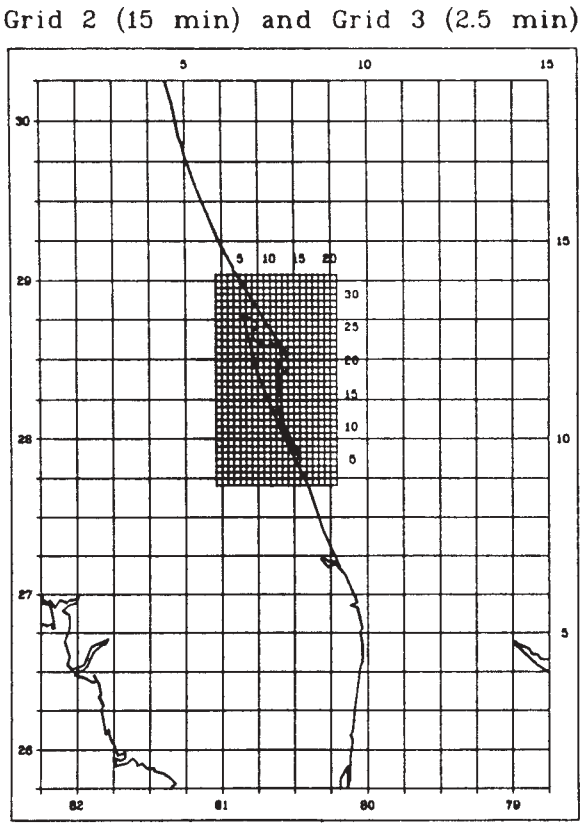


Figure 10 - Wave model grids #2 and #3 used in Canaveral/Sebastian hindcasting validation.

## 5.3 Model Validation Techniques

This project was performed to demonstrate the validity of hindcasted winds and waves for the Sebastian Inlet area. Offshore wind and hindcasted wave fields were validated against available marine buoys which reflect over-water winds and measured waves. Many offshore buoys were used throughout the Atlantic Ocean for assessing the performance of the modeling; however, the closest offshore buoy to the Sebastian Inlet area (41009) was used for a quantitative assessment. Buoy 41009 is a 6-meter NOMAD buoy located at 28.50N/80.18W in water depth of 42m, as indicated in Figure 1. Since March 1996, the buoy reports wind, wave and temperature conditions but no wave directions.

Nearshore wave conditions were validated against the PUV directional wave gage (pressure gage/current meter) deployed locally offshore of Sebastian Inlet at 27.866N/80.446W since August 1996. The gage is in approximately 8 meters of water, with the pressure transducer about 1.3 meters above the seabed.

## 5.4 Results - Offshore Waves at Cape Canaveral

Time histories for September and December, 1996, are shown in Figures 11 and 12. Field data were taken from NOAA Buoy 41009. Statistics for the entire period from August to December are shown in Figures 13 and 14. Both the time histories and statistics indicate an excellent validation of the wave model against measured offshore wave heights, where a correlation coefficient of 0.91 was achieved. Generally, the modelled wave heights are slightly underpredicted with some extreme events having more deviation from the measurements. As mentioned earlier, fine scale storm characteristics such as frontal boundaries and low pressure cells are not resolved at the scale of the wind fields used for this hindcast, but can be enhanced using supplemental data if improved accuracy is needed for more energetic, less frequent events.

Wave period validations exhibit a correlation of 0.64. Generally, wave period, here defined as spectral peak period, is a more difficult parameter to compare because spectral peakedness, bimodality, and other such characteristics of the wave spectrum can greatly affect the period selected as the peak period. For example, a bimodal spectrum with a high frequency (sea) peak and a low frequency (swell) peak may have similar amounts of energy in both peaks. The modeled spectrum may indicate that one peak is greater by a small amount, and the measurements may indicate the other is greater, whereas both could justifiably be selected as the spectral peak given the confidence limits on the estimated spectrum. Another example would be a broad spectrum, where energy is spread somewhat equally across several adjacent energy bands and the peak could be chosen at frequency bands across the range of the flat peak.

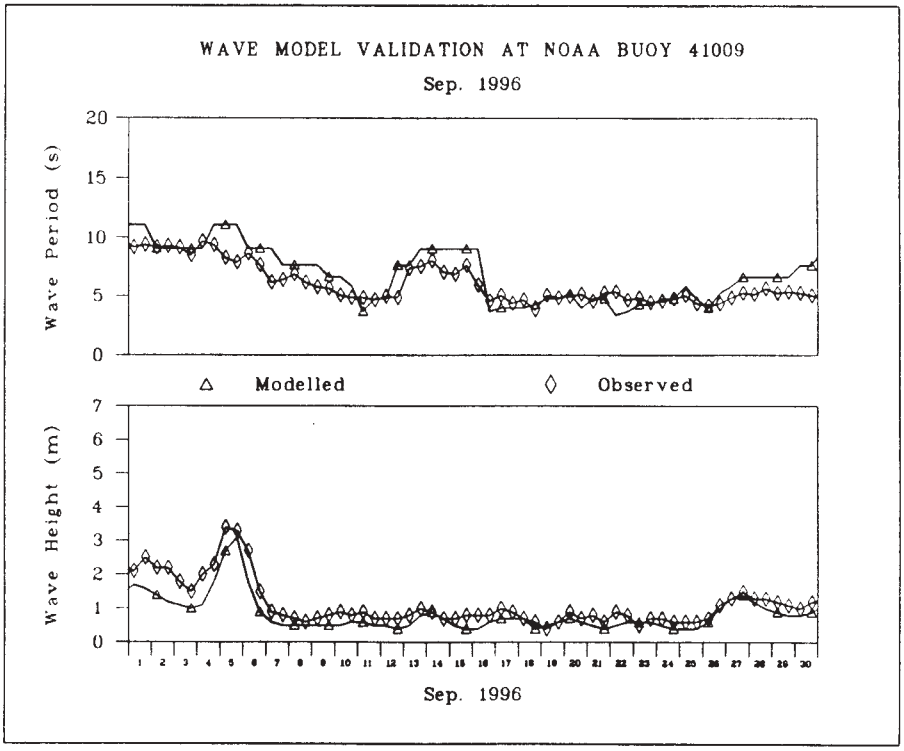


Figure 11 - Comparison of wave model results off Cape Canaveral to NOAA Buoy 41009 during September, 1996.

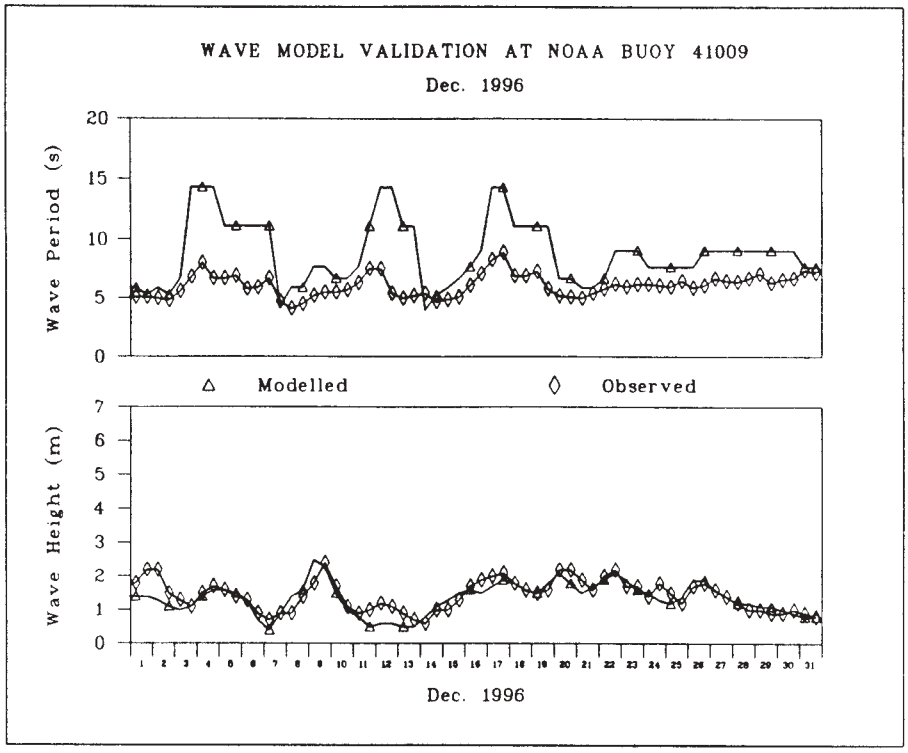


Figure 12 - Comparison of wave model results off Cape Canaveral to NOAA Buoy 41009 during December, 1996.

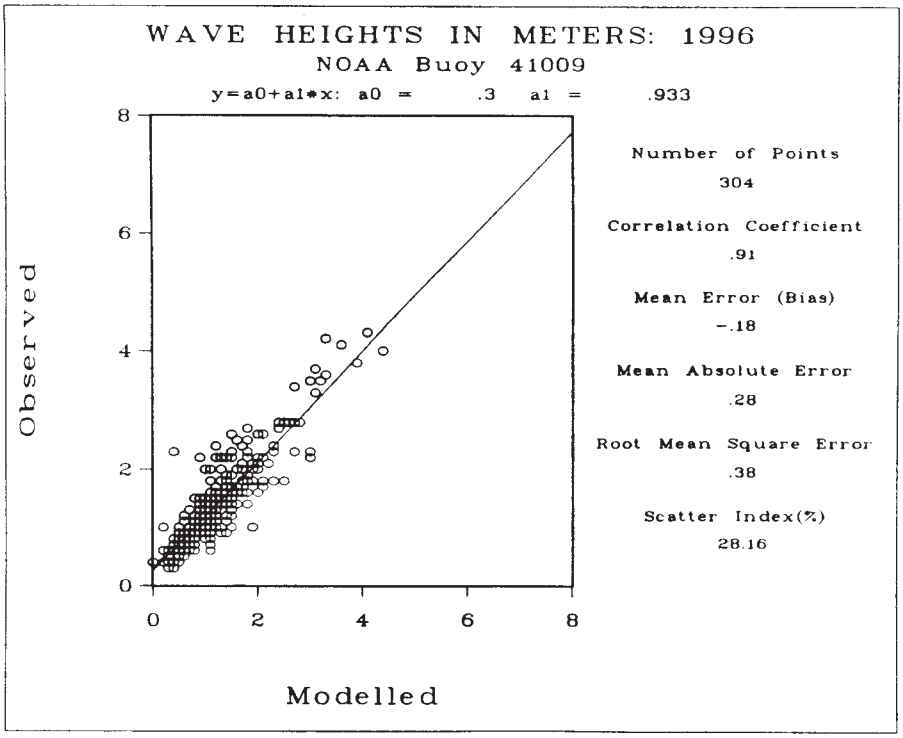


Figure 13 - Correlation of modelled heights off Cape Canaveral to NOAA Buoy 41009 during Aug.-Dec., 1996.

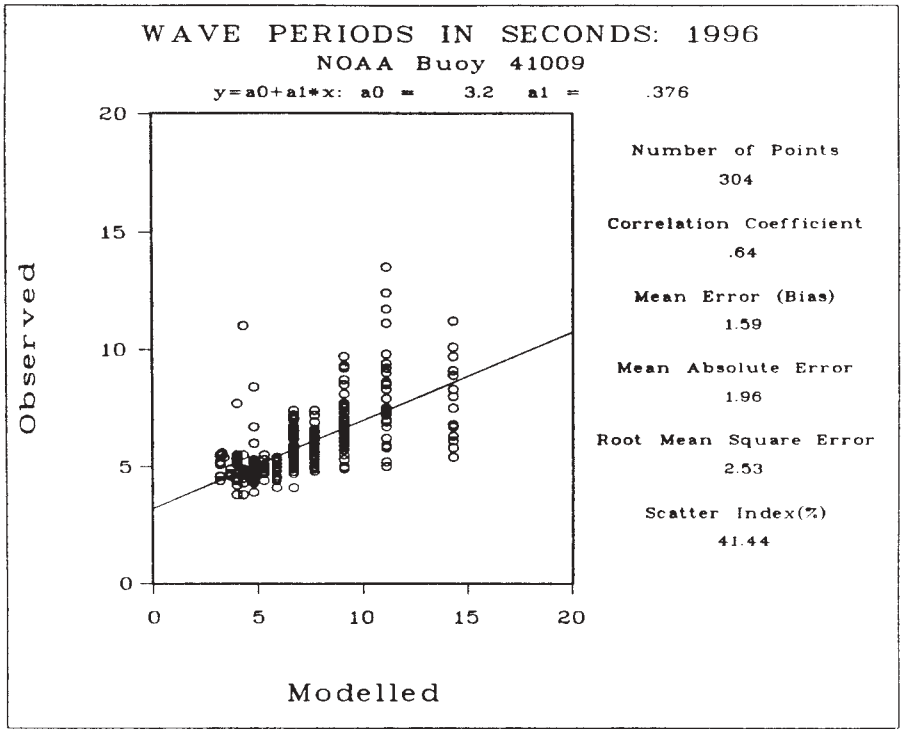


Figure 14 - Correlation of modelled periods off Cape Canaveral to NOAA Buoy 41009 during Aug.-Dec., 1996.

5.5 Results - Nearshore Waves at Sebastian Inlet

Time history comparisons from the Sebastian gage and the wave model for $H_{mo}$, $T_p$, and $\theta_p$ for August, October, and November, 1996, are shown in Figures 15, 16, and 17. Statistics for the same period are shown in Figures 18, 19, and 20. Both the time histories and statistics indicate an excellent validation of the wave model against measured wave heights, where a correlation coefficient of 0.84 was achieved (Figure 18). The fitting statistics are very similar to those found at the offshore buoy; however, in reviewing the time history it appears that deviations from measurements may be more likely due to model waves on a finer nested grid in order to include local bathymetric detail. Note that the model now exceeds the measurements during high-energy events, indicating that wave breaking and/or bottom friction may be important.

Wave period has a correlation of 0.57 (Figure 19) but with less error and scatter than found at the offshore gage. Here it appears that the field data analysis has produced a highly varying peak period, whereas the model produces a smoother representation of the same time history.

Directionally, the wave model appears to track the behavior of the measurements fairly well, with correlation of 0.56 (Figure 20). However, the measurements display fine-scale temporal variability that the model does not represent, resulting in mean errors on the order of 10-20 degrees. Also, as with the peak period, the spectral peak direction is a parameter that can be unstable when sea and swell energies are comparable.

Although correlation of $T_p$ and $\theta_p$ are somewhat less than satisfactory, much of the disagreement occurs when $H_{mo}$ is less than 0.3m. In addition to the model itself, this could indicate a problem with gage response during low energy conditions, due to the fact that the Sebastian instrument is bottom - mounted.

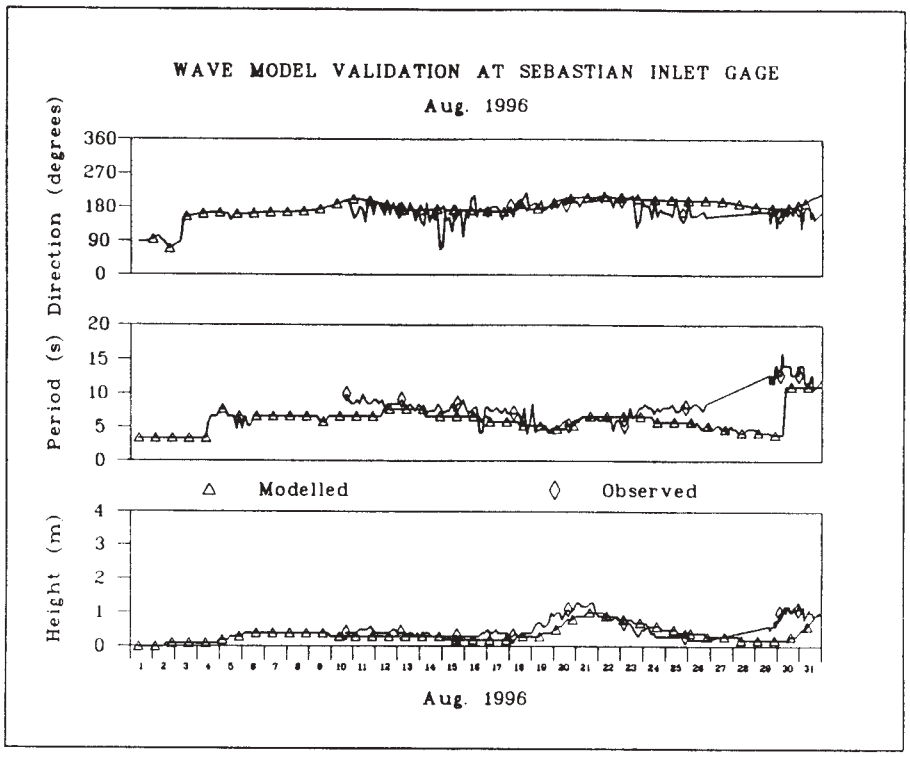


Figure 15 - Comparison of wave model results to PUV data at Sebastian Inlet for August, 1996.

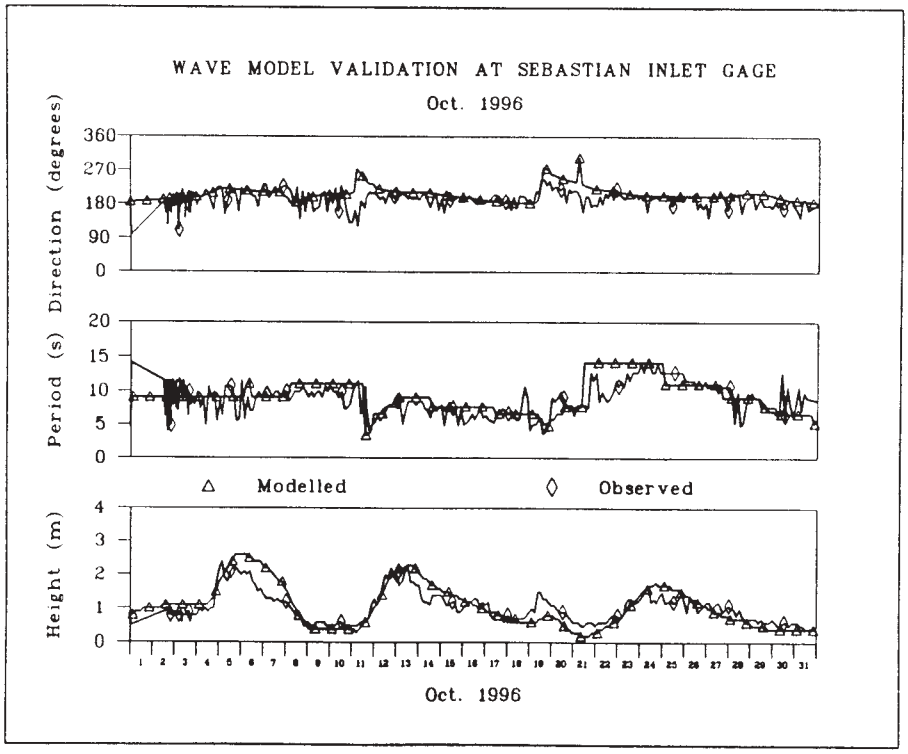


Figure 16 - Comparison of wave model results to PUV data at Sebastian Inlet for October, 1996.

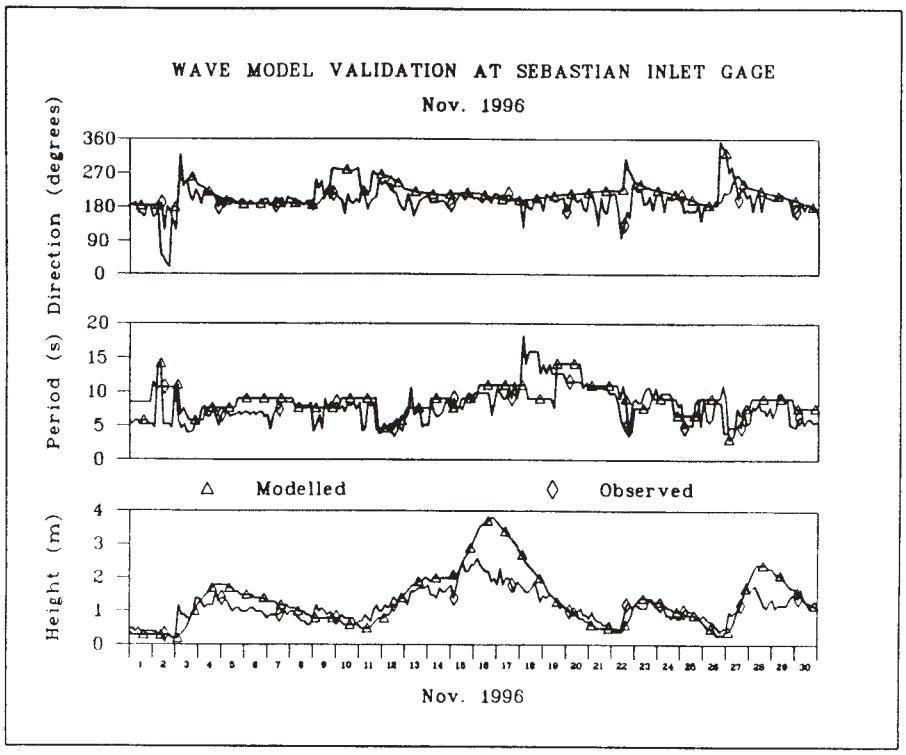


Figure 17 - Comparison of wave model results to PUV data at Sebastian Inlet for November, 1996.

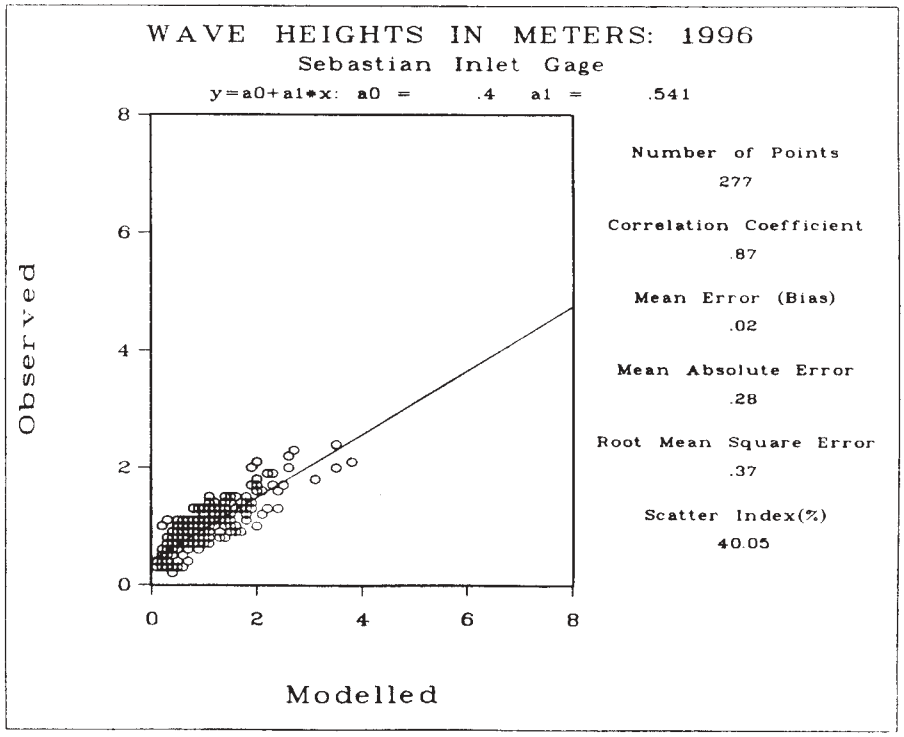


Figure 18 - Correlation of modelled heights to Sebastian PUV gage during August-December, 1996.

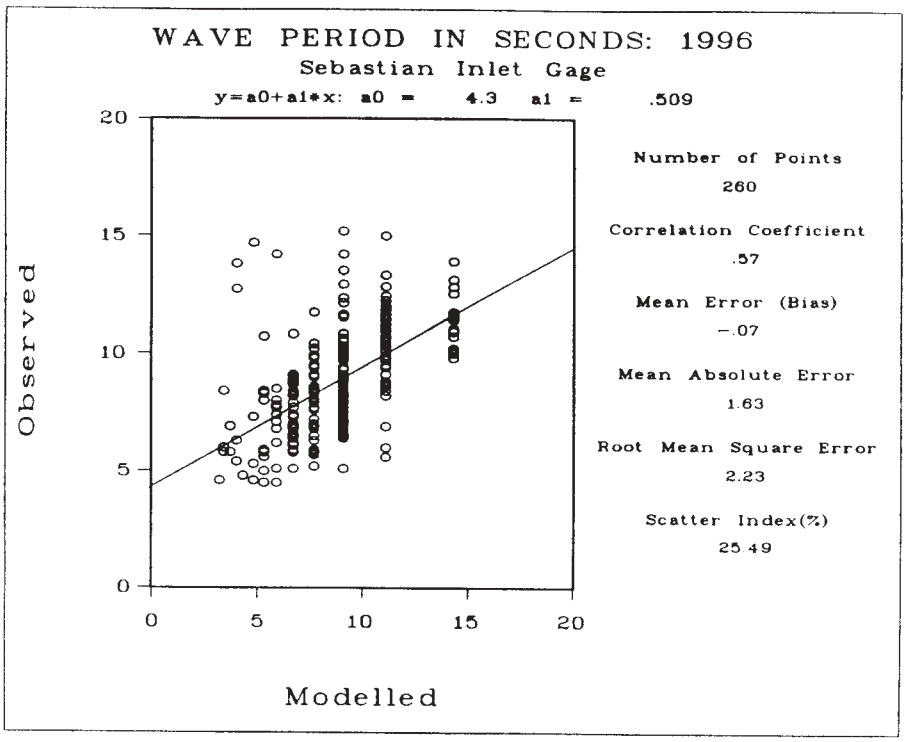


Figure 19 - Correlation of modelled periods to Sebastian PUV gage during August-December, 1996.

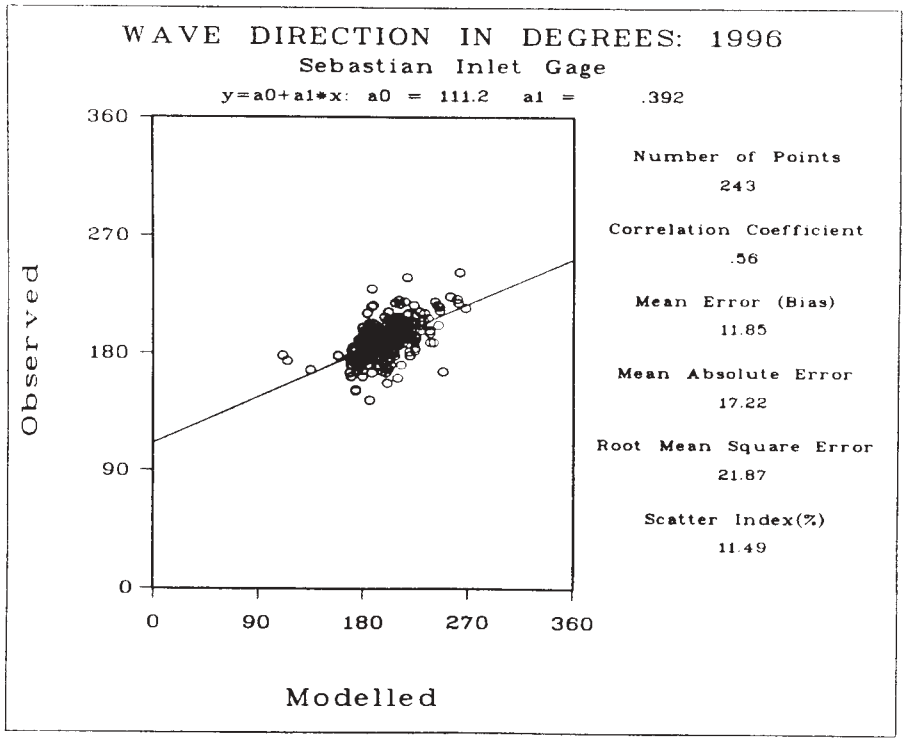


Figure 20 - Correlation of modelled directions to Sebastian PUV gage during August-December, 1996.

## 6.0 CONCLUSIONS

Based on comparisons and correlations of the WISWAVE hindcasts to buoy measurements in relatively deep water (24m) and PUV measurements in relatively shallow water (8m), it can be concluded that the wave model provides reliable estimates of the total wave energy contained in the spectrum, as parameterized by $H_{mo}$. However, the model does not predict spectral peak period and direction as well. This may be due to inherent instability in these parameters when sea and swell components are comparable in energy. To resolve this issue, period and direction should be tested using parameters that are more stable, as well as more meaningful to the intended application (e.g. sediment transport). One possible method would be to simply compute the total root mean square error in energy density from a bin-by-bin comparison of the frequency spectrum and direction spectrum, individually.

Finally, when atmospheric information becomes available for the 1997 calendar year from NCAR, the period January 1997-August 1997 will be hindcasted as well, to complete a full year of comparison. If successful, the WISWAVE model and improved NCAR weather data will then be used to develop historic hindcasts for the Sebastian Inlet region, and the long-term probabilistic modeling then revisited.

## 7. REFERENCES

Brooks, R.M. and Brandon, W.A., 1995, "Hindcast wave information for the U.S. Atlantic coast: update 1976-1993 with hurricanes," WIS Report 33, U.S. Army Engineer Waterways Experiment Station, Vicksburg, MS.

Kalnay, et al., 1995, National Weather Service Bulletin.

Leyden, V.M., 1997, "Probabilistic modeling of long-term wave climate," MSc. Thesis, Florida Institute of Technology, 124pp.

Resio, D.T., 1981, "The estimation of wind wave generation in a discrete spectral model," J. Physical Oceanography 11(4).

Acknowledgments - Portions of this study were financially supported by the Sebastian Inlet Tax District Commission.

# WIND-WAVE CLIMATE OF THE BLACK SEA AND THE TURKISH COASTS (NATO TU-WAVES PROJECT)

**Erdal Özhan and Saleh Abdalla**

*Ocean Engineering Research Center, Middle East Technical University*
*06531 Ankara, Turkey*

## 1. INTRODUCTION

Reliable data on the wind-wave characteristics affecting any coastal region are essential for almost all coastal and marine activities. This information may be either of statistical nature, derived from wave data covering a sufficiently long period of time (i.e. wave climate), or of daily predictive type, obtained by routine wave forecasting. The former type of data is needed for planning, design and management purposes, whereas the later type is required for all daily coastal and marine operations such as shipping, sailing and coastal construction activities.

Reliable wave data do not exist for the Turkish coast, which runs in excess of 8,300 km in length and extends along the Black Sea, the Aegean Sea, the Mediterranean, and the inland Sea of Marmara. In order to fill this gap, an extensive project, called NATO TU-WAVES Project (Özhan and Abdalla, 1992, 1993a, 1993b, 1997a, 1997b and 1997c, and Özhan et al. 1995), which includes systematical wave measurements, wave modelling and wave climate computations is being carried out with a partial financial support from the NATO Science for Stability (SfS) Programme - Phase III.

The main objectives of the project are as follows:

- To obtain detailed knowledge on wind waves affecting the Turkish coast and the whole of the Black Sea basin and to establishing a reliable data bank,
- To verify and implement a third generation wind-wave model for the seas surrounding Turkey (Black Sea, Sea of Marmara, Aegean Sea and the Eastern Mediterranean), and
- To construct a wave atlas for the Turkish coasts and the whole of the Black Sea basin in order to provide statistical information on sea state parameters.

The NATO TU-WAVES Project is led by Ocean Engineering Research Center of Middle East Technical University (METU-KLARE). Three other national organizations; namely: Department of Navigation, Hydrography and Oceanography of Turkish Navy (TN-DNHO), General Directorate of State Meteorological Services (SMS), and Ministry of Transport - General Directorate of Railway, Harbor and Airport Construction (MT-RHAC GD); are taking part in the project.

The Black Sea wind-wave climate is an international dimension of the project. This outreach component is being handled in collaboration with eight institutes from four Black Sea riparian countries as follows: Institute of Oceanology (IO), Varna, Bulgaria; the National Institute of Meteorology and Hydrology (NIMH), Bucharest, and the Rumanian Marine Research Institute (RMRI), Constantza, Rumania; Arctic and Antarctic Research Institute (AARI), St. Petersburg, Moscow State Technological University (MSTU), Moscow, and the P.P. Shirshov Institute of Oceanology (SIO), Gelendzhik, and State Oceanographical Institute (SPOGOIN), St. Petersburg, Russia; and Marine Hydrophysical Institute (MHI), Sevastopol, Ukraine.

## 2. WAVE GAGING AND ANALYSIS

To achieve the objectives of TU-WAVES Project, a national wave gaging network of six stations (at Alanya on the Mediterranean coast; Dalaman and Bozcaada on the Aegean Sea coast; Sinop and Hopa on the Black Sea coast; and finally Marmara Ereğlisi in Sea of Marmara) was set-up as shown in Fig. 1. A Black Sea gaging network was also set-up with four stations at the other Black Sea riparian countries (at Gelendzhik of Russia; Katziveli and Karkinitskaya Oil Platforms of the Ukraine; and Gloria Oil Platform of Romania) in addition to the two national stations at Sinop and Hopa. For the locations and the other detailed characteristics of each station the reader is

referred to Özhan and Abdalla (1997a, 1997b and 1997c).

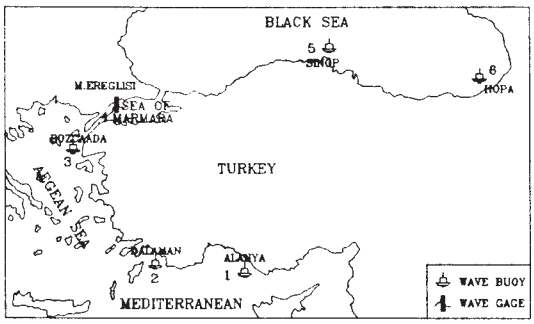


**Fig. 1:** The national wave gaging network.

The data collected at the gaging stations are gathered at the project center which is located at METU-KLARE. The data were used for short term statistical analysis to understand the characteristic of the wind waves affecting the Black Sea and the remaining Turkish coasts (e.g. Turhan, 1996 and Özhan et al., 1997). The measurements have been used for verification of the wave models and the sources of the wind fields to be used for the wave climate computations.

## 3. WAVE MODELING

Wave atlas, which is the ultimate goal of the TU-WAVES Project, will be an invaluable tool for coastal and marine planning, management, and operations along the Turkish coast, as well as the whole Black Sea. Wave climatology and wave atlas computations require wave data which cover the whole sea area of interest for a relatively lengthy period of time (few decades). Therefore, wave measurements alone are not enough for constructing the wave climatology or the wave atlas due to their limited spacial (few locations only) and temporal (few years only) coverage. Wave modelling solves this problem. Two advanced wave models are utilized for this purpose: METU3 and WAM. METU3 is a third generation wind-wave model developed at METU (Abdalla, 1991; and Abdalla and Özhan, 1994). WAM is a well known third generation wave model used for operational forecasts at several meteorological centers (the WAMDI Group, 1988). Both models has been used in extensive hindcasting exercises over the Eastern Mediterranean (including the Aegean Sea), the Black Sea and the Sea of Marmara. Typical hindcasting results are presented in Fig. 2 where the measured and predicted (using both WAM and METU3) significant wave height, mean wave period and mean wave direction at the gaging station Sinop during the whole month of November 1994. As can be seen in Fig. 2, in general both models give rather good agreement with the measured quantities with minor differences between the predictions of both models. Most of the disagreement between model results and the measurements can attributed to the possible errors in the wind fields which were obtained from the European Centre for Medium-Range Weather Forecast (ECMWF).

It is rather well known that the third generation wave models are satisfactorily reliable for many practical applications. Therefore, for reliable wave prediction, it is essential to have reliable input wind fields. Obtaining these fields may be the most problematic task of wind-wave prediction, especially for an extended period of time. Regardless of the degree of reliability, this type of data is usually obtained from the meteorological models operated by some meteorological organizations like ECMWF and the U.K. Meteorological Office (UKMO).

A survey for the available wind sources for the Eastern Mediterranean, Aegean, Marmara and the Black Seas was conducted (Özhan et al., 1995). The following wind sources were evaluated for possible use in generating the wind fields needed for the long-term wave hindcasting:

- ECMWF forecast and analysis wind fields: ECMWF runs a global operational weather forecasting system for more than 15 years by now. Surface wind components ($U_{10}$) are among the several weather parameters computed by the model. The model provides both objective analysis fields for the last 24 hours by assimilating available observations, and daily forecasts for a number of days (10 days in the current version) both at 6 hours intervals. The forecasting system has undergone several modifications and enhancements over the years. The system predictions (especially the analysis fields) are of acceptable quality for wave prediction only since September 1991 when the model was upgraded to what is called T213 spectral model, with a nominal horizontal resolution of about 80 km and vertical resolution of 31 levels. The wind fields of the model during 1987-1991 were of lower quality basically due to the coarser resolutions. These fields can not be used for reliable wave predictions (Cavaleri et al., 1991). However, they can be used for qualitative descriptions and as initial and boundary conditions for local area models (LAM's). The ECMWF wind fields before 1987 are not recommended to be used for wave predictions at all (Cavaleri, personal communications).

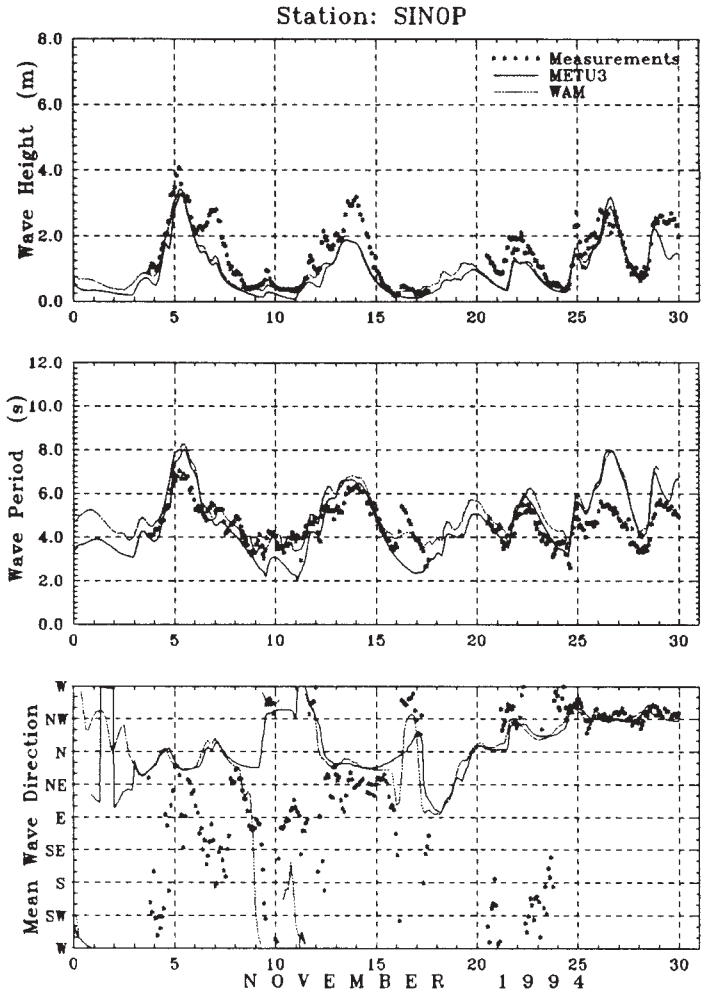


**Fig. 2:** Time histories of significant wave heights and mean wave periods and directions at Sinop.

- UKMO assimilated winds: UKMO runs a global operational weather forecasting model similar to that of ECMWF. Furthermore, they run a Limited Area Model (LAM) that covers the grid extending from 80°W to 40°E and from 30°N to 80°N. This covers the area of interest to TU-WAVES Project except the eastern end of the Black Sea. The grid resolution of the LAM, between October 1986 - June 1991, was 0.75° latitude x 0.9375° longitude (this resolution was enhanced in June 1991). The model provides both assimilated winds (similar to the analysis fields of ECMWF) and forecast fields on hourly basis twice a day. The model predictions were found recently, to underestimate the high wind speeds (exceeding 11 m/s). This problem is due to a wrong treatment of the surface boundary layer and was overcome early this year (Cavaleri, personal communications). The assimilated wind fields produced by the UKMO-LAM could be used for the period October 1986 - June 1991 due to its enhanced resolution over the ECMWF at that time. However, they were not used for this Project since the model does not cover the whole Black Sea and, more important, the cost of obtaining this information is very high for the budget of a basic research project.

- Use of wind models: It is also possible to use one of the available wind models to estimate the wind fields. This seems to be the only alternative for the period before 1986. Wind models can be divided into two groups: simple geostrophic or gradient models and complicated 3-D. models. Models of the first group are simple enough but are probably of lower reliability. The second group models are expected to be more reliable, but they are computationally very expensive and require an appreciable amount of input data as well as initial and boundary conditions. Synoptic pressure values, which are the basic input data for

both classes of wind models, can be obtained from any meteorological organization operating globally like ECMWF. Synoptic maps prepared by the local meteorological organizations like SMS and Russian (or the former USSR) Navy can be digitized for the same purpose to cover the period of 25 years (1970-1995) for the extreme storms.

Wave models were forced using several wind sources and the wave predictions were compared to wave measurements at the project gaging stations. Fig. 3 shows typical comparison between the wave predictions using the ECMWF forecast and analysis wind fields and the forecast wind fields of the LAM Eta Model (which is an experimental model used at the ICSC-Mediterranean Research Center, Erice, Italy). The wind fields of the Eta model were not successful to produce good wave predictions as compared to ECMWF wind fields. Fig. 2 also was obtained using the ECMWF analysis wind fields. In general, it was realized that the ECMWF analysis wind fields are of acceptable quality for wave prediction in the Eastern Mediterranean and, to a certain degree, in the Black and the Aegean Seas only since September 1991 (when the resolution of the ECMWF meteorological model was enhanced). These wind fields are of lower quality during 1987-1991 basically due to the coarse resolution of the ECMWF model at that time.

The ECMWF wind fields since 1991 (more than 6 years of continuous data) are being used to compute the corresponding wave fields in order to estimate the long term (operational) wave statistics. On the other hand, the need for extreme wave data for an extended period of time (26 years) motivated the use of the simpler, yet more oriented to local conditions, gradient wind models. The gradient wind model of Cavaleri et al. (1996) and that of Lavrenov et al. (1995) were considered in a pilot study to check the reliability of such models. The procedure followed was to digitize

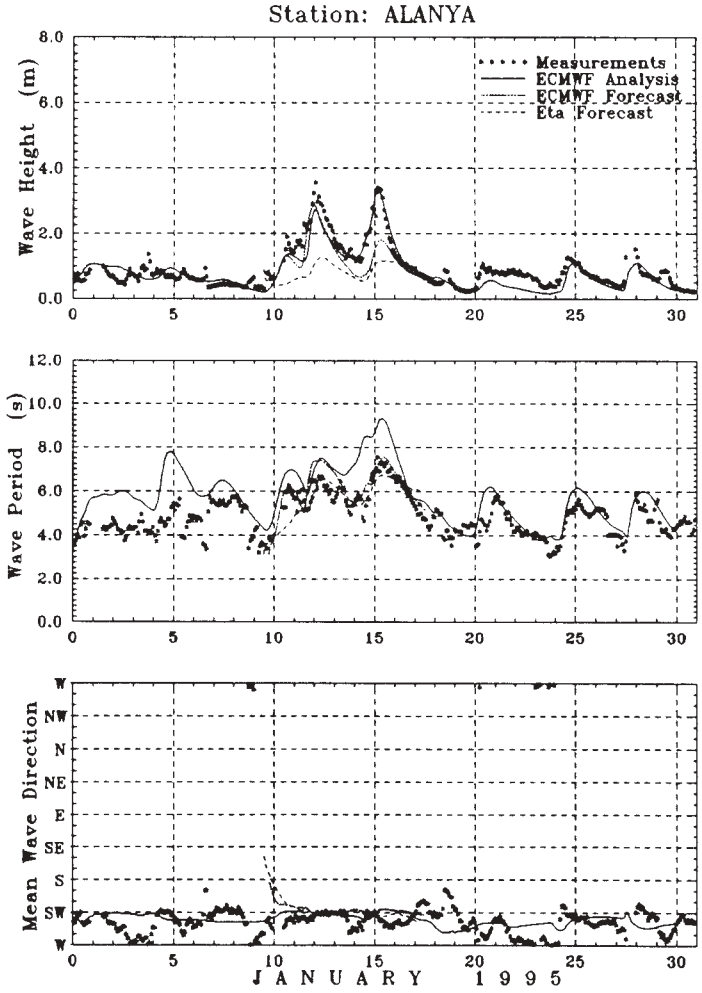


**Fig. 3:** Time histories of significant wave heights and mean wave periods and directions at Alanya.

the synoptic maps available at some of the state organizations dealing with meteorological matters in the Black Sea riparian countries (e.g. the Turkish State Meteorological Services and the Russian Navy). The digitized pressure fields were used to compute the corresponding gradient wind fields, which were later reduced to estimate the surface wind fields using some empirical reduction coefficients used for this purpose. The surface wind fields were used to drive the WAM model and the predicted wave characteristics were compared with the corresponding wave measurements at the TU-WAVES gaging stations. Fig. 4 shows one of the results of this exercise which is a storm over the Black Sea during 4-9 November 1994. The wave predictions using both the wind fields produced by the gradient model from the digitized synoptic maps ("digitize" fields) and the ECMWF analysis wind fields are not so much successful in reproducing the measured wave characteristics. But the overall results can be accepted. The worst hindcasting results obtained using the ECMWF analysis wind fields is the wave predictions at Hopa during 25-27 January 1995. Fig. 5 shows this situation with the wave hindcasts using the "digitize" wind fields are much better than those produced using the ECMWF fields. There is a shift of the peak of the storm in the case of the "digitize" fields. This should not be of significant problem as far as the wave climate is considered. It is worthwhile to mention that the predictions using both wind sources gave comparable wave predictions at the other gaging stations. Unfortunately there was no measured wave data to compare the prediction results

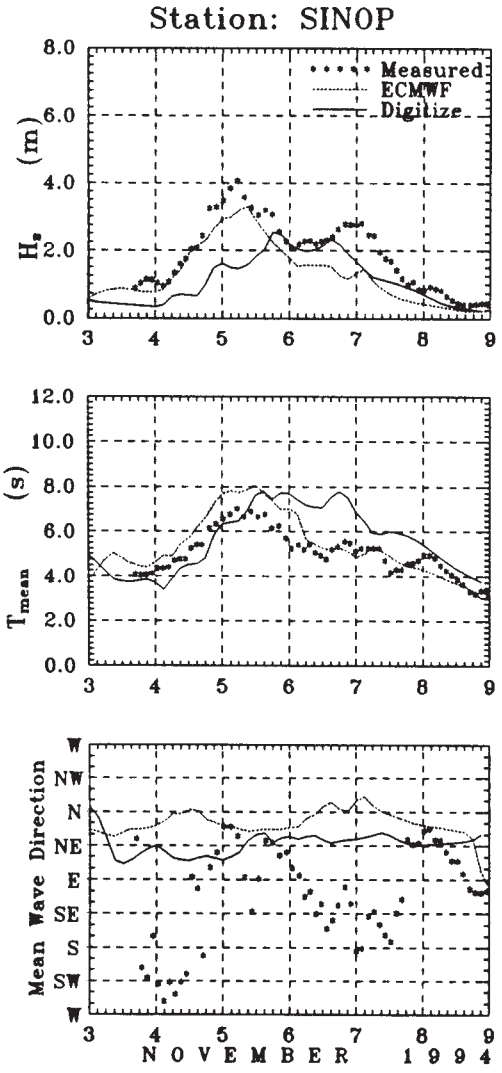


**Fig. 4:** Significant wave heights and mean wave periods and directions at Sinop.

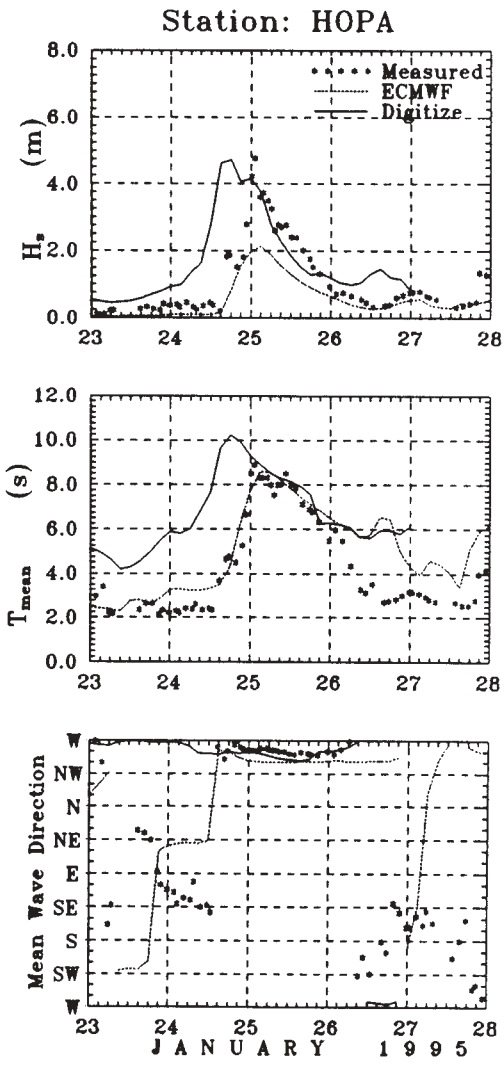


**Fig. 5:** Significant wave heights and mean wave periods and directions at Hopa.

with at the other stations. The one dimensional (1-D) wave spectra at Hopa around the storm peak is shown in Fig. 6. Furthermore, the corresponding 2-D wave spectra are given in Fig. 7 for 21:00 UT on 25 January, Fig. 8 for 00:00 UT on 26 January and Fig. 9 for 03:00 UT on 26 January. It seems that the wind was highly changeable during that storm on that part of the Black Sea (which is a typical criteria for that region). The 6-hour synoptic interval between the fields may be too coarse to resolve the temporal resolution of this changeability. It is also possible that the wind and the wave models are not able to cope correctly with this rapid change (e.g. swell may be dissipated and/or absorbed at higher rates than the true ones). Actually, detailed investigation is needed for this case. While the mean directions of the predictions (using both fields) agrees with the measurements, there is a tendency of the model to overestimate the mean wave period.

Finally, the main conclusions of this pilot study were in favour of the use of this digitization procedure and gradient wind models. There was no significant difference between the results produced by the two gradient wind models nor by the two synoptic map sources tested in the study.

## 4. MAJOR STORMS DURING 1970-1995

Wind and wave data covering few decades are needed to compute the wind and wave climate. To reduce the amount of work (wind and wave prediction), the preliminary step of identifying the major storms is vital.

A comprehensive survey for all storms recorded at the meteorological stations along the Turkish coasts of the Black, Mediterranean, Aegean and Marmara Seas was carried out by Erkal et al. (1996). The "hourly wind tables" at 32 coastal meteorological stations were investigated. "Storm" for the purpose of selecting severe storms for digitization was used in this study in a totally different manner than the usual definition of the storm. The Black Sea and the remaining Turkish coasts were divided into seven regions as: Eastern Black Sea, Western Black Sea, Marmara, Northern Aegean, Southern Aegean, Western Mediterranean and Eastern Mediterranean. The identified storms at each station of a region were tabulated yearly for helping the visual judgement for the significant storms in each region.

Although this work would give good idea about the existence and the severity of the different storms, it can not be used for wave prediction directly. Synoptic

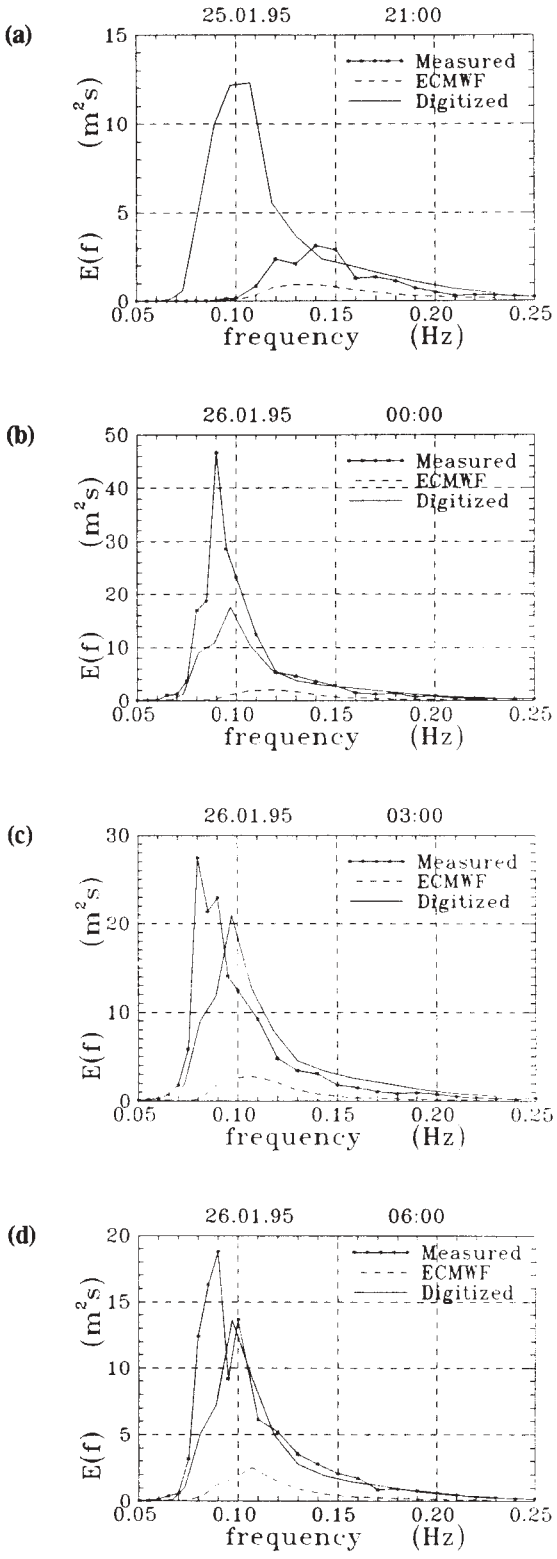


**Fig. 6:** 1-D wave spectra at Hopa at: **(a)** 21:00 UT on 25.01.95, **(b)** 00:00 UT on 26.01.95, **(c)** 03:00 UT on 26.01.95, and **(d)** 06:00 UT on 26.01.95.

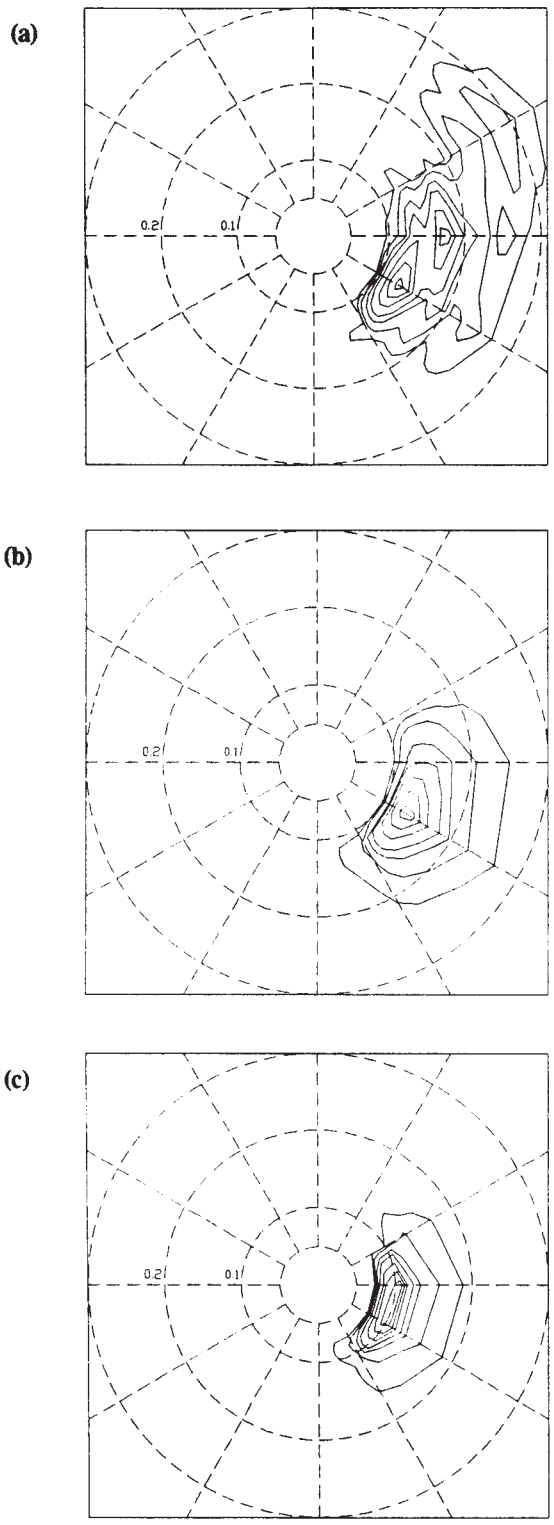


**Fig. 7:** 2-D wave spectra at Hopa at 21:00 UT on 25.01.1995: **(a)** measured, **(b)** modeled using ECMWF winds, **(c)** modeled using "digitize" winds. (Contours from outside are 0.05, 0.1, 0.2, 0.3, 0.5, 0.7 and 0.9).

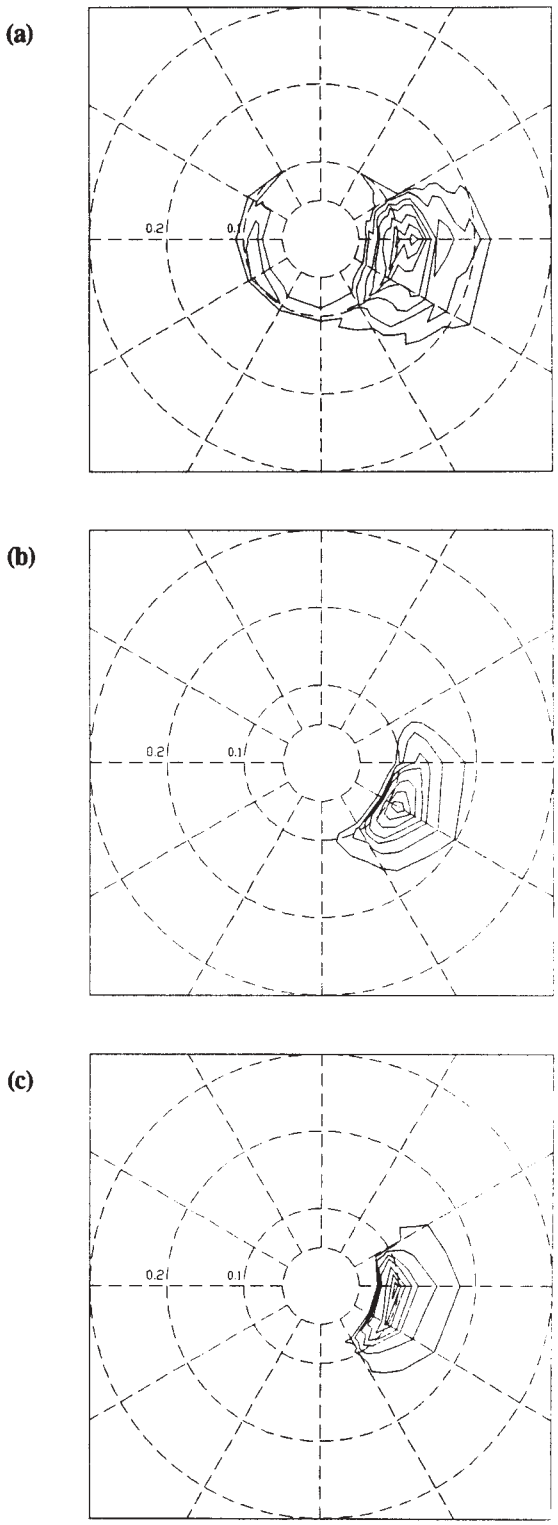


**Fig. 8:** 2-D wave spectra at Hopa at 00:00 UT on 26.01.1995: **(a)** measured, **(b)** modeled using ECMWF winds, **(c)** modeled using "digitize" winds. (Contours from outside are 0.05, 0.1, 0.2, 0.3, 0.5, 0.7 and 0.9).

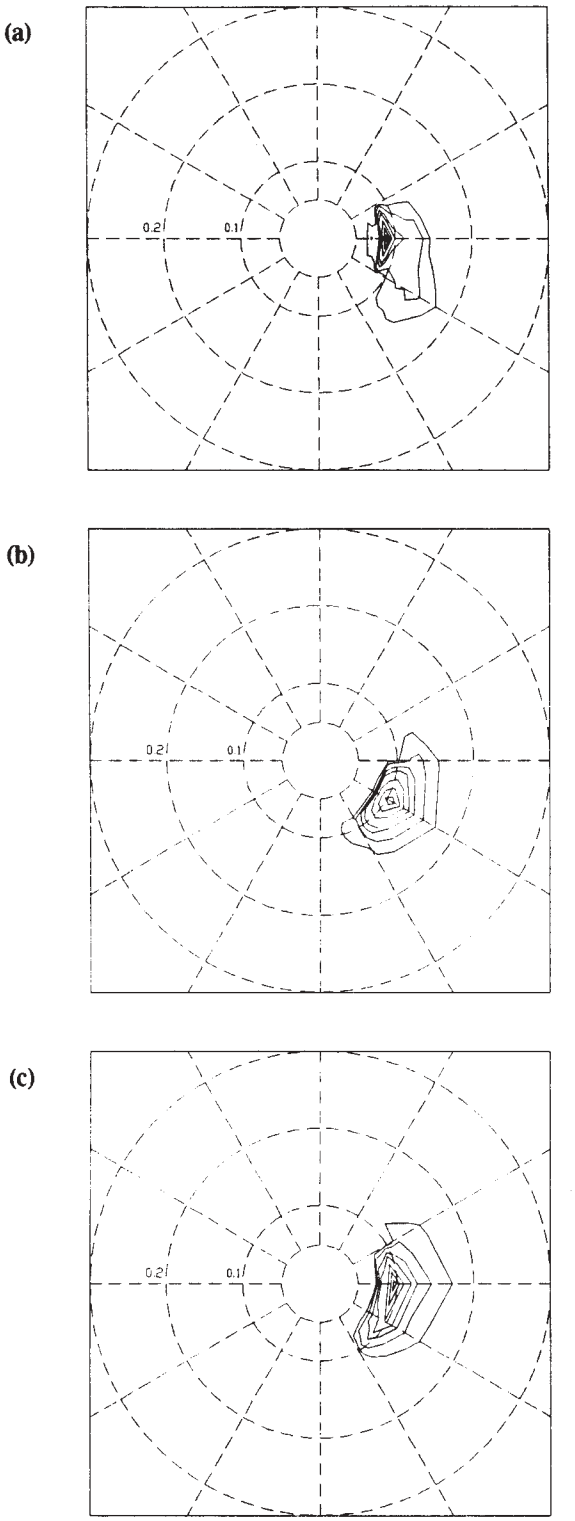


**Fig. 9:** 2-D wave spectra at Hopa at 03:00 UT on 26.01.1995: **(a)** measured, **(b)** modeled using ECMWF winds, **(c)** modeled using "digitize" winds. (Contours from outside are 0.05, 0.1, 0.2, 0.3, 0.5, 0.7 and 0.9).

maps archived at the Turkish State Meteorological Services have been obtained for the selected storms based on the current work and digitized to compute the wind fields needed for wave prediction.

Since the number of storms, thus the number of synoptic maps to be digitized is too large, only representative extreme storms were selected. Table 1 shows the annual number of significant storms, total number of stormy days and the approximate number of synoptic maps to be digitized for the Black Sea. As can be seen from Table 1, a total of 6582 synoptic maps are considered for digitization for the period 1970-1995 for the Black Sea. More than 5500 maps already have been digitized so far. Similarly, the numbers related to the significant storms affecting the remaining Turkish coasts are shown in Table 2. The amount of the additional synoptic maps to be digitized for the storms covering the Turkish coasts on the Mediterranean and the Aegean Sea is 8551 maps as can be seen in Table 2.

## 5. WIND AND WAVE MODELING FOR THE SEA OF MARMARA

The Sea of Marmara is a small inland sea of Turkey connecting the Aegean Sea with the Black Sea. Sea of Marmara has a length of 250 km (in the east-west direction) and a width of 90 km (in north-south direction). Global models (such as the ECMWF T213 operational meteorological model) produce wind fields which are reliable enough for wave computations over large basins. However, due to their relatively coarse resolutions, the global models fail to resolve local events, which make the predictions of these models rather poor for small water basins like the Sea of Marmara. On the other hand, the Sea of Marmara is so small that the errors produced during the digitization of synoptic maps would be significant and can not be recovered as in the case of larger basins. Therefore, the procedure used for the Black Sea, which is composed of the digitization of synoptic maps and the use of gradient wind models, is not proper for the Sea of Marmara. Furthermore, the wind velocities measured at coastal meteorological stations can not be utilized for wind field computations over the basin due to the effect of roughness and topography.

A wind model based on the atmospheric pressure records of the meteorological stations surrounding the water basin was developed by Erkal (1997). The pressure measurements are not affected by roughness (and are very slightly affected by topography). The pressure records at 14 stations surrounding the Sea of Marmara were used. The pressure values were passed

**Table 1:** Annual distribution of extreme storms affecting the whole Black Sea and their durations.

| Year | No. of Storms | No. of Days | No. of Maps |
|---|---|---|---|
| 1970 | 8 | 36 | 144 |
| 1971 | 9 | 49 | 196 |
| 1972 | 8 | 44 | 176 |
| 1973 | 11 | 54 | 216 |
| 1974 | 9 | 61 | 244 |
| 1975 | 10 | 45 | 180 |
| 1976 | 8 | 47 | 268 |
| 1977 | 13 | 61 | 427 |
| 1978 | 10 | 46 | 321 |
| 1979 | 12 | 68 | 486 |
| 1980 | 5 | 45 | 280 |
| 1981 | 11 | 67 | 449 |
| 1982 | 7 | 34 | 248 |
| 1983 | 6 | 21 | 135 |
| 1984 | 5 | 22 | 157 |
| 1985 | 9 | 38 | 250 |
| 1986 | 8 | 40 | 242 |
| 1987 | 8 | 42 | 296 |
| 1988 | 7 | 37 | 259 |
| 1989 | 8 | 44 | 304 |
| 1990 | 11 | 47 | 338 |
| 1991 | 7 | 39 | 212 |
| 1992 | 10 | 37 | 193 |
| 1993 | 9 | 43 | 230 |
| 1994 | 8 | 34 | 174 |
| 1995 | 7 | 33 | 157 |
| Total | 224 | 1134 | 6582 |

**Table 2:** Annual Distribution of Storms and Their Durations affected the Turkish Coasts on the Mediterranean and the Aegean Sea.

| Year | No. of Storms | No. of Days | No. of Maps |
|---|---|---|---|
| 1970 | 14 | 56 | 224 |
| 1971 | 13 | 66 | 264 |
| 1972 | 11 | 58 | 232 |
| 1973 | 13 | 67 | 268 |
| 1974 | 10 | 65 | 260 |
| 1975 | 12 | 57 | 228 |
| 1976 | 11 | 59 | 301 |
| 1977 | 12 | 82 | 571 |
| 1978 | 16 | 58 | 426 |
| 1979 | 10 | 65 | 442 |
| 1980 | 9 | 62 | 302 |
| 1981 | 12 | 79 | 483 |
| 1982 | 13 | 59 | 424 |
| 1983 | 11 | 49 | 346 |
| 1984 | 12 | 62 | 453 |
| 1985 | 12 | 50 | 336 |
| 1986 | 10 | 47 | 309 |
| 1987 | 13 | 55 | 406 |
| 1988 | 14 | 54 | 365 |
| 1989 | 10 | 40 | 281 |
| 1990 | 12 | 47 | 323 |
| 1991 | 13 | 66 | 406 |
| 1992 | 15 | 54 | 298 |
| 1993 | 12 | 46 | 183 |
| 1994 | 12 | 56 | 283 |
| 1995 | 8 | 31 | 137 |
| Total | 310 | 1490 | 8551 |

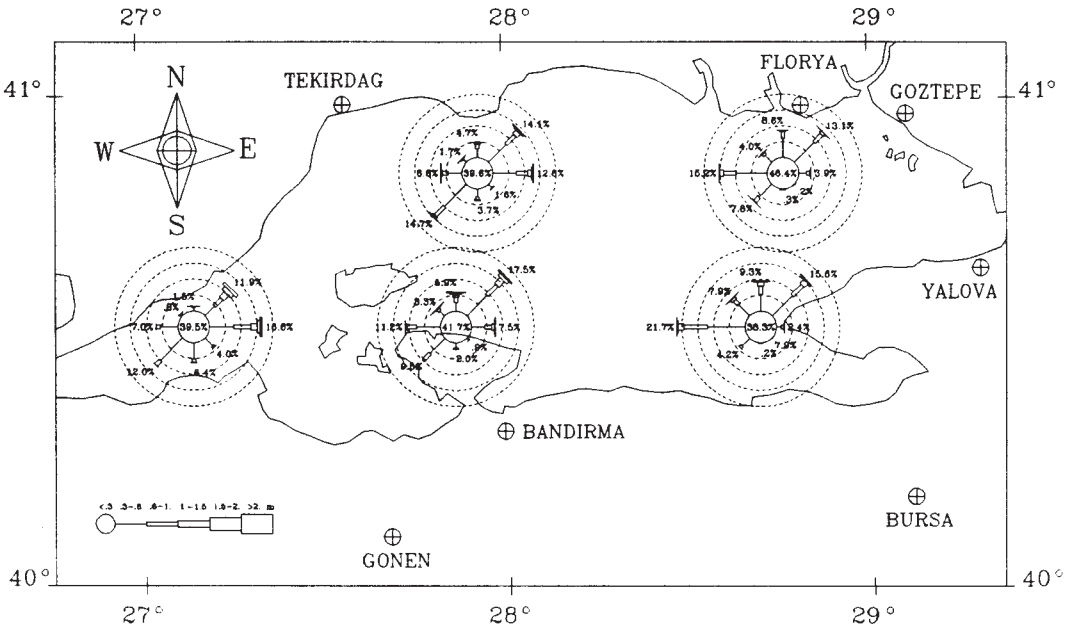


**Fig. 10:** Wave roses at five different regions of Sea of Marmara for the period of 1991-1994.

through a quality control process to discard the values which appeared as erroneous. The pressure field over the whole basin was then computed by using a surface fitting method called "quadratic distance-weighted". The gradient of the surface representing the pressure field was calculated and used to calculate the geostrophic wind. The geostrophic wind was then reduced to the 10-meter height (surface wind) by using the classical empirical reduction table of Findlater et al. (1966) and the monthly averaged stability factors for each region (Sea of Marmara was divided into three stability regions depending on the air-sea temperature differences). For verification purposes, the model was used to predict the wind fields of two months (September 1990, January 1991). Offshore wind measurements are available for those two months. The model results showed reasonably good fit to the measurements with RMS error about 3.5 m/s and bias about - 0.5 m/s (Erkal, 1997 and Abdalla et al., 1997b).

The wind and wave fields over the Sea of Marmara were calculated continuously for four years from 1991-1994; inclusively (Abdalla et al., 1997b). WAM model was used for the wave computations. The wave roses for five regions of the sea for the four years data is shown in Fig. 10. Work is being carried out to extend the temporal coverage of the data in order to perform more reliable wave climate computations for the Sea of Marmara.

## 6. WIND AND WAVE ATLAS

For the long term (operational) wind and wave statistics, the ECMWF analysis wind fields will be used together with the two third generation wave models mentioned before (METU3 and WAM). However for the extreme wind and wave statistics, a special software, developed by a team from AARI called "ALL-WAVES", is used for the digitization of the synoptic maps corresponding to the selected significant (extreme) storms. The gradient wind model of Lavrenov et al. (1995) is an integral part of this software giving it the ability to produce the wind fields from the digitized data. The produced wind fields together with METU3 and WAM models will be used to compute the wave fields from which the extreme wave statistics will be derived.

The wave atlas will be prepared in two forms: electronic (PC software) and printed atlas (book-like). The printed atlas will contain only the standard type of engineering data. On the other hand, there will be two versions of the electronic atlas: standard for engineering applications and a rather detailed one which can be used for scientific purposes as well as the engineering applications.

The electronic atlas is a form of a data-base software to present the wind and wave climate. This software is being prepared at Alkyon Hydraulics

Consultancy and Research (a Dutch firm). The software will use the results of the wave climate computations within the framework of TU-WAVES project and make the suitable presentations of all possible combination of data for practical usage. There will be two versions of the software: one for the Black Sea and the other for the whole Turkish coasts.

## 7. CONCLUDING REMARKS

Significant progress has been achieved during the first 48 months of the NATO TU-WAVES Project, which is a major collaborative effort at an international scale for establishing wave climate over the Black Sea basin and along the remaining part of the Turkish coast. The first goal of the project, that is the systematic measuring and archiving of the wind waves, has been achieved. Similarly the second goal which is related to reliable wave modelling has also been achieved through implementing and verifying two third generation wave models (METU3 and WAM).

The main ongoing efforts are directed towards the preparation of the wave atlas. The long term (operational) wind and wave statistics that covers six years will be based on the wind fields of ECMWF. The extreme wind and wave statistics will cover more than 20 years. This work is based on the digitization of the available synoptic maps for the significant storms which will be used to run a gradient wind model to estimate the corresponding surface wind fields. METU3 and WAM models will be used to compute the wave fields for the significant storms and the extreme statistics will be calculated. Finally, the results of the computations will be fed in a data-base software, which is being prepared as well, to achieve the electronic wave atlas. The engineering type of information will be published as a standard printed book-like wave atlas. At this stage, the task of the digitization of synoptic maps for the Black Sea has been completed. Several studies related to the long term wave statistics have been carried out to select the suitable distribution models (e.g. Buharalı, 1997, Abdalla and Buharalı, 1997 and Abdalla et al., 1997a).

## ACKNOWLEDGMENT

NATO TU-WAVES Project is financially supported by the NATO Science for Stability Programme (Phase III).

## References

Abdalla, S. (1991). "*Development of a third generation wind wave model applicable to finite depths*", PhD Thesis, Middle East Technical University, Ankara, Turkey.

Abdalla, S. and Buharalı, G. (1997). "The analysis of long-term statistics of wind waves at Alanya", *Proc. of the 1st. Nat. Conf. on the Coastal and Marine Zones of Turkey*, E. Özhan (ed.), MEDCOAST Publications, Ankara, Turkey, 629-638 (In Turkish).

Abdalla, S. and Özhan, E. (1994). "*METU models for wind-wave prediction*", METU-KLARE Special Report, Middle East Technical University, Ankara, Turkey.

Abdalla, S., Özhan, E. and Buharalı, G. (1997a). "Long term probability distribution of significant wave heights along the Turkish Mediterranean coast", *Proc. of the 3rd. Int. Conf. on the Mediterranean Coastal Environment, MEDCOAST 97*, E. Özhan (ed.), MEDCOAST Publications, Ankara.

Abdalla, S., Özhan, E. and Erkal, S. (1997b). "Wind and wave climate of the sea of marmara", *3rd. Int. Symp. on Ocean Wave Measurement and Analysis, WAVES 97*, 3-7 November, 1997, Virginia Beach, Virginia, USA.

Buharalı, G. (1997). "*Long term characteristics of wind wave along the Turkish Mediterranean coast*", MS Thesis, Middle East Technical University, Ankara, Turkey (In progress).

Cavaleri, L., Bertotti, L. and Lionello, P. (1991). "Wind wave cast in the Mediterranean Sea." *J. Geophys. Res.*, 96(C6), 10739-10764.

Cavaleri, L., Bertotti, L. and Tescaro, N. (1996). "Long term wind hindcast in the Adriatic Sea", *Il Nuovo Cimento*, 19C(1), 67-89.

Erkal, S. (1997). "*Wind modelling in Sea of Marmara*", MS Thesis, Middle East Technical University, Ankara, Turkey.

Erkal, S., Elmalıpınar, E. and Arıkan, Ş.E. (1996). "*Major storms recorded by the meteorological stations along the Turkish coast*", Special Report of NATO TU-WAVES Project, Middle East Technical University, Ankara, Turkey.

Findlater, J., Harrower, T.N.S., Howkins, G.A. and Wright, H.L. (1966). "*Surface and 900 mb wind relationships*, Scientific Paper 23, Meteorological Office, London.

Lavrenov, I., Dymov, V. and Pasechinik, T. (1995). "Different scales wind wave computation program ALL-WAVES", presented at the *Third Workshop of NATO TU-WAVES / Black Sea*, Mar. 31-Apr. 2, 1995, Ankara, Turkey.

Özhan, E. and Abdalla, S. (1992). "*Wave climatology of the Turkish coast: measurements-analysis-modeling, NATO TU-WAVES*", Project Plan presented to the NATO Science for Stability Program.

Özhan, E. and Abdalla, S. (1993a). "*Wave climatology of the Turkish coast: measurements-analysis-modeling, NATO TU-WAVES*", Amendments to the Project Plan presented to the NATO Science for Stability Program.

Özhan, E. and Abdalla, S. (1993b). "Wave climatology of the Turkish coast: NATO TU-WAVES Project", *Proc. of the 1st. Int. Conf. on the Mediterranean Coastal Environment, MEDCOAST 93*, E. Özhan (ed.), MEDCOAST Publications, Ankara, Turkey, 1221-1227.

Özhan, E. and Abdalla, S. (1997a). "Studies on the Wind-Wave Climate of the Whole Black Sea and the other Turkish Coasts", *Proc. of the 1st. Nat. Conf. on the Coastal and Marine Zones of Turkey*, E. Özhan (ed.), MEDCOAST Publications, Ankara, Turkey, 603-608 (In Turkish).

Özhan, E. and Abdalla, S. (1997b). "Wind-Wave Climatology of the Black Sea (NATO TU-WAVES)", *The 1st. Int. Conf. on Port, Coast and Environment (PCE'97)*, 30 June-4 July 1997, Varna, Bulgaria.

Özhan, E. and Abdalla, S. (1997c): "Wind-Wave Climatology of the Black Sea: Progress of the NATO TU-WAVES Project", *Proc. of the Deep Water Drilling and Production Tech. Symposium (Black Sea 97)*, 2-3 Oct. 1997, Ankara, Turkey, 20-26.

Özhan, E., Abdalla, S., Seziş-Papila, S. and Turhan, M. (1995). "Measurements and Modelling of Wind Waves along the Turkish Mediterranean Coasts and the Black Sea.", *Proc. of the 2nd. Int. Conf. on the Mediterranean Coastal Environment, MEDCOAST 95*, E. Özhan (ed.), MEDCOAST Publications, Ankara, 1899-1910.

Özhan, E., Abdalla, S. and Turhan, M. (1997). "Short term statistical characteristics of wind waves off the Turkish coast", *Proc. of the 3rd. Int. Conf. on the Mediterranean Coastal Environment, MEDCOAST 97*, E. Özhan (ed.), MEDCOAST Publications, Ankara.

Turhan, M. (1996). "*Short-term statistical analysis of wind-wave characteristics measured along the Turkish coast*", MS Thesis, Middle East Technical University, Ankara, Turkey.

WAMDI Group (1988). "The WAM model - A third generation ocean wave prediction model." *J. Phys. Oceanog.*, 18, 1775-1810.

# WAM VALIDATION OF PACIFIC SWELL

P. A. Wittmann

Fleet Numerical Meteorology and Oceanography Center, Monterey, California

W. C. O'Reilly

Department of Oceanography, Naval Postgraduate School, Monterey, California

## 1. INTRODUCTION

The third generation Wave Model (WAM) has been has been employed by most of the operational weather forecasting centers around the world to produce ocean wave forecasts. WAM has been extensively tested and validated by various groups using buoy and satellite data measurements (WAMDI Group, 1988; Zambresky, 1989). Many of these studies were conducted in fetch limited regions of the world's oceans and focused on the integrated wave energy, parameterized by significant wave height. In the central and eastern Pacific Ocean, frequency spectra are often bi- or tri-modal owing to the presence of both low frequency swell energy arriving from distance sources and higher frequency windsea energy from local wind generation. Once generated, long period swell attenuates slowly and can travel great distances (Snodgrass et al., 1966), and its prediction requires both accurate generation and propagation algorithms. WAM results in swell dominated areas have shown a tendency to underpredict significant wave height during swell events (Wittmann et al., 1994). Therefore, the accuracy of the WAM predictions as a function of frequency are of interest.

The limitations of the present first-order WAM wave propagation scheme is recognized for excessive diffusion of wave energy (Lionello et al., 1992; Bender, 1996). The accuracy of the lowest swell frequencies is not well established. Here we compare the low frequency portion of the U.S. Navy Fleet Numerical Meteorology and Oceanography Center (FNMOC) global WAM frequency spectra to deep water pressure sensor and buoy measurements off southern and central California for a 3 month period, March through May, 1997 (Figure 1.).

The ground-truth wave measurements and the FNMOC implementation of the WAM model are briefly described in section 2, and the model-data comparisons are presented in section 3. A bias towards underprediction at the lowest swell frequencies ($f < 0.06Hz$) is found at both comparison locations. In addition, it is shown that WAM tends to underpredict the peak wave heights of swell events and overpredict the low wave heights between swell events, resulting in relatively large RMS errors in WAM energy densities at swell frequencies.

In section 4, ray tracing methods are described to bypass the WAM propagation algorithm and transform WAM swell energy from the source regions to the measurement sites along great-circle paths. The hybrid WAM-ray tracing predictions are compared to the measurements in section 5, and the results are summarized in section 6.

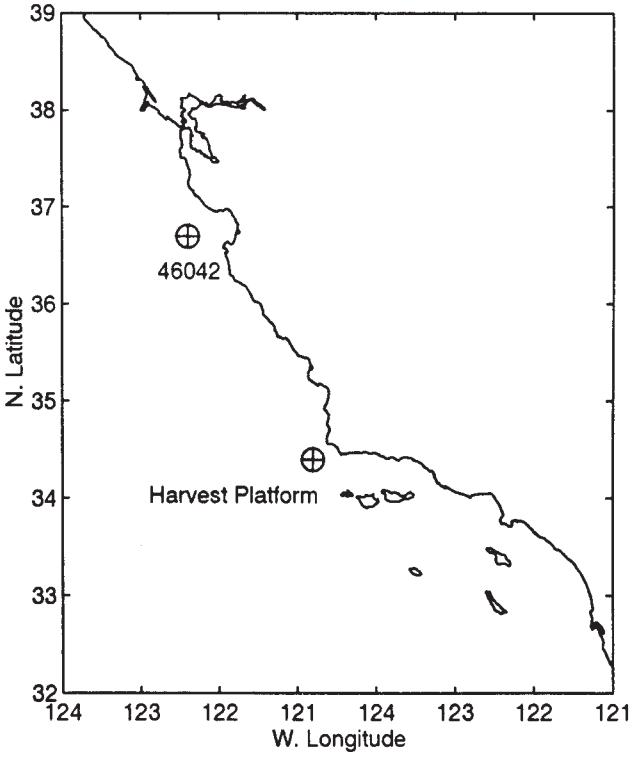


Fig. 1. Locations of NOAA Buoy 46042 and Chevron's Harvest Platform measurement sites.

## 2. MODEL AND MEASUREMENT METHODS

Cycle 4 of the third generation WAM has been implemented on a global 1 degree latitude/longitude grid (Wittmann and Clancy, 1993). Wind forcing comes from the Navy Operational Global Atmospheric Prediction System (NOGAPS), a T159, 18 vertical level, spectral atmospheric model (Hogan and Rosmond, 1991). Surface winds are input to WAM every 3 hours into the forecast. The model runs on a 6 hour update cycle, forecasting to 120 hours on the 0000 GMT and 1200 GMT synoptic times. Output is the directional wave energy spectrum at each grid point, from which integrated parameters, such as significant wave height, are derived.

The WAM frequency spectra at forecast time 0 (analysis) at grid point 37N, 123W are compared to that measured by NOAA buoy 46042, a 3-m discus buoy deployed in 2000 meters water depth offshore of Monterey, CA (36.75N, 122.41W; Figure 1.). Wave spectra from the NOAA buoy, archived by the National Ocean Data Center (NODC), are based on approximately 20 minute long data records collected hourly and reduced onboard to a frequency spectra with $0.01Hz$ resolution in the $0.03$-$0.35Hz$ frequency range (Steele et al. 1992). A second comparison is made between the WAM at grid point 35N, 121W to that measured from Chevron's Harvest Platform, located in 200 meters water depth, 10 kilometers west of Point Conception, CA (Figure, 1). An array of pressure sensors are attached to the platform at 14 meters depth, and continuous data is collected by the Coastal Data Information Program (CDIP) at Scripps Institution of Oceanography. Hourly wave frequency spectra, based on a 34 minute record segment (sample rate = $1Hz$) and corrected to the surface elevation using linear theory, were obtained from CDIP's Internet database for the 3 month comparison period.

Both the NOAA buoy and the platform pressure sensors are considered to be accurate sources of ground-truth frequency spectra. A recent intercomparison of swell energy measurements from Harvest Platform and the nearby NOAA 3-m discus buoy 46051, showed excellent agreement between the two instrument systems (O'Reilly et al., 1996).

## 3. MODEL-DATA INTERCOMPARISONS

FNMOC WAM spectra from daily 0000 GMT and 1200 GMT analysis runs are compared to the buoy and platform measurements from the same hours for the 3 month period of March-May, 1997, and includes swell events arriving from both the North and South Pacific. These results are summarized in Tables 1 and 2 as mean, bias, and RMS errors of the modeled energy densities at swell frequencies. To provide an overall view of the WAM vs. the measured swell, spectral energy in the frequency range $0.045$-$0.105Hz$ was combined to estimate "swell significant wave heights" for the 3 month period (Figure 2.). At both measurement sites, the WAM model was found to underpredict the maximum heights of most swell events and overpredict swell heights during the lulls between events. This is seen as relatively large RMS errors in the frequency spectra compared to the biases in Tables 1 and 2, and is consistent with the expected errors from the WAM first-order propagation algorithm with distant sources.

| Frequency (Hz) | Mean | Bias | RMS Error |
|---|---|---|---|
| 0.0418 | 0.0008 | -0.0480 | 0.1638 |
| 0.0459 | 0.0629 | -0.4431 | 1.3222 |
| 0.0505 | 0.2347 | -0.2725 | 1.2001 |
| 0.0556 | 0.7729 | -0.9986 | 3.2972 |
| 0.0612 | 1.8681 | 0.0893 | 3.4297 |
| 0.0673 | 3.0276 | -0.0601 | 2.8010 |
| 0.0740 | 3.8391 | 0.7459 | 2.5701 |
| 0.0814 | 4.1452 | 0.0039 | 2.9338 |
| 0.0895 | 3.6829 | -0.2579 | 2.7763 |
| 0.0985 | 3.1577 | 0.0583 | 1.8813 |
| 0.1083 | 2.6883 | 0.3047 | 1.2851 |

Table 1. WAM-NOAA 46042 energy density ($m^2/Hz$) comparisons as a function of WAM central frequencies for March-May, 1997.

| Frequency (Hz) | Mean | Bias | RMS Error |
|---|---|---|---|
| 0.0418 | 0.0007 | -0.0417 | 0.0417 |
| 0.0459 | 0.0470 | -1.0599 | 2.6227 |
| 0.0505 | 0.2058 | -0.9023 | 2.4820 |
| 0.0556 | 0.8086 | -0.9300 | 2.3039 |
| 0.0612 | 1.9998 | 0.2522 | 2.5770 |
| 0.0673 | 3.2229 | 0.6165 | 2.8182 |
| 0.0740 | 3.9818 | 0.3191 | 2.9847 |
| 0.0814 | 4.1261 | 0.4623 | 2.3684 |
| 0.0895 | 3.6072 | 0.4814 | 2.2815 |
| 0.0985 | 3.0556 | -0.0660 | 2.4358 |
| 0.1083 | 2.6217 | -0.2993 | 2.1098 |

Table 2. WAM-Harvest Platform energy density ($m^2/Hz$) comparisons as a function of WAM central frequencies for March-May, 1997.

AUTHOR INDEX

TABLE OF CONTENTS

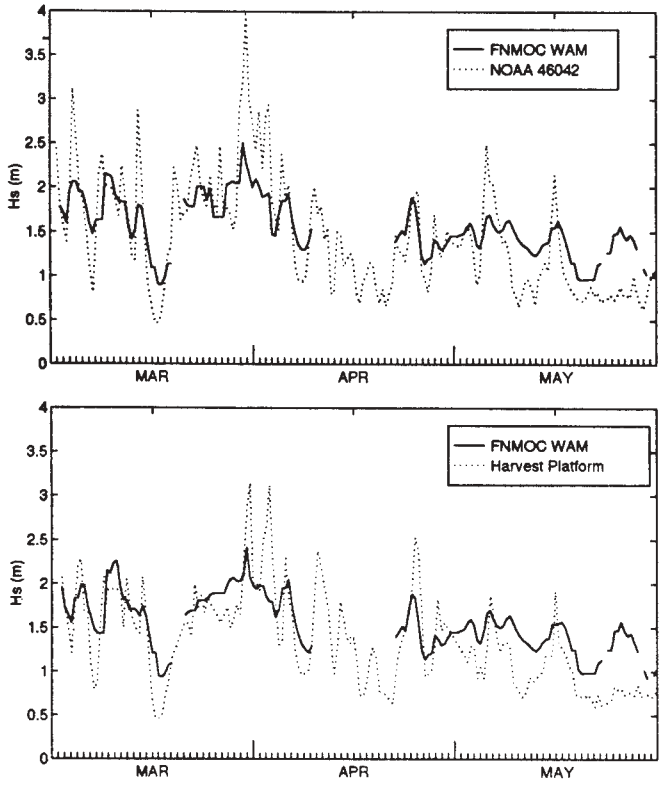


Fig. 2. Comparisons of "swell significant wave height" ($f$=0.045–0.105$Hz$) between the WAM model and NOAA buoy 46042 (upper panel) and Harvest Platform (lower panel) for March-May, 1997.

The underprediction of swell peaks could result from excessive numerical dispersion of the source swell energy over the Northeast Pacific as the swell propagates towards California, and the overprediction during the lull periods would result from the diffuse arrival of energy from distant sources that in reality do not generate significant wave energy along directional paths to the measurement sites. In other words, the overall effect of the excessive directional spreading of the propagating wave spectra is to damp variations in the swell energy from distant sources.

While Figure 2. is consistent with excessive directional spreading, it does not eliminate the possibility that insufficient low frequency wave energy is being generated in the source regions, contributing to the underestimation of the peak swell heights. Model and measured wave spectra averaged over the entire 3 month period (Figure 3.) show a bias towards underprediction of swell energy densities at frequencies less then 0.06 Hz at both the buoy and the platform (and as negative biases at the lower frequencies in Tables 1. and 2.). This suggests that too little energy is being generated by the WAM at low frequencies. However, it could also be argued that the west coast might have been a "focal point" for low frequency swell energy during this time period. (i.e., many of the Pacific storm fetches were preferentially oriented along great circle paths to the west coast). If this were true, excessive directional spreading could lead to an overall trend towards underprediction, although it is unclear why this would manifest itself only at the lowest frequencies. Of course, this assumes the surface wind forcing at the source region is accurate, which seems reasonable in view of the good model-data agreement in the windsea portion of the frequency spectrum. The RMS error of the NOGAPS surface wind speed analysis is approximately 2.5 m/s, when compared to the NDBC buoys (Wittmann and Clancy, 1993).

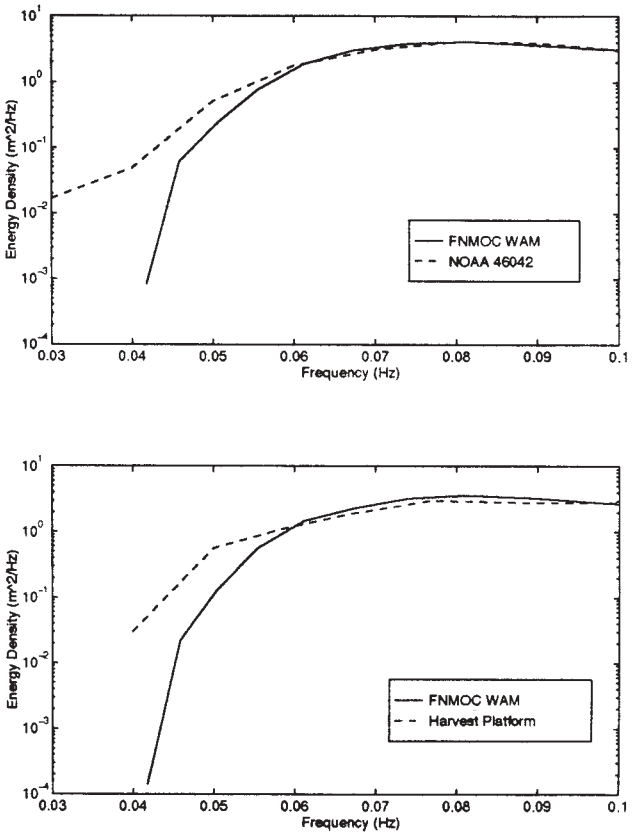


Fig. 3. Comparisons of mean swell frequency spectra ($f$ <0.10$Hz$) between the WAM model and NOAA buoy 46042 (upper panel) and Harvest Platform (lower panel) for March-May, 1997.

## 4. WAM SWELL PROPAGATION ALONG GREAT CIRCLE ROUTES

In order to gain some insight into the source of the low frequency swell underprediction, simple wave ray tracing methods are used here to transform WAM spectra from distant sources to NOAA buoy 46042 along great-circle paths.

Barber (1958) demonstrated that spectral energy density of propagating waves is conserved along the great-circle path between any two locations,

$$E_1(t,f,\theta_1) = E_2(t-\tau,f,\theta_2) \qquad (1)$$

where $\theta_1$ and $\theta_2$ are the starting and ending directions of the great-circle between two sites, and $\tau$ is the time lag for wave energy to propagate along the path.

Equation (1) assumes there are no losses along the path owing to dissipation or nonlinear interactions, and can be viewed as a mapping of wave energy density from one location to another based on great-circle paths and group propagation speeds. Here we use (1) to look back along ray paths ending at the buoy to see how much energy was propagating towards the site in earlier WAM analysis runs. Swell energy at a single location and time, $t$, based on the WAM analysis at a previous time, $t-\tau$, is constructed by mapping energy densities from the output WAM wave spectra at more distant lat-lon grid points, as dictated by the great-circle ray paths. Stated in terms of the buoy arrival direction, $\theta_a$,

$$E_{Buoy}(t,f,\theta_a) = \qquad (2)$$
$$E_{WAM}[\, t-\tau\,,\, f\,,\, \theta(\tau,f,\theta_a), \phi(\tau,f,\theta_a)\,,\, \lambda(\tau,f,\theta_a)\,],$$

where $\theta$ is direction of the great-circle path at the WAM grid point with latitude and longitude of $\phi$ and $\lambda$ respectively. Equation (2) was modeled by backward ray tracing in spherical coordinates from the buoy. Great-circle ray paths were calculated over all possible arrival directions using small increments of $\theta_a$. At selected energy propagation time lags $\tau$ (every 12 hours) the present ray direction $\theta$ and location $(\phi,\lambda)$ were saved.

## 5. THE SEARCH FOR MISSING SWELL ENERGY

To assess whether the underprediction of low frequency swell is primarily a generation or propagation problem, Eq. (2) is used to look back along great-circle routes in time to see if there were larger amounts of energy at these frequencies closer to the source. Complete WAM spectra for the Pacific Ocean were saved for the time period between April 22 and May 20, 1997. Starting with arrival time $t$= 0000Z on May 1, Eq. (2) was used transform WAM spectra from all approach directions, and estimate the swell significant wave height in the 0.045-0.055Hz frequency band based on WAM analysis output from 12 hrs to 10 days prior to $t$. This procedure was repeated in 12 hr arrival time steps until May 20. The maximum wave height found approaching along great-circle paths for each time step is shown in Figure 4 along with the corresponding 0000Z WAM estimate and the NOAA buoy 46042 measurement.

Figure 4. shows that the 0000Z WAM analysis at low frequencies does not correlate well with the measurements during this time period. A swell arrival during the first week of the month is particularly underpredicted. In addition, the analysis of WAM wave energy along great-circle paths shows some smoothing of the peak swell energy on May 10 and 16, presumably due to directional diffusion, but it failed to find any additional energy during the first week of the month. Therefore, we conclude that either the WAM model failed to generate sufficient energy at low frequencies for this event, or generated the energy in a directional band that was not oriented along great-circle paths towards central California.

## 6. SUMMARY

The damping of WAM swell predictions (Figure 2.) and the significant underprediction of energy at the lowest swell frequencies (Figure 3.) motivated a comparison of WAM analysis output at NOAA buoy 46042 to earlier WAM output closer to the swell source along great-circle routes (Figure 4.). Our preliminary conclusion is that the underprediction at low frequencies is primarily owing to generation errors, either in magnitude and/or direction, rather than propagation errors. Some damping of the swell peaks as they travel along great-circle routes is also observed, but it is unclear at this point if this can explain the damping of the entire swell spectrum seen in Figure 2. The May 1997 time period was not very energetic at the lowest swell frequencies compared to other time periods in the buoy record, and more comprehensive comparisons are planned in the near future.

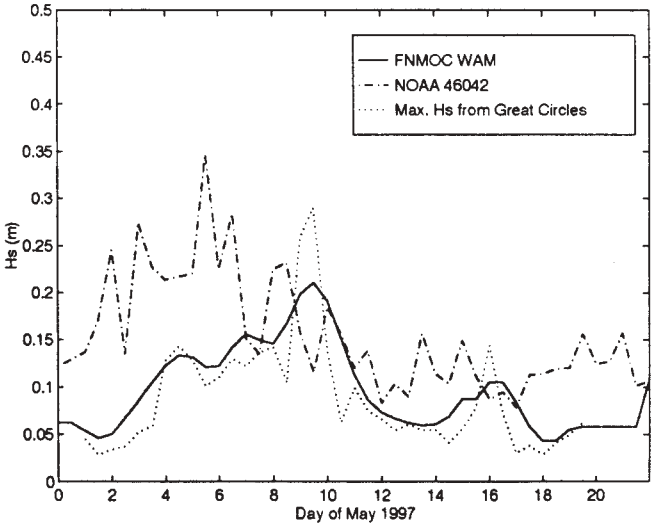


Fig. 4. Comparisons of swell significant wave heights in a low frequency band ($f$=0.045–0.055$Hz$) between the WAM model and NOAA buoy 46042 for May, 1997. The dotted line represents the maximum wave height found approaching the buoy along great-circle paths for up to 10 days prior to the arrival time.

AUTHOR INDEX

TABLE OF CONTENTS

Acknowledgements

The Harvest Platform wave data used in this study was collected by the Coastal Data Information Program, supported by the U.S. Army Corps of Engineers and the California Department of Boating and Waterways. Harvest wave data acquisition is supervised by David Castel and Julie Thomas. W.C. O'Reilly is sponsored by the ONR Waves BE and Coastal Sciences Programs.

## REFERENCES

Bender L.C., 1996: Modification to the Physics and Numerics in a Third-Generation Ocean Wave Model. J. of Atmospheric and Oceanic Technology, 13, 726-750.

Hogan, T.F and T.E. Rosmond, 1991: The Description of the Navy's Operational Global Atmospheric Prediction System's Spectral Forecast Model. Monthly Weather Review, 119, 1786-1815.

Lionello P., H. Gunther and P. Janssen, 1992: Assimilation of altimeter data in a global third generation wave model. ECMWF Tech. Report No. 67.

O'Reilly W. C., T. H. C. Herbers, R. J. Seymour, and R. T. Guza, 1996: A comparison of directional buoy and fixed platform measurements of pacific swell, J. of Atmos. and Oceanic Technology, 13(1), 231-238.

Steele, K.E., C.C. Teng, and D.W.C. Wang, 1992: Wave direction measurements using pitch-roll buoys. Ocean Eng., 19(4), 349-375.

Snodgrass, F.E., G.W. Groves, K.F. Hasselmann, G.R. Miller, W.H. Munk, and W.H. Powers, 1966: Propagation of ocean swell across the Pacific Ocean. Phil. Trans. Roy. Soc. London, A259, 430-497.

WAMDI Group, 1988: The WAM model - A third-generation ocean wave prediction model. Journal of Physical Oceanography, 18, 1775-1810.

Wittmann, P.A. and R.M. Clancy, 1993: Implementation and Validation of a Global Third-Generation Wave Model at Fleet Numerical Oceanography Center. In Ocean Wave Measurement and Analysis, Proceedings of the Second International Symposium, 25-28 July 1993, New Orleans, O.T. Magoon and J.M. Hemsley, Editors, American Society of Civil Engineers, 345 East 47th Street, New York, NY 10017-2389, pp. 406-419.

Wittmann, P.A., Clancy, R.M. and T. Mettlach, 1994: Operational Wave Forecasting at Fleet Numerical Meteorology and Oceanography Center. In 4th International Workshop on Wave Hindcasting and Forecasting, 335-342 pp. Banff, Alberta.

Zambresky L. F. 1989: A Verification Study of the Global WAM Model, December 1987 - November 1988. ECMWF Tech. Report No. 63.

# HINDCASTING WAVES FROM STORMS IN THE TASMAN SEA

Andrew K. Laing and Steve J. Reid

National Institute of Water and Atmospheric Research
Wellington, New Zealand

## 1. INTRODUCTION

The west coast of South Island, New Zealand is exposed to storms in the Tasman Sea. Since it lies at latitudes south of continental Australia it is also exposed to the Southern Ocean, and has a high level of background wave energy from the southwest. The weather in New Zealand is dominated by systems in the Tasman Sea which travel from west to east across the country. Low pressure systems predominate to the south and high pressure systems to the north, generating disturbed westerly flows containing fronts or troughs. These features commonly affect the west coast of South Island.

The resulting wave environment on the west coast is energetic but largely unspecified. For this coastline, and for most sites around New Zealand, wave measurements and observations are inadequate to accurately specify wave conditions. Hence, wave studies invariably require a substantial input from the synthetic data generated in wave hindcasts. This particularly requires accurate simulation of wave conditions during severe events.

In Laing *et al.* (1997) the wave conditions in the Karamea Bight (see Fig. 1) were described for the investigation of a vessel loading facility in the Bight. Since there were few wave measurements, data were extended by synthesizing new data with a six year hindcast for the site. The hindcast used a second-generation spectral ocean wave model with winds from numerical weather prediction models. The hindcast showed reasonable skill, producing good estimates of the significant wave height ($H_s$) and identifying major storms. It also generated a good distribution of storm maxima. However, within this selection of storms there were both over-estimated and under-estimated events. Because design wave errors of 1 m to 2 m can make a large impact on the economics of coastal structures, better definition of the climate of extreme waves is required.

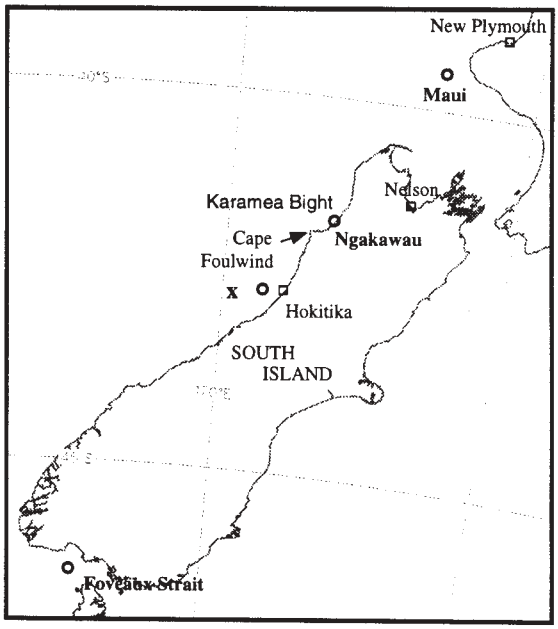


**Fig. 1.** Map of study area. "o" indicate the wave measurement sites mentioned in the text and "x" the position of the meteorological buoy.

In this study we have attempted to gain details of extreme events for the west coast of South Island coastline by selecting the most severe storms based on a screening procedure using weather observations and charts. The wave conditions are then estimated by performing hindcasts. It will be shown that the hindcasts give a plausible selection of severe events, but where comparisons are possible, they are often from different storms than indicated by the highest measured waves. The scope of this paper is confined to testing the storm selection criteria and analysing some of the discrepancies between modelled and measured storms.

Successful hindcasts depend on accurate wind fields deduced from meteorological analyses. It is recog-

nised that the largest gains in modelling ocean waves are to be made from improving the definition of these winds (pers. comm. P. Janssen ECMWF 1996, Graber *et al.* 1995). Unfortunately, the dearth of meteorological data in the Tasman Sea leaves considerable scope for errors in analyses. Hence, hindcasts based on routinely available model winds may not adequately define the important winds.

It has also been noted (e.g. Cardone *et al.* 1995) that routinely available model winds resolve only synoptic weather events and do not adequately resolve many small, intense wind features. In the present situation New Zealand presents a major barrier to the westerly airflow often resulting in strong wind bands near the coast (Laing and Brenstrum 1996). Further, Laing *et al.* (1997) observed that the most severe events in the Karamea Bight had a history of high winds over the sea before the winds reached the coast but also maintained their intensity near the coast. Hence, the wind fields used to simulate extreme events affecting the west coast of South Island will need to resolve the local effects of the orography on the winds, especially in coastal waters.

In the present study winds from both synoptic-scale models and digitised manual analyses are used to drive the simulations. The latter have also been redrawn to include data which became available after the original analysis time. The importance of using all available data is demonstrated in section 5 by the improvements which re-analysis of surface charts can make to hindcasts of selected storms. In particular, small changes in the position of a front or the orientation of a fetch can have a large impact on waves at the coast. Further, lack of detail in the analyses may produce excessively long fetches and substantial over-estimates of wave conditions.

In section 2 the available measurements and meteorological data are identified and in section 3 the wave modelling is described. Section 4 outlines the storm selection procedures and section 5 presents hindcasts of a number of storms affecting the west coast. These hindcasts illustrate the necessity of careful analyses of meteorological conditions in the Tasman Sea for good diagnoses of wave conditions.

## 2. STORM DATA

### 2.1 Wave data

No substantial wave data exist for this exposed coastline. Some information about the climate over the sea adjacent to the west coast of South Island has been obtained from the weather reports from ships. From these reports, estimates of wave height and direction and wind speed and direction indicate a predominance of swell from the southwest (50%) and the west (26%). The most frequent observed swell height is 2 m, although heights of up to 9 m have been reported. The southwest (21% of observations) is also the predominant direction for winds.

***Maui*** To the north, at the Maui Oil and Gas Field (see Fig. 1), a measured wave record over several years has shown a wave climate dominated by waves from the southwest (see Ewans and Kibblewhite 1992), with a significant wave height ($H_s$) often exceeding 2.5m. Over the 11 years of data this occurred for 37% of the time, $H_s$ exceeded 5 m 1.7% of the time and the maximum measured $H_s$ was over 10 m.

***Foveaux Strait*** To the south, a shorter record (1 year) in Foveaux Strait (see Fig. 1) with higher exposure to the Southern Ocean, indicates energetic (mean $H_s$ of 2.8 m) high period waves (mean peak period of 12.6 s) from the southwest quarter. However, this site is sheltered from the northwesterlies preceeding Tasman Sea troughs.

***Karamea Bight*** The longest measurement record for the west coast of South Island is from a Waverider which was deployed during 1980–82 in 20 m of water near Ngakawau in the Karamea Bight (see Fig. 1), 1.9 km offshore at 41°36'S, 171°51'E. These data indicate a mean $H_s$ of 1.3 m and zero-crossing period of 7.7 s with a standard deviation in the height of 0.7 m. During this period the maximum recorded $H_s$ was 6.0 m, and it exceeded 3.0 m during 29 events. The measurement site is sufficiently sheltered from the southwest by Cape Foulwind to limit the penetration of southwest swell (although we will present a case in section 5.1 in which significant westerly swell does reach the coast here). Hence, the highest waves appear to occur in situations where a trough in the Tasman Sea is preceded by a period of strong northwest winds extending in a long northwest fetch across the Tasman Sea. The measurements have been reported and analysed by Valentine and Macky (1984).

Shorter wave records were also available from Westport and Carter's Beach. Both these sites are also sheltered from the southwest by Cape Foulwind.

These measurements are all close to the coast in shallow water. This introduces complications to the interpretation of wave data from storms. Refraction and shoaling are significant, and modelling waves at

these sites may be quite sensitive to small differences in fetch orientation.

***Hokitika*** A recent deployment off the west coast of South Island has provided the first deep-water measurements for this coast. Since September 1996 a Waverider buoy has been moored west of Hokitika at 42.64°S, 170.85°E in a depth of 104 m. This site is fully exposed to the Tasman Sea (see Fig. 1).

### 2.2 Meteorological data

Several sources of meteorological information were used for the storm selection procedures and the wind field analyses.

***Model data*** Model wind fields for the storm simlations were derived from pressure analyses and surface winds provided by the European Centre for Medium Range Weather Forecasting (ECMWF) Numerical Weather Prediction (NWP) model. In the present study only the 6-hourly (and in some cases 12-hourly) fields were used.

***Weather charts*** The most suitable charts for this study were high resolution charts from the New Zealand Meteorological Service, extending from the east coast of Australia to east of 180°E. These were available for 3-hourly analyses and were retrieved from archived microfilm or large bound bundles.

***Coastal observations*** There are a number of regularly reporting observations stations along the west coast of South Island. For storm identification the stations at Nelson, Hokitika, and New Plymouth (see Fig. 1) were selected as being strategically located and for having consistent long-term records. For example, no good record exists in the Karamea Bight but the winds at Hokitika were used as they are under similar orographic constraints from the Southern Alps and respond in similar ways to storms.

***Buoy data*** A meteorological buoy has been moored west of Hokitika for extended periods during 1994–1997 (see Fig. 1). The buoy has a 3-metre discus-shaped hull supporting a 4 m tower. It has provided new pressure, wind and temperature data which were not available for either the model analyses or the manual analyses from the Meteorological Service.

***Ships' observations*** For each storm the data base of ships' observations was searched for all Tasman Sea observations. These often complemented those indicated on the weather charts. The ship data also provided air-sea temperature differences which were used in diagnosing surface winds from the weather charts.

***Satellite data*** The re-analysis of storms also used satellite images dating from the 1970s and, for storms after 1991, scatterometer wind data from the ERS1/2 satellite missions.

## 3. WAVE MODELLING

### 3.1 Model Description

The model used in the simulations has been detailed by Laing (1992b). It is a 2nd-generation spectral model with a total of 15 frequencies from 0.045 Hz to 0.32 Hz, defined by $0.045 \times 1.15^{n-1}$ (n=1,2, ...,15) and a directional resolution of 20° (18 bands). The physics is limited to deep-water processes including wind generation, dissipation due to white-capping and a simple parameterisation of the weakly nonlinear wave-wave interactions, which redistribute wave energy within the spectrum. Advection is by 4th-order finite differencing. From the modelled spectra the wave height $H_s$ is taken as $4\sqrt{m_0}$, where $m_0$ is the integral of the spectrum, and the period $T_z$ is taken as $\sqrt{(m_0/m_2)}$, where $m_2$ is the second frequency-moment of the spectrum. These parameters are comparable to the significant wave height and zero-crossing period respectively.

In each present application a cartesian grid on a polar stereographic projection was used. Since New Zealand is surrounded by open ocean these applications were over limited domains with some open-ocean boundaries. At these boundaries a condition was devised which allowed some influx of energy. However, the present interest is severe storms in the Tasman Sea and during these events the influence of distant swell, from outside the model domain, was not considered important.

### 3.2 Hindcasts using model winds

Storms for which wave data are available are confined to two periods, in the early 1980's with the Karamea Bight data, and in 1996 with the data from the central coast, west of Hokitika. Hindcasts based on model winds were made for both periods. For the early 1980s a pre-existing continuous hindcast was applied, but for the 1996 storms short periods around the storms were specifically hindcast for this study.

#### *Storm hindcasts for 1980–85*

A hindcast of the wave conditions in New Zealand environs was performed by Laing (1992a, 1993).

This hindcast covered the period 1980–1989 and included the deployments of the Waverider buoy at Ngakawau. The grid covered the entire New Zealand Exclusive Economic Zone (EEZ) with sufficient space around the borders to ensure that most events generating waves which affect the New Zealand EEZ were captured. A polar stereographic projection was used with a grid spacing of 190 km at 60°S. For the model integration this hindcast used a 3-hour timestep.

The wind information for forcing the wave model was derived from ECMWF pressure analyses. These winds were used to drive a diagnostic marine planetary boundary layer model from which the surface friction velocities (or equivalent 10 m winds for a neutrally stable atmosphere) were obtained at 6-hourly intervals. For intermediate 2-hourly time steps the winds were interpolated (separately in speed and direction as described in section 3.3).

Since the Karamea Bight site at Ngakawau is in shallow water we first describe how wave conditions at the Waverider site were derived from these hindcast wave data.

### *Calibration*

Validations of the second-generation model reported in Laing (1993) cover 5 months in mid-1989 and use satellite altimeter data from Geosat and Waverider data from the western Foveaux Strait (Fig. 1). The hindcasts were shown to be almost unbiased compared to the Waverider measurements and about 0.2 m lower than the open-ocean Geosat measurements (see Table 1). However, it now appears that the winds used to drive the wave model during this late period of the hindcast were inconsistent with the earlier period. Comparisons with measurements during 1980–81 from the Waverider deployed at the Maui-A oil and gas production platform (see Fig. 1), and with Geosat radar altimeter measurements for 1986–88 (corrected as per Carter *et al.* 1992) revealed a 30% over-generation of waves. This led to the discovery that the surface winds used to drive the model were over-estimated by 15% during the period 1980–87.

Since the scope of the study precluded a complete rehindcast of the period, the model results were calibrated to be consistent with the Maui data, as described in Laing *et al.* (1997). This was achieved by transforming the energy density spectrum using a scaling of the magnitude in conjunction with scaling the frequency domain, following Lionello *et al.* (1992). We here consider only the hindcast data from 1980–85.

### *Coastal effects*

Application of the hindcast data at the coastal site required modifications for the effects of refraction and shoaling. Specifically, we transformed each frequency-directional component of the (calibrated) hindcast spectra from the deep-water gridpoints to the site of measurements at Ngakawau. To determine the appropriate transformation, wave ray tracing was applied to each spectral component, i.e. for each direction and each period (wavelength) a monochromatic wave of specified energy and with the appropriate frequency and direction is traced to the site. The procedure enables refraction and the dissipation associated with shoaling to be traced as waves approach the shore. The new direction of the component is then determined and the new energy density provides a scaling factor.

**Table 1**. Summary of comparisons of hindcast (modelled) $H_s$ with measurements. Columns show the source of verification data, exposure, correlation ($\rho$), bias (model-measurements), mean (measured) and the number of comparisons ($N$). (* indicates calibrated values as per Carter *et al.* 1992). Note that the model estimates at Ngakawau have been calibrated and refracted.

| | Exposure | ρ | Bias (m) | Mean (m) | *N* |
|---|---|---|---|---|---|
| Foveaux St 1989 | Deep | 0.80 | -0.04 | 2.52 | 500 |
| Geosat* 1989 | Open ocean | 0.68 | -0.21 | 3.60 | 3519 |
| Ngakawau 1980-82 | Coastal | 0.76 | 0.19 | 1.29 | 4551 |

### *Verification*

Spectra derived from the hindcast were now available for the Waverider site off Ngakawau. The significant wave heights were calculated and compared to values from the zero-crossing analysis of the Waverider data. The results are shown in the bottom line in Table 1. Whilst the correlation indicates that less than 60% of the variance in the measured $H_s$ is explained by the model, direct visual comparisons between the time series indicate that the model picks most of the major events and has the magnitude of the significant events correctly estimated.

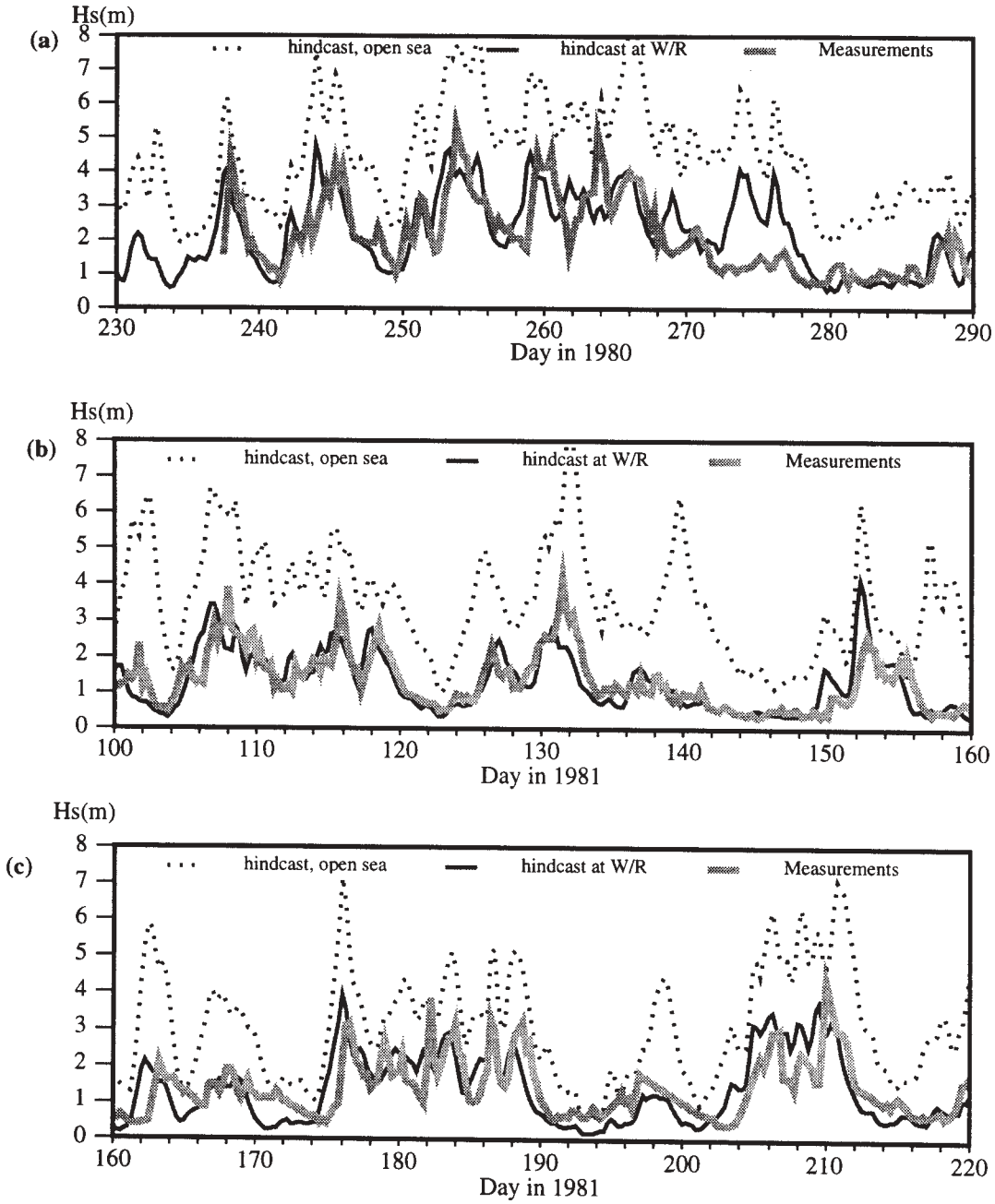


**Fig. 2.** Time series of $H_s$ from Waverider (W/R) measurements and hindcast, the latter being both for nearby deep water and at the W/R site.

Fig. 2 shows two sequences of the $H_s$ series, the first a 60-day sequence in September–October 1980 and the second a 120-day sequence from April to July in 1981. On each chart the series for the deep-water value at the nearest model grid-point is also shown (dotted lines). The standard deviation of the heights from the model estimates (0.96 m) is higher than from measurements (0.71 m) because of the occasional storm which is modelled with high waves but which is not reflected in measurements (e.g. Fig. 2a, day 275).

The maximum measured and hindcast waves are also well matched. The measurements at Ngakawau indicated that $H_s$ of over 6 m may be expected reasonably often. The hindcast data over the period 1980–85 also indicated that the 6 m value was breached several times in the 6 year period modelled and there

were 14 independent events during which $H_s$ exceeded 5.0 m.

***Storm hindcasts for 1996***

For the 1996 events, new hindcasts using model winds were made. To drive the model, ECMWF surface winds fields from the ECMWF/TOGA Level III surface data set were interpolated onto the grid described below (Fig. 3). Time-interpolation to 3-hourly fields was by the same method as described below in section 3.3. The model was applied with a 1 hour timestep, so each wind field was applied over 3 consecutive time steps.

### 3.3 Hindcasts using weather charts.

Manually analysed surface weather charts were also used as the basis for deriving wind fields for driving the wave model. These analyses often provided more detail than the model-based fields, and they also provided a basis for subsequent re-analysis of storms.

The modelling procedure involved 3 stages. Firstly the synoptic surface pressure charts for the period leading up to the storm were digitised. The fetches affecting the area were usually only active in the 2-day period leading up to the storm maximum, and a 4-day period was considered sufficient to capture all the wave growth which would affect the site.

Secondly, winds were derived on the model grid (see Fig. 3). The pressures were first analysed using a 3-pass Cressman scheme, providing first-guess fields for two further iterations using an optimal interpolation scheme which included dynamic constraints dictated by geostrophic balance. Gradient wind fields for the 1000 hPa level were calculated and a boundary layer model reduced these to the 10 m level for input into the wave model. The air-sea temperature difference indicated by ships' observations within the dominant fetch was assumed (e.g. for spring 1996 this was usually 1°C to 2°C).

The analyses were performed at 6-hourly intervals during the period leading up to each storm and at 3-hourly intervals during the peak of the storm. Interpolation was used to complete 3-hourly time series of wind fields. This interpolated the eastward and northward components by Fourier analysis of the component field, with linear interpolation of the phase and (squared) amplitudes. Since the wave model uses a one hour time step, each wind field was applied over 3 consecutive time steps. The wave model was then run to generate full frequency-direction spectra at the deep-water grid points. For coastal sites these spectra were then transformed to the site as described in section 3.2.

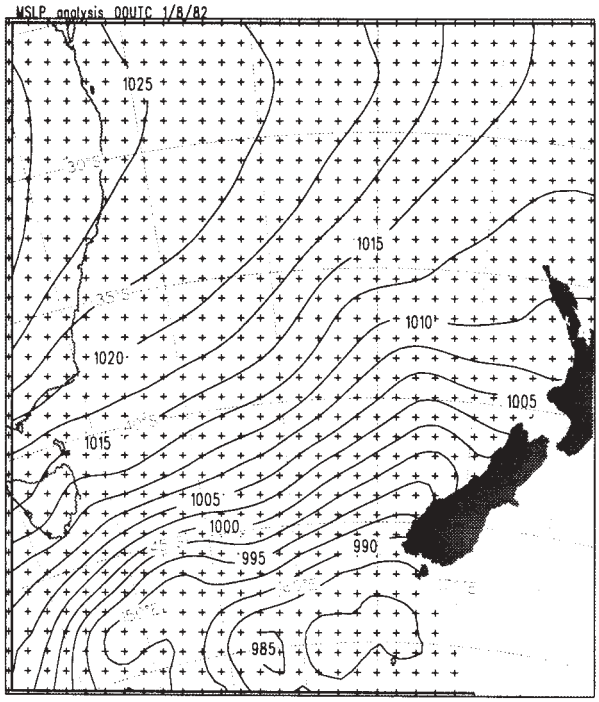


**Fig. 3.** Pressure analysis at 00UTC on August 1, 1982, with the grid used for the wind analysis and wave model.

## 4. STORM SELECTION

The process of detailing extreme events for the west coast of South Island requires both the identification of the potentially severe storms and successful modelling these storms.

***Basic criteria***

Laing *et al.* (1997) have discussed storm selection for a wave hindcast project on the West Coast for the period 1974–1993 (inclusive). Because the climate of extreme waves was required and there were no wave measurement data covering the whole period, an attempt to gain details of the extreme waves was made by selecting the most severe storms based on a screening procedure. This used a combination of indicators from meteorological station data and weather charts.

The primary indicators were:

- pressure difference Nelson —Hokitika > 5 hPa
- pressure difference New Plymouth — Hokitika > 13 hPa
- Hokitika wind speed > 12 $ms^{-1}$
- duration of wind-speed > 12 $ms^{-1}$

The stations: Nelson, Hokitika and New Plymouth, which were used in the selection process were all Meteorological Service Branch Office stations for most of the period. During the earlier years they provided hourly observations covering the full day. For this reason they are the best stations to use for investigations requiring the most comprehensive data sets. For the local wind conditions Hokitika is reasonably representative for this coast, as winds there are under typical orographic constraints from the Southern Alps and, whilst the site is subject to some very localised influences in major storms it is reasonably representative.

The two pressure difference indicators were chosen to detect periods of high pressure gradient in which the isobars were approximately perpendicular to the coast. Reid (1981) has shown that indicators of this type succeed in detecting storms which have been identified as major events from independent criteria e.g. damage. The thresholds were set empirically so as to eliminate all but the largest events.

A list of dates and times at which these criteria were exceeded was extracted from a climatic data base. The list was edited to remove occasions with only one criterion above the threshold and those for which the time above the threshold was less than 10 hours, unless one of the measures was particularly high. A resulting master list of 70 storms was obtained for the 20-year period and was used as a basis for a further selection process which will be described below.

The success of the selection process could be tested in the period 1980–1985 when wave measurements were made over varying lengths of time at three sites near Westport. Further, the hindcast of this period noted in section 3.2 provides a consistent data set, so that for this period we can also compare the selection with a more comprehensive list of hindcast events with high $H_s$. Comparisons between the number of storms selected by the above criteria during each of the wave data periods (measured and hindcast), and the hit and miss occurrences of storms with waves over 4 m and 6 m are given in Table 2.

The hit rate is under 50%, indicating that the coast-based criteria do not detect a large proportion of the storms with $H_s$ over 4 m, and pick a large number with lower waves. This is not surprising because the evolution of the wave systems depends on fetch, duration, wave propagation from distant sources, and weather system propagation and evolution. This degree of complexity cannot be simply monitored by any simple index based on coastal data. A greater proportion of the selected storms during the hindcast period are hits because there is a relatively greater number of > 4 m wave events.

The maximum wave heights in the hindcast wave events with $H_s$ above 4 m have also been regressed against the selection criteria. The value of the criteria for predicting wave height is in the order in which they are listed above. The pressure difference criteria were the strongest predictors and wind persistence had little effect. Together, the predictors could explain a little under half the variance of the wave heights.

**Table 2.** Number of selected storms coincident with wave events with heights over 4 m and 6 m as identified from wave data at 3 measurement sites and from hindcast results (last column).

| | Ngakawau | Carters Beach | Westport | H'cast |
|---|---|---|---|---|
| **Selected storms** | **16** | **4** | **12** | **22** |
| Hit (>4m) | 5 | 1 | 3 | 17 |
| Miss(>4m) | 5 | 2 | 3 | 28 |
| Hit (>6m) | 0 | 0 | 0 | 1 |
| Miss(>6m) | 1 | 0 | 1 | 1 |

### *Additional selection criteria*

In Laing *et al.* (1997) the list of 70 storms over the 20 year period (1974–1993) was further reduced by examining the weather charts over the storm periods. The New Zealand Meteorological Service charts which extend from the east coast of Australia to east of 180°E were used for this purpose. It was inferred that the storms picked up by the initial screening tended to be of 3 or 4 relatively distinct types:

1. depressions moving southward to the west of New Zealand with intense, northerly airstreams affecting the West Coast.
2. north-northwest airstreams ahead of complex troughs in the Tasman Sea.
3. long-fetch, linear, northwest airstreams extending over much of the Tasman Sea.
4. westerly airstreams intensified locally on the north sides of depressions.

Type 4 situation is known to be the predominant cause of high waves but it is thought that the situ-

ations of Type 1 to 3 are likely to lead to the highest waves.

The selection criteria in the last section are not particularly good for detecting intensifications of Type 4 storms and this is one of the reasons for their poor performance. Therefore, wave data series for Ngakawau, Westport and Carters Beach were also used to examine the edited list for completeness. The list of hindcast waves with heights over 4 m were included in the data series and used in a similar way to the other criteria. On some occasions, storms which had been previously eliminated were reintroduced.

The final screening yielded a number of storms which were not only intense near the coast but had a history of high winds over the sea before the winds reached the coast. In almost all these cases there were onshore winds and the wave directions were narrowly spread around 140°, normal to the local bathymetry.

For further hindcasting, six storms covering the situations 1 to 3 were chosen and the case with the highest waves in the Ngakawau record (a Type 4 event) was also chosen.

***Storms in spring 1996***

During the 1996–97 deployment off Hokitika, the spring period in October and November 1996 included 4 energetic events. The Waverider data indicated $H_s$>5 m on each of these occasions.

Since this site is fully exposed to the Tasman Sea and relatively free of complications of the coastal sites in Karamea Bight, it was instructive to perform hindcasts for each of these storms.

## 5 STORM HINDCASTS

We present results for storms from both measurements periods. Two occurred during the measurement period at Ngakawau, one for which the hindcast performed well and one for which it appeared not to. We also hindcast two periods during spring 1996.

### 5.1 August 1982

This storm produced the highest measured $H_s$ at Ngakawau (6 m). The fetch was a persistent, strong westerly with several embedded fronts. The surface pressure field near the height of the storm is shown in Fig. 3. This storm was more westerly than typical for this site, with a large swell component from intense fetches in the south Tasman Sea. (Note that the surface winds will be approximately 20° more clockwise oriented than the alignment of the isobars.)

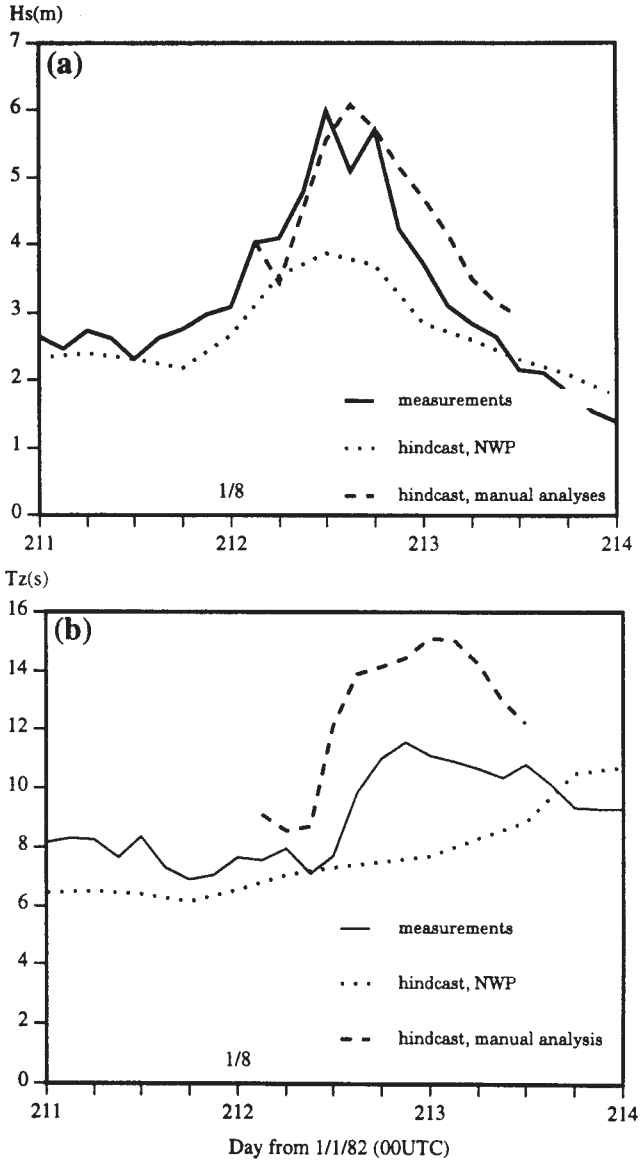


**Fig. 4.** Comparisons of $H_s$ (a) and $T_z$ (b) for hindcasts of August 1982 showing Waverider measurements and estimates from hindcasts based on NWP winds, and winds derived from surface charts (manual analysis).

The modelled waves (Fig. 4a) agreed very well with the nearby measurements, producing a peak $H_s$ of 6.2 m. The open ocean $H_s$ hindcast values exceeded 8 m, and the difference from the coastal values shows the large amount of energy spreading and shoaling resulting from the oblique approach of the waves to the coast. Also shown in Fig. 4 are results from the original hindcast, made using NWP winds.

These indicates considerably under-estimated wave heights.

The derivation of surface winds based on manual analyses has provided more detail than the NWP fields. A disturbance in the west-southwesterly flow in the manual analysis produces a more westerly orientation of the fetch (see Fig. 3) than the west-southwest orientation of the NWP model analysis.

The orientation of the fetch plays a significant role in the result at the coast. As the wave energy approaches the coast it refracts and diverges, so much of the energy from south of west does not reach the site. In the open ocean the NWP-based hindcast produced a $H_s$ of over 9 m, and the chart-based hindcast 8.4 m. The transformation at the coast to 3.9 m and 6.2 m respectively indicates the impact of this change in fetch orientation.

In Fig. 4b the zero-crossing period $T_z$ from the new hindcast correlates much better with the measurements than that derived from the hindcast based on NWP fields. However, periods are biased high.

### 5.2 October 1980

An intense northwest fetch, associated with a depression to the west of South Island and a front extending into the central Tasman Sea (see Fig. 5) here generates waves for which the hindcast $H_s$ reaches 5.5 m (see Fig. 6a). The original, NWP-based, continuous hindcast of the storm also produced a $H_s$ of 5.5 m but the measurements at Ngakawau only indicate 3.3 m at the peak of the storm.

Whilst the intensity of the storm satisfied the criteria for selection, the fetch was apparently not analysed correctly, resulting in a considerable over-estimate of $H_s$ at the coast. The zero-crossing period ($T_z$) in Fig. 6b is modelled as reaching over 10.5 s during the peak of the storm, 1.5 s above the measured maximum value.

#### *Manual re-analysis*

Since the winds for the modelling were derived from surface pressure analyses, which in turn were derived from isobaric analysis of limited data over the sea, errors are inevitable. To determine possible causes for errors in the hindcast we have re-analysed the storm. Firstly, the original surface pressure analyses were examined, and it was noted that there were few observations in the central Tasman Sea. As a result the analysis had been drawn to show a long, intense northwesterly fetch. However, a number of additional wind observations from ships indicated that the situation was more complex.

Re-analysing the surface charts to account for these observations produces a shift in the position of the trough (front) in central Tasman Sea and a shorter, more north-northwesterly fetch in the eastern Tasman Sea. Reprocessing these new analyses as described in section 3.3 produces a revised set of surface pressure fields. To illustrate the difference the re-analysed surface pressure field has been included in Fig. 5.

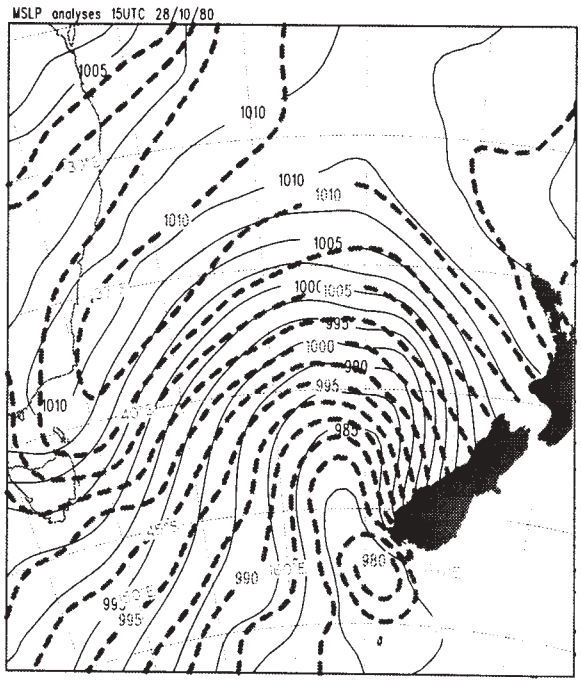


**Fig. 5.** Pressure analysis at 15UTC on October 28, 1980 (thick dashed lines). Also shown is the re-analysed pressure field (thin continous lines).

We also noted from the observations that the sea-surface temperatures in this fetch were about 1°C cooler than the surface air temperatures. This stable situation is quite reasonable for the time of year (spring) and the region preceding a trough. It makes a significant difference to the derivation of surface winds, which originally used a fixed, slightly unstable air–sea temperature difference of -2°C. In stable conditions less momentum is transferred downwards to the surface, and the 10 m windfields are less intense.

New hindcast estimates are included in Fig. 6. A considerable difference is noted in both $H_s$ and $T_z$. Both now closely match the measurements.

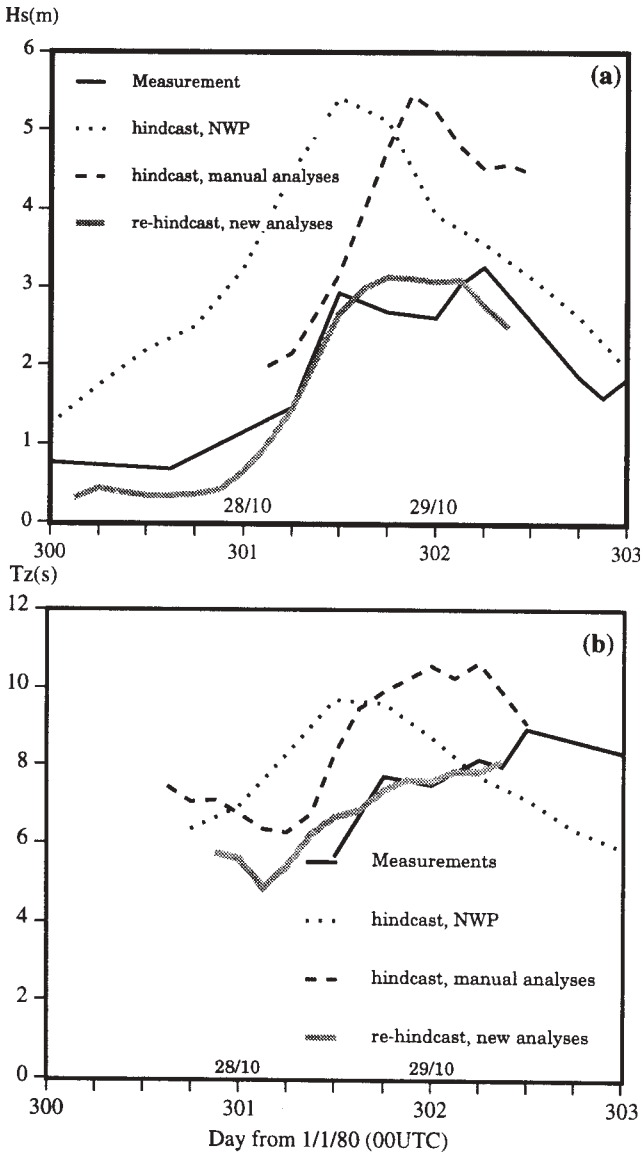


**Fig. 6.** Comparisons of $H_s$ (a) and $T_z$ (b) for hindcasts of October 1980, showing Waverider measurements and wave estimates from hindcasts based on NWP winds, surface charts (manual analyses) and re-analysed charts (new analyses).

The more north-northwesterly fetch has produced more northerly winds than in the previous hindcast. The impact of the change in direction is quite marked. The wave energy at the coast is now oblique to the bathymetry and diverges as it approaches the site, especially for low frequencies. Hence, the new hindcast estimates waves at the coast which are lower (lower $H_s$) and less energetic at low frequencies, resulting in lower $T_z$.

### 5.3 October 1996

The hindcast site for the 1996 storms is in deep (104 m) water and fully exposed to the Tasman Sea. In validating the hindcasts the values of $H_s$ and $T_z$ from the nearest grid-point were used directly in the comparisons.

During September 30 and October 1 a complex trough approached New Zealand across the Tasman Sea. This was preceded by an intense north to north-northwest fetch. Wave measurements off Hokitika peaked with a $H_s$ of 5.5 m and $T_z$ of 8.6 s. One week later a similar storm with slightly more westerly winds (about 20° more anti-clockwise) approached and the peak of this event produced very similar waves. The results are shown in Fig. 7. The hindcast results based on surface charts were very well correlated with the measurements but biased high by about 1 m.

Also shown are the results based on model winds. These are clearly not nearly as well correlated. The first event is prolonged with a 5 m swell which can be traced to high gradients east of Tasmania as the trough passed by. The second event is too intense.

The surface analyses used to hindcast these events did not incorporate data from the meteorological buoy (see Section 2.2 and Fig. 1). Hence the winds from the buoy were available as an independent measure to validate the analyses derived from the weather charts. Comparison with the derived winds at the nearest wave-model gridpoint (65 km to the north) is shown in Fig. 8. Unfortunately the buoy record is not complete, but the comparisons are good, with a slightly high bias in the winds used in the modelling. Even accounting for the increase in speed from 4.2 m (the buoy measurement height) to 10 m, this bias explains most of the over-estimation in the wave heights seen in Fig. 7.

A feature of this event is the number of observations in the Tasman Sea. At the peak of the storm, in addition to 5 ships within the weather system, there were 4 drifting buoys providing additional pressure data. Hence, the analysis is reasonably well-defined.

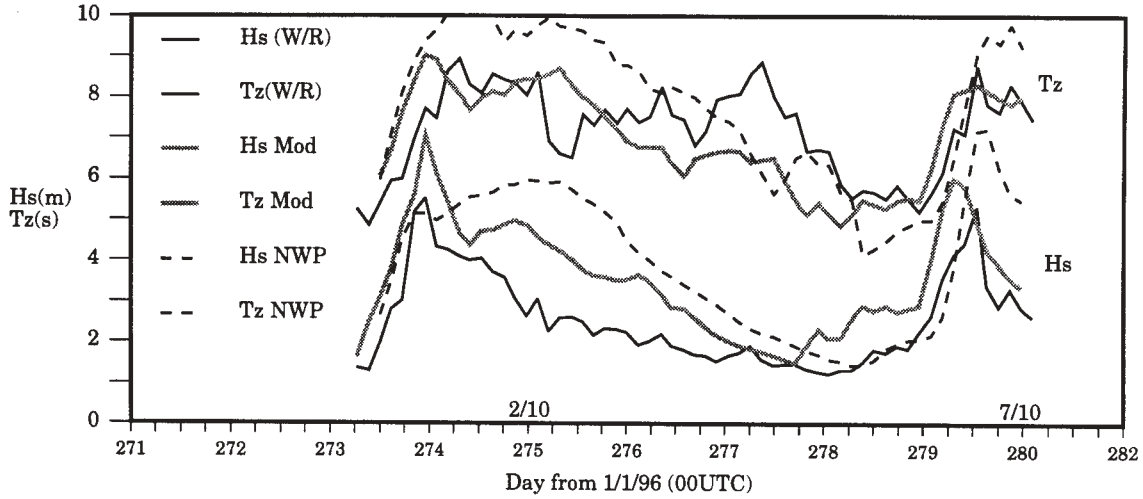


**Fig. 7**. Comparisons of $H_S$ (lower) and $T_Z$ (upper) for hindcasts of October 1996, showing Waverider measurements (W/R) and estimates from hindcasts based on NWP model winds (NWP), and surface weather charts (Mod).

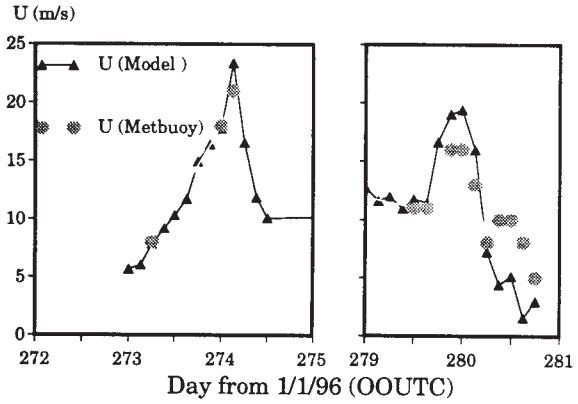


**Fig. 8**. Windspeed for hindcasts of October 1996 showing meteorological buoy measurements and estimates from objective analyses based on surface charts.

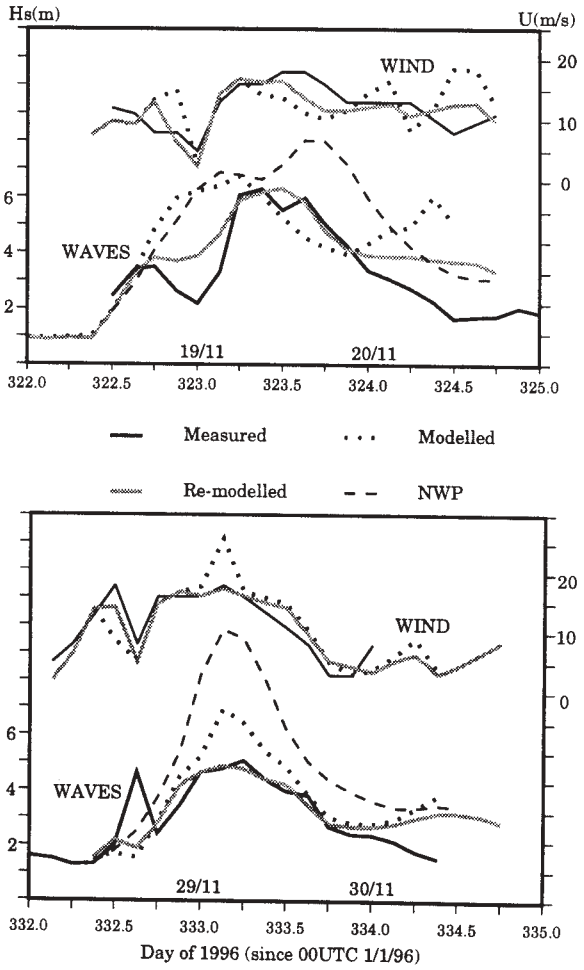


**Fig. 9**. Comparisons of $H_S$ and windspeed for hindcasts of November 1996, showing buoy measurements and estimates from hindcasts based on surface weather charts (Modelled), re-analysed charts (Re-modelled) and NWP model winds (NWP)

### 5.4 November 1996

During late November 1996 two considerably more developed systems crossed the west coast of South Island. In both cases a deep low-pressure centre crossed the coast bringing a short-duration but intense northerly fetch, followed by a change to strong southwesterly winds. The measured waves reached 6 m on November 19 and 5 m on November 29. The hindcasts and measurements are shown in Fig. 9. The winds at the nearest model grid-point and at the meteorological buoy are also shown.

The hindcasts were also repeated using winds from the ECMWF model data set. The results are included in Fig. 9 (as "NWP") and indicate that these winds do not resolve the storms well. They successfully identify the storms, but the airflow is generally too

AUTHOR INDEX



TABLE OF CONTENTS

zonal, resulting in longer, more intense, westerly fetches and over-estimated waves.

### *Manual re-analysis*

The wind comparisons in Fig. 9 highlight problems with the surface charts. In the first storm, ERS2 wind scatterometer data for 12UTC on November 18 and 00UTC on November 19 indicate reasonable analyses at these times, and Fig. 9 shows good agreement with the buoy winds at those times. However, at 18UTC on November 18 the wind used in the hindcast is considerably too high. The surface charts indicate a northwest fetch, with derived winds exceeding 15 $ms^{-1}$, whilst the measured winds were only 8 $ms^{-1}$ from the northeast. While there were adequate observations in the central Tasman Sea, there were none in the east Tasman Sea. Hence the east of the low was analysed with little available information.

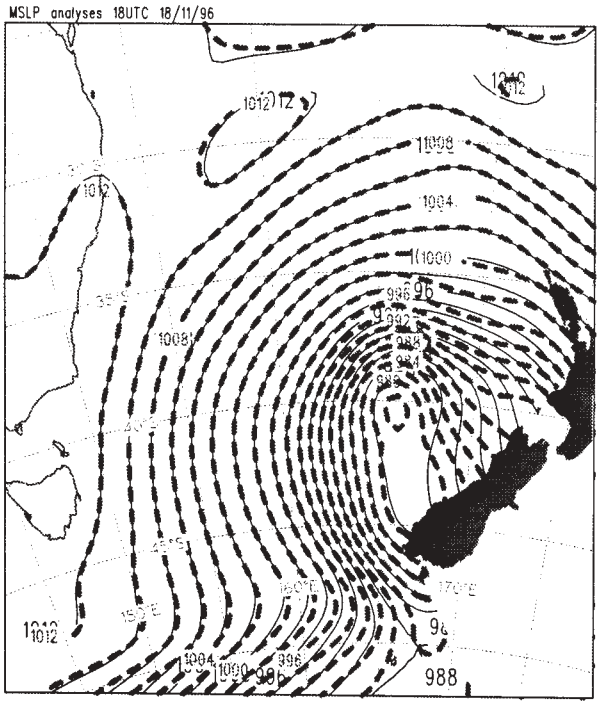


**Fig. 10.** Original pressure analysis at 18UTC on November 18, 1996 (thick dashed lines) with the re-analysed pressure field (thin continous lines).

A re-analysis using the original data, the ship data, satellite images and the additional buoy data, results in the fetch to the east of the low being oriented north-south (Fig. 10), with much lower winds from the northeast at the buoy. The impact of these changes is to substantially reduce the over-estimated wave conditions. The new results are included in Fig. 9.

Other modifcations were made to the analyses during the southwest flow following the passage of the low across the country. The impact of these changes is also quite evident in the hindcast in Fig. 9. However, it is also clear that the modifications do not completely rectify the original errors in the hindcast. There are two possible reasons for this. First, windfields driving the wave model are only changed every three hours, although they are applied at one hour timesteps. Thus, the temporal resolution of the winds is still quite coarse and unable to resolve rapid changes in the weather system, particularly as it crosses the coast. Secondly, the detailed hindcasts performed for this study suggest that the model has insufficient energy dissipation. Waves do not decay as rapidly as the measurements indicate following a wave event. In the present case this occurs following the northerly (at 00UTC on November 19) and following the ensuing southwesterly.

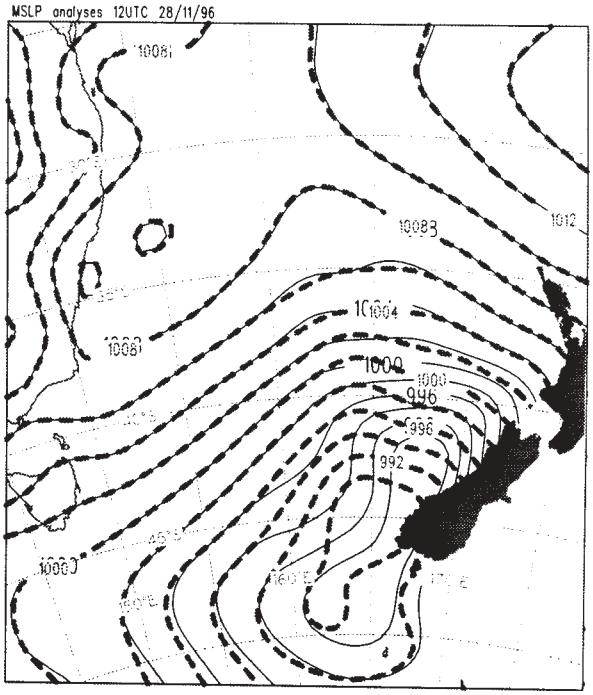


**Fig. 11.** Pressure analyses at 12UTC on November 28, 1996 (as for Fig. 10).

In the second storm the problem with winds in the northerlies preceding the low centre is similar, although this time the winds from the original analysis were too low. The buoy indicated 18 $ms^{-1}$ from the northeast at 12UTC on November 28, but the analysis yielded only 9 $ms^{-1}$. Scatterometer data for

1218UTC also indicated 16 $ms^{-1}$near the buoy site, but they also identify a southwesterly of 18 $ms^{-1}$ immediately off the southwest corner of South Island, and an apparent centre of circulation at about 43°S, 167.5°E. The original analysis and subsequent re-analysis are shown in Fig. 11. The analyses for the southwesterly flow following the passage of the low were also modified to accommodate the pressure and wind data from the buoy. The results of these changes are evident in Fig. 9, with the re-modelled wave heights improving considerably. However, the problems seen in the first storm are evident again: the short-duration northerly does not result in waves to match the measurements, and there is insufficient decay of waves arriving from the mid-Tasman on November 30.

## 6. CONCLUSIONS

We have hindcast storms affecting the west coast of South Island for two sites: the coastal environment of the Karamea Bight, and the open-ocean environment west of Hokitika. For the coastal site, the first attempt, using a continuous 6-year hindcast based on winds from numerical prediction models, produced good estimates of $H_s$ with small overall bias (less than 0.2 m). The hindcast waves also give a plausible selection of severe events, but where comparisons are possible, they are sometimes different storms than indicated by the highest measured waves. Over-estimated and under-estimated events were relatively equally represented. In general, while winds from routinely available atmospheric models depicted the major wave events, they do not accurately replicate details of particular events.

The severe events identified by the hindcast also differed from those identified using a set of objective criteria based solely on meteorological data from land stations. These criteria succeed in selecting only about 50% of the storms with significant wave heights over 4 m. Although the most severe events maintained their intensity near the coast, they also had a history of high winds over the sea. Therefore, the modest success of the selection criteria also serves to emphasise the significance of storm evolution over the open sea in events affecting the coast.

It was apparent that severe waves in the Karamea Bight occurred during periods of strong northwest winds, and that these extremes were very sensitive to the surface analysis from which the winds were derived. Consequently, some of the storms which affected the area during the measurement period were re-hindcast using surface winds derived from an archive of manually-drawn surface pressure analyses. These hindcasts generally improved the estimates of wave conditions but there were still storms which were not well hindcast. For these storms we re-analysed surface pressure fields in the Tasman Sea, taking heed of all observations. This produced changes to the shape of the critical fetches which had considerable influence on the resulting hindcast estimates. These changes were sometimes quite subtle. For example, for a shallow water site the orientation of the fetch is critical. Small changes in direction alter the angle at which waves approach the coast and affect the influence of refraction on the wave spectrum.

For the open-ocean environment the coastal effects are not so critical, but once again the hindcasts highlighted the impact of the shape of the critical fetch in a storm. For two events in November 1996 the original weather charts lacked data in the east Tasman Sea, and the resulting analyses produced winds and waves which did not verify well against measurements. Re-analyses altered the orientation of these fetches and the pressure gradients, and improved the resulting wave hindcasts.

These cases also highlighted the need for adequate temporal resolution to resolve rapidly evolving weather systems. This is particularly relevant in an environment where orographic influences have a strong affect on approaching systems. Three-hourly analyses did not always provide sufficient continuity.

***Acknowledgements***: We would like to thank Solid Energy N.Z. Ltd for commissioning the initial investigation in the Karamea Bight and for permission to reproduce some of those results. The Maui wave data were made available by Shell Todd Oil Services Ltd. The re-analysis of storms was carried out under Foundation for Research, Science and Technology contract CO1620.

## REFERENCES

Cardone, V.J., H.C. Graber, R.E. Jensen, S. Hasselmann and M. Caruso, 1995: In search of the true surface wind field in SWADE IOP-1: Ocean wave modelling perspective. *The Global Atmosphere-Ocean System.*

Carter, D.J.T., P.G. Challenor and M.A. Srokosz, 1992: An assessment of Geosat wave height and wind speed measurements. *J. Geophys. Res.*, **97**(C7), 11,383-11,392.

Ewans, K.C. and A.C. Kibblewhite, 1992: Spectral features of the New Zealand deep-water ocean wave climate. *N.Z. J. Marine and Freshwater Res.*, **26**, 323-338.

Graber, H.C., R.E. Jensen and V.J. Cardone, 1995: Sensitivity of wave model predictions on spatial and temporal resolution of the wind field. *4th International Workshop on Wave Hindcasting and Forecasting*, Banff, Canada, October 1995, pp 149-158.

Laing, A.K., 1992a: Hindcasting a wave climate for the New Zealand region. *3rd International workshop on wave hindcasting and forecasting, Montreal*, 19-22 May, 1992, 222-231.

Laing, A.K., 1992b: A spectral model for the sea-state with explicit forcing terms. *Applied Ocean Res.*, **14**, 341-351.

Laing, A.K., 1993: Estimating wave height data for New Zealand waters. *N.Z. J. Marine and Freshwater Res.*, **27**(2), 157-175.

Laing, A.K. and E. Brenstrum, 1996: Scatterometer observations of low-level wind jets over New Zealand coastal waters. *Weather and Forecasting* **11**(4), 458-475.

Laing, A.K., S.J. Reid and G. Hooper, 1997: Wave conditions in the Karamea Bight, New Zealand from measurements and modelling. *Proceedings of Pacific Coasts and Ports 97, the 13th Australasian Coastal and Ocean Engineering Conference*, Christchurch, New Zealand, September 1997, pp 989-994.

Lionello, P., H. Gunther and P.A.E.M Janssen, 1992: Assimilation of altimeter data in a global third-generation wave model. *J. Geophys. Res.*, **97**(C9), 14,453-14,474.

Reid, S.J. 1981: Extreme winds over the seas around New Zealand. *New Zealand J. of Science*, **24**, 51-58.

Valentine, E.M. and G.H. Macky, 1984: Sea wave climate at Ngakawau, Westport and Carters Beach. Ministry of Works and Development, Report No. 3-84/4, Vols I and II.

# INTERCOMPARING THIRD-GENERATION WAVE MODEL NESTING

R. Padilla[1], P. Osuna[1], J. Monbaliu[1] and L. Holthuijsen[2]

[1]Hydraulics Laboratory, K.U.Leuven, de Croylaan 2, B-3001 Heverlee, Belgium
[2] Civil Engineering, T.U. Delft, Stevinweg 1, 2628 CN Delft, the Netherlands

## 1 INTRODUCTION

To forecast or hindcast coastal wave conditions with numerical models, nesting of computational grids is often necessary. In the present study, wave conditions in the southern North Sea have been generated on a coarse grid (50 x 50 km$^2$) using the WAM Cycle 4 model. As a first step towards a high resolution (1 x 1 km$^2$) coastal wave prediction model for the Belgian coastal area, a nested grid with an intermediate spatial resolution (10 x 10 km$^2$) was implemented. For the nested runs both the WAM cycle 4 and SWAN cycle 2 model have been used.

For coastal engineering studies wave information is required in shallow water areas where wind growth, bottom dissipation and wave-current interactions may play an important role. An accurate and efficient wave model is essential. In the present paper, the WAM-model in its standard version, as well as the SWAN-model are used for the nested runs. The WAM-model is considered state-of-the-art up to intermediate water depth but has a number of limitations and shortcomings in shallow water. Note that extensions and modifications to the WAM model have been made or are being developed. They include amongst others, the incorporation of five different bottom friction dissipation formulations, the addition of depth-induced wave breaking according to the Battjes-Janssen formulation (Luo and Monbaliu, 1994; Luo, 1995) and the introduction of a more efficient numerical scheme. This last item reduces the computational effort for shallow water applications considerably (Luo et al., 1997). These and some other features are currently being put together and tested in the EC- Marine Science and Technology program PROMISE (Pre-Operation Modelling In the Seas of Europe). However these modifications were not yet used for this study.

A nearshore third-generation wave model SWAN has been developed at Delft University (Ris *et al.*, 1997) and it has been released recently into public domain. This model is also a third-generation, fully spectral model. Like the WAM model, it solves the wave action density transport equation without *a priori* spectral constraints. It takes into account depth-induced wave breaking and triad interactions. Triad interactions are not included in the WAM model but are considered important for wave evolution in nearshore areas. Attractive aspects of the SWAN model are its computational efficiency since the model uses an implicit scheme allowing the use of a large time step (greater than the CFL limit), and the ability to easily chose between different computational options. Note that SWAN can also be run in a first and in a second-generation mode.

The objective of this paper is to investigate and compare in more detail the nesting of WAM in WAM and SWAN in WAM and to point out a number of findings. Note that the non-stationary version of the SWAN-model is still under development and what is described below can therefore be seen as a contribution to this development. The SWAN model was used in its version 30.20.

In the following, the WAM and SWAN models are briefly described in section 2. In section 3, a wave hindcast study was carried out for the southern North Sea and model results are compared to buoy measurements. In section 4 the results are analysed and discussed in more detail by turning on and off different options in the SWAN model and by looking at the spectra at different locations. Finally, the paper ends with conclusions in section 5.

## 2 MODEL DESCRIPTION

### 2.1 The WAM model

The WAM (Cycle 4) model is a third-generation wave model, which solves the wave transport equation explicitly without any *ad hoc* assumption on the shape of the wave energy spectrum. The basic equation in Cartesian co-ordinates is

$$\frac{\partial F}{\partial t}+\frac{\partial}{\partial x}(c_x F)+\frac{\partial}{\partial y}(c_y F)+\sigma\frac{\partial}{\partial \sigma}(c_\sigma \frac{F}{\sigma})+\frac{\partial}{\partial \theta}(c_\theta F)=S_{tot} \quad (1)$$

where $F(\sigma, \theta)$ is the wave energy spectrum, $t$ is the time. $\sigma$ is the intrinsic angular frequency, $\theta$ is the wave direction measured clockwise from true north, $c_x$, $c_y$, are the propagation velocities in geographical space, $c_\sigma$ and $c_\theta$ are the propagation velocities in spectral space (frequency and directional space). The left-hand side of the above equation represents the local rate of change of wave energy density, propagation, shifting of frequency due to time variation in depth, and refraction. The right hand side represents all effects of generation and dissipation of the waves, including wind input $S_{in}$, whitecapping dissipation $S_{ds}$, non-linear quadruplet wave-wave interactions $S_{nl}$ and bottom friction dissipation $S_{bf}$. A detailed description of the WAM model can be found in Günther *et al.* (1992) and Komen *et al.* (1994).

The WAM (Cycle 4) can run for deep and shallow water conditions, can include depth and current refraction (steady depth and current field only), and can be set up for any local or global grid with a prescribed topographic dataset. The model solves the wave propagation equation using a first-order, upwind, explicit scheme. Therefore, the propagation time step is limited by the CFL condition. The propagation can be computed on a spherical or a Cartesian grid. The source term integration is solved by a semi-implicit scheme. Nesting of grids is possible for WAM. The boundaries of a nested fine grid have to be pre-defined in the set-up of a coarse grid run. The corner points of the nested fine grid have to coincide with nodes of the coarse grid. The coarse and fine grid model runs are separate. At the interface boundary, the wave spectra are output at the boundary points of the fine grid from the coarse grid run, and then interpolated in space and time to the boundary points of the fine grid. They are consequently used as boundary condition for the nested fine grid run (one-way nesting).

### 2.2 The SWAN Model

The SWAN (Simulation of WAves in Nearshore areas) model is based on the action balance equation since the wave energy density is not conserved in presence of currents, whereas action density is conserved. The equation solved by the SWAN model is

$$\frac{\partial N}{\partial t}+\frac{\partial}{\partial x}(c_x N)+\frac{\partial}{\partial y}(c_y N)+\frac{\partial}{\partial \sigma}(c_\sigma \frac{N}{\sigma})+\frac{\partial}{\partial \theta}(c_\theta N)=\frac{S_{tot}}{\sigma} \quad (2)$$

where $N(\sigma,\theta)$ is the wave action density ($=F(\sigma,\theta)/\sigma$). The other symbols are identical to the ones used for the WAM-model description (see section 2.1). The source terms in SWAN include the wave energy growth by wind input, wave energy transfer due to wave-wave non-linear interactions (both quadruplets and triads), the decay of wave energy due to whitecapping, bottom friction and depth-induced wave breaking. For the wind energy input into the spectrum, two different formulations can be used, i.e. the Komen et al. (1984) and the Janssen (1989, 1991) formulation. The first formulation refers to the wind input term expression of Snyder et al. (1981) but it has been rescaled in function of the air friction velocity. The second formulation refers to the wind input term expression of Janssen (1989, 1991) which takes the interaction between the waves and the wind explicitly into account. For each of these wind input term formulations, a corresponding whitecapping dissipation term is used. A detailed description of the SWAN (Cycle 2) model can be found in Ris (1997) and Ris *et al.* (1997).

The basic spectrum considered in SWAN (Cycle 2) is the action density spectrum. The model propagates the wave action density of all components of the spectrum across the computational area using an implicit scheme. It has the great advantage that the propagation time step is not limited by a numerical stability condition since the implicit scheme is unconditionally stable in geographic and spectral

space. Therefore, for high-resolution applications in shallow water, the computational effort required is expected to be reduced compared to WAM since a longer time step can be used in SWAN. In geographical space the scheme is a first-order upwind and it is applied to each of the four directional quadrants of wave propagation in sequence (i.e., divided into four sweeps). In the spectral space the scheme is a user-controlled combination of an upwind scheme and a central scheme. The propagation is done in a Cartesian co-ordinate system. The numerical scheme used for the source term integration is user defined. The users can chose between a fully implicit, a semi-implicit or an explicit scheme. SWAN can be run in several modes: first-, second- or third-generation mode, according to the chosen level of parameterisation. Nesting of grids is possible in SWAN. The idea of nesting in SWAN is similar to that in WAM. However, the corner points of the nested fine grid in SWAN do not have to coincide with nodes of the coarse grid. A description on the nesting of a finer SWAN run into a WAM coarse run can be found in Luo and Flather (1997).

# 3 NESTED RUNS

## 3.1 Application to the southern North Sea

A hindcast study for the period of February 1993, using nesting techniques was carried out in the southern North Sea. A severe storm occurred on the 21st of February. To account for swell generated in the Norwegian Sea and propagating into the southern North Sea, a WAM coarse grid covers the whole North Sea from 48° N to 70° N latitude and from 7° W to 12° E longitude on a grid of 25 x 48 points. The spatial resolution is about 50 km. Note that a stereographic projection was used to run the model on a Cartesian grid.
The model was implemented with a nested grid. Close to the Dutch and Flemish coasts, a finer grid with a spatial resolution of about 10 km was set up, nested into the coarse grid. The WAM coarse grid model was run for the whole month of February 1993. The nested fine grid was run for the period February 14 to 25 using both the WAM and the SWAN model.

To analyse the results from both models in more detail, buoy measurements from two locations were used for comparisons. The Dutch Europlatform (EUR) buoy is close to the fine grid model input boundary and in relatively deep water (model water depth of 26 m), while the Belgian A2B buoy is close to the coast in relatively shallow water (model water depth of 7 m). Figure 1 shows the nested fine grid model bathymetry and the exact locations of the two buoy stations.

The wind fields used come from the United Kingdom Meteorological Office (UKMO) atmospheric model. Analysed fields or forecasts are used depending on their availability. They were interpolated to the WAM coarse and fine grid.

# 4 ANALYSIS OF THE RESULTS

## 4.1 Time series WAM and SWAN

To intercompare the WAM and SWAN results, SWAN was run with option Janssen (excluding triads and depth-induced wave breaking), i.e. the WAM-Cycle4 physics, but also with the option Komen, i.e. the WAM-Cycle3 physics. The difference between these two SWAN options is in the source term formulation for wind input and whitecapping dissipation.

Comparisons between the computed results from WAM and SWAN, and buoy data were carried out. The time series of significant wave height during extreme conditions from February 17 to 23 are shown in Figures 2 and 3. In Figure 2 one can see that significant wave height at the EUR location is underestimated by both WAM and SWAN, and this mainly at the peak of the storm. Luo (1995) pointed out that UKMO predicted winds tend to be underestimated but the main reason for this underestimation is of course the underestimation of the energy from the coarse grid WAM computation. This underestimation will be propagated into the computational domain by the WAM and SWAN nested runs. In location A2B WAM reproduces quite well the measured values, which is somewhat surprising considering the underestimation at the boundary. SWAN is more

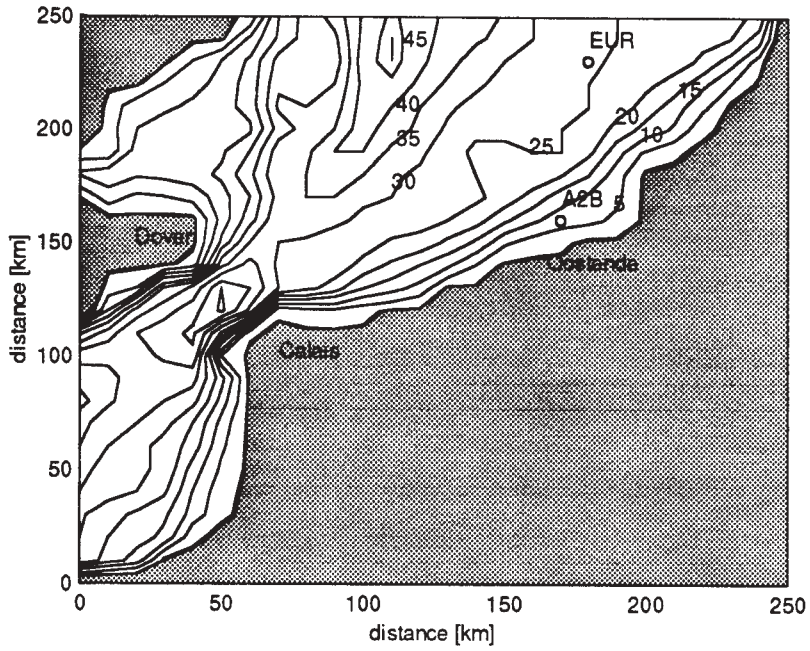


**Figure 1. Bathymetry of the nested area with indication of buoy location**

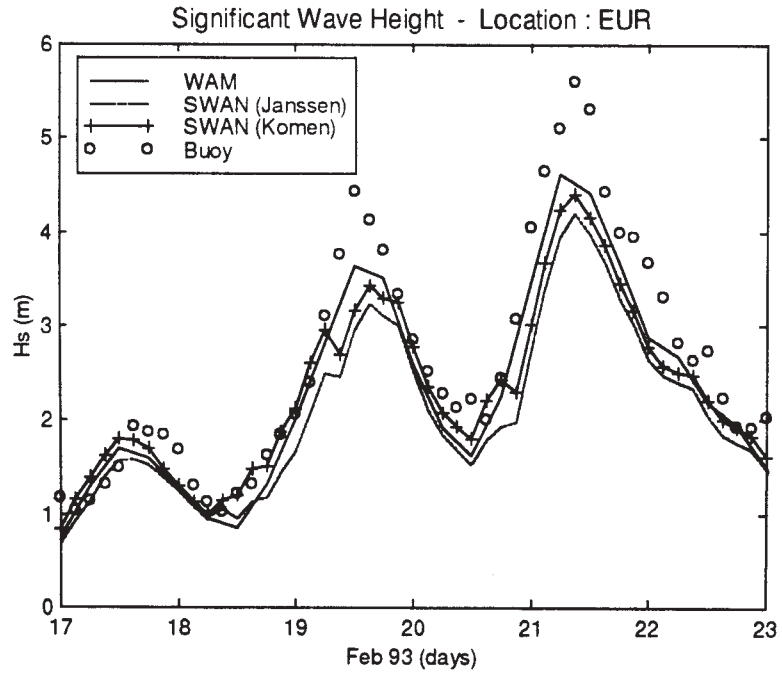


**Figure 2. Time series of significant wave height at the EUR location.**

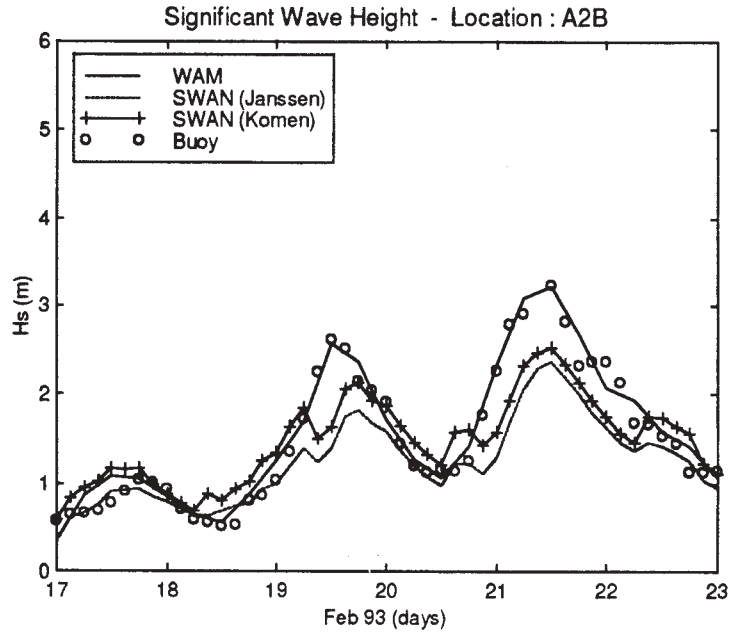


**Figure 3. Time series of significant wave height at the A2B location.**

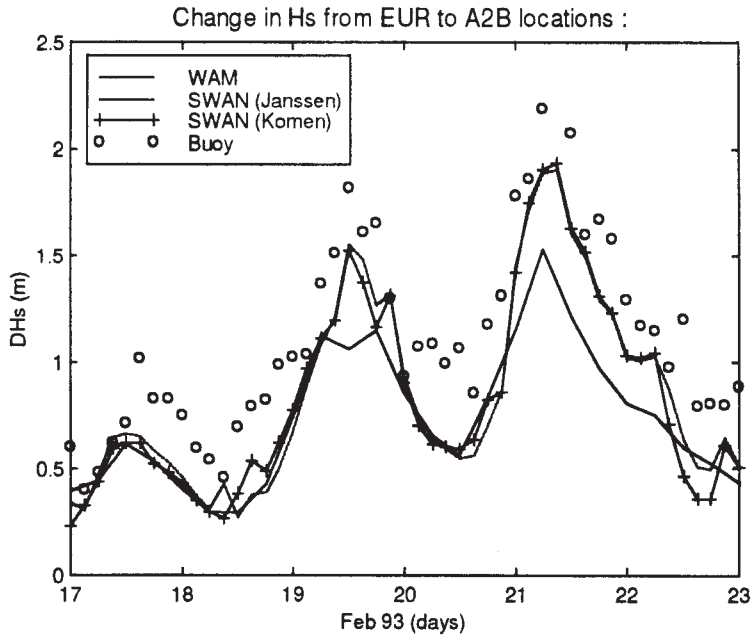


**Figure 4. Computed change (ΔHs) in wave height (Hs in EUR minus Hs in A2B).**

consistent with the boundary conditions coming from the WAM coarse grid run (see Figure 2). In model intercomparison the computed change in wave height ($\Delta Hs$) is probably a more relevant parameter to consider. The absolute wave height is affected too much by the wrong boundary conditions (in comparison with the observations). The computed $\Delta Hs$ is therefore compared with the $\Delta Hs$ from the observations, see Figure 4. It can be seen that the results from WAM in location A2B compensate for the low energy levels entering from the north boundary (from the coarse WAM run).

At the A2B location the water depth is about 7 m and bottom friction might play an important role in the wave dynamics, see also section 4.2 and 4.3. Another possible cause of discrepancy may be the directional resolution. For these runs a resolution of 30 degrees was used, which is according to Luo and Flather (1997) not the most appropriate resolution. It could be too poor for shallow water regions, especially when there are significant spatial gradients. Although not attempted in this study, it might be worthwhile to tune source term coefficients, in particular the bottom friction. However, it seems premature at this stage to put a lot of effort into this. It is more important to gain more experience with the model set-up by understanding better the sensitivity of the models to the different source terms. Therefore, in the next sections, propagation only and SWAN without bottom friction have been investigated.

## 4.2 Pure propagation

The purpose of this test is to point out how the propagation scheme in WAM and SWAN works in the nested runs. All the source terms were turned off. Figures 5 and 6 show the resulting time series for the wave height at the EUR and A2B locations. At the first location the output from both models match perfectly. This is due to the fact that the station EUR is very close to the boundary where the wave conditions obtained from the coarse WAM run, are imposed at the boundary every ten minutes and the waves have only propagated over a very short distance from the boundary (20 km). This however shows that the boundary conditions are read and incorporated into the numerics of SWAN properly without any changes in the total energy. However, in location A2B the energy level is lower in SWAN than the level of energy in the WAM run without source terms. This is an indication that the implicit scheme used in SWAN for the wave propagation is more diffusive than the explicit scheme used in WAM. The case considered here is for the SWAN model, in concept developed for relatively small coastal areas, beyond the intended limit in terms of spatial extent. It is intuitively clear that the behaviour of the source terms in the WAM and the SWAN model will be influenced by the diffusivity of the propagation. The source terms are related to and influenced by the shape or energy content of the spectrum.

## 4.3 Role of bottom friction

### 4.3.1 SWAN without bottom friction

To investigate the importance of the bottom friction in SWAN, the SWAN model was run with bottom friction turned off. The results can be seen in Figures 7 and 8. The wave heights from SWAN at location EUR are only slightly modified compared to the run with bottom friction on (see Figure 2). At the A2B location hindcasted wave heights seem to have 'improved', especially the predicted peak wave heights. However after the peak of the storm, wave heights are overestimated. Wave growth seems to be given at the "right time", but the decay of the energy is too slow. Bottom friction seems to be a dominating source term and plays an important role for the prediction of wave heights at the coastal location A2B. Luo *et al.* (1996) has shown that the bottom dissipation has quite significant effect on the energy balance using different bottom friction formulations, reporting difference as big as 80% of the total energy along the Belgian coast.

## 4.4 Role of triads and depth in induced breaking

This has not been looked at, but it is anticipated that these source terms will not play a significant role in this particular set-up, where due to still a relatively coarse grid resolution, local bathymetric effects such as sandbars have been smoothed out. These source terms might however play an important role when the grid resolution will be further reduced. Then it will be possible to resolve the different sandbanks and it will become important to take these effects into account.

### 4.5 The wind input term

It can be seen in Figures 2 and 3 that there are several occasions where the wave energy predicted by SWAN is larger than the results from WAM. This happens precisely at times when the wind speed increases and changes its direction (Figure 9a and 9b). SWAN responds faster than WAM, building up new components in the spectrum. The main reason can be traced back to the fact that the wind-input term in SWAN is the sum of two expressions, a linear input term and an exponential input term. The linear terms puts energy from the wind into the wave field at the early stages of wave development. Afterwards the exponential term becomes much more important. This is also illustrated in more detail in the Figures 10 and 11. Note that the spectra have been plot when there is an increase of energy and that the spectra have been normalised with the peak value ($E_{max}$) of the WAM spectrum. From the spectral distributions, one can see that SWAN responds faster than WAM when waves are building up in a direction considerably different from the wave direction of the energy peak of the spectrum.

## 5 CONCLUSIONS

Nesting WAM and SWAN in a coarse WAM run has been successfully applied to simulate the waves in the southern North Sea. The intercomparison reveals that the incorporation of the spectral distribution from WAM to SWAN is done properly despite the differences in numerics in both models. The largest differences between the output of both numerical models can be found in the shallowest locations. Although WAM at first sight seems to give better results at the shallow A2B location, SWAN is more consistent with the imposed boundary conditions. SWAN reproduces better the differences in wave height between the location EUR at the boundary of the nested grid and the location A2B close to the coast.

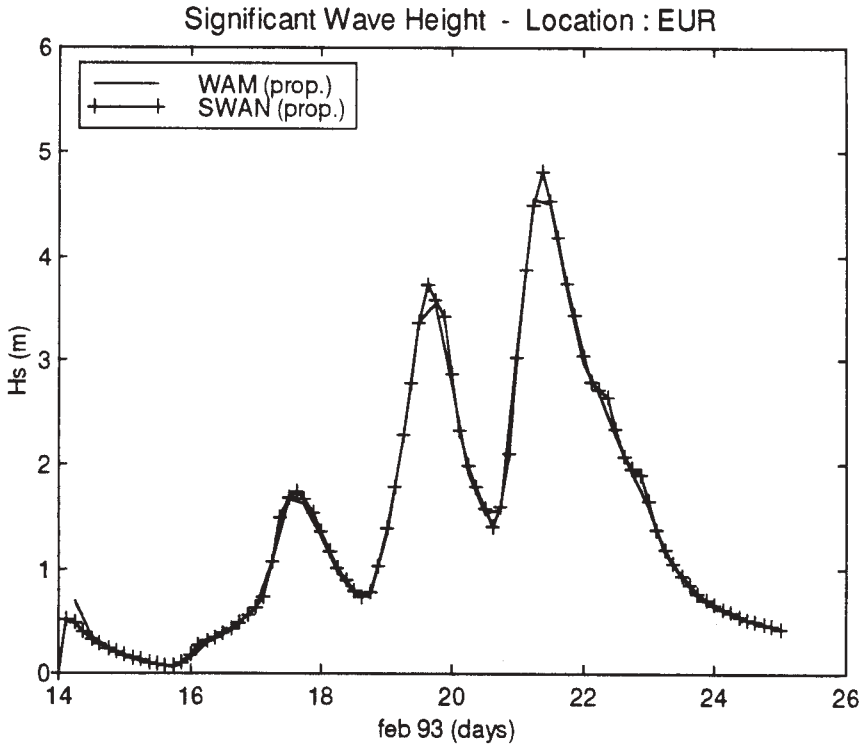


**Figure 5. Time series of wave height at the EUR location, pure propagation case.**

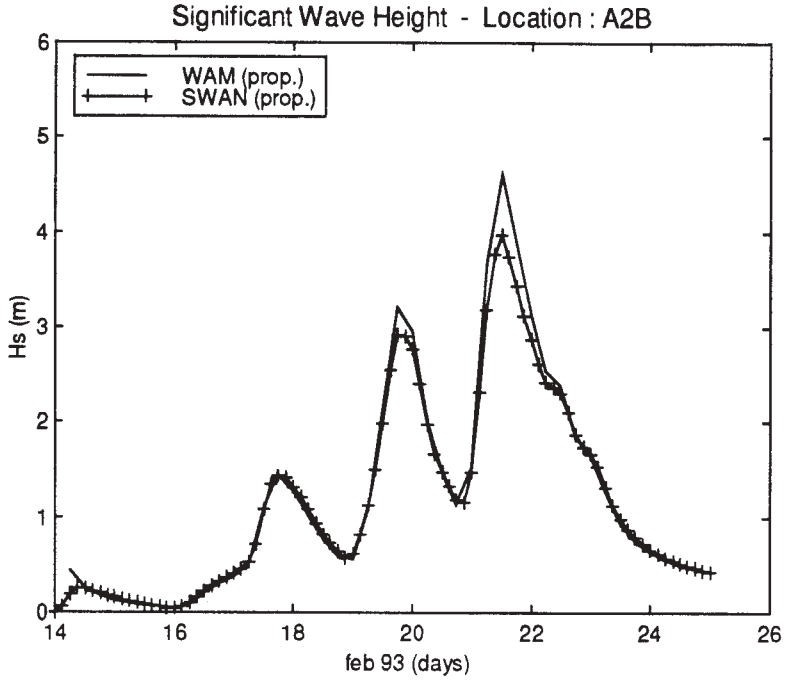


**Figure 6. Time series of wave height at the A2B location, pure propagation case.**

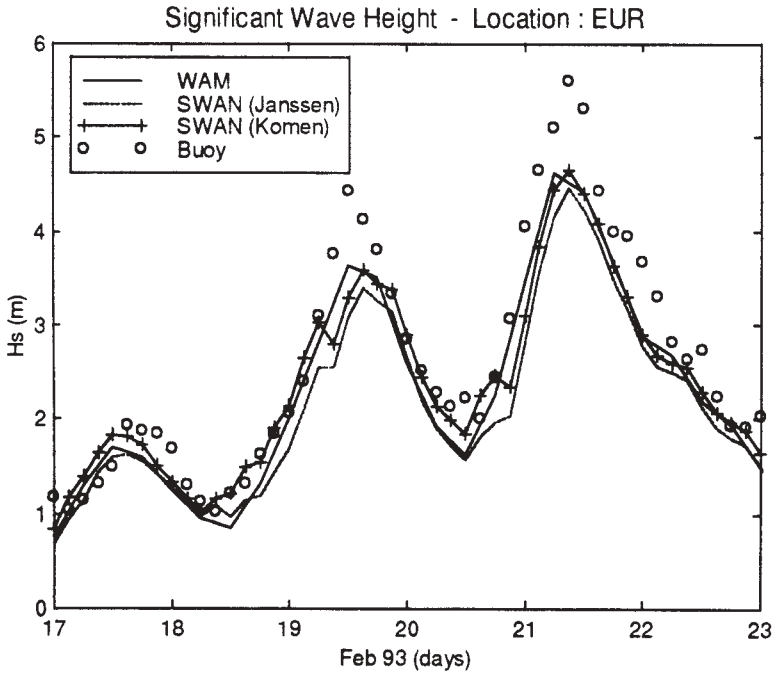


**Figure 7. Time series of wave height at the EUR location, friction off case.**

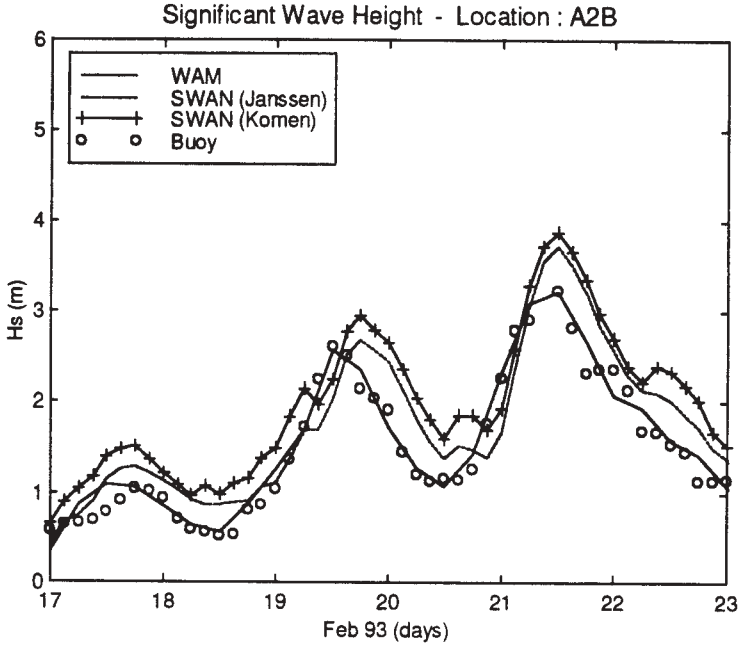


**Figure 8. Time series of wave height at the A2B location, friction off case.**

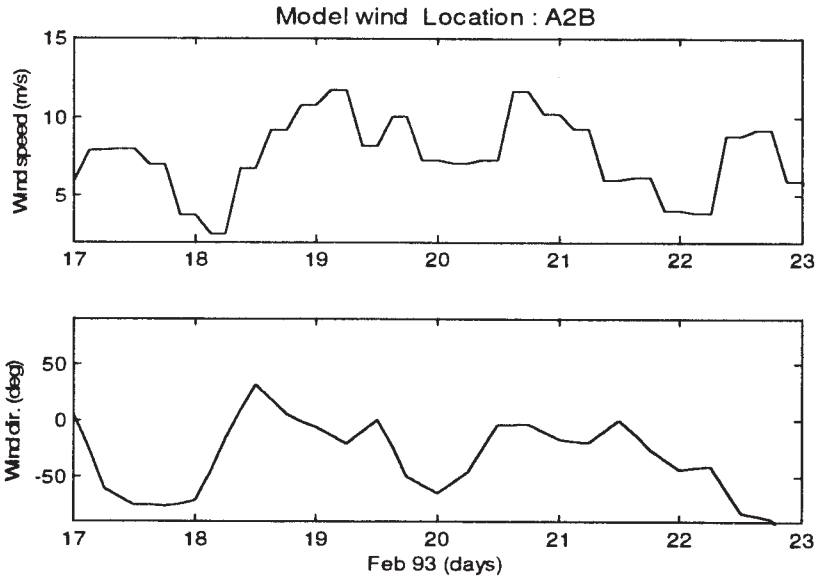


**Figure 9. Model wind speed (on top) and wind direction (on bottom) at the A2B location.**

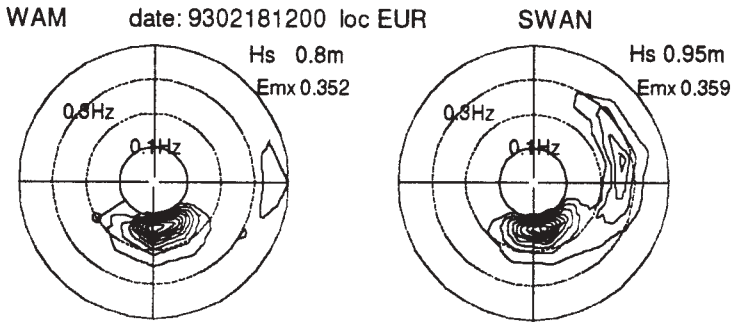


**Figure 10. Spectral energy distribution at the EUR location. The line indicates wind direction (going to).**

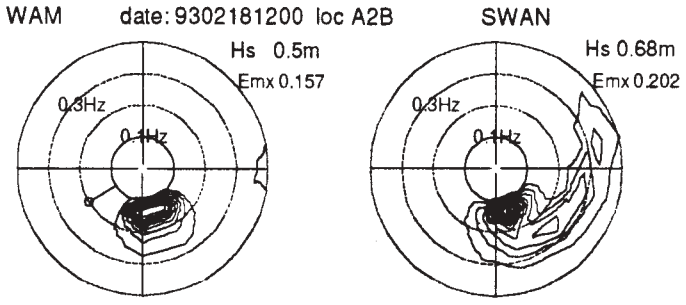


**Figure 11. Idem Figure 10 but at the A2B location.**

SWAN is in concept a shallow water wave model applicable to small areas. If it is applied to large areas, numerical diffusion due to the implicit propagation scheme used, is apparent. The exercise described in this paper is probably close to the SWAN limit of applicability in terms of spatial extent.

SWAN responds quickly to changes in the wind field. The linear term in the wind input source term formulation adds energy in the high frequency spectral bins.

Bottom friction plays an important role in this shallow water region. Tuning of the bottom friction parameter could improve the model results. However depth-induced wave breaking and triads were not taken into account for this study. Further tests with a finer grid in order to resolve the complex bathymetry of this region have to be made in order to estimate the importance of the different processes involved.

Acknowledgements

This study was partially carried out with financial support from the EC-MAST III PROGRAME, contract MAS3 CT 9500025.
We thank RIKZ (the Netherlands) and AWK (Belgium) for supplying the buoy data at the EUR and A2B location respectively.

## 6 REFERENCES

Günther, H., S. Hasselmann, & P.A.E.M Janssen, 1992: The WAM model Cycle 4, Report No. 4, Hamburg.

Janssen, P.A.E.M., 1989: Wave-induced stress and the drag of air flow over sea waves, *J. Phys. Oceanogr.*, **19**, 745-754.

Janssen, P.A.E.M., 1991: Quasi-linear theory of wind-wave generation applied to wave forecasting, *J. Phys. Oceanogr.*, **21**, 1631-1642.

Komen, G., S. Hasselmann, and K. Hasselmann, 1984: On the existence of a fully developed wind-sea spectrum, *J. Phys. Oceanogr.*, **14**, 1271-1285.

Komen, G.J., L. Cavaleri, M. Donelan, K. Hasselmann, S. Hasselmann & P.A.E.M. Janssen, 1994: Dynamics and Modelling of Ocean Waves, Cambridge University Press, Cambridge, 532p.

Luo W. and J. Monbaliu, 1994: Effects of bottom friction dissipation formulation on the energy balance for gravity waves in shallow water, *J. Geophys. Res.*, **99** (C9), 18,501-18,511.

Luo, W., 1995: Wind wave modelling in shallow water with application to the southern North Sea, Ph.D. thesis, K.U.Leuven, Belgium, ISBN 90-5682-003-6.

Luo W. and J. Monbaliu and J. Berlamont, 1996: Bottom friction dissipation in the Belgian coast regions, Proc. of the 25th International Conference on Coastal Engineering, 836-849.

Luo, W. and R. Flather, 1997: Nesting a nearshore wave model (SWAN) into an ocean wave model (WAM) with application to the southern North Sea", in Computer Modelling of Seas and Coastal Regions III, edited by J. R. Acinas and C.A. Brebbia, Computational Mechanics Publications, 253-264.

Luo, W., R. Flather and J. Monbaliu, 1997: An efficient computational scheme for the use of the third generation WAM model in coastal regions, submitted for publication in *J. of Waterway, Port, Coastal, and Ocean Engineering.*

Ris, R.C., 1997: Spectral modelling of wind waves in coastal areas. Ph.D. thesis, Delft University of Technology, the Netherlands.

Ris R.C., N. Booij, L.H. Holthuijsen and R. Padilla-Hernandez, 1997: SWAN Cycle 2 User Manual - Simulation of WAves in the Nearshore Zone, Delft University of Technology, the Netherlands.

Snyder, R.L., F.W. Dobson, J.A. Elliot and R.B. Long, 1981: Array measurements of atmospheric pressure fluctuations above surface gravity waves, *J. Fluid Mech.*, **102**, 1-59.

# WIND-WAVE MODELLING IN WATERS WITH RESTRICTED FETCHES

Henrik Kofoed-Hansen[1,2], Hakeem K. Johnson[2], Jørgen Højstrup[3] and Bernhard Lange[3]

[1] *International Research Centre for Computational Hydrodynamics (ICCH), Hørsholm, Denmark*
[2] *Danish Hydraulic Institute, Agern Allé 5, Hørsholm, Denmark*
[3] *Risø National Laboratory, Roskilde, Denmark*

## 1. INTRODUCTION

The WAM model of the WAMDI group (1988) was developed for oceanic waters and shelf seas. The concept of this model is used today in several third-generation wind-wave models covering global and regional scales in forecast and hindcast mode, and the models have performed quite well, Komen et al (1994). In recent years, considerable effort has been put on spectral modelling of wind generated waves in coastal and restricted waters, eg Ris (1997) and Benoit et al (1996). Basically, the shallow water models are an extension of the deepwater third-generation (3G) wave models which describe the change of wave action density due to wind input, dissipation due to white-capping and nonlinear energy transfer. In addition to the deepwater processes, various source functions such as bottom dissipation, depth-induced wave breaking and nonlinear energy transfer due to triad-wave interaction have been incorporated as well as shoaling and refraction due to varying depths and currents. A third-generation wind-wave model, MIKE 21 OSW 3G, including these processes was recently developed at the Danish Hydraulic Institute, Johnson (1997). The model is based on WAM physics.

As a part of ongoing Danish research project on wind-wave interaction in coastal and shallow waters, the problem of wave growth in fetch-restricted waters has been investigated using measured data and MIKE 21 OSW 3G. For strong winds ($U_{10}$~ 10-15 m/s), the wind stress and the significant wave height are considerably overestimated with a corresponding underestimation of the peak frequency. Similar overprediction has also been found by Hersbach (1997) in Lake George, Australia, using WAM Cycle 4. Detailed comparisons between numerical results and measured data indicate that most of the discrepancies may be explained by too low bottom dissipation and an overprediction of the wind friction velocity as calculated by Janssen's theory.

Section 2 presents a concise description of our third-generation wind-wave model. This paper considers two different fetch-restricted waters. The first area is located at Vindeby, Denmark, where the RASEX (Risø Air Sea EXperiment) study took place at an offshore wind-turbine site in 1994, see Johnson et al (1997a). The measurement site is located in relatively shallow water (water depth 3-4 m) in an area where the waves are predominantly fetch-limited (maximum fetch of about 20 km). The second area is located in the Great Belt between Funen and Zealand, Denmark. This paper considers winds from W-SW for this area, where the fetch is 3-7 km and 15-20 km, respectively, at the two measurement buoys. The water depth at the two buoys is about 20 m and 30 m, respectively. Section 3 describes the two areas and the available measured data, and Section 4 presents the basic model set-up. Section 5 presents and discusses comparisons between model results and measured data. Section 6 gives the conclusions.

## 2. WIND-WAVE MODEL

DHI's third-generation wind-wave model, MIKE 21 OSW 3G, has been used to calculate the two-dimensional wave spectrum. The

model is based on numerical integration of the spectral energy balance equation

$$\frac{DF}{Dt} = S_{in} + S_{nl} + S_{ds} + S_{bot} + S_{brk} \qquad (1)$$

where F(f,θ;x,t) represents the spectral energy density, **x** is the space co-ordinate, t is time, f is frequency and θ denotes the wave propagation direction. The left-hand side of Eq 1 describes the wave propagation in space and time using linear theory. The right-hand side represents superposition of source functions describing various physical processes: the wind input, $S_{in}$, nonlinear transfer due to four-wave interaction, $S_{nl}$, dissipation due to white-capping, $S_{ds}$, sea bottom dissipation, $S_{bot}$, and bottom induced wave breaking, $S_{brk}$.

### 2.1 Source Functions

The default settings in DHI's 3G wind-wave model are identical to the WAM model (Cycle 4) as described in Günther et al (1992) and Komen et al (1994). The wind input, $S_{in}$, is based on Janssen's quasi-linear theory of wind-wave generation (Janssen, 1989, 1991), where the wind friction velocity, $u_*$, and sea surface roughness, $z_0$, not only depend on the wind, but also the sea state itself. The nonlinear transfer of energy, $S_{nl}$, through the resonant four-wave interaction is approximated by the Discrete Interaction Approximation (DIA) originally proposed by Hasselmann and Hasselmann (1985a, 1985b). Although this parameterisation of the Boltzmann integral only considers a small subset of wave number configurations, the DIA approach reproduces the fundamental properties of quadruplet wave interactions reasonably well. The source function describing the dissipation due to white capping is based on the theory of Hasselmann (1974) and Janssen (1989).

*Shallow Water*

As waves propagate into shallow water, the orbital wave velocities penetrate the water depth and the source functions due to wave-bottom interaction become important. Furthermore, the deepwater source functions are modified due to depth effects.

A review of the different wave-bottom interaction processes is given by Shemdin et al (1978), who consider dissipation due to friction in the turbulent boundary layer, percolation into a porous bottom, motion of a soft bottom and scattering on bottom irregularities. According to Shemdin et al, bottom friction is generally dominant when the sediment is composed of fine sand ($d_{50}$= 0.1-0.4 mm) or when sand ripples are present. This condition is satisfied in Vindeby and partly in the Great Belt case investigated in this paper.

In the past decades, different formulations for the bottom friction term have emerged in the literature, see for example Luo and Monbalieu (1994). All formulations based on linear theory can be generalised into an equation for the dissipation rate due to bottom friction, Weber (1991a)

$$S_{bot}(f,\theta) = -C_{fw}\frac{k}{\sinh 2kh}F(f,\theta) \qquad (2)$$

where k is the wave number, h is water depth and $C_{fw}$ is a bottom dissipation coefficient which generally depend on the near-bed orbital velocity and sediment properties. Many expressions for the dissipation coefficient, $C_{fw}$, have emerged in the literature. These expressions can be broadly classified into three categories, namely:

- Purely empirical values, eg $C_{fw}$= 0.0078 m/s for swell waves (Hasselmann et al, 1973) or $C_{fw}$= 0.0136 m/s for storm waves (Bouws and Komen, 1983).
- Expressions based on the drag law turbulent friction model. This can be based on the assumption of a constant friction factor (Hasselmann and Collins, 1968; Collins, 1972), constant geometric roughness, $k_N$ (Madsen et al, 1988) or constant median bed sediment size, $d_{50}$ (Tolman, 1994).
- Expressions based on the eddy viscosity model (Weber, 1991b).

In MIKE 21 OSW 3G, the three categories for the dissipation coefficient are implemented as follows:

- A constant bottom dissipation coefficient as found in the JONSWAP experiment for swell waves or by Bouws and Komen

(1983) for storm waves. This will be called the JONSWAP friction model (JONF).

- A constant geometric roughness size, $k_N$, as suggested by Weber (1991a) in which the dissipation coefficient is based on the wave friction factor using the expression of Jonsson and Carlsen (1966) and the near-bottom orbital velocity. This approach will be called the constant roughness friction model (CRF).
- A constant median sediment size, $d_{50}$, in which the bed is modelled as a mobile bed. An example of this approach is described by Tolman (1994). However, our approach differs con-siderably in the details. Instead of using the Grant and Madsen model for determining ripple dimensions (as used by Tolman), we use the empirical expressions of Nielsen (1979) based on field measurements. The bed roughness is calculated using the expression by Swart (1976). Finally, the bottom dissipation coefficient is computed from the wave friction factor using the ex-pression of Jonsson and Carlsen (1966) and the bottom orbital velocity. We denote this approach the mobile bed friction model (MBF).

Further details about the bed friction models can be found in Johnson and Kofoed-Hansen (1997).

In very shallow water and especially in the surf zone, the energy dissipation caused by depth-induced wave breaking is an important process. The WAM model does not consider this process. A formulation by Eldeberky and Battjes (1996) based on Battjes and Janssen (1978) has been implemented in MIKE 21 OSW 3G. The dissipation rate is assumed proportional to the spectral energy density. Hence, the process is considered as a frequency independent process.

Although quadratic nonlinearities become important in very shallow water, the nonlinear energy transfer due to three wave interactions is not considered in this paper.

### 2.2 Integration of the Energy Balance Equation

The wave energy balance Eq 1 is formulated in Cartesian coordinates. The integration of Eq 1 is divided into two steps: a propagation step and a source function integration step. The propagation step is solved using either a second order semi-Lagrangian scheme or a first order Eulerian upwind scheme. The latter scheme is used in WAM. In this paper, we have used both transport schemes. The source integration is carried out using the method suggested by Hersbach and Janssen (1997).

### 2.3 Limitation on Wind-Wave Growth

Recently, Hersbach (1996) and Hersbach and Janssen (1997) found that the universal scaling laws for fetch-limited wind-wave growth is violated in the WAM model for small-scale applications, ie small grid spacing and time step. Typically, the WAM model underpredicts the wave height which was found to be as the result of a too restrictive limitation on the wind-wave growth. The so-called limiter was originally introduced to ensure a stable integration and was formulated as a limit on the change in the spectral density per time step. This limit was set to a certain fraction of Phillips' universal $f^{-5}$ equilibrium spectrum, and it is proportional to the time step. For small-scale applications with small time step, this limiter does not allow the waves to grow.

In order to be consistent with the WAM physics, a new limiter based on a Toba spectrum has been suggested by Hersbach and Janssen (1997):

$$\max\{\Delta F\} = 3.0 \cdot 10^{-7} g f_c f^{-4} \Delta t \cdot \max\{u_*, g f^*_{PM}/f\} \quad (3)$$

where $f^*_{PM} = 5.6 \cdot 10^{-3}$ is the dimensionless PM peak frequency, $f_c$ is the highest prognostic frequency and $\Delta t$ is the time step.

This new limiter has been implemented in MIKE 21 OSW 3G and is used throughout this paper.

## 3. DESCRIPTION OF MEASUREMENTS

The data used in this paper are a selected subset of measured data obtained from the RASEX (Risø Air Sea EXperiment) study at Vindeby,

Denmark, and from buoy measurements in the Great Belt, Denmark. A detailed field campaign has been initiated recently at Rødsand near Gedser, Denmark, in Fehmer Belt between Germany and Denmark. Measured data from this site will be available in 1997/98 and presented in near future.

### 3.1 RASEX Experiment

Figure 1 shows the RASEX site at Vindeby. The measurements took place at an offshore wind-turbine site during a spring and a fall campaign in 1994. One of the main objectives of the RASEX experiment is to investigate the exchange of momentum at the air-sea interface. Compared with other similar experiments, RASEX site is characterised by being located in relatively shallow waters (3-4 m water depths at the site) in an area where the waves are predominantly fetch-restricted (maximum fetch of about 20 km).

The experiment comprises two 48-m offshore towers (SMW and SMS in Figure 1) and one land mast (LM). In this paper, we use the mean wind speed measured at the lowest cup anemometer at 7 m above MSL from the offshore tower SMW. The estimated accuracy is about two per cent.

The wind friction velocity was derived from the lowest sonic anemometer (Solent, 3-component research type) mounted on SMW at 3 m above MSL. Data were logged as 30 minutes time series with a sampling frequency of 20 Hz. The estimated accuracy of the wind friction velocity is about ten per cent.

An acoustic wave recorder (AWR) was placed on the sea bottom about 30 m WNW from the SMW tower, measuring the surface elevation with a sampling frequency of 8 Hz. Spectral analyses were performed on 30-minute time series with a cut-off frequency of 2 Hz. Based on the frequency spectrum, characteristic integral measures were obtained. These are: significant wave height, $H_{m0}$, peak period, $T_p$, and mean wave periods, $T_{01}$ and $T_{02}$.

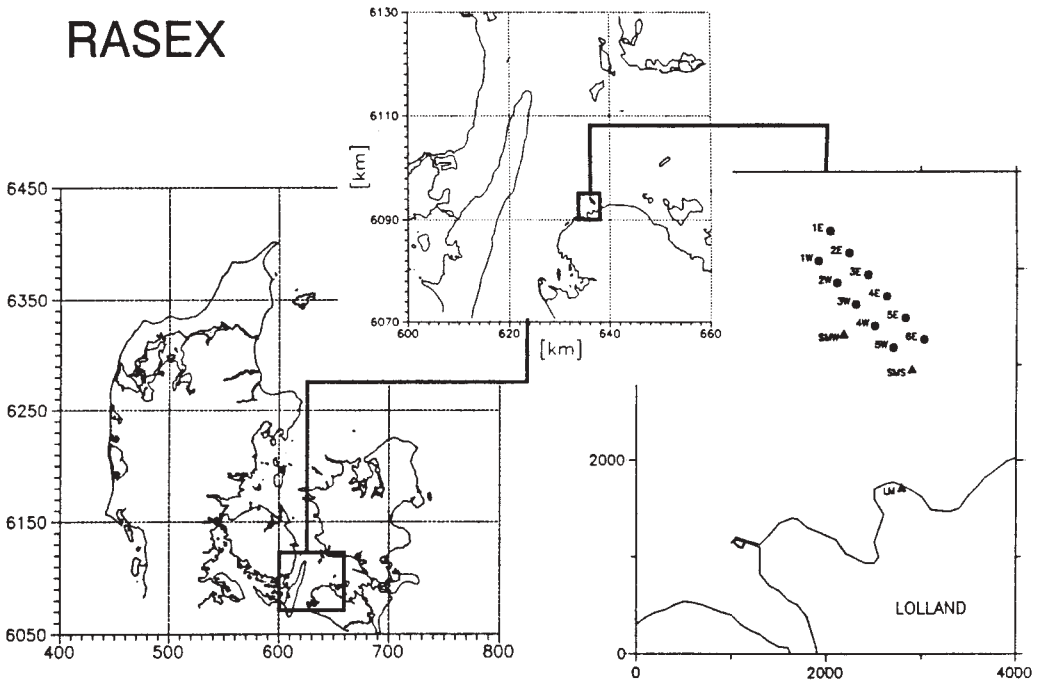


**Figure 1** RASEX site at Vindeby. From left to right: Denmark, Langeland/Lolland and close-up of site. The filled circles are wind-turbines, the triangles are the two offshore towers and land mast. The data used in this paper were measured at the SMW tower situated west of the wind-turbines. Distances on the two leftmost figures are in km, on the close-up in meters.

### 3.2 Wave and Wind Measurements in the Great Belt

In connection with the construction of the Great Belt Link, an extensive monitoring system was established in the Great Belt in the spring of 1989. The total system layout is indicated on the monitoring station plan shown in Figure 2. The waves were measured at stations SBF-05 (Sprogø NE) and SBF-07 (Vesterrenden) using Datawell Waverider buoys. The buoys were placed at 30 m and 20 m water depth, respectively. Time series of surface elevation was measured continuously for 20 minutes every three hours with a logging frequency of 2.56 Hz. The Waverider measurements were stopped October 1993.

An acoustic wave recorder (AWR) similar to the AWR used at Vindeby was incorporated in the monitoring system during the period from July 1991 to May 1992. Throughout the entire 10-month period, data were logged for 20 minutes every three hours for the calculation of $H_s$ and $T_z$. The sampling frequency was 4 Hz. The AWR was placed some 350 m from the Waverider buoy at station SBF-07 at approximately 20 m water depth.

Risø National Laboratory carried out the measurements of the mean wind speed and direction at the land station SBF-08 located on the island of Sprogø. The wind speed and directions are measured at level 10 m and 69 m above MSL. Data are recorded continuously and integrated to represent a ten-minute mean wind based on the average of ten one-minute records.

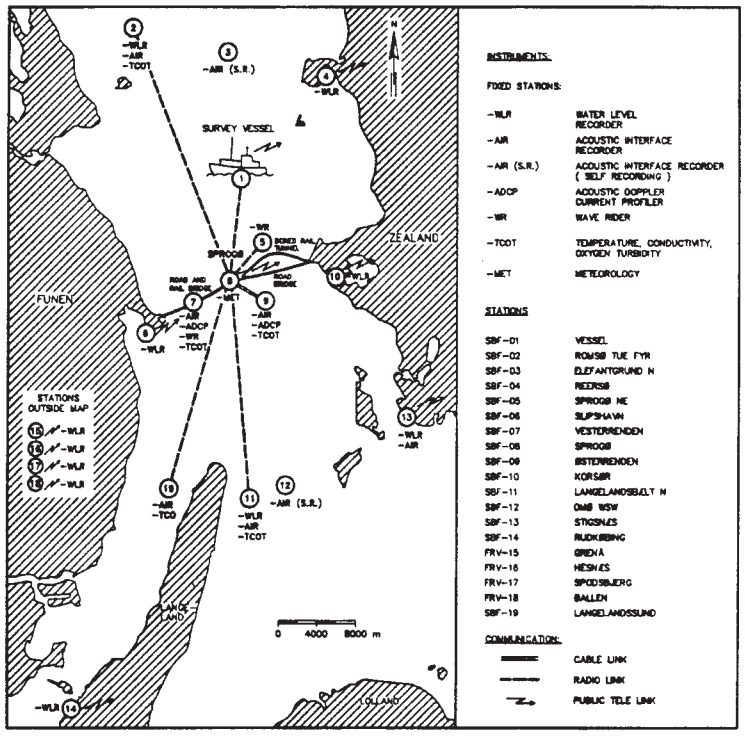


**Figure 2** The Great Belt Monitoring System. The wave data were collected at stations SBF-05 and SBF-07 by a Waverider buoy. The mean wind speed and direction are measured by Risø National Laboratory at station SBF-08 on the island of Sprogø.

## 4. SET-UP OF WIND-WAVE MODEL

The third-generation wind-wave model, MIKE 21 OSW 3G, was set-up for the two coastal areas where the waves are predominantly fetch-limited: Vindeby and Great Belt. Main emphasis will be laid on the Vindeby case where also the wind friction velocity was measured.

### 4.1 Vindeby Model

The digitised bathymetry is depicted in Figure 3, where the origin is at 10°44.4' E and 54°45.0' N. A constant grid spacing of 1000 m is used and the integration time step is 60 s for the propagation part and 30 s for the integration of the source functions. The first order upwind transport scheme has been used in this case. The prognostic part of the spectrum is resolved by 28 discrete logarithmic distributed frequencies ($f_1$= 0.1 Hz and $f_{i+1}$= 1.1$f_i$) and 12 directions ($\Delta\theta$= 30°). The model is initialised using a JONSWAP spectrum (fetch= 2 km, $\gamma$= 1.5 and $\alpha$= 0.018) and a $\cos^2\theta$ directional function.

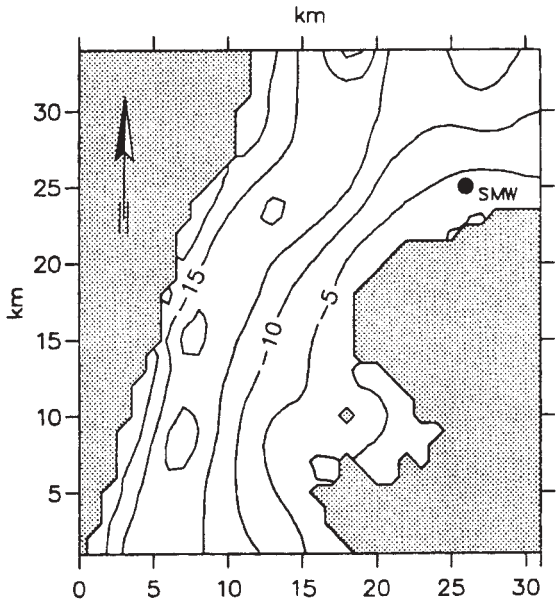


**Figure 3** Bathymetry used for the Vindeby model. The water depth is in meter and relative to MSL.

In this paper, two events were selected from the RASEX data set and compared with the numerical results. The first event is characterised by moderate winds ($U_{10}$~ 10 m/s) and the second event by relatively strong wind ($U_{10}$~ 15 m/s). Figure 5 shows time series of the measured wind. The $U_{10}$ wind was obtained from the measured $U_7$ wind using the 1/7 power law. The direction was not changed.

### 4.2 Great Belt Model

The model bathymetry is shown in Figure 4, where also the position of the Waverider buoys (SBF-05 and SBF-07) and the meteorological station (SBF-08) is indicated.

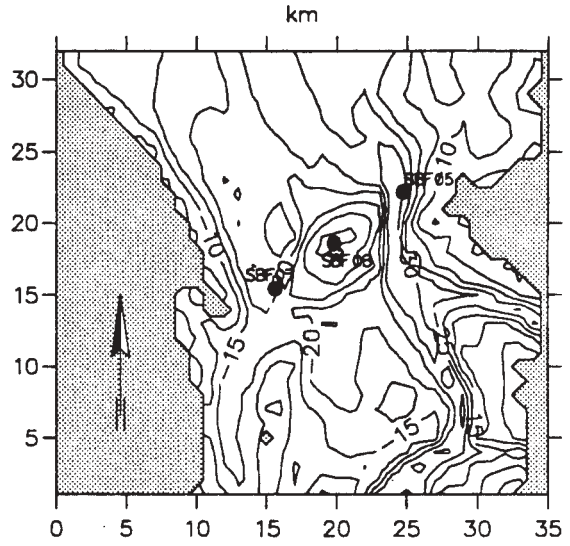


**Figure 4** Bathymetry used for the Great Belt model. The water depth is in meter and relative to MSL.

The origin of the model grid is at 10°38.9' E and 55°10.2' N. As for the Vindeby model, the horizontal resolution is 1000 m. Integration time step is 100 s for the propagation part and 50 s for the source functions. The frequency and directional resolutions as well as the initialisation are similar to those used in the Vindeby model. The semi-Lagrangian scheme has been used to integrate the transport equation.

MIKE 21 OSW 3G is used in this paper to simulate the wave growth in the Great Belt for a single event characterised by relative strong winds ($U_{10}$~ 15 m/s) from WSW. Time series of the measured wind at SBF-08 is shown in Figure 6. Although measurements were made at the 10 m reference level, these measurements are not used as the $U_{10}$ wind is affected by lee

effects from obstacles on Sprogø Island. The $U_{10}$ wind is found by multiplying the $U_{69}$ wind by a factor of 0.85, whereas the wind direction has not been changed.

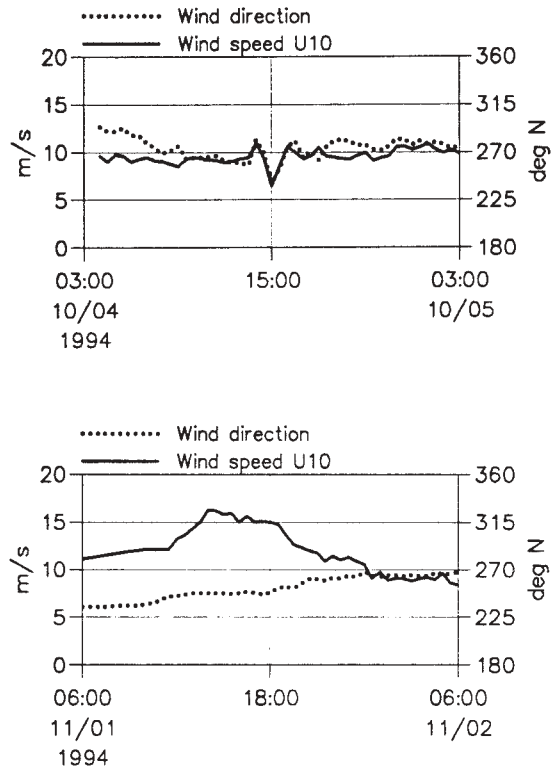


**Figure 5** Measured wind conditions during the two selected periods. From station SMW, Vindeby. Upper panel: event 1, lower panel: event 2.

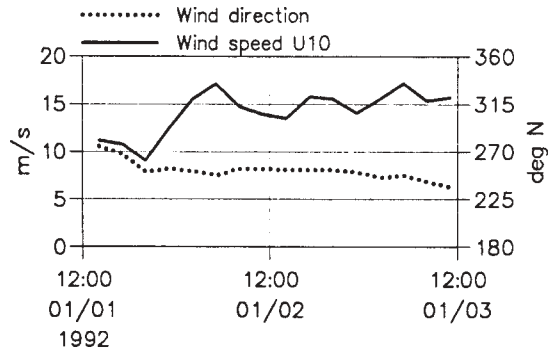


**Figure 6** Measured wind conditions during the selected period. From station SBF-08, Great Belt.

## 5. RESULTS AND DISCUSSION

### 5.1 WAM Source Functions and Measured $U_{10}$ Winds

The computation is performed with the standard WAM Cycle 4 source functions and spatial constant surface winds as shown in Figures 5 and 6, respectively, for the two areas.

*Vindeby*

Figure 7 shows the calculated isoline pattern of the significant wave height, $H_{m0}$, and the peak wave period, $T_p$, at maximum wind speed ($U_{10}$ ~ 16.3 m/s on 1 November 1994 14:30 UTC) during event 2. It is seen that the significant wave height reduces slightly from the open water to the measurement site due to lee effects and shallow water processes.

The performance of the model is shown by a comparison between calculated and measured significant wave height, peak wave period, $T_p$, and wind friction velocity, $u_*$, see Figure 9. The significant wave height and the peak wave period and wind friction velocity are overpredicted using the standard WAM Cycle 4 source functions. For the strong wind event, an overprediction of the wave height of more than 100 per cent is observed, as also found by Johnson et al (1997b) using the WAM model.

*Great Belt*

The calculated wave field is shown in Figure 8 in terms of $H_{m0}$ and $T_p$ at maximum wind speed ($U_{10}$= 17.2 m/s on 2 January 1992 05:00 UTC). The shallow water area around the island of Sprogø seems to have only local influence on the wave field.

In the two panels of Figure 10, the model results at the two stations are presented. For both stations, it can be seen that the significant wave height and mean wave period are overpredicted by the model. This was also found in the Vindeby model for a similar wind speed. In the Great Belt case, we use the second order transport scheme. Comparisons with first order scheme show that the semi-Lagrangian scheme results in only slightly higher $H_{m0}$.

The measured mean wave period at station SBF-07 is in general rather high for an upwind fetch of approximately 5 km and a wind speed

of $U_{10}$~ 15 m/s. Further, the mean period is part of the time even larger than the measured mean period at station SBF-05. The largest wave periods were expected at SBF-05.

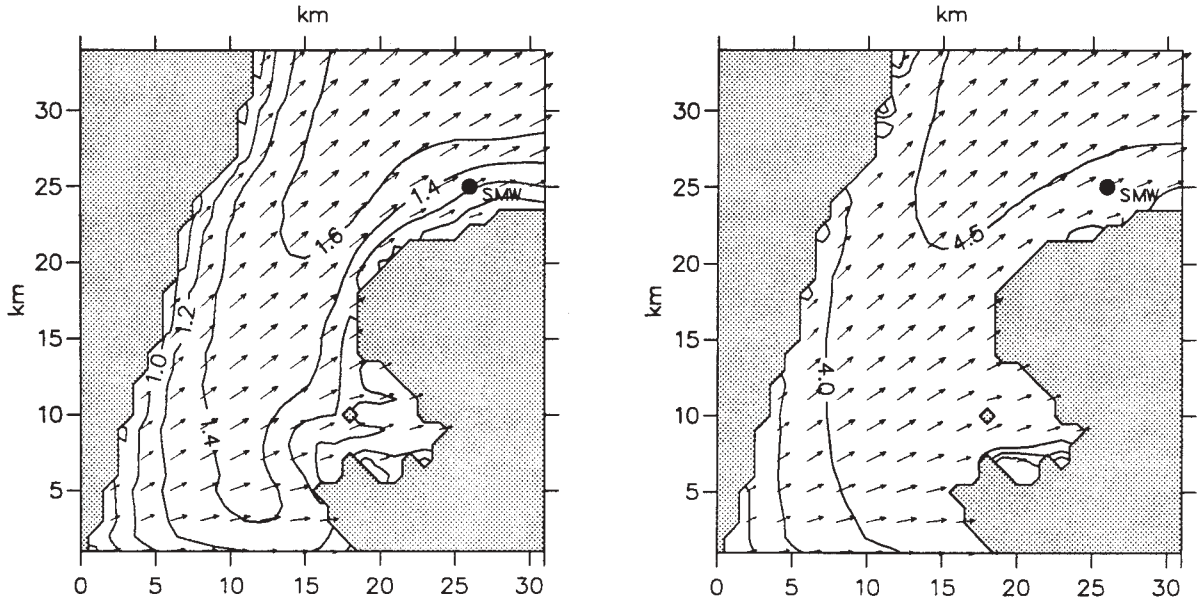


**Figure 7** Calculated significant wave height, $H_{m0}$ (left panel), and peak wave period, $T_p$ (right panel), using WAM Cycle 4 source functions with spatial constant wind. Vindeby, 1 November 1994 14:30 UTC (event 2). The arrows indicate the wave direction scaled with $H_{m0}$.

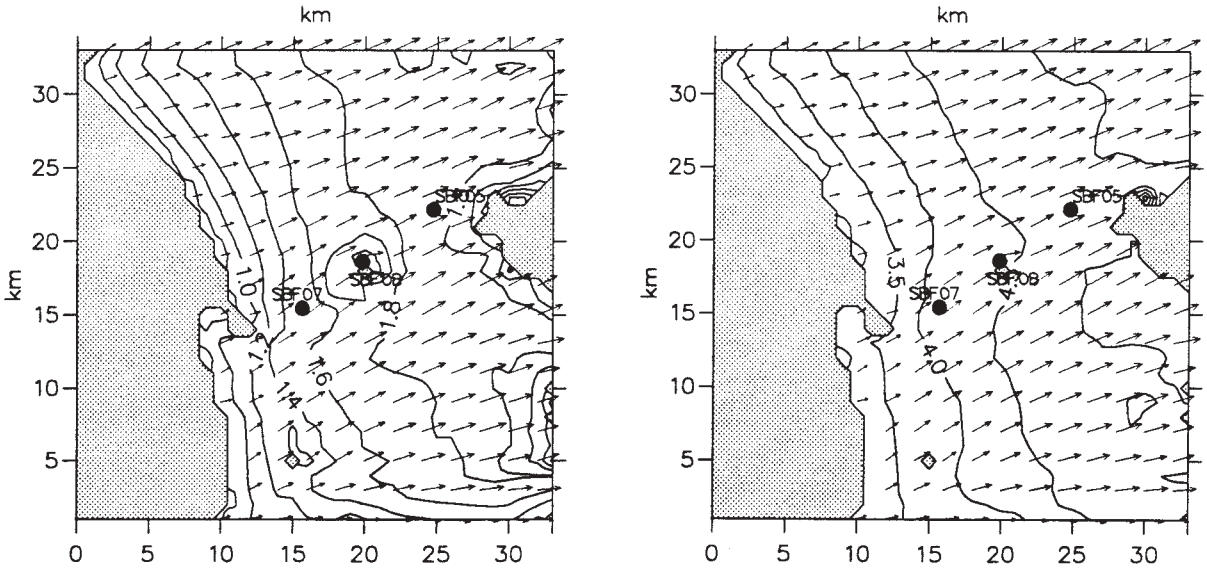


**Figure 8** Calculated significant wave height, $H_{m0}$ (left panel), and peak wave period, $T_p$ (right panel), using WAM Cycle 4 source functions with spatial constant wind. Great Belt, 2 January 1992 05:00 UTC. The arrows indicate the wave direction scaled with $H_{m0}$.

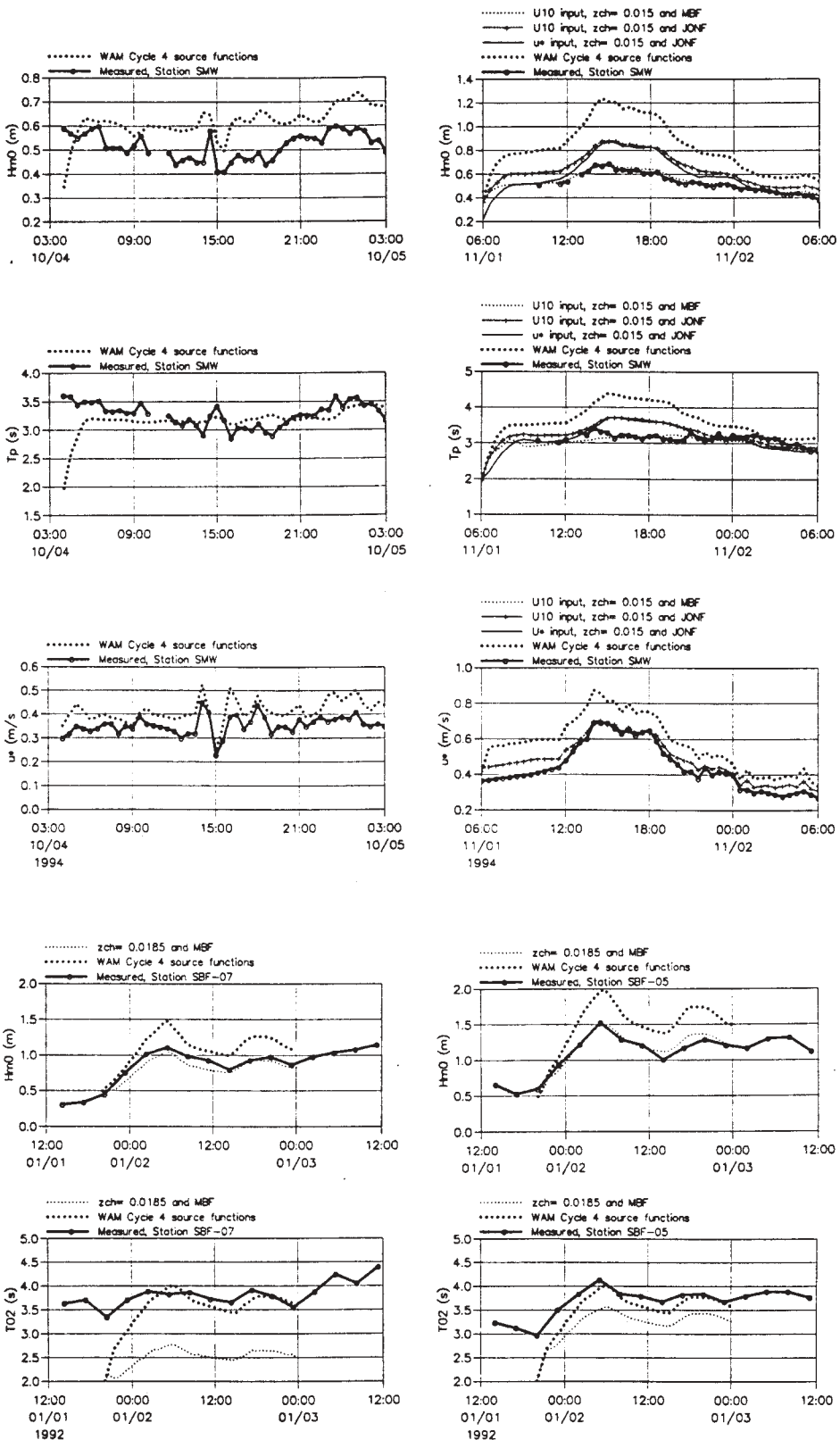


**Figure 9** Vindeby model. Comparison between model results and measured data for event 1 (left) and event 2 (right). Upper panel: significant wave height, $H_{m0}$, middle panel: peak wave period, $T_p$, and lower panel: wind friction velocity, $u_*$.

**Figure 10** Great Belt model. Comparison between model results (significant wave height, $H_{m0}$, and peak wave period, $T_p$) and measured data at the two stations SFB-07 (left) and SFB-05 (right).

A comparison between the Waverider data and AWR data at station SBF-07 made by Weiergang (1992) shows that the Waverider buoy gives slightly lower wave heights and larger wave periods than the AWR. Based on a comprehensive field evaluation of directional wave measurement instruments carried out in the North Sea, Allender et al (1989) made a similar conclusion that the high-frequency waves ($f > 0.3$-$0.4$ Hz for $H_{m0}= 1$-$2$ m) are underestimated by the Waverider having a natural frequency of 0.8 Hz. Thus, the discrepancies between the numerical model results and the measurements may partly be explained by the underestimation of the high-frequency waves by the Waverider. The effect will be largest at station SFB-07 for westerly winds.

### 5.2 WAM Source Functions and Measured $u_*$

The overprediction of the wave height and wave period may be linked to the overprediction of the wind friction velocity used in the wind input source function.

*Vindeby*

In order to investigate the influence of the sea roughness theory on the model results, a simulation for the Vindeby case was performed using the measured wind friction velocity together with a constant Charnock parameter of 0.015 that corresponds to the average measured value during the period (event 2). The comparison between the model results and measured data in Figure 9 shows a significant improvement. Hence, some of the explanation of the overprediction may be found in the calculation of the wind friction velocity using Janssen's theory.

### 5.3 Constant Charnock Parameter

By combining different field data, Johnson et al (1997a) found that there is strong evidence for a wave-age dependent sea roughness and that the Charnock parameter may be estimated using the expression $z_{ch}= 1.89(c_p/u_*)^{-1.59}$. They also concluded that for a relative small range of wave ages, characteristic for small area applications, a constant Charnock parameter may be used in the wind input source function. In order to investigate the effect of using a constant Charnock parameter, a decoupled simulation was performed for the two model areas.

*Vindeby*

For the strong wind event (event 2), the simulation was made using the constant Charnock parameter of 0.015. As seen from Figure 9, the wave height and wave period are very similar to the case where the measured $u_*$ are used to drive the model.

*Great Belt*

A constant Charnock parameter of 0.0185 as suggested by Wu (1980) was used in the simulation. The comparison between model results and measured wave data presented in Figure 10 clearly shows a significant improvement for the wave height at both stations compared to the standard (WAM) coupled results. The mean wave period is underestimated by 10-15 per cent, probably due to the inherent overestimation of the wave period using a Waverider buoy as discussed above.

From the two cases, it can be concluded that Janssen's theory seems to overestimate the sea roughness and thus the wind input in small-scale applications.

### 5.4 Effect of Depth-Induced Breaking

Johnson et al (1997b) have investigated the influence of the depth-induced wave breaking on the calculations of the wave conditions at Vindeby. They concluded that the inclusion of a wave breaking source function leads to a small improvement in the wave height and wave period, but practically no effect on the wind friction velocity. It is expected that the friction velocity is invariant with respect to wave breaking as this process is modelled as a frequency independent process.

### 5.5 Effect of Bottom Friction Dissipation

The investigation into bottom friction dissipation is here carried out using a mobile bed friction (MBF) model with fixed median grain size as described in Section 2.1.

*Vindeby*

Field observations suggest that the bed material consists of fine sand. A mean grain size of $d_{50}=$

0.25 mm is used here. The model was run for the period with the strong wind (event 2) using a constant Charnock parameter of 0.015.

Figure 11 shows a comparison between the calculated bottom dissipation coefficient, $C_{fw}$, and the constant value in the JONSWAP model, 0.0078 m/s. The bottom dissipation coefficient is in average about a factor 3 larger than the empirical JONSWAP value. This is due to the presence of wave-formed ripples enhancing the friction at the bed.

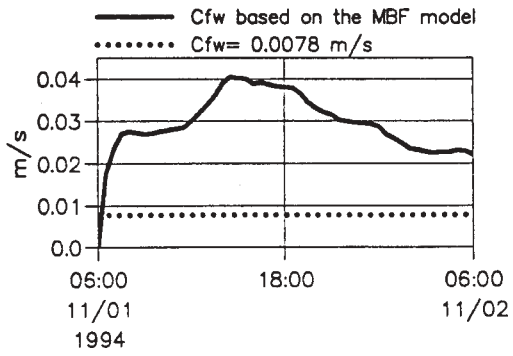


**Figure 11** Time series of the calculated bottom dissipation coefficient, $C_{fw}$, at station SMW, Vindeby, using $U_{10}$ wind and a constant Charnock parameter of 0.015. The constant value $C_{fw}$= 0.0078 m/s typically used in WAM is also indicated.

Figure 9 shows a comparison between the measured waves and prediction using the MBF model. The agreement is quite good. Also the calculated wind friction velocity is in better agreement with measurements.

*Great Belt*

The influence of bottom friction on the wave growth is expected to be small due to the relative large water depths in the Great Belt. However, the shallow water around the island of Sprogø may have an effect on the otherwise deepwater area. The possible influence on the wave field is investigated by using the MBF model with a fixed grain size of $d_{50}$= 0.25 mm.

The results are presented in Figure 12 in terms of a chart showing the difference in significant wave height between a run using the JONSWAP model (JONF), $C_{fw}$= 0.0078 m/s, and a spatial varying $C_{fw}$ obtained by the MBF model. Janssen's theory for the wind input is used here. The effect of bottom friction is seen to be small.

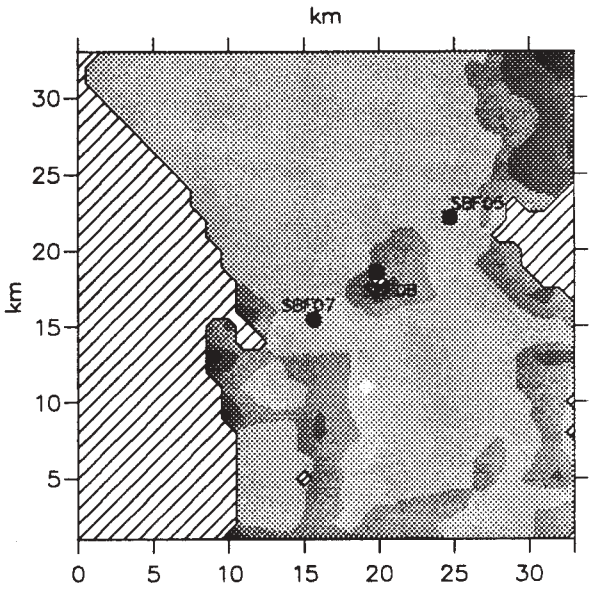


**Figure 12** Contours of the difference between $H_{m0}$ calculated by using the JONF model ($C_{fw}$= 0.0078 m/s) and spatial bottom dissipation coefficient simulated by the MBF model. The computations were made with WAM Cycle 4 source functions. The chart is for 2 January 1992 05:00 UTC, Great Belt. The isolines represent wave height differences (0 to 0.2 m, interval 0.05 m).

### 5.6 Effect of Land/Sea Roughness Changes

For wind-wave modelling in waters with restricted fetches, it is important to take the roughness change from land to sea into account. This is particularly important for small fetches. The influence of the generated internal boundary layer on the wind field can be estimated using the relationship given by Taylor and Lee (1984) as used by eg Young and Verhagen (1996) in Lake George, Australia. Here, we will take a somewhat different engineering approach and use part of the wind resource prediction model WASP (Wind Atlas Analysis and Application Programme), Troen and Petersen (1989).

Originally, this model is not meant to be used for calculating the wind field for a specific

event, but to predict the wind resource of a site from an average wind climate or from long-term measurements. Although the WASP model is used for a different task than intended, comparisons between measured winds and WASP predictions indicate that the approach gives reasonable results with an accuracy of about ten per cent for the mean wind speed of a single wind direction sector.

In this paper, three surface roughness classes have been used; water areas ($z_0$= 0.0002 m), agricultural areas ($z_0$= 0.05 m) and forests and cities ($z_0$= 0.4 m). In principle, the sea state dependent sea roughness obtained from the wave model should be used. A constant value was adopted here for simplicity. No orographic information was used in the calculations.

Based on artificial wind data, so-called scaling maps have been calculated for each of the 12 azimuth sectors. The maps have been used as basis to obtain the wind speed variation in the model area by multiplying the measured time series of $U_{10}$ by the corresponding map. The wind direction is assumed spatial constant and represented by the measured wind direction. An example of a calculated single wind field is shown in Figure 13 for the Great Belt using the time series shown in Figure 6.

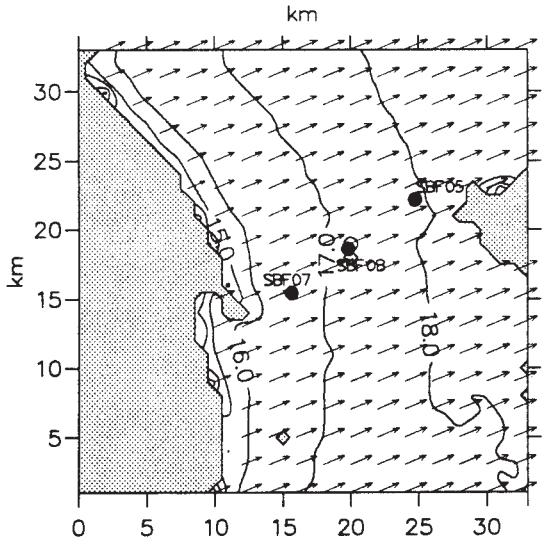


**Figure 13** Example of estimated wind field using the WASP model, Great Belt. The predicted wind field is valid on 2 January 1992 05:05:04 UTC and is based on wind measurements at station SBF-08.

For the WSW wind considered in this case, the WASP model estimates that the land-sea transition results in about ten per cent lower wind speed at station SBF-07. This implies a smaller wave height and wave period at station SBF-07. The effect is negligible at station SBF-05. Figure 14 shows the percentage difference in the significant wave height by using the WASP predicted winds compared by using a spatial constant wind. The roughness change around the island of Sprogø was not considered in the WASP model.

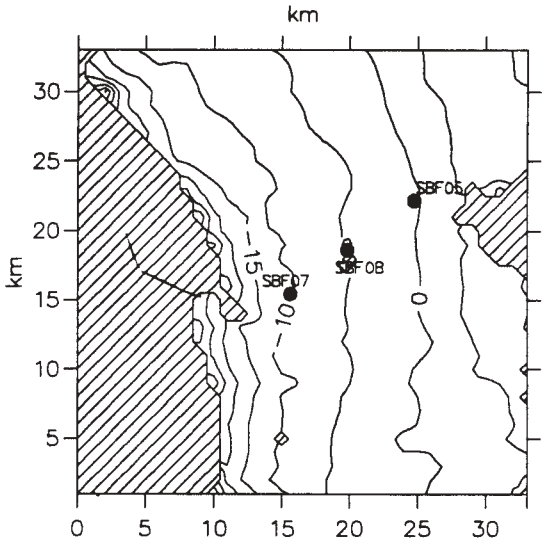


**Figure 14** Percentage difference between $H_{m0}$ calculated by using winds estimated by WASP and a spatial constant wind. The computations were made with WAM Cycle 4 source functions. The chart is for 2 January 1992 05:00 UTC.

### 5.7 Frequency Spectrum and Source Functions

Figure 15 shows a comparison between the calculated and measured frequency spectrum at station SMW, Vindeby. The corresponding source functions are shown in Figure 16. The calculation was made with a constant Charnock parameter of 0.015. The MBF model was used for the calculation of the bottom dissipation. It is seen that the calculated spectrum is in good agreement with the measured spectrum, whereas the standard WAM source functions clearly overestimate the wave energy.

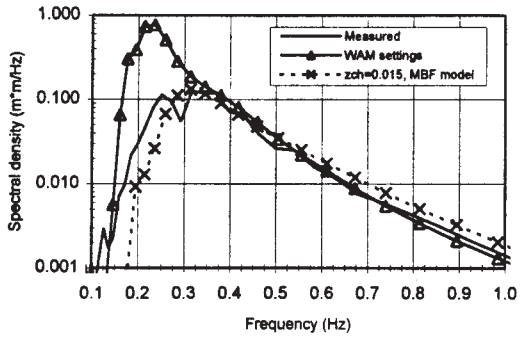


**Figure 15** The simulated and measured frequency spectrum at station SMW, Vindeby. The wind conditions are as shown in Figure 5 (lower panel). The spectrum is for 1 November 1994 15.00 UTC.

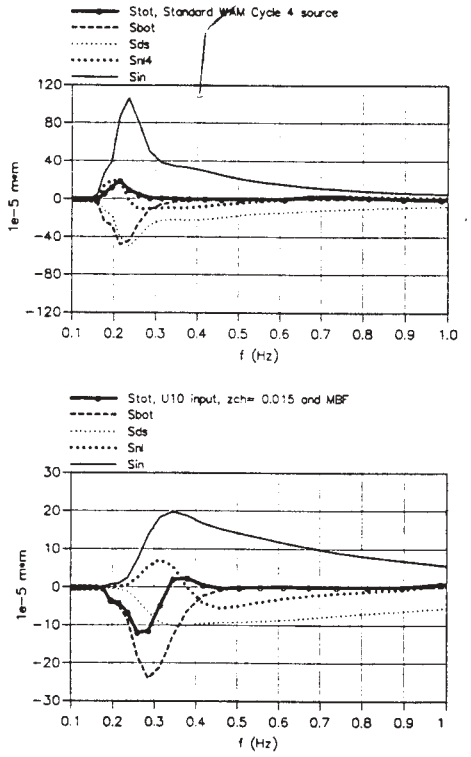


**Figure 16** Directional integrated source functions modelled at station SMW, Vindeby, using the standard WAM source functions (upper panel) and a constant Charnock parameter of 0.015 and the MBF model (lower panel). The sources are for 1 November 1994 15:00 UTC. Note the different scale on the ordinate axis.

From Figure 16, it is seen that the standard WAM source functions result in a net wave growth at SMW (water depth 3.5 m) on the forward face of the spectrum, whereas the sum of the source functions using $z_{ch}$= 0.015 and the MBF model results in a net decay. The WAM source functions imply that the dissipation terms, $S_{bot}$ and $S_{ds}$, almost balance the wind input term, $S_{in}$, around the spectral peak. The case with the large bottom dissipation results in a major sink on the forward face, and the wave growth is retarded at a higher peak frequency.

## 6. CONCLUSIONS

The third-generation wind-wave model, MIKE 21 OSW 3G, has been used to study the problem of wave growth in fetch-restricted coastal and shallow water. This paper considers two fetch-restricted water areas: Vindeby and Great Belt, Denmark. Comparisons between numerical results obtained with MIKE 21 OSW 3G and measured data show that the WAM source functions lead to a significant overprediction of the significant wave height and an underprediction of the peak and mean wave periods for strong winds. Furthermore, Janssen's theory leads to an overprediction of the wind friction velocity as also found by Johnson et al (1997a).

For the Vindeby case, the large overprediction can be eliminated by using the measured wind velocity together with a constant Charnock parameter (0.015) and modelling the bottom friction dissipation assuming a mobile bed with a grain size of $d_{50}$= 0.25 mm. The bottom dissipation coefficient was in average nearly three times higher than the JONSWAP value of 0.0078 m/s used as default in the WAM model. Our results are consistent with the findings of Hersbach (1997) for Lake George, Australia, using the ADWAM model (the adjoint of WAM Cycle 5) for inverse modelling.

Due to the relative large water depths in the Great Belt, the bottom friction dissipation is very small. Thus, wave-bottom interaction processes cannot explain the overprediction of the significant wave height. Quite good agreement was obtained for the significant wave height using a constant Charnock parameter of 0.0185. The mean wave period is underestimated in the Great Belt. Some of the discrepancies between

the model results and measured data may be explained by the fact that the Waverider underestimates the high-frequency waves (f > 0.3-0.4 Hz). Other reasons for the discrepancies may be find in the wind field and/or wave-current interaction.

The influence of land/sea roughness changes was investigated using the wind resource prediction model WASP. For WSW winds in the Great Belt, it was found that $H_{m0}$ is reduced by 10-15 per cent in a 5-km upwind area compared to the results obtained using a spatial constant wind.

## 7. REFERENCES


Allender, J., T. Audson, S.F. Barstow, S. Bjerken, H.E. Krogstad, P. Steinbakke, L. VartDal, L.E. Borgman and C. Graham, 1992: *The Wadic project: A comprehensive field evaluation of directional wave instrumentation*, Ocean Engng, 16, 5/6, 505-536.

Battjes, J.A. and J.P.F.M. Jensen, 1978: *Energy loss and set-up due to breaking of random waves*, Proc. 16th Int. Conf. on Coastal Engrg., ASCE, 569-587.

Benoit, M., F. Marcos and F. Becq, 1996: *Development of a third-generation shallow-water wave model with unstructured spatial meshing.* Proc. 25th Int. Conf. on Coastal Engrg, ASCE, Orlando, 465-487.

Bouws, E. and G.J. Komen, 1983: *On the balance between growth and dissipation in an extreme, depth-limited wind-sea in the southern North Sea.* J. Phys. Oceanogr., 13, 1653-1658.

Collins, J.I., 1972: *Prediction of shallow water spectra.* J. Geophys. Res., 77, 2693-2707.

Eldeberky, Y. and J.A. Battjes, 1996: *Spectral modelling of wave breaking: Application to Boussinesq equations.* J. Geophys. Res., 101, C1, 1253-1264.

Günther, H., S. Hasselmann and P.A.E.M. Janssen, 1992: *Wamodel Cycle 4 (revised version)*, Technical Report No 4, Deutsches Klimarechenzentrum, Hamburg, October, 102 pp.

Hasselmann, K., T.P. Barnett, E. Bouws, H. Carlson, D.E. Cartwright, K. Enke, J.A. Wing, H. Gienapp, D.E. Hasselmann, P. Kruseman, A. Meerburg, P. Müller, D.J. Olbers, K. Ricter, W. Sell and H. Walden, 1973: *Measurements of wind-wave growth and swell decay during the Joint North Sea Wave Project (JONSWAP)*, Dtsch. Hydrogr. Z. Suppl. A (12), 95 pp.

Hasselmann, K., 1974: *On the spectral dissipation of ocean waves due to white capping*, Boundary Layer Meteorol., 6, 107-127.

Hasselmann, K and J.I. Collins, 1968: *Spectral dissipation of finite-depth gravity waves due to turbulent bottom friction.* J. Mar. Res., 26, 1-12.

Hasselmann, S., and K. Hasselmann, 1985a: *Computations and parameterisations of the nonlinear energy transfer in a gravity-wave spectrum, Part 1: A new method for efficient computations of the exact nonlinear transfer integral.* J. Phys. Oceangr., 15, 1369-1377.

Hasselmann, S., K. Hasselmann, J.H. Allender and T.P. Barnett, 1985b: *Computations and parameterisations of the nonlinear energy transfer in a gravity-wave spectrum, Part 2: Parameterisations of the nonlinear energy transfer for applications in wave models.* J. Phys. Oceangr., 15, 1378-1391.

Hersbach, H., 1997: *Application of the adjoint of the WAM model to inverse modelling.* Submitted to J. Geophys. Res.

Hersbach, H. and P.A.E.M. Janssen, 1997: *Improvement of short-fetch behaviour of the WAM model.* Submitted to J. Atmos. and Ocean Tech.

Janssen, P.A.E.M., 1989: *Wave induced stress and the drag of airflow over sea waves.* J. Phys. Oceanogr., 19, 745-754.

Janssen, P.A.E.M., 1991: *Quasi-linear theory of wind-wave generation applied to wave forecasting.* J. Phys. Oceanogr., 21, 1631-1642.

Johnson, H.K., 1997: *MIKE 21 OSW 3G, Technical Documentation.* Danish Hydraulic Institute, February.

Johnson, H.K., J. Højstrup, H.J. Vested and S.E. Larsen, 1997a: *On the dependence of sea surface roughness on wind waves.* Accepted for publication in J. Phys. Oceanogr.

Johnson, H.K., J. Vested, H. Hersback, J. Højstrup and S.E. Larsen, 1997b: *On the cou-*

*pling between wind and waves in the WAM model dependence of sea surface roughness on wind waves*. Submitted to J. Atmos. Ocean Tech.

Johnson, H.K., and H. Kofoed-Hansen, 1997: *The role of bottom friction in shallow water wind-wave modelling*. Manuscript planned to be submitted to J. Phys. Oceanogr.

Jonsson, I.G. and N.A. Carlsen,, 1976: *Experimental and theoretical investigations in an oscillatory rough turbulent boundary layer*. J. Hydraul. Res., 14, 45-60.

Komen, G.J., L. Cavaleri, M. Donelan, K. Hasselmann, S. Hasselman and P.A.E.M Janssen, 1994: *Dynamics and modelling of ocean waves*. Cambridge University Press, 532 pp.

Luo, W. and J. Monbaliu, 1994: *Effects of the bottom friction formulation on the energy balance for gravity waves in shallow water*. J. Geophys. Res., 99, C9, 18501-18511.

Madsen, O.S., Y.-K. Poon and H.C. Graber, 1988: *Spectral wave attenuation by bottom friction: Theory*, Proc. 21st Int. Conf. on Coastal Engrg, ASCE, 492-504.

Nielsen, P., 1979: *Some basic concepts of wave sediment transport*. Institute of Hydrodynamic and Hydraulic Engrg (ISVA), Technical University of Denmark, Series Paper 20.

Ris, R.C., 1997: *Spectral modelling of wind waves in coastal areas*. PhD thesis, Communications on Hydraulic and Geotechnical Engrg, Report No 97-4, June, Faculty of Civil Engrg, Delft University, 160 pp.

Shemdim, P., K. Hasselmann, S.V. Hsiao and K. Herterich, 1978: *Non-linear and linear bottom interaction effects in shallow water*, pp 347-372 in: Turbulent fluxes through the sea surface, wave dynamics and prediction, A. Favre and K. Hasselmann (eds); Plenum, New York, 677 pp.

Swart, D.H., 1976: *Predictive equations regarding coastal transports*, Proc. 15th Int. Conf. on Coastal Engrg, ASCE, 1113-1132.

Taylor, P.A. and R.J. Lee, 1984: *Simple guidelines for estimating wind speed variations due to small-scale topographic features*, Climatol Bull, 18, 3-32.

Tolman, H.L., 1994: *Wind waves and moveable bed bottom friction*, J. Phys. Oceanogr., 24, 994-1009.

Troen, I. and E.L. Petersen, 1989: *European Wind Atlas*, Risø National Laboratory, Denmark, 565-593.

WAMDI group: S. Hasselmann, K. Hasselmann, E. Bauer, P.A.E.M. Janssen, G.J. Komen, L. Bertotti, P. Lionello, A. Guillaume, V.C. Cardone, J.A. Greenwood, M. Restad, L. Zambresky and J.A. Ewing, 1988: *The WAM model – a third-generation ocean wave prediction model*. J. Phys. Oceanogr., 18, 1775-1810.

Weber, S., 1991a: *Bottom friction for wind sea and swell in extreme depth-limited situations*. J. Phys. Oceanogr., 21, 149-172.

Weber, S., 1991b: *Eddy viscosity and drag law models for random ocean wave dissipation*. J. Fluid Mech., 232, 73-98.

Weiergang, J., 1992: *Wave measurements by a single beam acoustic profiling*. European Conference on Underwater Acoustics, Luxembourg, 14-17 Sept., 157-160.

Wu, J., 1980: *Wind stress coefficients over sea near neutral conditions – a revisit*. J. Phys. Oceanogr., 10, 727-740.

Young, I. and L.A. Verhagen, 1996: *The growth of fetch-limited waves in water of finite-depth. Part I and Part II*. Coastal Engrg, 29, 47-99.

## ACKNOWLEDGEMENTS

The research was funded by the Danish Technical Research Council (STVF) and the International Research Centre for Computational Hydrodynamics (ICCH) as part of the project "Wind-wave interaction in coastal and shallow water". Their financial support is greatly appreciated.

ONR (Office of Naval Research and ELKRAFT) sponsored the measurements at Vindeby.

8125-hkh/ybr/psd/paper – 14.11.97

# INTEGRATION OF SOURCE TERMS IN WAM

J.C. Hargreaves & J.D. Annan.

Proudman Oceanographic Laboratory, Birkenhead, Merseyside, United Kingdom

## 1 Introduction

### 1.1 Wave models for shallow water applications

WAM (Komen *et al.*, 1994) was the first wave model which modelled the evolution of the wave spectrum through time, space, frequency and direction without making assumptions on the shape of the frequency spectrum. The model was originally designed to run on the global scale with a spatial resolution of about 100km.

In recent years research effort has been directed towards development of a third generation model for use in areas of shallower water. Some groups have written entire models from scratch specifically designed to work in very small scale areas (eg. SWAN (Ris, 1997)). When the time dependent version of the SWAN model becomes available it should be straightforward to nest this inside a coarser WAM grid.

As far as the physical representation of the wave spectrum is concerned both WAM and SWAN use the same physical description so there is, in principle, no reason why the two models cannot both run on equally small scales. For WAM, the problem is one of CPU time. The model uses an explicit scheme for the propagation of the wave energy and this must comply with the CFL criterion, leading to small timesteps for fine resolution grids. SWAN, with an implicit propagation scheme, does not suffer from this problem, but must be used with care as accurate results will only be obtained if the wave spectrum on the boundary of the grid changes on a larger timescale than the time it takes the energy to propagate across the grid.

Because of this limitation, SWAN will only work accurately on grids of up to about 30km across. So while research is being continued into making SWAN work on larger scales, WAM is being adapted for use on finer scales.

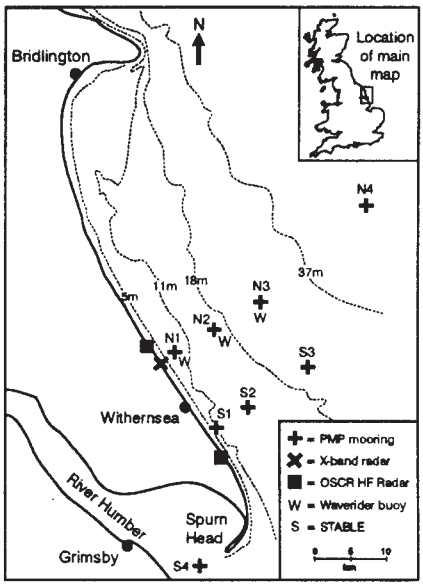


Figure 1: The area of the Holderness experiment, showing waverider and radar deployment sites.

We report here on work completed at the Proudman Oceanographic Laboratory which has been aimed at adapting WAM for use in shallow water areas.

### 1.2 Wave data

Over the winters of 1994/1995 and 1995/1996, wave and sediment measurements were made off the Holderness coast of the UK (Wolf, 1996). The wave measurements consisted of wave buoys, satellite and radar measurements and are shown in Figure 1. It is the wave climate observed during this experiment that we wish to model. Our aim is to use the WAM model with a grid resolution of about 1.2km over this area. Fur-

ther wave modelling research on the region surrounding the OSCR radar which has range up to about 30km offshore is being performed, using SWAN, by Sofia Caires at Sheffield University.

# 2 WAM in Shallow Water

The application of WAM to shallow water areas is limited by several factors. We shall now discuss each of these in turn along with the adaptions that have been incorporated into the POL version of the WAM code. Hereafter the WAM Cycle 4 code is refered to as WAMC4 and the version now implemented at POL is called POLWAM.

## 2.1 Computational efficiency

As mentioned in the previous section, the reason why it is impractical to use WAMC4 to calculate the wave field on fine scale grids is the computational effort involved. The CFL criterion required by the explicit computation of the propagation leads to the model not running much faster than real time for a grid of 79x79 points at 2.4km resolution running on a workstation (100MHz HP-9000). By way of contrast, a 49x52 North Sea grid of 36km resolution can run at the rate of one model day in about one hour. Most of the CPU time (75% ) is, however, spent on the calculation of the source terms rather than the propagation. This part of the integration does not need to be confined by the CFL criterion. In POLWAM, the code has been changed to allow the timestep of the source term calculation to exceed that of the propagation calculation.

This is the most important change to the coding, and has made it practical to run WAM on fine scales. For details see Luo & Sclavo, 1996 and references therein.

The time variables in the WAMC4 code are recorded in minutes rather than seconds, meaning that the timesteps must be an integer number of minutes. Once we get down to scales as fine as 1km we require the propagation to be of the order of one minute. The coding in POLWAM is such that all times are recorded in seconds and so this constraint on the timesteps is relaxed accordingly.

The frequency spectrum that is calculated by WAMC4 covers an order of magnitude in frequency. Since the same timestep is used for all frequencies, it is the lowest frequency waves which limit the timestep. This timestep is an order of magnitude smaller than that required for the highest frequency. Additional computational efficiency and accuracy can be achieved by introducing different timesteps for different frequencies. Work on this has been started in POLWAM by introducing two timesteps, one for the lowest frequency and the other for all the other frequencies.

## 2.2 Propagation Scheme

WAMC4 uses a first order upwind scheme for the propagation of wave action. This scheme is simple and therefore computationally efficient but suffers from high numerical diffusion. This can result in too much energy being lost from the edges of the computational grid. The problem is most aparent when energy is being propagated parallel to the coastline and at 45 degrees to the grid. As a partial solution to this problem POLWAM now incorporates the option of an octant propagation scheme. The specifics are discussed in Sclavo & Luo, 1997 and references therein.

## 2.3 Physics

In her thesis Luo (Luo, 1996) discussed the use of several formulations of the dissipation through bottom friction. Any of the five formaulations she discussed can be implemented as options in POLWAM, as well as two further formulations which include the effect of current on bottom dissipation. A routine to account for energy dissipation due to depth induced breaking is also included in POLWAM.

# 3 Source Term Numerics

With the timestep for propagation independent of that for the source terms in POLWAM (section 2.1) it has become possible to investigate the source term numerics independently of the propagation numerics. As more fully reported in Hargreaves & Annan, 1997, we discovered that while running the model with a small source

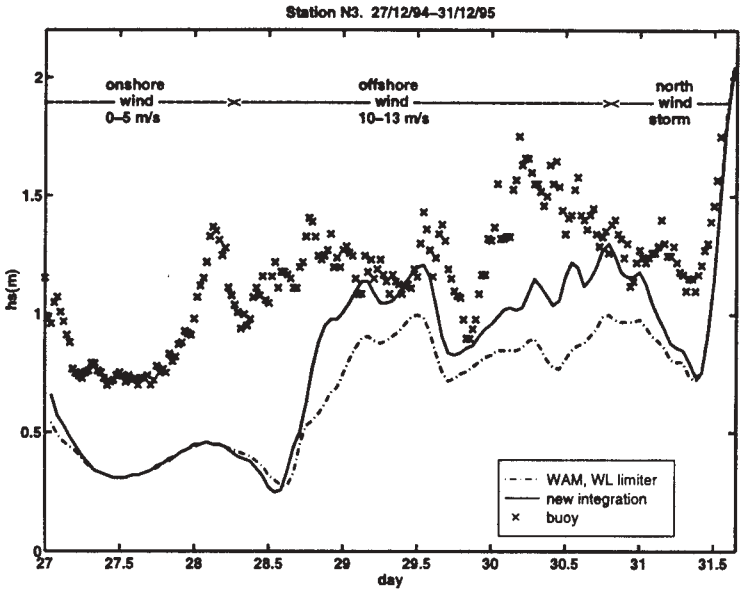


Figure 2: Comparison between WAM with the WL limiter and WAM with the new integration of source terms. Two days through the period the wind changes from light onshore to moderate offshore and the results from the two models diverge. They converge again as the wind becomes northerly with the approach of the storm. The results shown are for the wavebuoy station N3 which was situated at a fetch of 15km

term timestep the model remained stable without the need for the source term limiter that is standard in WAMC4. For larger source term timesteps the limiter, which places a maximum value on the amount that the energy can increase in a timestep, is required for the model to remain stable.

The use of the limiter is undesirable as it imposes a predefined spectral shape, rather than allowing the model to solve the equations.

Further investigation has resulted in the discovery of several inaccuracies in the calculation of the source terms in WAMC4.

## 3.1 Theory

In WAM, the action balance equation is approximately solved by an operator splitting technique. First, the advection of energy is calculated across the grid, and then the source terms are evaluated at each grid point. Here we are only concerned with the pointwise (in space) solution of the evolution equation given by

$$\frac{\partial F}{\partial t} = S \qquad (1)$$

where $F$ is the integrated energy content of the wave spectrum, and $S = S(F)$ is the source term. Equation (1) can be solved with the use of the following finite difference approximation:

$$\frac{F_1 - F_0}{\Delta t} = (1-\alpha)S(F_0) + \alpha S(F_1). \qquad (2)$$

Here $F_0$ is the initial energy level, $F_1 = F_0 + \Delta F$ is the energy level after a finite time interval $\Delta t$ has passed, and $\alpha$ is a parameter which can be chosen in the range $[0, 1]$.

In the WAM code the calculation is performed by setting $\alpha = 0.5$. This leads to the following semi-implicit equation for the change in enegry.

$$\Delta F = \frac{\Delta t \cdot S(F_0)}{1 - 0.5\Delta t \cdot S'(F_0)}. \qquad (3)$$

When $S'(F_0)$ is positive, the explicit formulation is used with $\alpha = 0$. This leads to the following equation for the change in the spectrum.

$$\Delta F = \Delta t \cdot S(F_0). \qquad (4)$$

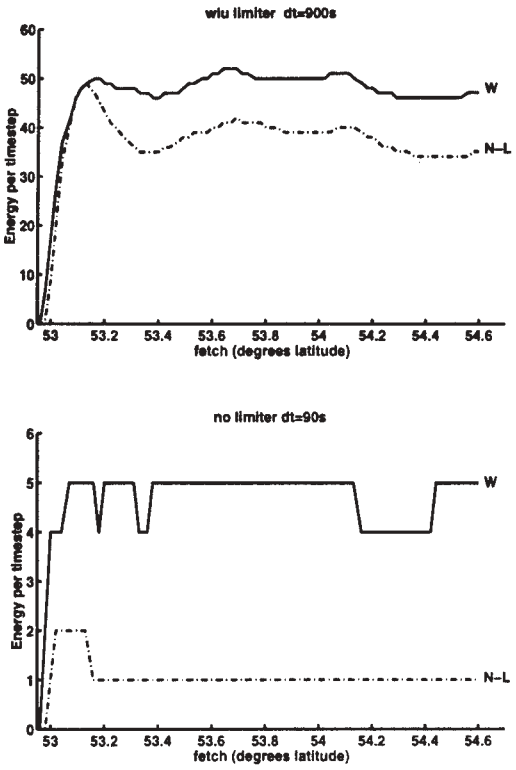


Figure 3: The solid lines show the energy per timestep that comes from the wind input term and the dot-dashed lines show the net input from the non-linear interactions. In the top plot, the input from the two source terms are of a similar size and in order to maintain stability the limiter subtracts almost half the calculated source term at each timestep. The bottom plots shows that for the model run with a 90s timestep, the net energy input from the nonlinear interactions is very small, and the model is stable.

### 3.2 Improvements to the integration sceheme

It was found that the use of an implicit scheme (ie with $\alpha = 1$) for integrating the source terms was more accurate and stable than the semi-implicit scheme. A semi-implicit scheme is inappropriate for long timesteps due to the oscillations which it can generate.

Changing the surface dissipation source term so that it is treated as cubic in energy gives a more accurate representation than the quasi-linear method of WAMC4. This representation additionally has the advantage that the source term integration can more often be integrated implicitly. This is advantageous as the explicit method is more generally prone to instabilities (Press *et al.*, 1994, Chapter16).

Figure 2 shows the importance of these results in a real situation. The diagram shows the difference between POLWAM run with the WL limiter (see Hargreaves & Annan, 1997; equivalent to the Hersbach limiter (Hersbach & Janssen, 1996) in this case) and the model run with our improvements to the integration routines.

### 3.3 Nonlinear interactions

Despite these improvements, a limiter was still required when running the WAM code with a large source term timestep. The model was unstable when the net source term was positive which was while the integration was being performed using the explicit formulation.

An investigation of the energy from each source term was made for runs using different source term timesteps. While the energy input and output to the spectrum from the wind input and dissipation source terms appeared to vary little, there was wide variation in the nonlinear interactions with different timesteps.

The nonlinear interaction source term is a result of resonant frequencies causing energy to move from one part of the frequency-direction spectrum to another. So it is to be expected that at a particular spatial grid point the sum of the energy from the nonlinear source term over the entire spectrum should be zero. We tested the WAM code for this property at different source term timesteps and Figure 3 shows the range of results. For large timesteps the nonlinear interaction calculation is not conservative.

We therefore conclude that it is this part of the calculation which is causing the instability to occur. The physical problem is that the timescale upon which the nonlinear interactions change is faster than the timestep we are trying to use to integrate the source terms.

## 4 Significance

This instability occurs only in high growth situations. The model implementation used in our experiments was a 2.4km resolution 79x79 grid centered on the sea off the Holderness coast. A

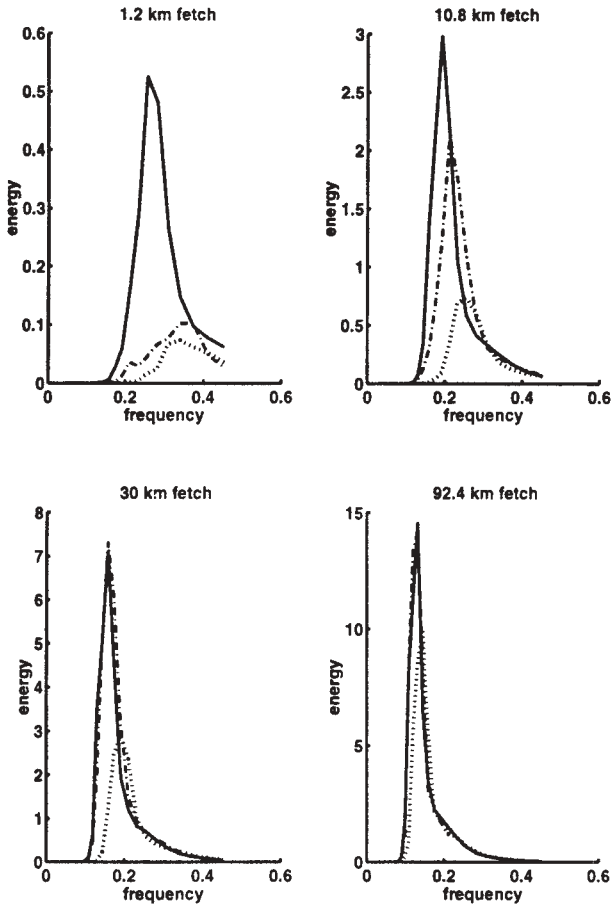


Figure 4: Spectra from fetch limited growth test case. Solid lines are the results from the stable small timestep run. The dot-dashed line is for 900s and the improved integration, and the dotted line shows the results from standard WAM with a 900s timestep.

fetch limited growth was simulated by setting up a $20ms^{-1}$ wind blowing offshore.

Figure 4 shows the spectra produced by this test case for fetches consistent with the positions of the wavebuoys at Holderness. The differences between the spectra produced from the stable small timestep (90s) runs and the runs using the limiter (900s timestep) are large at these small fetches. At fetches of 100km, the distinction between the two test case runs is less apparent. This experiment shows that the inaccuracy produced by using the limiter is important only for fine scale resolution implementations.

# 5 Possible Solutions

The instability is caused by rapid growth and is not a new phenomenum caused by using the model on fine resolutions. The limiter is standard to the WAMC4 code. However the problem is more important at fine resolution because at small fetch, unresolved by global scale models, the inaccuary caused by using the limiter is large.

One solution to this problem would be to resort to using a small source term timestep. A timestep of about 90 seconds would be reasonable for the $20ms^{-1}$ wind on 2.4km resolution test case that was discussed earlier. However, when there are stronger winds an even smaller timestep would be required. As we remarked right at the start of this paper, this approach is infeasible due to the CPU time required.

An alternative approach is to use a smaller timestep only for those places at which the limiter would otherwise be required. A similar scheme is implemented in the model WAVEWATCH (Tolman, 1992). In order for a similar scheme to be implemented in WAM the order of the integration over the spectrum has to be reversed.

Another solution would be to find a way of calculating the nonlinear interaction source term that would avoid the instability. It is hard to see how this would be achieved if we are correct with our suggestion that it is the physical time scale of the variation which is the underlying cause of the instability. At present it is the calculation of the non linear interactions that are the most consuming of CPU time in the program, and research is required into finding

a more efficient and accurate means of calculation.

## 6 Acknowledgements

This work was carried out with funding from the EC MAST programme (SCAWVEX and PROMISE projects) and UK Ministry of Agriculture, Fisheries and Food (CAMELOT project).

## References

J.C. Hargreaves, J.D. Annan, 199r. Integration of source terms in a third generation wave model. *Journal of Geophysical Research.* (submitted).

H. Hersbach, P. Janssen, 1996. Improvement of the short fetch behavious in the WAM model. *Journal of Atmospheric and Oceanographic Technology.* (submitted).

G. J. Komen, L. Cavaleri, M. Donelan, K. Hasselmann, S. Hasselmann, and P. A. E. M. Janssen, 1994. *Dynamics and modelling of ocean waves.* Cambridge University Press.

W. Luo, M. Sclavo 1997. Improvement of the third generation WAM model (cycle 4) for application in nearshore regions *POL Internal Document* No. 116

W. Luo, 1995. Wind wave modelling in shallow water. *Katholieke Universiteit Leuven, PhD Thesis*

W. H. Press, S. A. Teukolsky, W. T. Vetterling, and B. P. Flannery, 1994. *Numerical recipes in Fortran: the art of scientific computing (2nd Ed.).* Cambridge University Press.

R.C. Ris, 1997. Spectral modelling of wind waves in coastal areas. *Communications on Hydraulic and Geotechnical Engineering*, ISSN 0169-6548, Report No. 97-4

M. Sclavo & W. Luo, 1997 On the ungrading of the WAM model advection scheme for application in coastal areas *POL Internal Documents* No. 117

H. K. Tolman, 1992. Effects of numerics on the physics in a third-generation wind-wave model. *Journal of Physical Oceanography*, 22:1095–1111.

WAMDI, 1988. The WAM model — a third generation ocean wave prediction model. *Journal of Physical Oceanography*, 18:1775–1810.

J. Wolf, 1996. The Holderness project wave data. *POL Internal Report 89.*

# COMPARISON OF 4 WAVE PREDICTION MODELS

Carlos Sánchez
Comisión Federal de Electricidad
México 03810, D.F.

Rodolfo Silva
Instituto de Ingeniería, UNAM
México 04510, D.F.

Georges Govaere
Instituto de Ingeniería, UNAM
México 04510, D.F.

Adolfo Contreras
Comisión Federal de Electricidad
México 03810, D.F.

## 1. INTRODUCTION

During hurricane season, from May to November, the coastlines of the Gulf of Mexico and the Pacific Ocean suffer considerable damage in human and material terms due to the occurrence of hurricane winds and waves, and also due to the lack of a reliable real time wave prediction model. The purpose of this paper is to designate a reliable wave prediction model for the specific case of the Gulf of Mexico. The theoretical results of four models, NOAA model I, Hydromet, Fujita model J and Bret model X are compared against actual wave data collected from the period when hurricane Gilbert reached Mexico. These four models were developed for hurricane situations and are frequently used for wave prediction for specific coastal areas. It is of vital importance that the warnings given at times of hurricane alert are as accurate as possible.

## 2. METHODOLOGY

The results obtained from four wave prediction models were compared with actual data from hurricane Gilbert. Two forms of analysis make up the comparison. Firstly, through study of the pressure field of the hurricane (measured by satellite), the typical form of the pressure profiles was determined. These profiles were compared with the theoretical profiles obtained from each model.

Secondly, a comparison was made of available wave registers, made by a NOAA measuring buoy and by satellite over the Gulf of Mexico (hurricane Gilbert, September 1988), against theoretical data obtained from each of the models.

From these two comparisons the theoretical model which best represents the pressure profiles and the wave field generated by a hurricane in the Gulf of Mexico can be determined.

## 3. DESCRIPTION OF MODELS

This section is based on the description given by SPM (1984) and Bretschneider (1990). The latter also offers a good comparison of models available for the prediction of waves generated by tropical storms.

A hurricane model is one in which the pressure profile is the same in all directions of the compass from the centre of the hurricane. The model gives concentric circles of constant pressure, known as isobars. The slope of the profiles gives a pressure gradient using the wind gradient equation. Along with other factors this determines the characteristics of the hurricane force winds and pressure field.

From these profiles, the cyclostrophic profile is calculated from the smoothed profile of the pressure gradient. All the theoretical pressure profiles are adjusted with the pressure profile data: Pr, R and ( max rdp/dr ). Similarly, the profiles are all very similar in the data of pressure profiles of the approximate range of $0.5R < r < 1.5 R$. Then biggest differences are seen in the values of the pressure gradients.

There are basically two groups of models to determine the pressure profile of a hurricane.

There is the Rankin Vortex Modified Model, of Holland, of which the Hydromet model is a special case. Then, in the second group, there is the Bret General Model from which other models are derived: the Bret Model-X, the Fujita Model and that of Jelesnianski.

The mathematical formulae for pressure profiles in both groups is:

$$\frac{P_r - P_0}{P_\infty - P_0} = Ae^{-B(R/r)}$$

$$\frac{P_r - P_0}{P_\infty - P_0} = 1 - \left(1 + a\left(\frac{r}{R}\right)^2\right)^{-b}$$

where

- Po is the pressure in the centre of the hurricane.
- Pr is the pressure at a radial distance r.
- $P_\infty$ is the pressure at an infinite distance.
- R is the radius of maximum cyclostrophic wind.

The following expression $A = B^{-1}$ and $a = b^{-1}$ should be maintained to satisfy the mathematical expression with which the cyclostrophic wind is calculated. In the first equation, presented by Holland, when $A = B^{-1} = 1$ this becomes the original equation of the Rankin Vortex model.

The second equation was proposed by Bretschneider for the analysis of pressure profiles. Here, when $a = b^{-1} = 1$ it becomes the Bret Model X. For $a = b^{-1} = 2$ this becomes the Fujita Model.

The adimensional quantity $N_c = fR/V_{cR} = (0.522R\sin\phi) / K\Delta P_0^{1/2}$ is known as the Rankin Vortex number and is very valuable in determining which of the models fits best to the meteorological phenomenon.

The following values are suggested for the quantities A, B, a and b of the models ( they can be validated or corrected with the analysis of data measurements).

| | |
|---|---|
| $0.00 < N_{cR} < 0.05$ | $A = B^{-1} = 1$ |
| $0.03 < N_{cR} < 0.08$ | $A = B^{-1} = 5/4$ |
| $0.03 < N_{cR} < 0.08$ | $a = b^{-1} = ½$ |
| $0.06 < N_{cR} < 0.15$ | $a = b^{-1} = 1$ |

The numerical bases of the four models follow. These represent adequately the most relevant variables ($P_r$, Rc, $P_{Rc}$ $V_{cR}$ y max r dp/dr, R dp/dr) in a hurricane and are necessary for wave prediction.

The variables and constants of interest which make up these models are:

- Ko Internal constant of the model (valid for all methods)
- C2 Internal constant of the model (varying according to the model, see table 1)
- K1 Theoretical constant depending on the model and the units used for pressures and velocities, varying K1 = 66 - 68 for velocity in knots and pressure in Hg inches and K1 = 11.34 - 11.68 with speed in knots and pressure in millibars. The variation is due to the changes in the air density.
- C1 Theoretical constant, depending on the model chosen, see table 1.
- $V_{cR}$ Maximum velocity of cyclostrophic wind.
- Pn-Po Pressure gradient between the centre of the hurricane and a point sufficiently distant.
- Po Pressure measured at the centre of the hurricane.
- Pr Pressure along a radial distance
- dp/dr Pressure gradients
- $\rho_a$ Air density

The following table shows the relation between coefficients C1 and C2 for each model.

| MODEL | C1 | C2 |
|---|---|---|
| Hydromet HM | 1/e | ---- |
| NOAA Model I | $1/\pi$ | 0.5 |
| Fujita Model J | $2/3\sqrt{3}$ | 0.4226 |
| Bret Model X | 2 | 0.5 |

Table 1. Theoretical constants

These equations are common to all the models

$$K_0 = 19.26 - 18.70$$

$$K_1 = \frac{K_0}{\sqrt{C_1}}$$

$$v_{cR} = k_0\sqrt{\max(rdp/dr)}$$

$$p_N - p_0 = \left(\frac{v_{cR}}{k_1}\right)^2$$

$$p_0 = p_R - c_2(p_N - p_0$$

### 3.1 Hydromet Model HM

The most common equations applied in this model are:

$$p_r = p_0 + (p_N - p_0) * e^{-R_c/r}$$

$$R_c\frac{dp}{dr} = (p_N - p_0)\left(\frac{Rc}{r}\right)^2 e^{-R_c/r}$$

$$r\frac{dp}{dr} = (p_n - p_0)\left(\frac{R_c}{r}\right)e^{-R_c/r}$$

$$V_{cr} = \left(\frac{p_N - p_0}{\rho_a}\frac{R_c}{r}e^{-R_c/r}\right)^{1/2}$$

### 3.2 NOAA Model I

The most common equations applied in this model are:

$$p_r = p_0 + (p_N - p_o)(2/\pi)\tan^{-1}(r/R_c)$$

$$R_c\frac{dp}{dr} = (p_N - p_0)\frac{2/\pi}{1+(r/R_c)^2}$$

$$r\frac{dp}{dr} = (p_N - P_0)\left(\frac{r}{R_c}\right)\frac{2/\pi}{1+(r/R_c)^2}$$

$$V_{cr} = \left(\frac{p_N - p_0}{\rho_a}\frac{(2/\pi)(r/R_c)}{1+(r/R_c)^2}\right)^{1/2}$$

### 3.3 Fujita Model J

The most common equations applied in this model are:

$$p_r = p_0 + \left(1 - \frac{1}{\sqrt{1+2(r/R)^2}}\right)(p_N - p_0)$$

$$R_c\frac{dp}{dr} = (p_N - p_0)\frac{2(r/R_c)}{(1+2(r/R_c)^2)^{3/2}}$$

$$r_c\frac{dp}{dr} = (p_N - p_0)\left(\frac{r}{R_c}\right)^2\frac{2(r/R_c)}{(1+2(r/R_c)^2)^{3/2}}$$

$$V_{cr} = \left(\frac{p_N - p_0}{\rho_a}\frac{0.87738*(r/R_c)}{(1+2*(r/R_c)^2)^{3/4}}\right)^{1/2}$$

### 3.3 Bret Model X

The most common equations applied in this model are:

$$p_r = p_0 + \left(\frac{(r/R_c)^2}{1+(r/R_c)^2}\right)(p_N - p_0)$$

$$R_c\frac{dp}{dr} = (p_N - p_0)\frac{2(r/R_c)^2}{(1+2(r/R_c)^2)^2}$$

$$r_c \frac{dp}{dr} = (p_N - p_0) \frac{2(r/R_c)^2}{(1+2(r/R_c)^2)^2}$$

$$V_{cr} = \left( \frac{p_N - p_0}{\rho_a} \frac{(r/R_c)}{1+2*(r/R_c)^2} \right)^{1/2}$$

In figures (1) and (2) the differences are shown for the four models regarding pressure profile gradient and the rdp/dr, which is a combination of pressure gradient (proportional to the wind) and the radius of the centre of the hurricane. It can be seen that the most important differences are for values of r/R less than 3.

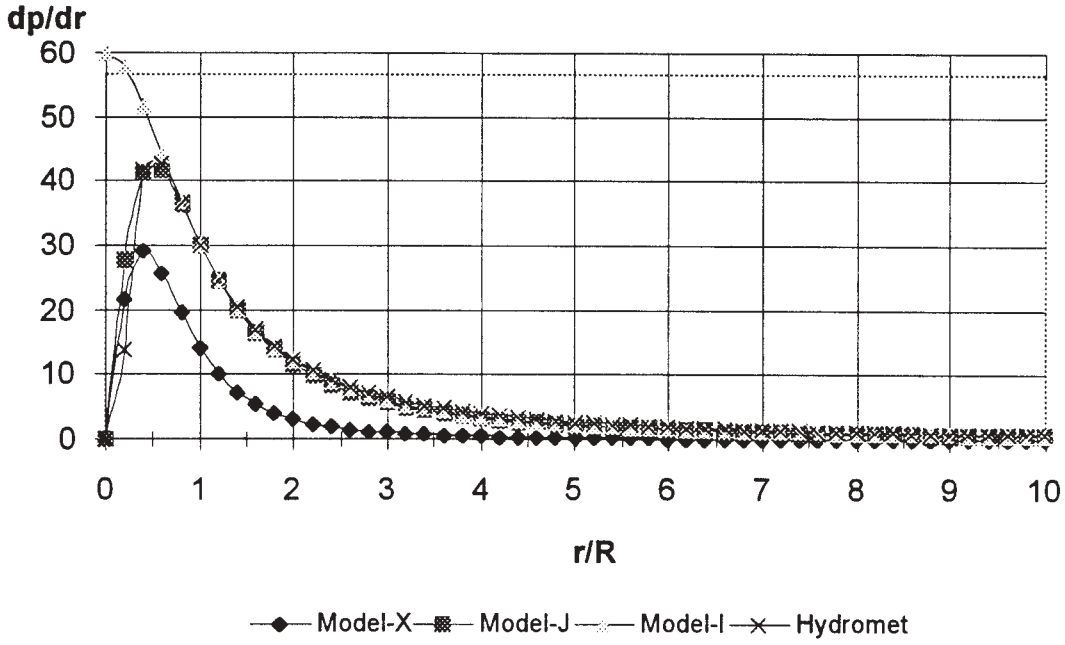


Figure 1. Results of (dp/dr) vs. (r/R) obtained from the four models

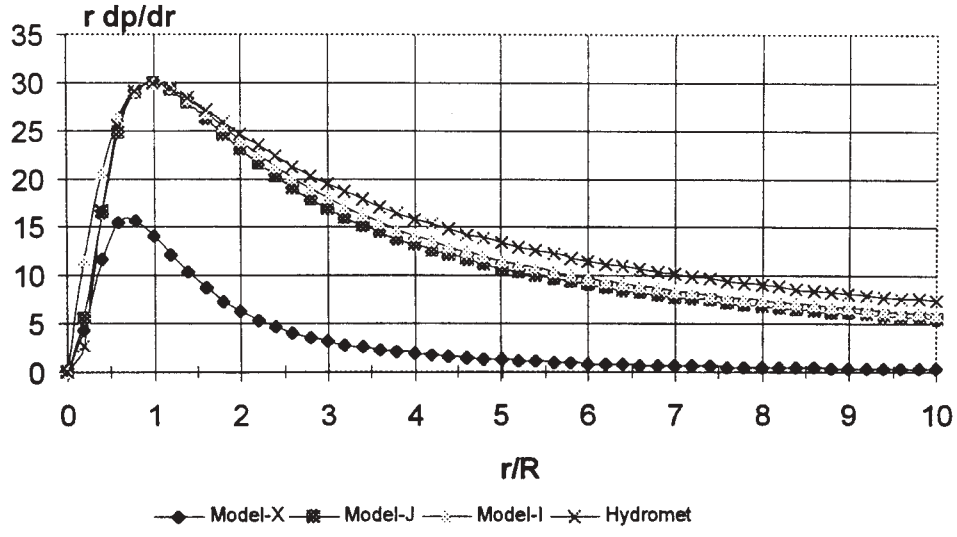


Figure 2. Results of r dp/dr vs. r/R obtained from the four models

## 4. HURRICANE GILBERT

Every year, between May and November at least twenty three tropical cyclones (tropical storms or hurricanes of varying intensity) approach the Mexican coastline; fourteen along the Pacific coast, nine on the Caribbean and Gulf of Mexico. It is estimated that the annual count of cyclones which actually penetrate inland Mexico is four.

In September 1988 hurricane Gilbert travelled over part of the Atlantic Ocean, Caribbean Sea and the Gulf of Mexico. Registering 888 mb minimum central pressure, Gilbert is the most intense hurricane of the century in the Gulf of Mexico, and caused tremendous damage along the coast.

The sharp pressure gradient brought sustained maximum winds of 296 km/hr with gusts of 319 km/hr at 0.00 GMT on 14 September 1988. As a result of the intensity throughout the length of his path in the Caribbean Sea and Gulf, all the ports in that area experienced heavy seas and were closed. The coastal city of Cancún in Quintana Roo recorded a storm tide of 3.5 m which penetrated up to 300 m inland damaging all structures within this area. Pushing inland, the hurricane caused floods and landslides. In Monterrey Nuevo Leon alone, 200 km from the coast, there were some 310 deaths.

The following table gives data, registered by the National Meteorological Service (NMS), showing location, pressure and sustained wind velocity in the centre of the hurricane Gilbert, as it passed over the Gulf of Mexico.

**Position data for hurricane Gilbert**

| Date (m/d/y) | Time (GMT) | Central Pressure (mb) | Wind (km/h) |
|---|---|---|---|
| 9/12/88 | 12 :00 | 960 | 203.72 |
| 9/12/88 | 18 :00 | 960 | 203.72 |
| 9/13/88 | 00 :00 | 960 | 203.72 |
| 9/13/88 | 06 :00 | 952 | 212.98 |
| 9/13/88 | 12 :00 | 934 | 231.50 |
| 9/13/88 | 18 :00 | 905 | 259.28 |
| 9/14/88 | 00 :00 | 888 | 296.32 |
| 9/14/88 | 06 :00 | 889 | 287.06 |
| 9/14/88 | 12 :00 | 892 | 268.54 |
| 9/14/88 | 18 :00 | 925 | 240.76 |
| 9/15/88 | 00 :00 | 944 | 185.20 |
| 9/15/88 | 06 :00 | 949 | 166.68 |
| 9/15/88 | 12 :00 | 950 | 157.42 |
| 9/15/88 | 18 :00 | 950 | 166.68 |
| 9/16/88 | 00 :00 | 949 | 185.20 |
| 9/16/88 | 06 :00 | 946 | 203.72 |
| 9/16/88 | 12 :00 | 948 | 212.98 |
| 9/16/88 | 18 :00 | 950 | 212.98 |
| 9/17/88 | 00 :00 | 964 | 148.16 |
| 9/17/88 | 06 :00 | 988 | 92.0 |
| 9/17/88 | 12 :00 | 996 | 64.82 |
| 9/17/88 | 18 :00 | 1000 | 55.56 |
| 9/18/88 | 00 :00 | 1002 | 55.56 |

### 4.1 Surface maps

As well as the data supplied by the NMS, surface maps, produced by the National Aerospace Service of Mexico (SENEAM, Servicio Nacional de Espacio Aéreo Mexicano), were analysed to calibrate the wind prediction models. These maps are available for the entire country and give isobars at 10 m ASML intervals and for specific points wind speed and direction. These maps were digitised in order to use them in computer.

The surface map shows the path of hurricane Gilbert, figures 3 and 4, over the Gulf of Mexico. The strong central depression is clearly visible.

### 4.2 Wave data

For the calibration of the model two sets of data were used to analyse waves produced by the hurricane as it crossed the basin of the Gulf.

NOAA buoy 42002, located at 93.5° longitude West, 26.0° latitude North, figure 4, recorded data of particular use in calibrating the model for east side of the cyclone.

Throughout the period of the cyclone wave height and wave period data in different part of

the Gulf was recorded by Geosat satellite. The World Wave Atlas programme, begun in 1982, which supplies wind and wave data via remote sensing. Figure 5 shows the path of hurricane with reference to buoy and satellite track.

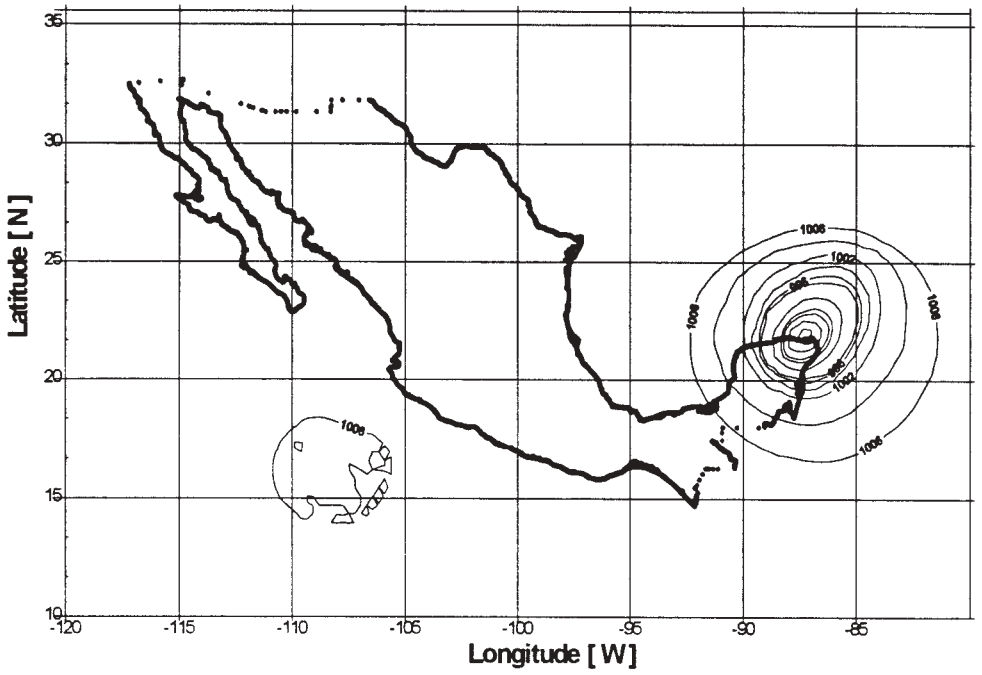


Figure 3 Surface map showing hurricane Gilbert, 14 September 00 :00 GMT

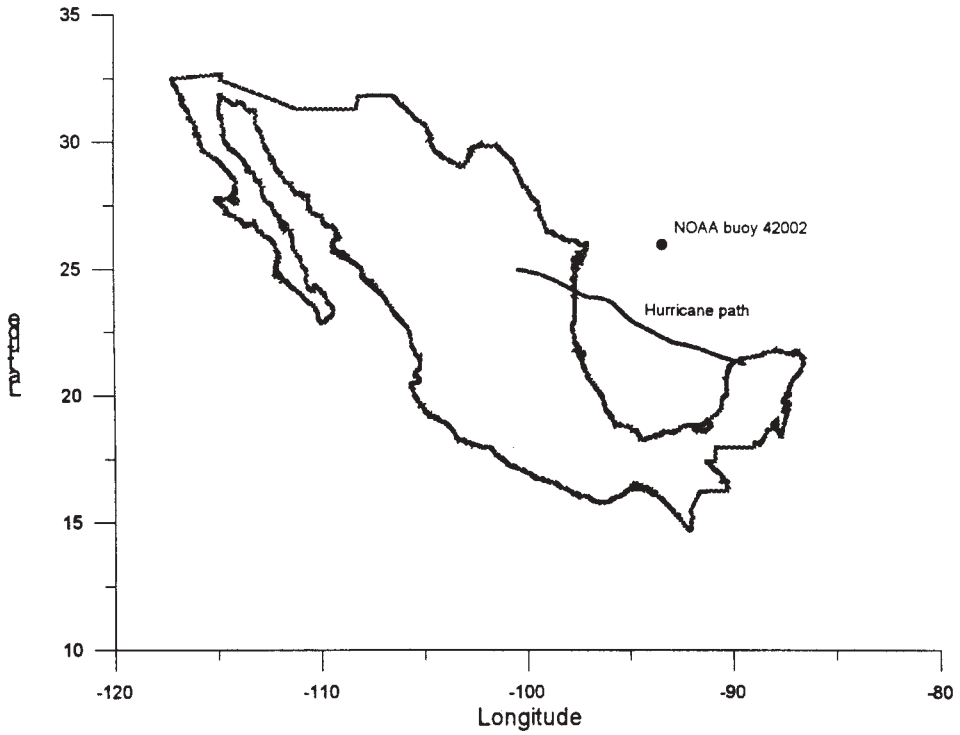


Figure 4. Location of NOAA Buoy 42002 and path of the eye of hurricane Gilbert.

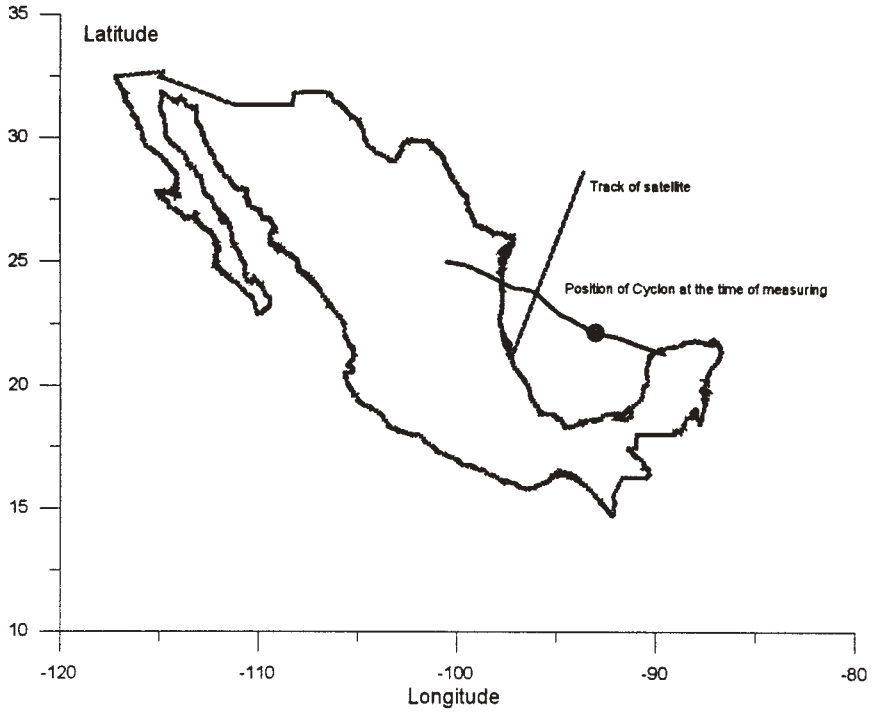


Figure 5. Position of cyclone as the satellite took measurements of wave characteristics. The satellite path follows a NNE direction.

## 5. COMPARISON OF RESULTS

In order to produce the pressure profile of a hurricane the corresponding isobars are traced onto the relevant surface maps with the relative distances of each isobar from the centre of the hurricane. The averaged pressure profile is built up by tracing eight concentric sections (from the centre of hurricane), figure 6, so that they cross the isobars. Next, the mean of the distances obtained is calculated giving pairs of values (pressure, distance), figure 7.

Thus the mean pressure profile of the hurricane is obtained with the basic data of the hurricane (pressure in the eye, radius of the maximum cyclostrophic wind). Theoretical profiles were built up for each of the four models studied.

Figure 8 shows the comparison of theoretical and measured results for the pressure at distances from the centre of the hurricane at one specific point in time. It can be seen that the Hydromet model offers the best fit. However it is important to note that close to the eye of the hurricane there are no pressure measurements.

For wave prediction two comparisons were made. Firstly the data from the NOAA buoy was used, figure 9, followed by satellite data, figure 10. The Hydromet model offered the best fit though once again wave data for the eye of hurricane is not available for comparison.

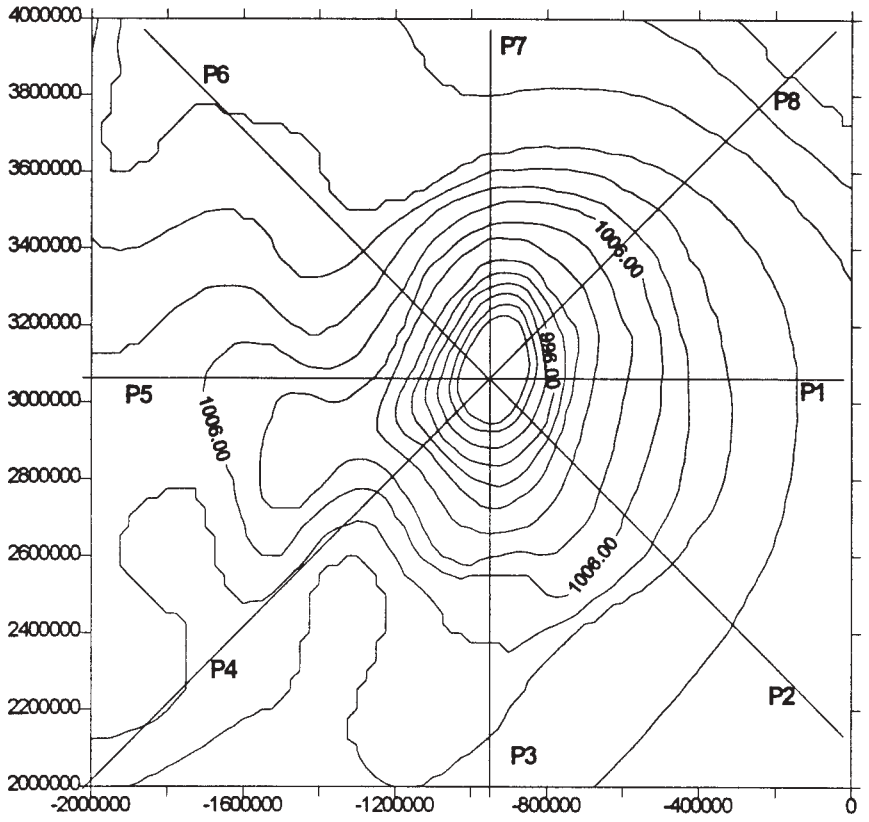


Figure 6. Example of tracing the eight concentric section. Hurricane Gilbert, pressure in mb and distance in meters.

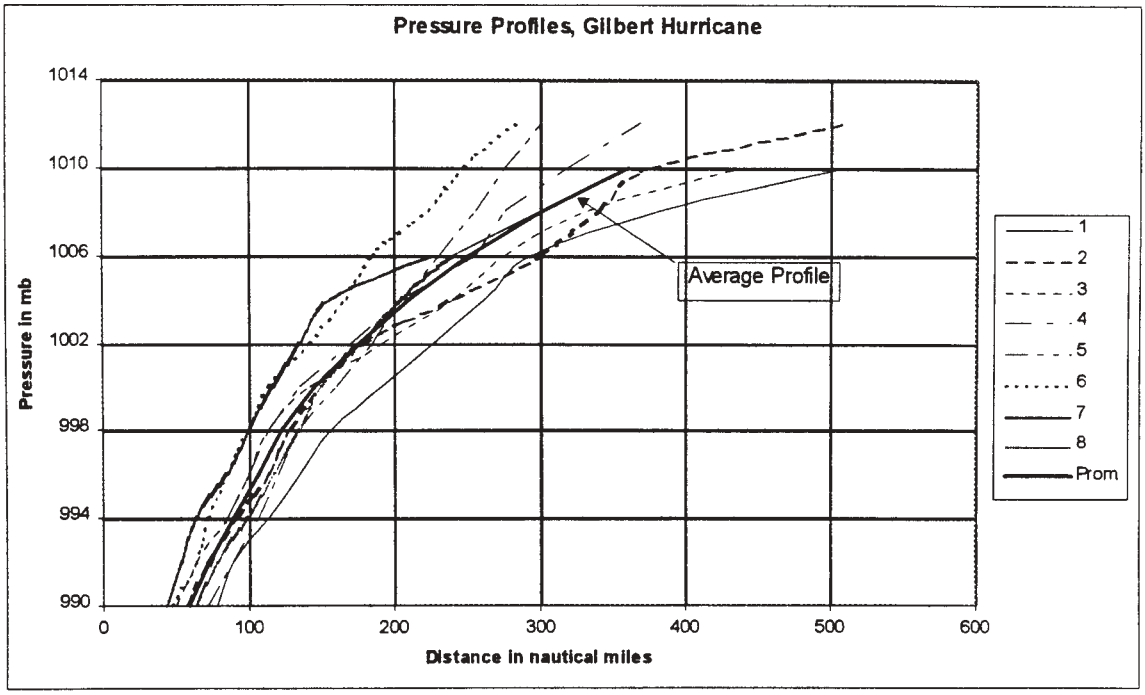


Figure 7. Example of calculation of mean pressure profile

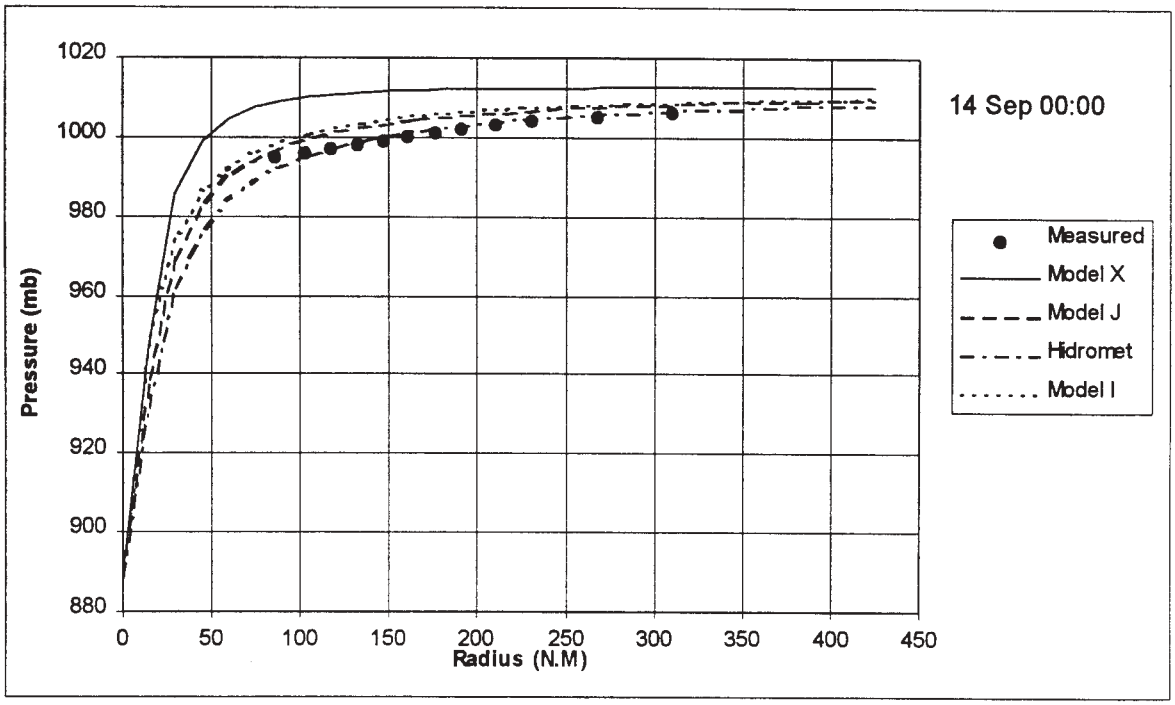


Figure 8. Comparison between theoretical and measured results pressure profiles

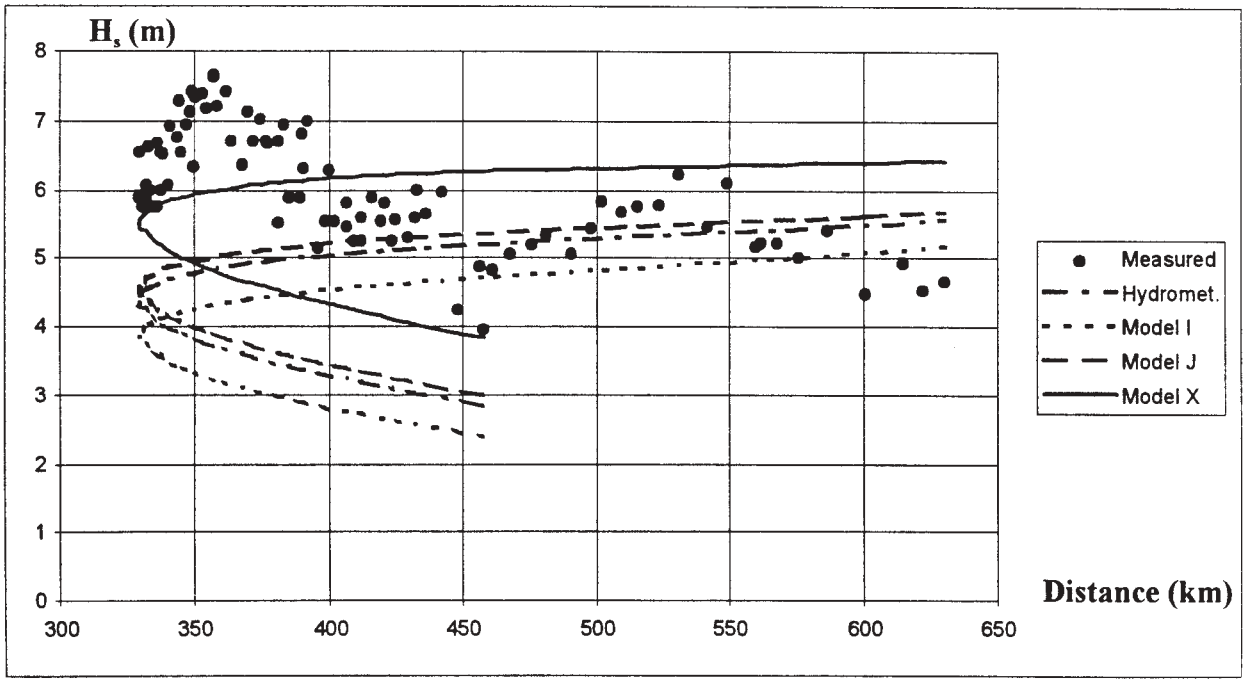


Figure 9. Comparison of theoretical and measured (Geosat) results for significant wave height

In figure 9 there is a very close relation between the data of the buoy (measurements taken every hour as the hurricane crossed the Gulf) and the results of all four models.

Figure 10 gives a comparison of the predicted and actual significant wave heights, as measured by the satellite. There is close approximation even for distances of 500 or 600 km. At around 350 km the real wave heights are subtancially greater than the predictions. This is due to the fact that in this area, south of the satellite track and west of the hurricane, the wave heights are the sum of two sea states: a SEA state, generated by the hurricane that time, and SWELL state, generated in the hours previous to that time, propagated into the zone being measured.

It should be remembered that the models assume that the hurricane is stationary, offering a correction for velocity and direction. If the hurricane moves very quickly it is possible to have these two sea conditions superimposed.

Figure 11 gives maps of significant wave heights for hurricane Gilbert at 00:00 GMT, 16 September. Whilst at first glance the difference between these appears small, in fact the differences are really quite substantial.

In table 3 the values are given for average significant wave heights for radii of 100 and 200 km from the eye of the hurricane. There are differences of up to 30% between the model predicting greatest wave heights (Bret model X) and that predicting the smallest wave heights (NOAA model I).

| Hs (m) | | | | |
|---|---|---|---|---|
| Radius \Method | Hydromet | NOAA Model I | Fujita Model J | Bret Model X |
| 100 km | **10.26** | **9.4** | **10.53** | **12.12** |
| 200 km | **8.83** | **8.04** | **9.08** | **10.54** |

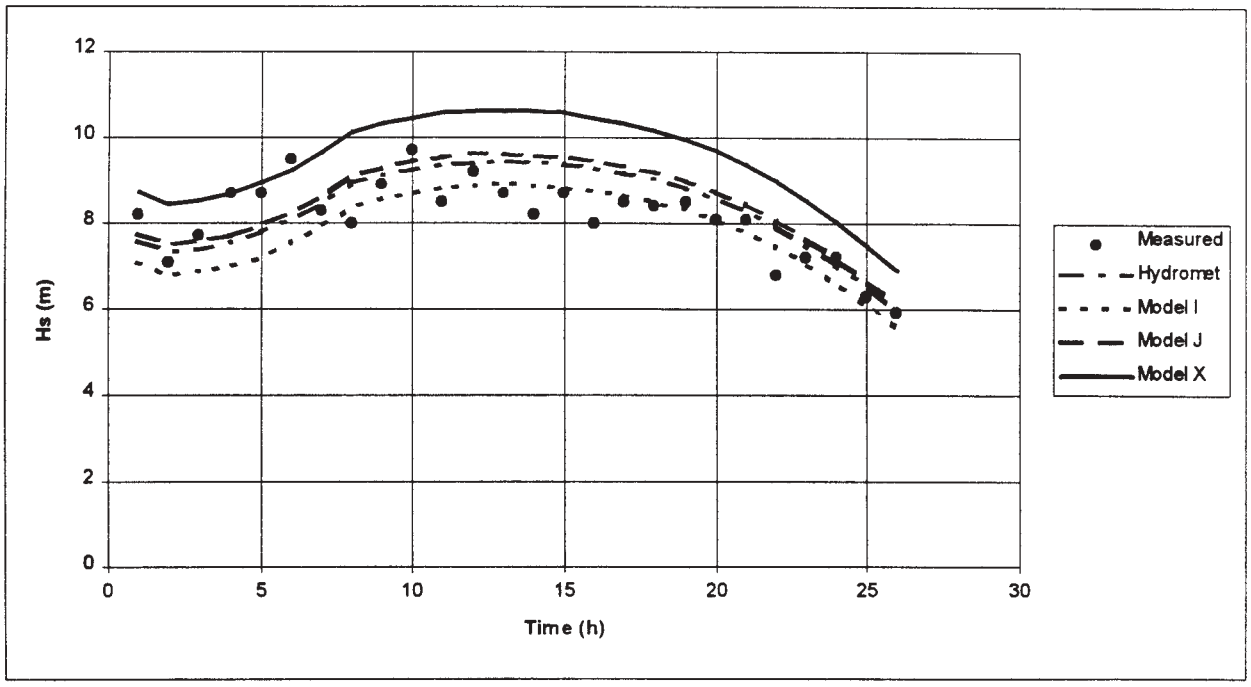


Figure 10 Comparison of measured significant wave height, NOAA Buoy, and theoretical results.

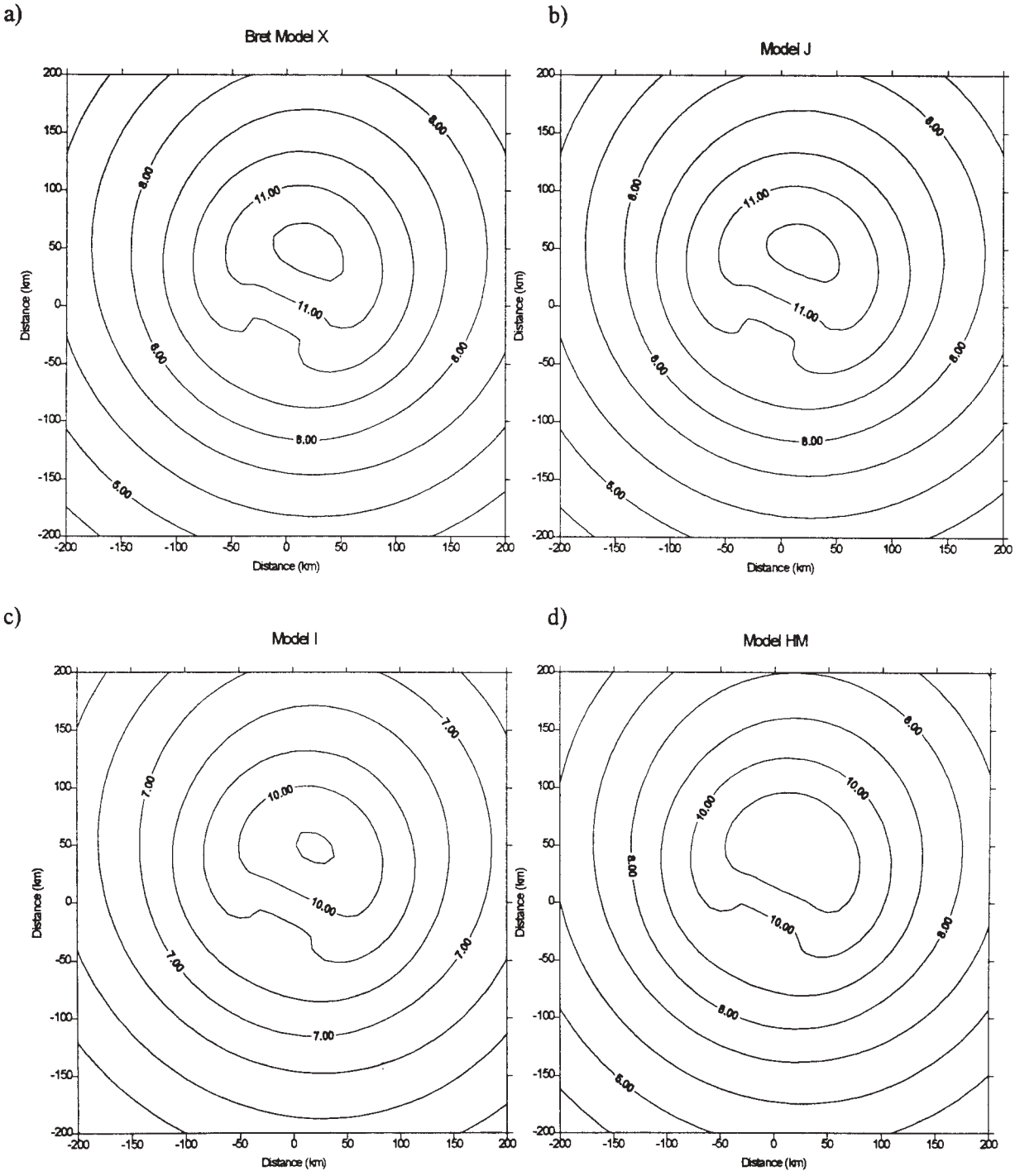


Figure 11. Hurricane Gilbert. Theoretical significant wave height in meters for: a) Bret Model X; b) Fujita Model J; c) NOAA Model I, and; d) Hydromet Model.

## 6. CONCLUSIONS

In general, the main conclusions of this paper are :

1- Normally, we have no pressure data available for the area close to the eye of the hurricane, which is the zone for which the models are most accurate.

2- The comparison of the models is made against data taken at great distance from the eye of the hurricane, beyond the recommended range of their use. Even so, the Hydromet and Fujita model J give very good results.

3- The upper boundary of wave height results was produced by the Bret model X. The lowest heights came from the results of NOAA model I.

4- The application of all four models is very straightforward.

5- The data from Geosat shows variations in wave conditions which cannot be explained by the SEA state. In some points (in the south of the hurricane path) there is clearly a combination of SEA with SWELL.

6- The methods described are valid only for offshore areas of deep water.

ACKNOWLEDGEMENTS

Special thanks are due to the Coastal Oceanographic Branch of the Coastal Engineering Research Center of the U.S. Army for providing the data from buoy 42002, and Secretaria Nacional del Espacio Aereo Mexicano (SENEAM) for providing the pressure maps.

## BIBLIOGRAPHY

Bretchsneider, C. 1990. Tropical cyclones. Gulf Publishing. Handbook on Ocean Engineering, Chapter 6.

Lorente, J.M. 1966. Meteorology. Edit Labor S.A. de C.V., Mexico, pp. 325.

Massel, S. R., 1996. Ocean Surface Waves : Their Physics and Prediction. Advanced Series on Coastal Engineering-Volume 11. World Scientific Publishing Co., N.J. 07661 USA, 222-252.

Shore Protection Manual (SPM), 1984. Coastal Engineering Research Center.

Young, I.R. 1988. Parametric hurricane wave prediction model. Journal of Waterway, Coastal and Ocean Engineering, v. 114 n 5

Wiegel, R. L.,1964. Oceanographical Engineering. Prentice Hall, Inc. Englewood Cliffs, N.J. Fluid Mechanics Series, Richard Skalak Editor.,238-239.

William, D. 1978. Meteorology. Edit Limusa S.A. de C.V., Mexico, pp. 412.

# REAL-TIME WAVE DATA COLLECTION SYSTEM AT SEBASTIAN INLET, FLORIDA

Lee E. Harris, Bartholomeus J. Winder, and Michael C. Perry

Florida Institute of Technology
Melbourne, Florida, USA

Earl F. Childress

Woods Hole Group
Cataumet, Massachusetts, USA

## 1. Introduction

This paper presents the real-time wave, weather and tide data collection system operated by Florida Institute of Technology at the Sebastian Inlet, Florida. Real-time wave, weather and tide data have been collected offshore of Sebastian Inlet since August 1996 (Harris and Perry, 1997). This paper details this oceanographic and meteorological data collection system and presents some of the results.

The purpose of this project, sponsored by the Sebastian Inlet Tax District, is to collect wave, tide and weather data for use in the management of the Sebastian Inlet. Wave, tide, and weather data are necessary for understanding the physical forces occurring at the inlet, and for performing calculations and engineering designs such as computing the longshore transport rate of sand and designing coastal structures. Directional wave data also can be used as input for hydrodynamic and sediment transport numerical models.

The aerial photograph in Figure 1 shows the location of the wave, weather and tide data collection system at the Sebastian Inlet. A weather and tide gage station are located at the seaward end of the north jetty, mounted on the light pole, so that the meteorological conditions occurring over the nearshore ocean waters can be measured. Weather and tide data are measured and recorded by the instruments on the north jetty, and the data are transmitted to a land-based computer in the shed in the State Park by a radio transmitter.

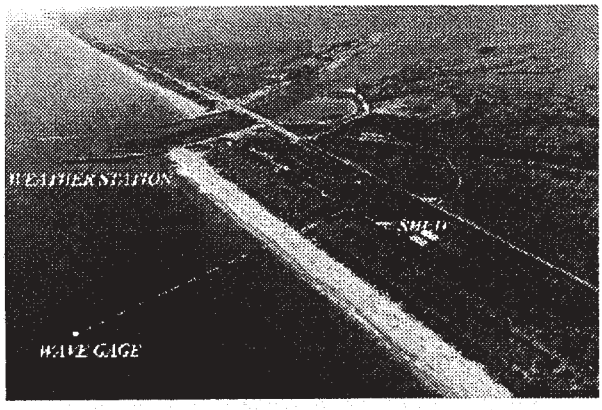


**Figure 1. Aerial photograph of the Sebastian Inlet showing the location of the data collection instruments.**

The wave gage is a submerged PUV directional wave gage, located in the Sebastian Inlet State Recreation Area, approximately 300 meters north of the north jetty, and approximately 300 meters offshore of the beach in a water depth of 8 meters. A 500-meter long double-armored steel cable runs to the shore and to a small shed in the State Park. The cable is used to send power out to the wave gage from shore, and to send wave data directly to shore as it is collected. This allows for continuous data collection and monitoring of the wave gage.

Details of the instrumentation, measurements, data collection and processing, and samples of the data collected by the wave, tide and weather data system are presented in the following sections.

## 2. Instrumentation

This project incorporates state-of-the-art instrumentation for measuring and recording wave, meteorological and tide data. Data are recorded internally in the instruments and transmitted to a shore-based computer to provide real-time data access. The internal recording of the data provides a backup of the data in the event of data transmission loss due to the loss of electricity or telephone service to the shore-based computer (especially during severe storm events).

### *2.1 Wave Measurement*

Two directional SeaPac™ 2100 PUV wave gages (named for the measured parameters of pressure and the two horizontal components u and v of the water particle velocity) manufactured by the Woods Hole Group (1997) are used for measuring, recording and transmitting the wave data. The second gage provides a backup for quick swapping of the gages for servicing, thereby minimizing data loss during wave gage service and maintenance.

The PUV wave gage consists of four sensors: Paroscientific pressure transducer to measure pressure variations due to water level changes (P), Marsh-McBirney electromagnetic (EM) current sensor to measure water particle velocity components (u and v), Paroscientific temperature sensor to measure seawater temperature (T), and KVH Industries digital fluxgate compass to determine wave and current directions. Specifications of the wave gage sensors are shown in Table 1.

**Table 1. SeaPac 2100 Directional PUV Wave Gage Sensor Specifications** (Woods Hole Group, 1997)

| WATER VELOCITY | |
|---|---|
| Sensor | 2-axis Marsh-McBirney EM sphere |
| Range | +/- 300 cm/sec |
| Resolution | 0.15 cm/sec (12-bits) |
| Threshold | 0.15 cm/sec |
| Response | 0.2 sec |
| Error | < 2cm/sec or 2% of signal |
| **DIRECTION** | |
| Sensor | KVH Industries digital fluxgate compass |
| Resolution | +/-0.1 degree |
| Accuracy | +/-0.5 degrees |
| Tilt Range | Operational +/-16 degrees |
| **TEMPERATURE** | |
| Sensor | Paroscientific temperature |
| Range | 0 to 35 degrees Celsius |
| Accuracy | +/-0.1 degree Celsius |
| Resolution | 0.01 degree Celsius |
| **PRESSURE** | |
| Sensor | Paroscientific Digiquartz |
| Range | 100 psi |
| Accuracy | 0.015% FS |
| Resolution | 0.0015% FS (24 bits) |

The wave gage sampling scheme is designed to resolve wave energy in the frequency range of 0.01 to 0.3 Hz (100 to 3 second wave periods). This is done by sampling the pressure field twice per second (2 Hz) for seventeen minutes. The sample burst interval was set to three hours, which is 8 times per day. Processing of the data was done using WavePro™ software, developed by the Woods Hole Group. This software is run in the MATLAB™ environment. A sample of the processed wave gage data is displayed in Table 2.

The high frequency pressure variations with periods from 3 to 100 seconds are used to determine the wave heights and periods, and the lower frequency water level variations (including the tides) are determined from pressure measurements averaged over 3.5-minute intervals. The wave direction is determined from the high frequency variations of the water particle velocity components (u and v) due to the waves. The lower frequency water current velocity components are measured by averaging the measured u and v components of the water particle velocities.

Figure 2 shows a SeaPac 2100 wave gage. Figure 3 shows the underwater wave gage installation at Sebastian Inlet, with the wave gage attached to the stainless-steel piling. The housing and all of the hardware used for the wave gage are stainless-steel, to resist the harsh forces of the marine environment and minimize corrosion, as well as being non-magnetic to avoid interfering with the compass.

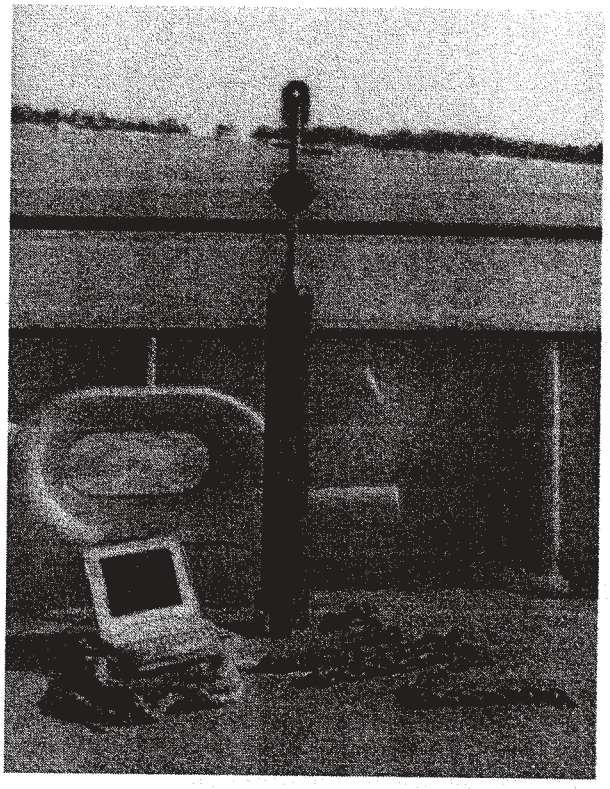

**Figure 2. Photograph of the SeaPac 2100 directional wave gage.**

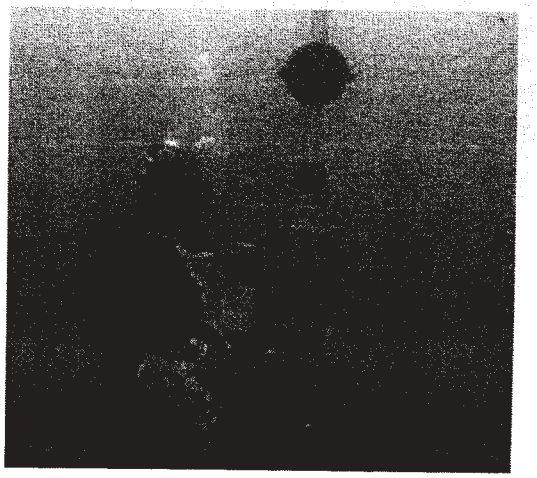

**Figure 3. Underwater photograph of the PUV wave gage.**

Figure 4 shows a diagram of the offshore wave gage installation. The wave gage is inspected and cleaned every two to four months, and swapped out every four to six months. The extra cable on the bottom is necessary so that the gage can be brought to the surface still connected to the cable.

**Table 2. Sebastian Inlet Wave Data**

| Date (M/D/Y) | Time (EST) | Depth (m) | Current (cm/s) | Current Dir. (degrees) | Hs (cm) | $T_p$ (s) | $T_z$ (s) | Wave Dir. (degrees) | Spread (degrees) |
|---|---|---|---|---|---|---|---|---|---|
| 11/07/97 | 00:00 | 8.48 | 18.80 | 163 | 74.8 | 7.1 | 6.4 | 258 | 39 |
| 11/07/97 | 03:00 | 8.33 | 18.01 | 161 | 65.2 | 9.8 | 6.5 | 250 | 32 |
| 11/07/97 | 06:00 | 7.77 | 13.17 | 155 | 69.3 | 8.5 | 6.8 | 252 | 35 |
| 11/07/97 | 09:00 | 7.80 | 13.61 | 163 | 66.6 | 8.5 | 7.4 | 240 | 33 |
| 11/07/97 | 12:00 | 8.52 | 14.34 | 167 | 72.6 | 8.5 | 8.2 | 248 | 40 |
| 11/07/97 | 15:00 | 8.54 | 15.11 | 173 | 61.5 | 8.5 | 8.3 | 254 | 33 |
| 11/07/97 | 18:00 | 7.91 | 15.81 | 158 | 60.8 | 9.1 | 8.5 | 250 | 30 |
| 11/07/97 | 21:00 | 7.72 | 14.99 | 162 | 58.6 | 9.8 | 6.6 | 259 | 27 |
| 11/08/97 | 00:00 | 8.31 | 17.92 | 159 | 59.3 | 8.5 | 7.2 | 254 | 35 |
| 11/08/97 | 03:00 | 8.55 | 25.70 | 156 | 74.8 | 10.7 | 6.2 | 258 | 27 |
| 11/08/97 | 06:00 | 7.99 | 21.24 | 149 | 82.7 | 12.8 | 6.3 | 262 | 17 |
| 11/08/97 | 09:00 | 7.73 | 21.23 | 152 | 85.7 | 11.6 | 6.6 | 250 | 19 |
| 11/08/97 | 12:00 | 8.34 | 29.44 | 152 | 86.5 | 11.6 | 7.3 | 256 | 19 |
| 11/08/97 | 15:00 | 8.71 | 31.86 | 157 | 85.5 | 16.0 | 8.2 | 280 | 39 |
| 11/08/97 | 18:00 | 8.24 | 28.25 | 156 | 87.0 | 14.2 | 8.2 | 268 | 31 |
| 11/08/97 | 21:00 | 7.68 | 12.12 | 155 | 66.2 | 11.6 | 7.5 | 259 | 13 |

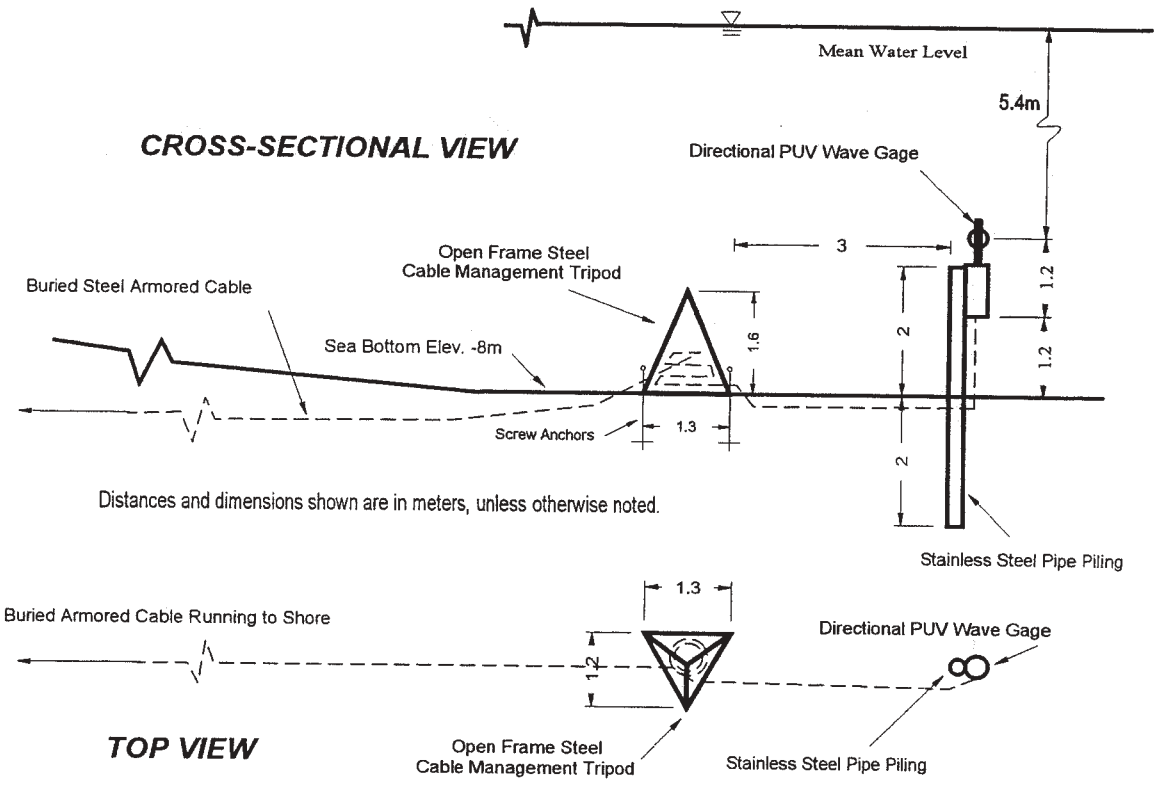


**Figure 4. Underwater bottom-mounted wave gage installation.**

### 2.2 *Meteorological Measurements*

A weather station is located at the seaward end of the north jetty, mounted on the light pole, so that the meteorological conditions occurring over the ocean waters can be measured. Data are recorded on a Vitel data recording system and transmitted to a land-based computer in the shed in the State Park by a radio transmitter. Two batteries with solar charging panels are used to power the equipment at the seaward end of the north jetty, which includes the instruments, data recorder, and radio transmitter, shown in the photograph in Figure 5.

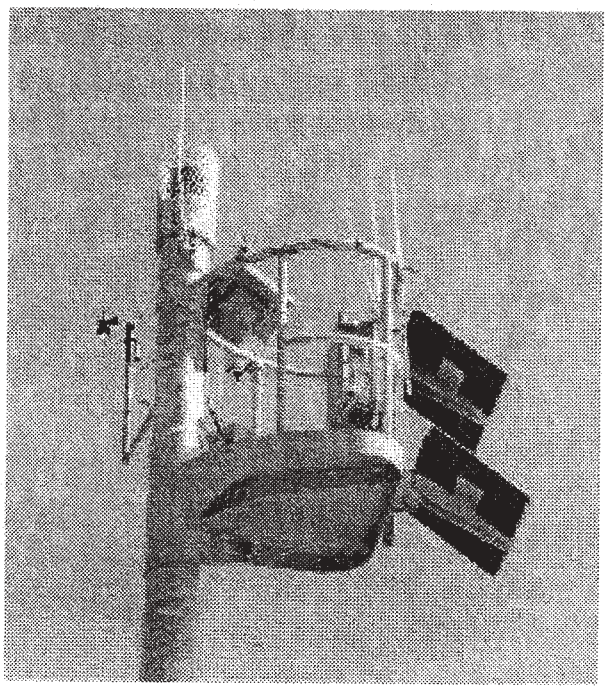

**Figure 5. Sebastian Inlet weather station, including the meteorological sensors, data logging system, radio transmitter, lightening rod, batteries and solar panels.**

A radio transmitter in the shed communicates with the weather system at the end of the north jetty, and is connected to a computer modem to allow for data transmission and control of the weather station from any other computer with a modem. The variables being measured include the wind speed and direction, barometric pressure, air temperature, and water level.

The weather/tide station is made up of 5 different sensors. The wind speed and direction sensor is an R.M. Young Wind Monitor. The monitor detects wind speed from a spinning propeller, with a range of wind speeds of 0 to 60 meters per second (0 to 134 miles per hour), and a maximum error of 1 meter per second ( 2.2 miles per hour). Wind direction is determined from the variance in current passing through a resistor as the whole wind sensor assembly rotates on its base. An R.M. Young analog output electrical barometer is used to measure air pressure, and has a range of 800 to 1100 millibars ( 23.6 to 32.5 inches of mercury). The air temperature is measured with a standard temperature gage. All of the sensors record the data in metric units. The data are stored in a data recorder at the weather station, and are sent by radio to the computer in the shed. The weather station is powered by batteries, which are recharged by 30 watt solar panels.

The data recorder has a capacity of 128 Kb and the data are stored in binary format The raw data files are stored on the PC hard drive, and can also be downloaded from the data recorder.

The sampling of the weather data is set so that accurate representation of changes in weather patterns can be detected, yet not overload the system with data. Sample rates are similar to meteorological standards used by other agencies. The water level is measured at 6-minute intervals, which allows for extremely accurate depiction of the rise and fall of the tide. The wind speed and direction are sampled every 10 seconds, and the average of the samples is logged at 15 minute intervals. Changes in wind direction and speed are therefore quickly noticed. The atmospheric pressure is sampled at 30 second intervals, and averaged every 30 minutes. The air temperature is sampled every 30 minutes.

The data files from the weather station computer are stored in binary format. They are converted into ASCII format using a translation software package. The data are then put into Excel™ spreadsheets and plotted. The plots are used to show trends and provide easily accessible information.

### 2.3 *Water Level Measurements*

An Aquatrak™ acoustic water level sensor is used to determine the water levels (including tides) at the north jetty, with a pressure sensor used as backup. An acoustic signal determines the elevation of the water surface with a resolution of one millimeter, and a maximum rise or fall rate of three meters per second. Water level data are recorded with the meteorological data on the Vitel data recording system and transmitted to the land-based computer in the shed in the State Park by radio transmitter. Differential leveling surveys from benchmarks to the water level gage are performed to ensure gage stability and to allow for long-term sea level changes to be measured.

## 3. Examples of Wave, Weather and Tide Data

Data from the directional wave gage for the month of November 1996 are shown in Figure 6. Water level data (which includes the tides), significant wave heights, peak wave periods, wave direction, and water temperature (which is used to adjust the EM current meter measurements) are determined from the gage measurements.

Data from the weather and tide station at the seaward end of the north jetty are shown in Figure 7, which includes water level from the acoustic sensor, atmospheric pressure, wind speed and direction, and air temperature for April 1997.

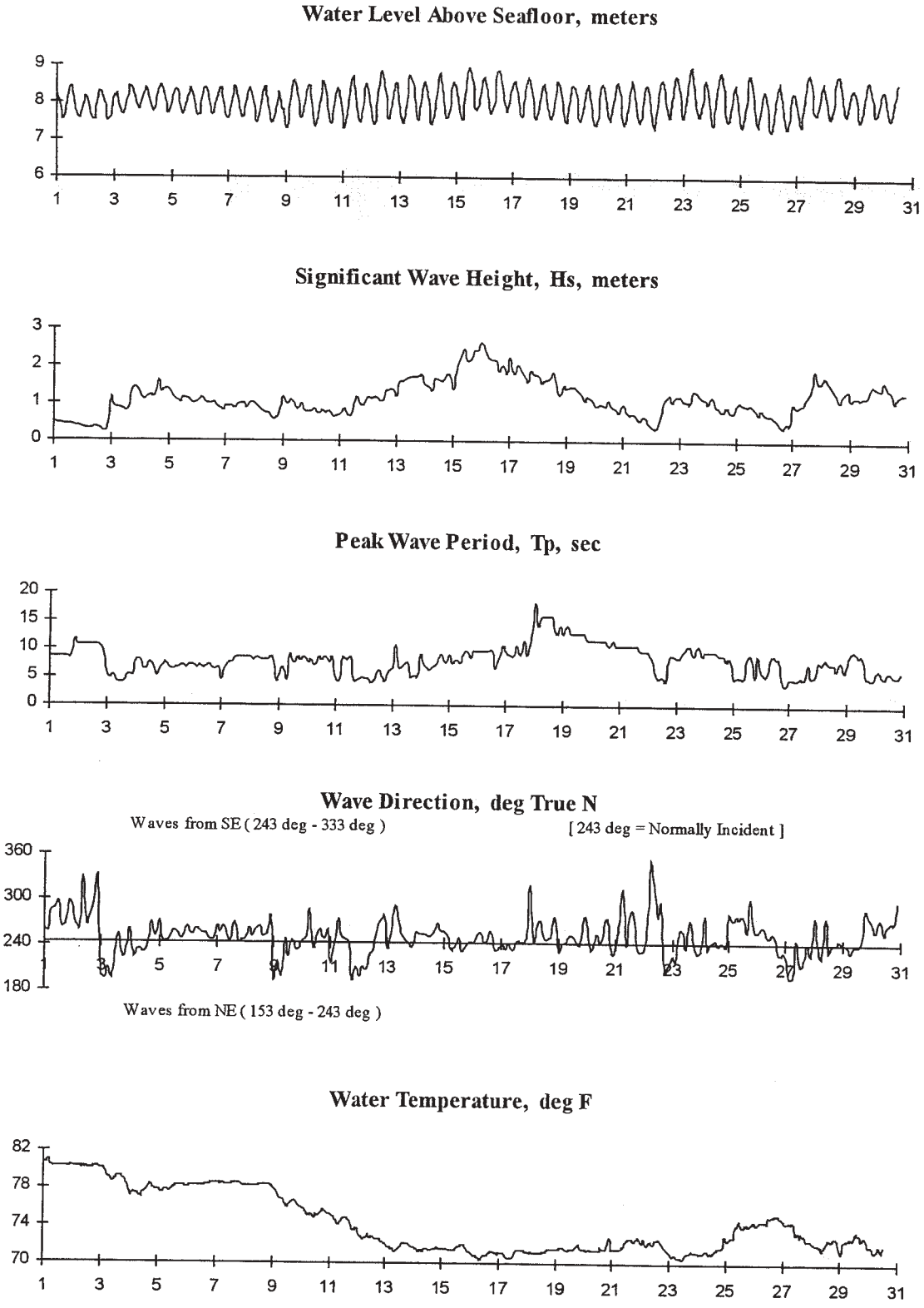


**Figure 6. November 1996 Data from Sebastian Inlet Wave Gage**

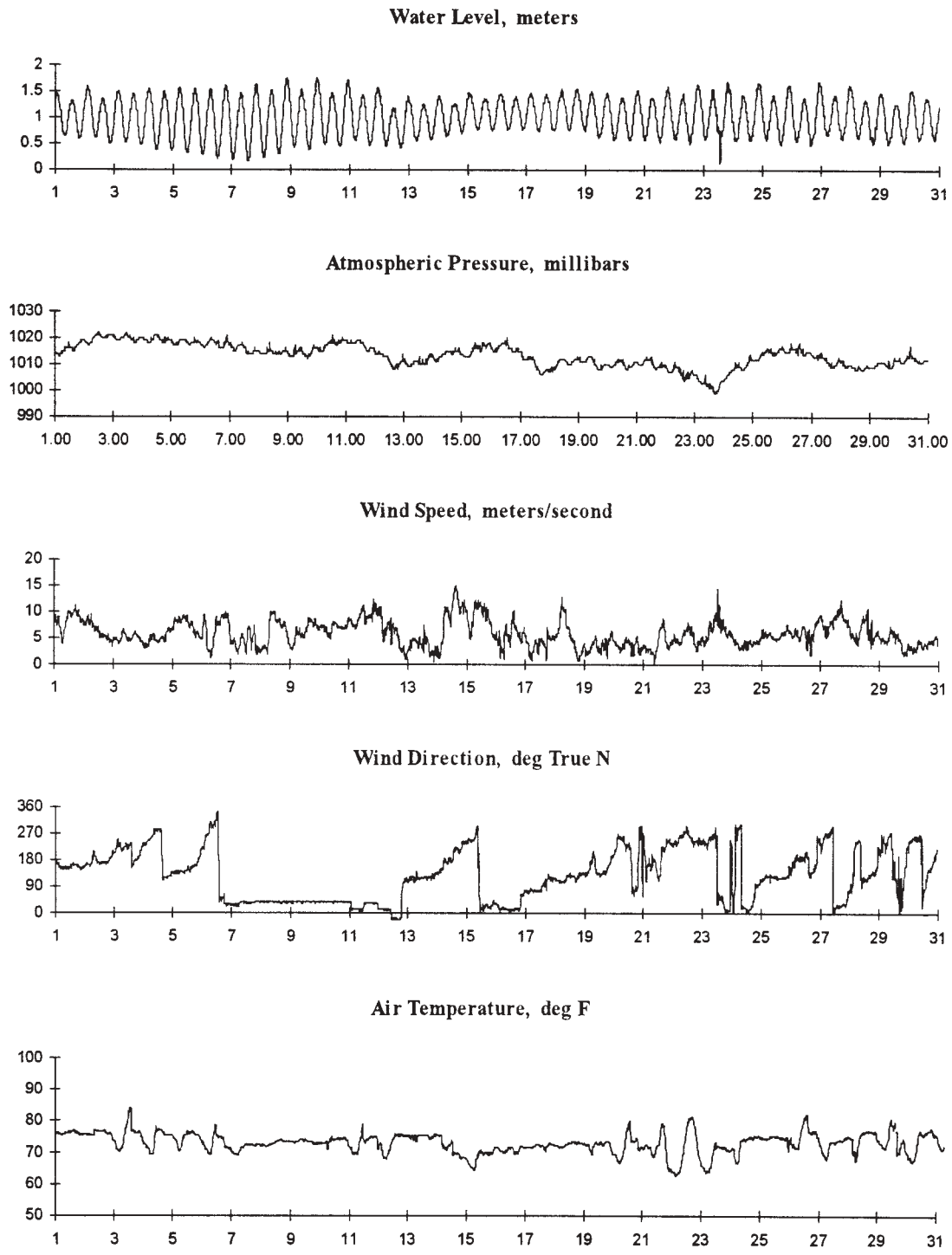


**Figure 7. April 1997 Data from Sebastian Inlet North Jetty Weather and Tide Station**

## 4. Real-time Data Posting to the Internet

The data collection, recording and posting to the Internet is a completely automated system. The shed computer in the State Park constantly receives wave data from the offshore wave gage via the cable, and weather and tide data from the north jetty station via radio transmission. These data are stored on the shed computer, and sent via telephone line to a computer at Florida Institute of Technology once every hour. The computer at Florida Institute of Technology stores the data, and ftps the data to an internet server, so that the data are posted on the internet within minutes of being measured, and updated hourly.

In addition to the real-time data, links to graphs of archived data, information on the instrumentation (including photographs), and other sites are included on the web page of the server at http://www.marine.fit.edu/~wavedata. Figure 8 shows an example of that web page for November 13, 1997.

In addition to providing oceanographic and meteorological data, the web page provides a mechanism that allows the operation of the system to be monitored from any computer in the world that has Internet access. The shed computer also can be operated remotely through the telephone line using appropriate computer software.

**Sebastian Inlet Online Wave and Weather Data**

**Wave Data**

| | |
|---|---|
| Date: | 11/13/97 |
| Time, EST: | 12:00 |

| Significant Wave Height in Meters | Peak Period in Seconds | Direction Coming From in Degrees |
|---|---|---|
| 0.59 | 5.1 | 118 |
| Significant Wave Height in Feet | Mean Period in Seconds | Direction Coming from |
| 1.92 | 5.3 | ESE |

The wave data were last uploaded Thursday, 13-Nov-97 12:35:37 EST

Recent Wave Statistics Data

**Weather Data**

| | |
|---|---|
| Date: | 11-13-97 |
| Time: EST | 12:00:09 |

| Data from the Sebastian Inlet North Jetty | Metric units | English units |
|---|---|---|
| Wind Speed ( m/s, mph ) | 5.2 | 11.6 |
| Wind Direction (direction coming from) | 178 | S |
| Barometric Pressure ( mb, inHg ) | 1006 | 29.7 |
| Air Temperature ( °C, °F ) | 27 | 80.6 |

The weather data were last uploaded Thursday, 13-Nov-97 12:35:38 EST

Wave Data Collection Information

Weather Data Collection Information

| Wave Data Archive | Weather Data Archive |
|---|---|

**Figure 8. Florida Tech Web Page**

The shed computer can be used to access the offshore wave gage and the weather and tide system, either using the shed computer directly, or by remote operation of the shed computer via the telephone line. This communication with the instruments can be used to retrieve the data that is stored internally in the instruments, and to set all of the data collection parameters for the instruments.

The data for each month is downloaded from the Sebastian Inlet wave, weather and tide station. The data are processed and monthly reports are submitted to the Sebastian Inlet Tax District. Both the raw data and the processed data are stored for future use. Monthly and annual histograms and other analyses of the data are presently being performed for the first year of this data collection project.

## 5. Conclusions

The existing wave, weather and tide data collection system at the Sebastian Inlet has been functioning for just over one year. A near continuous data set has been recorded, from which monthly and annual wave statistics are being determined. The real-time system is closely monitored to ensure accurate and continuous data collection by checking the data posted on the Internet, and by using a remote computer to communicate directly with the shed computer. Routine service and maintenance are performed at regularly scheduled intervals, and repairs are performed when needed.

The continuous collection of wave and weather data is essential so that the oceanographic and meteorological factors that influence the inlet are known. Wave and weather data provide the information necessary to determine the forces that drive the changes occurring at the inlet. This includes the determination of the amount and direction of longshore sand transport, the wave and weather forces accompanying storms, the interaction between the waves and current for inlet navigation, and the information needed upon which to base engineering designs and management decisions.

## 6. References

Harris, L.E. and M.C. Perry, 1997: Sebastian Inlet wave, weather and tide data annual report April 1996 to April 1997. Report submitted to the Sebastian Inlet Tax District, Indialantic, FL.

Woods Hole Group, 1997: SeaPac 2100 Directional Wave, Tide and Current Gage, Cataumet, MA.

*Acknowledgements*

Funding for this project is provided by the Sebastian Inlet Tax District.

# HIGH-RESOLUTION DIRECTIONAL WAVE MEASUREMENTS FROM AIR-SEA INTERACTION SPAR BUOY IN THE GULF OF MEXICO

**[1]Mark A. Donelan, [1]Hans C. Graber, [1]W.M. Drennan, [2]Eugene A. Terray**

[1]Rosenstiel School of Marine and Atmospheric Science
University of Miami
Miami, FL 33149 - 1098

[2]Applied Ocean Physics and Engineering Department
Woods Hole Oceanographic Institution
Woods Holes, MA 02543

## ABSTRACT

We have deployed a newly-developed Air-Sea Interaction Spar (ASIS) buoy in the Gulf of Mexico to study meteorological forcing and ocean wave dynamics. This buoy is specially designed to produce little surface disturbance, and to be a partial wave follower at low frequencies. The relative location of the interface is measured by an array of 8 capacitance wave staffs, while the motion of the buoy is monitored using linear accelerometers and rate gyros. This combination permits high resolution measurement of wave directional properties from 10 cm to 600 m. We have computed directional frequency and wavenumber spectra using minimum variance and wavelet methods, respectively. The resulting spectra are compared to directional frequency spectra obtained from 3-meter discus buoy located roughly 1 km away.

# SEPARATION OF SEAS AND SWELLS FROM NDBC BUOY WAVE DATA

David Wang[1] and David Gilhousen[2]

[1]Computer Sciences Corporation
Stennis Space Center, MS 39529
[2]National Data Buoy Center
Stennis Space Center, MS 39529

## 1. INTRODUCTION

The National Data Buoy Center (NDBC) operates more than 50 buoy stations that report wave spectral data hourly. From these spectra, real-time reports of significant wave height and dominant wave period have been posted on several Internet home pages for the last 2 years. One frequent request from the maritime public using these postings was to add swell height and period measurements. Indeed, wind seas and swells have different characteristics that are important for seakeeping safety, small boat operation, ship passages over harbor entrance and surfing forecasting (Earle, 1984). The statistical description of individual wind sea and swell wave system provides information needed to investigate the influence of swell on wind sea growth and dissipation in open ocean (Hanson, 1996). The presence of swell could also affect the relationship between wind stress and sea state (Dobson et al. 1994).

Gerling (1992) developed a spectral-partitioning method to divide each wave energy spectrum into its distinct peaks. Based on this method, a wave spectral partitioning scheme with automated swell tracking and storm source identification capabilities was developed (Kline and Hanson, 1995; Hanson, 1996). This approach require information of both directional wave and wind data, which may not be always available. Earle (1984) proposed that the frequency separating wind seas and swells for a given wave spectrum can be related to the peak frequency of the Pierson-Moskowitz spectral model, which is determined from a given local wind speed. This approach is similar to the concept that wind seas are in the frequency range of wave spectrum where the wave phase velocity is less than wind velocity component in the direction of wave propagation (The WAMDI Group, 1981; Dobson et al., 1994). Vartdal and Barstow (1987) , based on the shape of mean JONSWAP spectral model, developed an algorithm to separate wind seas and swells for a given wave spectrum, which does not require wind data.

In this study, in addition to the algorithms by Earle (1984) and by Vartdal and Barstow (1987), a new algorithm for separation of wind seas and swells based on wave steepness was introduced. The three algorithms were examined using directional wave and wind data collected from a buoy station off the coast of Alabama in the Gulf of Mexico.

## 2. ALGORITHMS FOR SEPARATION OF WIND SEAS AND SWELLS

The separation of wind seas and swells is carried out by determining the separation frequency, $f_s$, for each wave spectrum. Wave energy at frequencies higher than $f_s$ is considered to be generated by local winds; wave energy at frequencies lower than $f_s$ is considered to be generated by swells. Three algorithms for determining $f_s$ are introduced here.

### 2.1 P-M Algorithm (P-M)

According to the Pierson-Moskowitz (P-M) spectral model, the peak frequency of a fully developed sea is related to the local wind speed by

$$f_p = \frac{1.25}{U} \qquad (1)$$

where $f_p$ in $Hz$ is the frequency of maximum spectral density and $U$ in $m/s$ is wind speed at 10 m height. Earle (1984) recommended the separation frequency can be related to the peak frequency by

$$f_s = C f_p \qquad (2)$$

where is $C$ is an empirically-determined constant. A value of 0.8 is used by Earle (1984). Very similar approach with additional consideration of wind and wave direction difference was developed by Vartdal and Barstow (1987). Equation (2) with a value of 0.8 for $C$ can be rewritten as the relation of wave phase velocity $V_s$ at $f_s$ and wind speed, which is

$$V_s = 1.56U \tag{3}$$

This suggests that Earle's algorithm is similar to the concept that wind-generated seas are in a specific frequency range of wave spectrum where wave phase velocity is less than 1.56 times of local wind speed.

2.2 Spectral Shape Algorithm (SPSH)

This spectral shape algorithm, denoted as SPSH, was developed by Vartdal and Barstow (1987). This algorithm is based on the shape of the mean JONSWAP spectrum. The first step is to determine the lowest frequency $f_l$ of wind-generated equilibrium range that has

$$S(f) * f^5 > 2.5 * 10^{-4} (m^2 Hz^4) \tag{4}$$

where $S(f)$ is the measured wave spectral density in $m^2/Hz$ and $f$ is frequency in $Hz$. The value $2.5*10^{-4}$ is half the asymptotic value of the Pierson-Moskowitz spectrum multiplied by $f^5$. The second step is to determine the wind sea peak, $f_{wi}$ , which is the frequency of maximum $S(f)$ in the range

$$0.75 f_1 < f < 1.25 f_1 \tag{5}$$

and take

$$f_s = C f_{wi} \tag{6}$$

as the separation frequency between swells and wind seas. $C$ is an empirically-determined constant. A value of 0.75 is used by Vartdal and Barstow (1987).

2.3 Wave Steepness Algorithm (STPN)

This wave steepness algorithm, denoted as STPN, is based on the assumption that wind seas have a higher steepness and swells have a lower wave steepness. A representative parameter describing the steepness of random waves is defined as

$$steepness = \frac{H_s}{L} = \frac{2\pi H_s}{g T_z^2} \tag{7}$$

where $H_s$ is the significant wave height, $L$ is the wave length associated with $T_z$ and $T_z$ is the average wave period that are computed from the *nth* moment of wave spectrum by

$$H_s = 4\sqrt{m_0}\ , \qquad T_z = \sqrt{\frac{m_0}{m_2}} \tag{8}$$

$$m_n = \int_{f_l}^{f_u} f^n s(f) df$$

where $f_u$ and $f_l$ are usually the upper and lower frequency limits of measured wave spectra, respectively. In this study, 0.03 Hz and 0.4 Hz are used for the lower and upper limits, respectively. A frequency-dependent parameter representing wave steepness over frequencies ranging from a specified $f$ to the upper limit $f_u$ is defined as

$$\xi(f) = \frac{2\pi H_s(f)}{g T_z(f)^2} \tag{9}$$

where $H_s(f)$ and $T_z(f)$ are computed from

$$H_s(f) = 4\sqrt{m_0(f)}\ , \qquad T_z(f) = \sqrt{\frac{m_0(f)}{m_2(f)}} \tag{10}$$

$$m_n(f) = \int_{f}^{f_u} f^n s(f) df$$

The separation frequency $f_s$ is estimated by

$$f_s = C\, f_x \tag{11}$$



AUTHOR INDEX TABLE OF CONTENTS

where $f_x$ is the frequency of maximum $\xi(f)$, and C is an empirically-determined constant. A value of 0.95 is used in this study. This algorithm does not require wind data and any assumption concerning wave spectrum.

## 3. FIELD DATA TESTING OF THE SEPARATION ALGORITHMS

The validity and reliability of the algorithms were examined using hourly-measured wind and directional wave data measured from an NDBC buoy station during a meteorological frontal passage accompanied by rapid wind speed and wind direction shift. The buoy was moored off the Alabama coast at a water depth of approximately 30 m. The buoy was equipped with an NDBC directional wave measurement system to estimate directional wave data using the buoy's heave, pitch, and roll motions. Winds were measured by an R. M. Young propeller-type anemometer mounted at the top of the buoy mast at approximately 5 m above waterline. The 5-m measured wind speed was convert to wind speed at 10 m height using a multiplication factor of 1.2.

As the wind direction remained approximately 140 degrees during the first 26 hours from December 13-15, 1993, the wind speed gradually increased from 5 to 15 m/s (see Figure 1a). The significant wave height increased from 0.5 to 4 m as the peak wave period increased from approximately 4 to 8 s (see Figure 1b). The wave condition during this period was dominated by wind seas generated by the long-fetch southeasterly winds over the Gulf of Mexico. In the early hours of December 14, the wind speed quickly dropped to less than 4 m/s as wind direction shifted to approximately 290 degrees. The wind speed then increased to approximately 10 m/s and both the wind speed and direction remained relatively steady for the rest of the period. The wave conditions during this period consisted of southerly swells and wind seas generated by the fetch-limited northwesterly winds.

Figure 2a shows a selected wave spectrum with significant wave height of 4.135 m and wind speed of 15.3 m/s before the frontal passage, which are the highest wave height and wind speed of the entire period. Figure 2b shows frequency-dependent mean wave direction that aligned well with the local wind direction as indicated by the horizontal dashed line. The separation frequencies derived from the P-M, SPSH, and STPN algorithms are indicated by the vertical dashed, dash-dotted and solid lines, respectively. The vertical dotted line indicates the frequency above which the deep-water wave phase velocity is less than the wind velocity component in the mean wave direction. As can be seen, separation frequencies from the above algorithms are lower than peak frequency at 0.13 Hz indicating wave energy is mainly generated by the local wind.

Figures 3a and 3b show a selected wave spectrum and mean wave direction of a bimodal sea after the frontal passage. As indicated by the mean wave direction and local wind direction, wave energy at frequencies lower than 0.17 Hz has a major peak at 0.13 Hz, which was caused by swells coming from 160 degrees. Wave energy at frequencies higher than 0.17 Hz has a peak at 0.21 Hz, which was from wind seas generated by the local winds. The separation frequency derived from the STPN algorithm is 0.16 Hz, which properly separates the wind seas and swells. However, the separation frequencies from the P-M and the SPSH algorithms do not separate the two energy sources properly. Using separation frequencies from these two algorithms for this bimodal wave spectrum overestimates wind sea energy and underestimates swell energy. Examinations on wave spectra from the rest of period show very similar results as the two examples discussed here.

The significant wave height and average wave period for wind seas and swells can be computed from Equation(8) by replacing $f_l$ with $f_s$ for wind seas and replacing the $f_u$ with $f_s$ for swells, respectively. Figures 4 and 5 show the time series of wind sea significant wave height, $H_{sw}$, and swell significant wave height, $H_{ss}$, obtained using the separation frequencies by the three algorithms. For comparison, reference significant wave heights for wind seas and swells are also shown. The reference wave heights are obtained by considering $f_s$ as the frequency above which the wave phase velocity less than the local wind velocity component in the mean wave direction. This separation frequency is indicated by the dotted vertical line as shown in Figures 2 and 3.

As can be seen in Figure 4, when wave field was dominated by the growing wind seas before the frontal passage, the $H_{sw}$ derived from the three algorithms all agree well with the reference $H_{sw}$. During coexistence of wind seas and swells after the frontal passage, the $H_{sw}$ by the P-M and the SPSH algorithms are significantly higher than the reference

$H_{sw}$. The $H_{sw}$ by the STPN algorithm agree well with the reference $H_{sw}$, except for a few hours when both wind speed and direction changed rapidly during the frontal passage.

As can be seen in Figure 5, when wave fields were dominated by the growing wind seas, the swell significant wave height $H_{ss}$ by the three algorithms and the reference $H_{ss}$ are generally less than 1 m and the differences between them are very insignificant. When the wave fields consisted of fetch-limited wind seas and swells, the $H_{ss}$ by the STPN algorithm agree well with the reference $H_{ss}$ while $H_{ss}$ by the P-M and SPSH algorithms significantly lower than the $H_{ss}$ by the STPN and the reference $H_{ss}$.

Figures 6 and 7 show the time series of significant wave height and average wave period of wind seas and swells by the STPN algorithm, respectively. When wave conditions was dominated by wind seas before the frontal passage, the significant wave height and average wave period are almost the same as those of wind seas. During coexistence of wind seas and swells after the passage on December 14, the separation algorithm provided a detailed and better description of the evolution of wave conditions. It shows that the gradually decreasing significant wave height $H_s$, in fact, consisted of a growing $H_{sw}$ and a decaying $H_{ss}$ with an average wave period of approximately 4 sec for wind seas and 7.5 sec for swells.

## 4. SUMMARY

Three empirically developed algorithms for separation of wind seas and swells were examined based on directional wave data and wind data from an NDBC buoy station during a meteorological frontal passage. All three algorithms provide similar estimation of separation frequency when wave conditions were dominated by wind seas from an uniform and long-fetch wind field before the passage. However, when wave conditions were contributed by both wind seas and swells after the passage, only the algorithm based on wave steepness (STPN) provides proper and consistent separations for wind seas and swells. The other two algorithms overestimate wind seas and underestimate swells.

The STPN algorithm, without requirements of wave direction, wind data and wave spectrum shape assumption, shows that the spectral-related steepness parameter can be used to separate wind seas and swells effectively. This simple algorithm can be easily implemented to report wave height and period of wind seas and swells in real time for operational purposes.

## 5. REFERENCES


Dobson F. W., S. D. Smith and R. J. Anderson, 1994: Measuring the relationship between wind stress and sea state in the open ocean in the presence of swell. Atmosphere-Ocean 32 (1), 237-236.

Earl, M. D., 1984: Development of algorithms for separation of sea ans swell. Technical Report MEC-87-1, National Data Buoy Center, pp. 53

Gerling, T. W., 1992: Partitioning sequences and arrays of directional ocean waves spectra into component wave systems. Journal of Atmospheric and Oceanic Technology, Vol. 9, 444-458.

Hanson, J. L., 1996: Wave spectral partitioning applied to the analysis of complex wave conditions in the north pacific ocean. Proceeding of the 8th Conference on Air-Sea Interaction and symposium on Goals, America Meteorological Society.

Kline, S. A. and J. L. Hanson, 1995: Wave identification and tracking system. Technical Report STD-R-2436, The Johns Hopkins University, Applied Physics Laboratory; Laurel, M.D.

Vartdal, L. and S. F. Barstow, 1987: A separation algorithm for wind sea and swell for applications to directional Metocean data buoy. Technical Report, Oceanographic Center, SINTEF Group, Trondheim, Norway, pp. 104.

The WAMDI Group, 1988: The WAM model-A third-generation ocean wave prediction model. Journal of Physical Oceanography, Vol. 18, 1775-1810.

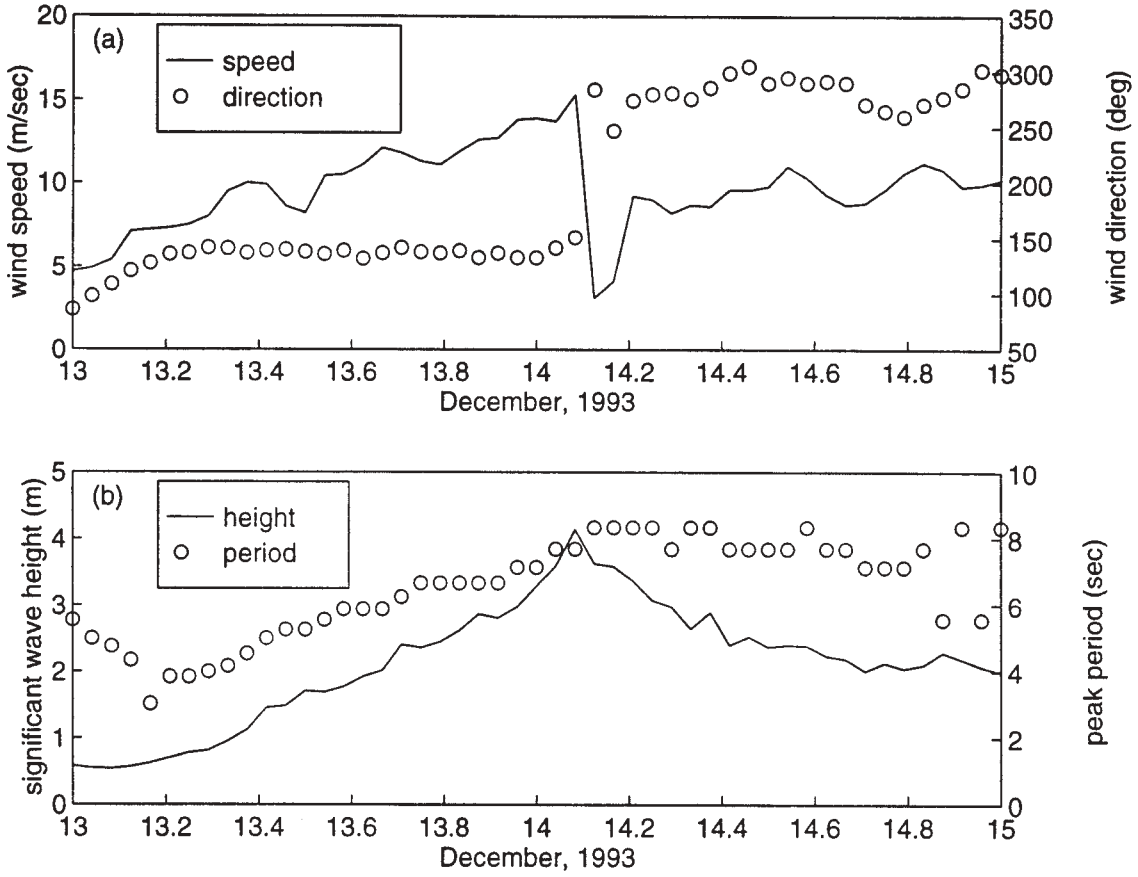


Figure 1. Time series of (a) wind speed and wind direction, (b) significant wave height and peak wave period.



AUTHOR INDEX TABLE OF CONTENTS

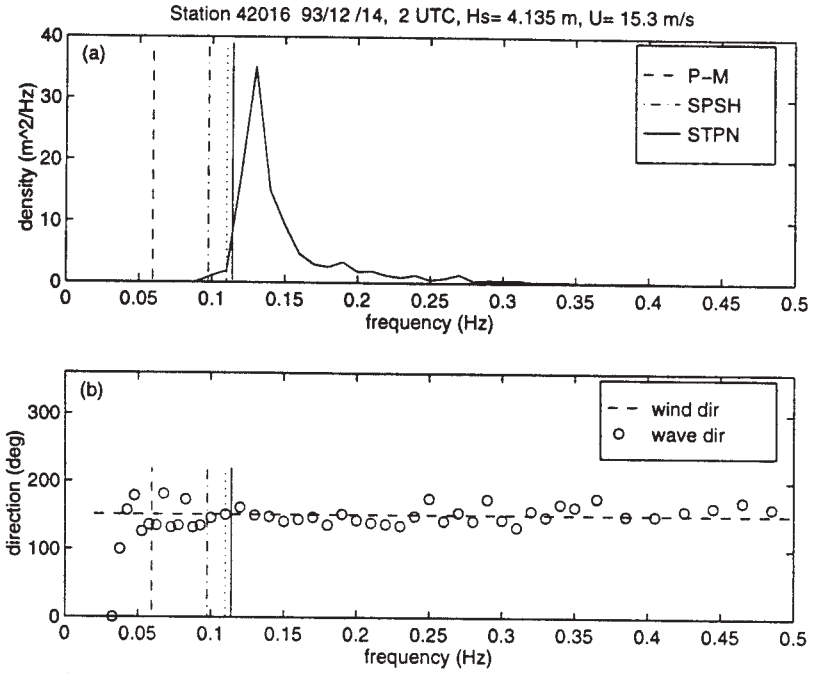


Figure 2. A selected (a) wave spectrum and (b) mean wave direction and wind direction before the frontal passage. The separation frequencies derived from the three algorithms are indicated by the vertical dashed, dash-dotted and solid line. The vertical dotted line indicates the frequency above which the wave phase velocity is less than the wind velocity component in the mean wave direction.

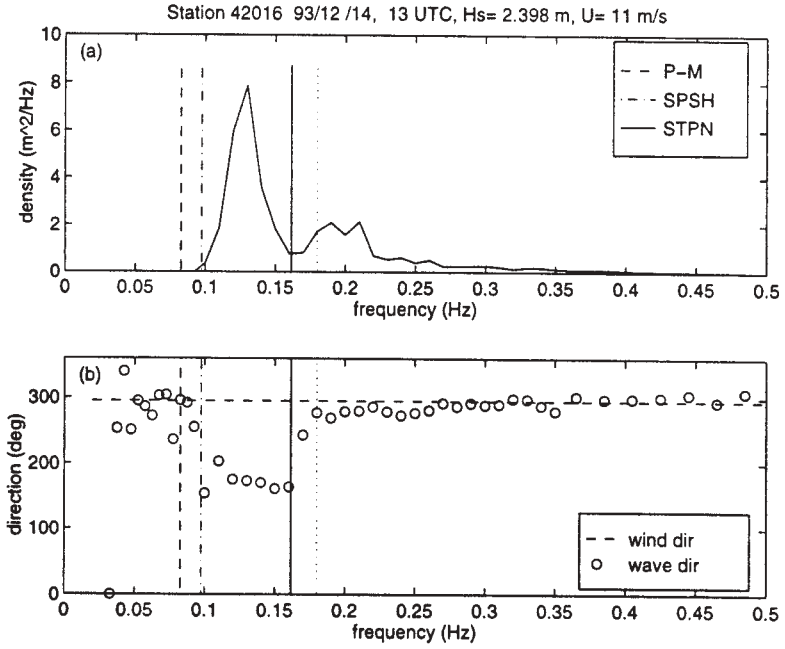


Figure 3. A selected (a) wave spectrum and (b) mean wave direction and wind direction after the frontal passage. The separation frequencies derived from the three algorithms are indicated by the vertical dashed, dash-dotted and solid line. The vertical dotted line indicates the frequency above which the wave phase velocity is less than the wind velocity component in the mean wave direction.

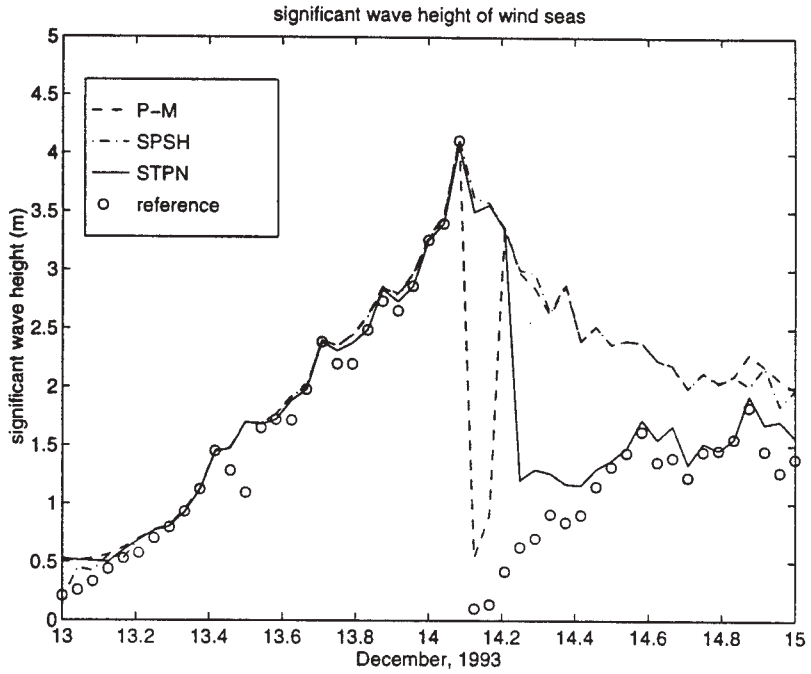


Figure 4. Time series of significant wave height of wind seas using the separation frequencies by the three algorithms. The reference significant wave heights for wind seas are obtained by using the separation frequency above which the wave phase velocity is less than the wind velocity component in the mean wave direction.

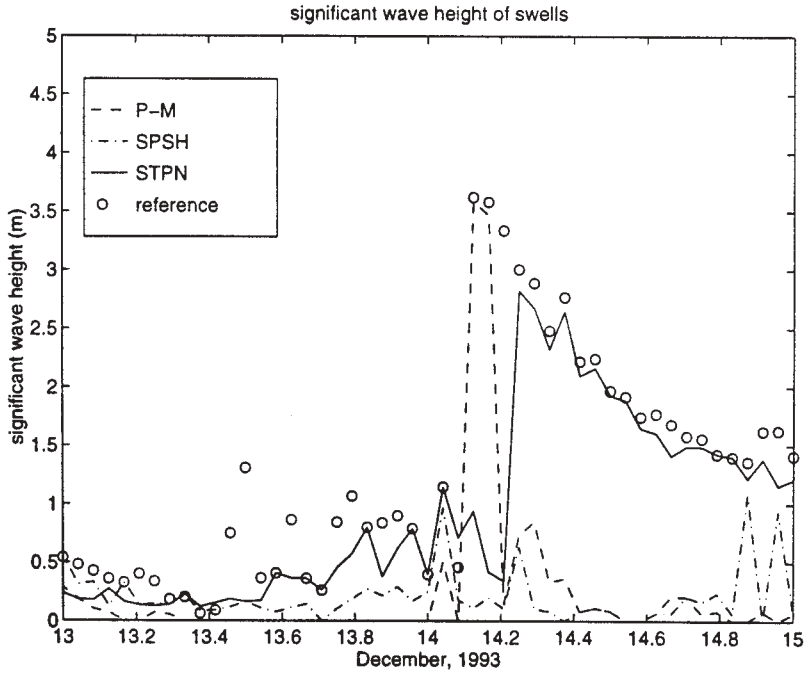


Figure 5. Time series of significant wave height of swells using the separation frequencies by the three algorithms. The reference significant wave height for swells are obtained by using the separation frequency below which the wave phase velocity is greater than the wind velocity component in the mean wave direction.

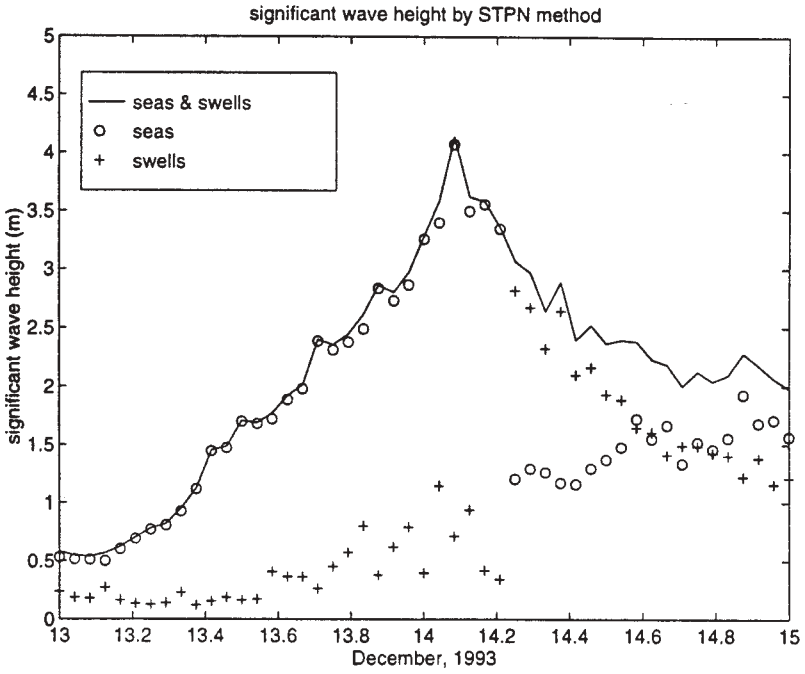


Figure 6. Time series of significant wave height of wind seas and swells by the wave steepness algorithm (STPN).

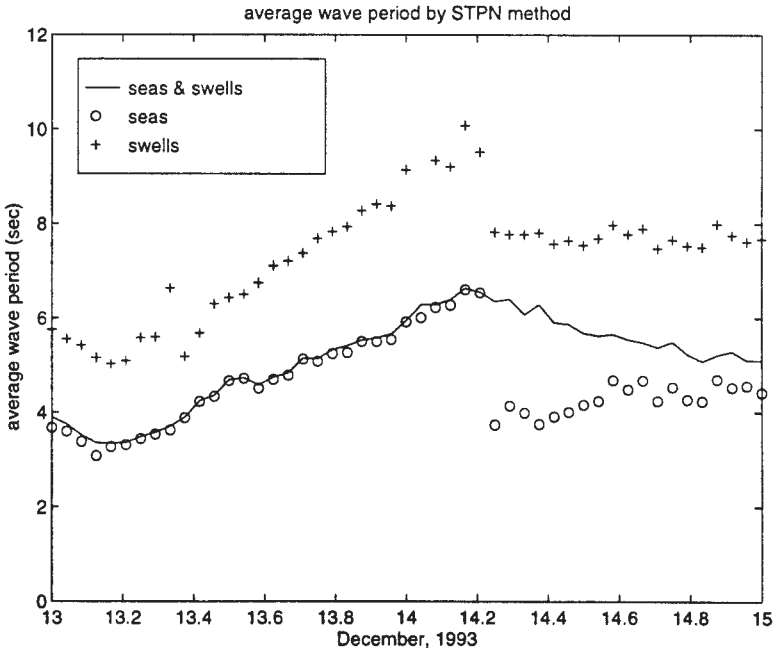


Figure 7. Time series of average wave period of wind seas and swells by the wave steepness algorithm (STPN).



AUTHOR INDEX TABLE OF CONTENTS

# MEASUREMENT OF WINDS AND WAVES FROM A NOMAD BUOY IN HIGH SEASTATES

S.G.P. Skey[1] , K. Berger-North[1] and V.R. Swail[2]

[1]Axys Environmental Consulting Ltd.
[2]Environment Canada, Downsview, Ontario

## 1.0 INTRODUCTION

In late October 1991 an intense extratropical storm developed in the Atlantic Ocean off the North American coast, and merged with the remnants of Hurricane "Grace". The combined storm, now known as the "Halloween Storm", raged for several days on the Atlantic coastal and offshore regions from Florida to New England and the Maritimes. High seas (waves and surge) affected most of the American and Canadian Atlantic coasts with extensive damage reported along the coast and the loss or damage of several vessels (Bigio, 1992). The high waves generated by the Halloween Storm exceed the 100-year return period at several locations (Cardone and Callahan, 1992).

As a result of this storm, concern was raised as to the ability to predict such extreme wave heights. There has been much speculation on the part of wave modellers that the wind measurements reported by weather buoys may be lower than the actual wind speed existing during high sea conditions. Several possible causes of the lower wind speed measured by the buoys have been advanced, including: sheltering of the buoy's anemometers by the waves; extreme buoy motion; and the methods of data presentation (averaging period and time). However, there is no consensus as to which factor may be the most prominent during high wave conditions, nor the relative magnitudes of these factors.

As a result of the 1991 Halloween Storm, Environment Canada commissioned a hindcasting study. The wind fields used in the hindcast study were generated form observations and pressure gradient fields by Oceanweather Inc. (Cardone and Callahan, 1992; Cardone, 1993, pers. comm.). The observed winds were increased by 5% to adjust the vector-averaged wind speed to a scalar-averaged wind speed following the findings of Gilhousen (1987), and then scaled to 20 m height (Cardone and Callahan, 1992).

The wave hindcasts undertaken by Oceanweather Inc. performed well in predicting peak waves measured at most buoys but could not reproduce the 17.4 m observed maximum significant wave at buoy #44137. Cardone (1993, pers. comm.) felt that a wind speed of 36-39 m/s would be required to generate a 17 m significant wave. The mean wind speed measured concurrent with this wave was 24.7 m/s, while the measured peak wind speed was 35 m/s. Cardone felt that more knowledge is needed of the wind field structure during storms, especially when the pressure gradients are tight. He also noted that several forecasting groups including Environment Canada's Pacific Weather Centre use the peak wind speed rather than the mean in their analyses.

The ability to forecast wave heights accurately during storm conditions is a prime objective for increasing marine and coastal safety. Accurate determination of wave properties during extreme weather is also essential to the development of design criteria for marine vessels, and coastal and offshore structures. Searches of the literature and discussions with experts in the field (Heidorn, 1993) have indicated that little is known about the airflow regime surrounding buoys, their motion in high seas, and the effects of averaging the data on the reporting of a true wind speed.

As a result of the uncertainties concerning wind measurements in sea states where the height of the significant wave is significantly greater than the height of the anemometer, the Storm Wave Study-1 (SWS-1) was initiated. A 6 m ship-shaped NOMAD weather buoy was deployed off the West Coast of British Columbia (approximately 10 miles south-west of Cape St. James) at the southern tip of the Queen Charlotte Islands in 2,000 m of water at WMO location #46147. This buoy, in addition to being part of the regular Canadian network of weather reporting buoys, was equipped with an additional payload designed to gather data (primarily wind speed and direction and wave height and period) at 2 Hz, and store it directly without any averaging.

The buoy was successfully deployed and, in the winter of 1994/95, recorded a number of storms, the worst being associated with a significant wave of 9.4 m. The SWS-1 program is described in Skey *et al.* (1993) and the preliminary analysis of the data was described in Skey *et al.*. (1995). Further findings of the SWS-1 data are described here as well as the details of the follow-on SWS-2 study which was initiated as a result of the recommendations from the SWS-1 study.

## 2.0 SWS PACKAGES

### 2.1 SWS-1

The SWS-1 package was installed on a standard Environment Canada NOMAD weather buoy. The buoy (WMO location #46147) is part of the network of weather buoys on the West Coast of Canada and, throughout the SWS-1 experimental period, it functioned as a regular buoy transmitting hourly messages as well as supporting the SWS-1 experiment. The SWS-1 package used some of the outputs from the buoy such as wind speed and direction, and wave height.

The SWS-1 program was designed to determine the following:

- whether significant variability in the wind field exists to suggest differences between the vector and scalar wind speeds greater than the 7 to 10% suggested by Gilhousen (1987);
- the extent to which the motion of the buoy increases/reduces the reported wind speed;
- whether high waves shelter the anemometers from the general air flow for a significant portion of the ten-minute averaging period, thus causing a reduced wind speed to be reported;
- the difference between the measured waves calculated from the strap-down accelerometer data and those calculated from the Datawell "gimballed" accelerometer data.

### 2.2 SWS-2 Package

On Saturday October 25th 1997, a follow up SWS-2 program was initiated with the deployment of an Environment Canada NOMAD buoy at 46°44.05'N, 48°48.13'W on the Grand Banks of Newfoundland in 81m of water on an all-chain mooring, 1.5 nautical miles to the south-west of the Hibernia platform. The buoy is transmitting regular hourly messages via GOES as well as storing (and transmitting via VHF to the Hibernia platform) the raw SWS-2 data gathered at 2 Hz. The SWS-2 program is based on the recommendations following the analysis of the SWS-1 data.

The main differences between SWS-1 and SWS-2 are:

- an additional strap down accelerometer located as close as possible to the Datawell heave sensor;
- a Solent Windmaster acoustic anemometer, an RMYoung 05305 AQ anemometer as well as an RMYoung 05106 anemometer on the aft mast;
- continuous sampling for period of deployment (c. 6 months) at 2 Hz;
- installation of a 3 Axis Solent Ultrasonic acoustic anemometer on the forward mast. This anemometer is part of a program being run by the Southampton Oceanography Centre;
- SWS-2 located near a fixed platform (Hibernia), a Directional Datawell Waverider and a Minimet Buoy. Data being measured on Hibernia includes wind speed and direction, and wave height and direction from a MIROS wave radar.

The measured parameters for a normally configured NOMAD buoy and for the SWS-1 and SWS-2 payload packages are summarized in Table 2.1.

## 3.0 WIND

### 3.1 Vector vs Scalar Winds

The high temporal resolution wind data provided by SWS-1 give an opportunity to investigate vector versus scalar averaging in considerable detail for a continuous range of sample durations in a wide range of sea and wind conditions.

Gilhousen (1986) investigated the difference between vector and scalar averaging of wind speeds by comparing the scalar averaged speeds measured at a C-MAN (Coastal-Marine Automated Network) station on a fixed platform at Chesapeake Light Station, Virginia, with the vector averaged speeds measured by a nearby

**Table 2.1**
**Configuration of NOMAD SWS-1 Buoy (46147) and SWS-2 Buoy (#44153)**

| Parameter/ System | Normal System for ODAS Buoys | Extra Systems for SWS-1 (WMO Buoy ID #46147) 1994/1995 | Extra Systems for SWS-2 (WMO Buoy ID #44153) 1997/1998 |
|---|---|---|---|
| Horizontal Wind Speed and Direction | Two RM Young anemometers (model # 05103/6) at 4.45m and 5.25m above sea level (ASL). | | Replaced #1 RMYoung anemometer with Solent Windmaster acoustic anemometer. Added an RMYoung AQ on aft extension of aft mast. |
| Vertical Wind Speed | | RM Young anemometer (model #05103), without vane, fixed vertically on horizontal axis 4.82m ASL. | SOC * Solent 3 axis Ultrasonic acoustic anemometer on forward mast. |
| Vertical Wind Direction | | RM Young anemometer (model #05103) on horiz. axis 4.82 m ASL. | SOC * Solent 3 axis Ultrasonic acoustic anemometer on forward mast. |
| Air temperature | YSI (model #703) with radiation shield at 4.27m ASL. | Increased sampling rate from .5 Hz. to 2 Hz. | Increased sampling rate from .5 Hz. to 2 Hz. |
| Buoy Attitude | | General Oceanics Inc. (model #6011 TAMS) three axis magnetic sensor. | Installed a Systron Donner motion sensor in SWS-2 package. |
| Wave Height and Period | On west coast - Datawell Mark II heave sensor (single axis vertically stabilised accelerometer); On east coast - strap down accelerometer. | Columbia Research Lab (SA 107B) single axis strap-down accelerometer. | Jewell LCA-100 accelerometer in SWS-2 package and another on top of Datawell sensor. |
| Barometric Pressure | Atmospheric Instrumentation Research Ltd (model AIR-SB-2A). | | |
| Water Temperature | YSI (model 44203) mounted in a s/s bolt below sea level. | | |
| Compass | Two Syntron (model FHS-AV-1) or KVH C100 fluxgate compasses (one for each anemometer). | One Syntron (model FHS-AV-1) fluxgate compass. | One KVH C100 fluxgate compass. |
| Mooring Strain | | Metrox TL101-25K tension load link mounted just below bridle. | Metrox TL101-25K tension load link in a modified mounting just below bridle. |
| Data Acquisition & Processing | ZENO 1200/Watchman 100 | SWS-1. Sampling and storage of raw data at 2 Hz under certain weather conditions. | SWS-2. Continuous sampling and storage of raw data at 2 Hz. |
| Data Transmission | GOES and ARGOS. | Repco RDS 1200 VHF transceiver. | Repco RDS 2400 VHF transceiver. |

3 m E-Buoy. The fixed platform was equipped with a Bendix Aerovane at a height of at 33.3 m, and the E-Buoy was similarly equipped with a Bendix Aerovane at a height of 3.6 m. For his analysis the wind speeds were adjusted to 10 m. The C-MAN Data Acquisition Control and Telemetry (DACT) payload for the platform samples wind speed every second for eight minutes. The General Service Buoy Payload (GSBP) used in the E-Buoy takes individual samples of the u and v components every second for 8.5 minutes. Average speed and

direction are then produced from the averaged components. Winds speeds reached 19.5 m/sec and the significant wave height reached 3.5 m for his analysis in extreme conditions with the passage of Hurricane Josephine. While the overall agreement for the buoy and platform speeds is good (the SD of the difference between the buoy and platform speeds is about the same as the SD of the difference between the platform's two anemometers), the buoy speeds are lower than the platform speeds for high wind speed events due to the averaging methods. Subsequent comparison of both averaging methods for the same anemometer at buoy station 41001 indicated that for speeds greater than 8 m/sec, the vector averaged speeds were about 7% lower than the scalar averaged speeds.

### 3.1.1 Calculation of SWS-1 Mean Wind Speeds

The SWS-1 anemometers are referenced directly to the fluxgate compass which is used for determining buoy heading. Both anemometers are referenced to the same compass, eliminating the source of error introduced if separate compasses were used. As the yaw component of buoy motion induces an apparent directional change in an otherwise stationary anemometer due to this directional reference, the buoy heading is subtracted from the wind direction value to provide true wind direction corrected for platform yaw.

From the SWS-1 data set instantaneous scalar wind speed $s_i$ and direction $\theta_i$ are computed from the 2.0 Hz output of the independent pulse counters into which are fed the frequency outputs of the port and starboard anemometers by dividing the integer values $p_s$ and $p_\theta$ in the digital pulse counter by the sample interval $L$ (Eqns. 1, 2). The difference in sample frequency from the standard ZENO processing has no effect on the calculation of scalar wind speed values for sample duration of equal length which are greater than the ZENO sampling period.

$$s_i = \left(\sum_{t=0}^{t=L} p_s\right) \Big/ L \tag{1}$$

$$\theta_i = \left(\sum_{t=0}^{t=L} p_\theta\right) \Big/ L \tag{2}$$

The scalar wind speed $u$ is computed by dividing the sum of the resultant instantaneous wind speeds $s_i$ by the number of samples $n$ in the sample duration (Eqn. 3)

$$u = \left(\sum_{i=1}^{n} s_i\right) \Big/ n \tag{3}$$

Vector wind speeds $\bar{v}$ are determined from the SWS-1 data set by computing the $v_x$ and $v_y$ components of the corrected wind direction and averaged over the number of samples $n$ in the appropriate gust length for instantaneous speed $s_i$ and instantaneous wind direction $\theta_i$ (Eqns. 4a-4f) .

$$v_{xi} = v(\sin\theta_i) \tag{4a}$$

$$v_{yi} = v(\cos\theta_i) \tag{4b}$$

$$\bar{v}_x = \left(\sum_{i=1}^{n} v_{xi}\right) \Big/ n \tag{4c}$$

$$\bar{v}_y = \left(\sum_{i=1}^{n} v_{yi}\right) \Big/ n \tag{4d}$$

$$\bar{v} = \sqrt{\bar{v}_x^2 + \bar{v}_y^2} \tag{4e}$$

$$\bar{\theta} = 270 - \arctan\left(\bar{v}_y / \bar{v}_x\right) \tag{4f}$$

### 3.1.2 Comparison of 10-Minute Vector and Scalar Means

Running 10-minute vector and scalar means ($v_{10}$ , $u_{10}$) are computed at one minute intervals for entire storms and the percentage difference

$\delta$ calculated (Eqn. 5). A typical time series is provided in Figure 3-1. Percentage differences between the vector and scalar values for all storms are summarized in Table 3.1.

$$\delta = 100\left(\frac{(u_{10} - v_{10})}{u_{10}}\right) \tag{5}$$

The average difference for all storms as reported in Table 3.1 is 3.1%, and is as low as 0.9% for the low wind and wave conditions of March 06, 1994. The only event that approximates Gillhousen's 7% value is the 8.61% value for the storm of December 05, 1994, which deserves closer investigation.

Time series plots of $\delta$ for this storm indicate two areas in which the difference exceeds an otherwise lower than average value of 2%. The first event is a sharp spike of an approximate magnitude of 35% which occurs just before the 4th hour of the storm; the second event is an increasing difference (which peaks at 70%) from hour 6 to the end of the data record. When this difference is plotted against the 10-minute scalar wind speed it becomes apparent that the spiking beyond hour 6 is attributable to the nature of the difference calculation in that the absolute value of the wind speed drops nearly to zero, causing any wind speed difference of a constant absolute magnitude to increase as a proportion of the diminishing absolute wind speed. This accounts for the spiking beyond hour 6 which can be ignored as the difference calculation becomes an inappropriate statistic for near-zero wind conditions.

When plotted against the 10-minute mean wind direction for the storm of December 05, 1994, the difference spike just prior to the 4th hour of the storm coincides with an abrupt change in wind direction of approximately 140° in 10 minutes. Inspection of the 10-minute scalar mean wind speed reveals a significant change in scalar wind speed at the same point. Surface Analysis Charts provided by Environment Canada's Pacific Weather Centre for 0600Z and 1200Z December 05, 1994 indicate that a frontal system passed over the SWS-1 moored buoy sometime between the two reports. This demonstrates that the first spike is attributable to the recording of a legitimate meteorological event.

Overall, the difference between 10-minute vector and scalar wind speeds are lower than anticipated in the extreme sea states recorded by SWS-1. While vector averaging is intuitively dependent on the high frequency variability of wind direction, further analysis of the wave sheltering effect on both wind speed and direction over individual waves suggests that the unexpectedly low difference between vector and scalar winds is partially attributable to the joint distribution of the high frequency variability of both wind speed and wind direction.

### 3.1.3 Comparison of Scalar and Vector Gusts

As high frequency variability in wind direction contributes to lower reported values of vector versus scalar 10-minute mean winds, it likewise contributes to lower values of vector versus scalar gusts of shorter periods. The algorithm for the computation of gusts is similar to that of the 10-minute mean (Eqns. 3, 4). The percentage difference $\delta$ (Eqn. 5) as a function of relative and cumulative frequency was computed for gusts of both five and eight seconds duration ($L$ = 5, $L$ = 8). Scalar and vector gusts were computed at one-second intervals for the duration of the storm of November 04, 1994, with over 86,000 points in the population sample. The difference distribution $\delta$ of this storm is representative of all the storms collected in the SWS-1 data set. Over 40% of both eight and five second gusts are within 0.5% of each other, independent of wind speed, wave height, or variability of wind direction. The cumulative frequency portion of the graph indicates that 95% of vector and scalar gust values are within 4% and 5% of each other for gusts of five and eight seconds respectively. This suggests that there is not a significant difference between the calculation of gusts (vector or scalar) for duration of five seconds (some of the US platforms) and eight seconds (the Canadian buoy network - now changing over to 5 second gusts).

## 3.2 Gust Factor Analysis

The gust $g_L$ of a sample is defined as the maximum scalar wind speed $u_L$ of duration $L$ over a record of period $T$ (Eqn. 6).

$$g_L = \max(u_L)\Big|_{t=o}^{t=T} \tag{6}$$

The gust factors $f_{uL}$ and $f_{vL}$ are defined as the ratio of the gust $g_L$ to the scalar mean $\bar{u}_T$ and vector mean $\bar{v}_T$ of period $T$ (Eqns. 7, 8).

$$f_{uL} = \frac{g_L}{\bar{u}_T} \tag{7}$$

$$f_{vL} = \frac{g_L}{\bar{v}_T} \tag{8}$$

A relation of gust factors as a function of sample duration was plotted by averaging all of the scalar gust factor values $f_{uL}$ and $f_{vL}$ over a given sample duration from *L=0.5 to L=30.0* seconds for a period *T=10* minutes, with *n=727* samples in the population (Eqns. 9, 10).

$$R_{uL} = \frac{\sum_{i=i}^{n} f_{uL}}{n} \tag{9}$$

$$R_{vL} = \frac{\sum_{i=i}^{n} f_{vL}}{n} \tag{10}$$

When plotted against sample duration *L*, mean gust factors $R_{uL}$ and $R_{vL}$ describe a general relation which might be used as a data quality control index for determining the validity of reported scalar gust values given the 10-minute vector or scalar mean wind speed (Figure 3-2). For sample duration *L=8* seconds, a scatter plot of $f_{uL}$ and $f_{vL}$ versus scalar and vector wind speeds (Figures 11,12) indicates the factor distribution and suggests a constant relation for wind speeds in excess of approximately 7 to 8 m/sec, with $f_{uL}$=1.23 (SD=0.08) and $f_{vL}$=1.27 (SD=0.11). The data for these calculations came from the November 4th storm.

**Table 3.1**
**Scalar vs. Vector Wind Speeds**
*Mean of 10-Minute Averages Computed Every One Minute*

| Date | Starboard | | | | | | Port | | | | | |
|---|---|---|---|---|---|---|---|---|---|---|---|---|
| | Scalar u (m/s) | Scalar std dev | Vector u (m/s) | Vector std dev | % Diff. | % Diff. std dev | Scalar u (m/s) | Scalar std dev | Vector u (m/s) | Vector std dev | % Diff. | % Diff. std dev |
| Nov04/94 | 11.92 | 2.35 | 11.54 | 2.3 | 3.45 | 1 | 11 | 3.04 | 10.65 | 2.97 | 3.43 | 1.09 |
| Nov06/94 | 8.16 | 1.19 | 7.83 | 1.11 | 4.29 | 1.3 | 7.44 | 1.72 | 7.14 | 1.67 | 4.26 | 1.24 |
| Nov12/94 | 8.68 | 1.42 | 8.43 | 1.43 | 3.08 | 1.53 | 7.79 | 2.47 | 7.58 | 2.43 | 2.82 | 0.81 |
| Nov14/94 | 9.39 | 0.82 | 9.2 | 0.83 | 2.11 | 0.51 | 8.84 | 0.6 | 8.66 | 0.61 | 2.2 | 0.58 |
| Nov27/94 | 11.36 | 1.2 | 10.89 | 1.24 | 4.39 | 3.05 | 10.96 | 1.17 | 10.67 | 1.13 | 2.74 | 0.56 |
| Nov30/94 | 12.94 | 1.9 | 12.63 | 1.86 | 2.45 | 0.41 | 12.47 | 1.79 | 12.17 | 1.75 | 2.52 | 0.43 |
| Dec02/94 | 9.69 | 2.79 | 9.35 | 2.71 | 3.78 | 1.34 | 9.4 | 2.8 | 9.08 | 2.7 | 3.56 | 0.81 |
| Dec05/94 | 10.77 | 6.95 | 10.22 | 6.7 | 8.61 | 8.19 | 10.62 | 7 | 6.17 | 6.82 | 7.23 | 6.64 |
| Dec06/94 | 7.44 | 2.61 | 7.2 | 2.64 | 4.24 | 3.03 | 6.99 | 2.65 | 6.76 | 2.67 | 4.32 | 3.04 |
| Dec07/94 | 8.68 | 1.08 | 8.43 | 1.06 | 2.95 | 0.6 | 8.45 | 1.07 | 8.2 | 1.04 | 3.06 | 0.6 |
| Dec19/94 | 10.98 | 1.46 | 10.69 | 1.44 | 2.77 | 0.63 | 11.05 | 1.42 | 10.76 | 1.39 | 2.74 | 0.6 |
| Dec22/94 | 15.97 | 1.24 | 15.57 | 1.21 | 2.56 | 0.45 | 16.07 | 1.28 | 15.67 | 1.25 | 2.53 | 0.43 |
| Dec30/94 | 6.96 | 0.74 | 6.76 | 0.47 | 3.08 | 0.43 | 6.76 | 0.45 | 6.62 | 0.45 | 2.09 | 0.32 |
| Jan 15/95 | 11.9 | 0.9 | 11.6 | 0.9 | 2.63 | 0.66 | 11.92 | 0.91 | 11.59 | 0.92 | 2.82 | 0.79 |
| Jan 18/95 | 4.7 | 0.44 | 5.69 | 0.44 | 1.64 | 0.41 | 6.61 | 0.43 | 6.5 | 0.43 | 1.75 | 0.37 |
| Jan 24/95 | 14.79 | 3.92 | 14.24 | 3.72 | 3.77 | 0.84 | 14.53 | 3.9 | 13.99 | 3.69 | 3.75 | 0.94 |
| Feb 10/95 | 10.61 | 0.64 | 10.48 | 0.64 | 1.2 | 0.21 | 9.77 | 0.68 | 9.66 | 0.68 | 1.1 | 0.21 |
| Mar06/95 | 7.31 | 0.57 | 7.25 | 0.57 | 0.9 | 0.1 | 7.2 | 0.57 | 7.13 | 0.56 | 1.07 | 0.13 |
| Mar29/95 | 10.43 | 0.38 | 10.28 | 0.38 | 1.55 | 0.13 | 9.98 | 0.39 | 9.93 | 0.38 | 1.53 | 0.11 |

### 3.3 Variability of Wind Speed and Direction

The flow of air over waves in extreme sea states is a complex issue. There is little data currently available to describe in detail the flow regime over individual waves as measured by a moored buoy.

Jeffreys (Sverdrup *et al.*, 1942; Wiegel, 1964) theorized that the flow field will exhibit separation behind solid obstacles (i.e., waves) due to eddy formation resulting from unequal air pressures on the windward and leeward sides of a perturbation of the water surface. This effect can only prevail when waves travel at a velocity smaller than the wind speed (Sverdrup *et al.*, 1942). Another school of thought contends that wind speed is unaffected by the waves in fully developed seas (wave speed equals wind speed) and that if waves affect the wind measurements, they do so by physical action on the buoy including knocking the buoy over by breaking waves (Heidorn, 1993).

The predictions of various theories of wind behaviour in high sea states are largely qualitative, and while this study may not definitively determine which models are correct, it provides data which can be used to quantify the magnitude of the various effects postulated.

Examination of wind direction over individual waves indicates significant variability. This variability typically decreases as a function of wave height. Zero crossing analysis is used to compute the joint distribution of the change in wind direction over an individual wave, with the frequency of these events for all storms summarized in Table 3.2. When the mean change in wind direction is computed as a function of wave height, a well-defined linear relationship becomes evident, with average changes of over 80° for wave heights in excess of 14 m (Figure 3-3). Regression coefficients for the fit of this relation are $m=3.6$ and $b=30.0$.

Wind speed demonstrates a similar degree of variability over individual waves in high sea states. While the wind speed appears to track the wave field quite closely in higher sea states, this correlation decreases in calmer seas. Table 3.3 contains the joint distribution of the decrease in wind speed and wave height for all storms. The decrease in speed is expressed as the percentage drop from the maximum instantaneous wind speed on the crest to the lowest instantaneous wind speed in the trough over a period of each corresponding zero crossing event. The mean decrease in wind speed calculated in this manner as a function of wave height is provided in Figure 3-4. Again a linear relation becomes evident, with regression coefficients of $m=2.29$ and $b=16.2$.

### 3.4 Effects of Buoy Motion on Wind Measurements

Another of the objectives of the SWS-1 project was to determine the effects of buoy motion in extreme sea states on reported wind speeds. Pond (1968) found that for buoy tilts of less than 10°, errors in wind speeds due to the varying tilt of the mast are negligible (less than 3%), increasing to 15% and 23% for tilts of 23° and 29° respectively. For the NOMAD hull design, Gilhousen (1986) computed the pitch response amplitude operators (RAOs), expressed in terms of degrees of pitch per meter of wave height, as a function of wave frequency. He found that the average pitch angles do not increase much for significant wave heights between three and 13 m, with the angles below 10° for significant wave heights under 11 m.

On the Canadian NOMAD buoys (including the SWS-1 buoy), the anemometers are fixed to the rear mast approximately 3.28 m aft of the centre of rotation (the bridle) at 4.45 m and 5.25 m elevation above the water line. With the centre of rotation 1.87 m below the water line, the effective length of the moment arm of the anemometers is 7.12 m and 7.48 m. The average additional induced wind speed (caused by the buoy motion on the anemometer) is computed for total tilts of 10°, 20°, 30° and 40° over a range of wave periods (Figure 3-5). As the degree of platform roll is symmetrical, it can be assumed that the pumping effect is approximately symmetrical over the individual wave with a zero net effect (vector averaged) as the anemometer accelerates into and out of the wind field. Maximum scalar values for this effect of less than 1.0 m/sec suggest that the larger variations in wind velocities over individual waves are attributable to sources other than buoy motion.

Examination of the magnetometer data from the November 4th storm indicates maximum

**Table 3.2**
**Change in Wind Direction vs. Wave Height**

| | | | | | | | | | | | | | | | | |
|---|---|---|---|---|---|---|---|---|---|---|---|---|---|---|---|---|
| 180 | 0 | 0 | 0 | 0 | 0 | 0 | 0 | 0 | 0 | 0 | 0 | 0 | 0 | 0 | 0 | 0 |
| 170 | 3 | 21 | 31 | 39 | 45 | 27 | 25 | 15 | 10 | 3 | 1 | 2 | 1 | 1 | 0 | 0 |
| 160 | 5 | 18 | 38 | 32 | 31 | 34 | 25 | 16 | 10 | 7 | 0 | 2 | 0 | 1 | 1 | 0 |
| 150 | 6 | 14 | 27 | 44 | 48 | 37 | 27 | 17 | 11 | 2 | 4 | 0 | 1 | 0 | 0 | 0 |
| 140 | 9 | 19 | 30 | 36 | 35 | 38 | 25 | 19 | 5 | 7 | 2 | 2 | 0 | 0 | 0 | 0 |
| 130 | 7 | 24 | 46 | 53 | 54 | 46 | 41 | 22 | 19 | 12 | 2 | 4 | 1 | 0 | 0 | 0 |
| 120 | 8 | 21 | 44 | 57 | 81 | 50 | 35 | 30 | 20 | 12 | 3 | 2 | 1 | 2 | 0 | 0 |
| 110 | 12 | 39 | 63 | 57 | 73 | 47 | 51 | 32 | 22 | 16 | 4 | 4 | 3 | 2 | 2 | 1 |
| 100 | 12 | 30 | 67 | 74 | 97 | 91 | 65 | 44 | 45 | 21 | 11 | 7 | 7 | 0 | 1 | 0 |
| 90 | 9 | 53 | 87 | 113 | 127 | 136 | 104 | 81 | 67 | 49 | 35 | 16 | 11 | 6 | 2 | 0 |
| 80 | 14 | 76 | 130 | 181 | 204 | 230 | 177 | 161 | 115 | 93 | 52 | 32 | 15 | 13 | 1 | 0 |
| 70 | 33 | 127 | 244 | 328 | 409 | 425 | 422 | 345 | 235 | 161 | 99 | 51 | 25 | 11 | 3 | 1 |
| 60 | 55 | 215 | 469 | 720 | 958 | 1056 | 906 | 729 | 480 | 249 | 169 | 60 | 29 | 19 | 2 | 1 |
| 50 | 102 | 488 | 1170 | 1706 | 2081 | 2040 | 1616 | 1026 | 632 | 340 | 144 | 53 | 15 | 7 | 4 | 0 |
| 40 | 318 | 1330 | 2562 | 3558 | 3586 | 3080 | 2082 | 1122 | 550 | 239 | 106 | 38 | 14 | 5 | 1 | 0 |
| 30 | 871 | 3184 | 4458 | 4561 | 3842 | 2610 | 1476 | 687 | 300 | 105 | 49 | 22 | 6 | 2 | 1 | 0 |
| 20 | 1859 | 4275 | 4041 | 2689 | 1721 | 900 | 471 | 189 | 76 | 26 | 14 | 4 | 1 | 0 | 0 | 0 |
| 10 | 2067 | 2133 | 1061 | 442 | 213 | 87 | 35 | 14 | 6 | 3 | 2 | 1 | 0 | 0 | 0 | 0 |
| 0 | 625 | 133 | 52 | 39 | 28 | 13 | 12 | 3 | 4 | 1 | 2 | 0 | 0 | 0 | 0 | 0 |
| | 0 | 1 | 2 | 3 | 4 | 5 | 6 | 7 | 8 | 9 | 10 | 11 | 12 | 13 | 14 | 15 |

Wave Height (m)

**Table 3.3**
**Percentage Decrease in Wind Speed from Maximum Crest Speed vs. Wave Height (m)**

| | | | | | | | | | | | | | | | | | |
|---|---|---|---|---|---|---|---|---|---|---|---|---|---|---|---|---|---|
| 100 | 32 | 85 | 167 | 198 | 227 | 150 | 105 | 57 | 22 | 18 | 6 | 3 | 4 | 1 | 0 | 0 | 0 |
| 90 | 3 | 9 | 6 | 14 | 13 | 15 | 6 | 3 | 6 | 3 | 0 | 2 | 1 | 0 | 0 | 0 | 1 |
| 80 | 0 | 3 | 10 | 10 | 17 | 13 | 4 | 4 | 0 | 2 | 2 | 1 | 1 | 1 | 0 | 0 | 0 |
| 70 | 4 | 5 | 7 | 15 | 13 | 13 | 5 | 9 | 10 | 13 | 10 | 7 | 7 | 5 | 1 | 0 | 1 |
| 60 | 4 | 12 | 13 | 16 | 34 | 58 | 73 | 69 | 72 | 56 | 42 | 26 | 14 | 7 | 4 | 0 | 0 |
| 50 | 4 | 21 | 61 | 138 | 265 | 386 | 442 | 364 | 260 | 189 | 91 | 46 | 14 | 11 | 5 | 0 | 1 |
| 40 | 12 | 134 | 447 | 889 | 1338 | 1539 | 1269 | 946 | 600 | 309 | 193 | 85 | 37 | 16 | 4 | 1 | 1 |
| 30 | 173 | 958 | 2111 | 3272 | 3844 | 3294 | 2317 | 1465 | 857 | 436 | 187 | 80 | 24 | 10 | 3 | 0 | 0 |
| 20 | 906 | 3241 | 4994 | 5247 | 4708 | 3499 | 2267 | 1167 | 560 | 254 | 126 | 39 | 16 | 13 | 2 | 2 | 0 |
| 10 | 2083 | 4408 | 4502 | 3569 | 2526 | 1584 | 850 | 406 | 191 | 73 | 38 | 8 | 11 | 4 | 0 | 0 | 0 |
| 0 | 2682 | 3129 | 2210 | 1348 | 749 | 391 | 210 | 84 | 32 | 9 | 4 | 3 | 1 | 0 | 0 | 0 | 0 |
| | 0 | 1 | 2 | 3 | 4 | 5 | 6 | 7 | 8 | 9 | 10 | 11 | 12 | 13 | 14 | 15 | 16 |

Wave Height (m)

total tilt values on the order of 60° for pitch and 35° for roll for individual extreme waves. Ninety-nine percent of roll and pitch values were recorded as being less than 30°.

## 4.0 Comparison of Heave Sensors

Both the Datawell gimballed heave sensor and the Columbia strap-down accelerometer are used to measure wave height in the Canadian data buoy network. While the NOMAD platforms on the West Coast are equipped with Datawell heave sensors, accelerometers are used in nearly all of the East Coast buoys. Concurrent sampling of the gimballed Datawell heave sensor and the strap-down Columbia accelerometer in SWS-1 permit direct intercomparison of the output of these sensors in extreme sea states. The off-angle response of the accelerometer is believed to contribute to an under-reporting by the accelerometer of wave height because the gravitational component of the output is reduced as the platform is tilted from a level of orientation. Sensor acceleration is doubly integrated to produce displacement values for both sensors.

Time series of the output of the two heave sensors demonstrate that overall the accelerometer reports lower values of heave than the Datawell, independent of sea state.

When the full frequency output of Datawell versus accelerometer heave values for the storm of 4 November 1994, (a data set comprised of over 86,000 data points) is plotted, there is a heave correlation of 0.85, and the slope of the accelerometer values relative to the Datawell values is 0.88. This relation is characteristic of all the storms collected by the SWS-1 package. When the mean value of the difference between the Datawell and the accelerometer is plotted as a function of wave height, it becomes evident that there is a linear relationship (Figure 4-1). For wave heights greater than 13 m, the linear relationship seems to break down, however the number of events in this range is very low (Table 4.1). This relationship, when expressed as a percentage mean difference between the two sensors and plotted against the individual trough to crest wave heights, is shown in Figure 26 for all SWS-1 storms. The difference increases steadily from about 2% or 3% for waves in the 2 m range, to about 10% for waves greater than 10 m. Beyond 13 m or so there are relatively little data and a corresponding decrease in the confidence of the results.

### 4.1 Calculation of Maximum Wave

The maximum positive wave amplitude (wave crest to mean sea level) is of considerable interest to the marine engineer computing the environmental loading factors in the design of offshore structures as project costs rapidly increase with wave height and air gap requirements. The wave analysis in the Canadian data buoy network assumes that the wave shape is symmetrical and reports a value for the maximum wave height, Hmax, which is calculated as twice the maximum positive wave amplitude. When the ratio of the total wave height (crest to trough) to the positive wave amplitude is plotted as a function of the total wave height for the Datawell sensor, it falls below 2.0 for wave heights exceeding 8 m, confirming that in extreme sea states the wave shape is not symmetrical. Thus, the Hmax as reported by some of the buoys in the Canadian network is misleading as an index of total wave height in extreme seas.

Over the next few years the processing packages in the Canadian buoys will change from a ZENO to a Watchman 100. The wave analysis software in the Watchman returns a true peak to trough value for the maximum wave. The key to determining whether a particular buoy is fitted with Watchman or a ZENO payload lies in the 912 maximum wind speed indicator group in the WMO formatted message. The key is as follows:

- If the maximum speed indicator group reads **921** then the payload is a ZENO and the maximum wave is calculated as twice the crest height.

**Table 4.1**
**Datawell/Accelerometer Comparison (All Storms)**

| Wave Height (m) | Difference (m) | Difference (%) | Number of Events |
|---|---|---|---|
| 0 | -0.25 | -81.05 | 2,354 |
| 1 | -0.06 | -6.0 | 11,324 |
| 2 | 0.06 | 2.98 | 16,059 |
| 3 | 0.16 | 5.24 | 17,886 |
| 4 | 0.26 | 6.57 | 17,348 |
| 5 | 0.37 | 7.44 | 15,220 |
| 6 | 0.47 | 7.84 | 11,131 |
| 7 | 0.58 | 8.38 | 7,076 |
| 8 | 0.71 | 8.89 | 4,225 |
| 9 | 0.8 | 8.95 | 2,280 |
| 10 | 0.96 | 9.68 | 1,182 |
| 11 | 1.05 | 9.6 | 550 |
| 12 | 1.42 | 11.94 | 232 |
| 13 | 1.29 | 10.0 | 119 |
| 14 | 2.03 | 14.64 | 48 |
| 15 | 2.49 | 16.67 | 9 |
| 16 | -0.06 | -0.36 | 6 |

- If the maximum speed indicator group reads **912** then the payload is a Watchman 100 and the maximum wave is reported as the greatest measured value of the peak to trough.

## 5.0 CONCLUSIONS AND RECOMMENDATIONS

### 5.1 Conclusions

In summary the data from SWS-1 data showed a number of interesting and important results. These were:

- wind speed and direction both demonstrated significant variabilities over individual waves. The so-called sheltering effect manifesting itself with reduced speeds and changes in wind direction in the wave troughs. These variabilities typically increased with increasing wave height. These variabilities were shown to have linear relationships with wave height;
- the effect of reporting vector mean winds as opposed to scalar mean winds seems to make a difference of only 3% or 4%. This is less than the 7% proposed by Gilhousen;
- the effect of the roll and pitch motions of the buoy had a negligible effect on the reported wind speeds;
- the strap-down accelerometer appears to read about 10% lower than the Datawell Mark II sensor under most wave conditions; and,
- the variability of wind and wave conditions within any one hour is quite large. The data that are reported on the hourly satellite broadcast is thus a factor of the conditions encountered, the sampling and averaging interval, and the processing algorithms.

Preliminary SWS-2 data from a three week period from the end of November/early December 1997 will be presented at the workshop if possible.

## 6.0 REFERENCES


Axys Environmental Consulting Ltd. 1996. Meteorological and Oceanographic Measurements from Canadian Weather Buoys. A review of sensors, data reduction, transmission, quality control and archival method. Environment Canada, Downsview, Ontario, March 1996. 43 pp.

Bigio, R. 1992. A sampling of damage reports from the Halloween 1991 Storm, Supplement - Proceedings of the 3rd International Workshop on Wave Hindcasting and Forecasting, Montreal, Quebec, May 1992. Atmospheric Environment Service, Environment Canada, Downsview, Ontario, pp. 45-70.

Cardone, V.J. and B.T. Callahan. 1992. Kinematic analysis of the surface wind field in the Halloween Storm and a preliminary spectral model wave hindcast, Supplement - Proceedings of the 3rd International Workshop on Wave Hindcasting and Forecasting, Montreal, Quebec, May 1992. Atmospheric Environment Service, Environment Canada, Downsview, Ontario, pp. 101-118.

Cardone, V.J., and V.R.Swail. 1995. Uncertainty in Prediction of Extreme Storm Seas (ESS). Proceedings of the 4th International Workshop on Wave Hindcasting and Forecasting, Bann, Alberta, October 16-20,1995. Environment Canada, pp. 1-20.

Earle, M.D. and J.M. Bishop. 1984. A Practical Guide to Ocean Wave Measurement and Analysis. Endeco, Inc., Marion, MA. 80pp.

Gilhousen, D.B. 1986. An accuracy statement for meteorological measurements obtained from NDBC moored buoys. National Data Buoy Center, NSTL, MS 39529.

Gilhousen, D.B. 1987. A Field Evaluation of NDBC Moored Buoy Winds. J. Atmos. Ocean. Technol., 4:94-104.

Heidorn, K.C. 1993. The Influence of High Waves on Buoy-Measured Wind Speeds. Atmospheric Environment Service, Environment Canada, Downsview, Ontario.

Pond, S. 1968. Some Effects of Buoy Motion on Measurements of Wind Speed and Stress. Journal of Geophysical Research, Vol. 73, No. 2:507-512.

Skey, S.G.P., K.C. Heidorn. S. Jarvin and V.R. Swail. 1993. The Measurement of Wind Speed in High Seas by Meteorological Buoys. Oceans '93, Victoria, B.C. IEEE.

Skey, S.G.P., K. Berger-North, V.R. Swail. 1995. Detailed measurement of winds and waves in high seastates from a moored NOMAD weather buoy. Proceedings of the 4th International Workshop on Wave Hindcasting and

Forecasting, Banff, Alberta, October 16-20, 1995. Environment Canada, pp. 213-223.

Sverdrup, H.U., M.W. Johnson, and R.H. Fleming. 1942. The Oceans: Their Physics, Chemistry and General Biology. Prentice-Hall Inc., Englewood Cliffs, NJ. 1087pp.

Wiegel, R.L. 1964. Ocean Engineering. Prentice-Hall, Inc., Englewood, NJ. 532pp.

Personal Communications

Dr. Vincent J. Cardone, President
Oceanweather Inc., Suite 1, 5 River Road, Cos Cob, CT 06807, USA.

Mr. Ken Steele
National Data Buoy Centre, NOAA, Stennis Space Centre, Bay St. Louis, Mississippi.

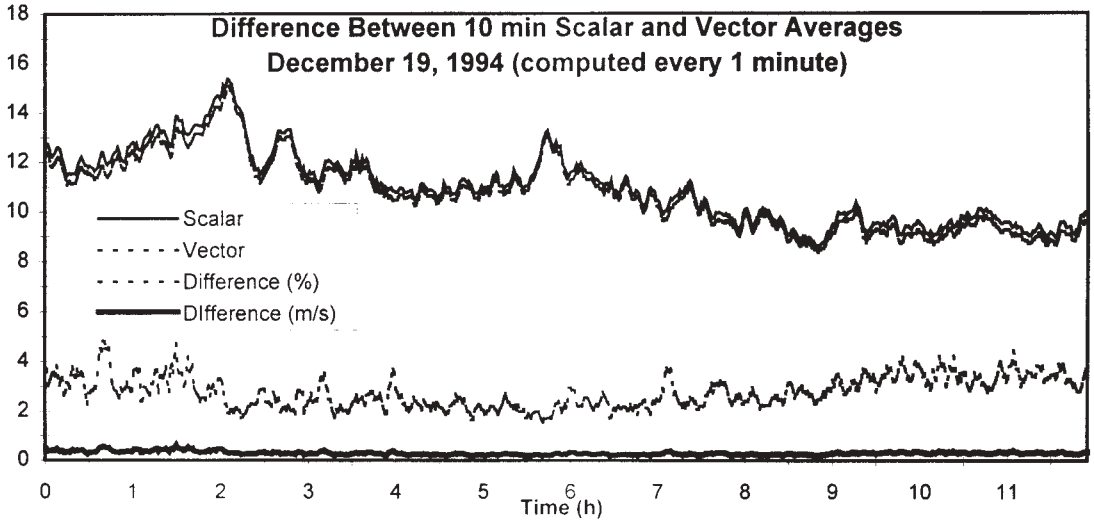


Figure 3-1

**Scalar Gust Factors vs Gust Length**

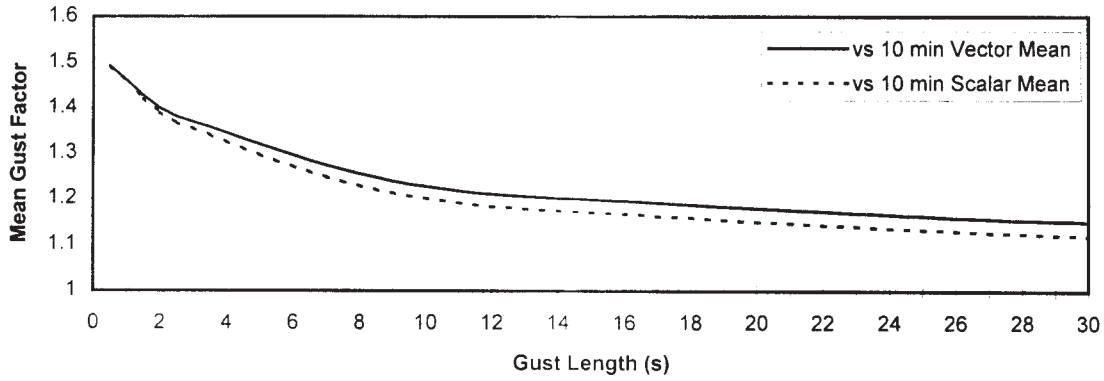


Figure 3-2

**Mean Change in Buoy Heading**

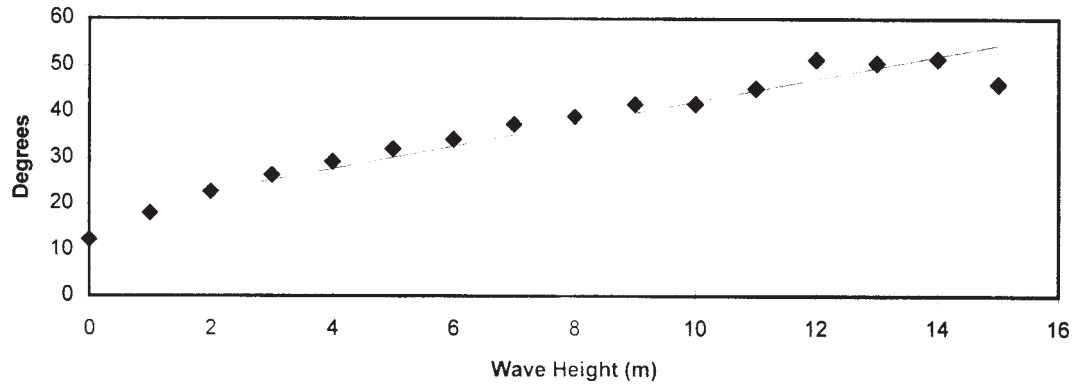


Figure 3-3

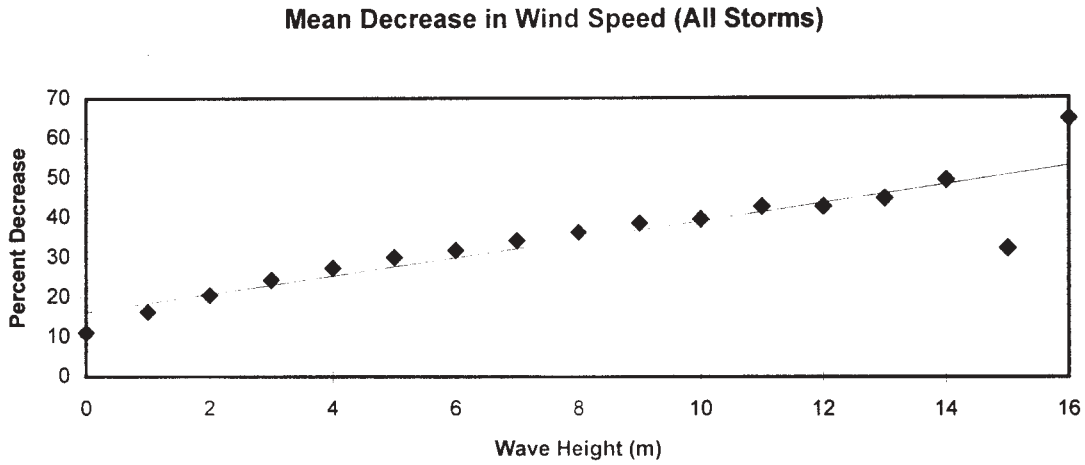


Figure 3-4

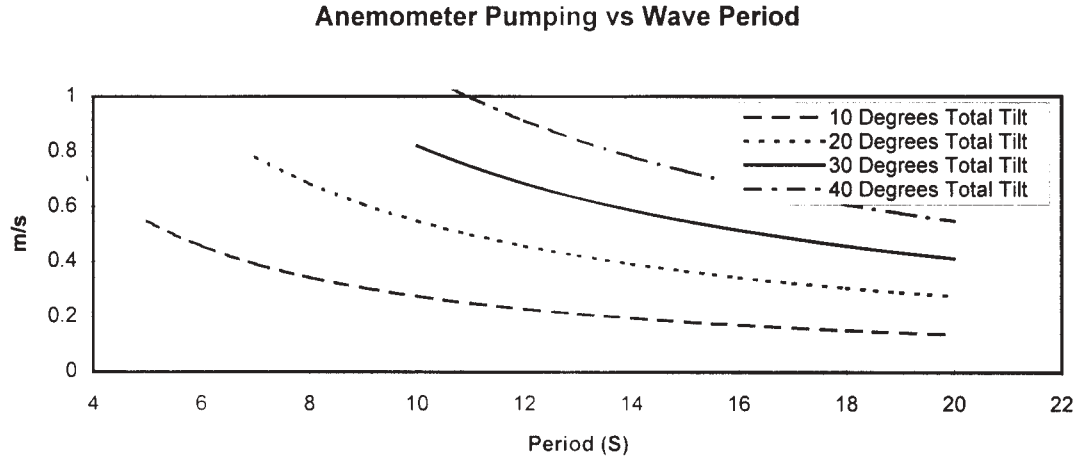


Figure 3-5

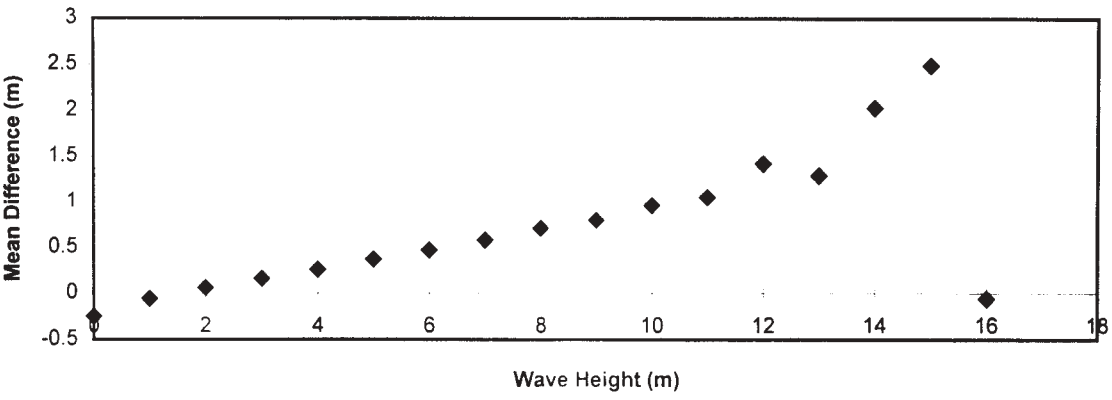


Figure 4-1



TABLE OF CONTENTS

AUTHOR INDEX

# WAVE MODELLING IN THE GREAT BARRIER REEF: INCORPORATING SUB-GRID SCALE EFFECTS

Thomas A. Hardy, Luciano B. Mason, and Jason D. McConochie

The School of Engineering
James Cook University
Townsville, Queensland, Australia

## 1. INTRODUCTION

Contrary to its name, the Great Barrier Reef (GBR) is far from a continuous barrier for much of its length. Instead the GBR is composed of over 2900 individual reefs (**Figure 1**). Although these reefs occupy approximately 20,000 square kilometres, this is only a small fraction of the area of the region. The individual reefs are spread in both the alongshore and cross-shelf directions. This reef matrix is contained in a band running more than 2000 kilometres along the tropical coast of northeastern Australia. The matrix is sometimes over 50 kilometres wide and its landward edge can be as much as 100 kilometres from the mainland. The individual reefs can be very irregular in geometry and groups of reefs can offer very complicated patterns.

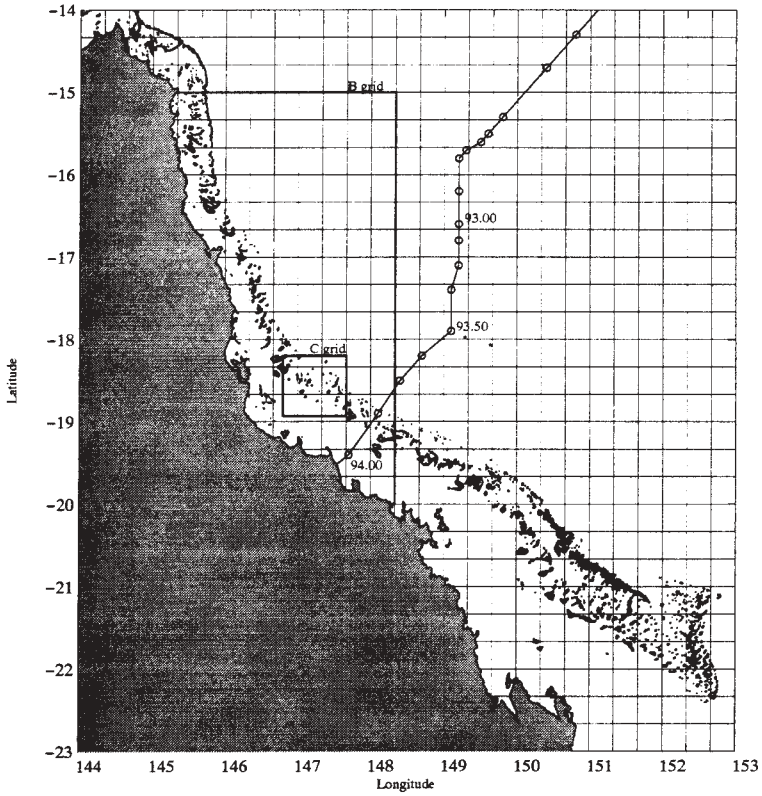


Figure 1. The northeastern coast of Australia and the Great Barrier Reef. Included are the western half of the *A* grid and *A*-grid lines. Boundaries of the *B* and *C* grids are indicated. Also included is the track of tropical cyclone Aivu. The numbers along the track indicate the day of the year; 93 is 3 April 1989.

A reef often creates a large and very abrupt change in bathymetry. The elevation of windward reef flats is approximately mean low water whereas the depth of the continental shelf surrounding reefs is often as much as 50 m. The transition between the relatively deep continental shelf and the shallow reef flat often occurs over only two or three wavelengths.

Wave prediction in the region presents several significant challenges. The porosity of the GBR to outside wave energy varies greatly. The size of individual reefs is often smaller than can be economically resolved in a wave generation model. The wide lagoon between the reef and the mainland allows for significant local generation. Design waves are caused by tropical cyclones. A fairly large tidal range allows energy to propagate across reefs at high tide.

We are in the process of modelling the wave climate from the population of tropical cyclones that threaten the GBR region. Preliminary estimates indicate that this process will require the simulation of several thousand tropical cyclones in order to predict accurately the wave climate over such a large region. Our first goal is create this wave climate at a 1 nautical mile scale (one minute of arc).

The modelling system is based on WAM (Komen *et al.* 1994) and we have established a series of nested computation grids in a spherical system. The outer "*A*" grid, covers the Coral Sea at a resolution of 20 minutes of arc (20 nautical miles). Multiple "*B*" grids have been established to cover the entire GBR at a resolution of 4 minutes of arc. Several "*C*" grids at resolutions of 1 minute of arc are being established for selected areas of interest. **Figure 1** shows the western half of the *A* grid, as well as the outlines of the *B* and *C* grids that are used for results presented in this paper. Grid lines in **Figure 1** indicate computational points in the *A* grid. Even for this nested three-grid system the computer resources will be substantial.

Since we are interested in wave information throughout the GBR, the choice of size and location of *B* and *C* grids is important. Points close the boundaries of a grid will suffer from the inaccuracies of the coarser parent grid. Overlapping the inner grids so that all locations would have a grid in which they were sufficiently removed from the boundary could ease this problem. This could be accomplished by either increasing the extent of the *B* and *C* grids or by increasing the number of *B* and *C* grids. However either of these options would greatly increase the computational expenses. A more attractive option is to increase the accuracy of boundary conditions so that fewer grids with less overlap will be needed.

**Figure 2** shows a typical intra-GBR location. Shown in this figure are the locations of *B* and *C* grid computational points. The *A*-grid computational points are at the corners of the figure. **Figure 2** clearly shows the difficulties in resolving reef geometry in the *A* and *B* grids. The result is inaccuracies not only in the computations inside the domains of these grids, but more importantly for boundary conditions from *A* to *B* and from *B* to *C* grids. Even the resolution of the *C* grid will not provide accuracy for project locations in highly sheltered regions. It is anticipated, that for engineering design input at those locations, a finer scaled modeling will be necessary that will include not only better resolution but also a better description of shallow water wave transformations. One possible scenario could be using *SWAN* (Booij, *et al*, 1996) for a *D* grid and perhaps a Bousinesq model (e.g. Madsen *et al.* 1996) for a very fine scale *E* grid.

In a previous modelling study in the region, Young and Hardy (1993) found that the presence of the GBR influences wave conditions for significant distances seaward of the outer reef edge. This is due to the orientation of the reef matrix parallel to most common wind direction (southeasterly). If the mean direction is parallel to the orientation of the reef matrix then the directional spread of energy is truncated by the reef even for points tens of kilometers seaward of the outer reef edge. Therefore boundary conditions are affected not only where the grids cross the reef at the northern and southern edges but also along the eastern boundary where the grid boundary is in proximity to the reef. Thus the inability to resolve the GBR in the coarser grids presents a problem for wave modelling in the region.

The primary purpose of this paper is to report on a sub-grid scale modeling technique that has shown promise especially for improving boundary conditions provided by coarser grids. The sub-grid scale sheltering mechanism provides a method to include the complexity of the reef geometry on a relatively coarse numerical grid.

## 2. ALTERATIONS TO WAM CYCLE 4.

Recent articles (Tolman, 1992 and Lin and Huang, 1996) suggested that the numerical propagation scheme used in WAM should be investigated to determine its suitability for both accuracy and efficiency. After considering several alternatives, the numerics in WAM were altered to include an implicit

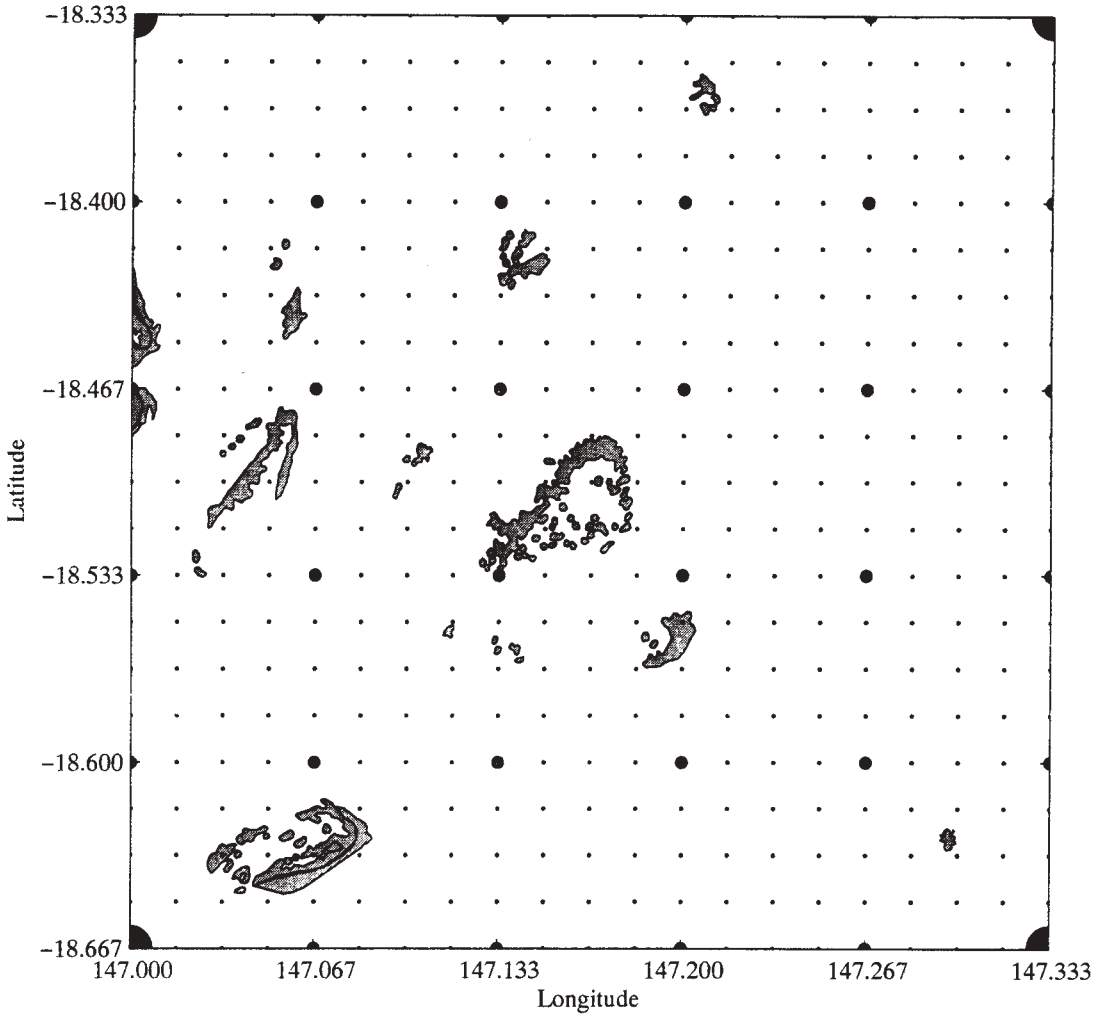


Figure 2. Typical reef location in Central Section of GBR. Corners of the figure are *A*-grid points. *B*-grid points are indicated by large dots. *C*-grid points are indicated by small dots.

scheme to increase computational efficiency. The full details of these tests and changes will be reported separately, however a brief summary is included in this section.

The explicit upwind finite difference algorithm used in WAM is stable only for Courant numbers less than one. However, during tests we found it difficult to obtain stable results over the complex bathymetry of the GBR without resorting to time steps that were much smaller than that indicated by $\mu_s \leq 1.0$, where the Courant number is given by

$$\mu_s = c_g \frac{\Delta t}{\Delta S}$$

where $c_g$ is the group speed, $\Delta t$ is the propagation time step, and $\Delta S$ is the spatial step. Since the numerical scheme in WAM operates over four dimensions; two spatial, angle, and frequency, it is necessary to check for the stability criterion in all four dimensions and not just for the spatial dimensions.

Investigations indicated that although $\mu_s < 1$, $\mu_\theta$ the Courant number in the angle domain can often be very large. The Courant number calculated as

$$\mu_\theta = \frac{d\theta}{dt}\frac{\Delta t}{\Delta\theta}$$

would often be as much as 20 in regions of rapid change in bathymetry.

In order to avoid stability problems, several implicit schemes were considered as alternatives to the present explicit scheme. Unfortunately the implicit schemes that were tested have poorer diffusive characteristics than the existing scheme. The scheme that we have chosen combines explicit and implicit upwind implementations so that diffusive characteristics are no worse than those of the explicit scheme, while at the same time avoiding the stability problems of the explicit scheme.

Another simple modification is the offset of the angle bins by $\Delta\theta/2$ so that no direction aligns itself with a grid axis. This reduces the asymmetry of the diffusion characteristics of the numerical scheme.

## 3. SUB-GRID SCALE FEATURE

Hardy *et al.* (1989) found that the ratio of significant wave height to water depth, $H_s/h$, reduced to less than 0.4 after the first several hundred metres of the windward reef flat. Even at higher tidal levels ($h \approx 3$m), deepwater cyclone waves (say $H_s = 10$m) are drastically reduced ($H_s \leq 1.4$m) after passing over the seaward edge of a coral reef. At mean tide levels ($h \approx 1.5$m) the reduction is more severe, and at low tide the dissipation is total. Hardy *et al.* (1989) also found that the friction coefficient for reef flats is an order of magnitude greater than that representative of sandy bottoms. Any energy left after the end of breaking is reduced even further by the enhanced bottom friction as waves continue across the reef and then eventually out the leeward side. Therefore, for the reef-induced attenuation we use the simple assumption that any wave energy that intersects a reef is dissipated. For large reefs (roughly the size of a grid cell or bigger) this can be simply achieved by treating them as land. For reefs that are significantly smaller than a grid cell, a sub-grid scale technique has been developed to include the dissipation of energy by reefs at a much finer resolution than that of the main computational grid.

### 3.1.1 Sub Grid Scale Technique Overview

The goal of the sub-grid dissipation scheme is to provide a simple and economical way to account for energy losses at a computational point due to sheltering of "up-wave" reefs. The key words here are simple and economical. The major assumption of the technique is that energy attenuation (breaking and bottom friction) is much more important than energy transformation (e.g. shoaling, refraction, diffraction, and three-wave interactions). The overall description of the scheme is as follows: At each computational point, energy that arrives at that point in each directional bin is assumed to travel in a straight line over a distance of (nominally) one grid spacing. If that line crosses one or more reef outlines the energy is dissipated. No attempt is made to account for other transformations caused by the abrupt change in bathymetry near reefs.

A digital data set of reef outlines has been developed which provides data on the location of reefs at a much finer scale ($\Delta x \leq 200$m) than that normally used in the computational grids ($A$ – 37,000m, $B$ – 7,400m). Simple closed polygons are created to represent the outlines of individual reefs by joining the digitized data with straight lines. At each computational point, this data set is used to determine the sheltering by upwind reefs as a function of wave direction. In general, for each direction a proportion (e.g. 60% or $s$ = 0.6) of the upwind direction that is sheltered is calculated. This sheltering coefficient is then used to calculate a porosity factor ($p = 1 - s$) for use in the propagation scheme. The porosity is included in the finite difference implementation of the spatial gradient of action density flux of the propagation scheme (Cartesian representation shown for simplicity),

$$\frac{\partial\left(C_{gx}N\right)_{i,j}}{\partial x} = \frac{\left(C_{gx}N\right)_{i,j} - p(C_{gx}N)_{i-1,j}}{\Delta S}$$

$$\frac{\partial\left(C_{gy}N\right)_{i,j}}{\partial y} = \frac{\left(C_{gy}N\right)_{i,j} - p(C_{gy}N)_{i,j-1}}{\Delta S}$$

where $C_g$ is the group velocity with component directions in $x$ and $y$ directions shown by subscripts, $N$ is the action density, and the subscripts $i$ and $j$, denote the spatial locations with the $i$–1 and $j$-1 locations at "up-wave" locations. The result of the inclusion of the porosity factor is to reduce the energy coming to the computational point to account for sheltering by reefs that are located in the grid space immediately up-wave of the point.

For simulations with the sub-grid scale dissipation scheme, the depth grid does not contain reef points.

Instead, the depth at each point is that which is characteristic (ignoring the presence of reefs) of the continental shelf in the vicinity of the point. Thus the model calculations do not consider the transformations induced by the rapid change in bathymetry at the reef front but they do include the transformations and source/sink inputs over the "reefless" continental shelf.

### 3.2 Calculation of the Porosity Factor, $p$

This very simple scheme of the sub-grid scale dissipation is not so straightforward to implement. Each computational grid point can be thought of as representing an area with dimensions $(\Delta s)^2$. Therefore, the sheltering cannot be determined by merely checking along lines radiating from the computation point at intervals of $\Delta\theta$, where $\theta$ is the direction of travel of a frequency component and $\Delta\theta = 22.5°$ is the angle resolution used in the modelling. Instead several methods were tested; several of which are described below.

The first method will be called the *rotated grid box method* (**Figure 3**). A square box with dimensions of one grid step is centred at the computational point and is rotated so as to extend "up-wave" parallel to each of the 16 directions used in the model calculations. At each rotation, 100 *counting lines* are drawn at equal spacing parallel to the wave direction. Each line is tested to determine if it crosses a reef polygon. For example, if 60 of the lines intersect at least one reef outline, then the sheltering, and the porosity are calculated as $s = 0.6$, and $p = 0.4$, respectively.

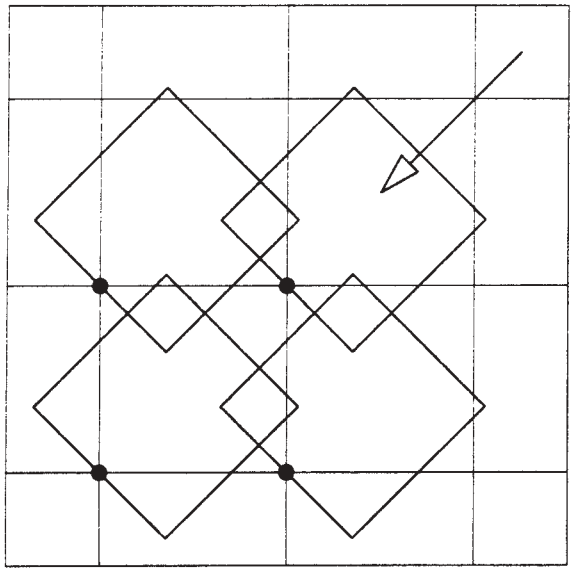

Figure 3. *Rotated box* method. Rotated for $\theta = 225°$.

The problems with the *rotated grid box method* can be seen in **Figure 3**. Boxes are draw at four adjacent grid points for waves going in a southwestery direction. The overlap between boxes is significant and this results in the double counting of reefs, which are located in this area. More importantly, gaps (areas are not included in any box) are also evident. These would cause sheltering to be ignored if reefs were located at these locations. For this reason the *rotated grid box method* was not used.

If the gaps are considered to be a more serious problem than the overlap, then the gaps can be eliminated by extending the square boxes to a rectangle with the long side equal to $\Delta S' = \Delta S(\cos\theta' + \sin\theta')$, where $\theta' = \text{Mod}(\theta, 90)$. These boxes are shown in **Figure 4** for the same wave direction ($\theta = 225°$) as in **Figure 3**. The gaps are eliminated but unfortunately the overlap is increased. A technique to reduce the overlap is shown in **Figure 5**. Here the small side of the rectangle is reduced to from $\Delta S$ to $\Delta S'' = \Delta S \cos\theta'$ and the overlap is reduced by approximately 50%. With this technique there are no gaps at any direction. The is no overlap for angles in multiples of 45°. The maximum overlap at $\theta = 22.5°$ is 34%.

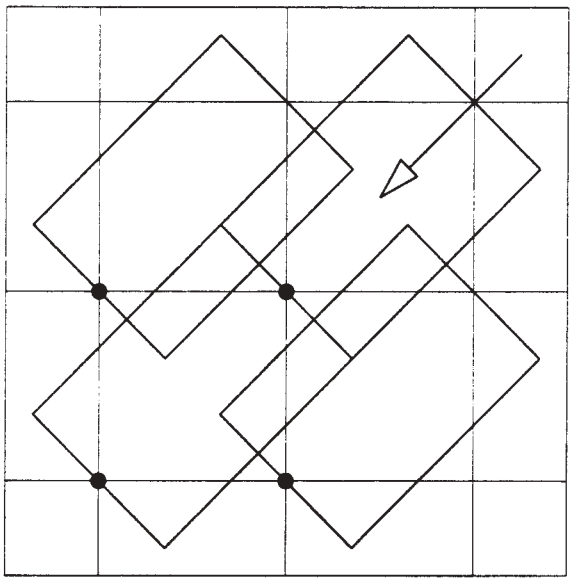

Figure 4. Rotated boxes extended to eliminate gaps.

Methods of correcting for the double counting of sheltering in the overlapped regions were investigated. None were considered satisfactory. To accurately account for the overlap requires extensive coding to determine answers to the following questions: If a counting line enters an overlapped

region, which other counting box shares that region? Are there multiple strikes along the counting line? If so, are some in the overlapped region and some in a non-overlapped region? Does a reef extend into more than one box? If so what percentage of sheltering should be assigned to each box? Such elaborate accounting defeats the purpose of the sub-grid scale scheme. It probably would be just as easy to use a grid with finer resolution.

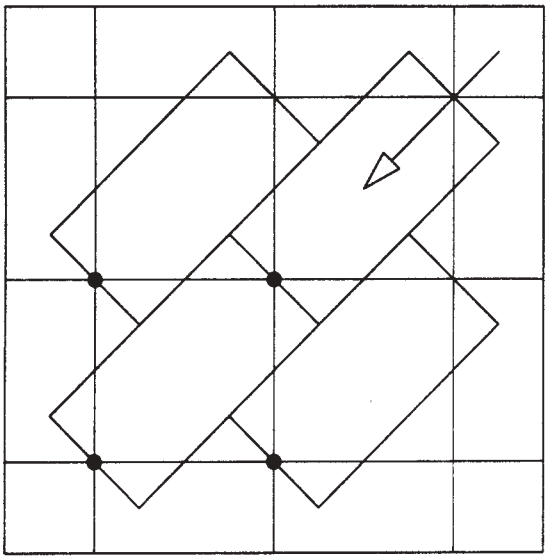

Figure 5. Width of box reduced to eliminate overlap.

The *Parallelogram* method (**Figure 6**) eliminates both gaps and overlaps, and is the method selected for use in the model. Parallelograms with a base width of $\Delta S$ along the grid axis and sides of length $\Delta S' = \Delta S/\cos\theta'$ parallel to the wave direction are constructed. The orientation of the base is flipped from $x$ to $y$ axis at $\theta = 45, 135, 225$ and $315°$ (**Figure 7**). For example, the base is on the $x$-axis for $315° < \theta < 45°$, and switches to the $y$-axis for $45° < \theta < 135°$.

The width of the boxes normal to the wave direction is equal to $\Delta S'' = \Delta S \cos\theta'$. If a constant spacing is used for the counting lines, the number of lines across a box will vary with direction, with 100 lines at $\theta = 0, 90, 180$ and $270°$ reducing to ~71 lines at $\theta = 45, 135, 225$ and $315°$.

If the sheltering represented by each line is set equal to the inverse of the total number of counting lines in a box (e.g.1/100 or 1/71) then a circular reef would cause sheltering that would vary with wave direction. In contrast, if the sheltering represented by each line remains constant (i.e. 1/100) then the model would allow energy to pass a series of reefs that should completely block the wave energy. The results of a simple propagation model (no source terms and assuming a Courant number equal to 1.0 are shown **Figure 8**. The upper number at each point indicates the porosity at the point ( $p = 1 - 70.7 \times 1/100 = 0.2929$ for the completed blocked boxes and $p = 1.0$ for those with no reef). The lower number indicates the energy (calculated by an explicit upwind scheme) given an input of 100 on the boundaries. For this worst case of $\theta = 45°$, approximately 12% of the energy passes through what should be a total blockage.

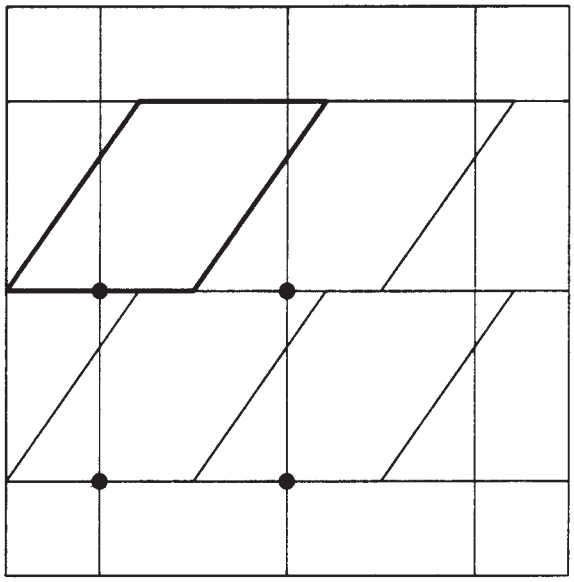

Figure 6. *Parallelogram method.* $\theta = 213.75°$.

## 4.0 MODEL RESULTS.

A comparison of results between models using the sub-grid scale scheme and the common practice of declaring reefs as land in the bathymetry grid is presented in this section. Several model simulations for *Tropical Cyclone Aivu* (April 1989) are presented. During 2 and 3 April, Aivu tracked in a generally southwesterly direction across the Coral Sea towards the Australian coast at speeds averaging 15 to 20 km/h. The lowest estimated central pressure during the lifetime of the storm was 935 hPa at 1600 on 3 April. Early on 4 April Aivu accelerated toward the coast and made landfall approximately 100 km southeast of Townsville at 1030. Estimated central pressure at landfall was 957 hPa with estimated wind gusts of around 200 km/h. The track is indicated in **Figure 1**.

Several combinations of nested grids were tested as indicated in Table 1, where *No reefs* indicates that

reefs were not included in bathymetry, *Land* indicates that reefs were input as land, and *Sub-grid* indicates use of the sub-grid scale technique.

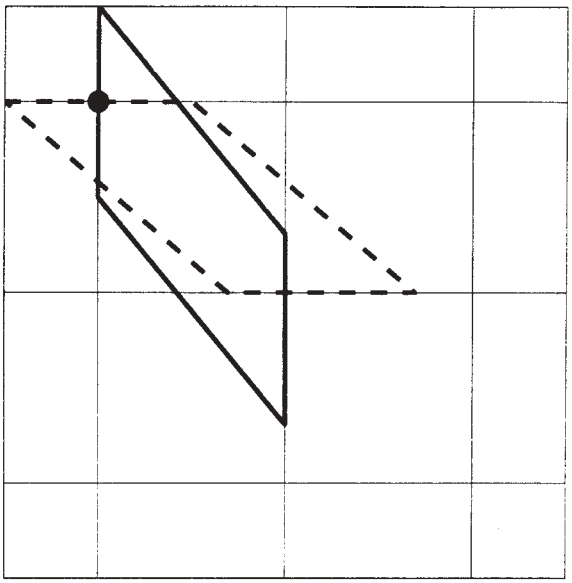

Figure 7. Base of parallelogram switches from $x$ to $y$ axis as wave direction changes from $\theta = 310^{\circ}$ (dashed box) to $\theta = 320^{\circ}$ (solid box).

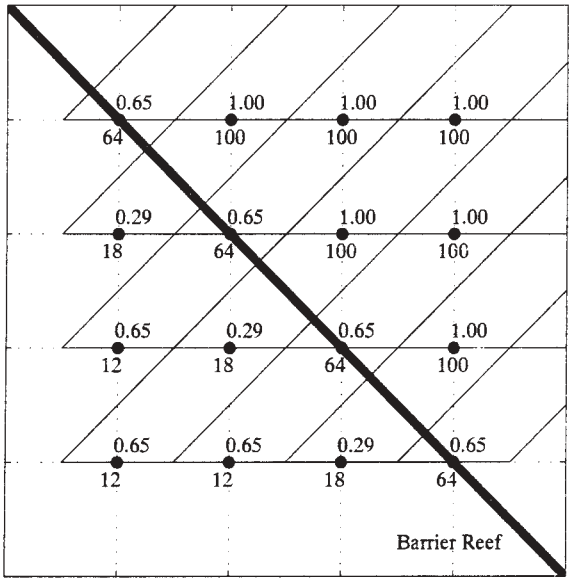


Figure 8. Propagation model results. Thick line is a continuous reef. Parallelograms are draw for $\theta = 225^{\circ}$. Top number at each grid point is porosity. Bottom number is action density.

Since one of the purposed benefits is improvement in boundary conditions provided by coarse grids, a point along the *B*-grid boundary will be investigated. **Figure 9** contains time series of significant wave height at a point on the eastern boundary of the *B* grid indicated on **Figure 10**. Three series are plotted, one each for *No reefs*, *Land* and *Sub-grid* simulations on the *A* grid. The timing and the shape of the three curves are similar with the maximum significant wave height occurring just before landfall. As would be expected the *No reefs* case produces the largest significant wave height (7.4 m), compared with 5.7 m for the *Land* case and 6.5 m for the *sub-grid* case.

Table 1
Grid and Technique Combinations in Model Simulations

| *A* | *B* | *C* |
|---|---|---|
| No reefs | Land | |
| No reefs | Sub-grid | |
| Land | Land | Land |
| Land | Sub-grid | |
| Sub-grid | Land | |
| Sub-grid | Sub-grid | Land |
| Sub-grid | Sub-grid | Sub-grid |

The worst aspect of the selection of which grid points are to be represented as land is the ad hoc nature of the assignment, especially if the grid spacing is much larger than typical reef sizes. As was discussed above, it is obvious that the geometry of the GBR cannot be resolved by the scale of the *A* grid, so that the determination of which *A-grid* points to choose as reef is very subjective. This subjective assignment implies that the accuracy of model results will vary with both location of the computational point relative to reef points and the direction of incident wave energy. For a given point the sheltering may be unrealistic for one wave condition but just fine for another. **Figure 10** shows the assignment of land (reef) points (large dots) for the *A*-grid *Land* case. Notice that the grid points immediately to the north and to the northeast of the output point are designated as reef. This selection should greatly reduce energy from those directions. The question here is not if some other combination of points could have been selected. Of course they could; there are many defensible possibilities. Other choices would change the pattern of the sheltering. For a grid where the resolution is 20 nautical miles and the reefs are at best 1/5 of that, the choice of which points represent reefs, and therefore the pattern of sheltering created, is somewhat arbitrary.

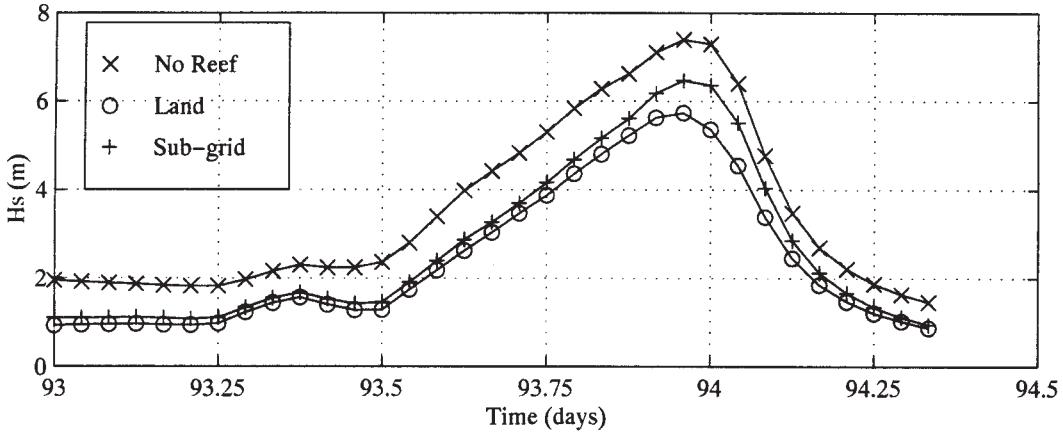


Figure 9. Time series of significant wave height from three different *A*-grid simulations at *B*-grid boundary location (shown in Figure 10). *No reefs* indicates that reefs were not included in bathymetry, *Land* indicates that reefs were input as land, and *Sub-grid* indicates use of the sub-grid scale technique.

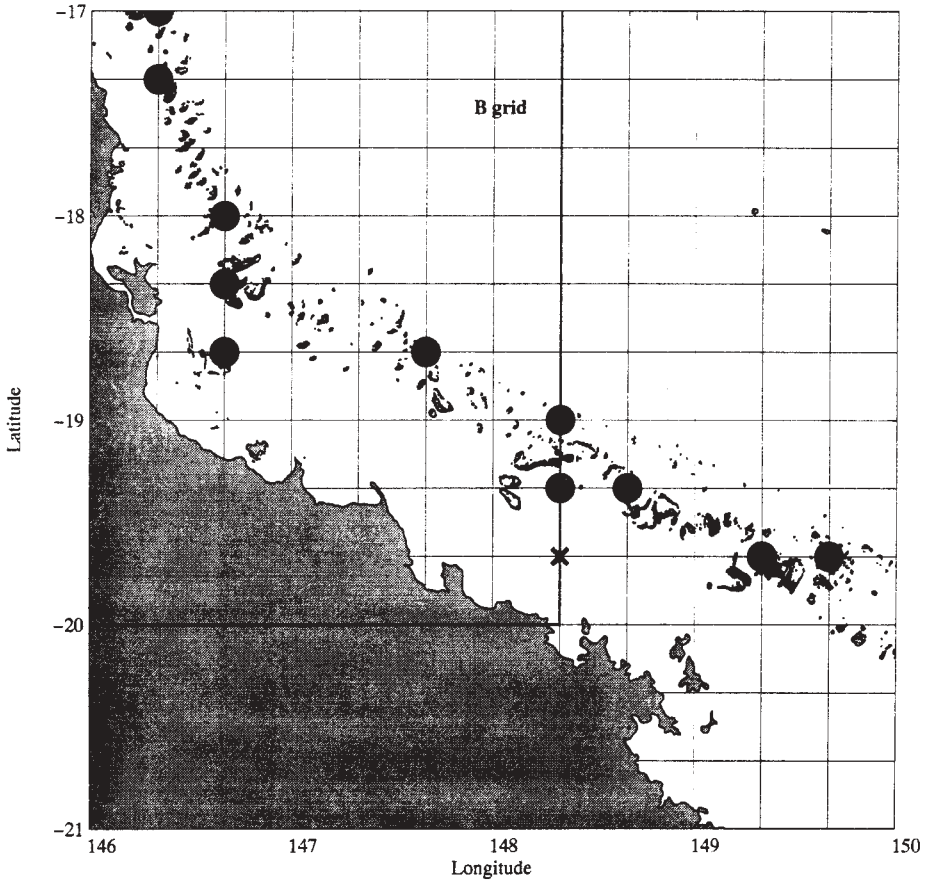


Figure 10. Assignment of land points in *A*-grid near *B*-grid boundary. Grid lines are from *A*-grid. Land points are shown as •. Results shown in Figures 9 and 11 are from point marked with ×.

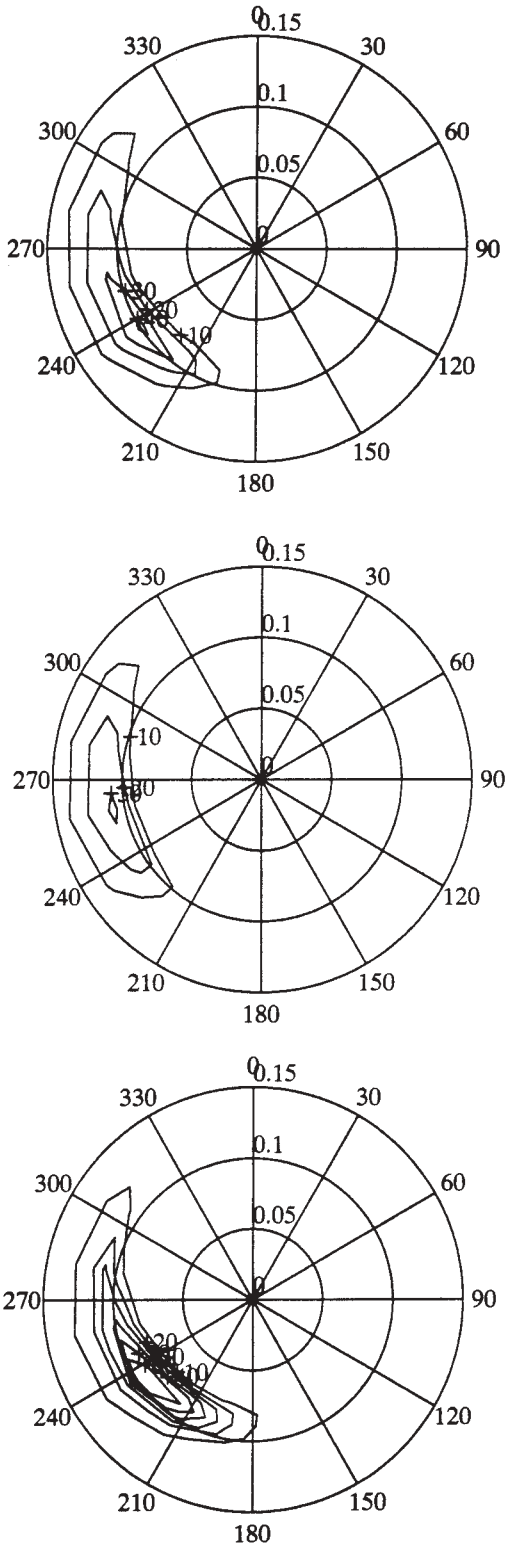


Figure 11. Direction spectra on *B*-grid boundary. Bottom – *No reefs*, Middle- *Reefs as Land*. Top –*Sub-grid*,

**Figure 11** contains polar plots of the directional spectra at the time of maximum significant wave height shown in **Figure 9**. Note that for the *No reef* case the peak direction is around 230°. In the *Land* case much of the energy traveling in this direction is blocked so the peak frequency is shifted towards 270°. Little energy is found in directions from 180° to 230°. The *Sub-grid* case allows some energy to come through the reef gaps and shows a smaller shift in peak frequency compared with the *Land* case.

The *Sub-grid* technique is much less arbitrary than the *Land* technique. The sheltering decisions at each grid point are not based on a coarse yes/no decision process, but rather they are based on a process that is much more smoothly varying and has much better spatial resolution.

Kelso Reef (**Figure 12**) is a site of a tourist pontoon. These permanently moored, barge-like structures are commonly used to provide a base for day use by reef visitors. Some pontoons are multi-million dollar, double decker structures with dimensions reaching 20 × 40 m. Accurate determination of design wave conditions are essential. **Figure 13** contains time histories of significant wave height for three combinations of grid simulations. Two labeled *Sub-grid:Sub-grid* and *Land:Land* represent *B*-grid results. For example the *Sub-grid:Sub-grid* signifies a simulation with an *A* grid using *Sub-grid* technique which provides boundary conditions for a *B* grid that uses *Sub-grid* technique. The *land:land:land* results represent *C*-grid results for a simulation with reefs represented as land on *A*, *B*, and *C* grids. This last case could be considered as the "best" answer that could be provided by the three-grid system without the introduction of the *Sub-grid* technique.

In **Figure 13** it is noteworthy that the *B*-grid results for the *Sub-grid:Sub-grid* match closely to the *C*-grid results for the *Land:Land:Land*. This implies that the *Sub-grid* technique provides this "best" answer at a coarser resolution, and therefore less cost than does the reefs as *Land* technique. Although we believe this to be true in general, the complexity of the reef geometry, coupled with he complexity of the cyclone wind field makes comparisons difficult. The quality of the results of the *Land:Land:Land* simulation will be sensitive to placement of reef points in the immediate vicinity of the output. It is not clear that the *Land:Land:Land* simulation, with all its problems

of resolving reef geometry, offers a result worthy to be labeled "best".

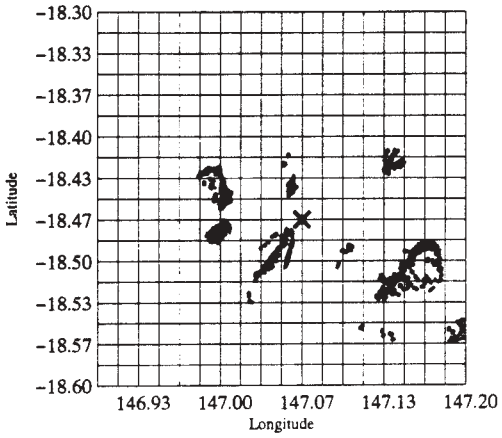


Figure 12. Section of C-grid in the vicinity of Kelso Reef. Output at location indicated with an × is shown in Figure 13.

## 5. CONCLUSIONS

A technique has been presented that incorporates sub-grid scale dissipation caused by coral reefs. The main assumptions of the technique are that (i) waves travel in a straight line in the grid box immediately up wave of the computational point. (ii) Wave energy that intersects a reef is totally dissipated. (iii) This dissipation is more significant than other possible sub-grid scale transformations. The technique has been shown to produce results that compare favorably with the traditional approach of representing the reefs as land. The technique offers promise for improving the boundary conditions provided by coarse grids that cannot adequately resolve reef geometry.

For the *Sub-grid* technique, ad hoc decisions about which points are selected as reef points are not needed. These assignments of reef points may allow reasonable results from standard models at some grid points for some wave directions, but will not provide uniformly good results for all points at all directions. The *Sub*-grid technique creates a smoother more realistic assignment of sheltering, especially for coarse grids

The *Sub-grid* technique is undergoing continued testing in preparation for modeling the ensemble of cyclone waves in the GBR region. Topics which are presently being investigated include: (1) allowing the reefs to be submerged and incorporating breaking into the sheltering mechanism; (2) replacing the sheltering technique presented above with a fine scale ($\Delta S \approx 100$m) propagation and breaking model that would be run for each grid cell as a pre-processor to the wave generation modeling. This simple model would be able to accurately resolve reefs as either land or submerged with multiple grid points. This continuing work will be presented at the workshop.

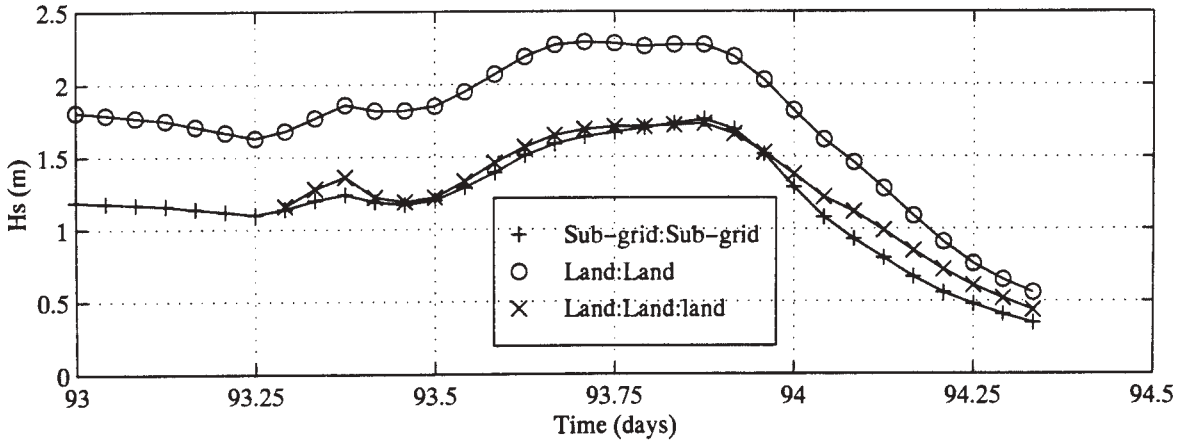


Figure 13. Time series of significant wave height in the vicinity of Kelso Reef. Output node indicated with an × in Figure 12. *Land:land:Land* (×) indicates *C*-grid results for *A-B-C* grid combination with *reefs as Land. Land:Land* (**O**) indicates *B*-grid results for *A-B* grid combination using *reefs as Land. Sub-grid:Sub-grid* (+) indicates *B*-grid results for an *A-B* grid combination using the *Sub-grid* technique.

## 6. REFERENCES


Booij, N, Holthuijsen, L.H., and Ris, R.C. 1996. *The SWAN wave model for shallow water*, Proc. 24th Int. Conf. Coastal Eng, ASCE Vol. 1, pp 668-676.

Hardy, T.A., Young, I.R., Nelson, R.C., and Gourlay, M.R. 1990. Wave attenuation of an offshore coral reef. , Proc. 22th Int. Conf. Coastal Eng, ASCE Vol. 1, pp 330-334.

Komen, *et al.* 1994. *Dynamics and Modeling of Ocean Waves* Cambridge University Press, p. 532.

Lin, R.Q., Huang, N.E. 1996. The Goddard coastal wave model. part 1: numerical method, *J. Physical Oceanography*, Vol 26, pp. 833-847.

Madsen, P.A. Banijamali, B. Schjaffer, H.A., Sorensen, O. 1996. Boussinesq type equations with high accuracy in dispersion and nonlinearity, Proc. 25th Int. Conf. Coastal Eng, ASCE

Tolman, H.L. Effects of numerics on the physics in a third-generation wind-wave model, *J. Physical Oceanography*, Vol 22, pp. 1095-1111.

Young, I.R. and Hardy, T.A. 1993. Measurement and modelling of tropical cyclone waves in the great barrier reef, *Coral Reefs*, Vol 12, pp. 85-95.

# USE OF COUPLED NUMERICAL WAVE MODELS TO SIMULATE THE LITTORAL ENVIRONMENT FROM DEEP WATER TO THE BEACH

Richard Allard, Larry Hsu
Naval Research Laboratory, Stennis Space Ctr, MS

Jane Mckee Smith
Coastal and Hydraulics Laboratory, Vicksburg, MS

Marshall Earle, Theodore Mettlach,
Neptune Sciences, Inc.

Kelley Miles
Sverdrup Technology, Inc.

## 1.0 INTRODUCTION

Development of numerical wave prediction models for purposes of wave forecasting and hindcasting has been a key part of wave research for several decades. Models generally address particular wave processes such as wave generation and propagation (in deep and/or shallow water), wave refraction/diffraction, or wave breaking. Each of these processes involves different physics, spatial scales, and numerical approaches. New types of amphibious systems and strategies require an integrated suite of models that provide predictive capability over a large region from deep-water to the beach and along the coast. Several state-of-the-art models have been developed to the point that they can be implemented operationally or are already used operationally.

The Surf Zone Environmental Representations (SZER) Program is identifying, linking, and operating a coupled suite of wave and surf models to provide automated calculations of wave conditions from deep-water to and along the beach. Unlike traditional wave forecasting and hindcasting, this effort's goal is to develop a methodology so that wave conditions can be calculated realistically over large regions for simulations of military systems and amphibious operations. Outputs ultimately will be used as inputs to simulation and visualization software. The developed methodology accommodates replacement of particular models with updated or improved models as they become available. Models that are incorporated into SZER are WAM, STWAVE, REFDIF1, and the Navy Standard Surf Model (NSSM). Model selection based on physics and practical implementation considerations, regions in which the models are most applicable, and model coupling techniques are described. Examples of coupled model output for Onslow Bay, NC, an important area for the military training and exercise community, are discussed.

## 2.0 MODEL DESCRIPTION

The SZER approach is to integrate a suite of physically consistent wave and surf models originating in deep-water and progressing to shallow water into the surf zone. Figure 1 illustrates the SZER approach implemented for Onslow Bay, NC in which a regional WAM model is independently coupled to the STWAVE and REFDIF1 shallow-water wave models. Outputs from one or both of these models are used as inputs to NSSM. In this paper, comparisons between STWAVE and REFDIF1, as well as recommendations for their implementation are made.

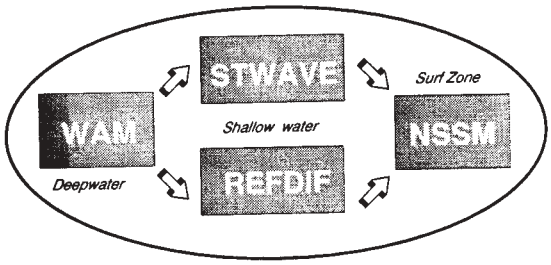


**Figure 1 SZER modeling approach in which the deepwater WAM model is coupled independently to the STWAVE and REFDIF shallow water wave models; the outputs from one or both of these models are used as inputs into NSSM.**

### 2.1 WAM

The WAM wave model is a spectral wave prediction model developed by the WAMDI Group (1988; also Komen et al. 1994), an international consortium of wave modelers. WAM describes the sea surface as a discretized two-dimensional (2-D) spectrum of sea surface elevation variance density.

The Fleet Numerical Meteorology and Oceanography Command and Naval Oceanographic Office (NAVOCEANO) run operational global and regional implementations of WAM Cycle 4 (Wittmann and Farrar 1997). WAM used in this study is the Carolina regional WAM run by NAVOCEANO with a 0.2° resolution and spectra saved at selected locations. This regional WAM is coupled to the 1° North Atlantic WAM. This implementation of WAM is not run routinely by NAVOCEANO. Rather, it is used for exercise support.

WAM is discretized into 25 frequency bands with center frequencies ranging from 0.04333 Hz to 0.32832 Hz, with each frequency being 1.1 times that of the next lower band. Direction is discretized into 24 bands of width 15°. WAM computes the wind-generated energy density of each spectral component. Energy is also propagated in space, with refraction due to depth variation, and dispersion due to the nature of the waves. Because WAM spatial resolution does not resolve bathymetric variations close to a coast, WAM's refraction calculations apply to offshore regions rather than to the regions covered by STWAVE and REFDIF1.

In this study, a 10-day period ranging from March 12-22, 1997 was selected in which WAM wave spectra were saved and subsequently used as inputs to the STWAVE and REFDIF1 shallow-water wave models. Figure 2 shows the WAM domain and locations of the spectra to be used as possible inputs to STWAVE and REFDIF1.

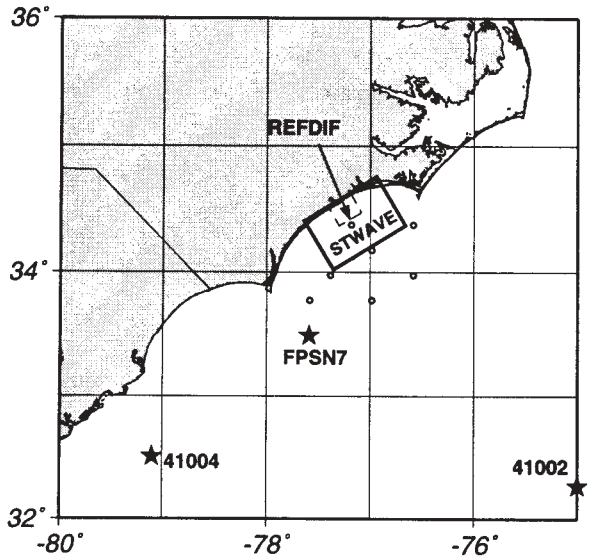


**Figure 2. WAM domain for Carolina coastal area. Buoy station (41002 and 41004) and CMAN station FPSN7 locations shown are used for model comparison. Also shown is the STWAVE and REFDIF model area.**

### 2.1.1 WAM Wind Forcing

The Navy Operational Regional Atmospheric Prediction System (NORAPS) for the Continental United States (CONUS) 10-m winds were used as inputs into the WAM (and STWAVE) hindcasts performed for the area including Onslow Bay, NC. CONUS NORAPS has a horizontal resolution of 0.5° and is run twice daily providing forecast products at 6-hourly intervals. The March 12-22, 1997 period was chosen to represent typical early-spring conditions which included a storm event on 14 March 1997 producing waves in excess of 4 m as indicated by buoy observations and model results discussed in Sec. 2.1.2.

Figure 3 depicts comparisons between observed winds at buoy stations 41002, 41004, and CMAN station FPSN7 (see Figure 2 for locations) and the NORAPS 10-m winds. Figures 3a-c show good agreement with the wind direction for all three locations with buoy station 41002 showing the highest correlation (r=0.92) and CMAN station FPSN7, located at Frying Pan Shoals, with the lowest value of r=0.82. The wind speeds shown in Figures 3d-f show correlations ranging between 0.75 and 0.85, with RMS errors between 2.21 and 2.42 m/s. Winds on 12 March were from the northeast ahead of a warm front which passed to the north of the area by 9Z on 14 March. The winds gradually shift from southerly ahead of an approaching cold front and shift to the northwest on 15 March near 12Z. Winds were strongest at CMAN station FPSN7 on 14 March 18Z with a speed of 20 m/s. Although NORAPS assimilates buoy observations into its analysis, the correlations shown here are reasonable considering that in addition to analyzed fields available every 12 hours, NORAPS 6-hr forecasts were included.

### 2.1.2 WAM Results

Typical frequency and directional energy distributions from March 1997 are shown in Figures 4-5 from WAM. Figure 4 shows the peak of the storm on 14 March 18Z, with a peak wave period of 9.6 sec, a wave height of 4.5 m, and a mean wave direction of 345° (relative to north). The winds at the peak of the storm, that are generating the waves, are over 18 m/sec from the SE and S (see Figure 3). Figure 5 shows the frequency and directional energy distribution 24 hours after the storm peak (15 March 18Z). The spectral peak from the storm is visible at a frequency of 0.1 Hz and a direction of 330°, but a second spectral peak around 0.17 Hz with a direction of 180° also appears. This second peak corresponds to a wind event with a wind speed of 15 m/sec from the north (see Figure 3).

Figure 6 depicts contours of significant wave height (m) for the entire WAM model domain on 14

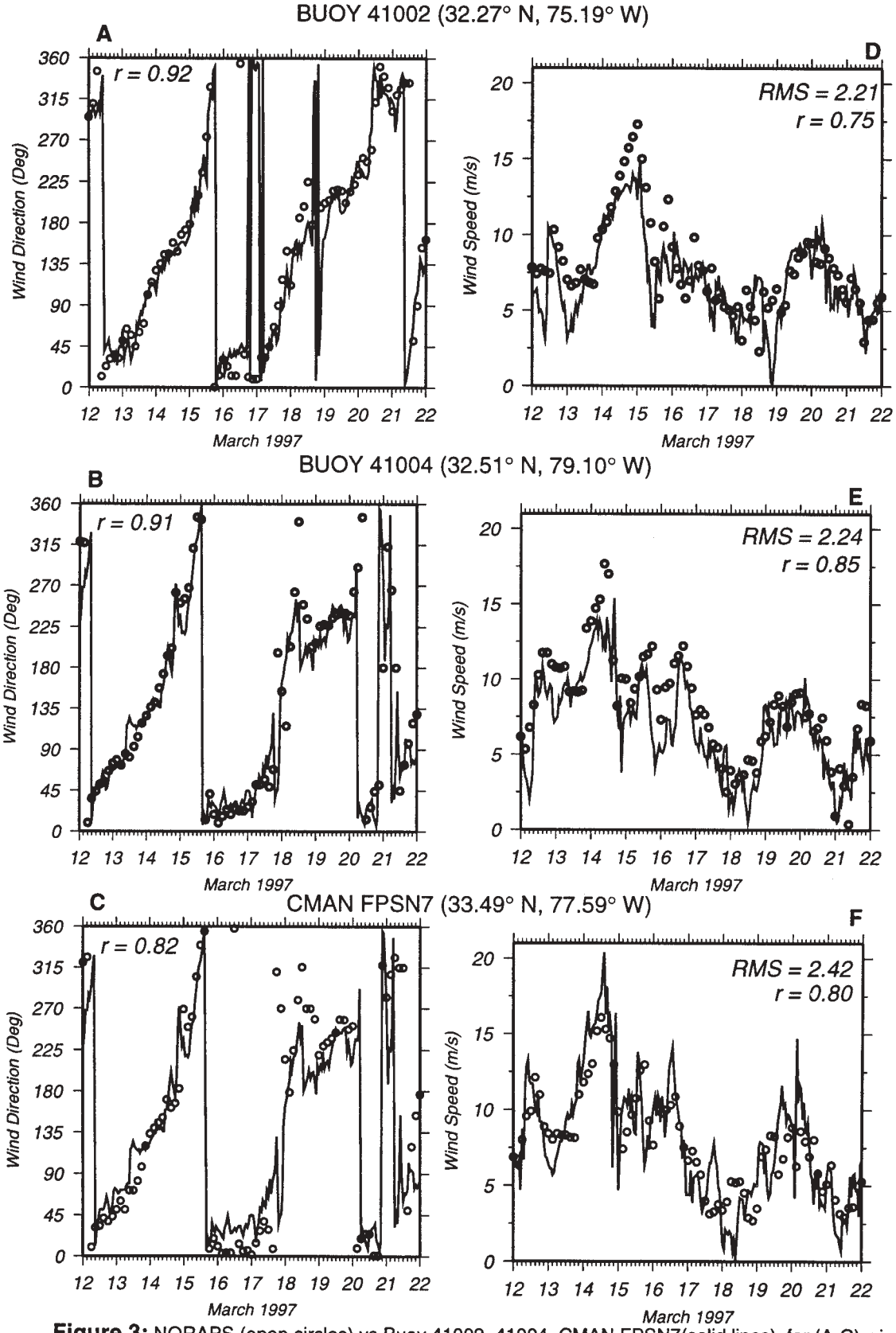


**Figure 3:** NORAPS (open circles) vs Buoy 41002, 41004, CMAN FPSN7(solid lines) for (A-C) wind direction and (D-F) wind speed during March 12-22, 1997.

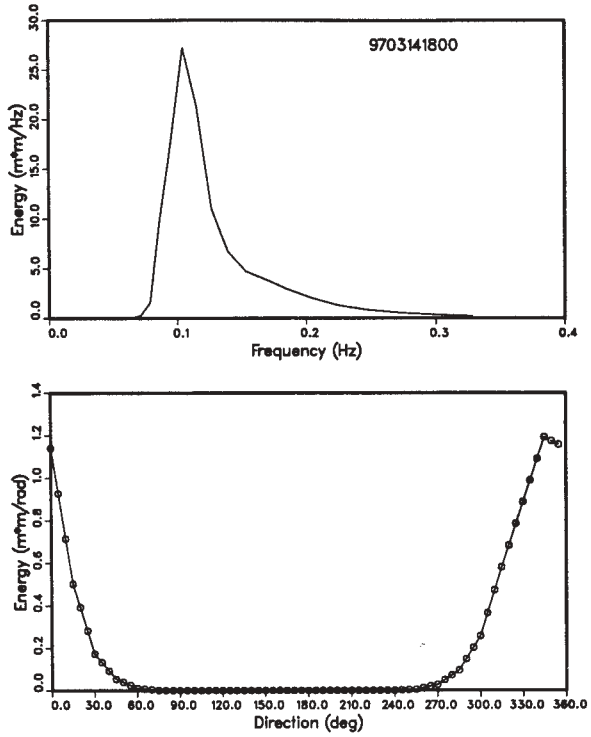


**Figure 4. WAM frequency and directional distributions of wave energy for 14 March 1997 18Z.**

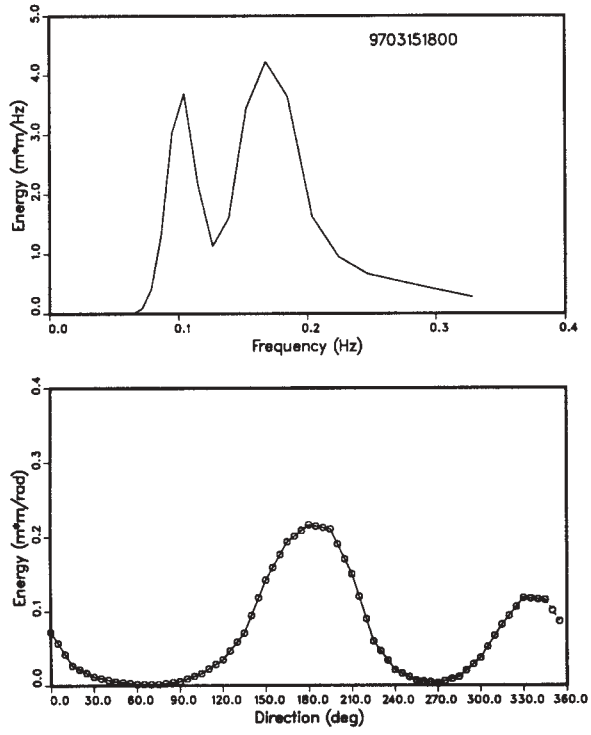


**Figure 5. WAM frequency and directional distributions of wave energy for 15 March 1997 18Z.**

March 18Z. Maximum heights are found in the central portion of the area with values near 4.5 m. Arrows show the direction the waves are moving, generally from the SSE.

Figures 7a-c depict comparisons of observed (solid line) versus WAM (open circles) significant wave height at buoy stations 41002, 41004, and CMAN station FPSN7. The closest WAM grid point to the buoy was chosen as the comparison location. Buoy station 41002, near the southeast corner of the model boundary, had the lowest correlation at 0.90 and a RMS error of 0.42 m. CMAN station FPSN7, closest to the STWAVE model grid, showed the highest correlation with r = 0.94 and an RMS error of 0.29 m. Although all three buoys are outside the area of interest for the shallow-water modeling effort, they demonstrate that the WAM spectra used as input to STWAVE and REFDIF1 are reasonable.

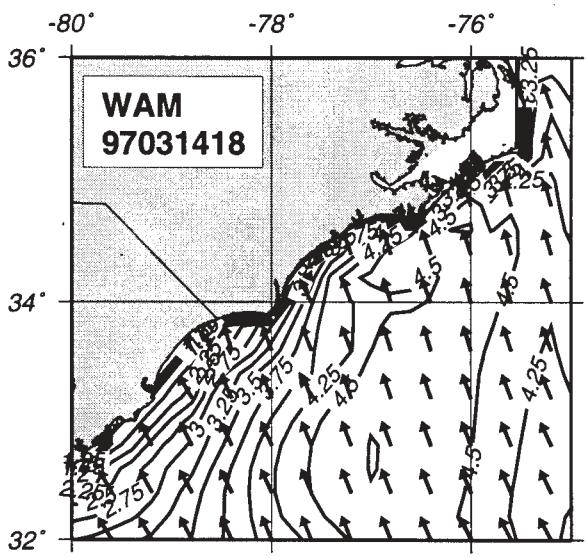


**Figure 6. WAM significant wave height (m) for 14 March 1997 18Z. Arrows show direction waves are propagating.**

Mean wave period from WAM versus observation is shown in Figures 7d-f. Wave periods range from 4-10 seconds, with the longest periods found during the peak of the storm on 14 March. Buoy station 41004 and CMAN station FPSN7 show reasonable correlations, however WAM data near 41002 are consistently 2 seconds higher than observation. This behavior may be a computational artifact because buoy station 41002 is near the southeast corner of the WAM boundary.

## 2.2 STWAVE

Due to time step limitations related to the grid resolution, WAM seldom runs at resolutions higher than 3 minutes (i.e. 5 km). Since bathymetry changes

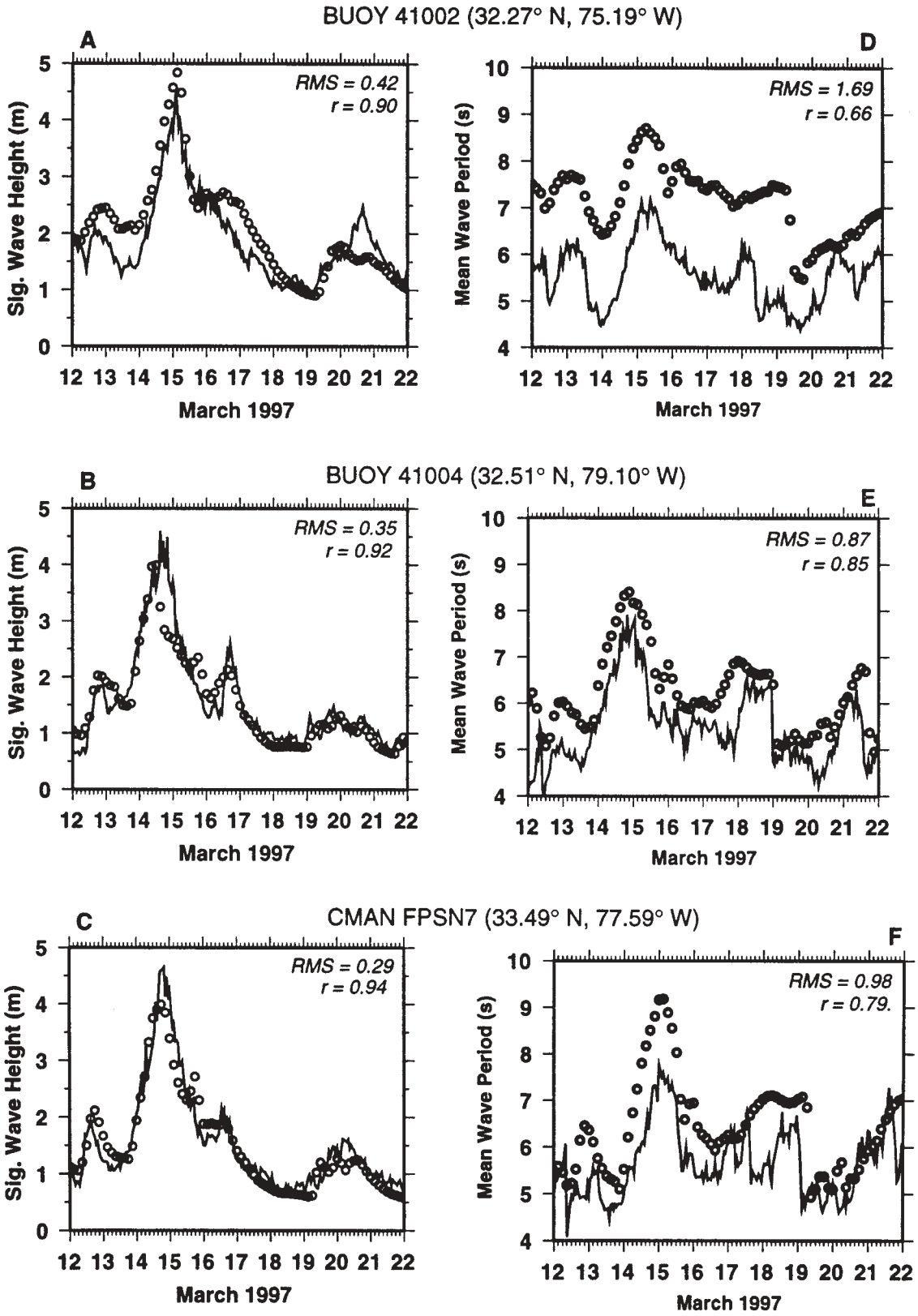


**Figure 7:** WAM (open circles) vs Buoy 41002, 41004, CMAN FPSN7(solid lines) for (A-C) significant wave height (m) and (D-F) mean wave period (s) during March 12-22, 1997.

more rapidly in shallow water, a smaller grid spacing in necessary for computing shallow water propagation. The spectral wave transformation model STWAVE (STeady-state spectral WAVE) (Resio, 1987, 1988a, 1988b, Davis 1992) was selected to transform offshore wave spectra that were hindcast using WAM into the nearshore. This 2-D, spectral wave model was selected because it simulates wave transformation over complex bathymetry with local wind input.

STWAVE numerically solves the steady-state spectral energy balance equation, in which the source terms include wind input, nonlinear wave-wave interactions, dissipation within the wave field, wave-bottom interactions, and depth-induced breaking. The assumptions made in STWAVE are mild bottom slopes, negligible wave reflection, spatially homogenous offshore wave conditions, steady wave and wind conditions, and linear refraction and shoaling.

### 2.2.1 STWAVE Setup

STWAVE operates on a flat grid with square grid cells. The optimal grid orientation is for the $y$ axis to be aligned with the bathymetry contours and the $x$ axis to be aligned normal to the contours. This orientation allows the greatest range of offshore wave angles and the most reliable modeling results.

The Naval Research Laboratory (NRL) supplied bathymetry for the Camp Lejeune region with a resolution of approximately 100 m. The bathymetry was based on data from a combination of sources: (1) National Ocean Service, (2) high-resolution bathymetry collected in April 1996 by the Naval Research Laboratory in support of the Purple Star Exercise (e.g. Nichols and Earle 1996) and (3) data provided by the Naval Oceanographic Office. A triangular irregular network (TIN) was used to create the 3 arc sec bathymetry. Hurricane Fran made landfall just south of Camp Lejeune in early September 1996. This bathymetry does not represent any local changes due to the hurricane.

The STWAVE grid was generated using the ACES2.0 URGG (Uniform Rectilinear Grid GUI[1]) software (Leenknecht and Tanner 1997). Using URGG, the digital bathymetry file (in the format of $x$, $y$, and $z$, with $x$ and $y$ in geographic coordinates and $z$ in meters) were imported and the coordinates were transformed into Universal Transverse Mercator coordinates. The orientation of the grid was selected to be 330° relative to North, so the grid was aligned with the shoreline and bottom contours. For Camp Lejeune, the grid was specified as 201 cells in the cross-shore and 301 cells in the longshore, with a grid resolution of 250 m. URGG uses Delauney triangulation to develop the grid and linear interpolation to assign elevations at each cell. After generation of the grid, the sea bed elevations (- values) were converted to depths (+ values), as required for STWAVE input.

The main driving for the nearshore waves is wave spectra input on the offshore boundary of the STWAVE grid. These input spectra are the output from the time-dependent WAM wave model runs, as discussed in Section 2.1.2. Figure 8 shows the STWAVE grid and the location where the WAM spectra were applied at the offshore boundary. STWAVE is run with the same frequency resolution as WAM. However, the STWAVE grid orientation and directional resolution differ from the WAM output. A 0° wave direction in WAM is a wave propagating to the north. In STWAVE, a 0° wave direction is propagating normal to the offshore edge of the grid. Thus, the WAM spectra were translated into the STWAVE orientation (STWAVE directions = 330° - WAM directions). Also, the directional coverage and resolution differ between the WAM output and the STWAVE input. WAM spectra cover a full 360° with a resolution of 15°. STWAVE spectra cover a half plane (180°) with a resolution of 5°. WAM spectra were truncated to a half plane (neglecting waves traveling away from the coast) and the resolution was linearly interpolated from 15° to 5°.

Figure 8 shows the depth contours over the STWAVE grid. The contours are in meters, with 0 m representing the shoreline. The foreshore slope is relatively steep out to a depth of 10 m, where it becomes very gentle. The contours are approximately parallel to the shoreline. The offshore edge of the grid is at a depth of 30 m. Since the bathymetry at Camp Lejeune is quite regular (reasonably straight and parallel contours), the wave transformation is fairly uniform along the shore. The dominant processes are wave shoaling, refraction, and depth-induced breaking.

Wind speed and direction are also input to STWAVE in the spectral input file. The wind parameters were supplied from NORAPS (see Section 2.1.1). The NORAPS wind speed and direction at the STWAVE grid offshore boundary (34.2° N and 77.0° W) were translated into the STWAVE reference frame for input to STWAVE. The wind speed and direction were assumed constant over the STWAVE model domain.

The hydrodynamical model ADCIRC-2DDI (Luettich et al. 1992, Westerink et al. 1994) was used to calculate water surface elevations which were input into STWAVE. The Advanced CIRCulation model (ADCIRC) is a 2D finite-element model which uses tidal constituents, winds and atmospheric pressure (from NORAPS) to compute water surface elevations.

[1]Graphical User Interface

ADCIRC also outputs depth-averaged currents, however, they were not used in the simulations discussed in this paper.

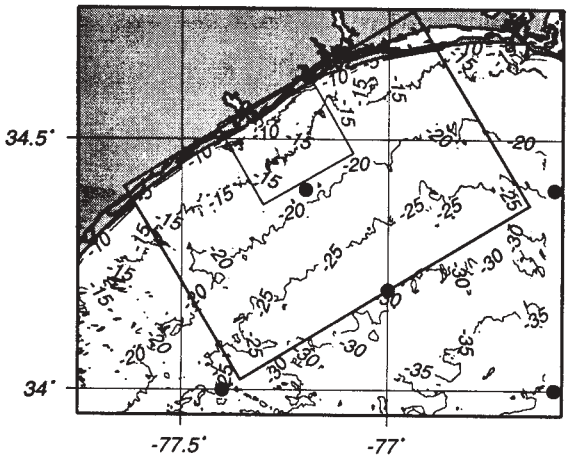


**Figure 8. STWAVE grid and bathymetric contours. Circles denote locations of WAM spectra. Inner-box denotes REFDIF1 model grid. STWAVE outer boundary is approximately parallel to the 30m isobath.**

### 2.2.2 STWAVE Results

The waves during the March 1997 simulation are representative of spring conditions with the growth and decay of waves from a large storm and from several smaller events. The wave heights ranged from 0.5 to 4.5 m and peak periods of 4 to 10 sec. The mean wave directions vary throughout the simulation period, but in the largest event waves are propagating toward the shore at 345°. Figure 9 shows transformed frequency and directional distributions of wave energy at four locations on the STWAVE grid (14 March 1997 18Z). The locations represent a cross-shore transect at the central section of the beach. The local water depths for Figure 9 are 25.3 m, 6.5 m, 4.1 m, and 1.6 m, respectively. The wave directions in Figure 9 are relative to the STWAVE grid, so 0° represents a wave propagating toward 330° relative to north, positive angles are more toward the west and south, and negative angles are more toward the north and east. The shape of the frequency spectra stays about constant for each location, but the energy level decreases due to wave breaking. The spectral shape stays constant because there is little or no additional wave growth between locations. The directional distribution of energy becomes narrower and more peaked in shallow depths due to refraction turning the waves so they are more shore normal.

Figure 10 shows contours of wave height for the same time period. The shoreline is at the right of the plot and the offshore is at the left. The offshore dashed line is the 4.5-m contour and the solid line in the center of the plot is the 4-m contour. The wave height shoals slightly between the 4.5-m and 4-m contours and then decays due to white capping. Very nearshore, the wave height decays due to depth-limited breaking.

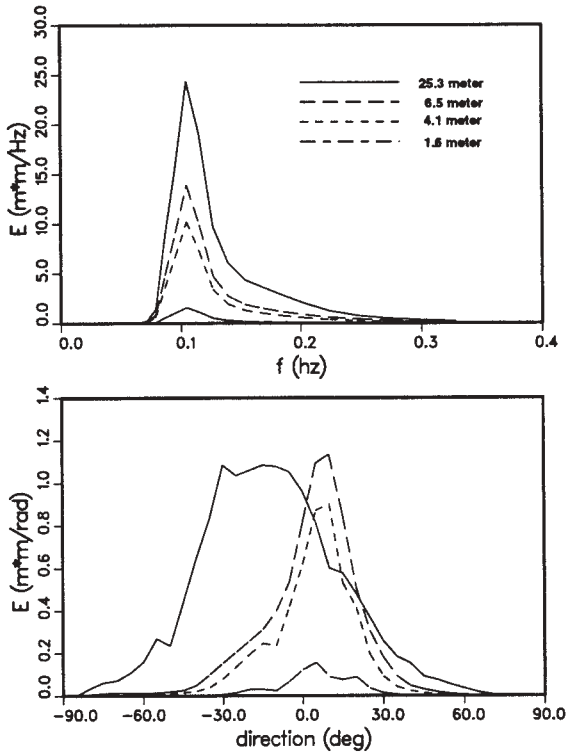


**Figure 9. STWAVE spectra at 25.3 m, 6.5 m, 4.1 m, and 1.6 m depths on 14 March 1997 18Z.**

## 2.3 REFDIF1

In shallow-water, many dynamic processes including shoaling, refraction, diffraction, and energy dissipation due to bottom friction and depth-induced breaking affect wave propagation. In the present operational Navy surf model, the RCPWAVE (Ebersole 1986) wave model was implemented for refraction and diffraction computations. However, RCPWAVE was developed only for open coasts with slowly varying bathymetry. In some cases, the bathymetry needs to be smoothed to achieve numerical stability. In addition, it cannot be applied accurately for locations with very complex bathymetry or surface-piecing features such as islands, or semi-enclosed areas. The coastal wave model REFDIF1 (Kirby and Dalrymple 1994) has a more robust formulation and does not suffer from these limitations.

The REFDIF1 model solves the mild slope equation with the parabolic approximation (Kirby and Dalrymple, 1983). Kirby (1986) extended the range of

model validity for a wider range of input wave angles. The model is solved in finite-difference form using an efficient Crank-Nicholson implicit scheme. Energy dissipation in the model permits treatment of bottom frictional losses due to rough, porous or viscous bottoms, surface film and depth-induced wave breaking. The model also includes the computation of wave-current interaction, which is important at areas near inlets and straits.


**Figure 10. STWAVE wave height contours (m) on 14 March 1997 18Z.**

The REFDIF1 model is designed for simulation of monochromatic and unidirectional wave train propagation. For any realistic wave condition consisting of various combination of wind waves and swell, the user needs to make independent REFDIF1 runs for wave components at fine frequency and direction bandwidths. The results of these separate runs are linearly combined. Outside the surf zone where depth-induced breaking rarely occurs, the superposition approximation is valid and was successfully applied to the Southern California Bight by O'Reilly and Guza (1993).

In wave simulation, REFDIF1 wave hindcasts, nowcasts, or forecasts can be used for each input wave condition each time or a transfer function approach can be applied. In the transfer function approach, calculations are made for all possible frequency and angular components, and the results are saved in a tabular form. The user only needs to derive the transfer function once for a given area assuming no changes in local bathymetry. The transfer function at any point in the model domain consists of amplitude and phase as functions of input wave conditions. For any given wave spectrum input, the spectrum is first divided into many wave components. The amplitude and direction of individual wave components is modified by the corresponding transfer function and then linearly combined with the results from other components to derive the final results.

### 2.3.1 REFDIF1 Setup

In this simulation, the transfer function approach is used. The model is run for every 2° ranging from -70 to +70 degree relative to the model grid. Frequency covers from 0.06 to 0.35 Hz with a total of 18 bands. From 0.06 to 0.2 Hz, model runs are conducted at 0.01 Hz interval. For high frequency waves above 0.2 Hz, the frequency interval increases to 0.5 Hz. All together, 1278 individual wave runs are conducted. The transfer functions are found to be highly variable over a directional spread of a few degrees. Similar variations have been reported by O'Reilly and Guza (1993). Smoothing is applied to the transfer functions to reduce the scatter. In view of the fact that most of the energy are within 50° (positive and negative) to the shore normal for the time period studied, no additional runs are performed for a rotated grid. In a parabolic model such as REFDIF1, the results are degraded for high incident angles beyond 50°. In such cases, grid rotation is often needed to consider high incident angles. Additional discussions about REFDIF1 modeling issues are covered in a paper by Kaihatu et al. (1997) in this proceeding.

### 2.3.2 REFDIF1 Results

The WAM spectra nearest to the shoreline, located at 34.4° N, -77.2° W, at a depth of 18.4 m, is used as input to REFDIF1. The time span covers the same period as described for the STWAVE hindcasts (Sect. 2.2.2) A sample comparison of frequency spectra between STWAVE, REFDIF1 (both at 7-m depth) and WAM (18-m depth) for 14 March 18Z is shown in Figure 11. The REFDIF1 spectra does not differ much from the input WAM spectra. This is to be expected since waves rarely lose energy at the 7-m depth due to breaking. The slight difference between STWAVE and REFDIF1 can be attributed to the inclusion of additional wave growth and white capping dissipation in STWAVE. The major change on wave characteristic in this case is the wave angle as shown in Figure 9. The evolution of sea state for 14 March (00–18 Z) is illustrated in Figure 12. The saturation of high frequency waves is evident. The peak frequency

changes from high to lower frequency, showing a typical wave growth due to wind.

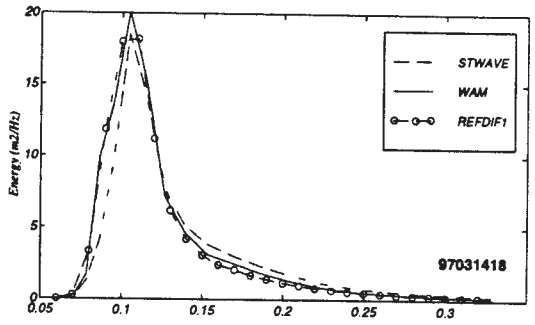


**Figure 11. Comparison of WAM, STWAVE and REFDIF1 wave spectra for 14 March 1997 18Z near Camp Lejeune, NC.**

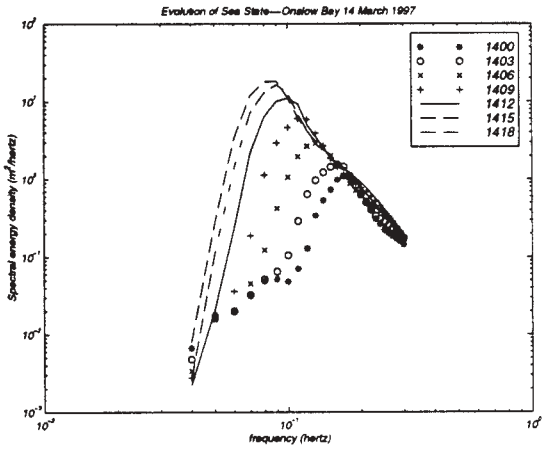


**Figure 12. REFDIF1 spectral density for March 14, 1997. Note changes in peak frequency from high to lower frequency due to wind induced wave growth.**

## 2.4 Navy Standard Surf Model /SURF96

The Navy Standard Surf Model (NSSM) was developed (Earle, 1988, 1989) because previous Navy surf forecasting techniques were largely manual, were based on methods dating to the 1950's, and did not adequately consider local shallow-water effects. NSSM is contained in the Geophysical Fleet Mission Program Library, the Tactical Environmental Support System, and the Mobile Oceanographic Support System. The NSSM has been used extensively by the Fleet and for several applications such as estimating climatological surf conditions at selected beaches for development of the Marine Corps' Advanced Amphibious Assault Vehicle (McDermid et al. 1997; Nichols et al. 1997)

The NSSM is composed of two main modules, a wave refraction model and the surf model itself, SURF96. The most recent version of the surf model, SURF96 incorporates several theoretical and numerical improvements (Earle et al.1997; Hsu et al. 1997) and was used for this work. The surf model's strengths are: rapid operation for field use and simulations, relatively simple operation and mathematical robustness for non-expert use, realistic depiction of breaking wave locations, and provision of detailed information (breaker heights, types, longshore currents) across the surf zone. The model automatically provides parameters for planing amphibious operations as described in the Joint Surf Manual (COMNAVSURFPAC/COMNAVSURFLANT, 1987).

SURF96 is a one-dimensional parametric model largely based on concepts developed by Thornton and Guza (1983, 1986). The assumptions include: (1) approximately straight and parallel bottom contours within the surf zone; (2) a directional wave spectrum that is narrow banded in frequency and direction; (3) a Rayleigh wave height distribution; and (4) linear wave theory. The directional wave spectrum used for model initialization can be obtained from a wave model (WAM, STWAVE, REFDIF) or measurements. If an offshore directional wave spectrum is used, it must be properly refracted, shoaled and diffracted to a starting depth which lies seaward of the breaker line. The directional wave energy distribution is reduced to three representative physical values; (1) the direction of the vertically averaged wave momentum flux, (2) the incident wave energy, and (3) the dominant wave frequency. The direction of the wave momentum flux is computed using radiation stress (e.g. Longuet-Higgins, 1970a,b). The model incrementally calculates wave energy from which wave heights are determined along a transect normal to the beach to very near the beach and still water level. As waves move through the surf zone, the average rate of energy dissipation due to wave breaking and frictional dissipation balances the gradient of the shoreward energy flux. Longshore current calculations at each increment are based on longshore current theory using radiation stress (e.g. Longuet-Higgins, 1970a,b). Current calculations include local wind stress effects. The longshore current module is being examined to provide improved performance for beaches with shallow offshore bars. Such a bar was not present for these data (Figure 13).

The percentage of breaking and broken waves across the surf zone is a model output. Surf zone width is considered as the most seaward point where ten percent of the waves are breaking or broken. Percentages of breaker type (spilling, plunging, or surging) are determined across the surf zone from the probability distribution of breaking waves using a widely accepted parameterization based on breaker height, breaker period, and bottom slope. Breaker height parameters specified in the *Joint Surf Manual*

are determined for regions where breakers are largest. The Modified Surf Index (MSI) defined in the *Joint Surf Manual* is calculated automatically. The MSI determines whether particular types of conventional landing craft (not air-cushion vehicles) can be used.

### 2.4.1 SURF96 Results

SURF96 hindcasts for the simulation period 12-22 March 1997 were performed using wave spectra from two sources: (1) REFDIF1 and (2) STWAVE. A Navy SEAL beach survey collected for the Purple Star Exercise was used as the beach profile in both sets of SURF96 model runs. Hourly wind speed and direction from the Marine Corps Air Station (34.7° N, 77.43° W) at New River, NC were used. NORAPS winds were available, however it was felt that observed winds would provide the most realistic input into SURF96. Because water elevations, including tides, affect surf, water elevations from ADCIRC were input into SURF96. The SURF96 code was adapted to accept wave spectra from REFDIF1 and STWAVE.

Shallow-water wave spectra from STWAVE and REFDIF1 hindcasts are saved for selected nearshore points. In this paper, the directional spectra from both models at a 7-m depth along the beach survey line are used as input to SURF96. The 7-m location is selected so that only a small probability of depth-induced wave breaking will occur at this location. This location was selected to assure that the assumption of no depth-induced breaking is valid for the REFDIF1 transfer function approach.

Figure 13 depicts SURF96 results for 15 March 03Z. The top panel shows the Navy SEAL beach team survey used as input to SURF96. The slope is rather steep from the coastline to approximately 250 meters offshore (at a depth of 4 m) where the slope levels off. Figure 13b shows significant wave height along the shore-normal transect to 900 m offshore. The solid line depicts SURF96 results with input from STWAVE and the open circles represent results in which REFDIF1 spectra were input. Figure 13c shows almost identical results of the percentage of breaking waves when comparing SURF96 output using inputs from REFDIF1 and STWAVE. The surf zone width (not shown) is defined as the offshore location where at least 10% of the waves break. This occurs at a distance of approximately 225 m. (Figure 14 depicts the variation of surf zone width with time). The waves do not begin to break until water depths become less than 4 m because the input significant wave heights are between 2 m and 3 m. Finally, Figure 13d shows the longshore current variation with distance and model input into SURF96. The maximum longshore current occurs at a distance of 150 m offshore. Currents using STWAVE input show larger magnitudes than those using REFDIF1 input in Figure 13 because STWAVE surf zone incident wave angles are slightly larger than those for REFDIF1. Wave directions are incident at small angles from a perpendicular to the beach so that currents are sensitive to small changes in wave directions just outside of the surf zone. At various times, slightly different wave directions rather than different wave heights seem to account for current differences between the two model inputs.

Figure 14 presents time series of SURF96 output during 12-22 March 1997. The top panel depicts wind speed and direction provided from the Marine Corps Air Station. Wind speeds are highest on 14 March in advance of a strong cold front as wind directions are generally from the south. The wind gradually veers to the west and northwest as the cold front passes through the area and become southerly on 18 March. Late in the day on 19 March the winds again shift to a direction from the north as yet another cold front passes through the area.

The second panel depicts the significant wave height, which is an input parameter to the surf model. The solid line represents the STWAVE whereas the open circles represent REFDIF1 output. Both models yield very similar results. The highest wave heights are associated with the major storm event occurring on 14 March.

The third panels shows the wave angle at the 7-m depth. 0° represents waves moving perpendicular to the shoreline. A positive breaker angle is shown to be for breakers moving toward the right flank relative to a sight line perpendicular to the beach. Again, results from SURF96 with REFDIF1 and STWAVE as inputs are similar. From 12 March 21Z to 13 March 18Z, REFDIF1 shows a wave direction approximately 10° more negative than STWAVE. Some of this variation may be attributed to wind forcing, which is included in STWAVE, but is not for REFDIF1.

The fourth panel depicts the surf zone width, which is defined as the offshore location where at least 10% of the waves are breaking. Throughout the 10-day hindcast period, surf zone widths are generally between 60-200 m. The exception occurs during an 18-hr period from 14 March 15Z to 15 March 03Z when the width exceeds 300 meters, when a major storm event affected the area. The effects of tides are evident by the modulation in surf zone width throughout the period.

The fifth panel shows the longshore current with magnitude maxima near 0.8 m/s on 14 March. There is a change in current direction associated with changes in wind and wave directions relative to the beach.

The final panel shows the modified surf index (MSI) which is derived using the maximum wave height, maximum longshore current, breaker angle,

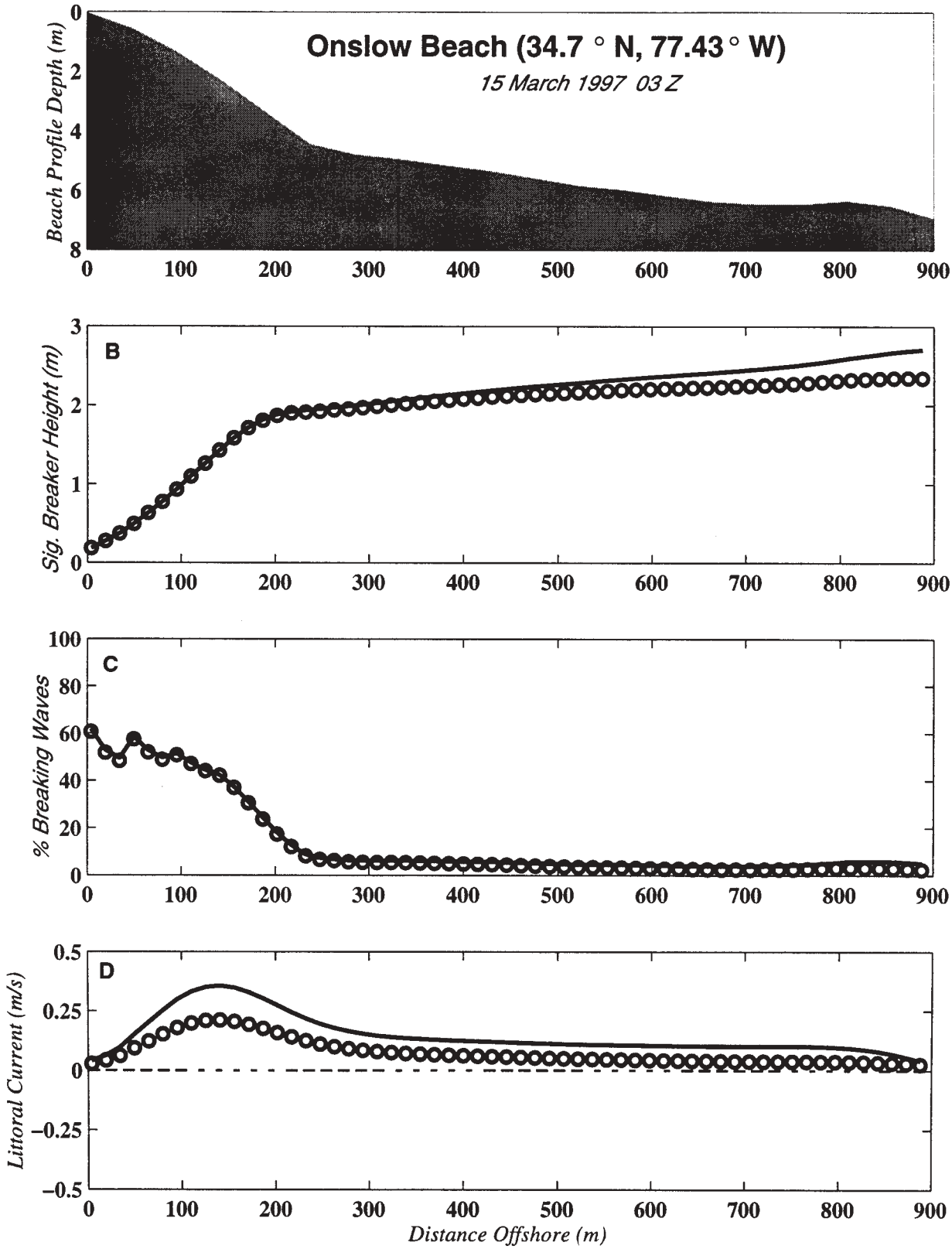


*Figure 13. SURF96 output valid on 15 March 1997 03Z. (a) Navy Seal Team beach profile used in SURF96 calculations. (b) significant wave height (m) based on REFDIF1 (circles) and STWAVE (solid) input. (c) % breaking waves (d) Longshore current (m/s).*

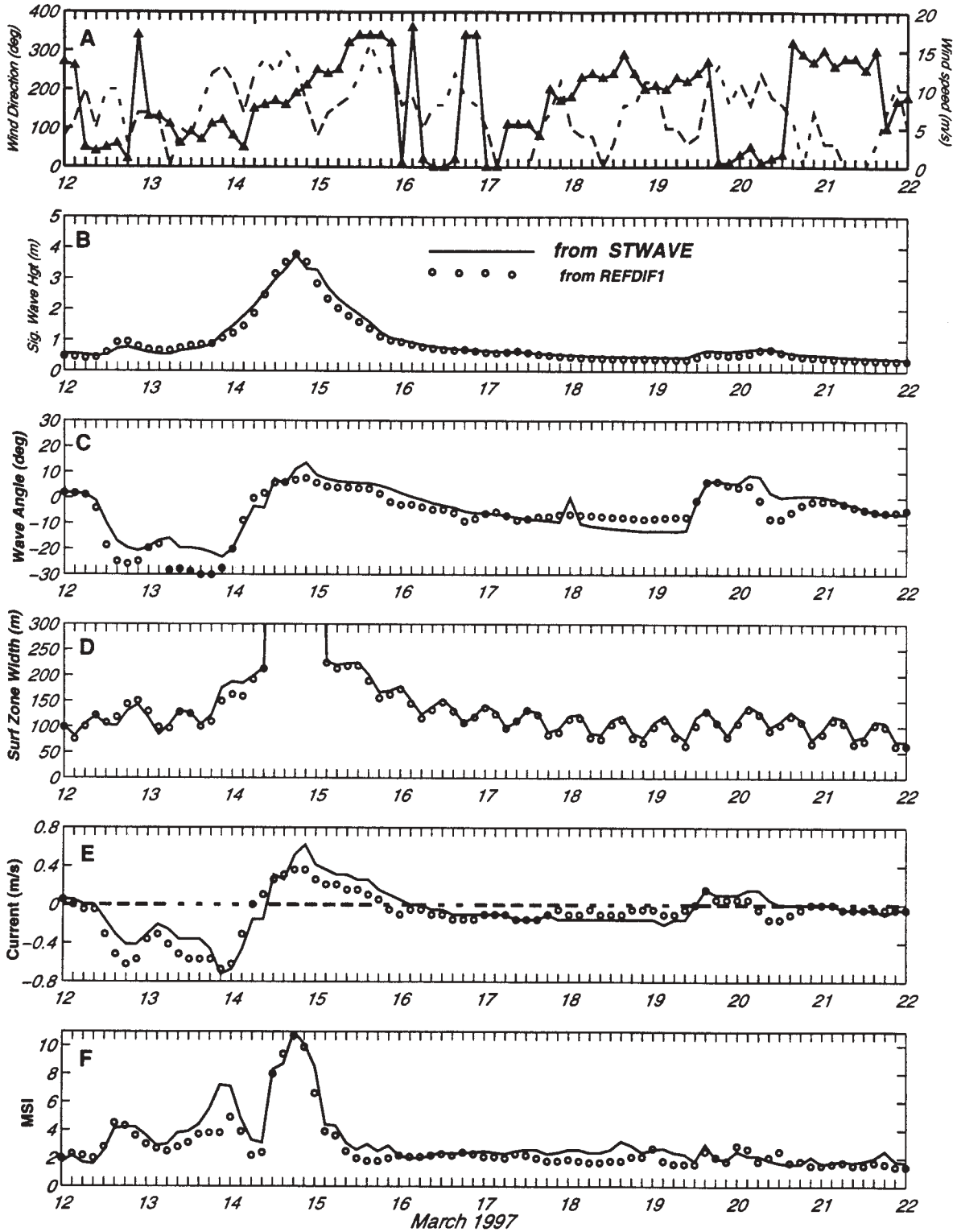


*Figure 14: Time series of (a) Wind direction (solid) and wind speed (dashed) near Onslow Beach, NC,(b) Significant wave height (m) from REFDIF1 (circles) and STWAVE (solid), (c) Wave angle (degrees), (d) Surf Zone Width (m), (e) longshore current and (f) Modified Surf Index (MSI).*

wave period, and breaker type and based on the *Joint Surf Manual*. Depending on the amphibious landing craft, large values of MSI beyond a critical threshold value would deem a potential landing as unsafe. High values late on 14 March would rule out use of most conventional amphibious landing craft.

## 3.0 SZER Model Validation

All the models contained in the SZER model suite have been validated and tested in either laboratory and/or field tests. Most recently, the Navy completed a validation report (Hsu et al. 1997) in which data collected at Duck, NC during the Duck Experiment on Low-Frequency and Incident-band Lonsghore and Across-shore Hydrodynamics (DELILAH) were used to validate the Navy Standard Surf Model in which REFDIF1 was used as the refraction module. However, this suite of coupled models has not been tested as a complete system of models.

During the period of 26 August – 5 September 1997, surf zone model validation data were collected at Onslow Bay, NC during the Joint Countermeasures Advanced Concept Technology Demonstration and Joint Training Fleet Exercise. Three directional wave buoys developed by the NRL Center for Tactical Oceanography Warfare Support (TOWS) Office and the Space and Naval Warfare Systems Command (SPAWAR) were moored in 3, 7, and 10 m of water. In addition, pressure sensor wave and tide gauges were deployed outside and within the surf zone. The surf zone environmental processes were monitored using video image processing techniques which allow quantification of both hydrodynamical and geological parameters including wave period, wave angle, wave speed, surf zone width, shoreline location, and sand bar structure. Estimates of longshore current and bathymetry can also be inferred. Fiscal Year 1998 plans call for running hindcasts of the models described in this paper for Onslow Bay, NC area and validating model output with data collected during this exercise.

## 4.0 SUMMARY

A coupled wave/surf model suite consisting of "off-the-shelf" wave and surf models is evaluated. A series of hindcasts are performed for the Onslow Bay, NC area during the period 12-22 March 1997.

The deepwater WAM model shows very good agreement with available buoy and CMAN data. WAM directional wave spectra are independently fed into two shallow-water wave models: (1) STWAVE and (2) REFDIF1. Model outputs from STWAVE and REFDIF1 are remarkably similar.

Outputs from STWAVE and REFDIF1 drive a recent version, SURF96, of the NSSM to provide detailed information across the surf zone. Surf parameters of interest for simulations of military systems and amphibious operations are similar for inputs from both models. Use of water elevations, including tides, from ADCIRC illustrates effects that varying water elevations can have on the surf zone width. Relatively high wave heights, large surf zone widths, and high MSI values on 14 March show how combined use of these models can simulate conditions that could adversely affect use of military systems and amphibious operations.

## ACKNOWLEDGEMENTS

This work was conducted under the sponsorship of the Ocean Executive Agent and the Defense Modeling and Simulation Office. Implementation of REFDIF1 for Navy use was sponsored by SPAWAR. The Office of Naval Research (ONR) and SPAWAR sponsored NSSM improvements resulting in SURF96. Pressure sensor wave and tide gauges used to collect nearshore validation data were provided by Janice Boyd (NRL). Surf zone video data were acquired by Todd Holland (NRL) and Professor Rob Holman (Oregon State University). The authors wish to thank Paul Farrar of NAVOCEANO for performing the WAM runs and providing WAM data, John Breckenridge and Doug May (NRL) for providing bathymetry, Mona Collins (NRL) for processing the WAM data, CPL Barber for providing hourly wind observations from the Marine Corps Air Station (MCAS) at New River, NC, Cindy McClure and the Florida State University Meteorology Dept. for providing weather maps and the National Data Buoy Center for providing buoy data. REFDIF1 computations were performed on the NAVO Cray C90 utilizing High Performance Computing Resources. The authors acknowledge the office of the Chief of Engineers, U.S. Army Corps of Engineers, for authorizing publication of this paper.

## 5.0 REFERENCES

COMNAVSURFPAC/COMNAVSURFLANT, 1987: Joint surf manual. Instruction 3840.1B.

Davis, J. E., 1992: STWAVE theory and program documentation, chapter 8 in coastal modeling system user's manual, instructional report CERC-91-1, supplement 1, M. A. Cialone (ed.), U.S. Army Corps of Engineers Waterways Experiment Station, Vicksburg, MS.

Earle, M.D., 1989: Surf forecasting software scientific reference manual. NORDA Technical Note 351,

Naval Research Laboratory, Stennis Space Center, MS, 1989, 261 pp.

Earle, M.D., 1988: Surf forecasting software user's manual. NORDA Technical Note 352, Naval Research Laboratory, Stennis Space Center, MS, 194 pp.

Earle, M.D., 1991: Surf forecasting software improvements. MEC Systems Corp. Report, Manassas, VA.

Earle, M.D., L.N. Migues, D.A. Osiecki, and T.R. Mettlach, 1997: Oceanographic and atmospheric master library Navy standard surf model, version 3.0, documentation. NRL Technical Report, Stennis Space Center, in preparation.

Ebersole, B.A., M.A. Cialone and M.D. Prater, 1986: Regional coastal processes numerical modeling system, report 1, RCPWAVE (A linear wave propagation model for engineering use). Dept. of the Army, Waterways Experimental Station, Technical Report CERC-86-4, 71pp.

Hsu, Y.L., T. Mettlach, E. Kennelly, and M. Earle, 1997: Interim report on validation of the Navy standard surf model. NRL Memorandum Report NRL/MR/7322—97-8054, Stennis Space Center, MS, 233 pp.

Kaihatu, J.M., W.E. Rogers, Y.L. Hsu and W.C. O'Reilly, 1998: Use of phase-resolving numerical wave models in coastal areas. Proceedings of the 5th International Workshop on Wave Hindcasting and Forecasting, Melbourne, Fl.

Kirby, J.T, 1986: Rational Approximations in the Parabolic Equation Method for Water Waves. *Coastal Eng.*, **10**, 355-376.

Kirby, J.T., and R.A. Dalrymple, 1983: A parabolic equation for the combined refraction-diffraction of stokes waves by mildly varying topography. *J. Fluid Mech.*, **136**, 543-566.

Kirby, J.T., and R.A. Dalrymple, 1994: Combined refraction (diffraction model REF/DIF1, Version 2.5, documentation and user's manual. Report 94-22, Center for Applied Coastal Research, University of Delaware.

Komen, G.J., L. Cavaleri, M. Donelan, K. Hasselmann, S. Hasselmann, and P.A.E.M. Janssen, 1994: Dynamics and modelling of ocean waves. Cambridge University Press, Cambridge, U.K. and New York, N.Y., 532 pp.

Leenknecht, D.A. and W.W. Tanner, 1997: Grid generation and data analysis for wave transformation models. Proceedings of the 4th Congress on Computing in Civil Engineering, Philadelphia, PA. (in press).

Longuet-Higgins, M.S., 1970a: Longshore currents generated by obliquely incident sea waves, 1. *J. Geo. Res.*, **75**, No. 33, 6778-6789.

Longuet-Higgins, M.S., 1970b: Longshore currents generated by obliquely incident sea waves, 2. *J. Geo. Res.*, **75**, No. 33, 6790-6801.

Luettich, R.A., Westerink, J.J., and Scheffner, 1992: ADCIRC: An advanced three-dimensional circulation model for shelves, coasts, and estuaries, report 1: theory and methodology of ADCIRC-2DDI and ADCIRC-3DL. Technical Report DRP-92-6, US Army Engineer Waterways Experiment Station, Vicksburg, MS.

O'Reilly, W. C., and R.T. Guza, 1993: A comparison of two spectral wave models in the southern California bight. *Coastal Eng.*, **19**, 263-282.

McDermid, J.G., M.D. Earle, D.C. Herringsaw, S.M. Mayfield, and C.R. Nichols, 1997: METOC conditions affecting AAAV ship-to-objective maneuver: a detailed analysis of power projection points sited along Iranian and Korean coasts, NRL Memorandum Report NRL/MR/717--97-8060.

Nichols, C.R.. and M.D. Earle, and J.G. McDermid , 1997: Coast types and wave statistics for strategic littoral regions. Draft report by Neptune Sciences, Inc., input for NRL-SSC report.

Nichols, C.R. and M.D. Earle, 1996: Use of a coupled wave buoy-surf model system to support combined joint task force exercise-96/Purple Star, Report for Center for Tactical Oceanographic Warfare Support Program Office, NRL, Stennis Space Center, MS.

Resio, D.T., 1987: Shallow-Water waves I: theory. *Journal of Waterways, Ports, Coastal, and Ocean Engineering*, **113** (3), 264-281.

Resio, D.T., 1988a: Shallow-Water waves II: data comparisons, *Journal of Waterways, Ports, Coastal, and Ocean Engineering*, **114** (1), 50-65.

Resio, D.T., 1988b: A steady-state wave model for coastal applications. Proceedings of the 21st Coastal Engineering Conference, ASCE, 929-940.

Thornton, E.B., and R.T. Guza, 1983: Transformation of wave height distributions. *J. Geo. Res*, **88** (C10), 5925-5938.

Thornton, E.B., and R.T. Guza, 1986: Surf zone longshore currents and random waves: field data and models. *J. Phys. Oceanogr.*, **16**, 1165-1178.

WAMDI Group, 1988: The WAM model – a third-generation ocean wave prediction model. *J. Phys. Ocean.* **18**, 1775-1810.

Westerink, J.J., C.A. Blain, R.A. Luettich, and N. Sheffner, 1994: ADCIRC: An advanced three-dimensional circulation model for shelves, coasts, and estuaries, Report 2: Users's manual for ADCIRC-2DDI. Technical Report DRP-92-6, US Army Engineer Waterways Experiment Station, Vicksburg, MS.

Wittmann, P.A. and P.D. Farrar, 1997: Global, regional and coastal wave prediction. *MTS Journal*, **31**, 76-82.

# MODELING WAVES AT PONCE DE LEON INLET, FLORIDA

Jane McKee Smith, Adele Militello, S. Jarrell Smith

USAE Waterways Experiment Station, Coastal and Hydraulics Laboratory
Vicksburg, Mississippi, USA

## 1.0 INTRODUCTION

Ponce de Leon Inlet, located on the Atlantic Ocean Coast of Florida, USA, experiences wave and current conditions that significantly impact coastal processes and navigation. Between 1981 and 1991, 347 vessels ran aground, 109 vessels capsized, and 20 lives were lost at the inlet (U.S. Army Corps of Engineers (USACE), Jacksonville District 1993). Maintenance problems exist at the inlet, including scour in the inlet throat near the north jetty, erosion of the north spit in the interior of the inlet, and migration of the navigation channel. The nearshore bathymetry at Ponce Inlet is complex due to the presence of the inlet, jetties, and a large ebb shoal. The tidal currents in the inlet throat can exceed 1 m/sec. Ponce de Leon Inlet is small enough to allow comprehensive measurements, yet large enough to experience substantial engineering problems.

To quantify wave conditions at Ponce de Leon Inlet, a steady-state, spectral wave model is applied together with a depth-integrated circulation model. These models are components of a system of integrated numerical models (wave, circulation, and sediment transport) to predict coastal inlet processes, which is an objective of the USACE Coastal Inlets Research Program (CIRP). Also, as part of CIRP, field measurements of waves and water levels at Ponce Inlet were made from September 1995 through October of 1997. Measurements for a storm in March 1996 are used to evaluate the performance of the wave model for a complex environment in the presence of currents.

The purpose of this paper is to present results from the application of a spectral wave model, with wave-current interaction, at Ponce de Leon Inlet for a storm in March 1996. First, the field measurements of waves, water levels, and bathymetry at Ponce Inlet are described. Then the characteristics of the March 1996 storm are discussed as background for model comparisons. The circulation model, which supplies current fields for the wave model, and circulation results are presented in Section 4. Section 5 presents the wave modeling and wave results. A summary and conclusions are given in the final section.

## 2.0 FIELD MEASUREMENTS

A field measurement program began in September 1995 to measure inlet processes at Ponce Inlet. Details of the measurement program are given by Howell (1996). The measurements of interest in this paper are water-surface elevations and waves for a storm in March 1996, and bathymetry. These measurements and the storm characteristics are described in this section.

### 2.1 Water Level Measurements

Water-surface elevations were measured at four locations in the back bay at Ponce Inlet (Gauge SPRSBAY1 - 1.8 km north of the inlet, SPRSBAY3 - 4.4 km south of the inlet, SPRSBAY2 - 2.6 km west of the inlet in the Intracoastal Waterway, and VITLBAY3 - at the Ponce Inlet Coast Guard Station 1.5 km south of the inlet) and at three ocean locations (DWG1INT1 - 1.7 km north of the inlet, DWG1EBB1 - on the ebb shoal, and DWG1OTH1 - in the outer throat). The locations of the gauges are shown in Figure 1, referenced to State Plane coordinates (grid markings are at approximately 1.5 km spacing). The gauges were all ParoScientific Digiquartz pressure sensors, with the exception of the gauge at the Coastal Guard Station, which was a stilling well tide gauge. The bay gauges were surveyed to the National Geodetic Vertical Datum (NGVD), and the ocean gauges were corrected to the same datum using a iterative minimization-of-residuals technique applied between the ocean and Coast Guard Station gauges over a six-month period (Howell 1996). The pressure gauges were corrected for atmospheric pressure. The bay water-level gauges recorded averages at 6-min intervals and the ocean gauges sampled at 0.2-sec intervals.

### 2.2 Wave Measurements

Waves were measured at the same three ocean locations as the water levels, north of the inlet, ebb shoal, and outer throat, at approximate water depths of 14, 7, and 5 m NGVD, respectively. Directional waves were measured with a 1.6-m base-line equilateral triangle pressure gauge array, using three ParoScientific gauges. The gauges were sampled continuously at 5 Hz. Thirty-four-minute

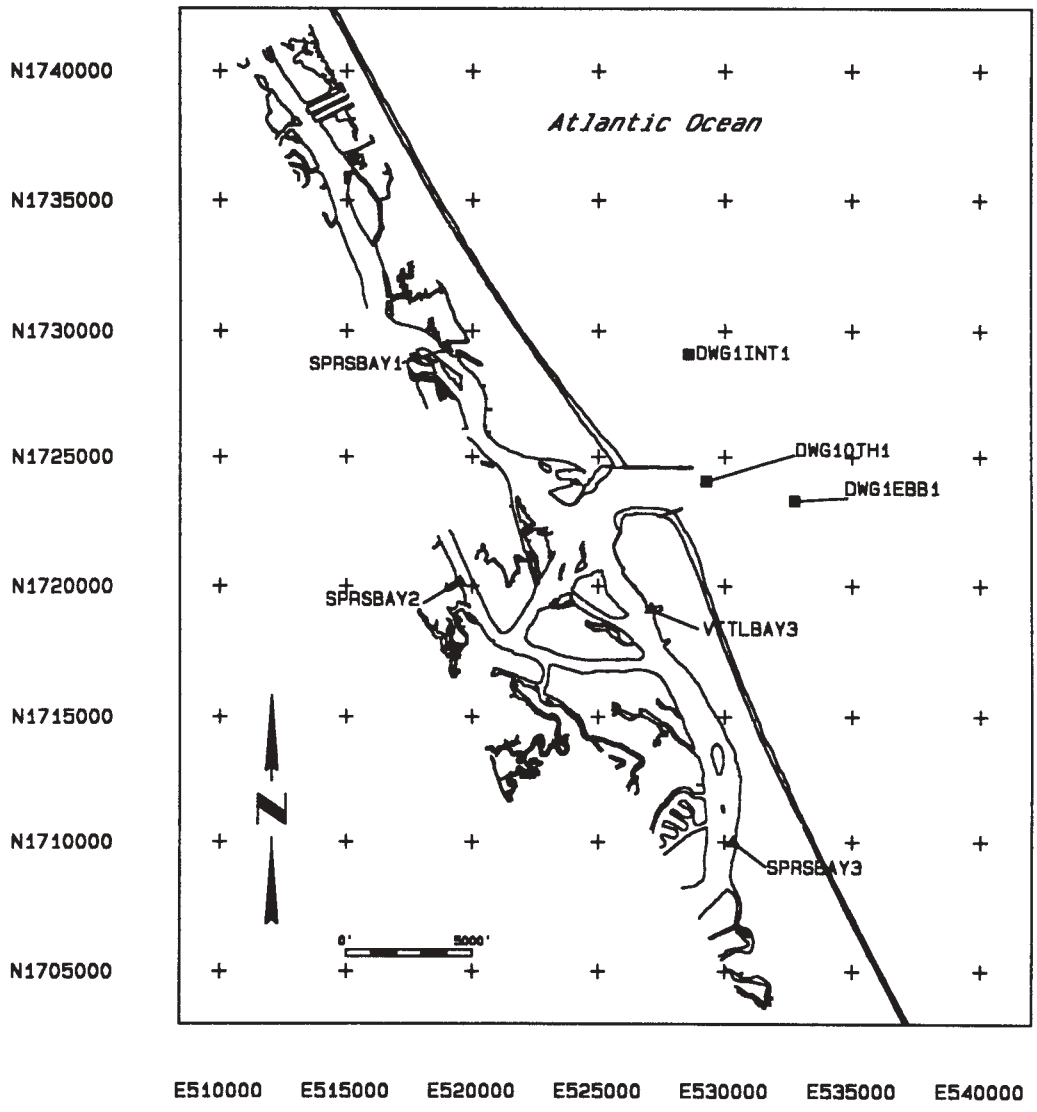


Figure 1. Location of gauges at Ponce de Leon Inlet.



AUTHOR INDEX TABLE OF CONTENTS

records were used to calculate hourly wave energy-frequency spectra and mean directions for each frequency. Modification of wavelength by the current was not included in the analysis.

### 2.3 Bathymetry

High-resolution bathymetry of the inlet and ebb shoal was obtained from the Scanning Hydrographic Operational Airborne Lidar System (SHOALS) (Lillycrop et al. 1996) survey performed in the fall of 1996. SHOALS data were supplemented with National Oceanic and Atmospheric Administration (NOAA) digital bathymetry (used to define offshore bathymetry) and shorelines. The SHOALS data resolution was approximately 4 m.

## 3.0 MARCH STORM

A 5-day segment of data from 10 March through 14 March 1996 was selected for evaluation of the wave model. This time period was selected because it included a significant storm with wave heights exceeding 5 m. Figure 2 shows the zero-moment wave height ($H_{mo}$) and peak wave direction during the data segment at the offshore gauge (DWG1INT1). The wave height peaks early on 11 March (all times are referenced to Greenwich Mean Time) at 4.0 m and then again late on 11 March at 5.4 m. The peak wave directions shift from NNE to ENE through the storm. Wave periods (not shown) grow from 6 sec on 10 March to 14 sec at the peak of the storm and remain at 12 to 14 sec through the end of the storm. The winds for the same period are given in Figure 3. Winds were recorded at the Battelle Research Station just north of the inlet, on the bay. The wind speeds reached 16 and 17 m/sec during the two storm peaks, with directions generally out of the north. After the second peak in the storm, the wind speed reduced to less than 10 m/sec with variable directions. Figure 4 shows water surface elevations from the gauge in the inlet throat. The typical tide range is on the order of 1 m. The water surface elevations were superelevated during the storm by approximately 0.4 m. The gap in recorded data on 11 March (shown in Figure 4) will be seen throughout the data comparisons. The ebb shoal gauge failed on 12 March and remained inoperable during the remainder of the simulation period.

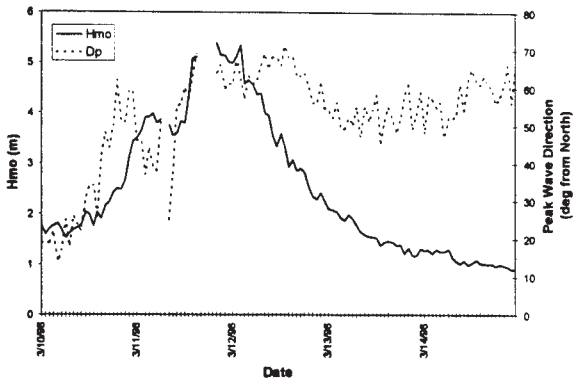


Figure 2. Wave height and peak direction at the offshore wave gauge (DWG1INT1) for March 1996 storm.

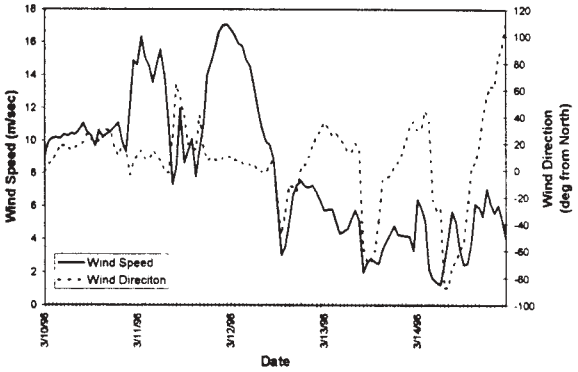


Figure 3. Wind speed and direction for March 1996 storm.

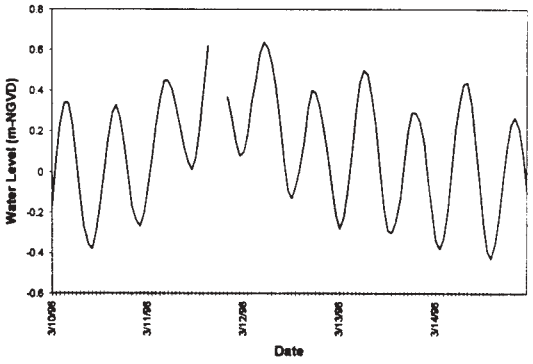


Figure 4. Water levels at the throat gauge (DWG1OTH1) for March 1996 storm.

## 4.0 CIRCULATION MODEL

### 4.1 Circulation Model Description

A two-dimensional, depth-integrated version of the ADCIRC (Advanced Three-Dimensional CIRCulation) model was applied for calculation of the circulation and water level at Ponce Inlet. ADCIRC is based on the Generalized Wave-Continuity Equation (GWCE) formulation of the depth-integrated continuity and momentum equations (Lynch and Gray 1979, Luettich et al. 1992). The GWCE in Cartesian coordinates is given by:

$$\frac{\partial^2\zeta}{\partial t^2}+\tau_0\frac{\partial\zeta}{\partial t}+\frac{\partial}{\partial x}\left(U\frac{\partial\zeta}{\partial t}-UH\frac{\partial U}{\partial x}-VH\frac{\partial U}{\partial y}+fVH\right.$$
$$\left.-H\frac{\partial}{\partial x}\left[\frac{p_s}{\rho_0}+g(\zeta-\alpha\eta)\right]-E_h\frac{\partial^2\zeta}{\partial x\partial t}+\frac{\tau_{sx}}{\rho_0}-(\tau_*-\tau_0)UH\right)$$
$$+\frac{\partial}{\partial y}\left(V\frac{\partial\zeta}{\partial t}-UH\frac{\partial V}{\partial x}-VH\frac{\partial V}{\partial y}-fUH\right.$$
$$\left.-H\frac{\partial}{\partial y}\left[\frac{p_s}{\rho_0}+g(\zeta-\alpha\eta)\right]-E_h\frac{\partial^2\zeta}{\partial y\partial t}+\frac{\tau_{sy}}{\rho_0}-(\tau_*-\tau_0)VH\right)=0 \quad (1)$$

where:

$E_h$ = horizontal eddy diffusion/dispersion coefficient
$f$ = Coriolis parameter
$g$ = gravitational acceleration
$H$ = total water depth ($\zeta + h$)
$h$ = still-water depth relative to a datum
$p_s$ = atmospheric pressure at the free surface
$t$ = time
$U, V$ = depth-averaged horizontal velocities
$\alpha$ = effective Earth elasticity factor
$\eta$ = Newtonian equilibrium tide potential
$\rho_0$ = density of water
$\tau_{sx}, \tau_{sy}$ = free-surface stresses
$\tau_* = C_f(U^2 + V^2)^{1/2}/H$
$C_f$ = bottom friction coefficient
$\tau_o$ = constant
$\zeta$ = free-surface elevation relative to a datum

In ADCIRC, the GWCE is solved together with the primitive form of the momentum equations:

$$\frac{\partial U}{\partial t}+U\frac{\partial U}{\partial x}+V\frac{\partial U}{\partial y}-fV=$$
$$-\frac{\partial}{\partial x}\left[\frac{p_s}{\rho_0}+g(\zeta-\alpha\eta)\right]+\frac{1}{H}M_x+\frac{\tau_{sx}}{\rho_0 H}-\tau_* U \quad (2)$$

$$\frac{\partial V}{\partial t}+U\frac{\partial V}{\partial x}+V\frac{\partial V}{\partial y}+fU=$$
$$-\frac{\partial}{\partial y}\left[\frac{p_s}{\rho_0}+g(\zeta-\alpha\eta)\right]+\frac{1}{H}M_y+\frac{\tau_{sy}}{\rho_0 H}-\tau_* V \quad (3)$$

where $M_x$ and $M_y$ represent depth-integrated horizontal diffusion/dispersion. The model can be applied in Cartesian or spherical coordinates. Forcing and resistance terms can include Coriolis, tidal potential, surface wind stress, atmospheric pressure, and bottom friction. In addition, the advective and diffusion/dispersion terms, as well as flooding and drying algorithms, can also be included in the computations. Inclusion of these optional terms, forcings, and algorithms are specified in an input file to ADCIRC. Input for ADCIRC includes:

*a.* Computational grid.
*b.* Run-specification file (includes options and settings).
*c.* Open-ocean, tidal-forcing boundary specifications.
*d.* Wind speed and direction.
*e.* Atmospheric pressure.

Model output can include any combination of the following:

*a.* Time series of global water elevation.
*b.* Time series of global velocity.
*c.* Time series of water elevation at specified locations.
*d.* Time series of velocity at specified locations.
*e.* Time series of global wind stress.
*f.* Harmonic analysis of water level at specified locations.

The numerical solution scheme applies a Galerkin finite-element (FE) method for triangular elements. The FE approach provides flexibility for grid generation allowing for a wide range of element sizes. Two benefits to this feature are: 1) high resolution can be applied in areas of interest, but is not required for other regions of the computational domain, and 2) forcing boundaries can be placed far from the local areas of interest, thus minimizing boundary effects.

### 4.2 Circulation Model Setup

Model setup consists of numerical grid generation, specification of forcing data, and model output configuration. Descriptions of these items are given here.

ADCIRC Grid. A 5504-node computational grid was developed for this study and is shown in Figure 5. The grid has longitudinal limits of 91.50 W and 73.87 W and latitudinal limits of 25.35 N and 33.96 N. The ratio of maximum to minimum element area is $1.17\times10^7$ with the largest elements placed in the deep ocean and smallest elements located in the inlet and back-bay regions. Figure 6 shows detail of the computational grid at the inlet and nearby back-bay region. The northern and southern grid limits of the back-bay region are 37 km north and 53 km south of Ponce Inlet (not shown in Figure 6), and encompass the entire Halifax River and Mosquito Lagoon. The significance of this coverage lies in the storage capacity of these reaches. The astronomical tides are severely damped in the far reaches

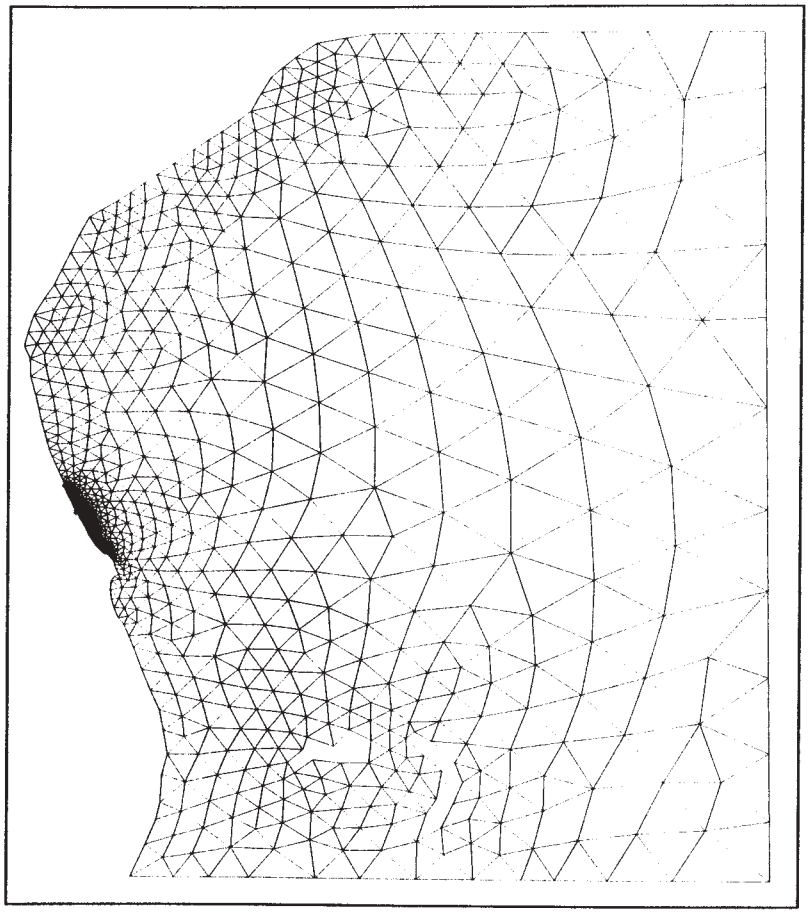

Figure 5. ADCIRC computational grid.

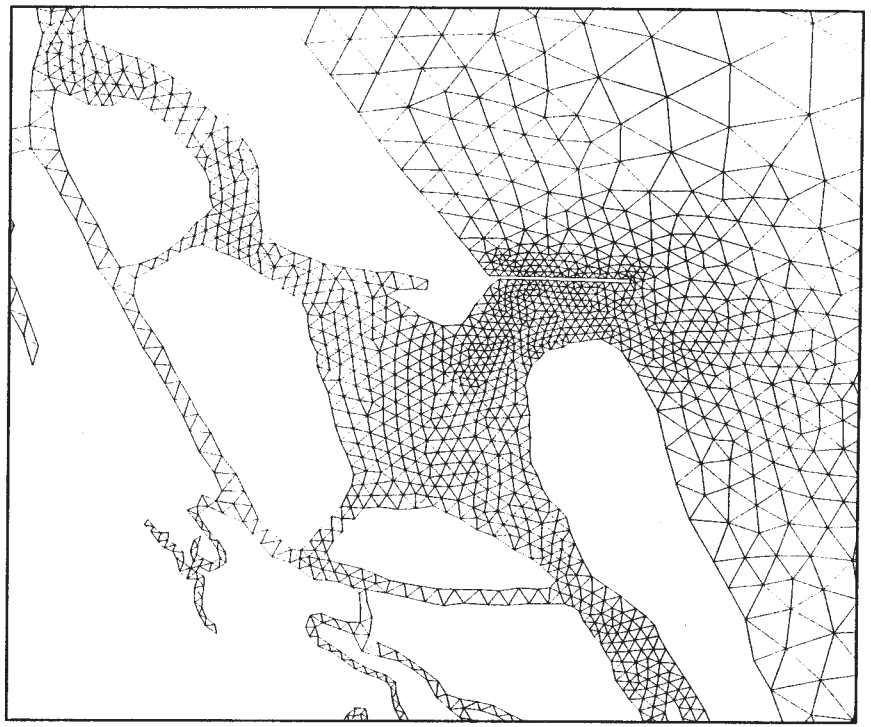

Figure 6. Detail of ADCIRC computational grid in vicinity of Ponce Inlet.

of the Halifax River and Mosquito Lagoon such that the still-water level is almost constant over a tidal cycle. Gradients in hydraulic head are produced between the inlet and north and south reaches, and contribute to the phase difference between the tidal elevation and current at the inlet.

The computational grid was developed from a larger-scale grid that encompassed the Western North Atlantic Ocean, Gulf of Mexico, and Caribbean (Westerink et al. 1993). Shoreline data for the East Coast of Florida, including Ponce Inlet, the Halifax River, and Mosquito Lagoon were obtained from the NOAA Medium Resolution Digital Vector Shoreline database. Bathymetry for Ponce Inlet, the ebb shoal, and limited back-bay channel areas were taken from the fall 1996 SHOALS survey. These bathymetry data were reduced to 23-m spacing for input into the grid. Bathymetry for the Halifax River and Mosquito Lagoon were taken from NOAA Chart 11485.

ADCIRC Input. Tidal elevations specified at 32 open-boundary nodes were calculated from the Western North Atlantic and Gulf of Mexico Tidal Database (Westerink et al. 1993). The four tidal constituents applied at the open boundaries were $M_2$, $S_2$, $N_2$, and $O_1$. Wind data were obtained from the NOAA National Center for Environmental Prediction (NCEP) Medium Range Forecast database in spatial increments of 1 deg and time increments of 6 hr. Atmospheric pressure was not included as a forcing input. The advective and nonlinear continuity terms, as well as flooding and drying, were included in the computations and the governing equations were solved on a spherical coordinate system. The time period of the simulation was 6 March through 17 March 1996, and the simulation time step was 5 sec.

ADCIRC Output. Global water level and current velocities were output at 20-min intervals starting 7 March 1996 and ending 17 March 1996. From the global velocity field, points in the vicinity of Ponce Inlet were extracted for input into the wave model. Time-series of water level at particular locations were extracted for comparison to measurements.

### 4.3 Circulation Model Results

Comparison of NCEP and Battelle wind data showed significant discrepancies from 8 March through 12 March, with the NCEP data having higher speed than the Battelle measurements. Although the Battelle gauge is sheltered with respect to the coastal ocean because of its placement on bay side of the barrier island, its measurements gave a good representation of timing of the frontal passage and changes in wind speed. The NCEP data showed the front passing through the study site a day ahead of measurements taken at the Battelle gauge. Because of the discrepancy in wind speed and timing between the two data sets, the NCEP wind speed values were reduced. The reduction in wind speed was varied and the resulting wind field input into the circulation model until a reasonable fit between measured and calculated water level was achieved. The winds specified for input into the model were reduced by the following formulation

$$W = \begin{cases} W_{NCEP} & \text{for } W_{NCEP} \le 8\,m/\text{sec} \\ W_{NCEP} - 0.3(W_{NCEP} - 8) & \text{for } W_{NCEP} > 8\,m/\text{sec} \end{cases} \quad (4)$$

where $W$ is the resultant wind speed applied as input into the circulation model, and $W_{NCEP}$ is the NCEP wind speed. A wind speed of 8 m/sec was selected as the cutoff for wind speed reduction because the overprediction of wind-induced water level occurred for NCEP winds above this value.

Results from the circulation model with the original NCEP data applied as input gave a wind-induced rise in water level at the coast ahead of the rise indicated by measurements. In addition, the calculated range in tidal elevation and surge during the storm peak were too large. Reduction of the wind speed resulted in a smaller surge and tidal-elevation range that match the measurements more closely. The surge calculated by the reduced winds still arrives at the study site a day early, but this surge is not a significant change in water level as compared to that at the storm peak.

Comparisons of measured and calculated water level are shown in Figures 7A and 7B for the outer throat and ebb shoal gauges, respectively. Prior to the storm, the calculated tidal water level closely matches the measurements in amplitude and phase for both locations. The storm surge is overpredicted by approximately 0.2 m at the onset of the event (9 and 10 March), then closely matches the measured surge elevations during the peak of the storm (11 and 12 March). One explanation for the high calculated surge at the beginning of the storm is the temporal resolution of the wind field. Linear interpolation of the storm front over a 6-hr time period may not provide accurate representation of the front location at any given time. The instantaneous increase in wind speed that typically occurs when a front arrives at a given location is calculated as a slower rise in wind speed that starts before the front actually arrives.

Current data were not available for model verification during March 1996. The maximum calculated current in

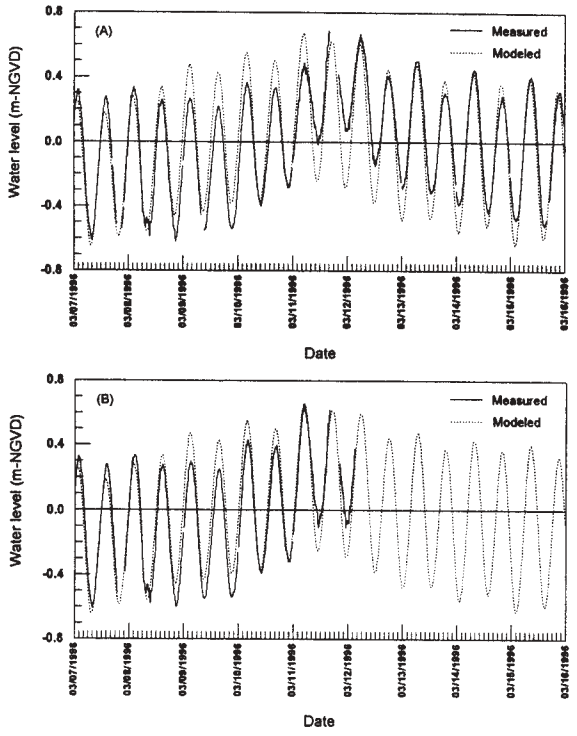


Figure 7. Comparison of measured and calculated water level: (A) OTH1 location, (B) EBB1 location.

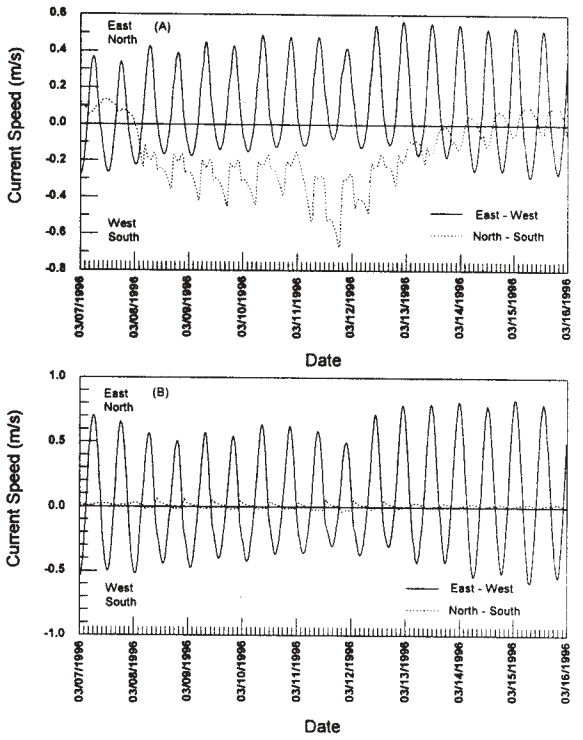


Figure 8. Decomposed current speed in the inlet: (A) OTH1 location, (B) middle throat.

the inlet throat is on the order of 1 m/sec, which is consistent with measurements taken during July and August, 1996, and August and September, 1997. Calculated currents for the outer throat (DWG1OTH1) and middle throat (within the northern third of the inlet, about one-third of the jetty length from the seaward end of the jetty) are shown in Figures 8A and 8B, respectively. The currents are decomposed into east-west and north-south components. The north jetty is aligned along an east-west axis. The tidal current at the outer throat location (Figure 8A) is dominant in the east-west component, while the wind- and surge-generated longshore current is dominant in the north-south component (wave-induced longshore current was not included in the circulation model calculations). The peak tidal current in the middle throat is reduced during the passage of the storm. This reduction may owe to the occurrence of the storm at neap tide and to elevated water level in both the back bay and along the coast that may decrease the normal water-surface gradient through the inlet.

Measured water level in the back bay rose approximately 0.75 m from pre-storm (7 - 8 March) to peak-storm (11 - 12 March) conditions, and water level in the ocean at DWG1INT1 rose approximately 0.67 m. The greater rise in water level in the back bay would enhance the ebb flow through the inlet and suppress the flood flow. However, the wind-induced setup along the coast would enhance the flood flow and reduce the ebb flow. The net effect of these forcings is an overall reduction in current speed through the inlet. In addition, the storm passed through the study site during the neap tidal cycle. Currents in the inlet are reduced during the neap cycle because the water level gradient between the ocean and far reaches of the back bay is not as great as during other parts of the tidal cycle.

## 5.0 WAVE MODEL

The spectral wave model STWAVE (Steady-state spectral WAVE) (Resio 1987, 1988a, 1988b, Davis 1992), modified for wave-current interaction, was applied at Ponce de Leon Inlet. The following subsections describe the model, the modeling procedure for Ponce Inlet, and model results.

### 5.1 Wave Model Description

STWAVE, which numerically solves the steady-state spectral energy-balance equation, was modified to solve the steady-state conservation of wave action:

$$\frac{\partial}{\partial x}\left(C_{ga_x}\frac{E(f,\theta)}{\omega_r}\right)+\frac{\partial}{\partial y}\left(C_{ga_y}\frac{E(f,\theta)}{\omega_r}\right)=\Sigma\frac{S}{\omega_r} \qquad (5)$$

where

$E$ = spectral energy density
$f$ = frequency of spectral component
$\theta$ = propagation direction of spectral component
$C_{ga}$ = absolute group velocity of spectral component
$x,y$ = spatial coordinates
$S$ = energy source/sink terms
$\omega_r$ = relative angular frequency (frequency relative to the current)

Currents enter into the wave model solution through the dispersion relationship and the calculation of the group velocities. The source terms include wind input, nonlinear wave-wave interactions, dissipation within the wave field, and depth-limited breaking. The terms on the left-hand side of Equation 5 represent wave propagation (refraction and shoaling) and the source terms on the right-hand side of the equation represent energy growth or decay in the spectrum. The assumptions made in STWAVE are:

*a.* Mild bottom slopes.
*b.* Negligible wave reflection.
*c.* Spatially homogeneous offshore waves.
*d.* Steady waves and winds.
*e.* Linear refraction and shoaling.
*f.* Linear wave-current interaction.

STWAVE includes two breaking mechanisms: depth-limited breaking and whitecapping. Based on laboratory data, Smith et al. (1997) showed that the whitecapping term was not sufficient to represent wave breaking in shallow water in the presence of an ebb current (see also Ris and Holthuijsen 1996). From these results, a steepness-based wave height limit in the form of the Miche (1951) criterion was applied in STWAVE for Ponce Inlet

$$H_{mo_{max}} = 0.1\ L\ \tanh kd \qquad (6)$$

where $L$ is wavelength, $k$ is wave number, and $d$ is water depth (corrected for tide/surge). STWAVE is a half-plane model, meaning that waves only propagate toward the coast. Waves reflected from the coast or waves generated by winds blowing offshore are neglected.

STWAVE is a finite-difference model and calculates the wave spectra on a rectangular grid with square grid cells using a backward ray-tracing scheme. The inputs required to execute STWAVE are:

*a.* Bathymetry and shoreline position.
*b.* Size and resolution of the grid.
*c.* 2D wave spectrum on the offshore grid boundary.
*d.* Wind speed and direction.
*e.* Current field.
*f.* Water level.

The model outputs zero-moment wave height ($H_{mo}$), peak spectral period ($T_p$), and mean wave direction ($\theta_m$) at all grid points, and the 2D spectrum at selected grid points.

### 5.2 Wave Model Inputs

Execution of the wave model requires specification of the following input information: a finite-difference grid, input spectra, and water level and current fields.

STWAVE Grid. STWAVE operates on a flat grid with square grid cells. The optimal grid orientation is for the $y$ axis to be aligned with the bathymetry contours and the $x$ axis to be aligned normal to the contours. This orientation allows the greatest range of incident wave angles and the most reliable modeling results. The STWAVE grid was generated using the ACES2.0 URGG (Uniform Rectilinear Grid GUI*) software (Leenknecht and Tanner 1997). Using URGG, the digital bathymetry (combined SHOALS and NOAA data) was imported, and the coordinates were transformed from geographical into Universal Transverse Mercator coordinates. The orientation of the grid $x$ axis was selected to be 236 deg relative to True North, so the grid was aligned with the shoreline and bottom contours. The offshore boundary of the grid is along the 18-m depth contour. The grid was specified with 53 cells in the cross-shore and 112 cells in the longshore, with a grid resolution of 50 m. URGG uses Delauney triangulation to develop the grid and linear interpolation to assign elevations at each cell. Figure 9 shows the depth contours within the STWAVE grid.

STWAVE Spectra. The nearshore waves were forced by wave spectra input on the offshore boundary of the STWAVE grid. These input spectra were specified such that the $H_{mo}$ and mean direction approximated the wave conditions measured at the offshore wave gauge (DWG1INT1). The spectra were generated using a TMA form (Bouws et al. 1985), with a spectral peakedness parameter, $\gamma$, of 3.3. Figure 10 shows a comparison of measured and generated frequency spectra. A $\cos^n$ directional distribution was applied to the spectra (only a mean direction for each frequency was available from the field data). The exponent $n$ was set to four for the building phase of the storm (peak periods of 6 to 12 sec) and to eight for the peak and waning phases of the storm

*Graphical User Interface

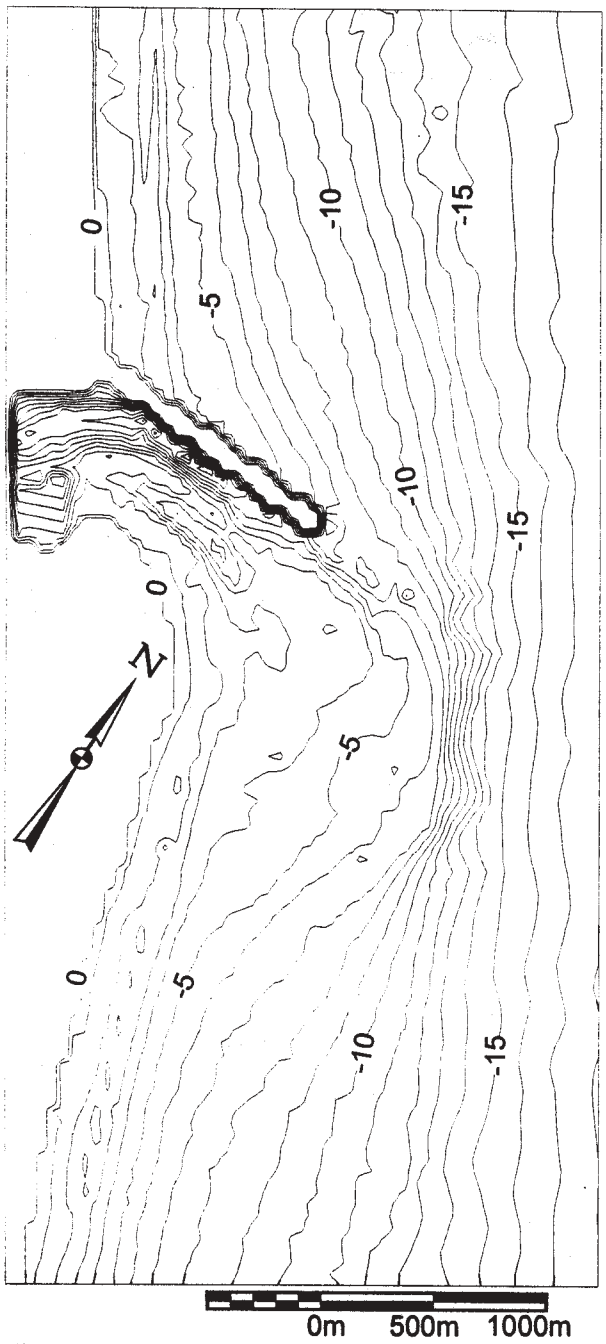


Figure 9. STWAVE bathymetry grid (contours in meters NGVD).

(peak periods of 12 to 14 sec). The generated spectra had 35 directions (5-deg bins) and 40 frequencies (0.0078 Hz increment, with the lowest frequency equal to 0.0312 Hz). Because STWAVE is a half-plane model, wave energy spread beyond +/- 87.5 deg from shore normal (offshore propagating wave energy) is truncated and neglected in STWAVE simulations.

For the Ponce Inlet simulations, local wave generation within the STWAVE grid was neglected. Because the

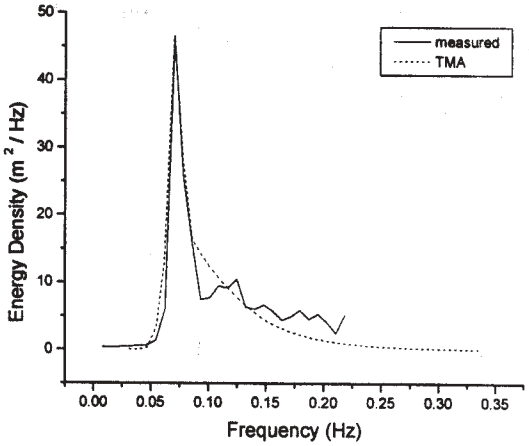


Figure 10. Example STWAVE input spectrum.

grid extent is relatively small, little additional wave growth is expected within the grid domain.

STWAVE Water Level and Current Fields. Water level fields were specified as spatially constant over the STWAVE grid and varying in time. The water level was set equal to values recorded at the gauge in the inlet throat (DWG1OTH1 in Figure 1). These measured water levels are plotted in Figure 4. The correlations in water level between the throat gauge and the other two ocean gauges (DWG1INT1 and DWG1EBB1) were 0.999 and 0.998, respectively, with offsets of 1 cm and slopes of 1.00 and 0.98. Thus, the assumption of a constant water surface elevation over the grid is reasonable. As seen in Figure 4, the water level varies from about -0.4 to 0.6 m during the storm. Water level fields could also have been specified from ADCIRC output.

Current fields over the STWAVE grid were specified from the ADCIRC output. To interpolate the ADCIRC results from the finite-element grid to the STWAVE finite-difference grid, the following procedure was used: first, it was determined which ADCIRC element contained the first STWAVE grid point, then the linear interpolation functions for each node of the element were calculated, and finally, from the interpolation functions, the weights to apply to each element node were calculated. This process was repeated for each STWAVE grid point. A lookup table was developed which specified each STWAVE grid point and the corresponding ADCIRC nodes and weights. After the ADCIRC current output was interpolated to the STWAVE grid point, the north and south current components were transformed to the STWAVE coordinate system.

### 5.3 Wave Model Results

STWAVE was run for 36 wave events during the storm 10-14 March 1996, at Ponce Inlet. The wave runs were selected at high, mid, and low tide, at approximately 3-hour increments (with the exception of the gap in measurements on 11 March). These time increments were chosen to include the range of water levels and currents. STWAVE was run both with currents as an input and without currents to isolate the impact of the currents.

Figure 11 shows contours of wave height at the peak of the March storm (2300 hours on 11 March). The contours show significant wave breaking on the outer edge of the ebb shoal, some wave focusing near the south jetty, and significant wave attenuation in the outer throat due to sheltering from the north jetty and wave breaking. Wave breaking occurs across the entire ebb shoal and in the outer throat.

Figures 12-14 show time history comparisons of STWAVE wave heights (with and without currents) to measurements at the gauge locations, offshore, ebb shoal, and outer throat, respectively. With-current results are labeled 'stwave', and without-current results are labeled 'stwave_nc'. Because the offshore gauge data were used as model input, it is expected that the model would reproduce the gauge data well. But, there are some slight differences caused by refraction and shoaling between the model boundary (depth of 18 m) and the gauge (depth of 15 m), truncation of the input spectra to a half plane, and differences between the true spectra and the TMA spectra with $\cos^n$ spreading used as input. The mean errors at the offshore gauge are less than 1 percent, and the root-mean-square (RMS) error is 2 percent. The current magnitudes at the offshore gauge are typically small (less than 0.3 m/sec), so STWAVE applied with and without current give about the same results.

Waves on the ebb shoal are attenuated by about 20 percent at the peak of the storm, due to a combination of refraction and breaking. At the ebb shoal gauge (Figure 13), STWAVE underpredicts the wave conditions early in the storm when the waves were steep and oblique (30-40 deg north of shore normal), but captures the building of the storm up to the peak well (the ebb shoal gauge failed at the storm peak). The current magnitudes on the ebb shoal are highly variable and reach as high as 0.6 m/sec, but differences in STWAVE with and without current are quite small. The mean errors in wave height are -7.5 and -8.5 percent for the with- and without-current simulations, respectively. The RMS errors are 11.9 and 12.6 percent for the with- and without-current situations.

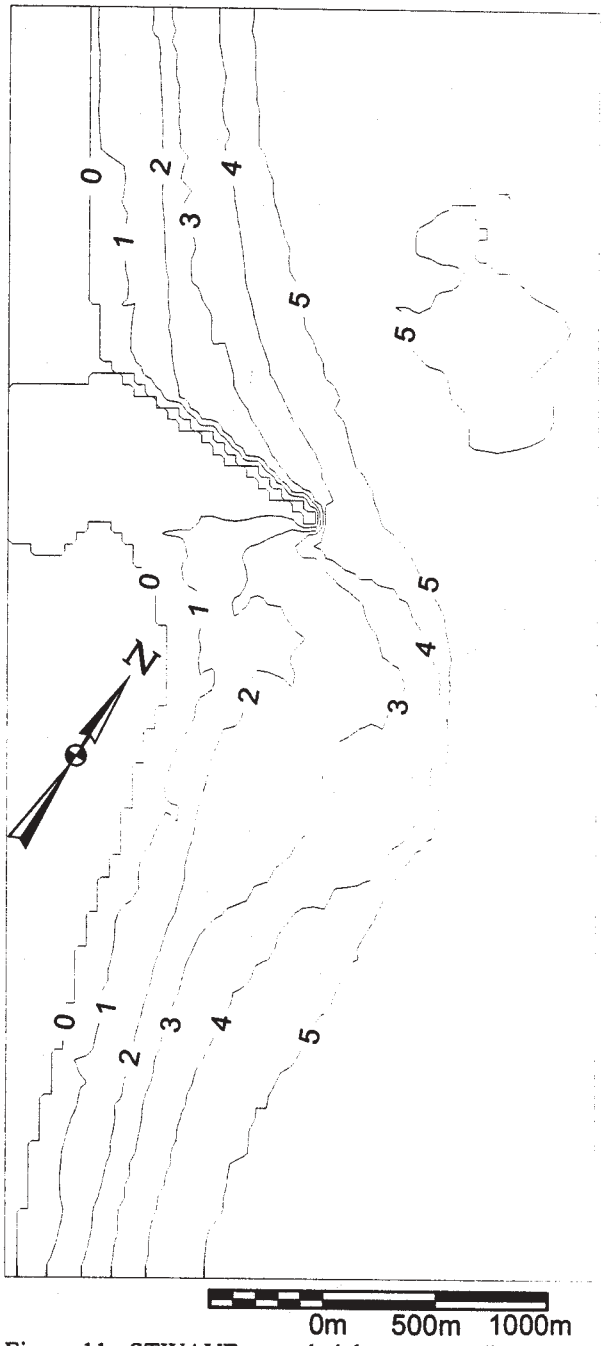


Figure 11. STWAVE wave height contours (in meters) for the storm peak (11 March at 2300 hours).

Of greatest interest are the wave heights predicted at the inlet throat. Figure 14 shows the model wave height comparisons with the throat measurements. The local peaks in wave height correspond to high water-level elevations, i.e., the greater water depth allowing larger wave heights. The attenuation of wave height between the offshore and throat gauges is 50 percent at the peak of the storm due to refraction, breaking, and sheltering by the north jetty. STWAVE tends to overpredict the steeper waves prior to the peak of the storm and

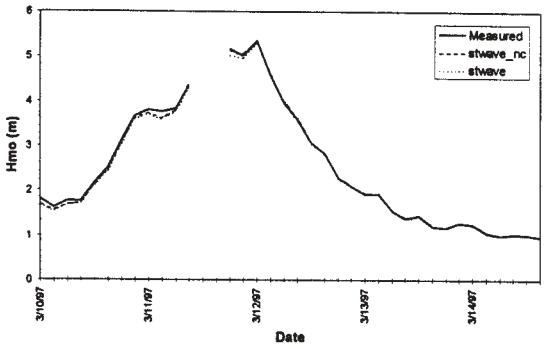


Figure 12. Comparison of STWAVE wave heights to gauge data offshore.

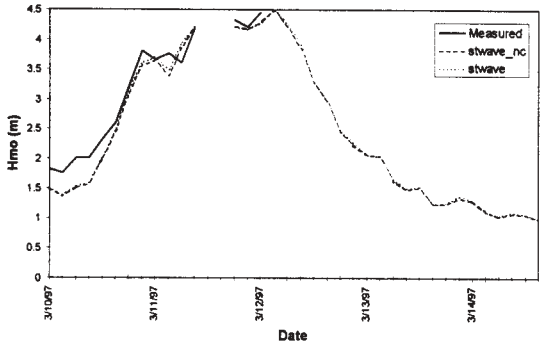


Figure 13. Comparison of STWAVE wave heights to gauge data on the ebb shoal.

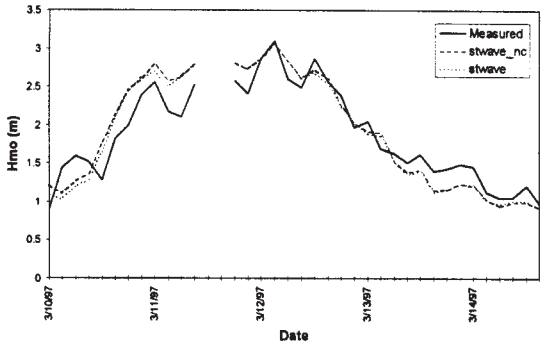


Figure 14. Comparison of STWAVE wave height to gauge data in the outer inlet throat.

underpredict low steepness waves after the peak. The agreement of the model with the data is reasonable, with mean errors of -1.0 and 0.5 percent and RMS errors of 14.3 and 15.2 percent for the with- and without-current simulations, respectively. The current magnitudes in the throat reach up to 0.6 m/sec for the cases modeled, but again, the impact of wave-current interaction on the wave height is small. Slight reductions in wave height are seen at high tides when the current is still flooding.

Summaries of the STWAVE wave height errors are given in Table 1.

**Table 1.** Error in Calculated Wave Height

| | | without current, percent | with current, percent |
|---|---|---|---|
| Offshore | mean | -0.6 | -1.2 |
| | RMS | 1.8 | 2.4 |
| Ebb | mean | -8.5 | -7.5 |
| | RMS | 12.6 | 11.9 |
| Throat | mean | 0.5 | -1.0 |
| | RMS | 15.2 | 14.3 |

Figures 15-17 show time history comparisons of STWAVE wave directions (with and without currents) to measurements at the gauge locations, offshore, ebb shoal, and outer throat, respectively. The wave directions given in Figures 15-17 can be related to true north by subtracting the wave direction from 56 deg. Summaries of the error statistics are given in Table 2.

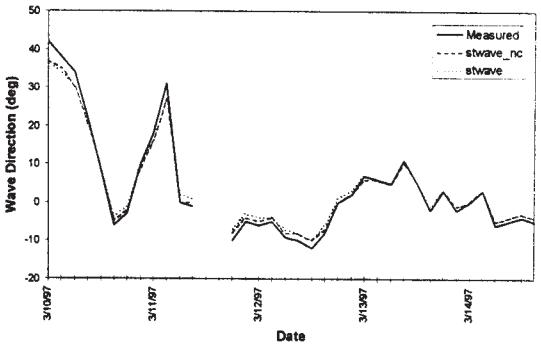


Figure 15. Comparison of STWAVE wave directions to gauge data offshore.

The wave direction at the offshore gauge is well represented by the model, which is again expected because the gauge served as model input. Small differences (RMS error of 2 deg) are due to refraction between the boundary and the gauge depth and due to truncation of the directional distribution to a half plane.

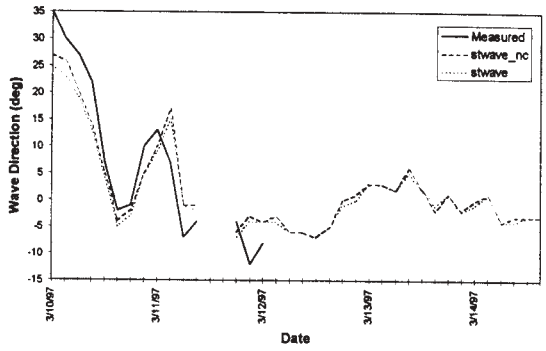


Figure 16. Comparison of STWAVE wave directions to gauge data on the ebb shoal.

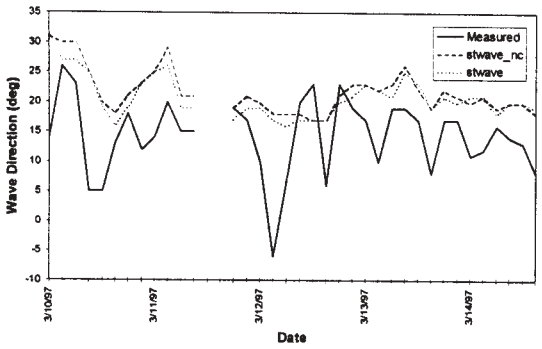


Figure 17. Comparison of STWAVE wave directions to gauge data in the outer inlet throat.

**Table 2.** Error in Calculated Wave Direction

| | | without current, deg | with current, deg |
|---|---|---|---|
| Offshore | mean | -0.1 | 0.3 |
| | RMS | 1.7 | 2.0 |
| Ebb | mean | -1.0 | -1.6 |
| | RMS | 4.6 | 4.8 |
| Throat | mean | 7.4 | 6.5 |
| | RMS | 9.4 | 9.0 |

The measured ebb shoal wave directions have a signature very similar to the offshore gauge, with slightly reduced wave angles relative to shore normal. Comparisons of wave direction at the ebb shoal gauge show reasonable agreement of the model with the measurements (RMS error of 5 deg). The difference in wave direction with and without currents in the STWAVE simulations is generally less than 1 deg.

At the inlet throat, STWAVE does not reproduce the wave direction measurements. As seen in Figure 17, the measurements show a highly variable wave direction (varying from +26 to -6 deg). The model results are far less variable ( +30 to +16 deg) with a mean error of 7 deg. The negative peaks in the measured wave direction occur at high tide and the positive peaks generally occur at mid tide. The reasons for the poor agreement of the model with the data are not clear. Possible contributing factors to the errors include errors in specification of the current field (current data were not available for verification), lack of diffraction in the wave model, poor representation and resolution of the north jetty in the wave model (jetty is porous and overtopped at high tide, jetty length is half a grid cell too short in the model), neglect of current effects in the analysis of the measurements, and differences in bathymetry in this highly dynamic region between the storm period and survey date (6-month time difference).

## 6.0 SUMMARY AND CONCLUSIONS

The inlet environment poses a number of complications to wave modeling, e.g., complex bathymetry, wave-current interaction, steepness and depth-limited wave breaking, specification of current fields, and small amount of field data for evaluation. Additionally, inlets are dynamic, and engineers have great need for accurate wave models to assist in solution of coastal inlet problems. In this study, the STWAVE spectral wave model, modified to include wave-current interaction and shallow-water steepness-induced breaking, was applied for a March 1996 storm at Ponce de Leon Inlet. Field measurements from offshore, the ebb shoal, and the outer throat were used to evaluate STWAVE. Depth-integrated current fields generated with the circulation model ADCIRC were used as input to STWAVE.

The ADCIRC simulations were driven by tidal constituents and wind fields. Comparison of calculated water levels to measurements showed an overestimate of storm surge by approximately 0.2 m during the onset of the storm, but good reproduction of the surge values at the storm peak. The coarse temporal resolution (6 hours) of the wind fields may have contributed to the overprediction in the early part of the storm. Measurements were not available to evaluate the accuracy of the current fields calculated by ADCIRC.

The STWAVE calculations compared well to measured wave heights at the inlet. Root-mean-square errors at the inlet throat were 14 to 15 percent. The model reproduced the overall growth and decay of the storm (small overprediction of wave heights during the building of the storm and underprediction during the waning of the storm) and the local wave height variations with changes in the tide level.

STWAVE did not reproduce the wave directions in the inlet throat well (7-deg mean error and 9-deg RMS error). The measured throat wave directions varied greatly through the storm (32 deg variation), whereas the modeled directions varied much less (14 deg variation). The reasons for the poor agreement are not clear, but are likely due to limitations in specification of the local boundaries (current, bathymetry, jetties). Also, the wave data analysis did not include current.

The differences in wave height and direction due to including currents in the STWAVE simulations are minor at the outer throat gauge location (differences of 10 percent in wave height and 3 deg in direction or less). The reasons the differences are small for this storm are probably a combination of the long wave periods (mostly 10-14 sec) and current velocities in the outer throat that are relatively low (0.5 m/sec or less). Deeper in the inlet throat where the velocities are higher (up to 1 m/sec) the wave-current interaction impacts are stronger.

This application is the first field evaluation of STWAVE with wave-current interaction for an inlet. Additional field data, including waves, water levels, current, and bathymetry have been collected at Ponce Inlet to provide a more thorough evaluation of both the circulation and wave models.

## 7.0 ACKNOWLEDGEMENTS

The research presented in this paper was conducted under the Inlet Modeling System work unit in the Coastal Inlets Research Program, of the Coastal and Hydraulics Laboratory, U.S. Army Engineer Waterways Experiment Station. The Prototype Measurements and Analysis Branch, Coastal and Hydraulics Laboratory, is acknowledged for design, deployment, and analysis of the Ponce de Leon Inlet field measurements. These efforts were led by Gary Howell and Sam Corson. SHOALS data were analyzed by Jennifer Irish. The authors also thank Nick Kraus and Bruce Ebersole for reviewing the manuscript. Permission to publish this paper was granted by the Office, Chief of Engineers, USACE.

## 8.0 REFERENCES

Bouws, E., H. Gunther, W. Rosenthal, and C.L. Vincent, 1985: Similarity of the wind wave spectrum in finite depth waves; 1. Spectral form. *J. Geophys. Res.*, 90(C1), 975-986.

Davis, J.E., 1992: STWAVE theory and program documentation. Chapter 8 in Coastal Modeling System User's Manual, Instructional Report CERC-91-1, Supplement 1, Ed. M. A. Cialone, USAE Waterways Experiment Station, Vicksburg, MS.

Howell, G.L., 1996: A comprehensive field study of tidal inlet processes at Ponce de Leon Inlet, Florida. *Proc.*, 25th Coast. Engrg. Conf., ASCE, 3323-3336.

Leenknecht, D.A., and W.W. Tanner, 1997: Grid generation and data analysis for wave transformation models. *Proc.*, 4th Cong. Computing in Civil Engrg., Philadelphia, PA, in publication.

Lillycrop, W.J., L.E. Parson, and J.L. Irish, 1996: Development and operation on the SHOALS airborne lidar hydrographic survey system. In Laser Remote Sensing of Natural Waters: From Theory to Practice, V.I. Feigels and Y.I. Kopilevich, Ed., *Proc.*, SPIE 2964, 26-37.

Luettich, R.A., J.J. Westerink, and N.W. Scheffner, 1992: ADCIRC: an advanced three-dimensional circulation model for shelves, coasts, and estuaries, Report 1: theory and methodology of ADCIRC-2DDI and ADCIRC-3DL. Technical Report DRP-92-6, USAE Waterways Experiment Station, Vicksburg, MS.

Lynch, D.R., and W.G. Gray, 1979: A wave equation model for finite element tidal computations. *Comp. Fluids*, 7, 207-228.

Miche, M., 1951: Le pouvoir reflechissant des ouvrages maritimes exposes a l' action de la houle. *Annals des Ponts et Chaussess*, 121e Annee, 285-319 (translated by Lincoln and Chevron, Univ. Calif, Berkeley, Wave Research Laboratory, Series 3, Issue 363, June 1954).

Resio, D.T., 1987: Shallow-water waves. I: theory. *J. Wtrway., Port, Coast., and Oc. Engrg.*, Vol. 113, No. 3, 264-281.

Resio, D.T., 1988a: Shallow-water waves. II: data comparisons. *J. Wtrway., Port, Coast., and Oc. Engrg.*, Vol. 114, No. 1, 50-65.

Resio, D.T., 1988b: A steady-state wave model for coastal applications. *Proc.*, 21st Coast. Engrg. Conf., ASCE, 929-940.

Ris, R.C., and L.H. Holthuijsen, 1996: Spectral modelling of current induced wave-blocking, *Proc.*, 25th Coast. Engrg. Conf., ASCE, 1247-1254.

Smith, J.M., D.T. Resio, and C.L. Vincent, 1997: Current-induced breaking at an idealized inlet. *Proc.*, Coastal Dynamics '97, ASCE, in press.

U.S. Army Corps of Engineers, Jacksonville District, 1993: Navigation study for Ponce de Leon Inlet, Volusia County, Florida -- 14310. Reconnaissance Report, USACE, Jacksonville District.

Westerink, J.J., R.A. Luettich, and N.W. Scheffner., 1993: ADCIRC: an advanced three-dimensional circulation model for shelves, coasts, and estuaries, Report 3: development of a tidal constituent data base for the western north Atlantic and Gulf of Mexico. Technical Report DRP-92-6, USAE Waterways Experiment Station, Vicksburg, MS.

# COMPARING THE SECOND-GENERATION "HISWA" WAVE MODEL WITH THE THIRD-GENERATION ""SWAN" WAVE MODEL

N. Booij, L.H. Holthuijsen and IJ.G. Haagsma

Delft University of Technology, Department of Civil Engineering,
Delft, the Netherlands

## 1. INTRODUCTION

Over the last decade, the traditional wave ray models to compute waves in coastal regions are being replaced by models that compute the waves on a regular grid. In analogy with ocean wave models, three generations of such grid models can be distinguished (depending on the degree of approximating the nonlinear wave-wave interactions). Here we intercompare the performance of a second- and third-generation model. The models are the second-generation wave model HISWA (Holthuijsen et al., 1989) and the third-generation wave model SWAN (e.g. Holthuijsen et al., 1996; Ris et al., 1994). In HISWA the wave-wave interactions are parameterized in the sense that a universal shape of the wave spectrum is assumed. The model has been in operation for about ten years in many institutions. In its successor, the recently developed SWAN model, the wave-wave interactions are formulated explicitly, allowing the wave spectrum to develop free of any a priori assumptions. In the present study both models are applied in stationary mode to five cases in three shallow water sites along the Dutch and German North Sea coast with (barrier) islands, tidal flats, local wind and ambient currents. For two cases the results are compared with observations in some detail. To judge cost against quality the differences between SWAN and HISWA in terms of prediction errors and computational effort are evaluated.

## 2. THE WAVE MODELS

### 2.1 Basic equations

The SWAN wave model (Simulating WAves Nearshore) is a discrete spectral model based on the action balance equation which for Cartesian coordinates is (e.g., Hasselmann et al., 1973):

$$\frac{\partial}{\partial t} N + \frac{\partial}{\partial x} c_x N + \frac{\partial}{\partial y} c_y N + \frac{\partial}{\partial \sigma} c_\sigma N + \frac{\partial}{\partial \theta} c_\theta N = \frac{S}{\sigma} \quad (1)$$

in which $N(\sigma, \theta, x, y, t)$ is the action density as a function of intrinsic frequency $\sigma$, direction $\theta$, horizontal coordinates $x$ and $y$ and time $t$. The first term in the left-hand side of this equation represents the local rate of change of action density in time, the second and third term represent propagation of action in geographical space (with propagation velocities in $x$- and $y$-space, $c_x$ and $c_y$ respectively). The fourth term represents shifting of the intrinsic frequency due to variations in depths and currents (with propagation velocity in $\sigma$-space, $c_\sigma$). The fifth term represents depth- and current-induced refraction (with propagation velocity in $\theta$-space, $c_\theta$). The expressions for these propagation speeds are taken from linear wave theory (e.g., Mei, 1983). The term $S$ $(= S(\sigma, \theta))$ at the right hand side of the action balance equation is the source term in terms of energy density representing generation of waves by wind, dissipation and nonlinear wave-wave interactions. A short description of the model is also given in the accompanying paper of Holthuijsen et al. (1998).

The HISWA model (HIndcasting waves in Shallow WAter) was developed to compute wave conditions with modest computer facilities. It is based on a parameterization of the above spectral equation. To retain the short-crested character of the waves (cross-seas due to refraction tend to be important in shallow water), the parameterization is limited to the frequency domain. It has been formulated in terms of the zero-th $(m_0)$ and first $(m_1)$ order moment of the spectrum in each spectral direction,

$$m_n(\theta) = \int_0^\infty \omega^n N(\omega, \theta)\, d\omega \quad (2)$$

Applying this definition operator to the spectral action balance equation results in the two evolution equations on which HISWA is based:

- an evolution equation for the zero-order moment of the action density spectrum for each spectral direction,

$$\frac{\partial}{\partial t}(m_0) + \frac{\partial}{\partial x}(c_x^* m_0) + \frac{\partial}{\partial y}(c_y^* m_0) + \frac{\partial}{\partial \theta}(c_\theta^* m_0) = T_0 \quad (3)$$

- an evolution equation for the first-order moment of the action density spectrum for each spectral direction,

$$\frac{\partial}{\partial t}(m_1) + \frac{\partial}{\partial x}(c_x^{**} m_1) + \frac{\partial}{\partial y}(c_y^{**} m_1) + \frac{\partial}{\partial \theta}(c_\theta^{**} m_1) = c_\omega^* m_0 + T_1 \quad (4)$$

The left-hand side of these equations represent propagation of the waves where $c_x^*$, $c_y^*$ and $c_\theta^*$ are the propagation speeds of the zero-th moment in x-, y- and $\theta$-space respectively. Similarly, $c_x^{**}$, $c_y^{**}$ and $c_\theta^{**}$ are the propagation speeds of the first moment in x- , y- and $\theta$-space. These speeds are approximated with the group velocity of the mean frequency $(m_1/m_0)$. The effect of time variations of currents and depth on the mean frequency is represented by the term $c_\omega^* m_0$, where $c_\omega^*$ is the propagation speed of the first moment in $\omega$-space (taken equal to the group velocity of the mean frequency). The source terms $T_0$ and $T_1$ are parametric versions of the above source term $S$ based on Eq. (2). Note that the wave components are directionally decoupled apart from some nonlinear coupling through the source terms.

One of the main operational differences between SWAN and HISWA is that SWAN considers wave propagation in all directions (the full 360°), whereas HISWA accounts only

for a limited directional sector (usually chosen to be 120° = 60° on either side of the incident mean wave direction, also in the present study).

### 2.2 Wind input

In SWAN the transfer of wind energy to the waves is described with the resonance mechanism of Phillips (1957) and the feed-back mechanism of Miles (1957). These mechanisms are implemented with the expressions of Cavaleri and Malanotte-Rizzoli (1981) for the resonance mechanism and two optional expressions for the feedback mechanism. The first is due to Snyder et al. (1981), rescaled in terms of friction velocity $U_*$ by Komen et al. (1984; used in the present study). The second is due to Janssen (1991).

In HISWA the simple expression of the Shore Protection Manual (CERC, 1973) for fetch-limited growth is used to simulate the wind induced evolution of the wave energy in each spectral direction independently. The wind-induced evolution of the mean frequency is based on an assumed universal relationship between wave energy and mean frequency (per spectral direction; deviations due to other processes are accounted for with a relaxation model). The effects of currents are accounted for in both models by using the apparent local wind speed and direction.

### 2.3 Dissipation

Whitecapping in SWAN is represented by the pulse-based model of Hasselmann (1974). Its coefficients have been obtained by Komen et al. (1984) and Janssen (1991) by closing the energy balance in fully developed deep water conditions. The coefficients that are used in SWAN are accordingly dependent on whether the wind input due to Komen et al. (1984) or due to Janssen (1991) is used. The effect of current is included through the steepness of the waves. In HISWA whitecapping is implicitly taken into account in the fetch-limited expression for wave growth. The effect of currents in HISWA is accounted for (in counter-current conditions) by instantaneously dissipating energy above the critical (blocking) frequency (assuming a $k^{-3}$ spectrum where k is wave number). This assumed shape of the spectrum also determines the corresponding effect on the mean frequency (shifting down).

Bottom friction in SWAN is represented by three options. The first is the linear, empirical model of JONSWAP (Hasselmann et al., 1973). It is used in the present study with the friction coefficient of Bouws and Komen (1983) as the applications concern wind sea rather than swell. The other two options are the drag-law model of Collins (1972) and the eddy-viscosity model of Madsen et al. (1988). In HISWA the quadratic friction model of Putnam and Johnson (1949) is used. For the corresponding effect on the mean frequency, bottom dissipation is concentrated in the lowest frequencies of the $k^{-3}$-spectrum (shifting the mean frequency up).

Depth-induced wave breaking in both SWAN and HISWA is modelled with the random-bore model of Battjes and Janssen (1978). In HISWA the original expression of Battjes and Janssen for the total energy is used (the depth-dependent part of that model with the maximum wave height-to-depth ratio $\gamma = 0.73$). In SWAN a simple spectral version of this model is used that retains the spectral shape. The rationale for the latter is that laboratory observations (e.g., Battjes and Beji, 1992; Vincent et al. 1994) have shown that the shape of initially uni-modal spectra propagating across (barred) beach profiles, is fairly insensitive to depth-induced breaking.

### 2.4 Nonlinear wave-wave interactions

Quadruplet wave-wave interactions transfer wave energy from the peak frequency to lower frequencies (thus moving the peak frequency to lower values) and to higher frequencies (where it is dissipated by whitecapping). In very shallow water, triad wave-wave interactions transfer energy from lower frequencies to higher frequencies (sometimes creating a secondary high-frequency peak). In SWAN the computations of the quadruplet interactions are carried out with the Discrete Interaction Approximation (DIA) of Hasselmann et al. (1985). The computations of the triad interactions are carried out with the Lumped Triad Approximation (LTA) of Eldeberky (1996). In HISWA the effects of quadruplet interactions are implicit in the assumed shape of the wave spectrum. The effects of triad interactions are accounted for by concentrating the (presumably simultaneously occurring) depth-induced breaking in the lowest frequencies of the $k^{-3}$ spectrum which shifts the mean frequency up.

### 2.5 The SWAN model and the WAM model

The above chosen formulations in the SWAN model for wind input, whitecapping, quadruplet wave-wave interactions and bottom dissipation are identical to the formulations in the WAM model (Cycle 3, the WAMDI group, 1988). In SWAN, the above triad wave-wave interactions and depth-induced breaking are added to these WAM Cycle 3 formulations.

## 3. FIELD CASES

SWAN and HISWA are applied to three sites that are located along the Dutch and German North Sea coast: the Haringvliet, the Friesche Zeegat and the Norderneyer Seegat (Fig. 1). Only the simplest case (the Haringvliet) and the most complex case (flood in the Friesche Zeegat) are described. The other cases are an ebb case in the Friesche Zeegat and a high-tide and a low-tide case in the Norderneyer Seegat (see the accompanying paper of Holthuijsen et al., 1998). The results of all cases will be considered statistically.

### 3.1 Haringvliet

The Haringvliet is a branch of the Rhine estuary that is separated from the main estuary by sluices. The bathymetry of the area and the locations of the (eight) observation stations are shown in Fig. 2. A local storm generated on October 14, 1982 waves from north-westerly directions and computations are carried out for 23:00 UTC on that day.

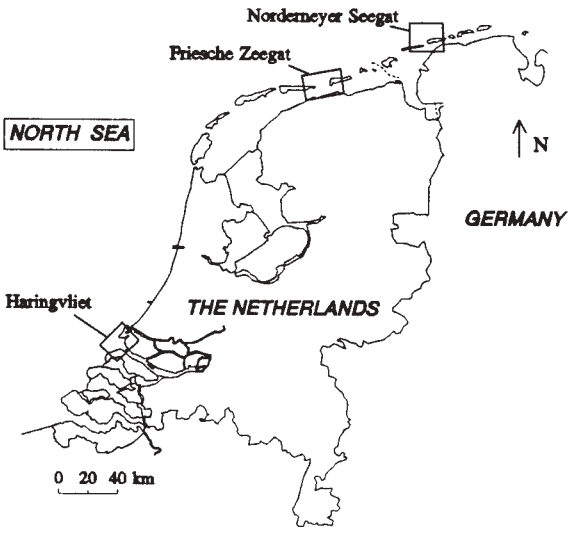


Fig. 1 The locations of the three verification sites along the Dutch and German coast in the southern North Sea.

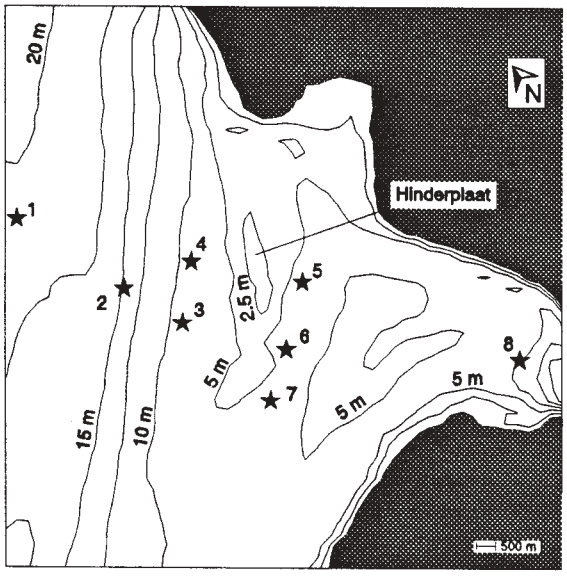


Fig. 2 The bathymetry of the Haringvliet with the locations of eight observation stations (numbered 1 through 8).

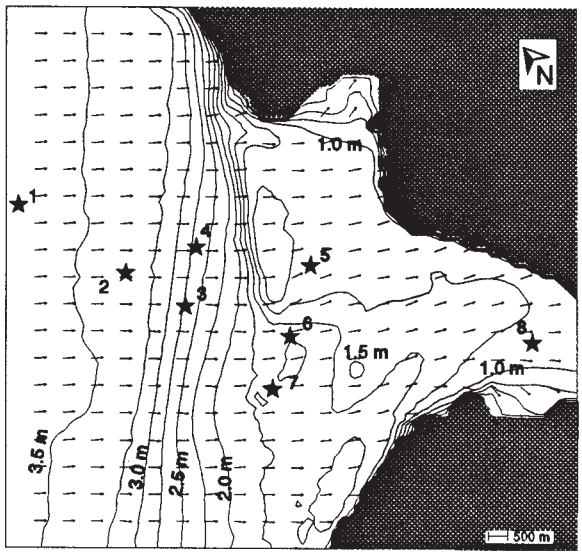


Fig. 3 The pattern of the significant wave height and mean wave direction (unit vectors) in the Haringvliet at 23:00 UTC on October 14, 1982, computed by SWAN.

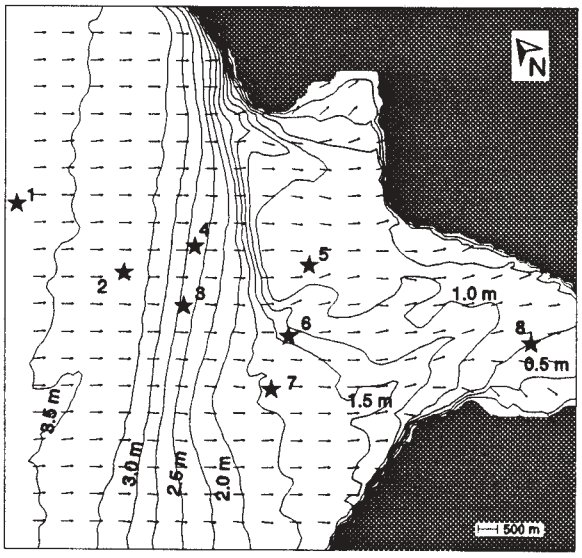


Fig. 4 As Fig. 3, computations by HISWA.

The incident wave conditions and the wind are given in Table 1 ($H_s \equiv 4\sqrt{m_o}$, $T_{m01} \equiv 2\pi m_0 / m_1$ and $U_{10}$ is the average wind speed at 10 m elevation). The waves approach the estuary from deep water and break over a shoal (the Hinderplaat, Fig. 2) with a reduction of significant wave height from about 3.6 m in deep water to 2.6 m in front of the shoal to about 0.7 m just behind the shoal. The local wind regenerates the waves behind the shoal to about 1.1 m at station 8. The mean wave period follows roughly the same pattern with an incident value of 6.7 s slowly decreasing to 6.5 s in front of the shoal with a rapid decrease to 3.2 s just behind the shoal. Beyond the shoal it slowly increases (due to the wind) to 4.0 s. The patterns of the significant wave height and the mean wave direction, computed with SWAN and HISWA are shown in Figs. 3 and 4. Obviously the patterns are very similar for both models. The pattern of the mean wave period computed with SWAN is shown in Fig. 5. In the HISWA

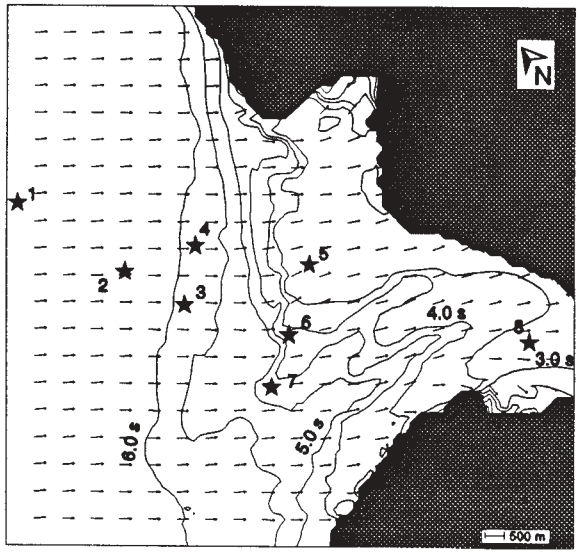


Fig. 5 The pattern of the mean wave period in the Haringvliet at 23:00 UTC on October 14, 1982, computed by SWAN.

results the mean wave period varies less than 1 s (except station 8, Fig. 10; pattern not shown here).

### 3.2 *Friesche Zeegat*

The Friesche Zeegat is located between the islands of Ameland and Schiermonnikoog in the northern part of the Netherlands (Figs. 1 and 6). The case that is considered is a flood case with maximum current speeds of 1.2 m/s (October 9, 1992, 05:00 UTC). The current velocities and water levels that are used in the computations have been obtained with the WAQUA circulation model (Les, 1996; Stelling et al., 1986) and are shown in Fig. 6. The incident wave conditions and the wind speed and direction are given in Table 1. The patterns of the significant wave height and mean wave direction, computed with SWAN and HISWA are shown in Figs. 7 and 8. Obviously the patterns are very similar for both models, except that the mean wave directions directly under the lee side of the islands are nearly reversed in the SWAN results (illustrating the larger directional freedom of SWAN). The patterns of the significant wave height are consistent with the pattern of the observations: the wave height gradually decreases between the deep water boundary and the entrance of the tidal inlet. The waves seem to penetrate deeper into the eastern channel than in the western channel. But repeated computations with and without wind show that this apparent penetration is due the wind which generates higher waves in the deeper eastern entrance than in the shallower western entrance (thus erroneously suggesting a difference in penetration). After the waves travel through the tidal gap they refract laterally to the shallower parts of the inlet. They completely reverse direction behind the two islands (not visible in the HISWA results because of the 120° directional limitation in the computations). The pattern of the mean wave period computed with SWAN is shown in Fig. 9. In the HISWA results the mean wave period varies less than 1 s (see Fig. 11; pattern not shown here). The

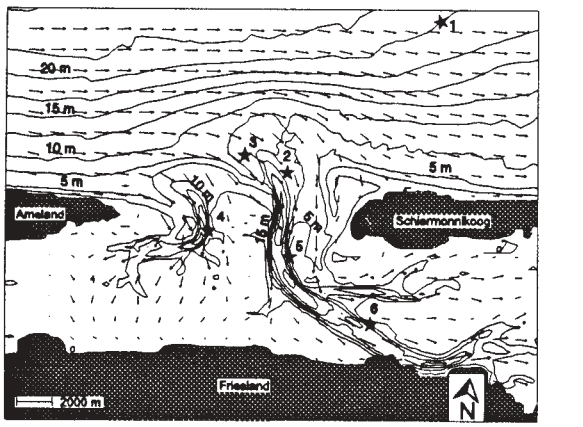


Fig. 6 Water depth and current velocity in the Friesche Zeegat during flood on October 9, 1992 (05:00 UTC) with the station locations.

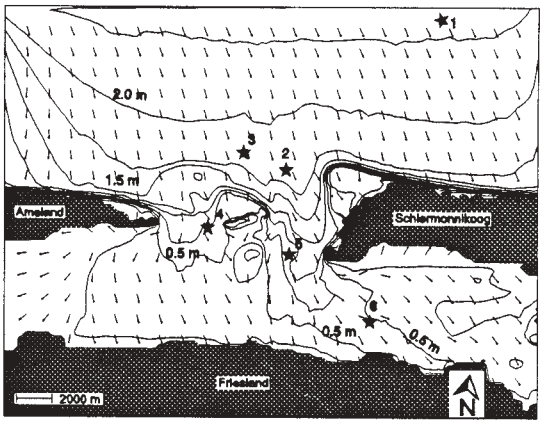


Fig. 7 The pattern of the significant wave height and mean wave direction (unit vectors) in the Friesche Zeegat during flood, computed by SWAN.

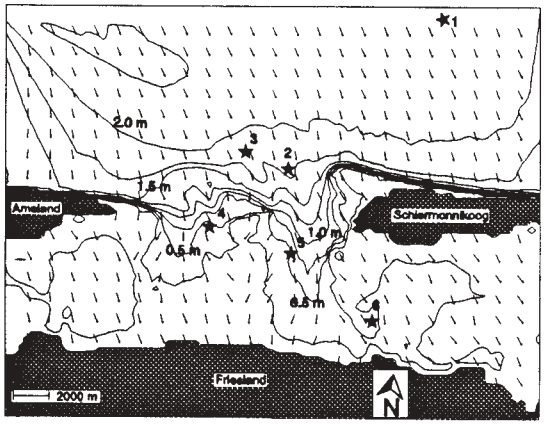


Fig. 8 As Fig. 7, computed by HISWA.



AUTHOR INDEX TABLE OF CONTENTS

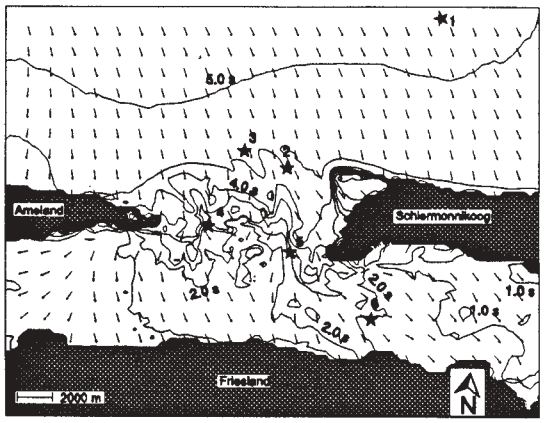


Fig. 9 The pattern of the mean wave period and mean wave direction (unit vectotrs) in the Friesche Zeegat during flood, computed by SWAN.

comparison with the observations (Fig. 11) indicates that the first pattern (SWAN) is probably more realistic than the second (HISWA). An essential difference between the two models is thus well illustrated: SWAN is able to account for multi-modal seas and HISWA not. This permits the mean frequency to shift upwards as the local wind generates a secondary, high-frequency peak in the spectrum. In contrast to this, HISWA assumes a uni-modal spectrum of which the mean frequency cannot be moved upward by the wind.

## 4. MODEL PERFORMANCE

A comparison with the observed significant wave height and mean wave period at the buoy locations for both models at both sites is given in Figs. 10 and 11. The wave observations in the Haringvliet case were not synchronous. Therefore the average of the two nearest observations on either side of 23:00 UTC is shown at each station. For the significant wave height the agreement with the observations is very reasonable for both models. A almost equally good agreement is obtained for SWAN for the mean wave period. That is, the errors seem to be acceptable for many coastal engineering problems. However, (a) both SWAN and HISWA tend to slightly overestimate the significant wave height, (b) SWAN tends to slightly underestimate the mean wave period and (c) HISWA significantly overestimates this period (for reasons explained above).

To quantify this performance of the models, a scatter-index, a model performance index, an operational performance index and a bias are defined. The scatter index (SI) is defined here as the rms-error normalized with the average observed value $\bar{X}$ (not including the incident value):

$$SI = \frac{rms_{error}}{\bar{X}} \tag{6}$$

where

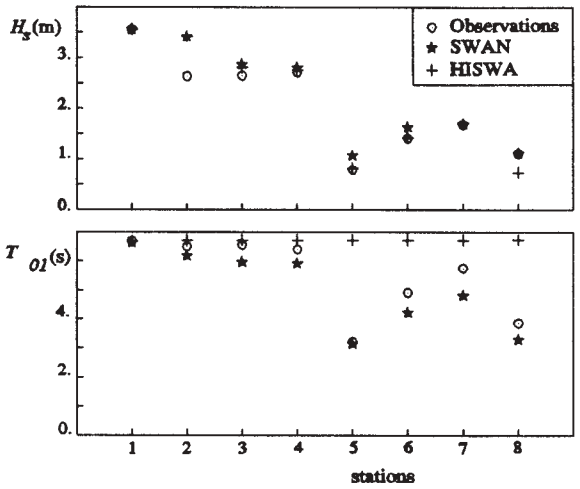


Fig. 10 The observed and computed significant wave height $H_s$ and mean wave period $T_{m01}$ in the Haringvliet on October 14, 1982 (SWAN and HISWA computations at 23:00 hr and average of observations around 23:00 UTC).

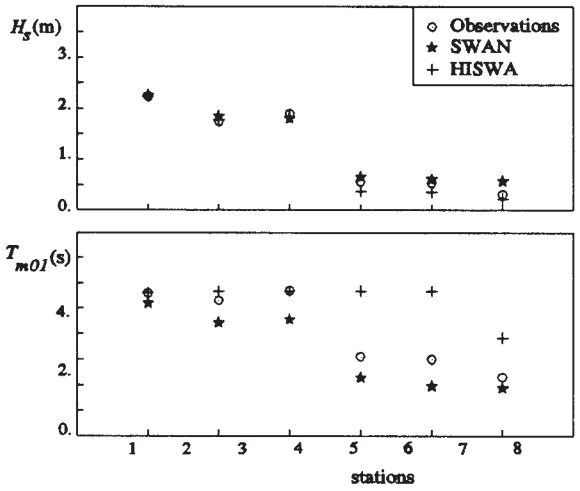


Fig. 11 The observed and computed significant wave height $H_s$ and mean wave period $T_{m01}$ in the Friesche Zeegat on October 9, 1992 (05:00 UTC; SWAN and HISWA computations).

$$rms_{error} = \sqrt{\frac{1}{N}\sum_{N}(X_n - Y_n)^2} \tag{7}$$

with $X_n$ the observed values, $Y_n$ the computed values and $N$ the number of observations. A diagnostic measure which indicates the degree to which the model reproduces the observed changes in the wave field is the model performance index (MPI) defined in terms of root-mean-square values:

$$MPI = 1 - \frac{rms_{error}}{rms_{changes}} \tag{8}$$

The definition of $rms_{changes}$ is identical to that of $rms_{error}$ except that all computed $Y_i$ values are replaced with the observed incident value $X_i$. For a perfect model ($rms_{error}=0$) the value of the MPI would be 1 whereas it would be 0 for a model that (erroneously) predicts no changes ($rms_{error}=rms_{changes}$). A more predictive and operationally more convenient measure is the operational performance index (OPI), defined as the rms-error normalized with the incident observed value:

$$OPI = \frac{rms_{error}}{X_i} \tag{9}$$

It is predictive in the sense that for a given value of the OPI (presumably a characteristic of the model and its implementation for a particular region), an error estimate can be made on the basis of incident wave conditions, prior to the computations. To determine the systematic part of the model performance, the bias is also considered. It is simply defined as the mean error (not including the incident values):

$$bias = \frac{1}{N}\sum_{N}(Y_i - X_i) \tag{10}$$

The average values of these error parameters for all five cases (one in the Haringvliet, two in the Friesche Zeegat and two in the Norderneyer Seegat) are summarized in Tables 2 and 3 (see accompanying paper of Holthuijsen et al. (1998) for details on the SWAN results). The parameter values are calculated per case and then averaged so that these averages generally do not obey the expressions 7, 8, 9 and 10. These values show that SWAN and HISWA perform equally well as regards the significant wave height (with only small differences). They both reproduce about 85% of the observed changes in the significant wave height from deep water and for both the rms-error is about 10% of the observed incident significant wave height. The values of the scatter index are is similar to those for the WAM model in oceanic applications (e.g., Zambreski, 1989, 1991; see also Komen et al., 1994; Romeiser, 1993; even if the definition is slightly different). As regards the mean period, SWAN performs significantly better than HISWA. SWAN reproduces about 75% of the observed changes whereas HISWA reproduces less than half of that. The relative rms-error in the SWAN results is about the same as for the significant wave height (i.e. 10% of the incident value) but for HISWA it is three times larger. (In fact, the poor performance of HISWA to reproduce the mean wave period in this kind of conditions was the main reason for developing SWAN.) The better overall performance of SWAN comes with a higher computational effort. The reasons are the following. In SWAN the waves are described with the full two-dimensional spectrum (over 360°) and in HISWA with only two moments per spectral direction (over only 120°). This represents more than one order of magnitude difference in the number of degrees of freedom of the models. The other difference is that in SWAN the formulations of the physical processes are considerably more involved than in HISWA, in particular the inclusion of quadruplet wave-wave interactions. To quantify the associated differences in computer requirements, the ratio of the actual computing (CPU) time and memory (SWAN/HISWA) of the cases of this study are listed in Table 4. It must be noted that accounting for currents in SWAN (as in the case of the Friesche Zeegat), is relatively expensive as in such cases an implicit propagation scheme is used in frequency domain (current-induced frequency shifting; in the absence of currents no such shifting occurs). It is obvious that HISWA is one to two orders of magnitude cheaper to run than SWAN. Also, if the "price" / "quality" ratio is considered (run time over OPI), HISWA is superior to SWAN as far as the significant wave height is concerned but the reverse is true for the mean wave period. But in comparing the qualities of HISWA and SWAN it must be noted that SWAN has the advantage of (a) giving spectral information, (b) permitting multi-modal seas and (c) providing a platform for implementing progress in the theoretical understanding of the physical processes involved. Moreover, since SWAN operates over the full 360° and HISWA only over 120°, it is expected that in refraction-dominated cases (possibly with reversal of wave directions, e.g. swell penetration), SWAN would provide better agreement with observations than HISWA.

## 4. CONCLUSIONS

In the rather complicated cases considered in this study of waves propagating across shoals or penetrating through a tidal gap onto tidal flats with currents and local wind, both HISWA and SWAN perform well in terms of significant wave height (rms-error ≃ 10% of the incident significant wave height). SWAN performs also well as regards the mean wave period (rms-error ≃ 10% of the incident mean wave period) but HISWA does not (rms-error ≃ 30% of the incident mean wave period). However, HISWA is one to two orders of magnitude more efficient than SWAN. On the other hand, the potential of SWAN for further developments on the basis of new scientific insights far exceeds that of HISWA.

## ACKNOWLEDGEMENTS

We thank John de Ronde, Joska Andorka Gal, Daan Dunsbergen, Miriam van Endt and their co-workers at the Ministry of Transport, Public Works and Water Management (the Netherlands) for providing us with the data of the Haringvliet and the Friesche Zeegat. We are equally indebted to Hans Niemeier and Ralf Kaiser of the State Coastal Research Station for Ecology in Norderney (Germany) for providing us with the data of the Norderneyer Seegat. Our special thanks go to Caroline Gautier who prepared the SWAN computations for the Norderneyer Seegat and to Bas Les who carried out the hydrodynamic calculations to determine the currents and water levels for the Friesche Zeegat cases.

## TABLES

| | $H_{s,i}$ (m) | $T_{m01,i}$ (s) | $\bar{\theta}_{wave,i}$ (°) | $\sigma_{\theta,i}$ (°) | $U_{10}$ (ms$^{-1}$) | $\theta_{wind}$ (°) |
|---|---|---|---|---|---|---|
| Haringvliet | 3.56 | 6.7 | 306 | 31 | 14.0 | 300 |
| Friesche Zeegat | 2.24 | 5.6 | 328 | 31 | 11.5 | 320 |

Table 1 The incident significant wave height, mean wave period, mean wave direction, directional spreading and wind speed and direction for the two cases that are treated in detail.

| | $H_{s,i}$ (m) | $\bar{H}_s$ (m) | bias (m) | rms (m) | SI (-) | MPI (-) | OPI (-) |
|---|---|---|---|---|---|---|---|
| SWAN | 2.99 | 1.00 | 0.15 | 0.29 | 0.37 | 0.86 | 0.09 |
| HISWA | 2.99 | 1.00 | -0.06 | 0.26 | 0.32 | 0.88 | 0.09 |

Table 2 The prediction errors for the significant wave height $H_s$ averaged over the five cases at the three sites of this study (Haringvliet, Friesche Zeegat and Norderneyer Seegat). The mean observed significant wave height is $\bar{H}_s$.

| | $T_{m01,i}$ (s) | $\bar{T}_{m01}$ (s) | bias (s) | rms (s) | SI (-) | MPI (-) | OPI (-) |
|---|---|---|---|---|---|---|---|
| SWAN | 6.6 | 3.9 | -0.6 | 0.7 | 0.20 | 0.73 | 0.12 |
| HISWA | 6.6 | 3.9 | 1.2 | 2.0 | 0.52 | 0.29 | 0.30 |

Table 3 The prediction errors for the mean wave period $T_{m01}$ for the five cases at the three sites of this study (Haringvliet, Friesche Zeegat and Norderneyer Seegat). The mean observed mean wave period is $\bar{T}_{m01}$.

| | CPU time SWAN / HISWA | memory SWAN / HISWA |
|---|---|---|
| Haringvliet | 53 | 200 |
| Friesche Zeegat | | |
| flood | 114 | 195 |
| ebb | 177 | 195 |
| Norderneyer Seegat | | |
| high tide | 55 | 195 |
| low tide | 55 | 195 |

Table 4 The ratio (SWAN/HISWA) of computing time (CPU) and memory for the five cases at the three sites of this study (Haringvliet, Friesche Zeegat and Norderneyer Seegat).

## REFERENCES


Battjes, J.A. and J.P.F.M. Janssen, 1978: Energy loss and set-up due to breaking of random waves, *Proc. 16th Int. Conf. Coastal Engineering*, ASCE, 569-587

Battjes, J.A. and S. Beji, 1992: Breaking waves propagating over a shoal, *Proc. 23rd Int. Conf. Coastal Engineering*, ASCE, 42-50

Booij, N., L.H. Holthuijsen and R. Padilla-Hernandez, 1997, A nonstationary, parametric coastal wave model, *Proc. Coastal Dynamics '97*, Plymouth, in press

Bouws, E. and G.J. Komen, 1983: On the balance between growth and dissipation in an extreme, depth-limited wind-sea in the southern North Sea, *J. Phys. Oceanogr.*, **13**, 1653-1658

Cavaleri, L. and P. Malanotte-Rizzoli, 1981: Wind wave prediction in shallow water: Theory and applications. *J. Geophys. Res.*, **86**, No. C11, 10,961-10,973

CERC, 1973: *Shore Protection Manual*, U.S. Army Corps of Engineers, Techn. Rep. No. 4, Vol. I

Collins, J.I., 1972: Prediction of shallow water spectra, *J. Geophys. Res.*, **77**, No. 15, 2693-2707

Eldeberky, Y., 1996: Nonlinear transformation of wave spectra in the nearshore zone, Ph.D. thesis, Delft University of Technology, Department of Civil Engineering, The Netherlands, 203 p.

Hasselmann, K., T.P. Barnett, E. Bouws, H. Carlson, D.E. Cartwright, K. Enke, J.A. Ewing, H. Gienapp, D.E. Hasselmann, P. Kruseman, A. Meerburg, P. Müller, D.J. Olbers, K. Richter, W. Sell and H. Walden, 1973: Measurements of wind-wave growth and swell decay during the Joint North Sea Wave Project (JONSWAP), *Dtsch. Hydrogr. Z. Suppl.*, 12, A8

Hasselmann, S., K. Hasselmann, J.H. Allender and T.P. Barnett, 1985: Computations and parameterizations of the linear energy transfer in a gravity wave spectrum. Part II: Parameterizations of the nonlinear transfer for application in wave models, *J. Phys. Oceanogr.*, 15, 11, 1378-1391

Hasselmann, K., 1974: On the spectral dissipation of ocean waves due to whitecapping, *Bound.-layer Meteor.*, **6**, 1-2, 107-127

Holthuijsen, L.H., Booij, N. and T.H.C. Herbers, 1989: A prediction model for stationary, short-crested waves in shallow water with ambient currents, *Coastal Engineering*, **13**, 23-54

Holthuijsen, L.H., R.C. Ris and N. Booij, 1996, A third-generation model for near-shore waves with ambient currents, *Proc. 25th Int. Conf. Coastal Engng.*, 668-676

Holthuijsen, L.H., R.C. Ris and N. Booij, 1998: A verification of the third-generation wave model SWAN, *Proceedings 5th Int. Workshop on Wave Hindcasting and Forecasting*, Melbourne, Fl., USA

Janssen, P.A.E.M., 1991: Quasi-linear theory of wind-wave generation applied to wave forecasting, *J. Phys. Oceanogr.*, **21**, 1631-1642

Komen, G.J., S. Hasselmann, and K. Hasselmann, 1984: On the existence of a fully developed wind-sea spectrum, *J. Phys. Oceanogr.*, 14, 1271-1285

Les, B.A.J., 1996: Flow computations in the Friesche Zeegat (Stromingsberekeningen in het Friesche Zeegat, in Dutch), M.Sc. thesis, Delft University of Technology, Department of Civil Engineering, The Netherlands

Madsen, O.S., Y.-K. Poon and H.C. Graber, 1988: Spectral wave attenuation by bottom friction: Theory, *Proc. 21st Int. Conf. Coastal Engineering*, ASCE, 492-504

WAMDI group, 1988: The WAM model - a third generation ocean wave prediction model, *J. Phys. Oceanogr.*, 18, 1775-1810

Mei, C.C., 1983: *The applied dynamics of ocean surface waves*, Wiley, New York, 740 p.

Miles, J.W., 1957: On the generation of surface waves by shear flows, *J. Fluid Mech.*, **3**, 185-204

Phillips, O.M., 1957: On the generation of waves by turbulent wind, *J. Fluid Mech.*, **2**, 417-445

Putnam, J.A. and J.W. Johnson, 1949: The dissipation of wave energy by bottom friction, *Trans. Am. Geoph. Union*, **30**, 67-74

Ris, R.C., L.H. Holthuijsen and N. Booij, 1994, A spectral model for waves in the near shore zone, *Proc. 24th Int. Conf. Coastal Engng.*, Kobe, Oct. 1994, Japan, pp. 68-78

Snyder, R.L., Dobson, F.W., Elliott, J.A. and R.B. Long, 1981: Array measurement of atmospheric pressure fluctuations above surface gravity waves, *J. Fluid Mech.*, **102**, 1-59

Stelling, G.S., A.K. Wiersma and J.B.T.M. Willemse, 1986: Practical aspects of accurate tidal computations, *J. Hydr. Eng.*, 112, 9, 802-817

Vincent, C.L., J.M. Smith and J. Davis, 1994: Parameterization of wave breaking in models, *Proc. of Int. Symp.: Waves - Physical and Numerical Modelling*, Univ. of British Columbia, Vancouver, Canada, M. Isaacson and M. Quick (Eds.), Vol. II, 753-762

# A VERIFICATION OF THE THIRD-GENERATION WAVE MODEL "SWAN"

L.H. Holthuijsen, R.C. Ris and N. Booij

Delft University of Technology, Department of Civil Engineering,
Delft, the Netherlands

## 1. INTRODUCTION

The third-generation wave model SWAN has been developed by Booij et al. (1997) to estimate wave conditions in small-scale, coastal regions with shallow water, (barrier) islands, tidal flats, local wind and ambient currents. The numerical implementation and the formulations of the various physical processes that are represented in the model have been successfully validated with academic tests but the model needs also to be verified in real field conditions. To this end the SWAN model is applied in stationary mode to three different sites in the southern North Sea. The results of the computations are presented and compared with observations.

## 2. THE WAVE MODEL

### 2.1 Basic equation

The SWAN wave model (Simulating WAves Nearshore) is a discrete spectral model based on the action balance equation which for Cartesian coordinates is (e.g., Hasselmann et al., 1973):

$$\frac{\partial}{\partial t} N + \frac{\partial}{\partial x} c_x N + \frac{\partial}{\partial y} c_y N + \frac{\partial}{\partial \sigma} c_\sigma N + \frac{\partial}{\partial \theta} c_\theta N = \frac{S}{\sigma} \qquad (1)$$

in which $N(\sigma, \theta, x, y, t)$ is the action density as a function of intrinsic frequency $\sigma$, direction $\theta$, horizontal coordinates $x$ and $y$ and time $t$. The first term in the left-hand side of this equation represents the local rate of change of action density in time, the second and third term represent propagation of action in geographical space (with propagation velocities in $x$- and $y$-space, $c_x$ and $c_y$ respectively). The fourth term represents shifting of the intrinsic frequency due to variations in depths and currents (with propagation velocity in $\sigma$-space, $c_\sigma$). The fifth term represents depth- and current-induced refraction (with propagation velocity in $\theta$-space, $c_\theta$). The expressions for these propagation speeds are taken from linear wave theory (e.g., Mei, 1983). The term $S$ $(=S(\sigma,\theta))$ at the right hand side of the action balance equation is the energy source term representing generation of waves by wind, dissipation and nonlinear wave-wave interactions.

### 2.2 Wind input

Transfer of wind energy to the waves is described with the resonance mechanism of Phillips (1957) and the feed-back mechanism of Miles (1957). The corresponding source term for these mechanisms is commonly described by the sum of linear and exponential growth:

$$S_{in}(\sigma,\theta) = A + B E(\sigma,\theta) \qquad (2)$$

in which $E(\sigma,\theta)$ is the two-dimensional energy spectrum and $A$ and $B$ are coefficients which depend on wave frequency and direction and wind speed and direction. The effects of currents are accounted for by using the apparent local wind speed and direction. The expression for the term $A$ is due to Cavaleri and Malanotte-Rizzoli (1981) but with a filter to avoid growth at frequencies lower than the Pierson-Moskowitz frequency (Tolman, 1992). Two optional expressions for the coefficient $B$ are used in the model. The first is due to Snyder et al. (1981), rescaled in terms of friction velocity $U_*$ by Komen et al. (1984; used in the present study). The second is due to Janssen (1991).

### 2.3 Dissipation

Whitecapping is primarily controlled by the steepness of the waves (e.g., the WAMDI group, 1988):

$$S_{ds,w}(\sigma,\theta) = -\Gamma \tilde{\sigma} \frac{k}{\tilde{k}} E(\sigma,\theta) \qquad (3)$$

where $\Gamma$ is a steepness dependent coefficient, and $\tilde{\sigma}$ and $\tilde{k}$ denote the mean frequency and the mean wave number. The value of $\Gamma$ depends on the wind input formulation that is used. Since two expressions are available for the wind input in the SWAN model, also two values for $\Gamma$ are available. The first is due to Komen et al. (1984; used in the present study). The second expression is an adaptation of this expression based on Janssen (1991).

Bottom friction can generally be represented as:

$$S_{ds,b}(\sigma,\theta) = -C_{bottom} \frac{\sigma^2}{g^2 \sinh^2(kd)} E(\sigma,\theta) \qquad (4)$$

in which $C_{bottom}$ is a bottom friction coefficient. In the SWAN model are available: the empirical coefficient of JONSWAP (Hasselmann et al., 1973; for swell) and Bouws and Komen (1983; for wind sea; this coefficient is used in the present study), the drag law model of Collins (1972) and the eddy-viscosity model of Madsen et al. (1988).

Depth-induced wave breaking can be modelled with the random bore model of Battjes and Janssen (1978). Laboratory observations (e.g., Battjes and Beji, 1992; Vincent et al. 1994) show that the shape of initially uni-modal spectra propagating across simple (barred) beach profiles, is fairly insensitive to depth-induced breaking. This has led to a simple spectral version of the energy dissipation:

$$S_{ds,br}(\sigma,\theta) = -\frac{D_{tot}}{E_{tot}} E(\sigma,\theta) \qquad (5)$$

in which $D_{tot}$ is the rate of total energy dissipation due to wave breaking. For this, the expression of Battjes and Janssen (1978) is used with the maximum wave height-to-depth ratio of $\gamma = 0.73$.

### *2.4 Nonlinear wave-wave interactions*

In deep water, quadruplet wave-wave interactions dominate the evolution of the spectrum. They transfer wave energy from the peak frequency to lower frequencies (thus moving the peak frequency to lower values) and to higher frequencies (where it is dissipated by whitecapping). In very shallow water, triad wave-wave interactions are more important, transferring energy from lower frequencies to higher frequencies (transfer to lower frequencies is not considered here). In the SWAN model the computations of the quadruplet interactions are carried out with the Discrete Interaction Approximation (DIA) of Hasselmann et al. (1985). The computations of the triad interactions are carried out with the Lumped Triad Approximation (LTA) of Eldeberky (1996).

The above chosen formulations in the present study for wind input, whitecapping, quadruplet wave-wave interactions and bottom dissipation are identical to the formulations in the WAM model (Cycle 3, the WAMDI group, 1988). In the SWAN model, the above triad wave-wave interactions and depth-induced breaking are added to these WAM formulations.

## 3. FIELD CASES

The SWAN model is verified here at three sites that are located along the North Sea coast of the Netherlands and Germany: the Haringvliet, the Norderneyer Seegat and the Friesche zeegat (Fig. 1).

### *3.1 Haringvliet*

The Haringvliet is a branch of the Rhine estuary in the south-west of the Netherlands that is separated from the main estuary by sluices. The bathymetry of the area and the locations of the (eight) observation stations are shown in Fig. 2. A local storm generated on October 14, 1982 waves from north-westerly directions and SWAN computations are carried out for 23:00 UTC on this day. The incident wave conditions and the wind are given in Table 1 (significant wave height $H_s$ and the mean wave period $T_{m01}$ defined as $H_s = 4\sqrt{m_0}$ and $T_{m01} = 2\pi (m_1 / m_0)$ where $m_n = \int \sigma^n E(\sigma,\theta)$).

The waves approach the estuary from deep water and break over a shoal (the Hinderplaat, Fig. 2) with a reduction of significant wave height from about 3.6 m in deep water to 2.5 m just in front of the shoal to about 0.6 m just behind the shoal. The local wind regenerates the waves behind the shoal to about 1.1 m significant wave height at station 8. Figure 3 shows the computed pattern of the significant wave height which is consistent with the pattern of the observations. A comparison with the observed significant wave height and mean wave period at the buoy locations is given in Fig. 4. The wave

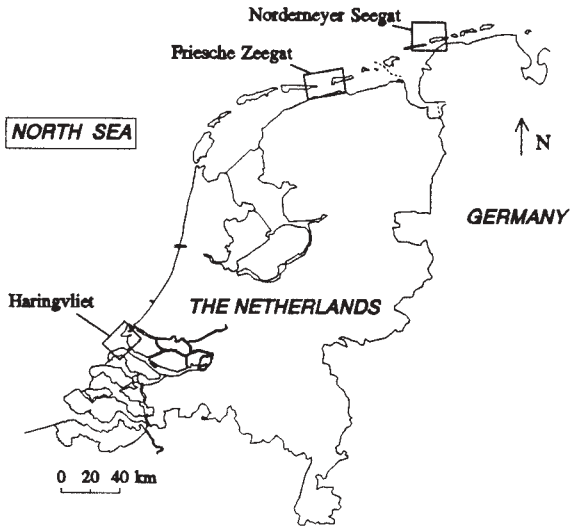


Fig. 1 The locations of the three sites along the Dutch and German coast in the southern North Sea.

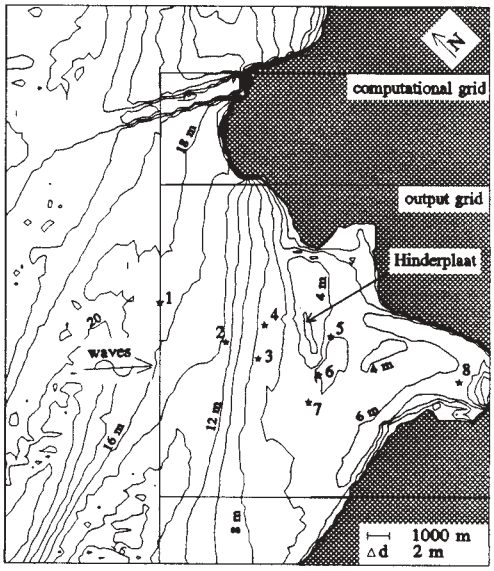


Fig. 2 The bathymetry of the Haringvliet with the locations of eight observation stations (numbered 1 through 8).

observations at the various stations were not synchronous. Therefore the two nearest observations on either side of 23:00 UTC are considered at each station. The agreement is generally reasonable although the model tends to slightly overestimate the significant wave height and to slightly underestimate the mean wave period.

The computed spectra are compared with the observed spectra in Fig. 5. The overall agreement is reasonable, particularly if allowance is made for the 20-fold variation in energy density scale of the spectra. But the decay of the primary peak and the regeneration at high frequencies



AUTHOR INDEX TABLE OF CONTENTS

beyond station 5 (see e.g. station 8) is poorly predicted. The variations in water level (0.6 m per hour) may have affected the evolution of the primary incident peak, particularly over the shoal. Computations at one hour before 23:00 UTC and one hour after, indicate that the evolution of this peak is indeed critically dependent on this temporal variation in water depth. Repeated computations without wind but with triad wave-wave interactions, and

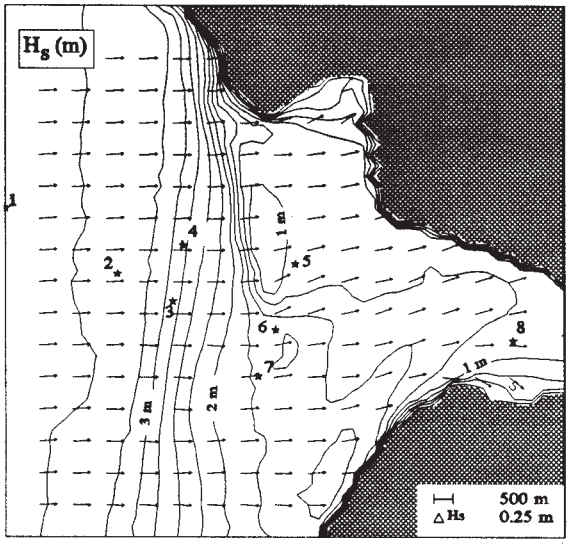


Fig. 3 The computed pattern of the significant wave height and mean wave direction (unit vectors) in the Haringvliet at 23:00 UTC on October 14, 1982.

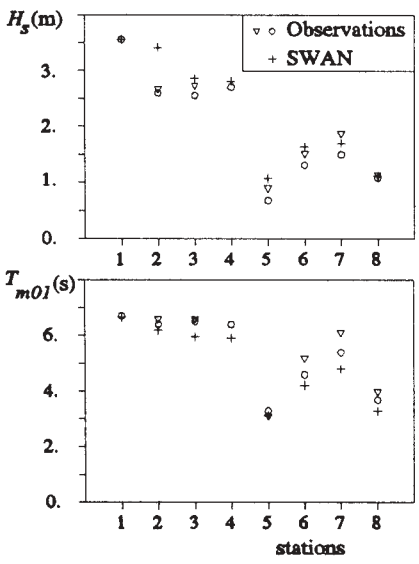


Fig. 4 The observed and computed significant wave height $H_s$ and mean wave period $T_{m01}$ in the Haringvliet on October 14, 1982 (computations at 23:00 hr and observations around 23:00 UTC).

vice-versa, show that both processes are equally responsible for the generation of the secondary, high-frequency peak at about twice the (incident) peak frequency at station 8.

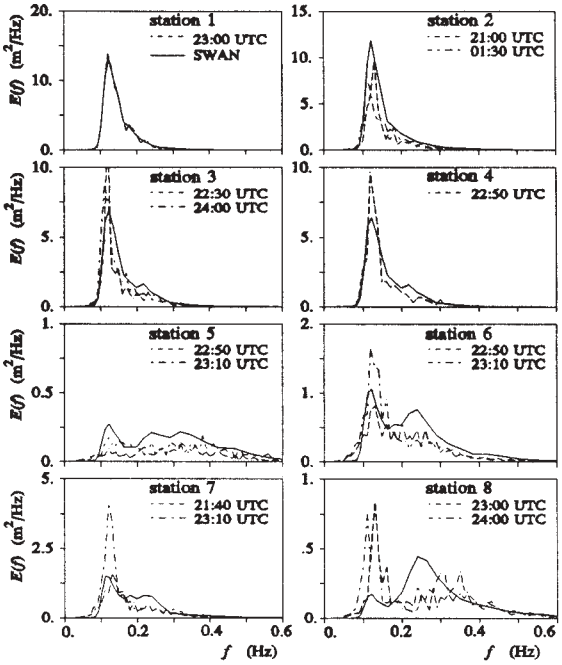


Fig. 5 The observed and computed spectra in the Haringvliet on 14 October, 1982 (computations at 23:00 hr and observations around 23:00 UTC). Note the 20-fold variation in energy density scale.

### 3.2 *Norderneyer Seegat*

The Norderneyer Seegat (Fig. 6) is a tidal gap between the barrier islands of Juist and Norderney in the northern part of Germany. The region behind this gap is an inter-tidal area with shoals and channels over a distance of 7.5 km to the main land. Two cases have been selected: a low-tide case (November 16, 1995, 22:00 UTC) and a high-tide case (November 17, 1995, 04:00 UTC). Since no current observations were available, a situation at the turn of the tide has been selected so that the effect of currents can be ignored. The incident wave conditions and the wind speed and direction are given in Table 1. As the waves propagate from deep water to the barrier islands the wave height gradually decreases from about 3 m to about 1 m (low-tide) or about 2.5 m (high-tide) at station 2. It is obvious from the observed spectra (Fig. 9) that the wave conditions behind the islands are dominated by local wind (the low frequency peak at station 1 is not present at stations 4 through 9). Figure 7 shows the computed pattern of the significant wave height for the low-tide case. This pattern is consistent with the pattern of the observations: the significant wave height reduces gradually from the deep water value of about 3 m to about 1 m in front of the tidal gap. As the waves propagate through the gap they refract out of the channels to the shallower parts where wave energy is dissipated rapidly. The local wind regenerates

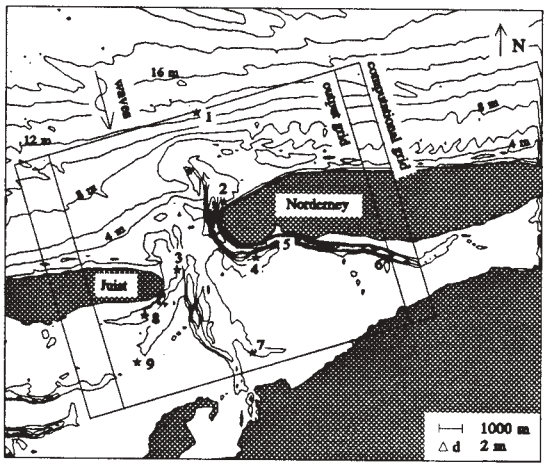


Fig. 6 The bathymetry of the Norderneyer Seegat with the locations of nine observation stations (numbered 1 through 9).

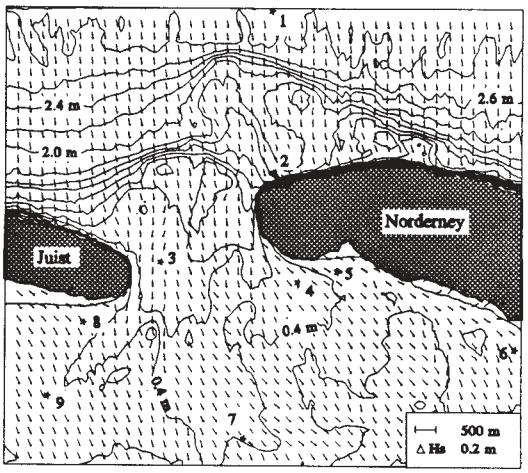


Fig. 7 The computed pattern of the significant wave height and mean wave direction (unit vectors) in the Norderneyer Seegat at low tide (22:00 UTC) on November 16, 1995.

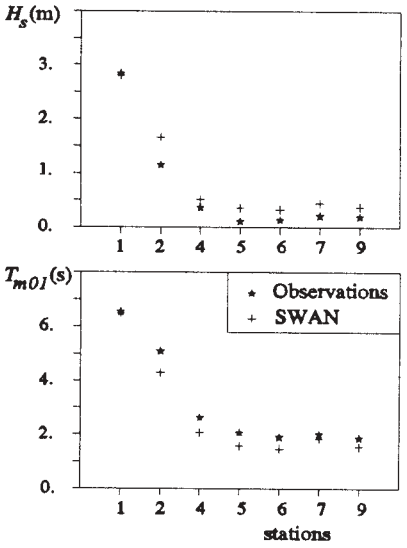


Fig. 8 The observed and computed significant wave height $H_s$ and mean wave period $T_{m01}$ in the Norderneyer Seegat at low tide (22:00 UTC) on November 16, 1995 (stations 3 and 8 missing from the data).

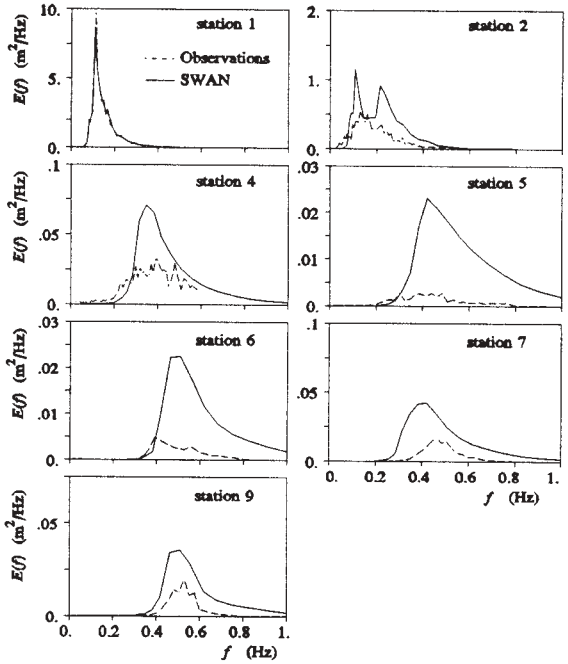


Fig. 9 The observed and computed spectra in the Norderneyer Seegat at low tide (22:00 UTC) on November 16, 1995. Note the 20-fold variation in energy density scale between the panels.

high-frequency waves in the interior region, thus decreasing the mean wave period from 6 s in deep water to about 2 s.

The comparison between the computed and observed significant wave height and mean wave period is reasonable, as is evident from Fig. 8. Generally, the model slightly overestimates the significant wave height and underestimates the mean wave period. A comparison between the computed and the observed spectra is shown in Fig. 9. It is obvious that the spectra are not well reproduced by the model but the 20-fold difference in energy levels between stations 1 and 9 should be noted.

The model overestimates the spectral levels particularly at stations 4, 5 and 6 which are located near an upwind coast. This suggests that local wind generation at very short fetches is much slower in the field than in the model. This may be due to an overestimation of the wind speed in the model which is assumed to be constant but a larger effect may be due to the presence of residual low-frequency wave energy from the open sea in the area behind the islands.

Such (low-frequency) background energy seems to reduce the wave growth by wind (e.g., Donelan, 1987; in idealized, fetch-limited conditions the model reproduces observed wave generation very well, Ris, 1997).

For the high-tide case the computed pattern of significant wave height and mean wave direction is very similar to that of the low-tide case. It is therefore not shown here. The agreement between the computed and observed significant wave heights and mean wave periods is again reasonable (not shown here), with the same degree of overestimating the significant wave height at the sheltered stations 4, 5 and 6 and (slightly more) underestimating the mean wave period.

### *3.3 Friesche Zeegat*

The situation of the Friesche Zeegat is geographically similar to that of the Norderneyer Seegat (Fig. 10), the main difference being that the inter-tidal area is larger and that the main channel crosses to the main land. Two cases have been selected: a flood case (October 9, 1992, 05:00 UTC) and an ebb case (October 9, 7, 1992, 11:00 UTC). The current velocities and water levels that are used in the computations have been obtained with the WAQUA circulation model (Les, 1996; Stelling et al., 1986) and are shown for the flood case in Fig. 10. The incident wave conditions and the wind speed and direction are given in Table 1.

The computed pattern of the significant wave height for the flood case is shown in Fig. 11. It is consistent with the pattern of the observations: the wave height gradually decreases between the deep water boundary and the entrance of the tidal inlet. The computed significant wave height and mean period at the six observation stations are given in Fig. 12. Again, the agreement with the observed significant wave heights is very reasonable but the mean wave period is underestimated by approximately 1 s.

Computations show that the currents in the area decrease the significant wave height and mean wave period in the channels. For instance, at station 5 the currents reduce the significant wave height from about 0.8 m to about 0.6 m and the mean wave period from about 2.9 s to about 1.9 s.

The computed spectra are compared with the observed spectra in Fig. 13 (05:00 UTC). The spectra that are observed at 06:00 UTC are also shown, indicating that the time variation in the conditions may have been relevant. It is obvious that the agreement between the observed spectra and the computed spectra is better than in the case of the Norderneyer Seegat (compare with Fig. 9). For the ebb case, the computed pattern of the significant wave height is similar to that of the flood case, except that the currents act to some extent as a wave guide (resulting in somewhat higher waves in the channels and mean wave directions which roughly follow the pattern of the channels).

## 4. MODEL PERFORMANCE

To quantify the performance of the model, a scatter-index, a model performance index, an operational performance index and a bias are defined. The scatter index

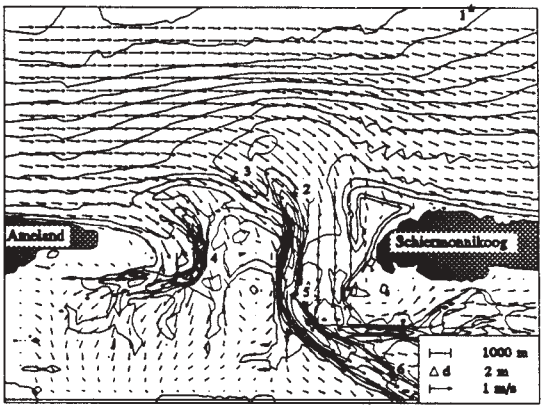


Fig. 10 Water depth (storm surge added to bathymetry) and current velocity in the Friesche Zeegat during the flood case (05:00 UTC on October 9, 1992).

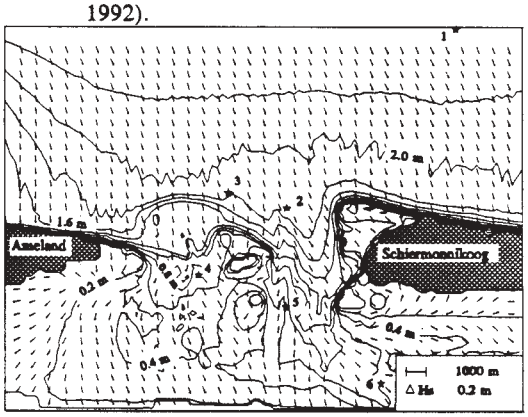


Fig. 11 The computed pattern of the significant wave height and mean wave direction (unit vectors) in the Friesche Zeegat during the flood case.

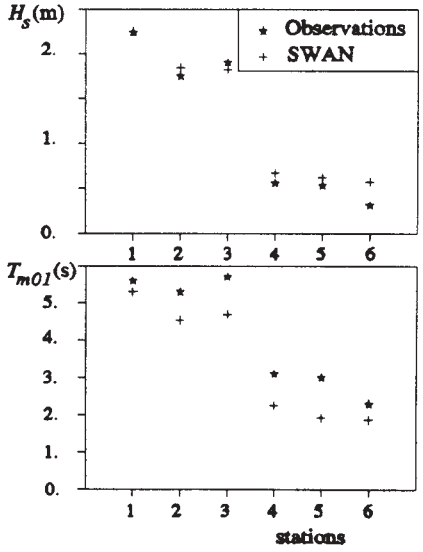


Fig. 12 The observed and computed significant wave height $H_s$ and mean wave period $T_{m01}$ in the Friesche Zeegat during the flood case.



AUTHOR INDEX TABLE OF CONTENTS

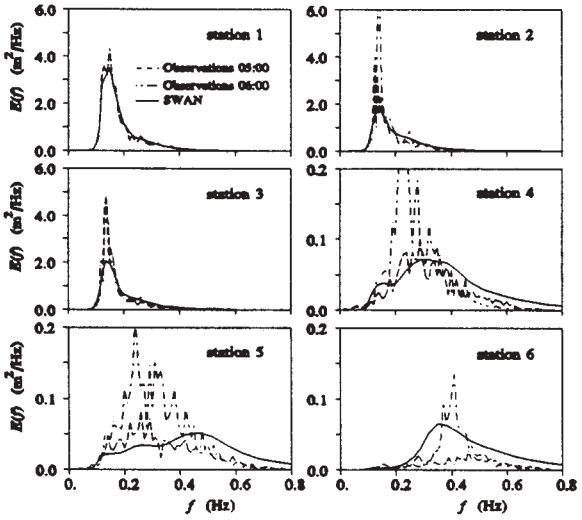


Fig. 13 The observed and computed spectra for the flood case in the Friesche Zeegat on October 9, 1992. Observed at 5:00 UTC and 6:00 UTC. Computed at 5:00 UTC. Note the 30-fold differences in energy density scale between the panels.

is defined here as the rms-error normalized with the average observed value $\bar{X}$ (not including the incident value):

$$SI = \frac{rms_{error}}{\bar{X}} \tag{6}$$

where

$$rms_{error} = \sqrt{\frac{1}{N}\sum_{N}(X_n - Y_n)^2} \tag{7}$$

with $X_n$ the observed values, $Y_n$ the computed values and $N$ the number of observations (not including the incident value). However, it is considered to be somewhat misleading for coastal wave models as the average significant wave height is usually rather small in coastal regions (an rms-error of 0.1 m in the significant wave height in complex field conditions seems quite acceptable but if the average value is only 0.5 m, the scatter index attains the rather high value of 20%). An alternative, diagnostic measure which indicates the degree to which the model reproduces the observed changes in the wave field is the model performance index (MPI) defined in terms of root-mean-square values:

$$MPI = 1 - \frac{rms_{error}}{rms_{changes}} \tag{8}$$

The definition of $rms_{changes}$ is identical to that of $rms_{error}$ except that all computed $Y_n$ values are replaced by the observed incident value $X_i$. For a perfect model ($rms_{error}=0$) the value of the MPI would obviously be 1 whereas it would be 0 for a model that (erroneously) predicts no changes ($rms_{error} = rms_{changes}$). A more predictive and operationally more convenient measure is the operational performance index (OPI), defined as the rms-error normalized with the incident observed value:

$$OPI = \frac{rms_{error}}{X_i} \tag{9}$$

It is predictive in the sense that for a given value of the OPI (presumably a characteristic of the model and its implementation for a particular region), an error estimate can be made on the basis of incident wave conditions, prior to the computations. To determine the systematic part of the model performance, the bias is also considered. It is simply defined as the average error (not including the incident values).

The values of these error parameters for the five cases of this study are summarized in Tables 2 and 3. These values show that the SWAN model performs well with the OPI values varying between 6% and 14% for significant wave height and between 8% and 16% for the mean wave period. The MPI values show that, on average, the model reproduces 86% of the observed changes in significant wave height and 73% of the observed changes in mean wave period. The values of the scatter index are similar to those for the WAM model in oceanic applications (e.g., Zambreski, 1989, 1991; see also Komen et al., 1994; Romeiser, 1993; even if the definition is slightly different). The relatively large values of the bias (compared to the rms-error) shows that these errors are systematic to a large extent.

## 4. CONCLUSIONS

In the rather complicated cases considered in this study of waves penetrating onto tidal flats behind barrier islands, the SWAN model performs well in terms of significant wave height and mean wave period. The model reproduces 86% of the observed changes in significant wave height and 73% of the observed changes in mean wave period. The rms-errors are about 10% of the incident values for both the significant wave height and the mean wave period. Behind the islands the computed waves are too low, presumably due to overestimating the local wave growth in the presence of residual wave energy from the open sea.

## ACKNOWLEDGEMENTS

We are very grateful to John de Ronde, Joska Andorka Gal, Daan Dunsbergen, Miriam van Endt and their co-workers at the Ministry of Transport, Public Works and Water Management (the Netherlands) for providing us with the data of the Haringvliet and the Friesche Zeegat. We are equally indebted to Hans Niemeier and Ralf Kaiser of the State Coastal Research Station for Ecology in Norderney (Germany) for providing us with the data of the Norderneyer Seegat. Our special thanks go to Caroline Gautier who prepared the SWAN computations for the Norderneyer Seegat and to Bas Les who carried out the hydrodynamic calculations for the Friesche Zeegat case.

TABLES

| | $H_{s,i}$ (m) | $T_{m01,i}$ (s) | $\bar{\theta}_{wave,i}$ (°) | $\sigma_{\theta,i}$ (°) | $U_{10}$ (ms$^{-1}$) | $\theta_{wind}$ (°) |
|---|---|---|---|---|---|---|
| Haringvliet | 3.56 | 6.7 | 306 | 31 | 14.0 | 300 |
| Nordemeyer Seegat: | | | | | | |
| Low tide | 2.84 | 6.5 | 335 | 45 | 13.0 | 315 |
| High tide | 2.98 | 6.8 | 375 | 45 | 8.0 | 338 |
| Friesche Zeegat | | | | | | |
| Flood | 2.24 | 5.6 | 328 | 31 | 11.5 | 320 |
| Ebb | 3.31 | 7.4 | 341 | 23 | 11.5 | 340 |

Table 1 The incident significant wave height, mean wave period, mean wave direction, directional spreading and wind speed and direction for the five cases at the three sites of this study (Haringvliet, Friesche Zeegat and Nordemeyer Seegat).

| | $H_{s,i}$ (m) | $\bar{H}_s$ (m) | bias (m) | rms (m) | SI (-) | MPI (-) | OPI (-) |
|---|---|---|---|---|---|---|---|
| Haringvliet | 3.56 | 1.86 | 0.23 | 0.33 | 0.18 | 0.82 | 0.09 |
| Nordemeyer seegat | | | | | | | |
| Low tide | 2.84 | 0.36 | 0.25 | 0.28 | 0.77 | 0.89 | 0.10 |
| High tide | 2.98 | 0.64 | 0.02 | 0.23 | 0.35 | 0.91 | 0.08 |
| Friesche Zeegat | | | | | | | |
| Flood | 2.24 | 1.01 | 0.09 | 0.15 | 0.14 | 0.90 | 0.06 |
| Ebb | 3.31 | 1.12 | 0.15 | 0.47 | 0.42 | 0.80 | 0.14 |
| Average | 2.99 | 1.00 | 0.15 | 0.29 | 0.37 | 0.86 | 0.09 |

Table 2 The prediction errors for the significant wave height $H_s$ for the five cases at the three sites of this study (Haringvliet, Friesche Zeegat and Nordemeyer Seegat). The mean observed significant wave height is $\bar{H}_s$.

| | $T_{m01,i}$ (s) | $\bar{T}_{m01}$ (s) | bias (s) | rms (s) | SI (-) | MPI (-) | OPI (-) |
|---|---|---|---|---|---|---|---|
| Haringvliet | 6.7 | 5.3 | -0.5 | 0.6 | 0.11 | 0.69 | 0.09 |
| Nordemeyer Seegat | | | | | | | |
| Low tide | 6.5 | 2.6 | -0.5 | 0.5 | 0.20 | 0.88 | 0.08 |
| High tide | 6.8 | 3.2 | -0.8 | 1.0 | 0.32 | 0.74 | 0.15 |
| Friesche Zeegat | | | | | | | |
| Flood | 5.6 | 3.9 | -0.9 | 0.9 | 0.23 | 0.59 | 0.16 |
| Ebb | 7.4 | 4.5 | -0.5 | 0.7 | 0.14 | 0.76 | 0.10 |
| Average | 6.6 | 3.9 | -0.6 | 0.7 | 0.20 | 0.73 | 0.12 |

Table 3 The prediction errors for the mean wave period $T_{m01}$ for the five cases at the three sites of this study (Haringvliet, Friesche Zeegat and Nordemeyer Seegat). The mean observed mean wave period is $\bar{T}_{m01}$.

REFERENCES


Battjes, J.A. and J.P.F.M. Janssen, 1978: Energy loss and set-up due to breaking of random waves, *Proc. 16th Int. Conf. Coastal Engineering*, ASCE, 569-587

Booij, N., R.C. Ris and L.H. Holthuijsen, 1997: A third-generation wave model for coastal regions. Part I: Model description and validation (stationary mode), submitted for publication.

Cavaleri, L. and P. Malanotte-Rizzoli, 1981: Wind wave prediction in shallow water: Theory and applications. *J. Geophys. Res.*, **86**, No. C11, 10,961-10,973

Donelan, M.A., 1987: The effect of swell on the growth of wind waves, *Johns Hopkins APL Technical Digest*, 8, 1, 18-23

Eldeberky, Y., 1996: Nonlinear transformation of wave spectra in the nearshore zone, Ph.D. thesis, Delft University of Technology, Department of Civil Engineering, The Netherlands, 203 p.

Hasselmann, K., T.P. Barnett, E. Bouws, H. Carlson, D.E. Cartwright, K. Enke, J.A. Ewing, H. Gienapp, D.E. Hasselmann, P. Kruseman, A. Meerburg, P. Müller, D.J. Olbers, K. Richter, W. Sell and H. Walden, 1973: Measurements of wind-wave growth and swell decay during the Joint North Sea Wave Project (JONSWAP), *Dtsch. Hydrogr. Z. Suppl.*, 12, A8

Hasselmann, S., K. Hasselmann, J.H. Allender and T.P. Barnett, 1985: Computations and parameterizations of the linear energy transfer in a gravity wave spectrum. Part II: Parameterizations of the nonlinear transfer for application in wave models, *J. Phys. Oceanogr.*, 15, 11, 1378-1391

Komen, G.J., S. Hasselmann, and K. Hasselmann, 1984: On the existence of a fully developed wind-sea spectrum, *J. Phys. Oceanogr.*, 14, 1271-1285

Komen, G.J., Cavaleri, L., Donelan, M., Hasselmann, K., Hasselmann, S. and P.A.E.M. Janssen, 1994: *Dynamics and Modelling of Ocean Waves*, Cambridge University Press, 532 p.

Les, B.A.J., 1996: Flow computations in the Friesche Zeegat (Stromingsberekeningen in het Friesche Zeegat, in Dutch), M.Sc. thesis, Delft University of Technology, Department of Civil Engineering, The Netherlands

WAMDI group, 1988: The WAM model - a third generation ocean wave prediction model, *J. Phys. Oceanogr.*, 18, 1775-1810

Mei, C.C., 1983: *The applied dynamics of ocean surface waves*, Wiley, New York, 740 p.

Ris, R.C., 1997: Spectral modelling of wind waves in coastal areas, *Communications on Hydraulic and Geotechnical Engineering*, Delft University of Technology, Ph.D thesis, 160 p.

Romeiser, R., 1993: Global validation of the wave model WAM over a one-year period using Geosat wave height data, *J. Geophys. Res.*, 98, C3, 4713-4726

Stelling, G.S., A.K. Wiersma and J.B.T.M. Willemse, 1986: Practical aspects of accurate tidal computations, *J. Hydr. Eng.*, 112, 9, 802-817

Zambreski, 1989: A verification study of the global WAM model, December 1987-November 1988, ECMWF Techn. Rep. 63, ECMWF, Reading

Zambreski, 1991: An evaluation of two WAM hindcasts for LEWEX, in: *Directional ocean wave spectra*, R.C. Beal (ed.), The Johns Hopkins University Press, Baltimore, 167-172

# MODELING OF EFFECTIVENESS OF WAVE DAMPING STRUCTURES IN WADDEN SEA AREAS

Hanz D. Niemeyer & Ralf Kaiser

Coastal Research Station of the Lower Saxonian Central State Board for Ecology P.O. Box 1221, 26534 Norderney/East Frisia, Germany

## 1. INTRODUCTION

In wave sheltered areas of the Wadden Sea sedimentation enabled the growth of supratidal salt marshes shoreward of the intertidal flats (Niemeyer 1979, 1983, 1995), partly supported by human activities. Traditionally they have been in human use, particularly for agricultural purposes but partly in the course of the last decades also for tourism. In order to increase the safety of these areas against flooding during summer allowing there seasonal safe keeping of e. g. cattle or small recreation facilities some of these areas have been enclosed by small earth walls called summer dykes (fig. 1). The crest of these summer dykes are lower than the design level but sufficiently high to give the summer polders shelter against flooding during the period of use in summer. The storm surges occuring then have generally set-ups which are lower than the crest heights of the summer dykes. If storm surges with a higher set-up occur the summer dykes are submerged and the summer polders are flooded.

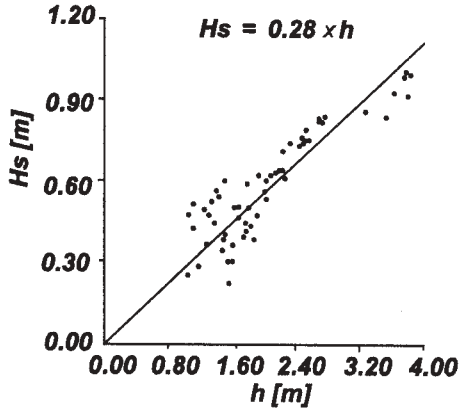


Fig. 2: Dynamical equilibrium of significant wave heights and water depths on tidal flats

Nowadays ecologists give salt marshes a much higher credit than summer polders. Most recently environmentalists demand increasingly for an ecological reinstatement of these areas to salt marshes by putting the summer dykes out of function, particularly as compensation for human impacts in the Wadden Sea like pipelaying or impoldering of tidal flats. In the past both supratidal salt marshes on their own and summer dykes have been regarded as wave absorbers in front of the sea dykes providing additional safety for them (Ingenieurkommission 1962; Erchinger 1971). This judgement based on comparison of measured wave run-up neglecting differences in local wave climate

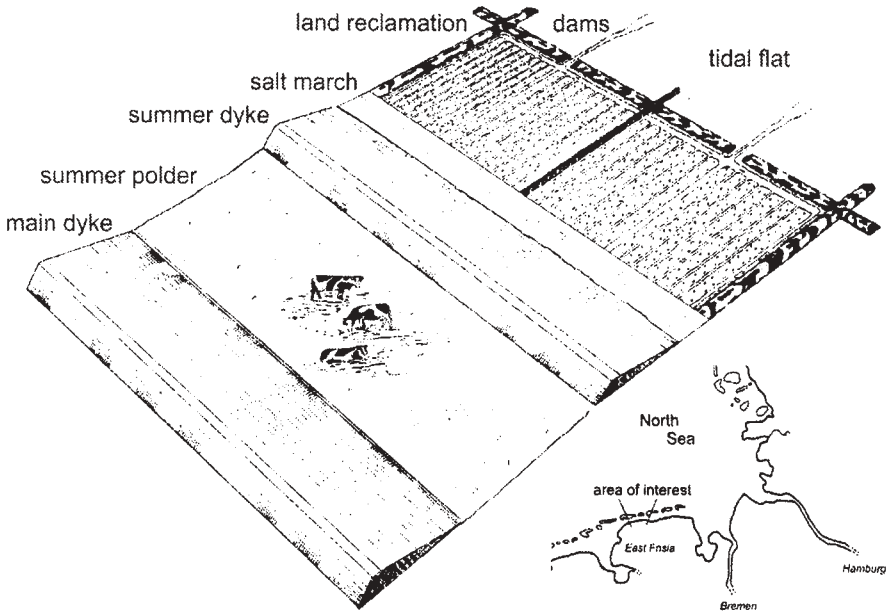


Fig. 1: Sceme of the nearshore area of the Wadden Sea with tidal flat, land reclamation dams, salt marsh, summer dyke, summer polder and main dyke and location of the area of interest



AUTHOR INDEX TABLE OF CONTENTS

due to governing boundary conditions. Meanwhile field investigations have made evident that there is no specific wave damping on salt marshes during severe storm surges (Ingenieurkommission 1979; Niemeyer 1979, 1983, 1991; Kaiser et al. 1995): The depth limited waves on tidal flats establish a dynamical equilibrium between wave heights and local water depths above MSL (fig. 2). Therefore they do not experience breaking at the edge of salt marshes because the wave height/water depth ratios do not exceed the critical value (Niemeyer 1979, 1983, 1991).

The self ruling communities in the coastal areas being responsible for the dykes claim that summer dykes create even for design conditions an evident wave attenuation leading to reduced wave loads on the sea dykes and increased safety of the hinterland. For that reason they object against the dismantling of the summer dykes. In order to deliver a sound basis for governmental decissions at the Coastal Research Station intensive studies have been carried out in the framework of a research project of the German Committee on Coastal Engineering Research. Major tool was the mathematical wave model HISWA (Holthuijsen & Booij 1987; Booij & Holthuijsen 1992) and the additional use of data from the Joint Research Facility Large Wave Flume Hannover and from intensive field investigations of CRS. HISWA incorporates all physical processes which are essential for suitable modeling of the interactions of waves with tidal flats, salt marshes and summer dykes. E. g. wave attenuation due to the effect of ebb delta shoals has been successfully modeled with HISWA (den Adel et al. 1991).

## 2. COMPARISON OF HISWA RUNS WITH DATA FROM THE LARGE WAVE FLUME

Tests in the Large Wave Flume in 1990 did also confirm the results of earlier field investigations (Niemeyer 1979, 1983) that no specific wave attenuation due to breaking will be created by salt marshes for the occurence of high storm surge levels. Friction is in the flume with its smooth bottom much smaller than e. g. tidal flats and salt marshes. The reduction of wave heights can be explained by shoaling effects, the relative water depth indicates those range of intermediate conditions for which wave heights decrease.

Data of these tests have been used as a basis for another verification of the mathematical wave model HISWA which has not been verified before with respect to such extreme shallow water conditions. The comparison of model and flume data show a general agreement, particularly for significant wave heights (fig. 3): differences do not exceed 10 %. Partly or

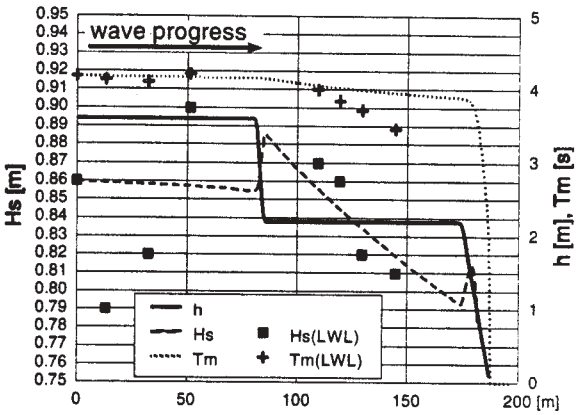

Fig. 3: Comparison of results from tests in the Large Wave Flume and HISWA model runs

even mostly they must be credited to small reflections in the flume though absorbtion was carried out in order to minimize reflection and maybe to the measuring devices in the flume. From a physical point of view the HISWA results with their clear tendencies deliver more reliable results than the scattering data of the flume. This successful verification encouraged to make use of HISWA for a systematic evaluation of the effectiveness of summer dykes on salt marshes in respect of wave damping.

Both the physical tests and the mathematical model runs make evident that there is no specific wave damping on supratidal salt marshes due to breaking for storm surge water levels and particularly not for design conditions. As already mentioned field investigations lead to the same conclusion (Niemeyer 1979, 1983, 1991). Earlier judgements (Erchinger 1971, 1977; Führböter 1974) giving credit for a remarkable wave energy dissipation in front of dykes to seawardly located salt marshes therefore do no longer hold stand.

## 3. BOUNDARY CONDITIONS OF MODEL TESTS

### 3.1 Water levels and waves

For water levels the range between the crest height of the summer dykes and design water level was taken into consideration by steps of 0,25 m. Water and bottom levels as well as heights of structures are referenced to German geodetic datum NN which is approximately equivalent to MSL. MHWL in the area of interest is currently about NN+ 1,25 m. The averaged yearly frequencies of storm surge peaks above MHWL due to German standard classification are 10 for a set-up of about 1,0 m; 0,5 for 2,0 m and 0,05 for 3,0 m. These values are estimates corresponding to a more thoroughful analysis of time series of the tidal gauge of

Norderney (Niemeyer 1987a). The highest recorded set-up in the area of interest was about 3,6 m in 1906.

The wave climate in this part of the Wadden Sea is definetely depth-controlled (Niemeyer 1979; 1983; Kaiser et al. 1995). Therefore wave conditions at the seaward boundary of the model could be determined by using relations between significant wave height and mean wave period with local water depth which have been derived from site measurements on both tidal flats and salt marshes (Niemeyer 1983):

$$H_s = 0{,}28 \cdot h \qquad \text{(fig. 2)}$$

$$T_m = (28{,}6 \cdot h \cdot g^{-1})^{0{,}5}$$

The relation for the significant wave height and local water depth is rather strict whereas for the wave periods the tendency is superimposed by a larger scatter due to effects of distinct swell conditions in the offshore area of the Wadden Sea (Niemeyer 1983). Model tests have been carried out as well for perpendicular as for nonperpendicular wave attack with deviations of 7,5°, 15°, 30°. Furthermore comparisons were made with respect to the impact of local wind on waves propagating on a salt marsh or respectively in a summer polder. The effectiveness of salt marshes with and without summer dykes is considered by wave conditions in front of the sea dyke sheltering the hinterland against inundation due to storm surges.

## 3.2 Morphology, structures and model bathymetry

The model tests have been carried out for three situations being representative for the East Frisian coast where most of the summer polders in Lower Saxony are located. For basic investigations considering the impact of dyke crest height variation, direction of

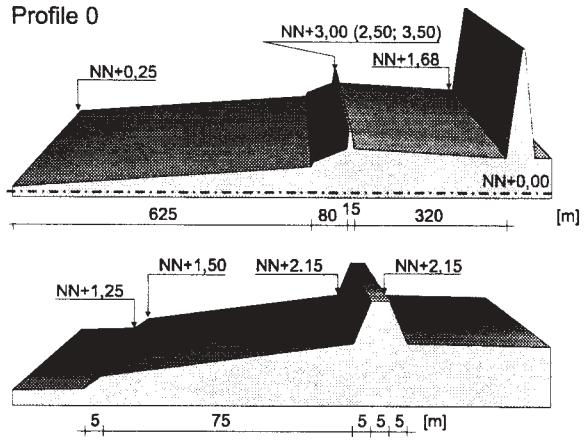


Fig. 4: Test profile 0 for model runs

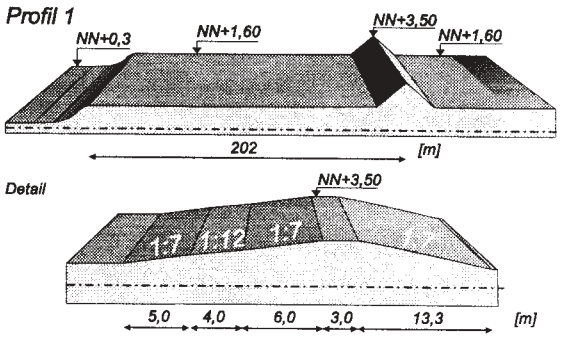


Fig. 5: Test profile 1 for model runs

wave attack and local wind effects a generalized model morphology incorporating intertidal flat, supra tidal salt marsh, main dyke without and respectively with a sum- mer dyke enclosing a part of the salt marsh (fig. 4). In order to achieve an insight into the effects of summer dyke profiles additionally two other profiles with a more complex summer dyke geometry have also been tested (fig. 5 + 6). All model runs were made comparatively as well for a profile including a summer dyke as for one whithout a summer dyke. The heights are referenced to German geodetic datum NN which is approximately equivalent to MSL.

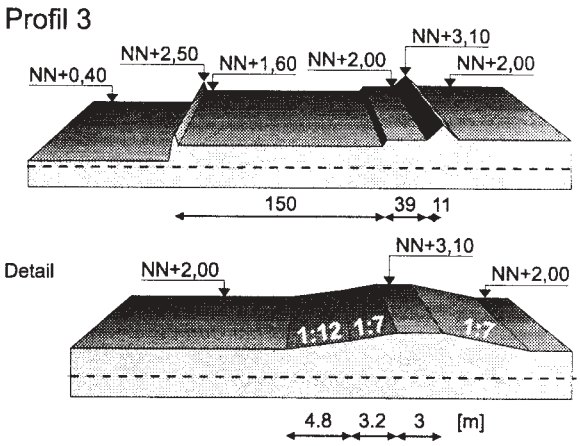


Fig. 6: Test profile 3 for model runs

The model bathymetry has generally a resolution of 2,5 m in x-direction which coincides approximately with the wave direction and perpendicular in y-direction 10 m. Since the bottom of intertidal flats and supratidal salt marshes are very flat the geometrical reproduction for model bathymetry causes no problems. The spatial resolution in x-direction is regarded as sufficient for the geometrical reproduction of the structure of a summer dyke, e. g. its crest is covered in x-direction by three grid points.

## 4. TEST RESULTS

### 4.1 Variation of crest heights

Model runs were carried out for profile 0 (fig. 4) with three distinct crest heights of the summer dyke for the described variation of water levels and wave conditions. For a summer dyke with a crest height of NN +2,5 m for still water levels exceeding it by 0,5 m and more no significant reduction of the significant wave heights is evident. The same holds stand for wave periods. For a crest height of NN +3,0 m the differences of significant wave heights in front of the sea dyke for profiles with and without summer dyke are for lower water levels more evident though the absolute values remain for both cases rather small. With increasing still water levels they tend to become smaller and decrease enormously if the still water levels exceeds NN + 4,25 m corresponding to a water depth of 1,75 m above the crest of the summer dyke to less than 5% (fig. 7), because the breaking of waves diminishes significantly. For the design water level of NN + 5,25 m the

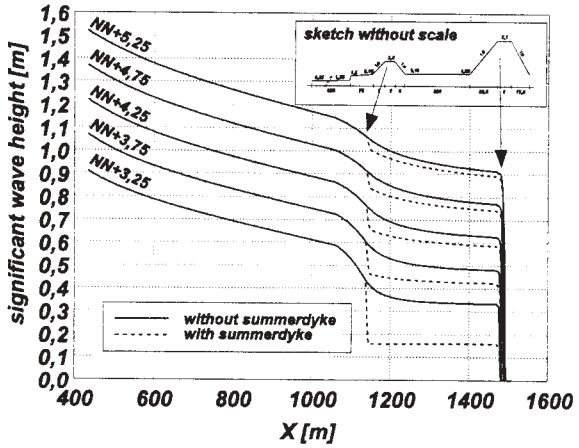


Fig. 7: HISWA test results for significant wave heights (profile 0; crest height: NN +3,0 m)

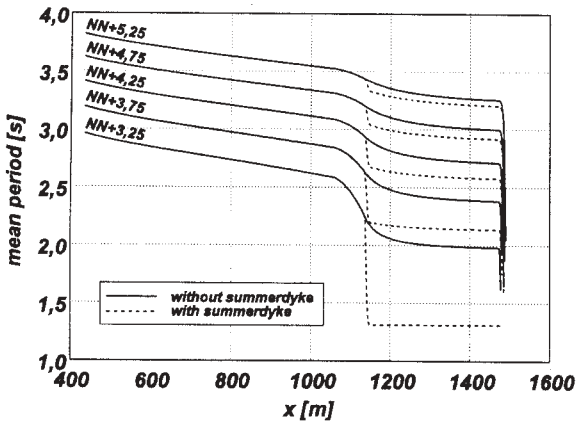


Fig. 8: HISWA test results for mean wave periods (profile 0; crest height: NN +3,0 m)

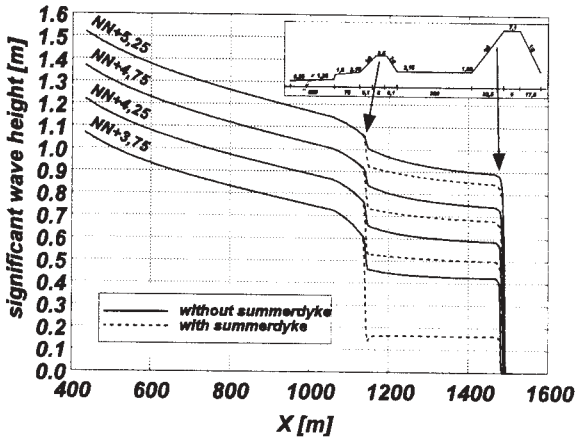


Fig. 9: HISWA test results for significant wave heights (profile 0; crest height: NN +3,5 m)

differences are smaller than 3% right off landward of the summer dyke and even smaller in front of the sea dyke. In general the differences decrease between the landward edge of the summer dyke and the sea dyke with the travel distance of the waves. For water depths above the summer dyke below 0,5 m mean wave periods are remarkably reduced. But if they exceed the value of 0,75 m corresponding to a still water level of NN + 3,25 m the differences are less than 0,2 s decreasing to less than 0,1s for design conditions being equivalent to approximately 2,5% (fig. 8).

A crest height of NN + 3,5 m of the summer dyke causes more increased wave breaking leading to a more intensive reduction of wave parameters, particularly for lower water levels (fig. 9 + 10): the periods are reduced by approximately one third for a water depth of 0,25 m above crest height. But with increasing water levels breaking obviously diminishes and also the differences between a situation with and one with a summer dyke: there is only a reduction of mean

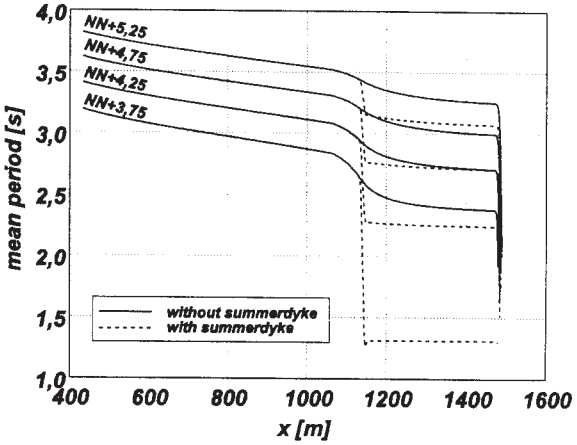


Fig. 10: HISWA test results for mean wave periods (profile 0; crest height: NN +3,5 m)

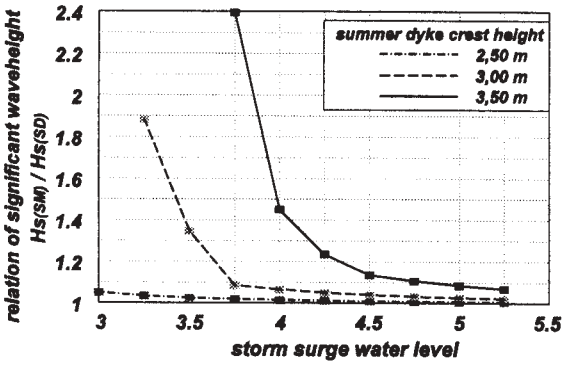


Fig. 11: Relation of significant wave heights in front of the main dyke with $H_s$ (SD) and without $H_s$ (SM) the shelter of a summer dyke for distinct summer dyke crest heights

wave period of 4,5% for design conditions (fig. 10). Similar processes occur with respect to wave height reduction (fig. 9): Whereas for a water depth of 0,25 the reduction of the significant wave height due to the effect of the summer dyke is about 60% from 0,48 m to 0,17 m, it decreases with increasing storm surge levels dramatically to less than 10% for design conditions, in this case from 1,02 m to 0,95 m.

In total the crest height of the summer dyke is of high importance for its effectiveness with respect to wave damping. A comparison of the relation of significant wave heights in front of a main dyke with and without the shelter of a summer dyke with distinct crest heights highlights this result. It summarizes the model test results for a range of storm surge levels up to design conditions (fig. 11): Whereas for a crest height of NN +2,5 m nearly no damping occurs the higher ones create a significant wave damping until a certain storm surge level has been exceeded. At least there is no specific wave damping effect being usable for the design of the main dyke.

## 4.2 Variation of structural shape

In order to get a deeper insight of the effects of a more complex structure of a summer dyke on wave damping additionally two profiles have been investigated which represent specific situations at the East Frisian coast (fig. 5 + 6). The profile 3 incorporates a summer dyke with a crest height of NN +3,1m which might be compared with the effectiveness of the summer dyke with a crest height of NN +3,0 m in profile 0. Furthermore there are a land reclamation dam at the seaward edge of the salt marsh and a small berm in front of the outer slope of the summer dyke. But the major difference for both cases is not the crest height but the level of the seawardly located intertidal flat (fig. 6). In this specific case the level is about 0,65 cm lower than for the previous one enabling the occurence of higher and longer waves for the same still water level (fig. 7 + 12). The differences do not create significant changes with respect to wave damping, particularly not for increasing water levels above NN + 4,0 m for which the additional damping effect is less than 10% and for design conditions even lesser than 5% (fig. 12). Taking additionally the slightly higher crest and particularly the more intensive wave climate due to the lower level of the intertidal flat into consideration a specific effect of the stuctural geometry is not realistic in this case.

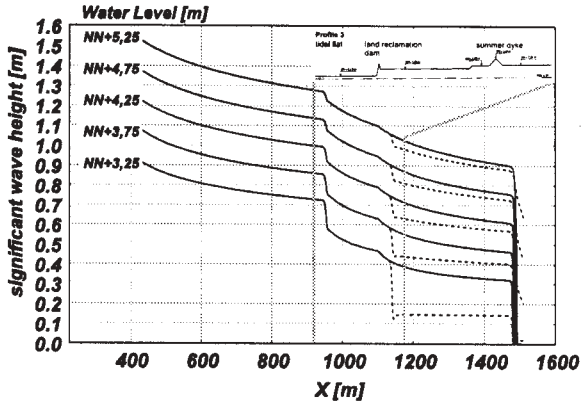


Fig. 12: HISWA test results for significant wave heights (profile 3; crest height: NN +3,0 m)

The profile 1 is also characterized by a geometrically more differentiated cross-section of the summer dyke, a very low level of the intertidal flat, a broad stretch of salt marsh seawardly of the summer dyke and a lower bottom level in the summer polder. Due to shoaling and partly friction on the broad salt marsh stretch seaward of the summer dyke the significant wave heights in front of the summer dyke are of the same order as

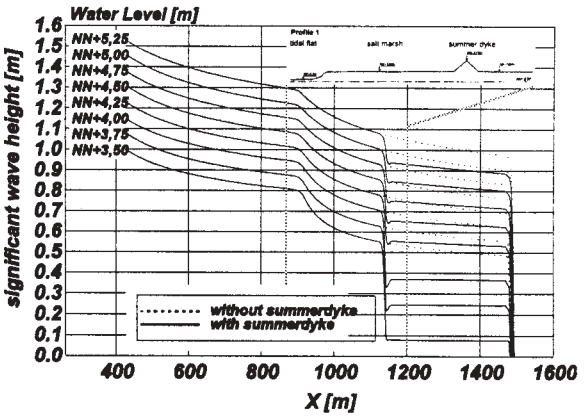


Fig. 13: HISWA test results for significant wave heights (profile 1; crest height: NN +3,5 m)

that one in profile 0 (fig. 9 + 13). The major differences between the two profiles is the bottom level in the summer polder: the higher one in profile 0 enforces a stronger wave attenuation as well with as without a summer dyke (fig. 13). The given boundary conditions deliver no evidence of a remarkable effect of the structural shape of summer dykes on wave damping.

### 4.3 Non-perpendicular wave attack

Considering non-perpendicular wave attack in the coastal sceme with the profile 0 and a crest height of the summer dyke of NN +3.0 m there is nearly no influence of the wave attack angle in front of the summer dyke (fig. 14). At the seaward edge of the summerdyke the isolines of significant wave height are nearly parallel to the coastline which has been caused by refraction. With water levels higher than NN +3.5 m the relation of significant wave heights of profiles without/with a summerdyke is independent of the wave attack angle.

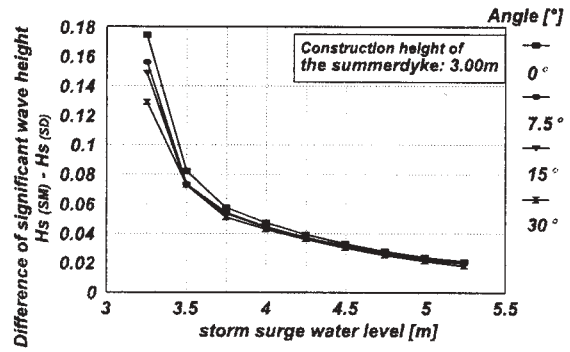


Fig. 14: Impact of non-perpendicular wave attack on the effectiveness of a summer dyke (significant wave heights; profile 0 with crest height NN +3,0 m)

### 4.4 Impact of local wind

In order to estimate the impact of local wind on the wave damping effects of summer dykes additional model runs were carried out for profile 0 with a crest height of NN+ 3,5 m. Chosen boundary conditions were storm with a velocity of 22,5 m/s at a water level of NN+ 4,25 m and for design conditions with a a velocity of 30 m/s. The wind direction is perpendicular to the summer dyke. Compared with a situation with no local wave impact (fig. 9) the significant wave height decreases lesser on the tidal flat due to the additional energy input causing a higher rate of energy dissipation at the seaward edge of the salt marsh (fig. 15 + 16). The higher reduction of the significant wave height caused by the summer dyke enables the local wind to transfer a higher rate of energy to the waves

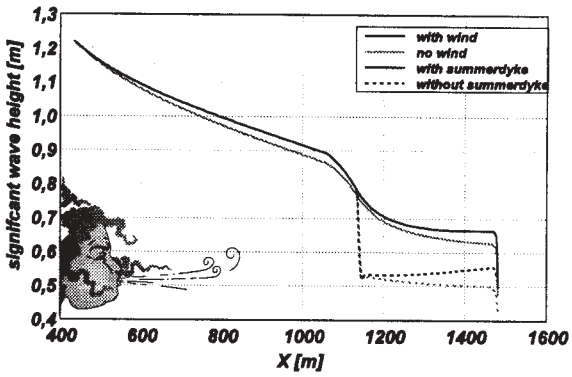


Fig. 15: Impact of local wind on the effectiveness of a summer dyke (significant wave height; u: 22,5 m/s; water level NN +4,25m; profile 0; crest height: NN +3,5 m)

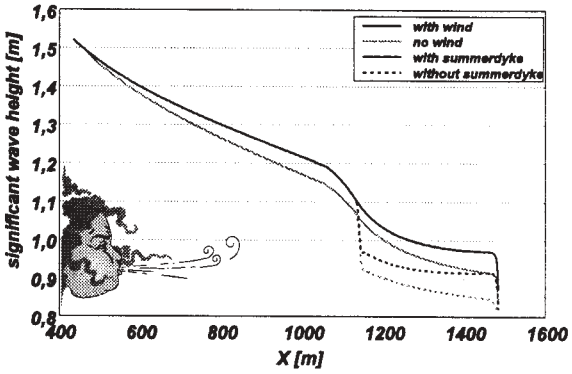


Fig. 16: Impact of local wind on the effectiveness of a summer dyke (significant wave height; u: 30 m/s; water level NN +5,25m; profile 0; crest height: NN +3,5 m)

approaching the sea dykes via the summer polder than to those travelling across a salt marsh without a summer dyke. For the water level of NN+ 4,25 m even an increase of the wave heights in the summer polder takes place (fig. 15). In total the differences between the wave heights at the edge of the sea dyke are smaller if local wind is taken into consideration (fig. 15 + 16) though the total figures are sufficiently small for allowing to neglect this effect for practical purposes.

## 5. COMPARISON WITH FIELD DATA

There are only a few prototype data available allowing estimates of the effectiveness of summer dykes. A beneficial comparison is e. g. possible by comparison of wave run-up on a sea dyke in the shelter of a seawardly located summer dyke with a crest height of NN+ 3,5 m for the storm surges of 19. 11. 1973 (Erchinger 1977) and 03. 01. 1976 (Ingenieurkommission 1979) which has been measured by levelling the benchmarks of floatsam after storm surges. For the



AUTHOR INDEX
TABLE OF CONTENTS

storm surge of November 19th 1973 with a peak of NN+ 3,88m corresponding to a set-up of about 2,6 m above MHWL in the shelter of the summer dyke a wave run-up of 0,1 m has been measured. The storm surge of January 3rd 1976 had a slightly higher peak of NN+ 4,15 m and set-up of about 3,0 m whereas the wave run-up in shelter of the summer dyke increases to 0,9 m. The overproportional rise with respect to that of the water level is due to the also overproportionally increase of water depth above the summer dyke crest leading to lesser or at least even to nearly no wave breaking. Tendencially this data confirm the results gained by mathematical wave modeling.

From these run-up of the storm surge of January 3rd 1976 the corresponding wave parameters in front of the dyke have been deducted by using the extrapolation-method for the determination of design wave run-up (Niemeyer 1977) which has been verified again on a larger data base recently (Niemeyer et al. 1995). The significant wave height is higher than those gained form the model run with similar boundary conditions (fig. 17), but of the same order of magnitude. The comparison is regarded as an indication for the capability of HISWA to match the problem.

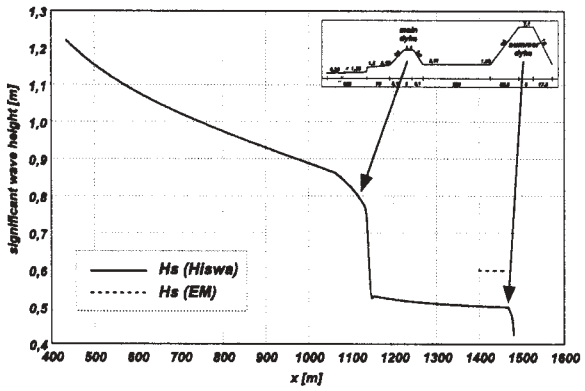


Fig. 17: Comparison of significant wave heights from HISWA model run $H_s$ (HISWA) and from deduction from wave run-up by Extrapolation method $H_s$ (EM)

## 6. CONCLUSIONS

The mathematical model HISWA incorporates all physical processes being relevant to reproduce wave energy dissipation caused by wave damping structures in the Wadden Sea like supratidal salt marshes or summer dykes. The model set-up allows a high spatial resolution which allows the pure geometrical reproduction of structures like summer dykes without the input of transmission coefficients gained from physical models or field data or simple estimates. The comparison with data from the Large Wave Flume highlights as well the suitability of this tool for this shallow water environment as earlier investigations did for other parts of the Wadden Sea. Furthermore as well the results from physical tests in the Large Wave Flume as those gained by using the mathematical model HISWA make evident that there is no specific wave damping on supratidal salt marshes due to breaking for storm surge water levels.

The model runs made evident that the impact of structural geometry, nonperpendicular wave attack and local wind have no significant impact for the range of boundary conditions being representative for Wadden Sea coasts. The most important boundary condition is the crest height of the summer dyke. But even the existing highest ones at the Wadden Sea will not effect a specific wave damping for higher storm surges and particularly not for the occurrence of design water levels.

## 7. LITERATURE


Adel, J.D. den, H. D. Niemeyer, A. F. Franken, N. Booij, J. Dekker & J. A. Vogel, 1991: Wave model application in a Wadden Sea area. Proc. 22nd Int. Conf. o. Coast. Eng. Delft/ The Netherlands, ASCE, New York

Booij, N. & L. Holthuijsen, 1992: HISWA user manual. Prediction of short-crested, stationary waves with ambient currents. TU Delft, Facult. Civ. Techn.

Erchinger, H. F., 1971: Land reclamation and groinbuilding in the tidal flats. Proc. 12th Int. Conf. Coast. Eng. Washigton D.C./USA, ASCE, New York

Erchinger, H. F., 1977: Wave run-up in field measurements with newly developed instruments. Proc. 15th Int. Conf. Coast. Eng. Honolulu,Hi./USA, ASCE, New York

Holthuijsen, L. H. & N. Booij, 1987: A grid model for shallow water waves. Proc. 20th Int. Conf. Coast. Eng. Taipei/Taiwan, ASCE, New York

Ingenieurkommission, 1962: Die Sturmflut vom 16./17. Februar 1962 im niedersächsischen Küstengebiet (in German: The storm surge at the 16th/17th of February 1962 at the Lower Saxonian coast). Die Küste, Jg. 10, H. 1

Ingenieurkommission, 1979: Erfahrungen und Folgerungen aus den Januar-Sturmfluten für den Küstenschutz in Niedersachsen (in German: Experiences and consequences for coastal protection in Lower Saxony gained due to the storm surges in January 1976). Die Küste, H. 33

Kaiser, R., G. Brandt, J. Gärtner, D. Glaser, J. Grüne, J. Jensen & H. D. Niemeyer, 1995: Wave climate study in Wadden Sea areas. Proc. 24th Int. Conf. Coast. Eng. Kobe/Japan, ASCE, New York

Niemeyer, H. D., 1979: Wave climate study in the region of the East Frisian Islands and Coast. Proc. 16th Int. Conf. Coast. Eng. Hamburg/Germany, ASCE, New York

Niemeyer, H. D., 1983: Über den Seegang an einer inselgeschützten Wattküste (in German: Waves at island sheltered Wadden Sea coasts). BMFT-Forschungsber. MF 0203

Niemeyer, H. D., 1991: Case study Ley Bay: an alternative to traditional enclosure. Proc. 3rd Conf. o. Coast. & Port Eng. i. Develop. Countr., Mombasa/Kenya

Niemeyer, H. D., 1995: Long-term morphodynamical development of the East Frisian Islands and Coast. Proc. 24th Int. Conf. Coast. Eng. Kobe/Japan, ASCE, New York

Niemeyer, H. D., J. Gärtner, R. Kaiser, K.H. Peters & O. Schneider, 1995: Estimation of design wave run-up on sea dykes under consideration of overtopping security by using benchmarks of flotsam. Proc. 4th Conf. o. Coast. & Port Eng. i. Develop. Countr., Rio de Janeiro/Brazil

# WAVE HINDCASTS FORCED BY SCATTEROMETER WIND FIELDS

W. Perrie, B. Toulany*, and M. Dowd†
Bedford Institute of Oceanography, Dartmouth, Nova Scotia

## 1 INTRODUCTION

Interpolation of remotely sensed SEASAT data, as suggested by Woiceshyn et al (1989), produced gridded wind fields at about 1-degree resolution. A similar study is shown on the cover of Aviation Week & Space Technology (1989) Vol. 130, (11). The interpolation uses values from earlier/later swaths, to achieve synoptic wind maps. Alternate studies are by Bentamy et al (1996a, 1996b) using kriging methods to get weekly wind fields, and Tang and Liu (1996), using succesive correction methods to get 12 hourly wind fields. Thus, wind fields with known/estimated errors and biases, can be constructed, without assistance of elaborate atmospheric models. Woiceshyn et al (1989) were able to use a second generation spectral wave model to show that SEASAT scatterometer data alone were sufficient for a viable hindcast, qualitatively and quantitatively competitive with wave hindcasts resulting from the ECMWF wind fields.

In this study we produce 1-degree spatial scale wind fields, synoptically every 12-hours and 6-hours, for the North Atlantic ocean. We use optimal interpolation, (hereafter OI) as implemented in the kriging analysis of Bentamy et al (1996). Error maps, produced in association with the kriging analysis, are also presented, to understand the results from OI constructed wind fields. We confine the present study to the Storm of the Century in March'93.

Verifications of OI constructed wind fields, will be presented, with (i) similar studies, for example Tang and Liu (1996), and (ii) in situ measurements of wind from buoys and dedicated experiments.

*Ocean Sciences Division, Fisheries and Oceans Canada, Bedford Institute of Oceanography, Dartmouth, Nova Scotia, Canada B2Y 4A2
†Satlantic Inc., Richmond Terminal, Pier 9, 3295 Barrington St., Halifax, Nova Scotia, Canada B3K 5X8

Wave hindcasts will be produced using the standard cycle 4 WAM model. For the storm event considered, we hope to show systematically that ERS scatterometer data alone is sufficient for a viable hindcast, competitve with (Canadian weather service) AES wind fields.

## 2 WIND FIELDS

As of the writing of this manuscript, wave fields have not been constructed. They form an ultimate test of the wind fields. A preliminary kriging analysis had been carried out on ERS scatterometer data. Our intent was to map wind vectors, from the satellite swaths, to gridded synoptic wind maps for the North Atlantic. The analysis focused on the so-called Storm of the Century (SOC), specifically March 14, 12:00GMT. At this time the center of the low pressure system was located near Long Island and moving rapidly to the northeast. An important reason for choosing this period is the presense of strong winds in the raw scatterometer data.

Nine scatterometer swaths were used in the analysis covering a total period of about 27 hours. The ERS orbital configuration allows each individual swath to cover the model domain in less than 20 minutes. This may be considered as essentially instantaneous in time, for the purpose of wind analysis. The swaths group naturally into three sets of three swaths each. The swaths within a given set are about 3 hours apart and the swath sets themselves are separated by about 12 hours.

The steps carried out for the scatterometer wind analysis, based on the kriging technique of Bentamy et al (1996), include the following:

1) Specification of a grid for the North Atlantic (based on a Scripps elevation database, to differentiate land and ocean). The 1° grid covered 20-60N (there are no data below 20N)



AUTHOR INDEX TABLE OF CONTENTS

and the full east-west range of the North Atlantic.

**(2)** The quality checked scatterometer data were binned to the nearest grid point (later to be replaced with bi-linear interpolation). This reduced the data volume by about an order of magnitude, an important consideration to ensure computational efficiency of the kriging algorithm.

**(3)** A kriging analysis was carried out to map the quasi-regular scatterometer data to the North Atlantic grid, using vector wind components.

Variogram values chosen for the temporal and spatial correlation scales were guided by those of Bentamy et al., which were tuned for the tropical Atlantic and weekly winds. As our analysis is for mid latitudes, and intended to capture the variability associated with individual storm events, the variogram values will have to be modified, possibly reducing the spatial and temporal correlation scales. We note that inital examination of the binned scatterometer winds indicates rapid changes occur in the wind fields in the 12 hours between swath sets (as much as 180° !). Thus, we use about one-half the temporal decorrelation scale compared to Bentamy et al.'s values.

The kriging algorithm was carried out for March 14, 1200GMT using the above variogram and scatterometer vector wind data from +/- 13 hours, as indicated above. The same variogram values have been used for both the u and v components of the wind. Although the usual practice is to filter data, eliminating distant observations, this has not been done here due to the limited data set considered. Resultant winds are shown in Fig. 1. Constructed winds from kriging compare well to CMC winds for the period. Apparent divergence in the fields, may result from lack of data, or lack of dynamical constraints. Associated error maps are shown in Fig. 2.

The errors are low where scatterometer swaths are nearby in space-time. Although their absolute values are probably not correct, their overall spatial pattern is reasonable, values are low when the scatterometer swaths are nearby in time.

# 3 CONCLUSIONS

The problem with inserting observed wind data into the output from operational atmospheric models is that inconsistencies arise within the resultant wind fields and the dynamical fields of as-

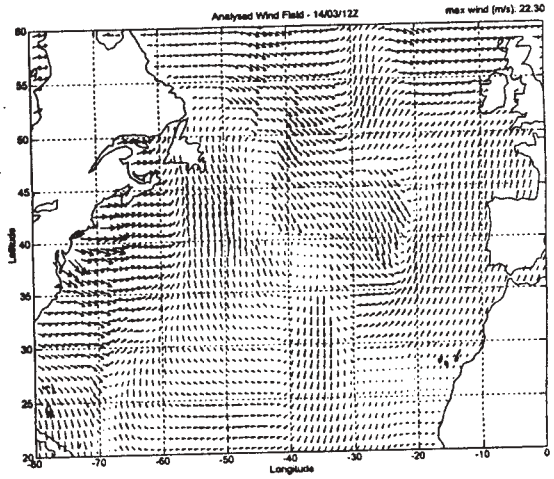


**Fig. 1.** Analysed wind field for March 14, 1200GMT as obtained from the kriging analysis. The maximum wind speed is indicated.

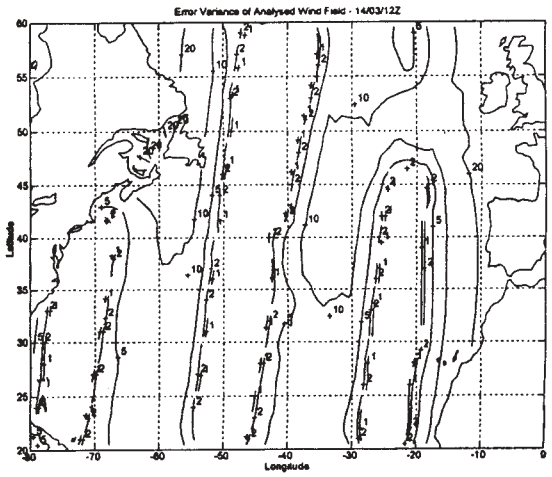


**Fig. 2.** Error map for the analysed wind field of March 14, 12Z, representing the square root of the variance between the true and estimated vector wind fields.

sociated dynamical atmospheric or marine boundary layer variables. This is discussed in Perrie and Wang (1995, 1997). The problem motivated the present study: can wind fields be constructed, solely from observed satellite data, with enough accuracy to be competitive with the estimated wind fields from atmospheric models, and of practical use for ocean/wave models?

Some years ago, Woiceshyn et al (1989) showed that this was possible, using simple data interpolation methods and SEASAT scatterometer data. In this study we have shown that we can construct realistic wind fields from ERS scatterometer data, using *"state-of-the-art"* data interpolation methods, namely kriging. To complete the study, we must re-compute the kriging variogram, and get final "best" estimates for associated wind fields. We must verify the wind fields with alternate data: measured winds from buoys, etc., kinematically anaylsed winds, as used by Cardone et al (1995). Ultimately, we must compute associated wave fields and compare wave estimates with measurements and also other SOC wave studies, for example Cardone et al (1995).

*Acknowledgements.* The marine wind program at BIO, responsible for this work, is funded by the Federal Panel on Energy Research and Development (Canada) under Project 24107.

## References

[1] Bentamy, A., Grima, N., Quilfen, Y., Harscoat, V., Maroni, C. and S. Pouliquen, 1996a: An atlas of surface wind from ERS - 1 scatterometer measurements. Report to the Département D'Océanographie Spatiale, IFREMER, 52pp + figs.

[2] Bentamy, A., Quilfen, Y., Gohin, F., Grima, N., Lenaour, M., and J. Servain, 1996b: Determination and validation of average wind fields from ERS - 1 scatterometer measurements. *The Global Atmosphere and Ocean System*, **4**, 1-29.

[3] Cardone, V. D., Jensen, R. E., Resio, D. T., Swail, V. R. and A. T. Cox, 1995: Evolution of contemporary ocean wave models in rare extreme events: "Halloween Storm" of October, 1991; "Storm of the Century" of March, 1993. *J. of Atmos. and Oceanic Tech.*, **13**, 198-230.

[4] Perrie, W. and L. Wang, 1995: On the overdetermination of friction velocity ($U_*$). *J. Phys. Oceanogr.*, **25**, 2177-2178.

[5] Perrie, W. and L. Wang, 1997: Implications of friction velocity on air-sea coupled dynamics. Proc. 5th International Workshop Wave Hindcasting & Forecasting.

[6] Tang, W. and W. T. Liu, 1996: Objective interpolation of scatterometer winds. JPL Publication 96-16, 16 pp.

[7] Woiceshyn, P. M., Wurtele, M. G. and G. F. Cunningham, 1989: Wave hindcasts forced by scatterometer and other wind fields. Proc. 2nd International Workshop Wave Hindcasting & Forecasting, 268-277.

# SHALLOW WATER WAVE MODELING WITH NONLINEAR DISSIPATION: APPLICATION TO SMALL SCALE TIDAL SYSTEMS

Christoph Schneggenburger, Heinz Günther, and Wolfgang Rosenthal

GKSS-Forschungszentrum Geesthacht GmbH
Geesthacht, Germany

## 1 INTRODUCTION

Wave modeling in small scale shallow water systems has moved into focus in recent years because wave understanding is essential for many questions related to coastal protection and sustainable development. An example is the influence of waves on suspended matter dynamics: mobilization of sediments is controlled by bottom shear stresses which to a large extend depend on the wave field.

The aim of the study presented in this paper is to show the performance of a shallow water wave model with nonlinear dissipation in simulations of small scale tidal systems. The model is internally called K-model. The name will be adopted in this article. As application of the model, an analysis of tidal current influences on the wind waves in the Sylt Rømø tidal basin located at the German Danish North Sea coast will be presented. The analysis consists of one case study and one hindcast simulation with the K-model. Both have been performed with currents taken into account and without. This allows a direct indication and quantification of current effects.

The K-model has been developed in the technical frame of WAM cy. 4 (Günther et al. 1992). Since the model has been designed for applications to nonuniform and instationary systems, the code was rearranged to have action densities in $(k, \theta)$ coordinates as prognostic fields. Various technical details were added to address the needs for small scale computations. A second major change was the replacement of white capping dissipation by a nonlinear dissipation source function. This source function accounts for turbulent diffusion in the momentum balance of the wave flow field as key dissipation mechanism (Rosenthal 1989). The balance of Snyder wind input and nonlinear dissipation reproduces common shapes of deep and shallow water self similar wave spectra (Günther et al. 1995). Nonlinear quadruplet interactions have been neglected so far, because there is not much knowledge about the relevance and technical details of this process in small scale nonuniform and instationary systems. For details on K-model formulation, test runs and validations in larger scale applications see Schneggenburger et al. (1997).

Wave modeling in small scale systems with dimensions of a few ten kilometers can be treated efficiently in stationary approximation in special cases (Holthuijsen et al. 1993). The approximation will be good if the external fields influencing the waves, i.e. wind, currents, and water levels, do not change considerably within a time period needed for wave energy at typical frequencies to propagate through the system. The wave group velocity at the spectral peak is an appropriate measure to decide in this question. If the wave spectrum mainly consists of an incoming near fully developed part with low frequencies, the corresponding dominant group velocity may be large enough to justify a stationary treatment. The waves in the Sylt Rømø tidal basin are in principal locally generated wind waves. The peak frequency of the spectra is usually well above 0.1 Hz. Group velocities of a few meters per second correspond to this, if water depths around five meters are assumed. As can be seen subsequently in the current model results, the currents in the tidal basin at a specified location can change by as much as 20 percent of the time maximum value at that location during only 15 minutes. Within this time period, wave energy in the described typical spectra can propagate only a few kilometers. Therefore, a stationary treatment of wave modeling is not appropriate in the Sylt Rømø tidal basin.

The formulation of the K-model in wave vector space is well adapted to an instationary treatment of the wave modeling problem. This will be shown below.

This paper is arranged as follows. An overview-

ing model description of the K-model is given in section 2. It covers the source functions, propagation and refraction, and aspects of instationary water level and current fields. In the third section we report on K-model applications to the Sylt Rømø tidal basin. The section is subdivided into subsections on the current modeling, technical aspects of the K-model setup, description and results of an artificial case study, and description and results of a hindcast simulation of an episode in April 1997 including comparisons with measurements. In a final section, we give our conclusions.

In our notation vectors appear as bold letters. Partial derivatives of a quantity, say $N$, with respect to a scalar quantity, e.g. time $t$, are indicated by "$\partial_t N$". Gradients in local space or $\boldsymbol{k}$-space of a quantity, say $N$, are written as "$\partial_{\boldsymbol{x}} N$" or "$\partial_{\boldsymbol{k}} N$", respectively. Dots between vectors denote their inner product.

## 2 OVERVIEW OF K-MODEL FEATURES

The K-model is a spectral discrete wave model. It solves the wave action balance equation in $\boldsymbol{k}$-space, using polar coordinates $(k, \theta)$ – the wave vector modulus and direction – as independent variables. In flux form, the balance equation for the wave action density $N \equiv E/\sigma$ in these coordinates reads

$$\partial_t N + \partial_{\boldsymbol{x}} \cdot (\dot{\boldsymbol{x}} N) + \partial_k (\dot{k} N) + \partial_\theta (\dot{\theta} N) = S(N) \ . \quad (1)$$

Here, $E$ and $\sigma$ are the wave energy density and wave intrinsic frequency. As usual, $N$, $E$, and $\sigma$ are functions of the wave vector coordinates, here $(k, \theta)$, and of location $\boldsymbol{x}$ and time $t$. The arguments have been dropped in our notation for reasons of clarity. $S(N)$ is the sum of sources of action density. In the K-model, the sum is

$$S(N) = S_{\text{in}} + S_{\text{phil}} + S_{\text{dis}} + S_{\text{bot}} \ , \quad (2)$$

consisting of a modified Snyder wind input, Phillips wind input, nonlinear dissipation, and bottom interaction dissipation.

For basic concepts and terminology of wave theory and modeling see Komen et al. (1994).

### 2.1 *Source Functions*

In order to give a complete description, the source functions of the K-model are briefly discussed in this subsection. Modified Snyder wind input and nonlinear dissipation are listed in detail, because both are nonstandard. For further discussion and details on all source functions we refer to Schneggenburger et al. (1997).

The Snyder wind input (WAMDI 1988) was modified to include the effect of wind gustiness. It reads

$$S_{\text{in}} = \beta \sigma G N(\boldsymbol{k}) \ . \quad (3)$$

The gustiness parameter is

$$G = \frac{\sigma_{u_*}}{\sqrt{2\pi} c_*} \exp\left[ -\frac{(c_* - u_*)^2}{2\sigma_{u_*}^2} \right] + \frac{1}{2}\left[ \frac{u_*}{c_*} - 1 \right] \left[ 1 - \Phi\left( \frac{c_* - u_*}{\sigma_{u_*}} \right) \right] \quad (4)$$

with

$$c_* \equiv \frac{\sigma}{28\, k \cos(\theta - \theta_{\text{w}})}$$

for the case of $\cos(\theta - \theta_{\text{w}}) > 0$ and $G = 0$ else. In the expression (4) the probability function

$$\Phi(x) \equiv \frac{2}{\sqrt{2\pi}} \int_0^x \mathrm{e}^{-\frac{t^2}{2}} \mathrm{d}t \quad (5)$$

appears. The quantity $\sigma_{u_*}$ is the standard deviation of the assumed normal distribution for the friction velocity. The parameters of the Snyder input are

$$\beta = 0.0006 \quad , \quad \frac{\sigma_{u_*}}{u_*} = 0.4 \ . \quad (6)$$

In the present state of development of the K-model the friction velocity in the input source functions was replaced by the wind speed in 10 m height using a fixed relation $28 u_* \rightarrow 1.667 u_{10}$. It was obtained from tuning the peak frequency of the deep water fully developed spectrum.

The nonlinear dissipation function in the K-model is given by

$$S_{\text{dis}} = -\gamma\, g\, k^5 \left( \coth 2kh + \frac{kh}{\sinh^2 kh} \right) N^2(\boldsymbol{k}) \ . \quad (7)$$

The symbols $g$, $k$, and $h$ denote the gravitational acceleration, modulus of the wave vector, and local water depth, respectively. The dissipation parameter $\gamma$ is a functional of $N$ and thus generates a coupling of different action bins in the model:

$$\gamma(N) = \gamma_0 \frac{p_1 (p_2 \frac{k}{\langle k \rangle})^q + 1}{(p_2 \frac{k}{\langle k \rangle})^q + 1} \ , \quad (8)$$

with the parameters

$$\gamma_0 = 0.06775 \ , \ p_1 = 12.0 \ , \ p_2 = 1.2 \ , \ q = 6.0 \ .$$

The Phillips input source function $S_{\text{phil}}$ was adopted from Cavaleri (1981) with the modification by Tolman (1992). This input term is needed to enable a model startup from initial zero energy sea states. It is further needed to enable a recovering of wave energy after zero wind periods. This feature is necessary in small scale partially enclosed systems where residual swell after calm periods is unlikely. The magnitude of the Phillips input was rescaled to one tenth of its original value according to Cavaleri (1981). This is necessary for small scale applications in which the wave height is of the order of one meter or less. In its original form, the source function would contribute too much energy to the spectra.

The bottom interaction dissipation function was adopted from Hasselmann (1973). The interaction parameter in this formulation is $\Gamma = 0.038\text{m}^2/\text{s}^3$ .

The numerical implementation of source functions in the K-model is similar to WAM cy. 4: a second order semi-implicit scheme is used.

For small scale applications, the K-model is tuned to match TMA wave heights and periods for fetches up to 50 kilometers and a water depth of 5 m.

### 2.2 *Propagation and Refraction*

Propagation and refraction in a spectral discrete wave model are represented by the $\boldsymbol{x}$ and $\boldsymbol{k}$ gradient terms in equation (1). Since a flux type balance equation is form invariant under a coordinate transformation applied to $\boldsymbol{x}$ and $\boldsymbol{k}$, the explicit propagation and refraction terms in a model are specified completely by the "dot terms" corresponding to the chosen set of physical and wave vector space coordinates.

The dot terms are obtained from the dispersion function $\Omega$ for linear water waves

$$\Omega(\boldsymbol{k}) = \sigma(\boldsymbol{k}) + \boldsymbol{k} \cdot \boldsymbol{u}_{\text{c}} \tag{9}$$

and the kinematical relations

$$\dot{\boldsymbol{x}} \equiv \partial_{\boldsymbol{k}} \Omega \quad , \quad \dot{\boldsymbol{k}} \equiv -\partial_{\boldsymbol{x}} \Omega \tag{10}$$

connected to it. Here, $\boldsymbol{u}_{\text{c}}$ denotes the current velocity vector.

In the case of the K-model, the dot terms $\dot{x_1}$, $\dot{x_2}$, $\dot{k}$, and $\dot{\theta}$ must be determined. The location dot terms are directly identified as components of the wave group velocities. The group velocities consist of two terms: the intrinsic wave group velocities $\partial\sigma/\partial k$ plus the superimposed current velocities, which thus enter the dynamical equation for the wave action density.

For the wave vector dot terms a short calculation leads to explicit formulas which indicate a further influence of the external fields on the wave dynamics:

$$\begin{aligned} \dot{k} &= -(\sin\theta\, \partial_{x_1}\Omega + \cos\theta\, \partial_{x_2}\Omega) \,, \\ \dot{\theta} &= -(\cos\theta\, \partial_{x_1}\Omega + \sin\theta\, \partial_{x_2}\Omega)\, k^{-1} \,. \end{aligned} \tag{11}$$

The dispersion function depends explicitly on water levels and currents. Therefore, derivatives of water levels and currents enter the action balance equation.

Note that only spatial derivatives of the dispersion function appear in equation (11). If frequency and direction are used as independent $\boldsymbol{k}$-space variables, partial time derivatives of the dispersion function will additionally appear in the dynamical equation.

If time derivatives of the dispersion function are present, a "quasistationary" approximation can be chosen. In it, time functions for the external fields are considered, but terms with partial time derivatives are neglected.

The K-model formulation is well adapted to tidal systems because the instationary dynamical equation can be solved without the need to worry about time derivatives of water level and current fields. This is a major difference to models which are formulated with frequency variables.

Propagation and refraction are implemented in the K-model with first order upwind schemes. Since water levels and currents appear in the dispersion function in different terms, propagation, depth refraction, and current refraction can be treated in separate subroutines with individual time steps. In the K-model, the CFL stability criterion is checked in its exact form. The individual terms of the CFL number can be observed separately. This enables an educated choice of time steps for the separate propagation and refraction routines.

### 2.3 *Influence and Treatment of Nonstationary Water Level and Current Fields*

Time varying water level and current field influences on wave spectra can be classified into

1. local effects resulting from time changing propagation

2. nonlocal effects by (time changing) refraction

3. local effects resulting from time changing source functions

4. and nonlocal effects resulting from an interplay of (time changing) source functions and propagation.

Corresponding examples are

1. Integrated wave period parameters at a grid point will change with changing currents at the same grid point due to Doppler shifts within the wave spectrum

2. Focusing or scattering of wave energy due to refraction will change with time varying spatial patterns of water levels and currents

3. The influence of the water level is manifold. It enters the bottom interaction and nonlinear dissipation functions explicitly. It has an implicit influence on all source functions via circular frequencies and wave phase and group velocities. All this can be taken into account easily.

   The influence of currents on the source functions is not as obvious. It is likely that the advection of waves with the current has an influence on the wind input, on the turbulent eddy viscosity entering the nonlinear dissipation, and on the bottom interaction dissipation. But it is not clear at present how to quantify these influences. They have therefore been neglected in this study.

4. Significant wave heights can vary due to the influence of (time changing) currents on the energy propagation velocities. Due to this, an effective fetch comes into play: with opposing currents, the effective fetch is enlargened because the waves are exposed to the wind longer. The reverse holds for equal wave and current directions.

We now give some technical details on the treatment of instationary water levels and currents in the K-model.

Time changing water levels may cause wet points in the model topography to become temporarily dry. In the K-model, water levels below 0.5 m are treated as dry points. At temporarily dry points, the wave energy is set zero after every propagation time step.

The CFL stability criterion for the first order upwind propagation in $(\boldsymbol{x}, \boldsymbol{k})$-space must be observed whenever new water level fields and current fields are provided. This is done in the K-model.

As described above, the K-model simulates fields of action density $N$ in $(k, \theta)$ coordinates. To be able to compare with measurements and other models, it is desirable to have fields of energy density $E$ in $(f, \theta)$ coordinates as model output. In the K-model, the action density spectra are transformed to energy densities at each output time and location. The energy spectrum has fixed frequency and direction axes at all locations and times. The axes can be chosen by the user. The transformation is performed utilizing an energy conserving method. Energy situated beyond the chosen output frequencies is lost, however.

Wave modeling with the dynamical equation (1) in $(k, \theta)$ coordinates is well suited to the presence of strong oppposing currents for which wave blocking can occur. There are no formal restrictions on the current velocity in our formulation, e.g. singularities in Jacobians or related problems. Since the wave numbers of plain waves are not changed by currents, the wave blocking feature comes up only in postprocessing, when energy spectra in frequency direction coordinates are calculated at specified output locations and times. The treatment is straight forward: if negative frequencies occur, the corresponding directions are reversed. Energy located close to the frequency origin is abandoned to avoid division by small numbers or zero.

## 3 APPLICATIONS TO THE SYLT RØMØ TIDAL BASIN

In this section, we report on applications of the K-model to the Sylt Rømø tidal basin. The Sylt Rømø tidal basin is located at the North Sea coast close to the Danish German border. The basin is enclosed by the islands Sylt and Rømø. Both are connected to the main land with artificial dams. This leaves only one opening to the North Sea. The bathymetry of the basin is shown in figure 1. The basin is approximately 30 km long and 20 km wide. The opening to the North Sea between Sylt and Rømø has a width of about 3 km. This opening is the only tidal inlet to the basin. Within the basin exist three tidal channels with depths of 5 m to 10 m. The remaining parts of the water body are less than 3 m deep. Large areas – the tidal flats – fall dry at low tide. The approximate tidal elevation is 2.3 m. Tidal currents can have velocities up to 1.5 m/s in the inlet. In the tidal channels the current velocities usually are less than 1 m/s. The currents over the tidal flats are weak in com-

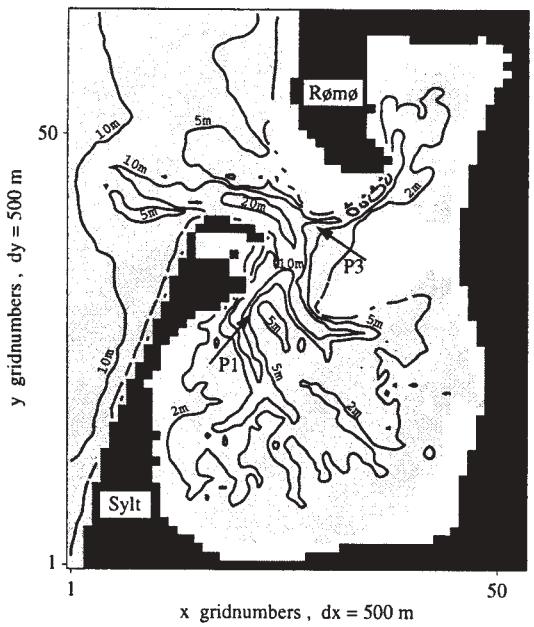


Figure 1: Bathymetry of the Sylt Rømø tidal basin. Water depths represent levels at a selected high tide. Contours show depths of 2 m, 5 m, 10 m, and 20 m. Arrows indicate the field station piles P1 Lister Ley and P3 Rømø Dyb.

parison to the channels. Figure 1 indicates the location of two measurement stations: the piles P1 Lister Ley and P3 Rømø Dyb.

Since there exists only one narrow opening to the North Sea, the wave regime in the Sylt Rømø tidal basin is expected to be dominated by wind waves. Waves over flooded tidal flats will be depth limited. Resulting from the short fetches, the wave velocities will be of the same order of magnitude as the current velocities. For this reason, a considerable influence of the tidal currents on the waves is expected.

Two wave modeling simulations were performed in the area. The first is an artificial case study assuming an east 20 m/s wind during two days of tidal varying hydrography. The second is a hindcast of a stormy six day period in April 1997. Technical details of the current and wave modeling will be discussed for both simulations together in the next two subsections.

### 3.1 *Water Level and Current Fields*

The time varying water levels and currents within the tidal basin were computed with the current model TRIM3D (Casulli et al. 1994). The model was applied in hydrostatic, barotropic, two-dimensional mode. The computational grid was rectangular, with grid steps in both horizontal directions of 100 m.

The model was forced by water levels on the model boundary located at the basin entrance, and by time interpolated, homogeneous winds provided from six hourly analysed wind fields of the DWD (German Weather Services) Europe model (in the case of the hindcast study). These wind fields will be abbreviated as "DWD winds" from now. The input boundary water levels were taken from measurements at the station Westerland which is located at the seaward coast of the island Sylt. The data were transformed to match water levels at the model boundary. For the case study with constant wind, a two day period in in February 1994 was picked out for the current modeling which matched the wind situation and in which water level measurements could be provided as boundary values. In this way, current and water level fields consistent to the prescribed wind situation were obtained.

Since it was convenient to establish the current model boundary at the bay entrance, time varying output current fields and water levels for the wave model input were restricted to the inner basin area. Outside the basin, the current fields were set to zero, the water levels were treated constant in time.

### 3.2 *K- Model Setup*

In this subsection we give some details on the K-model setup for the two Sylt Rømø tidal basin applications.

The wave model grid is the same as shown in figure 1. Its resolution is 500 m × 500 m. Water levels and currents were mapped from the TRIM3D 100 m resolution output to the wave model 500 m grid by a simple grid reduction: values for the 500 m grid were taken for all grid points from a fixed location within the grid box. This location was chosen to give a realistic mapping of the land sea patterns from the fine current model grid to the coarser wave model grid. In a second step, the water depths at the grid boxes representing the two measurement piles were matched to the measured depths to insure correct values for the local processes in the wave model at these points.

The spectral resolution was 25 wave numbers and 12 directions. The output frequency grid ranged from 0.1 Hz to 1 Hz. The directional dis-

cretization was shifted to have different main grid and propagation directions.

Time steps were 60 s for the source functions, 20 s for propagation and current refraction, and 4 s for depth refraction. It was made sure that a time step mismatch between propagation and source integration would not lead to oscillatory peaks as observed before in other small scale applications (Schneggenburger et al. 1997 WISE). Note that the small depth refraction time step is no major obstacle, because depth refraction is only a small part of all refraction and propagation computations. The depth refraction time step is a consequence of large water level gradients in the model topography.

Wind, water level, and current field time steps were 15 minutes, no time interpolation was performed.

For the April 1997 episode it turned out that the DWD winds did not have sufficient time varability. For this reason, the wave model was forced with measured winds from field station P3 Rømø Dyb. These were transformed to wind at 10 m height using a logarithmic scaling and the Charnock relation. The obtained wind was used homogeneously in the complete basin. There are shortcomings of this approach, but it is the best we could do without running a mesoscale atmospheric model.

To provide wave information at the wave model open boundary, the K-model was run on a North Sea grid for the month of April 1997. DWD wind fields were used for the forcing. The grid size of the North Sea model was 25 km × 25 km. The quality of this model was shown in Schneggenburger et al. (1997). One gridpoint was identified as located close to the island of Sylt. The water depth – 12 m – matches approximately the depth on the westward boundary of the small scale model. The spectral output at this North Sea wave model grid point was transformed to the wave number direction grid of the small scale K-model, and distributed to all boundary points with water depths greater than 3 meters.

### 3.3 *An Artificial Case Study: Strong East Wind*

To indicate and find orders of magnitude of tidal current effects on the waves in the Sylt-Rømø tidal basin, an artificial case study was carried out for the case of a constant east 20 m/s wind in 10 m height. The wind direction allows a neglection of wave boundary spectra at the open west boundary of the model grid. It was chosen for this reason.

As pointed out above, the current model was run for two days in February 1994 to get currents and water levels consistent with the chosen artificial wind situation. The wave model was run for two days with the according current model output and forced by a time constant, homogeneous east 20 m/s wind.

Results will be discussed with the help of time series at one location and snapshots of wave parameter and current fields at one chosen time.

#### 3.3.1 Time Series

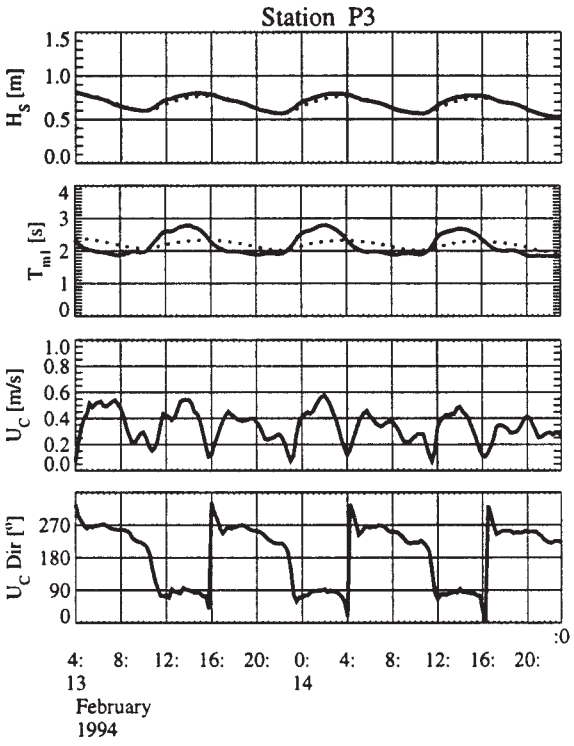


Figure 2: Time series of wave and current parameters at field station P3 Rømø Dyb for the east 20 m/s case study. Full lines are computations with tidal currents, dottet lines without.

Figure 2 shows time series of significant wave height and $T_{m1}$ period as computed by the K-model, and current velocities and directions as used in the K-model, at the location P3 Rømø Dyb. The field station is located at the side of one of the three tidal channels in the basin. Water levels varied within the tide cycle between 2.5 m and 5 m (not shown here). The current velocities are moderate, not exceeding 0.6 m/s. The flood current is little stronger than the ebb current. Note that the current can change consid-

erably within 15 minutes. This makes an instationary treatment inevitable, see our discussion in the introduction. Current directions are roughly to the east for the flood current, and to the west for the ebb current. They are thus antiparallel and parallel to the dominant wave direction (not shown here) which will approximately equal the wind direction to the west.

Comparing the curves for wave model computations with and without tidal currents, a dominant influence of currents on the $T_{m1}$ period can be seen at this station. It can be credited to the Doppler shift resulting from the advection of the waves with the currents. The period can change by as much as 25 percent. The influence in case of opposing currents is larger. This mainly stems from the nonlinearity of the dispersion function, and a little from the flood ebb asymmetry of the current velocity. The Doppler shift does not influence the energy content of the wave spectrum directly. This can be seen in the significant wave height time series. Here, only a small effect of a few centimeters change can be seen by comparing the curves for currents present and not. This stems from nonlocal effects, probably mainly the change of effective fetch in the presence of currents.

The tide signal in the wave parameters computed without currents can be explained by the varying water depths resulting in a change of local dissipation, and in a change of fetch due to dry falling areas during low tide.

Time series of the parameters at P1 Lister Ley (not shown here) show a much less pronounced effect of currents. This can be explained by the fact that the main current direction in the tidal channel Lister Ley is north- south, which is perpendicular to the dominant wave direction in this case study.

### 3.3.2 Parameter Fields

Figure 3 shows a snapshot of the current field in the Sylt Rømø tidal basin at a chosen time roughly one hour before high tide. In this and the following field plots, black areas are land, grey areas are wet points, and white areas are points which have fallen dry due to tidal water level variations. The arrows indicate the current directions, the length of the arrows are proportional to the velocities. In this snap shot, the maximum velocity was 1.2 m/s, occuring in the tidal inlet. Arrows appear only within the basin, because the TRIM3D

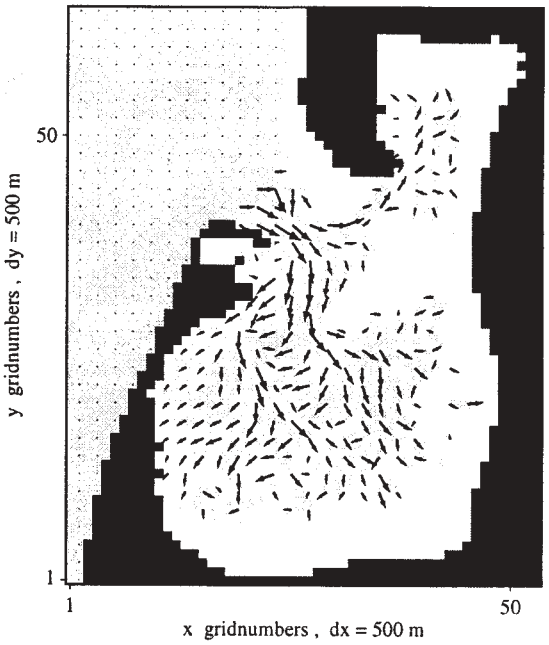


Figure 3: Current field one hour before high tide. Arrows indicate current directions, arrow lengths are proportional to current velocities. The maximum velocity is 1.2 m/s.

modeling was restricted to this area, see subsection 3.1.

The current influence on the $T_{m1}$ period and significant wave height parameter fields at the time of the snapshot is visualized in the figures 4 and 5. The differences of the respective parameters computed with and without currents are given as contour plots. Positive differences are full line contours, negative differences are dotted contours.

In figure 4 for the periods the maximum difference is 0.95 s. It corresponds to a period of 3.66 s (computed with currents). The relative change is 26 percent. The minimum difference is -0.42 s. It is smaller because we have an inflow situation, in which the strong currents mainly oppose the wave direction (to the west).

The Doppler shift of the wave periods already indicated in the time series is clearly visible in the difference field plot. The period is enhanced whereever the current has a component against the dominant wave direction. It is reduced at gridpoints where the current has a component into the wave direction. No major effect is visible in areas where the current is in north-south direction.

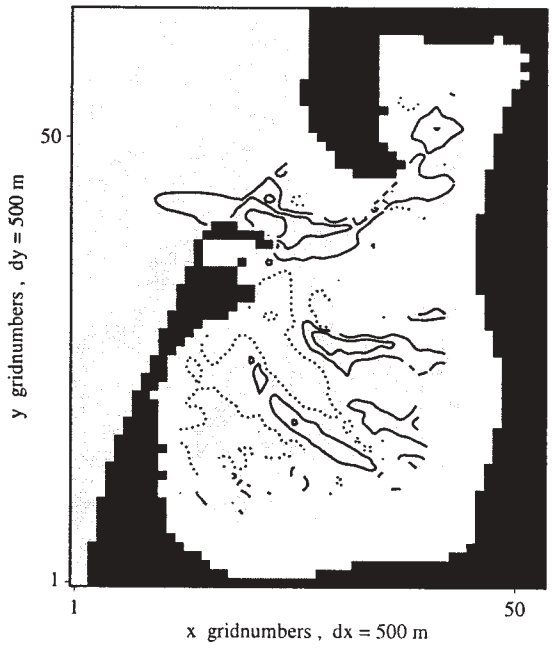


Figure 4: Difference field of $T_{m1}$ periods, computed with and without currents. Contours represent differences of 0.8 s, 0.5 s, 0.2 s, -0.1 s, and -0.4 s. Contour lines indicating negative differences are dotted.

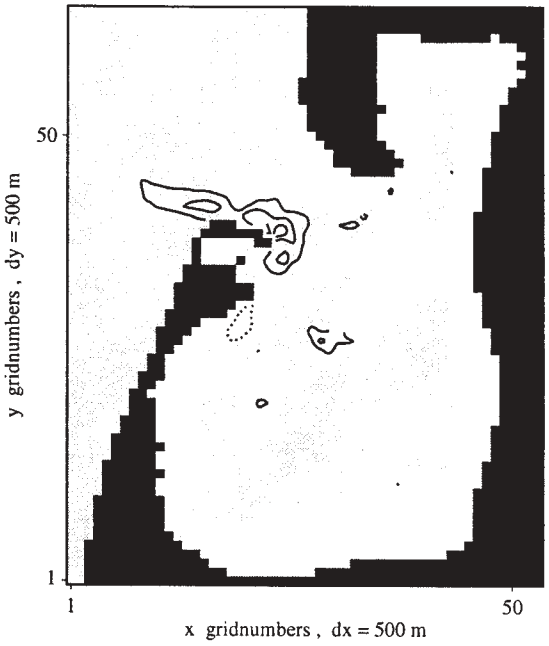


Figure 5: Difference field of significant wave heights $H_S$, computed with and without currents. Contours represent differences of 0.15 m, 0.1 m, 0.05 m, and -0.05 m. Contour lines indicating negative differences are dotted.

In figure 5 for the wave heights the maximum difference is 0.18 m occuring at a wave height of 1.19 m (with currents). The relative change is 15 percent. The mimimum difference is -0.09 m. The figure indicates a less pronounced effect, in contrast to the case of the periods. This is explained by the fact that the Doppler shift has no effect on the total spectral energy, compare the discussion of time series in subsection 3.3.1. There are only two smaller areas for which a difference is visible in the plot at all. Both can be explained by the nonlocal effect of an increase of effective fetch: note that the areas to the east of the two patches are both dominated by opposing currents. However, the effect on the wave heights is not uniquely creditable to one process. E.g. focusing and scattering of wave energy by current refraction can take further influence.

The difference fields of the wave parameters show that the tidal current fields can form considerable spatial patterns in the wind wave field. This effect adds to the known influences of fetch, wind patterns, and water level patterns on the waves.

### 3.4 *An Episode in April 1997*

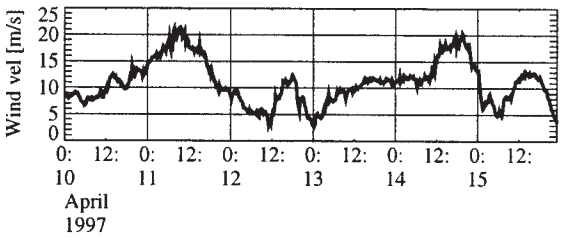


Figure 6: Time series of wind speed $u_{10}$ measured at field station P3 Rømø Dyb.

A six day hindcast of a storm period in April 1997 was performed to quantify the indicated current influences in a real situation. For this task, hindcast simulations were performed with and without tidal currents. The hindcast also allowed a validation of the K-model with measurements from two field stations in the Sylt Rømø tidal basin.

The selected period was a spring storm in 1997.

Figure 6 shows a time series of the wind velocity in 10 m height. The winds exceeded 20 m/s at two storm peaks. The wind directions were mainly between west and north, at both storm peaks roughly northwest. For this reason, a coarse grid run of the wave model to deliver boundary spectra was inevitable.

### 3.4.1 Measurements available

Field campaigns in the Sylt Rømø tidal basin were performed within the frame of the European Union MAST III programme PROMISE in the years of 1996 and 1997. Wind, wave, and current measurements (plus other parameters not needed here) are available at the two measurement piles P1 Lister Ley and P3 Rømø Dyb. One dimensional wave energy spectra were obtained from floater time series. From the spectra, the wave height and different wave period parameters were computed via integration. The quality of wave height measurements at P3 Rømø Dyb could be cross-checked by comparing with a nearby wave rider buouy. The floater wave heights and $T_{m1}$ periods at both stations roughly fulfill the energy frequency relations following from a TMA spectral shape. This can be seen as a quality check for the period measurements. The periods obtained from the wave rider buouy data deviated from the floater measurements in the case of wave heights below 0.2 m. The wave rider periods are unplausible in these cases.

### 3.4.2 Time Series

Time series of wave parameters at the two stations are given in figures 7 and 8. Further parameters are included in figure 7 to enable a detailed discussion of time series at station P1 Lister Ley.

In the first time series of figure 7 the significant wave heights modeled with and without currents and the measured wave heights can be compared. The influence of currents on the modeled wave heights is rather weak. The model agrees with the measurements fairly well. The second plot in figure 7 shows the corresponding $T_{m1}$ periods. There is a pronounced difference between model results with and without currents. The tidal current signal is also present in the measurements, but in most cases not as strong, in some cases stronger. These deviations of the model results from the measurements need not be credited to poor wave model performance, but can be explained qualitatively by an analysis of the measured currents and the currents used by the wave model. The third curve in figure 7 shows model current velocities and measured current velocities. The ebb semi-cycle of the tidal current velocities is represented remarkably well in the wave model. There are moderate differences in the flood semi-cycle, mainly consisting of the short peak in the measurements at the beginning of the flood current. The fourth time series in figure 7 shows the measured current directions and the ones used in the model, and the modeled mean wave directions. Note that the current directions in model and measurement deviate by approximately 70 degrees througout all of the shown ebb current periods, whereas the directions match better in most of the flood current periods.

Since the major differences in the wave periods of model and measurements occur in the ebb current semi-cycle, we will restrict the discussion to this part. The differences can be credited to the poor representation of the current directions in the wave model at this location. It can be checked that in cases where the $T_{m1}$ period is too high in the model, the model current opposes the mean wave direction, whereas the measured current directions are almost perpendicular to the modeled wave directions. In cases where the modeled periods are low, the reverse is true. Thus, the differences of the wave model periods to the measured periods can be explained by a wrong capture of the local effect of Doppler shift in the wave periods. However, it has to be stressed that this discussion is only qualitative. The complex interplay of many effects cannot be quantified in this way. It remains open if the overall wave model performance will be considerably better with better represented current directions or not.

For completeness, the time series of wave parameters at station P3 Rømø Dyb are given in figure 8. Again, the model results agree fairly well with the measurements. The current effect on the wave heights is small. The effect on the periods is considerable. At this station, the Doppler shifts agree better with the measurements. This can be credited to a better agreement of current parameters measured and used in the model at this station. This improved agreement of currents is purely accidental: it depends on whether the currents used in the 500 m wave model grid are by chance representative for the 100 m resolution current model grid point representing the measurement station.

For more clarity, the time series of wave rider

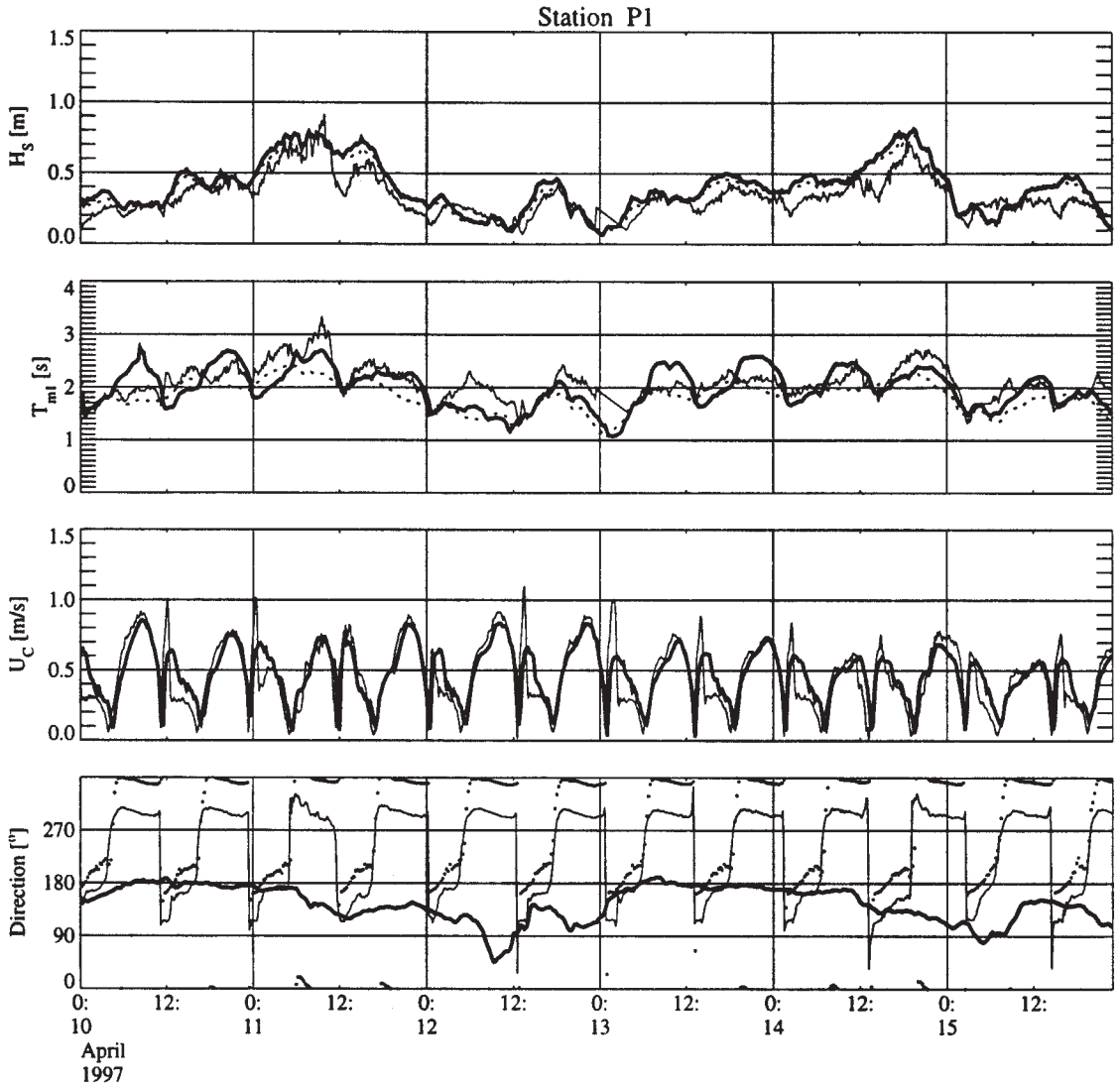


Figure 7: Time series of wave parameters at field station P1 Lister Ley. Dottet lines are computations without tidal currents. Thin lines are floater measurements. The last time series shows simulated mean wave directions (thick line), current directions in the model (dottet), and measured current directions (thin line).

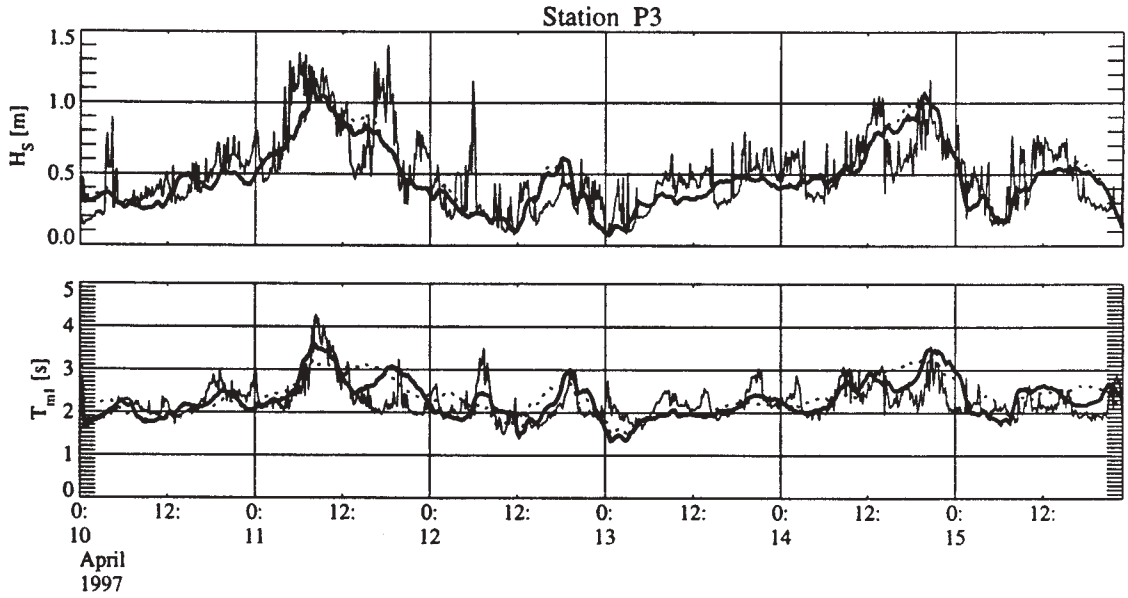


Figure 8: Time series of wave parameters at field station P3 Rømø Dyb. Dottet lines are computations without tidal currents. Thin lines are floater measurements.

measurents have been excluded from the figure.

### 3.4.3 Validation Statistics

The validation statistics for the parameters significant wave height and $T_{m1}$ period are given in the tables 1 and 2. Model results of K-model computations with and without tidal currents are statistically compared with floater measurements at two stations and wave rider measurements at one station. A large number of points could be considered in all cases. The wave model output time step was 15 minutes. Measurement points were identified to model output if the time lag between both did not exceed 7.5 minutes. Three statistical parameters are listed in the table. The bias is defined as difference of the mean of model results to the mean of measurements. The root mean square error is the square root of the sum of squared differences of model results to measurements. The scatter index is defined as standard deviation of model results with respect to the measurements divided by the mean of measurements and multiplied by 100.

Since both field stations are located at sites where the current influence on the significant wave heights was small during the hindcast period, no considerable difference in the statistics of the models with and without inclusion of tidal currents can be seen in table 1. The wave height statistics are quite acceptable. The biases are small, and r.m.s. errors are between 10 cm and 20 cm. The scatter indices lie around 25. Larger scatter indices around 35 for the model results compared with floater measurements at P3 Rømø Dyb can be understood by the much enhanced short term time variability of wave height measurements at this station, as can be seen in the time series. These enhanced fluctuations probably result from differences in the sampling and postprocessing of measurement time series. The wave rider measurements at the same station are smoother, compare the statistics with respect to these.

It should be expected to see an improvement in validation statistics for the model computations with currents taken into account in the case of the $T_{m1}$ periods, since the Doppler shift is clearly visible in the time series for both stations. This is true for station P3 Rømø Dyb. In the case of P1 Lister Ley the deviation of model and measurements discussed in subsection 3.4.2 leads to a small decrease in model performance quality if currents are included: the tidal current signal is present, but it is exaggerated by the model. Note that the bias of the wave model with respect to the wave rider period is large. It corresponds to a poor measurement quality in the case of small wave heights, see the discussion in subsection 3.4.1. As is the case for the wave heights, the overall statistical results are quite acceptable for the periods. The biases

Table 1: Validation statistics for significant wave height for three measurement stations within the Sylt Rømø tidal basin. Statistics for the K-model with currents taken into account and without.

| Location/ method | Number of points | Mean of measurements [m] | Model version | Bias [m] | R.m.s. error [m] | Scatter index |
|---|---|---|---|---|---|---|
| P1 floater | 555 | 0.34 | with currents | 0.07 | 0.11 | 24 |
| | | | without | 0.05 | 0.09 | 22 |
| P3 floater | 574 | 0.51 | with currents | -0.04 | 0.18 | 34 |
| | | | without | -0.03 | 0.19 | 36 |
| P3 waverider | 202 | 0.47 | with currents | 0.05 | 0.12 | 24 |
| | | | without | 0.06 | 0.14 | 26 |

Table 2: Validation statistics for $T_{m1}$ period for three measurement stations within the Sylt Rømø tidal basin. Statistics for the K-model with currents taken into account and without.

| Location/ method | Number of points | Mean of measurements [s] | Model version | Bias [s] | R.m.s. error [s] | Scatter index |
|---|---|---|---|---|---|---|
| P1 floater | 555 | 2.08 | with currents | -0.06 | 0.30 | 14 |
| | | | without | -0.22 | 0.32 | 11 |
| P3 floater | 574 | 2.27 | with currents | 0.04 | 0.37 | 16 |
| | | | without | 0.09 | 0.43 | 19 |
| P3 waverider | 159 | 2.86 | with currents | -0.38 | 0.53 | 13 |
| | | | without | -0.33 | 0.59 | 17 |

are again small. It is remarkable that the scatter indices are below 20 in all cases.

### 3.4.4 Critical Discussion of Hindcast Results

The time series and statistical analysis presented show that the hindcast performance for the wave parameter $T_{m1}$ – as quantified by comparison with local measurements from field stations – cannot be improved by the inclusion of currents into the wave model. The current influence on $T_{m1}$ is mainly local: the Doppler shift of the period at a grid point depends on the current at the same grid point. Since the comparatively coarse resolution of the wave model is not able to capture details of the small scale spatial variability of the current field in many cases, the hindcast cannot be improved. If interest is emphasized on local forecast or hindcast of wave parameters which are mainly locally influenced by currents, we conclude that the wave model must be applied with the same spatial resolution as the current model, in our case 100 m × 100 m (it can be shown that the 100 m resolution of the TRIM3D model is sufficient to capture the small scale spatial variability of the current field in the Sylt Rømø tidal basin).

Neither for the significant wave height did the hindcast analysis in the previous subsections reveal an improvement of wave model performance by inclusion of currents. But the reason in this case is that validation was performed at stations where the current influence on this parameter was almost neglectably small. The current influence on the wave height is nonlocal. It does not essentially depend on the sub-grid variability of the currents at the local grid point. We guess that if a validation had been possible at locations where a larger infuence of currents on the waves was detected, a current effect on the wave heights would have been quantified by the statistics. For wave parameters depending nonlocally on the currents, the used wave model grid resolution can be sufficient to improve the wave model hindcast performance by inclusion of currents.

## 4 CONCLUSIONS

In this paper, the influence of tidal currents on the wind waves in a small scall tidal system – the Sylt Rømø tidal basin – has been analysed. The K-model is a spectral discrete wave model with nonlinear dissipation. Further development resulted in the ability to take into account time and space varying water levels and currents in an instationary treatment. The K-model was applied to the tidal basin in one artificial case study and one hindcast simulation. In both cases, the model was run with and without tidal currents. The results allow direct insight into the effect of currents on the waves. The following conclusions can be drawn.

1. An artificial case study of an east 20 m/s wind situation shows considerable effects of tidal currents on the waves in the Sylt Rømø tidal basin. The effects are more pronounced for the $T_{m1}$ periods than for the significant wave heights. But even for the latter, relative changes of up to 15 percent can be seen. We conclude that inclusion of current effects into wave modeling for small scale tidal systems can remove systematical errors.

2. A hindcast of a six day storm period in the Sylt Rømø tidal basin showed a good wave model performance of the K-model. The performance was quantified by validation statistics at two field stations.

3. The statistical validation does not show an improvement of model performance through the inclusion of tidal currents in the wave modeling. Regarding the sigificant wave heights this can be explained by the fact that the measurement stations are located at spots where current effects on the wave heights were minor during the hindcast period. The current influence on wave periods depends to a large part on the local current field. It turned out that the wave model resolution was not sufficient to give a quantitative improvement of modeled wave periods through inclusion of current effects. It is expected, however, that a wave model resolution comparable to the current model resolution would give an improvement.

4. Although the forecast and hindcast performance of the K-model in its present resolution is limited with regard to wave parameters mainly locally affected by currents, the model is nevertheless a valuable tool for qualitative and quantitative coastal wave analysis. It can be used e.g. for further case studies with different wind situations to provide an understanding of changing current effects on the waves in different weather situations. Resulting spatial patterns of current induced wave height changes can give important additional information on the distribution of bottom shear stresses, which are responsible for the mobilization of sediments. This is one example for a useful application of the developed wave modeling technique.

## ACKNOWLEDGEMENTS

Field measurements and current modeling presented in this paper were carried out by coworkers of the Institute of Hydrophysics, GKSS-Forschungszentrum Geesthacht GmbH, Germany. This work, as well as a part of the wave modeling study, was performed within the frame of the European Union MAST III programme PROMISE, MAS3 CT 9500025, "PRe-Operational Modelling In the Seas of Europe". Corresponding financial support is gratefully acknowledged.

## REFERENCES

[1] V. Casulli and E. Cattani, *Stability, accuracy and efficiency of a semi-implicit method for three-dimensional shallow water flow*, Computers Math. Applic. **27** (1994), no. 4, 99–112.

[2] L. Cavaleri and P. Manalotte Rizzoli, *Wind wave prediction in shallow water - theory and application*, J. Geophys. Res. **86** (1981), 10961–10973.

[3] H. Günther, S. Hasselmann, and P. A. E. M. Janssen, *The WAM model cycle 4.0. user manual.*, Deutsches Klimarechenzentrum Hamburg, technical report no. 4, October 1992.

[4] H. Günther and W. Rosenthal, *A wave model with a non-linear dissipation source function*, Proc. 4th Int. Workshop Wave Hindcasting and Forecasting (Banff, Canada), October 1995.

[5] K. Hasselmann, T. P. Barnett, E. Bouws, H. Carlson, D. E. Cartwright, K. Enke,

J. A. Ewing, H. Gienapp, D. E. Hasselmann, P. Krusemann, A. Meerburg, P. Müller, D. J. Olbers, K. Richter, W. Sell, and H. Walden, *Measurements of wind-wave growth and swell decay during the Joint North Sea Wave Project (JONSWAP)*, Dtsch. Hydrogr. Z. Suppl. **A 8 (12)** (1973), 95p.

[6] L. H. Holthuijsen, N. Booij, and R. C. Ris, *A spectral model for the tidal zone*, Proc. Int. Conf. WAVES, 1993.

[7] G. J. Komen, L. Cavaleri, M. Donelan, K. Hasselmann, S. Hasselmann, and P. A. E. M. Janssen, *Dynamics and modelling of ocean waves*, Cambridge University Press, 1994.

[8] W. Rosenthal, *Derivation of Phillips $\alpha$-parameter from turbulent diffusion as a damping mechanism*, Radar Scattering from Modulated Wind Waves (G. J. Komen and W. A. Oost, eds.), Kluwer Academic Publishers, 1989, pp. 81–88.

[9] C. Schneggenburger, H. Günther, and W. Rosenthal, *Shallow water wave modeling with nonlinear dissipation: application to small scale systems*, Presentation at WISE San Francisco, April 1997.

[10] C. Schneggenburger, H. Günther, and W. Rosenthal, *Shallow water wave modeling with nonlinear dissipation*, Dt. Hydrogr. Z. **49** (1997), no. 2/3, xxxxxx.

[11] The WAMDI group: S. Hasselmann, K. Hasselmann, E. Bauer, P. A. E. M. Janssen, G. J. Komen, L. Bertotti, P. Lionello, A. Guillaume, V. C. Cardone, J. A. Greenwood, M. Reistad, L. Zambresky, and J. A. Ewing, *The WAM model – a third generation ocean wave prediction model*, J. Phys. Oceanogr. **18** (1988), 1775–1810.

[12] H. L. Tolman, *Effects of numerics on the physics in a third-generation wind-wave model*, J. Phys. Oceanogr. **22** (1992), 1095–1111.

# WAVE-WAVE INTERACTIONS IN A NEW COASTAL WAVE MODEL

Ray Q. Lin*and W. Perrie†
David Taylor Model Basin, Bethesda, Maryland

## 1 INTRODUCTION

In this study, our objective is to find a computationally cost-effective method of evaluation for the the nonlinear source function, $S_{nl}$, motivated by the Hasselmann (1962) or Zakharov (1968). Since 1962, when Hasselmann obtained a first formulation for $S_{nl}$, three different integration methods have been proposed. Firstly, there is the traditional integration method by Hasselmann and Hasselmann (1981), in which a stretched grid is used to reduce the six-dimensional integration to a five-dimensional integration. Secondly, there is the scaling similarity method (SSM) of Tracy and Resio (1982). Thirdly, there is the hybrid method by Snyder et al. (1993), in which a two-stage integration scheme is used, whereby spectrum-independent components of the evaluation are pre-computed and pre-summed before the main integration is performed. Both SSM and the hybrid method can improve the computational time by an order of magnitude, for the frequency-direction resolution used in this study. However, the DIA method is still about 10,000 times faster than the formulation of Hasselmann and Hasselmann (1981). Therefore, SSM and the hybrid method still need to be improved in order to be practical for almost-operational applications. In the study presented in this paper, we introduce a new integration method, which achieves a reduction of the integration dimensions in order to speed up the integration. We will show that the full six-dimensional singular integration can be reduced to a quasi-line integration, which we denote the reduced integration approximation, RIA.

*Hydormechanic Directorate, Code 5030, David Taylor Model Basin, NSWC, Carderock Division, 9500 MacArthur Boulevard, west Bethesda, MD 20817-5700, USA

†Ocean Sciences Division, Fisheries and Oceans Canada, Bedford Institute of Oceanography, Dartmouth, Nova Scotia, Canada B2Y 4A2

## 2 RIA MODEL

From Lin and Perrie (1997a), we know that the nonlinear action transfer rate from wave-wave interactions in finite depth water is given by

$$\frac{\partial A_{(\vec{k}_4)}}{\partial \tau} = 4\pi \int\int\int_{-\infty}^{\infty} T^2_{4,1,2,3}\delta(\vec{k}_4+\vec{k}_1-\vec{k}_2-\vec{k}_3)\,\delta[\omega_{(\vec{k})}+\omega_{(\vec{k}_1)}-\omega_{(\vec{k}_2)}-\omega_{(\vec{k}_3)}]\{A_{(\vec{k}_1)}A_{(\vec{k}_2)}[A_{(\vec{k}_1)}+A_{(\vec{k}_4)}]-A_{(\vec{k}_1)}A_{(\vec{k}_4)}[A_{(\vec{k}_3)}+A_{(\vec{k}_2)}]\}d\vec{k}_1 d\vec{k}_2 d\vec{k}_3, \quad (1)$$

where coupling coefficients $T_{i,1,2,3}$ are presented in Lin and Perrie (1997a). The resonant conditions (Phillips, 1960) are:

$$\vec{k}_3 = \vec{k}_4+\vec{k}_1-\vec{k}_2, \quad \omega_{(\vec{k}_4)}+\omega_{(\vec{k}_1)} = \omega_{(\vec{k}_2)}+\omega_{(\vec{k}_3)} \quad (2)$$

which are represented by the delta functions in Eq. (1). These limit part of the integral to a contour, the locus of interaction, thereby effectively reducing its dimensions. Following Webb (1978) and Tracy and Resio (1982), we let $B(\vec{k}_1)$ equal the argument of angular frequency delta function. Setting $B(\vec{k}_1) = 0$, the two resonant conditions in Eq. (2) can be combined into a single relation:

$$B(\vec{k}_1) = 0 = \omega_{(\vec{k}_4)}+\omega_{(\vec{k}_1)}-\omega_{(\vec{k}_2)}-\omega_{(\vec{k}_4+\vec{k}_1-\vec{k}_2)}, \quad (3)$$

Introducing $(\vec{n}, \vec{s})$ coordinates, normal and tangential to the interaction locus defined by Eq. (3), we may rewrite Eq. (1) as:

$$\frac{\partial A_{(\vec{k}_4)}}{\partial \tau} = 4\pi \int_{-\infty}^{\infty} d\vec{k}_2\{\int\int d\vec{s}d\vec{n}(\delta[B(\vec{s},\vec{n})])\}\, T^2_{4,1,2,3}\{A_{(\vec{k}_3)}A_{(\vec{k}_2)}[A_{(\vec{k}_1)}+A_{(\vec{k}_4)}]- A_{(\vec{k}_1)}A_{(\vec{k}_4)}[A_{(\vec{k}_3)}+A_{(\vec{k}_2)}]\} \quad (4)$$

and using the Dirac delta function, as in Lin and



AUTHOR INDEX TABLE OF CONTENTS

Perrie (1997b), to reduce the dimension of the integral, we obtain,

$$\frac{\partial A_{(\vec{k}_i)}}{\partial \tau} = 4\pi \int_0^\infty dk_2 \int_0^{2\pi} d\theta [2 \oint ds |\frac{\partial B(\vec{s},\vec{n})}{\partial n}|^{-1}] T^2_{i,1,2,3} \theta_{(x)} \{A_{(\vec{k}_3)} A_{(\vec{k}_2)} [A_{(\vec{k}_1)} + A_{(\vec{k}_i)}] - A_{(\vec{k}_1)} A_{(\vec{k}_i)} [A_{(\vec{k}_3)} + A_{(\vec{k}_2)}]\}, \tag{5}$$

where

$$|\frac{\partial B(\vec{s},\vec{n})}{\partial n}| = |\frac{\partial [\omega_{k_1} - \omega_{(|\vec{k}_i - \vec{k}_2 + \vec{k}_1|)}]}{\partial k_{1x}} \hat{i} + \frac{\partial [\omega_{k_1} - \omega_{(|\vec{k}_i - \vec{k}_2 + \vec{k}_1|)}]}{\partial k_{1y}} \hat{j}|, \tag{6}$$

and the Heaviside function is:

$$\theta_{(x)} = 1 \qquad if \qquad x > 0,$$
$$\theta_{(x)} = 0 \qquad if \qquad x < 0, \tag{7}$$

and $x = |\vec{k}_i - \vec{k}_3| - |\vec{k}_i - \vec{k}_2|$. Eq. (5) reduces the original six-dimensional singular integration Eq. (1) to a three-dimensional regular integration by eliminating two delta functions and evaluating the integral along a resonant orbit (Webb: 1978, Eq. 6.1, and Tracy and Resio: 1982, Eq. 7).

Analysis of the $T_{i,1,2,3}$ coupling coefficients in Lin and Perrie (1997b) implies $T_{i,1,2,3} \simeq T_{i,1,i,3} + T_{i,1,2,i}$. Furthermore, we can express $\vec{k}_3$ in terms of $\vec{k}_2$ by using resonant conditions when $\vec{k}_i$ and $\vec{k}_1$ are fixed. From Eq. (6), we see that if $\vec{k}_i \rightarrow \vec{k}_2$, then $|\frac{\partial B}{\partial n}| \rightarrow 0$ and the right hand side of the Eq. (5) $\rightarrow$ maximum. Therefore, we do not need to integrate $k_2$ from 0 to $\infty$, but only from $k_i - \Delta k$ to $k_i + \Delta k$. As only very limited $k_i$ domain ($\Delta k$) is therefore involved, Eq. (5) becomes quasi-two dimensional, rather than three-dimensional. In fact, we can further reduce the integration to a quasi-line integration, because the limitation on $\vec{k}$ restricts the angle ($\Delta\theta$) of integration on $\vec{k}_2$. Thus, we have finally,

$$\frac{\partial A_{(\vec{k}_i)}}{\partial \tau} = 4\pi \int_{k_i - \Delta k}^{k_i + \Delta k} dk_2 \int_{\theta_i - \Delta\theta}^{\theta_i + \Delta\theta} d\theta [2 \oint ds |\frac{\partial B(\vec{s},\vec{n})}{\partial n}|^{-1}] T^2_{i,1,2,3} \theta_{(x)} \{A_{(\vec{k}_3)} A_{(\vec{k}_2)} [A_{(\vec{k}_1)} + A_{(\vec{k}_i)}] - A_{(\vec{k}_1)} A_{(\vec{k}_i)} [A_{(\vec{k}_3)} + A_{(\vec{k}_2)}]\}. \tag{8}$$

This constitutes the reduced integration approximation, RIA. For tests implemented in this study, the integration limits on Eq. (8) are constrained by $\Delta\theta = 30^o$ and, in terms of frequency, $\Delta f = 0.4 f_p$, where $f_p$ is the spectral peak frequency.

# 3 $S_{nl}$ COMPARISONS

The formulations compared in this study assume deep water waves. The frequency increments are given by $df_i = 0.08 f_{i-1}$, and the angular discretization ($d\theta$) is 7.5°. The number of frequency bands are 35 and the number of angular bands are 48. Fig. 1 is the nonlinear action transfer rate from Eq. (5) as a function of angles and frequency.

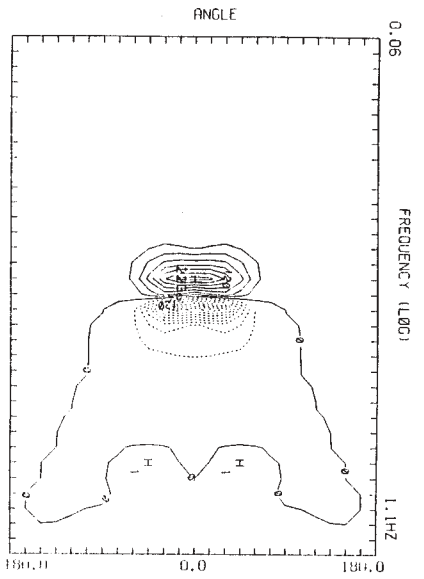


**Fig. 1.** The exact integral of the nonlinear action transfer from wave-wave interactions over deep water with linear dispersion (Lin and Perrie: 1997b) from Eq. (5) (Depth = 1,000 m) in frequency and direction coordinates. The increment between two contour lines is $3x10^{-6}$.

Fig. 2a shows $S_{nl}$ as computed by DIA in the WAM model, which is quite different from Fig. 1. Fig. 2b shows the Hasselmann (1962) formulation; Fig. 2c, the SSM Webb (1978) formulation as evaluated by Resio and Perrie (1991); and Fig. 2d, the Zakharov (1968) formulation evaluated in Lin and Perrie (1997a, 1997b).

Except for DIA, all other formulations give similar results. DIA differs in four major features. Firstly, DIA implies that $S_{nl}$ covers a far wider frequency domain than the original spectrum, as a result of its parameterization scheme. Secondly, a large amount of the DIA energy shift is to both high and low frequency directions, which is not prominent in any of the results from the other formulations. The other formulations show that most of the energy shift is to low frequency. The flux of



AUTHOR INDEX TABLE OF CONTENTS

energy to the high frequency, though necessary as discussed by Zakharov and Filonenko (1966), Zakharov (1991), and Resio and Perrie (1991), is only a very small fraction of the flux to low frequency.

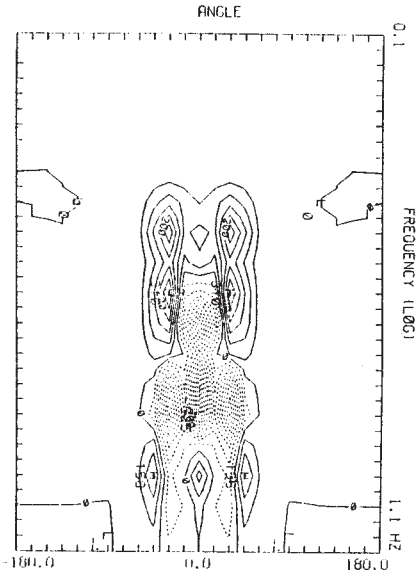


**Fig. 2a.** Comparisons of the different nonlinear action transfer formulations computed for deep water: DIA. Contour increment = $3 \times 10^{-7}$.

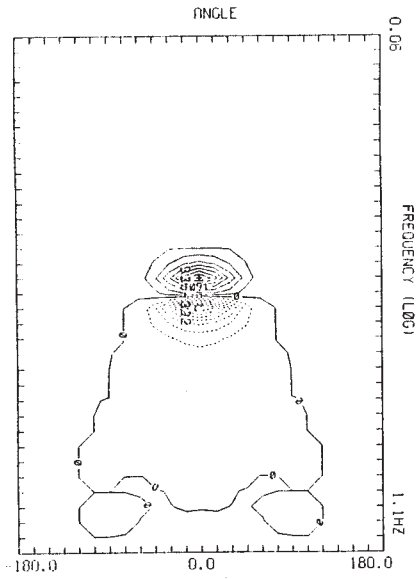


**Fig. 2b.** Improved Hasselmann and Hasselmann (1985). Contour increment = 3 $times 10^{-6}$.

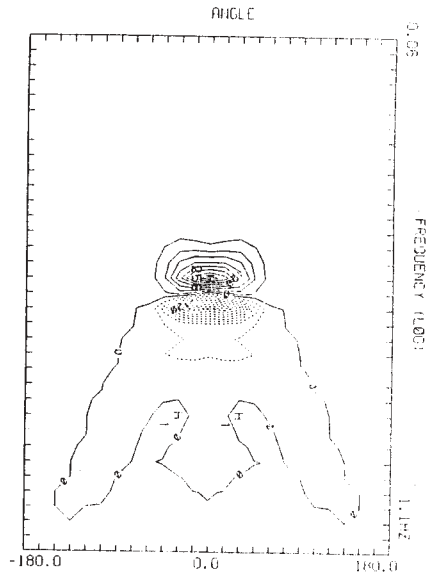


**Fig. 2c.** SSM (Resio and Perrie, 1990). Contour increment = $3 \times 10^{-6}$.

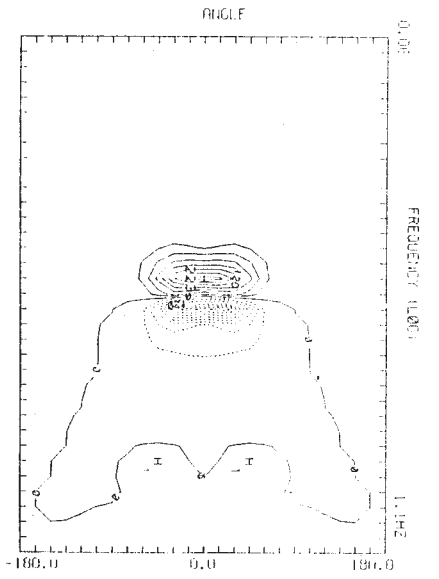


**Fig. 2d.** (d) Zakharov (1968). Contour increment = $3 \times 10^{-6}$.

Thirdly, the DIA result shows a pronounced splitting of the energy in both the down and up shift directions. The energy source and sink regions are very lumpy, a reflection of the discretization of the interacting components in the approximation process. Finally, the magnitude of the action transfer rate by DIA is about one order smaller than the other formulations in this test. Therefore, the increment between contour lines is $3x10^{-7}$ in Fig. 2a, as compared to $3x10^{-6}$ in Figs. 2b-d. This results from the large angular discretization ($d\theta = 30^o$) which is built into DIA as implemented in the WAM model. As discussed below, an angular discretization of less than about $7.5^o$ is necessary to accurately evaluate $S_{nl}$.

Based on these comparisons, we conclude that DIA results bear little physical resemblance with the exact results. Whether this lack of resemblance has impact on dynamics or not, needs to be studied rigorously. The fact that operational models, having totally different physics can all predict the sea state with equal success (Cardone et al 1995) is an intriguing phenomenon. This lack of resemblance with exact results must have been noticed by previous investigators. In fact, in proposing the DIA form, Hasselmann et al (1985) stated that 'the most critical test of a parameterization of $S_{nl}$ was its ability to reproduce the correct wave growth, rather than a ***superficial visual*** agreement of the transfer-function computations for individual spectra.' If we follow this suggestion, there is no difference between the WAM model and the heavily tuned models of the previous generations. We suggest that more rigorous study is needed on this problem.

Although Zakharov's (1968) algebraic formulation is much simpler than that of Hasselmann (1962), Zakharov's result as shown in Fig. 2d is almost exactly the same as Fig. 1, computed as in Lin and Perrie (1997b). The corresponding RIA integration, presented in Fig. 3, compares well with Figs. 1 and 2b-d and has a computation time which is several orders of magnitude faster than the integration of the Hasselmann and Hasselmann (1981) formulation. For 35 frequency bands and 48 angle bands, the RIA speed is about 25 times slower than DIA.

In fact, Dychenko and Lvov (1994) have analytically shown that the formulations by Zakharov and Hasselmann are identical, for the one-dimensional case. In our computations, summing maximal $S_{nl}$ values over all angles, we found that the difference between Hasselmann's and Zakharov's formulations is less than 8% and between

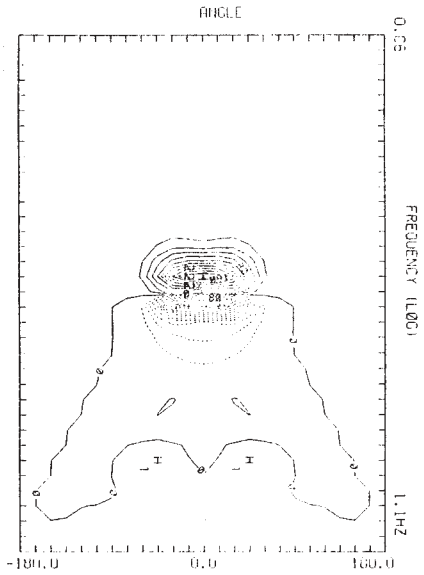


**Fig. 3.** The nonlinear action transfer rate computed from the reduced integration approximation, RIA in Eq. (8). Contour increment $= 3 \times 10^{-6}$.

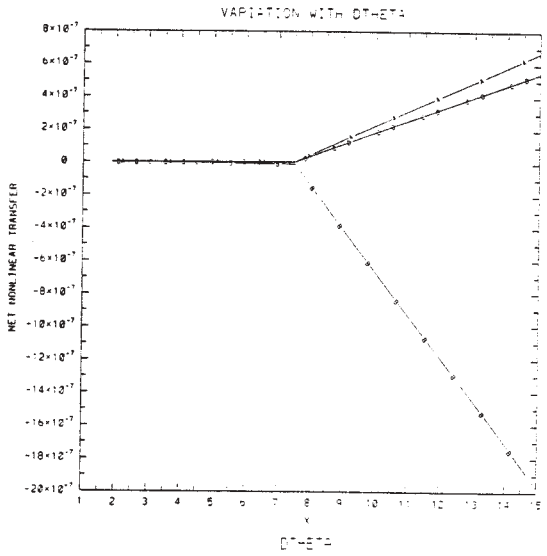


**Fig. 4.** Comparison of the net nonlinear transfer from various integral schemes as a function of angle discretization: where A, B, C, and D represent Zakharov, Hasselmann, Resio-Perrie and RIA.

Webb's and Zakharov's formulations is 9.7%, if $d\theta \leq 7.5^o$. The differences increase drastically for $d\theta$



AUTHOR INDEX TABLE OF CONTENTS

$> 7.5^o$. Among all the formulations, the one by Hasselmann is the most sensitive to the angular discretization size when $d\theta > 7.5^o$. To show this in a quantitative comparison, we plotted the net nonlinear transfer, which is the total integral of $\frac{DA}{Dt}$ over the entire frequency and direction range, plotted as a function of angular discretization sizes, in Fig. 4. In this figure, lines A, B, C, and D represent the formulations of Zakharov, Hasselmann, Webb and RIA respectively. DIA results are too small to be shown. Since $S_{nl}$ is conservative, the net nonlinear transfer should be zero. However, because numerical computational errors accumulate throughout the calculation, all formulations show a rapid deterioration of action conservation as the angular discretization increases. This becomes a serious problem when $d\theta > 7.5^o$ as shown in Fig. 4. Therefore, the angular discretization should always be less than $7.5^o$ in any wave model, regardless what formulation is used for $S_{nl}$.

# 4 CONCLUSIONS

We have compared formulations for $S_{nl}$ as given by DIA in the WAM model, Hasselmann and Hasselmann (1981), Zakharov (1968), Resio and Perrie (1991) and Lin and Perrie (1997b). Except for DIA, results from all formulations are quantitatively similar. The DIA formulation of Hasselmann et al. (1985) differs from the other formulations as follows:

**(1)** DIA spreads the energy far beyond the frequency domain of the original energy spectrum.

**(2)** Direct cascades of energy (or action), from low to high frequencies, are much greater in DIA, relative to inverse cascades from high to low frequencies, compard with other $S_{nl}$ formulations, where the direct cascade is typically an order of magnitude smaller than the inverse cascade.

**(3)** In magnitude, the maximal $S_{nl}$ values, as computed by DIA, are much smaller than corresponding values obtained in the other formulations, resulting from the coarse $d\theta = 30^o$ angular resolution implemented in DIA.

**(4)** DIA has a directional distribution which is completely unlike the other formulations, for a given input spectrum, giving nonlinear energy transfer to both high and low frequencies, which splits near $\pm$ $20^o$ from the dominant wave propagation direction, as seen in Fig. 3a. The other formulations give $S_{nl}$ plateaus at low frequencies and simple depressions at high frequencies, as shown in Figs. 1, 2b-d and 3.

Therefore, suggestions by Cardone et al (1995), that the 1st, 2nd, and 3rd (WAM) generation models all (i) perform very well for high wave conditions up to 12 m, (ii) all underpredict the most extreme seastate, (iii) and all have deficiencies in wave model physics, are hardly surprising. The DIA formulation within the WAM model necessitates considerable *tuning*, just as was necessary in earlier 1st and 2nd generation models.

The new finite-depth nonlinear transfer formulation, as developed in Lin and Perrie (1997a, 1997b) was also considered in this study. We found that an approximation to this formulation, denoted RIA, compared well with $S_{nl}$ formulations of Hasselmann (1962), Zakharov (1968) and Resio and Perrie (1991). Moreover, results indicate that RIA is only about 25 times slower than DIA, given an integration grid of 35 frequency bands and 48 angle bands. This is several orders of magnitude faster than the other $S_{nl}$ formulations making RIA a very practical formulation. Efficiency combined with simplistic algebra and low memory requirements, imply that RIA is definitely a strong competitor for future applications.

*Acknowledgements.* This research is funded in part by Physical and Coastal Oceanography program of the Office of Naval Research. The wave modeling program at BIO is funded by the Federal Panel on Energy Research and Development (Canada) under Project 6B3006. The authors would like to express their thanks to Professor Zakharov of the University of Arizona and Shirshov Institute of Oceanology (Moscow) for his valuable discussions. We would also like to thank Drs. Dychenko and Lvov both of the University of Arizona for sharing their results with us.

# References

[1] Cardone, V. D., Jensen, R. E., Resio, D. T., Swail, V. R. and A. T. Cox, 1995: Evolution of

contemporary ocean wave models in rare extreme events: "Halloween Storm" of October, 1991; "Storm of the Century" of March, 1993. *J. of Atmos. and Oceanic Tech.*, **13**, 198-230.

[2] Dychenko, A. I. and Y. V. Lvov, 1994: On the Hasselmann's and Zakharov's approaches to the kinetic equations for the gravity waves. In press in *Physica.*

[3] Hasselmann, K., 1962: On the nonlinear energy transfer in a gravity-wave spectrum Part I. General theory. *J. Fluid Mech.* **12**, 481-500.

[4] Hasselmann, S. and K. Hasselmann, 1981: A symmetrical method of computing the nonlinear transfer in a gravity - wave spectrum. *Hamb. Geophys. Einzelschriften Reihe A: Wiss. Abhand., 52*, 138pp.

[5] Hasselmann, S. and K. Hasselmann, 1985: Computation and parameterizations of the nonlinear energy transfer in a gravity-wave spectrum. Part I: A new method for efficient computations of the exact nonlinear transfer integral. *J. Phys. Oceanogr.*, **15**, 1369-1377.

[6] Hasselmann, S., K. Hasselmann, J. H. Allender, T. P. Barmett, 1985: Computations and parameterizations of nonlinear energy transfer in gravity-wave spectrum. Part II: Parameterizations of the nonlinear energy transfer for application in wave models. *J. of Phys. Oceanogr.*, **15**, 1378-1391.

[7] Lin, R. Q., and W. Perrie, 1997a: A New Coast Wave Model: Part III: Nonlinear wave-wave interaction for wave spectral evolution. *J. Phys. Oceanogr.* Vol. 27, No. 9, 1813-1826.

[8] Lin, R. Q., and W. Perrie, 1997b: A New Coast Wave Model: Part IV: Nonlinear source function. Submitted to *J. Geophys. Res.*.

[9] Phillips, O. M., 1960: On the dynamics of unsteady gravity waves of finite amplitude. *J. Fluid Mech.*, **9**, 193-217.

[10] Resio, D. and W. Perrie, 1991: A numerical study of nonlinear energy fluxes due to wave-wave interactions. Part I. Methodology and basic results. *J. Fluid Mech.*, **223**, 603-629.

[11] Snyder, R. L., W. C. Thacker, K. Hasselmann, S. Hasselmann, and G. Barzel, 1993: Implementation of an efficient scheme for calculating nonlinear transfer from wave-wave interaction. *J. Geophys. Res.*, **98**, No. c8, 14507-14525.

[12] Tracy, B. A. and D. T. Resio, 1982: Theory and calculation of the nonlinear energy transfer between sea waves in deep water. *WIS REP. 11, US Army Engineering Waterways Experiment Station*, Visksburg, MS. 50pp.

[13] Webb, D. J., 1978: Non-linear transfers between sea waves. *Deep-Sea Research*, **25**, 279-298.

[14] Zakharov, V. E., 1968: Stability of periodic waves and finite amplitude on the surface of deep fluid. *Zhurnal Prikladnoi Mekhaniki Tekhnicheskoi Fiziki*, **3**, No. 2, 80-94.

[15] Zakharov, V. E., 1991: Inverse and direct cascade in wind-driven surface wave turbulent and wave-breaking. *In breaking waves IUTAM Symposium*, M. L. Banner and R. H. J. Grimshaw (Editors), Sydney, Australia. 69-91.

[16] Zakharov, V. E. and N. N. Filonenko, 1966: The energy spectrum for stochastic oscillation of fluid's surface. *Doklady Akad. Nauk.*, **170**, 1292-1295.

# NONLINEAR SOURCE FUNCTION IN A NEW COASTAL WAVE MODEL

Ray Q. Lin*and Weijia Kuang†
David Taylor Model Basin, Bethesda, Maryland

## 1 INTRODUCTION

Nonlinear wave-wave interactions are the major source function in the evolution of surface waves. Phillips (1960, 1977) first found that the resonant mode can be specified by four-wave interactions and Hasselmann (1962) obtained the nonlinear transfer rate for four-wave interactions by applying fifth-order small perturbation theory. Since that time, for more than three decades, ocean scientists have been studying the nonlinear wave-wave interactions. However, in spite of this, it is still not been possible to efficiently obtain an accurate nonlinear source function for even four-wave interactions. Hasselmann and Hasselmann *et al* (1981, 1985) used a classical integrational method, based on Hasselmann (1962), and derived the formulation EXACT-NL. The formulation is so tedious that it is practically useless. More recently, a discrete interaction approximation (DIA) by Hasselmann *et al* (1985) was applied in an operational wave model (WAM). However, the DIA formulation has several major problems (Lin and Perrie,1997b):

**(1)** the direct cascade and the inverse cascade are about the same order of magnitude, resulting in energy loss due to four-wave interactions (they should be conservative);

**(2)** the energy transfer rate is about one-order smaller than the simulations using 'EXACT-NL',

**(3)** the inverse cascade is not in the - down wind direction.

Resio and Perrie (1991) applied Webb's simplified formulation and obtained results similar to those of Hasselmann and Hasselmann (1981 and 1985), and Hasselmann *et al* (1985), although the formulation is 20× faster than EXACT-NL. However, the method is only for the deep ocean and is not efficient enough for operational wave modelling. Zakharov (1968, 1991) used Hamiltonians to obtain the nonlinear transfer rate, obtaining a formulation that is equivalent to, but much simpler than EXACT-NL, based on Hasselman (1962). Thus, he was effective in shedding light on the aproach to obtaining an efficient accurate simulation of the nonlinear transfer rate for wave modelling. Krasitskii (1994) and Lin and Perrie (1997a and c) extended Zakharov's work to finite depth water. To obtain an exact solution for four-wave interactions, six integrals are needed, which is computationally expensive. Lin and Perrie (1997b) analysed the real solutions interaction locus and reduced the six-dimensional integrations to a quesi - line integration, formulating the Reduce Integration Approximation (RIA). The RIA formulation agrees well with well known existing methods, such as EXACT-NL by Hasselman and Hasselman *et al* (1981 and 1985) and Resio and Perrie (1991) in deep water. Moreover, RIA is a thousand times faster than EXACT-NL and only 20 times slower than DIA, which is an operational wave model.

Su (1982a and b) observed that three-dimensional instabilities occur in the deep ocean when the wave steepness ($ak$) is greater than 0.28. At about the same time, through an application of instability analysis, McLean (1982) found that five-wave interactions are greater than four-wave interactions when the wave steepness (ak) is greater than 0.28 and the water depth is 2 meters. Moreover, the experimental results of Su and Green (1984) suggested that two-dimensional instabili-

*Hydormechanic Directorate, Code 5030, David Taylor Model Basin, NSWC, Carderock Division, 9500 MacArthur Boulevard, west Bethesda, MD 20817-5700, USA

+EPS/Harvard University, 20 Oxford street, Cambridge, MA 02138, USA



AUTHOR INDEX TABLE OF CONTENTS

ties can trigger three-dimensional instabilities in deep water, as long as initial waves exhibit at least moderate steepness. Lin and Perrie (1997c) found that the five-wave interactions indeed can dominate over the four-wave interactions when the normalized wave steepness ($ak\frac{3+\tanh^2 kh}{4\tanh^3 kh}$) is greater than 0.3 in shallow water. The numerical simulation by Lin and Su (1997) shows that in deep water, the coupling of four-wave and five-wave interactions indeed causes the three-dimensional wave-wave interactions to dominate. This occurs not because of wave steepness, but because of the width of the spectrum. Therefore, five-wave interactions are indeed important when the wave amplitude is large. Therefore, the perturbational method, even RIA, as developed by Lin and Perrie (1997b), is not suitable for operational wave modelling. Thus, although RIA reduced six-dimensional integrations, representing the four-wave interactions, to a one-dimensional integration, it is limited because it is based on a perturbative anlysis.

In this paper, we will apply a pseudospectral method to study the nonlinear source function terms representing wave-wave interactions. The method is global. Unlike previous integration methods, it includes all wave-wave interactions within the truncation limit, instead of only four or five wave interactions studied before. A possible difficulty for the method may arise from the fact that the grid sizes of the operational wave model are much larger than the typical wavelengths. In the following we shall describe in detail how we solve this problem. The results will also be compared with well known other methods:

**(1)** deep water linear dispersion wave-wave interactions of Hasselman and Hasselman (1981, 1985); Resio and Perrie (1991) and Lin and Perrie (1997b).

**(2)** shallow water nonlinear dispersion wave-wave interactions of Lin and Perrie (1997b).

**(3)** coupling of four-wave and five-wave interactions in deep water of Lin and Su (1997).

# 2 MATHEMATICAL MODEL

Zakharov (1968) first used a Hamiltonian representation to obtain the four-wave interactions source function for deep water by applying the small perturbation theory up to the third-order equation. Krasitskii (1994), Lin and Perrie (1997a and 1997c) extended Zakharov's work to finite depth water and included five-wave interactions. However, small perturbation theory has its limitations. First of all, it is not appropriate for large amplitude wave-wave interactions because the nonlinear wave-wave interactions could be of the same order as the linear terms. Also, the method demands significant CPU time for evaluating integrations over the spectral (wave number vector) space, even when the solutions are in Hamiltonian form and the corresponding six-dimensional integation is reduced to a quesi-line integation (Lin and Perrie, 1997b). Furthermore, it is impossible to implement five-wave interactions into the operational wave model.

By examining the experimental data (Lake et al, 1977) and the theories, Crawford et al (1981) showed that it is not necessary to have a very high wave number cutoff in studies of the finite-amplitude wave-wave interactions.

Spectral methods have been applied in linear stability analysis in oceanic studies, such as McLean (1982). But none has been utlized to study the nonlinear source function, which is generally carried out with small perturbation theory. Here, we introduce a pseudo-spectral method in our wave-wave model, so that apart from the computational efficiency of the method, we shall also be able study large amplitude wave-wave interactions.

In this section, we will describe the basic equations of the waves and a brief review of the Hamiltonian solutions we employed. Then we describe in detail the spectral method we intend to apply for nonlinear interactions and other quantities of interest, such as the energy transfer rate.

## 2.1 Basic Equations and Boundary Conditions

**(A)** Continuity Equation:

$$\nabla_H^2 \phi + \frac{\partial^2 \phi}{\partial z^2} = 0, \qquad for \qquad -h \le z \le \eta, \tag{1}$$

where

$$\nabla_H = \vec{i}\frac{\partial}{\partial x} + \vec{j}\frac{\partial}{\partial y}.$$

**(B)** Boundary Conditions:

**(1)** At the free surface: $z = \eta$



AUTHOR INDEX TABLE OF CONTENTS

a) Kinematics:

$$\frac{\partial \eta}{\partial t} + \nabla_H \phi \cdot \nabla_H \eta = \frac{\partial \phi}{\partial z}, \qquad (2)$$

b) Dynamics:

$$\frac{\partial \phi}{\partial t} + \frac{1}{2}(\nabla_H \phi)^2 + \frac{1}{2}(\frac{\partial \phi}{\partial z})^2 + g\eta = 0, \quad (3)$$

**(2)** At the bottom: $z = -h$

$$\frac{\partial \phi}{\partial z} = 0. \qquad (4)$$

Variables denoted as $t$, $H$, $h$, $g$, $\eta$, and $\phi$ are time, the horizontal coordinate, the local depth of the ocean, the gravity acceleration, the free surface elevation, and the potential function.

## 2.2 Hamiltonian Variation Principle

In this section, we simply follow Zakharov (1968, 1991) to obtain the Hamiltonian form for the pseudospectral method.

Lets assume $\psi_{(\vec{r},t)} = \phi_{(\vec{r},z,t)}|_{z=\eta}$, implying

$$\frac{\partial \psi}{\partial t} = \frac{\partial \phi}{\partial t} + \frac{\partial \eta}{\partial t}\frac{\partial \phi}{\partial z}|_{z=\eta}, \qquad (5)$$

Substitute Equations (2) and (3) into Equation (5), we obtain:

$$\begin{aligned} &\tfrac{\partial \psi}{\partial t} = -g\eta - \tfrac{1}{2}[(\nabla_H \phi)^2 + (\tfrac{\partial \phi}{\partial z})^2] \\ &-[\nabla_H \eta \cdot \nabla_H \phi - \tfrac{\partial \phi}{\partial z}]\tfrac{\partial \phi}{\partial z}|_{z=\eta} \\ &= -g\eta - \tfrac{1}{2}(\nabla_H \phi)^2 + \tfrac{1}{2}(\tfrac{\partial \phi}{\partial z})^2 \\ &-\tfrac{\partial \phi}{\partial z}(\nabla_H \eta \cdot \nabla_H \phi), \end{aligned} \qquad (6)$$

The Hamiltonian Forms are:

$$\frac{\partial \eta}{\partial t} = \frac{\delta E}{\delta \psi}, \qquad \frac{\partial \psi}{\partial t} = -\frac{\delta E}{\delta \eta}, \qquad (7)$$

where E is total energy:

$$E = \frac{1}{2}\int d\vec{r}\int_{-h}^{\eta}[(\nabla_H \phi)^2 + (\frac{\partial \phi}{\partial z})^2]dz + \frac{1}{2}g\int \eta^2 d\vec{r}, \qquad (8)$$

and

$$\begin{aligned} &\delta E^* = \tfrac{1}{2}\int_s [\delta\psi_{(s)}\tfrac{\partial \phi_{(s)}}{\partial n} + \psi_{(s)}\tfrac{\partial \delta\phi_{(s)}}{\partial n}]ds \\ &= \int[\tfrac{1}{2}(\nabla_H \phi)^2 - \tfrac{1}{2}(\tfrac{\partial \phi}{\partial z})^2 + (\nabla_H \eta \cdot \nabla_H \phi)\tfrac{\partial \phi}{\partial z}]|_{z=\eta} \\ &\delta\eta_{(\vec{r})}d\vec{r}, \end{aligned} \qquad (9)$$

Using Fourier Transform:

$$\begin{aligned} &\eta_{(\vec{r},t)} = \tfrac{1}{2}\int_0^{2\pi} Q_1(k)[a(k)e^{i(\vec{k}\cdot\vec{r}-\omega t)} \\ &+a^*(k)e^{-i(\vec{k}\cdot\vec{r}-\omega t)}]d\vec{k}, \end{aligned} \qquad (10)$$

$$\begin{aligned} &\psi_{(\vec{r},t)} = -\tfrac{i}{2}\int_0^{2\pi} Q_2(k)[a(k)e^{i(\vec{k}\cdot\vec{r}-\omega t)} \\ &-a^*(k)e^{-i(\vec{k}\cdot\vec{r}-\omega t)}]d\vec{k}, \end{aligned} \qquad (11)$$

where

$$Q_1(k) = (\frac{k}{\omega})^{1/2},$$

$$Q_2(k) = Q_1(k)^{-1},$$

$k$ is wave number, and $\omega$ is frequency (Whitham, 1974):

$$\omega^2 = g\,k\tanh kh[1+a^2k^2\frac{9\tanh^4 kh - 10\tanh^2 kh + 9}{8\tanh^4 kh}].$$

The Hamiltonian form, Equation (7) can be written as:

$$i\frac{\partial a(k)}{\partial t} = \frac{\delta H}{\delta a^*(k)}, \qquad (12)$$

Rewriting Equation (12) as:

$$ia^*(k)\frac{\partial a(k)}{\partial t} = E = H,$$

$$\begin{aligned} &ia^*(k)\tfrac{\partial a(k)}{\partial t} = \omega a(k)a^*(k) + \tfrac{1}{2\pi}\int_0^{2\pi}[\tfrac{1}{2}(\nabla_H \phi)^2 \\ &-\tfrac{1}{2}(\tfrac{\partial \phi}{\partial z})^2 + (\nabla\eta \cdot \nabla\phi)\tfrac{\partial \phi}{\partial z}]a^*(k)e^{-i\vec{k}\cdot\vec{r}}d\vec{r}, \end{aligned} \qquad (13)$$

## 2.3 Pseudospectral Method in The Wave Model

We intend to work on the nondimensional equations by introducing the following scalings:

$$\begin{cases} x \rightarrow L_x x, \\ y \rightarrow L_y y, \\ z \rightarrow h z, \end{cases} \qquad \begin{cases} t \rightarrow \sqrt{h/g}\,t, \\ \phi \rightarrow h\sqrt{hg}\,\phi, \\ \eta \rightarrow h\eta, \end{cases} \qquad (14)$$

where $L_x$ and $L_y$ are typical length scales of the system in horizontal dimensions.

With the above scalings, the equations (1)–(3) can be rewritten as the following nondimensional forms:

$$\nabla_H^2\phi + \tfrac{\partial^2\phi}{\partial z^2} = 0, \text{ for } -1 \le z \le \eta, \qquad (15)$$

$$\tfrac{\partial \eta}{\partial t} + \nabla_H \phi \cdot \nabla_H \eta = \tfrac{\partial \phi}{\partial z}, \qquad (16)$$

$$\tfrac{\partial \phi}{\partial t} + \tfrac{1}{2}(\nabla_H \phi)^2 + \tfrac{1}{2}(\tfrac{\partial \phi}{\partial z})^2 + \eta = 0, \qquad (17)$$

where

$$\begin{cases} \nabla_H^2 = \epsilon_x\,\partial/\partial x\,1_x + \epsilon_y\,\partial/\partial y\,1_y, \\ \epsilon_x = h/L_x, \quad \epsilon_y = h/L_y. \end{cases} \qquad (18)$$

In our system, $\epsilon_x$ and $\epsilon_y$ are very small. The nondimensional equation for the surface stream function

$$\psi(x,y,t) \equiv \phi(x,y,t,z=\eta)$$

at the surface $z=\eta$ is

$$\frac{\partial\psi}{\partial t} = -\eta - \frac{1}{2}(\nabla_H^2\phi)^2 + \frac{1}{2}\left(\frac{\partial\phi}{\partial z}\right)^2 - \left(\frac{\partial\phi}{\partial z}\right)(\nabla_H^2\eta)(\nabla_H^2\phi). \quad (19)$$

The equations (15), (16), (17) and (19) are solved in the region

$$-\pi \le x \le \pi \quad \text{and} \quad -\pi \le y \le \pi. \quad (20)$$

We expand our solutions into the following spectral series:

$$\eta(x,y,t) = \frac{1}{2\pi}\sum_{m=0}^{M}\sum_{n=0}^{N}\hat{a}_{mn}(t)\, e^{i(mx+ny)} + C.C., \quad (21)$$

$$\psi(x,y,t) = \frac{1}{2\pi}\sum_{m=0}^{M}\sum_{n=0}^{N}\hat{b}_{mn}(t)\, e^{i(mx+ny)} + C.C., \quad (22)$$

where $C.C.$ stands for the complex conjugate. The numbers $(M,N)$ in the above expansions are the truncation order of our method. Consistent with the expansions (21–22), we can also expand the stream function $\phi$ as

$$\phi(x,y,z,t) = \frac{1}{2\pi}\sum_{m=0}^{M}\sum_{n=0}^{N}\hat{c}_{mn}(t)\, e^{i(mx+ny)} \cosh K_{mn}(1+z), \quad (23)$$

where

$$K_{mn} = \sqrt{\epsilon_x^2 m^2 + \epsilon_y^2 n^2} \quad (24)$$

is the wave number.

Substituting (21)–(23) into the equations (16) and (19), we obtain the following equations of the expansion coefficients

$$\frac{\partial\hat{a}_{mn}}{\partial t} = \hat{N}_{mn}^{(1)} \quad (25)$$

$$\frac{\partial\hat{b}_{mn}}{\partial t} + \hat{a}_{mn} = \hat{N}_{mn}^{(2)}, \quad (26)$$

where $(\hat{N}^{(1)}, \hat{N}^{(2)})$ are the spectral coefficients of the nonlinear interaction terms. They are solved via a collocation-point method.

We apply an implicit second order Cranken-Nicholson method for the linear terms and an explicit third order Runger-Kutter method for the nonlinear terms. The equations (25) and (26) can be rewritten as follows:

$$\frac{\partial\hat{f}}{\partial t} + \hat{L}\hat{f} = \hat{N}(\hat{f}), \quad (27)$$

where

$$\hat{f} \equiv (\hat{a}_{mn}, \hat{b}_{mn})^T, \qquad \hat{N} \equiv (\hat{N}_{mn}^{(1)}, \hat{N}_{mn}^{(2)})^T, \quad (28)$$

and $\hat{L}$ is a linear operator. Our numerical algorithm can then be written as

$$A_1\hat{f}_1 = A_2\hat{f}^{(k)} + \left(\frac{\Delta t}{2}\right)\hat{N}(\hat{f}^{(k)}), \quad (29)$$

$$A_1\hat{f}_2 = A_2\hat{f}^{(k)} + \left(\frac{3\Delta t}{4}\right)\hat{N}(\hat{f}_1), \quad (30)$$

$$A_1\hat{f}^{(k+1)} = A_2\hat{f}^{(k)} + \left(\frac{\Delta t}{9}\right)\left[2\hat{N}(\hat{f}^{(k)}) + 3\hat{N}(\hat{f}_1) + 4\hat{N}(\hat{f}_2)\right], \quad (31)$$

where

$$A_1 = I + \frac{\Delta t}{2}\hat{L}, \qquad A_2 = I - \frac{\Delta t}{2}\hat{L}, \quad (32)$$

and $\Delta t$ is the time step. It is determined by the CFL condition in the simulation. Therefore, for a given initial state $\left[\hat{a}_{mn}^{(0)}, \hat{b}_{mn}^{(0)}\right]$, we can integrate our solutions over time with the above algorithm.

# 3 MODEL RESULTS

In the above section, we described how to apply the pseudospectral method to study nonlinear source function in wave model. The pseudospectral method should represent the total sum of the wave-wave interactions, such as 4-wave, 5-wave, 6-wave, etc. The results of pseudospectral method also includes harmonic forcing. The following results are truncated to 25 waves in 101x25 points. The results should capture the dominant interaction mechanism for different ocean sea state conditions:

**(1)** two-dimensional wave-wave interactions dominate, when water is deep ($kh \le 1.363$) or normalized wave steepness satisfies, $\epsilon = ak\frac{3+\tanh^2 kh}{4\tanh^3 kh}$ less than 0.3;

**(2)** three-dimensional wave-wave interactions dominate when water is shallow ($kh < 1.363$) and normalized wave steepness satisfies $\epsilon$ greater or equal to 0.3 (Su 1981a and b; McLean, 1982; Lin and Perrie, 1997c).

**(3)** three-dimensional wave-wave interactions can dominate in deep ocean if the interaction time is long enough (Su and Green, 1984; Lin and Su, 1997).

To facilitate comparison, we will use the same JONSWAP spectrum as applied in the small perturbative method (Lin and Perrie, 1997a, b, c; Lin and Su, 1997). The spectral function is show in Figure 1.

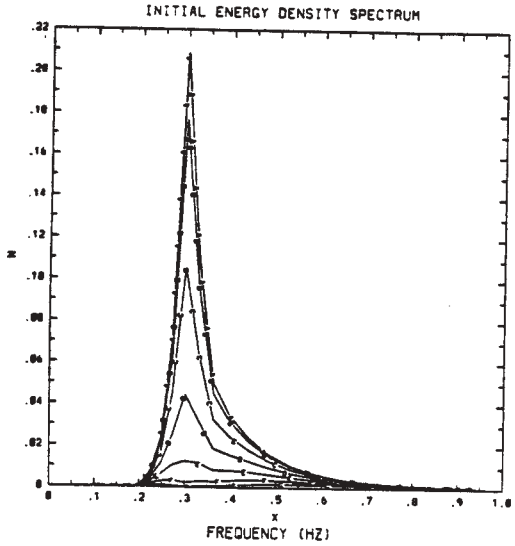


**Fig. 1** The reference JONSWAP gravity wave spectrum with Hasselmann - Mistsuyasu directional spreading, where lines A, B, C,...,G represent the angles $0^o$, $30^o$, $60^o$,..., $180^o$, with $0^o$ towards east.

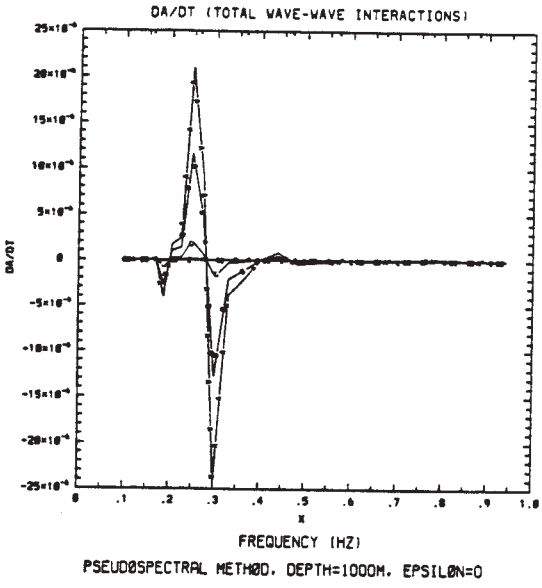


**Fig. 2** Total nonlinear transfer (sum of 4-wave, 5-wave, 6-wave, etc. interactions are truncated at 25) in deep water by pseudospectral method with linear dispersion, where lines A, B, C, D, E, F, and G represent the angles $0^o$, $30^o$, $60^o$, $90^o$, $120^o$, $150^o$, and $180^o$.

However, as of the writing of this manuscript, we only obtained the small amplitude nonlinear source function in deep water, which is shown in Figure 2, where $\epsilon = 0$, and lines A, B, ..., G are associated with those in Figure 1. Figure 2 is very similar to the nonlinear transfer rate due to 4-wave interactions in Figure 2 of Lin and Perrie (1997a), who used a Hamiltonian variation principle up to third-order equation. This result is very encouraging and it means that the 4-wave two dimensional wave-wave interactions indeed dominate in the deep ocean, especially for the linear dispersion case (very small wave steepness). The other results, which are related to large amplitude and shallow water will be shown in a related paper.

# 4 CONCLUSIONS

The pseudospectral method has been developed for calculating the general and global wave-wave interactions. The results of the pseudospectral method should able to capture the dominant interaction mechanism for the different ocean sea state conditions:

**(1)** two-dimensional wave-wave interactions are dominate in deep ocean, with nonlinearity as much as 0.3;

**(2)** nonlinear transfer rate decreases with water depth;

**(3)** when the water is shallow and nonlinearity, $\epsilon$ equal to 0.3, the three-dimensional wave-wave interactions become dominate.

However, at the writing of this paper, we only obtain the nonlinear transfer rate for small wave amplitudes in deep water, which agree well with the well known methods of (Lin and Perrie, 1997b). This is very encouraging. A related paper will present further results in the near future.

*Acknowledgements.*

We want to thank Dr. Perrie for reading the manucript critically. This work has been supported by grants from the Office of Naval Research under the Coastal and Physical Oceanography Programs.

## References


[1] Canuto, C., M. Y. Hussaini, and T. A. Zang, 1986: *Spectral Methods in Fluid Dynamics*, Springer Series in Computational Physics, Springer-Verlag.

[2] Crawford, D. R., B. M. Lake, P. G. Saffman and H. C. Yuen, 1981: Stability of weakly nonlinear deep-water waves in two and three dimensions. *J. Fluid Mech.*, Vol. 105, 177-191.

[3] Hasselmann, K., 1962: On the nonlinear energy transfer in a gravity-wave spectrum, Part I. General Theory. *J. Fluid Mech.* Vol. 12, 481-500.

[4] Hasselmann, S. and K. Hasselmann, 1981: A symmetrical method of computing the nonlinear transfer in a gravity-wave spectrum. *Hamb. Geophys. Einzelschriften Reihe A. Wiss. Abhand., 52*, 138pp.

[5] Hasselmann, S., K. Hasselmann, 1985: Computations and parameterizations of nonlinear energy transfer in a gravity-wave spectrum. Part I: A new method for efficient computations of exact nonlinear transfer integral. *J. of Physical Oceanogr.* Vol. 15, 1369-1377.

[6] Hasselman, S., K. Hasselmann, J. H. Alleder, T. P. Barmett, 1985: Computations and parameterizations of nonlinear energy transfer in gravity-wave spectrum. Part II: Parameterizations of the nonlinear energy transfer for application in wave model. *J. of Phys. Oceanogr.* Vol. 15, 1378-1391.

[7] Komen, G. J., L. Cavaleri, M. Donelan, K. Hasselman, S. Hasselman and P.A.E.M. Janssen, 1994: Dynamics and Modelling of ocean waves. Cambridge university press, 523pp.

[8] Krasitskii, V. P., 1994: On reduced equations in the Hamiltonian theory of weakly nonlinear surface waves. *J. Fluid Mech.*, Vol. 272, 1-20.

[9] Lake, B. M. Rungaldier, H. and Ferguson, W. E., 1977: Nonlinear deep-water waves: theory and experiment. Part 2. Evolution of a continuous wave train. *J. Fluid Mech.*, Vol. 83, 49-53.

[10] Lin, R. Q. and W. Perrie, 1997a: A new coastal wave model. Part III. Nonlinear wave-wave interactions. *J. Phys. Oceanogr.* Vol 27, No. 9, 1813-1826.

[11] Lin, R. Q. and W. Perrie, 1997b: Wave-wave Interactions in a new coastal wave model. Submitted to JGR.

[12] Lin, R. Q. and W. Perrie, 1997c: A new coastal wave model, Part V. Five-wave interactions. *J. of Physical Oceanogr.* Vol 27, No. 10, 2169-2186.

[13] Lin, R. Q. and M. Y. Su, 1997: Three-dimensional wave-wave interactions in deep water. In preparation.

[14] McLean, J. W., 1982: Instabilities of finite-amplitude gravity waves on water of finite depth. *J. Fluid Mech.*, Vol. 114, 331-341.

[15] Phillips, O. M., 1960: On the dynamics of unsteady gravity waves of finite amplitude. *J. Fluid Mech.*, Vol. 9, 193-217.

[16] Phillips, O. M., 1977: The Dynamics of the Upper Ocean. *Cambridge University Press.*

[17] Resio, D. and W. Perrie, 1991: A numerical study of nonlinear energy fluxes due to wave-wave interactions. Part I. methodology and basic results. *J. Fluid Mech.* Vol. 223, 603-629.

[18] Su, M. Y., 1982a: Three dimensional deep-water waves, Part I, Experimental measurement of skew and symmetric wave patterns, *J. Fluid Mech.*, Vol. 124, 73-108.

[19] Su, M. Y., 1982b: Evolution of groups of gravity waves with moderate to high steepness, *Phys. Fluids*, Vol. 25, 2167-2174.

[20] Su, M. Y. and W. Green, 1984: Coupling two- and three- dimensional instabilities of surface gravity waves. *Physical Fluids*, Vol. 27, 2595-2597.

[21] Whitham, G. B., 1974: *Linear and Nonlinear Waves.*, John Wiley & Sons, New York, 628pp.

[22] Zakharov, V. E., 1968: Stability of periodic waves of finite amplitude on the surface of deep fluid. *Zhurnal Prikladnio Mekhaniki Tekhnicheskoi Fiziki*, Vol. 3 No.2, 80-94.

[23] Zakharov, V. E. and E. Shulman, 1980: Degenerative dispersion law, motion invariants and kinetic equation, *Physica D.*, 192-202.

[24] Zakharov, V. E., 1991: Inverse and direct cascade in the wind-driven surface wave turbulence and wave-breaking. *M. L. Banner, R. H. Grimshaw, Eds. Breaking Waves IUTAM Symposium Sydney/Australia.*

# NEW PERSPECTIVE ON THREE-WAVE RESONANT INTERACTIONS IN SHALLOW WATER OCEAN SURFACE WAVES

**A. R. Osborne**

*Dipartimento di Fisica Generale dell'Università*
*Via Pietro Giuria 1, Torino 10125, Italy*

**M. Petti**

*Dipartimento di Ingeneria Civile, Sezione Idraulica*
*Via S. Marta 3, 50139 Firenze, Italy*

## 1. INTRODUCTION

The focus of this paper is to address new perspectives on shallow water wave resonances. We consider the problem from theoretical, numerical and experimental points of view. We discuss the problem in terms of the Korteweg-deVries equation, which is the prototypical, nonlinear partial differential equation for unidirectional, shallow water wave motion. Our main analysis tool is the inverse scattering transform solution of the KdV equation in terms of cnoidal wave basis functions. We discuss how solutions of KdV, for periodic boundary conditions, may be addressed in terms of a simple Cnoidal Wave Theorem: All solutions can be expressed as a linear superposition of particular cnoidal waves plus nonlinear interactions among the cnoidal waves. We show how to use this formulation to revisit and to enhance our understanding of the problem of resonances in shallow water waves.

In the last half of the twentieth century a number of important theoretical developments have been made with regard to the understanding of nonlinear wave propagation [Novikov, et al, 1980; Ablowitz and Segur, 1981; Dodd, et al, 1982; Newell, 1985]. Of particular relevance to the present work has been the discovery of large classes of *nonlinear wave equations* whose solutions may be computed without approximation using a new technique referred to as the *inverse scattering transform (IST)*. IST may be viewed as a kind of *nonlinear Fourier analysis*, valid for fully nonlinear wave motion, which has many of the nice features that render ordinary Fourier analysis such a useful tool for the analysis of oceanic wave motions. Practical implementation of IST has been made possible by a number of theoretical advances [Boyd, 1981, 1990; Date and Tanaka, 1976; Dubrovin, et al., 1976; Flaschka and McLaughlin, 1976; Its and Matveev, 1975; McKean and Trubowitz, 1976] with regard to the case for *periodic boundary conditions* and by a recent paper of Osborne [1995] in which techniques are developed for the simple exploitation of the method from physical, mathematical and numerical points of view. The approach has been cast in terms of a kind of *nonlinear Fourier analysis* which, in the small amplitude limit, reduces to the ordinary, linear Fourier transform. It is for this reason that the nonlinear Fourier approach may be viewed as a generalization of linear Fourier analysis.

In the present paper we are concerned with nonlinear shallow water wave motion as governed by the Korteweg-deVries equation [1895]:

$$\eta_t + c_o \eta_x + \alpha \eta \eta_x + \beta \eta_{xxx} = 0 \qquad (1a)$$

where the constant coefficient coefficients are given by: $c_o = \sqrt{gh}$, $\alpha = 3c_o / 2h$ and $\beta = c_o h^2 / 6$; $h$ is the water depth and $g$ is the acceleration of gravity. A normalized version of this equation, commonly used in inverse scattering theory, is given by:

$$u_t + 6uu_x + u_{xxx} = 0 \qquad (1b)$$

Herein we exploit the fact that the KdV equation is completely integrable by the inverse scattering transform for periodic boundary conditions.

This paper is organized as follows. In Section 2 we briefly discuss certain aspects of linear Fourier analysis useful in the present work. We give a terse introduction to *nonlinear* Fourier analysis and the inverse scattering transform in Sections 3, 4. An overview of our perspective on shallow water resonances from the points of view of multiscale analysis and inverse scattering theory is given in Section 5. Section 6 provides a simple numerical example in which resonances play an important role. Finally, in Section 7, we discuss the search for resonances in laboratory data. Section 8 summarizes and discusses some of the implications of the present results on the modelling of shallow water ocean waves.

## 2. LINEAR FOURIER ANALYSIS

Fourier analysis allows the construction of linear wave trains, $\eta(x,t)$, by a linear superposition of sine waves:

$$\eta(x,t) = \sum_{n=1}^{N} \eta_n \sin(k_n x - \omega_n t + \phi_n) \qquad (2)$$

In the present case there are $N$ sine waves which are interpreted as "degrees of freedom" or "Fourier components" in the wave train. In Eq. (2) the $\eta_n$ are the Fourier amplitudes, the $k_n$ are the wave numbers, the $\omega_n$ are the frequencies and the $\phi_n$ are the phases. The relationship between the frequencies, $\omega_n$, and the wave numbers, $k_n$, is given by the dispersion relation, written symbolically: $\omega_n = \omega_n(k_n)$. The dispersion relation defines the physics via the correspondences

$$\frac{\partial}{\partial t} \leftrightarrow -i\omega, \qquad \frac{\partial}{\partial x} \leftrightarrow ik$$

For example the simple dispersion relation for *long waves in shallow water* is given by

$$\omega = c_o k - \beta k^3 \text{ or } \Delta(\omega,k) = \omega - c_o k + \beta k^3 = 0 \quad (3)$$

which has the associated partial differential equation (the linearized Korteweg-deVries equation):

$$\eta_t + c_o \eta_x + \beta \eta_{xxx} = 0 \qquad (4)$$

The simplest periodic solution to (4) is a travelling sine wave

$$\eta(x,t) = \eta_o \sin(k_o x - \omega_o t + \phi_o) \qquad (5)$$

from which the general Fourier solution for $N$ components may be constructed by (2). The important point is that the *amplitudes of the sine waves and their phases are constants of the motion, provided that the motion is linear.* In oceanic applications one is often interested in the analysis of time series, i.e. measurements of the wave amplitude, $\eta(0,t)$, taken at a fixed spatial location over some convenient time interval; this implies setting $x = 0$ in (2) and (5).

## 3. NONLINEAR FOURIER ANALYSIS

It is well recognized that the Fourier transform is one of the most useful tools ever devised for the mathematical analysis of wave trains, for the analysis of experimental data and for engineering design purposes. Fourier analysis is, however, somewhat limited in its scope, primarily because ocean waves are effectively nonlinear. In sufficiently shallow water, where the waves may be considered long with respect to the depth, the waves 'feel' the presence of the bottom. Nonlinear effects typically manifest themselves by causing changes in the shape of the waves, i.e. nonlinear waves generally have crests which are higher and narrower than for a sine wave; likewise the troughs are less deep and broader than for a sine wave. The simplest nonlinear shallow water wave equation for which this occurs is the Korteweg-deVries equation (1) which is the same as (4) except for the presence of the nonlinear convective derivative term prefixed by the constant coefficient, $\alpha = 3c_o / 2h$. While the general solution of (4) for periodic boundary conditions is easily found using the linear Fourier transform, the general IST solution to the nonlinear equation (1) required an additional 170 years of mathematical progress! The simple travelling wave, periodic solution of (1) is the *cnoidal wave*, well known in shallow water oceanography and offshore engineering [Weigel, 1964; Whitham, 1974; Miles, 1980]:

$$\eta(x,t) = \frac{4k^2}{\lambda} \sum_{n=1}^{\infty} \frac{n(-1)^n q^n}{1-q^{2n}} \cos[nk_o(x - Ct) + \phi_o] =$$

$$= 2\eta_o cn^2 \left\{ (K(m)/\pi)[k_o x - \omega_o t + \phi_o]; m \right\} \qquad (6)$$

where $\lambda = \alpha / 6\beta = 3/2h^3$. The modulus, $m$, of the elliptic function, $cn$, the nonlinear phase speed, $C$, and the nome, $q$, depend explicitly on the amplitude, $\eta_o$ [see for example Osborne, 1993]; $\omega_o = Ck_o$. Note that the series in (6), suitably truncated to $N$ terms, is the shallow-water, $N$th order Stokes wave. In the limit as the modulus $m \to 0$ the cnoidal wave reduces to a sine wave; when $m \to 1$ the cnoidal wave approaches a solitary wave or soliton. Intermediate values of the modulus correspond to the Stokes wave with various levels of nonlinearity.

With regard to (1) and (5) an important problem in mathematical physics and related practical applications has remained open for a century. While it is well known that linear Fourier analysis works well for linear wave equations with sine wave basis functions, the more difficult question as to whether there exists a generalization of linear Fourier analysis which uses cnoidal wave basis functions has remained unresolved from a theoretical point of view until the work of [[Boyd, 1981, 1990; Date and Tanaka, 1976; Dubrovin, et al., 1976; Flaschka and McLaughlin, 1976; Its and Matveev, 1975; McKean and Trubowitz, 1976]; for practical perspective on this problem, see Osborne [1995]. Thanks to these papers, nonlinear Fourier analysis has been formulated in a physical and mathematical form simple enough that oceanographic and engineering applications of the method can now be made. This approach is based upon the general periodic solution to the KdV equation (1) in terms of the so-called *$\theta$-function representation* :

$$\lambda\eta(x,t) = 2\frac{\partial^2}{\partial x^2} \ln \Theta_N(x,t) \qquad (7)$$

where:



AUTHOR INDEX TABLE OF CONTENTS

$$\Theta_N(x,t) = \sum_{M_1=-\infty}^{\infty} \sum_{M_2=-\infty}^{\infty} \cdots \tag{8}$$

$$\cdots \sum_{M_N=-\infty}^{\infty} \exp\left[ i\sum_{n=1}^{N} M_n \eta_n + \frac{1}{2}\sum_{m=1}^{N}\sum_{n=1}^{N} M_m B_{mn} M_n \right]$$

Here $N$ is the number of cnoidal waves in a (broad-spectrum) solution to the KdV equation. The summation indices $M_n$ $(1 \le n \le N)$ are integers summed from $-\infty$ to $\infty$. The $\theta$-function phases have the same form as in linear Fourier analysis: $\eta_n = k_n x - \omega_n t + \phi_n$. Explicit computation of the period matrix, $\mathbf{B} = \{B_{mn}\}$, the wave numbers, $k_n$, the frequencies, $\omega_n$, and the phases, $\phi_n$, is discussed elsewhere in terms of the algebraic geometric loop integrals of periodic theory (see for example Osborne [1995] and cited references). The period matrix $\mathbf{B}$ is constant and negative definite and defines the cnoidal wave amplitudes and moduli (diagonal terms) and their nonlinear pair-wise interactions (off-diagonal terms). Equations (7), (8) are discussed in detail for the particular case $N = 2$ in Boyd [1990].

Recently Osborne [1995, 1996] has shown that the $\theta$-function (8) may be written in the alternative useful forms:

$$\Theta_N(x,t) = \sum_{l=1}^{\infty} C_l e^{-i(K_l x - \Omega_l t + \Phi_l)} =$$

$$= \sum_{n=-\infty}^{\infty} c_n'(t) e^{-i(k_n x - \omega_n t)} \tag{9}$$

where

$$C_l = \exp\left[ \frac{1}{2}\sum_{i=1}^{N}\sum_{j=1}^{N} M_i^l B_{ij} M_j^l \right] \tag{10}$$

and $c_n'(t)$ in discussed in detail in Section 5. In the first of (9) we have written the $N$ nested sums in the $\theta$–function as a single sum in terms of an "ordering parameter" $l$. The wave numbers, $K_l$, frequencies, $\Omega_l$, and phases, $\Phi_l$, are defined by:

$$K_l = \mathbf{M}_l \cdot \mathbf{k} = \tag{11a}$$

$$= \left[M_1^l, M_2^l, \ldots, M_N^l\right] \cdot [1, 2, \ldots, N] \Delta k = \Delta k \sum_{j=1}^{N} j M_j^l$$

$$\Phi_l = \mathbf{M}_l \cdot \phi = \tag{11b}$$

$$= \left[M_1^l, M_2^l, \ldots, M_N^l\right] \cdot \left[\phi_1, \phi_2, \ldots, \phi_N\right] = \sum_{j=1}^{N} M_j^l \phi_j$$

Note that the superscripts on the indices $M_j^l$ refer to the sequential summation over the first expression in Eq. (9). Thus the vector of indices $[M_1^l, M_2^l, \ldots, M_N^l]$ is obtained and associated with a particular $l$ value which is incremented each time one of the indices $M_j^l$ is changed in the nested sum of (8). The first equation in (11) says that the frequencies in the $\theta$-function are integer multiples of the lowest frequency, $\Delta k = 2\pi / L$, where $L$ is the period of the wave train:

$$K_l = I_l \Delta k; \qquad I_l = \sum_{j=1}^{N} j M_j^l \tag{12}$$

## 4. SPECTRAL DECOMPOSITION OF NONLINEAR FOURIER ANALYSIS

The $\theta$-function solution (7), (8) to the KdV equation (1) can be written in the following form:

$$\eta(x,t) = \frac{2}{\lambda}\frac{\partial^2}{\partial x^2} \ln \Theta_N(x,t) =$$

$$= \underbrace{\eta_{cn}(x,t)}_{\substack{\text{Linear superposition} \\ \text{of } N \text{ cnoidal waves}}} + \underbrace{\eta_{\text{int}}(x,t)}_{\substack{\text{Nonlinear interactions} \\ \text{among the } N \text{ cnoidal waves}}} \tag{13}$$

$$= 2\sum_{n=1}^{N} \eta_n cn^2\left\{ \left(K(m_n)/\pi\right)\left[k_n x - \omega_n t + \phi_n\right]; m_n \right\} +$$

$$+ \eta_{\text{int}}(x,t)$$

This result essentially states that *Shallow water wave trains governed by the KdV equation can be represented by a linear superposition of N cnoidal waves plus their mutual nonlinear interactions.* How is this formulation related to linear Fourier analysis? This is seen by letting the wave amplitudes become so small that the cnoidal wave components become sine waves and the nonlinear interactions tend to zero. In this way linear Fourier analysis is recovered from the nonlinear theory. An important aspect of (13) is that the *amplitudes of the cnoidal waves and their phases are constants of the motion for KdV evolution.*

## 5. OVERVIEW OF RESONANCES

In this Section we first review some important considerations with regard to resonances using multiscale expansions. We then go on to develop entirely new perspective on this problem using the inverse scattering transform.

### *5.1 Multiscale Expansions*

An often used procedure for studying resonances [LeBlond and Mysak, 1978; Mei, 1983] is to take KdV (or some other nonlinear wave equation) and to use the method of multiple scales to write a perturbed solution the equation. One discovers, for example, that for two initial sine waves (in the initial conditions of the KdV equation) of frequencies $\omega_1$ and $\omega_2$, these two



AUTHOR INDEX TABLE OF CONTENTS

waves will interact with each other and create other waves which will lie at all the sum and difference frequencies

$$\omega_3 = 0; \qquad \omega_3 = \pm 2\omega_1 \qquad (14)$$

$$\omega_3 = \pm 2\omega_2; \qquad \omega_3 = \pm(\omega_1 \pm \omega_2)$$

and similarly for the wave numbers.

A convenient way to summarize all of these possibilities is to use the elegant resonant interaction equations:

$$\omega_1 + \omega_2 + \omega_3 = 0; \quad k_1 + k_2 + k_3 = 0 \qquad (15)$$

where the case

$$\omega_m = \omega_n; \quad k_m = k_n$$

is also allowed ($m$ and $n$ range over 1, 2, 3). Now the usual multiscale expansion gives rise to nonlinear perturbations of the form:

$$u(x,t) = \varepsilon(u_1 + u_2) + \varepsilon^2 u_3 + \ldots$$

where

$$u_3(x,t) = \qquad (16)$$

$$\sum_{\substack{\text{All sign}\\ \text{combina-}\\ \text{tions in (14)}}} \frac{C\exp[i(k_3 x - \omega_3 t) + C^* \exp[-i(k_3 x - \omega_3 t)}{\Delta(\omega_3, k_3)}$$

Note that the interaction terms (i.e. the interactions among the two initial sine waves) consist of a summation of sinusoids each with its own amplitude $C$. The total solution to second order consists of the linear superposition of sinusoids, $\varepsilon(u_1 + u_2)$ plus $\varepsilon^2 u_3$ such the later is a small correction *provided that the linear dispersion relation is not satisfied.* Instead, if the linear dispersion relation (3), $\Delta(\omega_3, k_3) = 0$, is satisfied or is nearly satisfied, then a resonance occurs. When this happens the solution becomes secular and the amplitude $\varepsilon^2 u_3$ initially grows linearly with time. Thus a resonant wave is a free wave which satisfies the linear dispersion relation and hence propagates with the frequency and wave numbers associated with the interference pattern of the two primary waves: $\omega_3 = -(\omega_1 + \omega_2)$ and $k_3 = -(k_1 + k_2)$. The analysis predicts that the resonant wave travels at the phase speed of the two primary waves and is continuously excited and grows in energy as it propagates. Of course this initial growth will not continue forever for physical reasons (wave solutions cannot go to infinity), but nevertheless the method gives us the essentials of three-wave resonances in shallow water waves, i. e. two initial sine waves inject energy into a third wave by the resonant interaction.

It is worth noting that *nonlinear, nondispersive waves* all interact resonantly, since all wave have the same phase speed (and hence have commensurable frequencies and wave numbers).

An alternative way to describe resonance effects is to suppose that solutions to the KdV equation can be written with Fourier coefficients which vary in time. The formal procedure allows computation of resonances to arbitrary order. Consider a generalization of the Fourier series (2) given by:

$$\eta(x,t) = \sum_{n=-\infty}^{\infty} c_n(t) e^{-i(k_n x - \omega_n t)}; \quad c_n^* = c_{-n} \qquad (17)$$

A standard method for solving nonlinear partial differential equations such as KdV is to use the ansatz (17). If this expression is substituted into the KdV equation one obtains [Zakharov and Kusnetsov, 1980; Bryant, 1973; Mei, 1983]:

$$\left(\frac{d}{dt} + ink^3\right)c_n + \left(\frac{d}{dt} + ink\right)^3 c_n + \qquad (18)$$

$$+3\left(\frac{d}{dt} + ink\right)\sum_{m=-\infty}^{\infty} c_m c_{n-m} = 0; \qquad n = 1, 2 \ldots N$$

These ordinary differential equation (ODEs) give the solution for the $N$ time-dependent Fourier coefficients, $c_n(t)$, in (17) which are highly nonlinearly coupled. This approach, i.e. to introduce a Fourier series into a nonlinear partial differential equation (PDE) in order to "reduce" the system to an infinite set of ODEs ($N \to \infty$) is quite standard in mathematical physics. One is often tempted to truncate the infinite set of ODEs to a small number $N$. Lorenz used this approach (for $N = 3$, often attributed to Galerkin) for a particular set of PDEs and opened the way to the modern study of chaotic dynamics.

From the point of view of the above set of ODEs (18) one finds that it is quite simple to introduce the concept of resonances for $N$ small. For short-time solutions, one finds that certain Fourier series coefficients grow at the expense of others. For long-time behavior the above ODEs must describe, for periodic boundary conditions, Fourier coefficients which are oscillatory, alternatively growing and decaying in time.

In the next Section we show how to extend the multiscale expansion to infinity and to effectively sum the series (17) using the inverse scattering method.

### *5.2 Inverse Scattering Transform*

The time dependent coefficients in the *second* summation in Eq. (9) are given by the following *Poincarè series* [Osborne, 1997]:



AUTHOR INDEX TABLE OF CONTENTS

$$c_n'(t) = \sum_{\substack{\text{sum over subset} \\ \text{of } l \text{ for which } I_l = n}} C_l e^{i(\Omega_l t + \Phi_l)}; \quad 1 \le n \le \infty \qquad (19)$$

This latter result, by virtue of the fact that the second of (9) and (17) are easily related by a simple transformation (7) leads to the exact solution of the nonlinearly coupled ODEs (18). Thus the temporal evolution of the Fourier coefficients (19), $c_n'(t)$, in the $\theta$–function (9) is given exactly and analytically by inverse scattering transform variables; and the coefficients $c_n(t)$ in the Fourier transform (17) are computed from (9) by a transformation (7). One often numerically integrates the ODEs (18), but in the present case this is not necessary because we have their exact solutions from combining (17) and (18). The inverse scattering transform thus solves the ODEs (18) to all orders.

To see explicitly how the inverse scattering transform solves the KdV equation we expand the $\theta$–function for *two* cnoidal waves, but sum only on the interval $(-2, 2)$ and find:

$$\begin{aligned}
\theta_2(x,t) = 1 &+ 2e^{-B_{11}/2}\cos(X_1) + 2e^{-2B_{11}}\cos(2X_1) + \\
&+ 2e^{-B_{22}/2}\cos(X_2) + 2e^{-2B_{22}}\cos(2X_2) + \\
&+ 2e^{-(B_{11}+2B_{12}+B_{22})/2}\cos(X_1+X_2) + \\
&+ 2e^{-2(B_{11}+2B_{12}+B_{22})}\cos[2(X_1+X_2)] + \\
&+ 2e^{-(B_{11}-2B_{12}+B_{22})/2}\cos(X_1-X_2) + \\
&+ 2e^{-2(B_{11}-2B_{12}+B_{22})}\cos[2(X_1-X_2)] + \\
&+ 2e^{-B_{11}/2-2B_{12}-2B_{22}}\cos(X_1+2X_2) + \\
&+ 2e^{-B_{11}/2+2B_{12}-2B_{22}}\cos(X_1-2X_2) + \\
&+ 2e^{-2B_{11}-2B_{12}-B_{22}/2}\cos(2X_1+X_2) + \\
&+ 2e^{-2B_{11}+2B_{12}-B_{22}/2}\cos(2X_1-X_2)
\end{aligned} \qquad (20)$$

where the dynamic phase, $X_n = k_n x - \omega_n t + \phi_n$, has wave numbers $k_n = 2\pi n / L$, frequencies, $\omega_n$, and phases, $\phi_n$, given by algebraic-geometric loop integrals in the inverse scattering transform formulation with periodic boundary conditions (see for example, Osborne [1995]).

If we further assume that the above Fourier components are small with respect to 1 then we can use:

$$\ln\theta_2(x,t) = \ln[1 + f(x)] \approx f(x)$$

Here $f(x)$ is the sum of all the cosine terms in (20). Thus the solution to KdV (1) in the small amplitude limit is just the second spatial derivative (7) of this latter expression. In this solution we thus have in (20) the same combinations of frequencies or wave numbers as in (15) plus (infinitely) many more. This result still holds when the amplitudes are *not* small. Thus the inverse scattering transform has all of the wave number combinations as the multiscale analysis discussed above, plus all other possible combinations. But, thanks to the completely integrable nature of IST, there are *no secular terms*. Instead there are time-oscillating Fourier coefficients, $c_n'(t)$, which are periodic functions computed by the Poincarè series (19) for period boundary conditions. The natural basis in the inverse scattering transform formulation is *not* the sine wave basis but is instead the cnoidal wave basis whose amplitudes and phases are *constants of the motion for KdV*.

### *5.2 Do Resonances Exit in Inverse Scattering Theory?*

We thus see that the cnoidal waves do not exchange energy amongst one another *and therefore IST for the KdV equation does not give rise to resonances.* This is one of the most important conclusions of our paper: By studying KdV evolution using sine waves (multiscale analysis) one has resonances; if instead one uses cnoidal waves (IST) one does not have resonances. This is the convenience of using higher order basis functions and inverse scattering.

## 6. CLASSICAL RESONANCES IN A SIMPLE MODEL SIMULATION

We now consider an example to illustrate how three-wave resonances arise in the evolution of a sine-wave initial condition. Fig. 1 shows a series of wave trains (a)-(e) which were computed by numerically integrating the KdV equation from a sine wave initial condition in 15 cm depth (panel (a)); the initial wave has amplitude 1 cm and wave length 256 cm. The wave train has been numerically integrated and halted at $t = 3.2$ sec (b), $t = 6.3$ sec (c), $t = 9.5$ sec (d) and $t = 12.9$ sec. The initial sine wave is seen to evolve into a Stokes wave plus something else (b). The wave motion in panel (c) evidently is a Stokes wave plus some another small component. The smaller wave migrates somewhat to the left in (d). Finally, in panel (e) the wave train has almost returned to the sine wave initial conditions, i.e. we have an example of Fermi-Pasta-Ulam (FPU) recurrence [Fermi, et al, 1955].

In Fig. 2(a)-(e) we show the Fourier spectra for each of the wave trains in Fig. 1(a)-(e). In the first panel (a) we find of course only one sine wave, that which matches the initial conditions. As



AUTHOR INDEX TABLE OF CONTENTS

the wave form evolves from Fig. 1(a) to Fig. 1(b) the Fourier spectrum reduces its amplitude and broadens as shown in Fig. 2(b). The spectrum of the wave form in Fig. 1(c) is shown in Fig. 2(c) and is seen to further broaden, but only slightly. However, by the time the evolution arrives at Fig. 1(d) the Fourier spectrum has begun to narrow again and its peak amplitude increases (Fig. 2(d)). Finally, for the final wave train in Fig. 1(e) the Fourier spectrum, Fig. 2(e), is seen to almost return to that in Fig. 2(a). This is the Fourier view of FPU recurrence, i.e. an initial, delta-function spectrum broadens during the evolution, but eventually (almost) returns to the initial conditions [Fermi, et al, 1955].

How do we interpret the numerical simulation in terms of resonances? Resonances occur because, as the wave motion evolves from panel (a) to (b) the initial sine wave is seen to loose energy and the nearby harmonics instead increase there energy linearly with time. This is exactly the picture that one obtains by doing a multiscale expansion of the KdV equation [see for example Mei and Ünlüata, 1972; Bryant, 1973; Mei, 1983]. However, in the present example we have continued the evolution to long times, beyond the applicability of the multiscale expansion, and find that the evolution, via FPU recurrence, reverses itself and the wave motion returns very nearly to the initial conditions after some recurrence time.

Another point of interest here with regard to Fig. 1(c) is that the space series is very similar to what is often found in wave tank experiments (see for example, the next Section). The wave maker attempts to generate a pure sine wave and one instead obtains a Stokes wave plus other small amplitude wave(s). From the multiscale analysis this phenomenon is easily described in terms of the resonance effect, i.e. higher order harmonics grow at the expense of the initial sine wave.

Let us now given an alternative interpretation of this simple numerical experiment using the inverse scattering transform. Instead of taking the Fourier transform of each of the space series in Fig. 1, we now take their inverse scattering transforms. The results are shown in Figs. 3-7. The first result, given in Fig. 3, is the cnoidal wave decomposition for space series (a) in Fig. 1. Note that the number of iterations in the numerical algorithm is given in the upper right hand corner. Shown, in vertical order from top to bottom, are the 5 cnoidal waves in the spectrum, the sum of these cnoidal waves, the nonlinear interactions and the reconstructed wave train. Note that only three of the cnoidal waves make a substantial contribution to the dynamics: the highest wave is a large amplitude Stokes wave with modulus 0.932;

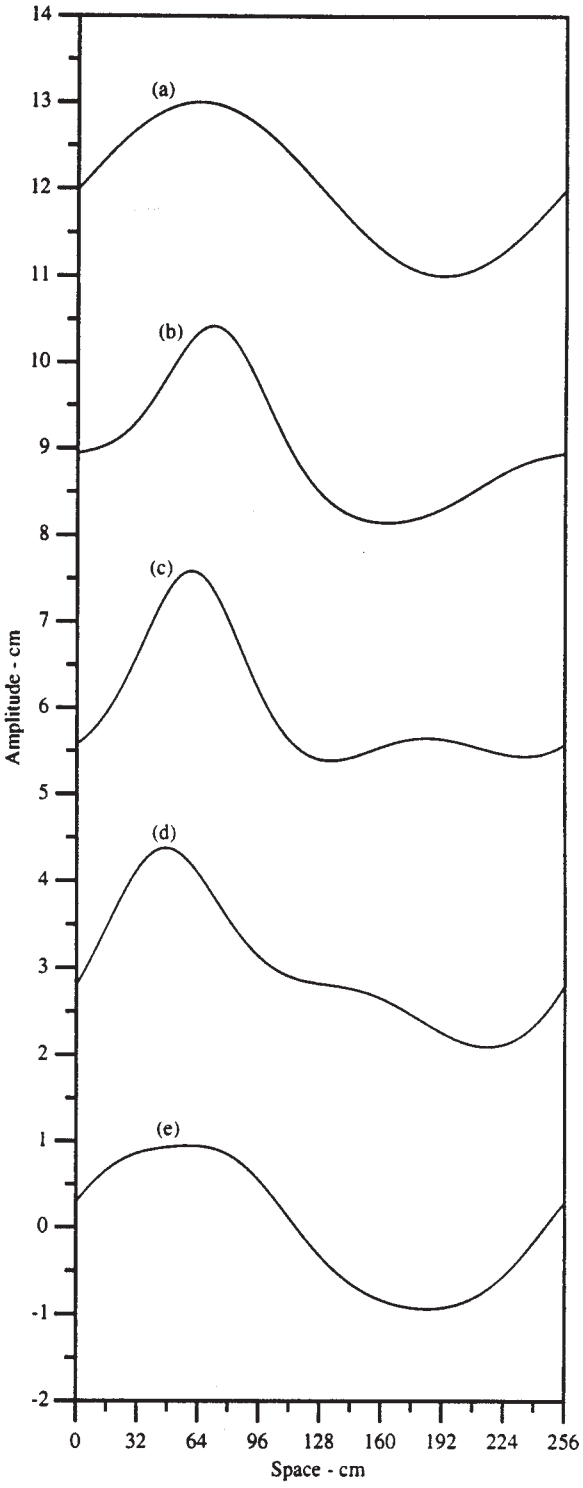


**Figure. 1.** Time evolution of an initial sine wave which is specified at $t = 0$ sec (a). The water depth is 15 cm, the initial wave amplitude is 1 cm and the wave length is 256 cm. Sequence of images (b) $t = 3.2$ sec, (c) $t = 6.3$ sec, (d) $t = 9.5$ sec and (e) $t = 12.9$ sec..



AUTHOR INDEX

TABLE OF CONTENTS

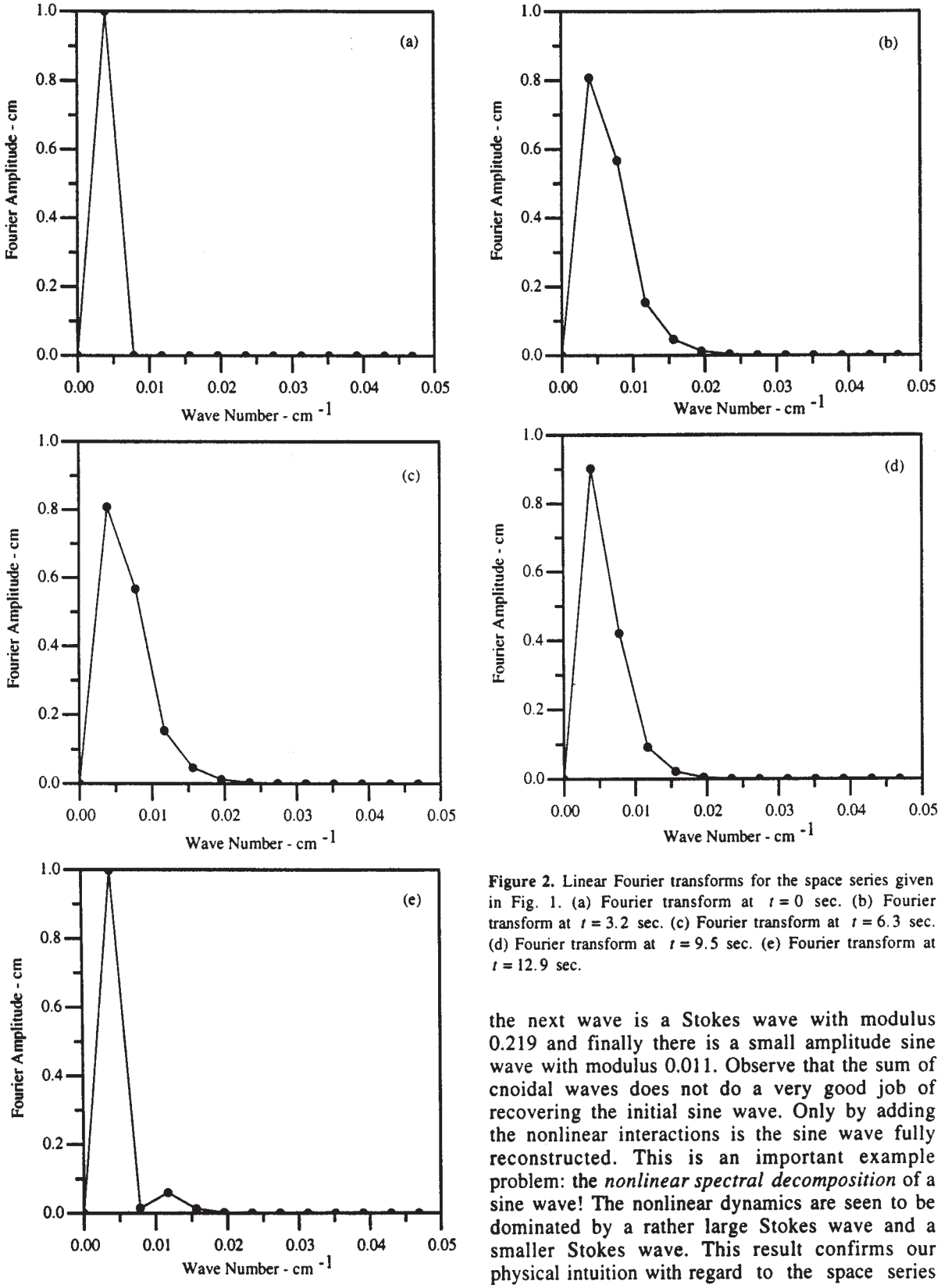


**Figure 2.** Linear Fourier transforms for the space series given in Fig. 1. (a) Fourier transform at $t = 0$ sec. (b) Fourier transform at $t = 3.2$ sec. (c) Fourier transform at $t = 6.3$ sec. (d) Fourier transform at $t = 9.5$ sec. (e) Fourier transform at $t = 12.9$ sec.

the next wave is a Stokes wave with modulus 0.219 and finally there is a small amplitude sine wave with modulus 0.011. Observe that the sum of cnoidal waves does not do a very good job of recovering the initial sine wave. Only by adding the nonlinear interactions is the sine wave fully reconstructed. This is an important example problem: the *nonlinear spectral decomposition* of a sine wave! The nonlinear dynamics are seen to be dominated by a rather large Stokes wave and a smaller Stokes wave. This result confirms our physical intuition with regard to the space series

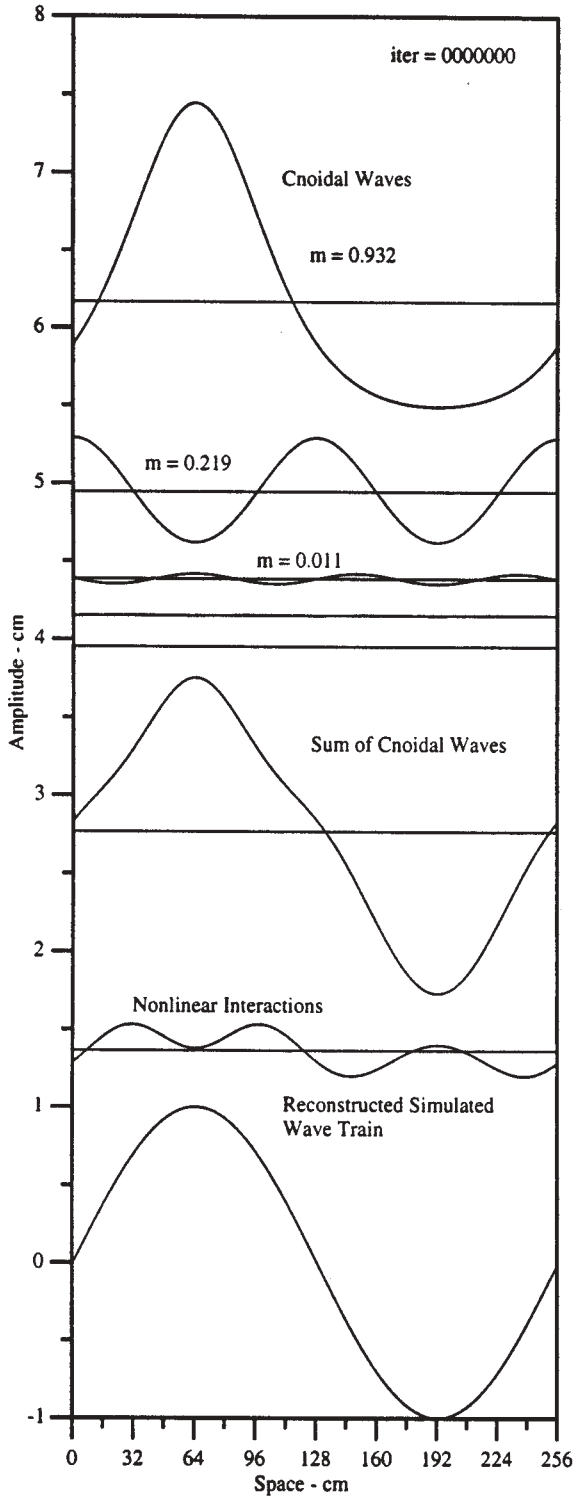


**Figure 3.** Cnoidal wave decomposition of wave train (a) ($t = 0$) in Fig. 1. Shown are the five cnoidal waves, their linear superposition, the nonlinear interactions and the reconstructed simulated wave train.

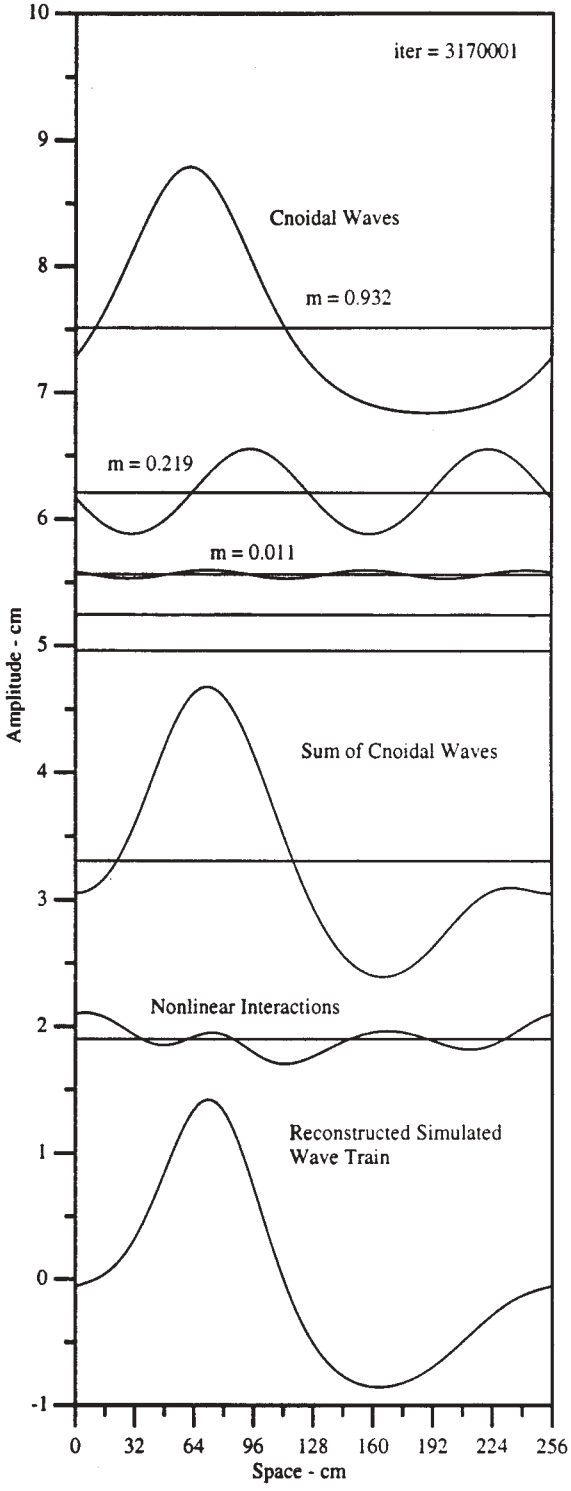


**Figure 4.** Cnoidal wave decomposition of wave train (b) ($t = 3.2$) in Fig. 1. Shown are the five cnoidal waves, their linear superposition, the nonlinear interactions and the reconstructed simulated wave train.



AUTHOR INDEX

TABLE OF CONTENTS

Fig. 1(c): An initial sine wave evolves into a large Stokes wave plus a smaller Stokes wave.

The spectral decomposition of the space series of Fig. 1(b) is given in Fig. 4. Note that the cnoidal waves in the spectrum are the same as those found in Fig. 3 (as they should be) but they are temporally phase shifted relative to their former positions. However, the nonlinear interactions have changed substantially. As a consequence, the wave motion is seen to be governed by the time-phase-shifted cnoidal waves together with the nonlinear interactions. Note, further, that the nonlinear interactions are different for different values of time, even though the cnoidal waves have the same amplitudes and moduli, i.e. the nonlinear interactions depend crucially on the temporal phases of the cnoidal waves.

In Fig. 5 we give the cnoidal wave decomposition of the wave train in Fig. 1(c). The main result is that the small amplitude Stokes wave has its maximum in the trough of the large amplitude Stokes wave, thus creating the small peak in the reconstructed wave train, hence recovering one of the important features in the numerical simulations. Note once again that the nonlinear effects are required to recover all the subtle features in the simulated wave train. In Fig. 6 we see the inverse scattering results for panel (d) of Fig. 1. Basically, this is very similar to the previous case except that the smaller Stokes wave has shifted slightly to the left. In Fig. 7 we give the decomposition of Fig. 1(e); these results are seen to be very similar to those of Fig. 3. This should not be surprising since we have almost recovered the initial conditions at this point in time of the nonlinear evolution.

It is now worthwhile addressing what the inverse scattering transform interpretation of this example has done to our perception of three-way resonances. First note that the basis functions in this case are the cnoidal waves and that they all have amplitudes which are *constants of the motion* for evolution governed by the KdV equation. The physics has been completely and fully captured by the nonlinear spectral decomposition. This is as it should be because the cnoidal waves are the *exact* basis functions of the KdV equation. This contrasts with our previous interpretation of resonances in terms of sine wave basis functions in which some waves gain or lose energy at the expense of others. However, the sine waves are not generally solutions of the KdV equation and, as pointed out with regard to equation (17), *this requires that the linear Fourier decomposition of KdV have temporally varying amplitudes.* Thus the traditional interpretation (multiscale analysis) is that resonances happen quite naturally. However, the inverse scattering transform with cnoidal wave

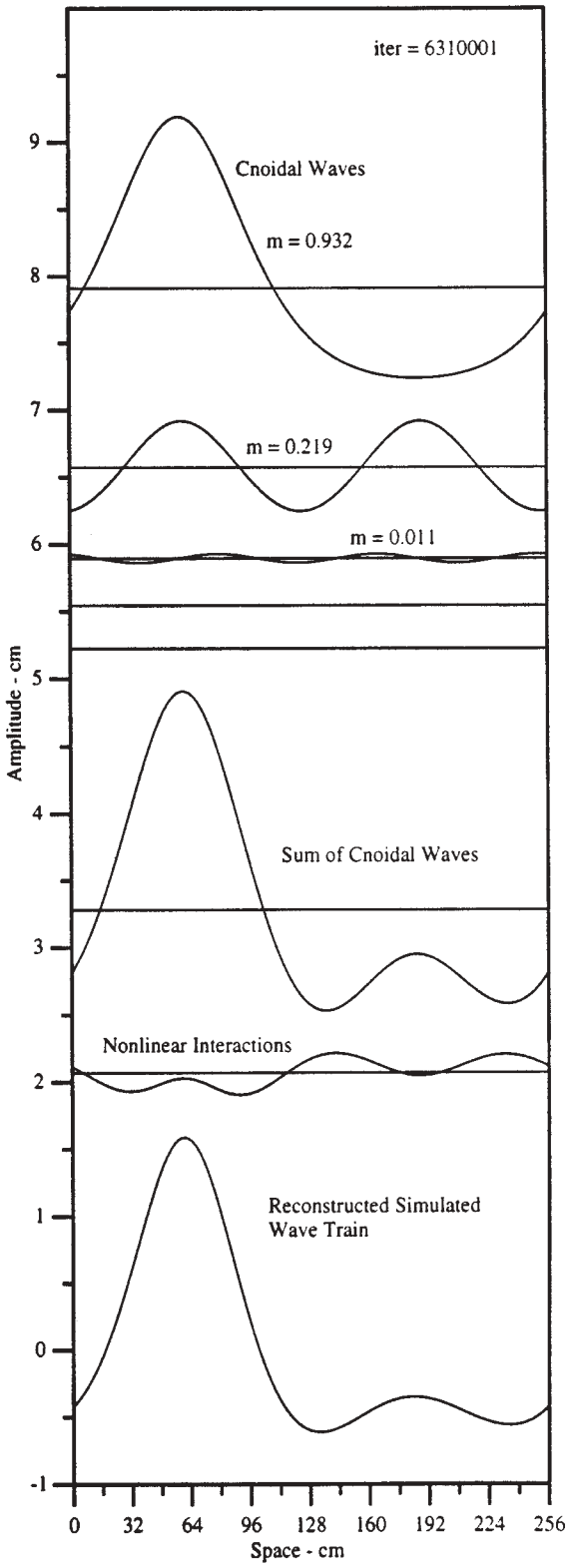


**Figure 5.** Cnoidal wave decomposition of wave train (c) ($t = 6.3$) in Fig. 1. Shown are the five cnoidal waves, their linear superposition, the nonlinear interactions and the reconstructed simulated wave train.



AUTHOR INDEX

TABLE OF CONTENTS

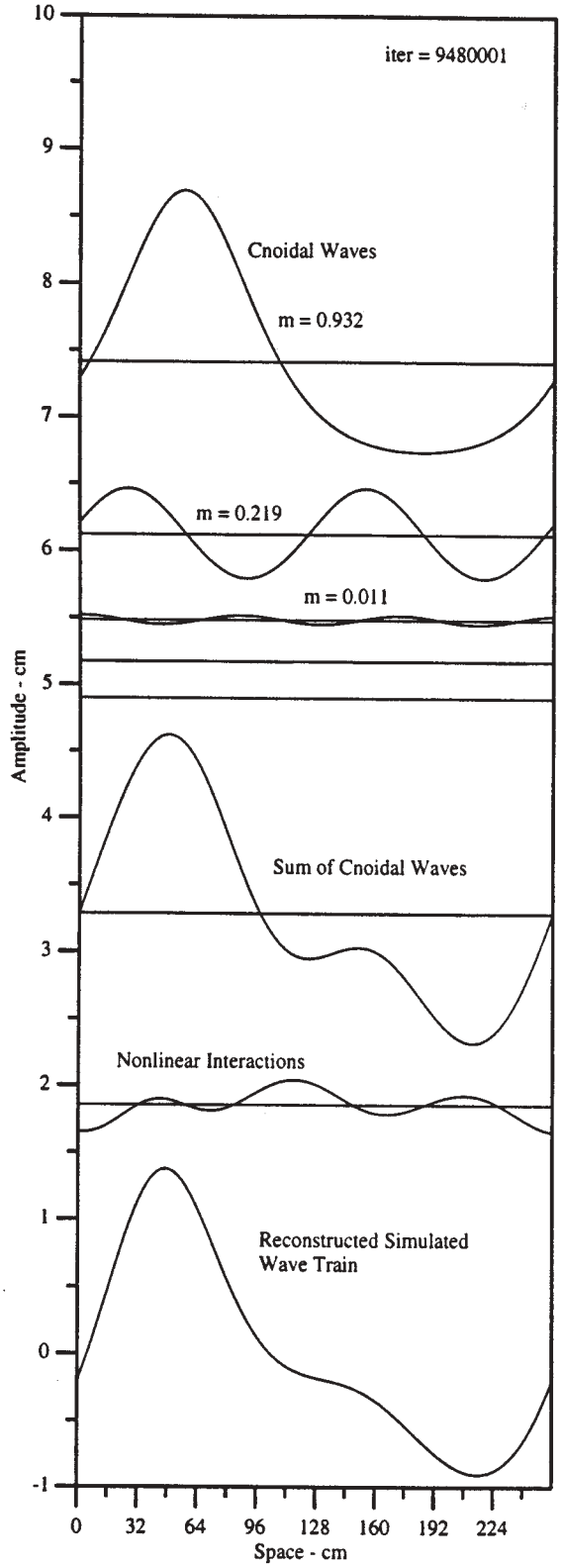


**Figure 6.** Cnoidal wave decomposition of wave train (d) ($t = 9.5$) in Fig. 1. Shown are the five cnoidal waves, their linear superposition, the nonlinear interactions and the reconstructed simulated wave train.

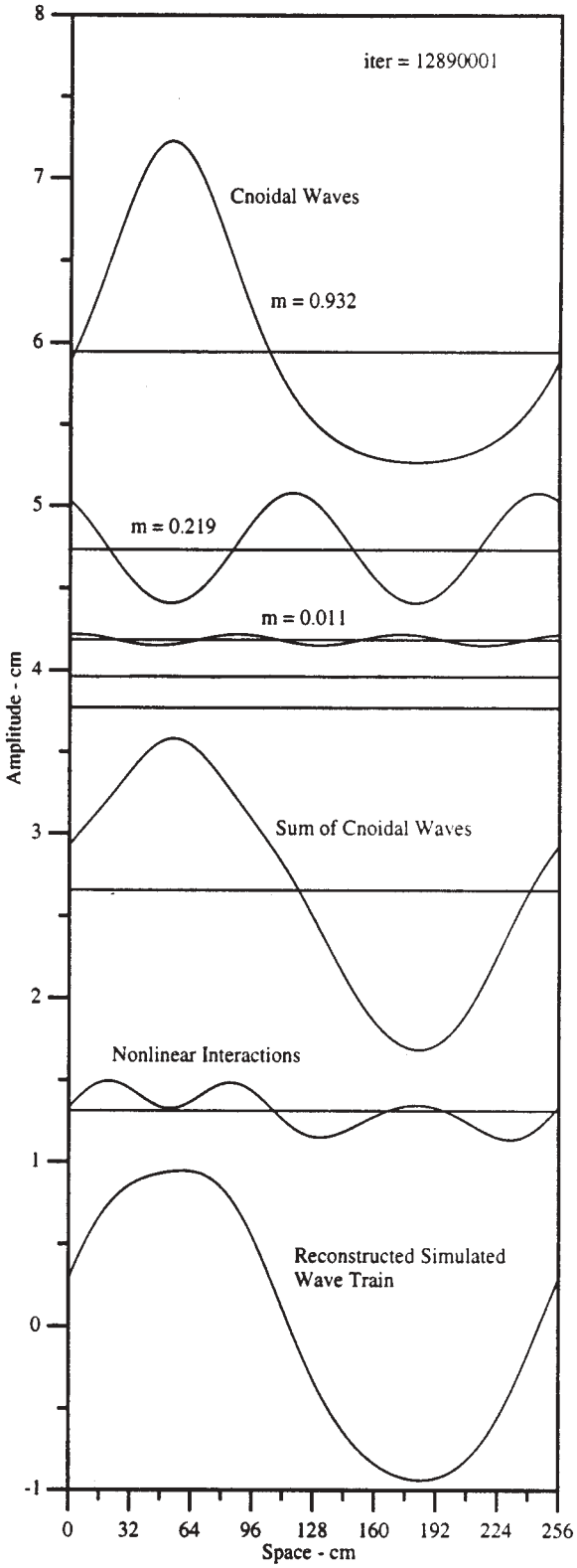


**Figure 7.** Cnoidal wave decomposition of wave train (e) ($t = 12.9$) in Fig. 1. Shown are the five cnoidal waves, their linear superposition, the nonlinear interactions and the reconstructed simulated wave train.

basis functions, does not predict resonances. This result simply states that, given the correct basis functions, one does not have resonances because there is no transfer of energy from one mode to the other, i. e. the mode amplitudes are simply constants of the motion. Basically we seem to be saying: Both the multiscale approach and the inverse scattering transform approach are equally good methods to apply to this problem. However, in the present case, inverse scattering modes are *the natural modes* of the physical problem and therefore no resonances occur from the point of view of this completely integrable Hamiltonian system.

## 7. SEARCH FOR RESONANCES IN LABORATORY DATA

We now consider the results of a simple wave tank experiment [for more details on the facility see Osborne and Petti, 1994]. The water depth was set to 40 cm and the wave maker was programmed to generate a sinusoidal initial wave. The period was selected to be 4 sec and we show in Fig. 8 the results of four probe measurements at 4.25, 7.01, 11.02 and 15.02 m from the wave maker. This experiment is somewhat more nonlinear that the computer experiments reported previously. Fig. 9 shows the IST spectrum at the first probe. Shown are the cnoidal wave amplitudes and moduli as a function of frequency. Note that we have taken *two periods of the generated wave trains*, i.e. the temporal length of the measured time series is 8 sec rather than 4 sec. It is easy to see that wave trains of this type are *quasi periodic* rather than perfectly periodic, since perfect periodicity is an improbable occurrence in the laboratory environment. For this reason the IST spectrum in Fig. 9 has the characteristic that the odd frequencies (1, 3, 5, 7, etc.) are much smaller than the even frequencies (2, 4, 6, 8, etc.). Further note that the first two components at low frequency have moduli which are very nearly 1, and hence these components are very nearly solitons. Thus a low frequency soliton ($\Delta\omega = 2\pi / T$ for the period, $T$=8 sec) is found to contribute to the lack of perfect periodicity in the measured wave trains.

In these experiments even the first probe is quite far from the sine wave initial conditions and the other probes are even further away. Furthermore, the presence of a ramp kept the test section to less than 20 m of the total 50 m length of the canal. For this reason we were unable to measure the presence of FPU recurrence. Nevertheless, it is clear that the Fourier spectra for the present experiment were quite broad banded and increasing in band width as the waves propagated down the tank.

Figs. 10-13 provide the details of the cnoidal wave decomposition of the four time series of Fig. 8. Fig. 10 give the analysis for Probe 1. Shown in the figure (in vertical order starting at the top) are the 12 cnoidal waves which comprise the spectrum, the sum of these cnoidal waves, the nonlinear interactions among the cnoidal waves and finally the reconstructed measured wave train. As mentioned above the first two components are essentially solitons and this is easily seen at the top of Fig. 10. Note that the top curve is a single soliton whereas the second curve is a double peaked soliton train. Furthermore, the single soliton is *phase locked* to one of the maxima in the soliton train; this can be verified to be the case also in Figs. 11-13. The third component from the top of Fig. 10 is a small amplitude sine wave, but the fourth component, with a modulus of about 0.55, is a rather robust Stokes wave. The remaining components have much smaller moduli, i.e. less than about 0.15, and are either Stokes waves or weak sine waves. The summation of the cnoidal wave components is shown near the middle of Fig. 10; this result differs quite a lot from the (reconstructed) measured wave train at the bottom of the figure. Only by adding the influence of the nonlinear interactions do we get good agreement between the reconstructed wave train and the measured wave train itself. Fig. 11 gives the IST spectral decomposition at probe 2. These results are quite similar to those in Fig. 10, except that there is more structure in the measured wave train and this is accounted for by the combined action of the temporally-phased cnoidal wave components and the nonlinear interactions. The observable structure in the measured wave train is seen to be considerably enhanced in Figs. 12, 13. Additional peaks are found to emerge from the initial wave train as the temporal phases of the cnoidal wave components shift relative to one another. These dynamics are seen to be quite complex and, to us, quite lovely.

In spite of the complex nonlinear interaction dynamics in the measured wave trains, the dynamics of the inverse scattering transform are seen to be quite simple as shown in Fig. 14. Here the main cnoidal wave amplitudes are found to change very little as the wave train propagates down the canal, i.e. they are essentially constants of the motion for KdV evolution and are nearly constant for the present wave tank experiments. This is the miracle of using IST as a tool for signal processing of shallow water waves: the experimental spectral, cnoidal wave decomposition demonstrates nearly constant amplitudes during the complicated evolution of an experimentally measured shallow water wave

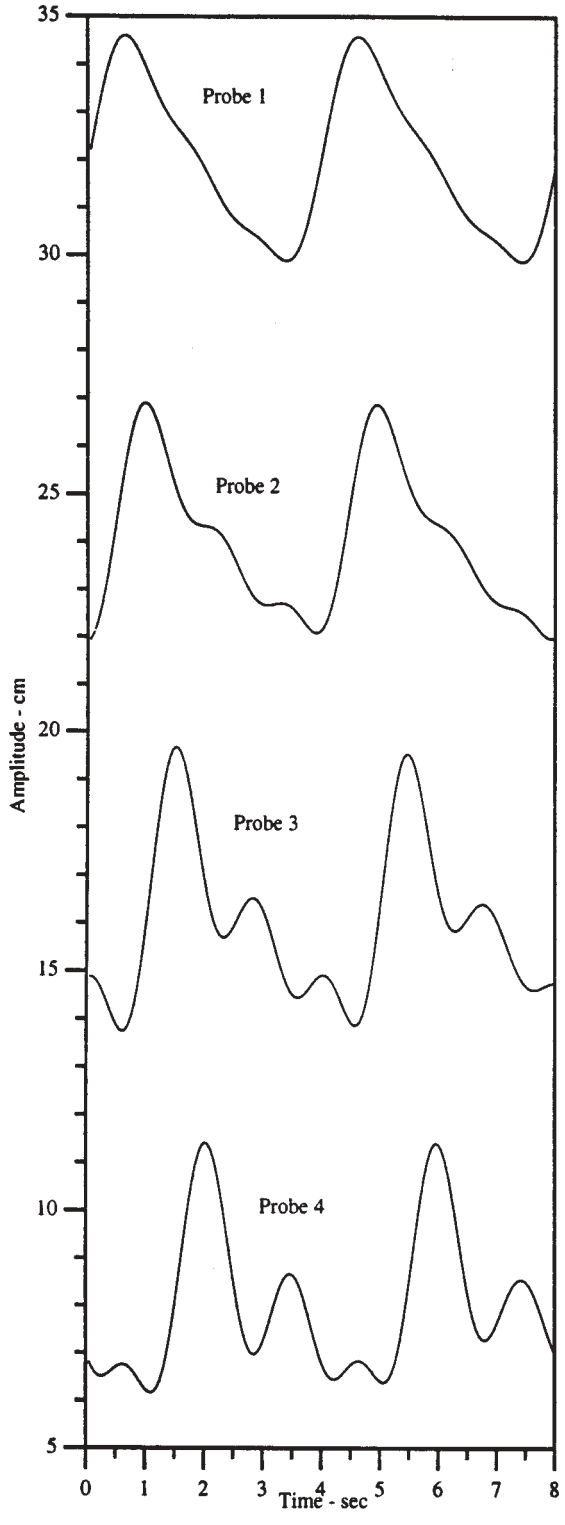


**Figure 8.** Wave tank experiments. The water depth is 40 cm and the probe locations relative to the wave maker are: Probe 1, 4.25 m; Probe 2, 7.01 m; Probe 3, 11.02 m and Probe 4, 15.02 m.

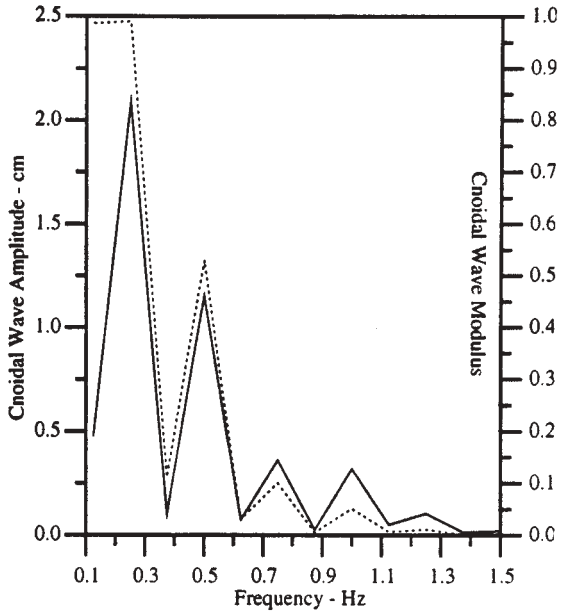


**Figure 9.** Inverse scattering transform analysis of Probe 1 signal in Fig. 8. Shown are the cnoidal wave amplitudes and moduli.

train; this is in contrast to the situation with sine wave basis functions which have considerable time evolution in their amplitudes as Fig. 15 demonstrates.

## 8. SUMMARY AND DISCUSSION

The inverse scattering transform in the $\theta$-function formulation is seen to provide new insight and perspective about the nonlinear dynamics of shallow-water wave trains. The propagation of shallow-water waves is seen to be governed by two considerations, namely, the space/time evolution of individual cnoidal waves with particular amplitudes and moduli, plus their mutual nonlinear interactions. The actual spectrum of the cnoidal wave components is seen to depend on the period or interaction matrix, **B**, whose *diagonal elements* define the cnoidal wave amplitudes and moduli and whose *off-diagonal elements* govern the nonlinear interactions. Both the synthesis of computer generated, shallow-water wave trains and the analysis of data are found to be feasible using recent methods developed in Osborne (1995). Both analytical and numerical results demonstrate that the nonlinear dynamics have no triad resonances in the $\theta$–function formulation. However, cnoidal wave resonances might themselves occur during adiabatic shoaling of nonlinear wave trains in shallow water regions. This is because KdV evolution is only approximately correct over variable bathymetry.

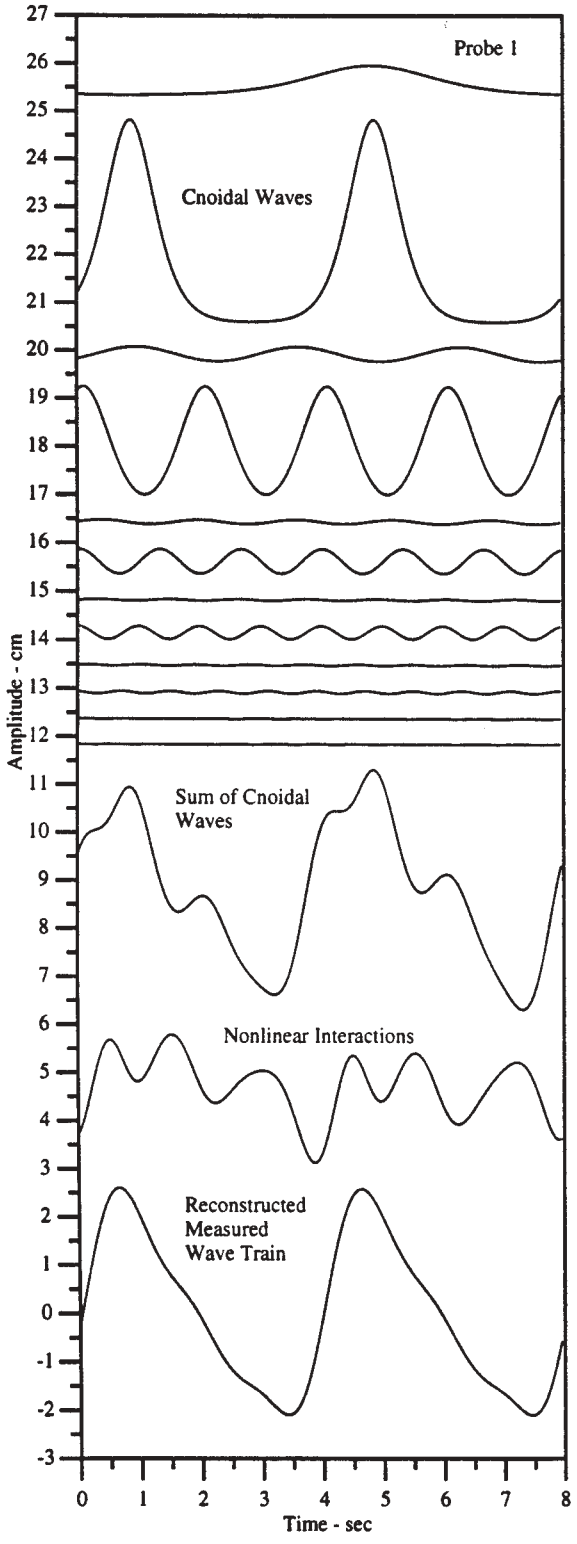


**Figure 10.** Cnoidal wave decomposition of wave train at Probe 1 (4.25 m from the wave maker) in Fig. 8. Shown are the twelve cnoidal waves, their linear superposition, the nonlinear cnoidal wave interactions and the reconstructed measured wave train.

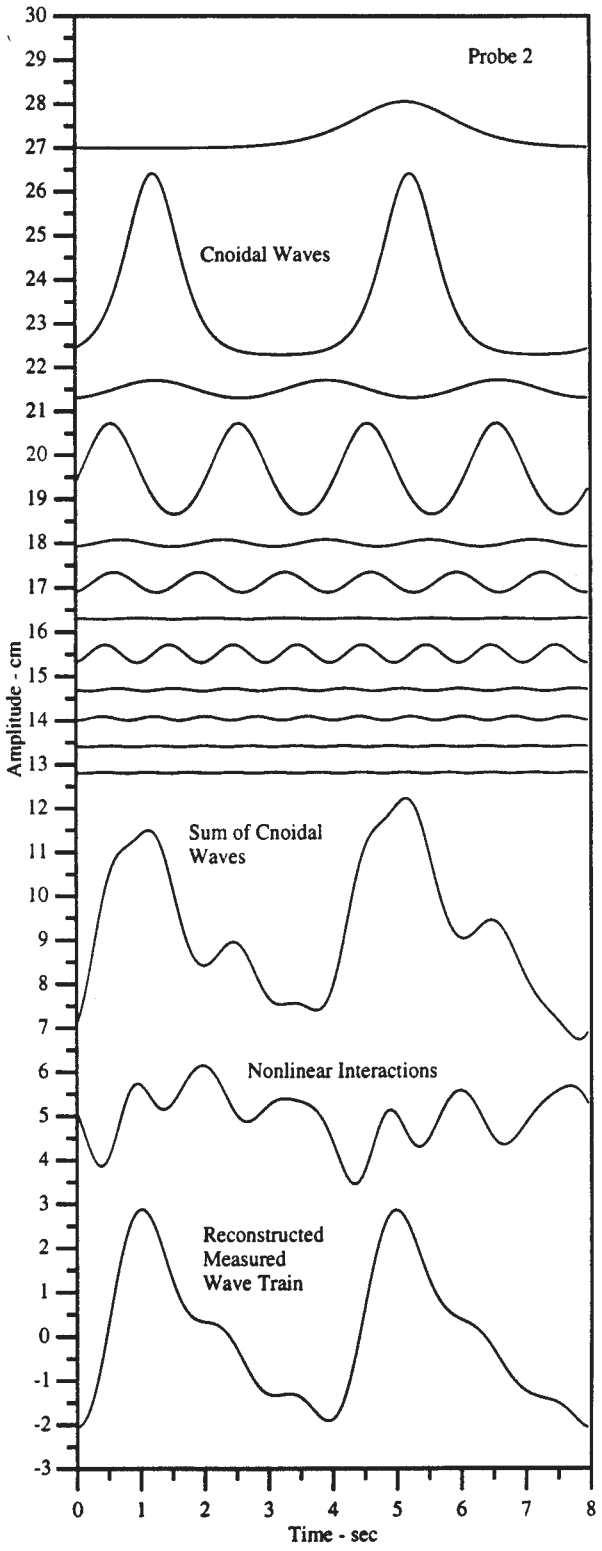


**Figure 11.** Cnoidal wave decomposition of wave train at Probe 2 (7.01 m from the wave maker) in Fig. 8. Shown are the twelve cnoidal waves, their linear superposition, the nonlinear cnoidal wave interactions and the reconstructed measured wave train.

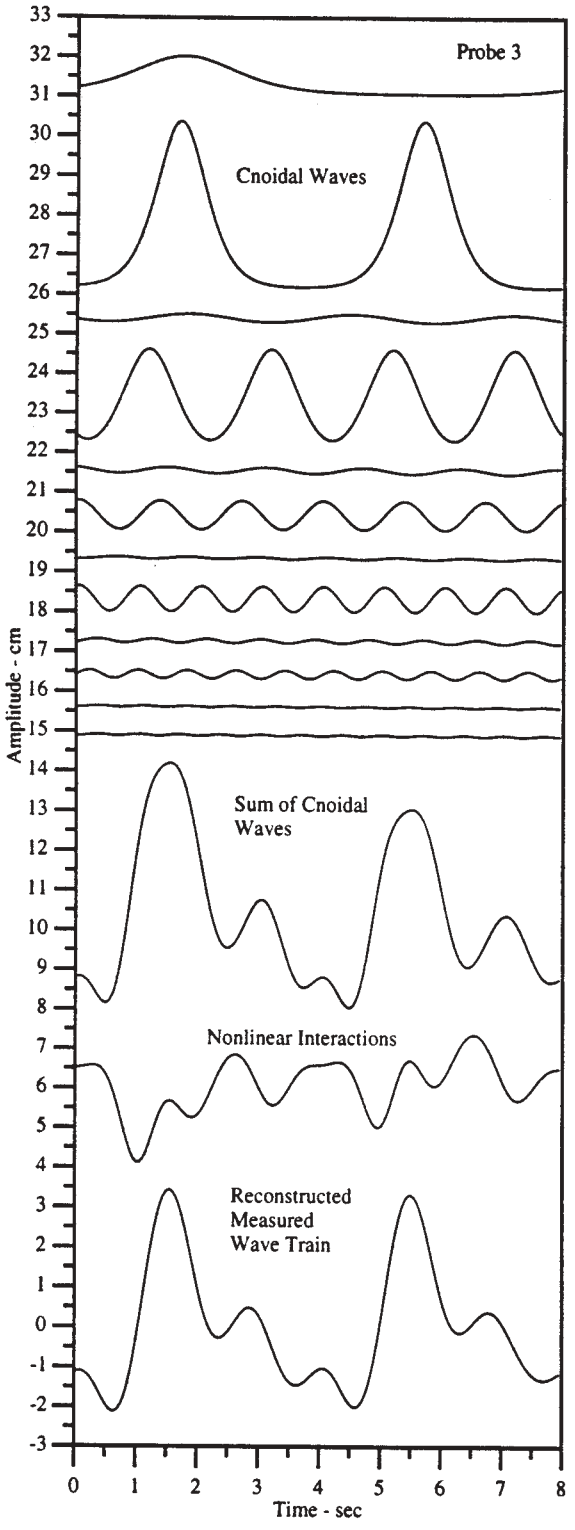


**Figure 12.** Cnoidal wave decomposition of wave train at Probe 3 (11.02 m from the wave maker) in Fig. 8. Shown are the 12 cnoidal waves, their linear superposition, the nonlinear cnoidal wave interactions and the reconstructed measured wave train.

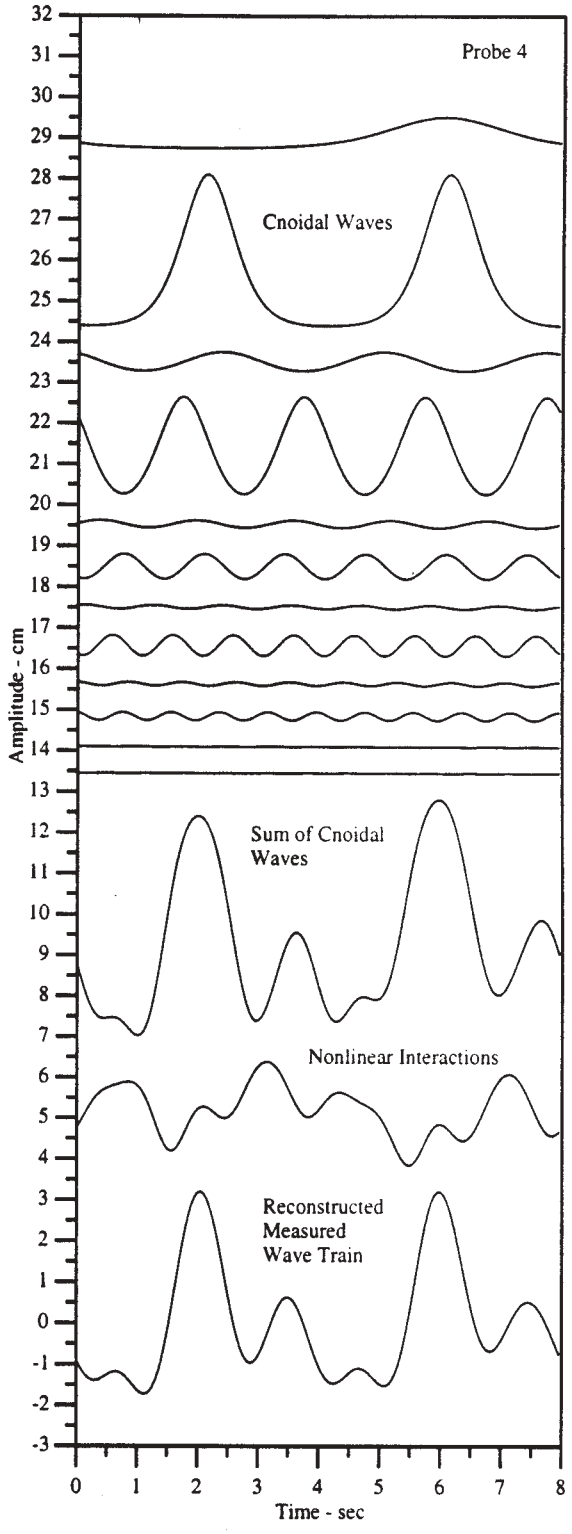


**Figure 13.** Cnoidal wave decomposition of wave train at Probe 4 (15.02 from the wave maker) in Fig. 8. Shown are the twelve cnoidal waves, their linear superposition, the nonlinear cnoidal waves interactions and the reconstructed measured wave train.

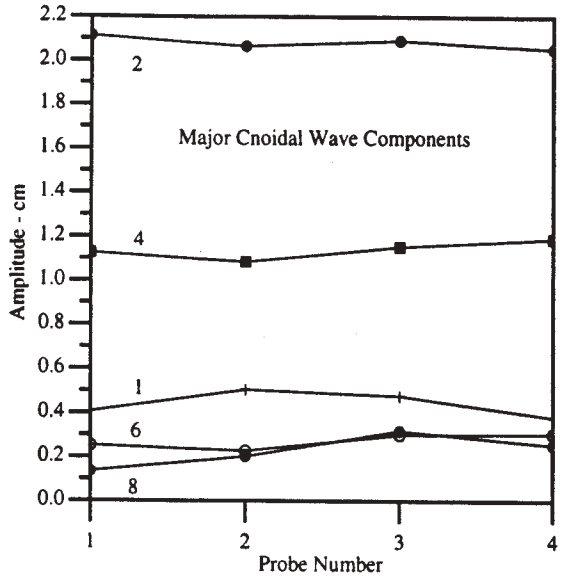


Figure 14 Variation of major cnoidal wave component amplitudes as a function of probe number for the data in Fig. 8.

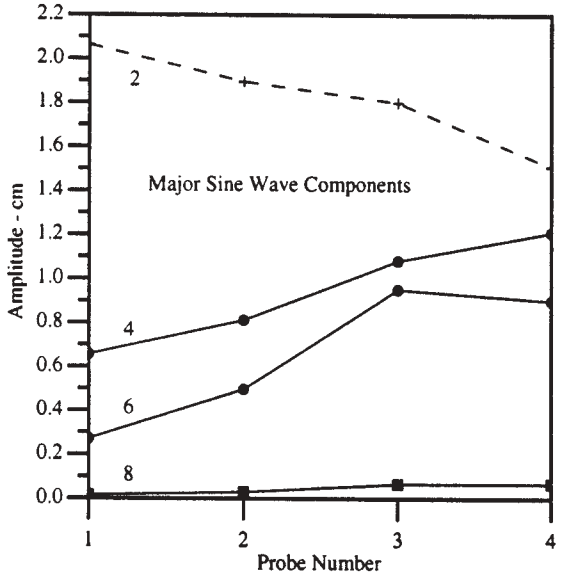


Figure 15. Variation of major sine wave component amplitudes as a function of probe number for the data in Fig. 8.

This work was supported in part by the Office of Naval Research of the United States of America and by two MURST (Ministero Università e Ricerca Scientifica Tecnologica) grants from Italy.

## REFERENCES

Ablowitz, M. J. and H. Segur, 1981: *Solitons and the Inverse Scattering Transform* (SIAM, Philadelphia).

Boyd, J. P., 1990: Adv. Appl. Mech, Vol. 27, 1.

Bryant, P. J., 1973: Periodic Waves in Shallow Water, J. Fluid. Mech. 59, 625-644..

Date, E. and S. Tanaka, 1976: Periodic multi-soliton solutions of Korteweg-deVries equation and Toda lattice, Prog. Theoret. Phys. Supp., Vol. 59, 107-126.

Dodd, R. K., J. E. Eilbeck, J. D. Gibbon and H. C. Morris, 1982: *Solitons and Nonlinear Wave Equations* (Academic Press, London).

Dubrovin, B. A., V. B. Matveev and S. P. Novikov, 1976: Nonlinear equations of Korteweg-deVries type, finite zoned linear operators, and Abelian varieties, Russian Math. Surv., Vol. 31, 59-146.

Fermi, E., J. Pasta and S. Ulam, 1974: *Studies of nonlinear problems, I*, Los Alamos Rep. LA1940, 1955; reprod. in Nonlinear Wave Motion, A. C. Newell, ed. (American Mathematical Society, Providence).

Flaschka, H. and D. W. McLaughlin, 1976: Canonically conjugate variables for KdV and Toda lattice under periodic boundary conditions, Prog. Theoret. Phys., Vol. 55, 438-456.

Its, A. R. and V. B. Matveev, 1975: The periodic Korteweg-deVries equation, Func. Anal. and Appl., Vol. 9(1), 67ff.

Korteweg, D. J. and G. deVries, 1895: On the change of form of long waves advancing in a rectangular canal, and on a new type of long stationary waves, Philos. Mag. Ser., Vol. 5(39), 422-443.

LeBlond, P. H. and L. A. Mysak, 1978: *Waves in the Ocean* (Elsevier, Amsterdam).

McKean, H. P. and E. Trubowitz, 1976: Hill's operator and hyperelliptic function theory in the presence of infinitely many branch points, Comm. Pure Appl. Math., Vol. 29, 143-226.

Mei, C. C. and U. Ünlüata, 1972: Harmonic generation in shallow water waves. *Waves on Beaches*, edited by R. E. Meyer (Academic, New York) 181-202.

Mei, C. C., 1983: *The Applied Dynamics of Ocean Surface Waves* (John Wiley, New York).

Miles, J. W., 1980: Solitary Waves, Annual Rev. Fluid Mech., Vol. 12, 11-43.

Newell, A. C., 1985: *Solitons in Mathematics and Physics* (SIAM, Philadelphia).

Novikov, S. P., S. V. Manakov, and M. P. Pitaevskii, V. E. Zakharov, 1980: *Theory of solitons. The Inverse Scattering Method*, (Consultants Bureau, New York).

Osborne, A. R., 1993: Numerical construction of nonlinear wave-train solutions of the periodic Korteweg-deVries equation, Phys. Rev. E, 48(1), 296-309.

Osborne, A. R., 1995: Solitons in the periodic Korteweg-deVries equation, the $\theta$-funtion representation, and the analysis of nonlinear, stochastic wave trains, Phys. Rev. E, Vol. 52(1), 1105-1122.

Osborne, A. R. and Petti, M., 1994: Laboratory-generated, shallow-water surface waves: Analysis using the periodic, inverse scattering transform, Phys. Fluids, Vol. 6(5), 1727-1744.

Osborne, A. R., Bergmasco, L., Serio, M., Bianco, L., Cavaleri, L., Drago, M., Iovenitti, L. and Viezzoli, D., 1996: Nonlinear shoaling of shallow-water waves: Perspective in terms of the inverse scattering transform, Il Nuovo Cimento, 19C(1), 151-175.

Weigel, R., 1964: *Oceanographical Engineering*. (Prentice-Hall, Englewood Cliffs, N.J.).

Whitham, G. B, 1974: *Linear and Nonlinear Waves* (John Wiley, New York).

# 5 WAVE INTERACTIONS IN THE SPECTRA OF SURFACE WAVES

**Valeri A. Kalmykov**

Department of Earth and
Planetary Sciences
Johns Hopkins University
Baltimore, MD 21218, USA

## 1. INTRODUCTION

In the state-of-the-art wave models such as WAM (Komen et al. 1994), the most important source term is due to the nonlinear wave-wave interactions. Though this source function is energy conserving, it is responsible for the wave field growth and its evolution by controlling the peak frequency downshift, without which the wave energy cannot grow. Because of its importance, the inclusion of this term in the third generation models greatly improves the physics of the model and the accuracy of the results. Though the importance of the nonlinear wave-wave interaction was first pointed out by Phillips (1960), the real applications were only possible after Hasselmann (1962, 1963) formulated it in terms of the wave spectrum. Even since then, the effective evaluation of the term in an operational model has been the goal of all wave modelers. Yet the complicated integrations involved have practically precluded the exact evaluation of it in operation. Rather, a parameterized source function was introduced in WAM, say. Due to its importance, however, exact evaluation is not only desirable but necessary in research, for the exact values are indispensable for guiding the parameterization. Because of this reason, many studies has been made on the nonlinear wave-wave interactions. Up till this time, however, most of the efforts were concentrated in the four-wave interaction conditions. The results by Fox (1976), Longuet-Higgins (1976), Masuda (1980) are all good examples. It is well known that the four-wave kinetic equation described these interactions is derived in an approximation accurate to the order of the cube of wave steepness. Its effects are primarily moving energy collinearly from high to low frequency, the so- called inverse cascade. In this note, we will examine the nonlinear wave-wave interactions to a higher order to investigate the effects of the term in an approximation accurate to the order of the fourth power of wave steepness. Past studies (see, for example, McLean (1982 a and b); Krasitski (1993); and Kalmykov (1993) and (1995)) indicated that this higher order nonlinear wave-wave interactions involved 5 gravity waves, and their primary function is to move energy away from the mean wave propagation direction; therefore, the mechanism might be important in the directional evolution of the spectral function.

The five-wave interactions were first discovered by Su (1982a and b) experimentally and McLean (1982a and b) theoretically. This type of interactions were designated by McLean as type II instability to be distinct from the known Benjamin-Feir instability as the instability of type I. The type I instability is primarily 2-dimensional; it provides the group structure of surface waves in direction of their propagation. According to the weak nonlinear theory, these wave groups can disappear and the monochromatic waves can reemerge, known as the Fermi-Pasta-Ulam recurrence (see, for example, Yuen and Lake 1982). But, when this happens, the frequency of the waves is invariably downshifted to a lower value, a process critical for wave growth (see, for, example, Huang et al., 1996). The type II instability is 3-dimensional. Its effects was first found by Su (1982a and b) in the formation 3-dimensional circular segments on the wave crests. Type II Insta-

bility was also investigated by Stiassnie and Shemer (1984, 1987) in spectral form. They derived the Zakharov equation in a cubic approximation of wave steepness for four and five wave-wave non-resonant interactions. The terms added by them to Zakharov's equation were the results of five wave-wave interactions.

The true spectral formulation was not completed till the full Hamiltonian formulation by Krasitski (1990, 1993, 1994). All details and theoretical foundation of applicability of this equation are contained in those papers. Some preliminary numerical results of based on Krasitski's formulation have been reported by Kalmykov (1993, 1995). In this note, we will report additional results from a systematic study of the five-wave interactions both in deep and shallow waters. By using various parametrical values in a JONSWAP spectrum with a cosine angular distribution function, we explored the effects on the five-wave interactions of the water depth, the spectral bandwidth in frequency space, and the spectral breadth in angular distribution. To show all these effects, we will first report the detailed computation of nonlinear transfer of energy by five wave-wave interactions in deep and shallow water. It is shown that wave energy is transferred by five-wave interactions from the main spectral maximum to high frequencies located at angles $\pm 70^0$ from the main direction. As expected, energy flux due to five-wave interactions is two orders of magnitude weaker than the four-wave interactions. The dependence of nonlinear energy transfer on the spectral bandwidth of frequency and breadth of angular distribution of the spectrum is also investigated.

Finally, we will also report the results from the detailed computation for finite water depth. A technique was developed to overcome the main difficulty of using the normalization method for the kernel function. As in the deep water case, the energy transfer in the water of finite depth is also from the spectral maximum to high frequency and move at an angle ranging from more than $\pm 70^0$ for deeper waters to about $\pm 60^0$ for the shallow case from the main wave direction. Although the magnitudes of the nonlinear energy transfer have increased by an order of magnitude in comparison with the deep sea, their over all values are still small compared to the 4-wave interactions. In all the cases, the energy fluxes from the Boltzmann integral at various depths are conserved as in the four-wave case. In the following section, we will start with the deep water case, for it is relatively easier.

## 2. EQUATION

In all the computation for the nonlinear transfer of energy by five -wave resonant interactions, we will use the kinetic equation derived by Krasitski (1993) as follows:

$$\frac{\partial n_1}{\partial t} = 12\pi \int_{-\infty}^{\infty} W^2_{1,2,3,4,5} n_1 n_2 n_3 n_4 n_5 \times$$
$$\times (\frac{1}{n_1} + \frac{1}{n_2} - \frac{1}{n_3} - \frac{1}{n_4} - \frac{1}{n_5}) \times$$
$$\times \delta(\omega_1 + \omega_2 - \omega_3 - \omega_4 - \omega_5) \times$$
$$\times \delta(\mathbf{k_1} + \mathbf{k_2} - \mathbf{k_3} - \mathbf{k_4} - \mathbf{k_5}) \mathbf{dk_{2345}} +$$
$$+ 18\pi \int_{-\infty}^{\infty} W^2_{5,4,3,2,1} n_1 n_2 n_3 n_4 n_5 \times$$
$$\times (\frac{1}{n_1} + \frac{1}{n_2} + \frac{1}{n_3} - \frac{1}{n_4} - \frac{1}{n_5}) \times$$
$$\times \delta(\omega_1 + \omega_2 + \omega_3 - \omega_4 - \omega_5) \times$$
$$\times \delta(\mathbf{k_1} + \mathbf{k_2} + \mathbf{k_3} - \mathbf{k_4} - \mathbf{k_5}) \mathbf{dk_{2345}} \quad (1)$$

in which $\mathbf{k}$ is the wave number vector, and $k = |\mathbf{k}|$; $\omega = [gk \cdot tanh(kh)]^{1/2}$ is the frequency which is related to the wave number by the dispersion relationship; $g = 9.81 m \cdot s^{-2}$ is the gravity acceleration; $h$ is the depth; $W_{1,2,3,4,5} =$



AUTHOR INDEX TABLE OF CONTENTS

$W(\mathbf{k_1}, \mathbf{k_2}, \mathbf{k_3}, \mathbf{k_4}, \mathbf{k_5})$ is the kernel function for arbitrary depth; $\delta(...)$ is the Dirac delta-function; $\mathbf{dk_{2345}} = \mathbf{dk_2 dk_3 dk_4 dk_5}$;

$$n_1 = n(\mathbf{k_1}) = \mathbf{S(k_1)}\frac{\mathbf{4\pi^2 g}}{\omega_1} \qquad (2)$$

is the spectrum of wave action (in canonical variables); $S(\mathbf{k})$ is the wave number spectrum of the surface waves. In order to simplify our presentation, we split the integral in equation (1) into two parts as follows:

$$\frac{\partial n_1}{\partial t} = I_5 = I_{51} + I_{52} \qquad (3)$$

where $I_{51}$- is the first term in equation (1) and $I_{52}$ - second one. To simplify the computation further, all computations are performed in nondinemsional form, thus, without loss of generality, we take $g = k_0 = \omega_0 = 1$, with $k_0$, and $\omega_0$ as the wavenumber and the frequency at the spectral peak. We treat the wave vector in pole coordinates; thus, $\mathbf{k} = (\omega^2, \theta)$ is a vector with amplitude $\omega^2$, and angle $\theta$ to X axis. According to equation (1), it is necessary to satisfy the following resonant conditions for five vectors and frequencies:

$$\mathbf{k_1} + \mathbf{k_2} + \mathbf{k_3} = \mathbf{k_4} + \mathbf{k_5} \qquad (4a)$$

$$\omega_1 + \omega_2 + \omega_3 = \omega_4 + \omega_5 \qquad (4b)$$

The degenerate case of interactions for five waves at $\mathbf{k_1} = \mathbf{k_2} = \mathbf{k_3} = (\mathbf{1, 0})$ for the different depths is shown on Figure 1a, which is analogous to the famous figure-8 curve for the four waves interactions (see, for example, Masuda, 1980). Figure 1a is shown only as an example, all other calculations are carried out for five different waves.

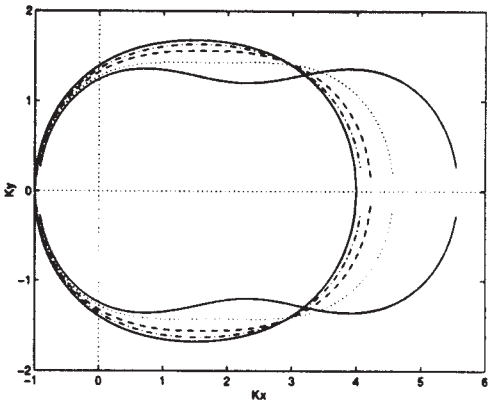


Figure 1a Diagram (4) for $k_1 = k_2 = k_3 = (1, 0)$ for the depths: h=0.5,1,1.5,2,10; (following from right to the left), h=10 - solid, h=2 - dash-dotted, h=1.5- dashed, h=1 - dotted, h=0.5- solid.

All the computation are performed in terms of action density spectra. Following Krasitski (1993), we write the action density spectrum (2) in term of the frequency-angular spectrum as follows:

$$n = S(\omega, \theta)\frac{4\pi^2}{2\omega^4} \qquad (5)$$

The factor $4\pi^2$ has to be included here because due to the canonical transformations, our action spectral form differs from the one used in Masuda (1980). Let us put

$$S(\omega, \theta) = \Psi(\omega)K(\theta) \qquad (6)$$

with $\Psi(\omega)$ as the frequency spectrum, and $K(\theta)$ as the angular distribution function. We also adopt the JONSWAP wave spectrum as the frequency function,

$$\Psi(\omega) = A\omega^{-5} exp^{-1.25\omega^{-4}} \gamma^{exp^{-\frac{(\omega-1)^2}{2\sigma^2}}} \qquad (7)$$

where $A = \Psi^{-1}(1)$, $\sigma = 0.07$ for $\omega \leq 1$, and $\sigma = 0.09$ for $\omega > 1$. The parameter $\gamma$ here offers a measure of the spectral width. The frequency of spectral maximum $\omega_0 = 1$ was chosen so that $\Psi(1) = 1$.

The frequency JONSWAP spectra with various $\gamma$ parameter values are plotted on Figure 1b.

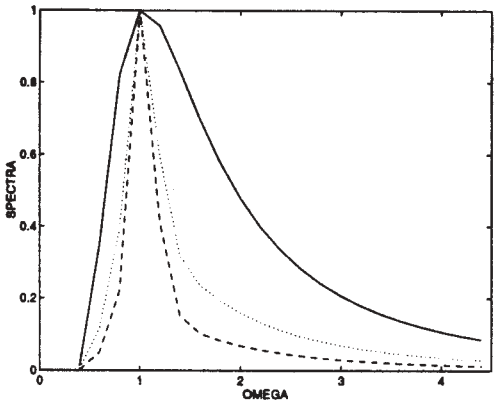


Figure 1b. Frequency JONSWAP spectra (7) $\gamma = 1$ -solid line, $\gamma = 3$ -dotted line, $\gamma = 7$ -dashed line.

The angular distribution function is assumed as

$$K(\theta) = B \cdot cos^m(\theta) \; for \; |\theta| \leq \pi/2 \quad (8)$$

where $B = \left[\int_{-\pi/2}^{\pi/2} K(\theta)d\theta\right]^{-1}$, so that $\int_{-\pi/2}^{\pi/2} K(\theta)d\theta = 1$. All results are presented in a nondimensional form as well as in (Masuda, 1980). To obtain dimensional values, the nondimensional energy transfer $\partial S / \partial t$ from (1) have to be multiplied by factor: $c_5 = \Psi^4(\omega_0)\omega_0^{16}g^{-6}$, and by a different factor $c_4 = \Psi^3(\omega_0)\omega_0^{11}g^{-4}$ for four-wave interactions. So, $c_5/c_4 = \epsilon^2$, with $\epsilon = k_0 a_0$ as the wave steepness. Therefore, the energy transfer rate for the five-wave interactions will only consist of a few percent of four-wave interactions. Consequently, it is reasonable to conclude that four-wave interactions remain dominant except for very steep waves, or for extremely shallow depth. But as will be shown later, even under such conditions, the five-wave interactions are still weak relative to the four-wave interactions.

## 3.1 DEEP WATER

In this section, we will present some numerical results of the five wave interactions. All the computations were performed using the following numerical parameters for external grid: for frequencies, $\omega_i = 0.8 + \Delta\omega \cdot (i-1)$; for angles, $\theta_j = -\pi/2 - \Delta\theta \cdot (j-1)$ for $\Delta\omega = 0.1$, $\Delta\theta = \pi/(M-1)$; for computation steps, i=(1,N), j=(1,M), N=20, M=21. Spectral parameters are: $\gamma = 1, 3, 7$; m=2,4. For internal grid $(\omega, \theta)$, we used N=10,15,20, M=15, $\Delta\omega = 0.1, 0.2$. As expected, the calculations with greater N give smoother results. When the action spectra density (5-8) is substituted in (3), the summary nonlinear transfer of energy calculated as

$$\frac{\partial S(\omega,\theta)}{\partial t} = I_{51} + I_{52} \quad (9)$$

and its 2-dimensional form is given as

$$\frac{\partial S}{\partial t} = \int_{-\pi/2}^{\pi/2} \frac{\partial S(\omega,\theta)}{\partial t} d\theta \quad (10)$$

Selected results from (9-10) are shown in Figure 2a,b corresponding to the spectrum from Figure 1b. (for Pierson-Moscovitz spectra only: $\gamma = 1$, $m = 2$).

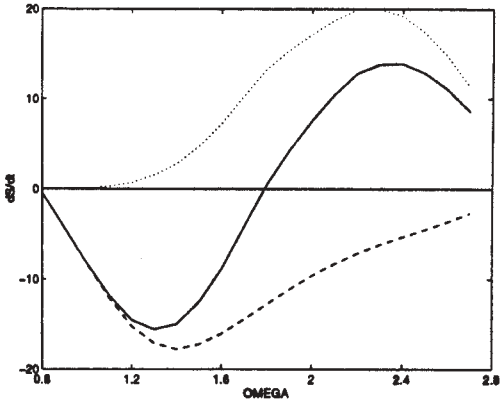


Figure 2a. Nonlinear transfer of energy (10) for Pierson-Moscovitz spectrum $\gamma = 1$, m=2): $I_{51}$- dotted line, $I_{52}$- dashed line, $I_{51} + I_{51}$- solid line.



AUTHOR INDEX TABLE OF CONTENTS

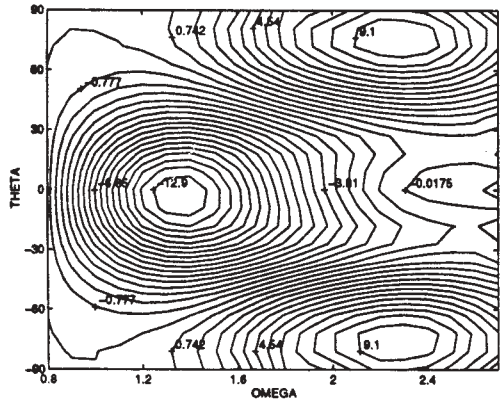

Figure 2b. Nonlinear transfer of energy (9)

It is revealed that energy transfer rates depend on the width of angular distribution of the spectrum: the rate for m=4 (10) is greater than for m=2. But this is only a small effect: the difference is only about 50 percent, yet the overall shapes of the energy transfer functions are essentially the same for different $m$ values. There is a much stronger dependence of the energy transfer rates on the bandwidth of frequency spectrum: the rate is higher for wideband spectra than the narrow band ones. The energy transfer rate given by (10) decreases as the wave spectrum frequency bandwidth becomes narrow and the volume of integration in (9) decreases. The difference can be orders of magnitude. The resulting trends is summarized in the next. Energy transfer rate is higher for wider spectra in frequency bandwidth, but slightly narrower angular distribution.

Because wave energy is conserved, hence from (10) it follows that (Krasitski,1993):

$$\int_{-\infty}^{\infty} \frac{\partial S(\omega)}{\partial t} d\omega = 0 \qquad (11)$$

Conservation of energy (11) is fulfilled always and was used for choosing of the integration step. It is evident from Figure 2a, that the wave energy by five-wave nonlinear interactions is transferred from spectral maximum to the high frequencies.

The direction of nonlinear energy transfer by five-wave interactions is directed oppositely in comparison with the four-wave cases for Pierson-Moscovitz spectrum ($\gamma = 1$)(Masuda, 1980). According to Zakharov (1997), a general rule governing the nonlinear energy transfer rate is as follows: For any odd number wave interactions, the energy transfer is the direct cascade pattern: from low frequency to higher frequency. The only exception is when the energy is almost collinear as the case treated by Dychenko and Zakharov (1995), in which the energy transfer could be in the inverse cascade pattern. Those cases can only be realized for swell propagation, but, even for those cases, the conditions are unstable to any cross wave perturbations. The fact that the five-wave interactions can move energy in the direct cascade pattern but with an off-the-main direction of propagation can be argued qualitatively as suggested by Zakharov (1997). Let us take the three of the five participating waves to be at the spectral peak with the frequency and wavenumber all at $\omega_0$ and $k_0$. Let also take the excited waves in the five-wave interactions to be $\omega_1$ and $k_1$. Then, from the resonant condition in (5), we have $3\omega_0 = 2\omega_1$; therefore $\omega_1 = 3/2\omega_0$, a direct cascade. Furthermore, $3k_0 = 2k_1 cos(\beta)$ thus, $\beta$ will have to be around $50^0$, an off main direction propagation. This is very close to what we have obtained, and also confirmed the results of McLean(1982b).

It should be pointed out that the five-wave interactions, being of higher order, are two orders of magnitude weaker than four-wave energy transfer. Therefore, in any given wave field, the four-wave interactions are the prevailing mechanisms. The five-wave interactions can only be of importance for the formation of the angular spectrum, because they transfer energy to the cross spectral wave modes while four-wave gives energy to the

collinear waves. But in consideration of the direct cascade pattern, the five-wave interactions can be significant in only influencing the directional distribution of the tail range of the spectrum. Even here, the four-wave interaction also has the same effect in moving the energy away from the main propagation as modeled by Banner and Young (1994).

Now let us examine the directional energy transfer rate for the five-wave interactions in detail. Figure 2b shows the contours of nonlinear transfer of energy by five wave-wave interactions (9). One can see that at the frequency of spectral maximum we have the negative minimum at or near $\omega_0 = 1$, $\theta_0 = 0$, and at or near $\omega_1 = 2$, $\theta_1 = \pm 70^0$ we have two positive maxima. It follows that the energy of waves is transferred by five-wave interactions from the spectral maximum to high harmonics propagating in angles $\pm 70^0$ from the main direction. It means, that the angular spectrum of high frequency waves will be wider, than those near the frequency of the main peak (Efimov and Solovjev, 1979). This result in some sense is obvious, as the kinetic equation itself dictates a slow spreading of wave energy in the frequency-angle domain if the mechanism that supports its narrow spreading (by the wind, say) is not available (Zakharov and Smilga, 1981). Value of an angle where instability of the type II is most unstable ($\pm 70^0$) also coinsides with its value from McLean (1982), and follows from the qualitative argument advanced by Zakharov (1997) discussed above. This is connected with the geometry of five interacting wave vectors from two terms in kinetic equation (1). The lateral spreading of energy could also help the effects of four-wave spreading of energy in the spectral tail modeled by Banner and Young (1994).

In summary, the four-wave interactions give the 2-dimensional instability of type I; the five-wave interactions gives the 3-dimensional instability of type II. The first type of instability is the most intensive for collinear waves (important for formation of frequency spectrum), while the second one is the most intensive for waves propagating almost in the cross direction from the main one (significant for the formation of an angular spectrum). This conclusion is in qualitative agreement with Stiassnie and Shemer (1984, 1987).

### 3.2 FINITE DEPTH WATER

The frequency-angular grid of integration for the finite depth is the same as in the deep water case. The special case of degenerate interaction of five waves is analogous to the case of deep sea as shown on Figure 1a for five depths h=0.5,1,1.5,2,10, with the cases of the largest and of the smallest depths shown by solid lines. It is seen that the diagram of wave-wave interaction for small depth is extended in X-axis and has the form of dumb-bell; for large depth it has the form of an egg. Angular distribution function (8) and the frequency spectrum (7), however, remain the same as in the deep water case ($\gamma = 1$, $m = 2$). Figures for the finite depth case are likely the same as for the deep water so they are not shown here. The main features of the Boltzmann integral for the different depths are kept the same as on the deep water and this is close to that pointed for four-wave case in Hasselmann and Hasselmann (1980). The energy is also conserved here. From these results one can also conclude that the nonlinear energy transfer is similar to the deep water case: from spectral maximum towards the high-frequency region and to the same angles located symmetrically at both sides from the main direction of wave propagation.

Due to the conservation of energy, the values of the positive and negative maxima are very close. Clearly, the magnitude of the energy transfer increases with decreasing depth. The values of the non-

linear energy transfer rate are up to an order of magnitude higher than that of the deep water cases. Even with this growth, the relative magnitudes of the five-wave interactions are still two orders smaller than the corresponding ones for the four-wave cases. At the deeper end, the energy is transferring from the peak to the wave modes propagating at $\pm 70^0$ from the main direction. At the shallower end, the energy is transferring from the peak to the wave modes propagating at $\pm 60^0$ from the main direction. Thus the decreasing depth has the effect of narrowing of the directional distribution of the spectrum even through the nonlinear wave-wave interactions.

## 4. CONCLUSIONS

Based on our study, we can draw the following conclusions: The energy in surface wave spectrum is transferred by five-wave interactions from the spectral peak to the high frequency range in an angle at $\pm 70^0$ from the main direction in the deep water, and at around $\pm 60^0$ in shallow water. The nonlinear energy transfer rate is higher for a narrower angular distribution of energy, and wider frequency bandwidth. The rate is also higher for decreasing depth. The form of the Boltzmann integral conserves its features as function of the depths. Although for shallow water depth, the energy transfer rate could be an order of magnitude higher than the corresponding values in the deep water, the energy transfer rate for the five-wave interactions is still much smaller relative to the four-wave interactions. Therefore, the only importance of the five-wave interactions is their effects in the formation of the directional spectrum tail. Even here, the five-wave interactions could only add to the widening effects of the four-wave interactions which can also widen the angular distribution of the spectral tail as reported by Banner and Young (1994).

## 5. ACKNOWLEDGEMENTS

The author would like to thank Dr. N. Huang, who has read the manuscript and suggested numerous improvements in the presentation of the results. I would also like to thank Professors O.M. Phillips and V. Zakharov for their generous sharing of their ideas, and stimulating discussions.

## 6. REFERENCES

**Banner, M. L. and I. R. Young** , 1994: Modeling spectral dissipation in the evolution of wind waves. Part 1: Assessment of existing model performance. *J. Physical Oceanogr.* 24, 1550-1571.

**Efimov V.V., Solovjev Y.P.** , 1979: The frequency-angular spectra and dispersion relation in wind waves. *Izvestija Akademii Nauk SSSR, Fizika Atmosferi i Okeana*, 15, 11, 1181-1196.

**Fox M.J.** , 1976: On the nonlinear transfer of the energy in the peak of a gravity wave spectrum. *Proc. Roy. Soc. London*, A 348, 467-483.

**Hasselmann K.** , 1962: On the nonlinear energy transfer in a gravity wave spectrum. Part 1. General theory. *J. Fluid Mech.*, 12, 481-500.

**Hasselmann K.** , 1963a: On the nonlinear energy transfer in a gravity wave spectrum. Part 2. Conservation theorems, wave-particle analogy: irreversibility. *J. Fluid Mech.*, 15, 273-281.

**Hasselmann K.** , 1963b: On the nonlinear energy transfer in a gravity wave spectrum. Part 3. Evaluation of the energy flux and swell-sea interactions for a Neumann spectrum. *J. Fluid Mech.*, 15, 385-398.

**Herterich K., Hasselmann K.** , 1980: A similarity relation for the nonlinear transfer in a finite depth gravity-wave spectrum. *J.Fluid Mech.*, 97, 215-224.

**Huang, N. E., S. R. Long, Z. Shen** , 1996: The mechanism for frequency downshift in nonlinear wave evolution. *Adv. App. Mech.* 32, 59-117.

**Komen G., L.Cavaleri, etc** , 1994: Dynamics and modeling of ocean waves. Cambridge University Press, 532 p.

**Kalmykov V.A.** , 1993: Numerical calculation of the nonlinear transfer of energy in the spectra of surface gravity waves by 5 wave resonant interactions. *Dokladi Akademii Nauk Ukraini*, 8, 101-104.

**Kalmykov V.A.** , 1995: Estimates of energy transfer in the spectra of surface gravity waves by nonlinearity of high order. *Dokladi Akademii Nauk Ukraini*, 11, 87-89.

**Krasitski V.P.** , 1990: About canonical transformation in the theory weakly nonlinear waves with nondisintegrated dispersion law. *JETP (Soviet Physics)*, 98, 5(11), 1644-1655.

**Krasitski V.P.** , 1993: 5 wave kinetic equation for surface gravity waves.*Marine Hydrophysical Journal*, 6, 17-25.

**Krasitski V.P.** , 1994: On reduced equations in the Hamiltonian theory of weakly nonlinear surface waves. *J. Fluid Mech.*, 272, 1-20.

**Longuet-Higgins M.S.** , 1976: On the nonlinear energy transfer of energy in the peak of a gravity wave spectrum: A simplified model. *Proc. Roy. Soc. London*, A 347, 311-328.

**Masuda A.** , 1980: Nonlinear Energy Transfer Between Wind Waves. *J. Phys. Oc.*, 10, 2082-2093.

**Mc Lean J.W.** , 1982a: Instabilities of finite amplitude gravity waves. *J. Fluid Mech.*, 114, 315-330.

**Mc Lean J.W.** , 1982b: Instabilities of finite amplitude gravity waves on water of finite depth. *J. Fluid Mech.*, 114, 331-341.

**Phillips, O. M.** , 1960: On the dynamics of unsteady gravity of finite amplitude, Part 1, The elementary interactions. *J. Fluid Mech.* 9, 193-217.

**Stiassnie M., Shemer L.** , 1984: On modification of Zakharov's equation of surface gravity waves. *J. Fluid Mech.*, 143, 47-67.

**Stiassnie M., Shemer L.** , 1987: Energy computations for evolution of class I and II instabilities of Stokes waves. *J. Fluid Mech.*,174, 299-312.

**Su M.Y.** , 1982a: Three-dimensional deep-water waves, Part 1, Experimental measurement of skew and symmetric wave patterns. *J. Fluid Mech.* 124, 73-108.

**Su M.Y.** , 1982b: Evolution of groups of gravity waves with moderate to high steepness. *Phys. Fluids*, 25, 2167-2174.

**Yuen G., Lake B.** , 1982: Nonlinear dynamics of deep-water gravity waves.- from Advances in applied mechanics, Ed. by Chia-Shun Yih,New-York, P. 67-229.

**Zakharov, V. E.** , 1997: The statistical theory of shallow water waves (under preparation).

**Dyachenko, A. I., Y. V. Lvov, etc** , 1994: Five-wave interaction on the surface of deep fluid. *Physica D.* 87, 233-261.

**Zakharov V.E., Smilga A.V.** , 1981: About quasi-uniform spectra in the weak turbulence. *JETP (Soviet Physics)*, 81, 4, 1318-1326.

# SWELL EVOLUTION IN THE SEA OF FINITE DEPTH

**Valeri A. Kalmykov**

Department of Earth
and Planetary Sciences
Johns Hopkins University
Baltimore, MD 21218, USA

## 1. INTRODUCTION

There are many works devoted to the numerical study of the four wave kinetic equation for surface gravity waves (including the finite depth case), for example: Fox (1976), Hasselmann (1962; 1963a,b) , Longuet-Higgins (1976), Masuda (1980), Hasselmann and Hasselmann (1985), etc. So, it is evident that the four wave-wave interactions play a key role in the formation of the spectrum of the surface gravity waves. Details of the nonlinear transfer of energy by the four wave-wave interactions have been studied quite extensively both theoretically and numerically. The exact and approximate numerical calculations of nonlinear energy transfer were carried out by different methods. They have been applied to various parametrizations of the nonlinear transfer of energy in the spectrum of surface gravity waves. These parametrizations have been used in wave prediction models , see Komen et al.(1994). But only two works can be seen to be devoted directly to the numerical solution of the kinetic equation in the deep sea: Polnikov (1990), Resio and Perrie (1991) and one to the sea of finite depth: Lavrenov (1991).

Before the discussion, let us note two points. First: this work will not deal with the idea of how to better perform nonlinear energy transfer calculations. Known methods will be applied to the spectral evolutions for the cases of infinite and finite depth. Second: the evolution of the surface waves is regarded in every case as a function of time for some constant depth. Only for a better presentation will all parameters be shown together in coordinates of time and depth. The case when waves are propagating from deep water into the shallow areas is not considered here. The present work is a further development of an earlier work Lavrenov (1991), where only the single nonlinear transfer of energy was estimated for an infinite depth. To obtain a finite depth energy transfer, a scaling factor for the depth required was used. Preliminary results of this work were presented in Kalmykov (1994,1995). Although the present work has no wind input and wave dissipation, this description may reflect real waves to some extent. A possible input of these terms to the spectral evolution will be discussed below. It may be noted that only the swell may be considered as an object for such study. It is well-known that the swell in the open ocean is propagated over large distances practically without dissipation. What will happen to such swell when it enters a sea of finite depth? This question is partly answered in Lavrenov (1991): the wave field being 3-dimensional on an infinite depth becomes 2-dimensional on shallow water. Beyond the concept of the studying of swell evolution for academic reasons, it will be interesting to apply these results to the wave prediction models, which are widely used. In comparison with the wave prediction models (as far as the transport equation is concerned), the kinetic equation is used here for the purpose of studying only the temporal spectral evolution. If one includes wind generation, dissipation, wave breaking and bottom friction in the kinetic equation, then the present results will differ from those obtained from only using the kinetic equation.

Another application of the numerical solution of kinetic equation will also be shown. Masson (1993) studied the interaction of swell and wind waves in one

spectrum by using the solution of the kinetic equation. The same work was performed earlier by Polnikov (1990). Here it is necessary to note that wave-wave interactions are the most intensive between the closest frequencies. Nonlinear interaction between short and long waves separated by large frequency interval will be very weak. From Masuda (1980), it is known that high-frequency wind waves in the spectrum disappear and their energy is transferred by nonlinear interactions to the low-frequency swell (if the swell amplitude is greater than that of the wind-wave). So the nonlinear transfer of energy always smooths any perturbations in the wave spectra. The nonlinear interactions always have a self-stabilizating role in spectral formation. This was first discussed in Hasselmann (1962). During the spectral evolution, the spectral form oscillated slightly near a stable condition. The same was noticed by Polnikov (1990).

A numerical study of the spectral evolution of surface gravity waves without energy input and wave dissipation makes it possible to answer the following questions: Does the steady wave spectrum exist after its long-time evolution due to its nonlinearity? What is the dependence of the spectral asympthotic form versus the depth? The first question is answered in Polnikov (1990): on deep water, the wave spectrum develops into some stable form. An answer to the second question will be given here. The term "spectral stability" is meant here in the asympthotic sense, because it is possible to expect a further, very slow broadening of the narrow wave spectrum without the wind: Zakharov and Smilga (1981). The numerical simulations performed here are very time-consuming and the upper time limit achieved here certainly may be increased using more powerful machines. We reached the time limit of an hour of real time (200-800 wave periods). It is the time when nonlinearity works even on deep water (at finite depth it is much quicker) and the phenomenon which was found is clearly seen. The spectra become practically saturated and keep their stable form, as will be seen from the figures below. Kinetic equation was solved numerically with the help of the Runge-Cutta method for deep and finite depth water. The main result for the finite depth case is the narrowing of the wave spectra at the depth $h = \lambda_0/2\pi$, where $\lambda_0$ is the wavelength of the spectral maximum.

In general, the spectral evolution shown here as well as by other authors is evident from the point of view of the structure of nonlinear energy transfer. A positive lobe of the nonlinear transfer of energy at low frequencies and a negative lobe at the high frequencies will indicate the growth of the spectral maximum and its frequency downshift. It must be noted that energy conservation makes the spectrum greater and narrower. When the spectrum become narrow, then the negative lobe of the energy transfer shifts slightly to the low frequencies just below the spectral peak. At the same time, the negative lobe at the high frequency becomes positive. As a result of this, three lobe structures of the nonlinear transfer become apparent: negative below the spectral peak and positive at both sides of the peak. This also means that the spectra will not grow more because energy is transferred from the spectral peak to other frequencies. However, spectra wouldn't become narrower either. As mentioned above, self-stabilization of the spectra by nonlinearity would take place. The time from the spectral growth to saturation will be denoted here as relaxation time. The most interesting aspect of this is the fact that the relaxation time is different for various depths. This narrowing of the spectrum has been shown in the experiments: Bouws et al. (1985), Davidan et al. (1995), but not as strong as will be shown here. The spectral form was paramertized by Bouws et al. (1985) by the TMA spectrum. (TMA means: T-Texel storm, M- Marine Remote Sencing Experiment, A- Atlantic Ocean Remote

Sensing Land-Ocean Experiment). They have shown that the spectral width is inversely proportional to the group velocity, which has a minimum at the depth $k_0 h = 1$. Hence, the spectrum will be narrowest at this depth.

It is necessary to note that the case of finite depth considered here is well described by the ordinary kinetic equation for tetradic wave interactions (1) and this is proved by works of Hasselmann and Hasselmann (1985). The case of the very shallow water (not considered here, $kh < 0.3$) is described by the Bussinesq equation for triadic wave interactions where the approximate dispersion relation of the small depth ($kh < 0.3$) is used: Frelich and Guza (1984). Strictly speaking, the triadic interactions are forbidden because they do not satisfy to the resonant conditions with the exact dispersion relation for the finite depth case.

## 2. KINETIC EQUATION

The kinetic equation for the four wave-wave interaction in a sea of arbitrary depth is taken from Krasitski (1993):

$$\frac{\partial N_1}{\partial t} = 4\pi \int_{-\infty}^{\infty} V^2_{1,2,3,4} N_1 N_2 N_3 N_4 \times \times (\frac{1}{N_1} + \frac{1}{N_2} - \frac{1}{N_3} - \frac{1}{N_4}) \times \times \delta(\omega_1 + \omega_2 - \omega_3 - \omega_4) \times \times \delta(\mathbf{k_1} + \mathbf{k_2} - \mathbf{k_3} - \mathbf{k_4}) \mathbf{dk_2 dk_3 dk_4} \quad (1)$$

Here $V_{1,2,3,4} = V(\mathbf{k_1}, \mathbf{k_2}, \mathbf{k_3}, \mathbf{k_4})$ is the kernel function of the four wave- wave interactions for arbitrary depth, see Krasitski and Kalmykov (1993); $\delta(\mathbf{k_1}+\mathbf{k_2}-\mathbf{k_3}-\mathbf{k_4})$ and $\delta(\omega_1 + \omega_2 - \omega_3 - \omega_4)$ are the delta-functions for the wave vectors $\mathbf{k}$ and frequencies $\omega = [gk \tanh(kh)]^{1/2}$, $k = |\mathbf{k}|$, where $h$ is the depth; and $g = 9.81 m \cdot s^{-2}$ where $g$ is the gravitational acceleration. Thus

$$N_1 = N(\mathbf{k_1}) = \mathbf{S(k_1)} \frac{\mathbf{4\pi^2 g}}{\omega_1} \quad (2)$$

gives the spectrum of wave action, where $S(\mathbf{k})$ is the spatial wave spectrum. To simplify the computations further, they are performed in nondinemsional form. Thus, without loss of generality, we take $g = k_0 = \omega_0 = 1$, with $k_0$, and $\omega_0$ as the wavenumber and the frequency at the spectral peak. We will rewrite formula (2) in a nondimensional form:

$$N = S(\omega, \theta) \frac{4\pi^2}{2\omega^4} \quad (3)$$

The factor $4\pi^2$ has to be included here. Due to the canonical transformations, our action spectral form differs from the one used in Masuda (1980). Let us put

$$S(\omega, \theta) = \Psi(\omega) K(\theta) \quad (4)$$

with $\Psi(\omega)$ as the frequency spectrum, and $K(\theta)$ as the angular distribution function. We also adopt the JONSWAP wave spectrum as the frequency function,

$$\Psi(\omega) = A\omega^{-5} \exp(-1.25\omega^{-4}) \gamma^{\exp(-\frac{(\omega-1)^2}{2\sigma^2})} \quad (5)$$

where $A = \Psi^{-1}(1)$, $\sigma = 0.07$ for $\omega \leq 1$, and $\sigma = 0.09$ for $\omega > 1$. The parameter $\gamma$ here offers a measure of the spectral width. The frequency of the spectral maximum $\omega_0 = 1$ was chosen so that $\Psi(1) = 1$. The angular distribution function is assumed to have a form

$$K(\theta) = B \cdot \cos^{n(\omega,t)}(\theta) \; for \; |\theta| \leq \pi/2 \quad (6)$$

where $B = [\int_{-\pi/2}^{\pi/2} K(\theta) d\theta]^{-1}$, so that $\int_{-\pi/2}^{\pi/2} K(\theta) d\theta = 1$, the angular part of the spectrum was taken as Mitsuyasu-Hasselmann one: $n(\omega, t) = n(t)\omega^{-2.34}$ for $\omega \geq \omega_0$ and $n(\omega, t) = n(t)\omega^4$ for $\omega \leq \omega_0$.

The parameter of angular width $n$, was taken (as well as a function of the frequency shown above) as constant, independent of the frequency. Numerical analysis shows that model practically does not indicate any difference between them. The angular spectrum evolves through the width parameter, $n(t)$. The frequency spectrum evolves through the parameter of narrowness, $\gamma(t)$, and the frequency of the spectral peak, $\omega_0(t)$. On each time step, the separation of the spatial spectrum to the angular and frequency parts is performed. The purpose here is to obtain spectral parameters versus time. The input for the $i+1$ time step is the spectra from the $i-th$ time step, but not the construction from its current $i-th$ parameters. The Boltzmann integral in equation (1) is estimated here in nondimensional form with the help of Masuda's (1980) method, modified for the case of finite depth.

We will rewrite equation (1) in the following form:

$$\frac{\partial S(\omega,\theta)}{\partial t} = I(\omega,\theta) \qquad (7)$$

where $I(\omega,\theta)$ is the right part of (1). To obtain the nonlinear transfer of energy in dimensional form, it is necessary to multiply $I$ by the factor $c_4 = S_0^3\omega^{11}g^{-4}$ where $S_0 = S(\omega_0)$ is the spectral maximum. In this factor, all values have their real units.

Next, the discrete system of equations (7) (in dimensional units) was solved numerically by the Runge-Cutta method of 4-th order accuracy. At every point, output spectra were used as input to the next time step. To get spectral parameters as functions of time on each step, the spatial wave spectrum (4) was separated on the frequency spectrum (5) and angular one (6). The frequency spectrum was adjusted to (5) using wave energy, and the angular spectrum to (6) with the help of the normalization factor $B$. After calculations, we had the following parameters as functions of time: the frequency of the spectral maximum $\omega_0(t)$, the spectral maximum $S_0(t)$, the breadth of the frequency spectrum $\gamma(t)$, and the width of the angular spectrum $n(t)$. Thus we have a simple parametrical model of the evolution of swell due to wave nonlinearity. The application of the parametrical model before the ordinary one (where the spectrum is defined in a frequency-angle grid) has some advantages. A similar calculation of (1) for the deep sea case using the ordinary model gave the ragged and asymmetric spectrum which was averaged on each step: Polnikov (1990). This doesn't happen in the parametrical model because the spectrum obtained here is always approximated by a smooth function of its parameters.

The wave spectrum in dimensional form is taken from Phillips (1980) as:

$$S(\omega,\theta) = 0.012g^2\omega_0^{-5}S(\omega/\omega_0,\theta) \qquad (8)$$

where $\omega_0 = 2\pi F_0$, $F_0 = 0.2$Hz, $S(\omega/\omega_0,\theta)$ is the nondimensional wave spectrum (4). The numerical Runge-Cutta scheme was checked on conservation of wave energy as a function of time. Appropriately, the time step was chosen. The wave energy:

$$E(t) = \int_{-\infty}^{\infty}\int_{-\pi/2}^{\pi/2} S(\omega,\theta)d\omega d\theta \qquad (9)$$

is thus practically constant in time. This indicates that numerical errors of the Runge-Cutta scheme were small. The main difficulty was to choose the proper time step that would be good for all wave harmonics, because in reality, the time step is different for different harmonics. Initial conditions for the spectrum were taken as:

$$S(t=0) = \Psi(\omega_0 = 1.1, \gamma = 1.1) \times \\ \times K(n=2; n=8) \qquad (10)$$

One can see in (10) two initial conditions: for $n = 2$ and $n = 8$.

## 3. RESULTS

A well known result of nonlinear energy transfer in the spectrum of surface gravity waves has shown that energy is transferred from high frequencies to the low ones. This means that the frequency of the spectral maximum will downshift toward the low frequencies, the spectral maximum will grow, and the breadth of the frequency spectrum will diminish. After a long time of spectral evolution on the deep water from the nonlinearity, we have the established angular spectrum $\cos^4(\theta)$ ($B = 0.98$ here and $B = 1$ in Polnikov (1990)). The time of spectral relaxation to the stable condition is approximately one hour, which is close to that of Resio and Perrie (1991). The exact calculations of equation (1) are very time consuming, because on each time step the Boltzmann integral is estimated four times. Thus, we can assume that in the deep sea case nonlinearity causes the establishment of medium width spectra ($\gamma = 4 \pm 1$) with angular distribution $\cos^4(\theta)$.

Estimation of the Boltzmann integral for the deep sea was performed by the method described above, but modified to the finite depth. We here assume that wave frequencies do not depend on the depth and that the wave numbers are derived from the dispersion relation for finite depth $\omega^2 = kh\tanh(kh)$. This equation was solved numerically by the tangential method with accuracy $10^{-6}$. As noted Herterich and Hasselmann (1980), the form of the Boltzmann integral $I$ is conserved for different depths, but differs by its value. The same we have here: collision integral (1) has the same form for different depths. This means that on the finite depth case, one might expect evolution of spectral parameters similar to those on the deep sea. As it was already said, the single computation of spectral evolution on the finite depth water was performed by Lavrenov (1991). However, the nonlinear integral there was estimated on deep water and through the known ratio of (7) at certain finite depth to the one at the deep water $R = 1 + 5.5/x(1 - 5x/6)\exp(-5x/4), x = kh$, it was reduced to the necessary depth. Spectral parameters as functions of time here seemed to become steady except for the smallest depth considered. As was mentioned in the introduction, the spectral evolution has two steps: first, when the spectra grow and narrow; second, when it becomes practically steady and of some constant width. This take place because of the self-stabilization of the nonlinearity. Nonlinearity try to keep some stable spectral form. Energy in the wide spectrum at the first stage is transferred from the higher frequencies to the lower ones and to the peak. On the second stage for the narrow spectra, the nonlinearity transfers energy from the peak to higher and lower frequencies. The relaxation time when second step is achieved depends upon the depth. As it was said above, broadening of the spectra at small depths was found by Bouws et al. (1985) and in the experiments in the shallow waters of the Black and Baltic Seas by Davidan et al. (1995). The spectral width was parametrizated as inversely proportional to the group velocity $C_g(x)/C_g(\infty) = 1+2x/\sinh(2x)$ ($C_g$ is group velocity, $x = kh$), which has a maximum at the depth $kh = 1$. Hence spectra are narrow at $kh = 1$ and broad at the other depths (Figure 1). The difference with the experiment is as follows. In the experiment, broadening of the spectrum was not so much as was found here, because the energy conserving computation procedure makes the spectrum very narrow. Actually, the spectrum is broadened by the subharmonics due to the depth. Subharmonics are always presented in the finite depth case and observed in the spectra measured in the wave tanks and shallow water. High wave modes make the wave's crests sharp on the shallow water. In the kinetic equation this effect is de-

scribed by three wave-wave (not resonant) interaction terms which are contained in the denominators of the kernel function.

Here the spectral parameters of one type as functions of time and depth are combined in one plot. They are shown on Figure 1 versus time and depth: wave energy $E(t,h)(m^2)$, frequency of spectral maximum $\omega_0(t,h)$ (nondimensional), spectral maximum $S_0(t,h)(m^2s)$, parameter of spectral width $\gamma(t,h)$, and width of the angular spectrum $n(t,h)$. The wave energy here remains practically constant in time for all depths. The energy shown in Figure 1a is obtained by integration of the spectrum, constructed from its parameters. During calculations, the energy is conserved with much better accuracy.

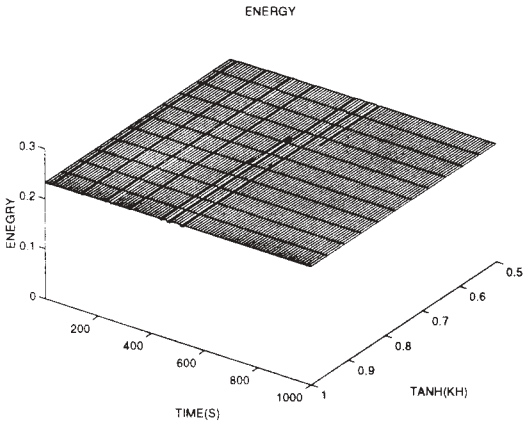


Figure 1. Spectral parameters as functions of time and depth from (7). Below perpective views are contour lines. a) energy $E(t)$ (9).

The most interesting result from Figure 1 is the narrowing of the frequency spectrum ($\gamma = 40$) and of the angular spectrum ($n = 40$), which takes place at the depth $k_0 h = 1$. The spectral narrowing obtained here is a new and very interesting result. A further reduction in depth would cause spectral broadening. Spectral narrowing is seen in all parameters: in dependence of the frequency of the spectral peak (Figure 1b)

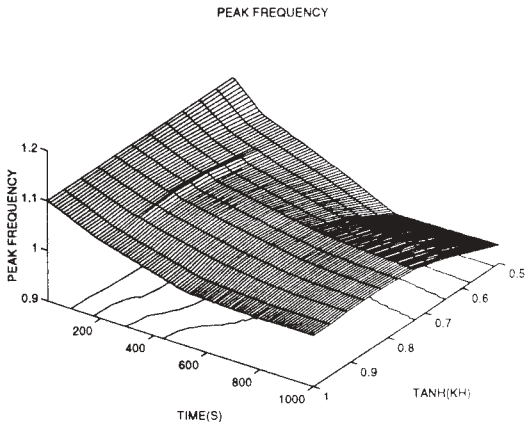


Figure 1b. Frequency of spectral peak $\omega_0(t)$.

of the spectral maximum (Figure 1c),

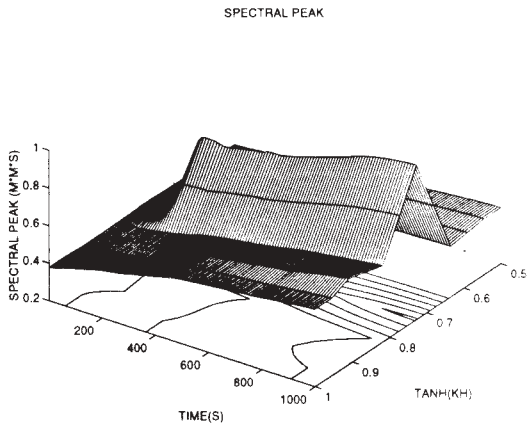


Figure 1c. Spectral maximum $S_0(t)$.

in the width of the frequency spectrum (Figure 1d),

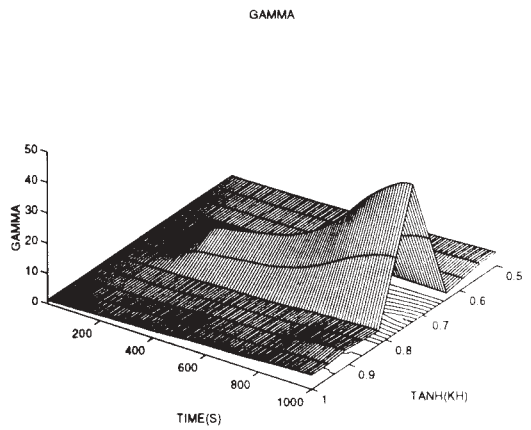


Figure 1d. Spectral sharpness $\gamma(t)$.



AUTHOR INDEX TABLE OF CONTENTS

and in the width of the angular spectrum (Figure 1e)

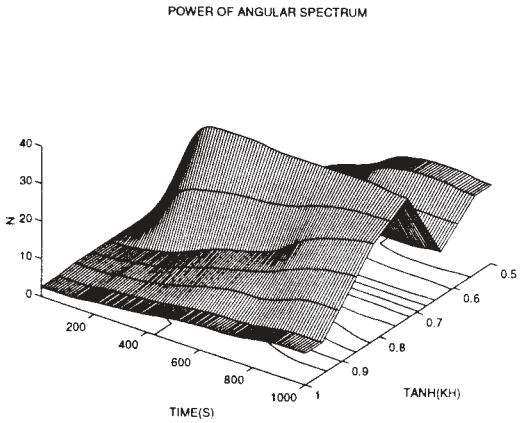


Figure 1e. Width of angular spectrum $n(t)$.

At the same time peak frequency $\omega_0(t)$ diminishes for all depths. One might suppose, that the wave field from the 3-dimensional on large depths becomes 2-dimensional in small depths. The degree of spectral narrowing becomes very large. The frequency narrowing in the model is much greater than in the experimental one, but the angular spectrum narrows to a value close to that of the experiment ($n = 40$). From the experiments in shallow water of the Black and Baltic Seas, the values of the Mitsuyasu-Hasselmann angular parameter were obtained. On Figure 2a are plotted the normalization factors $B$ from(6) (dashed line) and of Mitsuyasu-Hasselmann $B = [\int \cos^{2n}(\theta/2)d\theta]^{-1}$ $(-\pi \leq \theta \leq \pi)$(solid line).

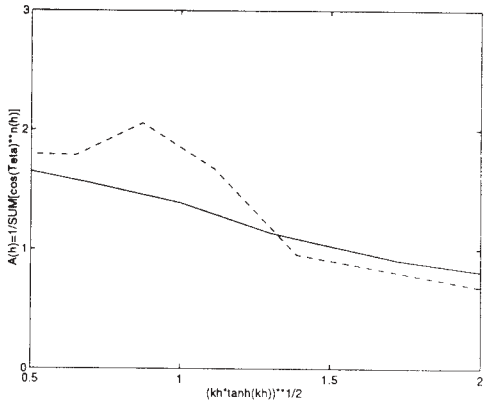


Figure 2a. Normalization for the angular spectra: (6)(- - - -) Mitsuyasu-Hasselmann: (——) Davidan et al. (1995).

One can see that they are close to each other: both the experimental and model angular spectra narrow with a reducing of the depth. The difference between them is that in the model, $n$ has a maximum at $kh = 1$, while in the experiment, it hasn't. If we include bottom friction in the model, which works as a low frequency filter $S_{bot} \sim \cosh^{-2}(kh)$, then the model graph on Figure 2a will go lower than at present and closer to the experimental curve. If wind generation is considered in the spectral peak ($S_{in} \sim S_0\omega_0(U/C_0\cos(\theta) - 1)$), for the wind input, where $U$ is the wind speed, and $C_0$ is the phase speed of the main wave components with frequency $\omega_0$), then the effect obtained will be revealed even more. Wave breaking obviously reduces spectral narrowing significantly.

Finally, let us show the conservation of the other two integrals: action and momentum from Phillips (1980). They are taken without factor $4\pi^2$ in (3). Action is:

$$F(t) = \int_{-\infty}^{\infty} N(\mathbf{k}, \mathbf{t})\mathbf{dk}, \qquad (11)$$

and the X-component of the momentum is:

$$M(t) = \int_{-\infty}^{\infty} N(\mathbf{k}, \mathbf{t})\mathbf{k}\cos(\theta)\mathbf{dk}. \qquad (12)$$

They as function versus depth and time are shown in Figure 2b,c. It is seen that action is conserved both in depth and time, while momentum is constant only in time and grows approximately 1.5 times with a reduction of the depth. This is because the wave number increases by 1.5 times if depth is diminished.

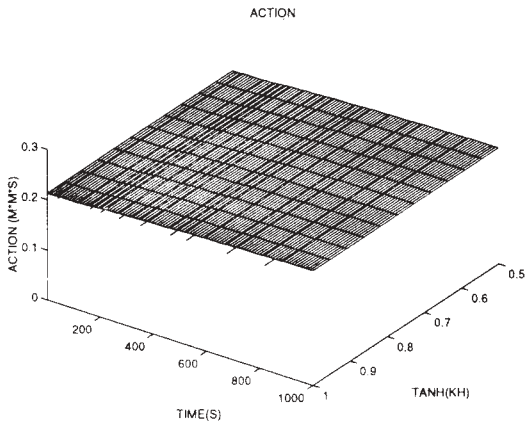


Figure 2b. Action $F(t)$ (11).

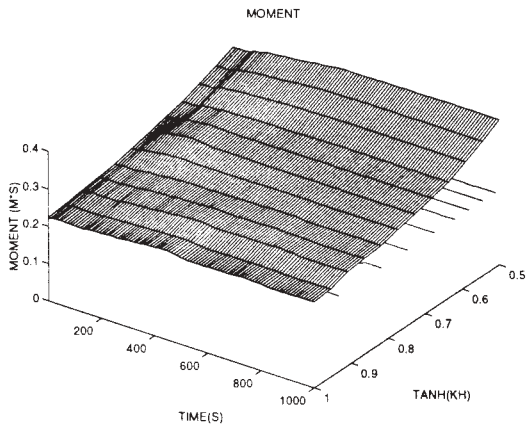


Figure 2c. Momentum $M(t)$ (12).

## 4. CONCLUSION

From the numerical analysis the following is concluded: 1) The realization of the steady angular spectrum after a long-term spectral evolution is due to nonlinearity. 2) In a sea of finite depth, the wave spectrum (a) considerably narrows at the depth which equals to $1/2\pi$ of the wavelength from the spectral maximum; (b) broadens if depth is reduced more.

## 5. ACKNOWLEDGEMENTS

The author would like to thank Dr. Norden E. Huang and Dr. Steven R. Long of NASA/GSFC, who have read the manuscript and suggested numerous improvements in the presentation of the results. I would also like to thank Professor O. M. Phillips of the Johns Hopkins University and Professor V. Zakharov of the University of Arizona for their stimulating discussions.

## 6. REFERENCES

**Bouws E., etc** , 1985: Similarity of the wind wave spectrum in finite depth water. *J. Geph. Res.*, 90, C1, 975-986.

**Davidan I.N., etc** , 1995: Problems of studing and mathematical modeling of wind waves.- St Petersbourg, Ed by Gidrometeoizdat, 472.

**Fox M.J.** , 1976: On the nonlinear transfer of the energy in the peak of a gravity wave spectrup. *Proc. Roy. Soc. London*, A 348, 467-483.

**Frelich M.H., Guza R.T.** , 1984: Nonlinear effects on shoaling surface gravity waves. *Phil. Trans. R. Soc. Lond.*, A 311, 1-41.

**Hasselmann K.** , 1962: On the nonlinear energy transfer in a gravity wave spectrum. Part 1. General theory. *J. Fluid Mech.*, 12, 481-500.

**Hasselmann K.** , 1963a: On the nonlinear energy transfer in a gravity wave spectrum. Part 2. Conservation theorems, wave-particle analogy: irreversibility. *J. Fluid Mech.*, 15, 273-281.

**Hasselmann K.** , 1963b: On the nonlinear energy transfer in a gravity wave spectrum. Part 3. Evaluation

of the energy flux and swell-sea interactions for a Neumann spectrum. *J. Fluid Mech.*, 15, 385-398.

**Herterich K., Hasselmann K.** , 1980: A similarity relation for the nonlinear transfer in a finite depth gravity-wave spectrum. *J. Fluid Mech.*, 97, 215-224.

**Hasselmann S, Hasselmann K** 1985: Computation and Parametrizations of the Nonlinear Energy Transfer in a Gravity Wave Spectrum. Part I: A New Method for Efficient Computation of the Exact Nonlinear Transfer Integral. *J. Phys. Oc.*, 15, 11, 1369-1377.

**Kalmykov V.A.** , 1994: Evolution of waves of swell in the shallow sea. *Dokladi Akademii Nauk Ukraini*, 10, 101-106.

**Kalmykov V.A.** , 1995: Evolution of the swell from nonlinear interactions in the water of finite depth. *Marine Hydrophysical Journal*, 5, 52-61.

**Krasitski V.P., Kalmykov V.A.** , 1993: About four-wave reduced equations for surface gravity waves. *Izvestija Akademii Nauk Rossii, Fizika Atmosferi i Okeana*, 29, 2, 237-243.

**Krasitski V.P.** , 1993: 5 wave kinetic equation for surface gravity waves. *Marine hydrophysical journal*, 6, 17-25.

**Lavrenov I.V.** , 1991: Weakly-nonlinear evolution of wave spectrum on shallow water. *Izvestija Akademii Nauk SSSR, Fizika Atmosferi i Okeana*, 27, 12, 1372-1378.

**Longuet-Higgins M.S.** , 1976: On the nonlinear energy transfer of energy in the peak of a gravity wave spectrum: A simplifyed model. *Proc. Roy. Soc. London*, A 347, 311-328.

**Masuda A.** , 1980: Nonlinear Energy Transfer Between Wind Waves. *J. Phys. Oc.*, 10, 2082-2093.

**Masson D.** , 1993: Nolinear Coupling, between Swell and Wind Waves. *J. Phys. Oc.*, 23, 6, 1249-1258.

**Phillips O.M.** , 1980: Dynamics of upper ocean.- Leningrad, Ed. by Gidrometeoizdat, 319 (translated to Russian).

**Polnikov V.G.** , 1990: Numerical calculation of kinetic equation for surface gravity waves. *Izvestija Akademii Nauk SSSR, Fizika Atmosferi i Okeana*, 26, 2, 168-176.

**Resio D., Perrie W.** , 1991: A numerical study of nonlinear energy fluxes due to wave-wave interactions. Part I. Methodology and basic results. *J. Fluid Mech.*, 223, 603-629.

**Komen G., L.Cavaleri, etc** , 1994: Dynamics and modeling of ocean waves. Cambridge University Press, 532.

**Zakharov V.E., Smilga A.V.** , 1981: About quasi-uniform spectra in the weak turbulence. *JETP (Soviet Physics)*, 81, 4, 1318-1326.

# NUMERICAL COMPUTATIONS OF THE NONLINEAR ENERGY TRANSFER OF GRAVITY-WAVE SPECTRA IN FINITE WATER DEPTHS

Noriaki Hashimoto, H. Tsuruya, and Y. Nakagawa,

Port and Harbour Research Institute,
Ministry of Transport,
Nagase, Yokosuka, Japan

**This paper was withdrawn from the workshop after the Preprints were sent to the printers; therefore, pages 301 - 321 have been removed.**

# USE OF TWO NCEP/NCAR REANALYSIS PRODUCTS TO HINDCAST THE WAVE CLIMATE AT NOME, ALASKA

Jon M. Hubertz

Applied Coastal Modeling
Vicksburg, Mississippi, USA

Willie A. Brandon

U. S. Army Engineer Waterways Experiment Station
Vicksburg, Mississippi, USA

## 1. INTRODUCTION

Wave climate information was required as part of a harbor renovation project at Nome, Alaska. No measurements were available, so a numerical hindcast was proposed. This project coincided in time with the availability of the National Center for Environmental Prediction (NCEP) and the National Center for Atmospheric Research (NCAR) Reanalysis Products, Kalnay (1996). Among these products is the global surface (10m) wind, which is considered the most accurate readily available source of winds for this hindcast project. These winds are available on compact disk (CD) for the period 1987-1996 for $10.00 per CD per year. These data are at an interval of 12 hours on the 192 by 94 point Gaussian grid. These same data at an interval of 6 hours on the same grid are available from NCAR as a special request at a much higher price. One part of this study examines the difference in wave results using the two different wind products.

Another part of this study examines the source of long period swell that interrupted dredging operations at the harbor during June of 1997. The passage of Typhoon Opal in the Western Pacific was identified as the source of this swell by conducting a hindcast of this storm.

Finally, to supplement the hindcast from 1987 through 1996, the period from 1976-1986 was examined to identify storms producing high waves at Nome. These storms were hindcasted to add to the extreme values of wave height at Nome.

## 2. HINDCAST APPROACH

Nome is located on the west coast of Alaska in the northeast corner of the Bering Sea, Figure 1. Potentially, the project site is open to waves from the Pacific Ocean propagating as swell through the Aleutian Islands or in a northeasterly direction across the Bering Sea. However, we feel most wave energy reaching the site has its origin in the Bering Sea and so limit the hindcast to this region.

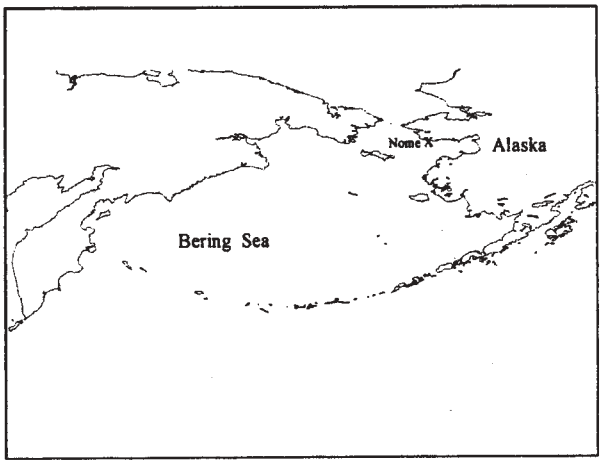


Figure 1. Hindcast study region.

The U. S. Army Corps of Engineers wave model WISWAVE 2.0, Hubertz (1992), was used to conduct the hindcast. This is a second generation, time dependent, directional spectral model, developed by Resio (1987, 1989), that can operate in a nested grid mode either in deep or shallow water. In this study it was applied in deep water over the Bering Sea on the same grid as the NCEP/NCAR reanalysis winds. This is referred to as the Level 1 grid. A nested grid with resolution four times that of Level 1 was used over the region to the east of St. Lawrence Island, the island to the west of Nome in Figure 1. The model was applied in the shallow water mode on this grid and referred to as the Level 2 grid.

Finally, spectral wave information was transformed from a point about 22 km offshore of the project site in

the Level 2 grid to a point 1 km from shore at a depth of 10 m using the U.S. Army Corps of Engineers model STWAVE, Resio (1988). The STWAVE model is a steady state, shallow water, directional spectral model that can account for the possible addition of wave energy over a reach due to wind input. This model was applied on a 0.5 nm grid extending about 10 nm on either side of the project site. This is referred to as the Level 3 grid. The Level 1, 2, and 3 grids are shown in Figures 2, 3, and 4, respectively.

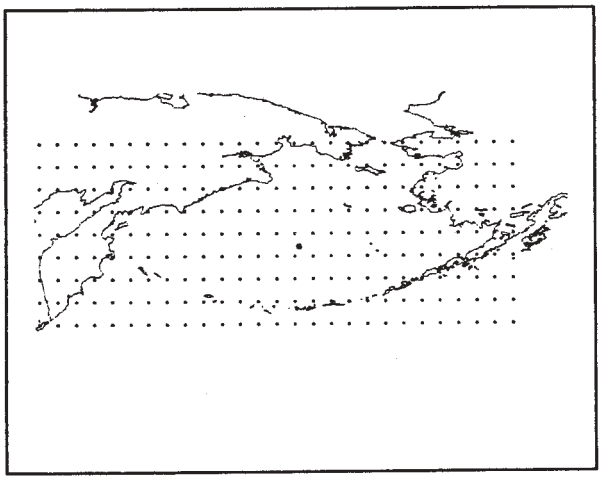

Figure 2. Level 1 grid. Circled point is location of buoy 46035. Filled box is location of Nome.

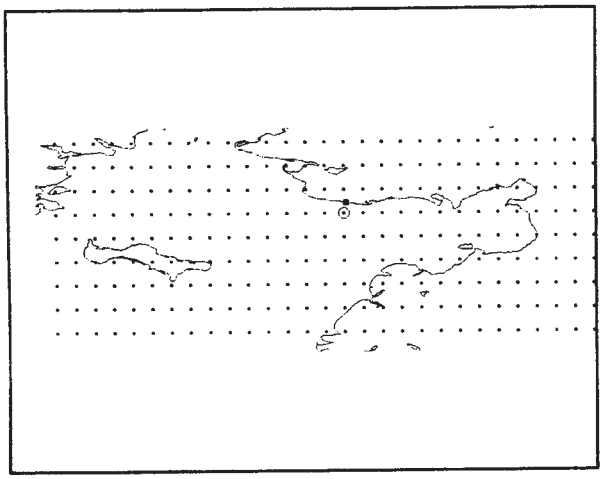

Figure 3. Level 2 grid. Results saved at circled point for input to Level 3.

## 3. MEASUREMENTS FROM BUOY

The National Oceanic and Atmospheric Administration (NOAA) maintained a buoy (46035) in the Bering Sea from 1987-1996. Wind and wave measurements were made from this buoy at the location shown in Figure 2. To our knowledge these are the only wave measurements available in the region for the hindcast period. Wave height and peak period results from the Level 1 grid point closest to the buoy were compared to measurements from the buoy to verify the hindcast results for this phase of the study. No directional measurements were available from the buoy.

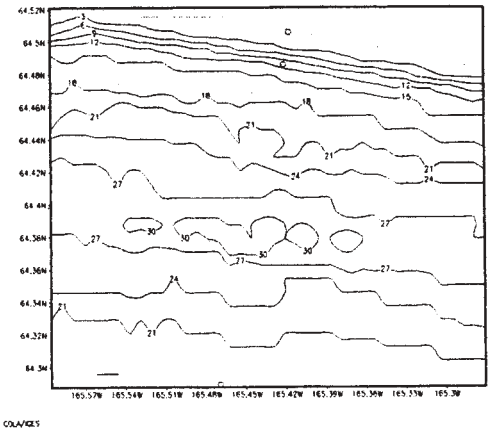

Figure 4. Level 3 depths (m). Input is at circled point offshore. Results saved at circled point near shore. Project site is at circled point on shore.

Wave height and peak period from the model and buoy were plotted for each year. An example from 1992 is shown in Figures 5-6, respectively. Gaps in the buoy record appear occasionally due to maintenance or repair. These plots give a qualitative indication of model performance. Both heights and periods show seasonal variation with largest values in the late fall, winter, and early spring months. Model wave heights accurately represent the occurrence of storm events in magnitude and time at this location. Model peak periods have a tendency to underpredict the magnitude and occurrence of long period events. This is partly a problem with the model and has been noticed in other studies but on a smaller scale. For example, in other studies of the Atlantic and Gulf of Mexico, Hubertz (1994), long period events may be underestimated by 1-2 seconds. The larger difference in this study, we believe, is due to long period swell propagating into the region from the Pacific Ocean (both North and South) which is not being modeled. Swell events in the winter months are probably due to North Pacific storms and in the summer months due to typhoons or from South Pacific winter storms. In the absence of measurements, we do not know how this translates to swell conditions at Nome. Interactions with islands

and bathymetry will have an effect. Model results include these effects and can be used as a best guess, but the percent occurrence of long period events may need to be adjusted upward to accurately represent the wave period climate at Nome.

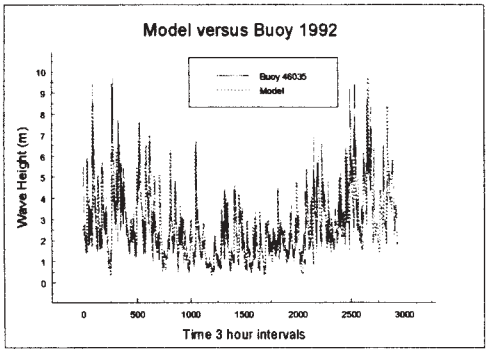


Figure 5. Model wave height results versus buoy measurements for 1992.

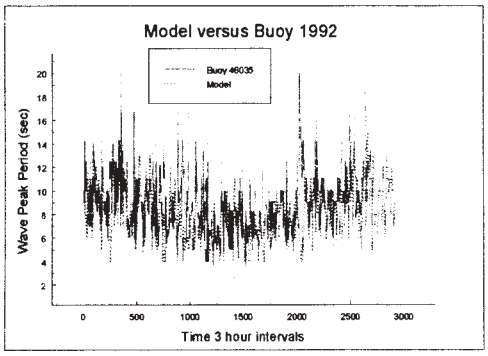


Figure 6. Model wave peak period results versus buoy measurements for 1992.

A quantitative indication of model performance is provided in Tables 1 and 2. These tables quantify by year the annual wave height and peak period means and the difference between means, the bias. The maximum height and period for each year for model and buoy are tabulated. These values do not necessarily occur at the same time. The measure of annual mean difference between model and buoy, regardless of sign, is provided as the root mean square difference (RMSD). There is negligible bias between model and buoy wave heights and typically a mean difference of 0.5 m. Maximum values are equivalent for each year. There is negligible bias for peak periods and a mean difference of about 5 seconds due mainly to an underestimate of long periods, as indicated by the differences between model and buoy maximum periods. The occurrence of wave heights in 0.5-m increments for model and buoy results is shown in Figure 7. The occurrence for peak period in 1-second increments for model and buoy results is shown in Figure 8. The distribution of model and buoy heights agrees well. The distribution of model and buoy periods also agrees well with the exception of an underprediction for periods 11 seconds and longer.

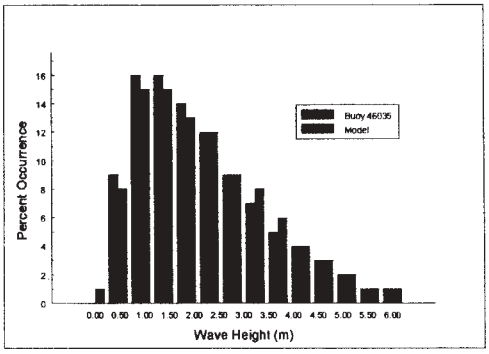


Figure 7. Percent occurrence of model versus buoy wave heights for 1987-1996.

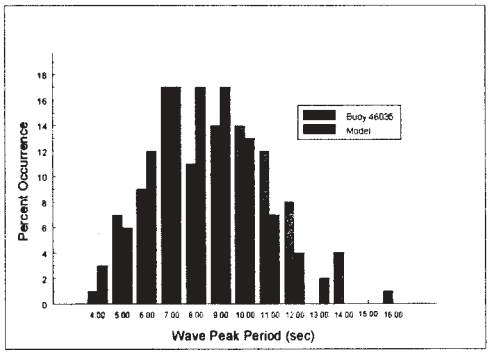


Figure 8. Percent occurrence of model versus buoy wave peak periods for 1987-1996.

Table 1. Comparison of hindcast wave heights (m) to measurements from buoys.

| Year | Mean | | | | Bias[1] | RMSD | Maximum | |
|---|---|---|---|---|---|---|---|---|
| | Buoy | No. | Model | No. | | | Buoy | Model |
| 1987 | 2.91 | 2334 | 2.72 | 2920 | -0.19 | 0.55 | 13.0 | 12.5 |
| 1988 | 2.42 | 2810 | 2.52 | 2928 | 0.10 | 0.44 | 10.2 | 9.3 |
| 1989 | 2.72 | 2734 | 2.80 | 2920 | 0.02 | 0.53 | 12.1 | 11.6 |
| 1990 | 2.51 | 2870 | 2.60 | 2920 | 0.09 | 0.52 | 11.4 | 12.7 |
| 1991 | 3.08 | 1720 | 2.64 | 2920 | -0.44 | 0.53 | 10.8 | 10.2 |
| 1992 | 2.56 | 2489 | 2.68 | 2928 | 0.12 | 0.49 | 9.7 | 9.8 |
| 1993 | 2.54 | 2457 | 2.62 | 2920 | 0.08 | 0.48 | 11.3 | 10.0 |
| 1994 | 2.96 | 1958 | 2.90 | 2920 | -0.06 | 0.68 | 11.4 | 12.3 |
| 1995 | 2.04 | 2143 | 2.48 | 2920 | 0.44 | 0.42 | 9.1 | 10.1 |
| 1996 | 2.66 | 1651 | 2.71 | 2441 | 0.05 | 0.72 | 9.2 | 10.0 |
| All Years | 2.64 | | 2.67 | | 0.03 | 0.54 | 10.8 | 10.8 |

[1] Model - buoy.

Table 2. Comparison of hindcast wave periods (sec) to measurements from buoys.

| Year | Mean | | | | Bias[1] | RMSD | Maximum | |
|---|---|---|---|---|---|---|---|---|
| | Buoy | No. | Model | No. | | | Buoy | Model |
| 1987 | 9.4 | 2334 | 8.3 | 2920 | -1.1 | 5.0 | 20.0 | 16.0 |
| 1988 | 8.7 | 2810 | 8.0 | 2928 | -0.7 | 4.4 | 16.7 | 13.0 |
| 1989 | 9.1 | 2733 | 8.4 | 2920 | -0.7 | 4.3 | 20.0 | 15.0 |
| 1990 | 9.0 | 2870 | 8.1 | 2920 | -0.9 | 5.5 | 20.0 | 16.0 |
| 1991 | 9.5 | 1720 | 8.2 | 2920 | -1.3 | 5.2 | 20.0 | 15.0 |
| 1992 | 8.9 | 2489 | 8.2 | 2928 | -0.7 | 6.4 | 20.0 | 15.0 |
| 1993 | 9.1 | 2457 | 8.2 | 2920 | -0.9 | 6.4 | 20.0 | 14.0 |
| 1994 | 9.3 | 1958 | 8.4 | 2920 | -0.9 | 4.8 | 25.0 | 15.0 |
| 1995 | 8.3 | 2143 | 8.0 | 2920 | -0.3 | 6.4 | 25.0 | 15.0 |
| 1996 | 9.3 | 1651 | 8.3 | 2441 | -1.0 | 6.6 | 20.0 | 16.0 |
| All Years | 9.1 | | 8.2 | | -0.9 | 5.5 | 20.7 | 15.0 |

[1] Model - buoy.

## 4. WIND INPUT AT 6 VERSUS 12 HOURS

These results were obtained using the reanalysis winds at a frequency of 6 hours, that is, the analysis wind fields at 00 and 12 UT and the forecast winds at 06 and 18 UT. In addition, we hindcast one year, 1992, using only the 00 and 12 UT, winds that are readily available on CD, to examine the differences in basic wave parameters as would be used in an engineering study. The minimum, maximum, mean, median, and standard deviation for wave height and peak period over 1992, as calculated using analysis and forecast winds, are identical to those values calculated using only analysis winds and linearly interpolating in time. The difference in wave heights, as calculated using the different wind inputs over the year, that is, Hs (06)-Hs (12), gave a minimum difference of -1.4 m, a maximum difference of 1.8 m, a mean difference of 0.03 m, a median difference of 0.0 m, and a standard deviation of 0.22 m. Similar values for peak period are -4.0, 4.0, 0.0, 0.0, and 0.58 seconds, respectively. The correlation coefficients for wave height and peak

period at 6- versus 12-hour inputs are 0.99 and 0.96, respectively. Other measures and plots, not included here, all indicate little, if any, difference in hindcast results using the different wind inputs.

## 5. LEVEL 2 HINDCAST

Boundary conditions linking the Level 1 grid to the Level 2 grid were saved at Level 1 points during the 10-year hindcast. Referring to Figure 2 and noting that the lower left grid point is I=1,J=1, boundary spectra were saved at Level 1 points upward and to the right from point (18,7), respectively, to the intersection of land. Level 1 winds were interpolated to the Level 2 grid that is four times as dense. The wave model was applied with these winds and boundary conditions as input, and results were saved at the circled point in Figure 3. The presence of St. Lawrence Island, shown on the left side of Figure 3, and shallow regions near coasts were included in the model application using a land-water matrix to allow calculation only at grid points over water and bathymetry values from navigational charts, respectively.

Level 2 results were saved as records containing condensed spectral information and referred to as a one-line file. An example is as follows:

1 87082903 5 9 5 173 3 265 0 0 0 107 0 0 0 0 0 0 0 0 0 0 1 3 6 81911 9121713 0 0 0 0 0 0 0 0 0 0 056555451504649494846

The first number (1) is a station identifier, i.e., Station 1. In this study there is only one station. The next eight numbers are the date and time, i.e., 1987 August 29 0300 referred to the universal time coordinate. The next number is the wave height in meters times 10, that is 0.5 meter, in this case. The next two numbers are the peak and mean periods in seconds, i.e., 9 and 5 seconds, respectively. The peak period is the reciprocal of the central frequency in the band containing the largest energy density in the spectrum. The mean period is the energy weighted mean across all frequencies. The next number is the mean wave direction in degrees from which the waves are coming. This is the mean across all frequency bands. It is related to compass directions, i.e., 173 degrees or almost directly from the south. The next two numbers are the wind speed (3) in meters/seconds and wind direction (265) in degrees with the same convention as the waves. The next three numbers are for water level and x, y components of current, which are not used in the study. The next number (107) is the total energy in the discrete part of the spectrum in meters$^2$ multiplied by 10,000. The remaining part of the record consists of two sets of 20 numbers each. The 20 increments are related to the 20 frequency bands used in the study. The first set is the percent of total energy density in each of the 20 bands. In this case, the band containing the largest energy density is band 15 containing 19 percent. The second set of 20 numbers is the mean direction in each of the 20 frequency bands expressed as a percent of 360 degrees. In this case, the mean at the peak frequency is 50 or 50 percent of 360 degrees or 180 degrees.

The detailed description above is given to help in explaining how this one-line file is used as input to the STWAVE model. The Level 2 one-line file consists of 10 years of information every 3 hours at this location. The program, which calculates the spectral input for STWAVE, first filters the information for records only occurring in the period May through November. This is based on the assumption the location is iced over from December through April. Second, it examines each frequency band for a given record to determine if there is energy in that band propagating toward shore in the STWAVE half plane from 95 to 265 degrees, Figure 4. Wave directions within 5 degrees of the model shoreline boundary are excluded. Next, the program calculates the total energy propagating toward shore on the input boundary. If this is equivalently less than 0.5 m, it is ignored. A spectrum is written for records passing these criteria by placing energy density in the appropriate frequency and directional bands of the STWAVE input spectrum. This input spectrum consists of the same 20 frequency bands used in Level 2 and 34 directional bands of 5 degrees each.

During the months of May through November for 1987-1996 there were 8,226 cases meeting the above criteria. Results are calculated for each case and saved at a point 1 km from shore at a depth of 10 m. The STWAVE grid is shown in Figure 4. It consists of 40 grid points in the along shore direction and 29 points in the offshore. The grid spacing is 0.5 nm. The Level 2 input and Level 3 output points are circled. The filled square is the project site. Depths at the grid points were obtained from files for U.S. coastlines, stored on the Coastal Engineering Data Retrieval System (CEDRS) maintained by the Coastal and Hydraulics Laboratory at the U.S. Army Engineer Waterways Experiment Station. Depths are referenced to mean lower low water (MLLW).

## 6. LEVEL 3 TRANSFORMATION

The STWAVE model can be run with wind input, which is assumed constant in speed and direction over the grid. In this mode the input spectrum is modified both by the wind input, wave interaction source terms, and refraction and shoaling. Without wind input only refraction and shoaling act. If the wind speed is greater than 5 m/second and toward a direction within +/- 10 degrees of the direction at the peak of the input spectrum, it is allowed to act. If not, the spectrum is propagated without wind input.

Results at the Level 3 point are saved as a series of wave heights, periods, and directions for all Mays, Junes, Julys, Augusts, Septembers, Octobers, and Novembers in the 1987-1996 period. Results for each group of months were sorted by direction into six directional bands, 30 degrees in width from 90 to 270 degrees. That is band 1 is from 90 to 120 degrees, band 2 from 120 to 150 degrees, etc. Within each of these directional bands, height and period occurrences were sorted by 0.5-m and 1-second intervals and joint distribution tables of height by period were formed for months and directions. An example of these results is shown in Table 3 for all Octobers and a water level at MLLW. There are no occurrences in bands 5 and 6 (210 to 270 degrees) for any of the months. This is assumed to be due to refraction which moves energy, which is contained in these bands offshore, into bands 4 or lower (210 degrees or less) by the time the energy propagates to the Level 3 point. Typically, 80-90 percent of incident wave energy is in bands 3 and 4 with little variation by month. About 90 percent of the wave heights are in the first two bands, or less than 1 m. Less than 1 percent of the cases are above 2.5 m with the maximum being 4.4 m. Largest heights occur in the months of October and November. Peak periods are more evenly distributed through the 4- to 16-second bands with most cases in the 6-10 seconds range. Longer periods, 13-16 seconds, occur in the months of September, October, and November.

The same 8,226 cases were applied on a water level elevated to 3.96 above MLLW. As an example, results for all Octobers are presented in Table 4. Energy is still absent in band 6 but now appears in band 5 because of less refraction due to deeper water. However 80-90 percent of the cases are still incident in bands 3 and 4. Most wave heights are now in the 0.5- to 1.4-m bands, with a little over 1 percent in the 3.0-m and greater bands. The maximum height is now 5.3 m. Periods are almost identically distributed, as in the MLLW case, since they are conservative with the exception of changes due to local wind effects. The complete set of results at the Level 3 output point will be used as the basis for determining input wave conditions for physical model tests of harbor entrance designs.

Table 3. All Octobers, 1987-1996, Level 3, MLLW. Joint distribution of wave height and peak period. Number of occurrences by 30 degree angle band.[1]

Angle band 1 90-120 degrees

| Hs(m) | Tp(sec) | | | | | | | | | | | | |
|---|---|---|---|---|---|---|---|---|---|---|---|---|---|
| | 4 | 5 | 6 | 7 | 8 | 9 | 10 | 11 | 12 | 13 | 14 | 15 | 16 |
| 0.0 | 1 | | | | | 1 | 1 | | | | | | |
| 0.5 | 1 | 3 | | 2 | | 1 | | | | | | | |
| 1.0 | | | | | | | | | | | | | |
| 1.5 | | | | | | | | | | | | | |
| 2.0 | | | | | | | | | | | | | |
| 2.5 | | | | | | | | | | | | | |
| 3.0 | | | | | | | | | | | | | |
| 3.5 | | | | | | | | | | | | | |
| 4.0 | | | | | | | | | | | | | |
| 4.5 | | | | | | | | | | | | | |
| 5.0 | | | | | | | | | | | | | |

Angle band 2 120-150 degrees

| Hs(m) | Tp(sec) | | | | | | | | | | | | |
|---|---|---|---|---|---|---|---|---|---|---|---|---|---|
| | 4 | 5 | 6 | 7 | 8 | 9 | 10 | 11 | 12 | 13 | 14 | 15 | 16 |
| 0.0 | 6 | 8 | 6 | 1 | 3 | 1 | 1 | 2 | | | | | |
| 0.5 | 6 | 19 | 13 | 3 | 11 | 3 | 9 | 2 | 1 | | | | |
| 1.0 | | 4 | 18 | 12 | 2 | | | | | | | | |
| 1.5 | | 1 | 2 | 7 | 2 | | | | | | | | |
| 2.0 | | | | 3 | 4 | 1 | | | | | | | |
| 2.5 | | | | | 3 | 2 | | | | | | | |
| 3.0 | | | | | | 4 | 1 | | | | | | |
| 3.5 | | | | | | | 1 | | | | | | |
| 4.0 | | | | | | | 2 | | | | | | |
| 4.5 | | | | | | | | | | | | | |
| 5.0 | | | | | | | | | | | | | |

Angle band 3 150-180 degrees

| Hs(m) | Tp(sec) | | | | | | | | | | | | |
|---|---|---|---|---|---|---|---|---|---|---|---|---|---|
| | 4 | 5 | 6 | 7 | 8 | 9 | 10 | 11 | 12 | 13 | 14 | 15 | 16 |
| 0.0 | 10 | 1 | 18 | 10 | 26 | 16 | 29 | 21 | 4 | 4 | 5 | | |
| 0.5 | 3 | 8 | 11 | 2 | 19 | 20 | 24 | 9 | | | | | |
| 1.0 | | 1 | 19 | 15 | 2 | 1 | 5 | | | | | | |
| 1.5 | | | 3 | 8 | 14 | 1 | | | | | | | |
| 2.0 | | | | | 9 | 9 | 1 | | | | | | |
| 2.5 | | | | | 2 | 4 | | | | | | | |
| 3.0 | | | | | | 2 | 1 | | | | | | |
| 3.5 | | | | | | 1 | 2 | | | | | | |
| 4.0 | | | | | | | 1 | | | | | | |
| 4.5 | | | | | | | | | | | | | |
| 5.0 | | | | | | | | | | | | | |

[1] Angles with respect to compass directions, i.e., 90 from east, 180 from south, 270 from west. Blank entries imply no occurrences.

(Continued)

Table 3. (Concluded)

Angle band 4 180-210 degrees

Hs(m) Tp(sec)

| | 4 | 5 | 6 | 7 | 8 | 9 | 10 | 11 | 12 | 13 | 14 | 15 | 16 |
|---|---|---|---|---|---|---|---|---|---|---|---|---|---|
| 0.0 | 15 | 22 | 36 | 60 | 56 | 69 | 148 | 84 | 60 | 35 | 18 | 8 | 3 |
| 0.5 | | 4 | 10 | 7 | 6 | 17 | 18 | 16 | 8 | | | 4 | 1 |
| 1.0 | | | 1 | 2 | 3 | 2 | 1 | 3 | 1 | | 2 | 1 | |
| 1.5 | | | | 2 | | 2 | 1 | 1 | 1 | | | | |
| 2.0 | | | | | | 1 | | 2 | | | | | |
| 2.5 | | | | | | | 1 | 1 | | | | | |
| 3.0 | | | | | | | | | | | | | |
| 3.5 | | | | | | | | | | | | | |
| 4.0 | | | | | | | | | | | | | |
| 4.5 | | | | | | | | | | | | | |
| 5.0 | | | | | | | | | | | | | |

Angle band 5 210-240 degrees

Hs(m) Tp(sec)

| | 4 | 5 | 6 | 7 | 8 | 9 | 10 | 11 | 12 | 13 | 14 | 15 | 16 |
|---|---|---|---|---|---|---|---|---|---|---|---|---|---|
| 0.0 | | | | | | | | | | | | | |
| 0.5 | | | | | | | | | | | | | |
| 1.0 | | | | | | | | | | | | | |
| 1.5 | | | | | | | | | | | | | |
| 2.0 | | | | | | | | | | | | | |
| 2.5 | | | | | | | | | | | | | |
| 3.0 | | | | | | | | | | | | | |
| 3.5 | | | | | | | | | | | | | |
| 4.0 | | | | | | | | | | | | | |
| 4.5 | | | | | | | | | | | | | |
| 5.0 | | | | | | | | | | | | | |

Angle band 6 240-270 degrees

Hs(m) Tp(sec)

| | 4 | 5 | 6 | 7 | 8 | 9 | 10 | 11 | 12 | 13 | 14 | 15 | 16 |
|---|---|---|---|---|---|---|---|---|---|---|---|---|---|
| 0.0 | | | | | | | | | | | | | |
| 0.5 | | | | | | | | | | | | | |
| 1.0 | | | | | | | | | | | | | |
| 1.5 | | | | | | | | | | | | | |
| 2.0 | | | | | | | | | | | | | |
| 2.5 | | | | | | | | | | | | | |
| 3.0 | | | | | | | | | | | | | |
| 3.5 | | | | | | | | | | | | | |
| 4.0 | | | | | | | | | | | | | |
| 4.5 | | | | | | | | | | | | | |
| 5.0 | | | | | | | | | | | | | |

Table 4. All Octobers, 1987-1996, Level 3, MLLW+3.96 m. Joint distribution of wave height and peak period. Number of occurrences by 30 degree angle band.[1]

Angle band 1 90-120 degrees

| Hs(m) | Tp(sec) | | | | | | | | | | | | |
|---|---|---|---|---|---|---|---|---|---|---|---|---|---|
| | 4 | 5 | 6 | 7 | 8 | 9 | 10 | 11 | 12 | 13 | 14 | 15 | 16 |
| 0.0 | 3 | | | | | | | | | | | | |
| 0.5 | | | | 1 | | | | | | | | | |
| 1.0 | | | 1 | 1 | | | | | | | | | |
| 1.5 | | | | | | | | | | | | | |
| 2.0 | | | | | | | | | | | | | |
| 2.5 | | | | | | | | | | | | | |
| 3.0 | | | | | | | | | | | | | |
| 3.5 | | | | | | | | | | | | | |
| 4.0 | | | | | | | | | | | | | |
| 4.5 | | | | | | | | | | | | | |
| 5.0 | | | | | | | | | | | | | |

Angle band 2 120-150 degrees

| Hs(m) | Tp(sec) | | | | | | | | | | | | |
|---|---|---|---|---|---|---|---|---|---|---|---|---|---|
| | 4 | 5 | 6 | 7 | 8 | 9 | 10 | 11 | 12 | 13 | 14 | 15 | 16 |
| 0.0 | 1 | 5 | 1 | 1 | 1 | | 1 | | | | | | |
| 0.5 | 6 | 15 | 4 | 1 | 2 | 1 | 1 | | | | | | |
| 1.0 | | 2 | 12 | 5 | 2 | | | | | | | | |
| 1.5 | | 1 | 2 | 2 | 2 | | | | | | | | |
| 2.0 | | | | 1 | 4 | | | | | | | | |
| 2.5 | | | | | | | | | | | | | |
| 3.0 | | | | | 1 | | | | | | | | |
| 3.5 | | | | | | 1 | | | | | | | |
| 4.0 | | | | | | | | | | | | | |
| 4.5 | | | | | | | | | | | | | |
| 5.0 | | | | | | | | | | | | | |

Angle band 3 150-180 degrees

| Hs(m) | Tp(sec) | | | | | | | | | | | | |
|---|---|---|---|---|---|---|---|---|---|---|---|---|---|
| | 4 | 5 | 6 | 7 | 8 | 9 | 10 | 11 | 12 | 13 | 14 | 15 | 16 |
| 0.0 | 1 | | 3 | 1 | 4 | 4 | 1 | | | | | | |
| 0.5 | 4 | 7 | 14 | 2 | 28 | 7 | 14 | 9 | 1 | | | | |
| 1.0 | 2 | 8 | 16 | 3 | 2 | 6 | 11 | 1 | | | | | |
| 1.5 | | 1 | 18 | 22 | 1 | | | | | | | | |
| 2.0 | | | 3 | 10 | 8 | | | | | | | | |
| 2.5 | | | | 1 | 14 | 3 | | | | | | | |
| 3.0 | | | | | 5 | 8 | | | | | | | |
| 3.5 | | | | | 1 | 6 | | | | | | | |
| 4.0 | | | | | | 2 | 1 | | | | | | |
| 4.5 | | | | | | 2 | 3 | | | | | | |
| 5.0 | | | | | | | 4 | | | | | | |

[1] Angles with respect to compass directions, i.e., 90 from east, 180 from south, 270 from west. Blank entries imply no occurrences.

(Continued)

Table 4. (Concluded).

Angle band 4 180-210 degrees

Hs(m) Tp(sec)

| | 4 | 5 | 6 | 7 | 8 | 9 | 10 | 11 | 12 | 13 | 14 | 15 | 16 |
|---|---|---|---|---|---|---|---|---|---|---|---|---|---|
| 0.0 | | 6 | 6 | 7 | 17 | 31 | 56 | 39 | 33 | 18 | 9 | | |
| 0.5 | 10 | 7 | 17 | 46 | 37 | 34 | 86 | 39 | 25 | 19 | 7 | 3 | |
| 1.0 | 9 | 15 | 24 | 13 | 9 | 28 | 37 | 31 | 6 | 1 | 7 | 5 | 4 |
| 1.5 | | 1 | 8 | 8 | 2 | 4 | 17 | 10 | 6 | 1 | | | 3 |
| 2.0 | | | | 6 | 7 | 12 | 1 | 4 | 3 | | 1 | 1 | 1 |
| 2.5 | | | | 1 | 3 | 3 | 2 | 2 | 1 | | 1 | | |
| 3.0 | | | | | | 2 | 1 | 2 | | | | | |
| 3.5 | | | | | | | 1 | 1 | | | | | |
| 4.0 | | | | | | | | | | | | | |
| 4.5 | | | | | | | | | | | | | |
| 5.0 | | | | | | | | | | | | | |

Angle band 5 210-240 degrees

Hs(m) Tp(sec)

| | 4 | 5 | 6 | 7 | 8 | 9 | 10 | 11 | 12 | 13 | 14 | 15 | 16 |
|---|---|---|---|---|---|---|---|---|---|---|---|---|---|
| 0.0 | | | | | 7 | 1 | 6 | 3 | | | | | |
| 0.5 | 1 | | | 1 | 1 | 2 | 1 | | | | | | |
| 1.0 | | 1 | 3 | | 4 | 1 | 3 | | | | | | |
| 1.5 | 2 | 2 | 5 | 1 | | | | | | | | | |
| 2.0 | 3 | | | | | | | | | | | | |
| 2.5 | | | | | | | | | | | | | |
| 3.0 | | | | | | | | | | | | | |
| 3.5 | | | | | | | | | | | | | |
| 4.0 | | | | | | | | | | | | | |
| 4.5 | | | | | | | | | | | | | |
| 5.0 | | | | | | | | | | | | | |

Angle band 6 240-270 degrees

Hs(m) Tp(sec)

| | 4 | 5 | 6 | 7 | 8 | 9 | 10 | 11 | 12 | 13 | 14 | 15 | 16 |
|---|---|---|---|---|---|---|---|---|---|---|---|---|---|
| 0.0 | | | | | | | | | | | | | |
| 0.5 | | | | | | | | | | | | | |
| 1.0 | | | | | | | | | | | | | |
| 1.5 | | | | | | | | | | | | | |
| 2.0 | | | | | | | | | | | | | |
| 2.5 | | | | | | | | | | | | | |
| 3.0 | | | | | | | | | | | | | |
| 3.5 | | | | | | | | | | | | | |
| 4.0 | | | | | | | | | | | | | |
| 4.5 | | | | | | | | | | | | | |
| 5.0 | | | | | | | | | | | | | |

## 7. TYPHOON OPAL

Maintenance dredging operations at the entrance to Nome harbor were halted June 21,1997, due to swell waves 1.2 m high. No storms were in the region. This is not an unusual situation as noted in dredging records. As mentioned above, records from buoy 46035 in the central Bering Sea indicate occurrences of long period waves in the summer months. It is reasonable that some of this is propagating toward Nome. The June 1997 shutdown of operations is attributed to Typhoon Opal. The track of Opal is shown in Figure 9.

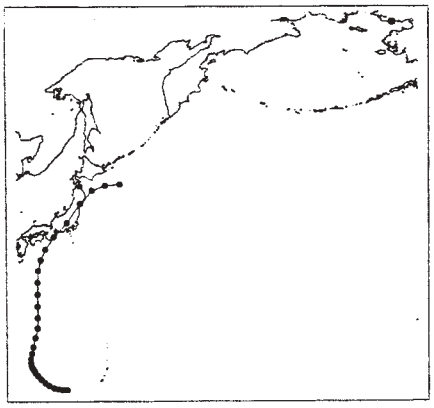

Figure 9. Track of Typhoon Opal 9706131200 to 97062106 UT at intervals of 6 hours

Maximum sustained wind speeds were in excess of 75 knots while the storm progressed from 17 to 34 degrees N. The storm was hindcast in the region shown in Figure 9 on a grid with spacing of 0.5 degrees. Wind fields due to the storm only were calculated with a planetary boundary layer tropical storm model and input to the wave model. The model predicted the arrival of 18-20 second swell with a height of 0.1-0.2 m on 21 June the same day dredging activity was shut down due to swell conditions, Figure 10. Even this somewhat general hindcast illustrates that typhoons in the Eastern Pacific can influence the wave climate at Nome and impact engineering activities.

## 8. EXTREME EVENTS, 1976-1986

The final part of this study was the identification of extreme storm events during the period 1976-1996 and calculation of return period wave heights. To supplement extreme events from the 10-year Level 3 hindcast results, a Level 1 hindcast was conducted for 1976-1986 and results saved at the point closest to the input boundary of Level 3. These results were examined to identify extreme events with waves toward Nome. The one-line files for these cases were transformed using the STWAVE model to obtain results at the Level 3 point near shore. The resulting wave heights were sorted and entered in the Automated Coastal Engineering System Extreme Wave Height Analysis Program, Leenknecht (1992). The results are summarized in Figure 11 and Table 5. Figure 11 is the resulting Fisher-Tippett Type I analysis, and Table 5 shows the percent chance of exceeding a 2-, 5-, 10-, 25-, or 50-year return period wave height over a period of 2, 5, 10, 25, or 50 years.

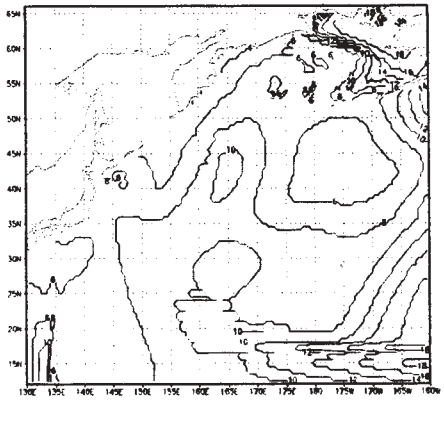

Figure 10. Contours of mean wave period (sec) on June 21, 1997.

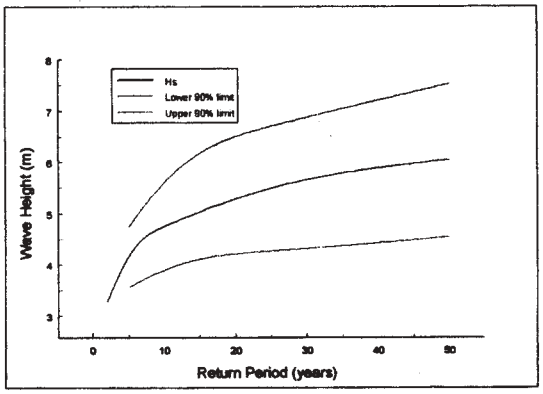


Figure 11. Wave heights at a depth of 10 m MLLW, 1 km from Nome for various return periods.

Table 5. Percent chance of equaling or exceeding a return period wave height in a certain number of years.

| Return Period HS | Number of Years | | | | |
|---|---|---|---|---|---|
| | 2 | 5 | 10 | 25 | 50 |
| 2 | 75 | 97 | 100 | 100 | 100 |
| 5 | 36 | 67 | 89 | 100 | 100 |
| 10 | 19 | 41 | 65 | 93 | 99 |
| 25 | 8 | 18 | 34 | 64 | 87 |
| 50 | 4 | 10 | 18 | 40 | 64 |

## 9. SUMMARY

A wave climate at the entrance to the harbor at Nome, Alaska, was calculated using wind fields from the NCEP/NCAR Reanalysis Project and the U.S Army Corps of Engineers wave model WISWAVE. The wave model was applied on two numerical grids. The Level 1 grid covered the Bering Sea region. The Level 2 grid resolved the bathymetry and land water boundary in the northeastern corner of the Bering Sea. A second Corps of Engineers model, STWAVE, was used to transform wave conditions over near shore bathymetry to a point 1 km from shore in a depth of 10 m.

One year of the 10-year hindcast was calculated using wind fields input to the wave model at analysis times, that is, at 0000 and 1200 UT. A separate hindcast for the same year was calculated using analysis times plus 6-hour forecast winds, that is at 0000, 0600, 1200, and 1800 UT. Comparison of results showed little, if any, difference in this case indicating the use of winds at an interval of 12 hours may be acceptable in place of winds at an interval of 6 hours. The global winds at an interval of 12 hours are readily available for a relatively low cost while winds at an interval of 6 hours are a special order product.

Wave results were compared to results from NOAA buoy 46035 during the period 1987-1996. There was negligible bias on an annual basis for wave height, and the RMSD between model and buoy was approximately 0.5 m. The difference between annual maximum values was approximately 1 m. The average over 10 years for both model and buoy was 10.8 m.

The value of annual peak periods tended to be approximately 1 second higher, as measured by the buoy versus as calculated by the model. Annual RMSD's were approximately 5 seconds. This underestimation by the model is attributed in part to swell propagating into the region from the North and South Pacific Oceans that was not part of the model region.

A separate wind and wave hindcast of Typhoon Opal confirmed that swell can reach Nome from tropical storms off the East Coast of Japan. It is also probable that swell from winter storms in the North Pacific and from storms in the South Pacific reaches Nome.

Waves at Nome arrive mainly from a window between the south and southwest. About 90 percent of the time, wave heights are 1 m or less and periods range between 6-10 seconds. Extreme values reach 5 m and have periods of 10 seconds. These are values determined from the hindcast between May and November. The period between December and April was excluded due to ice coverage.

## 10. ACKNOWLEDGEMENTS

The authors wish to acknowledge Mr. Kenneth Eisses for sponsoring the study and Mr. Edward Sorenson for contributions as technical monitor, both of whom are with the U.S. Army Corps of Engineers District, Alaska. We acknowledge Ms. Dee Hubertz for preparation of the manuscript and the Office of the Chief of Engineers, U. S. Army Corps of Engineers for authorizing publication of this paper.

## 11. REFERENCES

Hubertz, J. M., 1992: User's guide to the Wave Information Studies (WIS) wave model, version 2.0. WIS report 27, U.S. Army Engineer Waterways Experiment Station, Vicksburg, MS.

Hubertz, J. M., R. M. Brooks, W. A. Brandon, and B. A. Tracy, 1994: Hindcast wave information for the U.S. Atlantic Coast. *J. of Coastal Res.*, 10(1), 79-100.

Kalnay, E., M. Kanamitsu, R. Kistler, W. Collins, D. Deaven, L. Gandin, M. Iredell, S. Saha, G. White, J. Woollen, Y. Zhu, M. Chelliah, W. Ebisuzaki, W. Higgins, J. Janowiak, K. C. Mo, C. Ropelewski, J. Wang, A. Leetmaa, R. Reynolds, R. Jenne, and D. Joseph, 1996: The NCEP/NCAR 40-year reanalysis project. *Bull. Amer. Met. Soc.*, 77(3), 437-471.

Leenknecht, D. A., A. Szuwalski, A. R. Sherlock, 1992: Automated Coastal Engineering System, user's guide. U.S. Army Engineer Waterways Experiment Station, Vicksburg, MS.

Resio, D. T., 1987: Shallow water waves, I theory. *J. Waterways, Port, Coastal and Ocean Eng.*, 113, 264-281.

Resio, D. T., 1988: A steady state wave model for coastal applications. *Proc., 21st International Conference on Coastal Engineering*, Malaga, Spain, 1, 929-940.

Resio, D. T., W. Perrie, 1989: Implications of an $f^4$ equilibrium range for wind generated waves. *J. of Phys. Oceanog.*, 19, 193-204.

# COMPARISON OF MODEL OUTPUT OF WIND AND WAVE PARAMETERS WITH SPACEBORNE ALTIMETER MEASUREMENTS

Paul A. Hwang[1], Steven M. Bratos[2], William J. Teague[1], David W. Wang[3], Gregg A. Jacobs[1] and Donald T. Resio[2]
[1] Oceanography Division, Naval Research Laboratory, Stennis Space Center, MS 39529-5004
[2] U.S. Army Engineer Waterways Experiment Station, Vicksburg, MS 39180-6199
[3] Computer Science Corporate, Stennis Space Center, MS 39529-5004

## 1. INTRODUCTION

One of the major issues in the hindcasting and forecasting of winds and waves is the difficulty of validation and verification. While comparisons with point measurements from discrete and sparsely distributed wave buoys provide some measure of statistical confidence, the spatial distribution of the modeled wind and wave fields cannot be easily assessed.

Remote sensing from space provides a synoptic view of the ocean wind and wave fields. For example, wind speed and significant wave height are standard output of spaceborne altimeters such as TOPEX/POSEIDON (hereafter referred to as TOPEX for brevity). Comparisons of the altimeter measured wind speed and wave height with surface buoy data have shown very positive agreement (e.g., Ebuchi and Kawamura 1994; Freilich and Challenor 1994; Gower 1996; Hwang et al. 1997). With an along-track resolution of 7 km, the spatial resolution of the spaceborne altimeter is comparable with that of the numerical models used for regional simulations. In the following, we present the results of a comparison study of WAM wave modeling of the Yellow and East China Seas (YES) with two of the TOPEX tracks in the region. In the next section the accuracy of TOPEX altimeter wind and wave measurements is summarized based on earlier studies of TOPEX and surface buoy comparisons. Section 3 describes the YES data sets and the background information about the numerical modeling and satellite tracks in the comparison region. Section 4 presents the results of the comparison in terms of statistics such as bias ($B$), rms difference ($\Delta$), regression coefficient ($c$ and $c_y$, to be further discussed later) and correlation coefficient ($R$). Since altimeter remote sensing provides a spatial coverage of the wind and wave fields along transects, we will explore the use of such information for the validation of wave height distribution from a numerical wave model output. The conclusions and summary are presented in the last section of the paper.

## 2. ALTIMETER MEASUREMENT OF WIND AND WAVES

Extensive studies of altimeter measurements of wind and wave parameters have been published (e.g., Brown et al. 1981; Chelton and Wentz 1986; Wu 1992; Witter and Chelton 1994; Freilich and Challenor 1994; Ebuchi and Kawamura 1994; Gower 1996; Hwang et al. 1997, and the references therein). These studies have shown consistently that the significant wave height derived from the altimeter is essentially identical to that measured by ocean surface buoys. Particularly, if the distances between the buoy location and the satellite footprints are within 10 km, the rms difference of the two sets of data is approximately 0.14 m. One exception is in the coastal region, where large disagreement often occurs. The cause of the discrepancy may be due to the land effect on radar backscatter or the greater spatial inhomogeneity of the coastal wave field within the radar footprint. There are no established rules relating the deterioration of wind/wave data to the land proximity. Factors effecting the distance of data deterioration include the satellite approach (from land or from sea), the local bathymetry gradient, and the plane geometry of the subject location and shoaling factor. From examining the satellite output, it is estimated that if the satellite approach is from land to sea, three to four footprint lengths (20 to 30 km) are needed for the signal to adjust to the change of backscattering characteristics between land and water. For the sea to land approach, this distance is reduced to one footprint (7 km), but other factors mentioned above may dictate the application distance from land. Since the issue concerning land proximity has not been thoroughly investigated, we will exclude data within 50 km of land in the following comparison.

Derivation of wind speed from microwave radars is based on the correlation of surface roughness and radar backscatter intensity (the normalized radar backscatter cross section, $\sigma_0$). For the spaceborne altimeters, specular reflection is the primary mechanism of radar backscatter. In this mode, roughness on the surface causes incident radar waves to diffuse and scatter away from the aperture of radar reception, and the smoother the surface the higher the backscatter is expected. On the ocean surface, short ocean waves are the primary contributor to the surface roughness. Because these short water waves are wind generated, higher $\sigma_0$ corresponds to lower wind speed and vise versa. Over the past two decades, the operational algorithms to

retrieve wind speed from the altimeter backscatter cross section, however, have been based on empirical formulae established on collocated databases of altimeter and surface measurements (e.g., Brown et al. 1981; Chelton and Wentz 1986; Witter and Chelton 1991) or on the statistical distributions of wind speeds and $\sigma_0$ separately (Freilich and Challenor 1994). These comparisons indicate that despite the continuous improvement of altimeter hardware and software, the progress of wind speed retrieval from various algorithms developed over the last 20 years only shows marginal improvement. For example, Freilich and Challenor (1994) report a very comprehensive analysis of eight algorithms. Results in terms of the mean error (bias), root mean square error, standard deviation, wind speed error trend and pseudo-wave age error trend are tabulated. The differences in all eight algorithms are relatively minor. In terms of mean square errors and standard deviations, 7 of the 8 algorithms produced less than 10% difference in these two error parameters (1.60 to 1.75 m/s rms error, 1.58 to 1.72 m/s standard deviation). When applied to a regional scale, the error statistics are slightly better. For example, comparison of 3.2 years of TOPEX data with 4 buoys in the Gulf of Mexico suggests that when the separation distance between the TOPEX footprint and the buoy location is less than 10 km, the rms difference is approximately 1.2 m/s (Hwang et al. 1997). Figure 1 shows an example of the comparison of significant wave height and wind speed measured by the TOPEX Ku-band altimeter and the surface buoys in the Gulf of Mexico.

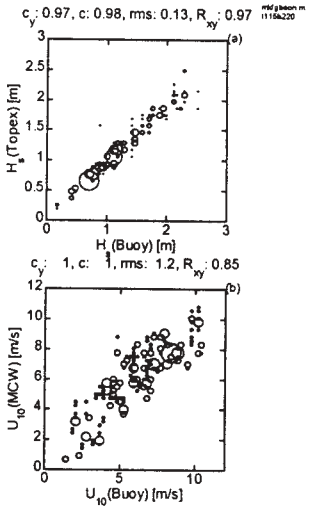


**Figure 1. Comparison of the significant wave height and wind speed measured by the TOPEX altimeter and the ocean buoys in the Gulf of Mexico (Hwang et al. 1997).**

The regression coefficient, rms difference and correlation coefficient for the wave height are 0.98, 0.13 m and 0.97, respectively; the corresponding statistics for the wind speed are 1.0, 1.2 m/s and 0.85 for this case.

*3. YELLOW AND EAST CHINA SEAS DATA SET*

As illustrated in the last section, the altimeter output of winds and waves represents a good source of wind/wave measurements for the study of regional wind/wave climate. The data can also be used for verification and validation of wave model output and offer insight into the spatial distribution, which can not be verified easily with point measurements. This is especially valuable in regions where in-situ data are either nonexistent or inaccessible.

The WAM model (Cycle 4) (WAMDI Group 1988; Janssen 1991) was recently applied to the Yellow and East China Seas to hindcast the wave climatology for 1994. The wave hindcast setup consisted of a global 1° Lat/Lon grid to generate input wave boundary conditions and a regional 0.25 ° Lat/Lon grid including the Yellow Sea, East China Sea, and the Sea of Japan shown in Figure 2.

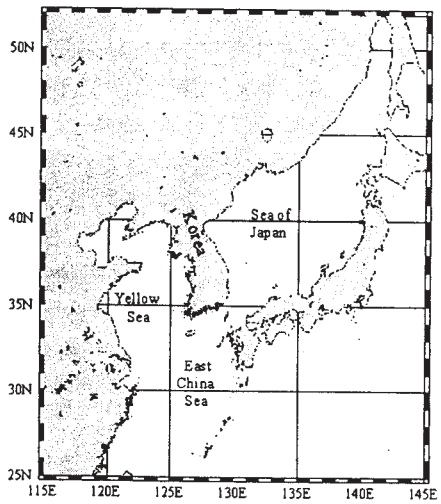


**Figure 2. The model domain of the WAM simulation for the year 1994 used in this simulation.**

A global wind product (Wobus and Kalnay 1995) from the National Centers for Environmental Prediction (NCEP, formerly the National Meteorological Center) was used to drive the global and regional wave model grids. The NCEP winds, which are provided at approximately 0.94° Lat/Lon resolution, were bilinearly interpolated to a 1° resolution for the global hindcast and a 0.25° resolution for the regional hindcast. The global hindcast was run with a temporal resolution of 6 hours, which is the resolution provided by NCEP. The NCEP



AUTHOR INDEX TABLE OF CONTENTS

winds were linearly interpolated to a 3 hour resolution for the regional hindcast.

Several researchers have suggested improvements to WAM (Tolman 1992; Lin and Huang 1996; Bender 1996). Bratos (1997) compared deepwater WAM results to National Data Buoy Center (NDBC) wave measurements along the US Atlantic coast using high quality winds (Cardone 1992) for five extratropical storms which included a variety of conditions ranging from extreme events to more moderate and variable events. One persistent tendency found in the WAM results was a low bias significant wave height (SWH), $H_S$. Figure 3 shows the relationship between wind speed bias and SWH bias for all buoy locations and storm events considered. For a well behaved model the SWH bias should correspond to the wind speed bias. The plot shows a tendency for WAM SWH to be biased low (0.0 m to -0.5 m) when the wind speed is biased high (0.0 m/s to 1.75 m/s).

One of the standard WAM output files includes the SWH, friction velocity $u*$, and drag coefficient $C_D$ at every grid point. The model wind speed at a 10 m elevation is given by $U_{10} = u_* C_D^{-1/2}$. The SWH and wind speed model parameters were extracted along the two TOPEX tracks for comparison. The first track is number 69, a descending track that runs along the central axis of the YES region (Figure 4), and the second track is number 26, which is an ascending track cutting across the entrance region.

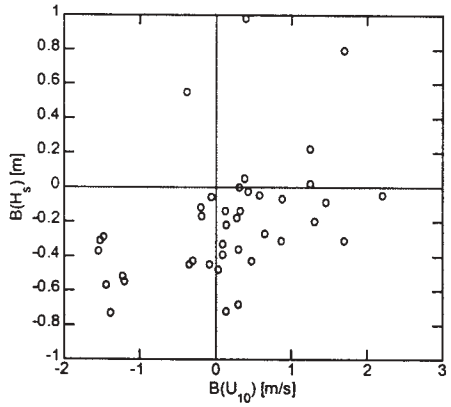


**Fig. 3. Example of WAM output compared with buoy measurements along the U. S. Atlantic coast [Bratos 1997].**

The extraction of the model output consisted of interpolation of the model parameters to the satellite track coordinates using two subroutines within the GMT-System (General Mapping Tools) (Wessel and Smith 1991). The subroutine *surface* ( Smith and Wessel 1990) creates a binary grid file using an adjustable tension continuous curvature algorithm. The subroutine *grdtrack* samples this 2-D binary grid file along tracklines 26 and 69 using bicubic interpolation. The numerical output and altimeter data are then merged together by linear interpolation using the latitude coordinate to a uniform spacing of 0.05 degree in latitude. The spacing between neighboring data points in the merged data set is between 6.0 to 6.3 km along track. The distances between the model data positions and the interpolated altimeter footprints are between 0.4 to 0.6 km. Over the one-year (1994) model run, 32 cycles are extracted for each track (4 of the missing cycles occur at Julian days 63, 172, 311 and 361 for track 26, and 76, 176, 315 and 324 for track 69.). The time differences between the model output and TOPEX measurement are distributed approximately evenly between 0 to 1.5 hours.

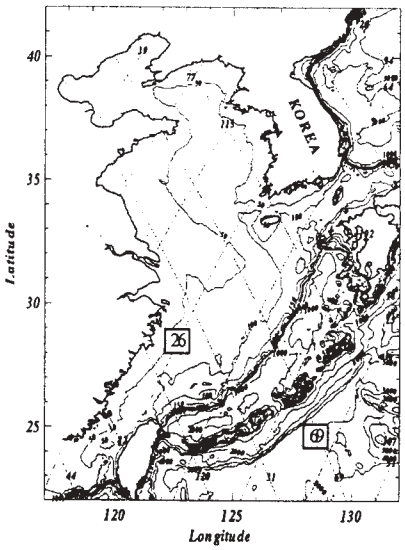


**Figure 4. A map of the Yellow and East China Seas (YES) region for this comparison study. TOPEX tracks are shown in dotted curves. Tracks 69 (from NW to SE going through the axis of the region) and 26 (from SW to NE across the YES entrance) are used for comparing with the WAM model simulation for the year 1994.**

## 4. COMPARISON AND DISCUSSIONS

### *4.1. Average Comparison*

We first study the wave and wind climate derived from TOPEX measurements and WAM output. The annual averages along the two tracks are listed in Table 1(A). The statistical distribution of the winds and waves in four different regions designated as are shown in Figure 5 (top half), in which the histogram of wind speeds and wave heights are displayed. These four regions are designated as D9, S3, M3 and N3 for 9 degrees (latitude), Southern 3 degrees, Middle 3

degrees and Northern 3 degrees along the two tracks. The limiting latitudes are tabulated in the first column of Table 1. From these tabulated statistics, it is found that the average properties of wind speed and wave height between the numerical simulation and the remote sensing measurement are in excellent agreement. Both the mean and standard deviation of these average quantities are mostly in agreement within 10 percent. Both TOPEX and WAM show that the average wave height decreases persistently northward. Along the central axis of YES (track 69) the 3-degree average wave height is reduced from 1.70 m at 29°, to 1.49 m at 32° and 1.16 m at 35° based on TOPEX measurements.

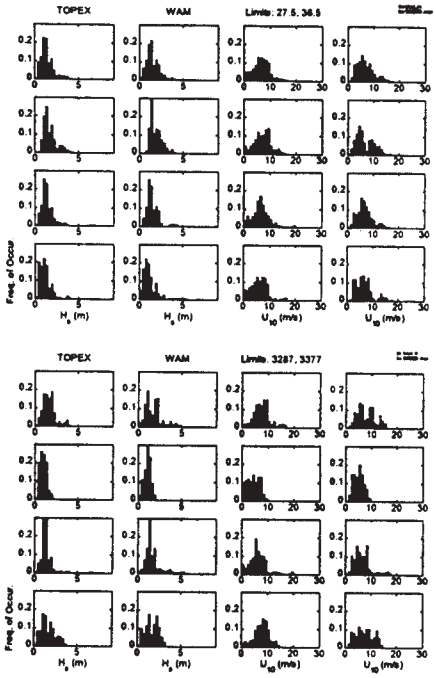


**Figure 5. Comparison of the histograms of wave heights and wind speeds from TOPEX measurements and WAM output. The plots are arranged as $H_S$ (TOPEX), $H_S$ (WAM), $U_{10}$ (TOPEX) and $U_{10}$ (WAM) in the first to the fourth column. The upper four rows of the plots are annual data within 9°, Southern 3° (S3), Middle 3° (M3), and Northern 3° (N3), respectively, along track 69. The lower four rows are the histograms of the wind and wave parameters in the 9° latitude along track 69, and over the first to the fourth 90-day period of 1994 data sets.**

The results show that the WAM hindcast of the wave heights are slightly higher, by 9%, 3% and 4% respectively, than the TOPEX data for the three regions (S3, M3 and N3). The average wave height along track 26 shows a similar trend, with 1.82 m at 27°, 1.63 m at 30° and 1.51 m at 33°. The WAM output again overpredicts the wave height by 9%, 11% and 2%, respectively. The distribution of the average wave heights can be measured in terms of the standard deviation (Table 1). In the along-axis direction (track 69), the dimensionless standard deviations (normalized by the mean) are 0.45, 0.65 and 0.58 from South to North based on the TOPEX data, and 0.37, 0.55, and 0.74, respectively, based on the WAM output. The standard deviations along track 26 of TOPEX and WAM are in much better agreement ([0.54, 0.47, 0.69] of TOPEX as compared to [0.52, 0.53, 0.61] of WAM). In general, the annual average predicted by WAM model agrees very well with the TOPEX measurement. One of the major sources of discrepancies is the wind speed or wind stress used to drive the model. As shown in Table 1, the average wind speed used in WAM is in general higher than the TOPEX observations. Except for one case (track 69, S3), the WAM average wind is 4 to 19% higher than the corresponding TOPEX data.

The comparison statistics of the seasonal average wave height and wind speed between TOPEX and WAM are also listed in Table 1(B). The histograms of the wave height and wind speed distributions are shown in Figure 5 (lower half). These statistics are based on the data along the full 9-degree tracks discussed above. The statistics over a smaller or larger distance can be generated also. Two of the notable features of the seasonal average are (1) the lower average occurs in the second quarter, and (2) the largest variation as represented by the standard deviation occurs in the third quarter (Table 1B). These features are consistent with the monsoon climate of the region, with predominantly northwesterly to northerly winds in the winter, and southwesterly to southeasterly winds in the summer. In the transition seasons, the winds fluctuate between the two dominant weather systems (e.g., Wang and Aubery 1987). The wind and wave properties are further complicated by the typhoons, which generally occur from July to October, and explain the large variation (standard deviation) of the seasonal statistics during the third quarter. The agreement of the mean properties derived from WAM output and TOPEX measurement is generally good, the ratio of the averages (WAM/TOPEX) ranges between 0.94 to 1.19. The agreement in the standard deviation statistics is also similar to that of the seasonal means. The larger difference in the seasonal means (up to 19% higher, as compared to 11% maximum in the annual means) is closely related to the wind condition used in driving the wave model. The maximum difference of the seasonal average wind speed is 36% (6.5/4.78=1.36; Track 26, Q2) as compared to 19% in the annual means (7.76/6.50=1.19; Track 26, M3).

We then compare the statistical correlation of the WAM and TOPEX along each track. The region of comparison, defined by the latitude distance along the tracks, is varied from less than 1 degree to 9 degrees. The mean properties averaged within the specified region will be presented below. The statistic parameters of the linear regression coefficients $c_y$ and $c$, the bias, the rms difference and the correlation coefficient are computed and summarized in Table 2. The coefficient $c$ is calculated by minimizing the orthogonal distances between data points to the linear regression curve. In the scatter plot of WAM data vs. TOPEX data with the intercept forced to zero, the regression fitting can be expressed as $y = cx$, where $y$ is the WAM wave height (wind speed) and $x$ is the TOPEX wave height (wind speed). The formula of the orthogonal regression coefficient is described in Bauer et al. (1992) and also in Romeiser (1993),

$$c = \tan\left[\frac{1}{2}\tan^{-1}\left(\frac{\langle 2xy\rangle}{\langle x^2\rangle - \langle y^2\rangle}\right)\right] \tag{1}$$

where angle brackets denote ensemble average. A slight modification to consider the condition that the magnitude of $\langle y^2 \rangle$ exceeds $\langle x^2 \rangle$ is given by Hwang et al. (1997)

$$c = \tan\left\{\frac{1}{2}\left[\tan^{-1}\left(\frac{\langle 2xy\rangle}{\langle x^2\rangle - \langle y^2\rangle}\right) + \pi\right]\right\}, \quad \langle x^2\rangle < \langle y^2\rangle \tag{1b}$$

The regression coefficient based on minimizing the orthogonal distance differs from those obtained from minimizing the mean square distances in the y-direction, $c_y$, or in the $x$-direction, $c_x$:

$$c_y = \frac{\langle xy\rangle}{\langle x^2\rangle}, \tag{2}$$

and

$$c_x = \frac{\langle y^2\rangle}{\langle xy\rangle}, \tag{3}$$

When the correlation of the two data sets are high, these three coefficients become indistinguishable (see discussions in Bauer et al. 1992).

The average wave height and wind speed of the WAM output and TOPEX data are in good agreement from cycle to cycle. Figure 6 shows an example of the results. For the wave height, the rms difference for the 9-degree average is approximately 0.3 m, with a correlation coefficient of 0.93 for both tracks (Table 1). The rms difference increases to approximately 0.4 m when the averaging distance decreases and the correlation coefficient also decreases, possibly due to a decrease of data points in the averaging process. For the wind speed, the rms difference is 1.92 m/s for track 26 and 1.33 m/s for track 69, with the correlation coefficients of 0.83 and 0.91, respectively for the 9-degree average. The statistics for the 3-degree (Southern, Middle, and Northern) averages are also tabulated in Table 2. In general, the agreement in wave height between TOPEX and WAM are good, considering that the wind input used for driving the model is considerable difference from the TOPEX measurements.

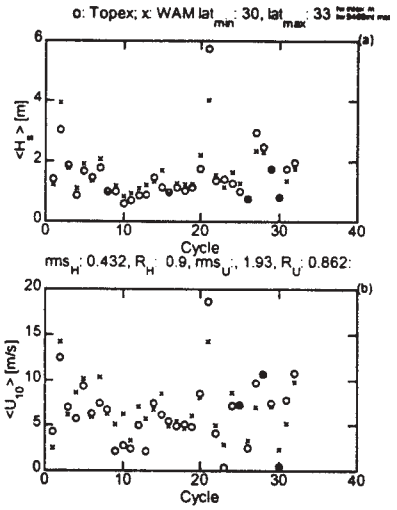


**Figure 6. An example of the mean wave height (a) and wind speed (b) averaged along the track of various distances. The example shown is the 3-degree average (M3, from 30 to 33 degrees latitude). O: TOPEX, × = WAM. The statistics of comparison are listed in Table 1.**

*4. 2. Spatial Distribution*

One of the most significant advantages of remote sensing measurements is the ability to provide a quasi-instantaneous measurement of the spatial distribution of the wave heights and wind speeds. For example, the 9° latitude transects of tracks 26 and 69 were completed in 168 and 190 s, respectively. The high spatial density of the measurements represents a unique source of wind and wave data that can be used for model comparison.

Figure 7 illustrates the cycle-by-cycle comparison of wave heights (top half) and wind speeds (bottom half) derived from WAM and TOPEX track 69. For this along-axis track, the WAM wave height output tends to be biased high in the first six to nine months of the year and the bias trend reverses toward the winter

months; however, the data scatter is quite large (Figure 8a). The bias trend of track 26 is slightly different, with the major negative bias appearing in the first four months, and positive the rest of the year. While there are apparent similarities of wave bias and wind bias, the scattering of data points is large. The average normalized bias relative to the mean wave height or wind speed, $B(H_S)/<H_S>$, is 0.09 for track 26 and 0.08 for track 69. For wind speed ($B(U_{10})/<U_{10}>$), the corresponding numbers are much larger, 0.39 and 0.57 for the two tracks.

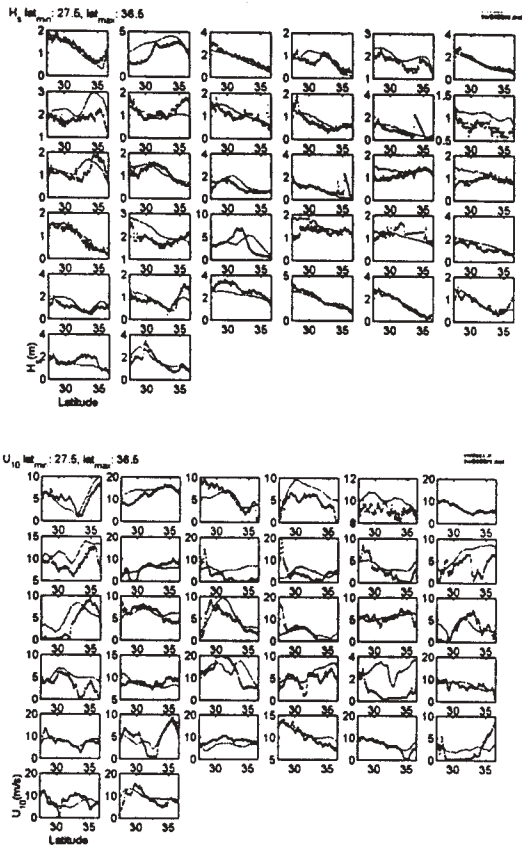

**Figure 7. Track-by track comparison of the wave height (top half) and wind speed (bottom half) from TOPEX (dots) and WAM (solid curve).**

The cycle-by-cycle normalized ($\Delta(H_S)/<H_S>$, $\Delta(U_{10})/<U_{10}>$) differences of wave heights and wind speeds are plotted in Figure 8c and 8d for tracks 26 and 69 respectively. The rms differences relative to the mean wave height are mostly less than 0.5, with an average value of 0.27 for track 26 and 0.24 for track 69. For wind speed, the corresponding numbers are 0.55 and 0.77 for the two tracks.

The linear regression coefficient, $c$, for tracks 26 and 69 is shown in Figures 8e and 8f. As can be seen from the plots, there are only small members of cases with $0.9 \le c \le 1.1$. The WAM output tends to over estimate the wave height, especially in the summer months. Many of the wave height over estimations can be associated with over estimation of the wind speed used as the input to the wave model. Exceptions are found in very low wind conditions, where the wave heights are mainly dominated by the swell components that are unrelated to the local wind condition.

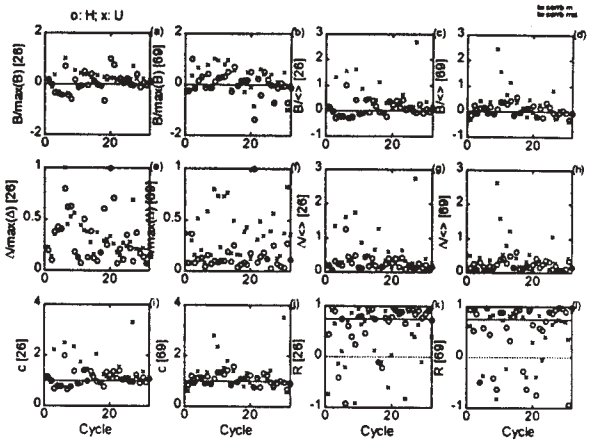


**Figure 8. Statistics of comparing spatial distributions of WAM output with TOPEX measurements. Bias normalized by the maximum for track 26 (a) and 69 (b); bias normalized by the mean wave height or mean wind speed for track 26 (c) and 69 (d); rms difference normalized by the maximum for track 26 (e) and 69 (f); rms difference normalized by the mean wave height or mean wind speed for track 26 (g) and 69 (h); regression coefficient for track 26 (i) and 69 (j); and correlation coefficient for track 26 (k) and 69 (l). o: wave height, x: wind speed. (M3 averages).**

The correlation coefficients between WAM and TOPEX data show the largest variation (Figure 8g and 8h) compared to the other statistical parameters. For the along-axis track 69, 7 out of 32 cycles show negative correlation coefficient, indicating that the opposite trends of wave height distribution along the altimeter track obtained from WAM modeling as compared to the altimeter measurements. In addition to the negative correlation cases, 9 more cycles have correlation coefficient of less than 0.75, so altogether one half of the cases examined for track 69 show poor correlation of WAM output with altimeter measurements. Similar to the wave correlation statistics, for the wind speed, there are 7 cycles of negative correlation and 9 additional cases of low correlation coefficients. While many cases of poor correlation in wind speeds correspond to those of poor correlation in wave heights, there are also many other mismatches.

Because the correlation coefficient is primarily a measure of proportionality of two variables (for example, when $y = cx^n$, where $c$ and $n$ are constant, the correlation coefficient always equals to unity) the correlation coefficient alone does not indicate the quantitative agreement of the two variables. The evaluation of data agreement needs to take into account other statistics such as the bias, rms difference and/or regression coefficient.

The cycle-by-cycle statistics of track 26 are not very different from those of track 69. For the wave height, there are 4 cases of negative correlation coefficient and 8 cases with $0 < R < 0.75$. For the wind speed, there are 9 negative correlation and 10 cases with $0 < R < 0.75$. Taking the statistics of the two tracks together, only in about one half of the cases are WAM output and TOPEX measurements in good agreement. The above conclusions are based on analyzing 32 cycles of 2 tracks over a 3-degree latitude stretch of the satellite tracks. Taking a different stretch, the statistics are not significantly different from the above results.

## 5. SUMMARY AND CONCLUSIONS

The wind speeds and wave heights measured by satellite altimeters have been compared with ocean buoy measurements with excellent agreement. They represent a good source of environmental data for the study of global and regional wave conditions. In this paper, we compare TOPEX altimeter measurements with WAM model output in the region of Yellow and East China Seas. Two of the satellite tracks passing through the region are selected for comparison. Track 69 passes through the central axis of YES and track 26 passes across the entrance to the enclosed seas. The comparisons are processed into two categories: (1) comparing the time series for a given location, and (2) comparing with the spatial distribution for a given time.

The first category is further divided into (a) average over a region from 3 to 9 degrees latitude along a track, and (b) seasonal average along a track. These average quantities from TOPEX and WAM are in good agreement in terms of mean and standard deviation of the statistics (Table 1). The difference between altimeter measurements and numerical simulations is approximately 10% with WAM overestimating most of the time. The median value of the rms differences is 0.4 m with a correlation coefficient of ~0.9 (Table 2). These figures are compared to 0.15 m and 0.97, respectively from TOPEX/buoy comparisons performed in the Gulf of Mexico region for comparable spatial and temporal separations (Hwang et al. 1997). The rms difference in wind speed in the YES/WAM comparison is ~2 m/s with a correlation coefficient of ~0.83. The corresponding values from TOPEX/buoy comparisons in the Gulf of Mexico region are 1.2 m/s and 0.9, respectively.

The comparison of spatial distributions of WAM simulations and TOPEX measurements is performed with 32 cycles each from the two tracks over 3 to 9 degrees latitude (Figure 7 shows the results of 9-degree processing). The quality of agreement between numerical simulations and altimeter measurements varies significantly from cycle to cycle. In many cases, opposite trends in the spatial distributions of wave heights and wind speeds are found. The statistics of bias, rms difference, linear regression coefficients and correlation coefficient from the 32 cycles of both tracks are analyzed (Figure 8 shows results of 3-degree averages). A rather large percentage (~50%) of cases show poor agreement based on a combination of low correlation and large rms difference or bias, and the regression coefficient differs significantly from one.

The comparisons presented here indicate that our numerical wave simulation skills are good in the projection of temporal evolution but relatively poor for the spatial variation of the wave field. The measurements from remote sensing devices, including spaceborne and airborne, are of spatial distribution in nature. These data represent a precious source for enhancing our understanding of the spatial properties of the wind and wave fields. The spaceborne data are especially useful for studying the regional wind and wave climate, in which case, the spatial density of in-situ measurements is usually not very high. Numerous comparison studies have shown that the accuracy of altimeter output of significant wave height and wind speed frequently exceeds the model output and is comparable in quality with in-situ ocean buoy measurements.

## ACKNOWLEDGMENT

This research is sponsored by the Office of Naval Research (NRL Job Orders 6800-08, 7405-A8 and 6725-A8), and the U.S. Army Corps of Engineers. The WAM hindcast was conducted as part of the Military RDT&E Program of the U.S. Army Engineer Waterways Experiment Station's Coastal and Hydraulics Laboratory. Permission was granted by the Chief of Engineers to publish this information. [NRL contribution PP/7332—97-0025].

## REFERENCES

Bauer, E., S. Hasselmann, and K. Hasselmann, , 1992: Validation and assimilation of Seasat altimeter wave heights using the WAM wave model, *J. Geophys. Res.*, 97, 12671-12682.

Bender, L. C., 1996: Modification of the physics and numerics in a third-generation ocean wave model.

*J. Atmos. and Ocean. Tech.*, **13,** 726-750.

Bratos, S. M., 1997: Comparison between third generation and second generation ocean wave models. Masters Thesis, In review, Texas A&M University

Brown, G. S., H. R. Stanley, and N. A. Roy, 1981: The wind speed measurement capability of spaceborne radar altimeters, IEEE *J. Oceanic Eng.*, OE-6, 59-63.

Cardone, V. J. , 1992: On the structure of the marine surface wind field. 3rd International Workshop of Wave Hindcasting and Forecasting, Montreal, Quebec, May 19-22, 54-66.

Chelton, D. B., and F. J. Wentz, 1986: Further development of an improved altimeter wind speed algorithm, *J. Geophys. Res.*, 91, 14250-14260.

Ebuchi, N., and H. Kawamura, 1994: Validation of wind speeds and significant wave heights observed by the TOPEX altimeter around Japan, *J. Oceanography,* 50, 479--487.

Freilich, M. H., and P. G. Challenor, 1994: A new approach for determining fully empirical altimeter wind speed model functions, *J. Geophys. Res.*, 99, 25051-25062.

Gower, J.F.R., 1996: Intercomparison of wave and wind data from TOPEX/POSEIDON, *J. Geophys. Res.*, 101, 3817-3829.

Hwang, P. A., W. J. Teague, G. A. Jacobs, and D. N. Wang, 1997: A statistical comparison of wind speed, wave height and wave period derived from satellite altimeters and ocean buoys in the Gulf of Mexico region, subm. *J. Geophys, Res.*

Janssen, P. A. E. M., 1991: Quasi-linear theory of wind wave generation applied to wave forecasting. *J. Phys. Oceanogr.*, **21,** 745-754.

Lin, R. Q., and N. E. Huang, 1996: The Goddard Coastal Wave Model. Part I: Numerical method. *J. Phys. Oceanogr.*, **26,** 833-847.

Romeiser, R., 1993: Global validation of the wave model WAM over a one-year period using Geosat wave height data, *J. Geophys. Res.*, 98, 4713-4726.

Smith, W. H. F. and P. Wessel, 1990: Gridding with continuous curvature splines in tension, *Geophysics*, **55,** 293-305.

Tolman, H. L., 1992: Effects of numerics on the physics in a third-generation wind-wave model. *J. Phys. Oceanogr.*, **22,** 1095-1111.

WAMDI Group, 1988: The WAM model - a third generation wave prediction model. *J. Phys. Oceanogr.*, **18,** 1775-1810.

Wessel, P., and W. H. F. Smith, 1991: Free software helps map and display data. *EOS Trans. Amer. Geophys. U.*, **72,** 441, 445-446.

Wobus, R. L., and E. Kalnay, 1995: Three years of operational prediction of forecast skill at NMC. *Mon. Wea. Rev.*, **123,** 2132-2148.

Wang, Y., and D. G. Aubrey, 1987: The characteristics of China Coastline, *Cont. Shelf Res.*, 7, 329-349.

Witter, D. L., and D. B. Chelton, 1991: A Geosat altimeter wind speed algorithm and a method for altimeter wind speed algorithm development, *J. Geophys. Res.*, 96, 8853-8860.

Wu, J., 1992: Near-nadir microwave specular returns from the sea surface - altimeter algorithm for wind and wind stress, *J. Atm. Oceanic Tech.*, 9, 659-667.

Table 1. Comparison of Mean and Standard Deviation of WAM and TOPEX Average Data.

| Latitude/Day limit | Wave Height | | | | Wind Speed | | | |
|---|---|---|---|---|---|---|---|---|
| | $\langle H_S \rangle$ (m) | | $\sigma_{Hs}/\langle H_S \rangle$ | | $\langle U_{10} \rangle$ (m/s) | | $\sigma_{U10}/\langle U_{10} \rangle$ | |
| | TOPEX | WAM | TOPEX | WAM | TOPEX | WAM | TOPEX | WAM |
| **A. Annual average over a region** | | | | | | | | |
| (a) Track 26 | | | | | | | | |
| D9 (25.5, 34.5) | 1.65 | 1.81 | 0.56 | 0.56 | 7.02 | 7.78 | 0.49 | 0.42 |
| S3 (25.5, 28.5) | 1.82 | 1.98 | 0.54 | 0.52 | 7.49 | 7.75 | 0.48 | 0.46 |
| M3 (28.5, 31.5) | 1.63 | 1.81 | 0.47 | 053 | 6.50 | 7.76 | 0.49 | 0.43 |
| N3 (31.5, 34.5) | 1.51 | 1.54 | 0.59 | 0.61 | 7.07 | 7.87 | 0.50 | 0.38 |
| (b) Track 69 | | | | | | | | |
| D9 (27.5, 36.5) | 1.45 | 1.55 | 0.58 | 0.54 | 6.66 | 6.94 | 0.51 | 0.49 |
| S3 (27.5, 30.5) | 1.70 | 1.85 | 0.45 | 0.37 | 7.19 | 6.99 | 0.46 | 0.51 |
| M3 (30.5, 33.5) | 1.49 | 1.53 | 0.65 | 0.55 | 6.66 | 6.97 | 0.52 | 0.45 |
| N3 (33.5, 36.5) | 1.16 | 1.21 | 0.58 | 0.74 | 6.15 | 6.84 | 0.53 | 0.50 |
| **B. Seasonal average along a track** | | | | | | | | |
| (a) Track 26 | | | | | | | | |
| Q1 (1, 90) | 1.69 | 1.59 | 0.42 | 0.40 | 7.51 | 7.42 | 0.43 | 0.36 |
| Q2 (91, 180) | 1.10 | 1.31 | 0.28 | 0.31 | 4.78 | 6.50 | 0.47 | 0.35 |
| Q3 181, 270) | 1.84 | 2.14 | 0.69 | 0.72 | 7.06 | 7.21 | 0.64 | 0.63 |
| Q4 (271, 360) | 1.90 | 2.14 | 0.43 | 0.36 | 8.33 | 9.76 | 0.29 | 0.23 |
| (b) Track 69 | | | | | | | | |
| Q1 (1, 90) | 1.63 | 0.76 | 0.48 | 0.56 | 7.60 | 8.10 | 0.41 | 0.44 |
| Q2 (91, 180) | 0.96 | 1.07 | 0.40 | 0.36 | 4.50 | 5.17 | 0.57 | 0.38 |
| Q3 (181, 270) | 1.46 | 1.67 | 0.69 | 0.55 | 6.47 | 6.74 | 0.55 | 0.51 |
| Q4 (271, 360) | 1.69 | 1.67 | 0.50 | 0.50 | 7.85 | 7.76 | 0.38 | 0.45 |

Table 2. Statistical Coefficients of WAM and TOPEX Correlations.

| | Wave Height, $H_S$ | | | | | Wind Speed, $U_{10}$ | | | | |
|---|---|---|---|---|---|---|---|---|---|---|
| Latitude Limit | $c_y$ | $c$ | $B$ (m) | $\Delta$ (m) | $R$ | $c_y$ | $c$ | $B$ (m/s) | $\Delta$ (m/s) | $R$ |
| (a) Track 26 | | | | | | | | | | |
| D9 (25.5, 34.5) | 1.06 | 1.07 | 0.13 | 0.33 | 0.93 | 1.10 | 1.13 | 1.07 | 1.92 | 0.83 |
| S3 (25.5, 28.5) | 1.07 | 1.09 | 0.17 | 0.43 | 0.92 | 1.02 | 1.04 | 0.37 | 1.73 | 0.87 |
| M3 (28.5, 31.5) | 1.07 | 1.09 | 0.15 | 0.41 | 0.91 | 1.16 | 1.21 | 1.60 | 2.56 | 0.78 |
| N3 (31.5, 34.5) | 1.03 | 1.06 | 0.06 | 0.41 | 0.90 | 1.09 | 1.13 | 1.20 | 2.52 | 0.75 |
| (b) Track 69 | | | | | | | | | | |
| D9 (27.5, 36.5) | 1.06 | 1.08 | 0.08 | 0.28 | 0.93 | 1.06 | 1.08 | 0.57 | 1.33 | 0.91 |
| S3 (27.5, 30.5) | 1.05 | 1.08 | 0.18 | 0.42 | 0.86 | 0.98 | 1.01 | 0.06 | 1.70 | 0.87 |
| M3 (30.5, 33.5) | 0.97 | 0.99 | 0.04 | 0.35 | 0.93 | 1.00 | 1.04 | 0.63 | 1.97 | 0.86 |
| N3 (33.5, 36.5) | 1.03 | 1.10 | 0.02 | 0.46 | 0.83 | 1.07 | 1.13 | 1.01 | 2.32 | 0.78 |

# IMPACT OF THE ASSIMILATION OF ERS-1 AND ERS-2 DATA INTO A NORTH ATLANTIC REGIONAL VERSION OF WAM

L. J. Wilson*
Environment Canada, Dorval, Québec

E. Dunlap
ASA Consulting Limited, Halifax, Nova Scotia

R. Olsen
Satlantic, Inc., Halifax, Nova Scotia

## 1. INTRODUCTION

Up until a few years ago, wave models ran without the use of any wave observations, mainly because too few observations were available to have an impact on the output of the models. With the launch of ERS-1 in July, 1991, the spatial and temporal frequency of wave observations increased dramatically, making their use to initialize wave models operationally practical. ERS-1 and ERS-2 wave observations are available in two forms, significant wave heights from the radar altimeter and information on the wave spectrum from the AMI instrument operating in SAR mode. While the former source has already seen considerable use in operational wave models (e.g. Lionello et. al., 1995), SAR data might prove more useful for wave modeling because it offers an estimate of the two-dimensional wave spectrum, which is the predictive variable of the wave model.

The general purpose of data assimilation is to nudge a model's estimate of the state of its geophysical variables toward their true state, using information obtained from observations. Both model and data are assumed to contain errors, which must be accounted for in the assimilation procedure. In our procedure, the errors and limitations of the SAR spectra are accounted for through the use of the Hasselmann and Hasselmann (1991) inversion procedure, which is a variational method for matching model and SAR estimates of the spectrum at the observation location. On the assumption that the errors in the wave spectrum are correlated in space, the corrections obtained from the Hasselmann algorithm are spread to nearby gridpoints using weights which are inverse functions of distance from the observation site, following Lionello et. al.(1995). The assimilation strategy is one-pass Cressman, that is, a single pass is made through the data with the pre-defined influence region of 5 model gridlengths and the non-linear weighting function. Further details of the full assimilation procedure are given in Dunlap et al., (1997).

Our goal was to develop a data assimilation system that would be sophisticated enough to give an initial assessment of the impact of SAR wave data on analysis and forecasts from the WAM model. To accomplish this, we put together a full assimilation system by adapting simple methods, and tested it on a variety of North Atlantic cases, including both extreme storm and non-storm situations. Results of these tests are described in this paper. The data and test method are described next, followed by the results.

## 2. TEST DATA AND METHODS

We have so far tested the assimilation on three separate periods, described in Table 1:

* Corresponding author address: L. J. Wilson, Environment Canada, 2121 route Transcanadienne, suite 500,Dorval, Québec, H9P 1J3, Canada. Phone 514-421-4726; fax: 514-421-2106; e-mail: Lawrence.Wilson@ec.gc.ca

**TABLE 1.** Dates and sources of data for the three wave data assimilation test periods.

| Case Number | Period | Model input data | | Verification data | | |
|---|---|---|---|---|---|---|
| | | Wind | SAR | Buoy | Altimeter | SAR |
| 1 | Mar. 11-21, 1993 | CMC forecast | off-line ERS-1 wave mode | 7 buoys, E coast US and Canada | OPR products, IFREMER | off-line ERS-1 wave mode |
| 2 | Mar 16 to April 16, 96 | CMC forecast | fast delivery ERS-1 wave mode | none available | fast delivery ERS-1 | fast delivery, ERS-1 wave mode |
| 3 | Dec 1 to Dec 31, 1996 | CMC forecast | fast delivery ERS-2 wave mode | none available | fast delivery ERS-2 | fast delivery ERS-2 wave mode |

The first case is a stormy period, dominated by the ``Storm of the Century`` in the North Atlantic, which produced a measured maximum significant wave height of 16.3 m south of Nova Scotia. The second period was quiet, with significant wave heights always below 8 m. The third period was also more typical for the season; with maximum measured wave heights around 8 m.

The atmospheric model used to provide the winds is the Canadian operational regional finite element model (RFE, Mailhot et.al., 1995) The model's grid length is 35 km over North America and the western Atlantic, but resolution decreases gradually outside this region. Wind analyses and forecasts from the model, valid every three hours to 48 hours were interpolated to the WAM grid for the purpose of running the wave model. WAM was run on a 1 degree by 1 degree grid for these experiments, corresponding to the Canadian operational version. The domain is 25 to 70 degrees N and 80 to 15 degrees W, giving a total of 2318 water points. Both wave model and atmospheric model were run twice daily through each test period, beginning at 00 UTC and 12 UTC. The wave model was also ``warmed up`` for at least two days of simulation in each case before verification was begun.

The wave model was run twice, once as a ``baseline`` run without the use of SAR data, and once with the assimilation of SAR data. Assimilation was carried out each three hours of the run, using all SAR data available over the model domain during the three hour period. For comparison with observations, the model data were interpolated to the observation points using bilinear interpolation, for the time steps before and after the observation, then interpolated in time to the observation time.

For assessment of the impact of assimilation, the ideal is to use completely independent data, preferably data which is considered to have a lower error level than the observations that are being assimilated. For ocean waves this is a difficult ideal to achieve, since few platforms measure the two dimensional wave spectrum and the observations that do exist are relatively sparse in space and time. For this study, we used buoy data, which contain non-directional spectra; altimeter data from ERS-1 and 2, which give estimates of significant wave height alone; and SAR data, which give an estimate of the full spectrum. Although we limited the verification with SAR data to data which was not used in the assimilation, this data still cannot be considered to be a completely independent data source. The other two datasets are more independent, but give less information about the spectrum. Thus, for buoy data, we could compare significant wave height (Hs) and average period (Tp), while for altimeter data, we could compare only Hs. For SAR data, we compared the three parameters of the spectrum, Hs, Tp, and average direction (Dir).

## 3. RESULTS

In order to assess the impact of SAR data assimilation throughout the Storm of the Century

(Case 1), we compared model output with buoy observations. The results, however, are dependent on the buoy locations. The available buoy data locations are along the western fringe of the North Atlantic, and are to windward of most of the satellite observations. Therefore, most of the wave systems and associated corrections arising from data assimilation propagate away from the buoy locations. The measurable impact is directly related to the region of influence and

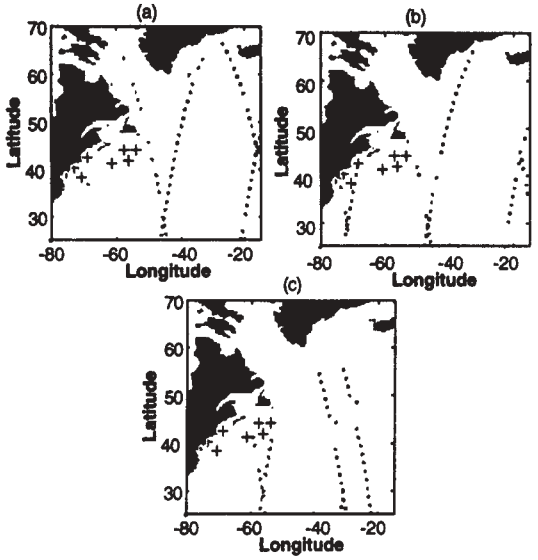


**Figure 1.** Coverage of assimilated SAR data in relation to buoys for Case 1: a) March 11, b) March 14, c) March 16. Each panel shows 24 hour coverage.

the spreading function applied. It is also very closely related to the spatial and temporal coverage of the SAR observations. In Figure 1, we show three examples of the 24-hour satellite coverage for 11, 14 and 16 March 1993. In Figures 2 and 3 we show time series comparing wave parameters from the model with buoy observations in the Gulf of Maine and off Long Island. The results are typical of all the buoy results and show that there is little difference in the two model runs, baseline and assimilation, early in the period, but greater impact later on, coinciding with satellite passes closer to the buoy locations. We also see that the assimilation of SAR data results in a reduced overall difference between the model and the buoy observations. The improvement is most pronounced during periods of decaying waves.

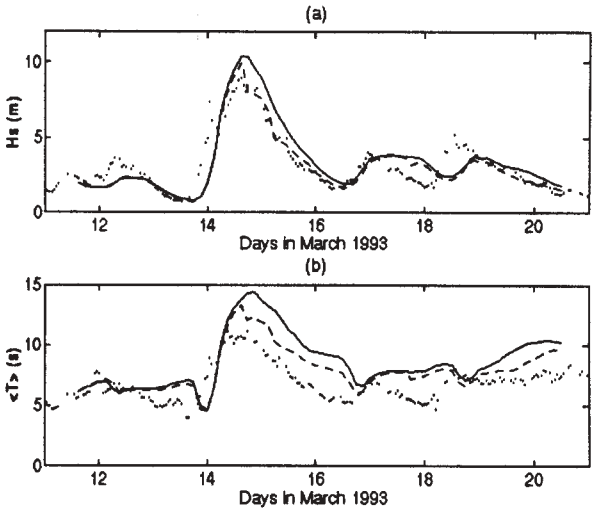


Figure 2. Comparison of hindcast series of wave height, (a), and mean period, (b), for buoy 44005 (Gulf of Maine), (Case 1). Modeled wave parameters with and without assimilation are indicated by dashed and continuous lines, respectively. Dots represent buoy observations.

Table 2 shows a summary of the impact of the assimilation for each of the buoys, in terms of the changes in scatter index and correlation between buoy significant wave height and period and model significant wave height and period. Results are averaged over the 9-day period of Case 1, and are based on about 183

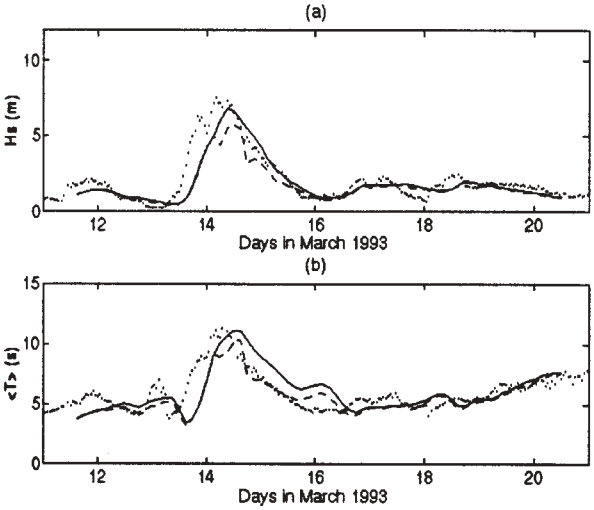


Figure 3. Same as Figure 2, but for buoy 44025 (Long Island)



AUTHOR INDEX
TABLE OF CONTENTS

**TABLE 2.** Change, Δ, in scatter index and correlation coefficient between buoy significant wave height and period and model significant wave height and period, due to SAR data assimilation.

| WAM & AWAM vs Buoys | | Hs (m) | | <T> (s) | |
|---|---|---|---|---|---|
| Station | N | $\Delta SI_D$ (%) | ΔCor. (%) | $\Delta SI_D$ (%) | ΔCor. (%) |
| 44005 | 187 | -2.46 | 0.23 | -3.13 | 0.28 |
| 44025 | 185 | 3.53 | 0.72 | -2.83 | 0.52 |
| 44004 | 182 | -2.18 | 1.08 | -1.91 | 0.64 |
| 44141 | 180 | 0.82 | -0.24 | -0.29 | -0.05 |
| 44139 | 185 | 1.59 | -0.22 | -3.36 | 0.34 |
| 44138 | 179 | -4.00 | 2.21 | -3.02 | 0.83 |
| 44137 | 184 | 2.95 | -0.18 | -1.40 | 0.03 |
| All buoys | 1282 | -0.30 | 0.21 | -1.55 | 0.26 |

observations for each buoy. Both the sample sizes and the observed changes are small. The overall scatter index is reduced by 0.3% and 1.55%, and the correlation is increased by 0.2% and 0.26% for the significant wave height and for the mean period, respectively. The impact on wave period is slightly greater than the impact on Hs. A typical example comparing wave height and period for one of the buoys on the Scotian Shelf is shown in Figure 4.

The small effect of the assimilation is consistent with the fact that the buoys were seldom within the influence region of ERS-1 data.

In order to further understand the effect of assimilating SAR data in the case of the Storm of the Century, we measured the impact against observations from the ERS altimeter. The comparisons were made in terms of both summary statistics for all the data and in terms of individual satellite passes. In Figure 5a, we show a selected satellite pass , which coincides with the storm area. The effect of assimilating the SAR observations for this pass, presented in Figure 5b (broken line), shows an improvement over the baseline case, (solid line). In this case, the scatter index is decreased from 21.33% for the baseline run to 16.03% for the assimilation run, while the correlation coefficient is increased from 98.42% (baseline) to 99.02% (assimilation). The altimeter data show a dip in wave height between 38° and 40° along the track, which

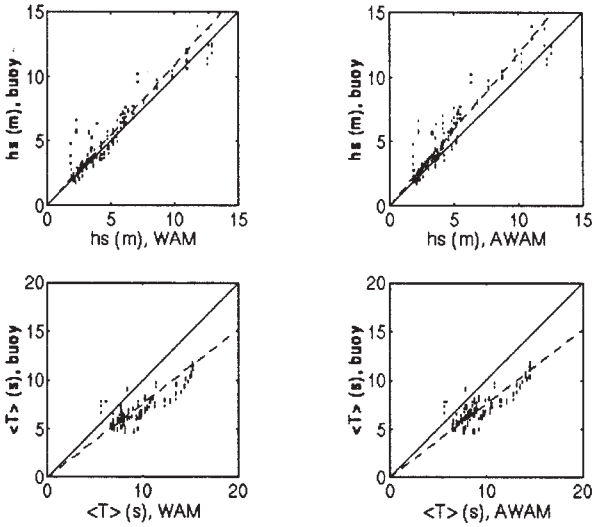


Figure 4. Comparison of buoy and model hindcast (top) wave heights and (bottom) mean periods for Scotian Shelf, (buoy 44137), including (left) baseline run results and (right) assimilation run results.

apparently was not resolved in the model. This feature is actually seen on several passes in the vicinity, and is therefore not simply an artifact in the data. A glance at the analysis maps for the time of these altimeter measurements suggests that the dip in the significant wave height is related to a trough and associated wind shift from W to NW. The gradient in this area was also slackening with time. The feature was apparently not resolved in the modeled wave field. Even

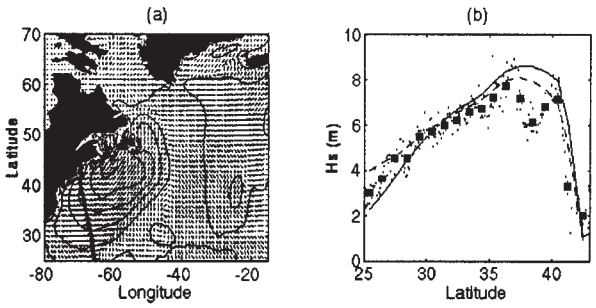


Figure 5. Comparison of altimeter and WAM significant wave heights along a specific satellite track for March 15, 0300 UTC. (a): The map showing contours of significant wave height and vector wave direction. Dots indicate location of averaged altimeter observations. (b): Significant wave height as a function of the latitude along the satellite track, for baseline run (solid line) and assimilation run (broken line) Altimeter data averaged over a distance of 1° are indicated by squares. Maximum model Hs=12.7m.

though the dip at the northern end of the track is not reproduced, the overall fit is better than without the assimilation.

Details of the comparison between the storm case (case 1) and the general case (case 2) are documented in Dunlap et. al. (1997). A comparative analysis of cases 2 and 3, which are climatologically similar, can give insights into the relative characteristics of data from ERS-1 and ERS-2. We start with a comparison of the WAM estimates of wave parameters vs. SAR estimates, before assimilation. Figure 6 shows scatter plots for Hs, Tp and Dir, for cases 2 and 3. Differences between the two test periods are small. In both cases, there is a tendency for the SAR Hs to be higher than WAM estimates, especially for higher wave heights. Tp and Dir appear to be nearly unbiased. Table 3, which contains statistics for all three cases, quantifies the results shown in Figure 6. In the table, bias is defined as (observation-WAM), the scatter index (SI) is the standard difference expressed as a percentage of the mean WAM value, and the slope is the symmetric slope. Case 1, the storm case, has a higher mean Hs, and lower scatter index than the other two cases. The higher bias is consistent with the tendency shown in Figure 6. The table also shows that Tp and Dir are nearly unbiased for all three cases, and correlation is high. There is a slight tendency toward higher correlation for ERS-2, but the difference may not be significant on one month of data.

**TABLE 3.** Statistics of the comparison between SAR wave parameters and WAM estimates of wave parameters.

| Case 1 | | | | | | |
|---|---|---|---|---|---|---|
| **548** | **mean (WAM)** | **bias** | **std** | **SI (%)** | **slope** | **corr** |
| **Hs(m)** | 4.09 | 0.43 | 1.09 | 23.35 | 1.10 | 97.7 |
| **<T>(s)** | 9.24 | 0.28 | 0.91 | 9.27 | 1.03 | 99.6 |
| **<dir>** | 140.9 | -2.38 | 46.25 | n/a | 0.98 | 95.9 |
| Case 2 | | | | | | |
| **1855** | **mean (WAM)** | **bias** | **std** | **SI (%)** | **slope** | **corr** |
| **Hs(m)** | 3.17 | 0.35 | 0.75 | 24.82 | 1.13 | 98.2 |
| **<T>(s)** | 8.55 | 0.21 | 0.77 | 9.2 | 1.02 | 99.6 |
| **<dir>** | 144.3 | -4.06 | 45.19 | n/a | 1.00 | 96.2 |
| Case 3 | | | | | | |
| **1901** | **mean (WAM)** | **bias** | **std** | **SI (%)** | **slope** | **corr** |
| **Hs(m)** | 3.68 | 0.38 | 0.78 | 22.45 | 1.11 | 98.4 |
| **<T>(s)** | 8.90 | 0.23 | 0.77 | 9.00 | 1.02 | 99.6 |
| **<dir>** | 169.7 | -1.61 | 44.89 | n/a | 0.99 | 97.1 |

One way of evaluating the performance is to evaluate the rate of success of inversion. For the inversion algorithm to work, there must be some basic level of agreement between the wave systems seen by the SAR compared to the wave systems seen by the model, which is used as a trial field in the inversion. The two main causes for failure of the inversion are excessive noise in the data (too low signal to noise ratio), which happens more often at low sea states, and too much difference between the model and SAR, which causes the inversion to fail to converge. Table 4 summarizes the inversion rate for the three cases. For case 3, the ERS-2 data result, there is a noticeable increase in the inversion success rate compared to the case 2 result. The success rate for case 1 is only slightly lower than for case 3, but this can be attributed to the higher mean wave height, and associated stronger average signal in the data. For case 3, the mean wave height is greater than for case 2 but considerably lower than for case 1.

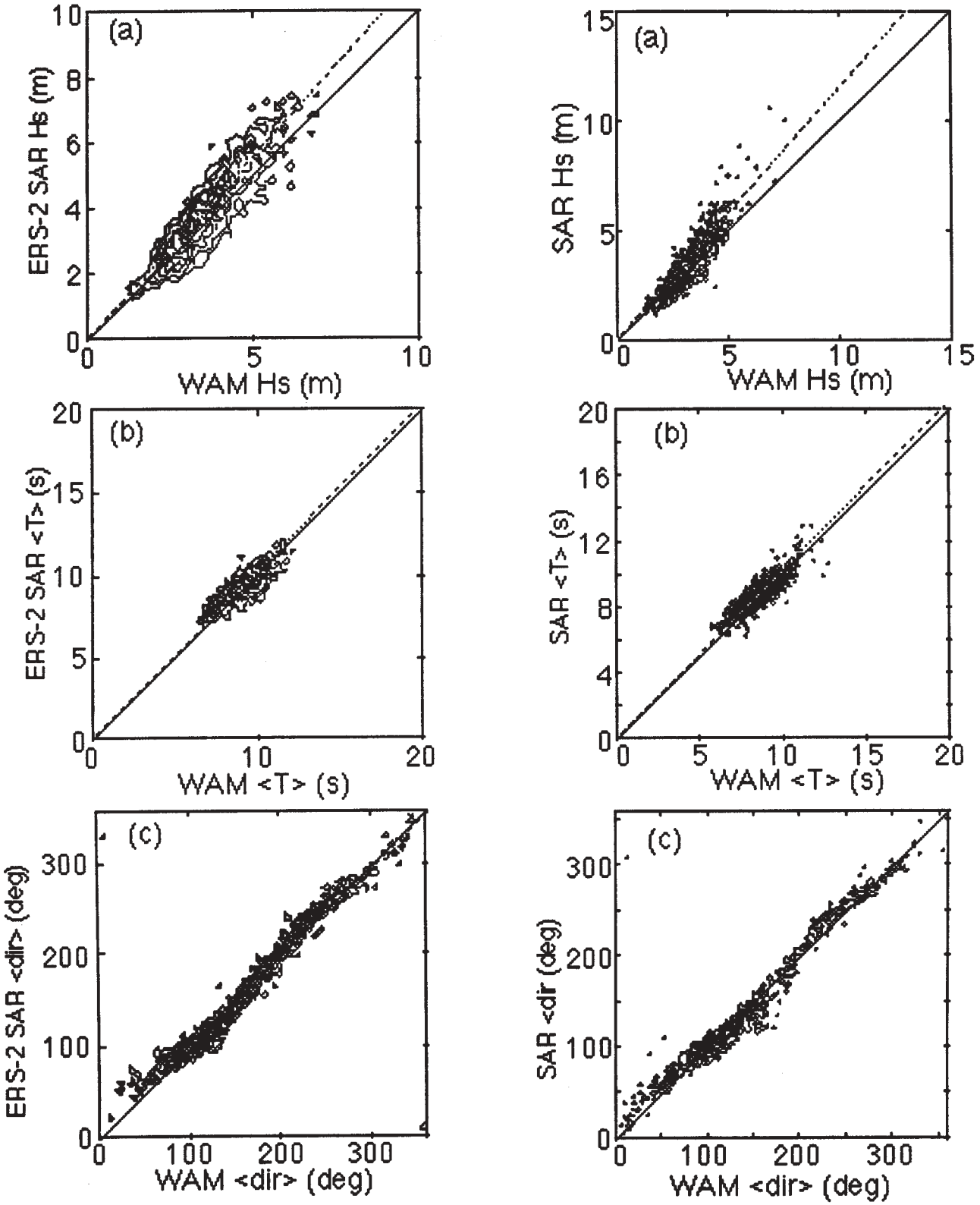


Figure 6. Comparison of WAM and SAR wave heights (a), average period (b), and direction (c), for one month of ERS-2 data (left) and one month of ERS-1 data (right).

**TABLE 4.** Statistics showing the relative success rate of the inversion for the three cases.

| Case | Total | Inverted | %Inverted | %rejected |
|---|---|---|---|---|
| 1 | 714 | 548 | 76.8 | 23.2 |
| 2 | 3504 | 2423 | 69.2 | 30.8 |
| 939999333 | 2468 | 1901 | 77.03 | 23.0 |

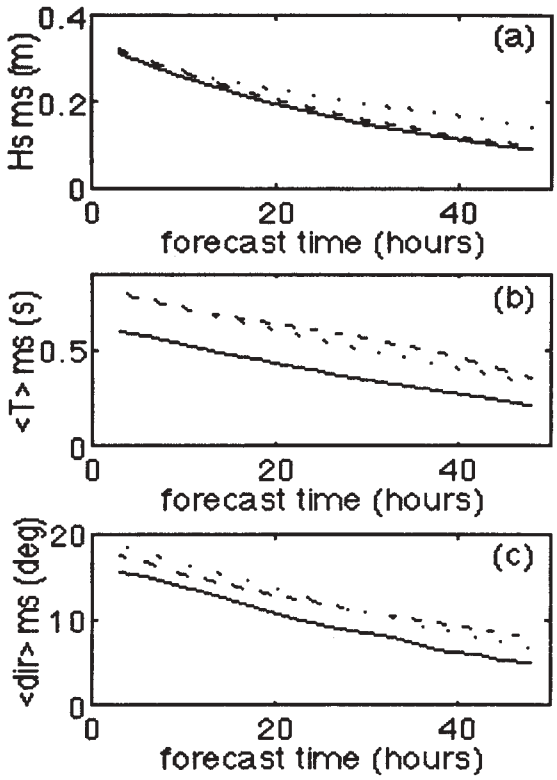


Figure 7. RMS difference between wave forecasts with and without assimilation as a function of forecast projection. (a) Wave heights; (b) average period, and (c) average direction. Case 1 is shown in dashed lines, Case 2 in solid, and Case 3 in dotted lines.

Results of the comparison of forecast Hs with and without assimilation vs. altimeter data are shown in Table 5. The table shows first of all that there is strong agreement between the WAM Hs and the altimeter Hs for ERS-2 data: It is more nearly unbiased (the negative bias has been largely corrected) and the scatter index is quite low, under 20%. This is consistent with results found by Janssen at ECMWF, using fast delivery data compared with the global version of WAM operating at ECMWF (personal communication). Agreement between WAM and the altimeter data is also better compared to case 1. It is not surprising to note that the assimilation of SAR data actually lowers the correlation of WAM with altimeter data. Since the SAR data is biased positive and the altimeter data is slightly negatively biased, the assimilation will tend to nudge the WAM forecasts in the wrong direction according to the altimeter. Table 5 shows this to be true for both the ``average`` situations, cases 2 and 3. For the storm case, however, the SAR assimilation has indeed increased the bias with respect to the altimeter, but nevertheless has improved the correlation and the scatter index.

Figure 7 shows the persistence of the impact on wave forecasts. The assimilation system was run up to each 12h initialization time, then stopped, and 48h forecasts were run from the corrected wave field. These forecasts were compared with forecasts initialized at the same time, but without assimilation. The figure indicates that the effects last at least 48 h; about 75% of the impact is lost during the forecast. This is consistent with the fact that the SAR sees mostly the swell part of the spectrum; swell waves can last several days and travel large distances.

## 4. CONCLUDING REMARKS

We have built and tested a simple assimilation system for ERS wave mode data. The system is used to correct the wave fields obtained from our North Atlantic version of the WAM model. The full system has been tested on three separate cases, one stormy period and two separate months of data, one during the operational period of ERS-1 and one during the operational period of ERS-2. We can conclude the following from our tests:

1. The impact of the assimilation is positive for the storm case, when compared against all available independent sources of data (buoys and altimeter observations). Positive results are stronger for period than for wave height.
2. The SAR observations of wave height tend to be higher on average than WAM wave heights, thus the assimilation tends to raise the modeled wave heights.
3. The impact of the assimilation for the two month-long periods was neutral to slightly negative, compared with altimeter observations of wave height. This is consistent with the observation that SAR wave heights are higher than WAM heights on

average, while altimeter wave heights are close to WAM wave heights without assimilation. We have not compared with buoy data, and have no independent sources of data to compare period and direction for these two months.

4. The overall difference between ERS and WAM wave heights is smaller for ERS-2 than for ERS-1, in agreement with other studies. This is true both for average difference and correlation.

**TABLE 5.** Statistics of the comparison of wave forecasts from WAM without (WAM) and with (AWAM) assimilation.

| Case 1 | | | | | | |
|---|---|---|---|---|---|---|
| | **mean (WAM)** | **bias** | **std** | **SI (%)** | **slope** | **corr** |
| WAM | 4.32 | -0.49 | 0.95 | 23.2 | 0.89 | 97.7 |
| AWAM | 4.45 | -0.62 | 0.89 | 21.5 | 0.88 | 97.9 |
| Case 2 | | | | | | |
| | **mean (WAM)** | **bias** | **std** | **SI (%)** | **slope** | **corr** |
| WAM | 2.68 | -0.15 | 0.71 | 27.4 | 0.94 | 96.9 |
| AWAM | 2.94 | -0.41 | 0.76 | 28.0 | 0.87 | 96.8 |
| Case 3 | | | | | | |
| **6620 cases** | **mean (WAM)** | **bias** | **std** | **SI (%)** | **slope** | **corr** |
| WAM | 3.32 | -0.04 | 0.64 | 19.3 | 0.98 | 98.5 |
| AWAM | 3.47 | -0.17 | 0.67 | 19.9 | 0.96 | 98.3 |

There is more work to be done to confirm the impact of the SAR data. First, the verification period is still quite short. A longer verification period not only will give more statistically significant results, but also it will allow for more collocations of independent data to directly confirm the impact. We will also need independent directional wave spectral data to define the impact in more detail.

Second, we intend to carry out a test implementation of the system which will enable us to test the impact from the point of view of reliability and timeliness of data ingest, as well as to accumulate additional statistics on the impact of the assimilation of the data on wave forecasts.

Third, the system is simple in concept. We intend to eventually use both sequential and time-dependent forms of variational methods, to improve our ability to optimally extract the information about the wave field from the data. Full operational use of such methods is still several years from realization, but time-dependent (``4-D``) variational methods will permit the optimal use of all sources of wind and wave observations to initialize a coupled atmosphere-wave forecast model.

## 5. REFERENCES


Dunlap, E.M., R.B. Olsen, L.J. Wilson, S. DeMargerie, and R. Lalbeharry, 1997: The effect of assimilating ERS-1 fast delivery wave data into the North Atlantic WAM model. *J. Geophys. Res.* (In Press)

Hasselmann, K., and S. Hasselmann, 1991: On the nonlinear mapping of an ocean wave spectrum into a synthetic aperture radar image spectrum and its inversion. *J. Geophys. Res.*, 96, 10,713-10,729.

Lionello, P., H. Günther, and B. Hansen, 1995: A sequential assimilation scheme applied to global wave analysis and prediction. *J. Marine Systems*, 6, 87-107.

Mailhot, J., R. Sarrazin, B. Bilodeau, N. Brunet, A. Methot, G. Pellerin, C. Chouinard, L. Garand, C. Girard, and R. Hogue, 1995: Changes to the Canadian regional forecast system: Description and evaluation of the 50 km version. *Atmosphere-Ocean* 33, 55-80.

# SEA21 - FORECASTING OPERABILITY OF MARINE INSTALLATIONS

Michael Stiassnie and Michael Glozman

Coastal and Marine Engineering Research Institute,
Technion City, Haifa 32000 Israel, Phone 972-4-8220642.

November 10, 1997

## 1 GENERAL APPROACH

The operability of marine installations like harbors or offshore terminals depends on the wind/wave conditions in open sea in a rather complicated way. The major factors, limiting the operability, are:

- Ability of ships to enter/exit the installation
- Cargo handling limitations for berthed ships

An integrated numerical model is being developed at CAMERI, to simulate, based on the predicted wind/wave conditions at deep sea, the entire physical process, from a deep sea storm to motion of moored ships. In order to simplify the simulation, we separate the physical process into three stages: wave shoaling from deep sea to the harbor entrance, wave diffraction and harbor oscillations, and wave-ship interaction in the harbor. Since the periods of resonance of the harbor and of the horizontal modes of motion (surge, sway, and yaw) of the moored ship, are in the range of long waves (more than about 20 seconds), and since the long waves are better transmitted into the harbor, it is very important to consider the long waves contribution to the ships motion in the harbor. Most of the energy in the long waves range, which exists at the harbor mouth, is a result of nonlinear wave-wave interactions in the shoaling zone. The dimensions of the harbor are assumed to be small enough to neglect nonlinear interaction within the harbor. The process is illustrated in Figure 1.

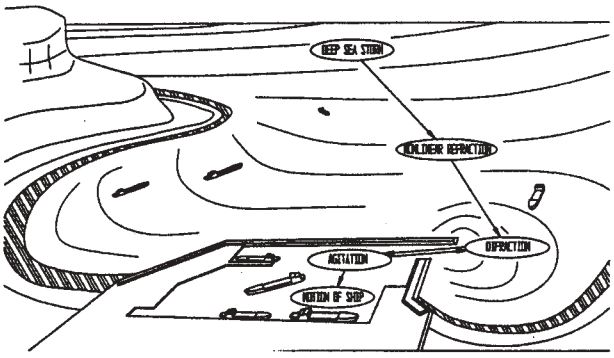


Figure 1: Illustration of the physical process, simulated by the model

The system will employ (at the first stage) the following numerical models:

- A nonlinear shoaling model, which will take as input frequency-directional spectrum at deep sea, and transform it into a new spectrum which characterizes waves at the harbor entrance. For later use this spectrum is decomposed into frequency/direction matrix.
- A linear agitation model, which produces maps of amplification coefficients and other wave parameters for each frequency/direction combination.

- A ship motion model, which computes responses of berthed ship in six degrees of freedom to input wave of unit height for each frequency/direction combination. To calculate characteristic ship motions during a storm, the above responses are multiplied by the corresponding amplitudes of the frequency/direction wave spectrum. The characteristic ship motions are used to predict operability, according to appropriate criteria.

- A navigation model, which will determine whether a specific ship with given loading conditions will be able to enter or exit the harbor.

The linear models will be run in advance and their results will be stored in look-up tables, whereas the nonlinear parts have to be executed in real time. The pilot version of the system will be installed at Haifa harbor by November.

# 2 DESCRIPTION OF MAJOR SYSTEM COMPONENTS

## 2.1 *Nonlinear shoaling model*

While several models are capable of describing of the nonlinear shoaling process (for example, different implementations of the Boussinesq equation), for the Haifa pilot Alexandru Sheremet has developed a semi-nonlinear model based on results of his D. Sc. thesis (Sheremet, 1996). In this approach, the original problem has been split into two problems linearly coupled; the first one, the linear shoaling and refraction of wind-waves over slowly varying bathymetry, is based on the geometrical optics approximation for steady conditions and negligible currents. The second one is a numerical model for the simulation of the long-wave generation based on an elliptic mild slope equation with a forcing term due to the wind waves.

In the elliptic equation no a-priori assumptions are made about the shape of the free surface. It provides a natural way to deal with the directionality of the wave spectrum. However, the integration of the equation on a realistically large domain requires very high numerical effort, taking into account many runs required to get the statistical picture.

WKB expansions bring the original elliptic equations to forms that no longer are capable to describe wave reflection. In exchange, one obtains a simpler evolution equation, more readily understood and much easier to solve. The basic assumptions of the model are that the gradient of the water depth is small (the mild slope assumption), the varying bathymetry affects the waves evolution on the same scale as the leading order nonlinear wave interactions, and the effect of background currents and wave setup/set down is negligible.

The shoaling model requires full spectral information about the sea state at the starting point (deep water), that is, both information about the spectral density and about the modal phases. As a rule, the former is available, but the phases are unknown. For any single run, the model generates the set of corresponding phases randomly, under the assumption that they are uniformly distributed. To obtain a statistical picture of the wave evolution, the results of a large number of such runs have to be averaged. Experience has shown, that the average results become rather stable for about 100 to 200 runs.

### 2.1.1 *Basic Equations*

The present work is based on the nonlinear mild slope equation, describing the spatial evolution of the amplitudes of the spectral components over arbitrary (mildly sloping) bathymetry (Sheremet, 1996). A unidirectional shoaling model may be derived from it by means of the WKB expansion, neglecting the wave reflection by the shore and assuming that the free surface may be represented as a superposition

of slowly modulated plane wave of the form

$$Ae^{i(\theta-\omega t)}; \quad \mathbf{k}=\nabla\theta; \quad \omega^2 = g\,|\mathbf{k}|\,tanh(|\mathbf{k}|\,h), \tag{1}$$

where $\theta$ is the phase function and the underlying assumption is that the wave-number vector $\mathbf{k}$ and the amplitude $A$ are slowly varying functions of position. The resulting equation is:

$$\frac{1}{2}A\nabla\cdot\mathbf{C}_g + \mathbf{C}_g\cdot\nabla A = \int_{-\infty}^{\infty}\mathbf{W}_{0:1,2}A_1A_2e^{-i\Delta^{\theta}_{0:1,2}}\delta^{\omega}_{0:1,2}d\omega_{1,2} \tag{2}$$

with

$$\mathbf{W}_{0:1,2} = \frac{1}{8\pi}(2\mathbf{k}_1\cdot\mathbf{k}_2+(\sigma_1\sigma_2)^2+k_1^2\frac{\sigma_2}{\sigma}+k_2^2\frac{\sigma_1}{\sigma}-\sigma^2\sigma_1\sigma_2)$$

Here $\mathbf{C}_g = C_g\mathbf{k}/k$ is the group velocity vector, $\sigma_j^2=\omega_j^2/g$, $\delta^{\omega}_{0:1,2}d\omega_{1,2}$ is shorthand for $\delta(\omega_0-\omega_1-\omega_2)d\omega_1d\omega_2$, $\Delta^{\theta}_{0:1,2}=\theta_0-\theta_1-\theta_2$ and $A_1A_2 = A(\ldots,\omega_1)A(\ldots,\omega_2)$.

Equation (2) does not describe wave reflection and thus is simpler to solve numerically than its elliptic counterpart. However, due to the nonlinearity, the information about the modal amplitudes and phases at a given point may be obtained only if all the upstream dependencies related to that point are resolved, that is, if the history of all the waves reaching that point is known. The key step in the further simplification of the problem is to somehow do away with the nonlinearity, while still preserving the essential mechanisms responsible for the long waves generation. This may be done by assuming that in the domain of interest the long waves amplitude is significantly smaller than the amplitude of the wind waves (we leave aside for the moment the problem of the exact definition of the long and wind waves bands). If $\beta$ denotes the order of magnitude of the ratio of the long- to wind-wave amplitudes, the leading order mechanism (in $\beta$) that transfers energy to the long waves is the triad interaction involving two components in the peak of the spectrum. The energy feedback from the long waves to wind waves is of higher order.

At the leading order in $\beta$, the equation separates into:

$$long\,waves: \quad \mathbf{L}(A_L)=\mathbf{N}(A_W,A_W) \tag{3}$$

$$wind\,waves: \quad \mathbf{L}(A_W)=0 \tag{4}$$

where $\mathbf{L}$ and $\mathbf{N}$ are notations for the linear and nonlinear operators acting on the unknown wind- and long-waves amplitudes ( $A_W$ and $A_L$ respectively).

The evolution of the wind-waves is *linear* and is independent of the long-waves evolution. The wind-waves system may be integrated by fast standard ray methods to obtain the wave field at any point. The long-waves system of equations is also linear, with a forcing term due to the wind-waves modes. The code developed to integrate the wind wave equations uses conventional ray methods. The numerical approach to the long-waves problem is presented the following subsections.

### 2.1.2 *The long waves generation model*

The numerical model used to solve the wind-waves equation deals with a fully directional spectrum. The discrete version of Equation (2), needed also for numerical integration purposes, is then:

$$\frac{1}{2}A_j\nabla\cdot\mathbf{C}_{g,j}+\mathbf{C}_{g,j}\cdot\nabla A_j = -i\sum_{\alpha,\beta}\mathbf{W}_{(j,\alpha,\beta)}A_\alpha A_\beta e^{-i\Delta^{\theta}_{j:\alpha,\beta}}\delta^{\omega}_{j:\alpha,\beta} + i\sum_{\alpha,\beta}2\mathbf{W}_{(j,-\alpha,\beta)}A^*_\alpha A_\beta e^{i\Delta^{\theta}_{\beta:j,\alpha}}\delta^{\omega}_{\beta:j,\alpha} \tag{5}$$

where $\mathbf{C}_{g,j} = C_{g,j}\mathbf{k}_j/k_j$ is the group velocity vector and

$$\Delta^{\theta}_{j:\alpha,\beta}=\theta_j-\theta_\alpha-\theta_\beta \qquad \nabla\theta_j=\mathbf{k}_j$$

Defining the wave ray as a curve everywhere tangent to the group velocity vector, after some quite standard transformations, one may write the linear term of equation (5) along the ray corresponding to mode "$j$":

$$\frac{1}{2}A_j\nabla\cdot\mathbf{C}_{g,j}+\mathbf{C}_{g,j}\cdot\nabla A_j = (\frac{C_{g,j}}{\sigma_j})^{1/2}\frac{d}{ds}(A_jC_{g,j}^{1/2}\sigma_j^{1/2}) \quad (6)$$

where $s_j$ is the coordinate along the ray corresponding to the spectral mode "$j$".

Introducing the notation:

$$B_j = A_j(C_{g,j}\sigma_j)^{1/2} \quad (7)$$

one may write for the long-wave spectral mode "$j$" the equation:

$$\frac{dB_j}{ds_j} = i(\frac{\sigma_j}{C_{g,j}})^{1/2}\sum_{\alpha,\beta\in W} 2\mathbf{W}_{(j,-\alpha,\beta)}A_\alpha^*A_\beta e^{i\Delta_{\beta:j,\alpha}^{\theta}}\delta_{\beta:j,\alpha}^{\omega} \quad (8)$$

where $W$ is the set of indices corresponding to the wind-wave band.

The problem is now an initial value problem for the long waves along the ray. To solve it, one needs to know the geometry of the long-wave ray and the wind-wave field along it, which may be calculated using Equation (4). Note that Equation (3) does not provide any information about the geometry of the long-wave ray; moreover, the long waves are nearly absent from the deep water spectrum (the long waves arise as a result of the nonlinear interactions, mainly in relatively shallow water) and therefore the ray cannot be computed from the deep water spectral data. In deep water, however, the second order long waves of radial frequency $\omega_j$ for example, may be represented as a superposition of bound waves forced by pairs of wind waves (see Sheremet 1996, App. A) of the form:

$$T_{j,\alpha,\beta}A_\alpha^*A_\beta e^{i\int(\mathbf{k}_\beta-\mathbf{k}_\alpha)d\mathbf{r}} \quad (9)$$

where $\mathbf{k}_L$ denotes the wave-number of the long wave, $T$ the interaction coefficient and

$$\omega_j = \omega_\beta - \omega_\alpha$$
$$\mathbf{k}_L = \mathbf{k}_\beta - \mathbf{k}_\alpha$$
$$\omega_L = gk_L tanh(k_Lh)$$

In deep water, a directional wind-wave spectrum will generate a complex, directionally spread spectrum of bound long-waves; however, if the wind-wave spectrum has a well defined peak and small angular spread, the main part of the energy in the locked long-wave band is concentrated on the direction of the peak.

Although the above heuristics are expected to fail at some point in shallower water, as the long waves will approach the status of the free waves, for the purpose of the present model, which is intended to simulate the long-wave generation up to the entrance of a harbor, at 10m-20m depth, the simplification we shall adopt in the sequel will be to identify the long waves rays with the spectral peak ray.

### 2.1.3 *Practical implementation*

The approach outlined in the preceding subsection allows for breakup of the whole numerical simulation into two distinct steps, as shown schematically in the following Figure 2.

The first package of programs does calculations related to the geometry of the problem and stores the results in files to be used by the second package. It requires only geometrical data such as the bathymetry matrix, the direction and the wavelength of the spectral peak in deep water. Given the deep water wind-wave spectrum, the spectral peak propagation ray up to the target point (harbor entrance) may be computed. The relevant parameters at this stage are only the peak frequency and direction in deep water. The data related to the ray (points, depth, refraction factor along the ray) are stored in a file. Once the spectral peak ray is computed, a second module is brought in to compute the transfer functions for all the points that describe the ray. The transfer functions are stored in a separate file for future use. Any incoming deep

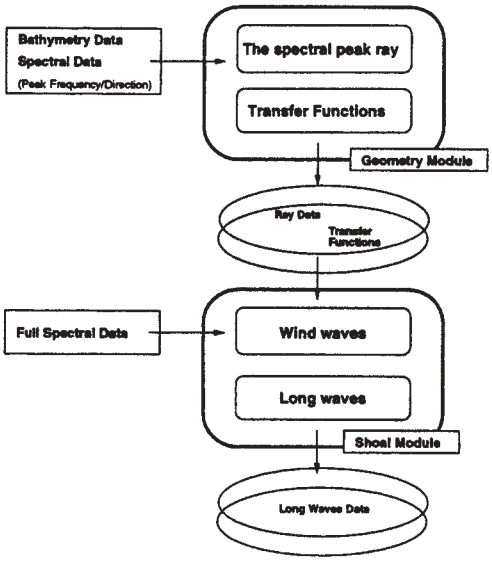


Figure 2: The components of the nonlinear shoaling model

water spectrum having the given direction and peak wave-length will be refracted and shoaled using the data produced by this module, so that the data is, in a certain sense, of general use.

The actual shoaling is done by the second package of programs. The data required is the full deep-water directional wind-wave spectrum, which is processed along the ray and using the transfer functions computed at the previous step. This package is itself designed to work in two steps:

- The linear refraction/shoaling model computes the transformation of the wind-waves along the given spectral-peak ray. For each point of the ray, it computes the corresponding refracted/shoaled directional spectrum. Then, for each frequency in the spectral representation, it computes the peak direction and integrates the spectrum over the directions such as to replace the directional spread at the given frequency with a single mode propagating in the direction of the peak (at that frequency). The data is saved in a file.

- The last module computes the "nonlinear" generation and shoaling of the long wave band using the Equations (3). First the phases of the wind-wave modes along the ray are computed with respect to the first point of the ray, generating a set of ready-made phases for all the wind-wave frequencies. A "realization" is generated by translating these phase arrays by random numbers uniformly distributed between 0 and $2\pi$. For each such realization Equations (3) are integrated to obtain the long-wave spectrum at the target point. For a physically meaningful result, the results for a number of such realizations have to be averaged.

In the present approach the full structure of the actual directional spectrum plays a role only at the later stages in the calculations; the first two modules deal only with the geometry of the problem, so that two spectra having the same peak parameters will be treated by the first group of programs in the model as the same spectrum, irrespective of the significant wave-heights, for example. This would allow the first package to be run only once for a given direction and peak frequency. Moreover, due to the inherent error in measuring directions, one could say that a given ray together with the corresponding transfer functions is representative of a certain angular aperture. Ray and transfer functions could then be pre-computed for discrete values of the propagation angles, and used directly by the second group of modules.

## 2.2 *The agitation model*

Many different numerical models were developed for harbor agitation. Our primary task was to choose the optimal one for our purposes, taking into account specific conditions within harbors. In a fully developed harbor there is a relatively small and well determined entrance; short waves, entering the harbor, undergo significant diffraction just beyond the entrance, so their amplitudes reduces quickly, and no significant long wave generation *within* the harbor can

be expected. Thus, a linear model will be appropriate for this purpose, with all the advantages that linearity provides. Another reason to use a linear monochromatic model, is the partial reflection from breakwaters and other marine structures. From the agitation point of view, this is the most important phenomenon in harbors. As determined by many field measurements and laboratory experiments, the coefficients of partial reflection vary significantly with wave period. In a time domain model, like that based on the Boussinesq equation, it is very difficult (if at all possible) to introduce boundary conditions or near-boundary sponge layers, which describe wave reflection correctly for all periods. So we have chosen the Elliptic Mild Slope (EMS) equation as the optimal one. This equation was originally derived by Berkhoff (1972). It is a linear equation describing the propagation of monochromatic waves over a bottom of slowly varying depth and accounting for refraction, reflection, diffraction and interference. The Elliptic Mild Slope Equation for purely harmonic motion

$$\phi(\mathbf{x},t) = Re\{\psi(\mathbf{x})e^{-i\omega t}\} \tag{10}$$

reads

$$\nabla \cdot (cc_g \nabla\psi) + k_u^2 cc_g \psi = 0 \tag{11}$$

for the complex potential $\psi(\mathbf{x})$, where $k_u(\mathbf{x})$, $c(\mathbf{x})$, and $c_g(\mathbf{x})$ are respectively the wavenumber, the celerity and the group velocity of linear waves in water of constant depth equal to the local depth at point $\mathbf{x}$.

The boundary conditions for (11) are:

$$\frac{\partial\psi}{\partial n} = 0 \tag{12}$$

for fully reflecting walls and

$$\frac{\partial\psi}{\partial n} = ik_u\psi_{in} \tag{13}$$

for a fully reflecting wavemaker, where $n$ is an outward normal, and $\psi_{in}$ is the prescribed potential of the incoming waves.

Partial reflection is modelled by introducing of sponge layers along the structures, in which artificial damping is present. The exact equations for such sponge layers depend on the numerical approach.

The EMS implementation currently in use at CAMERI is MIKE21 EMS developed by DHI. CAMERI has purchased it several years ago for a rather large project: the development of Haifa and Ashdod harbors. CAMERI gained a lot of experience with this model, it was extensively tested and calibrated against physical models of the same harbors. This model solves the hyperbolic form of the mild slope equation by introducing pseudo-fluxes and by removing the harmonic dependency using complex variables and pseudo-time (see Madsen and Larsen, 1987).

Generally, the EMS model is used to compute the agitation database, which is further used by the ship motion modules. This model runs only at CAMERI. The required wave directions are determined from wave statistics for each location. The set of frequencies includes the standard ones ( 20 equally spaced frequencies, from 1/160 Hz to 20/160 Hz), and possibly additional resonant frequencies, which can be determined from simple geometrical considerations, or by running a time domain model with a continuous spectrum. A model based on Saint Venant equation, developed at CAMERI, will be used for this purpose (see Sladkevich and Rubin, 1992). As this model runs with fully reflecting boundaries, the resonant effects will be overestimated. Thus only the strongest resonants must be picked out for further validation by monochromatic model, running with partial reflection.

As we mentioned above, the proper choice of reflection coefficients is extremely important. Separate sets of reflection coefficients were carefully chosen for external breakwaters, for internal sides of breakwaters and seawalls, and for beaches. They were extensively verified against experiments with monochromatic waves of various periods and directions for both Ashdod and Haifa harbors. An example for the Haifa harbor

is given in Figure 3.

Currently a new EMS module is being developed at CAMERI. When available, it will provide many advantages:

- ability to work with sloped and curvilinear boundaries, not just grid-aligned
- high-order model with less grid points per wavelength
- any number of phased array wavemakers, so directional spread can be introduced
- improved sponge layers.

## 2.3 *The ship motion model*

### 2.3.1 *The VIP (Vessel In Port) model*

The VIP model is basically a three dimensional wave diffraction program, which solves numerically the linear wave-body interaction problem for a floating body of general geometry. The program implements the Boundary Elements Method with a wave source Green's function. The basic code was developed as a part of a D. Sc. thesis (Drimer, 1994), which was limited to a box shaped vessel. The generalization of the model for a body of general geometry, was made as a part of Sea21 project.

The uniqueness of the VIP model is its ability to solve the hydrodynamics of a vessel berthed to a quay in a port. In the classical linear wave-body hydrodynamic problem, at open sea, the exciting flow field is defined by the theoretical velocity potential function of a monochromatic plane wave. However, the flow field inside a port is much more complicated. In order to solve the diffraction problem for a vessel in port, a special interface program reads the binary output file of the agitation module, and calculates the values of the velocity potential and its derivatives at the centroids of the boundary elements of the ship model. These values are then transferred to the VIP model as an input for the evaluation of the exciting forces applied on a vessel in port, instead of the open sea exciting forces.

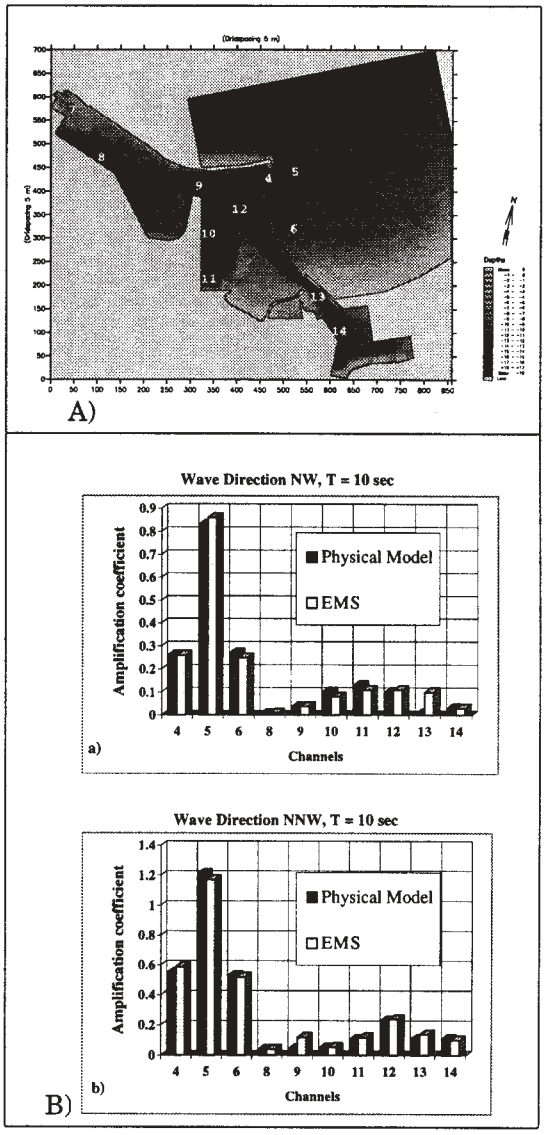


Figure 3: Comparison between the results of numerical and physical models for the Haifa harbor:
A) Location of wave gauges in the physical model
B) Comparison histograms:
a) Waves from NW, T = 10 sec; b) Waves from NNW, T = 10 sec

The scattering problem (a fixed vessel is excited by the harbor flow field), as well as the six radiation problems (the vessel oscillates in one degree of freedom, with a unit amplitude, and radiate waves in a domain which was otherwise calm), are solved with boundary conditions which represent the vertical quay at which the vessel is berthed. The results of the radiation problems are the added mass and damping coefficients. The re-reflection of waves by all boundaries except the quay at which the ship is berthing, is neglected.

After solving the seven hydrodynamic problems (diffraction and six radiation problems), the exciting forces and the hydrodynamic coefficients are substituted in the equations of motion of the ship, which are solved to obtain the amplitudes of motion of the moored ship.

The VIP model as well as the EMS-VIP interface program were developed in CAMERI.

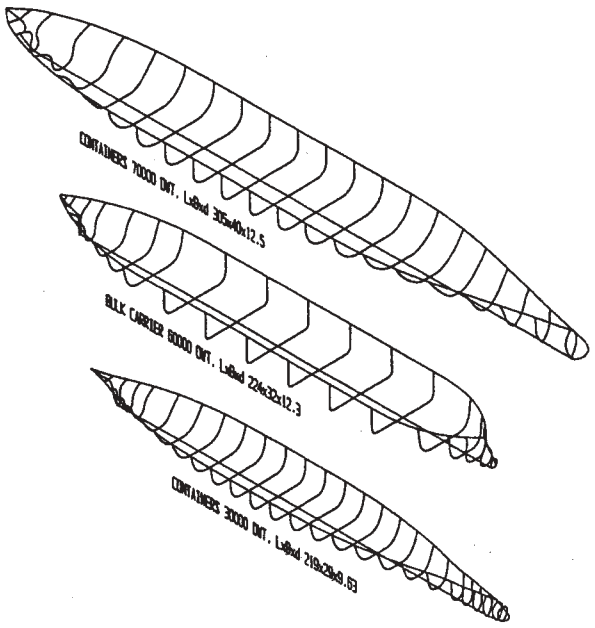

Figure 4: Isometric view of the wetted surface of three typical ships

### 2.3.2 *Ship characteristics*

Detailed ship characteristics are used in the analysis. They include general dimensions, loading conditions and exact shell geometry, which is approximated by finite number of boundary elements. An example is given in Fig. 4. The figure presents the three hulls in the same scale.

The resolution of the numerical representation was verified by means of comparison of calculated hydrodynamic coefficients and exciting forces, with published experimental results.

Beside the shell geometry, some hydrostatic and dynamic properties are needed as an input for the ship motion analysis; these include: metacentric heights, roll and pitch periods, waterline area and waterline moments of inertia.

In order to obtain the appropriate roll and pitch periods, the corresponding moments of inertia were calibrated according to the following process:

The natural periods of oscillations are given by:

$$(\frac{2\pi}{T_4})^2 = \frac{G_{Mt}\Delta}{I_{44} + a_{44}} \qquad for\ roll$$

and

$$(\frac{2\pi}{T_5})^2 = \frac{G_{Ml}\Delta}{I_{55} + a_{55}} \qquad for\ pitch$$

Where:

$T_4$ - roll period

$T_5$ - pitch period

$G_{Mt}$ - transverse metacentric height

$G_{Ml}$ - longitudinal metacentric height

$\Delta$ - displacement

$I_{44}$ , $I_{55}$ - roll and pitch moment of inertia, respectively

$a_{44}$ , $a_{55}$ - roll and pitch added mass, respectively

$a_{44}$ and $a_{55}$ were evaluated by applying the VIP model for a ship in an open sea, for the given roll or pitch periods. Then $I_{44}$ and $I_{55}$ were calculated to satisfy the above equations.

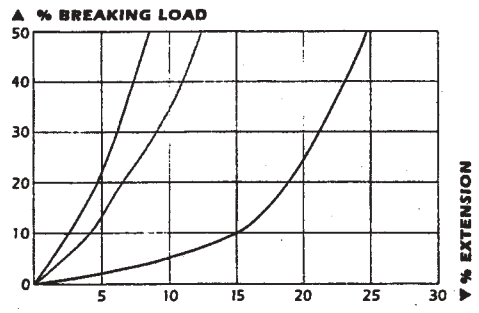


Figure 5: Typical deflection curves of mooring lines

### 2.3.3 *Representation of mooring*

In general the reaction of the mooring system is nonlinear. Examples of load deflection curves of mooring lines, are given in Fig. 5

In the linear numerical model only one spring constant may be used for each mooring line. The approach used to handle this difficulty was to solve the equations of motion with two different mooring types and then to make a logical engineering decision among the resulting amplitudes of motion.

The two mooring types are:

1. Free mooring
2. Actual mooring, where each mooring line is represented by the spring constant appropriate for the line used by the actual ship. This spring constant is determined from linearization around equilibrium state due to steady forces (like wind, current or wave drift).

The consideration of the free mooring is required, because the purely linear system has very strong resonances, which do not exist or are largely attenuated in a real (nonlinear) physical system. In the case of such resonant behavior, the appropriate motions are taken from the free mooring case.

The restoring forces of the modes heave, roll and pitch are dominated by hydrostatic forces, which may be considered linear for small amplitudes of motion. These modes of motion are hardly affected by the mooring restoring forces. Hence, free mooring is used for the heave, roll and pitch equations of motion.

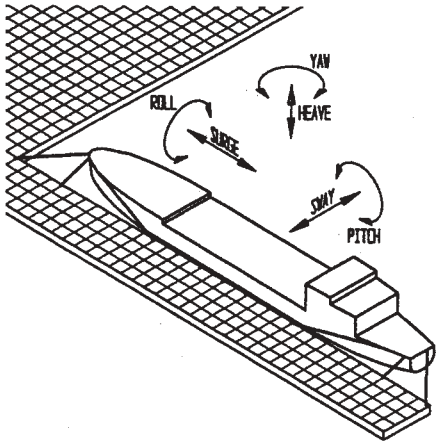


Figure 6: Six degrees of freedom of a moored ship

The six modes of motion are illustrated in Figure 6.

### 2.3.4 *Prediction of operability*

The final results of the entire modeling process are operability conditions of the berthed ships. Disturbance to loading or unloading operations may be caused by large motions of the vessel which disturb the cargo handling, or by the breakage of mooring lines.

In the present numerical models the operability criteria consider movements of ships and do not account for mooring forces. The nonlinear reaction curves of the mooring lines make it very difficult to predict reliable mooring forces using a linear model. Practically, the combination of the motion criteria, which were adopted, and the characteristics of typical mooring systems, make the probability of occurrence of a line breakage prior to exceeding of the motion criteria to be very small. In general, a stiff mooring system will reduce movements of ships but will break before a compliant mooring system which enables larger movements. The approach used for the representation of mooring (see 2.3.3), where

two mooring systems are investigated, is expected to provide reasonably good predictions.

After reviewing several operability criteria, which were published or used in the past (PIANC reports, PIANC, 1995), as well as several reports about problems during operation, which happened at the Haifa East quay, CAMERI decided to use the following operability criteria, based on characteristic ship motions, for Haifa East:

**Operability criteria**

**Characteristic ship motion (2*Sqrt(2)*RMS)**

| Type of Vessel | Surge | Sway | Heave | Roll | Pitch | Yaw |
|---|---|---|---|---|---|---|
| | m | m | m | deg | deg | deg |
| Container | 0.8 | 0.5 | 0.5 | 2.0 | 0.8 | 0.6 |
| Bulk Carrier | 1.0 | 0.8 | 0.5 | 3.0 | 0.8 | 1.5 |

For other harbors appropriate criteria will be derived based on local conditions, and in cooperation with the client.

#### 2.3.5 *Future developments*

The nonlinear reactions of mooring lines and fenders cause in many practical situations motions of the moored ship which exceed the limit of applicability of a simulation approach based on linear dynamics in the frequency domain. The range of validity of the model may be increased in such a situation by adopting a combined frequency-time domain approach. The principle of this approach is first to solve the linear hydrodynamic problem for a set of frequencies, and then to transform the obtained hydrodynamic coefficients to retardation functions which are substituted in a set of integro-differential equations of ship motions in the time domain. The equations of motion in the time domain may handle nonlinear effects such as nonlinear reactions of mooring lines and fenders, nonlinear roll damping and others. This approach has been used in the past for oil terminals in the open sea, but not for a vessel in port. This time domain approach is now under intensive development at CAMERI, and significant progress has already been achieved.

Another important module currently under development at CAMERI is the Navigation In The Approach Channel module, that should become an integral part of future Sea21 installation in harbors. This module will get its input data regarding waves from the wave database, built by the EMS module, regarding currents from the current database, built by the the hydrodynamic module, regarding winds from the local prognostic data and regarding tides from a harmonic tide predictor. The navigation module will determine whether a particular ship with specific loading conditions will be able to enter or exit the installation safely at any time within the 48 hours prognostic period.

## 3 AUXILIARY MODULES

### 3.1 *Objective Oriented Wave Forecasting*

The purpose of this auxiliary module is to determine the site targeted, forecasted wave and wind parameters. This is necessary if the deep sea wave and wind forecast, being drawn from the external information source (like a local weather bureau, etc.), is available on a large scale only. The module is working in real-time mode, and is activated automatically each time when a new data forecast is retrieved. It analyzes the wave propagation from the given locations in the deep sea to the neighborhood of the target site, taking into account the local wind and bathymetry. The output of this module includes the forecasted wave and wind parameters in the vicinity of the target site. These data serve as a basis for the whole structure of the Sea21 system. If the required prognostic data in the neighborhood of the target location is available, this module is deactivated.

### 3.2 *Wave and Wind Measurements and Prognostic Data Correction*

Sea21 is able to retrieve data automatically from local wave and wind measuring equipment (radio buoys, for example), with the desired frequency, and to store them. When measured data are available, the Prognostic Data Correction (PDC) module can be utilized. The PDC module will be activated each time when new data (forecast or measurements) are retrieved. The just obtained prognostic data will be analyzed, and corrected if needed, in accordance with the measurements. The PDC module will utilize an algorithm of statistical trend analysis, based mainly on previous experience. It means that, the more "experienced" the program becomes with time, the more reliable and precise the forecast of the wave and wind parameters will be.

### 3.3 *Harbor and near shore hydrodynamics*

The hydrodynamic module, which also requires "in-house" computations, will be employed in cases where currents are important. It can be used to precompute the current fields for the region of interest for a set of most typical wind/wave conditions.

The 3-D numerical model, developed at CAMERI (see Sladkevich, Militeev and Kit 1997), provides accurate, reliable solutions for the near-shore zone. This 3-D model is able to take into account temperature variations in the water, as well as the concentration of dissolved contaminants and other passive scalars. This hydrodynamic model was already successfully applied in several projects.

## 4 PRACTICAL REALIZATION

All computational modules are linked together by the Graphical User Interface (GUI, see Fig 8). The GUI ensures continuous, managed activity of the system, provides easy access to the stored information, and allows user-friendly, simple data input and output. The automation feature of the interface guarantees minimum requirements from the operator. The human interference will be required only in the case of possibly dangerous weather conditions. The GUI manages communication to the external information sources and automatic data retrieval. The wide range of communication methods, including the direct modem connection and the Internet http and ftp connection, is supported by Sea21. The system provides automatic communication error correction, and the operator is notified in the case of unrecoverable error occurrence.

### 4.1 *Possible system configurations*

Being a modular, multi-purpose system, Sea21 may be pre-designed and installed to suit the customer's specific needs and interests. A wide range of system installations can be constructed with different levels of sophistication. The main goal of each one of them is to facilitate improved usage of a certain marine installation, taking into account the local conditions and its specific requirements. A few possible configurations are described below.

- **Local wave forecasting**
  The output of this simplified system is a wave field in the local region of interest, forecasted up to 48 hours. The installation includes a pre-programmed personal computer, GUI, a communication module, a data correction module (if needed), and an Objective Oriented Wave Forecasting module. This system was designed for operators of marinas and small (fishing) harbors, who are interested in a more detailed wave forecasting than that available from the media.

- **Operability Forecasting for an Open Sea Terminal**
  The output of such a system, in addition to local wave and current fields, is a fore-

cast concerning the possibility to run loading/unloading operations, the need to reinforce the mooring system, and in extreme conditions the need to leave the terminal. The installation includes a pre-programmed personal computer and most of the system modules, as needed. This system may be installed at any type of loading/unloading terminals in open seas, like multi buoy terminals, mono buoy terminals and jetty type terminals.

- **Operability Forecasting for Ships Berthing in a Harbor**
  This is the most sophisticated system, which includes all the relevant software modules. The operator is provided with all the forecasted data available, including local wave and current field and operability conditions for all ships berthed in the port, as well as measured waves, wind and currents, where applicable.

## 4.2 *How does the system work*

The most heavy numerical tasks, requiring a large amount of computer time, are carried out in advance at CAMERI. The results are stored in the form of look-up tables, covering all the statistically possible cases. These results, together with the invariable data, like port layout, region and harbor bathymetry, characteristics of vessels, mooring and fendering systems, etc., compose the so-called static database. The results of all the calculations performed "on-site" are stored for a required period of time in the dynamic database. The Figure 7 presents a simplified data flow chart of the system. Detailed structure is given in Figure 9. The working cycle of the system is as follows:

- The large scale deep water wave and wind prognostic data are automatically retrieved from the external source (local weather bureau, etc.), by modem connection or via the Internet connection, with a desired frequency (2 - 4 times per day, as needed).

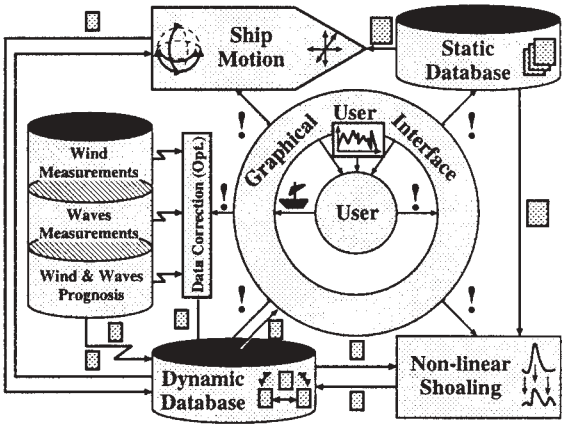


Figure 7: Simplified structure of the Sea21 system

- Further, these data are transformed to yield the near site deep water wave and wind prognostic data, if needed.

- Where applicable, measured wave and wind data are automatically retrieved with a high frequency (each 3 - 6 hours). The prognostic data correction, based on measurements, allows to avoid rough mistakes in the near site deep water wave and wind prognosis.

- The prognostic data are analyzed and, if a specified criterion is not exceeded, the system remains in the sleep-mode. Otherwise, the non-linear refraction module is activated. This module computes the wave spectrum transformation from deep water to the port entrance, including long wave generation. The results obtained are reanalyzed, and if normal "near-port conditions" are obtained, the system returns to the sleep-mode.

- If there is any change of conditions for the worse, the operator is notified both by visual and audio alarms, and is prompted to enter data related to ships scheduled to be in the port within the following 48 hours. The be-

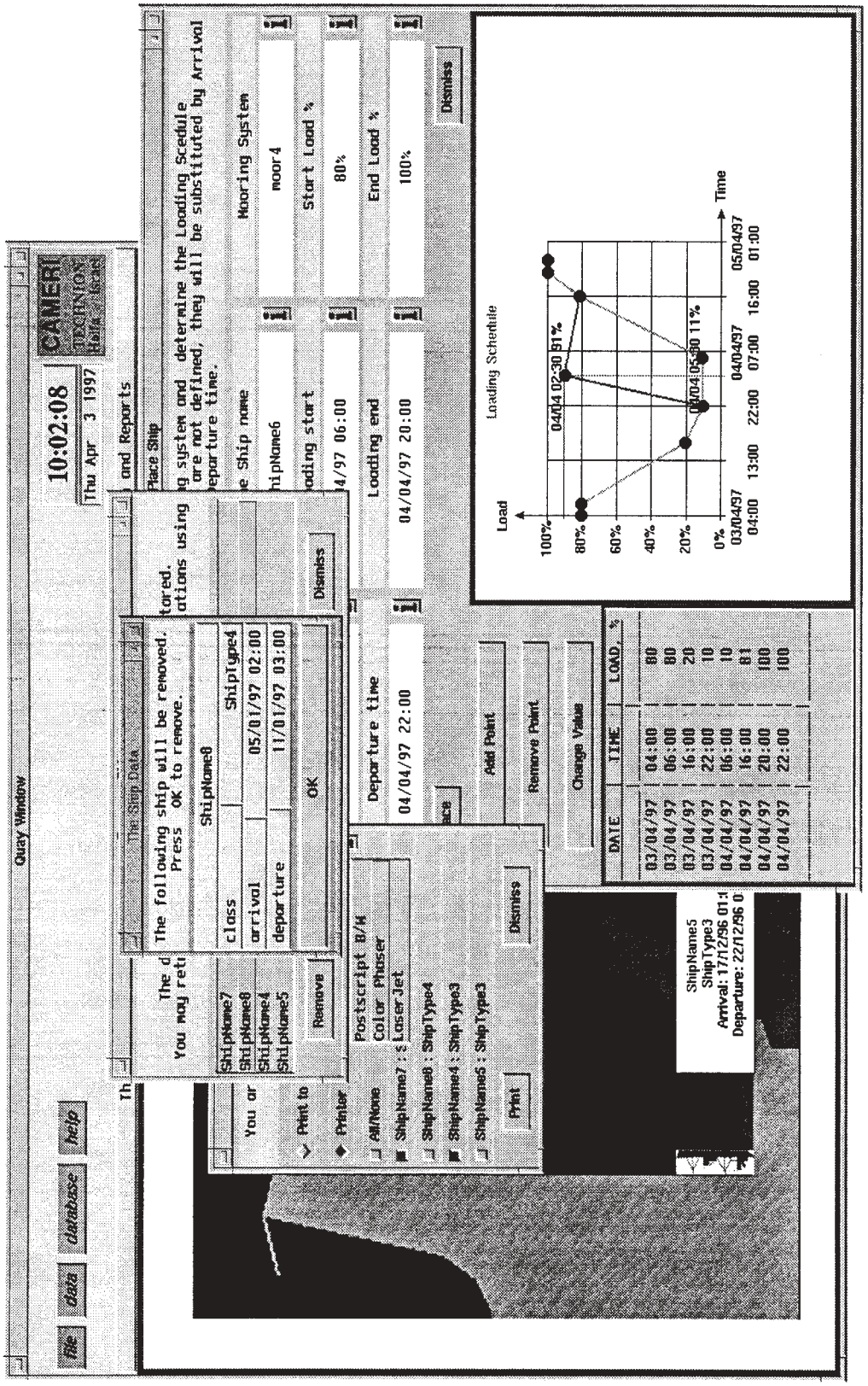


Figure 8: Sea21 GUI at work

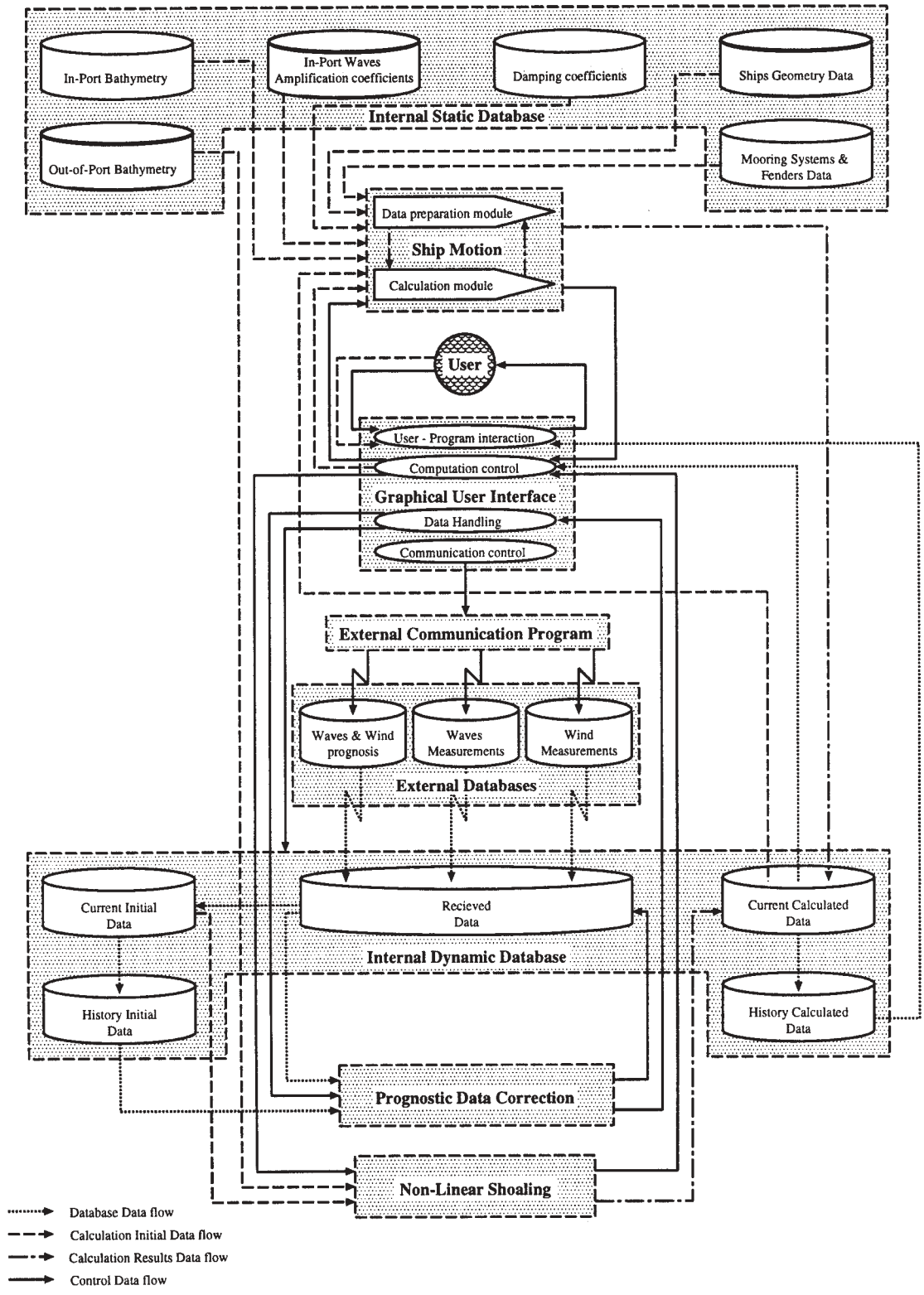


Figure 9: Detailed structure of the Sea21 system

havior of vessels, that the system was notified about them, is calculated automatically. The data stored in the static database are consequently retrieved and interpolated in accordance to the current conditions. This provides the wave and current fields in the port. In addition, harmonic predictor provides the tidal information.

- In the last stage of the cycle, the Vessel-In-Port module computes the operability conditions for the ships berthed in the harbor.

The operator has access to any required data stored in the system and may force the system, at any time, to leave the sleep-mode.

## ACKNOWLEDGMENTS

Sea21 is being developed by CAMERI's research staff, which in addition to the authors includes: Prof. Yehuda Agnon, Dr. Nitai Drimer, Dr. Dmitry Dveyrin, Prof. Eliezer Kit, Dr. Alexandru Sheremet, Dr. Michael Sladkevich, Dr. Gregory Zilman.

The authors acknowledge the assistance of their colleagues at CAMERI in the preparation of this report.

## REFERENCES

1. Berkhoff, J. C. W., 1972: "Computation of combined refraction - diffraction", *Proc. 13th Conf. Coastal. Eng., ASCE* **1,** 471 - 490.

2. Drimer, N., 1994: "The interaction of gravity waves with marine structures", D. Sc. thesis, Technion - Israel Institute of Technology, Haifa32000, Israel.

3. Madsen, P. A. and J. Larsen, 1987: "An efficient finite-difference approach to the mild slope equation", *Coastal Engineering,* **11,** 329 - 351.

4. Permanent International Association of Naval Congresses (PIANC), 1995: "Criteria for movements of moored ships in harbours. A practical guide", *Report of Working Group no. 24 of Permanent Technical committee 2. Supplement to bulletin N 88.*

5. Sheremet, A., 1996: "Wave interactions in shallow water". D. Sc. thesis, Technion - Israel Institute of Technology, Haifa32000, Israel.

6. Sladkevich M. and H. Rubin, 1992: "Sea currents and contaminants transport at the coast of Tel-Aviv", in *French - Israeli Symposium on the continental margin of the Mediterranean sea,* Haifa.

7. Sladkevich, M., A. N. Militeev and E. Kit, 1997: "Numerical models of pollutant transport in coastal environments", in *Numerical Methods in Laminar and Turbulent Flow*, vol. 10, Pineridge Press, Swansea, UK.

# A WAVE FORECASTING SYSTEM FOR THE SPANISH HARBOURS

Juan Carlos Carretero Albiach
Marta Gómez Lahoz
Enrique Álvarez Fanjul
Marta de Alfonso Alfonso-Muñoyerro
José Damián López Maldonado

Clima Marítimo - Puertos de Estado
Madrid
SPAIN

## 1. INTRODUCTION

A wave forecasting system developed to predict waves at the coast is run on a twice a day cycle by **Clima Marítimo (CM)**, a group dependent on the Spanish Holding of Habours. This system is based on two wave generation models: the WAM model, the WAMDI group (1988), Komen et al (1994), and the WAVEWATCH model, Tolman (1991, 1992), and on a propagation model: the PROPS model, Garci (1996), Rivero and Arcilla (1993), and is driven by wind fields supplied by **Oceanweather Inc. (OWI)**. The system is designed to provide a wave forecast of 72 hours of horizon to the Spanish harbours in the Atlantic and in the Mediterranean coasts of Spain. The mixture of scales involved in the system : basin scale to coastal scale, needed to predict waves in the coast, makes the difference with other operational forecasting systems run by national met-offices which are usually developed to predict waves in open waters.

The system described in the present paper, is based on two implementations of the WAM model, one for the Atlantic Ocean, and one for the Mediterranean Sea. To obtain a high resolution close to the Spanish coast without resorting to high resolutions in the deep ocean, a two-way nesting scheme for the WAM model has been developed and implemented at CM. The WAM grid then provides boundary conditions to applications of a high resolution wave generation model (WAVEWATCH) and a phase averaged monochromatic wave propagation model (PROPS). For this last coupling of WAM and PROPS, a new approach has been developed. The coupling, which has an extremely low computation cost, is based on linear theory and provides solutions only on those points of interest.

## 2. WIND FORECAST

Twice a day, OWI produces a wind forecast for CM, the main features of this wind fields are shown in Table 1.

TABLE 1. Main features of the OWI wind forecast produced for CM

| Variable | Value |
|---|---|
| Northern limit | 50° |
| Southern limit | 25° |
| Eastern limit | 16° |
| Western limit | 20° |
| Grid spacing | 0.5° |
| Analyzed fields | -18 to 0 every 6 hours |
| Forecasted fields | +6 to +72 every 6 hours |
| Cycles | two, for 0Z and 12Z |

The specification of analysis and forecast surface wind fields for the eastern North Atlantic Ocean and western Mediterranean Sea for CM in the present application makes use of a new Interactive Objective Kinematic Analysis/Forecast (IOKA) system, Cox et al. (1995) developed at Oceanweather Inc. (OWI) and introduced into its operational global real time forecast operation in 1994.

The IOKA system is used for both the "analysis" wind fields and the wind fields at the "forecast" horizons. At analysis time steps, the data consist of a background analysis taken from the latest global analyses available from the OWI global forecast system plus reports of surface wind

from transient ships, buoys and coastal and island reporting stations deemed to be representative of over-water conditions, as transmitted over the global telecommunications system. The analyst then is able to modify these data and add kinematic control points to effect desired modifications. At forecast horizons, the background surface wind fields are derived from surface pressure fields taken from NOAA's global spectral AVN model using OWI's planetary boundary model, see e.g. Cardone et al. (1996). These fields are then manipulated by the forecaster using a workstation.

The area covered by these wind fields is smaller than the WAM grid for the Atlantic application, so the AVN model winds are also retrieved on a coarse grid and interpolated to be used as a complement for the OWI fields to the South, West and North of the grid.

## 3. WAVE FORECAST

### 1. Basin scale

The present system is designed to forecast waves in the coast but swell generated far away from the coast has to be considered and basin scale applications have to be developed, i.e. the whole North Atlantic Ocean has to be modelled to forecast waves in the Atlantic Coast of Spain. Two applications of a wave generation model at basin scale had to be developed: the first one covering the North Atlantic Ocean and the second one covering the Western Basin of the Mediterranean Sea. The model run for this purpose is the standard WAM model cycle 4, Günther et al. (1991), with some modifications carried out and implemented by CM in the model, although the physics in the standard cycle 4 version of the model remains untouched.

a) WAM model

The WAM cycle 4 wave generation model integrates the basic transport equation ( 1) describing the evolution of a two-dimensional ocean wave spectrum $F(f,\theta,\lambda,\phi,t)$ with respect to frequency $f$ and direction $\theta$ without any additional ad hoc assumptions regarding the spectral shape

$$\frac{\partial F}{\partial t} + (cos\phi)^{-1}\frac{\partial}{\partial \phi}(\dot{\phi} cos\phi F) + \frac{\partial}{\partial \lambda}(\dot{\lambda} F) + \frac{\partial}{\partial \theta}(\dot{\theta} F) = S \qquad (1)$$

where $S$ is the net source function describing the change of energy of a propagating wave group travelling along a great circle path. The three source functions ( 2) for the deep water case describing the wind input, non-linear transfer, and white capping dissipation respectively,

$$S = S_{in} + S_{nl} + S_{ds} \qquad (2)$$

are prescribed explicitly and are integrated by means of implicit second-order, centered difference equations given by

$$F_{n+1} = F_n + \frac{\Delta t}{2}(S_{n+1} + S_n) \qquad (3)$$

where $\Delta t$ is the time step and the index $n$ refers to the time level. For the propagation, a first order upwind scheme is applied

$$F_j^n - \sum_k \frac{\Delta t}{\Delta x_k \cos\theta_j}[(u\cos\phi F^n)_j - (u\cos\phi F^n)_{k\_}] = F_j^{n+1} \qquad (4)$$

the index $k\_$ refers to the neighbouring grid point in the upstream propagation direction relative to the reference grid point $j$. The index $k$ runs over the three propagation directions $\lambda$, $\theta$ and $\phi$. $u_k$, $\Delta x_k$ denote the velocity component ($\lambda$, $\theta$, $\phi$) and grid spacing respectively in the relevant direction. This wave model was developed by a wide group of scientists from different research institutes (The WAMDI Group), following the recommendations derived from the Sea Wave Modeling Project, SWAMP group, (1985). One of the objectives of the group was the implementation of an operational global version of the model at the ECMWF centre, and was achieved in 1992, Günther et al. (1992). CM has been a member of the group since 1986 and has been involved in different aspects of the work, Carretero and Günther (1992). The final report of the group has been recently published, Komen et al (1994).

b) Two-Way nesting in the WAM model

The grid spacing required to resolve the coast should be of no more than 0.5°, but the computer costs makes prohibitive to consider such a high resolution for all the area. Roughly speaking, the computational effort varies linearly with the number of grid points and this number is increased with the square of the increase in grid spacing.

Nesting was introduced as an option in cycle 4 of the model. This option enables the user to run the model on a coarse grid in order to produce boundary conditions for a smaller area, included in the first one, for which a higher resolution is needed. The advantages of chosing a one-way nesting scheme to increase the resolution in an area as

oposed to covering the whole basin with a fine grid are evident, but it was found that this nesting procedure is not applicable when the resolution has to be enhanced drastically, unless intermediate grids are placed between the coarse and the fine grid areas. This solution, in turn, requires an excess of computing resources. Technical problems of one-way nesting have also to be considered. For each propagation time step, wave spectra at all boundary points are stored on disk and this file is kept until the run is completed. Of course, computer time spent writing and reading boundary conditions from disk should also be taken into account.

Being the purpose of our nested application to produce boundary conditions for coastal applications of a wave model, we will need to enhance our resolution to spacings of a few kilometers. As already noted, the enhanced resolution in a nested scheme should be gradual, and this implies that for this application many grids should be nested. But this option will multiply the problems mentioned above in proportion to the number of grids used, to the extent of making it non-viable.

In order to minimize the previously mentioned problems, a two-way nesting approach was finally chosen. This scheme, developed for CM's application, Gómez Lahoz M., Carretero J.C. (1997), works in practice as a variable grid spacing scheme in the sense that all grid points are integrated at the same time and that the grid spacing depends on the area. The resolution is enhanced through consecutive rectangles of regular spacing. At the boundaries of these rectangles, the grid is not continuous, and some grid points obtain energy by interpolation and others by advection. Interpolation is still present, but the resolution can be enhanced gradually, and this fact minimizes the problems produced by linear interpolation. This method enables the user to enhance the resolution for more than one area in the same grid, and allows one to reach resolutions sufficiently high so as to produce boundary conditions for coastal applications, i.e. propagation models developed for harbours, etc.

To implement such a scheme in the model implies a new organization of the grid, and to modify the advection routine so as to make it compatible with the new grid arrangement (the first order numerical scheme has been kept for the advection). The problem is solved by covering the whole area with a grid as fine as the finnest grid spacing defined by the user. Grid points are activated or deactivated to define different resolutions in different areas (all points will be considered active in the finnest grid area). Neighbouring points for energy advection are computed considering the resolution defined for the area, in practice this means that non active points are skipped in the advection. The propagation time step has to be reduced to satisfy the Courant-Friedrich-Lewy (CFL) criterion, and to avoid reducing the source term integration time step as required in the standard version of the model, the code has been changed at CM so as to allow a propagation time step smaller than the source term integration time step.

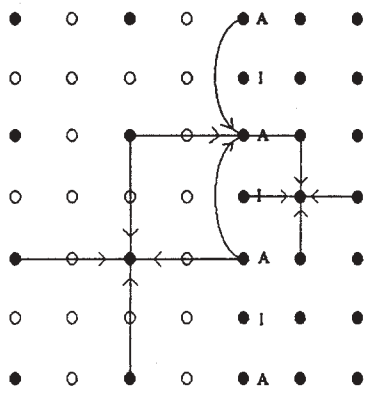


FIG.1. Wave advection in the limit of areas with different resolution. A-points get energy by advection and I-points by interpolation.

Figure 1 shows the advection scheme for a grid portion containing a border between rectangles of different resolution, filled circles indicate active grid points, and blank circles are deactivated points. It shows how there are two types of grid points in the boundary, some get energy by advection (A) and some others by interpolation (I). For I type grid points, the standard algorithm implemented in the model for spectra interpolation is carried out. For A type grid points, the distance to the neighbours has to be taken into account when advecting energy. The grid spacing is dependent on $\Delta\lambda$ and $\Delta\phi$ which in turn, are dependent on the location of the grid point to be computed. Additionally, $\Delta\lambda$ and $\Delta\phi$, depend on which is the up-stream neighbouring grid point, so this makes these variables dependent also on the direction $\theta$ of the spectrum component which is advected. The numerical implementation of the advection equation was modified to take into account these new dependences and an easy way for the user to define the grid was included in the user input files of the model.

c) North Atlantic Ocean

The coverage and grid points of the two-way nested application are shown in Figure 2, and the main specifications are described in Table 2.

TABLE 2: Model and grid specifications for the North Atlatic Ocean

| Variable | Value |
|---|---|
| Model version | Deep water |
| $\Delta t$ for propagation | 600 s |
| $\Delta t$ for source terms | 1200 s |
| Spectral directions | 24 |
| Spectral frequencies | 25 |
| Lowest frequency | 0.041772 Hertz |
| Highest frequency | 0.41145 Hertz |
| Northern limit | 69° |
| Southern limit | 18° |
| Western limit | 60° |
| Eastern limit | 9° |
| Coarsest grid spacing | 3° |
| Finest grid spacing | 0.25° |

d) Mediterranean Sea

The coverage and grid points of the two-way nested application are shown in Figure 3, and the main specifications are described in Table 3.

TABLE 3: Model and grid specifications for the Mediterranean Sea

| Variable | Value |
|---|---|
| Model version | Shallow water |
| $\Delta t$ propagation | 300 s |
| $\Delta t$ source terms | 1200 s |
| Spectral directions | 24 |
| Spectral frequencies | 25 |
| Lowest frequency | 0.041772 Hertz |
| Highest frequency | 0.41145 Hertz |
| Northern limit | 45° |
| Southern limit | 34° |
| Western limit | 7° |
| Eastern limit | 17° |
| Coarsest grid spacing | 0.25° |
| Finest grid spacing | 0.125° |

## 2. Local scale

The resolution of the WAM grid can be enhanced easily in different areas with the two-way nesting scheme but still it is not possible to reach resolutions of around 1 minute for areas where this resolution is needed and where wave generation, wave bottom and wave current interaction has to be carefully considered. The most practical option for this areas, is to nest in a one-way scheme a high resolution application of a wave generation model to the WAM application, in the present system, the WAVEWATCH model, is used for this purpose.

a) The WAVEWATCH model

The ocean wind wave model WAVEWATCH-II, which is a further development of WAVEWATCH, developed by Dr. Hendrik L. Tolman, is a third generation wave model which integrates a wave action conservation equation explicitly considering wave growth and decay, wave-wave interaction and dissipation due to whitecapping and wave-bottom interaction. It furthermore incorporates effects of unsteady and inhomogeneous currents on ocean waves. This model has been developed for high resolution applications in shallow waters considering interaction with ocean currents. The model has been modified at CM to make it cappable of working as a nested application for a certain area, receiving boundary conditions from other spectral models. Another modification to the code has been to introduce the possibility for the user to define a propagation time step smaller than the source term integration time step.

b) WAVEWATCH APPLICATION FOR THE STRAIT OF GIBRALTAR

As can be seen in figures 2 and 3, the WAM grids developed for the Atlantic Ocean and Mediterranean Sea are not connected through the Strait of Gibraltar. Waves generated in the Atlantic Ocean entering the Mediterranean Sea through the strait are not considered by the WAM model and this area has to be modelled with a resolution not smaller than 1 minute to obtain reasonable results. For this reasons the WAM forecast is not valid for the area, were three harbours: Algeciras, Ceuta and Cadiz are located.

A local application of the WAVEWATCH model has been developed, covering the Gulf of Cadiz, Strait of Gibraltar and partially the Alboran Sea. This application is nested to the WAM grids for the Atlantic Ocean and the Mediterranean Sea, the boundary conditions are the WAM energy spectra modified as wave action spectra and interpolated in space and time.

The coverage and grid points of the application are shown in Figure 4, and the main specifications are described in Table 4.

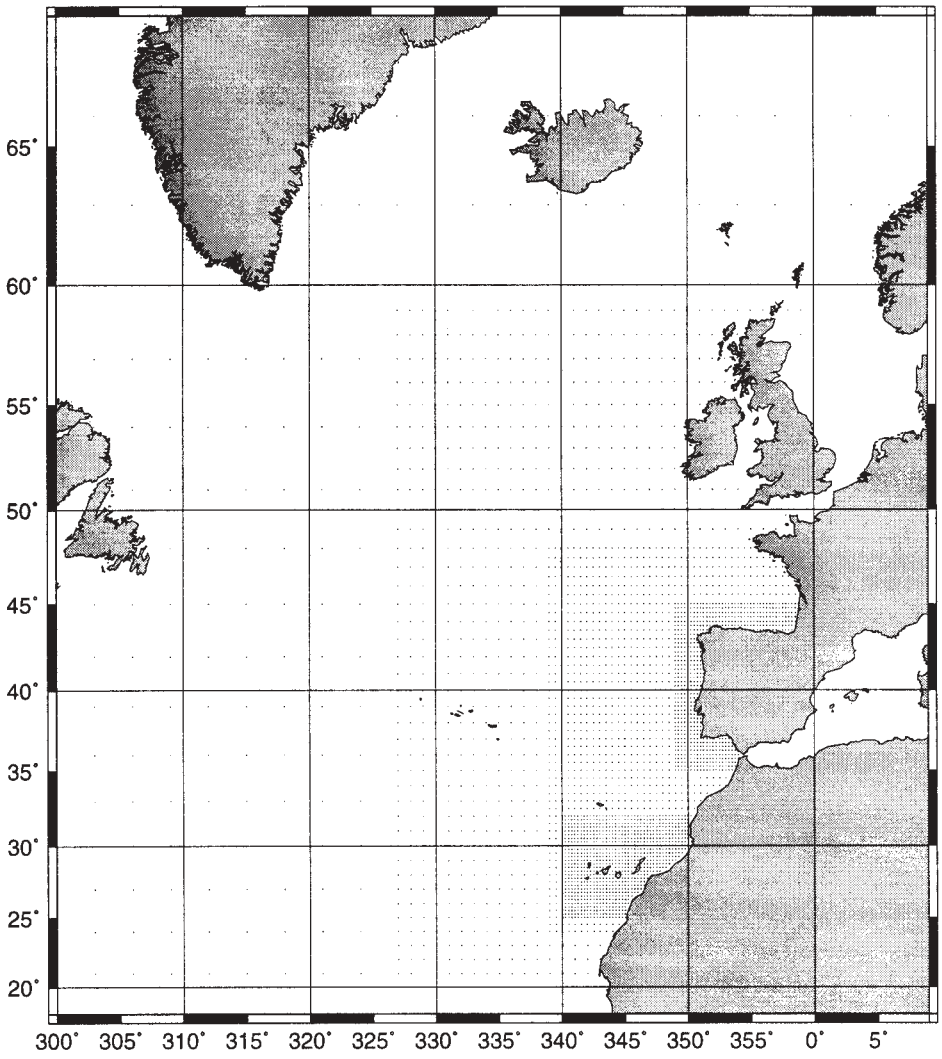


FIG. 2. WAM grid for the North Atlantic Ocean.

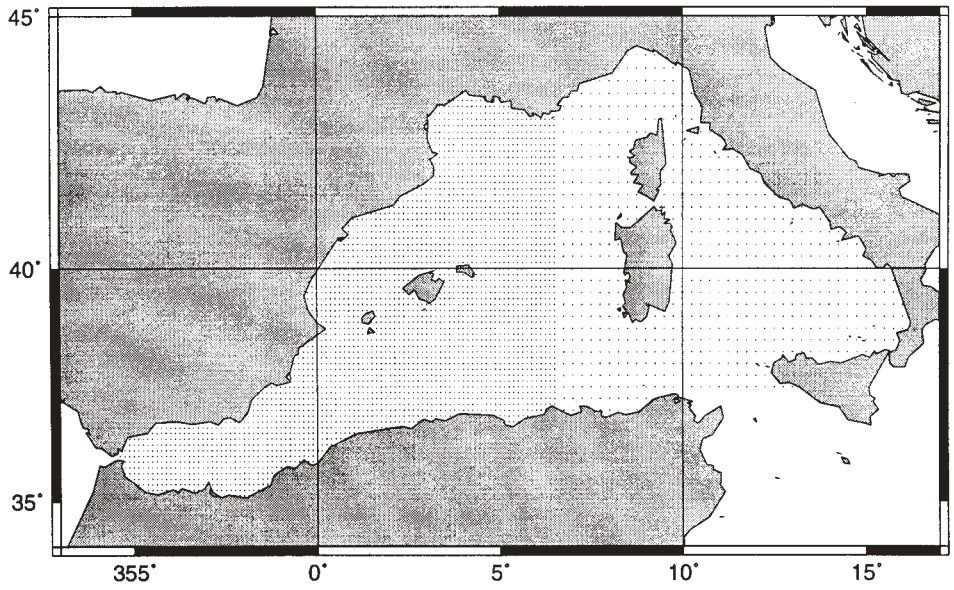


FIG. 3. WAM Grid for the Mediterranean Sea.

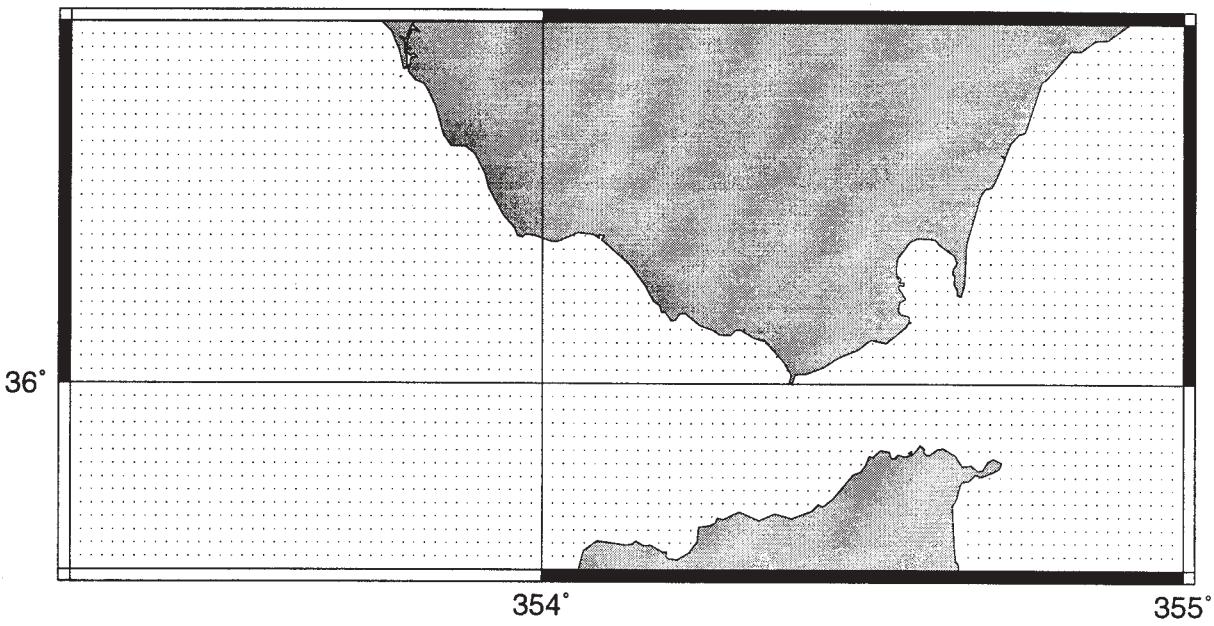


FIG. 4. WAVEWATCH grid for the Strait of Gibraltar

TABLE 4: Model and grid specifications for the Strait of Gibraltar

| Variable | Value |
|---|---|
| Model version | Deep water |
| $\Delta t$ propagation | 300 s |
| $\Delta t$ source terms | 1200 s |
| Spectral directions | 24 |
| Spectral frequencies | 25 |
| Lowest frequency | 0.041772 Hertz |
| Highest frequency | 0.41145 Hertz |
| Northern limit | 45° |
| Southern limit | 34° |
| Western limit | 7° |
| Eastern limit | 17° |
| Grid spacing | 0.25° |

### 3. Local propagation

Although the two-way nesting allows a drastic improvement in the resolution at the coast, a grid size of 0.250 is still not enough to accurately describe the changes in water depth at the coastal shelf and nearshore. On the other hand, for the Atlantic application of the model, only a few grid points can be considered as shallow water, and thus, the deep water version is used. There is a gap, in average, of 10 Km between the nearest WAM grid point and the coastline, precisely where waves are mostly affected by bottom variations, and the transformation of the waves when propagated to the coast cannot be modelled by the operational application of the WAM model. A different scheme, based in the propagation of the wave generation model spectra in shallow water, has to be applied.

#### a) DESCRIPTION OF THE SPECTRAL WAVE MODEL PROPS.

The PROPS model is an spectral wave propagation code able to propagate wave spectra into very shallow waters. The code solves the combined effects of shoaling, refraction, diffraction, wave-current interaction and energy dissipation due to wave breaking and bottom friction. In order to propagate a spectrum, the code follows this sequence; first, the wave spectra is discretized into a finite number of components (bins), then each component is propagated and, finally, the spectra is reconstructed. The model is a phase-averaged wave propagation code based on the wave action conservation equation, the irrotationality of the wave number, the dispersion relationship and, in order to take diffraction effects into account, the eikonal equation.

#### b) ONE POINT SPECTRAL PROPAGATION

A direct coupling between PROPS and WAM is not possible because of time constraints in an operational system. A new approach (hereafter called one point spectral propagation), based on the idea of providing solutions only on those points of interest and not in the complete simulation domain has been developed at CM, Alvarez *et al* (1997). The new coupling system was developed

under the assumptions that wave generation is negligible and linear theory can be applied. Under these assumptions, the coupling to provide wave spectra in a selected point is established as follows:

Pre-operational stage:

1) For a given simulation domain, the PROPS is employed as a linear monochromatic model to propagate a set of regular wave trains corresponding to each component of the WAM spectra between the WAM point nearest to the coast (generally located in deep waters due to the narrow Spanish shelf) and the selected point. Simulations are performed for all the WAM frequencies and the directions corresponding to waves travelling to the coast. No breaking or bottom friction are herein considered.
2) As a result of the simulations, the direction of propagation and the value of the coefficient K (the ratio between the propagated and incident wave height) are obtained in the selected point for each spectral component and stored. The input variables of those tables are the angles and frequencies in which the WAM spectra is discretized and the output are the values of K and of the direction of propagation angle $\alpha$ in the selected point.

Operational stage:

1) The one-point spectral propagation code makes use of those tables to compute the propagated spectra. First, the energy density of each WAM spectrum component is multiplied by the square of the corresponding value of K. The new value, computed with this method and corresponding to each component of the initial spectrum, is allocated in the new spectrum in components of the same frequency (linear theory) and directions obtained by the corresponding angle $\alpha$. The propagated spectrum is computed by addition of the results of applying this process to all the components of the WAM spectrum.
2) Finally, the integrated parameters, such us significant wave height or mean direction, are computed from the shallow water reconstructed spectrum.

The main advantage of this system is the extremely low computational cost. This allows to perform the WAM spectra propagation to the coastal points of interest without a representative computational effort in addition to the prediction system. Results obtained from this method are identical to those obtained with the linear version of the PROPS spectral model in the point of interest.

## 4. VERIFICATION

The output of the system, both predicted and analyzed waves, is regularly verified against measurements from the Spanish network of directional and scalar buoys. An example of the performance of the system is shown here, it corresponds to the skill of the analyzed and predicted values of significant wave height (Hs) during the period May 97 to October 97 both inclusive when compared with buoy measurements. The value of Hs for the model is derived in the usual way from the full bidimensional spectrum, and it is derived from the frequency spectrum for the buoy data ( 5).

$$H_s = 4\sqrt{\int_f S(f)df} \qquad (5)$$

The scalar buoys belong to the REMRO network and are of the *Waverider* type from *Datawell*. Directional buoys belong to the EMOD network, made up of *Wavescan* type buoys from *Seatex* and to the RAYO network, made up of *Seatex* buoys from *Oceanor*. Table 5 shows the main features of the buoys which are used in this verification, and figures 5, 6 7 and 11 show their location.

For this verification, no time or space interpolation has been applied to the model output. The nearest model grid point for coincident output times has been compared with the bouy data.

TABLE 5. Characteristics of the buoys used in this verification

| Location | Network | Type | Water depth(m) | Latitude N | Longitude W |
|---|---|---|---|---|---|
| Estaca de Bares | RAYO | Seatex | Deep water | 44.065° | 7.62° |
| Bilbao | REMRO | Waverider | 50 | 43.4° | 3.14° |
| Gijon | REMRO | Waverider | 23 | 43.57° | 5.65° |
| Las Palmas | RAYO | Seatex | Deep water | 28.2° | 15.8° |
| Mahon | EMOD | Wavescan | 300 | 39.72° | −4.44° |
| Puerto de Cadiz | EMOD | Wavescan | 65 | 36.46° | 6.30° |

The comparison of this two sets of data has been carried out in the following way:

Let $\{X(t_i); i = 1, ..., N\}$ be the time series of Hs measured by a buoy, and $\{Y(t_i); i = 1, ..., N\}$ the time series of Hs computed by the model for the nearest grid point to the buoy and for the same period and time step.

Mean value of buoy measurements:

$$\overline{X} = \mathbf{E}[X] = \frac{1}{N}\sum_{i=1}^{N} X(t_i) \tag{6}$$

Mean value of model measurements:

$$\overline{Y} = \mathbf{E}[Y] = \frac{1}{N}\sum_{i=1}^{N} Y(t_i) \tag{7}$$

Slope of the linear regression (least square):

$$m = \frac{\mathbf{E}[X\,Y] - \mathbf{E}[X]\,\mathbf{E}[Y]}{\mathbf{E}[X^2] - \mathbf{E}[X]^2} \tag{8}$$

Interception of the linear regression (least square):

$$b = \overline{Y} - m\overline{X} \tag{9}$$

Correlation index:

$$IC = \frac{\mathbf{E}[X\,Y] - \mathbf{E}[X]\,\mathbf{E}[Y]}{\{\,\mathbf{E}[X^2] - \mathbf{E}[X]^2\,\}^{\frac{1}{2}}\ \{\,\mathbf{E}[Y^2] - \mathbf{E}[Y]^2\,\}^{\frac{1}{2}}} \tag{10}$$

Root mean square error:

$$RMSE = \frac{1}{N}\,[\sum_{i=1}^{N} (Y(t_i) - X(t_i))^2\,]^{\frac{1}{2}} \tag{11}$$

Bias.

$$Bias = \overline{Y} - \overline{X} \tag{12}$$

Scatter index:

$$SI = \frac{RMSE}{\overline{X}} \tag{13}$$

### 1. WAM output

Tables 6, 7 and 8 show the skill of the WAM model output for the analyzed and the forecasted waves when compared with buoy measurements. Three buoys have been used for this purpose: Estaca, Las Palmas and Mahon. These buoys are representative for three areas (see figures 5, 6 and 7) with different wave climate: the Cantabric Coast of Spain, subjected to waves produced by frontal depressions travelling form West to East; the Canary Islands, with waves frequently produced by trade winds; and the Mediterranean Sea

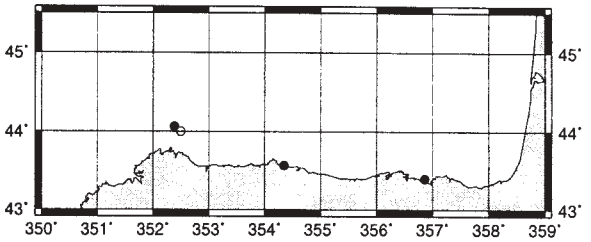


FIG.5. Buoys from Table 5 moored in the Cantabric Coast. Black dots corresponds to actual location of the buoys. The white dot corresponds to the nearest grid point to the Estaca de Bares buoy.

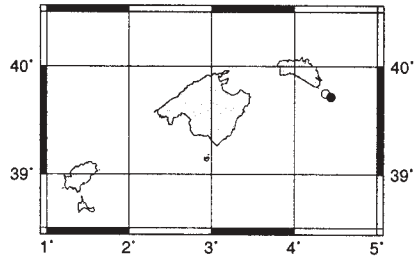


FIG.6. Buoy from Table 5 moored in the Balearic Islands. The black dot corresponds to actual location of the buoy and the white dot corresponds to the nearest grid point.

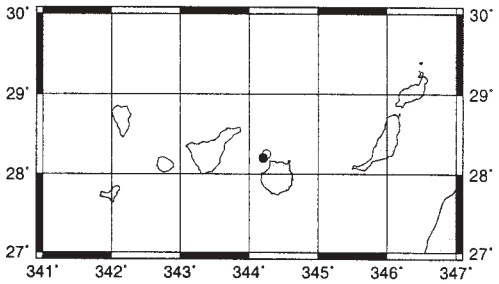


FIG.7. Buoy from Table 5 moored in the Canary Islands. The black dot corresponds to actual location of the buoy and the white dot corresponds to the nearest grid point to the buoy.

with highly variable winds which are very much determined by the orography of the mountains sorrounding the basin. Although near the coast, these buoys are in deep water and not sheltered by the coast, except for Las Palmas buoy, where directions sheltered by the islands can not be accurately reproduced by the model at this resolution.

Figures 8, 9 and 10 show time series of Hs for the month of October compared with the buoy measurements. Analyzed and forecasted values produced by the model are plotted along with buoy measurements. It can be seen that being a sum-

mer period, the mean values for both model and buoy outputs are low with very few storms in the period. Unfortunately, these fact reduces the representativity of the derived statistics.

Analyzed values from the model follows quite well the measurements except for Las Palmas were a more accurate definition of the coastline of the islands is needed to better reproduce the directions sheltered by other islands. A tendency to underestimate peaks can be observed, this fact makes slopes of the regression fitting smaller than one, wind fields every 3 hours would probably produce a more accurate reproduction of the peaks.

Storms are forecasted correctly with 24 hours of anticipation, both for the Atlantic and Mediterranean coasts.

With 36 hours of anticipation, the forecast is still correct for the main features of the storms, but for the 72 hours forecast, some storms in the Mediterranean Sea are not predicted, something coherent with the variability of wind fields in the area. In tables 6, 7 and 8, it can be seen from the scatter and the correlation values how the forecast skill is good up to the 48 hours horizon and acceptable for the 72 horizon for the Atlantic buoys, but the correlation is lost for the Mediterranean 48 hours forecast.

A clear improvement in the skill of the Mediterranean Sea will come through the increment of the number of observations provided to OWI to be assimilated during the production of the forecasted winds, something in which CM is working at present.

TABLE 6. Statistical results of the comparison of Hs between the model output for analysis and +24, +48 and +72 forecast and the Estaca buoy measurements

| Output | Sample | Mean buoy | Mean WAM | Corr. | Slope | Interc. | RMSE | Bias | Scat. |
|---|---|---|---|---|---|---|---|---|---|
| Analysis | 496 | 1.712 | 1.568 | .855 | .72 | .33 | .416 | -.143 | .243 |
| 24 forec. | 229 | 1.747 | 1.602 | .825 | .72 | .35 | .459 | -.145 | .263 |
| 48 forec. | 229 | 1.747 | 1.572 | .768 | .68 | .39 | .528 | -.175 | .302 |
| 72 forec. | 228 | 1.685 | 1.483 | .670 | .55 | .55 | .593 | -.202 | .352 |

TABLE 7. Statistical results of the comparison of Hs between the model output for analysis and +24, +48 and +72 forecast and the Las Palmas buoy measurements

| Output | Sample | Mean buoy | Mean WAM | Corr. | Slope | Interc. | RMSE | Bias | Scat. |
|---|---|---|---|---|---|---|---|---|---|
| Analysis | 445 | 1.393 | 1.231 | .751 | .72 | .23 | .319 | -.161 | .229 |
| 24 forec. | 206 | 1.413 | 1.210 | .754 | .65 | .29 | .341 | -.203 | .242 |
| 48 forec. | 206 | 1.402 | 1.194 | .752 | .63 | .30 | .348 | -.208 | .248 |
| 72 forec. | 205 | 1.424 | 1.189 | .709 | .58 | .37 | .379 | -.235 | .266 |

TABLE 8. Statistical results of the comparison of Hs between the model output for analysis and +24, +48 and +72 forecast and the Mahon buoy measurements

| Output | Sample | Mean buoy | Mean WAM | Corr. | Slope | Interc. | RMSE | Bias | Scat. |
|---|---|---|---|---|---|---|---|---|---|
| Analysis | 1199 | 1.061 | 1.032 | .834 | .71 | .28 | .430 | -.029 | .405 |
| 24 forec. | 279 | 1.068 | .907 | .787 | .65 | .21 | .525 | -.161 | .492 |
| 48 forec. | 281 | 1.051 | .734 | .637 | .43 | .28 | .701 | -.316 | .668 |
| 72 forec. | 282 | 1.043 | .664 | .533 | .35 | .30 | .786 | -.379 | .754 |

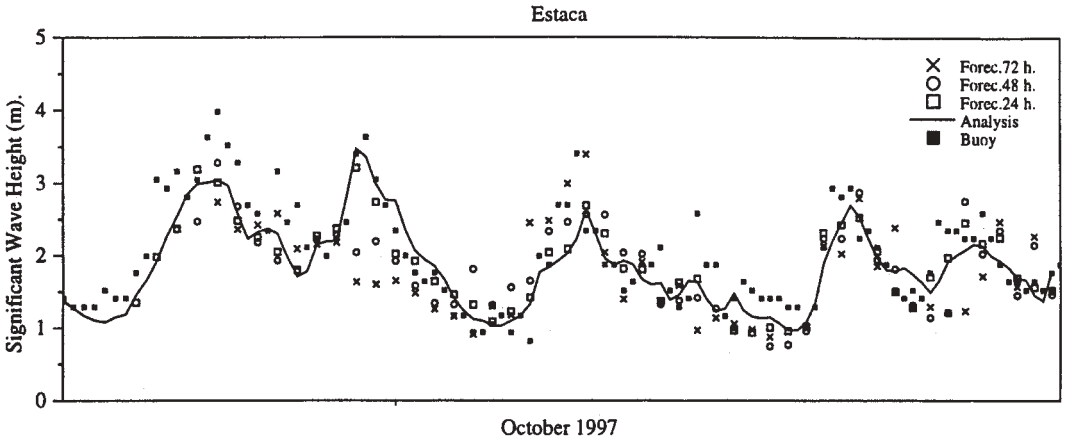


FIG.8. Model and forecasted Hs values compared with the Estaca buoy measurements. The solid line corresponds to the analyzed model values, squares to the +24 forecast, circles to the +48 forescast and crosses to the +72 forecast. Filled black squares correspond to buoy measurements.

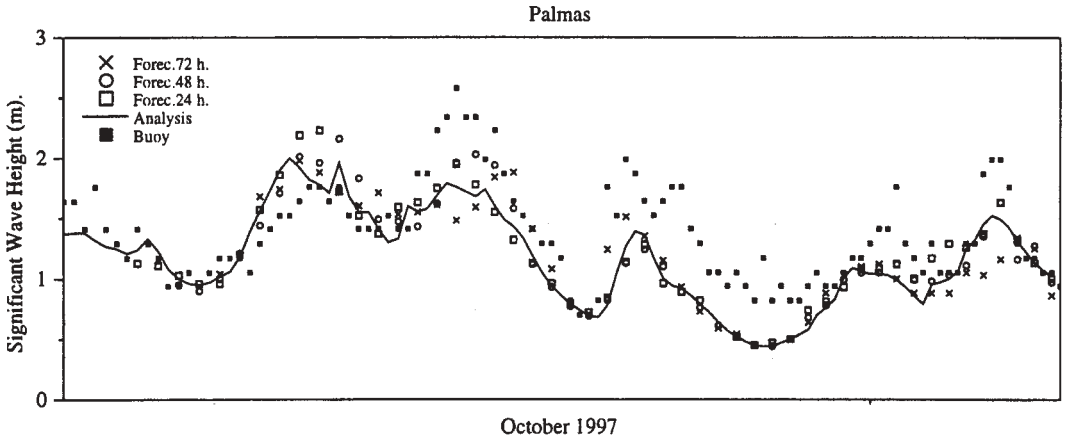


FIG.9. Model and forecasted Hs values compared with the Las Palmas buoy measurements. The solid line corresponds to the analyzed model values, squares to the +24 forecast, circles to the +48 forescast and crosses to the +72 forecast. Filled black squares correspond to buoy measurements.

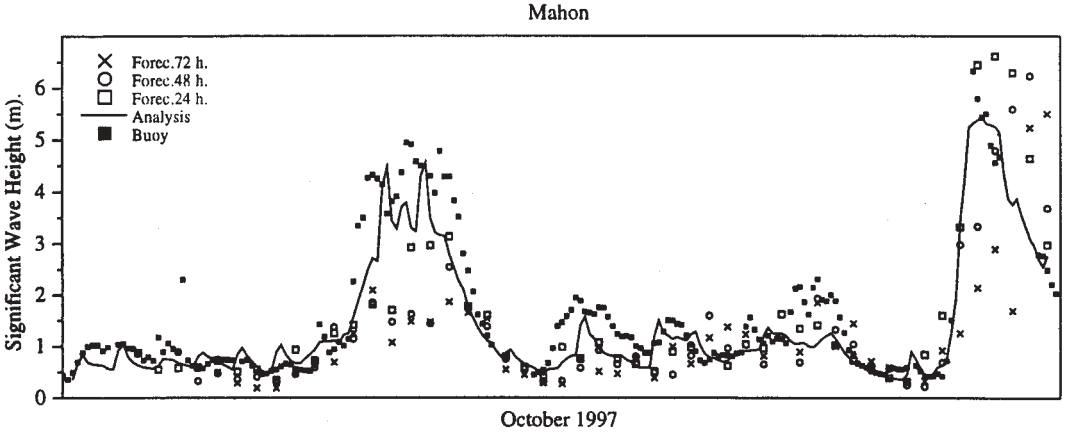


FIG.10. Model and forecasted Hs values compared with the Mahon buoy measurements. The solid line corresponds to the analyzed model values, squares to the +24 forecast, circles to the +48 forescast and crosses to the +72 forecast. Filled black squares correspond to buoy measurements.

TABLE OF CONTENTS
AUTHOR INDEX

## 2. WAVEWATCH output

The verification of the WAVEWATCH output in this example has been carried out with the measurements of a bouoy moored at the Harbour of Cadiz (see Figure 11).

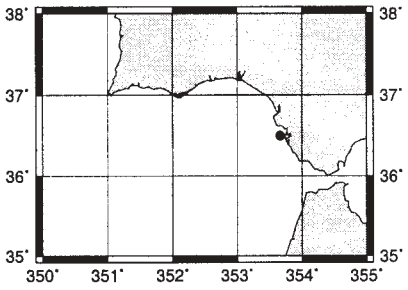


FIG.11. Buoy from Table 5 moored in the harbour of Cadiz. The black dot corresponds to actual location of the buoy.

This buoy is measuring waves subjected to refraction and atenuation by shoals in front of the harbour.

The small mean values of Hs, with long periods of time with waves below 1 meter, produce statistical results for the verification that are not really representive of the skill of the analyzed waves produced by the model. But by observation of Figure 12, if can be seen a very good reproduction of the Hs peaks, something that has been observed since the implementation of the model. From Table 9, we see how the skill of the prediction decays very much after the 48 hour forecast.

Although in this example it is not intended to show verifications of the peak period, it has to be mentioned the extremely good prediction of this parameter for the harbour, something much more relevant in this case than waveheight due to resonance problems in the harbour.

TABLE 9. Statistical results of the comparison of Hs between the model output for analysis and +24, +48 and +72 forecast and the Cadiz buoy measurements

| Output | Sample | Mean buoy | Mean WW | Corr. | Slope | Interc. | RMSE | Bias | Scat. |
|---|---|---|---|---|---|---|---|---|---|
| Analysis | 684 | .759 | .849 | .733 | .87 | .19 | .309 | .090 | .407 |
| 24 forec. | 89 | .715 | .809 | .652 | 1.09 | .03 | .357 | .094 | .500 |
| 48 forec. | 88 | .729 | .780 | .544 | .92 | .11 | .435 | .051 | .597 |
| 72 forec. | 90 | .728 | .658 | .580 | .83 | .06 | .365 | -.070 | .502 |

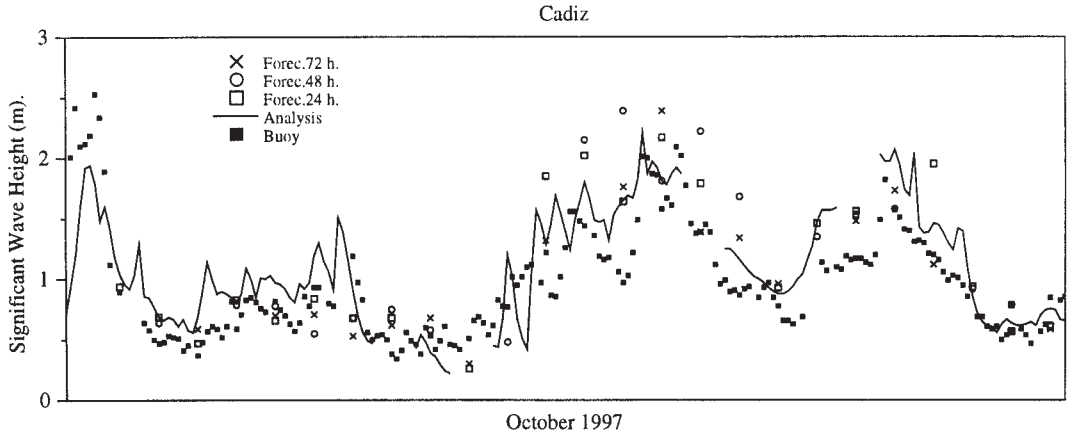


FIG.12. Model and forecasted Hs values compared with the Cadiz buoy measurements. The solid line corresponds to the analyzed model values, squares to the +24 forecast, circles to the +48 forescast and crosses to the +72 forecast. Filled black squares correspond to buoy measurements.

## 3. PROPS output

The one point spectral propagation coupling between WAM and PROPS is carried out to improve the WAM output by taking into accout coastal effects not resolved by the WAM model, but of course the skill of the forecast will be the same one as that of the WAM model which supplies the input to the PROPS model. For this reason only analyzed values are shown in this section. Results from the coupling can be seen on figures 12 and 13.

The clear improvement in the Bias (see tables 10 and 11), specially for Gijon, shows clearly the need of this coupling if waves at the mouth of the harbour are intended to be predicted. Statistical analysis of other time periods (not presented in this paper) show that the coupled system is providing the better results during storm events, when a accurate prediction is really needed.

TABLE 10. Statistical results of the comparison of Hs between the WAM analysis and WAM-PROPS analysis and the Bilbao buoy

| Output | Sample | Mean buoy | Mean model | Corr. | Slope | Interc. | RMSE | Bias | Scat. |
|---|---|---|---|---|---|---|---|---|---|
| WAM | 388 | 1.047 | 1.131 | .819 | .90 | .19 | .358 | .084 | .343 |
| PROPS | 388 | 1.047 | 1.043 | .880 | .98 | .02 | .289 | -.003 | .276 |

TABLE 11. Statistical results of the comparison of Hs between the WAM analysis and WAM-PROPS analysis and the Gijon buoy

| Output | Sample | Mean buoy | Mean model | Corr. | Slope | Interc. | RMSE | Bias | Scat. |
|---|---|---|---|---|---|---|---|---|---|
| WAM | 400 | .979 | 1.340 | .870 | 1.04 | .32 | .465 | .361 | .475 |
| PROPS | 400 | .979 | 1.032 | .839 | .92 | .13 | .304 | .053 | .310 |

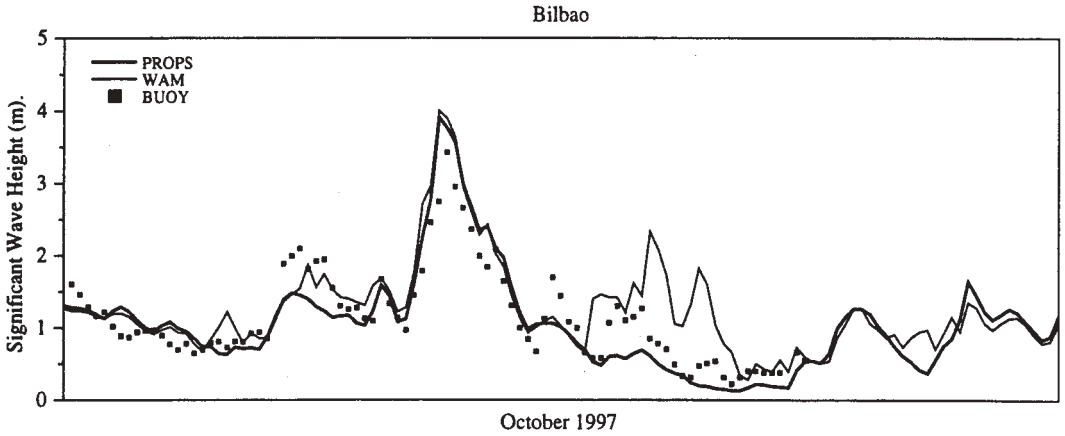


FIG.12. Analyzed WAM and WAM-PROPS values of Hs compared with Bilbao buoy measurements. Gross line corresponds to the WAM output, fine line to the WAM-PROPS output and filled black squares correspond to buoy measurements.

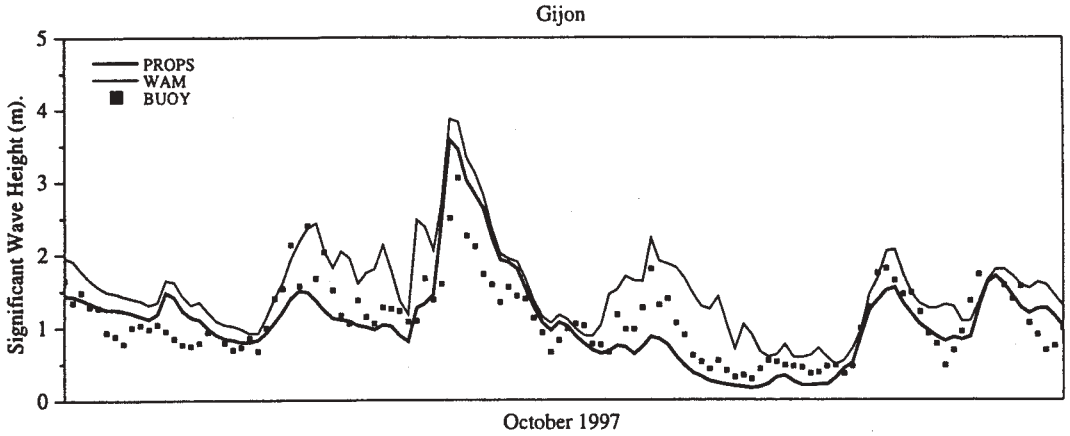


FIG.13. Analyzed WAM and WAM-PROPS values of Hs compared with Gijon buoy measurements. Gross line corresponds to the WAM output, fine line to the WAM-PROPS output and filled black squares correspond to buoy measurements.

## 4. DISTRIBUTION

The forecast is distributed to the users in the three following ways: **WWW**. The users can find at CM's server the forecast along with other information. This information includes an alert system for the harbours with alert warnings which depend on different thresholds defined by the user, reall time verification with coastal buoys, statistics, etc. **Fax**. An automatic fax distribution system is available for the users. This is an expensive and cumbersome system that anyhow has to be offered as many users are not yet connected to the WWW. **Local networks**. The forecast is also distributed through a digital link to the local networks in the harbours. This allows multiple connection points for big organizations such as harbours where only a few connections to the WWW are available.

## REFERENCES

Alvarez, E., M. Gómez, J.C. Carretero, P. Vega and F.J. Rivero, 1997. Coupling of two spectral wave models in the frame of an operational wave forecast system. Wind over wave Couplings, Congres proceedings,1997. The Salford University.

Cardone, V.J., 1996: Specification of the wind distribution in the marine boundary layer for wave forecasting. Report TR-69-01, Geophys. Sciences Lab., New York University, 137pp.

Carretero J.C. and H. Günther, 1992: Wave Forecast performed with the WAM model at the ECMWF. Statistical analysis of a One Month Period (November 1988). ECMWF Technical Report No. 68, UK.

Cox, A.T., J.A. Greenwood, V.J. Cardone, and V.R. Swail, 1995: An interactive objective kinematic analysis system. Fourth International Workshop on Wave Hindcasting and Forecasting, October 16-20, 1995, Banff, Alberta, Canada.

Garci, E., 1996. A spectral wave propagation model. MSc thesis, UPC, Barcelona, Spain. 117p.

Gómez M. and Carretero J.C., 1997: A Two-way Nesting Procedure for the WAM Model: Application to the Spanish Coast. J. Offshore Mechanics and Artic Engineering, Feb 1997, Vol. 119

Günther H., S. Hasselman, P.A.E.M. Janssen, 1991: Wamodel Cycle 4. Technical Report No .4, Deutsches KlimaRechenZentrum, Germany.

Günther H., P. Lionello, P.A.E.M. Janssen, L. Bertotti, C. Brüning, J.C. Carretero, L. Cavaleri, A. Guillaume, B. Hansen, S. Hasselman, K. Hasselman, M. de las Heras, A. Hollingsworth, M. Holt, J.M. Lefevre, R. Portz, 1992: Implementation of a third generation ocean wave model at the European Centre for Medium-Range Weather Forecasts, ECMWF Technical Report No. 68, UK.

G.J Komen, L. Cavaleri, M. Donelan, K. Hasselmann and P.A.E.M. Janssen, 1994: Dynamics and Modelling of Ocean Waves, Cambridge University Press, UK.

Rivero F. J. and A. S. Arcilla 1993: Propagation of linear gravity waves over slowly varying depth and currents. Proceedings on "WAVES'93" Symposium. New Orleans, USA, 518-532.

SWAMP Group, 1985: Sea Wave Modelling Project (SWAMP). An intercomparison study of wind wave prediction models. Part 1: Pricipal results and conclusions. Ocean Wave Modelling. Plenum Press.

Tolman, H.L., 1991: A third-generation model for wind waves on slowly varying, unsteady and inhomogeneous depths and currents. J. Phys. Oceanogr. 21, 782-797

Tolman, H.L., 1992: Effects of Numerics on the Physics in a Third-Generation Wind-Wave Model. J. Phys. Oceanogr., 22, 109 5-1111.

WAMDI Group: S. and K. Hasselman, P.A.E.M. Janssen, G.J. Komen, L. Bertotti, P. Lionello, A. Guillaume, V.C. Cardone, J.A. Greenwood, M. Reistad, L. Zambresky, J.A. Ewing, 1988: The WAM model - A third generation ocean wave prediction model. J. Phys. Oceanogr., 18, 1775-1810.

# A 2-D WAVE ENERGY SPECTRUM MODEL IN THE SHALLOW WATER

Angelidis K. and C. Koutitas
Div. of Hydraulics and Environmental Eng., Dep. of Civil Eng.
Aristotle University of Thessaloniki, AUT
540 06 Thessaloniki, Greece

## 1. INTRODUCTION

In the nature, there are almost always spectral energy waves. In order to deal with the problem of the wave propagation in the nearshore zones, there are many simplifications, from the practical point of view, as the adaptation and use of monochromatic waves for the calculation of the nearshore coastal structures and the relative with them parameters. This and other simplifications have cause lost of informations for the intermediate water region (just out of a harbour, some miles of continental shelf etc.). This work deals with this particular zone.

A linear wave propagation model is presented here. It is based in a finite difference scheme. The model computes the wave energy distribution in the shallow water region. Kinematic and dynamic procedures are involved in this model. The interaction of the wind and waves and the consequent non linear processes (wave generation, dissipation, breaking) are examined here. The bottom topography is also taken into account (processes as refraction, diffraction, shoaling e.t.c.).

Many researchers have contributed on the explanation and understanding of the physical processes and their consequences on this field during the last 25 years. Some of them are, Barnett(1968), Chen(1983), Collins(1972), Divoky(1970), Karlsson(1969), Longuet-Higgins and Stewart (1960,61,64), Miles(1957,59,62), Phillips(1957,77) Wang(1981) and others.

The set of the equations have been used are then presented. The presentation of some phenomena due to the wind and the wave iteraction is following. The numerical solution using the finite difference method is also presented. And finally there are the applications and the conclusions of this work.

## 2. MATHEMATICAL MODEL

### 2.1 The basic equations

The equations of the wave kinematics are derived on the basis of the conservation equation for the wave number k and the wave number irrotationality (Phillips,1977). So we have used the equations,

$$\frac{\partial}{\partial t}(k\cos\theta)+\frac{\partial \sigma}{\partial x}=0 \qquad (1)$$

$$\frac{\partial}{\partial t}(k\sin\theta)+\frac{\partial \sigma}{\partial y}=0 \qquad (2)$$



AUTHOR INDEX TABLE OF CONTENTS

where
x and y the co-ordinates parallel and perpendicular to the shore, in the xOy co-ordinate system
θ the angle of the incident wave
k the wave number
σ the angular frequency

and the other one that express the relationship between the wave number k and the angular frequency σ for regions where the d and u,v are slowly vary is given by,

$$\sigma = (gk \tanh kd)^{1/2} + uk\cos\theta + vk\sin\theta \tag{3}$$

where
d is the water depth
u, v are the velocities of the current, if there is any.

The computation of the wave spectral energy which is related with each frequency and wave angle propagation in this specific zone is then given by the wave energy transportation equation, Longuet-Higgins και Stewart (1960,61,64),

$$\rho g \frac{\partial E}{\partial t} + \rho g \frac{\partial}{\partial x}\left[E(u + c_g \cos\theta)\right] + \rho g \frac{\partial}{\partial y}\left[E(v + c_g \sin\theta)\right]$$
$$+ S_{xx}\frac{\partial u}{\partial x} + S_{xy}\frac{\partial v}{\partial x} + S_{yy}\frac{\partial v}{\partial y} + S_{yx}\frac{\partial u}{\partial y} = -\varepsilon_d(f) + \varepsilon_s(f) \tag{4}$$

where
$c_g$: is the wave group velocity
$E(f,\theta)$ is the wave directional spectrum
$\varepsilon_s$ : is the rate of energy generation
$\varepsilon_d$: is the rate of energy dissipation
$S_{xx}, S_{xy}, S_{yy}$: are the radiation stresses given by Longuet - Higgins and Stewart (1960,61,64).
f : is the wave frequency component
θ : is the wave propagation angle

The above set of equations is the basis of the development of the whole process.
Then we examine the mechanisms that are involved in the generation and dissipation of the waves due to the wind - wave interaction.

## 2.2 Wind wave iteraction

### 2.2.1 Wave generation

Two mechanisms have been developed for the generation of waves due to the wind. The Phillips(1957) linear mechanism for the initial stage of the wave energy development, is given by,

$$S_p = \rho g \alpha \tag{5}$$

where a is a linear coefficient
and the Miles(1957,59) mechanism for the last stage of the wave energy development, and given by,

$$S_M = \rho g \beta(E) \tag{6}$$

where β is an exponential coefficient. The composite wave energy mechanism is given by,

$$\varepsilon_S = S_p + S_M \tag{7}$$

### 2.2.2 Wave dissipation

At first is the loss due to the bottom friction, Collins(1972) suggest the following expression, depending on the frequency f,

$$\varepsilon_d(f) = \frac{\rho C_d g^2 k^2}{\sigma^2 \cosh^2 kd}(U_b)E \tag{8}$$

where $C_d$ the bottom friction coefficient
$U_b$ is the orbital velocity in the bottom of the sea.

The loss of energy due to the unsteadiness of the wave can be expressed by the term of energy generation of the wind (α+βE) plus a coefficient I, where I=1 for the non saturated condition and I=0 for the saturated one.

Finally when the wave approaches the shoreline, the wave breaking become the dominant effect. The calculation of the significant wave height (and the wave energy) is then given by an empirical criterion, the restriction proposed by Divoky et al. (1970),

$$\left(\frac{H_s}{L}\right)_b = 0.12 \tanh(kd)_b \tag{9}$$

where
$H_S$ is the wave height, $H_s = 2.828\sqrt{E}$
E is the total energy of the wave spectrum
L is the wave length
b refers to the breaking point.

The above mechanisms are part of the wave dissipation term $\varepsilon_d$ in eqn. (4).

## 3. NUMERICAL PROCEDURE

We have solved the equations using the finite difference scheme for the kinematic and dynamic processes. Among various explicit and implicit schemes, a first order upwind scheme has been chosen. Then the kinematic procedure is given by Angelidis(1995), Angelidis et al.,(1996-97), Koutitas(1988),

$$\frac{(k\cos\theta)_{ij}^{n+1}-(k\cos\theta)_{ij}^{n}}{\Delta t}+\frac{\sigma_{ij}^{n}-\sigma_{i-1j}^{n}}{\Delta x}=0 \tag{10}$$

$$\frac{(k\sin\theta)_{ij}^{n+1}-(k\sin\theta)_{ij}^{n}}{\Delta t}+\frac{\sigma_{ij}^{n}-\sigma_{ij-1}^{n}}{\Delta y}=0 \tag{11}$$

$$\sigma_{ij}=\left(gk_{ij}\tanh k_{ij}d_{ij}\right)^{1/2} \tag{12}$$

Solving the above set of equations, with proper initial and boundary conditions, and get the certain values of the variables k, θ and σ with the wave group velocity $c_g$, we use these values for the dynamic part of the process, the energy transport equation, that is solved using also a upwind first order finite difference scheme,

$$\frac{E_{ij}^{n+1}-E_{ij}^{n}}{\Delta t}+\left(c_g\cos\theta\right)_{ij}^{n}\frac{E_{ij}^{n}-E_{i-1j}^{n}}{\Delta x}+\left(c_g\sin\theta\right)_{ij}^{n}\frac{E_{ij}^{n}-E_{ij-1}^{n}}{\Delta y}=-\varepsilon_{dij}^{n}+\varepsilon_{sij}^{n} \tag{13}$$

By solving the wave energy equation with the appropriate initial and boundary conditions we got the energy distribution for a certain frequency and angle on each grid point (and the wave height also).

## 4. APPLICATIONS

Two tests are presented using the above model. The first refers to waves propagating at an angle to the shoreline, which is compared to the analytical solution (fig.1 and fig 2).

There is an application as a mildly slope depth profile (10m -1m), with grid dx=dy=10m
The evolution of the wave energy spectra has been computed with a given wave spectrum in the outer boundary of the computed region. The change of the spectrum in a area very near to the shore is also presented, second test.

The boundary conditions are periodic in the left and the right boundary and the absorbed condition has been used on the shore boundary.
The initial value for the energy spectrum is E0=1. The wave energy spectrum consist of frequencies from 0.1 - 0.5 Hz and the wave angle propagation has a range of $0^0$-$45^0$ (0 - 0.78534rad)
The initial wave energy spectrum is a top-hat shape, a continuous distribution and is then changed to an almost pointed wave spectrum. The whole process has been presented in fig3, 4 and 5.
Particularly, in fig.3 it is seen the change of the wave angle propagation of a specific band ($0$-$45^0$).for a range of frequencies (0.1 - 0.5Hz) to a very small range of wave angles 57-$72^0$, (1 -1.24 rad), nearshore.
In fig.4 the concentration of the initial wave enegry spectrum in a small wave angle range 57-$72^0$, related with certain frequencies is given.
In fig.5 there is a section of the transformed wave energy spectrum for the band of the frequencies (0.1-0.5Hz), for a particular wave angle propagation in the nearshore region.

## 5. CONCLUSIONS

The concentration of the wave energy spectrum in a nearshore area in a small range for the given initial wave angles might happen in areas with extended continental shelf, so it must taken into account, if it is decided the establishment of ports, marines or other facilities. A practical problem is the computation of the wave height due to storms as they propagate towards the shore, a parameter that is involved in the design of coastal structures.

Using this model, we have examined the wave propagation and the transport of the wave energy in the shallow water where certain phenomena, as refraction, diffraction, shoaling and breaking are taking place. It has been tested on areas of some square kilometers The conclusions have been encouraging, compared with other field observations and analytical solutions, where it was possible.

## 6. REFERENCES


1. Angelidis K., 1995, Propagation of the non-steady wind waves in waters of intermediate depth, Ph. D thesis, AUT, Dec..

2. Angelidis K. and Koutitas Cr., 1995 "Numerical propagation model of non steady waves in shallow waters", *6th Conference of Hellenic Hydrotechnical Association)*, Thessaloniki, 22-26 May.

3. Angelidis K., Th. Karambas and C. Koutitas, 1996 "Refraction - diffraction wave models in the inshore zone", *HYDROSOFT' 96*, 10/12 Sept., Penang, Malaysia.

4. Angelidis K. and Koutitas Cr., 1997, Spectral wave energy distribution in shallow waters, 7th Conference of Hellenic Hydrotechnical Association, Patra, 14-18 Oct.

5. Barnett, T.P., 1968, On the generation, dissipation and prediction of ocean wind waves, J. Geoph Res., 73, 513-530

6. Chen, Y. H. & Wang, H. Numerical model for nonstationary shallow water spectral transformation, *J. Geoph. Res.*, 1983, Vol. 88, C14, 9851-9863.

7. Collins J.L., 1972, Numerical models for nonstationary shallow water and spectral transformation, *J. Geoph. Res.*, Vol. 88, pp 9852-9863.

8. Divoky et. al., 1970, Breaking waves on gentle slopes, *J. Geoph. Res.*, 75, 1681-1692.

9. Karlsson T., 1969, Refraction of continuous ocean wave spectra, *J. Water. Harb. & Coastal Eng. Div.*, ASCE, 95, WW4, 437-448.

10. Koutitas C., 1988, *Mathematical Models in Coastal Engineering*, Pentench Press Ltd., London.

11. Longuet-Higgins M. S. and R. W. Stewart, 1960, Changes in the form of short gravity on long waves and tidal currents, *J. Fluid Mech.*, 8, 565-583.

12. Longuet-Higgins M. S. and R. W. Stewart, 1961, The changes in amplitude of short gravity waves on steady non-uniform currents, *J. Fluid Mech.*, 10, 529-549.

13. Longuet-Higgins M.S. and Stewart R.W., 1964. Radiation stresses in water waves; a physical discussion with applications. Reprinted from pp. 529-540, 561-562 of *Deep-sea research* 11:529-562

14..Miles J.W., 1957, On the generation of surface waves by shear flows, *J. Fluid Mech.*, 3, 185-204.

15. Miles J.W., 1959a,b On the generation of surface waves by shear flows, J. *Fluid Mech*, 6, 568-598.

16 .Miles J.W., 1962, On the generation of surface waves by shear flows, *J. Fluid Mech.*, 13, 433-448.

17. Phillips O.M., 1957, On the generation of waves by turbulent wind, *J. Fluid Mech.*, 9, 417-445.

18. Phillips O.M., 1977, *The Dynamics of the Upper Ocean,* 2nd ed, 23-24, Cambridge Univ, Press, New York.

19. Wang H. & W.C. Yang, 1981, Wave spectral transformation measurement at Sylt. North Sea , *Coastal Eng.*, 5, 1-34.

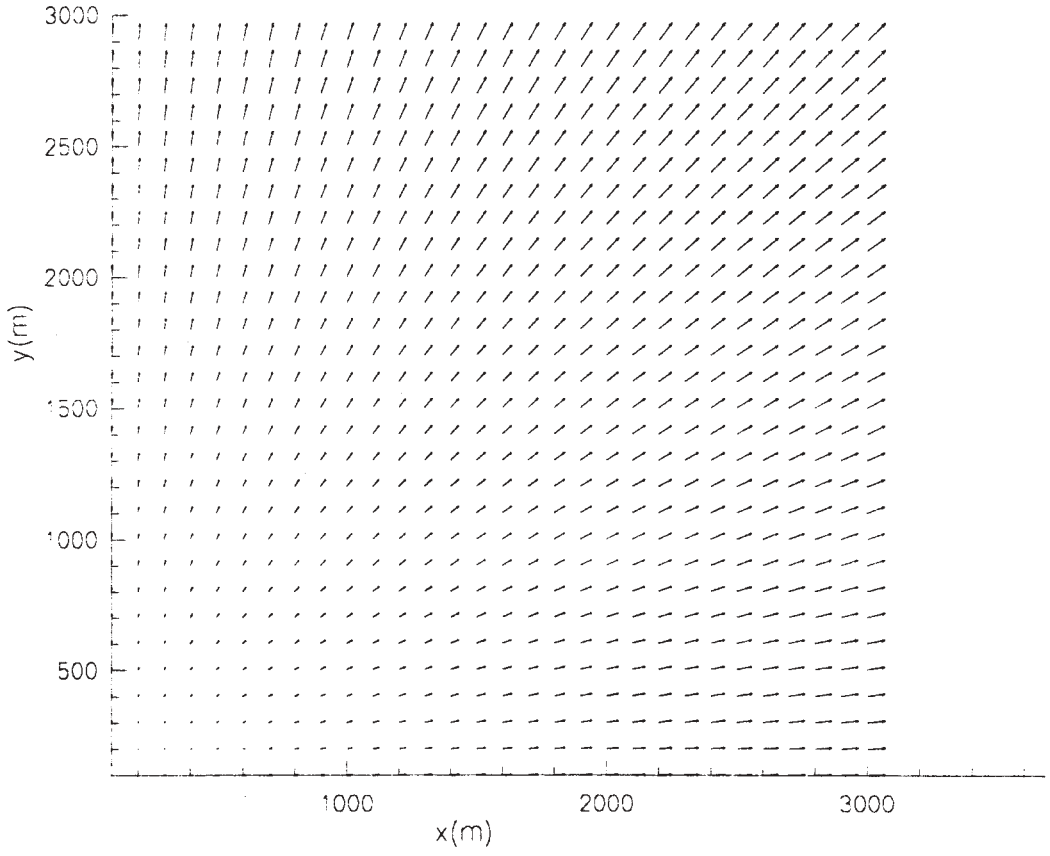


fig. 1 Wave propagation at an angle to the shore.
Change of the wave number

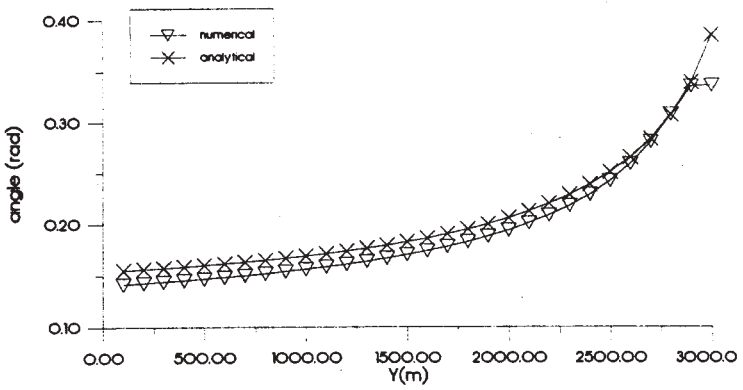


fig.2 Comparison of the numerical with the analytical solution for the proposed model

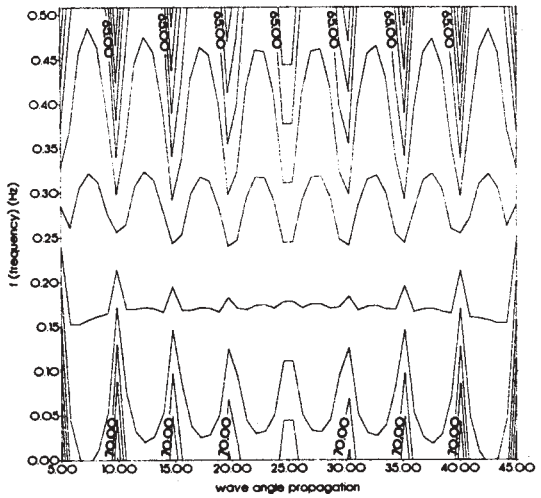


fig.3 Change of the incident wave propagation angles related with a frequency band, nearshore

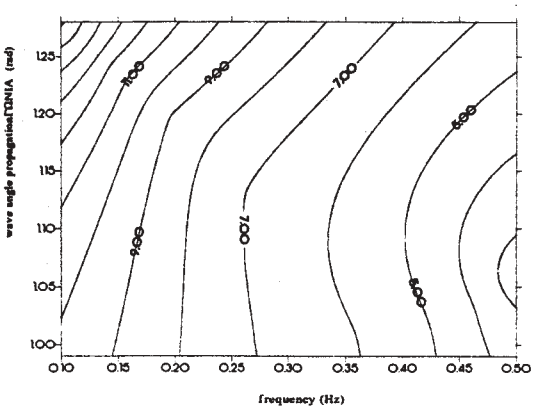


fig.4 Wave energy concentration in the nearshore zone, related with certain range of angles and frequencies.

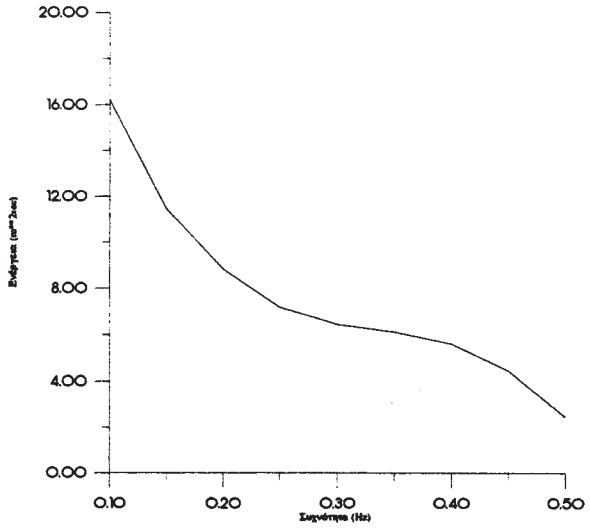


fig 5 A section of an angle of the propagated waves with a certain frequency band, shows the distribution of the wave energy, in the nearshore zone.

# USE OF PHASE-RESOLVING NUMERICAL WAVE MODELS IN COASTAL AREAS

James M. Kaihatu[1], W. Erick Rogers[2], Y. Larry Hsu[1], and William C. O'Reilly[3]

[1]Oceanography Division, Code 7322
Naval Research Laboratory
Stennis Space Center, MS 39529-5004

[2]Planning Systems, Inc.
MSAAP Building 9121
Stennis Space Center, MS 39529-5004

[3]Department of Oceanography
Naval Postgraduate School
Monterey, CA 93943

## 1. INTRODUCTION

The choice of a particular wave model for use in nearshore wave climate forecasting or hindcasting is usually contingent upon the site to be considered and the processes to be modeled. Phase-averaged spectral models such as SWAN (Booij et al. 1996), WAM (Komen et al. 1994) or STWAVE (Resio 1988) are source-based energy models which treat the wave field as a stochastic phenomenon. This particular formulation allows for the consideration of wind-wave generation, among other source terms. These models (particularly STWAVE and SWAN) are able to simulate irregular wave propagation over coastal areas relatively efficiently; however, the propagation terms in these models are derived from ray theory and do not handle bathymetrically-induced diffraction, which may be important in coastal areas. (It should be noted that STWAVE does contain some accounting for diffraction as a diffusion of wave energy in the source terms). Phase-resolving models such as REF/DIF1 (Kirby and Dalrymple 1994), REF/DIF-S (Kirby and Ozkan 1994) and RCPWAVE (Ebersole et al. 1986), by contrast, treat the wave field deterministically, tracing the free surface evolution over the domain. The irregular nature of the wave field can be accounted for by running several wave frequencies/directions through the model and calculating the statistics from the model results. This is often done by discretizing an input spectrum into frequency and direction bins, calculating the waveheight in each bin and then running them through the model. This formulation is most useful in the case of complex bathymetry and predominantly swell-like conditions. Models in this latter class cannot account for wind-wave generation.

For performing wave hindcasting or forecasting, however, it may be reasonable to use a "telescoping" approach. In this scenario, a phase-averaged model (usually WAM) is used to transport wave energy from deep water to the edge of the coastal zone, at which point this energy is then input into a coastal wave model to propagate this energy over the interior domain. The nearshore model would be either a coastal phase-averaged model or a phase-resolving model.

In this study we investigate the use of the phase-resolving wave model REF/DIF1 as a forecasting/hindcasting tool. We will look at both narrow shelf (West Coast) and broad shelf (East Coast) problems; each of these areas has unique bathymetric characteristics and thus requires different approaches. For the narrow-shelf problem, we will outline the use of REF/DIF1 in a forecast mode for a stretch of the Southern California coast. We then investigate the sensitivity of the model results to discretization of the spectrum in both frequency and direction, to confirm that our original discretization for the forecast system was sufficient. We then look at the broad shelf problem and note the frequency and directional discretization effects in this situation.

## 2. BACKGROUND

The difficulty in using phase-resolving wave models to simulate irregular wave evolution is that each monochromatic component exhibits a strong and unique variability over most nearshore bathymetry. In times when computational power was at a premium, the usual method for modeling irregular waves was to use a pseudo-monochromatic approach. This was done by representing the wave spectrum in terms of significant wave height $H_{1/3}$, peak period $T_p$ and peak direction, and running the wave model with these parameters. Unfortunately the resulting wave field is

still highly variable, and thus the use of these results to calculate such quantities as sediment transport can lead to unrealistic results. This difficulty can be surmounted by running many wave components (representative of a wave spectrum) and then calculate the associated wave statistical parameters; this usually leads to a smoother, more realistic waveheight field. This can be done in either a component-by-component fashion (REF/DIF1 and RCPWAVE) or by running all components simultaneously (REF/DIF-S).

It is not clear, however, how the spectrum should be discretized in order to simulate irregular wave evolution. The frequency and direction bands of the input spectra are usually determined by the measuring instrument and the associated processing software. Nonetheless, the adequacy of representing each frequency-direction band with a single monochromatic component at the center frequency and direction remains an open question. In this study we will investigate the effect of subdividing these prespecified frequency-direction bands into finer bins, and then averaging the waveheights from each individual bin across all bands in order to obtain an averaged result. This average would then represent the band. To this end, O'Reilly and Guza (1993) investigated the effect of spectral discretization on the smoothness of the waveheight field in the Southern California Bight. They initialized their parabolic refraction-diffraction model with spectra recorded at the Harvest Platform (located offshore of Point Conception), and simulated the wave evolution over a domain $300km$ by $300km$. A phase-resolving model was necessary for this application because the wave evolution process needed to account for several large offshore islands in the Bight. O'Reilly and Guza (1993) determined that a significant level of variation in nearshore waveheight (leeward of the islands) existed for a small amount of variation in offshore wave angle (seaward of the islands). Using a nominal spectral discretization of 5° in direction and $0.01Hz$ in frequency, they found that there was a substantial difference between waveheights on the coast calculated using one representative frequency and direction for this band, and those calculated by subdividing this bandwidth into finer bins and then averaging the resulting waveheight fields over the band. It can be supposed that the great variability is due to the presence of the islands; small differences in the wave frequency or direction may lead to large differences in the refraction/diffraction pattern around these features, thus clarifying the need for a relatively fine discretization. It is not clear, however, that this is required for an open coast. (We note that different frequency and directional distributions would require different spectral discretizations by virtue of their shape; we do not address this issue in this study.)

## 3. THE NUMERICAL MODELS

The primary model under consideration in this study is REF/DIF1 (Kirby and Dalrymple 1994). This model is monochromatic, and looping of the code to run through desired frequencies and directions is required. The model is a phase-resolving, frequency-domain parabolic approximation of the mild-slope equation for water wave propagation (Berkhoff 1972). The parabolic approximation (Radder 1979) reduces the elliptic mild-slope equation to a parabolic form, thereby allowing the solution to march forward as an initial value problem. Solution of this approximate equation is relatively efficient in memory, since values along only two longshore grid rows need be retained for any one forward step. However, the parabolic approximation assumes that the wave is propagating primarily along the cross-shore ($x$) direction of the domain, and thus significant errors are possible if the wave approaches the grid at angles over about 20° to the $x$ direction. Additionally, the approximation disallows back reflection of waves, and thus only forward scattered or propagating waves may be represented.

The formulation in REF/DIF1 utilizes the wide-angle approximation of Kirby (1986). This approximation yields additional terms that serve to reduce the angular error between the parabolic approximation and the full elliptic solution without adding any discernible computational difficulty. Waves approaching the domain at angles up to 45° from the $x$ direction can be modeled without significant error. However, for this study we rotated the grid to several orientations in order to keep the angle of incidence small.

The model REF/DIF1 utilizes the decay model of Dally et al. (1985). This formulation is problematic for irregular waves because each individual wave in the wavetrain has its own decay characteristic and incipient breaking condition. We will detail how this is handled for the West Coast case in the next section.

The model used to generate forcing conditions for the forecast is WAM (Komen et al. 1994). This phase-averaged model is used operationally by oceanographic centers worldwide for wave climate forecasting. It is based on a description of wave evolution as a random phase process. The model contains source/sink terms that account for wave propagation, whitecapping, wind-wave generation, nonlinear interaction, and bottom friction. The wind forcing for the WAM model is provided by the Navy Operational Regional Atmospheric Prediction System (NORAPS), and the $10m$ elevation winds are used.

## 4. WEST COAST – NARROW SHELF CASE

We first investigated the use of REF/DIF1 in a forecast mode in modeling a section of the Southern California Bight near Oceanside and Camp Pendleton. We outlined an area near Oceanside, about 0.5° on each side, to run the model; the domain is shown in Figure 1. The narrow width of the shelf is apparent. For bathymetry we used the 3 second by 3 second grid discussed in O'Reilly and Guza (1993) and derived from the National Ocean Survey (NOS) database; this bathymetry was interpolated onto a grid with $\Delta x$=$\Delta y$=100m. The seaward-most point in the grid corresponded to a location where wave spectra from the WAM model were available. This point was chosen because it appeared to not be affected by the offshore islands. The WAM model is presently being run operationally by the Naval Oceanographic Office (NAVO) at Stennis Space Center, MS, and 48 hour forecasts are run twice daily for selected regional locations, with predicted spectra made available at several points in the Bight. These regional WAM simulations are forced by global WAM results, also run by NAVO. Details on the operational implementation of WAM can be found in Wittmann and Farrar (1997). Furthermore, a Datawell directional buoy was installed near the local shelf break offshore of Oceanside Harbor (33.1789° latitude, 242.5311° longitude).

As mentioned above, REF/DIF1 contains a wide-angle

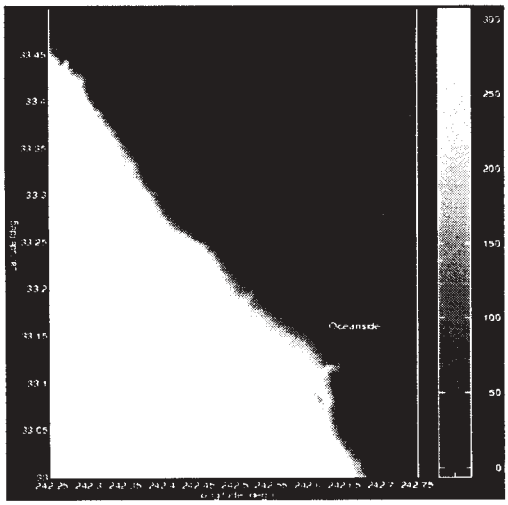


**Figure 1: Domain of Study – Southern California Bight. Depths Are In Meters.**

correction that allows for fairly large incident angles without a corresponding increase in error. However, we were able to orient the grid so that we could keep the incident angles reasonably small for all directions except for waves approaching from the northwest, where the incident angles were at most 45° to the $x$-axis. We had originally intended to orient the grid such that the waves approaching from this direction would have a small incidence angle; however, the close proximity of the coast along the lateral boundary of the grid caused significant noise in the transformation coefficients. Additionally, waves approaching from this direction during this time of year do not make up a significant part of the overall wave climate. Thus, we used the east-west oriented grid to model waves approaching from this sector. The grid orientations used are shown in Figure 2. The west-east and south-north grids had resolutions of $\Delta x$=$\Delta y$=100$m$, while the

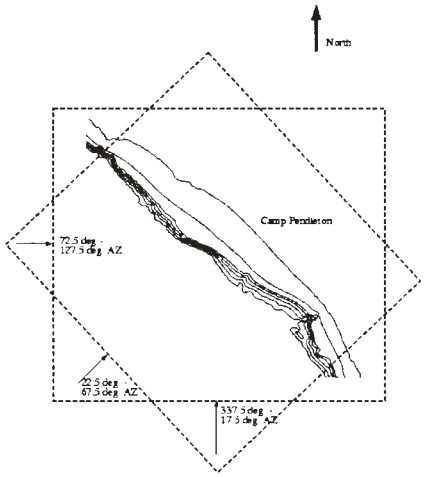


**Figure 2: Grid Orientations for Parabolic Model. Grid Overlap Not to Scale.**

southeast-northwest grid had resolutions of $\Delta x$=$\Delta y$=70.71$m$; this was done so that the points from the three grids overlapped. During the time of the forecast, when the WAM spectra were discretized and component wave heights through the domain calculated and summed, the results from all three grids were mapped onto the east-west oriented grid.

In anticipation of long computational times we used the "transformation coefficient" approach of O'Reilly and Guza (1993). First, a range of frequencies and directions was chosen, and subdivided into frequency-direction bins. Each bin was then initialized with a unit wave height and run in REF/DIF1, generating fields of transformation coefficients to be stored. A sample

transformation coefficient field is shown in Figure 3. During the forecast time, WAM spectra at the offshore point would then be discretized into the same bands used to run the REF/DIF1 model. Waveheights would be calculated in each band, and this waveheight multiplied by the transformation coefficient field associated with this band. The individual component fields would then be summed to yield significant wave heights and peak direction. We handled the problem of irregular wave breaking by setting all significant waveheights in water less than $2m$ depth to zero. We also tried to eliminate any anomalously high significant waveheights in the region by restricting their maximum values to be 0.78 of the water depth, corresponding to a pseudo-monochromatic approach.

Based on a sample WAM run from the last week of May 1997, a frequency range of 0.04-0.13$Hz$ and a directional range from 337.5°-127.5° azimuth (where 0° refers to a wave moving from south to north) were used. This frequency range was denoted the "swell range" and thus required the model runs for simulation of wave transformation. In the interests of time we utilized Snell's Law for the frequency range beyond 0.13 $Hz$, on the supposition that wave energy in this range would not be substantial. The frequency and direction ranges were subdivided into 0.01 $Hz$ and 5° intervals. (For reference, the WAM forecasts from NAVO are discretized at 15° directional intervals,

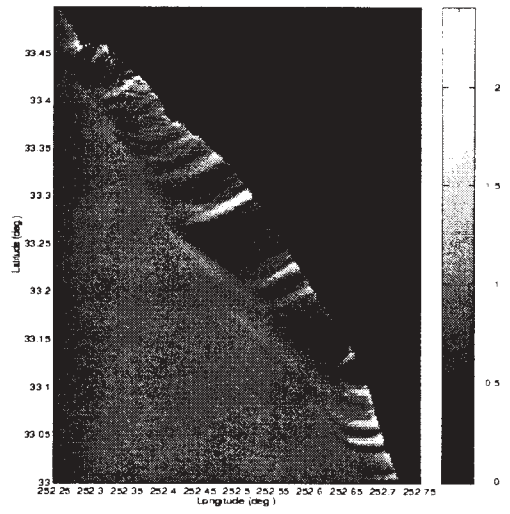


**Figure 3: Transformation Coefficient Field for 25$s$ Wave Propagating at 112.5 ° AZ.**

while the frequency intervals increase logarithmically with increasing frequency.) We then ran each bin in the spectrum through the model, and stored the resulting transformation coefficient fields. Once the WAM spectra were obtained, we ran this spectrum over the transformation coefficient fields, calculated and plotted significant wave height fields and peak direction, and put the plot on a Web page for user access; example are shown in Figures 4 and 5. Some difficulties were encountered with the WAM forecast spectra for this time frame, precluding direct comparison of results with the Datawell buoy. Investigations into the causes of these problems are continuing as of the time of this writing.

However, it is still important to investigate whether the chosen frequency-directional bins were sufficiently fine to bring about smooth wave fields. We noted that O'Reilly and Guza (1993) found that the wavefield resulting from a wave condition at the center of a 5° bin was substantially different from an averaged bin of equal width if the offshore islands were included in the domain. Additionally, we wished to incorporate the spectra from the Datawell buoy into the model. Thus we repositioned the domain somewhat so that the offshore boundary of a grid oriented southwest-northeast was located near both the buoy and the closest WAM output location. We employed the same three-grid system as before. The rotated (southwest-northeast oriented) grid had corners at 33.0227° latitude, 242.6826°longitude; 33.2773° latitude, 242.3774°longitude; 33.5319° latitude, 242.6826° longitude; and 33.2773°latitude, 242.9878° longitude. The north-south and east-west grids were defined to envelop the rotated grid completely. Then the rotated grid was truncated to eliminate the large number of land points. For the ensuing sensitivity tests we used both the rotated grid ($x$-direction close to shore normal) and the east-west oriented grid.

The rotated grid is tested first. We first tested the sensitivity of the model results with small variations in frequency. This was done for waves with frequencies of 0.05 $Hz$ and 0.10$Hz$. We defined a frequency bandwidth of 0.01$Hz$, as was done for the forecast, and first ran a single wave component with unit wave height at the central frequency over the domain. We then ran waves with frequencies of ±0.001 $Hz$ from the central frequency over the domain and averaged these bands together to create an averaged bin. Figure 6 shows the results for a 0.05 $Hz$ centered frequency. The top figure shows the results for a single wave component of unit wave height at 0.05 $Hz$. The middle figure shows the result of an averaged bin in which three frequencies of 0.045 $Hz$, 0.05 $Hz$ and 0.055 $Hz$ were averaged. The lower figure shows a result of an averaged bin consisting of all 11 frequencies between 0.045-0.055 $Hz$. There appears to be no substantial

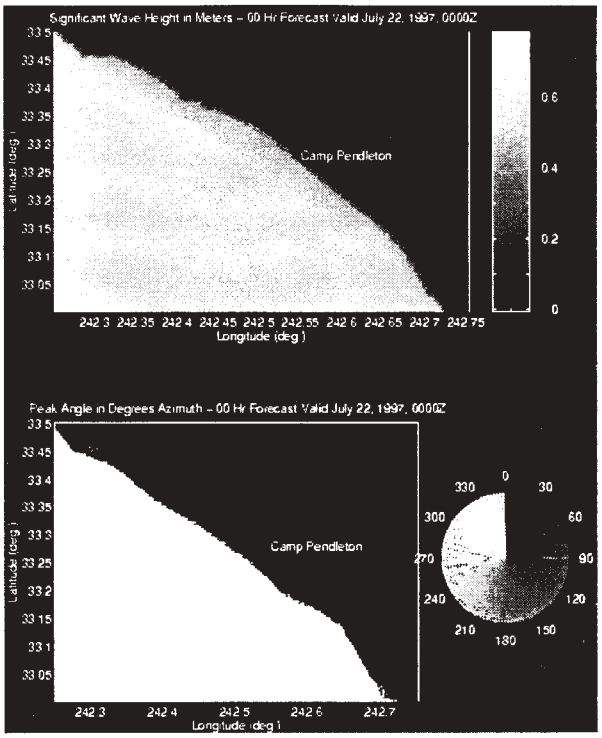


**Figure 4: 00Z Hr. Forecast for July 22, 1997**

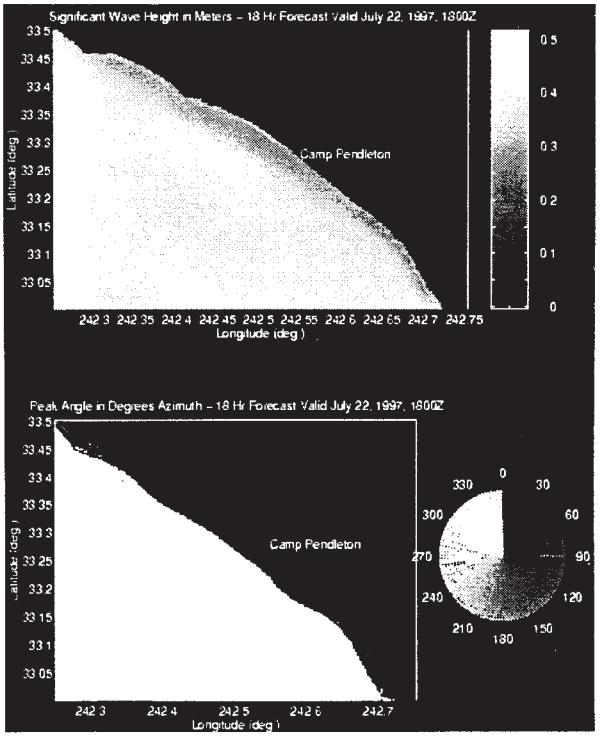


**Figure 5: 18Z Hr. Forecast for July 22, 1997**

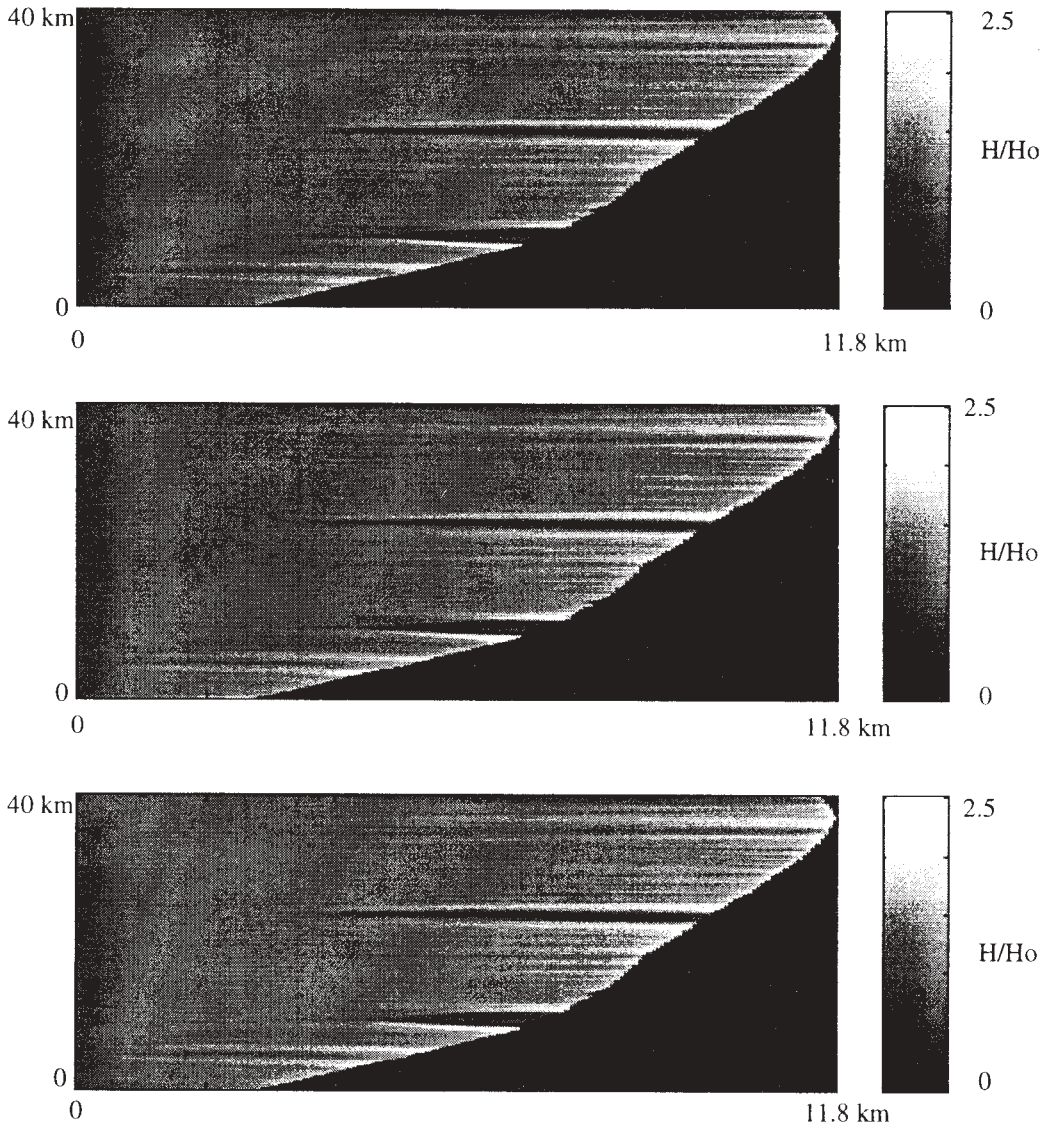


**Figure 6: Comparison of Frequency Discretization Methods, Narrow Shelf Case, Rotated Grid, $T$=25$s$, Mean Direction 45°Azimuth. Top: H/Ho Field for Single Wave Component at Center Frequency and Direction. Middle: H/Ho Field from Average of Three Components Within Band. Bottom: H/Ho Field from Average of Eleven Components Within Band. Note: Scale of Abscissa Distorted Relative To Ordinate.**

difference between the three plots. Tests were also performed for a wave condition with a centered frequency of 0.10 *Hz*, where frequencies of 0.095-0.105 *Hz* were modeled. The results showed similar insensitivity to discretization finer than 0.01*Hz*. This shows that the 0.01 *Hz* bins used for the forecast seem to be sufficiently fine for waves approaching from the southwest.

The sensitivity of the results with respect to incident wave direction was also studied on the rotated grid. We used the same directional bandwidth as the forecast (5°) and used a centered angle of 45° azimuth. We define nine directional bins, each of 0.625° bandwidth, from 42.5° to 47.5° azimuth. We then tested the sensitivity of the model by running waves of 0.05*Hz* frequency with unit offshore wave height at these directions, and then averaging the results of several bands together. This test was repeated for the 0.10*Hz* wave. As with the wave frequency sensitivity, there was little difference between the results for different discretizations for either frequency, confirming that the 5° directional bins used in the forecasting system were also sufficiently fine for waves approaching from the southwest.

Additionally, the tests were repeated for the east-west oriented grid for a wave approaching at 110° azimuth. This was thought to be a more severe case of wave transformation. Waves moving in this direction would likely undergo a high rate of turning in order to refract around and approach the shoreline. Thus it seems reasonable to believe that there would be appreciable differences in refraction/diffraction patterns between waves of closely-spaced frequencies moving in a narrow band of directions. We performed these tests in the same manner as was done on the rotated grid, and found that very little difference existed between the wavefields calculated either at the centered frequency and direction or in averaged frequency and direction bands. Thus it seems reasonable to conclude that waves approaching from the west to northwest were well represented by the spectral discretizations we chose for the forecast system. (We note here that in the above tests, similarity between wavefields resulting from various discretizations was confirmed by comparison of transects cut through the wavefields. These are not shown, since the waveheights virtually overlaid each other.)

The fact that the model results exhibit little sensitivity to the spectral discretization into bins finer than those used for the forecasting system indicates that the sensitivity to discretization bandwidth seen by O'Reilly and Guza (1993) in the same region is due primarily to the presence of the offshore islands in their domain. In this case, the offshore boundary condition for the modeling was located well leeward (and out of the shadow zone) of the islands.

Having confirmed the adequacy of the frequency and directional resolution used for the forecast, we then use model on the repositioned grid to simulate the propagation of the wavefield recorded at the buoy location into the domain. At the time of this writing the results for all grids were still undergoing analysis. Thus we show several realizations using only the rotated grid and only calculating the portion of energy in the buoy spectra in which the waves are approaching the coast between 27.5° and 72.5° azimuth, and have frequencies between 0.04*Hz* and 0.13*Hz*. It is noted here that this was not usually the sector containing the greatest portion of wave energy. Figures 7 and 8 show the results for several realizations of buoy spectra.

It should be noted that the implications of these results on general modeling practice are limited. The sampling of the bathymetry plays a large role. As noted above, the bathymetry used in this study was taken from the NOS database, and not taken specifically for this study. The resolution at which the raw bathymetric soundings were taken varies widely. Interpolation onto a regular latitude by longitude grid can smooth out local features, which are further smoothed by interpolation onto a 100 *m* by 100 *m* grid.

We mention here that no attempt to find the "ideal" spectral discretization was made with regard to the narrow shelf case. Our primary intent was to confirm the adequacy of our chosen spectral discretizations for the forecasting system. This is probably sufficient, in light of the relative smoothness of the bathymetry. In the next study, wave propagation over more complex. broad-shelf bathymetry will be examined.

## 5. EAST COAST – BROAD SHELF CASE

The model REF/DIF1 was also used in a forecast mode near Camp Lejune, NC. Rather than relying solely on the National Ocean Survey database for bathymetry for this area, NRL surveys and a bathymetry database from NAVO were also used and blended in to the NOS bathymetry to better resolve the small scale features in the nearshore area. This is shown in Figure 9. The resolution used here was $\Delta x=\Delta y=92.5m$. The incorporation of WAM spectra from NAVO for use in a wave modeling system is detailed in Allard et al. (1998, this conference). Here we will discuss the impact of the spectral discretization on the model results.

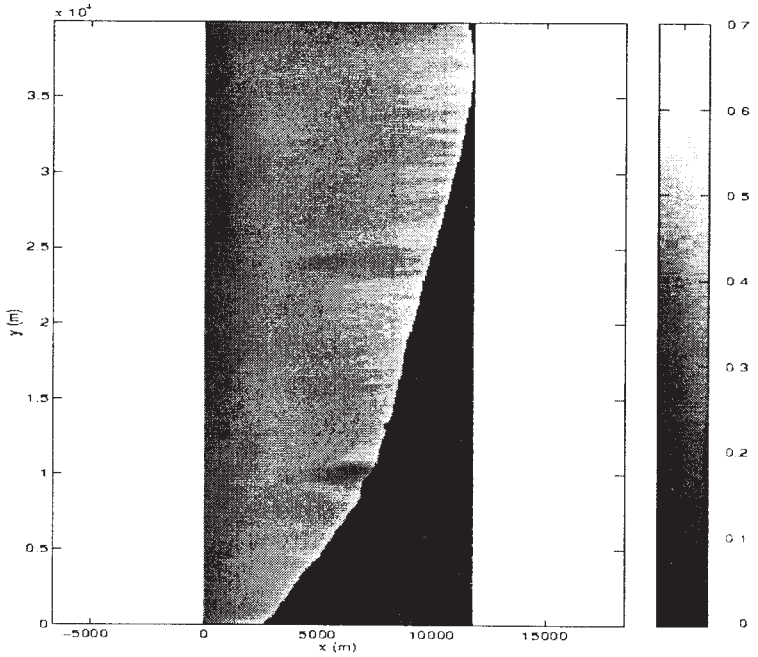


**Figure 7: Partial Wave Height Field for July 30, 1997, 1036PST. Model Forced with Portion of Buoy Spectrum (27.5°-72.5° AZ and 0.04-0.13*Hz*). Heights are in Meters.**

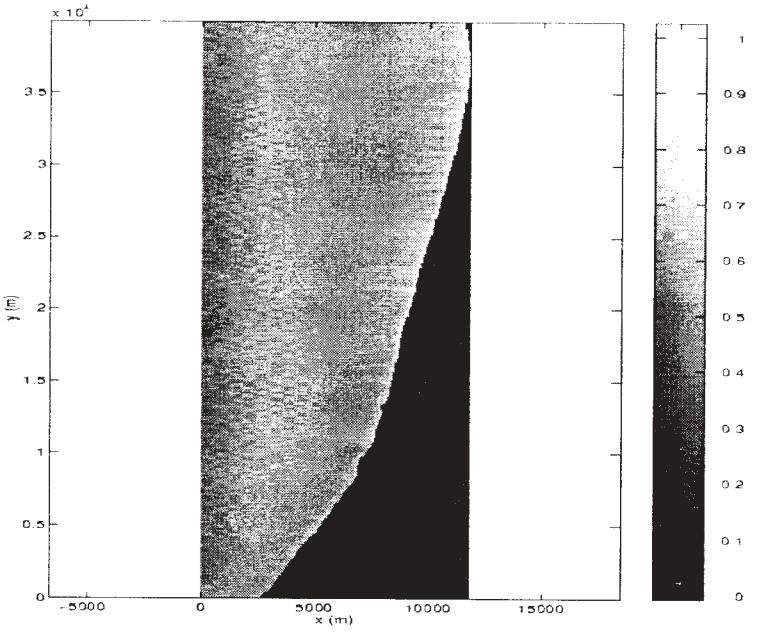


**Figure 8: Partial Wave Height Field for August 11, 1997, 908PST. Model Forced with Portion of Buoy Spectrum (27.5°-72.5° AZ and 0.04-0.13*Hz*). Heights are in Meters.**

The REF/DIF1 model was run for the domain shown in Figure 9. Allard et al. (1998, this conference) used a 2° angular resolution for directions ranging from –70 to +70 degrees relative to the model grid $x$ direction. No grid rotation was used to model higher incident angles. The frequency resolution for waves up to $0.2Hz$ was $0.01Hz$.

Because the shelf is broad, with some bathymetric complexity in the nearshore, some sensitivity of the forecasting system to spectral discretization would be apparent. We analyze the discretization effects in the same manner as was done for the West Coast narrow shelf case. We first investigated the effect of angular discretization on the resulting wave height fields. A bandwidth of 5.5° was established around the mean direction. Six different levels of sub-bandwidth discretization were used:

1) One bin with 5.5° bandwidth.
2) Two bins of 2.75°bandwidth.
3) Four bins of 1.375° bandwidth.
4) 11 bins of 0.5° bandwidth.
5) 22 bins of 0.25° bandwidth.
6) 44 bins of 0.125° bandwidth.

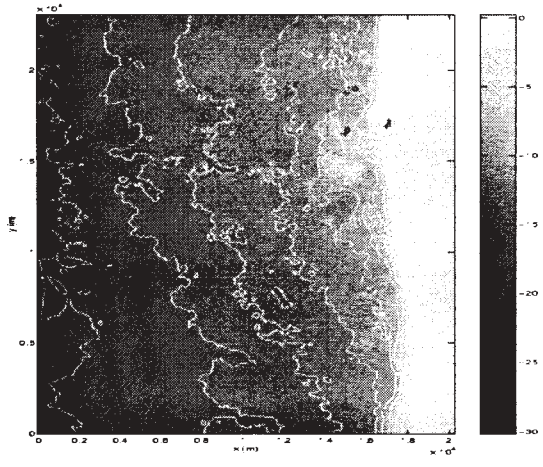

**Figure 9: Domain of Study - Camp Lejune, NC. Depths Are In Meters.**

This was done for several mean periods, and each frequency-direction bin was given a unit wave height. Figure 10 shows a result for a $17s$ wave with a mean direction of –20° to the $x$-axis of the grid. The bottom panel shows a single wave angle of –20°. The middle panel shows the result of averaging four bins of 1.375° bandwidth and the top panel displays the result of averaging 44 bins of 0.125° bandwidth. Unlike the West Coast case, there seems to be a distinct difference between the single component result and the averaged band results.

We also investigated the effect of averaging over several frequency bins within a single frequency band in order to represent the propagation of wave energy in that band. Seven sub-bandwidth levels of discretization were used:

1) One bin with $0.06Hz$ bandwidth.
2) Two bins with $0.03Hz$ bandwidth.
3) Six bins of $0.01Hz$ bandwidth.
4) Ten bins of $0.006Hz$ bandwidth.
5) 20 bins of $0.003Hz$ bandwidth.
6) 40 bins of $0.0015Hz$ bandwidth.
7) 50 bins of $0.0012Hz$ bandwidth.

As before, this was done for several mean periods and a direction of -20° from the $x$ direction of the grid. All components were initialized with a unit wave height. Figure 11 shows a result for a wave with a mean period of $12.5s$. The lower panel shows the result for a single component at the mean period. The middle panel shows the result of six bins comprising a total bandwidth of $0.06Hz$ about the mean frequency. The top panel shows the result of averaging over 50 bins within the $0.06Hz$ bandwidth. There is some difference between the single component run and the averaged band results, again in contrast to the West Coast case.

It is instructive to investigate the variations of the individual bands comprising a bin prior to averaging, and compare their behaviors to that of the single component result as well as the averaged result. Figure 12 shows the waveheights and nearshore wave angles resulting from each of the individual 11 components making up a 5.5° band with a mean angle of -20° to the grid. The nearshore point was located at $x$=13800$m$, $y$=12900$m$, and the period $T$=17$s$. The water depth at this point was $9.6m$. The incident wave directions used at the offshore boundary are noted above each point. These are compared to the result from a single component with the mean offshore angle (solid black line), as well as the result of the average of all 11 components (dashed line). Not only is the scatter about the single component result significant, but there is a significant difference between this single component and the average of the 11 individual components comprising this band. As the directional resolution increases, both the amount of scatter and the value of the average vary less for increasing resolutions.

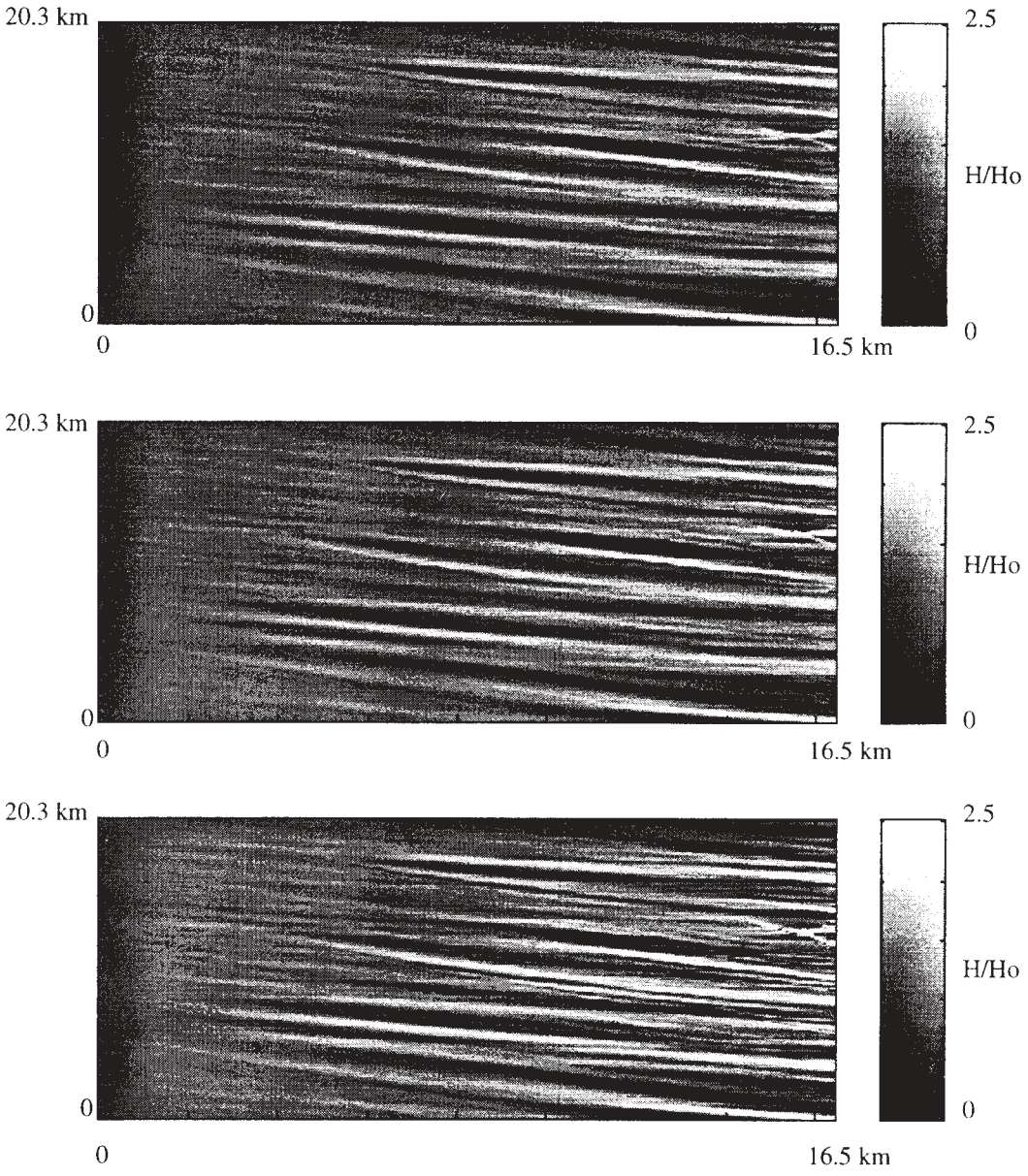


**Figure 10: Comparison of Directional Discretization Methods, Broad Shelf Case, $T$=17$s$, Mean Direction -20° With Respect To Grid. Top: H/Ho Field from Average of 44 Components Within Band. Middle: H/Ho Field from Average of Four Components Within Band. Bottom: H/Ho Field from Single Wave Component at Mean Frequency and Direction. Note: Scale of Abscissa Distorted Relative To Ordinate.**

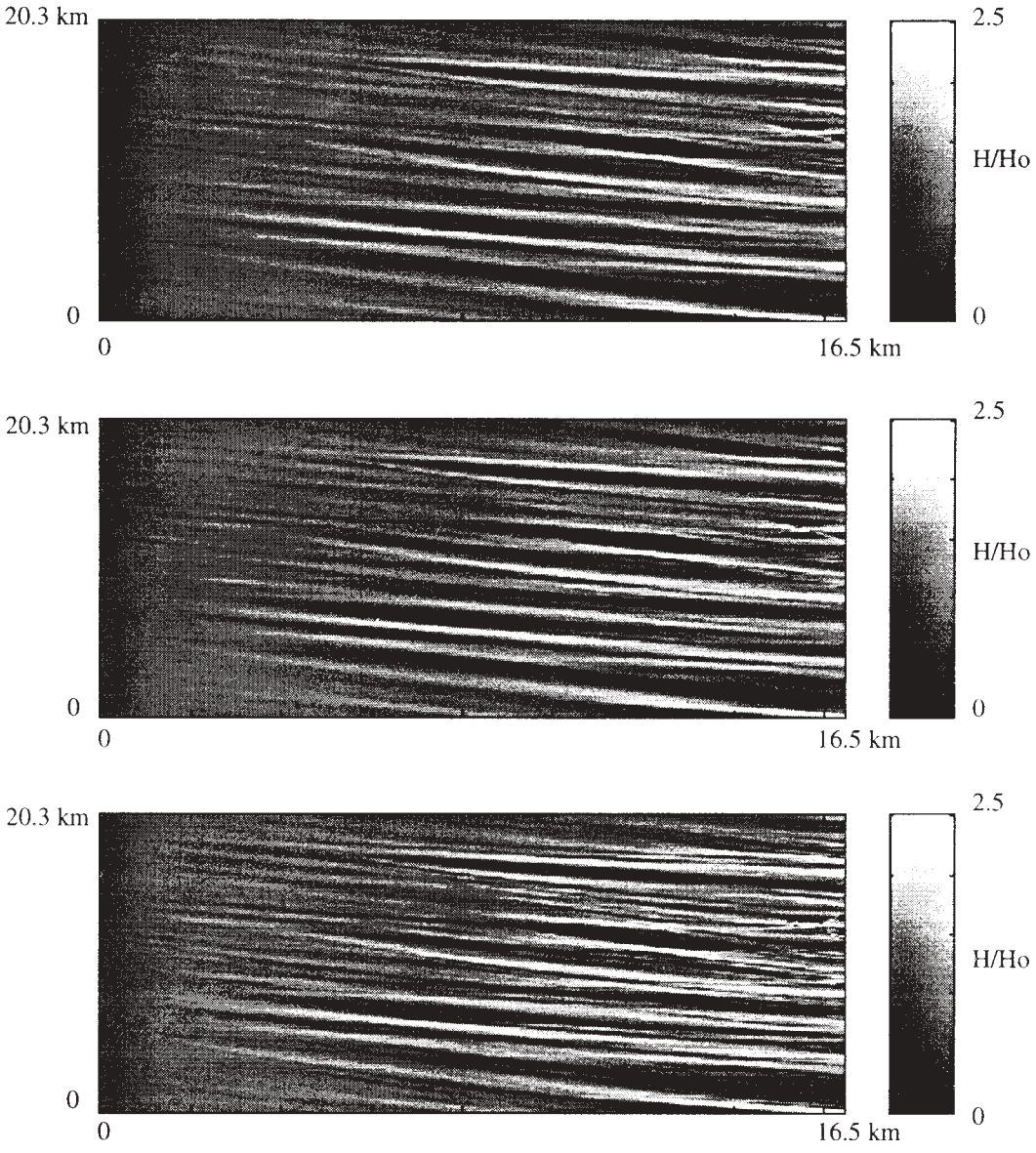


**Figure 11: Comparison of Frequency Discretization Methods, Broad Shelf Case, $T$=12.5$s$, Mean Direction -20° With Respect To Grid. Top: H/Ho Field from Average of 50 Components Within Band. Middle: H/Ho Field from Average of Six Components Within Band. Bottom: H/Ho Field from Single Wave Component at Mean Frequency and Direction. Note: Scale of Abscissa Distorted Relative To Ordinate.**

In order to analyze the effect increasing the spectral resolution has on the wave height prediction, we investigated the convergence of the waveheight prediction to a particular waveheight field as the spectral resolution increases. Both frequency and directional resolution were analyzed. In the case of angular discretization, the highest directional resolution (44 bins, each of 0.125° bandwidth, comprising a 5.5° band about an incident angle of -20°) was taken to be

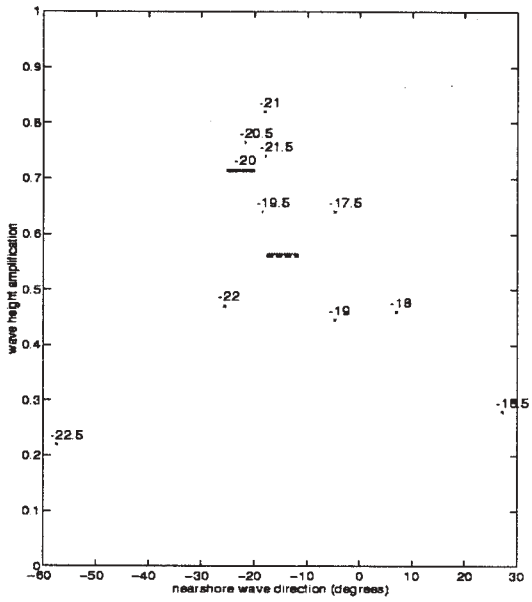


**Figure 12: Predicted Nearshore H/Ho and Wave Angles for $T$=17$s$, $x$=13800$m$, $y$=12900$m$. Offshore Wave Angles are Noted Above Each Point. Black Dots: Results for 11 Individual Components Comprising a 5.5°Band. Solid Line: Result for Single Component at the Center Frequency and Direction. Dashed Line: Average of 11 Components.**

the baseline for our comparisons. Differences between this baseline and the waveheights found using the other spectral resolutions were calculated and then averaged over the area of the grid seaward of the point of breaking. This yielded a "global mean error" for the particular discretization. Figure 13 shows the trend of the global mean error with decreasing directional bandwidth. The $T$=10$s$ (top panel) and $T$=17$s$ (lower panel) are shown in the figure. The convergence is almost exponential with bandwidth size. The 17$s$ wave seems to exhibit a slightly smaller overall error than the 10$s$ wave. It is apparent that the transformation characteristics of waves in the shallow water range do not vary as much with small variations in incident angle as intermediate depth waves. The exponential behavior of the convergence curves also reveals the relative sensitivity of the results with variations in directional bandwidths for the larger bandwidth sizes.

A similar analysis was also performed for the frequency resolution. The highest frequency resolution used (50 bins with width of 0.0012$Hz$, comprising a total frequency bandwidth of 0.06$Hz$) was used as the baseline in this case. Differences between the waveheight field from this baseline and those of the other frequency resolutions employed were calculated and averaged over the entire domain seaward of the point of breaking. Figure 14 shows the result of this analysis. The top panel displays the result for $T$=3.33$s$, the middle panel shows the result for $T$=7.14$s$, and the bottom panel shows the result for $T$=12.5$s$. Unlike the case of angular discretization, the convergence rate is linear rather than exponential. This indicates that the results would not be as quick to degrade relative to the baseline with degradation in frequency resolution as with degradation in angular resolution. Additionally, it also attests that the refraction/diffraction patterns for waves closely spaced in frequency are more similar than for waves closely spaced in direction. Additionally, also unlike the angular discretization case, the longer period wave has higher error for any particular frequency discretization than waves of lower period. This is sensible since a given frequency difference translates into a greater range of wavelengths for the lower frequencies. The above analyses for the broad shelf case indicates that the chosen frequency and direction discretizations used by Allard et al. (1998) are likely sufficient for the waveheight predictions.

It should be emphasized that the analyses outlined above were initialized with unit wave heights and performed in areas outside the surf zone. Thus the results are applicable to this bathymetry and the analyzed wave periods and directions regardless of initial wave height. However, extrapolation of these results to other domains should be done with care.

## 6. CONCLUSIONS

Phase-resolving numerical models offer an accurate description of monochromatic swell wave propagation over highly variable bathymetry. The simulation of irregular wave propagation using these models requires some care in how the spectra are discretized, since the smoothness of the resulting waveheight fields are often contingent on the fineness of the discretization.

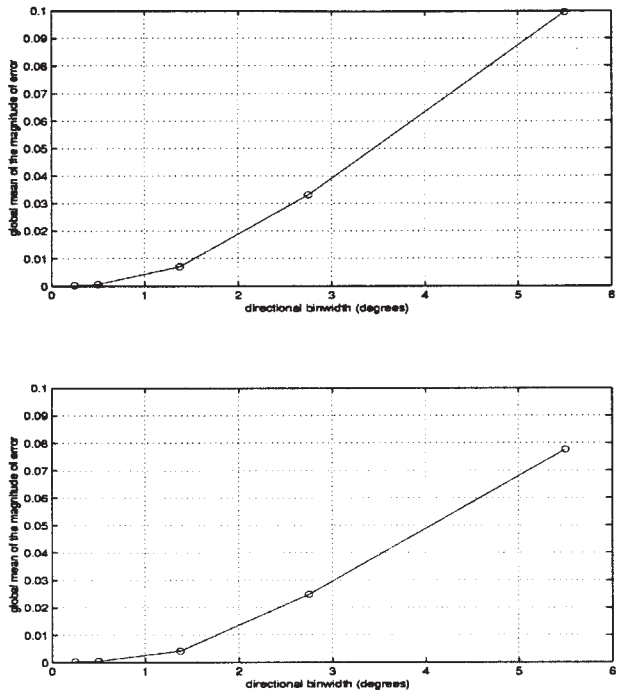


**Figure 13: Rate of Convergence of Waveheight Results For Different Directional Binwidths to Baseline Waveheight Field. Top: $T$=10$s$. Bottom: $T$=17$s$.**

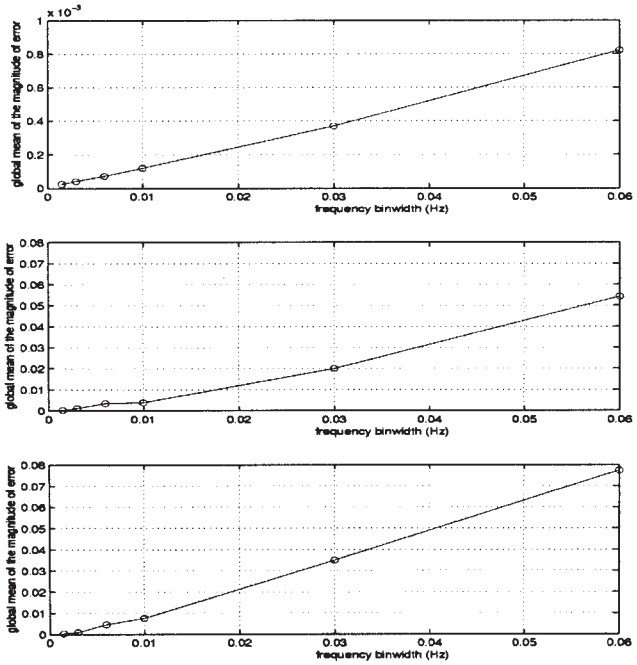


**Figure 14: Rate of Convergence of Waveheight Results For Different Frequency Binwidths to Baseline Waveheight Field. Top: Mean Period=3.33$s$. Middle: Mean Period=7.14s. Bottom: Mean Period=12.5$s$.**

We investigated two sites: Oceanside/Camp Pendleton, CA, and Camp Lejune, NC. A narrow shelf and relatively smooth bathymetry characterize the West Coast site, while the East Coast site has fairly complex bottom contours and distinct bottom features. We detailed the development of a forecasting system for the West Coast site, and also determined that the spectral discretization used in this system was sufficiently fine in frequency and direction. This was due to the fact that our grid was situated well leeward of the islands in the Southern California Bight, and thus did not have to account for the variations with frequency and incident direction in the refraction and diffraction patterns around them.

The East Coast Site did exhibit some sensitivity to the spectral discretization used, though it was determined that the frequency and direction bins used by Allard et al. (1998, this conference) appeared to be sufficiently fine to yield smooth waveheight fields. Exploring this further, we looked at the convergence of the waveheight field found by averaging over various numbers of subintervals in a frequency/direction band, to a set baseline. The convergence of the waveheight field to the baseline was found to be nearly exponential when varying the directional discretization, and nearly linear when varying the frequency discretization.

The general conclusion of this study is that spectral discretization can play a potentially important role in the accuracy and smoothness of a prediction of waveheight (and ensuing processes), and its importance seems to be in direct proportion to the complexity of the underlying bathymetry. The study also emphasizes the need to model irregular wave fields in multi-component (rather than pseudo-monochromatic) fashion, since wave response characteristics may vary greatly with small variations in frequency and/or incident direction.

## 7. ACKNOWLEDGMENTS

Both JMK and WER were supported by the Office of Naval Research through the Naval Research Laboratory, Stennis Space Center, MS, under the 6.2 "Coastal Simulation" NRL Core project. YLH was supported by Space and Naval Warfare Systems Command. BOR was supported by the State of California Department of Boating and Waterways. Discussions with Dr. Robert Jensen (Coastal and Hydraulics Laboratory, U.S. Army Waterways Experiment Station, Vicksburg, MS) and Mr. Paul Wittmann (Fleet Numerical Meteorological and Oceanographic Center, Monterey, CA) concerning the WAM model were very informative. This paper, NRL contribution PP/7322-97-0042, is approved for public release; distribution unlimited.

## 8. REFERENCES

Allard, R.A., Y.L. Hsu, J.M. Smith, M.D. Earle, T. Mettlach, and K. Miles, 1998: Use of coupled numerical wave models to simulate the littoral environment from deep water to the beach. Proceedings of the 5th International Workshop on Wave Hindcasting and Forecasting, Melbourne, FL.

Berkhoff, J.C.W., 1972: Computation of combined refraction-diffraction. Proceedings of the 13th International Conference on Coastal Engineering, 471-490, Vancouver, BC.

Booij, N, L.H. Holthuijsen, and R.C. Ris, 1996: The SWAN wave model for shallow water. Proceedings of the 25th International Conference on Coastal Engineering, 668-676, Orlando, FL.

Dally, W.R., R.G. Dean, and R.A. Dalrymple, 1985: Wave height transformation across beaches of arbitrary profile, *J. Geophys. Res.*, **90**, 2035-2043.

Ebersole, B.A., M.A. Cialone, and M.D. Prater, 1986: Regional coastal processes numerical modeling system: RCPWAVE – a linear wave propagation model for engineering use. Technical report CERC-86-4, Coastal Engineering Research Center, U.S. Army Waterways Experiment Station, Vicksburg, MS, 71p.

Kirby, J.T., 1986: Higher order approximations in the parabolic equation method for water waves, *J. Geophys. Res.*, **91**, 933-952.

Kirby, J.T., and R.A. Dalrymple, 1994: Combined refraction/diffraction model REF/DIF1, version 2.5, documentation and user's manual. CACR report 94-22, Center for Applied Coastal Research, University of Delaware, Newark, DE, 171p.

Komen, G.J., L. Cavileri, M.A. Donelan, K. Hasselmann, S. Hasselmann, and P.A.E.M. Janssen, 1994: Dynamics and modeling of ocean waves, Cambridge University Press, Cambridge, U.K., 532p.

O'Reilly, W.C., and Guza, R.T. 1993: A comparison of two spectral wave models in the Southern California Bight, *Coast. Eng.*, **19**, 263-282.

Radder, A.C., 1979: On the parabolic equation method for water wave propagation, *J. Fluid Mech.*, **95**, 159-176.

Resio, D.T., 1988: A steady state model for coastal applications, Proceedings of the 21st International Conference on Coastal Engineering, 929-940, Malaga, Spain.

Wittmann, P.A., and P.D. Farrar, 1997: Global, regional and coastal wave prediction. *MTS Journal*, **31**, 76-82.

# IMPLICATIONS OF FRICTION VELOCITY ON AIR-SEA COUPLED DYNAMICS

W. Perrie, L. Wang, B. Toulany and J. Yang*
Bedford Institute of Oceanography, Nova Scotia, Canada

As is well know, waves are driven by wind-stress at sea surface, sometimes expressed in terms of friction velocity. From an observational point of view, it is easier to measure the wind at a reference height, such as 10 meters $U_{10}$, than friction velocity $U^*$. A lot of empirical formulae trying to relate the drag coefficient $C_d$ (or $U^*$) and $U_{10}$ have been produced by observations. Oceanographers usually ask meteorologists to provide $U_{10}$ data from an atmospheric - boundary layer model. They then use this $U_{10}$ data as input, with an empirical formula to calculate $U^*$, to drive wave models. There are several problems with this process.

Equations for the atmospheric boundary layer relate wind speed $U_{10}$, drag coefficient $C_d$, friction velocity and sea surface roughness, $Z_o$. For neutral conditions, implementation of an empirical formula, such as Wu (1980), relating drag coefficient to wind speed $U_{10}$, leads to an over- determination of the atmospheric-boundary layer system of equations, as given in Perrie and Wang (1995).

A given wind profile is specified by $U^*$. However, at a given reference height such as 10 m, although the wind speed $U_{10}$ may have a single value such as $20m/s$, there may be a myriad of differing possible wind profiles. Each wind profile is associated with a different friction velocity $U^*$, depending on the stability conditions. Each different $U^*$ drives different waves systems. Thus wave models should be driven by $U^*$, as inferred from atmospheric models. The wind field, $U_{10}$, is not sufficiently unique to give adequate description of the forcing field responsible for the waves.

Empirical relations, try to express sea surface roughness $Z_o$ in terms of other marine boundary layer parameters. Yelland and Taylor (1996) try to relate $C_d$ to $U_{10}$, in a relation which is similar to that of Wu (1980). Smith et al (1992) try to couple roughness to wave parameters, relating $Z_o$ to seastate. An ongoing problem is to decide the appropriate variables needed to specify the sea suface roughness field. As yet measurements are unable to provide vital insight into this question.

Within the context of models that couple the atmospheric boundary layer to the ocean-wave surface, we show, implicitly, that the HEXOS results of Smith et al (1992) are better respresented by a seastate-dependent $Z_o$, than an uncoupled $C_d$ relation, as suggested by Yelland and Taylor (1996). Specifically, our present study is concerned with modelling the Storm of the Century.

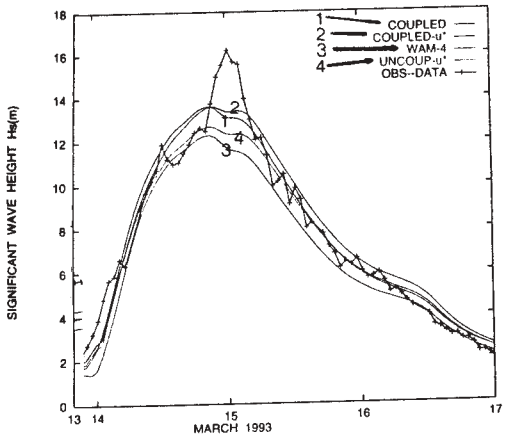


**Fig. 1.** Comparison of wave height estimates for Storm of the Century (SOC), from COUPLED, COUPLED-$U^*$, WAM-4, UNCOUP-$U^*$ models in comparison with measured data, OBS–DATA.

*Ocean Sciences Division, Fisheries and Oceans Canada, Bedford Institute of Oceanography, Dartmouth, Nova Scotia, Canada B2Y 4A2



AUTHOR INDEX TABLE OF CONTENTS

The Storm of the Century (SOC) occurred in March 1993. It has been reported in several papers and will not be described in detail, here. SOC involved very high waves, as presented in the study of Cardone et al (1995). These waves are the focus of our present study. Our UNCOUPLED model uses $U^*$ to drive the waves, in a 'one-way' manner, which is 'uncoupled'. Our COUPLED model uses the seastate dependent roughness $Z_o$ from the HEXOS experiment of Smith et al (1992) to force the waves, and an iteration process which continues until $U^*$ has converged to a limiting value.

As presented in Fig. 1, our COUPLED model is driven by $U_{10}$, COUPLED-$U^*$ is driven by $U^*$, WAM-4 is driven by $U_{10}$, UNCOUP-$U^*$ is the uncoupled model driven by $U^*$, and observed data is indicated as OBS-DATA. It is evident that, in terms of simulating the SOC peak wave heights, the COUPLED-$U^*$ model is most succeessful, and WAM-4 is least successful. WAM cycle 3, as given by Hasselmann et al (1988), is not shown in Fig. 1. It is qualitatively less good than WAM-4, compared to the data, OBS-DATA.

*Acknowledgements.* Wave modeling studies at BIO are funded by the Federal Panel on Energy Research and Development (Canada) under Project 534201.

## References

[1] Cardone, V. D., Jensen, R. E., Resio, D. T., Swail, V. R. and A. T. Cox, 1995: Evolution of contemporary ocean wave models in rare extreme events: "Halloween Storm" of October, 1991; "Storm of the Century" of March, 1993. *J. of Atmos. and Oceanic Tech.*, **13**, 198-230.

[2] Hasselmann et al. (The WAMDI) Group, 1988: The WAM Model - a third generation ocean wave prediction model. *J. Phys. Oceanogr.*, **18**, 1775 - 1810.

[3] Komen, G. J., L. Cavaleri, M. Donelan, K. Hasselmann, and P. A. E. M. Janssen, 1994: Dynamics and Modelling of Ocean Waves. *Cambridge University Press*, Cambridge, 512pp.

[4] Perrie, W. and L. Wang, 1995: On the overdetermination of friction velocity ($U_*$). *J. Phys. Oceanogr.*, **25**, 2177-2178.

[5] Smith, S.D., R.J. Anderson, W.A. Oost, C. Kraan, N. Maat, J. DeCosmo, K.B. Katsaros, K.L. Davidson, K. Bumke, L. Hasse and H.M. Chadwick, 1992: Sea surface wind stress and drag coefficients : The HEXOS results. *Bound. Layer Meteor.*, **60**, 109-142.

[6] Wu, J., 1980: Wind-stress coefficients over sea surface near neutral conditions - A revisit. *J. Phys. Oceanogr.*, **10**, 727-740.

[7] Yelland, M. and P. K. Taylor, 1996: Wind stress measurements from the open ocean. *J. Phys. Oceanogr.*, **26**, 541-558.

# A BI-DIRECTIONAL COUPLING BETWEEN AN ATMOSPHERIC MODEL AND AN OCEAN WAVE MODEL PART 1: ATMOSPHERIC ASPECTS

Serge Desjardins*, Jocelyn Mailhot*, Roop Lalbeharry**, and Laurie Wilson *

Meteorological Research Branch, Recherche en Prévision Numérique
*Atmospheric Environment Service, Dorval , Québec, Canada
** Atmospheric Environment Service, Downsview, Ontario, Canada

## 1. INTRODUCTION

Many studies (e.g. Mailhot and Chouinard, 1989, Perkey et al., 1991) have shown that explosive marine cyclones often have their prime thermodynamics sources in the air-sea interaction. This air-sea interaction depends on many parameters such as stability, wind speed and the ocean surface roughness which has a sea state dependence. Better parameterizations of the surface ocean roughness will certainly affect the interaction of the ocean and the atmosphere through variations of the surface energy fluxes. Differences in these fluxes could help to explain changes in larger features of a storm such as the low level jet, the fronts, or even the behaviour of the storm such as its trajectory, its deepening or its filling. Atmospheric models for many years have used the Charnock relation (Charnock 1955) to parameterize the roughness of the ocean. The Charnock constant (Wu, 1980) supposes an old or mature sea and therefore does not parameterize well the higher roughness of younger generated waves (Donelan,1982).

In more recent studies, several numerical experiments were done using a coupled atmospheric and ocean wave system. The results of these studies (Doyle, 1994, Doyle and Janssen., 1997, and Janssen, 1994) indicate there is a beneficial impact of such two-way interaction between the atmosphere and the ocean, although the response from this coupling is often modest. This study concerns the application of a coupled model system to simulate the "Storm of the Century" of March 1993. Our goal was to investigate the impact of the coupling on the atmosphere with two different parameterizations of the sea state dependence, the wave-induced stress of Janssen (1989), and the wave age of Smith et al. (1992).

## 2. COUPLED ATMOSPHERE-OCEAN WAVE MODEL SYSTEM

The coupled atmosphere-ocean wave system is composed of an atmospheric model and a wave model exchanging information between them at the end of a given number of model time steps. The coupling is bi-directional since both models influence each other throughout the integration. The information does not flow directly between models but goes through an interface module where interpolation on the receiving model grid is done. For this study, the coupled atmosphere-ocean wave system is constructed with the atmospheric model known as the Mesoscale Compressible Community (MC2) model and the Cycle-4 version of the ocean wave model WAM (The WAMDI group, 1988, and Komen et al., 1984). More details on WAM are provided by Lalbeharry et al. (1997, this Workshop), hereinafter referred to as LDMW.

### 2.1 *Numerical models*

The atmosphere is simulated with the MC2 model (Benoit et al. (1997)). The MC2 is based on the full-elastic nonhydrostatic model of Tanguay et al. (1990). The model solves the fully compressible Euler equations on a limited area cartesian domain of the polar projection with time-dependent nesting of the lateral boundary conditions. The MC2 model includes a complete physics package, comprising a TKE-based planetary boundary layer, a Kuo-type convection parameterization, an explicit moist scheme based on Sundqvist et al. (1989) and detailed radiation. All simulations were done with a time step of 600 s and at a resolution of 75 km on a grid including the whole wave model grid. Figure 1 shows the grid used in this study.

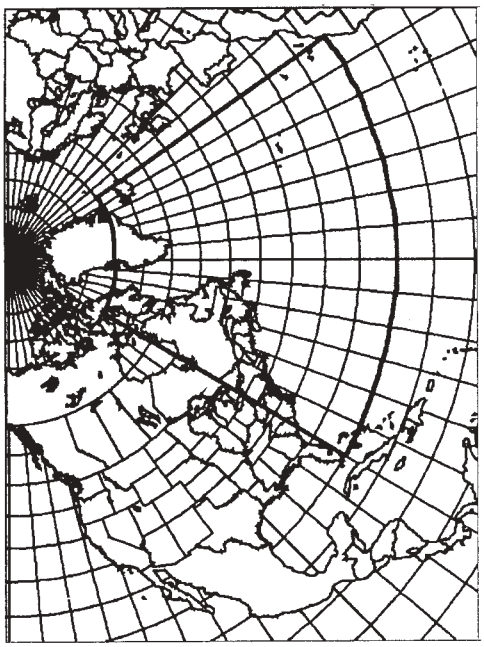

Figure 1: MC2 model grid used. The WAM grid is enclosed with the darker lines.

2.2 *Coupling parameter*

In an uncoupled system, the surface roughness length over sea is calculated by Charnock's relation (Charnock, 1955):

$$Z_0 = \frac{\beta u_*^2}{g} \qquad (1)$$

where $u_*$ is the friction velocity, g is the gravitational acceleration, and $\beta$ is the Charnock constant taken to be 0.018, a typical value for a mature sea. The Charnock relation makes no reference to sea state and is not a good representation of younger and rougher wind-generated waves.

In a coupled system, to improve the Charnock relation, $\beta$ loses its status as a constant and becomes a function of the sea state, that is, $\beta = \beta(\eta)$ where $\eta$ is the sea state forecast by a wave model. The sea state dependence can be expressed in terms of the wave-induced stress (Janssen et al., 1989) or the wave age (Smith et al., 1992). For more details on the two parameterizations of the Charnock parameter the reader is referred to LDMW. Equation (1) is reformulated as follows:

$$\beta(\eta) = 0.01/\{1-(\tau_w/\tau)\} \quad \Rightarrow \quad \text{wave induced stress}$$

$$Z_0 = \frac{\beta(\eta)\, u_*^2}{g} \qquad \text{where} \qquad (2)$$

$$\beta(\eta) = 0.48\, u_*/c_p \quad \Rightarrow \quad \text{wave age}$$

2.3 *Marching procedure*

The coupling mechanism has been developed to allow communication between both models at an arbitrary number of time steps. Let $t_n = T_o + n\Delta t$ where $T_o$ is the run time, $\Delta t$ the coupling input timestep and n the number of exchanges or couplings done between models. In our case, the coupling interval is $\Delta t$ = 1800 s and the MC2 model time step is 600 s so that the wind field passed to WAM is generated after 3 model time steps. In the marching procedure, the wind produced by the MC2 model at $t_{n-1}$ is used as WAM input wind valid at $t_n$ to allow both models to perform their respective integrations forward in time simultaneously without either one of them waiting on the other. WAM passes to the MC2 model at time $t_n$ the Charnock parameter $\beta$ defined in (2) based on the wave-induced stress of Janssen (1991) or the wave age of Smith et al. (1992). The Charnock parameter is computed using the previous wind field inputs. The MC2 model then uses $\beta$ provided by WAM and its own friction velocity $u_*$ to compute the sea-state dependent roughness length $z_0$ from (2) and then integrates forward in time to produce a new wind field for passing to WAM at the next coupling input time. WAM uses the input winds valid at $t_n$ and at $t_{n+1}$ to integrate forward in time to generate new wave parameters such as the Charnock parameter valid at $t_{n+1}$.

The simulation of each storm case consists of three phases, namely, the spin-up phase lasting for 48 hours, the transition phase lasting for 24 hours, and the evaluation phase lasting for 48 hours. The MC2 model is initialized at the start of each phase and after 24 hours into the spin-up run. The coupled model system runs in a control or uncoupled mode only in the spin-up phase and in either the coupled or uncoupled mode in the other phases. In the spin-up run WAM starts from a flat sea (cold start). This run is done once only and is based on the wave-induced stress. It provides the same initial sea-state to be used as input to all transition runs in warm start. The initial sea-state for the evaluation run in warm start is different for each run in this phase.

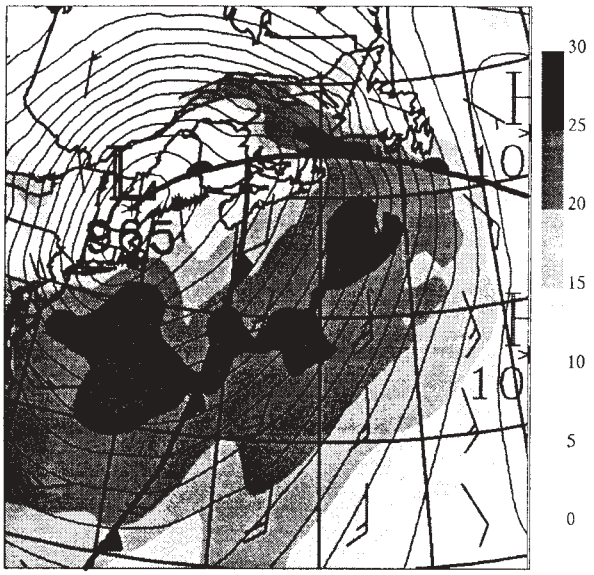


Figure 2: Synoptic surface situation from MC2 12HR forecast valid at 1200 UTC on March 14 1993. Solid lines represent pressure at sea level (4 hPa). Wind barbs (gray scale) are in m/s.

2.4 *Case Study*

The Blizzard of March 1993, better known as the Storm of the Century, was chosen as a first case to study the impact of the coupling. The storm was characterized by very strong winds and its extreme wave heights. As a brief description of the synoptic situation, at 0000 UTC March 13 1993, a strong cyclonic low pressure system at 996 hPa was located in the Gulf of Mexico. It continued to intensify to reach a central pressure of 963 hPa at 0000 UTC March 14 over the state of Delaware. Afterwards, it slowly filled to reach a central pressure of 968 hPa over Anticosti Island at 0000 UTC March 15 1993. Southerlies of 10-25 m/s gradually shifted to westerlies 15 to 30 m/s during the period over the ocean and generated significant wave heights up to 15 m. Figure 2 gives a snapshot of the pressure and its wind at 1200 UTC March 14 1993. The meandering effect in the wind field, especially ahead of the cold front, was caused by the details in the SST as studied in Desjardins et al. (1997).

## 3 RESULTS

### 3.1 *Numerical impact*

In the model simulations, the "control" run or "uncoupled" refers to the one-way interaction run in which the MC2 uses a constant value of $\beta = 0.018$ in the Charnock relation. On the other hand , the "coupled" run refers to the two-way interaction run in which the atmospheric model computed its roughness length using (2) where $\beta$ is supplied by the wave model, using either the wave-induced stress or the wave age as a parameterization of the sea state dependence.

One expects that the main effect of the coupling on the atmospheric model will appear in the surface wind fields. Figure 3 shows the 10 m wind speed difference between the "control" run and a coupled run superimposed with the coupled wind field for the same time as in Figure 2. Figure 3a shows the case using the wave-induced stress while Figure 3b shows the case with wave age. Both couplings generated a very

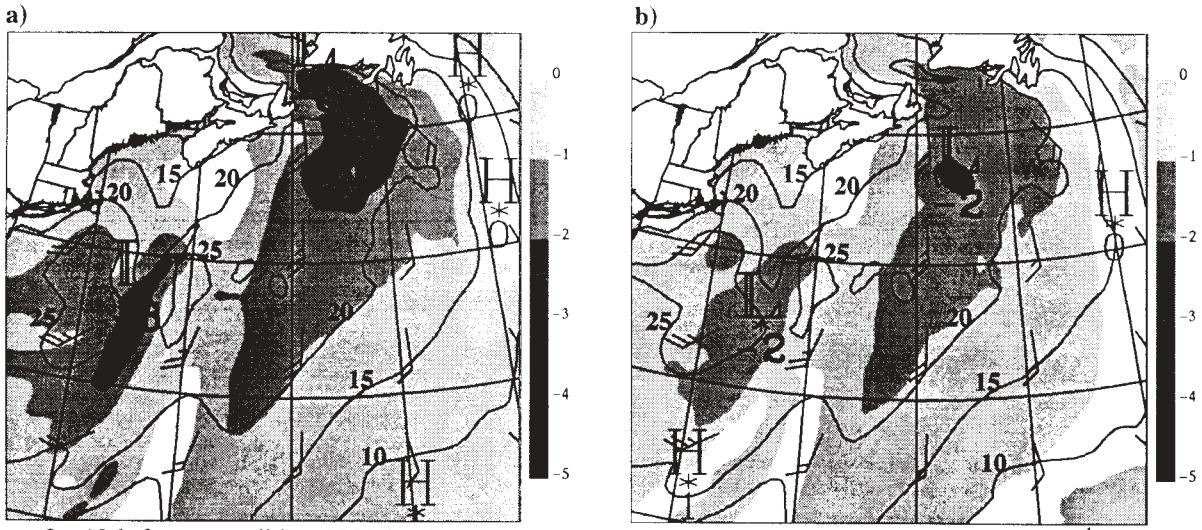


Figure 3: 12-h forecast valid at 1200 UTC 14 March 1993 of the 10 m wind speed difference [1 m $s^{-1}$, gray scale] between coupled and uncoupled simulations superimposed with the coupled wind field [5 m $s^{-1}$, black and labelled] for a) wave-induced stress and b) wave age.

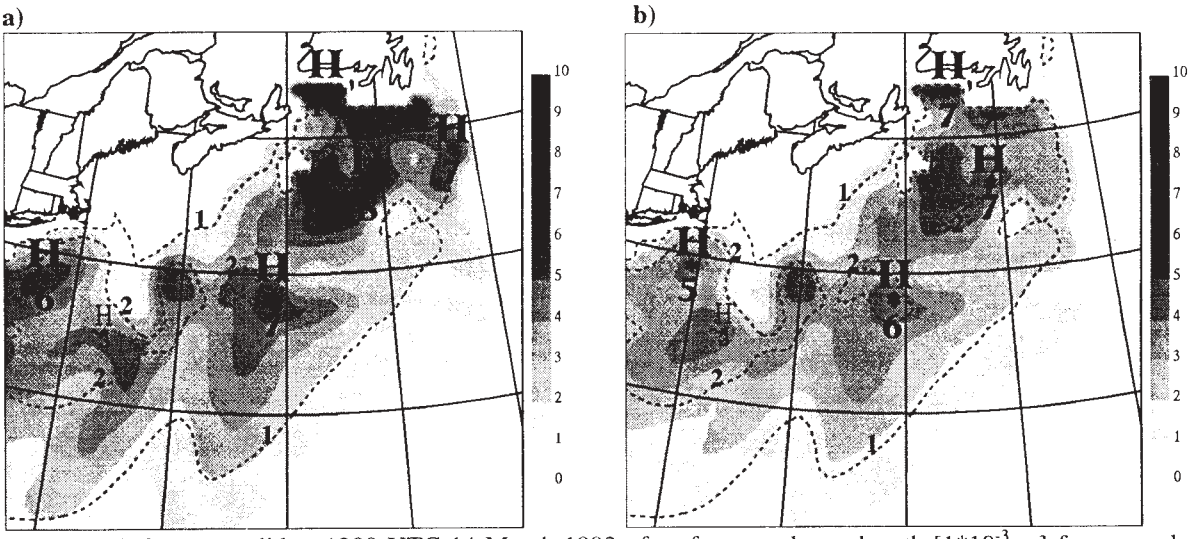


Figure 4: 12-h forecast valid at 1200 UTC 14 March 1993 of surface roughness length [$1*10^{-3}$ m] from coupled (grayscale) and uncoupled (dashed and labelled) runs for a) wave-induced stress and b) wave age.

similar wind field pattern with decreased wind values over the main domain when compared with the "control" run. The wind speed differences between the control run and the coupled run with wave-induced stress were found slightly larger than those in the wave age. East of the cold front (see Figure 2 for front positions), the southerly jet was decreased by about 1-2 m/s in both coupled simulations. Wave-induced stress seemed to have reacted more to the change in the wind direction found in the vicinity of the warm front. Both coupled simulations reacted similarly to the weaker winds found just behind the cold front by reducing them, by about 2 m/s. Again, the run with the wave-induced stress generated slightly bigger differences and therefore had a greater effect on the maximum wind speed in the unstable air behind the cold front.

Figure 4 shows the corresponding roughness length computed from (2) using both the wave-induced stress and the wave age superimposed with the "control" (Charnock constant) run. As noticed in the wind field, both coupled runs generated similar roughness length fields shaped as in the "control" run but more intense. Also by looking at Figure 3 in LDMW, one can see that the Charnock parameter reached values higher than the standard value (=0.018) over most of the domain. Over regions of "younger" waves (e.g. to the eastern part of the storm) the 2 mm isoline from the coupled run closely corresponds to the 1 mm isoline of the "control" run. This shows that the coupling results in roughness length above 1 mm with winds of 15 m/s instead of 25 m/s (see Figure 2) when uncoupled. On the other hand, the western edge isoline of 1 mm corresponds closely in both coupled and uncoupled simulations suggesting the presence of older seas or swells in that region. Persistent southerly winds for at least 6 hours may have generated this "older" sea/swell area.

Other atmospheric fields such as momentum, heat and vapor fluxes or precipitation rate were also examined. In general, fluxes are modified on average by 5-10 % with maximum variation of 15-25 % over regions of large $z_0$. Also, wave age modified the fluxes less than the wave-induced stress, by a factor of 5 % less. Figure 5 shows the difference in the precipitation rate between the uncoupled run and the wave-induced stress run (wage age gave similar results). The coupled run generated less precipitation over the warm front and in the main precipitation band ahead of the cold

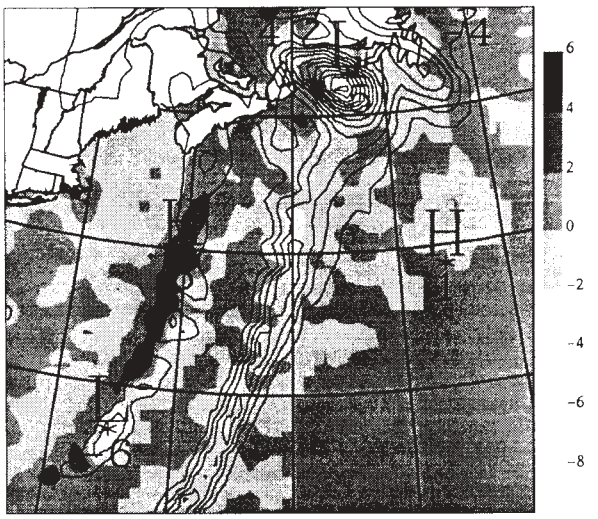


Figure 5: 12-h forecast valid at 1200 UTC 14 March 1993 of the precipitation rate [$10^{-7}$ m/s, gray scale] difference between coupled run with wave-induced stress and the uncoupled run. The precipitation rate in the uncoupled run is shown by the solid lines.

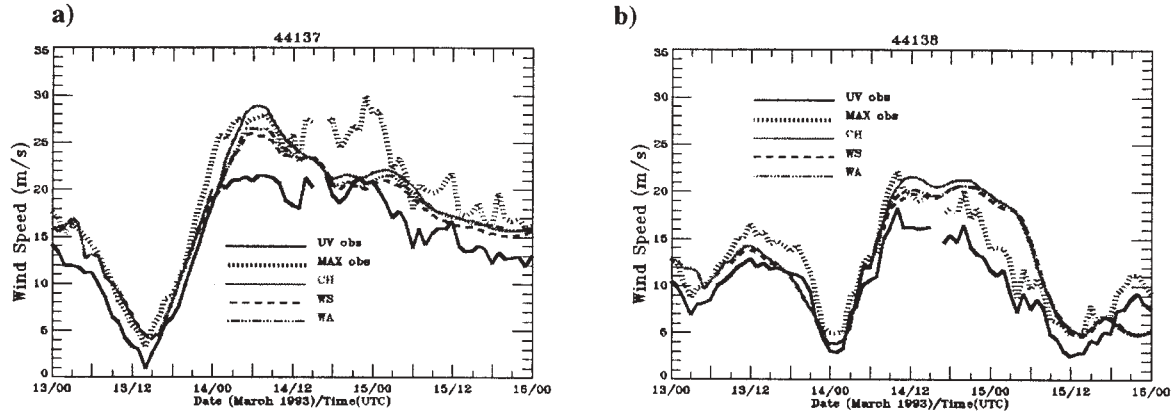


Figure 6: Times series of 10 m wind speed (m/s) for a) East Scotian Slope (44137) and b) Banquereau (44138) buoys. Solid lines indicate buoy observations and dashed lines are for the model forecasts. For the definition of lines, see legend in graph. CH refers to the uncoupled run, WS to the wave-induced stress run and WA to the wave age run.

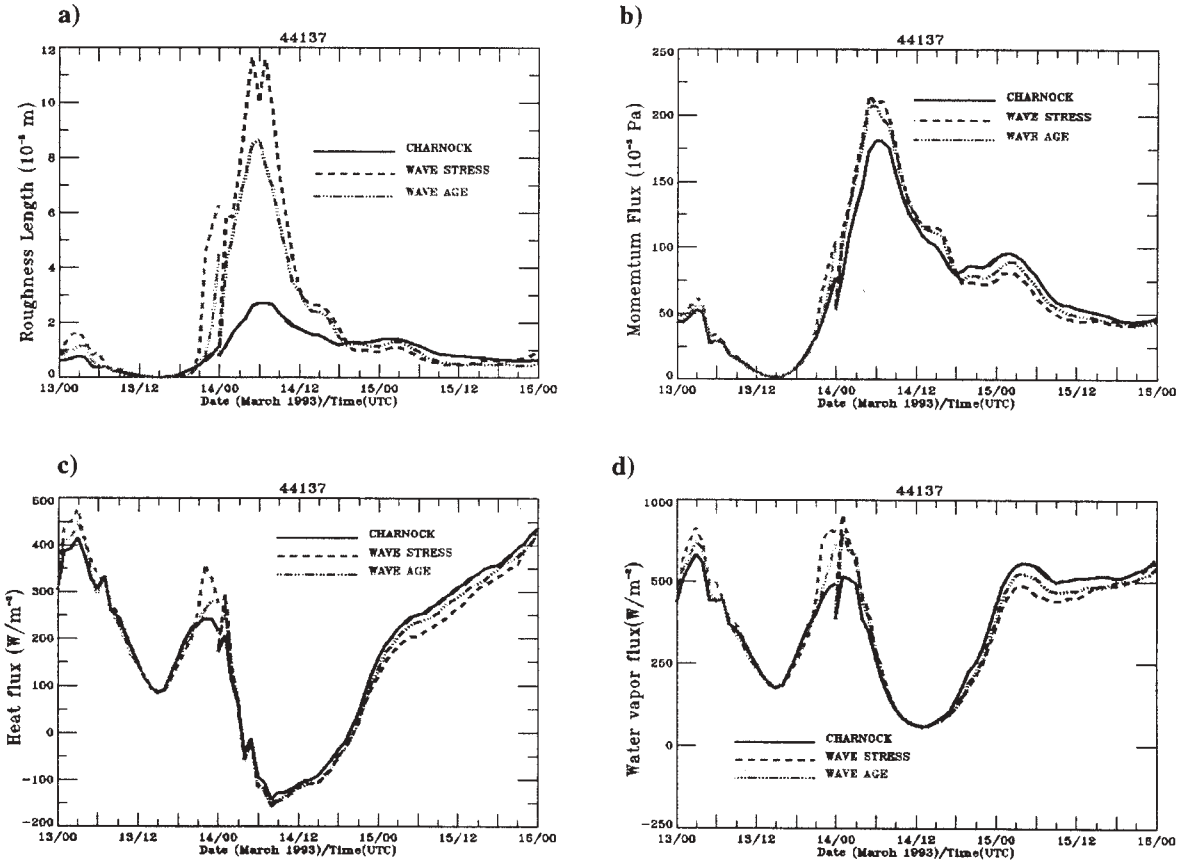


Figure 7: Times series of numerical grid point value representing East Scotian Slope buoy 44137 for a) surface roughness length, b) momemtum flux, c) heat flux and d) vapor flux. Solid lines indicate the contol run and dashed lines the coupled runs. For the definition of lines, see legend in graph.

front. The precipitation associated with the cold front was more intense in the coupled run and, moreover, had a phase difference with the uncoupled one.

### 3.2 *Numerical output versus observations*

In this section, a comparison between the model wind speed and the buoy observations is described. Canadian buoys report winds as a 10-minute vector average and maximum wind speeds are extracted from the highest running 8-second maxima (Skey et al., 1995). Figure 6 gives the 10 m level wind speed time series for East Scotian Slope (buoy 44137) and Banquereau (buoy 44138) buoys. East Scotian Slope was located at 41.2N and 61.1W, in a warm eddy while Banquereau was located at 44.2N and 53.6 W, in cold water. Following Smith (1981), 5 m wind speed were converted to a height of 10 m. This conversion added little to real buoy wind speed observations. No correction was done on the wind direction itself. Figure 6 indicates that the model overestimated the wind speed. The "control" run overestimated the wind speed the most. Both coupled runs helped to decrease this overestimation. Consistent with Figure 3, the wave-induced stress decreased the wind speed more than the wave age. At buoy 44138, the coupling had less impact. The possible reasons for this are that 1), winds were weaker and 2), the difference between uncoupled and coupled $z_0$ (not shown here) was between 3 and 5 mm while at buoy 44137, it was between 6 and 9 mm (see Figure 7a). As seen before in Figure 4, wave-induced stress generated the highest $z_0$ values. Figure 7a shows also that most of the time, the Charnock relation is good since both coupling runs converge to it except at specific periods where 'younger' waves are present. By looking at Figure 6a and Figure 7a after 1800 UTC on 14 March, one can understand why the coupling does not have a strong impact on the wind, despite a wind speed of 20 m/s; this is because all 3 roughness lengths converge to the same value indicating that the sea is mature (Charnock relation).

As indicted in Figure 7, generally, slight impact is found on the fluxes except for short periods of time . Coupling caused more impact on the water vapor fluxes. Both couplings slightly decreased the fluxes behind the front (i.e., after 1800 UTC on 14 March) because the roughness length was smaller in the coupled runs than in the uncoupled runs (see Figure 7a).

## 4 CONCLUSIONS

A coupled atmosphere-ocean wave model system was developed and tested on the "Storm of the Century" of March 1993 to assess the impact of such a coupling on the atmosphere and on the ocean waves. This storm produced very strong winds which generated extreme sea states. The coupling slightly altered the behavior of the storm. The main effect of the coupling was a reduction of surface wind speed over most of the domain due to the presence of higher roughness length. The largest impact was found at the eastern edge of the storm where winds generated "younger" and therefore rougher seas. It was also found that the importance of the coupling was dependent on the wind speed. Stronger winds generating "younger" waves increased the effect of the coupling on the atmosphere. Behind the storm, even with persitent winds up to 20 m/s, the sea state was considered as mature or old by the wave model and consequently very little impact of the coupling was found.

Two different wave coupling parameterizations were tested in this study. The wave-induced stress was found to generate the largest differences between uncoupled and coupled runs. It seemed also more sensitive to changes in the wind direction. However, the atmospheric response to both couplings was very small and one of the main reasons is that this storm is known to be somewhat insensitive to sea surface fluxes. Another case more sensitive to sea surface fluxes is currently being studied. Results from this case and possibly other will be presented at this Workshop.

## 5. REFERENCES

Benoit, R., M. Desgagnes, P. Pellerin, S. Pellerin, Y. Chartier and S. Desjardins, 1997: The Canadian MC2: A Semi-Lagrangian, Semi-Implicit Wide Band Atmospheric Model Suited for Fine-Scale Process Studies and Simulation. Mon. Wea. Rev., 117, 1726-1750.

Charnock, H., 1955: Wind stress on a water surface. Quart. J. Roy. Meteor. Soc., 81, 639-640.

Desjardins S, V. Swail and R. Benoit, 1997: The Influence of Meso-Scale Feature of the Sea Surface Temperature Distribution on Marine Boundary Layer Winds Off the Scotian Shelf during the "Storm of the Century", submitted in publication in MWR.

Donelan, M.A, 1982. The dependence of the aerodynamics drag coefficient on wave parameters. Proc. First Int. Conf. On Meteorology and Air-Sea Interaction of the coastal zone, The Hague, 381-387.

Doyle, J.D., 1994: Air-sea interaction during marine cyclogenesis. Proc of the international symposium on the life cycles of extratropical cyclones, Vol. III, June 27 - July 1, Bergen, Norway, 61-66.

Doyle, J.D. and P.A.E.M. Janssen, 1997: Experiments with ECMWF coupled ocean wave/atmosphere modelling system. Presentation made at WISE (Wave In Shallow water Environments) Meeting, 13-17 April, San Francisco, USA.

Janssen, P.A.E.M., 1989: Wave-induced stress and the drag of air flow over sea waves. J. Phys. Oceanogr., 19, 745-754.

Janssen, P.A.E.M., 1994: Results with a coupled wind wave model: ECMWF Tech. Rep. No. 71, 60p.

Komen, G.J., L. Caveleri, M. Donelan, K. Hasselmann, S. Hasselmann and P.A.E.M. Janssen, 1994: Dynamics and modelling of ocean waves. Cambridge University press, 532p.

Mailhot, J. and C. Chouinard, 1989: Numerical forecast of explosive winter storms: Sensitivity experiments with a meso-$\alpha$ model. Mon Wea. Rev., 117, 1311-1343.

Perkey, D. J. W. M. Lapenta, F. R. Robertson and C. W. Kreitzberg, 1991: The role of sea surface temperature distribution on numerically simulated cyclogenesis during Erica IOP-4. First Symposium on Winter Storm, Jan. 14-18 1991, New-Orleans, Louisiana, 418-422.

Skey S. G., K. Gerger-North and v. R. Swail, 1995. Detailed measurement of winds and waves in high sea states from a moored NOMAD weather buoy. Proc. 4$^{th}$ International workshop on Wave Hindcasting and Forecasting, October 16-20, 1995, Banff, Alberta, pp. 213-223.

Smith, D.S., R.J. Anderson, W.A. Oost, C. Kraan, N. Maat, J. DeCosmo, K.B. Katsaros, K.L. Davidson, K. Bumke, L. Hasse, and H.M. Chadwick, 1992: Sea surface wind stress and drag coefficients: The HEXOS results. Bound.-Layer Meteor., 60, 109-142.

Smith, S. D., 1981. Factors for adjustment of wind speed over water to a 10 m height. Report Series/BI-R-81-3/March 81. Bedford Institue of Oceanography. Bedford, N. S. 29 p.

Sundqvist, H., E. Berge and J. E. Kristjansson, 1989: Condensation and cloud parameterization studies with a mesocscale numerical weather prediction model. Mon. Wea. Rev., 117, 1641-1657.

Tanguay, M., A. Robert and R. Laprise, 1990: A semi-implicit semi-lagrangian fully compressible regional forecast model. Mon. Wea. Rev., 118, 1970-1980.

WAMDI Group, 1988: The WAM model - A third generation ocean wave prediction model. J. Phys. Oceanogr., 18, 1775-1810

Wu, J. (1980), Wind-stress coefficients over sea surface neutral conditions: A revisit. J Phys. Oceanogr., 10, p. 727-740

# A BI-DIRECTIONAL COUPLING BETWEEN AN ATMOSPHERIC MODEL AND AN OCEAN WAVE MODEL PART 2: OCEAN WAVE ASPECTS

Roop Lalbeharry*, Serge Desjardins**, Jocelyn Mailhot**, and Laurie Wilson **

Meteorological Research Branch, Recherche en Prévision Numérique
* Atmospheric Environment Service, Downsview, Ontario, Canada
** Atmospheric Environment Service, Dorval , Québec, Canada

## 1. INTRODUCTION

Several studies in recent years have indicated that the airflow over the oceans is sea-state dependent in which there is a bi-directional or two-way interaction between winds and waves (Donelan et al., 1993, Maat et al., 1991, Smith et al., 1992). Janssen (1989, 1991) developed a theory of this two-way interaction, which was implemented as Cycle-4 of the ocean wave model WAM (The WAMDI Group, 1988, Komen et al., 1994). In Janssen's theory the total stress is the sum of the atmospheric turbulent stress and the wave-induced stress with the latter being a significant fraction of the total stress, especially for young waves. In the marine atmospheric boundary layer wind-generated ocean waves may play an important role by modulating the response to deepening and/or filling of mesoscale and synoptic scale weather systems through the modulation of the surface fluxes of momentum, heat, and moisture.

In more recent studies several numerical experiments were performed using a coupled ocean-wave atmospheric model system to investigate the impact of the two-way interaction (Doyle, 1994, Doyle and Janssen, 1996, Janssen, 1994) and the results of these studies indicate that there is a beneficial impact. In this study a coupled model system is being applied to a rapidly deepening western Atlantic storm to further examine the impact of the two-way interaction.

## 2. COUPLED ATMOSPHERE-OCEAN WAVE MODEL SYSTEM

The wave model used in this study is a regional version of Cycle-4 of the ocean surface wave model WAM (The WAMDI Group, 1988), in which the atmospheric boundary layer is coupled to the wave model following Janssen's scheme (Janssen, 1989, 1991). The WAM grid has a spacing of 0.5° in both latitude and longitude directions extending from 25° N to 70°N and from 80°W to 15°W in the north Atlantic. The Cycle-4 version of WAM (WAM4) describes the evolution of the directional wave spectrum $E(f,\theta,\varphi,\lambda,t)$ for deep water physics by solving the wave energy transfer equation for 25 frequencies logarithmically spaced from 0.042 Hz to 0.41 Hz at intervals of $\Delta f/f = 0.1$ and 24 directions at 15° apart. Here, f is frequency, $\theta$ is wave direction, $\varphi$ is latitude, $\lambda$ is longitude, and t is time. The net source term consists of the wind input term $S_{in}$ and the dissipation term $S_{ds}$, both of which are based on Janssen's (1991) formulation, and the nonlinear wave-wave interaction term $S_{nl}$ from Hasselmann et al. (1985). In Janssen's formulation $S_{in}$ includes the square of the inverse of the wave age $c/u_*$ , c being the phase speed and $u_*$ the friction velocity, and has a higher growth rate than WAM Cycle-3 (WAM3). The WAM4 $S_{ds}$ is the WAM3 dissipation term plus an additional term proportional to the fourth power of the frequency to compensate for the higher growth rate of WAM4 $S_{in}$ (Bender, 1996).

In WAM4 the model roughness parameter, $z_o$, is given by the Charnock equation (Charnock,1955) in terms of $u_*$ and the acceleration due to gravity, g, as

$$z_o = \beta u_*^2/g \qquad (1)$$

where the Charnock parameter $\beta$ is a sea-state dependent parameter. Without any sea state dependence, $\beta$ is a constant. The value $\beta = 0.018$ is used by Canadian Meteorological Centre (CMC) operational numerical weather prediction model in the determination of $z_o$ over the ocean. In terms of

Janssen's formulation $\beta$ is modified to include the wave-induced stress, that is,

$$\beta_J = \alpha/\sqrt{\{1 - (\tau_w/\tau)\}};\ \alpha = 0.01 \quad (2)$$

in which the sea state dependence is reflected through the wave-induced kinematic stress, $\tau_w$, obtained from the integration of the model wind input source term over all frequencies and directions. In (2) the total kinematic stress $\tau = \tau_a + \tau_w$ where $\tau_a$ is the atmospheric turbulent kinematic stress from flow over a rigid flat surface. In terms of the formulation of Smith et al. (1992) using the HEXOS dataset $\beta$ is modified to include the wind sea parameter called wave age, $\xi = c_p/u_*$, that is,

$$\beta_S = 0.48/\xi \quad (3)$$

where $c_p$ is the phase speed of the peak of the spectrum. The 10 m level drag coefficient under neutral conditions is given by

$$C_D = u_*^2/u_{10}^2 \quad (4)$$

where $u_{10}$ is the neutral 10 m level wind given by

$$u_{10} = (u_*/\kappa)\ln(10/z_o) \quad (5)$$

where $\kappa = 0.41$ is the von Karman constant. From (4) and (5)

$$z_o = 10\exp(-\kappa/\sqrt{C_D}) \quad (6)$$

and from (1)

$$\beta_J = gz_o/u_*^2 \quad (7)$$

Given $u_{10}$ and $\tau_w$, (5) can be solved for $u_*$ iteratively. $C_D$ is now obtained from (4), $z_o$ from (6), and $\beta_J$ from (7). Given $u_{10}$ and $c_p$, the various parameters obtained using wave-induced stress can be similarly obtained using wave age. It should be noted that $\beta_J$ is valid for mixed wind sea, swell situation while $\beta_S$ is valid for pure wind sea.

The ocean wave model WAM is coupled in a bi-directional mode to the atmospheric model called MC2 described by Desjardins et al. (1997, this Workshop), hereinafter referred to as DMLW. The coupling parameter used is $\beta_J$ based on wave-induced stress or $\beta_S$ based on wave age, both as defined in (7). The results of the experimental runs presented are based on these two formulations of the coupling parameter.

Let $t_n = T_o + n\Delta t$ where $T_o$ is the run time, $\Delta t$ the exchange or coupling interval, n the number of exchanges or couplings done between models, and $t_n$ refers to the time as used by WAM. In the marching procedure the wind produced by the MC2 model at $t_{n-1}$ is used as WAM input wind valid at $t_n$ to allow both models to perform their respective integrations forward in time simultaneously without either one of them waiting on the other. WAM passes to the MC2 model at time $t_n$ the Charnock parameter $\beta$ as defined in (7) based on the wave-induced stress of Janssen (1991) or the wave age of Smith et al. (1992) and, in return, receives the MC2 model wind to be used as WAM input wind valid at $t_{n+1}$. The MC2 model then uses $\beta$ provided by WAM and its own friction velocity $u_*$ to compute the sea-state dependent roughness length $z_o$ from (1) and then integrates forward in time to produce a new wind field for passing to WAM. WAM uses the input winds valid at $t_n$ and at $t_{n+1}$ to integrate forward in time to generate a $\tau_w$ valid at $t_{n+1}$. It uses this $\tau_w$ and the wind at $t_{n+1}$ to produce a new $\beta$ valid at $t_{n+1}$ for passing to the MC2 model. In the coupling experiment WAM uses a propagation time step of 300 s, a source term growth integration time step equal to the propagation time step, and an exchange or coupling interval of $\Delta t$ = 1800 s so that the $\beta$ provided by WAM to the MC2 model is generated after 6 WAM propagation/growth time steps.

In the model simulations, the "control" or "uncoupled" run is referred to as the one-way interaction run in which the MC2 model uses not the $\beta$ provided by WAM but a constant value of $\beta$ = 0.018 over the entire MC2 model grid. On the other hand, the "coupled" run is referred to as the two-way interaction run in which the MC2 model receives from WAM the sea-state dependent parameter $\beta$ and WAM, in return, receives from the MC2 model the 10 m level wind field generated using the $\beta$ provided by the wave model.

The simulation of each storm case consists of three phases, namely, the spin-up phase lasting for 48 hours, the transition phase lasting for 24 hours, and the evaluation phase lasting for 48 hours. The MC2 model is initialized at the start of each phase and after 24 hours into the spin-up run. The coupled model system runs in a control or uncoupled mode

only in the spin-up phase and in either the coupled or uncoupled mode in the other phases. In the spin-up run WAM starts from a flat sea (cold start). This run is done once only and is based on the wave-induced stress. It provides the same initial sea-state to be used as input to all transition runs in warm start. The initial sea-state for the evaluation run in warm start is different for each run in this phase.

When wave age instead of wave-induced stress is used as the coupling parameter, WAM uses the WAM3 dissipation source term and a parametric high-frequency tail of the spectrum proportional to $f^{-4.5}$ instead of $f^{-5}$ as in WAM4 for frequencies greater than the model-calculated cut-off frequency. This is in keeping with some of the options used by the Bedford Institute of Oceanography in its ocean wave modelling work.

## 3. RESULTS OF ONE-WAY AND TWO-WAY INTERACTIONS OF THE COUPLED MODEL SYSTEM

The WAM results obtained in the evaluation phase from the two-way interaction are compared against those from the one-way interaction. Both these results are also compared against buoy observations whose locations are given in Table 1 to give a measure of the impact of the coupled model system.

Table 1: Locations of buoys used in model verification.

| Buoy | Latitude (°N) | Longitude (°W) |
|---|---|---|
| 44137 | 41.2 | 61.1 |
| 44138 | 44.2 | 53.6 |
| 44139 | 44.3 | 57.4 |
| 44141 | 42.1 | 56.2 |

A series of simulations using the coupled model system were obtained in respect of a storm case which pertains to the blizzard of March 1993, dubbed as the "storm of the century". The storm developed over the panhandle region of Florida, U.S.A., and moved rapidly through the U.S. Atlantic seaboard along a track from Florida to the Gulf of St. Lawrence in the Canadian east coast offshore (see Brugge, 1994, and Figure 2 in DMLW). The storm generated extreme sea states with significant wave heights of 13-16 m at several buoy locations in the Scotian Shelf region of the Canadian Atlantic.

Figure 1 shows the time series plots of observed and model-generated significant wave heights (SWH) in metres in coupled and uncoupled modes based on the wave-induced stress $\tau_w$ (left panels) and the wave age $\xi$ (right panels) at four buoy locations in the Scotian Shelf region during the evaluation period from 0000 UTC on 14 March to 0000 UTC on 16 March 1993. The SWH is, in general, overpredicted with greater overprediction when the coupled model system runs in the control mode. In the coupled mode the overprediction is reduced with greater reduction associated with $\tau_w$. The reductions associated with both $\tau_w$ and $\xi$ improve the agreement between observed SWH and model-generated SWH.

Figure 2 gives a snapshot of the SWH in metres based on $\tau_w$ (left panels) and $\xi$ (right panels) at 1200 UTC (upper panels) and 1800 UTC (lower panels) on 14 March. The region in shades of gray gives the difference in SWH (coupled mode SWH minus control mode SWH), the range of values of each shade of gray being given by the vertical gray-scale bar to the right. The superimposed contours with large labels are the SWH generated by the model system in the uncoupled mode. It can be seen that the SWH in coupled mode is lower than the SWH in uncoupled mode by 1-3 m using wave-induced stress and by 1-2 m using wave age. The area less than -1 m difference is in good agreement with the reduction in the MC2 model winds in the coupled mode (see Figure 3 in DMLW). In general, however, higher differences are associated with wave-induced stress rather than with wave age.

In Figure 3, the upper panels give the WAM-generated Charnock parameter $\beta$ x 100 and the lower panels the corresponding drag coefficient $C_D$ x 1000 valid at 1200 UTC on 14 March. The left panels are for model runs using wave-induced stress and the right panels for those using wave age. The regions in shades of gray with central values are for model runs in the coupled mode while the solid black lines with labels are for runs in the uncoupled mode. In the region to the southeast of Newfoundland there is stronger wind speed gradient ( see Figure 3 in DMLR) which gives rise to relatively larger values of $\beta_J$ (upper left panel) and $\beta_S$ (upper right panel), that is, younger waves with a maximum value of $\beta_J$ close

to 0.14. Here, the subscripts J and S refer, respectively, to runs based on wave-induced stress and wave age. In general, $\beta_J > \beta_S$ indicating that the sea states generated using $\tau_w$ are younger and rougher than those generated using $\xi$. The areas of maxima of $\beta_J$ and $\beta_S$ match closely those corresponding to the drag coefficients of $C_{DJ}$ (lower left panel) and $C_{DS}$ ( lower right panel), respectively. An examination of the drag coefficient in the coupled mode indicates that $C_D \geq 3 \times 10^{-3}$ lies in a region of wind speed in excess of 20 m/s (see Figure 3, DMLW). Here, the $C_D$ due to wave age approximates that due to wave-induced stress, that is, as the wind speed increases, the difference in drag coefficients between the pure wind sea and the mixed wind sea/swell decreases (Donelan et al., 1997).

## 4. CONCLUSIONS

In this study an attempt is made to further examine the ocean-wave impact of a coupled atmosphere-ocean wave model system. Results based on one case study suggest that there is some beneficial impact, especially in areas of extreme sea states. Both the control and coupled runs overpredicted the extreme sea state for this case study, but the SWH generated from the two-way interaction run, however, is in better agreement with the buoy observed SWH. The SWH based on wave age is generally greater than the SWH based on wave-induced stress and this may be ascribed to the smaller WAM3 dissipation source term used in runs based on wave age. More case studies will be done to determine whether the roughness length formulation based on wave-induced stress is superior to that based on wave age and to provide a better assessment of the impact of the coupled model system with a view for operational implementation.

## 5. REFERENCES


Bender, L.C., 1996: Modification of the physics and numerics in a third-generation ocean wave model. J. Atmos. Oceanic Technology, Vol. 13, No. 3, 726-750.

Brugge, R., 1994: The blizzard of 12-15 March 1993 in the USA and Canada, Weather, Vol. 49, No. 3, 82-89.

Charnock, H., 1955: Wind stress on a water surface. Quart. J. Roy. Meteor. Soc., 81, 639-640.

Donelan, M.A., W. Drennan and K.B. Katsaros, 1997: The air-sea momentum flux in conditions of wind sea and swell. J. Phys. Oceanogr., 27, 2087-2099.

Donelan, M.A., F.W. Dobson, S.D. Smith and R.J. Anderson, 1993: On the dependence of the sea surface roughness on wave development. J. Phys. Oceanogr., 23, 2143-2149.

Doyle, J.D., 1994: Air-sea interaction during marine cyclogenesis. Proc of the international symposium on the life cycles of extratropical cyclones, Vol. III, June 27 - July 1, Bergen, Norway, 61-66.

Doyle, J.D. and P.A.E.M. Janssen, 1997: Experiments with ECMWF coupled ocean wave/atmosphere modelling system. Presentation made at WISE (Waves In Shallow water Environments) Meeting, 13-17 April, San Francisco, USA.

Hasselmann, S., K. Hasselmann, J.H. Allender and T.P.Barnett, 1985: Computations and parameterizations of the nonlinear energy transfer in a gravity-wave spectrum. Part II: Parameterizations of the nonlinear transfer for application in wave models. J. Phys. Oceanogr., 19, 745-754.

Janssen, P.A.E.M., 1989: Wave-induced stress and the drag of air flow over sea waves. J. Phys. Oceanogr., 19, 745-754.

Janssen, P.A.E.M., 1994: Results with a coupled wind wave model: ECMWF Tech. Rep. No. 71, 60p.

Janssen, P.A.E.M., 1991: Quasi-linear theory for wind-wave generation applied to wave forecasting. J. Phys. Oceanogr., 21, 1631-1642.

Komen, G.J., L. Caveleri, M. Donelan, K. Hasselmann, S. Hasselmann and P.A.E.M. Janssen, 1994: Dynamics and modelling of ocean waves. Cambridge University press, 532p.

Maat, N., C. Kraan and W.A. Oost, 1991: The roughness of waves. Bound.-Layer Meteor., 54, 89-103.

Smith, D.S., R.J. Anderson, W.A. Oost, C. Kraan, N. Maat, J. DeCosmo, K.B. Katsaros, K.L. Davidson, K. Bumke, L. Hasse, and H.M. Chadwick, 1992: Sea surface wind stress and drag coefficients: The HEXOS results. Bound.-Layer Meteor., 60, 109-142.

WAMDI Group, 1988: The WAM model - A third generation ocean wave prediction model. J. Phys. Oceanogr., 18, 1775-1810.

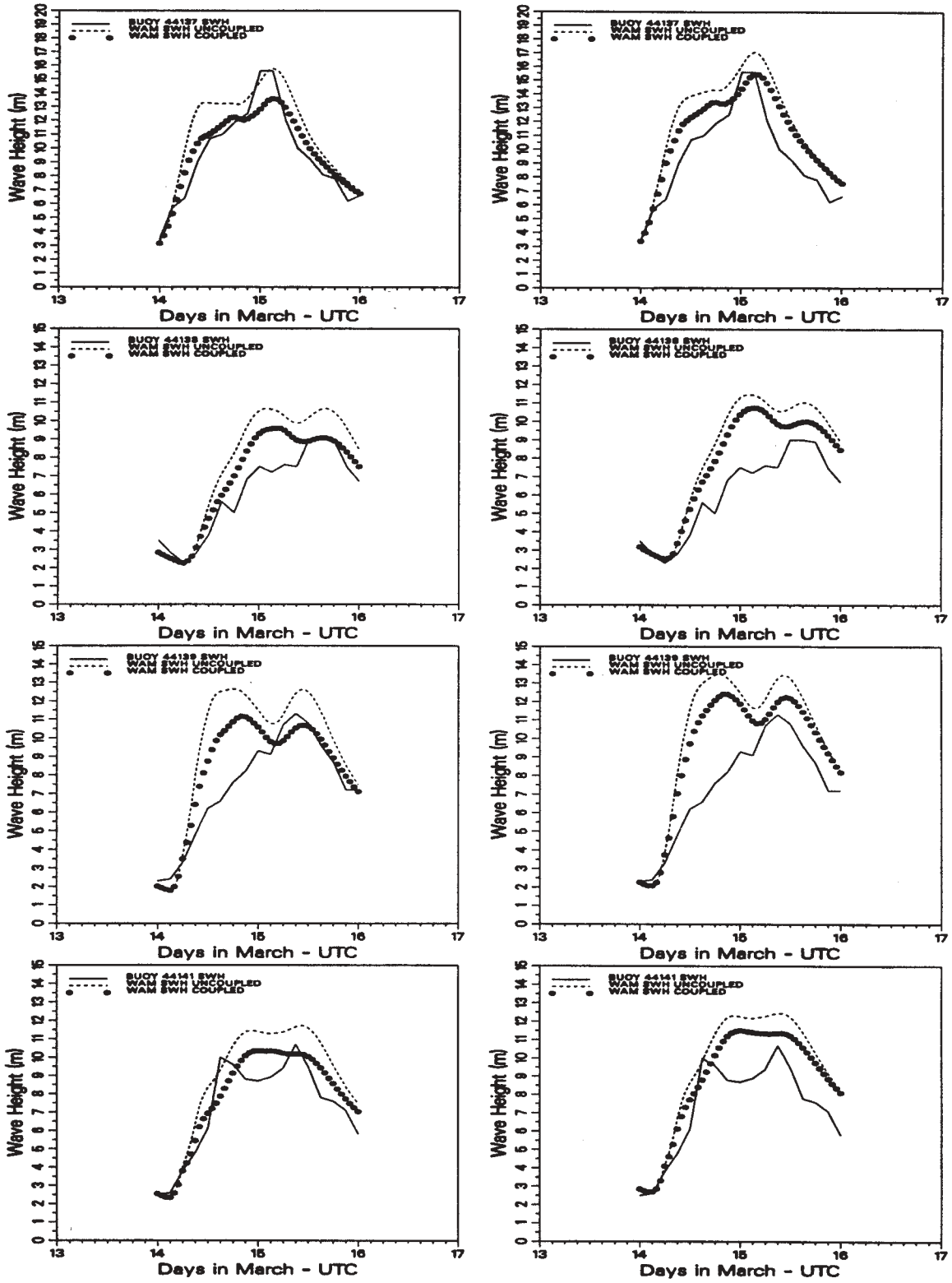


Figure 1: Time series plots of SWH in metres at buoys 44137, 44138, 44139, and 44141 based on wave-induced stress $\tau_w$ (left panels) and wave age $\xi$ (right panels). Solid lines indicate buoy observations, the dashed lines SWH generated using the uncoupled system, and the solid circles that using the coupled system.

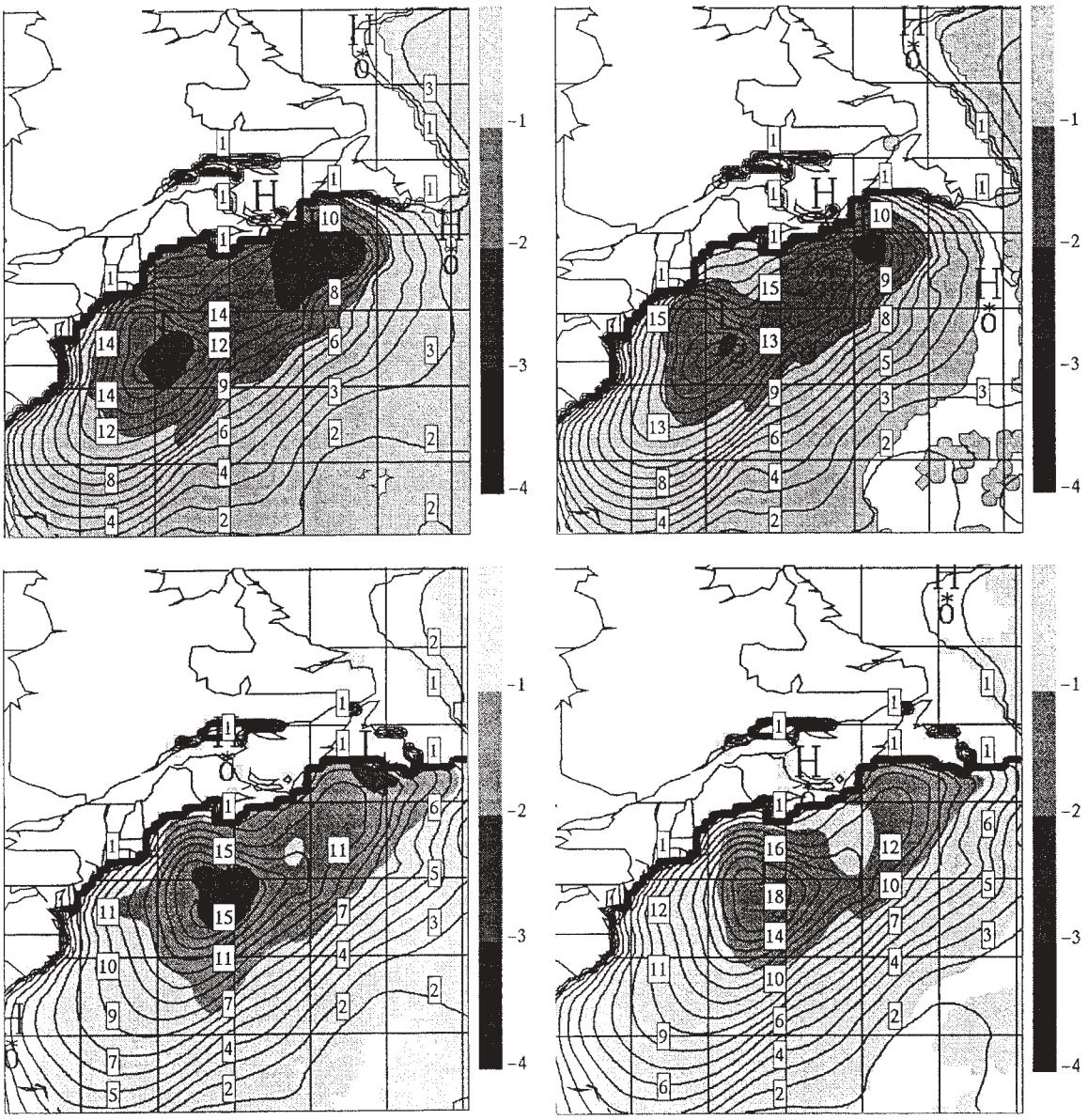


Figure 2: WAM model-generated SWH in metres based on wave-induced stress (left panels) and wave age (right panels) valid at 1200 UTC (upper panels) and 1800 UTC (lower panels) on 14 March 1993, respectively. The shaded regions with central values are SWH differences (coupled mode SWH minus control mode SWH). The range of values for each shade of gray is given by the vertical gray-scale bar to the right. The superimposed contours with labels are the SWH corresponding to the uncoupled system.

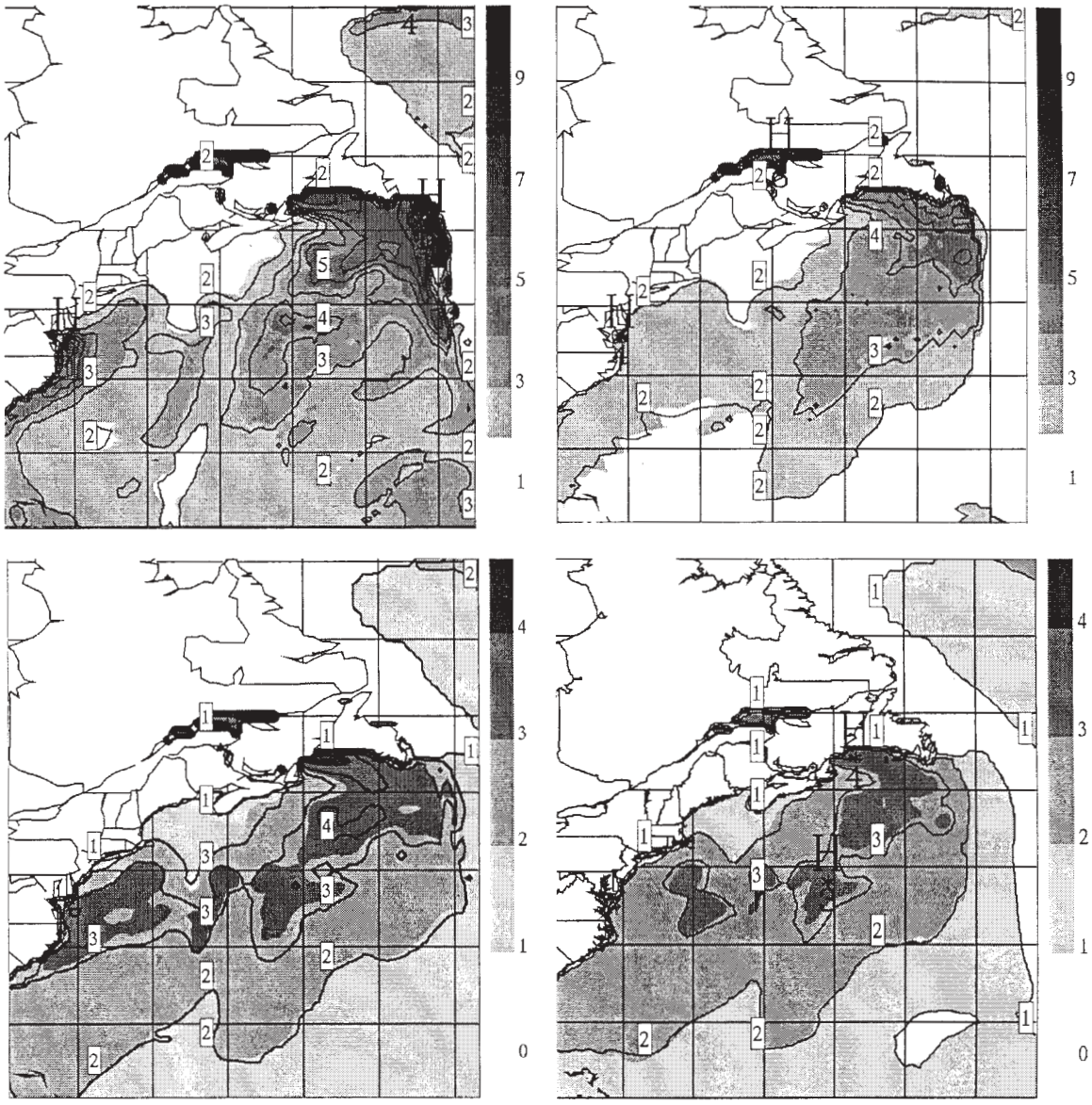

Figure 3: WAM-generated Charnock parameter β x 100 (upper panels) and drag coefficient $C_D$ x 1000 (lower panels) valid 1200 UTC on 14 March 1993. The left panels are for model runs using wave-induced stress and the right panels are for those using wave age. The regions in shades of gray with central values correspond to runs in the coupled mode while the solid lines with labels correspond to runs in the uncoupled mode.

**ERRATUM**

Please replace Figure 3 in Lalbeharry et al. in the preprint volume with this new Figure 3.

# THE EFFECT OF THE SEA FLOOR EROSION ON WAVE HINDCASTING IN COASTAL AREAS OF BOHAI SEA

Li Luping
First Institute of Oceanography, SOA. P. O. Box 98 Qingdao 266003

## 1. INTRODUCTION

The shallow water area of the southern Bohai sea is rich in oil and gas resources. With the expansion of product scale of oil and gas, hydraulic architecture and equipment in this area are increasing quickly. To guarantee the safety and reliability of coastal engineering, it is very important to study and forecast the evolution of sea bottom, coastline, and wave parameters in this area in the coming ten years or a longer period. In the past twenty years, many wave observation programs are carried out in this area. The main purpose of these programs is to collect wave data for estimating ocean environment design parameters and analyzing operation conditions in the sea. In the executive process of the programs, It was found out that the wave depth increased consecutively for identical observation points. This means that the bottom in the sea area is eroded and is unstable. In shallow water the change in the bottom will cause the change in wave parameters for identical external conditions, therefore, the uncertainty of waves due to the bottom erosion makes it difficult to determine the design wave parameters for this area. It is well—known that wind waves is one of the main external loads of ocean structures, and the study of the uncertainty of wind waves is of great importance. As many researchers pointed out (Guedes and Moan 1983, Liu 1988), the uncertainty of design wave heights is about 55% of the resultant uncertainty caused by nine factors which include wave height, wave pe-



AUTHOR INDEX TABLE OF CONTENTS

riod, current, the diameter of cylinder, the roughness of cylinder, the parameters of calculating wave forces, Cd and Cm etc.. In normal conditions the uncertainty of design waves include the uncertainty of stochastic analysis methods and probability models, the uncertainty of data samples, and the uncertainty of statistics, etc.. It should be pointed out that for shallow water waves the long—term erosion of the sea bottom and the retreat of the coastline caused by storm waves will result in the deformation of the bottom and the change in water depths, therefore, will yield the uncertainty of design waves. It is expected that the effect of this uncertainty on the design waves might be higher in orders of magnitude than the effects of the uncertainties mentioned above. However, the uncertainty of design waves due to bottom erosion has not been considered in the calculation of design waves yet. In order to solve this problem, it is necessary to study wave — bottom interaction and the evolution of wave and bottom.

The deformation of the sea bottom caused by action of waves has been studied for a long time. This study concentrates in bottom friction models (Weber 1991), the estimate of bottom roughness, friction coefficent (Shemdien 1987), and sediment to transportation (Grant and Madsen 1979). These studies are very important to discove the mechanism of wave—bottom interaction. However, the determine of some parameters such as diameter of sand grain, bottom roughness, and friction coefficient is very difficult. The arbitrary for chosing these parameters will influence theoretically the results. Because of the complication of the problem, it is very difficult to present a theoretical model for wave—bottom interaction to quantitatively predict the evolution of waves and bottoms. It is also difficult to obtain field observation da-

ta and such an observation program is very expensive. Therefore, we know little about the consequence of wave—bottom interaction, but the knowledge of the evolution of wave and bottom is necessary to ocean engineering design.

In this paper, HISWA model is used to investigate the effects of the sea floor erosion on storm waves and the evolution of wave parameters due to the bottom erosion on a typical shallow water area in the southern Bohai sea, based on the depth measurements of 1976 and 1993 and the typical storm wave data, without considering the mechanism of the erosion. Some new results are presented.

## 2 THE DESIGN OF THE COMPUTATION FOR HISWA MODE

The description of HISWA model is given by Holthuijsen et. al.. The typical sea area calculated by HISWA model locates 118°43′—119°04′E, 38°06′—38°18′N. In the design of the computation, the bottom grids coincidence with the grids of water depth measurements of 1976 and 1993 with the space step of 1′×1′, that is, the number of the grid is Mx=21, My=13. the lengths of the mesh are chosen as Dx=1666.6m, Dy=1852m, considering the position of this area. The computation grid is chosen as Mx=60, My=40, the direction interval $M_\theta$=12. Because the angle between the x direction of the bottom grid and the x direction of the computation grid is 270°. Therefore, the lengths of the computation grid Dx=370.4m, Dy=874.65m. In the computation the effects of bottom friction dissipation and depth breaking dissipation on the frequence are considered. The input of wave parameters of deep water boundary conditions is on the basis of the measuring data of storm wave in this area, that is, Hs=3.52m, T=8.0s, local wind speed U10=17.2m/s. As for direction-

al spread width, there is no measurement data available to be used, we used the deep water wave model DOLPHIN to calculate the storm waves due to a typhon invaded Bohai sea. The results show that the directional spread is about 30° and very stable. Therefore, in the computation the directional spread width is chosen as 2.

## 3 THE EFFECTS OF THE SEA FLOOR EROSION ON THE WAVE HINDCASTING

The water depth measurements of 1976 and 1993 of the typical sea area show that this area is unstable. The depth field in shallow water was severely eroded in the past 17 years. Along the profiles from deep water to the coastal line, that is, along the x direction of the computation grid the eroded depths of the sea bottom increased gradually, reached the maximum value, and then dereased. Fig. 1 gives three measured depth profiles of 1976 and 1993. The other profiles are alomst the same shapes as these profiles.

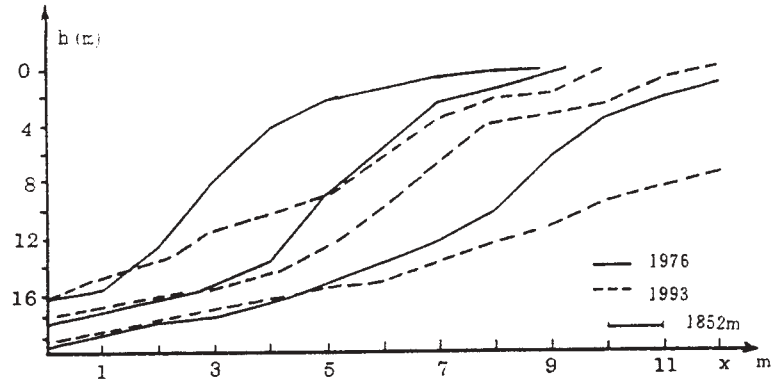


Fig. 1 the profiles of water depth measurement of 1976 and 1993

Using the computation design of HISWA model in sector 2, the wave parameters calculated on the bottom grids of 1976 and 1993 show that the increase of the water depth caused by erosion of the sea bottom results in the strengthening of the wave

fields. From the wave parameters of 1976 and 1993´ two wave fileds it is easy to obtain the relationship between the erosion depth and the increments of the significant wave height, the mean wave length, and the maximum value of the near—bottom orbital velocity (see Fig. 2a, b, c).

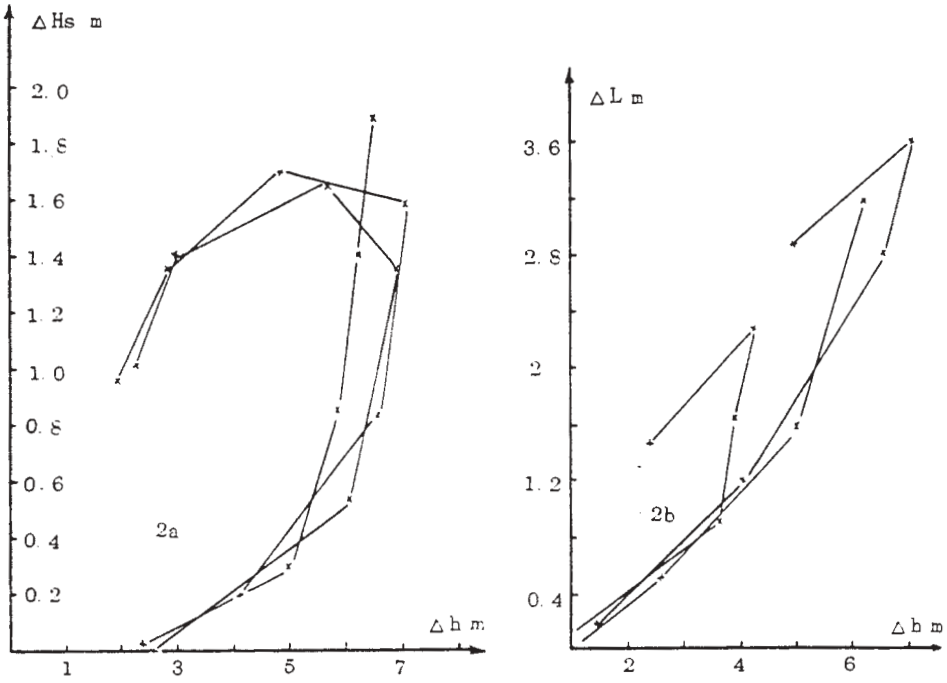


Fig. 2 the relationship between the erosion depth and the increment of Hs and L

Fig. 2a,b show that along the profiles of x direction for the computation grid the increments of wave parameters mentioned above changed from small to large with the erosion depth, reached the maximum value, and then decreased, as the erosion depth changed. But the increment of the wave parameters mentioned above had much higher values in the shallower water than that in the deeper water for the same erosion depths.

Fig. 2c shows that the increment of the maximum of near—bottom orbital velocity decreased with increasing erosion depth at first, and then increased with decreasing

erosion depth. In particularly, the increment of the maximum of the near—bottom orbital veocity increased greatly in the shallower water.

The comparisons between Fig. 2a,b and Fig. 2c show that:

1, in the deeper water area the wave field was strengthened because of the erosion of the sea bottom; but the maximum of the near—bottom orbital velocity decreased, therefore, the erosion of the sea bottom for the deeper water due to storm waves will be weakened.

2, in the shallower water area the wave field was much strengthened because of the erosion of the sea bottom; but the maximum of the near—bottom orbital velocity increased, that is, the current field of the sea bottom was strengthened, therefore, the erosion of the sea bottom fot the shallower water due to storm waves will be much more strengthened.

Along the profile of x direction for the computation grid the distribution between the peak values of the maximum of the near—bottom orbital velocity and the water depth and the distribution between the peak values of the dissipation due to bottom friction and the water depth are given in Fig. 3a,b.

From Fig. 3a it can be seen that the peak values of the maximum of the near—bottom orbital velocity were decreased with the shift of the time, and the corresponding water depth were increased. This indicates that strengthening of wave field will be increased with the time, but the erosion of sea bottom will be decreased.

From Fig. 3b the distribution between the peak values of the dissipation due to bottom friction and the water depth, it can be seen that in 1976 the peak values of the dissipation due to bottom friction increased with increasing in water depth, and the higher

dissipation values located in deeper water; in 1993 the peak values of the dissipation due to bottom friction decreased with increasing in water depth, and the higher dissipation values located in shallower water. This indicates that the severe erosion of this sea area has been moved from the deeper water area of 1976 to the shallower water area of 1993.

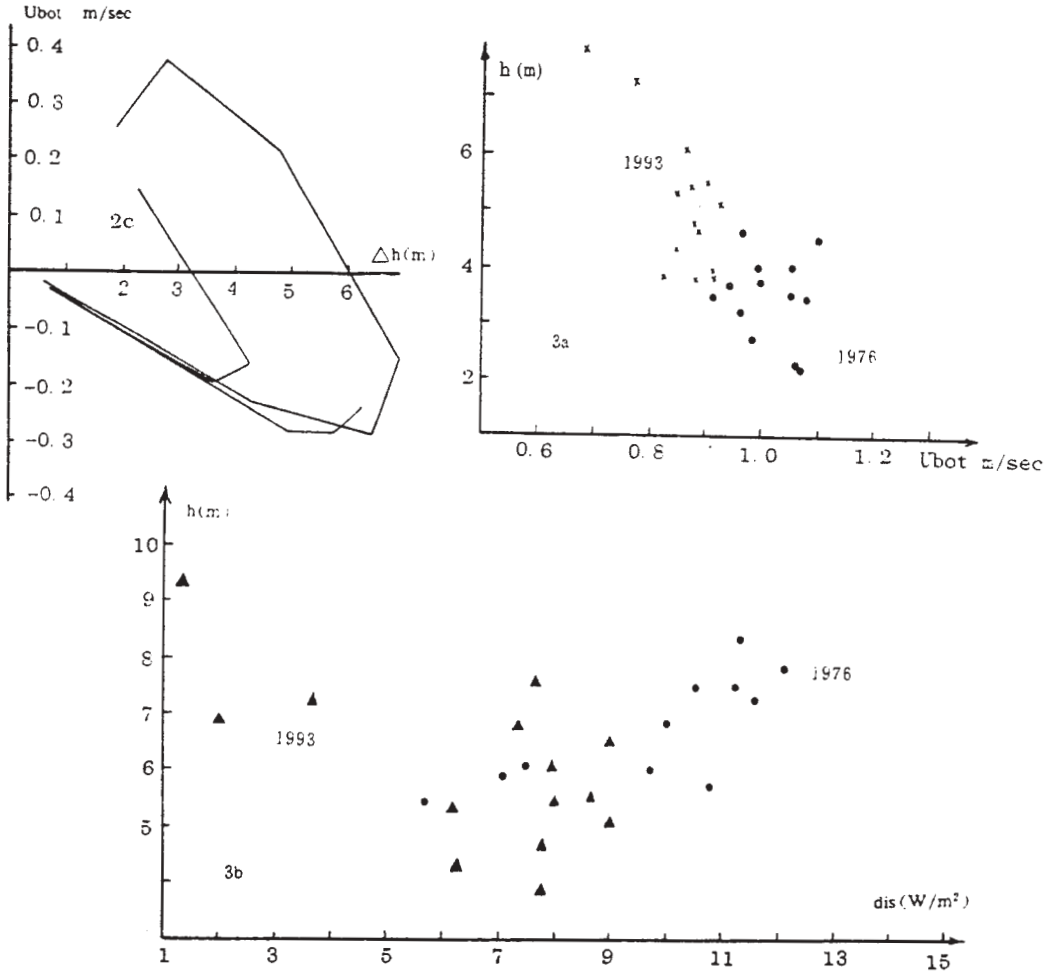


Fig. 3 the distribution between the peak values of the maximum of the near—bottom orbital velocity and the water depth and the distribution between the peak values of the dissipation due to bottom friction and the water depth.

The numerical results mentioned above are obtained on the basis of the water depth measurements of 1976 and 1993. The results show that the change in the mean wave



AUTHOR INDEX TABLE OF CONTENTS

direction caused by the different bottoms is small, and the maximum of the change in the mean wave direction is less than 15°. This means that the effect of wave direction on the wave parameters is not important.

Based on the observations of storm waves of this area, in the deeper water the significant wave height is 3. 52m, and the mean wave period is 8s. These are the boundary input values of HISWA model. The numerical results shows that the increments of significant wave height and the mean wave period due to the bottom erosion in this area during 1976—1993 reached up 1. 8m and 3. 2s. Therefore, the uncertainty of the design wave due to the erosion of the bottom extremely affect the analysis of the design wave parameters.

In order to solve this uncertainty of the design waves due to the erosion of the bottom, we must estimate the change in sea bottom in this area at first. So the study of the erosion action of waves on the sea bottom is very important.

## 4. THE ACTION OF STORM WAVES ON SEA BOTTOM EROSION

Many studies show that in shallow water, storm waves is the main dynamic factor resulted in the bottom erosion. Many researchers have studied the ripple formation of the sea bottom by waves for a long time. That the ripples formed and washed out results in the bottom erosion, therefore, the ripple formation is prerequisite to produce the erosion of the bottom. Researchers recognize that the ripple formation of the sea bottom is related to the ability of waves to move sediment, which in turn is governed by the Shields number, that is:

$$\psi = \frac{\tau_b}{\rho(s-1)gD} \tag{1}$$

where $\tau_b$ is the bottom friction, $\rho$ is the density of water, s is the relative density of the sediment $\rho_s/\rho(=2.65$ for quartz sands), and D is the representative grain diameter. Studies indicate that sediment motion starts when the Shields number becomes larger than its critical value which is estimated as $\psi_c=0.04\sim0.06$ For clean, well —sorted sands (Madsen and Grant 1976). For a given sea area, Shields number depends on bottom friction $\tau_b$:

$$\tau_b = 1/2\ fu^2 \tag{2}$$

where f is the friction factor, u is the near—bottom orbital velocity. Therefore, for a given sea area the near—bottom orbital velocity is only the parameter of determining Shields number. And the near—bottom orbital velocity corresponded by the critical Shields number is seen as the start velocity, the corresponding water depth is seen as the maximum depth of bottom erosion, and the sea area from this depth to the coastal line is the erosion area.

Tolman presented the Shields number expressed by wave parameters in his study on the dissipation of bottom friction for the numerical wave prediction model, which is easy to be used in practical application. The critical Shields number $\psi_c$ and the critical wave height Hc have the following relation:

$$\frac{Hc^2}{dD} = 8(s-1)\frac{1.2\psi_c}{\alpha^2 f}\frac{\sinh 2Kpd}{Kpd} \tag{3}$$

where d is the water depth, $\alpha$ is the shape factor depending on relative water depth Kpd and the spectral shape, Kp is the spectral peak wavenumber. Eq. (3) shows that in shallow water, that is, sinh Kpd=Kpd, the critical wave height is not related to the wave period; but in deep water the critical wave height is controlled by sinh function, and strongly depends on the wave period.

In this sea area, the water depth measurements of 1976 and 1993 show that during the 17 years the bottom slope, in which the water depth was relatively stable and the bottom was not eroded, kept to be $0.45\times10^{-3}$. On this slope the near—bottom orbital velocity due to waves calculated by HISWA model basically unchanged and is about 0.53cm/s～0.60cm/s, which is the maximum velocity that sediment is not eroded. Using Eq. (1), it is estimated that in this area the representive grain diameter of the sediment in the sea bottom is about 2.17mm～2.78mm with the critical values $\psi_c=0.04$ and 0.06, respectively, and friction coefficient $f=0.01$. Then using Eq. (3), the critical wave height that the bottom starts to be eroded can be calculated. Fig. 4 gives the distributions of the critical wave height and the calculated wave height related to the water depth.

Fig. 4 indicates that the significant wave heights computed by HISWA are higher than the mean values of the critical wave heights in the whole sea area. Because the critical Shields number is related to the sediment of the sea bottom, it is difficult to accurately estimate the critical Shields number. Therefore, Fig. 4 can only qualitatively show the erosion of the bottom in this area in the future. From Fig. 4 we see that the significant wave heights of 1976 were higher than that of 1993 in the shallow water area of less than 10m; the curve of the change in the significant wave height of 1993 was more close with the curve of the change in the critical wave height. This means that although the erosion of the sea bottom in this area will be continuous, the strength of the erosion will be weakened, and will be occurred in shallow water region. This conclusion is in agreement with that in section 3.

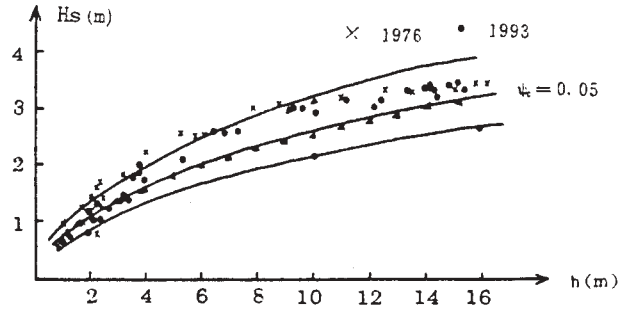


Fig. 4 the distributions of the critical wave height and the calculated wave height related to the water depth.

## 5. CONCLUSION

Based on the water depth measurements of 1976 and 1993 and typical storm wave data in a coastal area of the southern Bohai Sea, HISWA model is used to hindcast wave parameters on the two bottoms to investigate the effect of the sea floor erosion due to attack of storm waves into this sea area on wave hindcasting. The results calculated by HISWA model show that the bottom erosion due to storm waves will be weakened in the deeper water region, and strengthened in shallower water region. As a result, the coastal line will be seriously eroded and the speed of the land retreat will be increased. Bottom erosions result in strengthening of wave fields and cause the uncertainties of the design waves, which will affect seriously the estimation of the ocean engineering environment and the analysis of the operation conditions in the sea. Therefore, it is very important to predict the evolution of the sea bottom in this area in the future.

## REFERENCE

Booij, N., Holthuijsen, L. H., Ddkker, J. and Schoonbeek, R., 1988: Standard tests for the shallow water waves model hiswa. Ddlft Univ. Technol., Dep. Civ.

Eng., Group. Hydraul, Geotech. Eng., Rep. No. 6—88,42pp.

Guedes Seares C. and T. Moan, 1983: On the uncertainties to the extreme hydrody—namic loading of a cylindrical pile, reliability theory and its application, Structure & Soil Mechanics, Mantiuns Nijhoft pub., Hague, 351—364.

Grant, W. D., and O. S, Madsen: 1979: Combined wave and current interaction with a rough bottom. J. Geophys. Res. 84. 1797—1808.

Holthuijsen, L. H., N. Booij and T. H. C. Herbers 1989: A prediction Model for Stationary Short—crested Waves in Shallow water with Ambient Current. Coastal Engineering. 13. 23—54.

Liu Tehfu and Wang Chao, 1988: Design wave criteria for offshore structure, Offshore Mechanics and Arctic Engineering, 404—409.

Madsen, O. S., and W. D. Grant, 1976: Quantitative description of sediment transport by waves Proc. 15th int. Conf on Coastal Engineering, Honolulu, ASCE, 1093—1112.

Shemdin, O., K. Hasselmann, S. V. Hsiao, and K. Heterich, 1978: Nonlinear and linear bottom interaction effects in shallow water NATO conf. Ser. V. Vol. 1,347—365.

Tolman, H. L., 1994: Wind Waves and Moveable—Bed Bottom Friction. J. phys. Oceangr. 24. 5. 994—1009.

Weber, S. L., 1991 a: Eddy—viscosity and drag—law models for random ocean wave dissipation. J. Fluid Mech., 232. 73—98.

Weber, S. L., 1991 b: Bottom friction for wind sea and swell in extreme depth—limited situations. J. phys. Oceanogr., 21. 149—172.

# ACTIVITIES OF THE WISE GROUP

L.H. Holthuijsen[1] and L. Cavaleri[2]

[1]Delft University of Technology, Department of Civil Engineering, Delft, the Netherlands
[2]Istituto Studio Dinamica Grandi Masse, Venice, Italy,

## 1. INTRODUCTION

Research of waves in the deep ocean has always had a strong international coordination (at least over the last few decades). Several dozen scientists and engineers participated in joint programmes, with field observations (e.g., JONSWAP; Hasselmann et al, 1973) and with numerical models (e.g., the SWAMP group, 1985). This has resulted in a reasonable understanding of the generation of waves by wind, their dissipation by whitecapping and their nonlinear wave-wave interactions in deep water. The sum total of this knowledge has been implemented in a computer code for ocean wave forecasting by the WAM group (the WAMDI group, 1988), which can also be used in intermediate-depth water (refraction and bottom friction are included). The fully operational WAM model was finalized in 1992 and it is now implemented at a large number of institutions all over the world (Komen et al., 1994).

Research of waves in coastal regions has never known this level of international coordination. Traditionally these waves have been studied by coastal engineers who faced (a) waves in a more complex physical environment and (b) a more competitive and commercially oriented working context. Progress towards a comprehensive operational wave model was consequently much slower than in deep water. Moreover, numerical codes for waves in coastal regions tended to concentrate on one (or at best a few) of the processes that affect the waves in shallow water. Nevertheless, a small group of coastal engineers borrowed some of the basic concepts of ocean wave modelling and developed a parametric shallow water version that integrated (almost) all processes in shallow water (the HISWA model; Holthuijsen et al., 1989), which like the WAM model, has been implemented at a large number of institutions all over the world. However, the operational capability of this model is limited due to (voluntary) computer constraints. Moreover, the representation of the physical processes is rather primitive compared with the WAM model.

## 2. AIM AND METHOD

When in 1992 the WAM model was completed, several members of the WAM group turned their attention to coastal regions where of course they encountered the coastal engineers with their large diversity of wave models. In 1993 members of the WAM group and of the HISWA group and others met to jointly approach the study of Waves In Shallow water Environments (WISE). The WISE group agreed to develop (operational) wave models for coastal regions in which all relevant physical processes would be represented explicitly. Three tasks were correspondingly defined: (i) to study the physical processes affecting waves in shallow water, (ii) to develop numerical codes to represent these processes in operational models and (iii) to verify these wave models in realistic coastal conditions.

The basic formulation for the shallow-water models is relatively open in the sense that, in contrast to ocean wave models, two families of models can be used effectively in coastal regions (depending on the horizontal scale of the problem area). These are (a) phase-resolving models which are based on vertically integrated, time-dependent mass and momentum balance equations and (b) phase-averaged models, which are based on a spectral energy balance equation. The phase-resolving models require a spatial resolution that is a small fraction of the wave length. They are therefore limited to relatively small areas of the order of a few dozen wave lengths. The phase-averaged models do not require such fine resolution so that they can be used in much larger areas, the limitation being the size of the ocean basin (with the conventional resolution for ocean applications of the order of 50 - 100 km). The reason for using both models is that some processes cannot be adequately handled in one or the other. For instance, diffraction and triad wave-wave interactions can at present not or only approximately be modelled in phase-averaged models whereas wind-generation cannot be modelled in phase-resolving models with any operational feasibility. During the five-year existence of the WISE group, the role of these types of models in the group has evolved. The interest of most WISE members is aimed at the region between the deep ocean and the surf zone (it includes islands, shoals, tidal flats and estuaries; e.g., Fig. 1). This has resulted in a support-oriented role of the phase-resolving models (source of basic results) and an operationally-oriented role for the phase-averaged models (source of operational products). It must be emphasized that this evolution in the WISE group does not distract from the operational importance of the phase-resolving models in small-scale areas where they may well perform better than any phase-averaged model (in particular when diffraction is important).

The WISE group is an informal group of some 50 active members (individuals) from some 15 countries, mostly from Europe and N. America but also from Australia, Japan, S. America and the Middle East. The home institutions of these members are both public and private with a wide range of interests from applied research to daily marine operations (e.g., ministries, harbour authorities, army & navy, universities, research institutions,

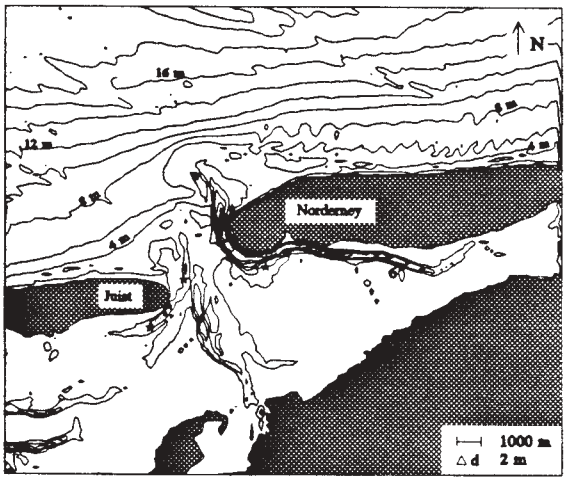


Fig. 1 An example of the type of area of interest to the WISE group: the Norderneyer Seegat (Germany)

consultants). The WISE group as a whole is coordinated by the present authors. The group meets once every year alternatively in Europe and N. America. Meetings were held in Greece (Thessaloniki, 1993), Mexico (Ensenada, 1995), Italy (Venice, 1996) and the USA (San Francisco, 1997). The next meeting shall convene in Belgium (Leuven, 1998). The WISE group has three working groups corresponding to the above three tasks. Each group communicates and coordinates common interests (e.g., joint funding, exchange of visiting scientists, computer codes and observational data).During the meetings scientific and operational progress in each group is reported in plenary meetings which are also used to discuss common interests such as large-scale joint efforts, funding opportunities and sharing of data and computer codes. The WISE meetings are organized in a very informal way, without any written report or proceedings, and with an open continuous discussion during and after the individual presentations. The latest findings are regularly shown at the meeting for constructive discussion about future steps. The WISE group as such is not funded by any agency but some (subgroups of) WISE members are funded contingent on their participation in the WISE group and their willingness to share results with other WISE members.

## 3. ACHIEVEMENTS

In task (i) most of the progress has come from the phase-resolving models, providing input for the development of the phase-averaged models. Madsen and Sørensen (1993) formulated a spectral version of the (phase-resolving) Boussinesq model which explicitly formulates the triad wave-wave interactions. In deep water these interactions can be ignored but in shallow water they often generate a secondary, high-frequency peak in the wave spectrum. This spectral Boussinesq model is phase-resolving in the sense that the phases of the wave components are an integral part of the formulation (in contrast to the random-phase assumption in phase-averaged models). But because of the spectral nature of the formulation, it allows a blending with phase-averaged model in a hybrid approach: the energy balance equation can be supplemented with a phase evolution equation. The first step in implementing this explicit formulation of triad interactions in a phase-averaged model was taken by Eldeberky and Battjes (1995). They used an approach somewhat similar to the discrete interaction approximation (DIA) of the quadruplet wave-wave interactions of Hasselmann et al. (1985) for deep water. Eldeberky and Battjes consider only self-self triad interactions in their model (the lumped triad approximation, LTA, Eldeberky, 1996) and they avoided the use of a phase-evolution equation by locally estimating the bi-phase of the wave components involved. The next step will be to fully blend the phase evolution with a spectral energy balance model. Another phase-resolving model, the mild-slope equation (Berkhoff, 1972) is the basis for an attempt to include diffraction in phase-averaged models. The essence is that diffraction modifies the conventional dispersion relationship from the linear wave theory and consequently the refraction term in phase-averaged models. Preliminary attempts are being made, but an adequate numerical formulation has not yet been developed. Progress with phase-averaged modelling in this task (i) as been mostly in depth-induced breaking. It has been observed in laboratory conditions (e.g., Battjes and Beji, 1992; Vincent et al., 1994) that depth-induced wave breaking hardly affects the shape of the wave spectrum (the changes in spectral shape are mostly due to triad wave-wave interactions). This has led to a simple spectral version of an earlier expression for the overall dissipation of waves breaking in shallow water that is based on a bore model (Battjes and Janssen, 1978; Thornton and Guza, 1983). However, the observations have been rather limited in their parameter range and the findings may be valid only for uni-modal incident spectra. Observations in the surf zone will further contribute to the understanding of this phenomenon.

In task (ii) the main progress has been achieved with new numerical codes of phase-averaged models and adaptations of the WAM code. A serious problem with the codes of phase-averaged ocean wave models such as the WAM model (but also similar third-generation models such as the WAVEWATCH model, Tolman, 1991) for applications in shallow water is that they are explicit in nature. This implies that they are subject to the Courant criterion of numerical stability: the time step in the computations is limited by the spatial resolution of the model. In open ocean applications this is usually not a problem (the spatial resolution is of the order of 100 km and the propagation time step is of the order of 15 min). For coastal applications however this is a problem because the required spatial resolution is often of the order of 100 m and the corresponding time step would be about 10 s in water of 10 m depth. This is operationally unacceptable and new ways for integrating the energy balance have to be found. One successful optimization has been to use a larger time step for integrating the physical processes than for

wave propagation (in the WAM model, Luo et al., 1997 and in the WAVEWATCH model). This permits reasonably efficient computations in realistic wave conditions down to a spatial resolution of about 1 km (in particular on vector machines, as these models vectorize well). Another attempt is being made with a hybrid scheme: piecewise propagation along rays between grid points (in the TOMAWAC model of Benoit et al., 1996). This numerical scheme is unconditionally stable but time steps larger than corresponding to the spatial resolution ignore the variations in the physical processes at that resolution. This approach is therefore still subject to the Courant criterion (for reasons of spatial resolution of the physical processes rather than numerical stability). An implicit scheme that avoids the stability problem has been developed by Booij et al. (1996) in their SWAN model. It sweeps through the computational area in four 90° quadrants thus propagating the waves in all directions. This scheme is unconditionally stable and does not suffer from the limitation of the hybrid approach. However, the present implementation is based on a first-order, upwind scheme which is rather diffusive. This seems acceptable for small-scale regions (25 km or less) but it needs to be replaced by a higher-order scheme for larger scales. It operates on arbitrarily small spatial resolution (varying from 1 km to 10 m in field conditions to 0.1 m in laboratory conditions). The SWAN model is an extension of the WAM model in the sense that it supplements the processes that are represented in the WAM model (Cycles 3 and 4 of that model) with the LTA of the triad wave-wave interactions, spectral depth-induced wave breaking and several options for bottom friction. However, vectorization has not been considered in the design of SWAN as it is aimed at relatively small computers. Like the WAM model, to all intents and purposes the SWAN model is available in the public domain (home page, http:// swan@ct.tudelft.nl).

To validate numerical wave models that are being developed, a standard test bank is under construction containing academic cases of wave propagation in deep and shallow water with and without ambient currents for which analytical solutions are available. Real field cases with detailed observations are also included. Some are fairly complex (e.g., tidal inlets), others are sufficiently simple that they can be generalized (e.g. idealized fetch-limited wave generation).

The wave models often need coupling to other models, either to be driven by models such as atmospheric and circulation models or to drive other models such as circulation models (with wave induced radiation stresses) and morphodynamic or ecological models. Also, some wave models need to be nested into other wave models to achieve high-resolution results or to shift to other physical processes (e.g. to include diffraction). Work in these aspects is being carried out at several levels in the WISE group. From a scientific point of view the effect of wind variations in coastal regions is being investigated by coupling coastal atmospheric models with coastal wave models (in particular orographic and boundary-layer effects along mountainous coastlines and behind barrier islands). The effects of tidal currents on the coastal wave climate are similarly investigated by coupling coastal wave models with tide-driven coastal circulation models. To numerically accommodate such interactions with circulation models, the TOMAWAC model is formulated on a triangular grid and the SWAN model has recently been adapted to operate on a non-orthogonal curvi-linear grid. To carry out computations from large scale to small scale, the SWAN model can be nested into the WAM model (SWAN accepts output directly from the WAM model; Luo and Flather, 1997). To pre- and post-process the input and output of such sets of models (both numerically and graphically), dedicated tools are being developed based on ARCINFO (Kaiser, 1994), ARCVIEW and MATLAB.

In task (iii) a number of fairly large field campaigns has been carried out with very useful results. A most interesting field campaign was carried out in nearly ideal shallow-water generation conditions in Lake George in Australia (e.g. Young and Verhagen, 1996). The observations of this campaign provide much needed characteristics of the wind-induced growth of waves in limited water depth. It has already served (and will continue to do so) to verify or calibrate models of the WISE group. Several other large field campaigns have been executed off fairly open coasts along the east coasts of the USA and England and along the rather convoluted coast in

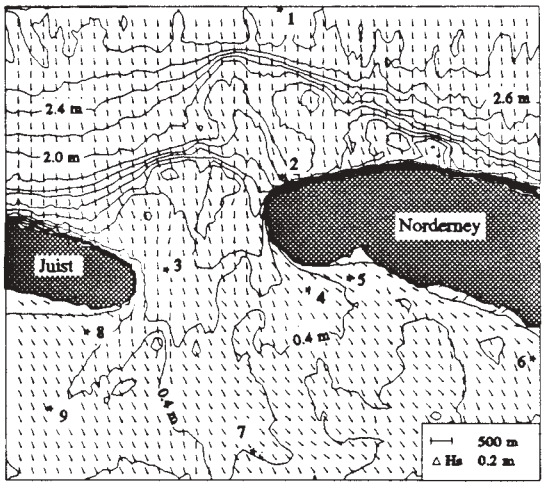


Fig. 2 Significant wave height and mean wave direction (unit vestors) computed with the SWAN model in the Norderneyer Seegat (Germany, see Fig. 1; six buoy locations indicated).

the north of the Netherlands and Germany. It is expected that the wave models of WISE members will be verified against these observations. Such verification has already been carried out for the SWAN model (Figs. 2 and 3). The rms-error of the significant wave height and mean wave period computed with SWAN in these (and other, similar) conditions was typically about 10% of the incident values (note that locally the relative error can be much larger as the local waves may be much lower).

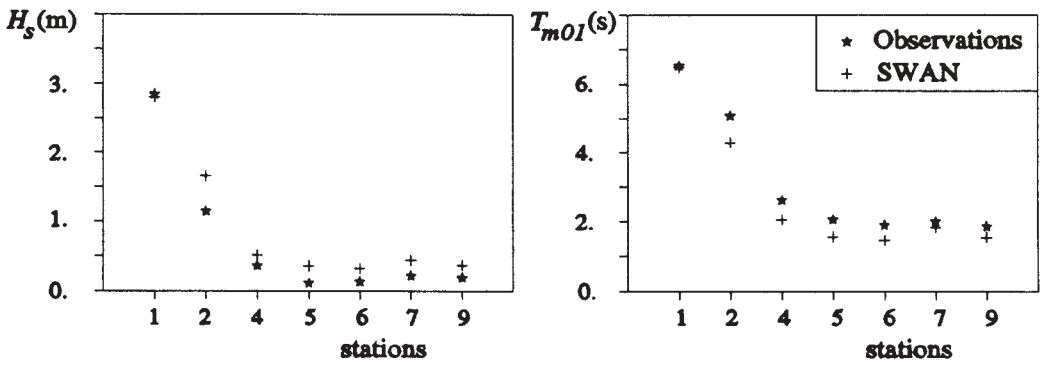


Fig. 3 The significant wave height and mean wave period in the Norderneyer Seegat (Germany, see Fig. 1) observed at the six buoy locations of Fig. 2 and computed with the SWAN model.

## 4. OUTLOOK

Although considerable progress has been made in the WISE group over the last few years, several basic aspects are still unresolved and the verification of the existing computer codes has been rather limited. Moreover, the numerical quality of the present codes pose unnecessary constraints on their operational applicability. With the present and future R&D programs of WISE members, these aspects will improve. In addition, relatively new model technology such as real-time data assimilation based on buoy and satellite observations will be introduced in the forecasting of waves in coastal regions. The outlook for these developments is optimistic because both in Europe and in the USA, funding is available to continue research and development at an increased pace. With the release of the SWAN model in the public domain, next to the WAM model, these developments can be concentrated in two widely available, supplementary computer codes.

## ACKNOWLEDGEMENTS

The achievements in the WISE group are a credit to individual members who, we hope, have benefitted from the discussions and interactions with other members. The group as a whole proceeds with its own momentum which we, as chairmen, hope to maintain with our logistical efforts.

## REFERENCES

Battjes, J.A. and J.P.F.M. Janssen, 1978: Energy loss and set-up due to breaking of random waves, *Proc. 16th Int. Conf. Coastal Engineering*, ASCE, 569- 587

Battjes, J.A. and S. Beji, 1992: Breaking waves propagating over a shoal, *Proc. 23rd Int. Conf. Coastal Engineering*, ASCE, 42-50

Benoit, M., F. Marcos and F. Becq, 1996: Development of a third-generation shallow-water wave model with unstructured spatial meshing, *Proc. 25th Int. Conf. Coastal Engineering*, ASCE, Orlando, in press

Berkhoff, J.C.W., 1972: Computation of combined refraction-diffraction, *Proc. 13th Int. Conf. Coastal Engineering*, ASCE, 471-490

Booij, N, L.H. Holthuijsen and R.C. Ris, 1996, The "SWAN" wave model for shallow water, *Proc. 25th Int. Conf. Coastal Engineering*, ASCE, Orlando, in press

Eldeberky, Y. and J.A. Battjes, 1995: Parameterization of triad interactions in wave energy models, *Proc. Coastal Dynamics Conf. '95*, Gdansk, Poland, 140-148

Eldeberky, Y., 1996: Nonlinear transformation of wave spectra in the nearshore zone, Ph.D. thesis, Delft University of Technology, Department of Civil Engineering, The Netherlands

Hasselmann, K., T.P. Barnett, E. Bouws, H. Carlson, D.E. Cartwright, K. Enke, J.A. Ewing, H. Gienapp, D.E. Hasselmann, P. Kruseman, A. Meerburg, P. Müller, D.J. Olbers, K. Richter, W. Sell and H. Walden, 1973: Measurements of wind-wave growth and swell decay during the Joint North Sea Wave Project (JONSWAP), *Dtsch. Hydrogr. Z. Suppl.*, **12**, A8

Hasselmann, S., K. Hasselmann, J.H. Allender and T.P. Barnett, 1985: Computations and parameterizations of the linear energy transfer in a gravity wave spectrum. Part II: Parameterizations of the nonlinear transfer for application in wave models, *J. Phys. Oceanogr.*, **15**, 11, 1378-1391

Holthuijsen, L.H., Booij, N. and T.H.C. Herbers, 1989: A prediction model for stationary, short-crested waves in shallow water with ambient currents, *Coastal Engineering*, **13**, 23-54

Kaiser, R., W. Liebig and H.D. Niemeyer, 1994: Mutual benefits of combined mathematical wave model and geographic information system application, *Proc. Int. Conf. Hydrodyn. '94*, Wuxi (China), China Ocean Press

Komen, G.J., Cavaleri, L., Donelan, M., Hasselmann, K., Hasselmann, S. and P.A.E.M. Janssen, 1994: *Dynamics and Modelling of Ocean Waves*, Cambridge University Press, 532 p.

Luo, W. and R. Flather, 1997: Nesting a nearshore wave model (SWAN) into an ocean wave model (WAM) with application to the southern North Sea, in: *Computer Modelling of Seas and Coastal Regions III*, J.R. Acinas

and C.A. Brebbia (eds.), Computational Mechanics Publications, 253-264.

Luo, W., R. Flather and J. Monbaliu, 1997: An efficient computational scheme for the use of the third-generation WAM model in coastal regions, *J. Waterway, Port, Coastal and Ocean Engineering*, in press

Madsen, P.A. and O.R. Sørensen, 1993: Bound waves and triad interactions in shallow water, *Ocean Engineering*, **20**, 4, 359-388

SWAMP group, 1985: *Ocean wave modelling*, Plenum Press, New York and London

Thornton, E.B. and R.T. Guza, 1983: Transformation of wave height distribution, *J. Geophys. Res.*, **88**, C10, 5925-5938

Tolman, H.L., 1991: A third-generation model for wind waves on slowly varying, unsteady and inhomogeneous depths and currents, *J. Phys. Oceanogr.*, **21**, 6, 782-797

Vincent, C.L., J.M. Smith and J. Davis, 1994: Parameterization of wave breaking in models, *Proc. of Int. Symp.: Waves - Physical and Numerical Modelling*, Univ. of British Columbia, Vancouver, Canada, M. Isaacson and M. Quick (Eds.), Vol. II, 753-762

WAMDI group, 1988: The WAM model - a third generation ocean wave prediction model, *J. Phys. Oceanogr.*, **18**, 1775-1810

Young, I.R. and L.A. Verhagen, 1996: The growth of fetch limited waves in water of finite depth. Part 1: Total energy and peak frequency, *Coastal Engineering*, **29**, 47-783

# WINTER CONDITIONS OF THE WAVE ACTIVITY AT RIO DE JANEIRO SIMULATED BY NUMERICAL WAVE MODELS

**[1]Valdir Innocentini and [2]Ernesto dos Santos Caetano Neto**

[1]Instituto Nacional de Pesquisas Espaciais
Sao Jose dos Campos, Brazil

[2]Instituto de Pesquisas Meteorologicas - UNESP
Bauru, Brazil

## ABSTRACT

During the South Hemisphere winter, oceanic waves in the South Atlantic are predominantly determined by cyclones originated from westerly baroclinic disturbances. They develop in the east side of Andes Cordillera, and intensify over the sea. Usually they displace southeastwards, producing high waves which are detected at coast of Rio de Janeiro(RJ) as swell. Rarely the cyclones travel eastwards. When this happens, intense wind-sea are produced, responsible for very high waves and damages at RJ.

In this research two wave models are used to hindcast the wave activity provoked by two cases of intense cyclones. The distinction between the cases is the cyclone displacement, important characteristic as pointed out. The wave models are a 2nd and a 3rd generation models. The former is used with two different features concerning the nonlinear parametrization; (1) with a rapid migration of energy in response to sudden wind variation, and (2) with a gradative migration of energy. The later is the WAM model with the migration of energy according to its nonlinear interaction parametrization. The great occurrence of cyclones and generation of swell during the winter in South Atlantic demonstrates the necessity of an appropriated initialization of wave models in the forecasing of sea conditions.

A careful analysis on the results produced by the 3 numerical models reveals a notable difference on the feature of the swell produced near RJ in the case of southeastwards cyclone, which is stronger in the WAM simulation.

# ESTIMATION OF THE EXTREME HEIGHTS OF WIND WAVES IN THE COASTAL SEA AREA

Dr. I.V. Lavrenov,
V.N. Bokov, V.I. Dymov, T.A. Pasechnik, N.P.Yakovleva
Arctic and Antarctic Research Institute State Scientific Center of the Russian Federation

Prof. I.N. Davidan
State Oceanography Institute St.Petersburg Department

## INTRODUCTION

Wind waves regime in the shelf areas, as a rule, has not been adequately studied because there are no in fact long-term foolproof observations, which could be used to calculate regime of extreme values. Estimations of wind waves elements, which are in different manuals, are rather non-uniqueness. Usually they are based on visual data observations carried out by ships crow during the navigation period (Wind and waves in oceans and seas, 1974; Davidan et al, 1985). There are not enough to have only visual estimations in order to estimate wind waves regime more reliably. It is connected with low quality and wide spatial nonhomogeneity of the wind waves field in the coastal shallow-water sea regions.

That is why method based on numerical modeling results would be appropriate for restoring the unavailable data. Let us see the example of such calculation for the Pechora Sea.

Pechora Sea is located within the south-eastern Barents Sea area, which is the most stormy area in Russia. Waves in the Barents Sea of the 8 m height and more can be repetitive in winter up to 3 percent, in summer - 0.1-0.2 percent. Wave heights intensity decreases from west to east. Extreme waves characteristics decrease moving in the direction from west toward east by 20-30 percent accordingly. These properties of the spatial waves distribution are of special features of the atmospheric circulation over the sea and properties of waves formation conditions (Wind and waves in oceans and seas, 1974; Hydrometeorological conditions of a shelf zone of USSR seas, 1985; Davidan et al, 1985; «USSR seas», 1990)

Wind waves and swell can penetrate to the Pechora Sea water area not only from the Barents Sea, but also from Norwegian and Greenland seas and the northern water areas of the Atlantic Ocean as well. It is necessary to take into consideration the sea ice cover, which can change the size of the water area open part, in order to estimate the waves regime of the Barents Sea water area and, to a greater extent, of the Pechora Sea. Local waves development in the Pechora Sea is essentially limited by region depth and distance from the nearest coasts. Waves intensity in all areas of the Pechora Sea is less than in the other parts of Barents Sea water area. Pechora Sea is open for waves appearance from central and southern part of the Barents Sea only from western and north-western directions. Over all points waves are defined by speed and duration period of local winds, depth and distance from the lee coast side.

## 1. WIND WAVE MODEL DESCRIPTION

FORMULATION PROBLEM. The evolution of two-dimentional spectrum $S(\vec{k},\vec{r},t)$ with respect to wave vector $\vec{k} = \{k_x, k_y\}$, as a fuction of horizontal vector $\vec{r} = \{x, y\}$ and time $t$ is governed by the equation (Davidan et al., 1985; Davidan et al 1988; Komen.et al 1994; Ocean wave modeling, 1985):

$$\frac{d\,S(\vec{k},\vec{r},t)}{d\,t} = \frac{\partial\,S}{\partial\,t} + \frac{\partial S}{\partial \vec{k}}\frac{d\,\vec{k}}{d\,t} + \frac{\partial S}{\partial \vec{r}}\frac{d\,\vec{r}}{d\,t} = G \qquad (1)$$

where $G$ - is source function describing physical mechanisms forming the wind waves spectrum.

$G$ - is function we will write as a sum of three terms $G = G_{in} + G_{nl} + G_{ds}$, where $G_{in}$ - energy input from wind to waves, $G_{ds}$ - dissipation of wave energy, $G_{nl}$ non-linear interaction in wind waves spectrum.

One can consider that dissipation of wave energy $G_{ds}$ is interpreted by two terms as follows: bottom friction $G_{ds}^{(1)}$ and crest wave breaking $G_{ds}^{(2)}$ in shallow water of surf zone.

As dissipation of wave energy function connected with bottom friction the recommendations of (Komen et al 1994) work are used.

$$G_{ds}^{(1)} = -\gamma \frac{k\,S}{g\,sh(2kH)} \qquad (2)$$

where $\gamma = 0.076\,m^2c^{-3}$. $G_{ds}^{(2)}$ will be defined later is parametric form.

Characteristics for equation (1) are the following proportions describing wave packets propagation in water with uneven bottom.

$$\frac{d\vec{r}}{dt} = \frac{\partial\omega}{\partial\vec{k}}, \qquad \frac{d\vec{k}}{dt} = -\frac{\partial\omega}{\partial\vec{r}} \qquad (3)$$

where $\omega = \sqrt{gk\,th(kH)}$, $H$ - depth.

Calculation task of waves spectrum is to solve a set of equations (1) - (3) with corresponding specified border and initial conditions. Initial data to solve the problem is wind field $\vec{u}(x, y, t)$ and depths field H(x, y).

To perform the model numerically let us pass from wave vectors spectrum $S(\vec{k}, \vec{r}, t)$ to wave numbers and angels spectrum $S(k, \beta, x, y, t)$ (where $k = |\vec{k}|$, $\beta = arctg(k_y/k_x)$).

Describing total time derivative in the left part of equation (1), let us pass to the following equation:

$$\frac{\partial S}{\partial t} + C_{gx}\frac{\partial S}{\partial x} + C_{gy}\frac{\partial S}{\partial y} = G - \frac{\partial S}{\partial k}\frac{dk}{dt} - \frac{\partial S}{\partial \beta}\frac{d\beta}{dt} \qquad (4)$$

where $C_{gx} = \frac{dx}{dt}$ and $C_{gy} = \frac{dy}{dt}$ - projection of group speed $C_g = \frac{d\omega}{dk} = \frac{1}{2}\frac{\omega}{k}\left(1 + \frac{2kH}{sh(2kH)}\right)$

The equation describing wave number and angle changing (3) can be written in the following form:

$$\frac{dk}{dt} = -\frac{\partial\omega}{\partial H}\frac{\partial H}{\partial x}\cos\beta - \frac{\partial\omega}{\partial H}\frac{\partial H}{\partial y}\sin\beta \qquad (5)$$

$$\frac{d\beta}{dt} = \frac{1}{k}\frac{\partial\omega}{\partial H}\frac{\partial H}{\partial x}\sin\beta - \frac{1}{k}\frac{\partial\omega}{\partial H}\frac{\partial H}{\partial y}\cos\beta \qquad (6)$$

## EQUATIONS FOR WIND WAVES SPECTRUM PARAMETERS

Parametric method of wave calculation consists of going from equation of energy spectral density (1) to equations of spectrum parameters (Davidan, 1988; Ocean wave modeling, 1985)

Parametric methods became traditional for wave calculation in deep water. Usage of these methods makes it possible to decrease significantly the calculations and to make up the deficiency of knowledge of physical mechanisms, forming the wind waves spectrum, through using of empirical proportions. Parametric models are based on hypotheses of obtaining stable form of wind waves spectrum being controlled by non-linear waves interactions.

Concerning wave development in the basin of final depth the same idea can be used there. According to experimental data (Bouws. et al, 1987) there is an invariance of spatial wind waves spectrums (in 'k' -space) in shallow-water basin. In addition, the authors of this work made a conclusion that bottom friction does not have an influence on form of wind waves spectrum. Bottom friction, of course, produces wave energy dissipation, but with wind activity its combination with the other mechanisms brings spectrum to its invariant form. Bottom friction may prevail if wind speed become lower the value, which generated the main energy, and during swell propagation.

The deduction of an equations for spectrum parameters is based on the usage of spectral equation (1). Deduction procedure does not differ from that proposed in works for deep water (Davidan et al, 1988; Theoretical bases and calculation methods of wind waves, 1988), but for shallow-water basin it should be used not frequency and angle spectrum but wave numbers $k$ and directions $\beta$ spectrum. It is a function of wave process dispersion $m_o$, wave number $k_{max}$ of spectrum maximum wave process dispersion (which can be in terms of $k_{max} = k_{max}(m_o)$ (Problems of investigation and math modeling of wind waves, 1995) and main direction of the $\bar{\beta}$ wave propagation. These parameters depend on spatial co-ordinates $\{x, y\}$ and time $t$. By this means the proportion between spectrum and arguments may be shown as $S = S(m_0(x, y, t), \bar{\beta}(x, y, t), k, \beta)$. Spectrum function can be divided, and it may be written as a product of wave numbers spectrum by angle distribution function: $S = S(m_0, k)\,Q(m_0, \bar{\beta}, k, \beta)$.

As a result of action of specially selected integral operators on equation of wave energy balance (1) one can get a set of non-linear differential equations for spectrum parameters as follows: equal to zero moment $m_o$ and main wave

propagation direction $\bar{\beta}$. Equation set for spectrum parameters is written as:

$$\frac{\partial m_0}{\partial t}+C_m\cos\bar{\beta}\frac{\partial m_0}{\partial x}+C_m\sin\bar{\beta}\frac{\partial m_0}{\partial y}-D_m\sin\bar{\beta}\frac{\partial\bar{\beta}}{\partial x}+D_m\cos\bar{\beta}\frac{\partial\bar{\beta}}{\partial y}=$$
$$=G_m^u\cos(\bar{\beta}-\beta_U)+G_m^{ref}+G_m^{ds}$$
$$\frac{\partial\bar{\beta}}{\partial t}+D_\beta\cos\bar{\beta}\frac{\partial\bar{\beta}}{\partial x}+D_\beta\sin\bar{\beta}\frac{\partial\bar{\beta}}{\partial y}-C_\beta\sin\bar{\beta}\frac{\partial m_0}{\partial x}+C_\beta\cos\bar{\beta}\frac{\partial m_0}{\partial y}$$
$$=G_\beta^u\sin(\bar{\beta}-\beta_U)+G_\beta^{ref} \qquad (7)$$

where $\beta_u$ - wind direction; $C_m, D_m, C_\beta, D_\beta$ - functional coefficients estimated by two-dimensional spectrum form; $G_m^u$ - generalized function of of wave energy generation by wind; $G_m^{ref}$ - effect function of refraction to wave energy; $G_m^{ds}$ - wave energy dissipation; $G_\beta^u$ - function of changing of the main direction of wave propagation as a result of wind direction changes $G_\beta^{ref}$ - function of the refraction influence to changing of wave distribution direction. Coefficients and functions described hereabove are the integral expressions from two-dimensional spectrums approximation and corresponding source function components shown in equation (4). Explicit values of coefficients and functions were described in (Lavrenov 1997) work. As a result of model calibration it appeared the possibility to get correspondence of calculation results and adopted manuals (Shore Protection Manual, 1984) and the results of (Davidan.,et al, 1988; Bouws.,et al 1987; Komen.,et al 1994) known works.

One should point some new details of the parametric equations set (7). This set is an extension of our earliest version for deep water conditions, which was used by us in spectral parametric model of wind waves (Davidan., et al 1988; Theoretical bases and calculation methods of wind waves, 1988). This model was tested in details on instrumental observations data during specialized expeditions of St.Petersburg Department of State Oceanography Institute at Black, Baltic, Barenz and others seas. Newness of the new version is in two aspects. First is connected with generalization of the model in case of final depth and with the wave refraction. In this case it was made the transfer from frequency-angle spectrum to spectrum of wave numbers and directions, in which the empirical relationship between zeroth moment $m_0$ and wave number of spectral maximum $k_{max}$ according to experiment data (Problems of investigation and math modeling of wind waves, 1995):

$$\tilde{m}_0 = 2.0\cdot 10^{-3}\,\tilde{k}_{max}^{-1.47}\ , \qquad (8)$$

where $\tilde{m}_0=\frac{g^2 m_0}{u_{10}^4}$, $\tilde{k}_{max}=\frac{k_{max}u_{10}^2}{g}$, $u_{10}$ - wind speed value at 10 m level.

Proportion (8) is valid both for waves in deep water and for shallow-water coastal water areas as well. One should point out that the feasibility condition of (8) is valid up to the depth $H_\omega = H\frac{\omega^2_{max}(k_{max})}{g}=0.16$.

Second correction of the model is connected with going from normalization on wind speed on 10-meters horizon to normalization on dynamic speed. One should point out that normalization on dynamic speed makes empirical proportions to be the most universal and makes it possible to use them for wave parameters calculation at large wind speeds and to forecast the most dangerous waves in more qualitative way (Lavrenov et al, 1996; Problems of investigation and math modelling of wind waves, 1995). In the model the following relation between waves development stage and sea roughness $Z$ is assumed:

$$Z^* = 0.4\,\omega^*(k^*_{max}) \qquad (9)$$

where * - normalization on dynamic speed $u_*$.

Proportion (9) was proposed by Davidan (Problems of investigation and math modelling of wind waves, 1995). It shows the decreasing sea roughness, which appear as waves develop. The substitution the expression (9) to a formula for logarithmic profile makes it possible to estimate the relation between resistance coefficient $C_d=\sqrt{u_*/u_{10}}$ and wave stage $\tilde{\omega}_{max}=\omega_{max}u_{10}/g$:

$$\ln C_d + 0.267/\sqrt{C_d} = 3.67 - 0.667\ln(\tilde{\omega}_{max}) - 1.333\ln(u_{10}) \qquad (10)$$

Spectral-parametric model with taking into account dynamic speed of wind waves except equations for wind waves spectrum parameters consists of sub-program for simulation swell refraction and propagation. Swell transformation is calculated in spectral form as a result of numerical solving of initial equation (1), in which wave refraction and bottom friction effect are being taken into consideration, but energy supply of waves by wind is overlooked. In this case the equations for (3) or (5)-(6) rays are solved by method of

characteristics with going to spherical variables. For numerical solving of spectral equation of total wave energy the semi-Lagrangian method (Lavrenov, 1997) is being used.

In spite of existence model of third generation (Komen et al, 1994), which have more fundamental physical background we will use Spectral-Parametric model which used normalization on Dynamic speed (SPD model). This model is based on reliable experimental data and can give enough good results by using much smaller CPU time.

## 2. CALCULATION AREA, NUMERICAL GRIDS

Let us make the numerical simulations of the wind waves elements in the south-eastern area of the Pechora Sea in the point with 19 meters depth, which is being measured relative to the min theoretical level (MTL). As it is shown earlier, the sea waves regime in water sea area is being formed by the local wind action and also as a result of penetrating of wind waves and swell from water area of the Barents Sea. Wave formation conditions and scales of changes of modeling wind wave fields in that and another case differ very much. In this instance it is better to use different approach for wave elements calculation in these two cases.

We will use the SPD model for deep water conditions in water area of the Norway, Greenland and Barents Seas. As we will be interested in extreme values of waves heights, as it was pointed out hereabove, using of this model, in which the normalization on dynamic speed is used, it makes possible to estimate waves parameters in storm conditions more exactly.

One will take the calculated area in rectangle form on the spherical surface, western boundary of which is coincident with 20° W, eastern - 61°E, southern - 60°N, northern -80°N (see Fig.1).

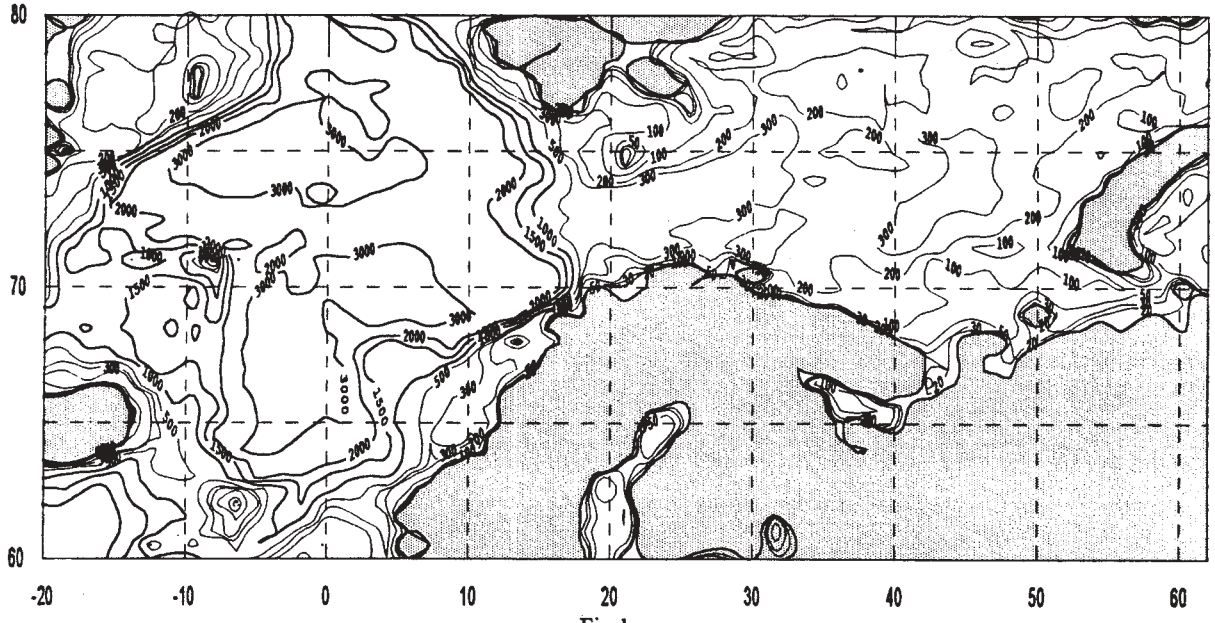


Fig.1

General chart of water area depths of waves calculation

In this calculated area the grid with 1.5 degree step along longitude and 0.5 degree along latitude had been used. For 70° latitude, on which the interested calculated point is located, it makes the same distance between two neighbor points equal 55 km Land regions and regions covered by ice are excluded from calculating area.

To perform the wave calculation in the Pechora Sea water area more fine resolution grid with a step of 0.75° along longitude and 0.25° along latitude (see Fig. 2). To take into consideration the wave transformation on shallow water in SPD model the detail depth information was used.

The problem solutions boundary of two models scales was «laced» along 52 meridian E.

## 3. INITIAL DATA FOR NUMERICAL SIMULATION.

Data of surface atmospheric pressure in the main synoptic terms within the period from 1960 through 1994 were used as a data base to perform



AUTHOR INDEX TABLE OF CONTENTS

the calculations of wind wave parameters. In total atmospheric pressure fields in 24158 synoptic terms over Norway, Greenland and Barents Seas water areas in without ice annual period (June-November). were used in calculations

It is necessary to take into consideration ice cover, which can change essentially size of open water sea area and correspondingly number of computed points. The location of ice cover edge was taken in correspondence with mean monthly means on long-standing data (Zubakin, 1987). It is worthy of note that in the first half of December there is a probability of ice cover lack in north-western Pechora Sea, which in combination with ice free sea surface in given point, is 25 percent. In some extreme storms and calculations in November-December ice edge was taken in correspondence with real data. It has been possible to point out only three strong storms in December with a height more than 6 meters used in calculations during performance of joint analysis of synoptic maps and maps of ice conditions.

One of the main factors in wind wave field formation in the Pechora Sea is bathymetry . To perform the numerical calculations the factual depth values ( in correspondence with that of min theoretic

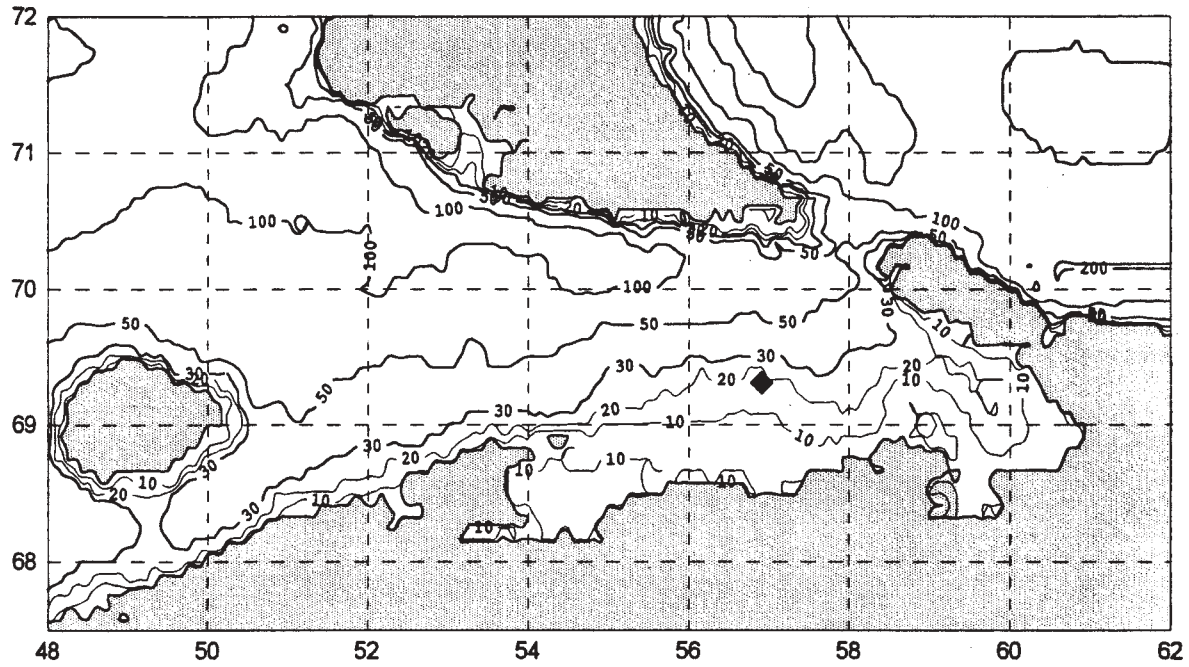


Fig. 2
Depths chart of the Pechora Sea

level - MTL) from navigation map were taken there, using which the regular calculation depth grid was developed. In this case the total correspondence restored depth with its factual mean in calculated point was developed. Total calculated area with isobaths, restored by interpolation to numerical values, is shown on Fig. 1. Calculated area for the Pechora Sea is shown in more details on Fig. 2.

Sea level, which can change the basin effective depth and in that way effect to waves, is an additional factor, which specify wave height in water area. Level oscillations relatively MTL, which specify depth showed on the map, can significantly change through two components as follows: astronomical tides and stormy surges. Wave parameters calculations in water area of the Pechora Sea are to be performed in extreme situations when wave height may be max. That is why in correspondence with estimations of max level changing, its increasing through tide and surge relatively MTL was taken equal 2.6 meters for western and north-western wind directions. For other cases level parameter was taken in correspondence with mean long-standing value (+0.45 m).

## 4. MODEL VERIFICATION BY NATURAL OBSERVATION IN PECHORA SEA.

In spite of model verification, described hereabove, one should remind that wave formation conditions in the Pechora Sea water area have some

specific features described in the beginning of the paragraph. In this case to perform the wind waves calculations in the Pechora Sea water area there appears the question about the model practicality. That is why it will be more convenient to point out the model calculation results and compare them with on location observation data carried out during one of the storms in the interested by us water area region.

In June 1984 in water area of south-eastern Barents Sea the special expedition investigations by St.Petersburg Department of State Oceanography Institute fellows on «*ROMBAK*» ship were carried out there. Instrumental wind and wave measurements were performed there. Sea wave was measured by GM-16M wavemeter. It is necessary to point out that wind and wave measurements were performed in water area located near the interested by us region in the Pechora Sea.

During work of the ship in given point (63°30' N - 53°08' E) within July 16-17, 1984 the conditions for storm wave development appeared there. Wind increasing was defined by increasing of atmospheric gradient between cyclone over gulf of Onega and anticyclone located to east from Novaya Zemlya. Wind direction within all storm period was defined by east direction with progressive changing from 130° to 70°. Max wave development was observed nightlong July 17.

For this case the comparison of calculated and measured wave heights means was performed. Comparison results are shown on Fig. 3. As it is

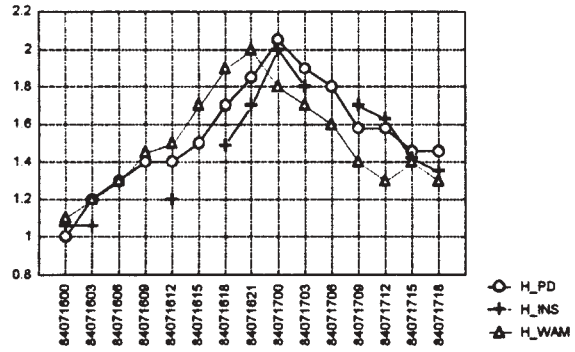


Fig. 3
Comparison of calculated by SPD (H_PD) model WAM (H_WAM) model and (H_INS) measured mean waves heights for the period 16-17.07.1984 (horizontal axes shows the synoptic term)

shown on Fig. 3 our calculation results correspond to waves height means. Mean error of calculations is $\Delta h$=0.139 m only, correlation coefficient between calculated and measured waves height means is r=0.95.

Comparison calculation results by SPD model and WAM model show their close correspondence with measuring data. But it is necessary to point out that WAM model gives more fast wave height increasing as it is follows from our model calculation and measuring data.

## 5. CALCULATION RESULTS OF WIND WAVES ELEMENTS.

Calculations of sea surface wind and waves were performed by using surface atmospheric pressure data in water area (see Fig. 1), where wind wave and swell may have influence on wave climate formation in the Pechora Sea region. So the continued wind wave calculations with duration period of 34 years has been carried out. In total 24158 means of wind wave elements in each point of computed area were calculated there.

Mean wave height gave opportunity to produce max. heights (0.1 percent probability) in correspondence with recommendations (Gluhovskiy, 1966). According calculations results cases were pointed out, when $h_{0,1\%}$ waves height is not less 8 meters in our interested region. In total within this

Table 1.
Max waves heights distribution in a calculated point.

| Sample ranges of waves heights (m) | Number of events | Probability (%) | 100%- Cum. probability |
|---|---|---|---|
| 0.00<h<0.50 | 49 | .20283 | 99.79717 |
| 0.50<h<1.00 | 2404 | 9.95115 | 89.84601 |
| 1.00<h<1.50 | 7619 | 31.53821 | 58.30781 |
| 1.50<h<2.00 | 5497 | 22.75437 | 35.55344 |
| 2.00<h<2.50 | 3465 | 14.34307 | 21.21037 |
| 2.50<h<3.00 | 2067 | 8.55617 | 12.65419 |
| 3.00<h<3.50 | 1240 | 5.13288 | 7.52132 |
| 3.50<h<4.00 | 724 | 2.99694 | 4.52438 |
| 4.00<h<4.50 | 455 | 1.88343 | 2.64095 |
| 4.50<h<5.00 | 270 | 1.11764 | 1.52330 |
| 5.00<h<5.50 | 158 | .65403 | .86928 |
| 5.50<h<6.00 | 98 | .40566 | .46361 |
| 6.00<h<6.50 | 59 | .24423 | .21939 |
| 6.50<h<7.00 | 24 | .09935 | .12004 |
| 7.00<h<7.50 | 18 | .07451 | .04553 |
| 7.50<h<8.00 | 6 | .02484 | .02070 |
| 8.00<h<8.50 | 2 | .00828 | .01242 |
| 8.50<h<9.00 | 1 | .00414 | .00828 |
| 9.00<h<9.50 | 2 | .00828 | .00000 |

period there were 5 such cases, when wave height in the calculated point increased given value. Distribution function means by range (in a half of one meter) in the calculated point are shown in Table 1. One of the strongest storms was that of October 28-29, 1973, when wave height in calculated point appeared as $h_{0,1\%}$=9.3 m. Taking into consideration the importance of this storm let us describe it.

Synoptic fields in 12 hours for each day of this storm are shown on Fig. 4a, b. As it is shown on

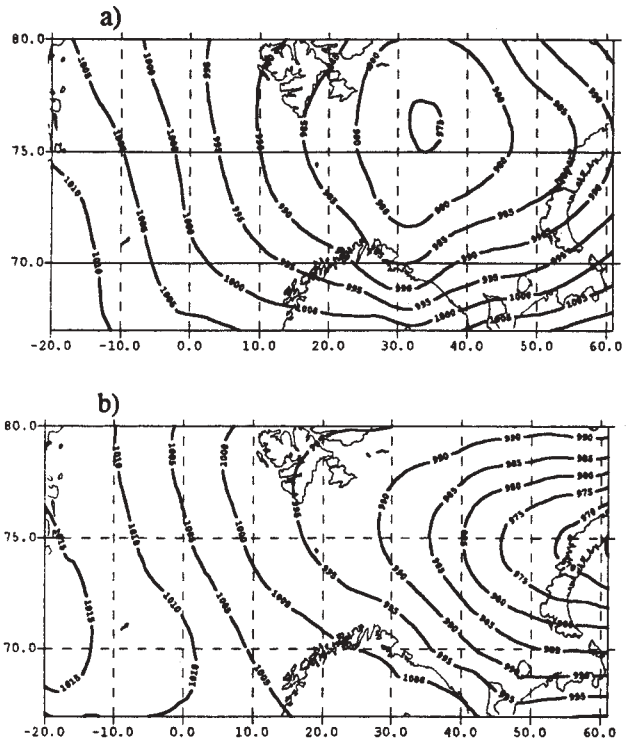


Fig. 4

Surface atmospheric pressure on 12 hours in the storm of October 28, 1973 (a) and October 29, 1973 (b)

Fig 4a, on October 28 the cyclone center (with pressure less than 980mbar) was in the center of the Barents Sea in the 75° latitude. Forward cyclone part was over given point. Wind speed with its direction about 240° reached 15.0 m/c. At that time near the coasts of the Kola Peninsula wind speed reached 20.0 m/c. In 6 hours pressure in the cyclone center decreased up to more than by 5 mbar, warm cyclone section has been over the given point yet. With its direction of 270° wind speed reached 17.5 m/c. At that time near the coasts of the Kola Peninsula wind speed reached 27.5 m/c, and at *Kanin Nos* Hydrometeorological Station it reached the value of 25 m/c. Further the cycle center moved to east in 75° latitude, and over the Pechora Sea (October 29) wind speed and its direction depended upon backward cyclone part (Fig. 4b). Wind speed in the region reached 22 m/c (00 hours GMT, October 29) with the 280° direction. It was observed the progressive wind speed decaying and storm amplifying.

With the purpose to estimate certainly waves heights in storm the calculations were performed not only on the SPD wind wave model, but on the WAM model. Calculation results of the mean wave height fields in the max time of storm increasing (by 03 and 09 hours) are shown on Fig. 5a, b for the SPD model,

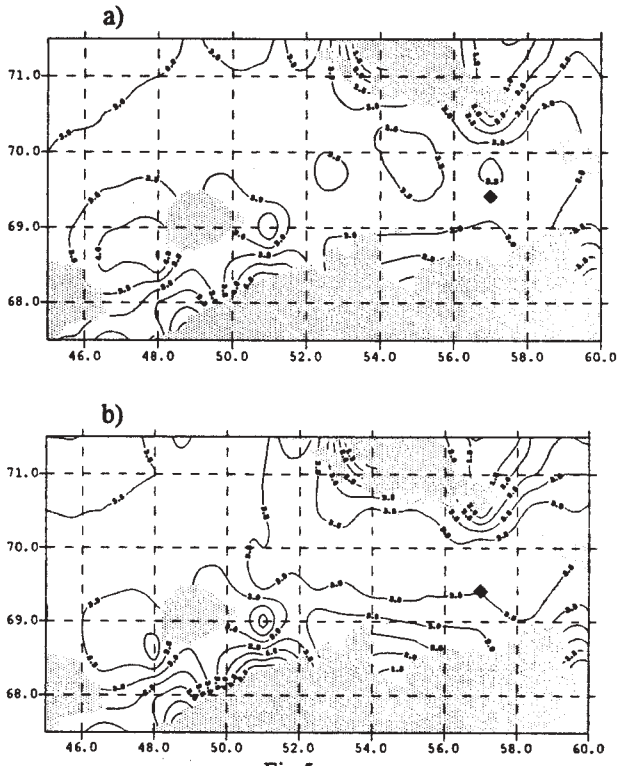


Fig.5

Mean wave heights by PD model in the storm of October 29, 1973 on 03 hours (a), on 09 hours (b)

and for WAM model - on Fig. 6a, b. As it is follows from the comparison of the calculation results the spatial distribution of wave fields is approximately the same on the both models. But, if for the WAM model the max wave means are observed in 03 hours, so on SPD model - in 09 hours. It means that wave development in WAM model is faster in time that on our model, that has been considered because of these empirical proportions, which were given in the models.

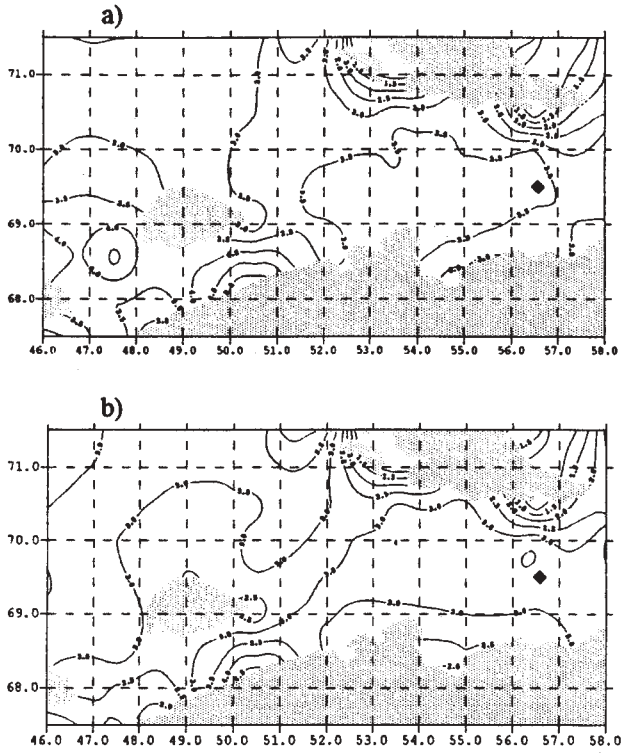


Fig. 6
Mean wave heights by WAM (cycl 4) model in the storm of October 29, 1973 on 03 hours (a), on 09 hours (b).

## 6. ESTIMATIONS OF THE EXTREME VALUES OF WIND WAVES ELEMENTS.

Waves calculation in the shallow point was performed in two stages. It is so because multiannual wave distribution proportions in shallow water contrary to deep water has not been practically investigated. It is impossible to calculate heights of waves beforehand, which can appear over the period limits, that is the initial temporal data set, received during observations or by calculation on pressure fields, if one does not know the multiannual wave distribution function with different proportion between wave height and place depth.

Because of that at first wave heights and wave periods were calculated on the math model in 35 years in deep and shallow water, and then waves were calculated beforehand, which can appear once in 50 and 100 years in this place.

Three methods (Davidan et al 1985) that are often used to estimate heights of waves, which appear once in so much years. Two of them are possible to use in the case when there are temporal sets of multiannual wave observations or multiannual continued wave calculations by barometric fields of atmospheric pressure. Third method is been used when there is no possibility to get multiannual continued wave sets and instead them waves are calculated in limited (more or less) storm situations. In this case one may do some assumptions of function of storm number distribution in time.

In our case there were reasonably large 35-year temporal sets of wave calculations, and that is why two first methods to estimate waves, which may appear once in 20, 50 and 100 years, were used there. The first is considered to estimate wave heights by parameters of asymptotic lognormal distribution with all calculated initial data in navigation period, the second - to estimate extreme wave heights on annual maximum waves using asymptotic Gumbel distribution. This method to estimate extreme waves is based on multiannual investigation results carried out in our country and abroad (Gumbel, 1965; Davidan et al, 1985; Matushevskiy, 1985; Building standards and rules, 1983).

Estimation of wave heights by lognormal distribution parameters was performed in the following way. Wave distribution data in the nearest deep water point with $\varphi$ = 70° 00 and $\lambda$ = 54° 00 coordinates, where depth is equal 100m (H=100 m) were chosen for the calculation. Function means of mean wave heights distribution by model calculations data during navigation period in 35 years from 1960 to 1994 by sample including data in 24158 terms are shown on Fig 7 on function grid

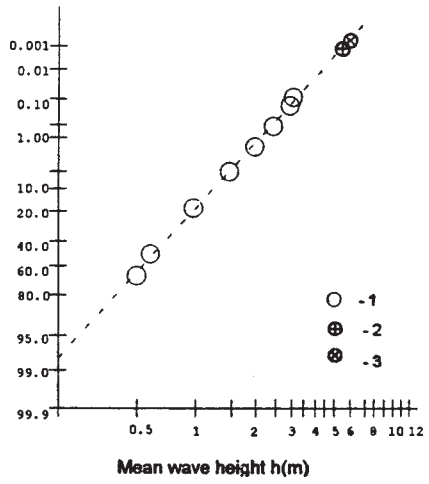


Fig. 7
Distribution function of mean wave heights in the 70° S, 54° E (H=100 m) point during June-November navigation period, 1- according to calculations within the period from 1960 through 1994; 2- mean height value of waves appearing once in 50 years (5.3 m); 3- mean height value of waves appearing once in 100 years (5.8 m);

of lognormal distribution. Calculation results are pointed by circles.

Dotted line corresponds to lognormal distribution with $h_{0,5}$=0.6 and s=1.85 parameters

$$F(h) = (s/\sqrt{2\pi})\int_{\tilde{h}}^{\infty}(1/\tilde{h})\exp\left[(-1/2)\ln^2(\tilde{h})'\right]d\tilde{h} \quad (11)$$

where, $h_{0.5}$ - median mean in multiannual distribution of mean wave heights in synoptic terms; $s=ln(h)/\sigma$ - standard deviations of their logarithms.

As it is shown on Fig. 7 calculated data are well corresponded with lognormal distribution function. It allows to use this distribution to estimate maximum height means of waves, which may appear in given point in deep water in one of synoptic terms in particular years amount.

Maximum height means of waves appearing once in 50 and 100 years calculated according to the (11) proportion are shown on Fig.7 by circles with cross lines. In the first case the mean height became equal 5.3 m, in second - 5.8 m.

On Fig.8 the calculated means of wave heights for autumn (September-October) are compared with the extension results of passing ship

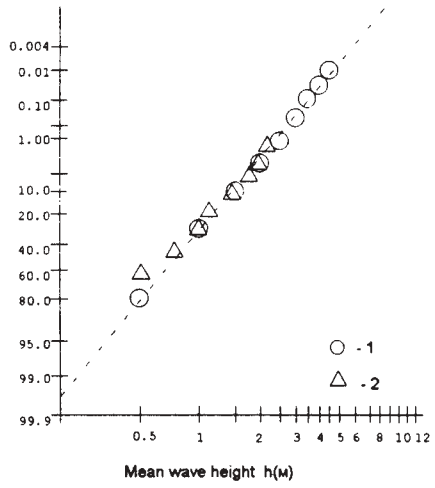


Fig. 8
Distribution function of mean wave heights in the 70° N, 54 W(H=100 m) point in navigation season (September-November) 1- by calculations within the period from 1960 through 1994; 2- by ship observation data.

observations. Distribution function means of mean wave heights by calculated data are shown by circles, lognormal distribution with $h_{0,5}$=0.74 and s=1.82 parameters is shown by dotted line, that shown by triangle - function distribution means by visual observation data in square close to a center where pointed out hereabove point is being located. Good agreement of calculated and observation data reinforces the assurance of performed calculations. Concerning waves that are with mean height less than 1 m, it must be taken into consideration that accuracy of visual estimations of weak waves is small.

Data of wave heights appearing once in 50 and 100 years, mentioned above, fall into the June-November period. In some cases even in December the ice conditions do not limit waves development in the viewed region. However, within the period from 1971 through 1992 in December there were only three cases when mean wave heights in deep water extended by 3 m.

From above data one can make a conclusion that in 20 years the *h=4.4 m* maximum mean is close to wave heights pointed out in October-November. Number of cases, when ice conditions were favorable for significant wave development, is few and it does not allow to get the quantitative statistic heights estimations of waves , which may appear once in 50 and 100 years.

Data (shown by circles) of distribution function of annual maximum values of mean wave heights in navigation period from 1960 through 1994 by the same temporal calculated data set are shown on Fig.9. Dotted line on Fig. 9 means

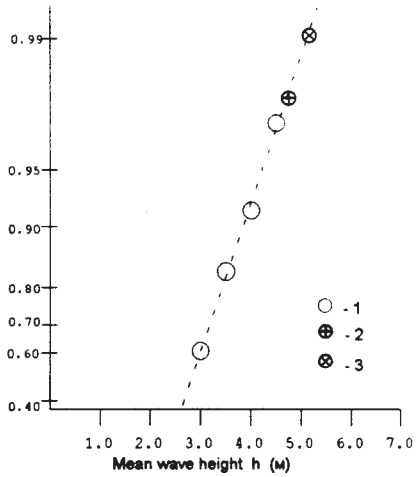


Fig. 10
Distribution function of maximum in a year mean wave heights in the 70° N, 54 W (H=100 m).
1- by calculation data by wind fields within the period from 1960 through 1994; 2- mean wave height appearing once in 50 years (4.8 m), 3- mean wave height appearing once in 100 years (5.2 m)



AUTHOR INDEX TABLE OF CONTENTS

asymptotic Gumbel distribution with $\alpha = 1.75$ and $\beta = 2.60$ parameters.

$$F(h) = \exp\left[-e^{-y}\right] \qquad (12)$$

As it is shown on the figure the calculated data of maximum values of mean wave heights in some years correspond very well with Gumbel distribution. Maximum values, which may appear on (12) proportion once in 50 and 100 years are shown on the figure by circles with cross lines. In the first case $h_{50}=4.8$ *m*, in the second $h_{100}=5.2$ *m*. It is known that the extreme waves calculated by annual maximums distribution usually are approximately less by 10 percent of calculated with all data set, that according to some investigators (Gumbel, 1965; Davidan et al., 1985; Matushevskiy , 1985; Problems of investigation and math modeling of wind waves, 1995 ) is followed from the fact that in some years there are some cases when wave heights are the same or very close in fact as to year maximums. Our calculations, as it is shown in $h_{50}$ and $h_{100}$ proportions, confirm the pointed out by the other scientists differences between results of these methods.

As the results, got by using the first from these used by us two methods, include significantly the initial data, so further wave heights are estimated in shallow water on the base of calculations on lognormal wave distribution.

## 7. CALCULATION OF EXTREME WAVES ELEMENTS IN SHALLOW WATER

Wave distribution in the calculated shallow-water point got on the base of model calculations in 35-year period is shown in Table 1. Height value (0.1 percent probability)waves , which may appear once in 20 years (see Table 2), was estimated according to the Table. As it was pointed out spectral-parametric model of a shallow sea was used in calculations.

Let us point out that it would be wrong to use this distribution to estimate wave heights, which are over the limits of 35-year set. To develop asymptotic distribution to estimate heights of waves appearing once in 50 and 100 years is considered to be conjectural because of the limited influence of depth to wave heights.

Taking into consideration the fact that in deep water the values of the regime wave heights distribution straighten well on the functional lgnormal grid, that is they may be approximated by corresponding asymptotic distribution. The following algorithm of extreme wave heights estimation (waves appear once in 50 and 100 years) in shallow-water region was proposed by Davidan. As the extreme waves in shallow-water region of interest come from deep water regions of the Barents Sea, it is possible to calculate their extreme values using the initial data of wave height in deep water with the help of lognormal distribution. Then, to estimate the corresponding values of mean wave heights in given shallow-water point using the SPD model of the shallow sea. Height of 0.1 percent probability with the depth influence is estimated by mean wave height. Mean wave period and waves period, the heights of which has 0.1% probability, are estimated by spectral maximum frequency.

However, it is necessary to know not only their mean heights in deep water, but wind speeds being observed in that case in order to calculate in that way shallow water waves. Wind speeds distribution for the cases, when waves transferred from the most dangerous north-western direction in navigation season in 35 years from 1960 up to 1994, is shown on Fig. 10 by circles. Approximation of calculated data by using the Weibull distribution is shown by dotted lines. The most probable wind speed values in one of synoptic terms appearing once in 50 years (27 m/c) and 100 years (28 m/c) are shown by circles with crossed lines.

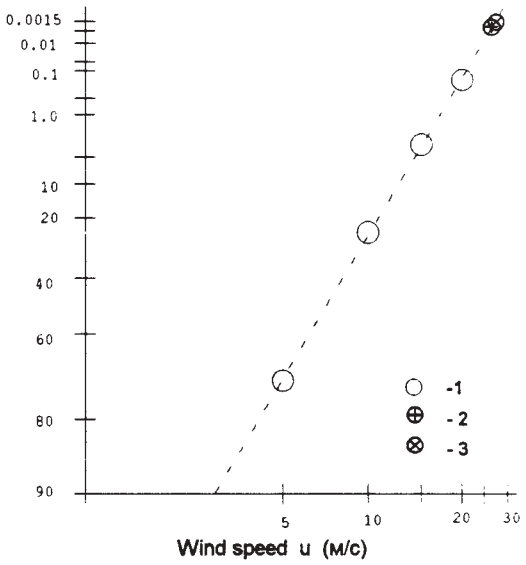


Fig. 11
Distribution function of mean wind speeds in the 70° N, 54° W (H=100 m), 1-with waves distribution from north-western direction; 2-wind speed appearing once in 50 years (27 m/c); 3- wind speed appearing once in 100 years (28 m/c)

So the initial wave and wind parameters in deep water are as follows $h_{50}$=5.3 m, $u_{50}$=27 m/c and $h_{100}$=5.8 m, $u_{100}$=28 m/c in the case when waves were calculated by lognormal distribution.

By using of these initial data one may consider the following $h_{0.1\%}$, $\bar{\tau}$ *and* $\bar{\tau} / h_{0.1\%}$ wave parameters in shallow-water points. Their values for the calculated point are shown in Table 2.

Table 2. Wave elements appearing once in 20, 50 and 100 years in a calculated point

| Year number | Wave height (m) (0,1 percent probability) | mean period (sek) | period of maximum wave (sek) |
|---|---|---|---|
| 20 | 8.7 | 8.5 | 10.1 |
| 50 | 9.5 | 9.1 | 10.8 |
| 100 | 9.9 | 9.5 | 11.3 |

## 8. PROBABAL LIMITS OF EXTREME WAVES ESTIMATIONS.

Proportion, given in monograph (Problems of investigation and math modelling of wind waves. 1995) was used to estimate the probable limits of above calculated wave heights got by lognormal distribution.

$$\sigma_{x_F} = \frac{x_F}{s}\left[\frac{2}{\alpha n} + \frac{u_F^2}{2\alpha n}\right]^{1/2} \qquad (13)$$

where $u_F$ - quantile of standard normal distribution $x_F = x_F^* \pm u_{x_F}\sigma_{x_F}$, $\alpha = 0.1$

For 95 percent confidence interval $u_F$ is equal 1,65 ($u_f$ = 1,65). Then for deep water with $h_{100}$ - 5,8 m one will get $\sigma_{X_F} \approx 0.1$, $x_F = 5.8 \pm 0.16$, $x_{F/x_F^*} = 1.028$

Accordingly with the shown proportion one may conclude that through selective variability with deep water wave heights approximation on lognormal law for 95 percent confidence interval, $h_{0,1\%}$ will change in range from 9.6 m to 10.2 m in the calculated point for waves, which may appear once in 100 years. Minimum confidence interval, which depends on number of temporal set terms, is shown there. To this we can add wave calculation accuracy and unknown beforehand trend in changes of the wave formation conditions in 50 and 100 succeeding years. Earlier performed model verification showed that there was not find the systematic error in calculations in rather large wave formation conditions range, and random errors are + 0,5 m for heights values.

## CONCLUSION

Estimations of the extreme heights of waves, which may appear once in 20, 50 and 100 years on a Gas Oil Field in the Pechora Sea, were performed in this work. Complex method based both on ship observations data analysis and for calculations on numerical model using synoptic data within 35-year period were used to perform calculations. In total the atmospheric pressure fields in 24158 synoptic terms were used in calculations, that made it possible to get the most quantity estimations of wave elements.

More sophisticated version of SPD model tested in details and verification by nature observation data was used in calculations. The most extreme situations were calculated by WAM model , that from one hand showed good agreement of calculation results, and from the other hand allowed to consider our calculations to be true.

Let us point out that the question about approximation of the regime asymptotic function of wave height distribution remains to be opened. In this work at first the parameters of lognormal wave height distribution function in the nearest deep water point were calculated, and then the extreme wave height values were recalculated to a shallow water point with their transformation.

As a result of the performance of statistic analysis of calculated temporal sets of wind wave elements it was found that the maximum height of wave, which may appear once in 100 years, in calculated point is equal 9.9 m. Taking into consideration 95 percent of confidence interval the values of maximum heights of waves, which may appear once in 100 years, change in the 9.6-10.2 m range.


## ACKNOWLEDGENENT

Investigation were performed under the support of the Russian Fund of Fundamental Investigations (96-05-65213 RFFI grant).


## REFERENCES


Bouws E., Gunther H., Rosenthal W., and Vincent C.L., 1987. Similarity of the wind wave spectrum in finite depth water. Part 2:Statistical relation between shape and growth stage parameters.-Deutsch. Hydrog. Zeitschrift., V.40, N1

Building standards and rules. Loads and influence on hydrotechnical constructions. 1983 - Moscow., Stroyizdat, 264 p.

Davidan I.N., Lopatukhin L.I., Rozhkov V.A., 1965 Wind waves in the World ocean.- Leningrad: Gidrometeoizdat, 285p.

Davidan I.N., Lavrenov I.V., Pasechnik T.A. and others, 1988. Math model and method of calculations of wind waves in USSR seas. Meteorologia i gidrologia, N 11, p.81-90

Hydrometeorological conditions of a shelf zone of USSR seas. The Barents Sea. 1985 - Leningrad: Gidrometeoizdat, V.6, 263 p.

Gluhovskiy B.H., 1966. Sea wave investigations.-L.: Gidrometeoizdat, 284 p.

Gumbel E., 1965. Extreme values statistics.-Moscow: Mir, 285p.

Komen G.J., Cavaleri L. Donelan M., Hasselmann S., Hasselmann K., Janssen P.A.E.M. 1994. Dynamics and Modelling of ocean waves. Cambridge, University press., 532 p.

Lavrenov I.V. and others., 1996. To carry out investigations with a purpose to develop improved numerical sea waves model as applied tosea conditions of the Arctic Ocean. AARI Report. St.Petersburg, 32 p.

Lavrenov I.V. 1997. Math modelling of wind waves in the spatial and heterogeneity ocean. St.Petersburg, 452 p.

Theoretical bases and calculation methods of wind waves. 1988.-Leningrad: Gidrometeoizdat, 264 p.

Matushevskiy G.V., 1985 Estimation method of climatic waves characteristics and estimations of their reliability. VNIGMI-MCD, Obninsk, 28 p.

Ocean wave modelling (SWAMP group) 1985. Plenum press, New York 285p.

Problems of investigation and math modelling of wind waves. 1995, St.Petersburg: Gidrometeoizdat, 465 p.

Shore Protection Manual. 1977, 1984 U.S. Army Engineering Research Centre, Washington, , Vol.1,2.

«USSR seas», Project. Hygrometeorology and hydrochemistry of USSR seas. The Barents Sea. Hydrometeorological conditions. 1990, -Leningrad: Gidrometeoizdat, V.1, Iss.1.

Wind and waves in oceans and seas. Manual data.1974 Leningrad: Transport 187p.

Zubakin G.K.,1987 Large-scale variability of ice cover conditions of the North-European Basin.- Leningrad: Gidrometeoizdat, 1987, 160 p.

# PROBABILISTIC DESCRIPTION OF CREST HEIGHTS OF OCEAN WAVES

Sverre Haver[1] and Daniel Karunakaran[2]

[1] Statoil, Exploration and Production Technology
[2] Sintef, Civil and Environmental Engineering

## 1 INTRODUCTION

In connection with stochastic response and fatigue analyses of marine structures, it is frequently assumed the surface elevation process can be modelled as a Gaussian process. The advantages of this are; the sea surface is for short term periods completely characterised (in a statistical sense) by the spectral density function, and a well-known theory for the probabilistic behaviour of maxima, minima, and threshold crossings become available. For a broad range of applications the Gaussian assumption is of a sufficient accuracy. Examples of such applications could be motions and global forces on ships and semi-submersibles. On the other hand if phenomena like green water on ships, wave - deck impacts on fixed and floating platforms, loads on slender fixed marine structures, and, possibly, ringing type of response are considered, it may be of importance to recognise that the real surface process is likely to slightly differ from a Gaussian process - even in deep waters.

That the real sea surface in most cases will deviate somewhat from a Gaussian model is rather obvious when looking at the sea surface. White capping and wave breaking will not occur within a Gaussian framework. The Gaussian assumption is in consistence with linear wave theory which is valid as long as the wave amplitude is very small as compared to the wave length. In severe sea states this is hardly fulfilled and we should expect a certain deviation from the Gaussian assumption. Thus the problem is mainly to quantify this expected deviation. To some extent this can be solved theoretically by modelling the wave process to a higher order, but at a present one will most probably also have to put some weight to empirical results based on wave measurements. In this connection it is very important that wave measurements are made by a sensor which can reflect a small deviation from the Gaussian assumption with a reasonable accuracy.

In shallow waters the deviations from the Gaussian assumption is very pronounced, see e.g. Jahns and Wheeler( 1972 ) and Ochi (1986 ). The steepness of waves are very much enhanced when the water depth becomes very shallow so a probabilistic model in agreement with linear wave theory can not be expected to be accurate. In the present paper we will consider waves in moderate water depths. By this we mean a water depth where the waves clearly feel the bottom, but the wave characteristics are not governed by bottom induced effects. As typical storm seas with wave periods in the band 10 - 20s move into shallower water depths, the wave asymmetry (ratio of crest height to wave height) changes rather slowly from deep water to a water depth of say 40 - 50m. As the water depth reduces further, the asymmetry changes rather rapidly. Most of the measurements considered herein are achieved at a water depth of 70 - 80m.

## 2 PREDICTION OF CREST HEIGHT FOR DESIGN

### 2.1 Long term distribution

In the time domain, the long term climate can be modelled as a sequence of stationary sea states. The length of each stationary sequence is more or less artificial and a 3-hour duration is frequently used. Provided the sea surface elevation within each stationary event can be modelled as a Gaussian process, the crest height distribution is very well modelled by the Rayleigh distribution. In the limit of a narrow banded surface process, this is in fact the exact distribution. Later on we will discuss the adequacy or, rather, lack of so for the Rayleigh distribution, and we will review the adequacy of some probabilistic models meant to reflect the non Gaussian structure of surface waves. At first, let us just denote the short term distribution by, $F_{C|H_{m0}T_p}(c|h,t)$, and show how we can predict crest heights corresponding to prescribed values of the annual exceedance probability.



AUTHOR INDEX TABLE OF CONTENTS

Probabilistically, the wave climate at a given site can be described by the joint density function of the significant wave height, $H_{m0}$, and the spectral peak period, $T_p$, $f_{H_{m0}T_p}(h,t)$. The long term probability of exceeding a particular crest height, $Q_C(c)$, is then given by:

$$Q_C(c) = \frac{1}{\bar{\nu}_0^+} \int_h \int_t \nu_0^+ (1 - F_{C|H_{m0}T_p}(c|h,t)) f_{H_{m0}T_p}(h,t)\, dtdh \tag{1}$$

where $\bar{\nu}_0^+$ is the long term mean zero-up-crossing frequency, i.e.:

$$\bar{\nu}_0^+ = \int_h \int_t \nu_0^+(h,t) f_{H_{m0}T_p}(h,t)\, dtdh \tag{2}$$

The exceedance probability obtained by Eq. (1) refers to the probability of exceeding the level $c$ by an arbitrary wave crest. For design purposes, target probabilities refer to annual exceedance probabilities, and for very small probabilities ($\bar{\nu}_0^+ \Delta_1 Q_C(c)$ much less than 1) the exceedance probabilities obtained by Eq. (1) can be transformed to annual exceedance probabilities by:

$$Q_C^{(1)}(c) = \bar{\nu}_0^+ \Delta_1 Q_C(c) \tag{3}$$

where $\Delta_1$ denotes 1 year in seconds.

Eq. (1) represents the most consistent approach for calculating for example the 100-year or 10000-year crest height. Of course it would be sufficient to include only sea states contributing significantly to the exceedance probabilities, but this must then be accounted for in the probability level corresponding to one year, i.e. $\Delta_1$ will then have to represent the expected accumulated duration of contributing sea states per year in seconds. Such a formulation will require a problem-dependent joint environmental model and this will not be very convenient for practical applications. The simplest thing is therefore to include all sea states, or at least all sea states exceeding a rather low significant wave height level.

The long term approach, Eq. (1), represents a straight forward method provided the short term distribution of the crest heights are known. This will be the case if the surface process can be modelled as a Gaussian process. For a general process the probabilistic structure of the crest heights is not that easy. Various models are suggested and we will discuss their adequacy later on. However, before proceeding with the short term distribution of crest heights, we will briefly discuss a simplified approach for predicting extremes corresponding to a particular annual exceedance probability. In this approach the target extreme value is estimated as the highest extreme value predicted for a proper sub set of sea states. This means that instead of determining the short term distribution for all sea states and thereafter weight the short term exceedance probabilities over all possible sea states, we merely predict extremes for some few sea states and then take the worst out of these as an adequate estimate for the wanted long term extreme value.

## 2.2 Contour line approach

A common way of establishing contour lines in the sea state space is to let them follow lines of constant probability density. An example of such a contour line is shown in Fig. 1. This particular contour line is determined by requiring it to go through the point given by the significant wave height corresponding to an annual exceedance probability equal to $10^{-2}$ and the conditional mean of the spectral peak period for this significant wave height. The duration of the sea states along this contour line should be taken to be 3 hours which is in consistence with the probability level used for predicting the 100-year value of the significant wave height.

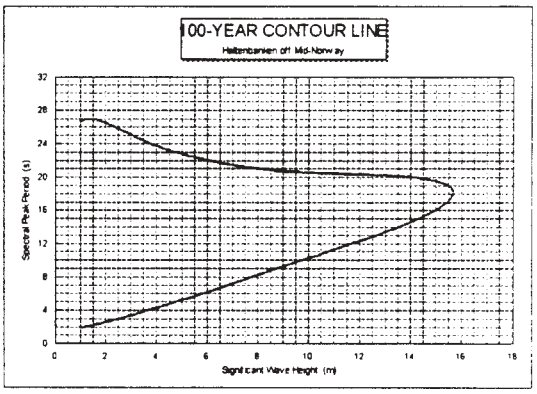


Fig. 1 100-year contour line for Haltenbanken. Sea state duration: 3 hours.

Let us for the sake of illustration assume that the surface elevation can be modelled as a Gaussian process. As a consequence of this one can model the short term crest height distribution by a Rayleigh model. From a long term analysis, Eq. (1), the 100-year crest height is found to be 16.2m. The joint model for $H_{m0}$ and $T_p$ is the same as is used for determining the contour line in Fig. 1. If now the most probable largest crest height in 3 hours is estimated for all sea states along the contour line, it is seen from Fig. 2 that even the worst value along the contour line is somewhat less than the 100-year value predicted from a long term analysis. This is not surprisingly and it is caused by the fact that the short term analysis neglects the variability of the short term extreme. If the short term extreme value along the contour line shown in Fig. 1 shall, for the most unfavourable sea state, equal the 100-year value, one has to adopt a higher fractile as the characteristic short term extreme value. From Fig. 2 it is seen that a very close approximation is obtained if the 85% fractile is adopted. For waves we will therefore recommend the 85% fractile to be

used in connection with a contour line obtained as the one shown in Fig. 1.

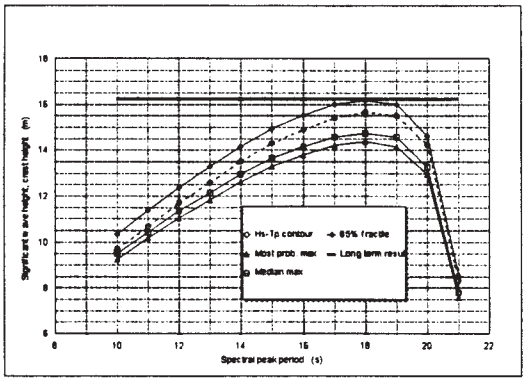


Fig. 2 Short term (3-hour) extreme crest heights

An alternative to select higher fractiles than the most probable extreme value is to artificially inflate the contour line until the most probable largest crest height in 3 hours equals the 100-year value obtained from the long term analysis. Regarding waves it is seen that this can be achieved by replacing the reference point used above by a significant wave height about 10% higher than the 100-year significant wave height.

A more general interpretation of the contour line concept is achieved using methods from the field of reliability analysis of marine structures. Usually the aim of a reliability analysis is to estimate the exceedance probability of a particular capacity or load level. This is very efficiently and, most often, very accurately done using the FORM-technique, see e.g. Madsen et al. (1986). The main idea behind this algorithm is that all physical variables which may be correlated to each other are transformed to standard, uncorrelated Gaussian variables, see e.g. Madsen et al. (1986). The actual reliability estimation is carried out in the latter space often referred to as the u-space. The physical failure surface (i.e. the boundary between the safe and the unsafe region in the physical parameter space) is also transformed to the u-space. The FORM-algorithm now first of all find the point on the failure surface that is closest to the origin. This point is often referred to as the design point and it is the most likely parameter combination as failure takes place. The next step of the FORM-algorithm is to approximate the true failure surface by a hyperplane in the design point. This plane is normal to the vector connecting origin and the design point. Denoting the length of this vector by $\beta$, the failure probability is simply given by $\Phi(-\beta)$, where $\Phi()$ is the distribution function for a standard Gaussian variable.

In connection with the contour line concept, we simply invert the procedure presented above. The situation is now that we know a target probability level. If we aim towards an annual exceedance probability of $10^{-2}$ and model the long term wave climate as a "continuous" step function of stationary 3-hour sea states, the target failure probability for an arbitrary 3-hour sea state is $10^{-2}/2920 = 3.42 \cdot 10^{-6}$. In a standard Gaussian distribution this corresponds to –4.5, i.e. the target distance from origin to the design point should be $\beta = 4.5$ in the standard Gaussian space, i.e. the u-space. For a two parameter problem this is represented by a circle in the u-space, while it becomes a sphere in case of a three parameter problem. If the target failure probability shall be met (within the accuracy of the FORM framework), the design point has to be located somewhere on this surface. The actual position on the surface will of course depend on the problem. The failure surface thus determined can now be transformed back to the space of physical parameters. The approach followed for determining contour lines is referred to as Inverse FORM (IFORM) and for a further discussion reference is made to Winterstein et al. (1993).

The contour line determined using the IFORM - algorithm is expected to be slightly more accurate than the contour lines following lines of constant probability density. It will coincide with the constant density lines in the reference point (100-year significant wave height and conditional mean spectral peak period), but it may differ slightly as one moves away from this point. However, a comparison for a number of North Sea locations has demonstrated that the difference is rather minor.

If the 100-year response is to be achieved by a short term analysis, one will also for the IFORM contour line have to use a higher fractile as the characteristic short term extreme value. The 85% fractile is expected to be a proper choice. An alternative approach is to include the short term extreme value as one of the variables in the IFORM-analysis, but this will then make the analysis problem dependent. An advantage of the contour line obtained using the IFORM-algorithm is that it can be extended to include other environmental parameters like wind speed and current speed, and, of course, the largest response (e. g. crest height) in the short term sea state.

In this paper, emphasis will be given to the first approach, i.e. the lines presented herein will follow lines of constant probability density. This will work very well for crest height problems since, for this type of problem, the most important part of the contour line is in the vicinity of the 100-year significant wave height. A proper estimate of the 100-year crest height is obtained by predicting the 85% fractile of the 3-hour maximum for all sea states along the contour line and then select the highest out of these.

At the end of the paper, the contour line approach is chosen as a simple way of demonstrating the impact of deviations of the Gaussian assumption.

## 3 ADEQUACY OF THE GAUSSIAN ASSUMPTION

### 3.1 Consequences of the Gaussian assumption

For Gaussian processes a well developed theory becomes available. Provided that the surface elevation process is not too broad banded, the crest heights of zero crossing wave cycles are very well modelled by the Rayleigh model, :

$$F_C(c) = 1 - \exp\left\{-\tfrac{1}{2}\left(\tfrac{c}{\sigma_\Xi}\right)^2\right\};\ c \geq 0 \qquad (4)$$

where $\sigma_\Xi$ is the standard deviation of the surface process.

Furthermore, it can be shown that the expected wave profile approaches asymptotically the auto correlation function of the surface process as the crest height increases, Boccotti (1983). This result is utilised in the so-called "New Wave Theory" suggested by Tromans et al. (1991). Of course actual realisations will show some scatter around this profile, but, on the average, the asymmetry of waves with large crests is clearly demonstrated in Fig. 3. This figure is based on simulation of a Gaussian process and it shows that even under the Gaussian assumption, waves with large crest heights are expected to show an asymmetric profile. It is important to recognise, however, that this has nothing to do with non-linearities. It is merely a consequence of bandwidth.

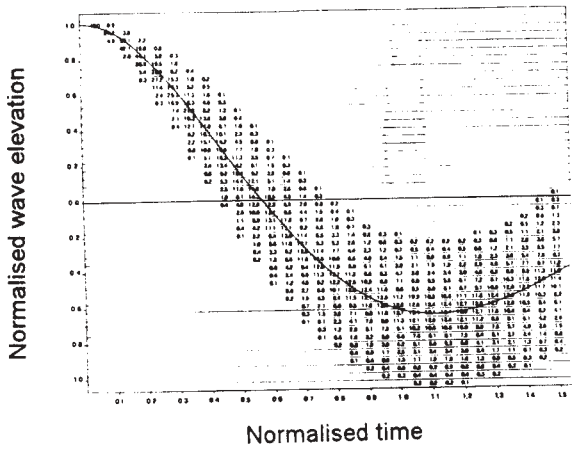


Fig. 3 Wave profile of waves with large crest height. From Boccotti (1983).

It is important to note that the asymmetry observed above is for waves with large crest heights. A similar negative asymmetry will, within the Gaussian framework, be observed for waves with large trough depths. In an average sense, however, a Gaussian process is symmetric. This is reflected by the fact that the coefficient of skewness, defined below, is equal to zero. Another parameter which is used for measuring the Gaussianity of stochastic processes is the coefficient of kurtosis. This coefficient involves the fourth moment of the process and is therefore rather sensitive to the tail behaviour of the population. The coefficients are given by:

$$\gamma_1 = \frac{m_\Xi^{(3)}}{\sigma_\Xi^3} \qquad (5)$$

$$\gamma_2 = \frac{m_\Xi^{(4)}}{\sigma_\Xi^4} \qquad (6)$$

where $m_\Xi^{(j)} = E(\Xi(t)^j)$ is the $j^{th}$ moment of the surface process. The mean value is without loss of generality assumed to be zero.

Subsequently, we will use these coefficients for assessing whether or not a measured sea surface can be considered as a realisation of a Gaussian process.

### 3.3 Properties of wave measurements

When assessing the adequacy of the Gaussian assumption in deep water, it is important that the measurements are made by a sensor which is able to recognise small deviations from the Gaussian hypothesis. Available types of sensors are floating buoys, down-looking radar or laser devices, and wave staffs. Both the down-looking sensors and the wave staffs require that a fixed platform is installed at the field. Furthermore, the platform should be rather transparent if the undisturbed incoming wave field should be accurately measured. If it is a large volume structure, diffraction effects will be very pronounced close to the platform. In such cases and for cases where no platform is installed at the field, wave measurements are most often made by means of floating buoys.

Wave measurements are also made by micro wave radars looking horizontally, but these do not provide any information about the detail surface structure. They mainly provide us with an estimate of the directional wave spectrum. The same can be said about satellite measurements. For both these sources, a prediction of crest heights rests completely on analytical tools. This will also be the case when it comes to hindcast data.

Both wave staffs and down-looking radar or laser devices should be able to measure a rather accurate time trace of the sea surface elevation. The main disturbance regarding these sensors is how they respond to foam and intense sea spray. When it comes to a floating buoy, the adequacy concerning a detail consideration of crest heights can be questioned. There is a number of reasons for believing that a floating buoy "gaussinize" the signal somewhat. The buoy floating under the action of the waves is likely to move around steep three dimensional crests, it may pass sharp wave crests in a more or less submerged condition, and, the buoy will move in the same direction as the wave profile at the wave crest and

against the wave profile in the trough. All these points will act in the same direction, i.e. making the realisation of surface process (the time series achieved by the buoy) more Gaussian than the underlying surface process.

A measure of the probabilistic structure of the surface process is the ratio of crest height to wave height. For a Gaussian process the average ratio should be equal to 0.5. In Fig. 4 the conditional mean value of this ratio is shown versus wave height for both down-looking lasers and buoys. A very clear difference in result is observed. The lasers clearly suggests an increasing asymmetry for increasing wave height. This suggests that the underlying process deviates slightly from a Gaussian process. Buoy data, on the other hand, indicate a rather different pattern. The buoys suggest that the asymmetry decreases slightly with increasing wave height. This is most likely a bias introduced by the buoy behaviour. The tendency we see in this figure is similar to what is observed for other cases.

For some Ekofisk data, the coefficient of skewness and coefficient of kurtosis are calculated both from Waverider data and a down-looking radar, Haver and Anfindsen (1988). For the skewness the results are shown in Fig. 5. A very clear difference is observed. For the kurtosis, however, there is in the average no difference between results from the two types of sensors.

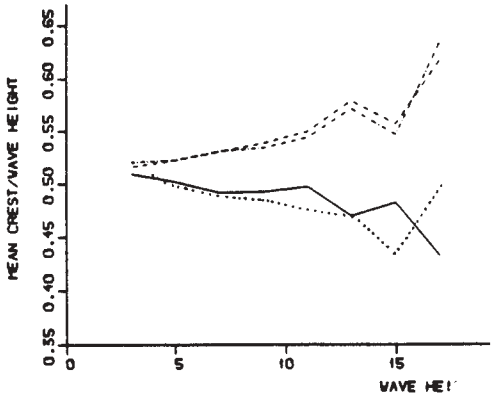


Fig. 4 Mean crest to wave height ratio for all instruments used in the WADIC Experiment. (- - - - ) and (- .- .- .) represent laser results, ( ____ ) and ( .....) represent buoy data, From Barstow et. al (1992).

3.4 Non-Gaussian characteristics

When assessing possible deviations from a Gaussian surface, emphasis is usually given to the coefficients defined in Eqs. (5 and 6). Based on the 3rd and 4th central sample moment, $m_{\Xi}^{(j)}, j = 3,4$ , of the observed time history, unbiased estimates for these parameters reads, Cramer (1951):

$$\hat{\gamma}_1 = \frac{m_{\Xi}^{(3)}}{s_{\Xi}^3} \tag{7}$$

$$\hat{\gamma}_2 = \frac{n+1}{n-1} \cdot \frac{m_{\Xi}^{(4)}}{s_{\Xi}^4} \tag{8}$$

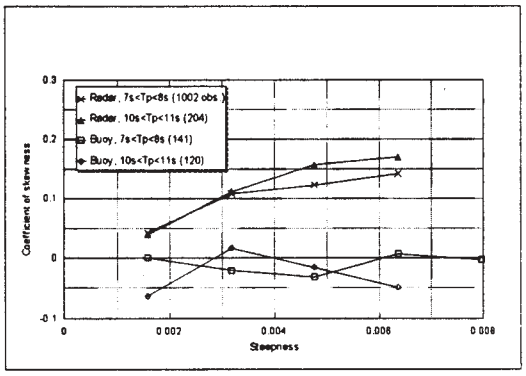


Fig. 5 Estimated coefficient of skewness for buoy data and radar data.

where $s_{\Xi}$ is the sample standard deviation. $n$ is the number of observations used for calculating the sample moments.

Standard deviations associated with these estimates are also given by Cramer(1951). However, these standard deviations assume that the individual observations involved in the calculation are independent. For time series typically sampled at a frequency close to 2 Hz this is far from fulfilled. The stability is in practise therefore much less than suggested by the standard deviations found in Cramer(1951). This is also the case when it comes to the bias correction included in Eq. (8). The bias is most probably somewhat larger than the correction factor. However, it is still a rather small bias, say typically less than 1%.

An alternative approach for establishing a more proper measure of the stability of the estimated coefficients is to simulate a large number of Gaussian time series, estimate the coefficients for each time series, and then estimate the standard deviation from these estimates. This is done in Haver(1980) for three different sea states; ($h_{m0}$ = 1.2m, $t_p$ = 4.5s), ($h_{m0}$ = 4m, $t_p$ = 6.5s), and ($h_{m0}$ = 8m, $t_p$ = 9.5s). Using these results, 90% confidence bands are shown in Figs. 6 and 7 for skewness and kurtosis, respectively.

It is clear from these figures, which of course should be taken as rather rough approximations, that a considerable deviation from the Gaussian values is required before it can be concluded that a particular time series deviates from a Gaussian process. However, when investigating the adequacy of the

Gaussian assumption, a lot of time series should be considered. Conclusions should be based on the mean coefficients for which the width of the corresponding confidence bands is significantly reduced.

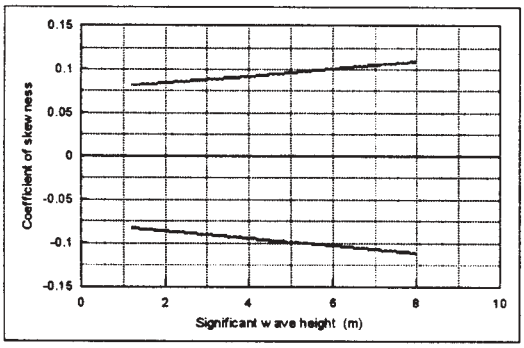


Fig. 6 90% confidence band for estimated skewness (n = 2048)

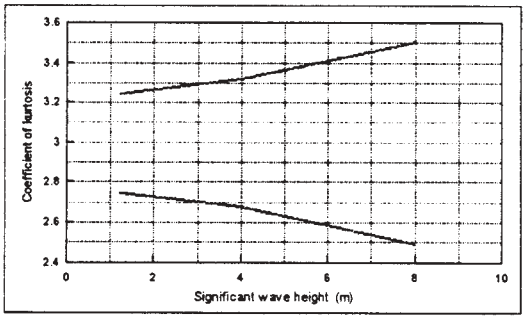


Fig. 7 90% confidence band for estimated kurtosis (n = 2048)

Using a second order description of the surface process, parametric models for the skewness and kurtosis of ocean waves in deep waters are presented by Vinje and Haver (1994). A consistent consideration of the kurtosis would require that the surface process is described to third order. The model for the kurtosis is therefore expected to be less accurate than the skewness model and may be one should rather consider the coefficient in front of the second term as a free parameter to be fitted to data. The models, which concerning skewness include an empirical correction for finite depth, read:

$$\gamma_1 \approx 34.4 \cdot \frac{h_{m0}}{g t_p^2} + 0.564 \cdot 10^{-6} \left( \frac{g t_p^2}{d} \right)^3 \qquad (9)$$

$$\gamma_2 \approx 3 + 3\gamma_1^2 \qquad (10)$$

In Vinje and Haver (1994), the wave spectrum is modelled by the Pierson Moskowitz spectrum, but the impact of a double peaked wave spectrum is demonstrated. The consequences of such a spectrum are mainly that the skewness will be reduced as compared to Eq. (9). For steep sea states, i.e. rapidly growing storm conditions, which often will be of a combined nature, Eq. (9) will significantly overestimate the expected skewness level.

Using a second order description of the surface process together with a Jonswap wave spectrum with a peakedness factor denoted $\gamma$, parametric models are also suggested by Jha (1997). His recommendations, which also include a depth correction for the skewness, are:

$$\gamma_1 = 34.2\gamma^{-0.084 \frac{h_{m0}}{g t_p^2}} + \left\{ \exp\left[ 7.41 \left( \frac{2\pi d}{g t_p^2} \right)^{1.22} \right] - 1 \right\}^{-1} \qquad (11)$$

$$\gamma_2 = 3 + 1.41\gamma^{-0.02} \cdot \gamma_1^2 \qquad (12)$$

It is seen that the results are not very sensitive to the spectral peakedness. It is probably more important to account for the double peakedness of spectra characterising steep sea states. For $\gamma = 1$, Eqs. (9) and (11) become, as they should, more or less equal, while a certain discrepancy is seen for the kurtosis. In Vinje and Haver (1994), Eqs. (9 and 10) are compared to wave measurements from a Northern North Sea site where the water depth is about 220m. The data are achieved by means of a down-looking laser and a reasonable good agreement is observed.

Herein we will compare the parametric models with coefficients estimated from data in a somewhat shallower location. The data are measured by a down-looking laser mounted at the corner of a transparent jacket platform in about 70m of water. For this depth, the depth correction factor has a rather little impact and it can very well be neglected. The measurements are made during some storm events occurring in the area in January 1995. The comparison is shown for skewness and kurtosis in Figs. 8 and 9, respectively. Although the models suggest a clear dependence on the steepness, $h_{m0}/(gt_p^2)$, this is not seen in the measurements. One possible reason may be that a lot of the included January 1995 data seem to correspond to rather confused sea systems characterised by double peaked spectra. However, this has not been investigated herein so it should merely be considered as a possible explanation.

A number of the time series correspond to so large coefficients that they obviously belong to a non-Gaussian population if the data quality is acceptable. A visual inspection has suggested that this is the case for the time series included herein.

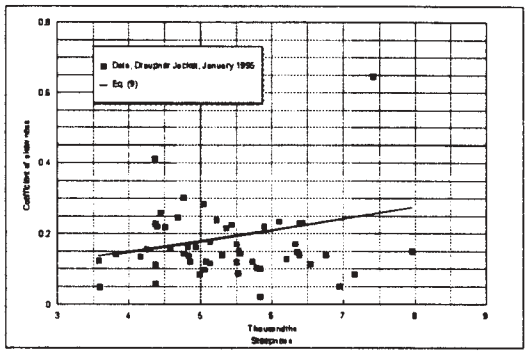

Fig. 8 Coefficient of skewness versus steepness

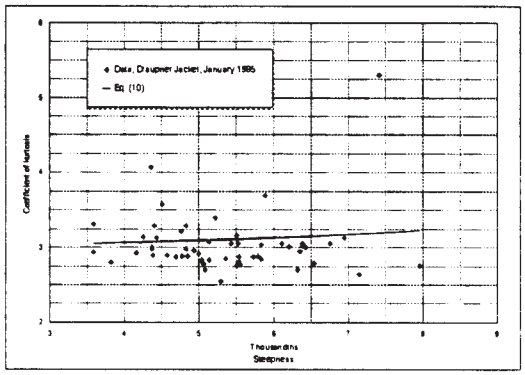

Fig. 9 Coefficient of kurtosis versus steepness

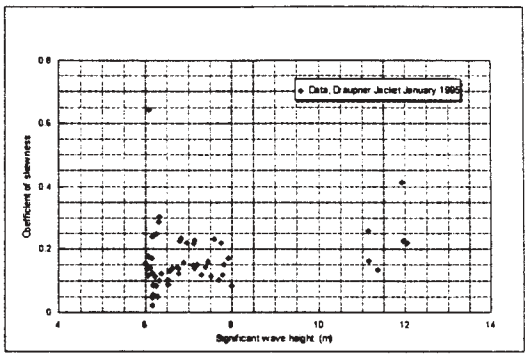

Fig. 10 Skewness versus significant wave height

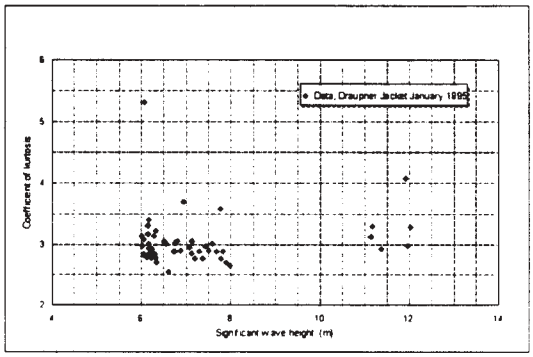

Fig. 11 Kurtosis versus significant wave height

The coefficient of skewness and kurtosis are shown versus significant wave height in Figs. 10 and 11. A rather large scatter is observed, but there seems to be an increasing deviation from the Gaussian assumption with increasing sea severity. We will take this as an indication of that when it comes to the most severe wave conditions, the non-Gaussian structure should be accounted for if the maximum crest height level is of concern.

It is seen from the figures that there is one event that is rather different from all the other. Both the skewness and the kurtosis attain very large values for this particular case. The time trace for this event is shown in Fig. 12. It is seen that a couple of extraordinary crest height occur at 900 and 950s. Whether these events are real waves or erroneous measurements is difficult to say. In Fig. 13 another time trace is shown. This time trace include one very severe crest height. We know this case is real because water was reported to have hit a temporary deck about 19m above mean sea level. If Fig. 13 is accepted as a valid time history, it is hard to reject Fig. 12 as false, although, it is of course more questionable with two extraordinary crests only some few wave cycles apart. Fig. 12 is therefore accepted as a valid measurement.

The wave spectra corresponding to these time series are shown in Figs. 14 and 15, respectively. It is seen that both seem to correspond to some degree of combined seas.

## 4 CREST HEIGHT MODELS FOR NON-GAUSSIAN PROCESSES

### 4.1 Second order model

Second order modelling has been frequently used for practical applications over the last few years. The resulting surface process, $\Xi(t)$, is then written as a Gaussian process ( first order term), $\Xi_1(t)$, plus a second order correction, $\Xi_2(t)$, i.e.:

$$\Xi(t) = \Xi_1(t) + \Xi_2(t) \qquad (13)$$

Herein we will not go into details of the second order model, reference is made to e.g. Marthinsen and Winterstein (1992), Stansberg ( 1993) and Jha (1997). Below we will mainly indicate the adequacy of second order models. In Fig. 16, the time series shown in Figs. 12 and 13 have been high pass filtered. The filter is set to a frequency slightly below two times the spectral peak frequency. It is clearly seen that in connection with the very large crest heights a rather

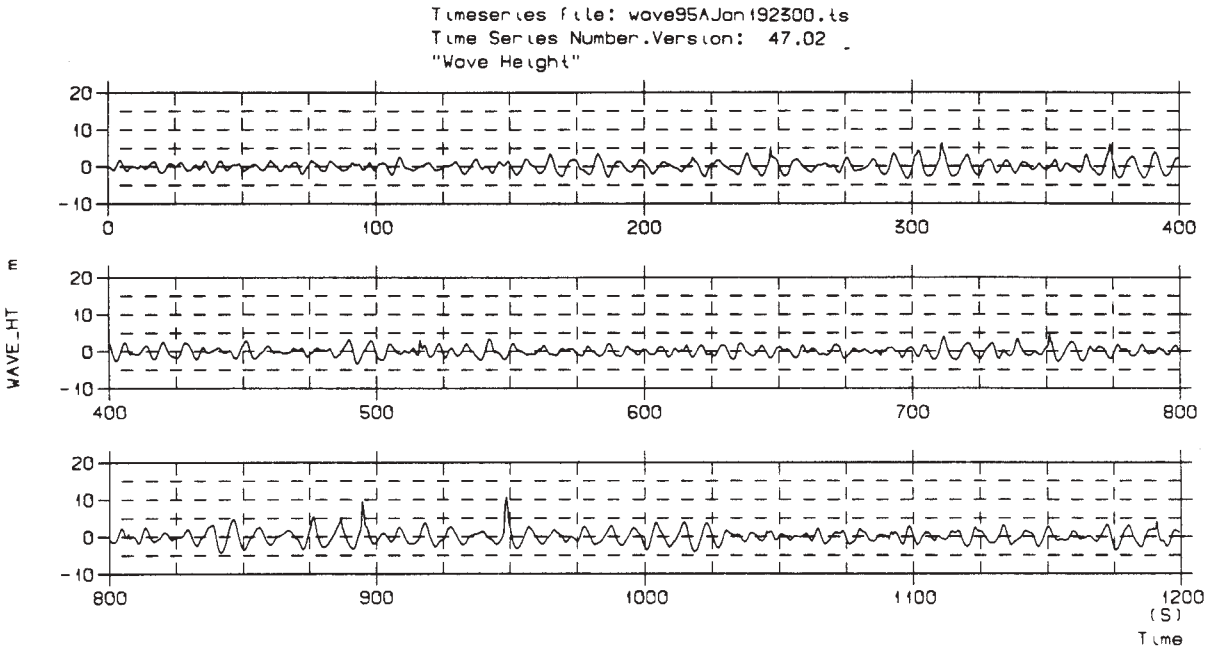


Fig.12 Time history of a case with very large skewness and kurtosis.

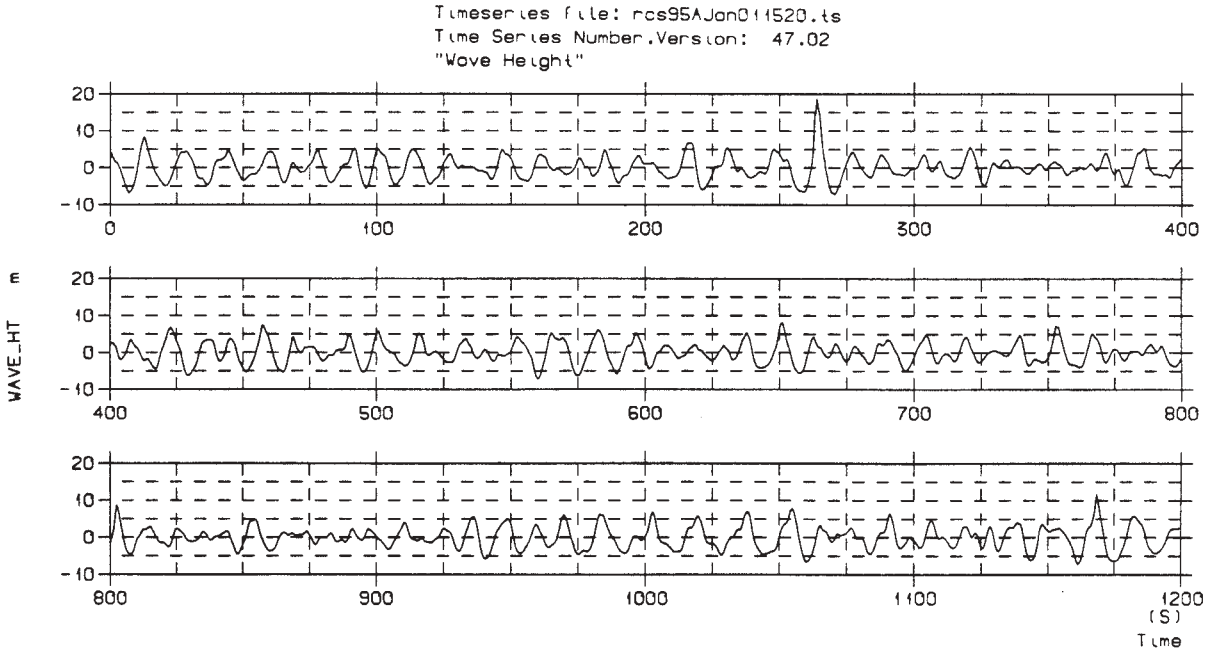


Fig.13 Time trace of the case with the largest crest height measured at the actual platform

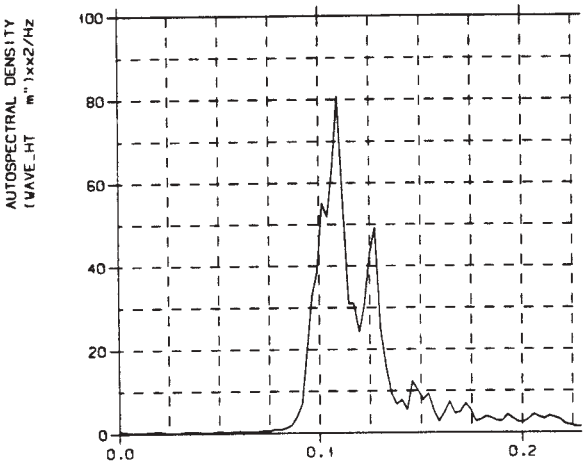


Fig. 14 Wave spectrum for the time history in Fig. 12

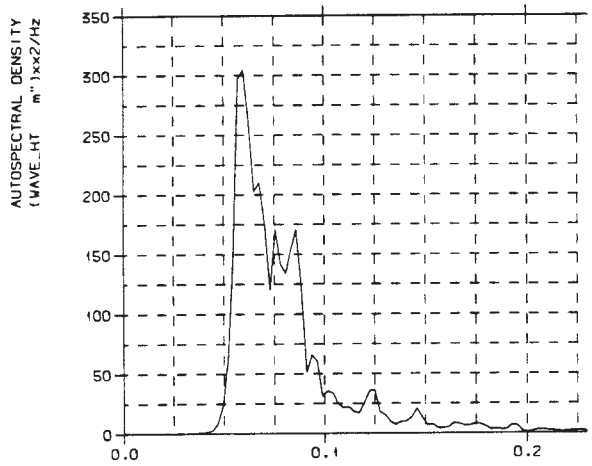


Fig. 15 Wave spectrum for the time history in Fig. 13.

pronounced crest is also observed in the high frequency process. The peak of the high frequency component seems to be perfectly in phase with the low frequency peak, suggesting that some sort of phase locking takes place. This indicates that higher order wave models are necessary in order to capture this type of extraordinary crest heights. Most probably a second order model will not be sufficient to capture crests like those included in these figures. In the future one should therefore aim towards higher order models for the surface elevation process.

Stansberg (1993) has compared second order reconstructions with measured surface processes and found, on the average, a rather good agreement. There is, however, a tendency that the reconstructed profile slightly underestimate the largest crests, indicating that higher order models are needed before the most extreme events can be reproduced numerically with a realistic frequency of occurrence. Jha (1997) presents a comparison of crest height distribution obtained from measurements with that obtained fram a simulated second order surface. These results are shown in Figs. 17 and 18. In Fig. 17, the measured time history is measured in a model basin and it has the following characteristics; $\gamma_1 = 0.15$ and $\gamma_2 = 3.14$. Fig. 18 shows a comparison with full scale data from the Ekofisk area characterized by $\gamma_1 = 0.11$ and $\gamma_2 = 3.01$. It is seen that the second order model does pretty well regarding the full scale data, while a clear underprediction of large crests is the case for the laboratory data. Again this clearly shows that second order models are not the final solution regarding numerical simulation of ocean waves. Concerning a prediction of extreme crests, one will probably have to rely on more or less empirically founded statistical models.

4.2 Probabilistic models for the crest height

Below we will briefly present probabilistic models that have been suggested in cases where the surface process deviates from the Gaussian assumption. An empirical modification of the Rayleigh distribution involving depth as a parameter is proposed by Jahns and Wheeler (1972):

$$F_C(c) = 1 - \exp\left\{-\tfrac{1}{2}c^2\left[1 - \beta_1 c\,\tfrac{\sigma_\Xi}{d}\left(\beta_2 - c\,\tfrac{\sigma_\Xi}{d}\right)\right]\right\};\ c \geq 0 \qquad (14)$$

$\sigma_\Xi$ is the standard deviation of the surface elevation process, $d$ is the water depth, and $\beta_1$ and $\beta_2$ are empirical coefficients. $\beta_1 = 4.37$ and $\beta_2 = 0.57$ are recommended by Haring and Heideman (1978). This recommendation is later on supported by Heideman and Schaudt (1987).

Another modification to the Rayleigh model is proposed by Stansberg(1993). The basis for this approach is the Rayleigh model given by Eq. (4) and the generalized crest height model is obtained by scaling the Rayleigh fractiles, $c_R$, by:

$$c = c_R \cdot \exp(c_R k_p) \qquad (15)$$

where $k_p = 2\pi/\lambda_p$, and $\lambda_p$ is the wave length corresponding to the spectral peak period.

Finally, we will also present the procedure proposed by Winterstein (1988). The basic idea underlying this approach is that instead of modelling the surface process as a Gaussian process, it is modelled as a Hermite expansion of a Gaussian process. The coefficients in the series expansion are determined such that the skewness and kurtosis of the model process approximately equals those actually measured or prescribed for a particular sea state. The fractiles of the distribution function of crest heights of a non Gaussian process can now be calculated by scaling

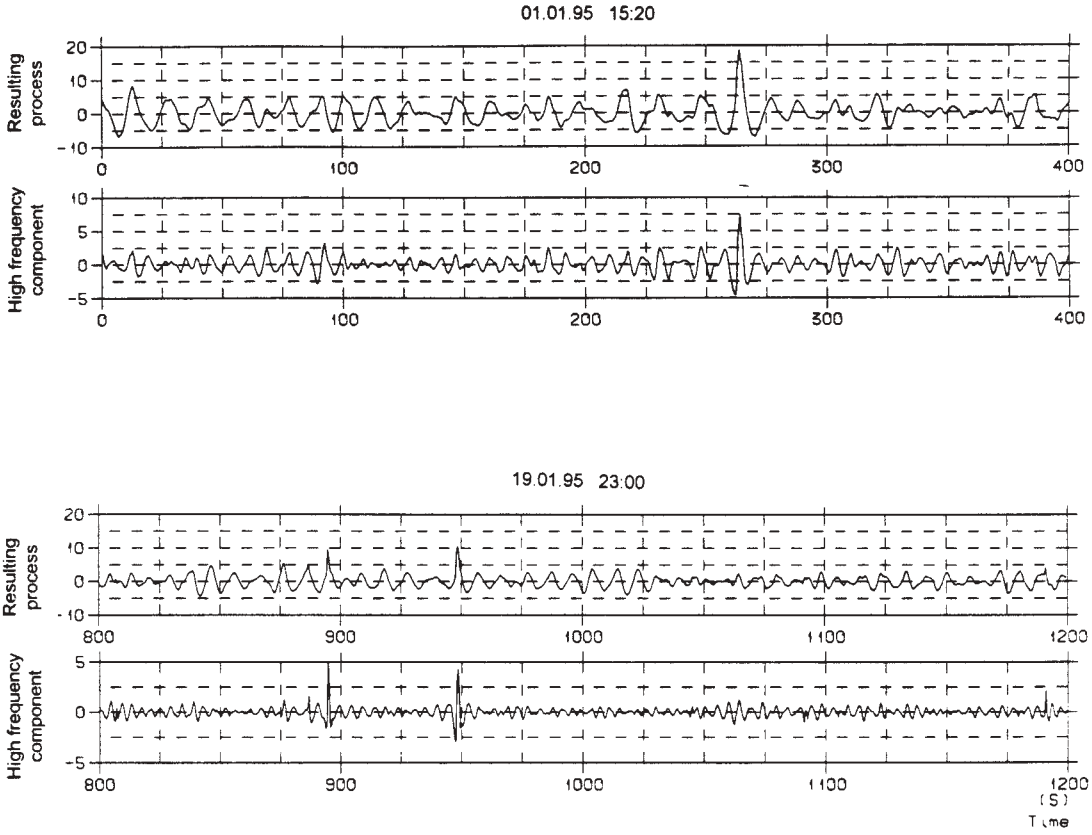


Fig. 16 High frequency component of the surface process versus the resulting process

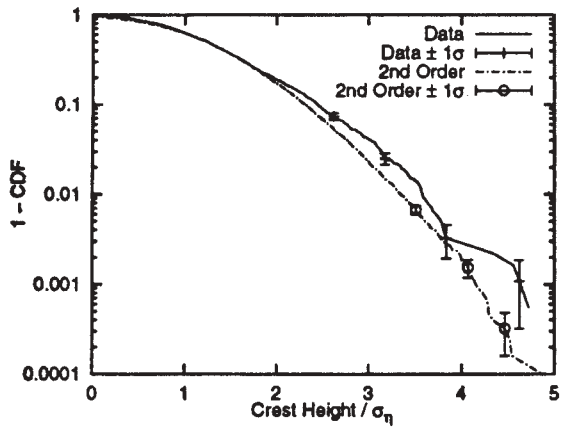


Fig. 17 Comparison of crest height distribution from measured time history (laboratory) and second order simulation. From Jha(1997)

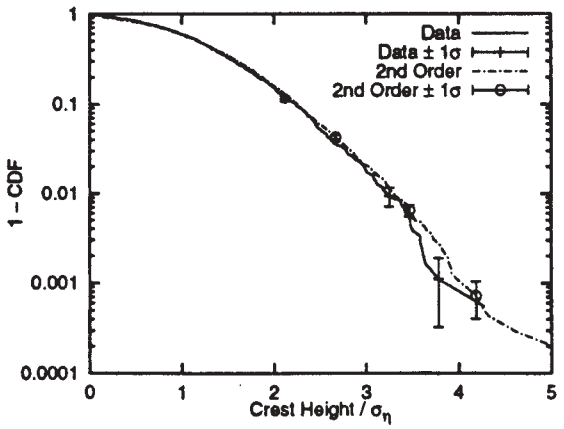


Fig. 18 Comparison of crest height distribution from measured time history (full sccale) and second order simulation. From Jha(1997)

the Rayleigh fractiles, $c_R$, according to the above mentioned Hermite expansion:

$$\tilde{c} = \kappa\left\{\tilde{c_R} + k_3\left(\tilde{c_R}^2 - 1\right) + k_4\left(\tilde{c_R}^3 - 3\,\tilde{c_R}\right)\right\} \qquad (16)$$

where ~ means that the crest heights refer to a normalized process, $\Xi(t)/\sigma_\Xi$, and

$$\kappa = \left(1 + 2k_3^2 + 6k_4^2\right)^{-0.5} \qquad (17)$$

$$k_3 = \frac{\gamma_1}{6(1+6k_4)} \qquad (18)$$

$$k_4 = \frac{1}{18}\left[\sqrt{1 + \frac{3}{2}(\gamma_2 - 3)} - 1\right] \qquad (19)$$

When applying this approach we start by calculating the fractiles, $c_R$, according to Eq. (4). Normalized fractiles, $\tilde{c_R}$, are obtained as $c_R/\sigma_\Xi$. When $\gamma_1$ and $\gamma_2$ are given, the Hermite coefficients can be calculated from Eqs. (17-19) and normalized fractiles of the crest height distribution for the non-Gaussian process are given by Eq. (16). Finally, physical fractiles are found by multiplying by the standard deviation, $\sigma_\Xi$.

The coefficients given by Eqs. (17-19) represent the simplest interpretation of the Hermite expansion technique. More resent implementations choose $k_3$ and $k_4$ such that the error in matching $\gamma_1$ and $\gamma_2$ is minimized under the requirement that Eq. (16) shall remain monotonic, Winterstein et al. (1994).

## 5 CREST HEIGHT DISTRIBUTIONS COMPARED TO DATA

### 5.1 Introduction

In this chapter we will consider the adequacy of the models suggested above in view of wave measurements. All measurements are made by down-looking wave sensors measuring the distance from the sensor to the instantaneous surface. Main focus will be on 1000 20-minute time histories achieved at the Ekofisk area during the years 1982 - 1990. Thereafter some severe storm measurements from the Draupner Jacket close to the Sleipner area in North Sea will adressed.

### 5.2 Ekofisk data

The Ekofisk analysis is based on about 1000 time series, Karunakaran (1994). The main focus of this study is the shape of the upper tail of the crest height distribution. A priori we did expect that this quantity could be effected by; steepness characterized by $(2\pi h_{m0})/(gt_p^2)$, a depth parameter given by $(gt_p^2)/(4\pi d)$, and the spectral shape characterized by $t_p/t_z$. The investigation did not demonstrate any clear dependency to these parameters and the data are therefore simply grouped in terms of the significant wave height. The groups and the group characteristics are given in Table 1. It is seen that the skewness seems on the average to increase with increasing sea states, while the kurtosis stays more or less constant. This is very similar to the observation we made for the Draupner Jacket, at least regarding skewness, see Fig.10.

Table 5.1 Grouping of the Ekofisk data

| Group no. | Significant wave height range (m) | No. of time series | Mean characteristics | | |
|---|---|---|---|---|---|
| | | | St. deviation (m) | Skewness | Kurtosis |
| 1 | 0 - 1 | 9 | 0.208 | 0.047 | 2.996 |
| 2 | 1 - 2 | 183 | 0.401 | 0.064 | 3.006 |
| 3 | 2 - 3 | 274 | 0.623 | 0.101 | 2.992 |
| 4 | 3 - 4 | 240 | 0.869 | 0.109 | 2.977 |
| 5 | 4 - 5 | 174 | 1.107 | 0.131 | 3.020 |
| 6 | 5 - 6 | 67 | 1.352 | 0.14 | 2.956 |
| 7 | 6 - 7 | 43 | 1.617 | 0.164 | 2.999 |
| 8 | 7 - 8 | 21 | 1.856 | 0.174 | 2.970 |
| 9 | 8 - 9 | 14 | 2.103 | 0.146 | 3.026 |
| 10 | 9 - 10 | 2 | 2.285 | 0.19 | 2.840 |
| 11 | 10 - 11 | 2 | 2.551 | 0.205 | 2.954 |

For each of the groups the average upper tail fractiles are calculated. Emphasis is given to fractiles corresponding to a cumulative probability of 0.9 or higher. The Jahns and Wheeler model and the Winterstein model are fitted to the mean characteristics of each group. For three of the groups the fit is illustrated in Figs. 19 - 21. It should be noted that regarding the Winterstein model Eqs. (17 - 19) are used for fitting purposes. It is possible that a better fit could have been obtained using a more advanced fitting procedure, Winterstein et al. (1994). With respect to the Jahns and Wheeler model, two fitted models are shown; the fit obtained using the original parameters provided by Jahns and Wheeler (1972), and the fit obtained using the parameters of Haring and Heideman (1978).

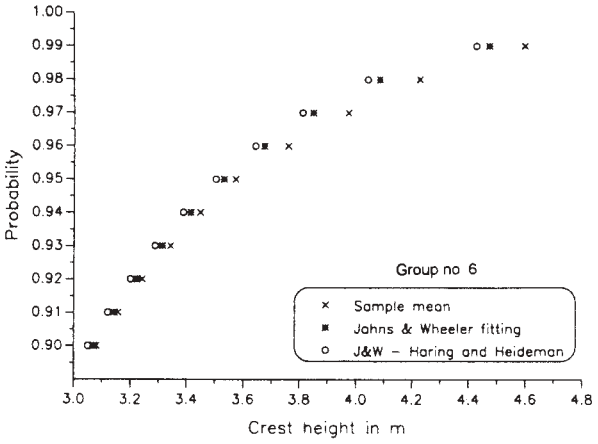


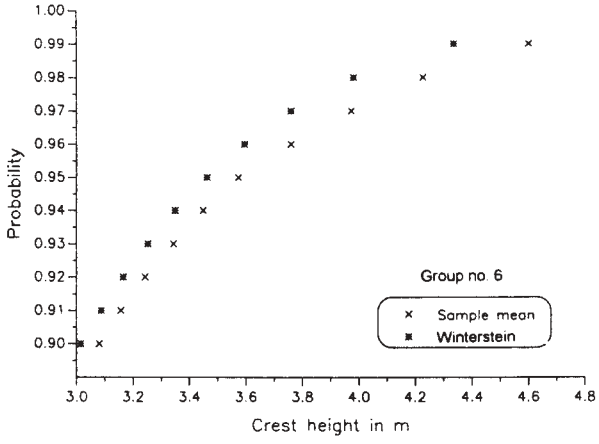


Fig.19 Fractiles of the crest height distribution, group no. 6

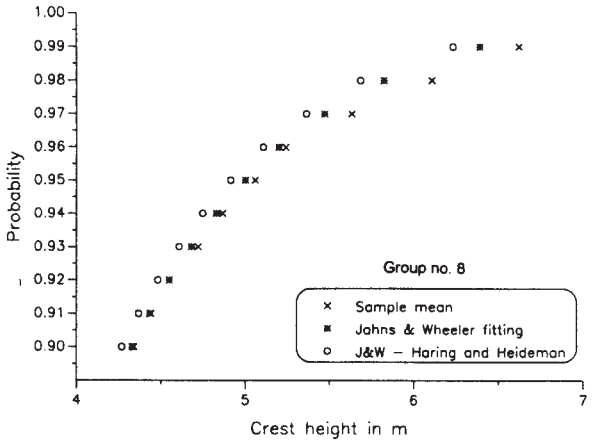


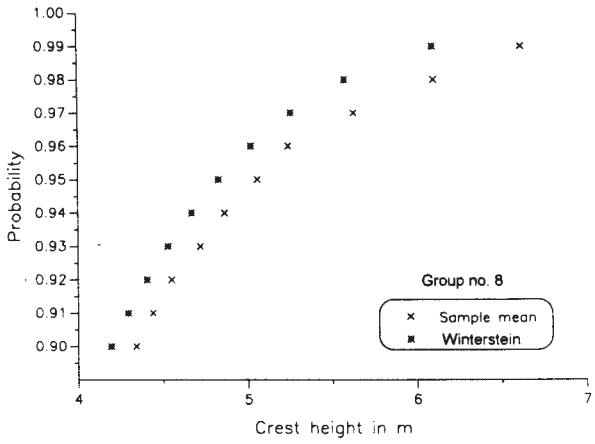


Fig. 20 Fractiles of the crest height distribution, group no. 8

From Figs. 19 - 21, it appears as if both the Winterstein model and the Jahns and Wheeler model slightly underestimate the mean fractiles calculated from the data. However, for the groups with a reasonable amount of measured time series, the underestimation is 5% or less. For these groups we typically observe that the original parameters of Jahns and Wheeler (1972) give a slightly better fit than the parameters suggested by Haring and Heideman (1978). For our cases the Jahns and Wheeler model appears to give a slightly better fit than the Winterstein model, but this could possibly be changed if an improved parameter estimation had been used for the latter model. With reference to the upper class, both models seem to underestimate the fractiles in the range 0.90 to 0.98. For the highest sea state group, however, they seem to approach the measured fractiles in the upper tail region. The no. of timeseries

in this group is on the other hand very limited so too much weight should not be given to this. Concerning the upper tail of severe sea states more data have to be considered.

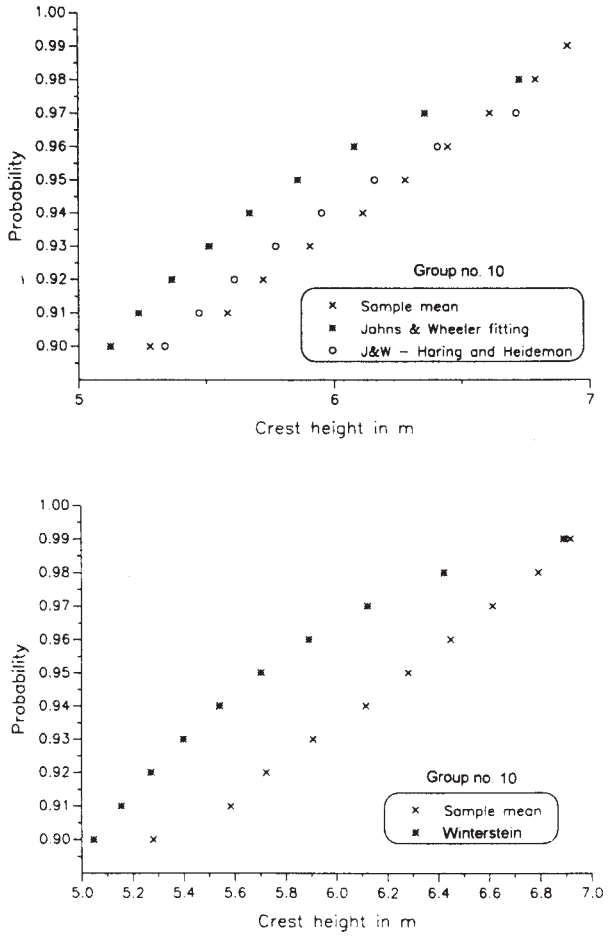


Fig. 21 Fractiles of the crest height distribution, group no. 10

5.3 Draupner jacket data

In January 1995, a rather severe storm hit the Central North Sea. At the Draupner Jacket the wave condition stayed at a significant wave height between 11 and 12m for a number of hours. Good quality wave measurements are available for this period, and the empirical crest height distribution is compared to the models suggested in Ch. 4 in Figs. 22 - 28. It is seen from these figures that the Rayleigh distribution severely underestimates the fractiles in the upper tail of the distribution. It is also seen that the empirical correction suggested by Stansberg(1993), do not provide a sufficient fat tail for capturing the observed deviation from the Gaussian hypothesis. The best models are again the Jahns and Wheeler model and the Winterstein model. If a simple fitting is used for the latter model, as is done herein, the Jahns and Wheeler model seems to give a better fit. On the average, however, both models seem to slightly underestimate the fractiles of the upper tail of the distribution. At least there is no reason to believe that any of these models are particularly conservative when it comes to predicting extreme crest heights.

For the cases with very extreme waves, none of the models are able to show a good tail fit. However, this should possibly neither be expected nor aimed for. The conditional return period in number of waves (average no. of waves between such crest heights within a particular sea state) of these events is most probably much longer than the no. of waves in the observed time series. Longer time series are needed for a more careful investigation the relative frequency of the very extreme events.

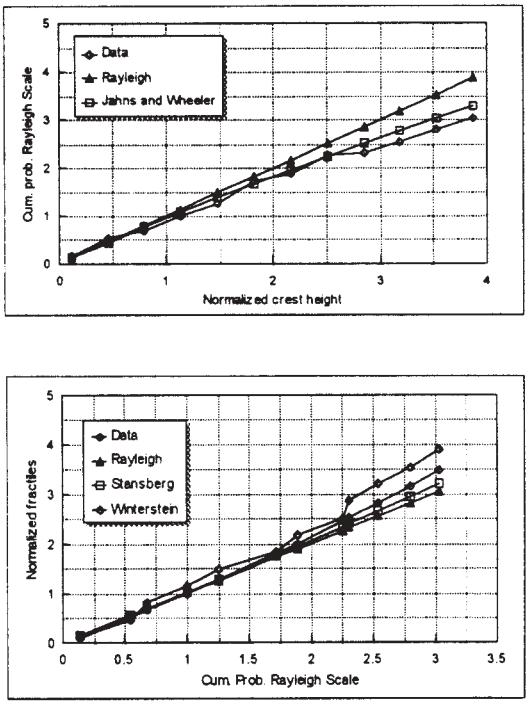


Fig.22 Crest height fit for time series 01.01.95 14:20

5.4 Consequences of deviations from the Gaussian assumption

From a practical point of view, the main concern is the impact of a possible deviation from the Gaussian assumption on, forexample, the 100 year crest height. This impact is demonstrated for Haltenbanken off Mid-Norway in Fig. 29. It is seen that adopting the Winterstein model for the short term extremes, the estimated 100-year value increases from 16.2m to

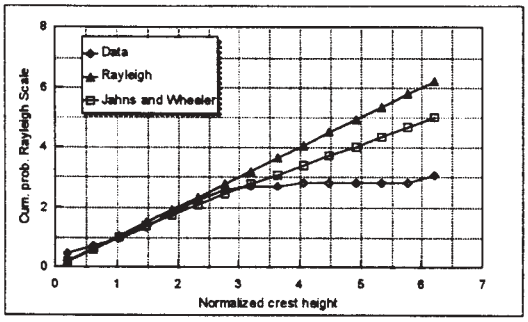


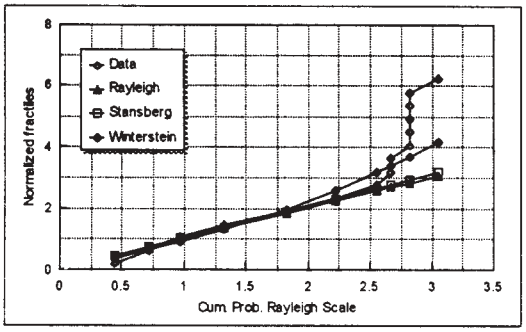


Fig. 23 Crest height fit for time series 01.01.95 15:20

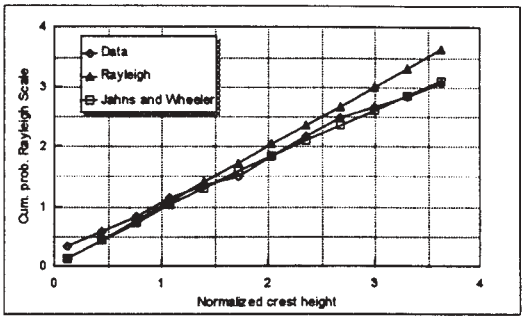


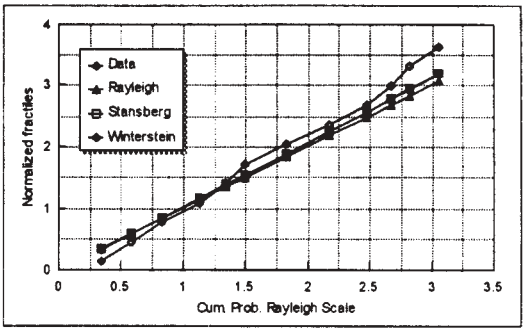


Fig. 25 Crest height fit for time series 01.01.95 17:20

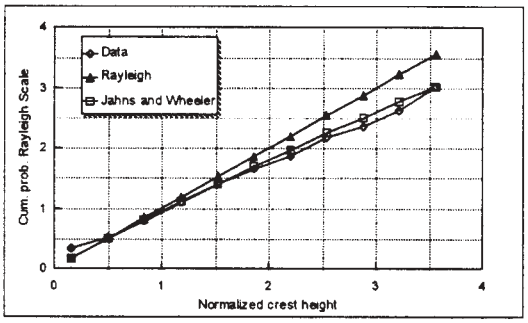


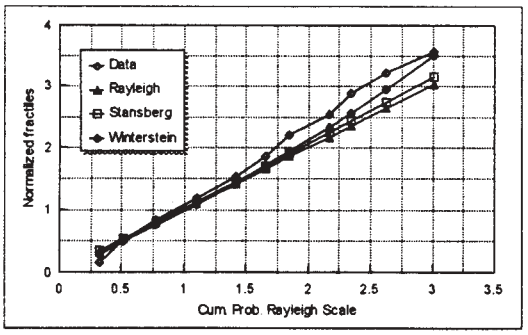


Fig.24 Crest height fit for time series 01.01.95 16:20

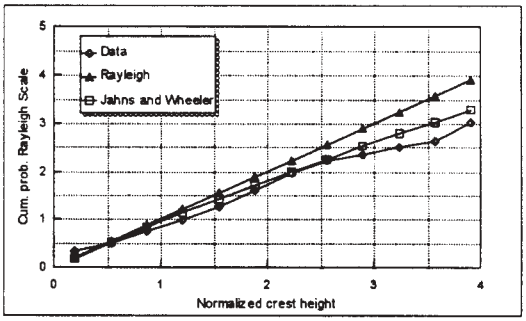


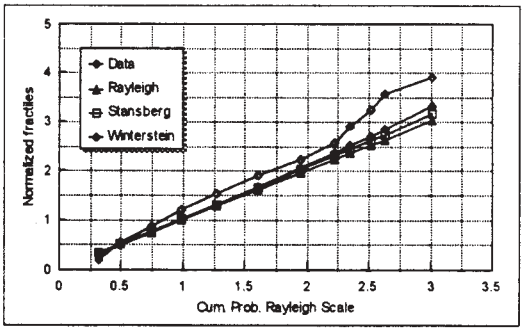


Fig. 26 Crest height fit for time series 01.01.95 18:20

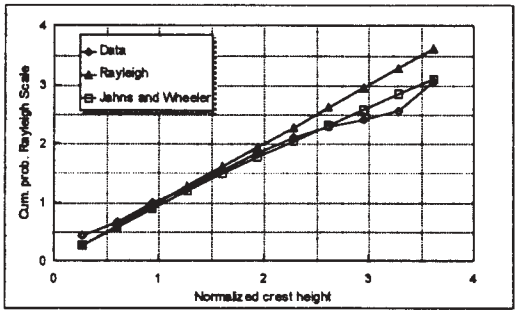


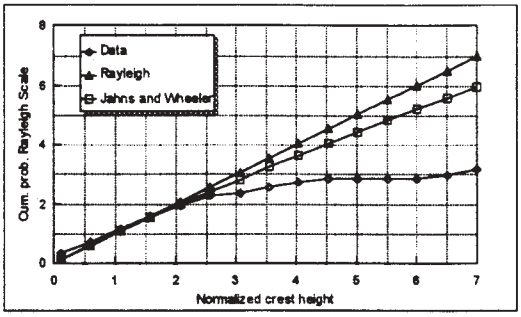


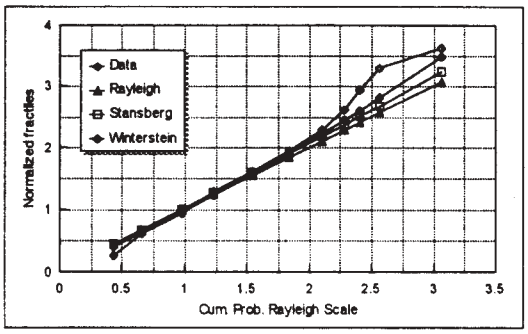


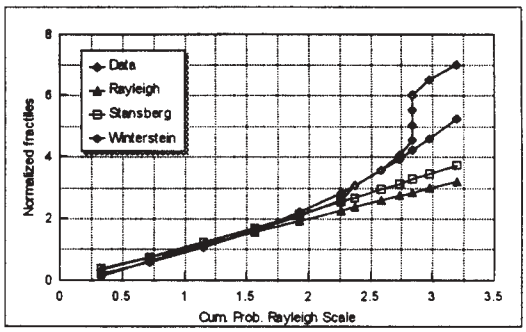


Fig. 27 Crest height fit for time series 01.01.95 19:20

Fig.28 Crest height fit for time series 19.01.95 23:00

about 18.7m, i.e. about 15%.The impact is expected to become even more as the 10000-year crest height is considered. It should also be kept in mind that the comparisons made herein does suggest that the Winterstein model may be on the low side when it comes to predicting the very extreme crest heights. At least this seems to be the case for moderate water depths (70m).

## 6 CONCLUSIONS

The probabilistic structure of ocean waves in deep and moderately deep waters is considered. Some suggested probabilistic models are compared with distribution functions estimated directly from measured time series.

From available litterature it seems as if a second order model reflects the sustained non linearity of the surface process. However, there appears to be a tendency of a certain underprediction regarding most extreme crest heights.

Both the Jahns and Wheeler model and the Winterstein model represent adequate models regarding a prediction of crest heights of non Gaussian processes. However, both models can be questioned regarding a modelling of the relative frequency of the very extreme crest heights, often referred to as freak waves. Whether these waves should be considered as rare events of a typical non-Gaussian process or as special events governed by different physical mechanisms should be further adressed in the future.

The Jahns and Wheeler model should be questioned as one approach deep water since the model approaches the Rayleigh model as depth increases.

It should also be noted that neither the Jahns and Wheeler model nor the Winterstein model appear to be conservative regarding a prediction of extreme crest heights.

For a deep water location in the Norwegian Sea, the impact of the likely deviation from the Gaussian assumption seems to be an increase of about 2.5m in the 100-year crest height. In percent this corresponds to about 15%.

## 7 ACKNOWLEDGMENT

Statoil is gratefully acknowledged for the permission to present this paper. The opinions expressed herein are those of the authors and should not be construed as reflecting the views of Statoil and Sintef.

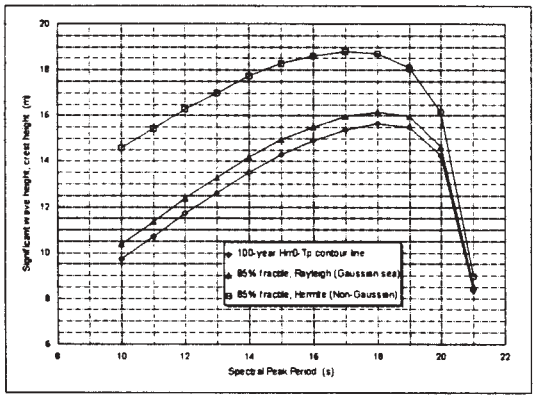


Fig. 29 Extreme crests (85% fractile ) along the the 100-year contour shown in Fig. 1

## 8 REFERENCES


Barstow, S., Bern, T.-I., and Krogstad, H (1992).: "Wave crest analysis for the Draugen field",OCN R-92093, Oceanor, Trondheim, 1992

Boccotti, P.(1983): "Some new results on statistical properties of wind waves", Applied Ocean Research, Vol. 5, No.3, 1983.

Cramer, H.(1951): "Mathematical methods of statistics", Princeton University Press, Princeton, 1951.

Haring, R.E. and Heideman, J.C.(1978): "Gulf of Mexico rare wave return periods", Offshore Technology Conference, OTC 3230, Houston, 1978.

Haver, S.(1980): "Analysis of uncertainties related to the stochastic modelling of ocean waves", Dr. Ing. thesis, Division of Marine Structures, The Norwegian Institute of Technology, Trondheim, 1980.

Haver, S. and Anfindsen, M.(1988): "On the adequacy of the Gaussian assumption regarding the sea surface elevation", Statoil, F&U-ST 88010, Stavanger, 1988.

Heidemann, J.C. and Schaudt, K.J.(1987): "Recommended equations for short term statistics of wave heights and crest heights", North European Storm Study (NESS) - memo, Solstrand Hotel, Bergen, 1987.

Jahns, H.O. and Wheeler, J.D.(1972): "Long -term wave probabilities based on hindcasting of severe storms", Offshore Technology Conference, OTC 1590, Houston, 1972.

Jha, A.(1997): "Nonlinear stochastic models for ocean wave loads and responses of offshore structures and vessels", Ph.D. - thesis, Departement of Civil Engineering, Stanford University, Stanford, 1997.

Karunakaran, D. (1994): "Ekofisk wave data processing and analysis", SINTEF Structures and Concrete, Memo, Trondheim, 1994

Madsen, H., Krenk, S. and Lind, N.(1986): "Structural safety", Prentice Hall Inc., Englewood Cliffs, New Jersey, 1986.

Marthinsen, T. and Winterstein, S.R.(1992): "On the skewness of random surface waves", Proceedings, ISOPE'92, San Fransisco, 1992.

Ochi, M.K.(1986): "Non-Gaussian random processes in ocean engineering", Probabilistic Engineering Mechanics, Vol. 1, No. 1, 1986.

Stansberg, C.T.(1993): "Second-order numerical reconstruction of laboratory generated random waves", OMAE'93, Glasgow, 1993.

Tromans, P.S., Anaturk, A.R. and Hagemeijer, P.(1991): "A new model for the kinematics of large ocean waves - applications as a design wave", ISOPE'91, Edinburgh, 1991.

Vinje, T. and Haver, S.(1994): "On the non-Gaussian structure of ocean waves", BOSS'94, Boston, 1994.

Winterstein, S.R.(1988): "Non-linear vibration models for extremes and fatigue", Journal of Engineering Mechanics, ASCE, 114 (10), 1988.

Winterstein, S.R., Ude, T., Cornell, C.A., Bjerager, P. and Haver, S.(1993): "Environmental parameters for extreme response: Inverse FORM with omission factors", ICOSSAR'93, Insbruck, 1993.

Winterstein, S.R., Lange, C.H. and Kumar, S.(1994): "FITTING: A subroutine to fit four moment probability distributions to data", Report RMS-14, Reliability of Marine Structures Programme, Civil Engineering Departement, Stanford University, Stanford, 1994.

# WAVE HINDCASTING AND FORECASTING - THEIR ROLE IN ENSURING THE SAFETY OF PERSONNEL INVOLVED IN OFFSHORE OIL AND GAS EXPLOITATION

**Dr. Donald Smith**

Offshore Safety Division of the UK Health and Safety Executive
315 Merton House
Stanley Road
Bootle, Mersyside, United Kingdom

## ABSTRACT

The paper will describe the new offshore oil and gas regulatory environment in UK waters (in particular the recently enacted Design and Construction Regulations) with a focus on the environmental data requirements for use in the design and assessment of offshore installations.

Particular emphasis will be given to understanding the role of the oceanographer and his/her models, methods, and data in the overall process of ensuring that offshore, installations realize an acceptable level of reliability against environmental overload.

The paper will draw on the experience gained by the HSE and industry in carrying out the North Sea Storm Study initial (2nd generation) and subsequent (3rd generation) hindcasts, some climate study work, crest height statistic studies, and the work being carried out to model the current climate in the North West Approaches area to the UK.

# AN ASSESSMENT OF WAVE MODELLING TECHNOLOGY

Vincent J. Cardone and Donald T. Resio

Oceanweather Inc.
Cos Cob, CT

USAE Waterways Experiment Station
Coastal and Hydraulics Laboratory
Vicksburg, MS

## INTRODUCTION

This year marks a decade since the publication of the first operational third-generation (3-G) wave model (WAMDI, 1988). Since 1988, 3-G models, and mainly 3G-WAM, have gradually replaced earlier 1-G and 2-G models in most but not all deep water wave prediction systems, though 1-G and 2-G models continue to be used in some important forecast and hindcast applications. The same decade has seen a significant expansion of the global base of wave measurements from both in-situ (data buoys and offshore platforms) and remote sensing (radar altimeter and synthetic aperture radars) systems. Measured data are used to evaluate wave models, validate wave predictions and sometimes to become part of the wave prediction process itself through data assimilation. Most of the operational wave prediction systems, global long term simulations and climate assessment applications of contemporary models and most wave data pertain to deep water. In the first part of this paper we review deep water models in terms of their performance, highlighting along the way remaining technical issues and areas which require further research and development.

With regard to shallow water wave modeling, the international wave modeling community is taking the first steps toward the development of a single community model (such as WAM for deep and intermediate water depth applications) , but it may be several years before such a model is ready for widespread operational use. Meanwhile, over the last 20 years or so, the number of wave models used in prediction of shallow-water wave conditions has proliferated. Data generated by these models play a critical role in a wide range of areas, including the design of shallow-water facilities (ports, harbors, oil production platforms), commercial navigation in coastal areas, force projection and sustainment in military operations, decision-making in coastal management, sediment transport related to beach erosion and dredging needs, and hazardous cleanup in coastal areas. Unlike in deep water, direct wave measurements are available only for a few sites around the world. Therefore, it is critical to ensure that shallow water wave models are accurate and appropriately applied. In spite of this, little has been done to date to quantify the performance of these models in a systematic fashion. In the second part of this paper, we shall present a framework for such quantification, with the intent that it will serve as a catalyst to generate future discussion in this area.

## 2. DEEP WATER WAVE PREDICTION

### 2.1 Review of Recent Wave Model Applications

The operational implementation of 3G-WAM began in Europe with both global and regional versions (see Komen et al, 1994) and has spread worldwide. Within the past two years, the U.S. Navy Fleet Numerical Meteorology and Oceanography Center (FNMOC) have implemented a global version of WAM (1° grid spacing) and regional versions (0.25° grid spacing) of WAM for the Indian Ocean, Mediterranean Sea and Korean waters (Wittmann et al., 1995). Forecast horizons extend to 144 hours for the global model and between 36 and 72 hours for the regional versions. In early 1996, the U.S. National Centers for Environmental Prediction (NCEP) adopted and began to distribute output from a global adaptation of WAM model (2.5° grid for forecasting to 72 hours) and from regional adaptations for the North Atlantic basin (1° grid), the Gulf of Mexico and Eastern Caribbean (1/4° grid). Early in 1996, the Atmospheric Environment Service of Canada (AES) replaced its 1-G operational model for the mid- and high-latitude parts of the North Atlantic and North Pacific Oceans with WAM (1° grid). A nested grid (3°/1°) adaptation of WAM for Australian waters has also been implemented at the Australian Bureau of Meteorology (ABM) (Bender, 1996).

Assimilation of ERS-1 satellite sensed wind and wave data into a wind/wave forecasting system ERS-1 has been reported by several groups. Bruning et al.(1994) made a preliminary evaluation of the assimilation of a 3-day sample of ERS-1 SAR wave mode data into the European Center for Medium Range Weather

Forecasting (ECMWF) global wave model. The retrieved SAR wave spectra show good agreement with the WAM wave spectra with mean wavelength and direction and directional spread in good agreement for low to moderate sea states and an approximately 15% overestimation for waves larger than about 5 m. Foreman et al.(1994) report a 3-month test of the assimilation of ERS-1 altimeter significant wave heights SWH estimates into the UKMO wave forecast system. The main impact was an increase in model swell especially in the central Pacific, and a reduction in the bias in the model by about 0.3 m. The potentially more powerful "adjoint" technique has been explored by Heras et al. (Heras et al., 1994). In this approach, an "adjoint" of the WAM model is constructed and is used to trace back in time the cause of a difference between the model result and some piece of measured wave data. Heras showed that assimilation of only SWH and mean wave direction is sufficient to control wind fields and wave spectra fields in a model consistent way. An unanswered question is the degree to which assimilation of global remotely sensed marine wind alone may control the wave field. The availability of global scatterometer sensed global marine surface winds from two satellites, ERS2 SCAT and ADEOS NSCAT during the 9-month period September, 1996 – June, 1997 may allow such an assessment.

The application of wind/wave hindcast models together with historical meteorological data continues to be the favored approach to describe the long-term operational and extreme wave climates for practical purposes and research. These models are typically applied on a single basin or regional basis and are often carried out by private companies and institutes as sponsored by the offshore and coastal engineering communities either by consortia of companies (joint projects), or individual companies for specific engineering projects. The results of such studies are proprietary to the study sponsors for a number of years. Major hindcast studies of both the operational and storm climates have been reported for the South China Sea (SEAMOS, Cardone and Grant, 1994) and the west coast of Africa (WAX, Cardone et al., 1995b. SEAMOS involved the hindcast of ten continuous years (1980-89) and 207 storms with a 3-G shallow model adapted on a 25-km grid (SEAMOS is believed to be the first application of a 3-G model to extreme wave climate assessment). The previously reported North European Storm Study (NESS; Peters et al., 1993) which included the hindcast of 25 continuous winters (1964-1989) with a 2-G model, has been completely rehindcast and updated to 1995 with a 3-G shallow water wave model. Similarly, a previous study which used a 1-G model to assess the extreme wave climate off the east Coast of Canada (CCC-91; Swail et al., 1995) was recently updated to include the many severe storms observed through 1995, with all previous and new storms (a total of 82 events between 1954-1995) rehindcast with a 3-G model. The updates to both the NESS and CCC-91 studies utilized a new interactive wind workstation (WWS) to hindcast the surface winds fields (Cox et al., 1995). WWS greatly reduces the degree of manual labor over classical kinematic analysis required to develop the most accurate wind fields possible for a given historical data set. Model verification studies conducted as part of the CCC-91 and NESS updates suggest that 3-G models provide slightly greater wave heights and lower periods than 1-G and 2-G models for the same wind fields. This result combined with the increased severity of storms observed off the Northwest Europe and the East Coast of the US in recent years has resulted in increases in the extreme wave climate specified in the update studies by about 10% over earlier estimates. The question of improvements of absolute accuracy of 3-G models over earlier formulations will be discussed in the next section of this paper.

The hindcast approach was used by Kushnir et al. (1995) to study the nature and cause of the recent increase in North Atlantic (NA) wave heights (Bacon and Carter, 1994). They found a link between the winter monthly mean NA wave height field (determined via hindcasting) and the sea level pressure field by canonical correlation analysis. The leading correlation patterns resemble the North Atlantic Oscillation (NAO) suggesting that the recent trend toward higher waves in the Northeast NA is a part of a longer term natural cycle with a periodicity of several decades. Interest in climate variability of the NA has stimulated two 40-year NA wave hindcast studies. The so-called European WASA project (WASA Group, 1995) used a 40-year file of surface wind fields compiled from US Navy and Norwegian Meteorological Institute operational products and a nested WAM. A Canadian sponsored project (Swail et al., 1998), is based upon the NOAA/NCAR NCEP Reanalysis (NRA) products . The alternative NRA wind products were first evaluated for accuracy (Cox et al., 1998) and the best of the alternative wind fields is itself reanalyzed using WWS mainly to improve resolution of tropical and extratropical storms. Before NRA was completed, ECMWF produced a 15-year global atmospheric reanalysis, which was subsequently used to drive the WAM model (Sterl et al., 1998).

### 2.2 Evolution of Source Term Algorithms

As to be expected, research and development of wave models has shifted almost exclusively to 3-G type models while existing proven 1-G and 2-G models continue to be exploited in their frozen states.

However, there has been remarkably little evolution of the physical formulation or numerics of deep water 3-G WAM over the past decade. Most of the above noted applications utilize either the so-called Cycle 3 (essentially the same model as described by WAMDI, 1988) or the Cycle4 version of WAM. Cycle 4 uses the coupled form of the atmospheric (wind) input source term (Janssen, 1991) as opposed to the uncoupled version of the earlier cycles. The effect of the coupled form is to enhance the wave growth of immature wind seas over that of older wind seas for the same wind. Cycle 4 also incorporates a different parameterization of wave dissipation (deep water) and the combination of source terms has been shown to produce somewhat higher global mean wave heights (Gunther et al., 1992).

All cycles of WAM use a simple first-order upwind differencing scheme in deep water to propagate the spectrum. Several centers (FNMOC, ABM) suspect that the first order scheme leads to under-prediction of swell. The replacement of the first-order scheme with a third-order propagation scheme in Cycle 3 of WAM in the ABM adaptation seems to produce the least biased predictions in the Southern Ocean in the operational ABM version.

An alternative version of 3-G WAM was developed at Oceanweather Inc (OWI3G, see Khandekar et al., 1994). That version combines the downstream interpolatory system of deep water wave propagation described by Greenwood et al. (1985) with a source term specification and integration scheme much like WAM-3 except that a second mode of the non-linear interactions are included within the DIA. This so-called DIA2 non-linear source term within OWI3G apparently leads to improved specification of the angular spread of pure wind seas (Forristall and Greenwood, 1998).

Presumably, future cycles of WAM and alternative 3-G type models will continue to evolve as the precise physical mechanisms of each source term become better understood, and are expressed more fundamentally in model algorithms as computing power increases allow. The atmospheric input source term used in WAM has been implicated as a possible source of the failure of most present 3-G models to specify the peaks in the wave spectrum observed at either side of the downwind direction, at least in limited fetch growth situations (Long et al. 1994; Ewans, 1995). It is suggested that the Phillips resonance mechanism is responsible for this bimodal directional behavior. That mechanism has already been incorporated into one alternative 3-G wave model (Khandekar et al. 1994). The dissipation source term has also been shown to need refinement (Banner and Young, 1994; Tolman and Chalikov, 1996) before wave models may reproduce the observed details of the spectral evolution as a function of fetch. Finally, while the non-linear quadruplet wave-wave interaction term source term is theoretically well described, the Discrete Interaction Approximation of the interactions has been shown to provide directional transfer rates that differ from the exact theory (e.g Resio, 1993). Young, Verhagen and Banner (1995) propose that a more exact non-linear source terms (e.g DIA2) is also required to model the bimodal directional distribution of fetch-limited wind seas. Lin and Huang (1996a,b) have developed a wave model based upon the action conservation equation rather than the transport equation and which uses the full non-linear dispersion relationship in water of arbitrary depth.

### 2.3 Model Performance

The performance of WAM in over a dozen early applications was reviewed by Komen et al., (1995). These included mainly Cycle 3 and early Cycle 4 case studies and forecast applications at the (ECMWF). A large number of additional wave model verification studies have been reported in the past few years. Those studies usually consist of the application of WAM in a case study, driven by winds obtained from an NWP center with the model predictions compared to measurements at one or two sites, though as noted above, 1G and 2G models continue to be applied, especially the ODGP2 model developed over 20 years ago (Cardone et al., 1976 or more recently Khandekar et al., 1994). Unfortunately, deficiencies in model performance are rarely related in these studies to particular source term or propagation deficiencies, which is perhaps why progress in further improvements in wave models has been so slow within the past decade.

Maximum Skill in Continuous Hindcasts. The recent SWADE hindcast study (Cardone et al., 1995) suggests that when wind fields are specified accurately in a hindcast mode using intensive reanalysis techniques which take advantage of the enhanced data coverage in areas of dense buoy and/or offshore platform measurement arrays (e.g. off the east and west coasts of North America and in and around the North Sea), well calibrated wave models specify the evolution of SWH with negligible bias and scatter near the lower limit set by accuracy and sampling variability in the wave measurements.. It is not as clear that the details of the 2-D spectrum and hence mean or peak spectral wave period or wave direction and angular spreading of waves are as well simulated. This SWADE IOP-1 11-day continuous hindcast with WAM-4 using kinematically reanalyzed wind fields probably best exemplifies the potential very high level

of skill in contemporary wave height predictions.. Table 1 gives the hindcast errors averaged over the deep water buoys in the area of maximum SWADE data density and hence the area with the most accurate wind fields. The SWH scatter index (SI) of 14% is unprecedented for continuous hindcasts . However, the mean negative error of about 0.4 seconds in peak period is apparently a real characteristic of this hindcast and remains unexplained.

Errors in hindcasts validated against wave measurements on the periphery of the SWADE array increased to levels probably more typical of continuous hindcasts of mid-latitude extratropical weather regimes with kinematically reanalyzed winds with SWH SI of 18%.- 20%. The SWH SI was found to increase to 25%-41% in the general SWADE area when WAM-4 was driven alternatively by wind fields derived from operational centers. The increase in SWH SI was highly correlated with increases in wind speed (WS) SI. The lower resolution of operational wind field is often indicted as a source of error in wave hindcasts . Graber et al. (1995) explored the effect of wind field resolution in the US East Coast extratropical cyclogenetical setting of SWADE IOP-1 by making a series of sensitivity hindcasts with WAM-4. The resolution of the baseline OW/AES reference SWADE IOP-1 wind field (spatial resolution of 0.5 degrees and temporal resolution of 1-hour) was systematically degraded for a series of alternative hindcasts with WAM-4. The wave height hindcast scatter relative to SWADE buoy-array wave measurements was found to increase approximately linearly with increasing temporal resolution between 1-hour and 12-hours. At most buoys sites, there was little error growth between spatial resolutions of 0.5 degree and 1 degree in general and about a 25 % degradation in skill at spatial resolution of 1.5 degrees. The exception to these general conclusions was found to be at sites in the path of the main surface wind jet streak propagating about the developing cyclone, where resolutions of 0.5 degrees and 3-hours was necessary to correctly specify the storm peak sea states. Another interesting finding of this study was that wind field resolution effects alone could explain only about 20-40% of the error observed in the alternative WAM-4 wave hindcasts made with various operational center wind fields reported by Cardone et al. (1995), leaving much of the remaining 60-80% of the error arising in errors in the operational center wind fields produced in October, 1990 for this period.

Marine wind field analyses produced at operational centers have tended to improve since 1990 due to more accurate and effective assimilation of surface and remotely sensed wind data and use of higher resolution NWP models in the analysis-forecast cycle. For example, ECMWF recently reanalyzed the 15-year period 1979-1993 using its current analysis scheme and a global WAM-4 continuous hindcast using these winds has been reported by Sterl et al. (1998). When that hindcast was evaluated at the same NOAA East Coast buoys used to evaluate the deep water SWADE hindcasts above, Sterl et al. find SWH SI in winter months of 27% when a 3 degree wave model grid is used and 22% when a 1.5 degree grid is used. They also report a negative hindcast bias in SWH of -0.7 m in this area for the 3 degree grid and -.5 m for the 1.5 degree grid. This bias is attributed mainly to underprediction of higher waves in storms. Still, these errors are significantly lower than exhibited by the SWADE hindcasts driven by ECMWF winds (i.e. SWH SI of 36%).

As part of a 40-year hindcast study of the North Atlantic Ocean using the NRA, Cox et al, (1998) evaluated the skill in deep water hindcasts of the North Atlantic Ocean with OWI3G driven by alternative estimates of the surface marine wind field. Table 2 shows results of hindcasts using the so-called 10m Gaussian grid surface wind fields for four selected months. The wave model grid spacing is 0.625 degrees in latitude by 0.833 degrees in longitude. The evaluation against all buoys moored in deep water offshore the US and Canadian East Coasts and off Northwest Europe indicates less skill than provided by kinematically reanalyzed winds with SWH SI of 26% overall months at the lower end of the range exhibited by wave hindcasts driven by the operational winds in SWADE. However, the SWH bias is satisfyingly small. The negative bias in wave period noted above is also evident in these hindcasts.

The AES 40-year North Atlantic hindcast project includes selective kinematic reanalysis of the NRA winds, mainly to resolve and enhance wind speeds in jet streaks which propagate about major storms and to add detail in wind fields in tropical storms (see Cox et al., 1998). Table 3 compares hindcasts made with these enhanced winds for March, 1993 with buoy and altimeter wave measurements for both the nominal OWI3G run and a comparison hindcast made with a model of the same grid system and propagation scheme as the nominal run but using the first generation ODGP2 source term algorithm. Comparison of the nominal run with enhanced winds with the run using unmodified NRA winds shows small improvement in global statistics: e.g at the buoys the negative bias is eliminated and there is about an 8% reduction in the SWH SI at the buoys from 24% to 22%. This is attributed mainly to reassimilation of buoys winds in the modification process. The altimeter comparisons

provide evaluation of the nominal run over the whole of the North Atlantic. For these comparisons, the ERS altimeter Fast Delivery 1 Hz estimates of SWH were first bin-averaged spatially over each wave model grid box using all estimates available within a 6-hour time window centered on the 6-hourly wave analysis times. The altimeter comparisons indicate a SWH bias of .05 m and SWH SI of only 21%. Comparable skill was found in the other three months evaluated in this manner. These evaluations indicate that the NRA reanalysis wind field products are a significant improvement in wind field accuracy over operational wind fields produced just a few years ago.

What is perhaps surprising about Table 3 is that the differences in SWH skill between ODGP2 and OWI3G are rather small with ODGP2 actually providing better statistics for wave period. The difference in altimeter SWH SI between the runs is only .02 and the bias overall is negligible. The variation of bias with SWH is shown in Figure 1 for each run. This figure compares the altimeter and hindcast in 0.5 meter altimeter SWH bins (bins with fewer than 5 comparisons are not shown) or one of the four months evaluated. In each bin we plot the mean difference and the standard deviation of the differences for all pairs within the bin. In bins up to SWH of 9 m (which contain 16,915 of the total of 16,915 comparisons) the two runs are virtual clones of each other while at higher SWH the bias remains negligible for OWI3G but becomes negative for ODGP2.

The relative effects of wind field accuracy and wave physics on wave prediction may also be examined through the results given in Cardone et al. ( 1995) in which one wave model, WAM-4, was driven alternatively by six different wind fields, and by Cardone et al. (1996) in which one high quality wind field was used to drive four different wave models. Both of those studies involved US East Coast extratropical storm regimes, used the same type of wave measurements to validate the wave hindcasts and controlled wave model variables of temporal and spatial resolution. The upper panel of Figure 2 shows the aggregate (i.e over 17 buoys used to evaluate the two hindcasts) SWH SI found for the four models used. All wave models were driven by the same wind field at the same resolution. The vertical bars denote plus and minus one standard deviation in the SI over the buoys and provide a measure of the consistency of the accuracy of the hindcast of a given model from area to area. The lower panel of the Figure 2 gives the aggregate SWH SI (over eight buoys) and SI standard deviation for the WAM-4 SWADE IOP-1 hindcasts made with six different wind fields. This figure clearly illustrates that the effect on wave hindcast skill on wind field accuracy is (at least for the four models used in this study ) more important than the choice of wave model.

Maximum Skill in Storm Peak Hindcasts. Skill in specification of storm peak sea states is important for extreme wave climate assessment for structure and ship design and for real-time wave forecasting. Figure 3 shows the skill in hindcasts of peak sea states (SWH, TP) in number of different tropical and extratropical storms made in several different basins with kinematically reanalyzed wind fields. OWI3G was used for all runs. The mean error in SWH (TP) is -.13 m (-.27 sec), the rms error is .98 m (1.64 sec) and the scatter index is 14% (15%). The skill seems to be invariant with wave height at least up to SWH of about 12 m, with a tendency to underestimate peak sea states in the most extreme storms in which SWH exceeds about 12 m. This underspecification in peak states was also observed with other wave models (Cardone et al., 1996) and may be associated with one or more of the following possibilities: (1) wind speeds measured from buoys in high seas states, which feed into operational as well as kinematically reanalyzed wind fields may be biased low; (2) wave model growth reaches saturation prematurely; (3) the source terms in wave models used for atmospheric input and wave dissipation, which are tuned even in 3G models, are being extrapolated beyond their applicable range; (4) spatially coherent small scale wind field features, such as rapidly propagating surface wind "jet streaks", which seem to be associated with several known occurrences of extreme storm sea states (Cardone et al. 1996) are not resolved accurately in even the best wind fields. These questions relate to assessment of wave models in general and are discussed in more detail below.

### 2.4 Principal Remaining Issues

Validation Data Given the importance of buoy measured wind and wave data to many wave modeling studies and to calibration of remote sensing systems for marine winds (altimeter and scatterometer) and wave height and period (altimeter), which are used increasingly to validate wave models, it is important to understand the bias and scatter in buoy wind and wave measurements, especially at higher wind speeds and sea states. A field program is underway to investigate the accuracy of wind and wave measurements from moored buoys in high sea states and preliminary results are presented at this conference (Skey et al., 1998).

Source Terms New source terms for atmospheric input and dissipation have been proposed (see e.g discussion above and papers at this conference) but few have found their way into fully working wave models

and thoroughly tested against real data. The ultimate objective is a wave model which includes source terms for atmospheric input and dissipation based upon correct physical processes and which are free of arbitrary tuning coefficients, and more accurate non-linear source term integration schemes. Such a model should correctly describe the wave evolution from flat calm initial conditions to a fully developed sea state if indeed such a state exists. Current 3G models are a step along the way toward such a model, but there is still a long way to go.

The concept of a fully developed sea continues to play a large role in wave models. In 1G and 2G models this limit to growth is usually explicitly invoked. In most 3G models, the dissipation source term is tuned such when the model is driven by constant winds the detailed balance leads to an equilibrium or very slowly evolving spectrum at large fetch or duration. Resio et al. (1998) have shown that a rescaling of the reference wind speed in a fully developed spectrum formulation (e.g. P-M) in terms of a dynamic reference height which increases with increasing wave height may explain the tendency of all models to underestimate extreme sea states (Figure 4.)

Directional Wave Spectrum Model performance has been assessed above mainly in terms of integrated properties of the spectrum. While it may be implied that a spectral model which attempts to model the detailed source term balance and which skillfully predicts the integrated properties, must also be modeling the entire 2-D spectrum correctly, this is not necessarily the case. For example, it has been noted above that while the 3G approach has led to somewhat more accurate specification of SWH in hindcasts, these models appear to have bias in specifications of wave period (not enough low frequency energy) in wind seas. Some users of operational wave analyses and forecasts (most of which are now based on some cycle of WAM) suspect a deficiency of swell not characteristic of previous forecast systems based on tuned 1G or 2G models (e.g. Whittman et al., 1995). This deficiency, if real, may be related to the deficiency of low frequency energy in the swell source zones which exhibits itself as a small negative bias in peak or average wave period.

Relatively few studies have been reported which compare model and measured directional spectra. For example, Jensen et al. (1995) compared WAM-4 hindcast and measured 2-D spectra at several data buoys off the US East Coast in two storm events (one tropical, one extratropical) in terms of mean wave direction and rms spreading. While generally good agreement was found for mean wave direction, systematic differences were often found for spreading. Forristall and Greenwood (1998) investigated the directional spread of various models as compared to measurements in both simple fetch and duration wave generation regimes and in tropical and extratropical storm hindcasts. To represent spreading, they adopted a measure based on second trigonometric moments of the wave spectrum which is equivalent to the square root of the "in-line variance ratio" defined by Haring and Heideman (1980). This ratio is an important measure of the wave load on an offshore structure. Figure 5 shows this spreading factor as a function of non-dimensional frequency for various models for a 20 m/s wind speed and 48 hour duration compared to measurements. Near the peak frequency model differences are small but all have spreading factors less than (therefore too broadly spread) the measured spreading. In the tail of the spectrum, the WAM-4 model (PHIDIAS in the figure) has a lower spreading factor than the measurements, while the OWI3G (which includes the aforementioned DIA2 non-linear source term algorithm) and EXACT-NL models agree more closely with the data, suggesting that the inclusion of a second mode of non-linear interactions in DIA2 is responsible for the improved spreading. The spreading exhibited by ODGP2 (not shown) actually agreed best with the measured data, but this is not surprising because in that model the spreading in a pure duration test is constrained to follow a prescribed empirical form (SWOP).

Forristall and Greenwood (1998) also found good agreement between modeled and measured spreading factors at two sites in the northern North Sea in a 5-year continuous hindcast made with OWI3G, but not so good agreement between hindcast and measurements at a site in the northern Gulf of Mexico on the left side of the track of severe hurricane Opal (1995). We have also observed less skill in OWI3G and WAM hindcasts of 2-D spectra details to the left of the tracks of tropical cyclones Frederic (1979) and Luis (1995) than hindcasts with ODGP driven by the same wind fields (unpublished).

Real Time Applications. Real time wave predictions provided by regional and global wave models are routinely verified at most centers against wave heights and period estimated by accelerometers mounted in moored data buoys, and wave heights measured from spaceborne radar altimeters (e.g. Khandekar and Lalbeharry, 1996; Wittmann et al, 1995 and Jannsen et al., 1997). In the FNWOC and ECMWF implementations the mean forecast error in wave height is slightly positive at all horizons, a characteristic believed due to slightly positively biased surface wind fields provided by atmospheric models. At centers at which the buoy and altimeter wave height

measurements are assimilated into the wave model, the measurements are less useful as independent indicators of model skill. When evaluated against a reference forecast such as persistence or climatology, the skill in extended range global wave forecasts such as those made at FNMOC, ECMWF and in the private sector (Lacey and Chen, 1995) varies from an extremely close simulation of nature at analysis time to virtually useless simulations at forecast horizons beyond about 120 hours.. This is shown, for example, at a buoy in the western North Atlantic over a full year in Figure 6a, which shows the error growth by quarter in terms of SWH S.I. and Figure 6b which shows the skill against a very stringent measure which is a linear combination of climatology and persistence (Murphy, 1992). The error growth is almost completely attributable to the inevitable growth of error in atmospheric forecasts to the chaotic limit of deterministic skill at about 7 days. However, there is evidence (e.g Cardone et al., 1995b) that forecast of swell from distant storms may be quite skillful somewhat beyond five days if there is high skill in meteorological analyses and short range forecasts in the swell source zones.

With so many centers adopting essentially the same wave model for operational analysis and forecasting, the variations in accuracy of the model predictions will differ from center to center mainly due to differences in the forcing wind fields and whether or not wind and wave data from unconventional sources (moored buoys, satellite) are assimilated in real time. Typically, each center takes the wind field to drive the wave model from the output of its own numerical weather prediction (NWP) system, with care taken that input (either 10m wind or wind stress) is consistent with the wave model requirement (Perrie and Wang, 1995). Nevertheless, the error structure in the "analysis" winds may vary considerably from center to center (e.g Cardone et al., 1995) and such errors are typically much larger than may be achieved in detailed hindcast studies. Growth of error in forecast winds is mainly a function of growth of error in the NWP model. On a global scale, such error growth varies little from center to center. On a regional basis, locally implemented high-resolution NWP models should outperform global models, though much depends on the regional model initialization and calibration. Further improvements in accuracy of real-time wave predictions depends almost entirely on improvements in operational wind fields, not on further refinement of wave models.

## 3. SHALLOW WATER WAVE PREDICTION

### 3.1 Overview

The maturity level of shallow-water models is far less than that of deep-water wave models. Therefore, this part of our paper cannot rely on the wealth of detailed studies and intercomparisons of model performance available in deep water. Presently, there is no real consensus on the governing physics for waves in shallow water and even less agreement on numerical methods. Some models treat propagation in great detail while neglecting source terms. Other models include a number of source terms while neglecting or poorly approximating part of the propagation effects. Some model applications even persist in using the concept of "equivalent" monochromatic waves even though clear evidence has been given that this does not work (Vincent and Briggs, 1988).

For our purposes, we shall concentrate here on coastal regions with negligible currents and with depths which are at least two times the zero-moment wave height ($H_{m0}=4E_0^{1/2}$). For practical purposes, this means we will be excluding inlet areas and shallow, surf zone areas from our analyses. Inlets are excluded since wave blocking, reflection, trapping, breaking, and coupling to current fields are still fairly poorly understood and depend critically on details of the current field, which are often not known. The surf zone is excluded since simple parameterizations of wave height appear to provide an adequate first approximation to the wave field for many purposes in this area. This does not imply that significant research on higher-order processes (such as nonlinear shoaling, nonlinear run-up processes, and shallow-water spectral shape) is not needed, but simply that it does not seem to be as critical to many of the data needs as getting the waves from deep water up to the edge of the surf zone.

A recent advantage for shallow-water modelers is the increasing availability of high-quality wave measurements in paired locations offshore (i.e. one farther offshore than the other). At the U.S. Army Engineer Field Research Facility (FRF) in Duck, North Carolina, an extensive climatology of wave spectra has been collected. In general, if we examine wave spectra with significant wave heights greater than 2 meters at the FRF as documented in Long (1994), we see that wave spectra appear to undergo substantial evolution in moving from deep to shallow water at this site. In some cases wave heights are larger at the 8-meter depth than at the closest offshore gage (located in a depth of about 18 meters). In other cases, the wave heights are lower. In some cases, the spectral shapes seem similar at the two sites. In other cases, spectral shapes change dramatically.

A general framework for understanding wave transformations in intermediate and shallow water is provided by the radiative transfer equation, assuming negligible diffraction, i.e.

$$\frac{DE(f,\theta)}{Dt} = \frac{\partial E(f,\theta)}{\partial k_x}\frac{\partial k_x}{\partial t} + \frac{\partial E(f,\theta)}{\partial k_y}\frac{\partial k_y}{\partial t} + \frac{\partial E(f,\theta)}{\partial t}$$

Where E(f,theta) is the energy density in the spectrum at frequency f and direction theta; $k_x$ is the component of the wave number vector in the x-direction and $k_y$ is the component of the wave number vector in the y-direction. The first two terms on the right side of this equation represent the effects of propagation on a particular frequency-directional element of the spectrum, whereas the third term represents the effects of source terms on this element of the spectrum. In the past, many scientists and engineers often neglected the third term in calculating wave conditions for shallow-water designs; however, it is not clear that this is a reasonable approach to this problem.

As discussed by Ris (1997), two broad classes of models are generally applied to coastal problems: phase resolving and phase averaged. The inclusion of wave phases into models is required for accurate solutions for wave diffraction and for deterministic solutions involving triad interactions. Phase resolving models can be solved in the time domain (for example: Madsen et al, 1991, 1992, and 1994) or in the frequency domain (for example: Berkoff, 1972; Radder, 1979; Kirby, ????). Frequency domain solutions are typically based on the mild-slope equation which assumes that the wave field is slowly varying over the spatial scale of a typical wavelength; whereas, time-domain solutions have far less restrictions in this area. Presently, a major drawback to the application of all phase-resolving models over large distances is their inability to include important source terms within their formulation.

Phase-averaged models are typically solved in the frequency domain and represent a large segment of what are commonly termed spectral models. Two models in this class gaining some popularity of late are SWAN (Ris, 1997) and STWAVE (Resio, 1988). Models of this type can either solve the complete radiative transfer equation or can assume a steady-state approximation for estimating wave conditions within the computational grid. A major drawback to this class of models has been the difficulty in incorporating wave diffraction into the propagation solution.

Previous assessments of shallow-water wave models have concentrated on demonstrating the importance of a particular term in a particular situation. Thus, if one examines monochromatic waves near an island, one will conclude that diffraction is essential (Dalrymple....). Or, if one examines waves inside a shallow barred area, one will conclude that triad interactions are very important (Eldeberky and Battjes, 1996). Or, if one observes an energy loss between two points, one can invoke a particular dissipation mechanism to explain this loss (Shemdin et al., 1988; Bertotti and Cavaleri, 1994). In this paper, we shall attempt first to establish some simple guidance to help us understand the relative importance of various terms in the total solution and second to formulate some recommendations for needed work in this area.

### 3.2 Assessment of Modeling Approaches

The strength of phase-averaged models seems to lie in their ability to include arbitrary (random-phase) source terms. The strength of phase-resolving models seems to lie in their ability to include diffraction and nonlinear propagation effects in wave transformations. Thus, it seems logical here (1) to estimate the magnitude of different source terms in certain situations relative to propagation effects and (2) to examine the potential magnitude of diffraction effects in coastal areas. This should assist in determining some approximate limits to the application of models without source terms as well as the applicability of models which neglect diffraction.

For simplicity here, we shall examine the integrated effects (over all frequencies and directions) of source terms and propagation effects. For wind input, white-capping, bottom friction and refraction, this will be estimated here by integrating over the range of frequencies 0 to $3f_p$. For 4-wave interactions, this will be estimated from the flux of energy into higher frequencies at $3f_p$.

### 3.3 Evaluation of Propagation Effects

To evaluate an approximate magnitude of refraction and shoaling effects, we will restrict bottom bathymetries to situations with depth contours which are locally parallel over a distance of at least a few wavelengths. In this case, diffraction effects should be very small, and refraction and shoaling along a wave ray will be governed by the equation

$$E(f,\theta)cc_g = constant$$

where $c_g$ is the group velocity.

Although many different mechanisms have been proposed for shallow water areas, the set of source terms which will be treated here includes only the following: wind input, nonlinear wave-wave interactions, wave breaking, and bottom friction. All of these terms depend on the selection of an initial

spectrum, and all except for wind input have forms which are nonlinearly related to water depth. In this paper we will represent our initial spectra in terms of JONSWAP parameterizations with a $\cos^{2n}$ directional spreading.

### 3.4 Evaluation of Wind Input

There is some agreement among researchers (Komen et al., 1994) that the wind input into the wave field can be represented by the sum of a linear and an exponential term, i.e.

$$S_{in}(f,\theta) = A(f,\theta) + B(f,\theta)E(f,\theta)$$

where the first term is typically a variation of Phillips (1957) theory for energy input by air pressure fluctuations advected by the wind, and the second term is a variation of Miles (1957) theory for the interaction between waves and shear in the atmospheric boundary layer. In this paper we shall use the form for the linear term which given in Ris (1997). This form is adapted from an equation originally proposed by Cavaleri and Malanotte-Rizzoli (1981). Given an initial spectrum, we can now integrate this equation to obtain the total energy input by the wind into the wave field over a fixed time.

### 3.5 Evaluation of Wave-Wave Interaction Fluxes

Considerable debate persists over the role of nonlinear source terms in shallow water. Two different types of nonlinear interactions have been postulated to have potential significance in shallow-water wave transformations, three-wave (triad) interactions and four-wave (quartic) interactions. The governing integro-differential equations for these forms of interactions can be found in Zakharov (1968) and Heterich and Hasselmann (1982). Neither of these equations reduces to a simple form but instead must be estimated numerically. The characteristic signatures of these two types of energy transfers are quite different from one another. Strong triad interactions tend to generate a secondary peak in the spectrum at about twice the frequency of the spectral peak while strong quartic interactions tend to force monochromatically decreasing spectral equilibrium forms with characteristic $k^{-n}$ shapes (where n is a positive real number).

In random-phase, homogeneous wave fields, only quartic interactions can transfer energy from one region of a spectrum to another. Long (1994) examined all wave spectra for wave conditions with heights of over 2.0 meters measured at the FRF during the interval September 1986 to July 1991. Examination of all spectra contained in this report shows that in none of the measured spectra is the energy content at the harmonic frequencies very large compared to the spectral peak itself; however, this is not to say that they are not important to certain processes sensitive to this type of nonlinearity (i.e. sediment transport, mass transport, etc.). Also, it should be noted that the bottom slope at this site is fairly shallow. Since rapid variations in depth can introduce inhomogeneities into the wave field, significant phase correlation can be generated over bars and steep slopes. Thus, this type of interaction will likely become more important for waves on steeper slopes than found at the FRF.

Little quantitative work has been done on shallow-water quartic interactions since Heterich and Hasselmann (1982). Recently however, Rassmussen (1995) reprogrammed the Heterich-Hasselmann form of this equation and Resio (unpublished) extended the deep-water form of Resio and Perrie (1991) to allow more efficient estimates of these interactions to be made. Comparisons of the results from these three different integration methods have shown them to produce essentially equivalent results. The shallow-water extension of the Resio-Perrie method will be used here for all calculations. Energy fluxes at $3f_p$ are explicitly calculated within the numerical code.

It is well known that wave-wave interactions vary in intensity as the depth changes. Figure 7 shows a set of full-integral estimates for $S_{nl}$ for a JONSWAP spectrum ($\alpha$=0.01, $f_p$=0.01, $\gamma$=3.3, $\sigma_a$=0.07, $\sigma_b$=0.09) in depths of 80, 40, 20, and 10 meters. As can be seen here, the results for 80 meters and 40 meters are quite similar. Further decrease in depth from 40 to 20 meters results in a source term with about the same form, but with increasing magnitude, consistent with the similarity-scaling formulation of Heterich and Hasselmann (1982). However, when the depth is decreased further to 10 meters, the source term not only becomes substantially larger but also changes its form. Numerical studies show that the equilibrium form of the spectrum shifts in a fashion which is consistent with the TMA spectral formulation (Figure 8). This figure shows an initial JONSWAP spectrum (normalized by a $k^{-2.5}$ multiplicative factor) which evolves under the action of $S_{nl}$ to an equilibrium form that has a constant $k^{-2.5}$ form, consistent with the observations of Miller and Vincent (1990).

### 3.6 Evaluation of Wave Breaking (Whitecapping)

Whitecapping as represented in both WAM and SWAN is related primarily to wave steepness. In this paper, we shall use the whitecapping form adapted by

WAMDI (1988)

$$S(f,\theta)_{ds,w} = -\Gamma \bar{f} \frac{k}{\bar{k}} E(f,\theta)$$

where

$\Gamma$ *is a steepness-dependent coefficient*

and the overbar over f and k denotes the average values for frequency and wavenumber, respectively.

3.7 Evaluation of Wave Breaking (Due to Depth Limitations)

Since we are mainly interested in waves outside the surf zone, we shall take this term to be negligible. This may not be a very good assumption as the surf zone is approached; however, it will suffice for our purposes here.

3.8 Evaluation of Bottom Friction

The form for the bottom friction source term used here is due to Bertotti and Cavaleri (1994)

$$S(f,\theta)_{ds,b} = C_b \frac{f^2}{g^2 \sinh^2(kd)} E(f,\theta)$$

where $C_b$ is a dimensionless coefficient. Although many papers have advocated using a highly variable representation for $C_b$, almost an equal number have advocated using just a simple constant value. For simplicity in this paper we shall adopt the latter approach and use a constant value of 0.038 for $C_b$.

3.9 Evaluation of Source Term Effects Relative to Propagation Effects

For a given spectral shape (TMA, JONSWAP, etc.), the magnitude of source terms listed above depends on wave height, peak frequency, and wind speed. Similarly, the magnitude of propagation effects will be a function of wave height, wave period, and bottom slope. Rather than vary all of these terms independently, let us restrict our analyses to three situations that are typical in most coastal areas: growing seas, fully-developed seas, and swell. We shall represent all three cases in terms of JONSWAP spectra with $\sigma_a$=0.07 and $\sigma_b$=0.09. Growing seas are characterized here by u=20 m/sec, $f_p$=0.167 hz, $\alpha$=0.015, and $\gamma$=3.3. Fully-developed seas are characterized by u=15 m/sec, $f_p$=0.1 hz, $\alpha$=0.0081, and $\gamma$=1.0. Swell will be characterized by u=10 m/sec, $f_p$=0.067, $\alpha$=0.0002, and $\gamma$=7. Source terms for these three types of spectra will be examined in depths of 80, 40, 20, and 10 meters. Slopes of 1/1000, 1/100, and 1/10 and mean angles relative to these slopes of 0-, 45-, and 90-degrees will be considered to cover the range of all of the pertinent parameters here.

Tables 4-6 present estimates of rate of change (i.e. total change in energy over 1 second) for all source terms and propagation effects times $10^6$. In this table the following notation is used:

| | | |
|---|---|---|
| S1 | - | nonlinear 4-wave interaction fluxes |
| S2 | - | wind input |
| S3 | - | whitecapping |
| S4 | - | bottom friction |
| S5a | - | refraction/shoaling on 1/1000 slope |
| S5b | - | refraction/shoaling on 1/100 slope |
| S5c | - | refraction/shoaling on 1/10 slope |

Growing seas

As shown in Table 4, nonlinear fluxes of energy toward higher frequencies represent a critical source term for growing seas. Only for the case of waves at $90^0$ to the bottom slope (maximum refraction effects) on a 1/10 slope does any other source term become larger. For slopes typical of the area off the FRF (1/300), it appears that $S_{nl}$ should play a very important role in the evolution of spectra propagating into the linear array in 8-meters depth. Wind input is the second largest source term in depths of 40 meters and greater and is of comparable magnitude to refraction even into a depth of 10 meters. For wind seas in depths of 20 meters and less, it appears that an accurate solution for spectral evolution must consider at least $S_{nl}$, wind input, and refraction. Present formulations for whitecapping and bottom friction do not appear to play a very significant role for this case.

Fully-developed seas

Since the waves are less steep in this case, $S_{nl}$ is smaller in deep water; however, in shallow water these interactions become even larger than for the wind-sea case. It is apparent in Table 5 that the importance of refraction has significantly increased over that for the wind-sea case, making it the largest source term in depths of 40 meters and less, for slopes of 1/100 and greater. Again, however, for slopes that are typical of the FRF area, $S_{nl}$ is still the largest source term even into depths as shallow as 10 meters. As was found for the wind-sea case, an accurate solution to the spectral evolution equation should consider at a minimum $S_{nl}$,

wind input, and refraction.

Swell

As shown in Table 6, the swell case is very much dominated by refraction effects. The low wave steepness and wind speeds for this case produce very small values for $S_{nl}$ and wind input. Surprisingly, bottom friction seems to only play a minor role in this case.

3.10 Assessment of the Role of Diffraction in Coastal Regions

As noted earlier, the major failing of models which incorporate random-phase source terms is the difficulty in treating combined refraction-diffraction within the phase-averaged formulation. Although some arguments have been given that diffraction "averages out" for the case of broad spectra (Ris, 1997), there has been little investigation into the potential magnitude of error due to its neglect. In order to investigate this error parametrically in this paper, we shall define wave characteristics behind a gap between two islands, with and without diffraction effects, $\cos^2$, $\cos^{16}$, and $\cos^{64}$ directional distributions. The estimate for the "exact" diffraction pattern comes from the Huygens-Kirchoff integral formulation

$$e(f,\theta,x,y)^{1/2} = \left| \int_{y_1}^{y_2} \frac{e(f,\theta,x_0,y)^{1/2}}{\sqrt{r}} \phi(\theta_0,\alpha_0) e^{ip(x,y)} dy \right|$$

where $e(f,\theta,x,y)^{1/2}$ is the wave amplitude at a point x,y beyond the island gap, $\phi$ is the obliquity factor, $\rho$ is wave phase, $y_1$ is the y-value at one boundary, $y_2$ is the y-value at the other boundary, and the subscript "0" denote values along a line between the two islands (i.e. at the boundary for this calculation). Since different directional bands will not be correlated in phase, the wave height at x,y is still estimated as $4E(x,y)_0^{1/2}$, where

$$E(x,y)_0 = \int_0^{2\pi} e(f,\theta,x,y) d\theta$$

An estimate for the wave energy without diffraction can be taken from geometric optics as

$$E(x,y)_0 = \int_0^{2\pi} e(x_0,y_c,\theta) H_1 H_2 d\theta$$

where $H_1$ and $H_2$ are two Heaviside functions used to ensure that a receiving point (x,y) is within the geometric beam of width $y_2$-$y_1$ centered at $y$ and traveling at angle $\theta$.

Figure 9a shows a comparison for the case of a $\cos^2$ directional spreading at a distance behind the gap of 16 wavelengths, for a gap width of 5 wavelengths and a principal propagation direction of $45^0$. Figure 9b shows the same situation except at a distance of 64 wavelengths past the gap. As can be seen here, the "no-diffraction" estimate for broad spectra is not too bad close to the gap, but degenerates into a "garden-sprinkler" pattern at larger distances.

Figure 10a shows a comparison for the case of a $\cos^{16}$ directional spreading at a distance behind the gap of 16 wavelengths, again for a gap width of 5 wavelengths and a principal propagation direction of $45^0$. Figure 10b shows the same situation except at a distance of 64 wavelengths past the gap. Once again, the "no-diffraction" estimate is not too bad close to the gap, but degenerates into a "garden-sprinkler" pattern at larger distances.

Figure ?? shows a comparison for the case of a $\cos^{64}$ directional spreading at a distance behind the gap of 16 wavelengths, again for a gap width of 5 wavelengths and a principal propagation direction of $45^0$. Figure ?? shows the same situation except at a distance of 64 wavelengths past the gap. In this case a somewhat different pattern emerges, with less "garden-sprinkler" effect, but larger error, due to narrowness of the directional distribution.

These comparisons show that, even for directionally distributed spectra, diffraction effects should be treated in certain situations where strong gradients in the wave field are created (such as propagation past gaps). In general, the agreement is worsened as the directional distribution becomes narrower; thus, for the case of waves (particularly swell) propagating through an inlet or past some offshore islands, it seems that the effect of diffraction does not seem to average out and should not be included into the propagation scheme. For cases with smaller (continuous) gradients in the wave field, the effects of diffraction will be much less than for the case of the discontinuous gradients shown here. Consequently, it is possible that the zero-diffraction solution might be adequate for offshore areas with no islands.

4. CONCLUSIONS

4.1 Deep Water

The SWAMP model intercomparison exercise carried out in the early 1980s painted a rather chaotic picture

of international state of wave modeling up to that time. A large variance in model formulation and tuning was found to provide a large scatter in model predictions in even the simplest wave generation regimes. Today, there is much greater homogeneity and accuracy in wave model performance resulting generally in more reliable global wave forecasts and wave climate assessments. This improvement is attributable to several main factors: (1) the widespread distribution and implementation of the WAM model and computer code; (2) the demonstration that a few of the 1G and 2G pre-SWAMP models actually provide skill comparable to WAM and, therefore, may continue to be exploited in a wide range of practical applications, especially where supercomputer power is not available; (3) improved marine wind field analyses and forecasts at global NWP centers, aided at some centers by the assimilation of remotely sensed wind and wave data.

Despite this progress, several problems areas are revealed, mainly through the biases in 3G model specification of the wave heights in very high sea states, errors in specification of details of the 2-D spectrum such as peak period and angular spreading in simple regimes, and large errors in specification of 2-D spectra in more complicated wave regimes such as tropical cyclones. In fact, in some of these respects, 3-G models may be outperformed by well-tuned 1G and 2G models, the latter admittedly constrained by empirical rather than physical formulations for spectral shape. There is certainly a need for further refinement of the source terms for input and dissipation and more accurate numerical approximation of wave-wave interactions. Fortunately, there is a growing base of high-quality wind fields and measured wave data becoming available to wave modelers to allow testing of more physically-based source terms. To the standard SWAMP test cases may be added the excellent SWAMP IOP data sets for which wind fields of unprecedented accuracy and resolution have been produced, data sets in a number of well-documented extratropical and tropical cyclones, and recently produced basin-wide global data sets where winds are based on results of major NWP center reanalysis projects and for which global wave data sets are provided by satellite radar systems. Work has begun at USAE CERC on the development of a virtual wave model test bed facility which assembles the drivers for the standard tests and the above noted wind fields and measured wave data sets for the real test cases in a convenient form for alternative wave model evaluation. This facility will also include a standard package for the statistical evaluation of model performance and will be made available to the international wave modeling community.

4.2 Shallow Water

From the analyses conducted here, the following conclusions can be drawn: (1) for many important wave conditions in coastal areas it is important to consider wind effects and nonlinear wave-wave interactions, as well as wave propagation effects; (2) diffraction may be negligible in offshore areas without islands but significantly affect wave conditions in areas behind islands.

Based on these results, it appears that both the phase-averaged and phase-resolving models may have an important role to play in the future. It seems logical to separate the solution into two parts, one covering the larger scale on which source terms are critical (10's of wavelengths and larger) and a second covering smaller-scale regions in which combined diffraction-refraction-reflection can be important (1's of wavelengths).

Due to the apparent importance of source terms (with perhaps only vaguely-known empirical constants in their formulations) to shallow-water wave predictions, it will be extremely important for careful benchmark studies to be conducted in the future. These benchmark tests should cover a wide range of growing sea, fully-developed, and swell conditions for a wide range of depths and wave periods. Only after such studies have been completed can we begin to put as much faith in shallow-water wave predictions as we do in deep-water predictions.

5. REFERENCES

Bacon, S. and D.J.T. Carter. (1994). "a connection between mean wave height and atmospheric pressure gradient in the North Atlantic." J. of Climatology. 13. 423-436.

Banner, M.L. and I.R. Young. (1994). "Modeling spectral dissipation in the evolution of wind waves. Part 1: Assessment of existing model performance." J. Phys. Oceanog., 24. 1550-1571.

Bender, L.C. (1996). "Modification of the physics and numerics in a third-generation ocean wave model." J. of Atmos. and Oceanic Technol. 13. 726-750.

Bruning, C., S. Hasselmann, K. Hasselmann, S. Lehner and T. Gerling. (1994). "A first evaluation of ERS-1 synthetic aperture radar wave mode data." The Global Atmosphere and Ocean System. 2. 61-98.

Bouws, E., H. Gunther, W. Rosenthal, and C.L. Vincent. (1985). " Similarity of the wind wave spectrum in finite depth water, 1. Spectral form." J. Geophys. Res. 90: 975-986.

Cardone, V. J., W. J. Pierson and E. G. Ward. (1976). "Hindcasting the directional spectra of hurricane generated waves." J. Petrol. Technol. 28, 385-394.

Cardone, V.J. and C. K. Grant. (1994). "Southeast Asia meteorological and oceanographic hindcast study (SEAMOS)." OSEA 94132. Offshore South East Asia 10th Conference & Exhibition. Singapore, 6-9 December 6-9.

Cardone, V. J., H.C. Graber, R.E. Jensen, S. Hasselmann and M. J. Caruso. (1995a). "In search of the true surface wind field in SWADE IOP-1: ocean wave modeling perspective." The Global Atmosphere and Ocean System. 3. 107-150.

Cardone, V.J., C.K. Cooper and D. Szabo. (1995b). "A hindcast study of the extreme wave climate of offshore West Africa (WAX)." OTC 007687 Offshore Technology Conference, Houston, 1-4 May. 439 -451.

Cardone, V.J., R.E. Jensen, D.T. Resio, V.R. Swail and A.T. Cox. (1996). "Evaluation of contemporary ocean wave models in rare extreme events: the "Halloween Storm" of October, 1991 and the "Storm of the Century" of March, 1993." J. Atmos. Oceanic. Technol. 13. 198-230.

Cox, A.T., J.A. Greenwood, V.J. Cardone and V.R. Swail. (1995). "An interactive objective kinematic analysis system." The International Workshop on Wave Hindcasting and Forecasting. Banff, Alberta, 16-20 October. 109-118. (Available from Atmospheric Environment Service, Downsview, Ontario.)

Cox, A.T., V. J. Cardone and V. R. Swail. (1998). Evaluation of NCEP/NCAR Reanalysis Project marine surface wind products for a long term North Atlantic wave hindcast. Proc. 5th International Workshop on Wave Hindcasting and Forecasting, Melbourne, FL, January 26-30, 1998.

Eldeberky, Y. and J.A. Battjes (1995). "Parameterisation of triad interactions in wave energy models." Proc. Coastal Dynamics Conf. '95., Gdansk, Poland, pp. 140-148.

Ewans, K.C.. (1995). "Observations the directional spectrum of fetch-limited waves off the west coast of New Zealand." 4th International Workshop on Wave Hindcasting and Forecasting. Banff, Alberta. 16-20 October. 263-278. (Available from Atmospheric Environment Service, Downsview, Ontario.)

Foreman, S.J., M.W. Holt and S. Kelsall. (1994). "Preliminary assessment and use of ERS-1 altimeter mode data." J. Atmos. Oceanic. Technol. 11. 1370-1380.

Forristall, G.Z. and J. A. Greenwood. (1998). "Directional spreading of measured and hindcasted wave spectra." Proc. 5th International Workshop on Wave Hindcasting and Forecasting, Melbourne, FL, January 26-30, 1998.

Graber , H. C., R. E. Jensen and V. J. Cardone. (1995). "Sensitivity of wave model predictions on spatial and temporal resolution of the wind field." 4th International Workshop on Wave Hindcasting and Forecasting. Banff, Alberta. 16-20 October. 263-278. (Available from Atmospheric Environment Service, Downsview, Ontario.)

Greenwood, J.A., V.J. Cardone and L. M. Lawson. (1985). "Intercomparison test version of the SAIL wave model." Ocean Wave Modelling, the SWAMPO Group, Plenum Press, 221-233.

Gunther, H.P.L. and 14 coauthors. (1992). "Implementation of a third generation ocean wave model at the European Center for Medium Range Weather Forecasts." ECMWF Tech. Rep. 68. European Center for Medium Range Weather Forecasting, Reading, United Kingdom. 34 pp.

Haring, R.E. and J. C. Heideman. (1980). "Gulf of Mexico rare wave return periods." J. Petrol. Tech ., 35-37.

Heras, M., G. Burgers and P.A.E.M. Janssen. (1994). "Variational data assimilation in a third-generation wave model." J. Atmos. Oceanic. Technol. 11. 1350-1369.

Janssen, P.A.E.M. (1991). "Quasi-linear theory of wind-wave generation applied to wave forecasting." J. Phys. Oceanog. 2. 1631-1642.

Janssen, P.A.E.M., B. Hansen, and J. Bidlot. (1997). "Verification of ECMWF wave forecasting systems against buoy and altimeter data." To appear in Weather and Forecasting ( December).

Khandekar, M.L., R. Lalbeharry and V.J. Cardone. (1994). "The performance of the Canadian spectral ocean wave model (CSOWM) during the Grand Banks ERS-1 SAR wave spectra validation experiment." Atmosphere-Ocean. 32. 31-60.

Khandekar, M.L. and R. Lalbeharry. (1996). "An evaluation of Environment Canada's operational ocean

wave model based on moored buoy data." Wea. Forecasting. 11. 137-152.

Komen G. J., L. Cavalieri, M. Donelan, K. Hasselmann, S. Hasselmann and P.A.E.M. Janssen. (1994). "Dynamics and Modeling of Ocean Waves." Cambridge University Press. 532pp.

Kushnir, Y., V.J. Cardone, J.G. Greenwood and M. Cane. (1995). "Link between North Atlantic climate variability of surface wave height and sea level pressure." 4th International Workshop on Wave Hindcasting and Forecasting. Banff, Alberta, 16-20 October 16-20. 59 - 64. (Available from Atmospheric Environment Service, Downsview, Ontario.)

Lacey, P. and H. Chen. (1995). Improved passage planning using weather forecasting, maneuvering guidance, and instrumentation feedback. Marine Technology, 32. 1-19.

Lalbeharry, R., L.J. Wilson, J. Mailhot, V. Lee, W. Perrie, L. Wang and B. Toulany. (1995). "Toward a consistent boundary layer formulation in operational atmospheric and wave models." 4th International Workshop on Wave Hindcasting and Forecasting. Banff, Alberta, 16-20 October. 199 - 212. (Available from Atmospheric Environment Service, Downsview, Ontario.)

Lin, R.Q. and N.E. Huang. (1996). "The Goddard coastal wave model. Part I: numerical method." J. Phys. Oceanog.. 26. 833-847.

Lin, R.Q. and N.E. Huang. (1996). "The Goddard coastal wave model. Part II: kinematics." J. Phys. Oceanog. 26. 848-862.

Long, S.R., N.S. Huang, E. Mollo-Christensen, F.C. Jackson, G.L. Geernaert. (1994). "Directional wind wave development." Geophys. Res. Lett.. 21. 2503-2506.

Madsen, P.A. and O.R. Sorensen. (1992). " A new form of the Boussinesq equations with improved linear dispersion characteristices, Part 2. A slowly-varying bathymetry." Coast. Eng., 18: 183-204.

Madsen, P.A.., R. Murray, and Sorensen. (1991). "A new form of the Boussinesq equations with improved linear dispersion characteristics." Coast. Eng., 15: 371-389.

Madsen, P.A., O.R. Sorensen, and H.A. Schaffer. (1994). "Time domain modelling of wave breaking, runup, and surf beats." 24th Int. Conf. On Coastal Engineering, Am. Soc. Civ. Eng., New York, NY, pp. 399-411.

Miller, H.C. and C.L. Vincent. (1990). " FRF spectrum: TMA with Kitaigorodskii's $f^{-4}$ scaling." ASCE J. Waterw. Port Coastal Ocean Div. 116:57-78.

Murphy, A.H. (1992). "Climatology, persistence and their linear combination as standards of reference in skill scores." Weather and Forecasting, 7, 692-698.

Perrie, W. and L. Wang. (1995). "a coupling mechanism for winds and waves." J. Phys. Oceanog.. 25. 615-630.

Peters, D.J., C.J. Shaw, C.K. Grant, J.C. Heideman and D. Szabo. (1993). "Modeling the North Sea through the North European Storm Study." OTC 7130, Offshore Technology Conference, Houston, 3-6 May. 479-493.

Resio, D.T. (1987). "Shallow-water waves. I: Theory." J. Wtrway., Port, Coast., Oc. Eng., 113 (3), 264-281.

Resio, D.T. (1988). "Shallow-water waves. II: Data comparisons." J. Watrway., Port, Coast. OC. Eng., 114 (1), 50-65.

Resio, D.T. (1993). "Full Boltzman discrete spectral wave model, implementation and nondimensional tests." Contract Report CERC-93-1. U.S. Army Waterways Experiment Station, Vicksburg, MS.

Resio, D. T., V. R. Swail, R. E. Jensen and V. J. Cardone. (1998). Wind speed scaling in fully developed seas. Submitted to J. of Phys. Oceanog.

Skey, S.G.P., K. Berger-North, V.R. Swail. (1995). "Detailed measurements of winds and waves in high sea states from a moored NOMAD weather buoy." 4th International Workshop on Wave Hindcasting and Forecasting. Banff, Alberta, 16-20 October. 213-224. (Available from Atmospheric Environment Service, Downsview, Ontario.) (see update this conference).

Sterl, A., G. J. Komen and P. D. Cotton. (1998). 15 years of global wave hindcasts using ERA winds: validating the reanalyzed winds and assessing the wave climate. To appear in J. of Geophys. Res. (Oceans).

Swail, V.R., M. Parsons, B.T. Callahan and V.J. Cardone. (1995). "a revised extreme wave climatology for the Canadian east coast." 4th International Workshop on Wave Hindcasting and Forecasting.

Banff, Alberta. 16-20 October. 81-92. (Available from Atmospheric Environment Service, Downsview, Ontario.)

Swail, V. R., V. J. Cardone and A. T. Cox. (1998). "a long term North Atlantic Wave hindcast." Proc. 5th International Workshop on Wave Hindcasting and Forecasting, Melbourne, FL, January 26-30, 1998.

Tolman, H. L. and D. Chalikov. (1996). "Source terms in a third-generation wind wave model." J. Phys. Oceanog. 26. 2497-2518.

Vincent, C.L. and M.J. Briggs (1988). "Refraction - diffraction of irregular waves over a mound." Submitted to J. Wtrway., Port, Coast., and Oc. Eng.

WASA Group (coordinator H. von Storch). (1995). "The WASA project: changing storm and wave climate in the northeast Atlantic and adjacent seas?" . 4th International Workshop on Wave Hindcasting and Forecasting. Banff, Alberta, 16-20 October. 31- 44. (Available from Atmospheric Environment Service, Downsview, Ontario.)

Wittmann, P.A., R.M. Clancy and T. Mettlach. (1995). "Operational wave forecasting at Fleet Numerical Meteorology and Oceanography Center, Monterey, CA.." 4th International Workshop on Wave Hindcasting and Forecasting. Banff, Alberta, 16-20 October. 335 - 342. (Available from Atmospheric Environment Service, Downsview, Ontario.)

Young, I.R., L.A. Verhagen and M.L. Banner. (1995). "a note on the bimodal directional spreading of fetch-limited waves." J. Geophys. Res., 100 (c1). 773-778.

**Table 1: Comparison of SWADE IOP-1 (22-31 October, 1990) WAM-4 hindcast driven by kinematically reanalyzed wind fields (OW/AES) against deep water buoys in inner SWADE array.**

| | WS (m/s) | θ (°) | SWH (m) | TP (s) |
|---|---|---|---|---|
| Bias | -0.05 | 0.6 | -0.13 | -0.39 |
| Rms | 0.97 | 22 | 0.37 | 0.82 |
| S.I. (%) | 10 | 6 | 14 | 13 |
| C.C. | 0.99 | - | 0.98 | 0.89 |

Bias: Hindcast-measured
Rms: Root mean square difference
S.I.: Scatter index (standard deviation/mean of measurements x 100%)
C.C.: Correlation coefficient

**Table 2: Validation of North Atlantic Ocean continuous hindcasts of indicated months with OWI3G driven by NRA surface winds, against buoy and ERS-1 altimeter wave measurements.**

| Year/Month | Variable | All Buoys | | | | ERS-1 Altimeter | | | |
|---|---|---|---|---|---|---|---|---|---|
| | | Num | Bias | rms | S.I. | Num | Bias | rms | S.I. |
| 9110 | WS | 882 | 0.12 | 2.96 | 0.34 | 16,808 | 0.34 | 2.13 | 0.29 |
| | SWH | 758 | 0.01 | 0.77 | 0.24 | 16,703 | -0.20 | 0.65 | 0.24 |
| | TP | 876 | -1.47 | 2.95 | 0.31 | - | - | - | - |
| 9303 | WS | 868 | -0.28 | 2.31 | 0.24 | 17,517 | 0.43 | 2.19 | 0.26 |
| | SWH | 871 | -0.07 | 0.73 | 0.24 | 16,972 | -0.05 | 0.61 | 0.20 |
| | TP | 871 | -1.08 | 2.76 | 0.32 | - | - | - | - |
| 9504 | WS | 600 | -0.15 | 2.30 | 0.33 | 17,693 | 0.37 | 1.97 | 0.27 |
| | SWH | 720 | 0.04 | 0.60 | 0.26 | 17,551 | -0.01 | 0.54 | 0.23 |
| | TP | 720 | -0.85 | 1.74 | 0.16 | - | - | - | - |
| 9509 | WS | 761 | 0.36 | 2.68 | 0.41 | 18,081 | 0.05 | 2.30 | 0.35 |
| | SWH | 834 | -0.11 | 0.62 | 0.30 | 18,059 | -0.46 | 0.74 | 0.25 |
| | TP | 832 | -1.30 | 2.30 | 0.26 | - | - | - | - |
| All Months | WS | 3,111 | 0.01 | 2.59 | 0.33 | 70,099 | 0.30 | 2.15 | 0.29 |
| | SWH | 3,183 | -0.03 | 0.68 | 0.26 | 69,285 | -0.18 | 0.64 | 0.23 |
| | TP | 3,299 | -1.17 | 2.48 | 0.27 | - | - | - | - |

**Table 3: Comparison of OWI3G and ODGP2 North Atlantic Ocean continuous wave hindcasts driven by modified NRA wind fields with wave measurements from moored buoy and ERS-1 altimeter for March, 1993.**

| Variable | Model | All Buoys | | | | ERS-1 Altimeter | | | |
|---|---|---|---|---|---|---|---|---|---|
| | | Num | Bias | rms | S.I. | Num | Bias | rms | S.I. |
| WS | OWI3G | 868 | 0.19 | 1.04 | 0.11 | 17,517 | 0.46 | 2.26 | 0.27 |
| | ODGP2 | 868 | 0.19 | 1.04 | 0.11 | 17,517 | 0.46 | 2.26 | 0.27 |
| SWH | OWI3G | 871 | 0.09 | 0.68 | 0.22 | 16,972 | 0.05 | 0.63 | 0.21 |
| | ODGP2 | 871 | 0.01 | 0.78 | 0.25 | 16,972 | -0.05 | 0.69 | 0.23 |
| TP | OWI3G | 871 | -0.99 | 2.76 | 0.32 | - | - | - | - |
| | ODGP2 | 871 | -0.58 | 2.78 | 0.34 | - | - | - | - |

**Table 4: Growing Sea**

0 Degrees

| Depth (m) | S1 | S2 | S3 | S4 | S5a | S5b | S5c |
|---|---|---|---|---|---|---|---|
| 10 | 212 | 33 | 1 | 1 | 8 | 38 | 76 |
| 20 | 104 | 30 | 1 | 0 | 9 | 47 | 94 |
| 40 | 93 | 29 | 1 | 0 | 1 | 4 | 8 |
| 80 | 93 | 29 | 1 | 0 | 0 | 0 | 0 |

45 Degrees

| Depth (m) | S1 | S2 | S3 | S4 | S5a | S5b | S5c |
|---|---|---|---|---|---|---|---|
| 10 | 212 | 33 | 1 | 1 | 19 | 92 | 175 |
| 20 | 104 | 30 | 1 | 0 | 11 | 53 | 106 |
| 40 | 93 | 29 | 1 | 0 | 1 | 4 | 8 |
| 80 | 93 | 29 | 1 | 0 | 0 | 0 | 0 |

90 Degrees

| Depth (m) | S1 | S2 | S3 | S4 | S5a | S5b | S5c |
|---|---|---|---|---|---|---|---|
| 10 | 212 | 33 | 1 | 1 | 45 | 224 | 446 |
| 20 | 104 | 30 | 1 | 0 | 3 | 16 | 33 |
| 40 | 93 | 29 | 1 | 0 | 0 | 0 | 1 |
| 80 | 93 | 29 | 1 | 0 | 0 | 0 | 0 |

**Table 5: Fully Developed Sea**

0 Degrees

| Depth (m) | S1 | S2 | S3 | S4 | S5a | S5b | S5c |
|---|---|---|---|---|---|---|---|
| 10 | 443 | 26 | 2 | 6 | 124 | 623 | 1256 |
| 20 | 99 | 17 | 3 | 2 | 9 | 44 | 90 |
| 40 | 35 | 13 | 3 | 0 | 18 | 91 | 181 |
| 80 | 25 | 13 | 3 | 0 | 6 | 27 | 55 |

45 Degrees

| Depth (m) | S1 | S2 | S3 | S4 | S5a | S5b | S5c |
|---|---|---|---|---|---|---|---|
| 10 | 443 | 26 | 2 | 6 | 38 | 228 | 539 |
| 20 | 99 | 17 | 3 | 2 | 24 | 111 | 203 |
| 40 | 35 | 13 | 3 | 0 | 25 | 123 | 204 |
| 80 | 25 | 13 | 3 | 0 | 6 | 29 | 59 |

90 Degrees

| Depth (m) | S1 | S2 | S3 | S4 | S5a | S5b | S5c |
|---|---|---|---|---|---|---|---|
| 10 | 443 | 26 | 2 | 6 | 380 | 1883 | 3733 |
| 20 | 99 | 17 | 3 | 2 | 135 | 675 | 1342 |
| 40 | 35 | 13 | 3 | 0 | 24 | 120 | 239 |
| 80 | 25 | 13 | 3 | 0 | 1 | 3 | 6 |

**Table 6: Swell**

0 Degrees

| Depth (m) | S1 | S2 | S3 | S4 | S5a | S5b | S5c |
|---|---|---|---|---|---|---|---|
| 10 | 16 | 0 | 1 | 4 | 148 | 742 | 1492 |
| 20 | 3 | 0 | 1 | 2 | 66 | 331 | 665 |
| 40 | 0 | 0 | 1 | 1 | 11 | 57 | 115 |
| 80 | 0 | 0 | 1 | 0 | 10 | 48 | 96 |

45 Degrees

| Depth (m) | S1 | S2 | S3 | S4 | S5a | S5b | S5c |
|---|---|---|---|---|---|---|---|
| 10 | 16 | 0 | 1 | 4 | 78 | 428 | 931 |
| 20 | 3 | 0 | 1 | 2 | 27 | 149 | 327 |
| 40 | 0 | 0 | 1 | 1 | 5 | 22 | 37 |
| 80 | 0 | 0 | 1 | 0 | 13 | 66 | 131 |

90 Degrees

| Depth (m) | S1 | S2 | S3 | S4 | S5a | S5b | S5c |
|---|---|---|---|---|---|---|---|
| 10 | 16 | 0 | 1 | 4 | 317 | 1567 | 3100 |
| 20 | 3 | 0 | 1 | 2 | 173 | 856 | 1700 |
| 40 | 0 | 0 | 1 | 1 | 70 | 348 | 693 |
| 80 | 0 | 0 | 1 | 0 | 13 | 64 | 128 |

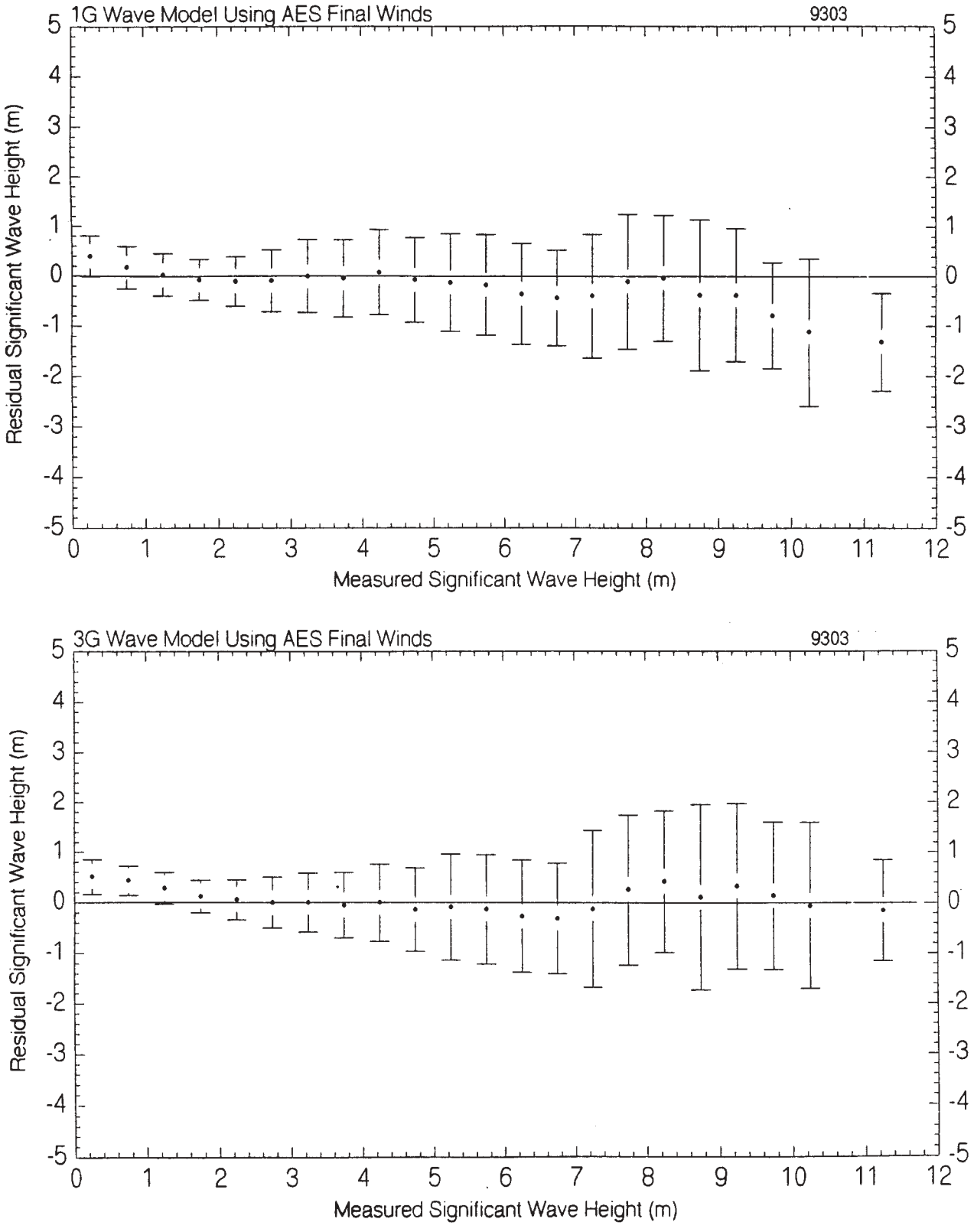


**Figure 1. Mean and standard deviation of differences between hindcast and ERS altimeter significant wave height in 0.5 m bins in hindcasts of the entire North Atlantic Ocean with 1G (above) and 3G (below) wave models for the month of March, 1993, driven by final wind fields produced in the AES 40-year study**

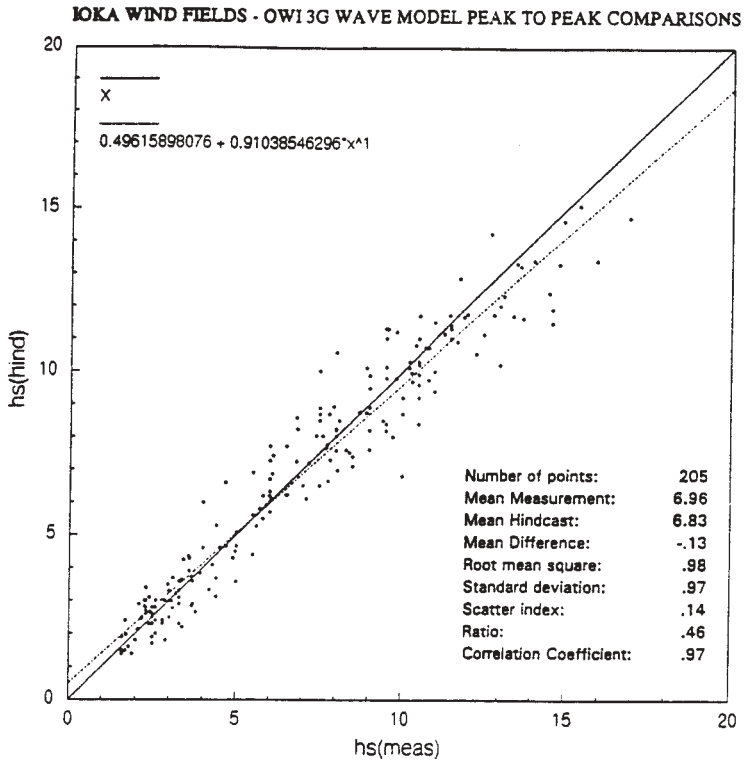


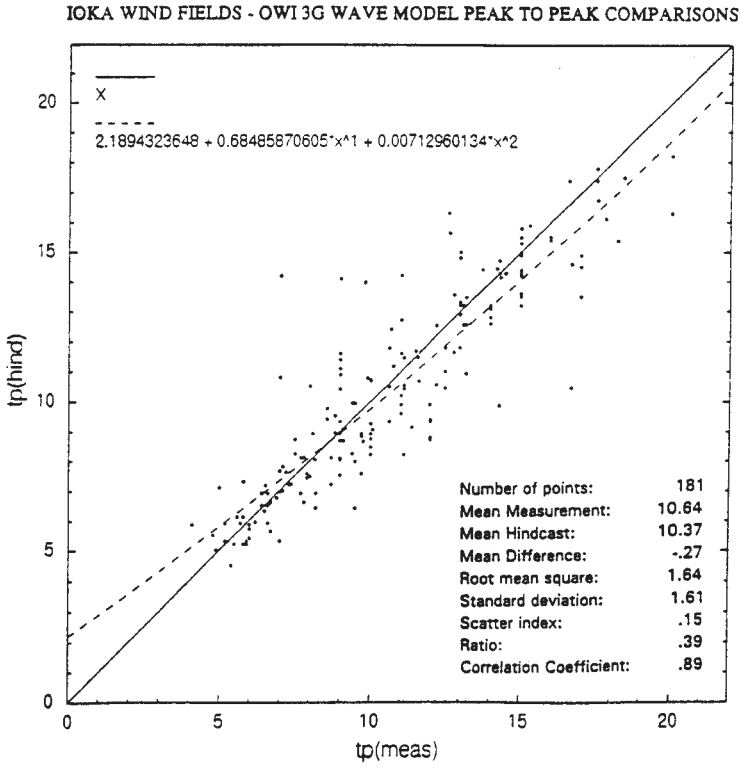


**Figure 2. Comparison of 3-G model hindcasts and measurements of peak storm significant wave height (above) and peak spectral period (below) for hindcasts in different basins and a wide range of storm types where the model is driven by reanlyzed wind fields.**

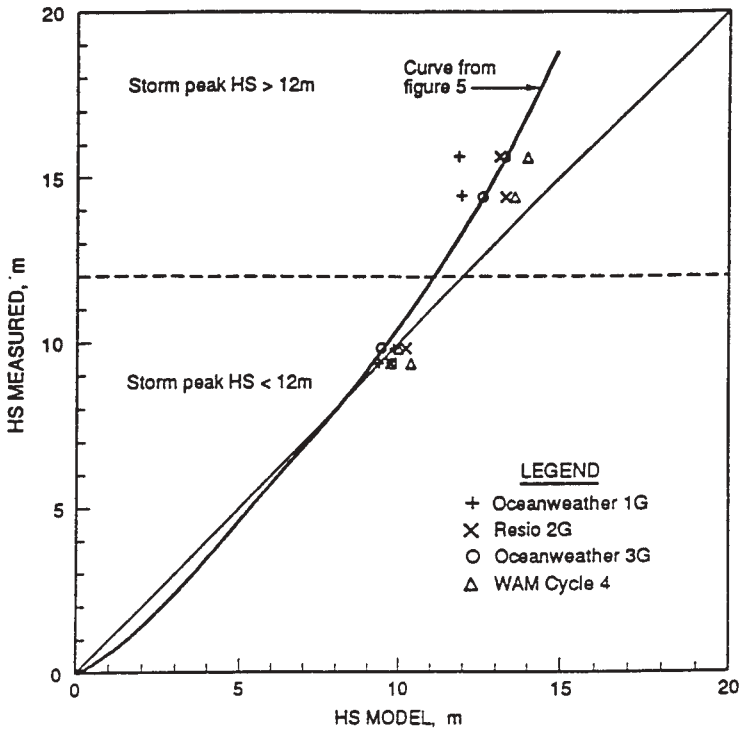


Figure 3. Comparison of theoretical relationship between fully developed wave heights based on dynamic scaling (x axis coordinate) of Resio et al. (1998) and fully developed wave height based on 10 m wind scaling (y axis coordinate) to averaged model wave height plots from Cardone et al. (1996)

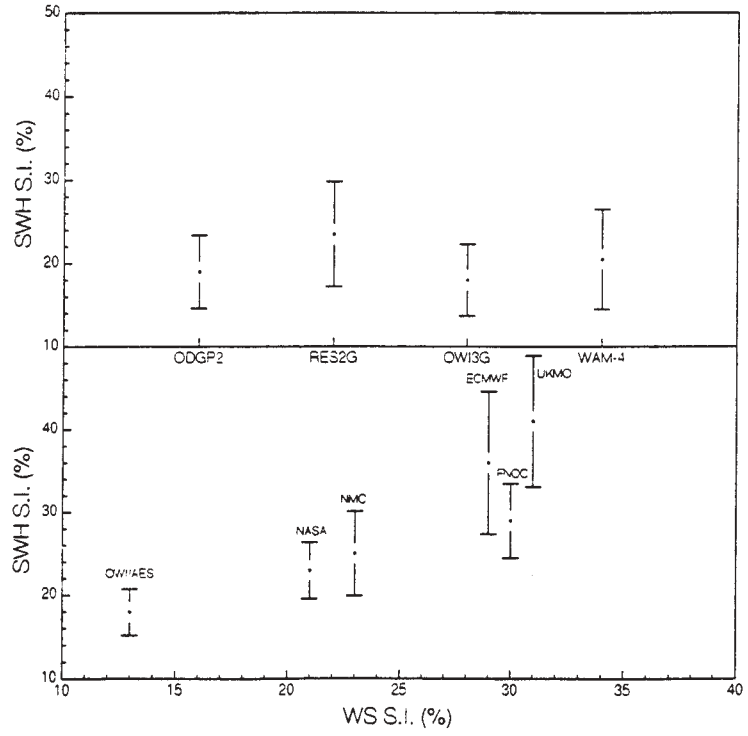


Figure 4. Significant wave height scatter index in hindcasts where one high-quality wind field is used to drive four wave models (above, from Cardone et al., 1996) compared to the same when one wave model (WAM-4) is driven by six different wind fields (below, from Cardone al., 1995)

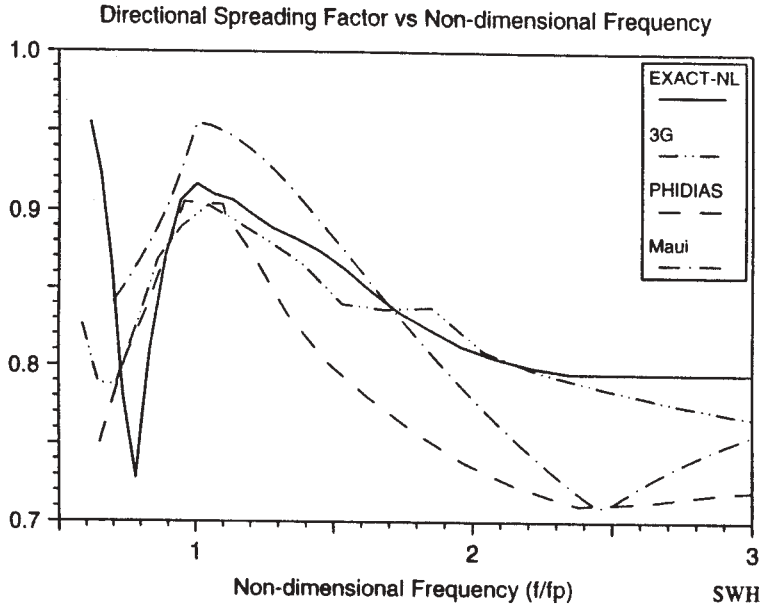


Figure 5. Directional spreading factor vs non-dimensional frequency from 20 m/s duration limited runs at 48 hours for indicated wave models compared to Maui field (New Zealand) measurements (from Forristall and Greenwood, 1998)

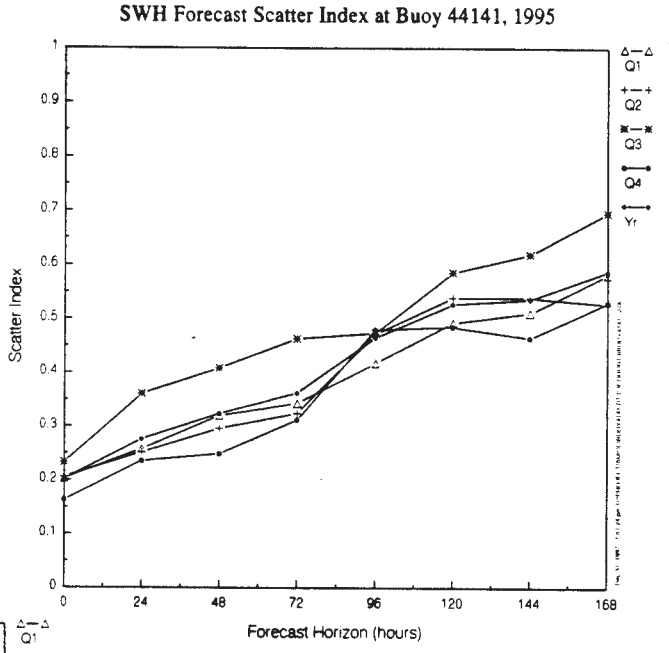


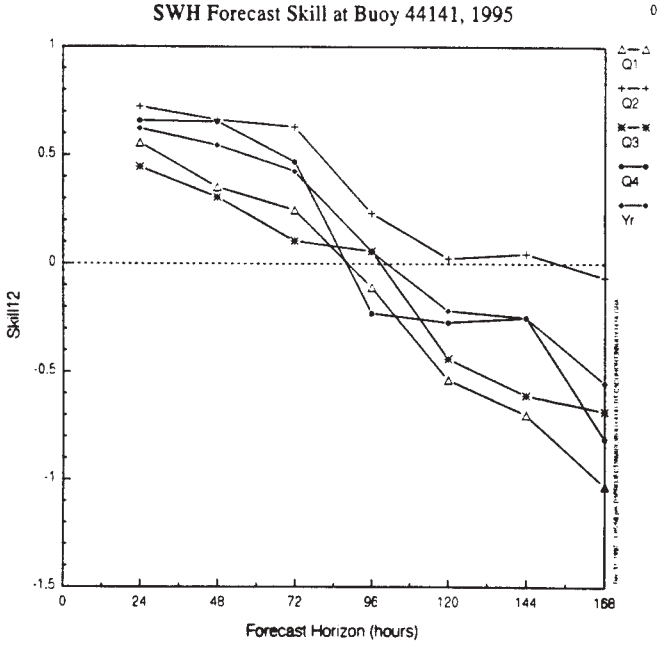


Figure 6. Growth of significant wave height scatter index (above), and skill versus linear combination of climatology and persistence (left) as a function of forecast horizon, in real-time wave analyses and forecasts for indicated quarters of 1995 exhibited in global IMDSS (Lacey and Chen 1995) wave prediction system validated against measurements from a data buoy moored near the main North Atlantic shipping lane.

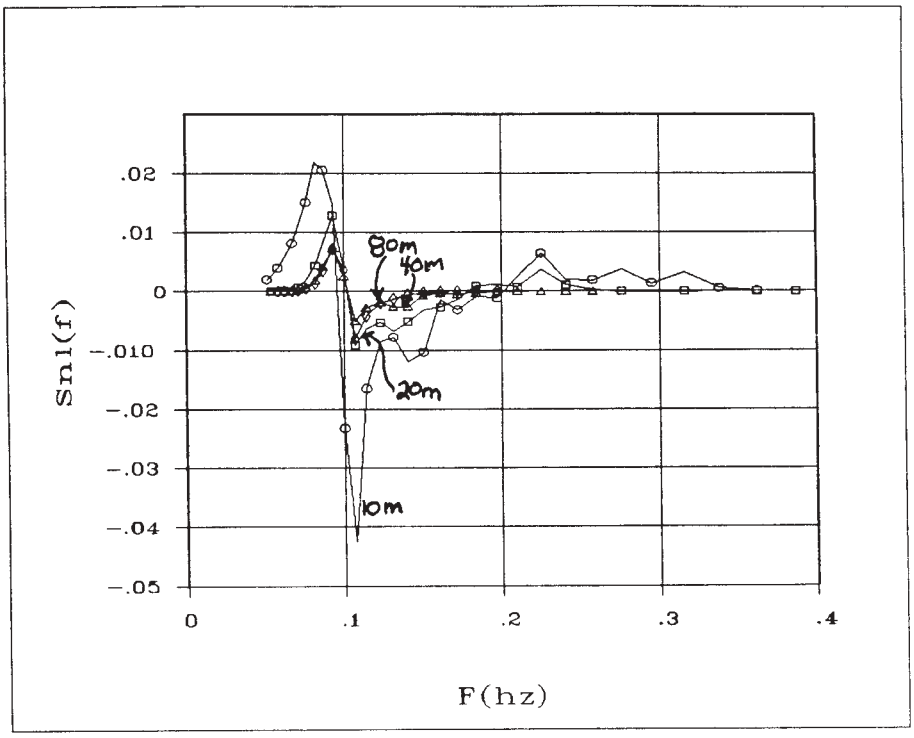


Figure 7. $S_{n1}$ for depths specified JONSWAP spectrum in depths of 80, 40, 20, and 10 meters.

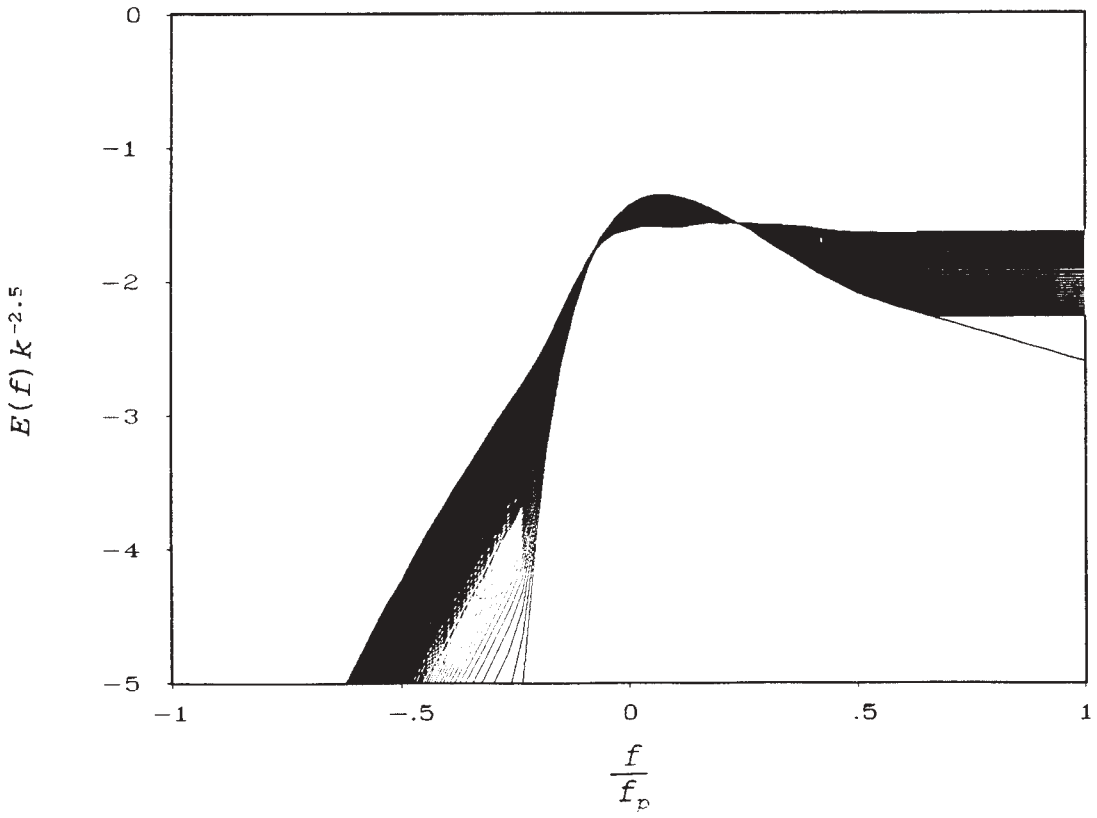


Figure 8. Evolution of wave normalized spectral densities from initial spectrum to $k^{-2.5}$ form due to nonlinear energy fluxes in shallow water. Initial spectrum was JONSWAP ($f^{-5}$) form.

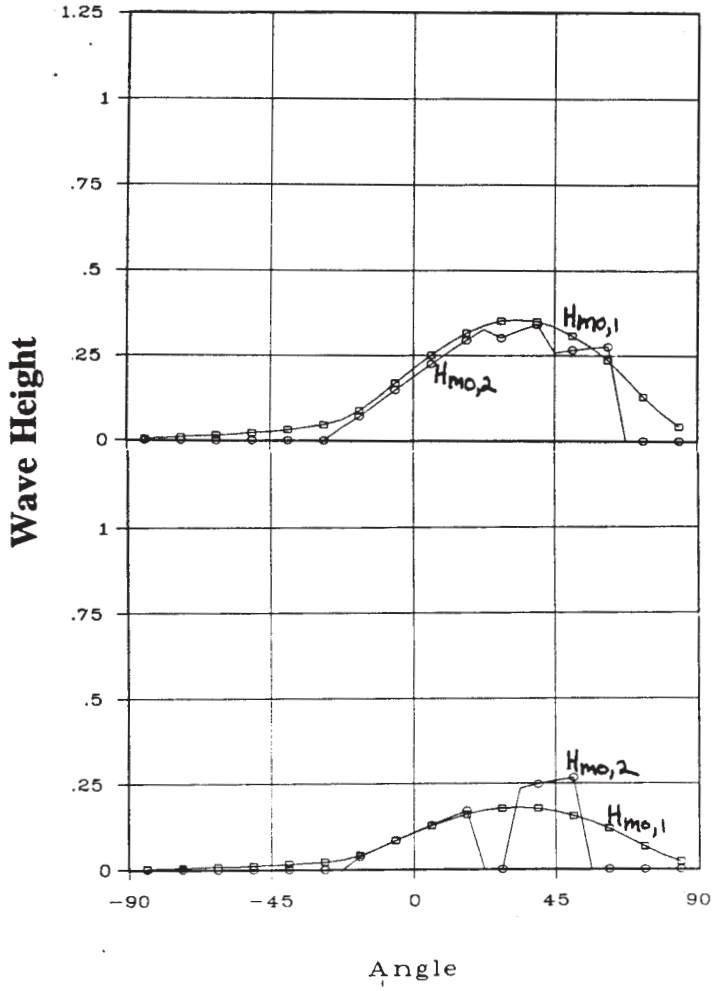


Figure 9. Comparison of wave heights at a distance of four wavelengths (top panel) and sixteen wavelengths (bottom panel) behind a gap between islands. Incident spectrum has $\cos^2 h$ directional spreading. $H_{m0,1}$ is wave height with diffraction. $H_{m0,2}$ is wave height without diffraction.

Figure 10. Comparison of wave heights at a distance of four wavelengths (top panel) and sixteen wavelengths (bottom panel) behind a gap between islands. Incident spectrum has $\cos^{16} h$ directional spreading. $H_{m0,1}$ is wave height with diffraction. $H_{m0,2}$ is wave height without diffraction.

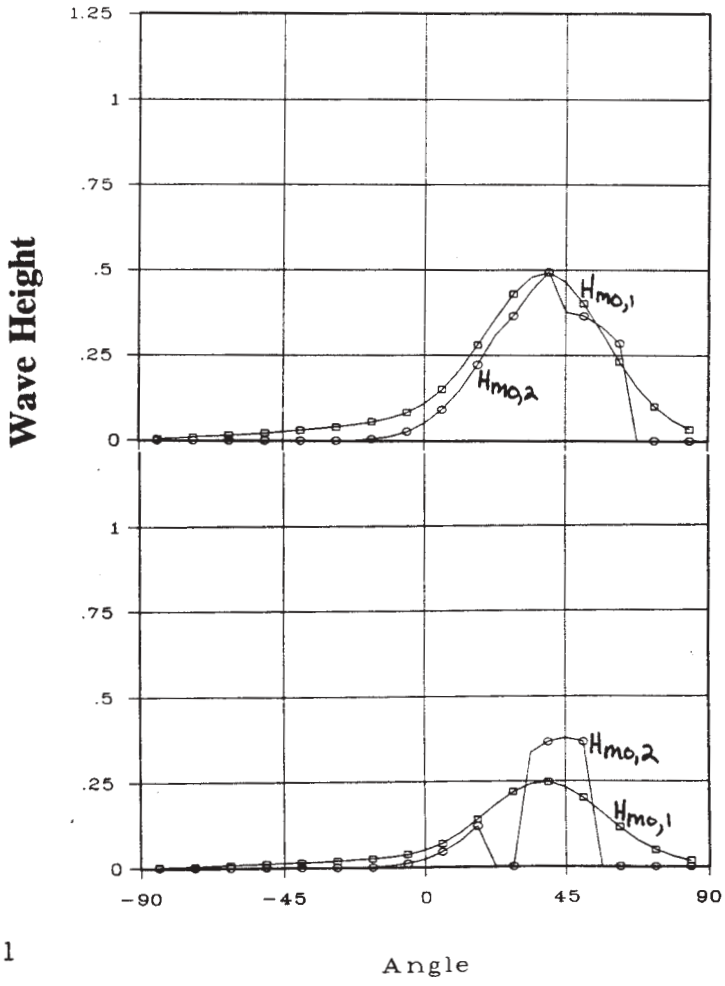

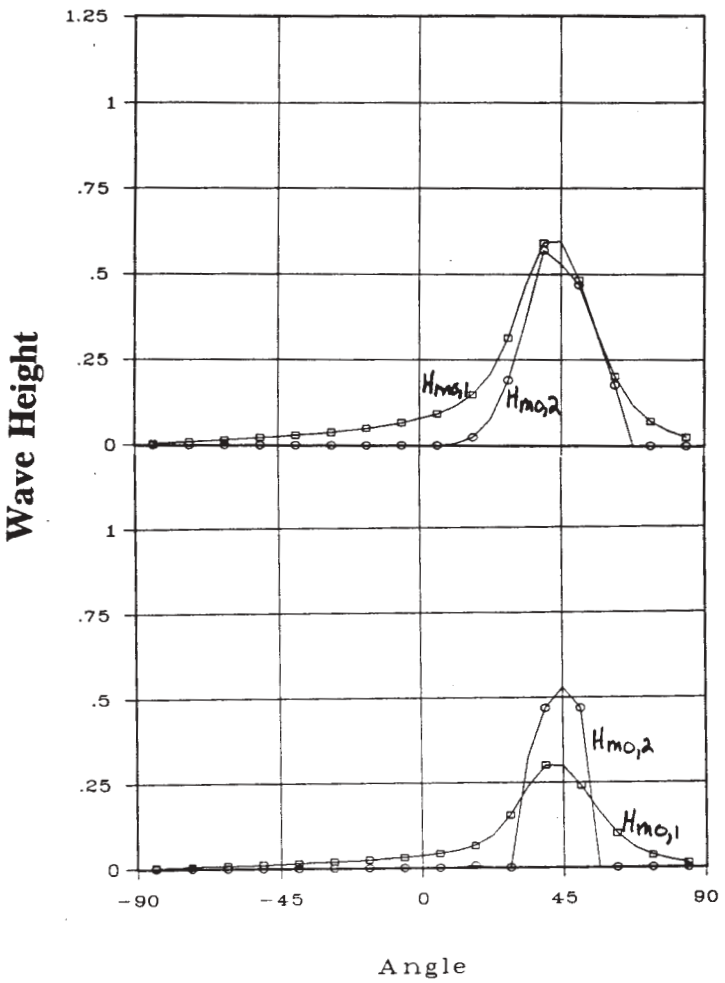


Figure 11. Comparison of wave heights at a distance of four wavelengths (top panel) and sixteen wavelengths (bottom panel) behind a gap between islands. Incident spectrum has $\cos^{64}$h directional spreading. $H_{m0,1}$ is wave height with diffraction. $H_{m0,2}$ is wave height without diffraction.

# Interaction of Sea and Swell In Ocean Wave Models

**Charles L. Vincent, PhD**
**Donald T. Resio, PhD**

Coastal and Hydraulics Laboratory
USAE Waterways Experiment Station
Vicksburg, MS 39180

## ABSTRACT

In ocean wave models such as WAM the ocean wave field is decomposed into spectral components each of which is propagated independently and influenced by various source and sink terms. To a very great extent however, wave systems whose spectral peaks are separated a modest bandwidth do not interact. The principle cross-spectral coupling mechanism, the 4-wave interactions are not sufficiently well represented in the DIA formulation in WAM to allow realistic transfer. Laboratory experiments and field data show evidence that the presence of a low frequency wave train can alter the dissipation of the higher frequency wave system even under forcing by the wind in the example of Banner and Phillips. The potential therefore exists for significant interactions among sea and swell components that are completely lacking in state of the art models.

In this paper, we explore the possible magnitude of both the 4-wave interactions and the induced breaking phenomena in order to ascertain what affects they may have and when they are important. The Full Boltzmann Integral code of Resio will be used to examine the interaction between sea and swell systems typical of a variety of wave generation scenarios: hurricane, extra tropical storm, and North Pacific multiple storm systems. The enhanced breaking mechanism will be parameterized and used to estimate the possible suppression of wind sea as a function of steepness of the swell. Wave-wave interactions have the potential of transferring energy from sea into a swell component. The enhanced breaking mechanism increases the relative size of the swell to the sea since these may be somewhat suppressed. The goal is to understand when these mechanisms are sufficiently strong to have practical impact in prediction models.

# Implications of Exact Solutions to the Nonlinear Wave-Wave Interaction Source Function

**Robert E. Jensen and Donald T. Resio**

USAE Waterways Experiment Station
Coastal and Hydraulics Laboratory
Vicksburg, MS 39180-6199

Telephone: (601) 634-2101
Email: jensen@madmax.wes.army.mil
Telephone : (601) 634-2018
Email: d.resio@cerc.wes.army.mil

## ABSTRACT

The implementation of exact solutions to the nonlinear wave-wave interaction source term (e.g. Hasselmann and Hasselmann 1981; Resio and Perrie 1991) is dependent on assumed characteristics of the high frequency tail. The full integral solution in the continuum extends from 0 to ∞; however, numerical solutions are unable to perform the integration past some cutoff wave number. Despite the exactness in these solutions, they are, in part controlled by the location of cutoff wave number as well as the parametric formulation of the high frequency tail. Historical studies have assumed eventually restricted their work to obtain a stable solution, performed academic tests (e.g. SWAMP 1983) using selective formulations for the atmospheric input and wave breaking source terms for detailed balance. Hence, the net effect of these assumptions governing the *parametric tail*, and prescribed boundary condition to the discrete region will greatly influence the overall solution.

The work presented herein will investigate various cutoff wave numbers, and boundary condition assumptions through controlled academic tests to determine the relative affect in the overall solution using the Full Boltzmann Model (Resio 1993), and compared to the operational version of **WAM** using the Discrete Interaction Approximation (Komen et al. 1994). Field investigations of trial balance derived from the Surface Wave Dynamics Experiment (Weller et al. 1991) for two cases, an energetic cyclo-genesis and a rapid wind shift to demonstrate the appropriateness of the cutoff wave number as well as the boundary condition between the parametric and discrete regions of the solution.

# EVALUATION OF SHALLOW WATER WAVE PREDICTION OVER THE INNER SHELF WITH HF RADAR AND IN-SITU MEASUREMENTS

**Hans C. Graber**
Division of Applied Marine Physics
Rosenstiel School of Marine and Atmospheric Science
University of Miami
Miami, FL 33149-1098
Tel: (305) 361-4935
email: hgraber@rsmas.miami.edu

**Robert E. Jensen**
USAE Waterways Experiment Station
Coastal and Hydraulics Laboratory
Vicksburg, MS 39180
Tel: (601) 634-2101
email: jensen@madmax.wes.army.mil

**Thomas H. C. Herbers**
Department of Oceanography, Code OC/He
Naval Postgraduate School
Monterey, CA 93943-5123
Tel: (408) 656-2917
email: herbers@oc.nps.navy.mil

The WAM-4 ocean wave model will be evaluated over the inner shelf region off Duck, North Carolina. Wave measurements from the DUCK94 experiment obtained from a HF Doppler radar (surface current vectors and wave heights only), two 3-m discus directional wave buoys and several bottom-mounted pressure gauges will be used to provide boundary conditions for the WAM model. The wave model will be implemented on a 1 km grid over a 25 km by 30 km domain with both options for shallow water wave physics and wave-current interaction. Directional wave spectra and wind observations from the buoys will be used in conjunction with the HF radar and pressure gauge measurements to provide the boundary conditions for the wave energy propagating into the domain and the local wind forcing field. High-resolution surface vector current measurements from the HF radar will be included to examine the effect of wave-current interaction over the continental shelf. Simulations will be made during a Nor'easter in October 1994 to evaluate the shallow water wave physics. Predicted model wave heights will be compared with wave height estimates from HF radar at 1 km resolution. Shoaling and refraction effects will be examined with energy spectra from the bottom pressure gauges and a linear array.

# Nested Wave Model for the Baltic Sea

**Lennart Funkquist**
**Swedish Meteorological and Hydrological Institute**
**S-601 76 Norrköping**
**Sweden**

*tel: +46 11158000*
*fax: +46 11170207*
*email: lfunkquist@ssmhi.se*

## ABSTRACT

A nested wave model for the Baltic Sea is composed of four different grids with a grid-spacing ranging form 22 km down to 500 m. The coarsest one covers the North Sea and part of the Norwegian Sea while the finest one covers the Sound, which is one of the narrow connections between the North Sea and the Baltic Sea. For each grid, a part of the atmospheric model output is cut out and interpolated to provide the local forcing.

As the frequency resolution is different between the grids, the energy transfer from a coarse grid to a finer one has to be modified. This is solved simply by putting the non-resolved low-frequency energy into the lowest frequency in the next grid.

Operational output is shown for the differ net grids as well an outline of the interactive graphical interface as part of the marine forecasting system.

# DIRECTIONAL SPREADING OF MEASURED AND HINDCASTED WAVE SPECTRA

George Z. Forristall[1] and J. Arthur Greenwood[2]

[1]Shell International Exploration and Production B.V.
Rijswijk, Netherlands

[2]Oceanweather, Inc.
Cos Cob, CT

## 1. INTRODUCTION

Numerical models based on the transport equation for wave energy are now routinely used to forecast and hindcast the directional spectrum of surface waves. Growth curves for total variance and peak frequency are fairly well established, and many studies have compared the results of the models to measurements of these parameters. Evaluations of the directional properties of the spectra created by the models are less common, and have concentrated on the mean direction of the spectral energy. Such studies include those of Cavaleri et al. (1991), Guillaume (1990) and Khandekar et al. (1994).

There is much more information in the directional spectrum than the mean wave direction. For many engineering purposes, the degree to which the spectrum is spread in direction is of considerable interest. Forristall and Ewans (1998) have shown that a spreading factor defined as the square root of the in-line variance ratio predicts the reduction in the in-line particle velocities under waves due to direction spreading. This spreading factor thus can be used to give the reduced wave force on a structure in a directionally spread sea compared to the force calculated from a two dimensional wave theory. It also gives a convenient and intuitive measure of the total amount of directional spreading in a wave spectrum. The spreading factor is 1.0 for unidirectional waves and 0.707 for omnidirectional waves.

Comparisons of measured and modeled directional spreading are thus an important part of the validation of numerical wave models, but few such comparisons are yet available. Ewans (1995) did make some limited comparisons between fetch limited measurements and calculations of duration limited spectra. The measurements, made at Maui in New Zealand, gave an average spreading factor of 0.910, which was apparently independent of wave age, and very similar to the value of 0.903 that was interpreted from the measurements of Donelan et al. (1985) in Lake Ontario.

Calculations by Banner and Young (1994) using a model that gives a full solution to the non-linear source term, the so-called Exact-NL model, gave a spreading factor of 0.887. An accurate calculation of the nonlinear source terms thus appears to give a reasonable approximation of the observations. On the other hand, calculations by van Vledder and Holthuijsen (1993) using PHIDIAS, which is an implementation of the WAM model using the standard discrete interaction kernel, gave an average spreading factor of 0.850. The difference is significant. The operational model produces waves that have considerably broader spreading than the observations, to the extent that it would be unconservative to use the results in engineering calculations.

The purpose of this paper is to make a considerably more detailed comparison between measured and hindcast directional spreading. We begin with a review of the definition of the spreading factor. Then we discuss the calculation of the nonlinear interaction terms in the Oceanweather implementation of a third generation (3G) wave model. This model includes a discrete interaction approximation with two interaction modes. The model is first applied to duration cases, and compared to measurements and other models. The 3G model is then used to hindcast waves in the North Sea from 1991 through 1994 where it is compared to measurements from buoys at two sites. Comparisons are also made to the wave spreading measured at the Bullwinkle platform during Hurricane Opal in 1995. The paper closes with conclusions and plans for future work.

## 2. DEFINITION OF THE SPREADING FACTOR

Given the directional spectrum $S(f,\theta)$, define the spreading function $H(f,\theta)$ by

$$S(f,\theta) = S(f)H(f,\theta)$$

where

$$\int_{\pi}^{\pi} H(f,\theta)d\theta = 1$$

Then expand $H(f,\theta)$ in the Fourier series

$$H(f,\theta) = \frac{1}{\pi}\{\frac{1}{2} + \sum_{n=1}^{\infty}[a_n(f)\cos n\theta + b_n(f)\sin n\theta]\}$$

The variances and covariances of the $u$ and $v$ velocity components are then

$$\alpha_{uu}^2 = \frac{1}{2}\int_0^{\infty} Q^2(f)S(f)[1+a_2(f)]df$$

$$\alpha_{vv}^2 = \frac{1}{2}\int_0^{\infty} Q^2(f)S(f)[1-a_2(f)]df$$

$$\alpha_{uv}^2 = \frac{1}{2}\int_0^{\infty} Q^2(f)S(f)b_2(f)df$$

where $Q(f)$ is the attenuation of velocity with depth. Forristall and Ewans (1998) showed that the most generally applicable spreading factor for force integrated over depth should be calculated by setting $Q(f) = 1$.

It is always possible to find a coordinate system $(a,b)$ in which the velocity components are statistically independent, i.e., $\alpha_{ab} = 0$. The angle between the $(x,y)$ and $(a,b)$ coordinate systems is given by

$$\tan 2\theta_p = \frac{2\alpha_{uv}^2}{\alpha_{uu}^2 - \alpha_{vv}^2}$$

where $\theta_p$ is defined as the principal wave direction. In the new coordinate system, the velocity variances at zero lag are given by

$$\alpha_{aa}^2 = \frac{1}{2}(\alpha_{uu}^2 + \alpha_{vv}^2) + r$$

$$\alpha_{bb}^2 = \frac{1}{2}(\alpha_{uu}^2 + \alpha_{vv}^2) - r$$

where

$$r^2 = \frac{1}{4}(\alpha_{uu}^2 - \alpha_{vv}^2)^2 + (\alpha_{uv}^2)^2$$

The velocity distribution in the principal wave direction is normal with standard deviation $\alpha_{aa}$. If all of the wave energy were in one direction, then the velocity distribution would have a standard deviation $\alpha$ given by

$$\alpha^2 = \alpha_{uu}^2 + \alpha_{vv}^2 = \int_0^{\infty} Q^2(f)df \int_{\pi}^{\pi} S(f,\theta)d\theta$$

Wave spreading thus reduces the rms velocity in the principal wave direction by the factor

$$\phi = \frac{\alpha_{aa}}{\alpha}$$

We define $\phi$ to be the wave spreading factor. Our spreading factor is the square root of the ``in-line variance ratio" defined by Haring and Heideman (1980), and our principal wave direction is equal to their ``dominant wave direction." It is relatively easy to measure accurately since it depends only on the second moments of the directional spectrum. All that is really required of the measurement system is that its response be the same in all directions.

## 3. THE DIA2 MODEL

### 3.1 DIA2 Discrete Interaction Approximation

In deep water the wave spectrum can be expressed as a function of radian frequency $\omega$ and direction $\theta$ or equivalently in terms of vector wave number $\tilde{k} = (k\cos\theta, k\sin\theta)$ where the scalar wave number:

$$k = \frac{\omega^2}{g}$$

In a full non-linear model (e.g. EXACT-NL), the contribution to spectral growth at $\tilde{k}_0$ is a multiple

integral, with a coupling coefficient that scales as $\omega^3 k^4$, of the product of spectral densities at $\tilde{k}_1, \tilde{k}_2, \tilde{k}_3$ where

$$\omega_0 + \omega_1 = \omega_2 + \omega_3 \quad ; \quad (\omega_i = [gk_i]^{\frac{1}{2}})$$

$$k_0 \cos\theta_0 + k_1 \cos\theta_1 = k_2 \cos\theta_2 + k_3 \cos\theta_3$$

$$k_0 \sin\theta_0 + k_1 \sin\theta_1 = k_2 \sin\theta_2 + k_3 \sin\theta_3$$

For computational convenience the factor $\omega^3 k^4$ is often replaced by $\omega^{11}$ or $f^{11}$; this substitution restricts the NL model to deep water.

A discrete interaction approximation (DIA) replaces the integral by a sum over a very small number of combinations of $\omega_i/\omega_0$ and $(\theta_i - \theta_0)$. For example, the DIA adopted in the widely used WAM model uses the sets

$$\omega_1 = \omega_0$$
$$\omega_2 = (1+\lambda)\omega_0$$
$$\omega_3 = (1-\lambda)\omega_0$$

$$\theta_1 = \theta_0$$
$$\theta_2 = \theta_0 \pm \alpha_2$$
$$\theta_3 = \theta_0 \pm \alpha_3$$

where

$$\lambda = 0.25$$
$$\alpha_2 = -\arccos(5/6)$$
$$\alpha_3 = \arccos(0.98)$$

Oceanweather's model DIA2 uses the two quartets aforesaid and the two additional quartets

$$\omega_1 = \omega_0$$
$$\omega_2 = (1+\mu)\omega_0$$
$$\omega_3 = (1-\mu)\omega_0$$

$$\theta_1 = \theta_0$$
$$\theta_2 = \theta_0 \pm \beta_2$$
$$\theta_3 = \theta_0 \pm \beta_3$$

where

$$\mu = 1 - (1-\lambda)^{2/3}$$

$\beta_2$ and $\beta_3$ are roughly –19.998 degrees and +9.725 degrees; more exact values are found by solving the equations balancing $k_0 \cos\theta_0$ and $k_0 \sin\theta_0$.

3.2 Duration Tests

DIA2 was applied to a pure duration test, run for 48 hours at a wind speed of 20 m/sec. It is well known, but probably worth mentioning once more, that a duration test is run by taking a full wave model and disabling the subroutine that effects propagation; the wave spectra so computed are the same as would be grown by a steady wind blowing for a finite duration over an unlimited fetch. The duration test was also run for ODGP2, a first generation model in use at Oceanweather Inc. for over 20 years (Cardone, Pierson and Ward, 1976; see also Khandekar et al., 1994 for a more recent model description). A duration run by PHIDIAS, a PC version of WAM Cycle 4, was provided by G. Ph. van Vledder. The growth of significant wave height and spreading as a function of time for these models is shown in Table 1. PHIDIAS HS lags the other models at short duration because of the lack of a self-starting mechanism in WAM. Beyond duration of about 24 hours the growth rates reflect mainly the tuning preferred by the model authors. Differences in spreading, however, between WAM and DIA2 reflect mainly the impact of the DIA2 non-linear source term within the detailed source term balance on the directional distribution of energy. For this run, phi averages .842 for PHIDIAS, .870 for DIA2, and .886 for ODGP2. Recall that for immature seas EXACT-NL provides an average spreading of 0.887. While the ODGP2 model actually provides the largest spreading factor, in better agreement with EXACT –NL, than the 3G models, it should be noted that in ODGP2, the directional spectrum is shaped

according to an imposed spreading based on the empirical SWOP form. In the 3G models the directional spreading is a consequence of the detailed balance of (in deep water) source terms for wave growth, dissipation and interaction.

Figure 1 shows the duration limited spreading factors from the various models (except ODGP) as a function of non-dimensional frequency. The calculations were all for a 20 m/sec wind and a 48 hour duration. The average spreading factors from the Maui measurements are shown for comparison, although they arose actually from fetch-limited situations. The frequency is non-dimensionalized by the frequency at the peak of the power spectrum.

All of the models and the measurements have the highest spreading factors near the peak of the spectrum. They agree with the well-known fact that the spreading is narrowest there. The measurements, however, have a higher spreading factor than any of the models near the peak. The spreading from the PHIDIAS model, which uses the standard DIA terms, remains lower than the measurements through the tail of the spectrum. The Exact-NL and DIA2 model results have higher spreading factors in the tail than the PHIDIAS model, and thus agree better with the measurements. The DIA2 model agrees very well with the EXACT-NL results, showing that the addition of the second interaction mode captures an important part of the nonlinear interactions that is missed by the standard DIA calculations.

Figure 2 shows the spreading factor, now integrated over the entire spectrum, as a function of wave age. The Maui data points and average value are again shown for comparison. The wave age is calculated from the frequency of the peak of the spectrum and the 10 m wind speed. Neither the measurements nor any of the models show any significant trends with wave age.

All of the models produce waves that are more broadly spread than the measurements. This is due to the fact that they all have a lower spreading factor at the peak of the spectrum, as shown in Figure 1, and much of the energy in the spectrum is near the peak. The PHIDIAS model, which uses the standard DIA terms, has the lowest spreading factor. The DIA2 model produces higher spreading factors, which agree well with the one EXACT-NL calculation, and the first generation ODGP model actually produces the highest spreading factors which agree best with the measurements.

## 4. NORTH SEA HINDCASTS

### 4.1 Hindcast Methodology

A long continuous hindcast including the period from January, 1991 through May, 1994 has recently been made with the DIA2 wave model adapted to a two-nest grid system covering the North Atlantic basin, including the North Sea and Norwegian Sea. The basin is modeled with a grid of 150 km spacing and the European shelf, including the entire North Sea, is modeled with a nest of 30 km spacing. The spectrum is resolved in 24 directions and 23 frequencies. The bin center frequencies range from 0.039 Hz increasing in geometric progression with a constant ratio 1.10064 to 0.32 Hz. Wind fields for this hindcast were derived by intensive kinematic analysis using a graphical workstation which incorporates an objective analysis program for winds. This analysis system assimilates all available historical data into a high quality background field and also allows the analyst to impose time and space continuity of major kinematic properties of storm wind fields and to add small-scale features (see e.g. Cox et al. (1995)).

### 4.2 Measurements

Measurements of directional wave spectra were made near the Auk and North Cormorant oil production platforms in the North Sea from 1991 through 1995. The Auk platform is located at 56° 24' N and 2° 03' E and the North Cormorant platform is at 61° 14' N and 1° 09' E. The measurements were made using WAVEC buoys, which are 2.5 m buoys manufactured by Datawell, with Datawell Hippy 120A sensors that measure the heave, pitch and roll of the buoy. The Fourier components of the directional spreading function were calculated from 20-minute samples, and the spreading factor was calculated from the Fourier components.

### 4.3 Comparison of Hindcast and Measurements

Figure 3 is a scatter plot of measured and hindcast spreading factors at North Cormorant. The straight line is a simple linear regression of the hindcasts against the measurements. Perfect agreement between the measurements and hindcasts would result in a line at 45 degrees. The hindcasts definitely show some skill in reproducing the measurements, but there is much scatter. The regression line also shows that there is a tendency for the hindcast spreading factor to be too large when the measured spreading factor is small and too small when the measured spreading factor is large.

Figure 4 is a similar plot for Auk. The scatter is somewhat less than at North Cormorant, but the regression line is more horizontal.

Forristall and Ewans (1998) found that there was a tendency for the spreading factor to be smaller at lower latitudes, both for the North Sea and their total data set. Figure 5 shows the average values of the spreading factor at the two sites for both the measurements and the hindcasts. All of the data series are averaged over 0.5 m bins in $H_s$. Both the hindcasts and measurements show a tendency for higher spreading factors at high wave heights, and there is reasonably good agreement between the hindcast and measured values at the two sites.

The hindcasts agree with the measurements in showing that the spreading factor is higher, i.e., the directional spreading is narrower, at Auk which is at a lower latitude than North Cormorant. The largest difference between the hindcasts and measurements is that the hindcasts do not show the continued increase of the spreading factor at Auk for significant wave heights greater than 7 m. The lower spreading factor in the hindcasts is consistent with the observation that the spreading factor for fetch limited seas was 0.91 in the measurements while it was 0.87 from the model.

## 5. HURRICANE OPAL

### 5.1 Hindcast

The availability of directional wave measurements at an oil platform in the Gulf of Mexico during the passage of a Category 4 hurricane, prompted a hindcast of hurricane Opal (1995) with DIA2 and ODGP2 and comparison of measured and hindcast spreading factor. The hindcast spanned the entire history of Opal in the Gulf of Mexico from two days before its emergence into the Bay of Campeche from Yucatan on 30 September as a tropical depression, to its rapid intensification as it accelerated north-northeastward on October 3 and 4 to its entrance into the Florida Panhandle late on the October 4 and rapid decay over Alabama during October 5. Maximum intensity was observed early on October 4 as the storm eye passed near 27.3° N, 88.5° W, where reconnaissance aircraft found a very small 10 nm diameter eye with central pressure of 916 mb with maximum sustained surface winds estimated at 130 knots.

The wave model was adapted to the entire Gulf of Mexico on a square grid laid out on a direct Mercator projection. The grid spacing ranged from 24.26 km at the south edge of the grid to 22.0313 at the north edge. The model integration time step is 30 minutes. In other respects, the model is the same as described above for the North Sea hindcast. Wind fields were generated by Oceanweather's latest numerical tropical cyclone boundary layer wind model (Thompson and Cardone, 1996).

### 5.2 Measurements

Measurements of the directional wave spectrum were made at the Bullwinkle platform, located at 27° 53' N and 90° 54' W, in 410 m of water. The measurements were made using a Baylor wave staff and a Marsh-McBirney electromagnetic current meter located nearby. The signals from the instruments were recorded continuously, and spectra were calculated from hour long samples of data. The Fourier coefficients of the spreading function were calculated from the time series, and the spreading factors were calculated from the Fourier coefficients.

### 5.3 Comparison of Hindcast and Measurements

Figure 6 shows the measured and hindcast significant wave heights during the peak of the storm at Bullwinkle. Since the center of the storm passed some distance from the measurement site, the wave heights show a gradual increase and decrease rather than a sharp peak. Both hindcasts track the measurements reasonably well, staying within one meter of the measured significant wave height. The peak waves from the DIA2 model are, however, considerably larger than the highest waves from the ODGP model. This tendency for DIA2 to run higher than ODGP2 on the left side of accelerating intense hurricanes has also been observed in other cases. Agreement between these models is usually very close on the right side of the storm. It is speculated (V. Cardone, personal communication) that this differential behavior may be due to differences in the algorithms for growth of wind seas in the presence of swell. The left side of hurricanes typically is invaded by wave energy propagated from the high-energy right front quadrant.

Figure 7 shows the measured and hindcast spreading factors during Opal. The spreading factors from the two hindcasts are rather similar, but they show behavior completely different from the measurements. The measured spreading factors decrease through the storm, indicating that the waves become more confused, but the hindcast spreading factors generally increase. The agreement between the hindcasts and measurements is poor while the storm is approaching, but reasonably good from the time of the closest approach of the storm center. Again this model anomaly might by due to the model having too much wave energy propagated to the left of the storm track from different quadrants. More detailed study of the directional spectra (modeled and measured) and of the

source term balance in the presence of swell are needed to resolve these questions.

## 6. SUMMARY AND CONCLUSIONS

The in-line variance ratio, based on the second trigonometric moments of a wave spectrum, is somewhat less intuitive than a measure of angular spreading based on first trigonometric moments, but is more easily interpreted in terms of wave loads on structures. When wave spectra are grown by using third-generation numerical models, the in-line ratio is only weakly dependent on the wave age (alternatively, on the non-dimensional total variance).

Unlike the total variance and the peak frequency, which follow recognized growth curves, the in-line ratio is very sensitive to the details of the discrete interaction approximation used to compute interactions in an operational 3G model. This sensitivity is illustrated by comparing the extensively used WAM model with the model DIA2 (discrete interaction approximation, two interaction modes) first exploited in 1991, applying each to fetch, duration, and limited growth tests. These comparisons show that the DIA2 model provides higher spreading factors, and hence narrower directional spectra than WAM. The main difference between WAM and DIA2 is the inclusion in DIA2 of a second mode of interactions in the discrete interaction of the non-linear source term, and this is believed to contribute to the higher spreading factors. This conclusion is supported also by the closer agreement between DIA2 and EXACT-NL than between WAM and EXACT-NL. The mean spreading factor of neither WAM nor DIA2 agrees as closely with EXACT-NL as does ODGP2, a 1G model which, in simple fetch and duration regimes, forces the 2-D spectrum to spread according to an empirical spreading form.

Comparison between measured wave spectra at two North Sea sites from January 1991 to May 1994 and spectra hindcasted for the North Sea using DIA2 adapted to a 30-km grid, demonstrates a gratifying agreement between the in-line ratio from hindcasts and measurements. Comparisons between hindcasts and measurements made in Hurricane Opal, 1995, are also given. These comparisons were found to be more difficult to evaluate in terms of source terms because of the effect on angular spreading of storm quadrant-quadrant wave propagation in the highly curved wind field environment.

The North Sea comparisons were also found to be consistent with a previously reported dependence of in-line ratio on latitude, but the latitude range between stations is small in these cases. This dependence will be further explored by analyzing the spreading in 2-D spectra in a 40-year continuous hindcast covering the entire North Atlantic basin to the equator, which is currently in production (Swail et al (1998)).

## REFERENCES


Banner, M.L. and I.R. Young, 1994. *Modeling spectral dissipation in the evolution of wind waves.* J. Phys. Ocean., 24:1550-1561.

Cardone, V.J., W.J. Pierson, and E.G. Ward, 1976. *Hindcasting the directional spectra of hurricane generated waves.* J. Petrol. Tech., 28, 385-394.

Cavaleri, L., L. Bertotti, and P. Lieonello, 1991. *Wind wave cast in the Mediterranean Sea.* J. of Geophysical Research., 96:10,739-10,764.

Cox, A.T., J.A. Greenwood, V.J. Cardone, and V.R. Swail, 1995. *An interactive objective kinematic analysis system.* Proc. 4th International Workshop on Wave Hindcasting and Forecasting, October 16-20, 1995, Banff, Alberta, p. 109-118.

Donelan, M.A., J. Hamilton, and W.H. Hui, 1985. *Directional spectra of wind-generated waves.* Philosophical Trans. Roy. Soc. London, A315:509-562.

Ewans, K.C., 1995. *Observations of the directional spectrum of fetch-limited waves off the west coast of New Zealand.* International Workshop on Wave Hindcasting and Forecasting, 4, 263-277.

Forristall, G.Z., and K.E. Ewans, 1998. *Worldwide measurements of directional wave spreading*, J. Atmospheric and Oceanic Tech., in the press.

Guillaume, A., 1990. *Statistical tests for the comparison of surface gravity wave spectra with application to model validation.* J. Atmos. and Oceanic Tech., 7:551--567.

Haring, R.E. and J.C. Heideman, 1980. *Gulf of Mexico rare wave return periods.* J. Petrol. Tech., p. 35-47.

Khandekar, M.L., R. Lalbeharry, and V.J. Cardone, 1994. *The performance of the Canadian spectral ocean wave model (CSOWM) during the Grand Banks ERS-1 SAR wave spectra validation experiment.* Atmosphere-Ocean, 32(1), 31-60.

Swail, V.R., V.J. Cardone, A.T. Cox. 1998. *A long term North Atlantic wave hindcast.* Proc. 5th International Workshop on Wave Hindcasting and Forecasting, Melbourne, FL.

Thompson, E.F. and V.J. Cardone, 1996. *Practical modeling of hurricane surface wind fields.* Journal of Waterway, Port, Coastal, and Ocean Engineering, July/August 1996, pp. 195-205.

van Vledder, G. and L.H. Holthuijsen, 1993. *The directional response of ocean waves to turning winds.* J. Phys. Ocean., 23:177-192.

Table 1: Duration test for wind speed (10m) of 20m/s for three wave models.

| Duration Hours | Significant Wave Height (m) | | | Spreading Factor | | |
|---|---|---|---|---|---|---|
| | ODGP | DIA2 | WAM | ODGP | DIA2 | WAM |
| 6. | 4.542 | 5.258 | 1.808 | 0.8918 | 0.8672 | 0.8254 |
| 12. | 6.609 | 7.071 | 4.539 | 0.8827 | 0.8782 | 0.8547 |
| 18. | 8.436 | 8.189 | 6.542 | 0.8844 | 0.8754 | 0.8477 |
| 24. | 9.548 | 8.883 | 7.515 | 0.8920 | 0.8725 | 0.8467 |
| 30. | 9.739 | 9.351 | 8.141 | 0.8879 | 0.8696 | 0.8450 |
| 36. | 9.794 | 9.694 | 8.559 | 0.8850 | 0.8675 | 0.8420 |
| 42. | 9.819 | 9.956 | 8.845 | 0.8836 | 0.8655 | 0.8403 |
| 48. | 9.833 | 10.164 | 9.045 | 0.8828 | 0.8639 | 0.8377 |

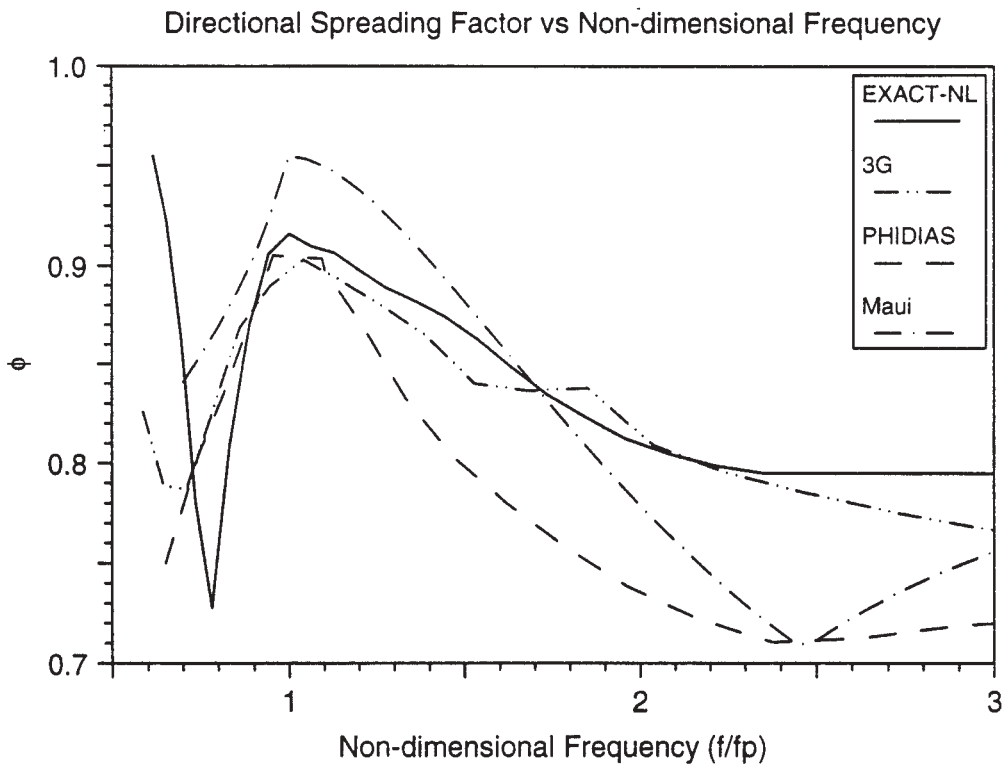


Figure 1



AUTHOR INDEX TABLE OF CONTENTS

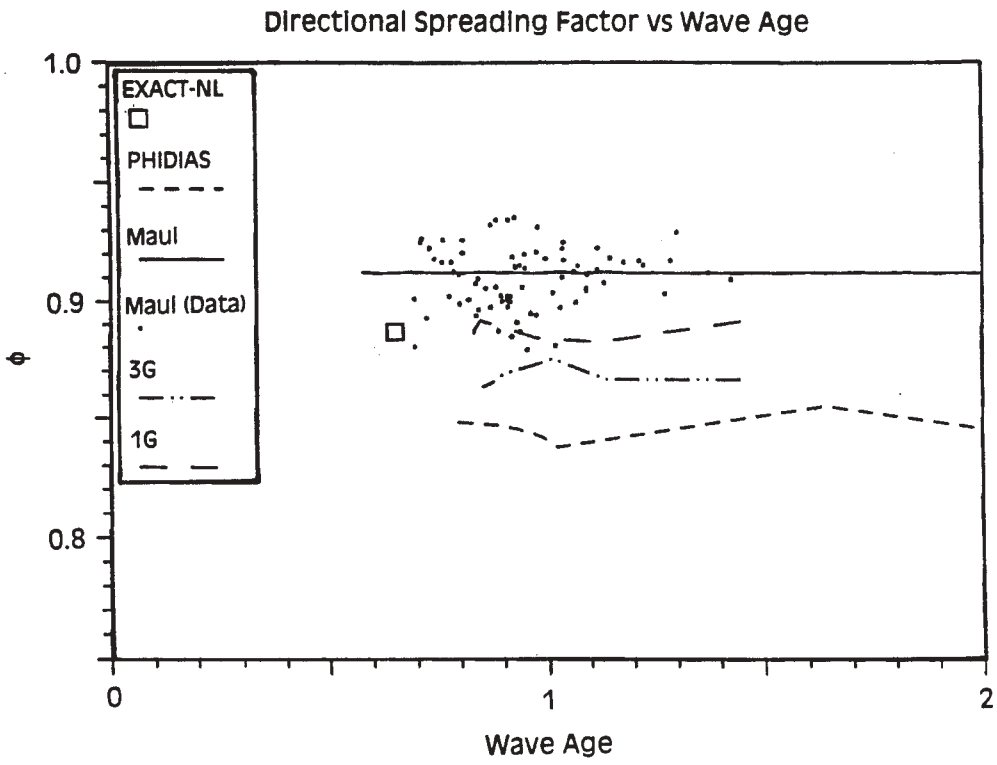


Figure 2

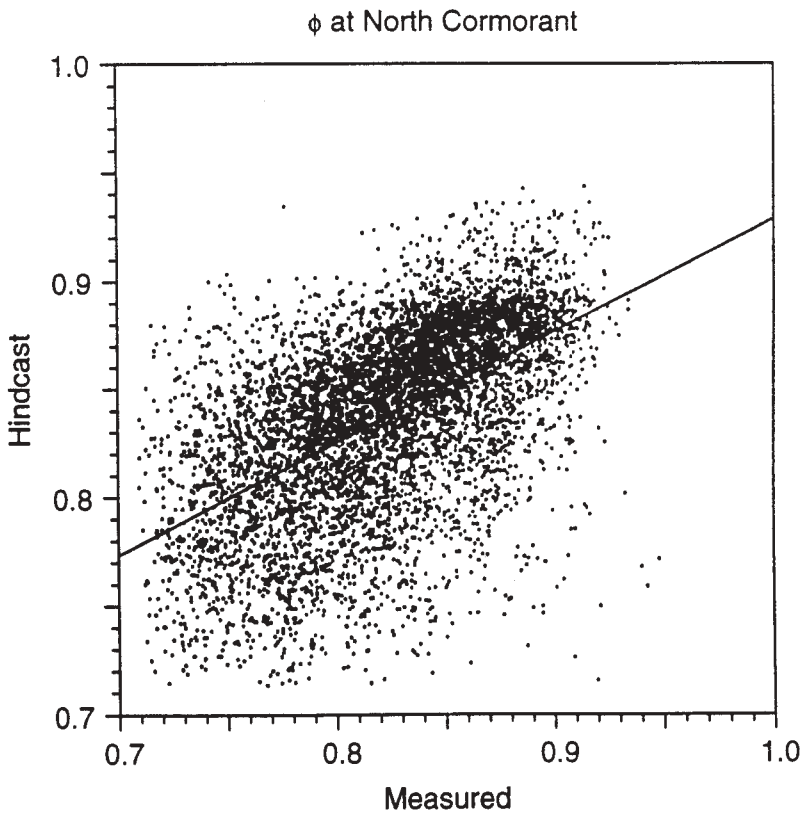


Figure 3



AUTHOR INDEX TABLE OF CONTENTS

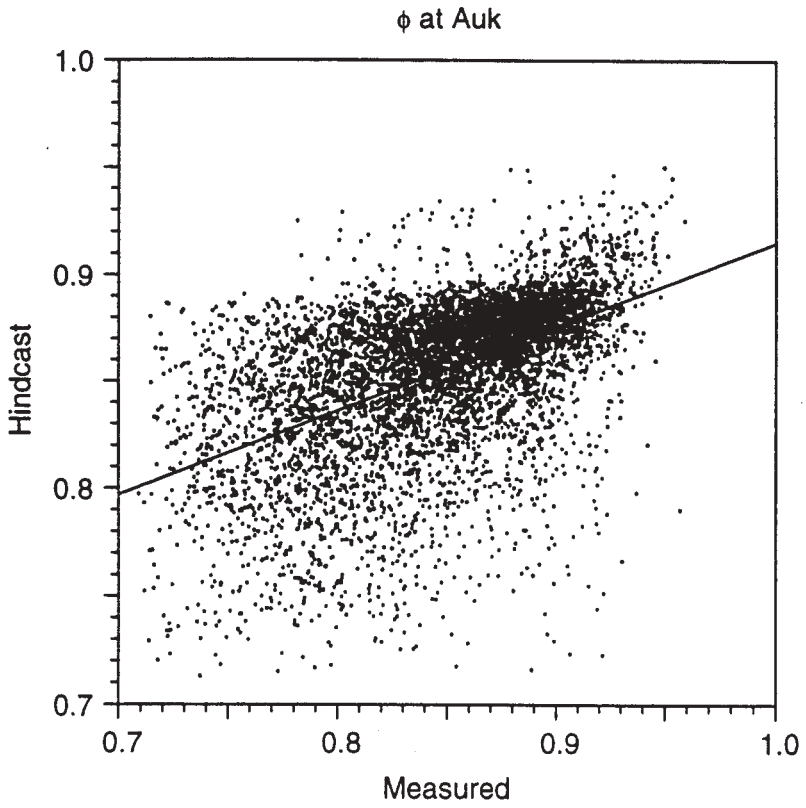


Figure 4

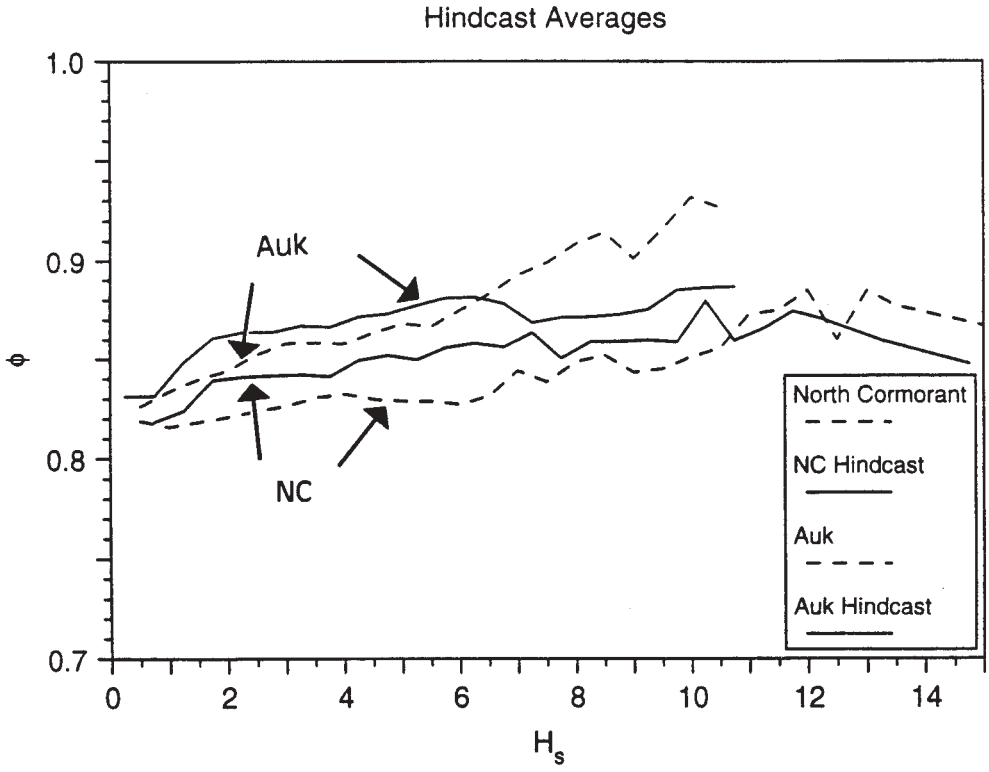


Figure 5

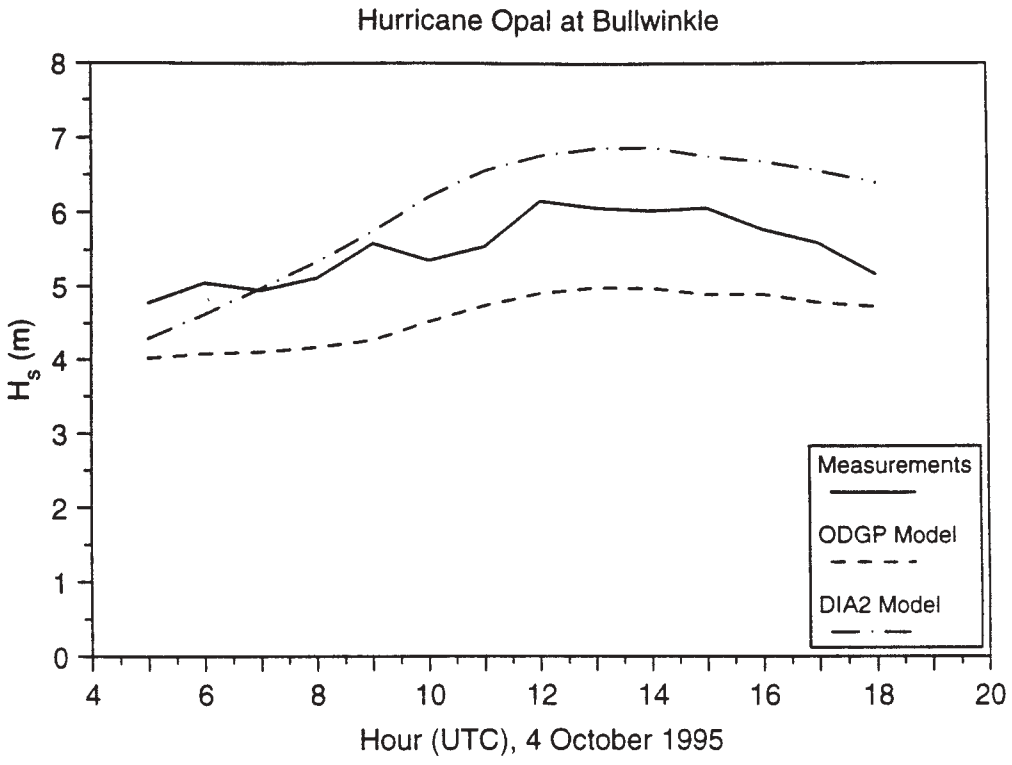


**Figure 6**

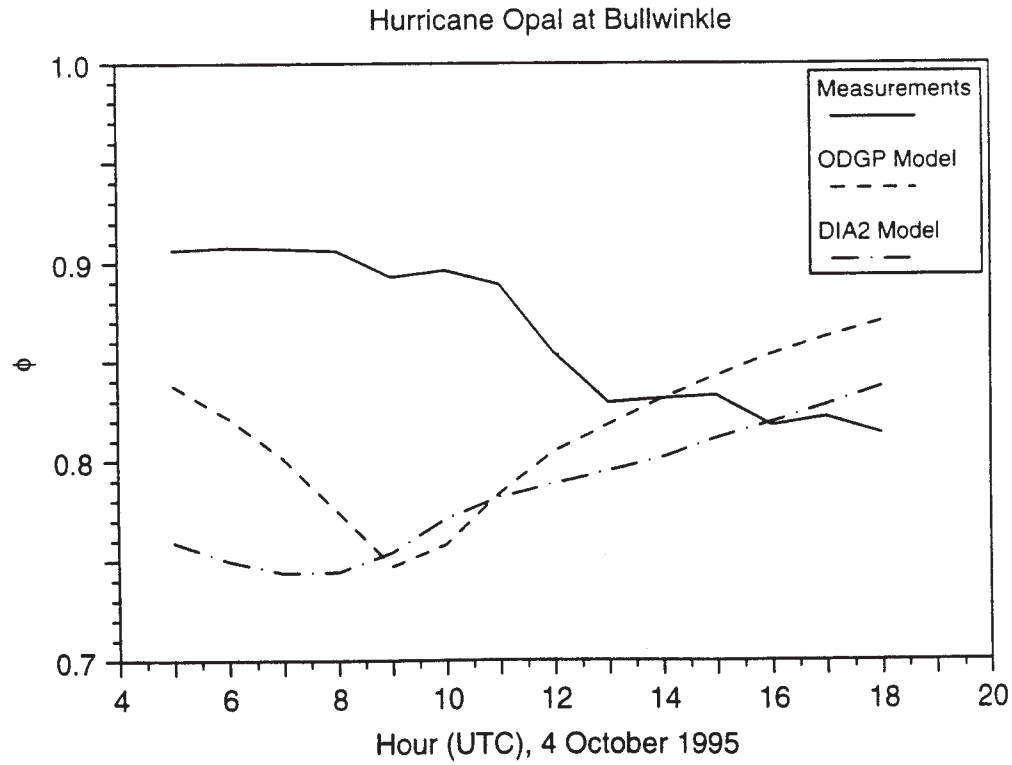


**Figure 7**



AUTHOR INDEX TABLE OF CONTENTS